



HAL
open science

Mécanismes d'action de complexes polypyridyle du Ruthénium (II) utilisés comme agents chimiothérapeutiques ou photosensibilisateurs pour la photothérapie dynamique

Marta Jakubaszek

► **To cite this version:**

Marta Jakubaszek. Mécanismes d'action de complexes polypyridyle du Ruthénium (II) utilisés comme agents chimiothérapeutiques ou photosensibilisateurs pour la photothérapie dynamique. Chimie thérapeutique. Université Paris sciences et lettres, 2020. Français. NNT : 2020UPSLC001 . tel-03224177

HAL Id: tel-03224177

<https://pastel.hal.science/tel-03224177v1>

Submitted on 11 May 2021

HAL is a multi-disciplinary open access archive for the deposit and dissemination of scientific research documents, whether they are published or not. The documents may come from teaching and research institutions in France or abroad, or from public or private research centers.

L'archive ouverte pluridisciplinaire **HAL**, est destinée au dépôt et à la diffusion de documents scientifiques de niveau recherche, publiés ou non, émanant des établissements d'enseignement et de recherche français ou étrangers, des laboratoires publics ou privés.



THÈSE DE DOCTORAT

DE L'UNIVERSITÉ PSL

Préparée à l'École Nationale Supérieure de Chimie de Paris

**Mechanisms of action of Ru(II) Polypyridyl Complexes
as Photodynamic Therapy Photosensitizers and
Chemotherapy Agents**

Soutenue par

Marta JAKUBASZEK

Le 19 Mai 2020

Ecole doctorale n° 406

**Chimie Moléculaire
de Paris Centre**

Spécialité

Chimie moléculaire

Composition du jury :

Christian, GAIDDON Directeur de recherche, Université de Strasbourg	<i>Président & rapporteur</i>
Mélanie, HAMON Directrice de recherche, Institut Pasteur	<i>Examineur</i>
Pascal, BIGEY Maître de conférences, Chimie ParisTech, PSL	<i>Examineur</i>
Bruno, GOUD Directeur de recherche, Institut Curie, PSL	<i>Examineur</i>
Caroline, MAAKE Professeur, Université de Zurich, Suisse	<i>Rapporteur</i>
Gilles, GASSER Professeur, Chimie ParisTech, PSL	<i>Directeur de thèse</i>



ParisTech

Acknowledgements

I greatly appreciated the involvement, help and scientific guidance of my supervisor Dr. Gilles Gasser through the three years of my PhD. Thank you Gilles for your motivation and patience. I will always be thankful for giving me an opportunity to work in your group in beautiful Paris. A big thank you also goes to my second supervisor Dr Bruno Goud and his group at the Institut Curie. I am very grateful for all the kind words, guidance, advice and encouragement.

During my PhD, I had the chance to work with many people. Thank you all for this stimulating and friendly environment. It is not always easy to be a biologist in a chemistry lab, but you made this a cheerful journey!

I wish to say thank you to all the collaborators with whom I have worked. Without them, this work would not have been possible.

Mazzarine and Chloé: you were the best students that I had the chance to teach. Working with you was a pleasure. I want to thank you for all of your hard work and commitment.

I want to thank all the people that helped me with data acquiring and analysis:

Dr. Bruno Saubamea and Dr. Patricia Le-Baccon from the microscopy cores.

Dr. Coralie Guerin, Dr. Lea Guyonnet and Dr. Annick Viguiet from the flow cytometry core.

Mickaël Tharaud for the ICP-MS measurements.

Dr. Johanne Seguin for introducing me to the world of *in vivo*.

Warm thanks go to Francine, Ali, Didier and Patrick Guezo. Merci!

Finally, importantly, I would like to thank the ERC for financially supporting this work (Consolidator Grant PhotoMedMet (GA 681679)).

Podziękowania

Chciałabym z całego serca podziękować wszystkim tym, którzy zainspirowali mnie bym podjęła studia doktoranckie, jak również tym, którzy byli dla mnie wsparciem w tej wędrówce.

Mamo, Tato dziękuję Wam przede wszystkim za miłość, wsparcie w moich decyzjach i zachęcanie mnie do pokonywania własnych barier. Nauczyliście mnie by próbować wszystkiego, co oferuje życie. Dzięki temu mogę się rozwijać a namacalnym dowodem na to jest ten manuskrypt. Jesteście zawsze przy mnie, gdy tego potrzebuję i wiem, że mogę na was liczyć w każdej sytuacji. Kocham Was!

Piotrze, dziękuję Ci za Twoją miłość, motywację i cierpliwość. Jesteś moją podporą. Dzięki Tobie nie oszalałam w tym trudnym okresie.

Dominiko, dziękuję Ci serdecznie za dobre słowa i wsparcie. Nikt nie zrozumie wyzwania, jakim jest doktorat tak dobrze jak osoba, która też bierze udział w tej przygodzie.

Dziękuję również mojej grupie przyjaciół i znajomych. Olgo, Asiu, Liliano, Kingo, Wojtku, Dawidzie i Kubo jesteście wspaniali. Dziękuję!

Table of contents

RÉSUMÉ	1
SUMMARY	9
CHAPTER 1- MECHANISMS OF ACTION OF RU(II) POLYPYRIDYL COMPLEXES IN LIVING CELLS UPON LIGHT IRRADIATION	17
CHAPTER 2- EVALUATION OF THE POTENTIAL OF COBALAMIN DERIVATIVES BEARING RU(II) POLYPYRIDYL COMPLEXES AS PHOTOSENSITISERS FOR PHOTODYNAMIC THERAPY	65
SUPPLEMENTARY INFORMATION	85
CHAPTER 3- SYNTHESIS AND CHARACTERIZATION OF AN EPIDERMAL GROWTH FACTOR RECEPTOR SELECTIVE RU(II) POLYPYRIDYL-NANOBODY CONJUGATE AS A PHOTOSENSITIZER FOR PHOTODYNAMIC THERAPY	101
SUPPLEMENTARY INFORMATION	141
CHAPTER 4- SYSTEMATIC INVESTIGATION OF THE ANTIPROLIFERATIVE ACTIVITY OF A SERIES OF RUTHENIUM TERPYRIDINE COMPLEXES	157
SUPPLEMENTARY INFORMATION	189
CHAPTER 5- RATIONALLY DESIGNED LONG-WAVELENGTH ABSORBING RU(II) POLYPYRIDYL COMPLEXES AS PHOTOSENSITIZERS FOR PHOTODYNAMIC THERAPY	233
SUPPLEMENTARY INFORMATION	259
CHAPTER 6- RUTHENIUM-INITIATED POLYMERIZATION OF LACTIDE: A ROUTE TO REMARKABLE CELLULAR UPTAKE FOR PHOTODYNAMIC THERAPY OF CANCER	371
SUPPLEMENTARY INFORMATION	393
CHAPTER 7- A RUTHENIUM(II) COMPLEX CONTAINING A REDOX-ACTIVE SEMIQUINONATE LIGAND AS POTENTIAL CHEMOTHERAPEUTIC AGENT: FROM SYNTHESIS TO <i>IN VIVO</i> STUDIES	425
SUPPLEMENTARY INFORMATION	481
CHAPTER 8- A MALTOL-CONTAINING RUTHENIUM POLYPYRIDYL COMPLEX AS A POTENTIAL ANTICANCER AGENT	509
SUPPLEMENTARY INFORMATION	551
CHAPTER 9- INCREASING THE CYTOTOXICITY OF RU(II) POLYPYRIDYL COMPLEXES BY TUNING THE ELECTRONIC STRUCTURE OF DIOXO LIGANDS	579
SUPPLEMENTARY INFORMATION	639
CHAPTER 10- NOVEL RUTHENIUM (II) POLYPYRIDYL COMPLEXES WITH FLAVONOID LIGANDS AS ANTICANCER DRUG CANDIDATES	705
SUPPLEMENTARY INFORMATION	745
CHAPTER 11- CONCLUSIONS	777

Résumé

Cette thèse de doctorat a pour dessein d'évaluer d'un point de vue chimique, mais surtout biologique les complexes polypyridyle Ru (II). Ces complexes métalliques peuvent être utilisés comme photosensibilisateurs (PS) pour la thérapie photodynamique (PDT), ou encore comme agents chimiothérapeutiques dans le traitement du cancer. La PDT est un traitement alternatif ou complémentaire à la chirurgie, la chimiothérapie ou la radiothérapie. Ses nombreux avantages lui confèrent un intérêt dans le traitement actuel du cancer. Son contrôle spatial et temporel est particulièrement intéressant, ce qui conduit à cibler les tumeurs tout en préservant les tissus sains. De plus, les résistances à répétition et les effets secondaires graves provoqués par la chimiothérapie incitent le monde scientifique à rechercher de nouveaux médicaments candidats anticancéreux. Les complexes de ruthénium sont l'un des groupes les plus prometteurs de médicaments candidats à base de métaux (comme chimiothérapeutiques ou PS) en raison de leurs multiples états d'oxydation stables. Cette thèse décrit un aperçu des modes d'action connus des complexes polypyridyle Ru (II) comme PS pour la PDT et introduit de nouveaux complexes, qui peuvent être utilisés pour des traitements PDT réguliers et ciblés. En outre, cette thèse se concentre également sur la caractérisation d'une nouvelle classe de complexes Ru générés comme agents anticancéreux potentiels pour la chimiothérapie, par coordination de différents dioxydants au noyau métallique. Cette thèse est composée de 11 chapitres et leur contenu est brièvement décrit ci-dessous

Chapitre 1

Ce premier chapitre se concentre sur l'introduction de complexes polypyridyle Ru (II) en tant que PS pour la PDT et, en outre, décrit le ou les mécanismes connus d'action de ces composés dans des cellules / souris vivantes lors d'une irradiation lumineuse. Malheureusement, à ce jour,

il y'a peu d'études décrivant le ou les mode (s) d'action de ces composés. Dans ce chapitre, seules les études biologiques, traitant de la phototoxicité et de la localisation cellulaire de certains complexes Ru (II), sont passées en revue, à partir des résultats obtenus avec le TLD-1433, le PS du groupe McFarland actuellement en essai clinique. À la fin de ce chapitre, une classification des complexes Ru (II) en fonction de leur localisation cellulaire est fournie. Il convient de noter que seuls les complexes de polypyridyle Ru (II) saturés de manière coordonnée et inertes par substitution sont discutés dans ce chapitre.

Chapitre 2

Cette section décrit la synthèse, les propriétés photophysiques et l'évaluation biologique des complexes de polypyridyle Ru (II) portant une fraction cobalamine. Les PS pour PDT actuels manquent de sélectivité pour les cellules cancéreuses. Pour remédier à cet inconvénient, , ce chapitre décrit la conjugaison de deux complexes de polypyridyle de ruthénium à la vitamine B₁₂ (cobalamine), afin de bénéficier de la solubilité et absorption active de celle-. Ainsi, nos résultats montrent que la voie de la transcobalamine n'est probablement pas impliquée pour la libération de ces PS à base de ruthénium, soulignant la difficulté de livrer avec succès des complexes métalliques aux cellules cancéreuses.

Chapitre 3

Ce chapitre présente la synthèse, la caractérisation et l'évaluation photophysique approfondie de nanocorps comportant un complexe conjugué de polypyridyle Ru (II) sélectif pour le récepteur du facteur de croissance épidermique (EGFR) en vue d'une PDT ciblée. Actuellement, un essor pour le développement de nouveaux PS de PDT est observé, ceux actuellement approuvés nn'étant pas entièrement satisfaisant. Parmi les composés testés, les complexes polypyridyle Ru (II) de type $[\text{Ru}(\text{bipy})_2(\text{dppz})]^{2+}$ et $[\text{Ru}(\text{phen})_2(\text{dppz})]^{2+}$ (bipy = 2,2'-bipyridine; dppz = dipyrido [3,2-a: 2', 3'-c] -phénazine, phén = 1,10-phénanthroline) ont déjà

été étudiés. Ces complexes ciblent sélectivement l'ADN. Cependant, comme l'ADN est omniprésent, l'objectif fût d'accroître la sélectivité de ces PS en les reliant à un vecteur de ciblage en vue de la PDT ciblée. Dans ce chapitre, les techniques ICP-MS et de microscopie confocale ont permis de démontrer que le nanocorps à base de complexe conjugué polypyridyle de Ru (II) a une sélectivité élevée pour le récepteur EGFR. Celui-ci a une importance particulière du fait qu'il soit une cible oncologique cruciale, en effet, celui-ci est surexprimé et / ou dérégulé dans une variété de tumeurs solides. Cependant, les expériences de coloration DCFH-DA ont indiqué qu'aucun ROS significatif n'était produit à l'intérieur des cellules. C'est très probablement la raison pour laquelle le complexe s'est révélé non phototoxique.

Chapitre 4

Ce chapitre présente une série de complexes Ru (II) portant des ligands de coordination 2,2':6',2''-terpyridine (terpy), moins étudiés que les complexes basés sur la coordination des ligands bidentés donneurs de N au noyau de ruthénium. Ici, 7 complexes du type [Ru (terpy) (terpy-X)]²⁺ (X = H (1), Cl (2), Br (3), OMe (4), COOH (5), COOMe (6), NMe₂ (7)) ont été étudiés comme agents chimiothérapeutiques potentiels et PS de PDT. Les composés ont été entièrement caractérisés, y compris par cristallographie aux rayons X. Il est important de noter que six des sept complexes se sont avérés stables dans le plasma humain ainsi que photostables dans l'acétonitrile lors d'une irradiation LED continue. La détermination des valeurs de logP pour les 7 complexes a révélé leur bonne solubilité dans l'eau. Le complexe le plus prometteur 7 s'est révélé être cytotoxique dans la gamme micromolaire dans l'obscurité et avoir une certaine phototoxicité lors d'une exposition à la lumière à 480 nm dans l'épithélium pigmentaire rétinien non cancéreux (RPE-1) et le carcinome cervical humain cancéreux (HeLa) cellules.

Chapitre 5

Cette section présente une tentative réussie de recherche guidée grâce à une étude DFT pour un PS de PDT efficace qui aura un fort décalage vers le rouge. Malgré les récents développements de la recherche, les traitements de thérapie photodynamique utilisent la lumière bleue ou UV-A pour obtenir un effet PDT. En conséquence, la profondeur de pénétration à l'intérieur du tissu est limitée et, la possibilité de traiter des tumeurs profondes ou de grande taille est affaiblie. Grâce à cette conception rationnelle, des complexes de ruthénium avec une forte absorption dans le rouge ont pu être préparés avec succès. L'un des complexes stable dans le plasma humain ainsi que lors d'une irradiation lumineuse, s'est révélé se localiser dans le cytoplasme des cellules HeLa. Lors de l'irradiation à 595 nm cliniquement pertinente, elle a entraîné une perturbation de la respiration mitochondriale et des processus de glycolyse dans les cellules monocouches 2D. De plus, il a été démontré que le composé était également photo-cytotoxique dans les MCTS 3D, qui sont un modèle tumoral beaucoup plus approprié que les cultures monocouches. D'autres recherches sur l'efficacité in vivo de ce composé prometteur sont prévues à l'avenir.

Chapitre 6

Ce chapitre décrit la synthèse de nanoconjugués par polymérisation d'ouverture de cycle du lactide initiée par un complexe polypyridyle de Ru non phototoxique et ne pénétrant pas dans les cellules (**RuOH**). Ces conjugués ont ensuite été formulés en nanoparticules par nanopréciipitation, puis caractérisés par spectrométrie de résonance magnétique nucléaire (RMN), désorption-ionisation laser de matrice couplée à la spectrométrie de masse à temps de vol (MALDI-TOF MS) et par diffusion dynamique de la lumière (DLS). Enfin, leur indice photothérapeutique ($\lambda_{exc} = 480 \text{ nm}$; 3.21 J.cm^{-2}) ainsi que celui du précurseur **RuOH** a été déterminé sur des cellules de carcinome cervical humain (HeLa) et sur des cellules non-

cancéreuses d'épithélium pigmentaire rétinien (RPE-1) et leur internalisation cellulaire a été évaluée par microscopie confocale et par spectrométrie de masse à plasma à couplage inductif (ICP-MS). Ces nanoparticules ont montré des propriétés photophysiques, telles que la luminescence et le rendement de production d'oxygène singulet, supérieures à celles du complexe seul ainsi qu'une internalisation cellulaire plus importante pouvant potentiellement résulter en une meilleure phototoxicité. Globalement, cette étude montre la possibilité de transformer un PS non phototoxique en un PS actif en employant une réaction de polymérisation simple et modulable.

Chapitre 7

Ce chapitre décrit la caractérisation d'un nouveau candidat médicament anticancéreux noté $[\text{Ru}(\text{DIP})_2(\text{sq})]\text{PF}_6$ (**Ru-sq**) (DIP = 4,7-diphényl-1,10-phénantroline ; sq = ligand semiquinonate). Le but de cette étude est de combiner le grand potentiel anticancéreux d'un complexe polypyridyle de Ru(II) avec les propriétés biologiques et redox particulières du groupement catécholate. Des résultats expérimentaux (cristallographie aux rayons X, résonance paramagnétique électronique, électrochimie) montrent que la forme semiquinonate est l'état d'oxydation prédominant du ligand dioxo de ce complexe. L'activité biologique de **Ru-sq** a ensuite été évaluée *in vitro* et *in vivo*, révélant le fort potentiel thérapeutique de ce complexe en tant qu'anticancéreux. En particulier, **Ru-sq** présente une cytotoxicité bien supérieure à celle du cisplatine (de l'ordre du nanomolaire) qui, contrairement au cisplatine, peut être expliquée en partie par l'induction d'une dysfonction mitochondriale. Les multiples cibles cellulaires de **Ru-sq** peuvent être la solution pour contourner un des désavantages du cisplatine (*i.e.*, l'apparition de résistances). De plus, **Ru-sq** a présenté une activité spectaculaire dans un modèle de sphéroïdes multicellulaires tumoraux (MCTS), menant à l'inhibition de la croissance tumorale 13 jours après traitement (20 μM). Notamment, ce composé a été bien toléré et a montré une activité prometteuse dans deux modèles *in vivo* différents.

Chapitre 8

En raison du fort potentiel exprimé par le candidat médicament anticancéreux noté **Ru-sq** ($[\text{Ru}(\text{DIP})_2(\text{sq})]\text{PF}_6$ (DIP : 4,7-diphényl-1,10-phénantroline, sq : ligand semiquinonate) décrit dans le chapitre 7, le chapitre 8 présente une étude de relation structure-activité (SAR) incluant une gamme plus large d'analogues résultant de la coordination de différents ligands dioxo analogues du catéchol sur le même centre $\text{Ru}(\text{DIP})_2$. Des catéchols portant des groupements électrodonneurs (EDG) ou électroattracteurs (EWG) ont été sélectionnés et les propriétés physicochimiques et biologiques de leur complexe ont été déterminées. Différents résultats expérimentaux démontrent que la coordination de catéchols portant des groupements électrodonneurs mène à la formation de complexes rouges profonds et positivement chargés (complexes **1-4**), dans lesquels l'état d'oxydation prédominant des ligands dioxo est la forme semiquinonate portant une unique charge négative. D'autre part, les complexes comportant un ligand catéchol portant un groupement électroattracteur (complexes **5** et **6**), sont des complexes neutres bleus/violets où le catéchol est doublement chargé négativement. L'évaluation biologique des complexes **1-6** a mené à la conclusion que les différences dans leurs propriétés physicochimiques ont un fort impact sur leur activité biologique. Ainsi, les complexes **1-4** présentent une cytotoxicité bien supérieure à celle des complexes **5** et **6**. Le complexe **1** est le composé le plus prometteur de la série et a donc été sélectionné pour une évaluation biologique plus poussée. Outre une remarquable cytotoxicité ($\text{IC}_{50} = 0.07\text{-}00.7 \mu\text{M}$ dans différentes lignées cellulaires), le complexe **1** est internalisé très efficacement par les cellules HeLa en suivant un mécanisme de transport passif. De plus, son accumulation modérée dans différents compartiments intracellulaires (*i.e.*, noyau, lysosomes, mitochondries et cytoplasme) est un avantage significatif dans la recherche d'un agent anticancéreux à modes d'action multiples. En complément, des études de la métallation de l'ADN et du métabolisme énergétique suggèrent une interaction directe du complexe **1** avec l'ADN ainsi que l'induction d'une

dysfonction mitochondriale. Les cibles multiples du complexe **1** ainsi que sa remarquable cytotoxicité en font un candidat médicament précieux dans le domaine de la recherche contre le cancer.

Chapitre 9

Le chapitre 9 décrit un analogue du complexe présenté dans le chapitre 7 noté **[Ru(DIP)₂(mal)](PF₆)**, portant un ligand maltol (mal), un exhausteur de goût approuvé par la FDA. Posséder un ligand approuvé par la FDA est essentiel pour un complexe dont le mécanisme d'action peut impliquer un échange de ligand. Dans ce chapitre sont décrites la synthèse et la caractérisation de **[Ru(DIP)₂(mal)](PF₆)**, l'étude de sa stabilité en milieu biologique ainsi que son évaluation biologique poussée. Des tests de cytotoxicités sur différentes lignées cellulaires dans un modèle 2D ainsi que dans un modèle de sphéroïdes multicellulaires tumoraux (MCTS) de cellules HeLa ont montré que ce composé présente une activité accrue comparée au cisplatine, actuellement commercialisé, justifiant une étude plus poussée. **[Ru(DIP)₂(mal)](PF₆)** est efficacement internalisé par les cellules HeLa en suivant une voie de transport passive, et affecte sévèrement le métabolisme mitochondrial.

Chapitre 10

Ce chapitre présente quatre nouveaux complexes monocationiques polypyridyles de Ru(II), synthétisés à partir de la formule générale **[Ru(DIP)₂flv]X**, où DIP correspond à la 4,7-diphényl-1,10-phénantroline, flv correspond à un ligand flavonoïde (5-hydroxyflavone dans le complexe **[Ru(DIP)₂(5-OHF)](PF₆)**, génistéine dans le complexe **[Ru(DIP)₂(gen)](PF₆)**, chrysine dans le complexe **[Ru(DIP)₂(chr)](OTf)**, et morine dans le complexe **[Ru(DIP)₂(mor)](OTf)** et X représente les contre-ions PF₆⁻ et OTf⁻ (triflate, CF₃SO₃⁻). Ces nouveaux composés ont été caractérisés et leur cytotoxicité contre différentes lignées cellulaires a été testée. L'activité biologique du complexe le plus prometteur **[Ru(DIP)₂(gen)](PF₆)** a

ensuite été étudiée. Des études du métabolisme énergétique ont montré que ce complexe affecte sévèrement la respiration mitochondriale. De plus, son accumulation préférentielle dans les cellules MDA-MB-435S (cellules de mélanome identifiées initialement comme des cellules cancéreuses de glandes mammaires ou du sein extraites d'un site métastatique situé dans un épanchement pleural), fréquemment utilisées pour l'étude des métastases, explique l'efficacité accrue du complexe dans cette lignée comparée à la lignée MCF-7 (carcinome canalaire humain).

Chapitre 11

Ce dernier chapitre contient un résumé ainsi que les conclusions finales de ces travaux de thèse portant sur l'étude du mode d'action de complexes polypyridyles de Ru(II) utilisés en tant que PS pour la PDT ou en tant qu'agent chimiothérapeutique. Il résume les désavantages actuels de ces complexes et propose des pistes d'améliorations pour cette classe intéressante de complexes organométalliques.

Summary

This PhD thesis aims to evaluate chemically and, more importantly, biologically Ru(II) polypyridyl complexes. These metal complexes can be used as photodynamic therapy (PDT) photosensitizers (PS) or as chemotherapeutic agents in cancer treatment. PDT is an alternative or complimentary treatment to surgery, chemotherapy or radiotherapy. Currently it draws a lot of attention due to its advantages. Especially interesting is its spatial and temporal control, which leads to targeting tumours while preserving healthy tissue. Additionally, repeatedly occurring resistances and severe side effects brought by chemotherapy urges the scientific world to search for new anticancer drug candidates. Ruthenium complexes are one of the most promising groups of metal-based drug candidates (as chemotherapeutics or PSs) owing to their multiple stable oxidation states, etc. This thesis describes an overview of the known modes of action of Ru(II) polypyridyl complexes as PDT PS and introduces new complexes that can be used in regular as well as targeted PDT. Additionally, this thesis also focuses on the characterisation of novel class of Ru complexes that were generated as potential anticancer agents for chemotherapy by coordination of different dioxoligands to the metal core. This thesis is composed of 11 chapters and their content is shortly described below.

Chapter 1

This chapter of the thesis focuses on the introduction of Ru(II) polypyridyl complexes as a class of PDT PSs and, in addition, describes known mechanism(s) of action of these compounds in living cells/mice upon light irradiation. Unfortunately, to date, there is a scarcity of studies exploring thoroughly the mode(s) of action of these compounds. In this chapter, only biological studies that show more than just the phototoxicity and the cellular localisation of some Ru(II) complexes are reviewed, starting from the results obtained with TLD-1433, the PS of the

McFarland group currently in clinical trial. To the end of this chapter, a classification of the Ru(II) complexes depending on their cellular localisation is provided. Of note, only coordinatively saturated and substitutionally inert Ru(II) polypyridyl complexes are discussed in this chapter.

Chapter 2

This section describes the synthesis, photophysical properties and biological evaluation of Ru(II) polypyridyl complexes bearing a cobalamin moiety. The current PDT PSs lack selectivity for cancer cells. To tackle this drawback, in view of selective cancer delivery, this chapter describes the conjugation of two ruthenium polypyridyl complexes to vitamin B₁₂ (cobalamin) to take advantage of the solubility and active uptake of the latter. Ultimately, our results show that the transcobalamin pathway is unlikely involved for the delivery of these ruthenium-based PDT PSs, emphasizing the difficulty in successfully delivering metal complexes to cancer cells.

Chapter 3

This chapter presents the synthesis, characterization and in-depth photophysical evaluation of a nanobody-containing Ru(II) polypyridyl conjugate selective for the epidermal growth factor receptor (EGFR) in view of targeted PDT. There is currently a surge for the development of novel PDT PSs since those currently approved are not completely ideal. Among the tested compounds, Ru(II) polypyridyl complexes with a [Ru(bipy)₂(dppz)]²⁺ and [Ru(phen)₂(dppz)]²⁺ scaffold (bipy = 2,2'-bipyridine; dppz = dipyrido[3,2-a:2',3'-c]-phenazine, phen = 1,10-phenanthroline) were previously investigated. These complexes selectively target DNA. However, since DNA is ubiquitous, it was of great interest to increase the selectivity of these PDT PSs by linking them to a targeting vector in view of targeted PDT. In this chapter, ICP-MS and confocal microscopy techniques allowed to demonstrate that the a nanobody-

containing Ru(II) polypyridyl conjugate had a high selectivity for the EGFR receptor, which is a crucial oncological target as it is overexpressed and/or deregulated in a variety of solid tumors. However, DCFH-DA staining experiments indicated that no significant ROS was produced inside the cells. This is most probably the reason why the complex was found to be non-phototoxic.

Chapter 4

This chapter presents a series of Ru (II) complexes bearing 2,2':6', 2''-terpyridine (terpy) coordinating ligands, which are less investigated than the complexes based on the coordination of N-donating bidentate ligands to the ruthenium core. Herein, 7 complexes of the type [Ru(terpy)(terpy-X)]²⁺ (X = H (**1**), Cl (**2**), Br (**3**), OMe (**4**), COOH (**5**), COOMe (**6**), NMe₂ (**7**)) were investigated as potential chemotherapeutic agents and PDT PSs. The compounds were characterized in-depth including by X-ray crystallography. Importantly, six of the seven complexes were found to be stable in human plasma as well as photostable in acetonitrile upon continuous LED irradiation. The determination of the logP values for the **7** complexes revealed their good water solubility. The most promising complex **7** was found to be cytotoxic in the micromolar range in the dark as well as to have some phototoxicity upon light exposure at 480 nm in non-cancerous retinal pigment epithelium (RPE-1) and cancerous human cervical carcinoma (HeLa) cells.

Chapter 5

This section presents a successful attempt of DFT guided search for an efficient PDT PS that will have a strong red shift. Currently photodynamic therapy treatments, despite the recent research developments, utilizes blue or UV-A light to obtain a PDT effect. As a result, penetration depth inside the tissue is limited and therefore, the possibility to treat deep-seated or large tumours is weakened. Thanks to this rational design, ruthenium complexes with a

strong red shift in their absorption profile could be successfully prepared. One of the complexes, while being stable in human plasma as well as upon light irradiation, was found to localize in the cytoplasm of HeLa cells. Upon irradiation at clinically relevant 595 nm, it led to the disturbance of mitochondrial respiration and glycolysis processes in 2D monolayer cells. Moreover, it was demonstrated that the compound was also photo-cytotoxic in 3D MCTS, which are a much more suitable tumour model than monolayer cultures. Further investigations of the *in vivo* efficiency of this promising compound are planned in the future.

Chapter 6

This chapter describes the synthesis of ruthenium-containing nanoconjugates from a non-cell-penetrating, non-phototoxic ruthenium(II) polypyridyl complex (**RuOH**), by a drug-initiated ring-opening polymerization of lactide. These conjugates were then formulated into nanoparticles by nanoprecipitation and characterized by means of nuclear magnetic resonance spectroscopy (NMR), matrix-assisted laser desorption/ionization - time of flight mass spectrometry (MALDI-TOF MS) and dynamic light scattering (DLS). Finally, their phototherapeutic activity ($\lambda_{exc} = 480 \text{ nm}$, 3.21 J.cm^{-2}) in cancerous human cervical carcinoma (HeLa) and non-cancerous retinal pigment epithelium (RPE-1) cells was tested alongside that of **RuOH** and their cellular uptake in HeLa cells was assessed by confocal microscopy and inductively coupled plasma - mass spectrometry (ICP-MS). All nanoparticles showed improved photophysical properties including luminescence and singlet oxygen generation, enhanced cellular uptake and, capitalizing on this, an improved photo-toxicity. Overall, this study demonstrates how it is possible to transform a non-phototoxic PDT PS into an active PS using an easy, versatile polymerisation.

Chapter 7

This chapter characterises a new chemotherapeutic drug candidate against cancer, namely $[\text{Ru}(\text{DIP})_2(\text{sq})]\text{PF}_6$ (**Ru-sq**) (DIP = 4,7-diphenyl-1,10-phenanthroline; sq = semiquinonate ligand). The aim of this study was to combine the great potential expressed by Ru(II) polypyridyl complexes and the singular redox and biological properties associated to the catecholate moiety. Experimental evidences (e.g., X-ray crystallography, electron paramagnetic resonance, electrochemistry) demonstrated that the semiquinonate is the preferred oxidation state of the dioxo ligand in this complex. The biological activity of **Ru-sq** was then scrutinised *in vitro* and *in vivo*, and the results highlight the auspicious potential of this complex as a chemotherapeutic agent against cancer. **Ru-sq** was notably found to have a much higher cytotoxic activity than cisplatin (i.e. in the nanomolar range), and, contrary to cisplatin, to have mitochondrial dysfunction as one of its modes of action. The multicellular targets of **Ru-sq** could potentially be the key to overcome one of the main drawbacks of cisplatin (i.e., the occurrence of resistance). Moreover, **Ru-sq** exhibited impressive activity on Multi Cellular Tumour Spheroids (MCTS) model, even leading to growth inhibition of the tumour 13 days after treatment (20 μM). Importantly, using two different *in vivo* models, this compound was found to be well-tolerated by mice and has very promising activity.

Chapter 8

Due to the great potential expressed by an anticancer drug candidate discussed in Chapter 7, namely **Ru-sq** ($[\text{Ru}(\text{DIP})_2(\text{sq})](\text{PF}_6)$ (DIP: 4,7-diphenyl-1,10-phenanthroline, sq: semiquinonate ligand), Chapter 8 presents a structure-activity relationship (SAR) that involves a broader range of derivatives resulting from the coordination of different catecholate-like dioxoligands to the same $\text{Ru}(\text{DIP})_2$ core. More in detail, catechols carrying either electron-donating or electron-withdrawing groups EDG or EWG were chosen and the physico-chemical

and biological properties of their complexes investigated. Several pieces of experimental evidences demonstrated that the coordination of catechols bearing EDGs led to deep red positively charged complexes **1–4**, in which the preferred oxidation state of the dioxoligand is the uninegatively charged semiquinonate. Complexes **5** and **6**, on the other hand, are blue/violet neutral complexes, which carry an EWG substituted dinegatively charged catecholate ligand. The biological investigation of complexes **1–6** led to the conclusion that the difference in their physico-chemical properties has a strong impact on their biological activity. Thus, complexes **1–4** expressed much higher cytotoxicities than complexes **5** and **6**. Complex **1** constitutes the most promising compound of the series and was selected for a more in-depth biological investigation. Apart from its remarkably high cytotoxicity ($IC_{50} = 0.07\text{--}0.7 \mu\text{M}$ in different cancerous cell lines), complex **1** was taken up by HeLa cells very efficiently by a passive transportation mechanism. Moreover, its moderate accumulation in several cellular compartments (*i.e.*, nucleus, lysosomes, mitochondria and cytoplasm) is extremely advantageous in the search of a potential drug with multiple modes of action. Further DNA metalation and metabolic studies pointed to the direct interaction of complex **1** with DNA and to the severe impairment of the mitochondrial function. Multiple targets, together with its outstanding cytotoxicity, make complex **1** a valuable candidate in the field of chemotherapy research.

Chapter 9

Chapter 9 focuses on structurally similar compound to the one from Chapter 7, namely **[Ru(DIP)₂(mal)](PF₆)**, carrying the flavour-enhancing agent approved by the FDA, maltol (mal). To possess an FDA approved ligand is crucial for a complex, whose mechanism of action might include ligand exchange. Herein, we describe the synthesis and characterisation of **[Ru(DIP)₂(mal)](PF₆)**, its stability in solutions and in conditions which resemble the physiological ones, and its in-depth biological investigation. Cytotoxicity tests on different cell

lines in 2D model and on HeLa MultiCellular Tumour Spheroids (MCTS) demonstrated that our compound has higher activity compared to the approved drug cisplatin, inspiring further tests. $[\text{Ru}(\text{DIP})_2(\text{mal})](\text{PF}_6)$ was efficiently internalised by HeLa cells through a passive transport mechanism and severely affected the mitochondrial metabolism.

Chapter 10

This Chapter presents four novel monocationic Ru(II) polypyridyl complexes that have been synthesized with the general formula $[\text{Ru}(\text{DIP})_2\text{flv}]\text{X}$, where DIP is 4,7-diphenyl-1,10-phenanthroline, flv stands for the flavonoid ligand (5-hydroxyflavone in $[\text{Ru}(\text{DIP})_2(\text{5-OHF})](\text{PF}_6)$, genistein in $[\text{Ru}(\text{DIP})_2(\text{gen})](\text{PF}_6)$, chrysin in $[\text{Ru}(\text{DIP})_2(\text{chr})](\text{OTf})$, and morin in $[\text{Ru}(\text{DIP})_2(\text{mor})](\text{OTf})$) and X is the counterion, PF_6^- and OTf^- (triflate, CF_3SO_3^-), respectively. These novel compounds were thoroughly characterised, and their cytotoxicity tested against several cancer cell lines. The most promising complex, $[\text{Ru}(\text{DIP})_2(\text{gen})](\text{PF}_6)$, was further investigated for its biological activity. Metabolic studies revealed that this complex severely impaired mitochondrial respiration and glycolysis processes, contrary to its precursor, $\text{Ru}(\text{DIP})_2\text{Cl}_2$, which showed a prominent effect only on the mitochondrial respiration. In addition, its preferential accumulation in MDA-MB-435S cells (a human melanoma cell line previously described as mammary gland/breast; derived from metastatic site: pleural effusion), that are used for the study of metastasis, explained the better activity in this cell line compared to MCF-7 (human, ductal carcinoma).

Chapter 11

The last section of this thesis contains the summary and final conclusions of introduced work regarding modes of action of Ru (II) polypyridyl complexes as PDT PSs and as chemotherapy drug candidates. It recapitulates on the current drawbacks and future directions for this interesting class of metal-based complexes.

Chapter 1- Mechanisms of Action of Ru(II) Polypyridyl Complexes in Living Cells upon Light Irradiation

Marta Jakubaszek^{a,b}, Bruno Goud^b, Stefano Ferrari^c and Gilles Gasser^{a,}*

^a Chimie ParisTech, PSL University, CNRS, Institute of Chemistry for Life and Health Sciences, Laboratory for Inorganic Chemical Biology, Paris, France.

^b Institut Curie, PSL University, CNRS UMR 144, Paris, France

^c Institute of Molecular Cancer Research, University of Zurich, Zurich, Switzerland.

* Corresponding author: Email: gilles.gasser@chimie-paristech.fr; www.gassergroup.com;
Tel. +33 1 44 27 56 02.

This chapter has been published in *Chemical Communications*, 2018, **54**, 13040-13059

Reproduced by permission of The Royal Society of Chemistry

(<https://pubs.rsc.org/en/content/articlelanding/2018/CC/C8CC05928D#!divAbstract>)

Contribution to the publication:

Marta Jakubaszek made the literature research and wrote the first draft of the review.

Marta Jakubaszek

A handwritten signature in blue ink that reads "Marta Jakubaszek".

19.05.2020

Gilles Gasser

A handwritten signature in blue ink that reads "Gasser".

Abstract

The unique photophysical properties of Ru(II) polypyridyl complexes make them very attractive candidates as photosensitisers in Photodynamic Therapy (PDT). However, to date, there are not many studies exploring in detail the mechanism(s) of action of such compounds in living systems upon light irradiation. This feature article provides an overview of the most in-depth biological studies on such compounds.

Introduction

The earliest reports on the use of light in combination with chemical entities in the field of medicine are more than 100 years old.¹ Since then, this medical technique, known as photodynamic therapy (PDT), has evolved to a successful alternative or complimentary treatment to chemotherapy, radiotherapy and surgery. Nowadays PDT is an approved and common treatment in dermatology. It is used to treat acne, psoriasis, keloid scars and port wine stains, helping patients to improve their appearance and quality of life.^{2, 3} PDT also gives another, new perspective for cancer therapy due to its spatial and temporal control.⁴ This treatment modality is currently approved for a wide range of cancer types using commercially available photosensitisers such as Photofrin®, Visudyne®, Foscan® or Levulan® (see Figure 1 for structures).^{5, 6}

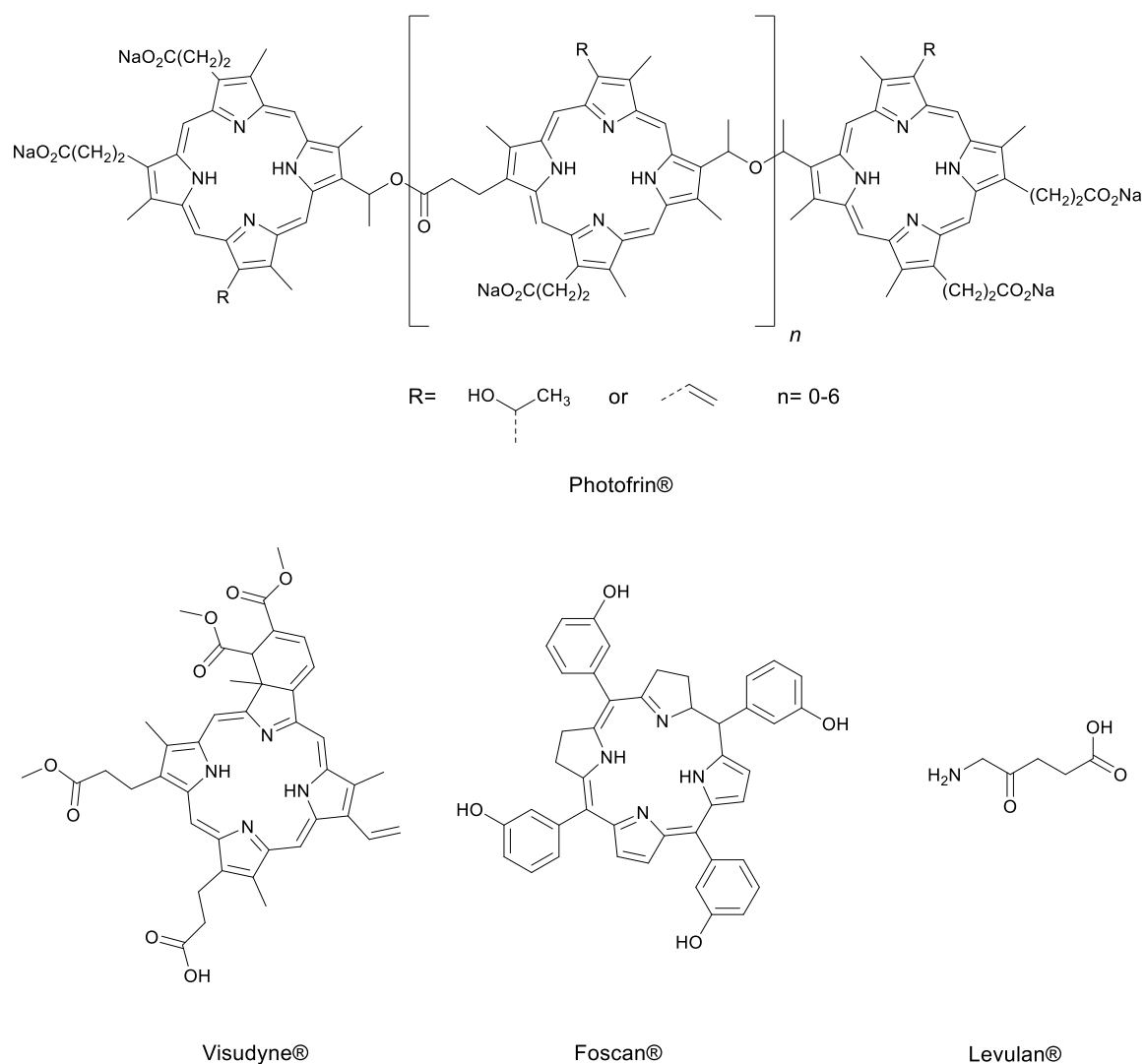


Figure 1. Chemical structures of Photofrin®, Visudyne®, Foscan® and Levulan®.

PDT usually requires three main components, namely a photosensitiser (PS), molecular oxygen ($^3\text{O}_2$) and light. After injection/application of the PS into/on the patient, the latter is irradiated at a specific, defined wavelength, allowing the PS to reach its singlet excited state $^1\text{PS}^*$. After intersystem crossing (ISC), the PS reaches an excited state, which has a triplet character ($^3\text{PS}^*$). It might then react in two different electron exchange mechanisms, resulting in the formation of very reactive singlet oxygen $^1\text{O}_2$ (Type II) or radical anions or cations, which can further react with oxygen producing other reactive oxygen species (ROS) like hydrogen peroxide H_2O_2 , superoxide O_2^- or hydroxyl radicals $\cdot\text{OH}$ (Type I). Both mechanisms, namely Types I and II, lead to the formation of products that impair metabolic pathways and eventually lead to

eukaryotic cell or bacteria death. The ratio between these two processes depends on the PS used as well as the concentrations of molecular oxygen and other biological substrates.⁷ The most attractive feature of PDT is its subsistent selectivity. Indeed, areas that are affected by PDT treatments are only those where the PS has accumulated and where light is applied. Additionally, due to the short life of generated $^1\text{O}_2$ (40 ns) and radicals, the area of action is estimated to be only 20 nm.⁸

Currently used PSs are based on cyclic tetrapyrrolic structures like porphyrins, phthalocyanines or chlorins.⁹ Although they fill the requirements of a PS, they also have a number of drawbacks. Photofrin®, for example, exhibits poor light penetration into the tumour as well as low clearance from the patients bodies that leads to photosensitivity.¹⁰ There is therefore a need for new PSs that overcome these unwanted effects and that have a higher uptake and selectivity towards cancer cells.¹¹ Recently designed molecules can be classified in two main classes, namely modified porphyrin-based PSs or porphyrin-free PDT systems.⁶ In the second class, inert Ru(II) polypyridyl complexes have raised great interest not only as alternatives to cisplatin but also as a novel PDT PSs because of their favourable photophysical properties (e.g. long excited state lifetimes, visible light absorption and two-photon excitation).^{6, 12-15} One of these compounds, namely TLD-1433, is currently undergoing a human clinical trial against invasive bladder cancer (Figure 2).⁵⁸

Understanding the mechanism(s) of action of these compounds in living cells/mice upon light irradiation is extremely important to establish their therapeutic potential and to design new generation PSs. Unfortunately, to date, there is a scarcity of studies exploring in depth the mode(s) of action of these compounds.¹⁶ In this feature article, we review only biological studies that describe more than just the phototoxicity and the cellular localisation of some Ru(II) complexes, starting from the results obtained with TLD-1433, the PS of the McFarland group currently in clinical trial. To the end of our feature article, we have decided to classify the Ru(II)

complexes depending on their cellular localisation. Of note, only coordinatively saturated and substitutionally inert Ru(II) polypyridyl complexes are discussed herein.

TLD-1433 and its derivatives

In 2013, the group of prof. McFarland reported two compounds, namely **TLD-1411** and **TLD-1433** (see Figure 2).¹⁷ Both molecules were first investigated for photodynamic inactivation (PDI) of pathogenic bacteria.

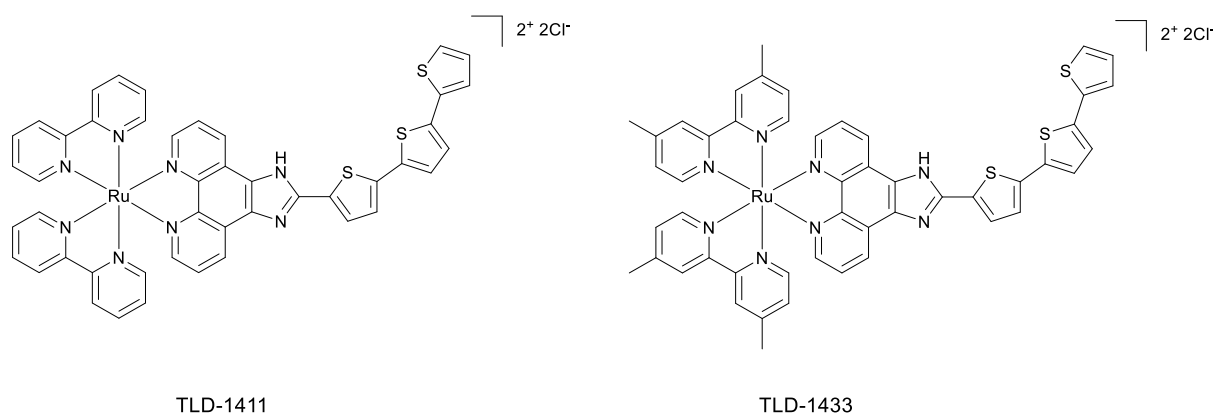


Figure 2. TLD-1411 and TLD-1433

The researchers pointed out that the 2-(2',2'':5'',2''')-terthiophene)-imidazo[4,5-f][1,10]phenanthroline (IP-TT) ligand in the compounds structure might be responsible for both Type I and Type II electron exchange mechanisms. The ability of the designed complexes to work in low oxygen conditions through a Type I mechanism corroborated the advantage of these compounds. Promising results obtained in bacteria led to further examinations of the compounds. In 2015, a study on **TLD-1411** and **TLD-1433** as PSs suitable for anticancer PDT *in vitro* and *in vivo* was reported by Lilge and co-workers.¹⁸ For *in vitro* studies, four cell lines were used, namely CT26 and CT25.26 (respectively wild type and N-nitroso-N-methylurethane-induced mouse colon carcinoma), U87MG (human glioblastoma cell line) and

F98 (rat glioblastoma). The Lethal Dose to kill 50 % of the cell population (LD_{50}) was determined for **TLD-1411** and **TLD-1433** on all four cell lines in the dark and after light irradiation. Concentration of 4 μM of **TLD-1411** and 1 μM of **TLD-1433** effectively killed 100% of CT-26 WT and U87MG cells upon light irradiation (green LED emitting at 525 ± 25 nm; 45 J cm^{-2}). U87MG cells were chosen to check whether these PSs could be used in hypoxic and normoxic conditions. A photodynamic effect was observed in normoxic conditions with concentrations of 18 μM (70% of cells killed). Unfortunately, **TLD-1411** and **TLD-1433** did not work in hypoxia conditions in human cell lines. The compounds were also tested *in vivo* using 8-10 week-old BALB/C mice injected with CT26.WT murine colon carcinoma. The maximum tolerated dose 50 (MTD_{50}) values for **TLD-1411** and **TLD-1433** were established to be $36 \text{ mg}\cdot\text{kg}^{-1}$ and $103 \text{ mg}\cdot\text{kg}^{-1}$, respectively. Mice treated with doses of **TLD-1411** higher than MTD_{50} showed sign of weakness, ataxia and died a couple of days post-injection. On the contrary, **TLD-1433** when given at higher doses than MTD_{50} did not cause death and all behavioural symptoms disappeared 24 h post-injection. Accumulation studies showed that both compounds were detectable in the tumour, liver and brain after 24 h. Tumour concentration of **TLD-1411** was lower than the one of **TLD-1433** (4.32 μM to 16.1 μM). The efficacy of PDT treatment was also tested using the same mouse model. Mice with grown tumours were injected with compounds and irradiated after 4 h thereafter with $190 \text{ J}\cdot\text{cm}^{-2}$ for 32 min in 30 s cycles. Tumours were significantly reduced when treated with $2 \text{ mg}\cdot\text{kg}^{-1}$ of **TLD-1411** and displayed a growth delay of 8 days. However, all tumours recurred. A higher dose of $5 \text{ mg}\cdot\text{kg}^{-1}$ of **TLD-1433** gave a tumour reduction and growth delay of 9 days. The researchers also checked whether continuous wave (cw lasers) or pulsed lasers would give better results with the tested PSs. Cw lasers are regularly used in PDT applications. Pulsed ones have the advantage of lowering down the local tissue heating, keeping the high power density. Mice treated with **TLD-**

1411 and **TLD-1433** showed significant increase in survival when higher doses of the compounds as well as cw light source was applied.

Upregulated receptors or cell surface markers in cancer cells are useful targets for therapeutic agents. Usually, targeting mosaic is conjugated with the complex. It is also common to use the association of the serum or membrane proteins with the active compound in non-covalent manner to improve compound uptake. Ru complexes are known to associate with human serum albumin (HSA) or transferrin.^{19,20} Transferrin is a 78 kDa glycoprotein necessary for chelating Fe³⁺ from the serum.²¹ Cancer cells display upregulated levels of transferrin receptors due to their higher demand for Fe³⁺ to grow.²² In 2016, Lilge *et al.* confirmed that the uptake of **TLD-1433** as well as ROS production upon light irradiation (96 laser diode array light source; 625 nm; $90 \pm 6 \text{ J cm}^{-2}$) were improved in cell free environment when the complex was mixed with transferrin.²³ **TLD-1433** associated with transferrin showed also lower dark cytotoxicity, probably due to enhanced Fe³⁺ delivery to the cancer cells, and resistance to photobleaching in contrary to **TLD-1433** alone.

Cell localisation of **TLD-1433** and its impact on cell metabolism by changing the cellular redox balance was published in a recent study.²⁴ Colocalisation studies performed by confocal and time-resolved laser scanning microscopy were inconclusive. Additionally, fluorescence signals of the tracking dyes vanished before the **TLD-1433** signal could be detected. It is possible that redox reactions and complex activation during laser scanning could be the reason for that unexpected phenomena.

The good results obtained with **TLD-1433** led to the preparation of a series of cyclometalated Ru(II) complexes similar to **TLD 1433** structure (**1-4**, Figure 3).²⁵

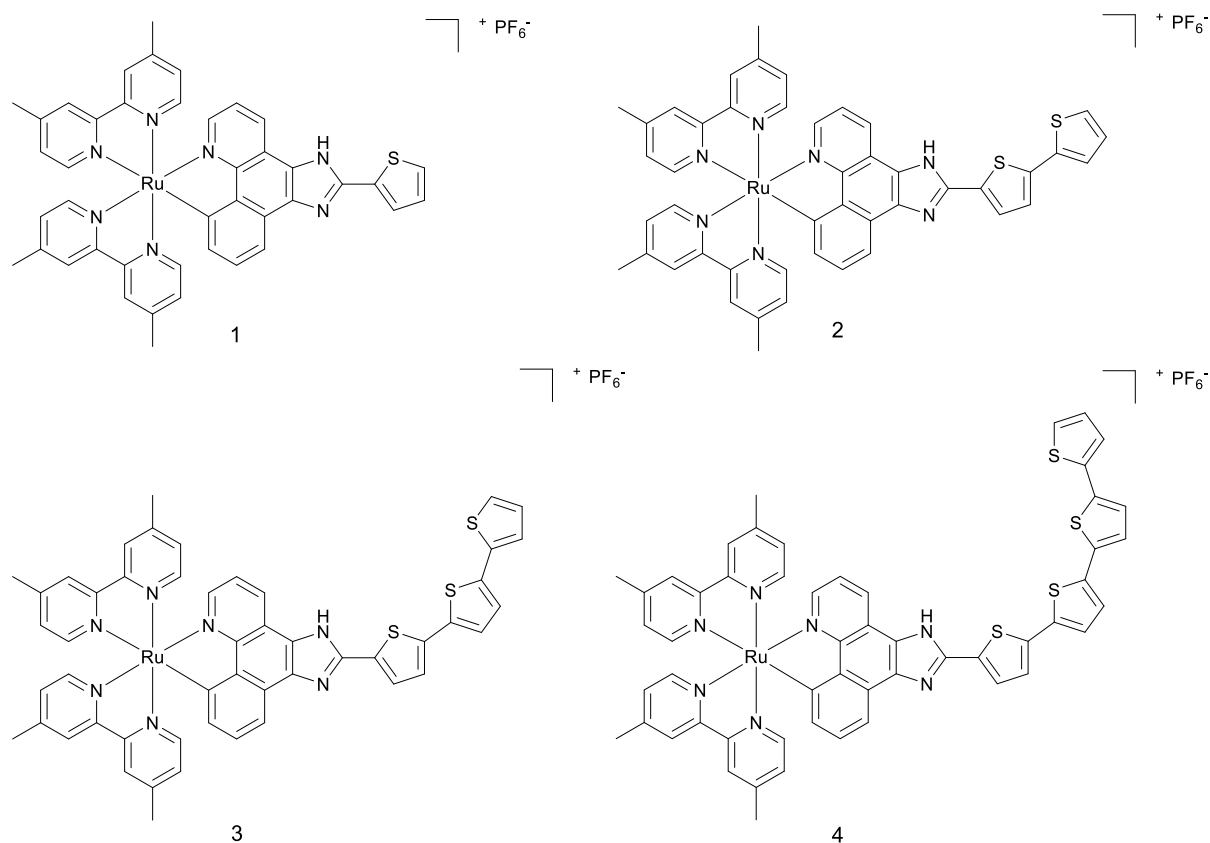


Figure 3. Structure of complexes **1-4**

Cyclometalated Ru(II) complexes are usually more photostable and their absorption spectra is red-shifted compared to diamine Ru(II) complexes. The (photo-)toxicity of the complexes was checked in two cell lines, namely SK-MEL-28 (melanoma) and CCD-1064Sk (normal skin fibroblasts). Complexes **1-3** were found to be highly cytotoxic in the dark towards melanoma cell line and were affecting much less normal skin fibroblasts. Complex **4** did not show any cytotoxicity in the dark. Upon irradiation with visible light (400-700 nm, $34.7 \text{ mW}\cdot\text{cm}^{-2}$), all complexes appeared to be extremely cytotoxic to melanoma cells. Particularly, complex **4** had a surprising PI of more than 1100, much higher than the three other complexes. To determine if complexes **1-4** would possibly bind to DNA, a mobility shift assay was performed. Upon light irradiation with visible light, the pUC19 plasmid formed aggregates in the presence of the complexes. No single-strand nor double-strand DNA breaks were observed under these conditions. Ethidium bromide staining with or without light irradiation was impaired,

presumably as a result of the intercalation of complexes **1-4** into DNA, or quenching of the ethidium bromide fluorescence. Confocal microscopy and DIC images were taken to assess compounds uptake and cells morphology before and after light treatment (400-700 nm, 34.7 mW·cm⁻², 50 J·cm⁻²). Complexes **1** and **2**, which had the highest uptake in melanoma cells, as determined by confocal microscopy, were not taken up by non-cancerous cells. Complexes **3** and **4**, despite their lower uptake in melanoma cells, caused impressive changes of cell shape upon light irradiation, contrary to complexes **1** and **2**.

Mitochondria targeting compounds

Mitochondria are the cell energy centres and play an important role in the intrinsic apoptotic pathway. DNA damage, metabolic stress or the presence of unfolded proteins might lead to the permeabilisation of mitochondrial outer membrane. The release of mitochondrial proteins into the cytosol (e.g. cytochrome *c*) activates an apoptotic signalling cascade and finally leads to cell death.²⁶ Generation of singlet oxygen or other ROS in this organelle might trigger a rapid apoptotic response in the targeted cell, making this cellular compartment an interesting target for PDT photosensitizers.

Two Ru(II) polypyridyl compounds that target mitochondria functionalized with tyrosine and tryptophan were designed in 2013 (Figure 4).²⁷ Both amino acids were chosen to improve the cellular uptake of the Ru complexes.

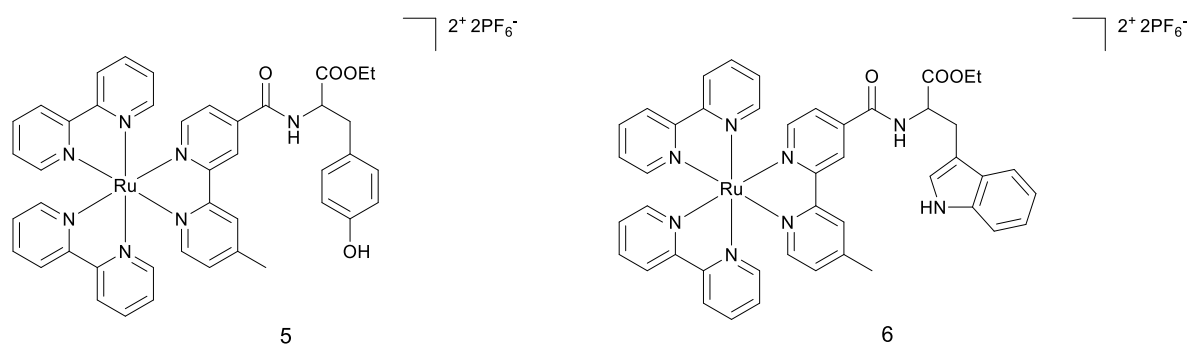


Figure 4 Structures of complexes **5** and **6**.

Cytotoxicity in the dark and upon light irradiation (4 h with visible light source $\lambda \sim 450\text{-}480$ nm, 10 J cm^{-2}) of both compounds was examined in A549 (pulmonary carcinoma) and HCT116 (colon cancer) cell line. Promising phototoxic index (PI) values in A549 cell line (>10 for complex **5** and >10 for complex **6**) and in HCT116 (>9 and >10 , respectively) encouraged the authors to perform further biological studies.

Singlet oxygen 1O_2 production upon light irradiation was confirmed and was suggested to be responsible for cell death. Fluorescence spectroscopy, UV-Vis absorption and isothermal titration calorimetry experiments showed that the Ru(II) complexes were able to bind CT-DNA in a non-covalent way, probably by intercalation into the DNA groove. Irradiation of pUC19 plasmid with the Ru(II) complexes led to photo-cleavage of the DNA, suggesting this mechanism as the main cause of cell death. This finding was further confirmed by single cell gel electrophoresis, which revealed DNA damage in treated A549 cells upon light irradiation. Confocal laser scanning microscopy helped identify the cellular localisation of the complexes in A549 cells. Unexpectedly, none of the compounds was found to localise in the cell nucleus. Signals from Mitotracker Green suggested the presence of the complexes in mitochondria and cell membranes. Microscopy studies after light irradiation would have been an interesting addition to the work since some of the compounds are known to modify their localisation after illumination of the cells.²⁸ Nevertheless, singlet oxygen is known to alter the mitochondrial

trans-membrane potential, which might trigger the apoptotic pathway. To further investigate the molecular mechanism of cell death, western blot analysis was performed. It revealed that caspase-3, a marker of apoptosis, was found to be overexpressed in irradiated cells. The researchers concluded that the mechanism of cell death included the disruption of mitochondria membrane potential that, in turn, triggered the caspase-3-dependent apoptotic pathway.

Biological evaluation on Ru(II) complexes containing pdppz ([2,3-h]dipyrido[3,2-a:2',3'-c]phenazine) ligands was published in 2015.¹⁶ Complexes **7** and **8** were expected to bind DNA because of their extended dppz ligand, while complex **9** was used as a control (see Figure 5 for chemical structures). Experiments confirmed that complexes **7** and **8** were able to intercalate DNA in non-cell environment. Incubation of complex **8** with the plasmid pBR322 upon light irradiation (390nm, 2 J cm⁻²) caused single and double breaks in the DNA. Such effect was not seen with complex **7**. It was shown that HeLa cells could actively uptake compounds **7** and **8** in a temperature-dependent manner. Confocal microscopy studies of complex **8** demonstrated that this compound colocalised with mitochondria and lysosomes, which clustered near the nucleus. It is possible that small amounts of **8** were also able to localise to the nucleus. Alkaline comet assay revealed DNA damage in treated and irradiated cells. ICP-MS experiments would have been an attractive addition to this study.

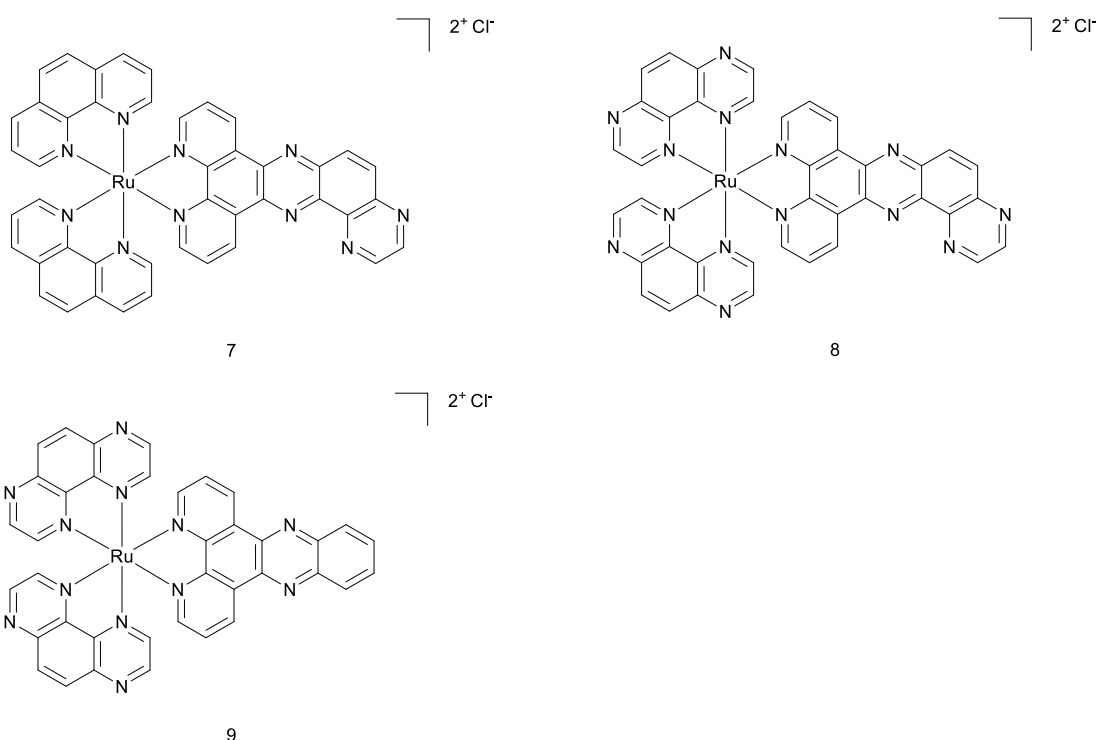


Figure 5. Chemical structures of complexes **7**, **8**, **9**.

Cytotoxicity of the complexes in the dark and light conditions (≥ 400 nm, ~ 18 J cm⁻²) was examined in HeLa (cervical cancer), two mesothelioma cell lines (CRL5915 and One58), in Mutu-1 (Epstein-Barr virus-related Burkitt lymphoma) and DG-75 (Burkitt lymphoma) cell lines. Complex **7** did not show any dark or light cytotoxicity. Complex **8** was moderately cytotoxic in the dark (Inhibitory concentration 50 -IC₅₀ values ranged from >100 to 40.2 μ M). Light irradiation of the treated cells caused phototoxic effect (IC₅₀ values ranged from 42.8 to 8.8 μ M). Pre-treatment of HeLa cells with N-acetylcysteine (NAC), an established antioxidant, confirmed that ROS were involved in cell death. HeLa cells were 50% more viable with the NAC treatment upon light irradiation. Real-time confocal microscopy demonstrated that HeLa cells treated with **8** displayed an apoptotic morphology upon light irradiation. Such result was confirmed by Fluorescent Activated Cell Sorting (FACS) analysis. Interestingly cell death could be prevented when cells were co-treated with VAD-fmk (inhibitor of caspases). Hence, these results demonstrated that **8** triggered apoptotic cell death in the treated cells.

Another set of four Ru (II) compounds that target mitochondria was synthesised by the Chao group in 2015 (see Figure 6 for structures).²⁹

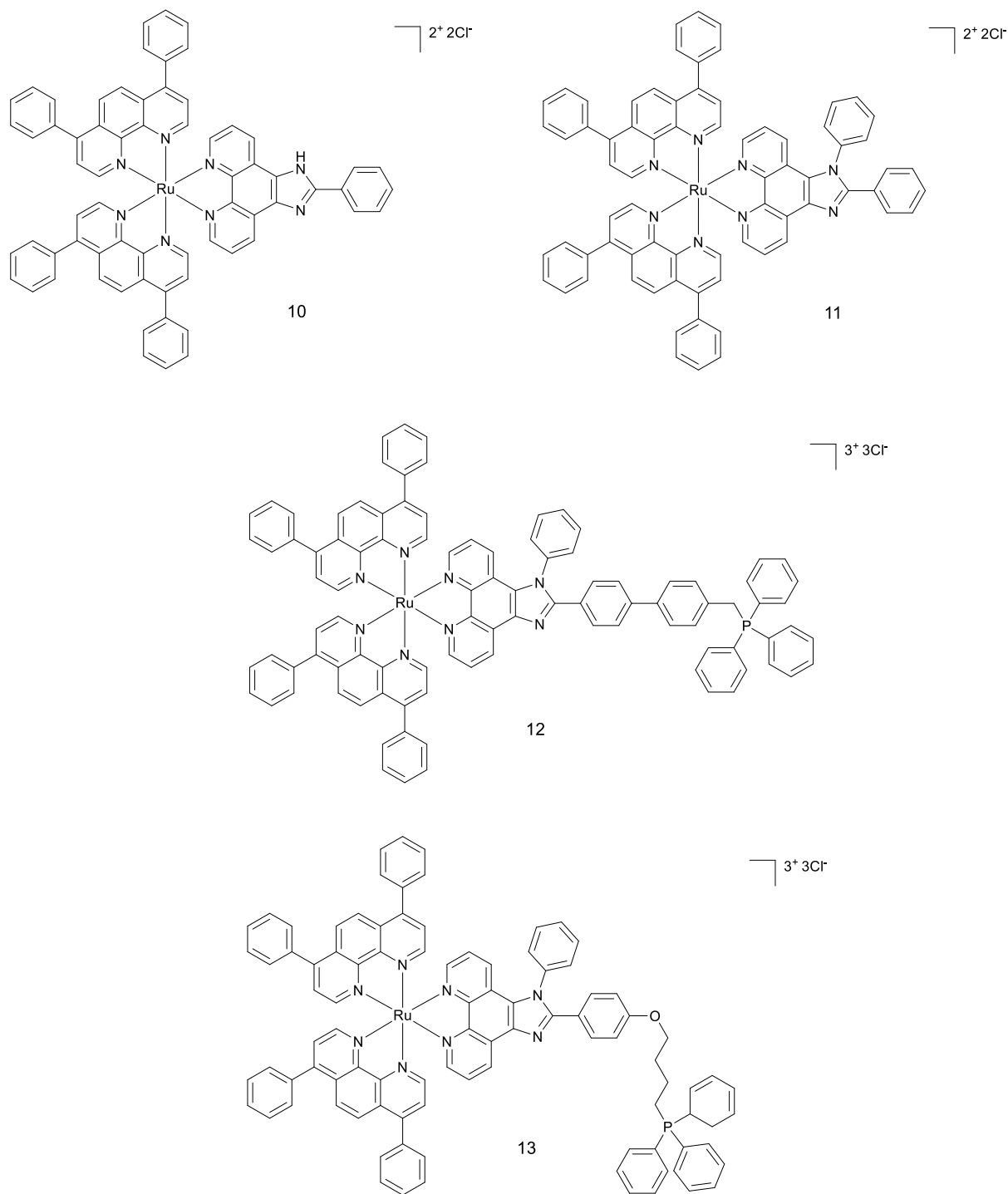


Figure 6. Chemical structures of complexes 7, 8, 9 and 10.

The triphenylphosphine (TPP) present in complexes **12** and **13** adds lipophilic character to the compounds, resulting in better mitochondria targeting abilities.³⁰ Confocal microscopy with Mitotracker Green in HeLa cell line revealed that complex **13** localises in the mitochondria. Three other compounds were found to moderately localise in that compartment. Localisation results were confirmed by ICP-MS analysis, showing that complexes **10-12** were present in higher amount in the cytoplasm (Figure 7).

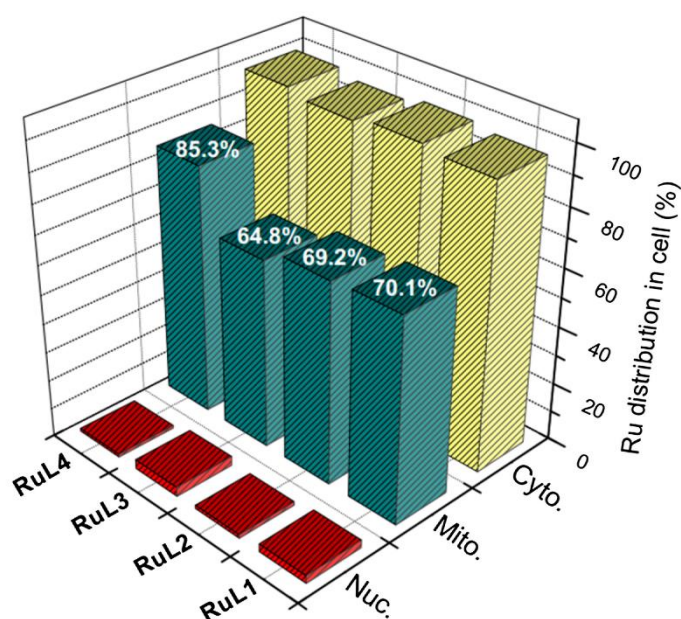


Figure 7. ICP-MS quantification of the internalized Ru by the HeLa cells. Figure taken from ref 30 with permission from Elsevier.

All four compounds were designed to produce singlet oxygen not only using a one-photon but also a two-photon irradiation process. Confocal microscopy images of HeLa cells taken before and after two-photon irradiation (810-830 nm for 3 minutes; 800 J cm^{-1}) with 2,7-dichlorodihydro-fluorescein diacetate (DCFH-DA) allowed verifying singlet oxygen production in all samples. Dark and light cytotoxicities of all compounds were tested under one-photon irradiation. Compounds were not toxic under dark conditions ($\text{IC}_{50} > 100 \mu\text{M}$). After irradiation (LED source; 450 nm; 12 J cm^{-2}), complexes **10-12** showed similar cytotoxicity, varying from 12.4 to $15.5 \mu\text{M}$. Probably due to its high concentration in mitochondria, complex

13 was found to be the most effective compound tested, with a PI >28. Since monolayer cell cultures are not a good model for tumour treatment, HeLa multicellular tumour spheroids (MCTS) were used for further tests. Diffusion of the compounds (10 μ M, 8 h treatment) was examined in 800 μ m MCTSs. Treated spheroids were imaged with one-photon and two-photon z-stack microscopy. The luminescence signal of the compounds was found in all depth sections of the spheroids. Two-photon microscopy showed deeper penetration of the complexes through spheroids than one-photon microscopy, probably due to its excitation wavelength in the therapeutic window. This confirmed the high permeability of the complexes through the MCTSs. Singlet oxygen generation with DCFH-DA was also investigated in MCTS. Enrichment of the singlet oxygen signal was observed in the treated spheroids. The results showed lower signal of produced singlet oxygen in the cores of the spheroids as compared to their surface. Compounds treatment also inhibited MCTSs growth after irradiation with two-photon technique. The best results were obtained again with complex **13**. All synthesised compounds exhibited good photodynamic therapy ability against the HeLa cell line. However, further investigations should include healthy cells to establish a possible therapeutic window for these compounds.

An interesting study was recently published by the same group, who designed mitochondria-localising Ru(II) complexes that can be activated by glutathione (GSH).³¹ The aim of the study was to improve the tumour selectivity of the Ru complexes that are used as PDT PSs. Complex **14** is a dinuclear Ru(II) complex, which is bridged by a GSH activating ligand 4,4''-azobis(2,2'-bipyridine) (Figure 8). Specific properties of the ligand cause quenching of luminescence of the Ru complex. Since intracellular concentration of GSH in cancer cells are higher than in healthy ones, the authors were hoping that the complex would be activated and transformed into complex **15** (Figure 8), and this mostly in cancer cells.

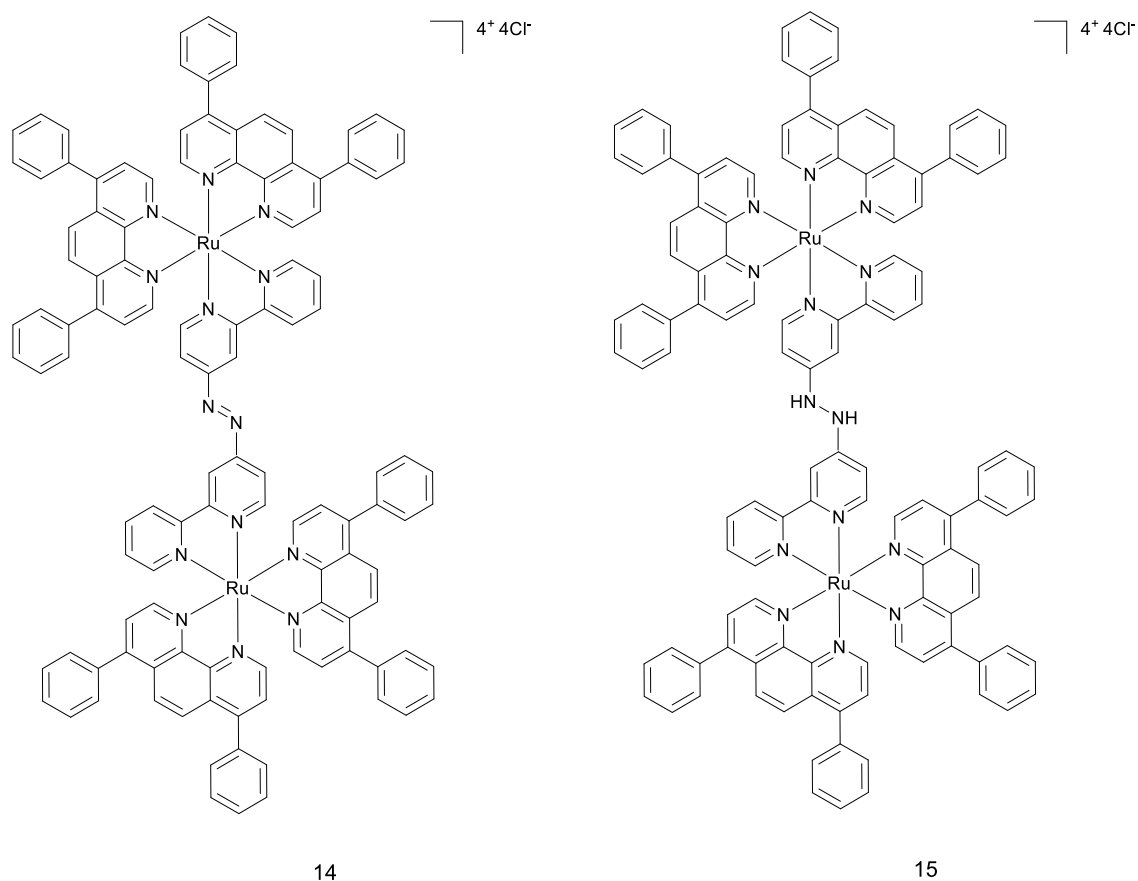


Figure 8. Chemical structures of complex **14** and complex **15**.

For the experiments, Chao and co-workers used two cell lines, namely HeLa and LO2 (human fetal hepatocyte- healthy control). Both were cultured in monolayers as well as in MCTSs. ICP-MS and confocal microscopy experiments confirmed that the mitochondria were the main target for complex **14**. As expected, LO2 cells displayed a much weaker accumulation of the complex compared to HeLa. Two-photon irradiation (810 nm, 100 mW, 80 MHz, 100 fs) was used to establish ROS generation in treated 2D and 3D cell cultures. A strong green fluorescence of the ROS indicator was detected, confirming that the complex was able to permeate the MCTSs and induce single oxygen production. Cytotoxicity studies demonstrated that complex **14** was not toxic in the dark ($IC_{50} > 70 \mu\text{M}$) for both cell lines. After 15 min irradiation at 450 nm ($20 \text{ mW}\cdot\text{cm}^2$), its cytotoxicity raised to about $5 \mu\text{M}$ for HeLa and $13 \mu\text{M}$ for LO2 cells. Similar results were obtained with cancer cell MCTSs. Complex **14** was not toxic in the dark ($IC_{50} >$

100 μM) and became more harmful on MCTSs after light irradiation (5.71 μM). Viability of the MCTSs was checked by Calcein AM staining. Irradiation of treated cells caused loss of the fluorescent signal from the dye, suggesting cell death. It is worth noting that MCTSs treated with complex **14** at 10 μM concentration stopped growing two days after two-photon irradiation, whereas the control group treated with the same concentration of cisplatin kept growing. Of note, annexin V and propidium iodide (PI) staining showed that apoptosis was the main cause of cell death.

In 2018, Stang, Chao and coworkers prepared a tetrametallic macrocyclic structure containing Ru(II) and Pt(II) atoms, that can be used in two-photon PDT (Figure 9).³²

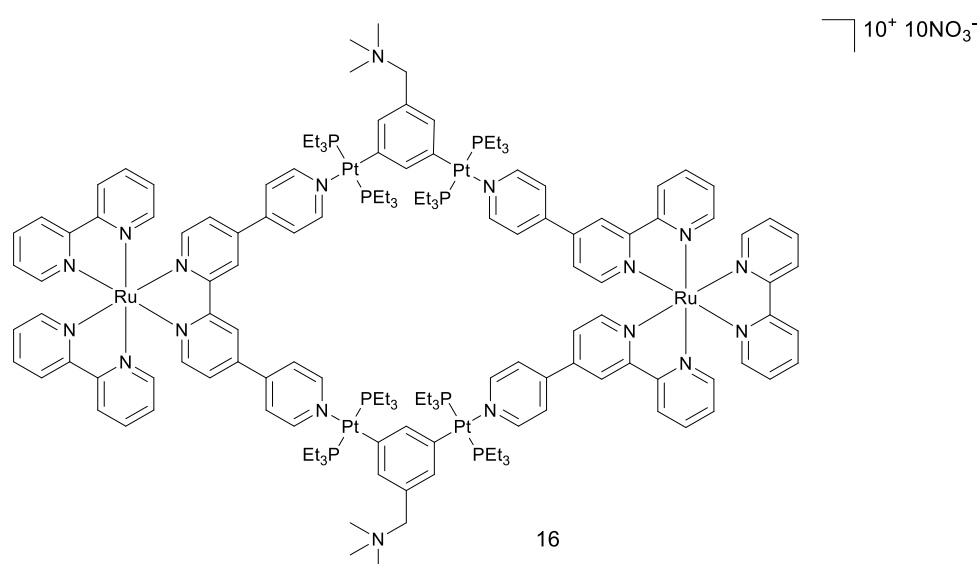


Figure 9. Chemical structures of complex **16**.

The addition of the Pt(II) moieties to the two Ru(II) complexes was made to enhance the intrinsic photophysical properties of the Ru(II) complexes. Impressive two photon absorption (TPA) cross-section values of 1371 GM were obtained, which were much higher than the one of $[\text{Ru}(\text{bpy})_3]^{2+}$ itself (66 GM). Moreover, the intersystem crossing process was enhanced, which elevated the singlet oxygen quantum yield value to 88% in methanol, when $[\text{Ru}(\text{bpy})_3]^{2+}$ was used as reference. Cellular localisation showed that metallacycle complex was

accumulating in the mitochondria and the nucleus. ICP-MS results corroborated those of microscopy, indicating that, after 2 h incubation, complex **16** (5 μ M) localised in mitochondria (67 %) and in the nucleus (25 %). Cellular uptake data revealed that complex **16** entered the cells through endocytosis pathway. Cytotoxicity experiments were performed on HeLa, A549, A549R (cisplatin resistant cell line), KV (multi-resistant human oral floor carcinoma) and PC-3 (prostate cancer) cell lines. The PI values ranged between 11.6- 114 (irradiation conditions: LED source; 450 nm, 21.8 mW cm⁻², 5 min). Since A549 cells displayed the highest PI, they were chosen as a model cell line for further studies. DCFH-DA staining and calcein AM/ethidium homodimer-1 (EthD-1) co-staining after two photon (TP) irradiation of the treated cells confirmed that compound **16** can generate singlet oxygen and cell death only in the irradiated area. Compound **16** caused cell apoptosis, confirmed by annexin V and PI staining as well as by elevated levels of caspase-3/7. To assess the impact of complex **16** in mitochondria and nucleus, several tests were performed. The mitochondrial membrane potential (MMP) was significantly lower in irradiated cells. TP irradiation also caused DNA fragmentation in the nucleus. Due to these promising results obtained *in vitro*, *in vivo* studies in mice were performed. To assess two photon photodynamic therapy (TP-PDT) efficacy of complex **16**, A549 tumour bearing nude mice were used. The group treated with complex **16** (0.5 mg kg⁻¹) and irradiated with TP laser (800nm, 50 mW, 20 s mm⁻¹) did not exhibit observable weight loss. The tumour volume of the treated group was reduced by 78%, while control mice groups showed 13-fold increase in tumour mass. Additionally, examination of tumour tissue of the treated group showed pathological changes, which were not observed in other organs like liver, kidney, heart, etc.

Nucleus targeting compounds

Besides mitochondria, another important target for PDT PSs is the nucleus. Generation of singlet oxygen or other ROS, in close proximity to the DNA, might allow for DNA damage, and finally lead to cell death. It is known that dipyridophenazine (dppz) ligands have the ability to intercalate within DNA.^{33, 34} That is why in 2014 six different $[\text{Ru}(\text{bpy})_2\text{dppz}]^{2+}$ derivatives **17-22** were investigated by our groups (Figure 10).³⁵

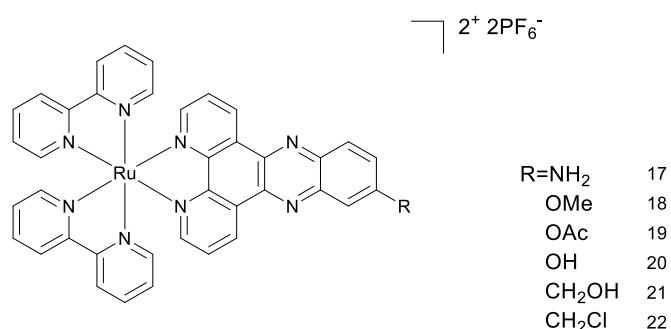


Figure 10. Chemical structures of $[\text{Ru}(\text{bpy})_2\text{dppz}]^{2+}$ derivatives.

Singlet oxygen production study showed that all compounds had a high efficacy for $^1\text{O}_2$ production but only in hydrophobic environment. The excited state of the complexes bearing a dppz ligand are quenched very fast in the presence of water molecules.³⁶ All synthesised complexes were found to be non-cytotoxic in the dark ($\text{IC}_{50} > 100 \mu\text{M}$) against HeLa and MRC-5 cells (normal lung fibroblast). Light cytotoxicity studies were performed using two different light treatments: 10 min at 350 nm ($2.58 \text{ J}\cdot\text{cm}^{-2}$) and 20 min at 420 nm ($9.27 \text{ J}\cdot\text{cm}^{-2}$). Among all compounds, only complexes **17** and **18** showed an interesting phototoxic effect. The PI value for complex **9** was higher than 150, while for complex **18** it was 42. The cellular uptake of the Ru compounds was investigated by High-Resolution Continuum Source Atomic Absorption Spectrometry (HR-CS AAS), showing that it correlated well with toxicity studies. The most cytotoxic complexes **17** and **18** had the highest accumulation in the HeLa cells (1.08 and 1.76 nmol Ru per mg protein). Accumulation of the compounds in the MRC-5 cell line was different

since only 0.76 and 0.18 nmol Ru per mg protein were determined. This indicates that the complexes penetrated the non-cancerous cell line to a lesser extent than the cancerous line. Cellular localisation of complexes **17** and **18** was investigated using confocal microscopy.

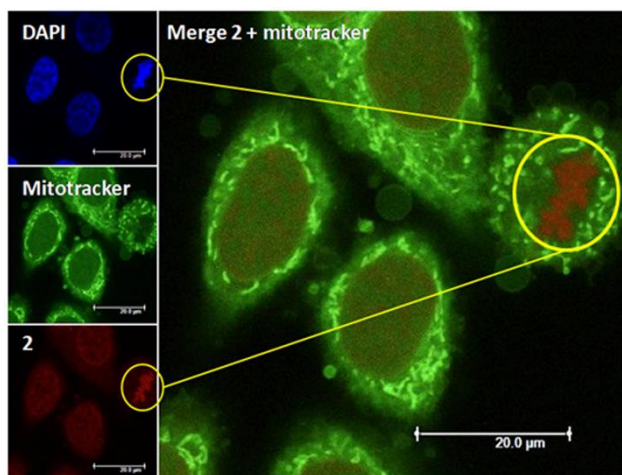


Figure 11. Cellular localisation of complex **18**. Figure taken from ref 36, with permission from John Wiley and Sons.

The first complex was difficult to detect even when cells were treated with high doses of compound. The low luminescence quantum yield is probably responsible for this result. On the other hand, complex **18** was able to accumulate preferentially in the nucleus. Because of the luminescent quenching effect of the complex in aqueous environment mentioned above, fluorescence microscopy localisation was supported by HR-CS AAS. The results showed that both complexes efficiently accumulated in the nucleus (0.43 ± 0.05 and 0.96 ± 0.06 nmol Ru per mg protein). To check if nuclear localisation and binding to DNA might have been the reason of toxicity, DNA photocleavage experiments were conducted. Treatment of pcDNA3 plasmid with complexes and irradiation at 420 nm for 20 min ($9.27 \text{ J}\cdot\text{cm}^{-2}$) showed that both complex **17** and **18** were able to cleave plasmid DNA. Administration of compounds in the dark did not cause cleavage of the plasmid. In a follow up study, our groups further explored the molecular cell death mechanism of complex **18**.³⁷ Mechanistic studies on the outcome of DNA binding led to the conclusion that irradiation of the intercalated compound caused oxidative

damage of purines in DNA. Importantly, alkaline comet assay supported these results in living cells. Confocal microscopy images of different cell lines such as U2OS (human bone osteosarcoma), MCF-7 (mammary gland adenocarcinoma) and RPE-1 (normal retina pigmented epithelium) confirmed that the complex was mainly localised in the nucleus³⁵. ICP-MS confirmed these results. The determination of the presence of specific markers of DNA damage response, analysis of DNA content and cytotoxicity studies after irradiation showed that cells underwent cell cycle arrest and loss of viability. Annexin V and PI staining experiments of interphase cells excluded classic apoptotic or necrotic cell death. Further analysis demonstrated that cell death was caused by DNA damage and endoplasmic reticulum-(ER) mediated stress response pathways. On the other hand, treatment and irradiation of mitotic cells caused death according to classic apoptotic pathways, indicating two distinct modes of cells death in interphase or mitosis and pointing to the potential of the use of these compounds in combination with established cancer therapeutics.

Further studies on Ru(II) polypyridyl complexes with dppz ligands were performed by our group in collaboration with the Chao group.²⁸ Two substitutionally inert complexes, namely $[\text{Ru}(\text{phen})_2(\text{dppz}-7,8\text{-(OMe)}_2)]^{2+}$ (complex **23**) and $[\text{Ru}(\text{phen})_2\text{dppz}-7,8(\text{OH})_2]^{2+}$ (complex **24**) were investigated (see Figure 12 for structures).

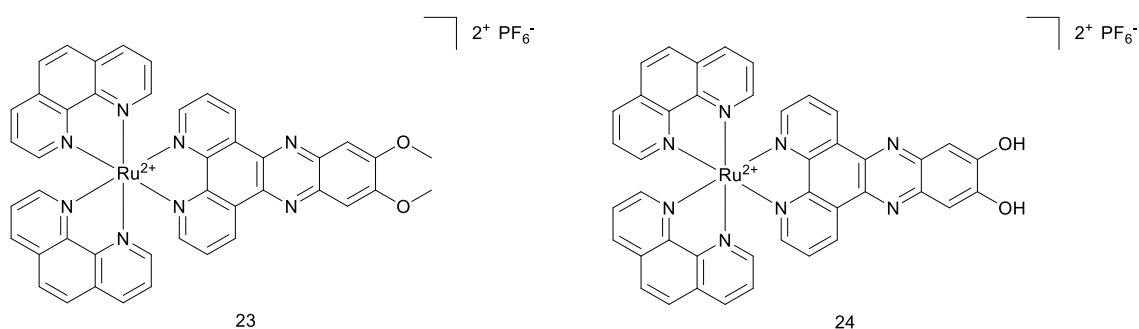


Figure 12. Chemical structures of complex **23** and complex **24**.

The aim of this study was to investigate if small structural differences could cause significant changes in the biological response. It is worth noting that both complexes were investigated for use in one-photon (OP) and two-photon (TP) PDT. Dark and light cytotoxicity studies on HeLa and MRC-5 cell line monolayers showed that the introduction of -OMe groups on the ligand enhanced toxicity compared to those bearing the -OH groups (decrease of the IC₅₀ value from $16.7 \pm 2.6 \mu\text{M}$ in -OH bearing compound to $3.1 \pm 0.6 \mu\text{M}$ in -OMe compound in HeLa). Both complexes were also much more effective than the positive control aminolevulinic acid (5-ALA), an approved PDT PS. Interestingly, the compounds were also studied on 3D multicellular tumour spheroid to provide a comprehensive overview on how Ru(II) complexes might act in solid tumours. Surprisingly, only complex **23** was active on MCTSs upon light irradiation (LED light source; IC₅₀ $32.5 \pm 6.8 \mu\text{M}$). To further explore the mechanism of action of the complexes, cellular localization and uptake of the compounds were studied. ICP-MS showed that the amount of complex **23** was much higher in HeLa cells than complex **24** (2.4 nmol Ru/mg protein to 0.9 nmol Ru/mg protein). This result might explain the differences between the IC₅₀ values obtained for both complexes in the dark and upon light irradiation. Confocal microscopy showed that the Ru complexes under study localised in different compartments of the cell. Complex **23** was found to accumulate in the nucleus and mitochondria while **24** localised in the outer cell membranes. Imaging was also performed after light irradiation. Complex **23** changed its localisation and moved completely into the nucleus, probably as result of damage generated by singlet oxygen in membranes, enabling the compound to reach the nucleus. Worthy of note, these Ru complexes might also localise in other compartments that escaped detection by confocal microscopy. Indeed, due to luminescence quenching in aqueous solution of these dppz-containing complexes, their detection is only possible in hydrophobic environment.³⁸ OP and TP absorption was also used to image both compounds in spheroids. For both complexes, TP imaging gave better results. In

this experiment, complex **23** completely permeated the MCTSs, while complex **24** could only be detected in the external parts of the spheroids (Figure 13 and Figure 14).

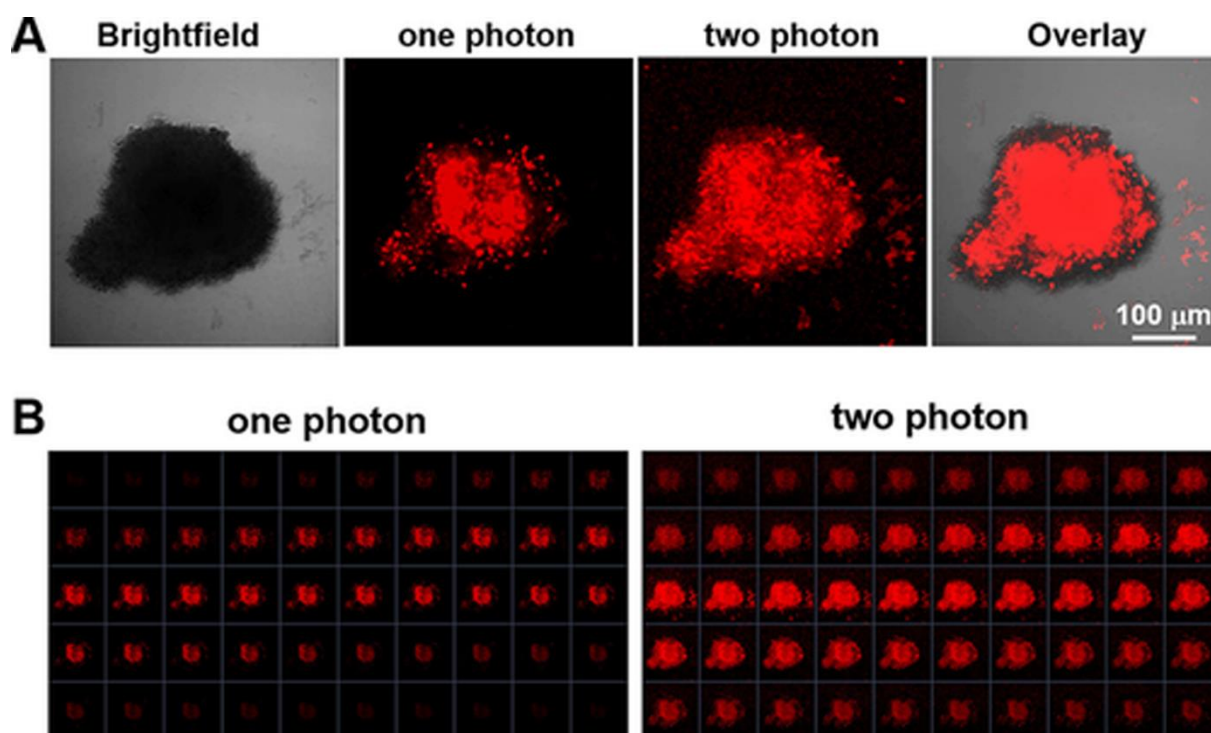


Figure 13. A. OP and TP images of **23** after incubation with HeLa spheroids for 12 h.

B stack images of the same HeLa spheroids captured every 5 μ m along the Z-axis.

Figure taken from ref. 29 with permission from John Wiley and Sons.

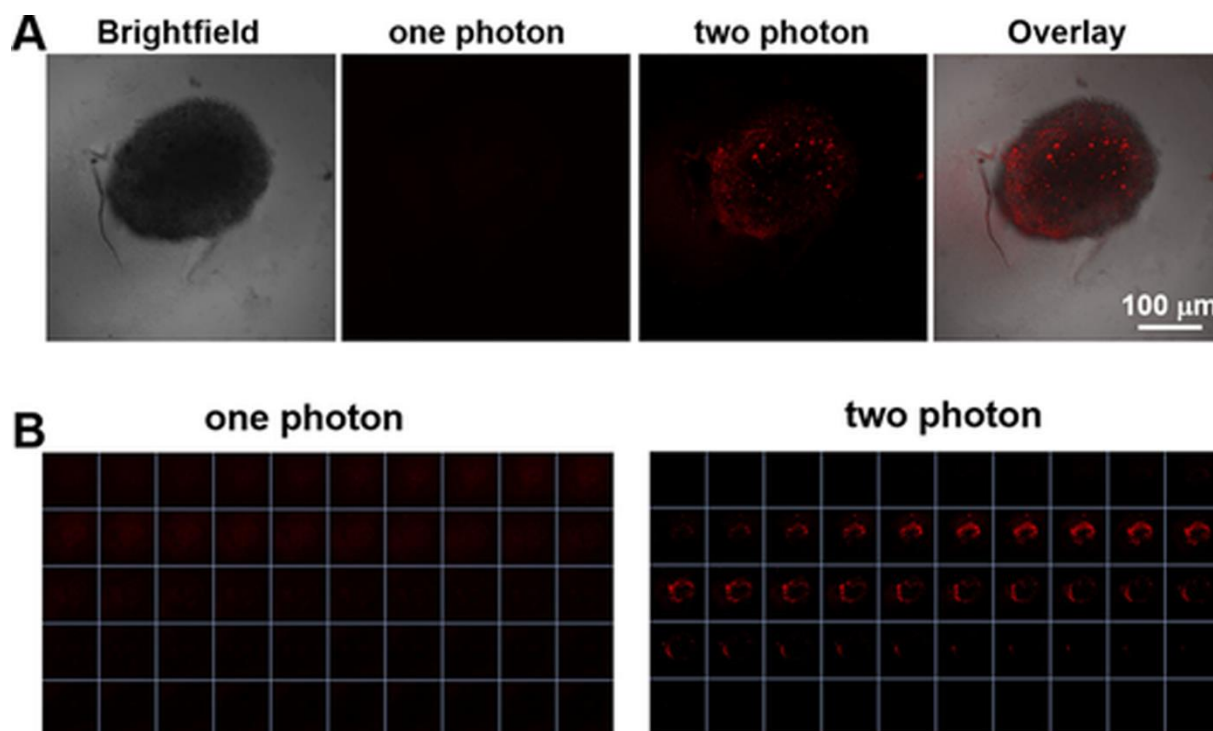


Figure 14. A. OP and TP images of **24** after incubation with HeLa spheroids for 12 h.

B stack images of the same HeLa spheroids captured every 5 μm along the Z-axis.

Figure taken from ref. 29 with permission from John Wiley and Sons.

Comparable results with structurally related compounds were obtained by the Glazer group in 2014.³⁹ Although complexes **25** and **26** have very similar photophysical properties (Figure 15), the differences in their overall charge and hydrophilicities led to distinct biological effects. While complex **25** localised in the mitochondria, complex **26** did not show specific organelle localisation and was found in the cytosol. Upon irradiation (30 s pulses; $>400\text{ nm}$; $7\text{ J}\cdot\text{cm}^{-2}$), complex **25** caused necrotic cell death distinct from complex **26** which turned on the apoptotic pathway. It is possible that the addition of sulfonic acid groups on complex **26** induced a different cell localisation and consequently a different type of cell death.

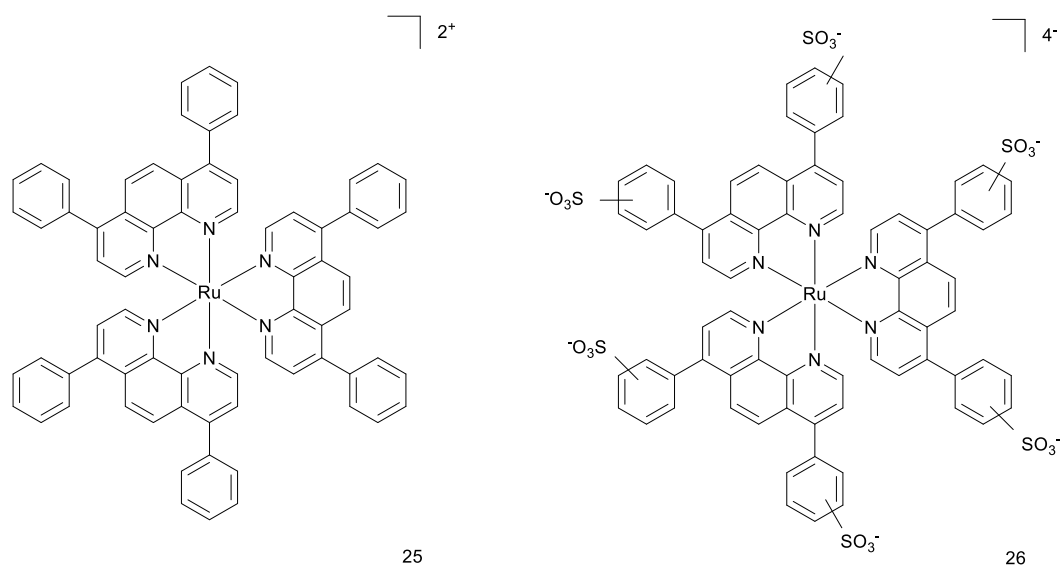


Figure 15. Chemical structures of complex **25** and **26**.

Similar conclusions were brought in 2015, when small changes in the structure of Ru(II)-based PSs cancelled phototoxicity of the complex.⁴⁰ In this case, two inert Ru(II) polypyridyl complexes with a nitrile containing ddpz ligand and two byridine or phenantroline ancillary ligands were tested. In contrast to previously described Ru(II) complexes with dppz ligands, both did not exhibit high singlet oxygen production (20% comparing to 50%-90%). This is probably why these complexes did not display any cytotoxic effect upon light irradiation (RPR 200 Rayonet chamber reactor; 420 nm; 9.27 J·cm⁻²).

A series of four cyclometallated Ru(II) complexes with π -expansive ligands were described by McFarland in 2015 (Figure 16).

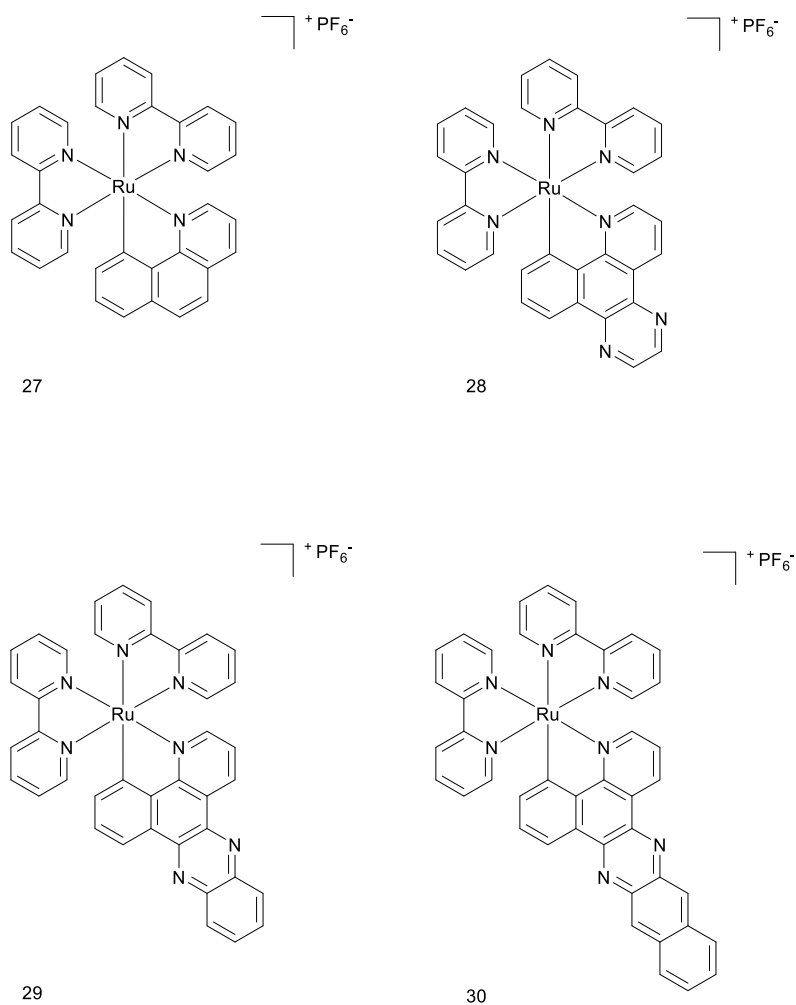


Figure 16. Chemical structures of complex **27-30**.

Cytotoxicity of the compounds was assessed in HL-60 (acute myeloid leukemia) and SK-MEL-28 cell lines. Complexes **27-29** were toxic to the cells in the dark and did not show high PI value (4-18) after irradiation (190 W BenQMS 510 overhead projector; visible light 400-700 nm; 34.2 mW cm^{-2}). On the contrary complex **30** showed an astonishing PI value, namely 1400. To assess if the complexes can interact with the DNA, a photocleavage assay was used. It was shown that all complexes could impair ethidium bromide staining due to induced DNA aggregation and precipitation. Because complex **30** was the most promising one, further tests were performed with it. Since **30** was generating singlet oxygen very weakly (less than 0.56% relative to $[\text{Ru}(\text{bpy})_3]^{2+}$), it was suggested that the other ROS is responsible for the phototoxic effect in cells. Indeed, tests with dihydroethidium (DHE) in HL-60 cells confirmed that

superoxide $O_2^{\cdot-}$ was responsible for cell death. It was also shown in SK-MEL-28 cells that complex **30** altered its localisation upon light irradiation (from nucleus to cytoplasm) and induced morphology changes in the cells.

Lysosome targeting compounds

In 2015, our group in collaboration with the Chao group introduced highly charged homoleptic complexes that are suitable for TP-PDT (see Figure 17).⁴¹

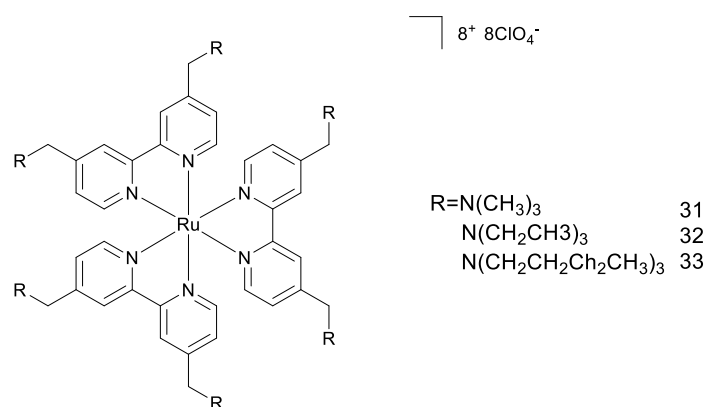


Figure 17. Chemical structures of highly charged complexes.

The compounds were found to be photostable and did not break down in bovine plasma. Electron paramagnetic resonance (EPR) experiments demonstrated that the main type of ROS generated by the three compounds at 450 nm irradiation was 1O_2 . Cellular localisation of complexes **31**, **32** and **33** was determined using confocal laser scanning microscopy in HeLa cell line monolayers as well as in HeLa multicellular tumour spheroids. All three complexes were found to localise in the lysosomes, probably entering the cell by endocytosis pathway. ICP-MS experiments confirmed the microscopy outcomes. All compounds were not cytotoxic in the dark. After OP irradiation (450 nm, $10 \text{ J}\cdot\text{cm}^{-2}$), complex **31** showed particularly high phototoxicity with IC_{50} value of $1.5 \mu\text{M}$ (PI 313). All complexes had a higher phototoxicity than 5-ALA, which was used as a control PS. The same trend was also observed for MCTSs.

Further investigations were performed with complex **31**, which was found to be the most promising compound of the series. Calcein AM staining and ROS indicator staining (DCFH-DA) showed that cell death was only limited to the place of irradiation. Morphology studies after TP light treatment showed that cells underwent shrinking and formed bubbles.

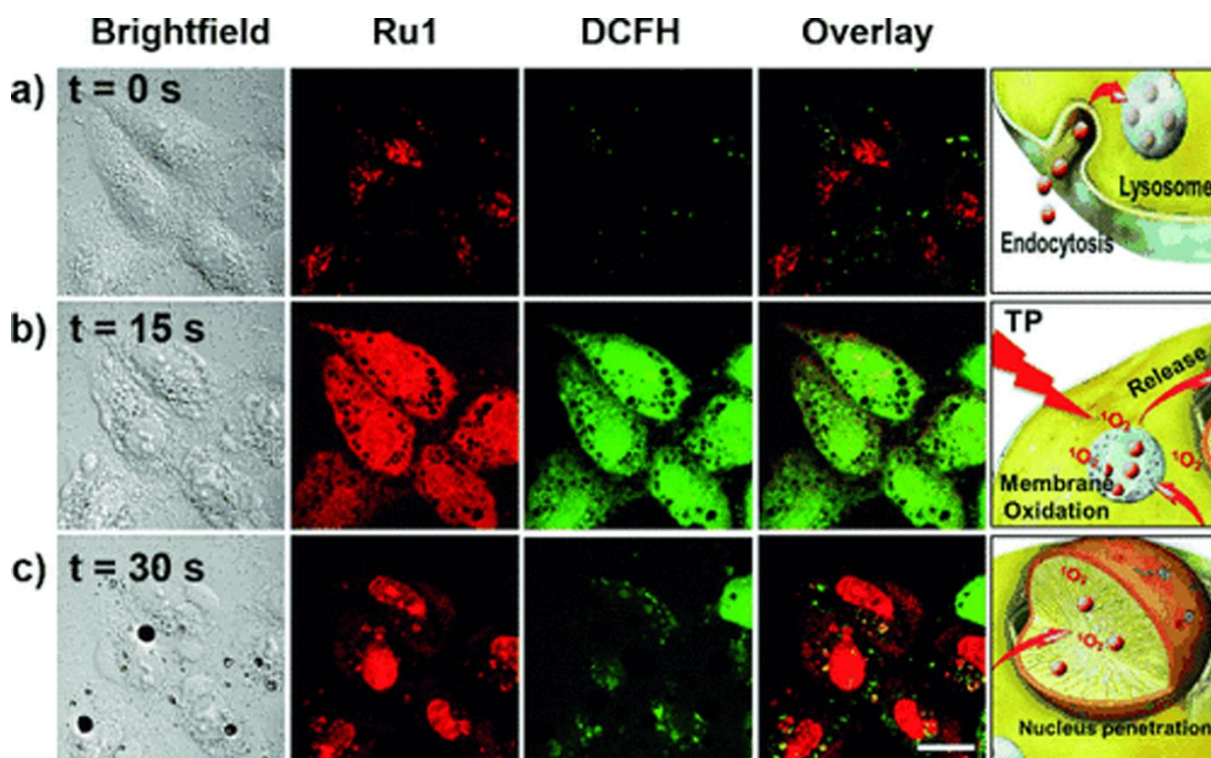
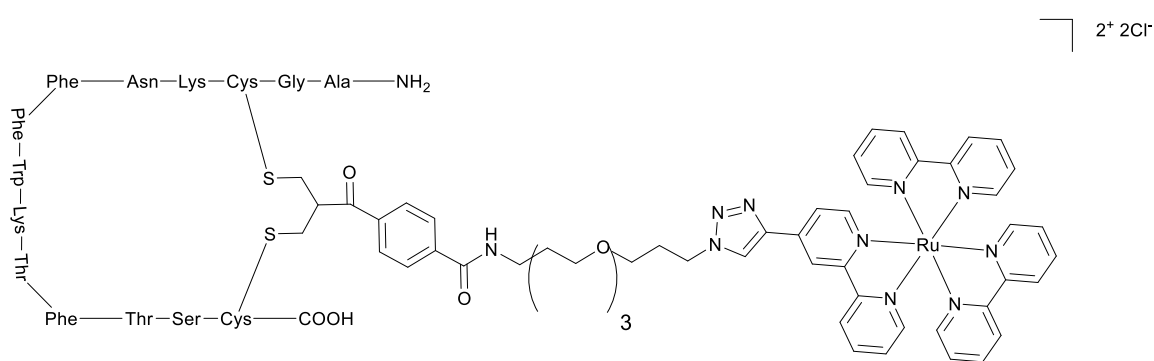


Figure 18. Micrographs of and ROS generation in HeLa cells incubated with complex **31** after irradiation with a two-photon confocal laser. Figure taken from ref. 42 with permission from John Wiley and Sons²²

The cellular localisation of complex **31** was also altered. After irradiation, the compound was found in the cytoplasm, nucleus and nucleoli (see Figure 18). Microscopy analysis indicated that cells died by a necrotic process, bursting their content into the extracellular space. Overall, this investigation revealed that lysosomes might be a good target for future PDT PSs.

Targeting conjugates

The need for new Ru(II) polypyridyl complexes with better selectivity towards cancer cells led to the design of compounds with tumour specific targeting moieties. Such moieties might be antibodies, cell surface receptors, aptamers, etc.^{42,43} In 2015, Weil and Rau introduced a Ru(II)-based PS that was conjugated to somatostatin,⁴⁴ a peptide hormone produced by δ -cells of the pancreas inhibiting the release of insulin and glucagon.⁴⁵ Somatostatin receptors are frequently overexpressed in many tumour cancer cells, making them a good target for anticancer agents.⁴⁶ In this study, $[\text{Ru}(\text{byp})_3]^{2+}$ derivative was conjugated to the peptide hormone to form complex **34** (Figure 19).



34

Figure 19. Chemical structure of complex **34**.

The cellular uptake of the conjugate was analysed by laser scanning confocal microscopy in A549 cells, which express different types of somatostatin receptors. The intensity of the compound emission was measured. A hundred times higher uptake of the somatostatin conjugate compared to the control was observed. Tumour selectivity was tested on wild type CHO-K1/Ga15 (Chinese hamster ovarian epithelial cell line expressing G α 15 alpha subunit protein) and cells overexpressing somatostatin receptor 2, CHO-K1/Ga15/SSTR2. Very high selectivity towards receptor overexpressing cells was confirmed by functional calcium flux

assay. The IC_{50} value for cytotoxicity by complex **34**, after light irradiation of A549 cells (LED array; 470 nm for 5 min; $6.9 \pm 0.9 \text{ J}\cdot\text{cm}^{-2}$), was $13.2 \pm 1.1 \mu\text{M}$. Interestingly, the compound did not show any dark cytotoxicity up to $300 \mu\text{M}$.

A different approach was utilised by the same research groups two years later, when a Ru(II) complex was conjugated to a protein carrier scaffold containing mitochondria targeting groups to yield complex **35** (see Figure 20 for Ru(II) complex structure).⁴⁷

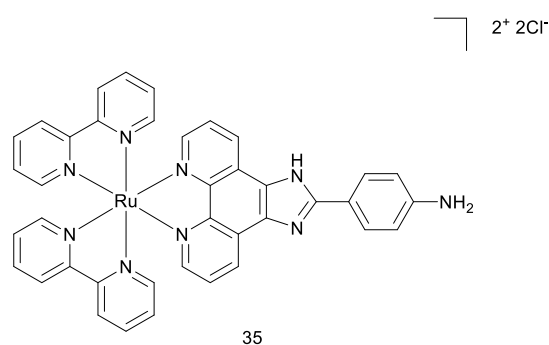


Figure 20. Chemical structure of Ru(II) complex that was conjugated to the protein carrier scaffold.

In this case, human serum albumin was the nanotransporter for the PS. Complex **35** was found to localise in mitochondria of HeLa cells within 240 min, thanks to the TPP-mitochondria targeting groups. An impressive PI value of 250 was determined for the conjugate after irradiation for 5 min (LED array; 470 nm, $\sim 20 \text{ mW}\cdot\text{cm}^{-2}$). Phototoxicity was also examined in A549, MCF-7 and CHO cell lines. IC_{50} values in the nanomolar range were obtained. Colony forming and cell proliferation assays revealed that complex **35** could relevantly reduce the colony growth of OCI-AML3 (myeloid leukemia cell line) (44% and 84.4%) and leukemic AE9a cell line (37% and 88%) when treated and irradiated for 2 min or 5 min, respectively. The conjugate reduced the healthy murine BM cells growth only by 10% and 28% upon light irradiation, clearly showing the specificity of the conjugate towards cancer cells. Since two photon absorbing PS offer deeper tissue penetration and better spatial resolution,⁴⁸ researchers

also looked at the TP properties of complex. Data obtained for **35** showed 5 times higher TP cross-section values for the conjugate than for the Ru(II) complex alone. This nanotransporter platform with enhanced cellular uptake, phototoxicity and specificity against a leukemic cell line is undoubtedly a successful solution for selective delivery of PDT PSs.

In 2018, a biological evaluation of the use of a Ru(II) complex conjugated with tamoxifen as a TP-PDT PS was published (see Figure 21 for structure).⁴⁹The Estrogen Receptor (ER) is highly overexpressed in breast cancer cells, making it a great target for anticancer therapy.⁵⁰ For over 30 years, tamoxifen has been an approved drug for the endocrine treatment of oestrogen-receptor-positive breast cancer.⁵¹

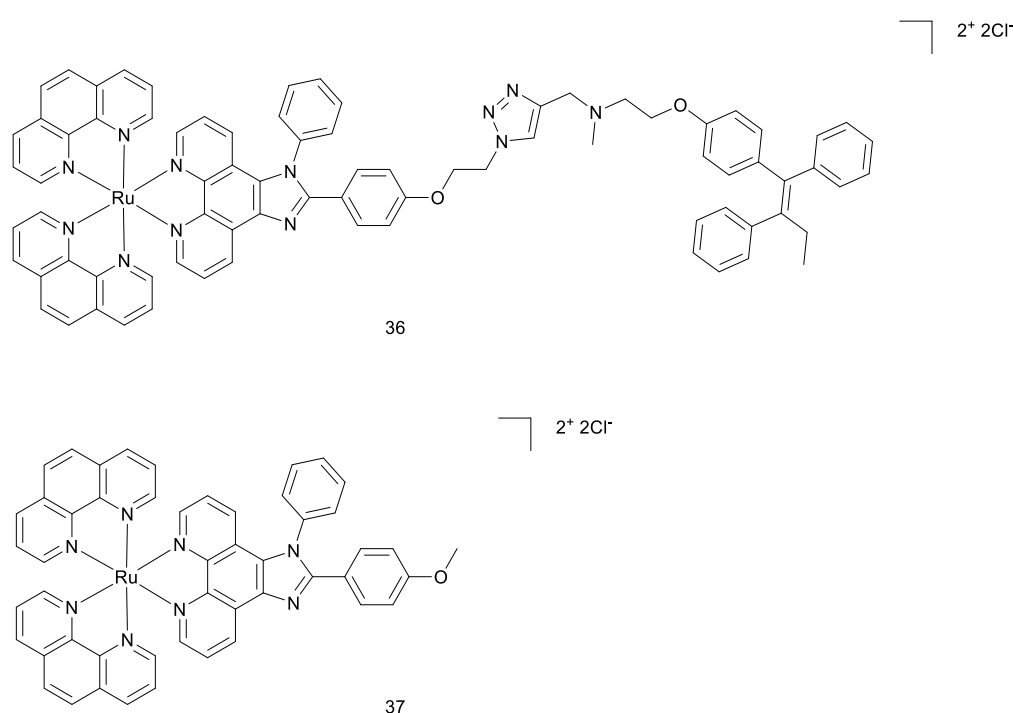


Figure 21. Chemical structure of complex **36** and **37**

The designed complex **36** demonstrated a large two-photon action cross section. The selectivity of complex **36** against cells overexpressing ER was confirmed by confocal microscopy in MCF-7 (ER positive), MDA-MB 231(ER negative) breast cancer cell lines as well as in HL-7702 (human liver) and COS-7 (monkey kidney) non-cancerous cell lines. Competitive assay with

17 β -estradiol (inhibitor of ER) showed that the uptake of complex **36** depended on interaction with the ER. Complex **36** as found to be non-toxic to cells in the dark. Upon light irradiation (450 nm, 12 J·cm⁻²) almost all MCF-7 cells treated with 16 μ M of complex **36** were killed (99%) in comparison to the control (complex **37** which is not conjugated to tamoxifen, Figure 21). Calcein AM and PI staining confirmed these cytotoxicity studies. Annexin V and PI assays showed that the treated and irradiated cells were in late apoptosis or necrosis. ROS generation of the complex **36** was verified by DCFH-DA. Moreover, upon addition of NaN₃ (singlet oxygen scavenger), only very weak fluorescence of the DCFH-DA was observed. Confocal microscopy studies showed that complex **36** localised in the lysosomes. Acridine orange (AO) staining demonstrated that upon light irradiation complex **36** caused lysosomes disruption. Very importantly, as a further confirmation of the mode of cell death action, complex **36** was found to generate singlet oxygen upon two-photon irradiation (fs, 820 nm) leading to cell death (calcein AM and PI staining).

Nanomaterials like carbon nanotubes or nanodots can also be used as carriers for different therapeutic drugs or diagnostic molecules.⁵² In 2015, Zhang *et al.* developed carbon nanotubes functionalised with TP-absorbing Ru(II) complexes for bimodal photothermal and photodynamic therapy.⁵³ Two years later, a full biological evaluation of carbon nanodots modified with ruthenium complex was published.⁵⁴ This study showed that the combination with Ru(II) polypyridyl complexes might improve their intercellular uptake as well as their features required for PDT. For the studies, two complexes were used: complex **38** alone and complex **38** conjugated to carbon nanodots (see Figure 22 for structure of Ru(II) complex). These compounds exhibited TP phosphorescence as well as higher ¹O₂ production in acidic environment than at neutral pH. Both compounds were taken up by A549 cells as well as normal LO2 cells, as confirmed by ICP-MS. The ruthenium content was estimated to be 10.6 \pm 0.3 ng/10⁶ cells for complex **38** and 16.2 \pm 0.4 ng/10⁶ for complex **38** with CDs in A549 cells and

$6.0 \pm 0.2 \text{ ng}/10^6$ and $6.4 \pm 0.2 \text{ ng}/10^6$ in LO2 cells, indicating that CDs might improve the uptake into the cancerous cells.

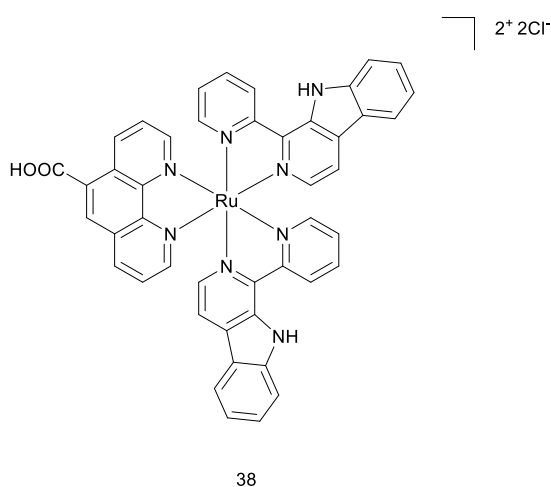


Figure 22. Chemical structure of complex **38**.

Cellular localisation performed by confocal laser microscopy showed that both compounds localised in the cytoplasm, specifically in the lysosomes. The cytotoxicity in the dark and after light irradiation (5 min; 450 nm; 20 mW·cm⁻²) was determined by cell proliferation assay (MTT) in A549 and LO2 cell lines. Complex **38** and complex **38** with CDs displayed high PI values (7.8 and 20.0 respectively) for the cancerous cell line compared to normal LO2 cells (>2.5 and 6.2). Complex **38** with CDs showed better results than the Ru (II) polypyridyl complex alone. To assess the type of mechanism causing cell death, the researchers performed multiple experiments. Cell morphology, annexin V staining, protein levels of caspase 3 and 7 as well as ATP levels in irradiated A549 cells confirmed that apoptosis was the main cause of cell death. This mechanism was likely triggered by the high amounts of ¹O₂ produced in lysosomes, which caused lysosomal permeability. This hypothesis was further confirmed with confocal microscopy and flow cytometry analysis. To further investigate if complex **38** and complex **38** with CDs would be efficacious in solid tumours, the researchers performed several experiments on MCTSs. Complex **38** and complex **38** with CDs were found to be able to penetrate 400 μm

A549 spheroids. Confocal microscopy studies with calcein AM staining corroborated that spheroids treated with the compounds in the dark condition were viable and that cell death was only limited to the irradiated area. Once again, complex **38** with CDs was found to be better than ruthenium complex alone. IC₅₀ values that were obtained on spheroids upon light irradiation (20 min; 810 nm; 100 mW; 80 mHz; 100 fs) were 12.0 μM for complex **38** (PI >8.3) and 2.2 μM for complex **38** with CDs (PI >45.5). Both compounds were successfully used as imaging agents in a living organism, namely zebrafish.

The PDT therapeutic potential of a PS is usually dependent on the oxygen levels in the targeted tissue since most of the PSs act with type II mechanism. In 2017, an interesting work on cyclometalated Ru(II) complexes, which act as Type I PSs, was published by Huang and co-workers.⁵⁵ The aim of this study was to design new PSs that could exhibit good PDT effects under hypoxia conditions. One of the designed PS contains a coumarin moiety (complex **39**) while the other one does not (complex **40**) (see Figure 23 for structures).

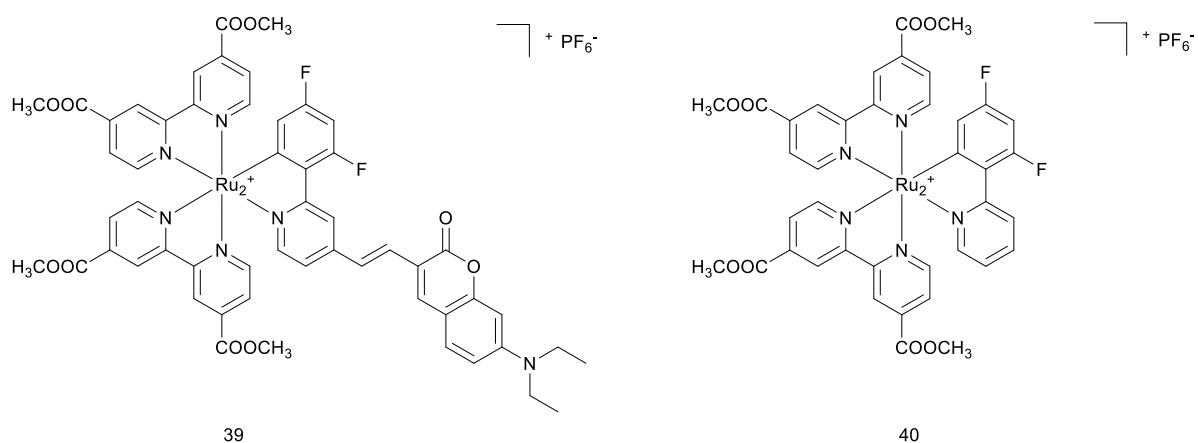


Figure 23. Chemical structure of complex **39** and complex **40**.

Coumarins have electron-donating and light-harvesting abilities. In both normoxia and hypoxia conditions, complex **39** showed low dark cytotoxicity and caused fast cell apoptosis after light irradiation in HeLa cells (white light; 400-800 nm, 30 mW cm⁻², 10 min). Cell death was confirmed with flow cytometry and fluorescent microscopy experiments. ROS generation

studies confirmed that complex **39** generated high level of ROS under hypoxic and normoxic conditions compared to complex **39** and Ru(byp)₃²⁺, which were used as a control. Highly-oxidative hydroxyl radicals were detected after light irradiation. Complex **40** was a far less effective PS compared to complex **39**. To further verify the effectiveness of complex **39**, *in vivo* studies (HeLa derived tumours in mice) were performed. Dosage of 5 mg kg⁻¹ of the PS caused tumour growth inhibition and serious tumour cell damage after irradiation (xenon lamp, 250 mW cm⁻², 15 min) (Figure 24). No side-effects during 14 days of treatment were observed. Histopathology as well as clearing time studies confirmed that complex **39** was not toxic for organs and was not accumulating in the body.

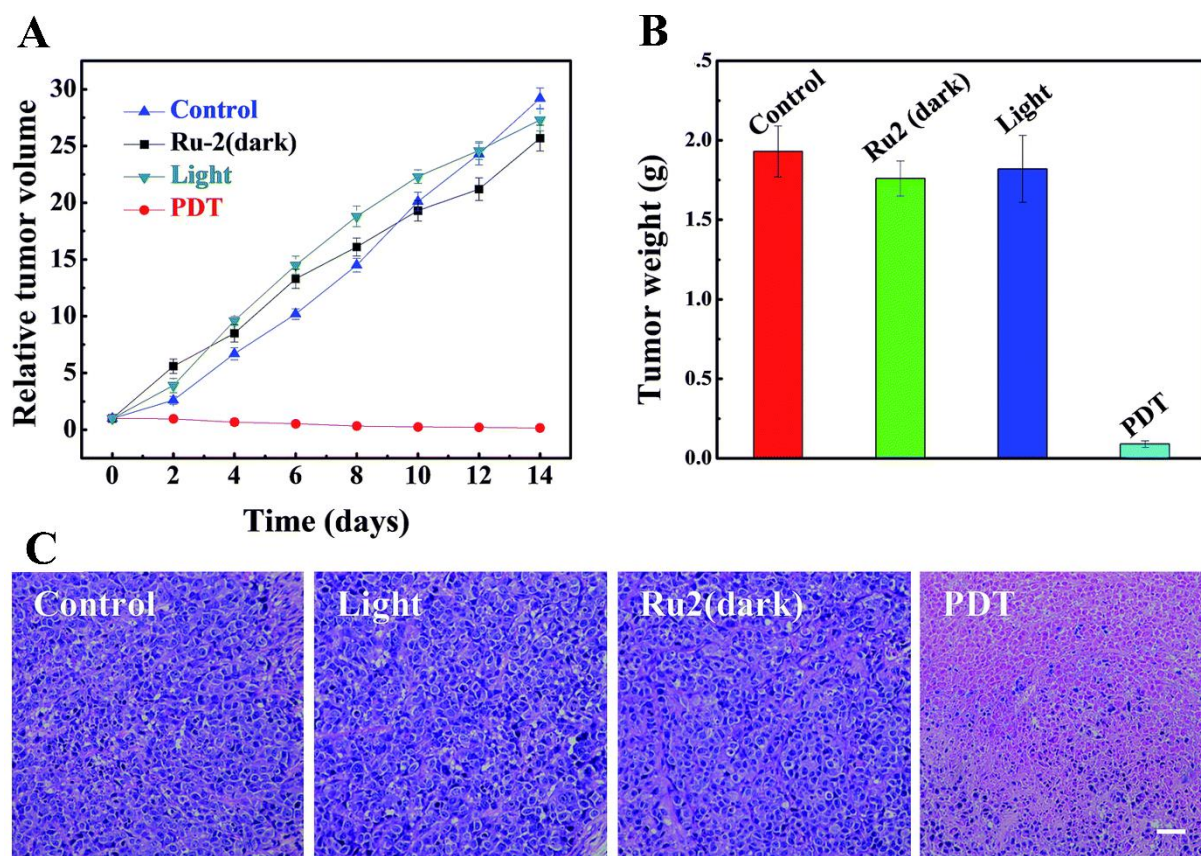


Figure 24.A. Relative tumor volume of different groups after various treatments. B Tumor weights of different groups after 14 days treatments. C. H&E stained tumor slices of different groups. Figure taken from ref.56 with permission from The Royal Society of Chemistry

Complex **39** can be considered as a promising PS that can work under hypoxic conditions.

A recent study published by Keyes and co-workers introduced a Ru(II) complex conjugated with nuclear localisation signal (NLS). Such signal sequence was derived from nuclear factor κ B (NF- κ B) (**41**, Figure 25),⁵⁶ a regulatory protein involved in the control of immune and inflammatory responses. Its activation is caused by different stimuli (e.g. growth factors, microbial components and stress agents)⁵⁷ and, mechanistically, requires nuclear translocation of the protein.

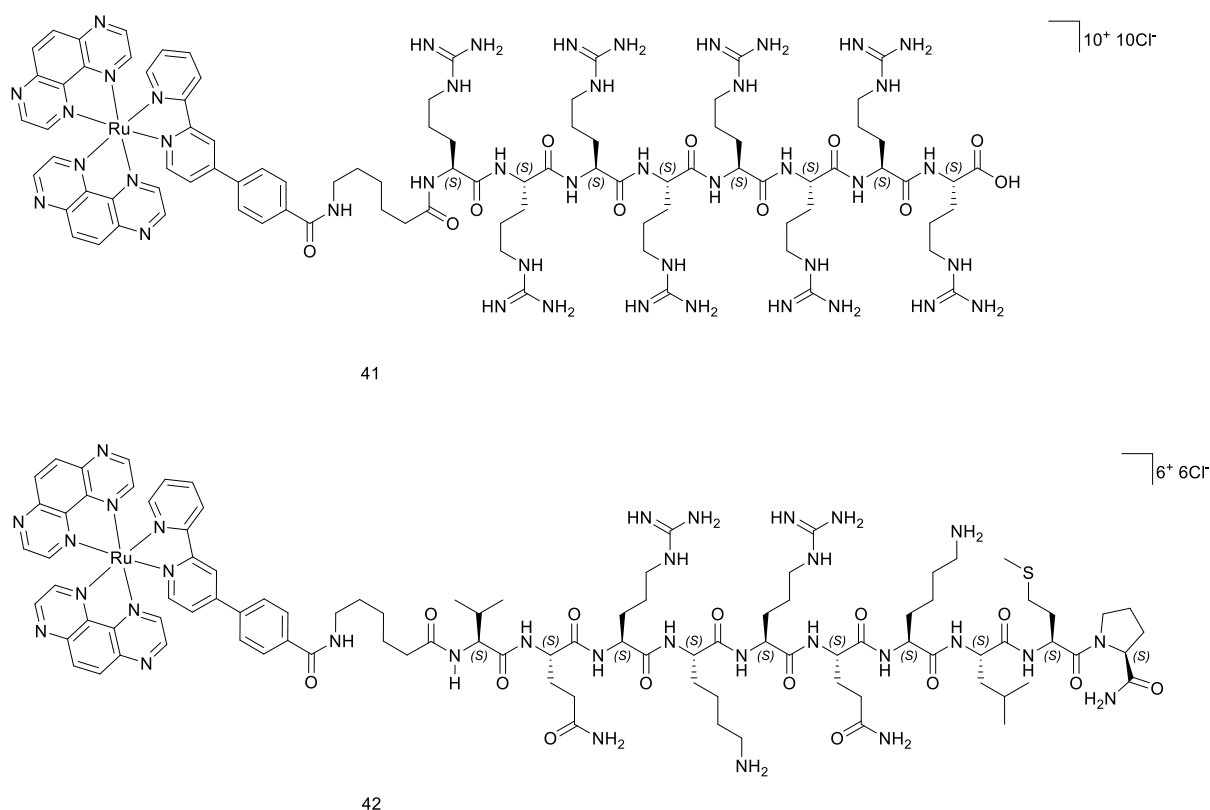


Figure 25. Chemical structure of complex **41** and complex **42**.

Complex **42** was found to localise in the cell nucleus of HeLa and CHO cell lines. On the contrary, complex **41** (Figure 18), which did not have a NLS but was conjugated with cell permeable peptide, remained in the cell cytoplasm. Complex **42** was found to be taken up by cells through an energy-dependend transport and to be not cytotoxic in the dark on HeLa cells

(IC₅₀ value of 83.4 μM). Light irradiation of treated cells at 440 nm (5 mW·cm⁻², 15 min) lowered the IC₅₀ value to 51.8 μM. Single cell irradiation experiments with cells treated with complex **42** or complex **41**, co-stained with nuclear dye DRAQ 7 (which only enters dead or permeabilised cells), demonstrated that the phototoxic effect of complex **42** was a result of its nuclear localisation. CT-DNA binding affinity studies along with photo-cleavage of pUC19 plasmid showed that complex **42** binds strongly DNA and is able to cleave it upon light irradiation. Tests with NaN₃ revealed that singlet oxygen was not responsible for DNA cleavage. It was proposed that either Type I mechanism of electron exchange or direct oxidative damage at the guanine bases was the cause of DNA damage.

Conclusions and outlook

In recent years, many Ru(II) polypyridyl complexes were studied as potential PDT PSs. Their strong absorption in the visible light, ability to produce singlet oxygen upon light irradiation, tunable photophysics and lack of cytotoxicity in the dark makes them very attractive candidates. Unfortunately, not many of them were analysed in-depth from a biological point of view. The mechanism of action of these compounds in living cells, a key factor in order to obtain their approval for a given indication, is very often still unknown or has only been superficially investigated. Worse, as shown in this Feature Article, there are only a few *in vivo* studies reported to date. However, despite this, one of such compounds has already entered clinical trial as a PDT PS against bladder cancer, clearly emphasising the potential of such complexes in this area of research. Further investigations in field of Ru(II) polypyridyl complexes as PDT PSs are of course needed. There is undoubtedly a necessity for new complexes that will exert their action by Type I mechanism. This is a crucial feature that will help fight very difficult to treat hypoxic tumours. During the designing process of the PDT PSs, adjustments will also need to be made in order to have PSs that can be activated at higher wavelengths. It is known that

longer wavelengths will allow for deeper penetration through tissue. As shown in this Feature Article, this can also be obtained by Ru(II) polypyridyl complexes that are activated by two photon irradiation. However, this technique will require further proofs of its suitability for in vivo models, since studies in this field of research, not only with Ru(II) complexes, are for the moment much too scarce. Overall, we are convinced that this field of research is still in its infancy and that very exciting results will be published in the near future.

Abbreviations

5-ALA- aminolevulinic acid

AO- Acridine orange

CDs- carbon nanodots

cw- Continuous Wave lasers

DCFH-DA- 2,7-dichlorodihydro-fluorescein diacetate

DHE- dihydroethidium

Dppz- dipyridophenazine

EPR- Electron paramagnetic resonance

ER- Endoplasmic reticulum/ Estrogen Receptor

EthD-1- ethidium homodimer-

FACS- Fluorescent activated Cell Sorting

GSH- glutathione

HR-CS AAS- High-Resolution Continuum Source Atomic Absorption Spectrometry

HSA- Human Serum Albumin

IC₅₀- Inhibitory Concentration 50

ICP-MS- Inductively Coupled Plasma Mass Spectrometry

IP-TT- 2-(2',2'':5'',2'''-terthiophene)-imidazo[4,5-f][1,10]phenanthroline

ISC- Intersystem crossing

LD₅₀- Lethal Dose 50

MB- Methylene Blue
MCTS- Multicellular Tumour Spheroids
MMP – mitochondrial membrane potential
MTD₅₀- Maximum Tolerated Dose 50
MTT- cell proliferation assay
NAC- N-acetylcysteine
NADPH- Nicotinamide Adenine Dinucleotide Phosphate
NLS- nuclear localisation signal
OP- One-photon
PDI- Photodynamic inactivation
Pdppz- ([2,3-h]dipyrido[3,2-a:2',3'-c]phenazine)
PDT- Photodynamic therapy
PI- Phototoxic index/ Propidium iodide
PS- Photosensitiser
ROS- Reactive oxygen species
TP- Two photon
TPA- two photon absorption
TPP- Trisphenylphospine
TP-PDT- Two photon photodynamic therapy

Cell lines mentioned

A549- pulmonary carcinoma
A549R- Cisplatin resistant cell line
AE9a- leukemia
BM- normal murine cells
CCD-1064sk- normal skin fibroblasts
CHO-K1/Ga- Chinese hamster ovarian epithelial cell line expressing Gα15 alpha subunit protein
CHO-K1/Ga15/SSTR2- Chinese hamster ovarian epithelial cell line expressing Gα15 alpha subunit protein and overexpressing somatostatin receptor 2

COS-7- monkey kidney cells
CRL5915- mesothelioma cell line
CT-26- wild type mouse colon carcinoma
CT-5.26- N-nitroso-N-methylurethane-induced mouse colon carcinoma
DG-75- Burkitt lymphoma
F98- rat glioblastoma
HCT116- colon cancer
HeLa- cervical cancer
HL-60- acute myeloid leukemia
HL-7702- human normal liver cells
HT1367- urothelial cell line
KV- multi-resistant human oral floor carcinoma
LO2- human fetal hepatocyte
MCF-7- mammary gland adenocarcinoma
MDA-MB 231- ER negative breast cancer
MRC-5- normal lung fibroblast
Mutu-1- Epstein-Barr virus-related Burkitt lymphoma
OCI-AML3- myeloid leukemia
One58- mesothelioma cell line
PC-3- prostate cancer
RPE-1 retina pigmented epithelium
SK-MEL-28- melanoma cell line
T24- urothelial cell line
U2OS- human bone osteosarcoma
U87 MG- human glioblastoma

Conflicts of interest

There are no conflicts to declare

Acknowledgments

This work was financially supported by an ERC Consolidator Grant PhotoMedMet to G.G. (GA 681679) and has received support under the program *Investissements d'Avenir* launched by the French Government and implemented by the ANR with the reference ANR-10-IDEX-0001-02 PSL (G.G.) and by grants from the Stiftung zur Krebsbekämpfung and the Stiftung für wissenschaftliche Forschung of the University of Zurich (S.F.) and by grants from the Institut Curie and the Centre National de la Recherche Scientifique (CNRS) (B.G.).

References

1. D. Kessel, *Photodiagn. Photodyn. Ther.*, 2004, **1**, 3-7.
2. X. Wen, Y. Li and M. R. Hamblin, *Photodiagn. Photodyn. Ther.*, 2017, **19**, 140-152.
3. S. Bonnet, *Dalton Trans.*, 2018, DOI: 10.1039/C8DT01585F.
4. J. Liu, C. Jin, B. Yuan, Y. Chen, X. Liu, L. Ji and H. Chao, *Chem. Comm.*, 2017, **53**, 9878-9881.
5. N. Malatesti, I. Munitic and I. Jurak, *Biophys. Rev.*, 2017, **9**, 149-168.
6. C. Mari, V. Pierroz, S. Ferrari and G. Gasser, *Chem. Sci.*, 2015, **6**, 2660-2686.
7. A. P. Castano, T. N. Demidova and M. R. Hamblin, *Photodiagn. Photodyn. Ther.*, 2004, **1**, 279-293.
8. J. Moan and K. Berg, *Photochem. Photobiol.*, 1991, **53**, 549-553.

9. P. Agostinis, K. Berg, K. A. Cengel, T. H. Foster, A. W. Girotti, S. O. Gollnick, S. M. Hahn, M. R. Hamblin, A. Juzeniene, D. Kessel, M. Korbelik, J. Moan, P. Mroz, D. Nowis, J. Piette, B. C. Wilson and J. Golab, *CA Cancer J. Clin.*, 2011, **61**, 250-281.
10. I. Yoon, J. Z. Li and Y. K. Shim, *Clin. Endosc.*, 2013, **46**, 7-23.
11. M. Triesscheijn, P. Baas, J. H. Schellens and F. A. Stewart, *Oncologist*, 2006, **11**, 1034-1044.
12. L. Zeng, P. Gupta, Y. Chen, E. Wang, L. Ji, H. Chao and Z.-S. Chen, *Chem. Soc. Rev.*, 2017, **46**, 5771-5804.
13. C. Mari and G. Gasser, *Chimia*, 2015, **69**, 176-181.
14. L. K. McKenzie, H. E. Bryant and J. A. Weinstein, *Coord. Chem. Rev.*, 2018, DOI: [10.1016/j.ccr.2018.03.020](https://doi.org/10.1016/j.ccr.2018.03.020).
15. X. Li, A. K. Gorle, M. K. Sundaraneedi, F. R. Keene and J. G. Collins, *Coord. Chem. Rev.*, 2017, DOI: [10.1016/j.ccr.2017.11.011](https://doi.org/10.1016/j.ccr.2017.11.011).
16. S. M. Cloonan, R. B. Elmes, M. Erby, S. A. Bright, F. E. Poynton, D. E. Nolan, S. J. Quinn, T. Gunnlaugsson and D. C. Williams, *J Med Chem*, 2015, **58**, 4494-4505.
17. Y. Arenas, S. Monro, G. Shi, A. Mandel, S. McFarland and L. Lilge, *Photodiagn. Photodyn. Ther.*, 2013, **10**, 615-625.
18. J. Fong, K. Kasimova, Y. Arenas, P. Kaspler, S. Lazic, A. Mandel and L. Lilge, *Photochem. Photobiol. Sci.*, 2015, **14**, 2014-2023.
19. O. Dömötör, C. G. Hartinger, A. K. Bytzeck, T. Kiss, B. K. Keppler and E. A. Enyedy, *JBIC J. Biol. Inorg. Chem.*, 2013, **18**, 9-17.
20. A. Levina, A. Mitra and P. A. Lay, *Metallomics*, 2009, **1**, 458-470.
21. S. Tortorella and T. C. Karagiannis, *J. Membr. Biol.*, 2014, **247**, 291-307.
22. S. V. Torti and F. M. Torti, *Crit. Rev. Oncog.*, 2013, **18**, 435-448.

23. P. Kaspler, S. Lazic, S. Forward, Y. Arenas, A. Mandel and L. Lilge, *Photochem. Photobiol. Sci.*, 2016, **15**, 481-495.
24. S. Kalinina, J. Brey Mayer, K. Reess, L. Lilge, A. Mandel and A. Ruck, *J. Biophotonics*, 2018, DOI: 10.1002/jbio.201800085, e201800085.
25. G. Ghosh, K. L. Colón, A. Fuller, T. Sainuddin, E. Bradner, J. McCain, S. M. A. Monro, H. Yin, M. W. Hetu, C. G. Cameron and S. A. McFarland, *Inorg. Chem.*, 2018, **57**, 7694-7712.
26. Y.-L. P. Ow, D. R. Green, Z. Hao and T. W. Mak, *Nat. Rev. Mol. Cell Biol.*, 2008, **9**, 532.
27. V. Ramu, S. Aute, N. Taye, R. Guha, M. G. Walker, D. Mogare, A. Parulekar, J. A. Thomas, S. Chattopadhyay and A. Das, *Dalton Trans*, 2017, **46**, 6634-6644.
28. J. Hess, H. Huang, A. Kaiser, V. Pierroz, O. Blacque, H. Chao and G. Gasser, *Chem. - Eur.J.*, 2017, **23**, 9888-9896.
29. J. Liu, Y. Chen, G. Li, P. Zhang, C. Jin, L. Zeng, L. Ji and H. Chao, *Biomaterials*, 2015, **56**, 140-153.
30. C. W. T. Leung, Y. Hong, S. Chen, E. Zhao, J. W. Y. Lam and B. Z. Tang, *J. Am. Chem. Soc.*, 2013, **135**, 62-65.
31. L. Zeng, S. Kuang, G. Li, C. Jin, L. Ji and H. Chao, *Chem. Comm.*, 2017, **53**, 1977-1980.
32. Z. Zhou, J. Liu, T. W. Rees, H. Wang, X. Li, H. Chao and P. J. Stang, *Proc. Nat. Acad. Sci.U.S.A.*, 2018, **115**, 5664-5669.
33. A. M. Angeles-Boza, P. M. Bradley, P. K. Fu, S. E. Wicke, J. Bacsá, K. R. Dunbar and C. Turro, *Inorg Chem*, 2004, **43**, 8510-8519.
34. A. J. McConnell, H. Song and J. K. Barton, *Inorg. Chem.*, 2013, **52**, 10131-10136.

35. C. Mari, V. Pierroz, R. Rubbiani, M. Patra, J. Hess, B. Spingler, L. Oehninger, J. Schur, I. Ott, L. Salassa, S. Ferrari and G. Gasser, *Chem. - Eur. J.*, 2014, **20**, 14421-14436.
36. A. E. Friedman, J. C. Chambron, J. P. Sauvage, N. J. Turro and J. K. Barton, *J. Am. Chem. Soc.*, 1990, **112**, 4960-4962.
37. V. Pierroz, R. Rubbiani, C. Gentili, M. Patra, C. Mari, G. Gasser and S. Ferrari, *Chem Sci*, 2016, **7**, 6115-6124.
38. A. J. McConnell, M. H. Lim, E. D. Olmon, H. Song, E. E. Dervan and J. K. Barton, *Inorg. Chem.*, 2012, **51**, 12511-12520.
39. M. Dickerson, Y. Sun, B. Howerton and E. C. Glazer, *Inorg Chem*, 2014, **53**, 10370-10377.
40. C. Mari, R. Rubbiani and G. Gasser, *Inorg. Chim. Acta*, 2017, **454**, 21-26.
41. H. Huang, B. Yu, P. Zhang, J. Huang, Y. Chen, G. Gasser, L. Ji and H. Chao, *Angew. Chem., Int. Ed. Engl.*, 2015, **54**, 14049-14052.
42. G. L. Zwicke, G. A. Mansoori and C. J. Jeffery, *Nano Rev.*, 2012, **3**.
43. C. M. A. Alonso, A. Palumbo, A. J. Bullous, F. Pretto, D. Neri and R. W. Boyle, *Bioconjugate Chem.*, 2010, **21**, 302-313.
44. T. Wang, N. Zabarska, Y. Wu, M. Lamla, S. Fischer, K. Monczak, D. Y. W. Ng, S. Rau and T. Weil, *Chem. Comm.*, 2015, **51**, 12552-12555.
45. P. Rorsman and M. O. Huising, *Nat. Rev. Endocrinol.*, 2018, DOI: 10.1038/s41574-018-0020-6.
46. L. C. Sun and D. H. Coy, *Current drug delivery*, 2011, **8**, 2-10.
47. S. Chakraborty, B. K. Agrawalla, A. Stumper, N. M. Vegi, S. Fischer, C. Reichardt, M. Kogler, B. Dietzek, M. Feuring-Buske, C. Buske, S. Rau and T. Weil, *J Am Chem Soc*, 2017, **139**, 2512-2519.

48. G. B. Magali, M. Youssef, R. Cédric, B. David, B. Ilaria, M. Marie, V. Ophélie, M. Olivier, B. D. Mireille, M. Alain, G. Marcel, D. Jean-Olivier and R. Laurence, *Angew. Chem., Int. Ed. Engl.*, 2011, **123**, 11627-11631.
49. X. Zhao, M. Li, W. Sun, J. Fan, J. Du and X. Peng, *Chem. Comm.*, 2018, **54**, 7038-7041.
50. S. I. Hayashi, H. Eguchi, K. Tanimoto, T. Yoshida, Y. Omoto, A. Inoue, N. Yoshida and Y. Yamaguchi, *Endocr. - Relat. Cancer*, 2003, **10**, 193-202.
51. V. C. Jordan, *Nat. Rev. Drug Discovery*, 2003, **2**, 205.
52. L. Muzi, C. Menard-Moyon, J. Russier, J. Li, C. F. Chin, W. H. Ang, G. Pastorin, G. Risuleo and A. Bianco, *Nanoscale*, 2015, **7**, 5383-5394.
53. P. Zhang, H. Huang, J. Huang, H. Chen, J. Wang, K. Qiu, D. Zhao, L. Ji and H. Chao, *ACS Appl. Mater. Inter.*, 2015, **7**, 23278-23290.
54. D. Y. Zhang, Y. Zheng, H. Zhang, L. He, C. P. Tan, J. H. Sun, W. Zhang, X. Peng, Q. Zhan, L. N. Ji and Z. W. Mao, *Nanoscale*, 2017, DOI: 10.1039/c7nr05349e.
55. Z. Lv, H. Wei, Q. Li, X. Su, S.-J. Liu, K. Y. Zhang, W. Lv, Q. Zhao, X. Li and W. Huang, *Chem. Sci.*, 2017, DOI: 10.1039/C7SC03765A.
56. C. S. Burke, A. Byrne and T. E. Keyes, *J. Am. Chem. Soc.*, 2018, DOI: 10.1021/jacs.8b02711.
57. T. Liu, L. Zhang, D. Joo and S.-C. Sun, *Signal Transduction And Targeted Ther.*, 2017, **2**, 17023.

Chapter 2- Evaluation of the Potential of Cobalamin Derivatives Bearing Ru(II) Polypyridyl Complexes as Photosensitisers for Photodynamic Therapy

*Marta Jakubaszek,^{a,b,#} Jeremie Rossier,^{c,#} Johannes Karges,^{a,#} Joachim Delasoie,^{c,#} Bruno
Goud,^b Gilles Gasser,^{a,*} and Fabio Zobi^{c,*}*

^a Chimie ParisTech, PSL University, CNRS, Institute of Chemistry for Life and Health Sciences, Laboratory for Inorganic Chemical Biology, F-75005 Paris, France, gilles.gasser@chimieparistech.psl.eu

^b Institut Curie, PSL University, CNRS UMR 144, Paris, France.

^c Chemistry Department, University of Fribourg, CH-1700 Fribourg, Switzerland, fabio.zobi@unifr.ch

* Corresponding authors: Email: gilles.gasser@chimie-paristech.fr; fabio.zobi@unifr.ch

these authors have contributed equally to the work.

This chapter has been published in *Helvetica Chimica Acta* 2019, **102** (7), e1900104

Reproduced by permission of Wiley-VHCA AG, Zurich, Switzerland

(<https://onlinelibrary.wiley.com/doi/full/10.1002/hlca.201900104>)

Contribution to the publication:

Marta Jakubaszek performed the cytotoxicity studies as well as the fluorescent microscopy experiments. She wrote the first draft of this publication.

Marta Jakubaszek



19.05.2020

Gilles Gasser



Abstract:

The current photosensitizers (PSs) for photodynamic therapy (PDT) lack selectivity for cancer cells. To tackle this drawback, in view of selective cancer delivery, we envisioned conjugating two ruthenium polypyridyl complexes to vitamin B₁₂ (Cobalamin, Cbl) to take advantage of the solubility and active uptake of the latter. Ultimately, our results showed that the transcobalamin pathway is unlikely involved for the delivery of these ruthenium-based PDT PSs, emphasizing the difficulty in successfully delivering metal complexes to cancer cells.

Keywords: bioinorganic chemistry • cobalamine • medicinal inorganic chemistry • photodynamic therapy • ruthenium polypyridyl complexes

Introduction

Photodynamic therapy (PDT) is an approved medical technique that relies on the use of a photosensitizer (PS) to ultimately generate reactive oxygen species (ROS) or radicals that can trigger cell death.^[1] The interest of this method is its spatio-temporal control. The PS is activated only when and where the physician applies light. In brief, upon irradiation at a specific, defined wavelength, an electron of the ground state of the PS reaches a singlet excited state ($^1\text{PS}^*$), which then reaches a triplet state ($^3\text{PS}^*$) through an intersystem crossing (ISC) event.^[2] The PDT process can then rely on two types of mechanism: 1) in Type I, an electron or proton transfer from the species $^3\text{PS}^*$ to a biological substrate that generates radicals which can further react with molecular oxygen and form superoxides, hydroxyl radicals or peroxides or 2) in Type II, an energy transfer from $^3\text{PS}^*$ to molecular oxygen in its ground triplet state ($^3\text{O}_2$) to generate the highly toxic singlet oxygen ($^1\text{O}_2$).^[3]

The currently used PSs in the clinic are mainly based on cyclic tetrapyrrolic scaffolds (chlorins, phthalocyanines and porphyrines ^[4]). Their main drawbacks are a lack of selectivity towards cancers cells, a low water solubility, an important photobleaching and, sometimes, serious problems of photosensitivity for the treated patients.^[5] Ru(II) polypyridyl complexes were found to be an interesting alternative to the current PDT PSs. Although the use of such compounds as PDT PS against cancer is relatively recent, the results are spectacular with one of such compounds, TLD-1433, having recently completed phase I clinical trial against bladder cancer.^[2, 6-10] We note that to reach the therapeutic window for PDT treatment (~ 600 to 800 nm), some Ru(II) polypyridyl complexes were found to be good PSs for two-photon PDT ^[11-13], further illustrating the versatility of ruthenium in medicinal chemistry. To further improve the properties of the Ru(II)-based PDT PSs, it is also possible to conjugate them with targeting moieties, or to associate them in non-covalent manner with serum or membrane proteins.^[14-16]

Another possible strategy envisioned by our group and by others is the encapsulation of the Ru(II)-based PDT agents in polymers or their functionalization to nanoparticles.^[17-19]

Vitamin B₁₂ is a vital nutrient that is characterized by a low bioavailability. Because it is playing an essential role in cell proliferation, it is crucial for fast growing cells.^[20] This interesting characteristic was already used in several studies^[21] in which cobalamin was used as a targeting moiety for metal complexes to direct them towards fast dividing malignant cells.^[22-24] With this in mind, in this work, we aimed at developing a system for improving the solubility and uptake of Ru(II)-based PSs into cancer cells. Our hope was that the resulting conjugates would have a good water solubility and an active cellular uptake.^[25, 26] Indeed, in the systemic circulation, Cbl is brought to the cells by a carrier protein named transcobalamin and ultimately taken up following a receptor-mediated endocytosis.^[13, 27] Therefore, two trisbipyridyl ruthenium(II) complexes were conjugated to vitamin B₁₂ (Cobalamin, Cbl). After characterization, the resulting conjugates were tested in vitro to evaluate their efficiency in PDT as well as their cellular uptake. This data were compared with the Ru(II) complexes themselves.

Results and Discussion

Compounds design and chemistry

As a cofactor, inside cells, cob(III)alamin is ultimately reduced to cob(I)alamin and during this process, the β -upper ligand of cobalamin becomes labile.^[28] This feature has been explored in the past to attach drugs/drug candidates at this position.^[29] However, chemical modifications at the β -position were for a long time restrained by synthetic constraints as well as the instability of the resulting derivatives.^[30] Recent advances in organometallic chemistry of cobalamin have allowed to generate stable derivatives and to rethink this prodrug approach.^[31, 32] As a prerequisite, the chosen compounds should bear an accessible alkyne group which can be directly attached to the cobalt center of Cbl following a copper-mediated reaction as described

by Gryko and coworkers.^[33] Two bispyridyl ruthenium(II) complexes were chosen and adapted to the need of this coupling reaction: a cytotoxic compound, which was previously reported to accumulate at the plasma membranes of ovarian carcinoma cell line A2780, $[\text{Ru}(\text{NNbpy})_3]^{2+}$ (where NNbpy = diethylamino-2,2'-bipyridine) and the standard $[\text{Ru}(\text{bpy})_3]^{2+}$ (bpy: 2,2'-bipyridine).^[34] These two compounds were synthesized asymmetrically in order to substitute one of the original bipyridyl ligands by a 4-ethynyl-2,2'-bipyridine ligand ($\text{C}\equiv\text{Cbpy}$), as previously reported to give $[\text{Ru}(\text{NNbpy})_2(\text{C}\equiv\text{Cbpy})]^{2+}$ (**1**) and $[\text{Ru}(\text{bpy})_2(\text{C}\equiv\text{Cbpy})]^{2+}$ (**2**) as shown in Figure 1.^[35, 36]

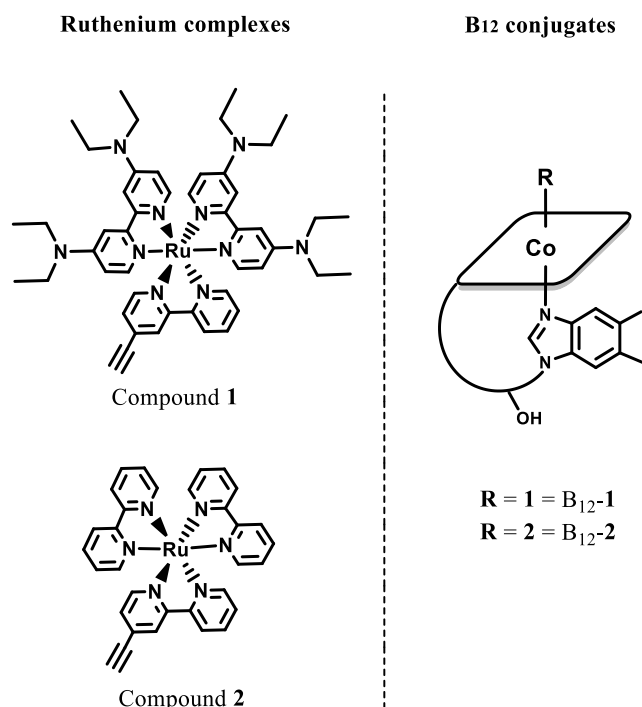


Figure 1. Ruthenium complexes and B₁₂ conjugates used in this study.

The complexes **1** and **2** were then coupled to cobalamin in good yield by adapting Gryko's procedure^[31] to give two B₁₂ derivatives: B₁₂-1 and B₁₂-2 (see Figure 1). The compounds were unambiguously characterized by ¹H NMR and HR-ESI-MS and their purity verified by HPLC (see ESI). Very importantly, all compounds were found stable in water for at least 7 days as well as light stable over the same time period.

Photophysical properties

With both compounds in hand, we investigated their photophysical properties to evaluate their potential as PDT PSs (Tables 1 and 2). As a first experiment, the absorption of the compounds was measured in MeOH and compared with their B₁₂-conjugates (Image 2). Since the necessary ³MLCT band centered at 450 nm did not significantly change, we assume that the photophysical properties of the conjugate should not be influenced through the conjugation. As a second experiment, the emission of the compounds was investigated upon excitation at 450 nm in CH₃CN. Compound **2** has an emission maximum at 635 nm and a luminescence quantum yield of 0.02. These values are in the same range as other Ru(II) polypyridine complexes.^[37, 38] However, the emission of **1** was barely measurable with the apparatus in our laboratory. As a third experiment, the luminescence lifetimes were determined and their influence on the presence of air investigated. Due to the very low emission of complex **1**, its lifetime was not detected. This contrasts with the lifetime of compound **2** which was found to be in the same range than other Ru(II) polypyridyl complexes.^[37, 38] Importantly, the excited state lifetime changed drastically upon the presence of oxygen indicating that ³O₂ is able to interact with the excited state of **2**.

Table 1. Photophysical properties of **1** and **2**. λ_{abs} = absorption maximum in MeOH, λ_{em} = emission maximum in CH₃CN, Φ_{em} = luminescence quantum yield in CH₃CN, τ = luminescence lifetime, n.d. = not detectable.

Compound	λ_{abs} / nm	λ_{em} / nm	Φ_{em}	τ / ns	
				air	degassed
1	Column 2	695	>0.001	n.d.	n.d.
2	Column 2	635	0.021	226	679

After showing that our compounds are able to interact with oxygen, we investigated quantitatively the production of singlet oxygen ($^1\text{O}_2$) upon light exposure. This is a crucial factor for a PS since $^1\text{O}_2$ is known to be the major active species for most applied PSs in the clinics. For this purpose, two different methods have been used: 1) direct by measurement of the phosphorescence of $^1\text{O}_2$, 2) indirect by measurement of the change in absorbance of a reporter molecule.^[39] Worthy of note, only singlet oxygen quantum yields over 20% can be detected via the direct method with our apparatus. The results shown in Table 2 demonstrate that compounds **1** and **2** are producing $^1\text{O}_2$ only poorly. This could be explained by the weak population of the excited state indicated by the poor luminescence properties of the complexes (Table 1) which is a necessary requirement for the production of $^1\text{O}_2$.

Table 2. Singlet oxygen quantum yields in CH_3CN and aqueous solution determined at 450 nm. Average of three independent measurements.

Compound	Indirect 450	Indirect 450
	nm CH_3CN	nm PBS
1	8 %	3 %
2	19 %	7 %

Evaluation of PDT activity

Dark and light cytotoxicity of the complexes was investigated in the cervical cancer cell line (HeLa) and non-cancerous retina pigmented epithelium (RPE-1) cell lines. It was expected that the B12 derivatives would be more toxic to both cell lines due to the presence of B₁₂ that should increase their uptake. Surprisingly, compound **2** and its derivative B₁₂-**2** showed no cytotoxicity both in the dark or upon light irradiation. On the contrary, complex **1** was found to be cytotoxic

in the dark (IC_{50} : $9.33 \pm 1.43 \mu\text{M}$ and $6.08 \pm 0.085 \mu\text{M}$ on HeLa and RPE-1 cell lines, respectively). Irradiation at 480 nm (10 min; $3.21 \text{ J}\cdot\text{cm}^{-2}$) did not significantly increase its toxicity. Photoindex (PI) values (IC_{50} dark/ IC_{50} light) of 1.3 and 1.1 for HeLa and RPE-1 cell lines, respectively, were determined. To our surprise, the **B₁₂-1** complex was found to be not toxic in the dark. Light irradiation of cells treated with **B₁₂-1** did not caused toxicity in the RPE-1 cell line or in the HeLa cell line (see results in Table 1). Overall, these studies did not show any correlation between the presence of vit B₁₂ and (photo-)toxicity, clearly emphasizing that the coupling of Cbl was not helping in the delivery of our Ru(II) complexes. An obvious reason could be the bulkiness of the Ru(II) complexes. In a more general context, these disappointing results highlight the difficulty in specifically delivering metal complexes to cancer cells.

Table 3. IC_{50} values of complexes incubated with RPE-1 or HeLa cell line in the dark and upon light irradiation (in μM).

Compound	RPE-1			HeLa		
	Dark	Light	PI value	Dark	Light	PI value
1	6.08 0.085	± 5.43 0.060	± 1.1	9.33 ± 1.43	7.14 ± 0.13	1.3
B₁₂-1	>100	>100	-	>100	>100	-
2	>100	>100	-	>100	>100	-
B₁₂-2	>50	>50	-	>50	>50	-

Ru(II) polypyridyl complexes are usually known to be highly luminescent.^[40] We have therefore used this characteristic to further investigate the cellular biodistribution of the complexes in cells, and confocal microscopy studies were performed. Disappointingly, these two Ru(II) complexes as well as their B₁₂ derivatives showed very weak or no luminescent signal in treated HeLa cells (see Fig S13). For this reason, cellular localisation could not be precisely determined, although localization in the cytoplasm could be faintly observed.

Conclusions

In this article, we have presented the synthesis and characterization of the trisbipyridyl Ru(II) complexes **1** and **2** conjugated with vitamin B₁₂. The resulting organometallic complexes were then evaluated as potential photosensitisers for PDT. The conjugation with cobalamin increased the water solubility of the compounds, especially for complex **1** which was found to be extremely poorly soluble in this solvent. Unfortunately, our ruthenium-containing conjugates were found to not have any significant phototoxic activity to the cell lines studied in this work. In addition, we could not precisely determine the cellular localization of the complexes by confocal microscopy due to either the lack of luminescence of the Ru(II) complexes or due to the very poor uptake of the compounds. Overall, this study suggests that the transcobalamin pathway is unlikely involved for the uptake of our Ru(II) conjugates. It would be interesting to assess if this is true with other Ru(II) polypyridyl complexes. More generally, this study highlights the difficulty in bringing selectively metal-based PDT PSs and, more generally, metal complexes to cancer cells.

Experimental Section

General experimental details

All chemicals were purchased from Sigma-Aldrich (St Louis, MO) and used without further purification. The ligand 4-ethynyl-2,2'-bipyridine was synthesized according to a published procedure as well as the Ru complexes **1** and **2** and the B₁₂ derivative B₁₂-**1**.^{15,16} HPLC analyses were performed on a Merck-Hitachi L7000. The analytical separations were conducted on a Macherey-Nagel Nucleodur PolarTec column (5 μm particle size, 110 Å pore size, 250 × 3 mm). The preparative separations were conducted on a Macherey–Nagel Nucleodur C18 HTec column (5 μm particle size, 110 Å pore size, 250 × 21 mm). HPLC solvents were water (A) and methanol (B). The compounds were separated using the following gradient: 0–5 min (75% solvent A), 5–35 (75% solvent A → 0% solvent A), 35–45 min (100% solvent B). The flow rate was set to 0.5 ml*min⁻¹ for analytical separations and 5 ml*min⁻¹ for the preparative ones. The eluting bands were detected at 320 nm. High resolution ESI-MS was performed on a Bruker FTMS 4.7-T Apex II (positive mode) and the UV/Vis spectra recorded on a Jasco V-730. NMR analyses were recorded on a Bruker Avance III 500 MHz. The corresponding ¹H and ¹³C chemical shifts are reported relative to residual solvent protons and carbons.

Synthesis and characterization of the derivative B₁₂-2

The following procedure was adapted from the literature to achieve the synthesis of the B₁₂ derivatives.¹³ A mixture of cyanocobalamin (20 mg, 0.013 mmol, 1 eq.), CuAcO (2.3 mg, 0.0013 mmol, 0.1 eq.) and the alkynes **2** (0.07 mmol, 5 eq.) in DMA (3.5 ml) was stirred until dissolution. DBU (0.01 ml, 0.7 mmol, 5 eq.) was added and the solution was allowed to react at room temperature for 4h. The respective crudes were precipitated by dropwise addition to a

stirred solution of diethyl ether/CH₂Cl₂ (50 ml, 1:1). The residue was dissolved in a mixture of CH₃OH and water (2 ml, 1:1), filtered again and purified by preparative HPLC. The eluting band containing the desired product was isolated and lyophilized.

B₁₂-2: Isolated as a brownish powder, yield 19.8 mg (70%). **¹H NMR** (500 MHz, MeOD-[d₄]): δ = 8.53 (t, J = 9.5 Hz, 4H), 8.25 (t, J = 9.37 Hz, 1H), 8.09-7.99 (m, 5H), 7.85-7.69 (m, 6H), 7.54 (dd, J = 6.0, 2.37 Hz, 1H), 7.40-7.32 (m, 5H), 7.29 (s, 1H), 7.14 (s, 1H), 6.82-6.76 (m, 1H), 6.50 (s, 1H), 6.37 (d, J = 3.2 Hz, 1H), 6.05 (d, J = 3.8 Hz, 1H), 4.38-4.23 (m, 2H), 4.13-4.07 (m, 1H), 3.95 (dd, J = 13.0, 2.45 Hz, 1H), 3.78 (dd, J = 13.0, 4.0 Hz, 1H), 3.62 (d, J = 14.3 Hz, 1H), 3.43-3.35 (m, 1H), 3.32-3.25 (m, 2H), 2.99 (dd, J = 9.0, 5.3 Hz, 1H), 2.79-2.32 (m, 18H), 2.27 (s, 6H), 2.14 (t, J = 12.0, 1H), 2.09-1.93 (m, 6H), 1.89-1.77 (m, 5H), 1.45 (d, J = 4.2 Hz, 3H), 1.40 (d, J = 3.4 Hz, 3H), 1.34 (s, 3H), 1.27 (d, J = 6.3 Hz, 3H), 1.18 (s, 3H), 1.15 (s, 3H), 1.13-1.02 (m, 2H), 0.52 (s, 3H) ppm; **UV/Vis** spectrum in methanol solution: λ_{\max} = 330, 363, 460, 519, 552; **HPLC**: t_R = 14.5 min; **HR-ESI-MS** (ESI⁺): [M]²⁺ = 960.8315, calculated for C₉₄H₁₁₁Co₁₁N₁₉O₁₄P₁Ru₁ = 960.8342.

Cell culture

HeLa cell line was cultured in DMEM (Gibco, Life Technologies, USA) supplemented with 10% of fetal calf serum (Gibco). RPE-1 cell were cultured in DMEM/F-12 (Gibco) supplemented with 10% of fetal calf serum. Cell lines were complemented with 100 U/ml penicillin-streptomycin mixture (Gibco), and maintained in humidified atmosphere at 37°C and 5% of CO₂.

Cytotoxicity studies

Dark and light cytotoxicity of the Ru(II) complexes and Ru(II) conjugates was assessed by fluorometric cell viability assay using resazurin (ACROS Organics). For light and dark cytotoxicity, HeLa and RPE-1 cells were seeded in triplicates in 96 well plates at a density of 4000 cells per well in 100 μ l, 24 h prior to treatment. Cells were then treated with increasing concentration of compounds for 48 h. After that time medium was replaced by fresh complete medium. For light cytotoxicity experiments HeLa and RPE-1 cells were exposed to 480 nm light for 10 min in a 96-well plate using a LUMOS-BIO photoreactor (Atlas Photonics). Each well was individually illuminated with a 5 lm LED at constant current (light dose 3.21 J cm⁻²). After 44h in the incubator medium was replaced by fresh complete medium containing resazurin (0.2 mg ml⁻¹ final concentration). After 4 h incubation at 37°C, fluorescence signal of resorufin product was read by SpectraMax M5 microplate reader (ex: 540 nm; em: 590 nm). IC₅₀ values were calculated using GraphPad Prism software.

Localisation studies

Cellular localisation of the Ru(II) compounds was assessed by fluorescent microscopy. HeLa cells were grown on the 12 mm Menzel–Gläser coverslips in 2 ml of complete medium at a density of 1.3 x 10⁵ cells per ml. Cells were then treated with the compounds (IC₅₀ concentration in the dark) for 2 h, with NucBlue (2 drops per 1 ml of media) for the last 25 min and with 100 nm Mitotracker Green FM for the last 15 min. HeLa cells were then fixed with paraformaldehyde solution in PBS (4%) and mounted on glass slides using Prolong Glass Antifade Mountant. Leica SP8 confocal microscope was used to analyse the samples. Ru compounds were excited at 488 nm and emission above 650nm was recorded. Images were

recorded in Cellular and Molecular Imaging Technical Platform, INSERM UMS 025 - CNRS UMS 3612, Faculty of Pharmacy of Paris, Paris Descartes University, Paris, France.

Acknowledgements

We gratefully acknowledge financial support from the ERC (Consolidator Grant PhotoMedMet (GA 681679) to G.G.) and the Swiss National Science Foundation (Grant# PP00P2_170589).

This work has received support under the program «Investissements d’Avenir » launched by the French Government and implemented by the ANR with the reference ANR-10-IDEX-0001-02 PSL (G.G.). We thank Dr. Philippe Goldner for access to a state-of-the-art laser apparatus.

Author Contribution Statement

M. J, J. R., J. K. and J. D. performed the experiments, analyzed the data and wrote the paper. B. G., F. Z and G. G. conceived and designed the experiments.

References

- [1] I. J. MacDonald, T. J. Dougherty, ‘Basic principles of photodynamic therapy’, *J Porphyr Phthalocya* **2001**, *5*, 105-129.
- [2] C. Mari, V. Pierroz, S. Ferrari, G. Gasser, ‘Combination of Ru(II) complexes and light: new frontiers in cancer therapy’, *Chem Sci* **2015**, *6*, 2660-2686.
- [3] C. Lottner, K. C. Bart, G. Bernhardt, H. Brunner, ‘Hematoporphyrin-derived soluble porphyrin-platinum conjugates with combined cytotoxic and phototoxic antitumor activity’, *J Med Chem* **2002**, *45*, 2064-2078.
- [4] P. Agostinis, K. Berg, K. A. Cengel, T. H. Foster, A. W. Girotti, S. O. Gollnick, S. M. Hahn, M. R. Hamblin, A. Juzeniene, D. Kessel, M. Korbelik, J. Moan, P. Mroz, D.

- Nowis, J. Piette, B. C. Wilson, J. Golab, 'Photodynamic therapy of cancer: an update', *CA Cancer J Clin* **2011**, *61*, 250-281.
- [5] I. Yoon, J. Z. Li, Y. K. Shim, 'Advance in photosensitizers and light delivery for photodynamic therapy', *Clin Endosc* **2013**, *46*, 7-23.
- [6] M. Jakubaszek, B. Goud, S. Ferrari, G. Gasser, 'Mechanisms of action of Ru(II) polypyridyl complexes in living cells upon light irradiation', *Chem Commun (Camb)* **2018**, *54*, 13040-13059.
- [7] F. Heinemann, J. Karges, G. Gasser, 'Critical Overview of the Use of Ru(II) Polypyridyl Complexes as Photosensitizers in One-Photon and Two-Photon Photodynamic Therapy', *Acc Chem Res* **2017**, *50*, 2727-2736.
- [8] L. Zeng, P. Gupta, Y. Chen, E. Wang, L. Ji, H. Chao, Z. S. Chen, 'The development of anticancer ruthenium(II) complexes: from single molecule compounds to nanomaterials', *Chem Soc Rev* **2017**, *46*, 5771-5804.
- [9] L. K. McKenzie, H. E. Bryant, J. A. Weinstein, 'Transition metal complexes as photosensitisers in one- and two-photon photodynamic therapy', *Coordin Chem Rev* **2019**, *379*, 2-29.
- [10] S. Monro, K. L. Colon, H. Yin, J. Roque, 3rd, P. Konda, S. Gujar, R. P. Thummel, L. Lilge, C. G. Cameron, S. A. McFarland, 'Transition Metal Complexes and Photodynamic Therapy from a Tumor-Centered Approach: Challenges, Opportunities, and Highlights from the Development of TLD1433', *Chem Rev* **2018**.
- [11] J. Hess, H. Huang, A. Kaiser, V. Pierroz, O. Blacque, H. Chao, G. Gasser, 'Evaluation of the Medicinal Potential of Two Ruthenium(II) Polypyridine Complexes as One- and Two-Photon Photodynamic Therapy Photosensitizers', *Chem Eur J* **2017**, *23*, 9888-9896.

- [12] Y. Chen, R. L. Guan, C. Zhang, J. J. Huang, L. N. Ji, H. Chao, 'Two-photon luminescent metal complexes for bioimaging and cancer phototherapy', *Coordin Chem Rev* **2016**, *310*, 16-40.
- [13] H. Huang, B. Yu, P. Zhang, J. Huang, Y. Chen, G. Gasser, L. Ji, H. Chao, 'Highly Charged Ruthenium(II) Polypyridyl Complexes as Lysosome-Localized Photosensitizers for Two-Photon Photodynamic Therapy', *Angew Chem Int Ed Engl* **2015**, *54*, 14049-14052.
- [14] S. Chakraborty, B. K. Agrawalla, A. Stumper, N. M. Vegi, S. Fischer, C. Reichardt, M. Kogler, B. Dietzek, M. Feuring-Buske, C. Buske, S. Rau, T. Weil, 'Mitochondria Targeted Protein-Ruthenium Photosensitizer for Efficient Photodynamic Applications', *J Am Chem Soc* **2017**, *139*, 2512-2519.
- [15] T. Wang, N. Zabarska, Y. Wu, M. Lamla, S. Fischer, K. Monczak, D. Y. Ng, S. Rau, T. Weil, 'Receptor selective ruthenium-somatostatin photosensitizer for cancer targeted photodynamic applications', *Chem Commun (Camb)* **2015**, *51*, 12552-12555.
- [16] X. Zhao, M. Li, W. Sun, J. Fan, J. Du, X. Peng, 'An estrogen receptor targeted ruthenium complex as a two-photon photodynamic therapy agent for breast cancer cells', *Chem Commun (Camb)* **2018**, *54*, 7038-7041.
- [17] E. Villemin, Y. C. Ong, C. M. Thomas, G. Gasser, 'Polymer encapsulation of ruthenium complexes for biological and medicinal applications', *Nature Rev Chem* **2019**, *3*, 261-282.
- [18] Y. Ellahioui, M. Patra, C. Mari, R. Kaabi, J. Karges, G. Gasser, S. Gomez-Ruiz, 'Mesoporous silica nanoparticles functionalised with a photoactive ruthenium(II) complex: exploring the formulation of a metal-based photodynamic therapy photosensitiser', *Dalton Trans* **2018**.

- [19] M. Appold, C. Mari, C. Lederle, J. Elbert, C. Schmidt, I. Ott, B. Stuhn, G. Gasser, M. Gallei, 'Multi-stimuli responsive block copolymers as a smart release platform for a polypyridyl ruthenium complex', *Polym Chem* **2017**, *8*, 890-900.
- [20] R. Green, L. H. Allen, A. L. Bjorke-Monsen, A. Brito, J. L. Gueant, J. W. Miller, A. M. Molloy, E. Nexø, S. Stabler, B. H. Toh, P. M. Ueland, C. Yajnik, 'Vitamin B12 deficiency', *Nat Rev Dis Primers* **2017**, *3*, 17040.
- [21] A. J. Wierzba, S. Hassan, D. Gryko, 'Synthetic Approaches toward Vitamin B12 Conjugates', *Asian J Org Chem* **2019**, *8*, 6-24.
- [22] F. Zelder, 'Recent trends in the development of vitamin B12 derivatives for medicinal applications', *Chem Commun (Camb)* **2015**, *51*, 14004-14017.
- [23] A. Pettenuzzo, R. Pigot, L. Ronconi, 'Vitamin B-12-Metal Conjugates for Targeted Chemotherapy and Diagnosis: Current Status and Future Prospects', *Eur J Inorg Chem* **2017**, 1625-1638.
- [24] J. Delasoie, J. Rossier, L. Haeni, B. Rothen-Rutishauser, F. Zobi, 'Slow-targeted release of a ruthenium anticancer agent from vitamin B12 functionalized marine diatom microalgae', *Dalton Trans* **2018**, *47*, 17221-17232.
- [25] C. Lottner, K. C. Bart, G. Bernhardt, H. Brunner, 'Soluble tetraarylporphyrin-platinum conjugates as cytotoxic and phototoxic antitumor agents', *J Med Chem* **2002**, *45*, 2079-2089.
- [26] F. Schmitt, P. Govindaswamy, G. Suss-Fink, W. H. Ang, P. J. Dyson, L. Juillerat-Jeanneret, B. Therrien, 'Ruthenium porphyrin compounds for photodynamic therapy of cancer', *J Med Chem* **2008**, *51*, 1811-1816.
- [27] C. Mari, V. Pierroz, R. Rubbiani, M. Patra, J. Hess, B. Spingler, L. Oehninger, J. Schur, I. Ott, L. Salassa, S. Ferrari, G. Gasser, 'DNA intercalating Ru(II) polypyridyl

- complexes as effective photosensitizers in photodynamic therapy', *Chem Eur J* **2014**, *20*, 14421-14436.
- [28] B. Krautler, 'Vitamin B12: chemistry and biochemistry', *Biochem Soc Trans* **2005**, *33*, 806-810.
- [29] E. Nexø, *Cobalamin Binding Proteins*, Jon Wiley & Sons, 2007.
- [30] K. L. Brown, 'Chemistry and enzymology of vitamin B-12', *Chemical Reviews* **2005**, *105*, 2075-2149.
- [31] B. Krautler, 'Organometallic chemistry of b(12) coenzymes', *Met Ions Life Sci* **2009**, *6*, 1-51.
- [32] M. Ruetz, R. Salchner, K. Wurst, S. Fedosov, B. Krautler, 'Phenylethynylcobalamin: a light-stable and thermolysis-resistant organometallic vitamin B(12) derivative prepared by radical synthesis', *Angew Chem Int Ed Engl* **2013**, *52*, 11406-11409.
- [33] M. Chrominski, A. Lewalska, D. Gryko, 'Reduction-free synthesis of stable acetylide cobalamins', *Chem Commun (Camb)* **2013**, *49*, 11406-11408.
- [34] O. Zava, S. M. Zakeeruddin, C. Danelon, H. Vogel, M. Gratzel, P. J. Dyson, 'A cytotoxic ruthenium tris(bipyridyl) complex that accumulates at plasma membranes', *Chembiochem* **2009**, *10*, 1796-1800.
- [35] J. Rossier, D. Hauser, E. Kottelat, B. Rothen-Rutishauser, F. Zobi, 'Organometallic cobalamin anticancer derivatives for targeted prodrug delivery via transcobalamin-mediated uptake', *Dalton Trans* **2017**, *46*, 2159-2164.
- [36] C. Herrero, A. Quaranta, S. El Ghachtouli, B. Vauzeilles, W. Leibl, A. Aukauloo, 'Carbon dioxide reduction via light activation of a ruthenium-Ni(cyclam) complex', *Phys Chem Chem Phys* **2014**, *16*, 12067-12072.
- [37] M. J. Cook, A. P. Lewis, G. S. G. McAuliffe, V. Skarda, A. J. Thomson, J. L. Glasper, D. J. Robbins, 'Luminescent Metal-Complexes .1. Tris-Chelates of Substituted 2,2'-

- Bipyridyls with Ruthenium(II) as Dyes for Luminescent Solar Collectors', *J Chem Soc Perk T 2* **1984**, 1293-1301.
- [38] A. Juris, V. Balzani, F. Barigelletti, S. Campagna, P. Belser, A. Vonzelewsky, 'Ru(II) Polypyridine Complexes - Photophysics, Photochemistry, Electrochemistry, and Chemi-Luminescence', *Coordin Chem Rev* **1988**, *84*, 85-277.
- [39] J. Karges, P. Goldner, G. Gasser, 'Synthesis, Characterization, and Biological Evaluation of Red-Absorbing Fe(II) Polypyridine Complexes', *Inorganics* **2019**, *7*.
- [40] V. Fernandez-Moreira, F. L. Thorp-Greenwood, M. P. Coogan, 'Application of d6 transition metal complexes in fluorescence cell imaging', *Chem Commun (Camb)* **2010**, *46*, 186-202.

Supplementary Information

Evaluation of the Potential of Cobalamin Derivatives Bearing
Ru(II) Polypyridyl Complexes as Photosensitisers for
Photodynamic Therapy

Marta Jakubaszek,^{1,2,#} Jeremie Rossier,^{3,#} Johannes Karges,^{1,#} Joachim Delasoie,^{3,#} Bruno
Goud,² Gilles Gasser^{1,*} and Fabio Zobi^{3,*}

¹ Chimie ParisTech, PSL University, CNRS, Institute of Chemistry for Life and Health
Sciences, Laboratory for Inorganic Chemical Biology, F-75005 Paris.

² Institut Curie, PSL University, CNRS UMR 144, Paris, France.

³ Chemistry Department, University of Fribourg, CH-1700 Fribourg.

* Corresponding authors: Email: gilles.gasser@chimie-paristech.fr; fabio.zobi@unifr.ch

these authors have contributed equally to the work.

Table of Contents:

FIGURE S1. 500 MHz ¹ H-NMR OF COMPOUND B ₁₂ - 2	87
FIGURE S2. NORMALIZED UV-VIS OF COMPOUNDS 2 , B ₁₂ - 2 AND OF CYANOCOBALAMIN (CN-CBL) IN METHANOL.	88
FIGURE S3. HPLC CHROMATOGRAM OF COMPOUND B ₁₂ - 2	89
FIGURE S4. HR-ESI-MS OF COMPOUND B ₁₂ - 2	90
FIGURE S5. CYTOTOXICITY OF COMPLEX 2 IN THE HeLa CELL LINE.	91
FIGURE S6. CYTOTOXICITY OF COMPLEX 2 IN THE RPE-1 CELL LINE.	92
FIGURE S7. CYTOTOXICITY OF COMPLEX B ₁₂ - 2 IN THE HeLa CELL LINE.....	93
FIGURE S8. CYTOTOXICITY OF COMPLEX B ₁₂ - 2 IN THE RPE-1 CELL LINE.	94
FIGURE S9. CYTOTOXICITY OF COMPLEX 1 IN THE HeLa CELL LINE.	95
FIGURE S10. CYTOTOXICITY OF COMPLEX 1 IN THE RPE-1 CELL LINE.	96
FIGURE S11. CYTOTOXICITY OF COMPLEX B ₁₂ - 1 IN THE HeLa CELL LINE.	97
FIGURE S12. CYTOTOXICITY OF COMPLEX B ₁₂ - 1 IN THE RPE-1 CELL LINE.	98
FIGURE S13. CELLULAR LOCALISATION OF THE COMPLEXES IN HeLa CELL LINE..	99

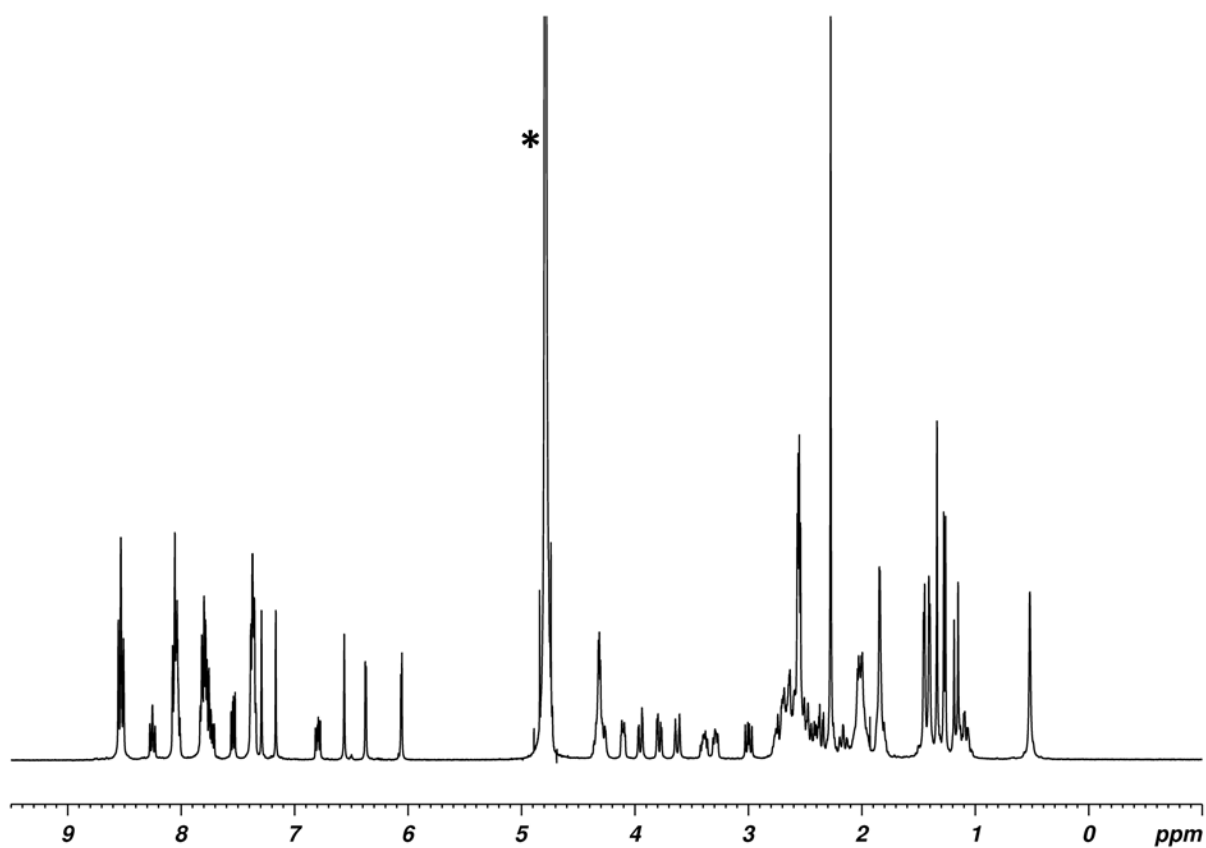


Figure S1. 500 MHz ^1H -NMR of compound B₁₂-2 (in D₂O, * = solvent residual peak).

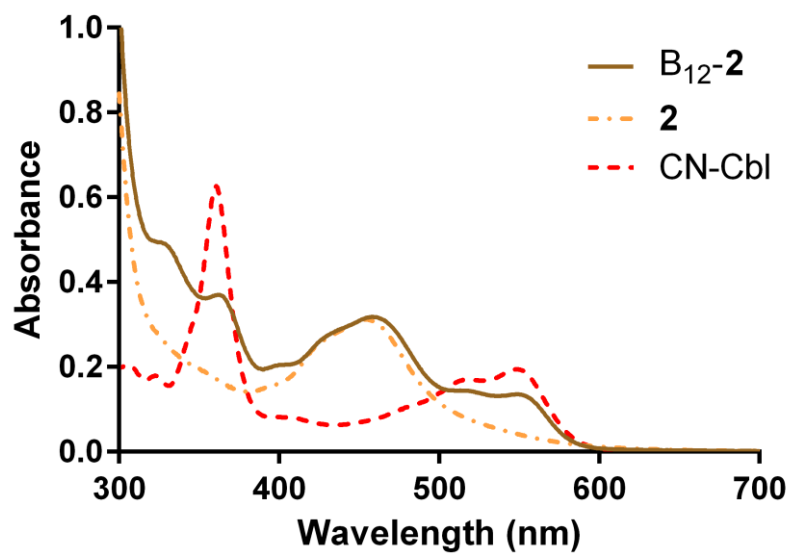


Figure S2. Normalized UV-Vis of compounds **2**, B₁₂-**2** and of cyanocobalamin (CN-Cbl) in methanol.

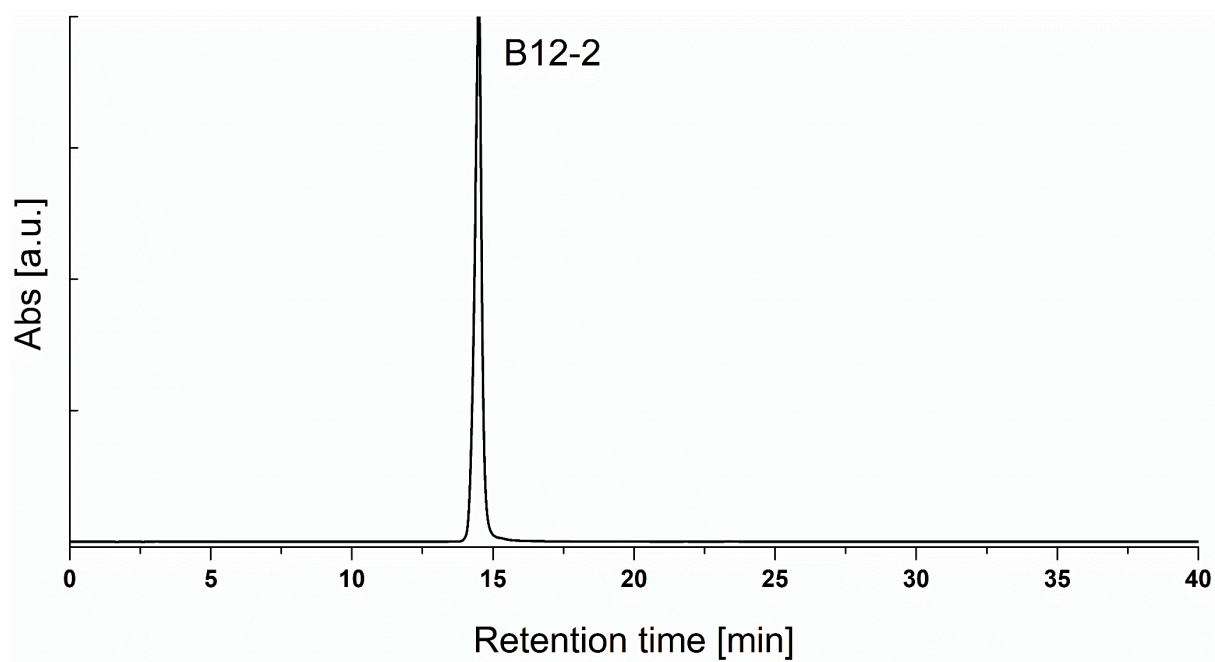


Figure S3. HPLC chromatogram of compound B₁₂-2.

Exact mass

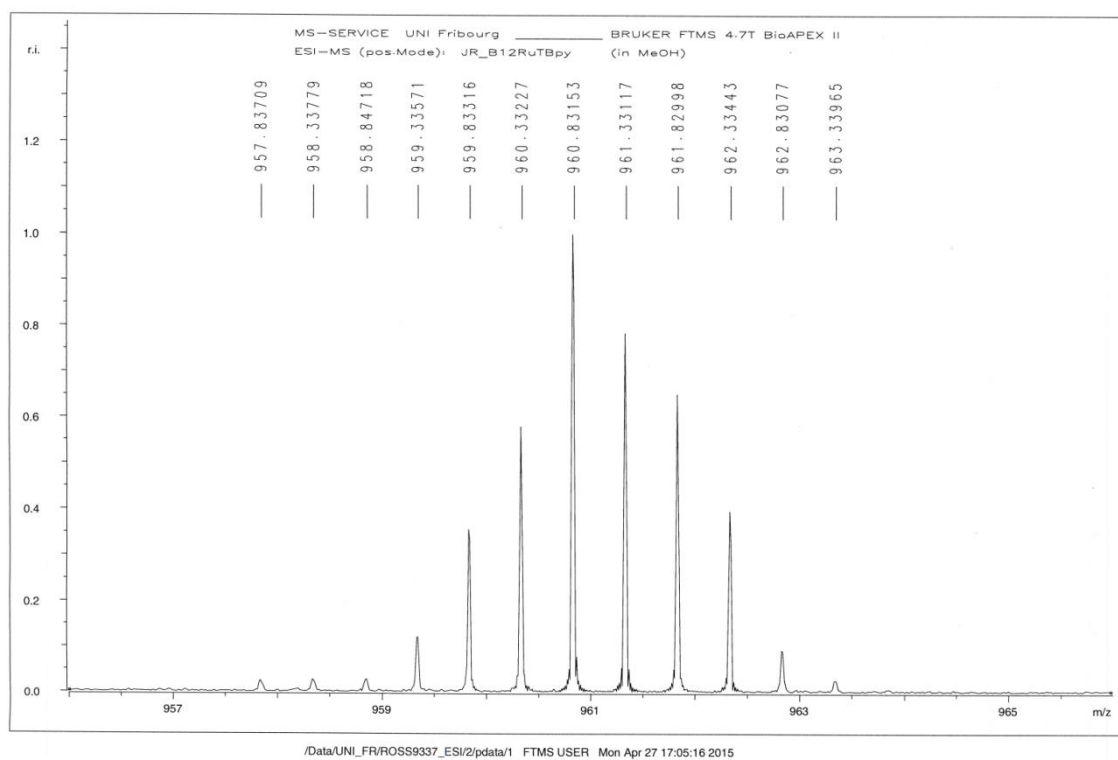
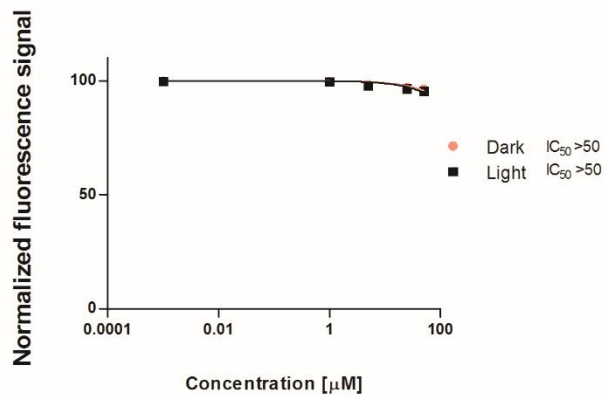
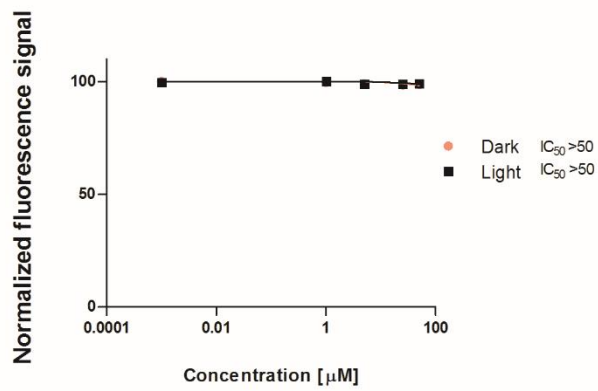


Figure S4. HR-ESI-MS of compound B₁₂-2.

Cytotoxicity of Complex 2 in HeLa -1st repeat



Cytotoxicity of Complex 2 in HeLa-2nd repeat



Cytotoxicity of Complex 2 in HeLa-3rd repeat

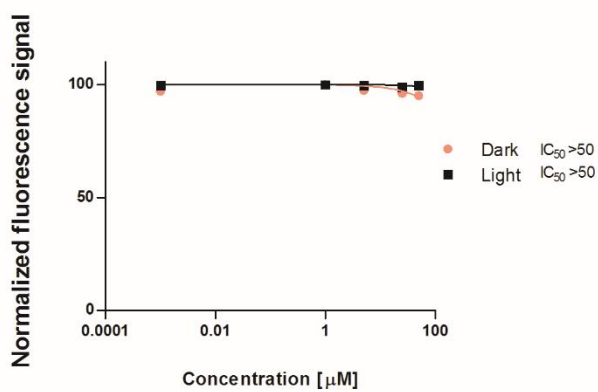
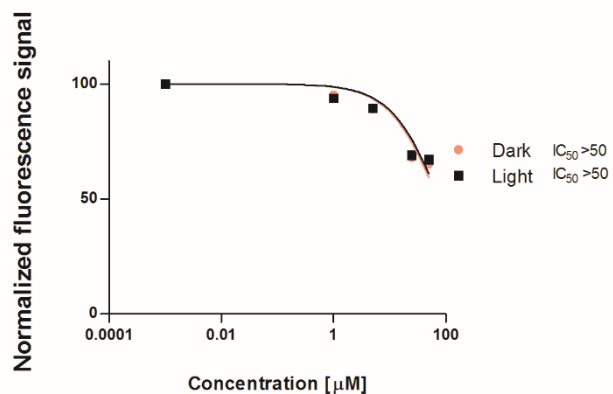
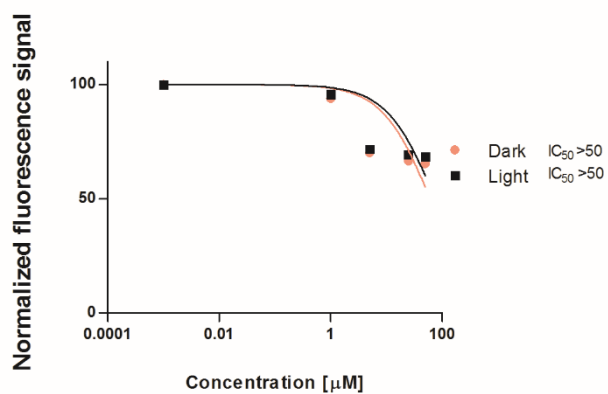


Figure S5. Cytotoxicity of complex 2 in the HeLa cell line.

Cytotoxicity of complex 2 in RPE-1 -1st repeat



Cytotoxicity of complex 2 in RPE-1 -2nd repeat



Cytotoxicity of complex 2 in RPE-1 -3rd repeat

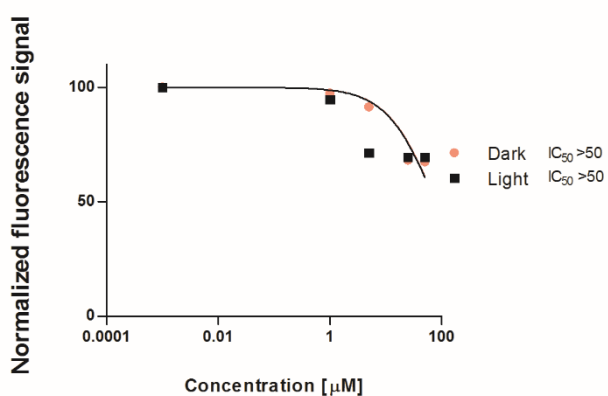
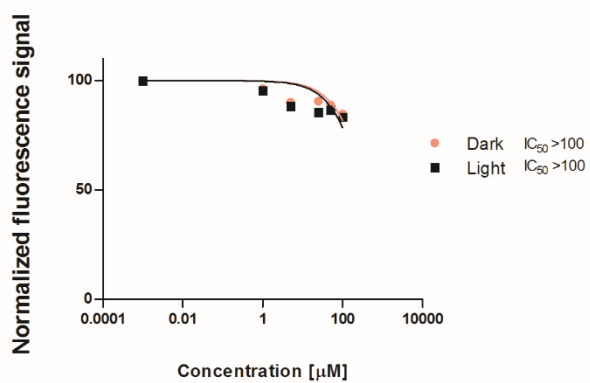
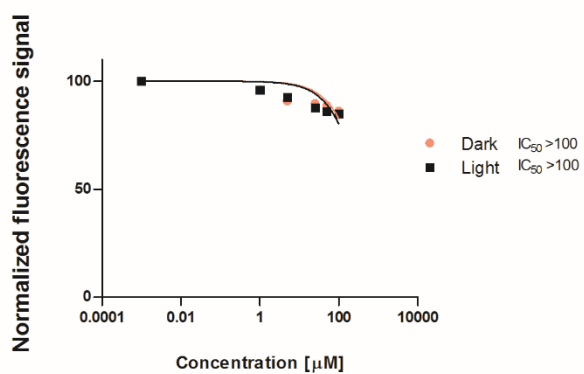


Figure S6. Cytotoxicity of complex 2 in the RPE-1 cell line.

Cytotoxicity of complex B₁₂-2 in HeLa -1st repeat



Cytotoxicity of complex B₁₂-2 in HeLa -2nd repeat



Cytotoxicity of complex B₁₂-2 in HeLa -3rd repeat

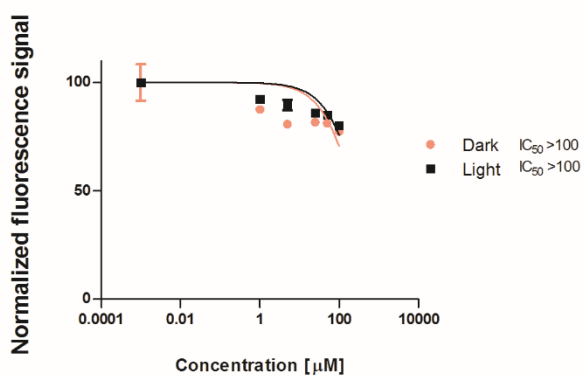
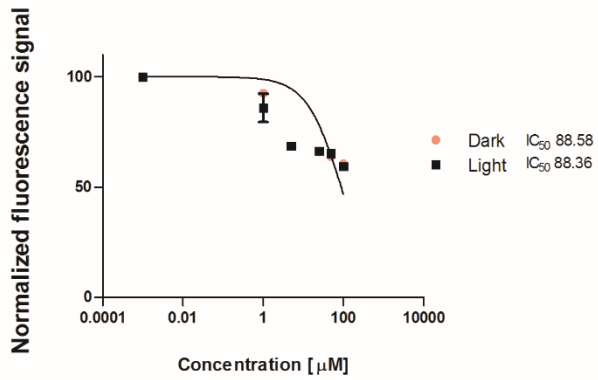
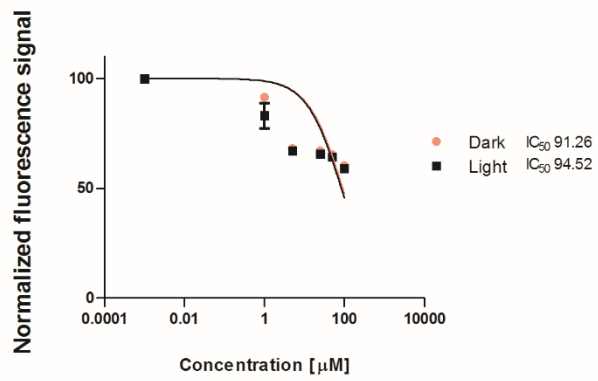


Figure S7. Cytotoxicity of complex B₁₂-2 in the HeLa cell line.

Cytotoxicity of complex B₁₂-2 in RPE-1 -1st repeat



Cytotoxicity of complex B₁₂-2 in RPE-1 -2nd repeat



Cytotoxicity of complex B₁₂-2 in RPE-1 -3rd repeat

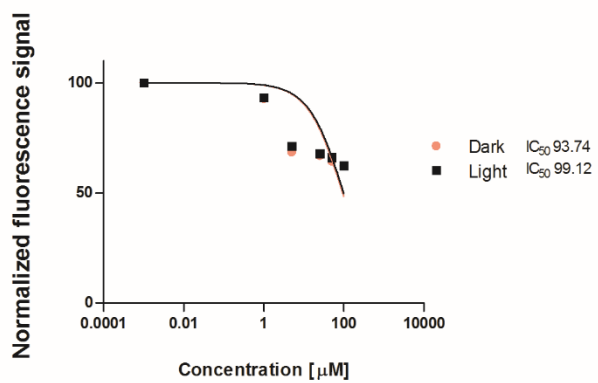
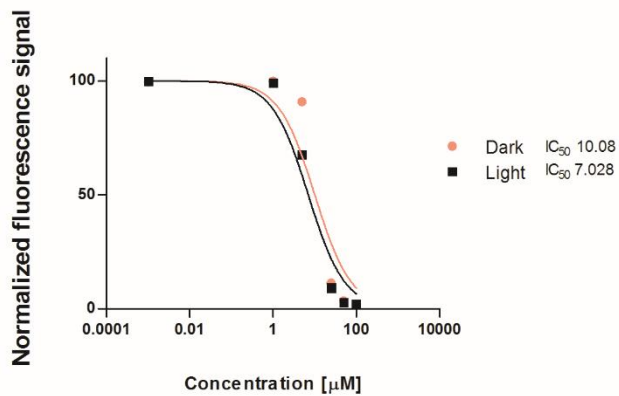
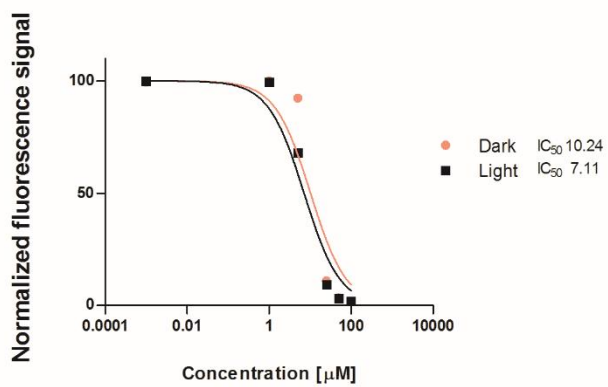


Figure S8. Cytotoxicity of complex B₁₂-2 in the RPE-1 cell line.

Cytotoxicity of complex 1 in HeLa -1st repeat



Cytotoxicity of Complex 1 in HeLa-2nd repeat



Cytotoxicity of Complex 1 in HeLa-3rd repeat

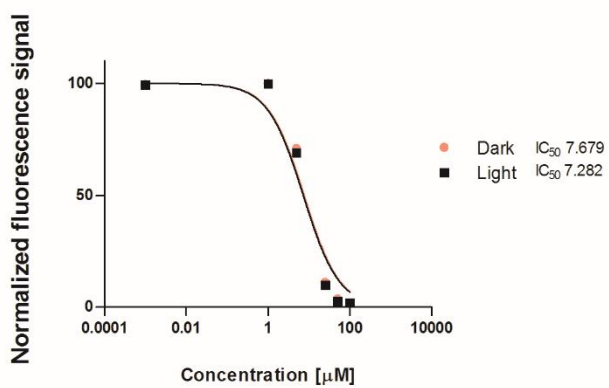
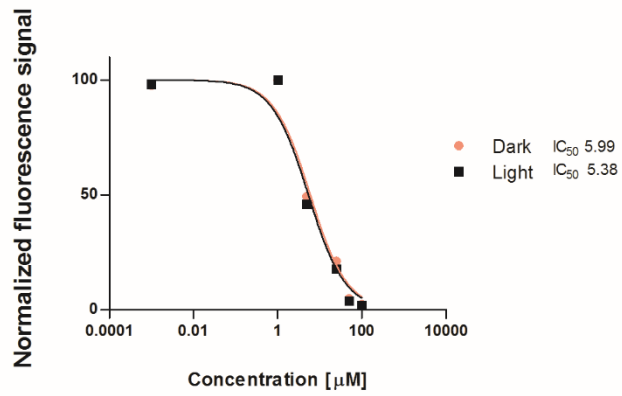
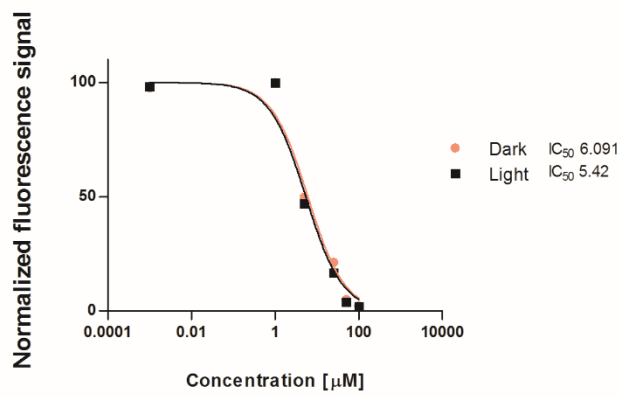


Figure S9. Cytotoxicity of complex 1 in the HeLa cell line.

Cytotoxicity of complex 1 in RPE-1 -1st repeat



Cytotoxicity of complex 1 in RPE-1 -2nd repeat



Cytotoxicity of complex 1 in RPE-1 -3rd repeat

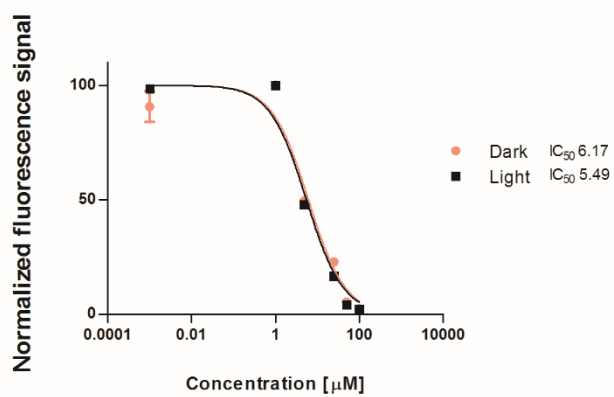
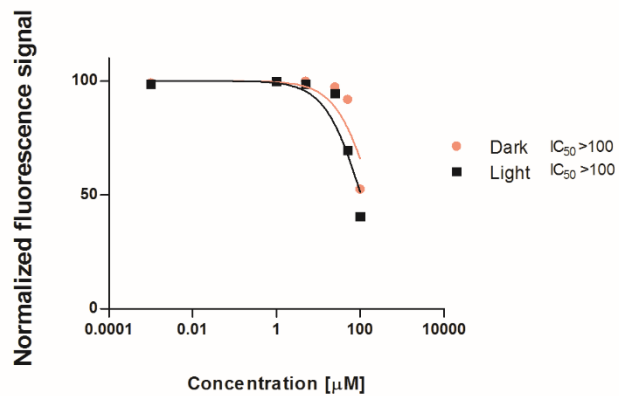
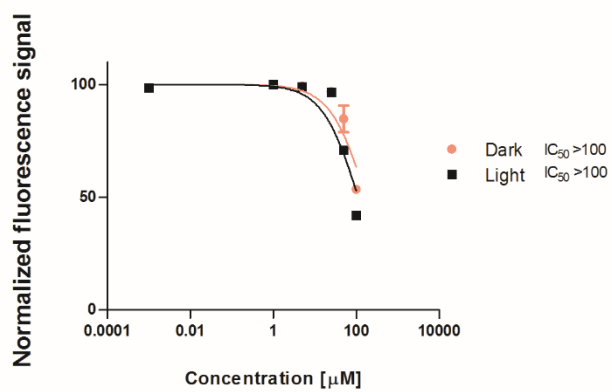


Figure S10. Cytotoxicity of complex 1 in the RPE-1 cell line.

Cytotoxicity of Complex B₁₂-1 in HeLa -1st repeat



Cytotoxicity of Complex B₁₂-1 in HeLa-2nd repeat



Cytotoxicity of Complex B₁₂-1 in HeLa-3rd repeat

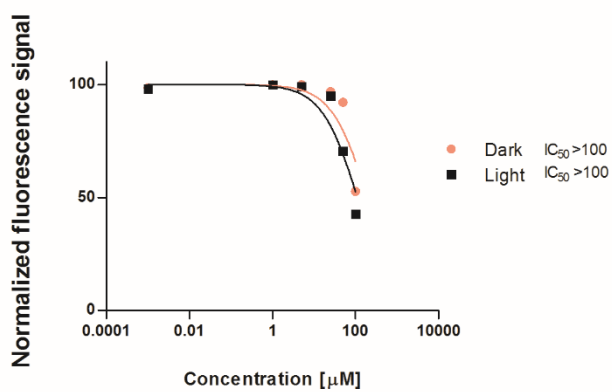
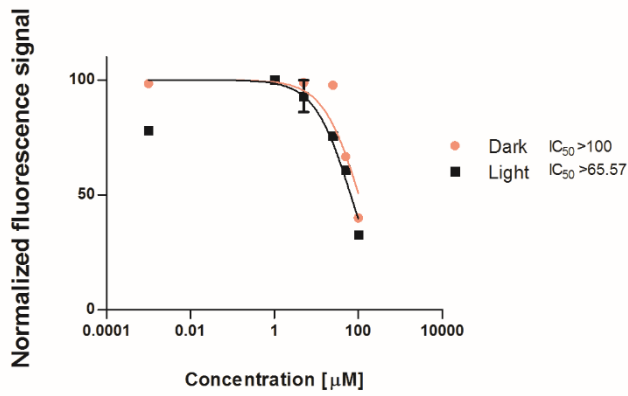
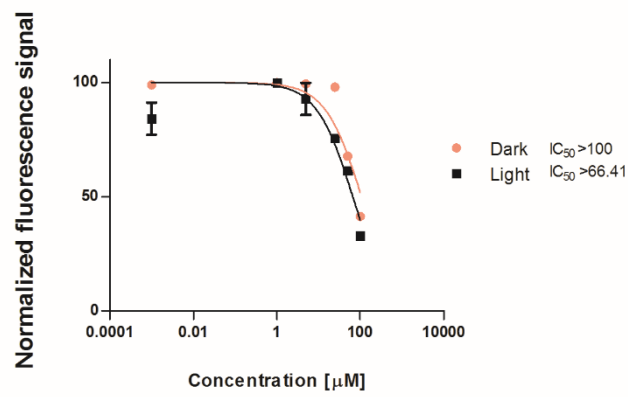


Figure S11. Cytotoxicity of complex B₁₂-1 in the HeLa cell line.

Cytotoxicity of complex B₁₂-1 in RPE-1 -1st repeat



Cytotoxicity of complex B₁₂-1 in RPE-1 -2nd repeat



Cytotoxicity of complex B₁₂-1 in RPE-1 -3rd repeat

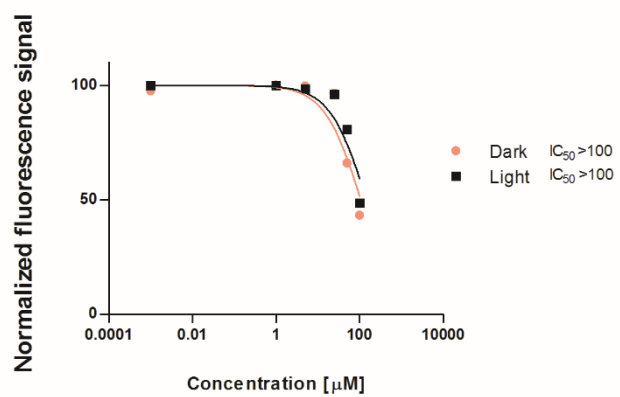


Figure S12. Cytotoxicity of complex B₁₂-1 in the RPE-1 cell line.

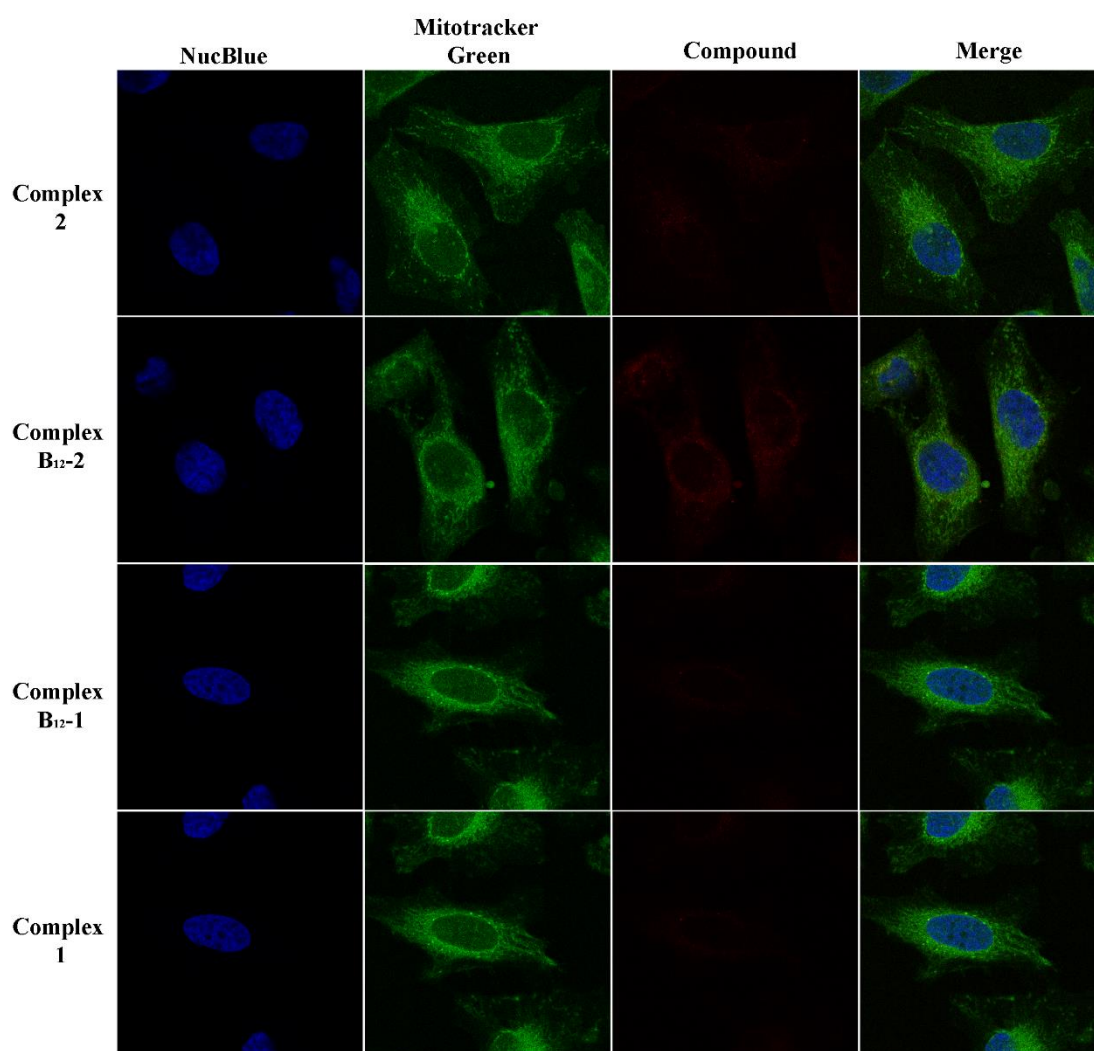


Figure S13. Cellular localisation of the complexes in HeLa cell line. Cells were treated with the compounds (IC_{50} concentration in the dark) for 2 h and co-stained with NucBlue and Mitotracker Green FM. Compounds were then removed, cells were fixed and visualised by confocal microscopy.

Chapter 3- Synthesis and Characterization of an Epidermal Growth Factor Receptor selective Ru(II) Polypyridyl- Nanobody Conjugate as a Photosensitizer for Photodynamic Therapy

Johannes Karges,^{a,#} Marta Jakubaszek,^{a,b,#} Cristina Mari,^{c,#} Kristof Zarschler^{d,#,} Bruno
Goud,^b Holger Stephan,^d and Gilles Gasser^{a,*}*

^a Chimie ParisTech, PSL University, CNRS, Institute of Chemistry for Life and Health Sciences, Laboratory for Inorganic Chemical Biology, F-75005 Paris, France.

^b Institut Curie, PSL University, CNRS UMR 144, Paris, France.

^c Department of Chemistry, University of Zurich, Winterthurerstrasse 190, CH-8057 Zurich, Switzerland.

^d Helmholtz-Zentrum Dresden - Rossendorf, Institute of Radiopharmaceutical Cancer Research, Bautzner Landstraße 400, D-01328 Dresden, Germany.

These authors have contributed equally to the work.

*Corresponding authors: Email: k.zarschler@hzdr.de, WWW:
www.hzdr.de/NanoscalicSystems, Tel. +49 351 260 3678; Email:
gilles.gasser@chimieparistech.psl.eu, WWW: www.gassergroup.com, Tel. +33 1 44 27 56 02.

This chapter has been published in *ChemBioChem* **2019**, in press (DOI [10.1002/cbic.201900419](https://doi.org/10.1002/cbic.201900419))

Reproduced by permission of Wiley-VCH Verlag GmbH & Co. KGaA.

<https://onlinelibrary.wiley.com/doi/full/10.1002/cbic.201900419>

Contribution to the publication:

Marta Jakubaszek performed the cytotoxicity studies as well as the flow cytometry experiments. She wrote the first draft of this publication.

Marta Jakubaszek



19.05.2020

Gilles Gasser

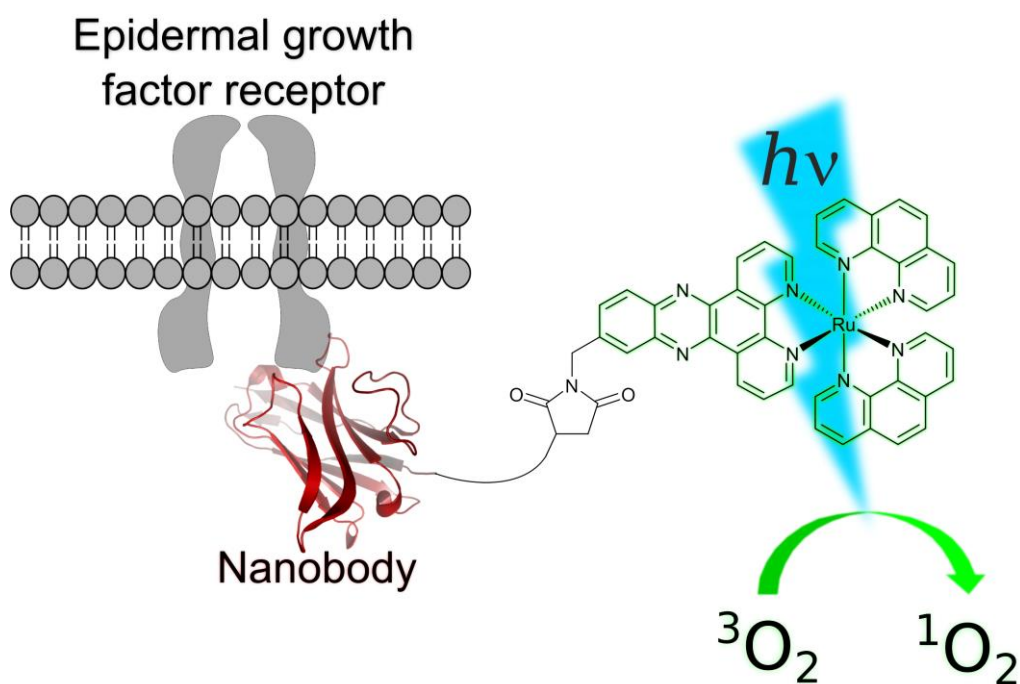


Abstract

There is currently a surge for the development of novel photosensitizers (PSs) for photodynamic therapy (PDT) since those currently approved are not completely ideal. Among the tested compounds, we have previously investigated the use of Ru(II) polypyridyl complexes with a $[\text{Ru}(\text{bipy})_2(\text{dppz})]^{2+}$ and $[\text{Ru}(\text{phen})_2(\text{dppz})]^{2+}$ scaffold (bipy = 2,2'-bipyridine; dppz = dipyrido[3,2-a:2',3'-c]-phenazine, phen = 1,10-phenanthroline). These complexes selectively target DNA. However, since DNA is ubiquitous, it would be of great interest to increase the selectivity of our PDT PSs by linking them to a targeting vector in view of targeted PDT. Herein, we present the synthesis, characterization and in-depth photophysical evaluation of a nanobody-containing Ru(II) polypyridyl conjugate selective for the epidermal growth factor receptor (EGFR) in view of targeted PDT. Using ICP-MS and confocal microscopy, we could demonstrate that our conjugate had a high selectivity for the EGFR receptor, which is a crucial oncological target as it is overexpressed and/or deregulated in a variety of solid tumors. However, contrary to expectations, this conjugate was found to not produce reactive oxygen species (ROS) in cancer cells and to be therefore not phototoxic.

Graphical abstract

The synthesis, characterization and in-depth photophysical evaluation of a nanobody-containing Ru(II) polypyridyl conjugate selective for the epidermal growth factor receptor (EGFR) in view of targeted PDT is presented.



Introduction

The use of photodynamic therapy (PDT) has expanded the possible techniques in medicine to treat various types of cancer (e.g., lung, bladder, oesophageal and brain cancer) as well as bacterial, fungal or viral infections. Its effect is caused by a combination of an ideally non-toxic photosensitizer (PS), oxygen and light. Upon light exposure, the PS is able to produce reactive oxygen species (ROS), such as singlet oxygen ($^1\text{O}_2$) or other radicals. Due to the high reactivity of the latter, these can cause oxidative stress and damage in different cellular compartments (e.g., membrane, nucleus, endoplasmic reticulum, lysosome, mitochondria), leading ultimately to cell death.^[1]

Next to the already approved PDT PSs, which are based on a tetrapyrrolic scaffold (i.e. porphyrins, chlorins, phthalocyanines), the development of Ru(II) polypyridyl complexes as PDT PSs is receiving more attention due to their ideal photophysical and photochemical properties, which include, among others, high water solubility, high chemical stability and photostability, intense luminescence, large Stokes shifts, high $^1\text{O}_2$ production.^[1a-d, 2] These attractive features have allowed one of such complexes, namely TLD-1433, to enter into clinical trial as a PDT PS against bladder cancer.^[3] Phase I has been recently completed.^[2f]

In this context, our group was able to demonstrate that Ru(II) complexes of the type $[\text{Ru}(\text{bipy})_2(\text{dppz})]^{2+}$ (bipy = 2,2'-bipyridine, dppz = dipyrido[3,2-a:2',3'-c]-phenazine) and $[\text{Ru}(\text{phen})_2(\text{dppz})]^{2+}$ (phen = 1,10-phenanthroline) were effective PDT PSs (Figure 1).^[1a, 2c, 4] As a highlight, we could demonstrate that some of these complexes were non-toxic in the dark and highly toxic upon light irradiation with IC_{50} values in the low micromolar range and a phototoxic index of up to >150 .^[2c] Based on the extended planar π -system of the dppz ligand, which is able to intercalate into the base pairs of the DNA, these compounds showed a preferable nuclear localization. Upon light exposure, these complexes caused oxidative stress,

as well as DNA photocleavage, suggesting that they impaired replication and integrity of the genetic material.^[1a, 2c, 4]

Highly proliferating cells like cancer cells are generally preferably targeted by such compounds over healthy cells, as it is the case for cisplatin.^[5] However, other frequently dividing cells in the organism (e.g. hair follicles, gastrointestinal tract, bone marrow) can be affected, leading to severe side-effects for the patients.^[4a, 6] Thus, it is extremely important to increase the selectivity of PDT PS, for example, with the development of a suitable delivery system.

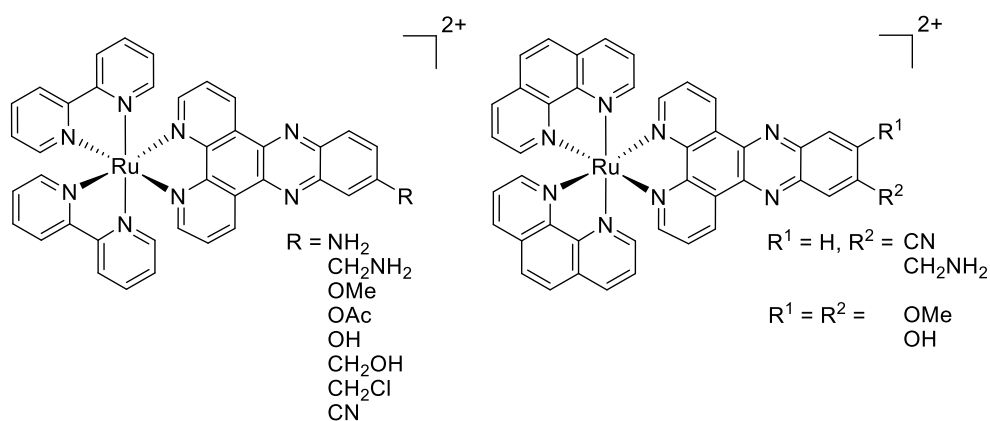


Figure 1. Structures of $[\text{Ru}(\text{bipy})_2(\text{dppz})]^{2+}$ and $[\text{Ru}(\text{phen})_2(\text{dppz})]^{2+}$ complexes as PSs developed by our group.^[1a, 2c, 4]

So far, the examples of Ru(II) polypyridyl complexes for targeted PDT are scarce, if we do not take into account polymer encapsulation/nanoparticle attachment.^[4a, 7] The group of Lilge could recently demonstrate that the premixing of TLD-1433 with transferrin was able to increase the extinction coefficient, prolongs the absorption range, reduced photobleaching, cellular uptake as well as overall toxicity of the compound.^[8] Our group previously demonstrated the efficiency of the coupling of a metal-based PDT PS to peptides, which are known to bind specifically to

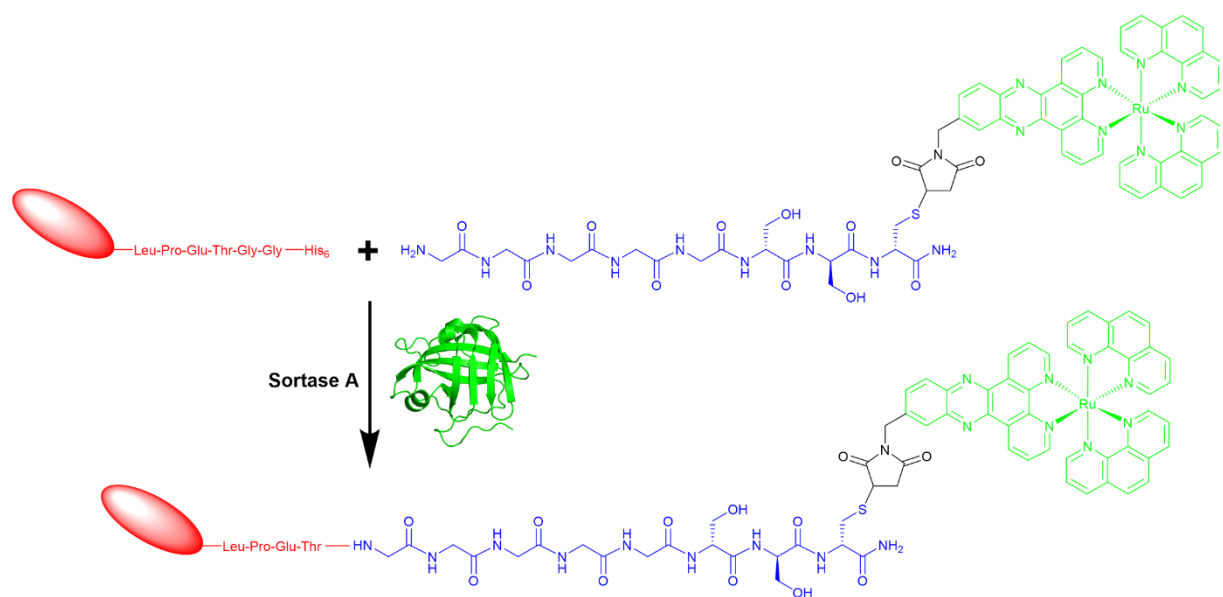
abundant molecular targets on malignant cells. More precisely, in those studies, bombesin, that is known to target the human gastrin-releasing peptide receptor as well as a nuclear localization signal peptide that facilitates the intracellular transport into the nucleus were coupled to Ru-based PDT PSs. We were able to demonstrate an increased uptake of the conjugate in the receptor-expressing cells in comparison to the free complex.^[4a] The groups of Weil and Rau were able to link the peptide hormone somatostatin to a PS and could show an 100-fold increased efficiency for somatostatin receptor-expressing cells compared to the free PS.^[7a] Recently, the authors described a macromolecular plasma protein serum albumin–PS conjugate with several Ru complexes bound to the protein surface. Using the protein as a nanocarrier, the PSs were delivered selectively to the mitochondria, where it showed an impressive phototoxicity with IC₅₀ values in the nanomolar range.^[7c] Worthy of note, a variety metal complexes as for example Re(I), Pt(II), Ru(II) or Ir(III) compounds have been successfully coupled to peptides to increase receptor selectivity.^[9]

Among the different established classes of delivery systems^[10] (e.g. oil-dispersions, encapsulation in polymeric particles/lysosomes, targeting peptide-PS conjugates, polymer-PS conjugates), the conjugation of PS to monoclonal antibodies (mAb) takes advantage of the excellent target specificity of the latter. However, despite their clinical success, the concept of utilizing mAb-PS conjugates is afflicted with several important drawbacks. These vector molecules are known for their high stability and prolonged serum half-life, slow pharmacokinetics and clearance from the body. This leads to an increase of the absolute level of the mAb-PS conjugate in the tumor alongside with an increased non-specific uptake in non-target tissues.^[11] Additionally, the treatment of solid tumors is limited due to penetration problems of the large conjugate into the tumor caused by poor vascularization, drainage, interstitial pressure and dense stroma.^[12] An attractive strategy to circumvent these limitations is the use of smaller oncotropic vector molecules like antibody fragments or nanobodies

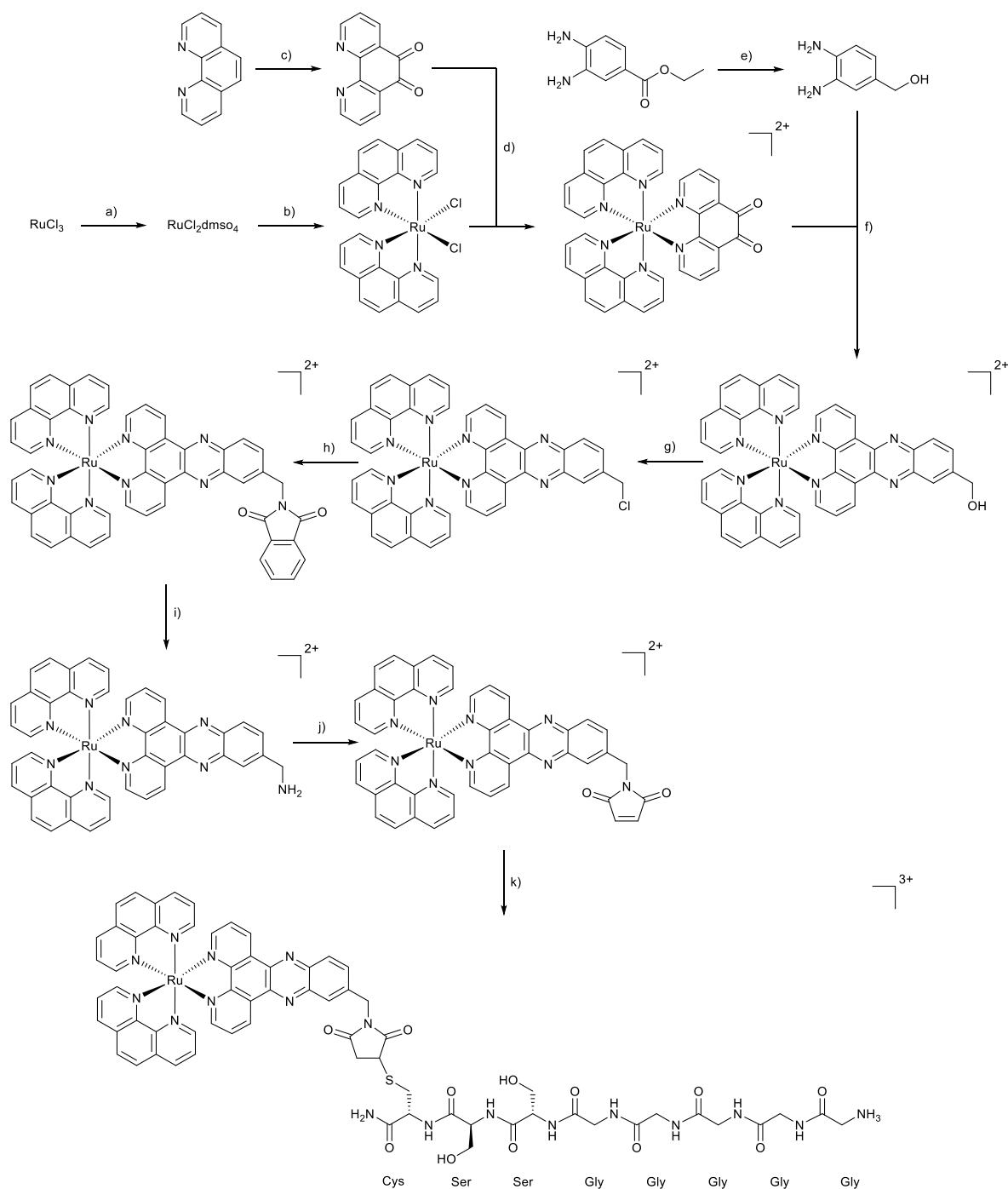
(NBs).^[13] NBs represent the antigen-binding domain of heavy-chain-only antibodies that occur in species belonging to the family of *Camelidae*. Their small size, stability, solubility, fast pharmacokinetics as well as high specificity and affinity for their cognate antigens make them powerful targeting agents for diagnostic imaging and targeted therapy.^[14] Noteworthy in this context, Caplacizumab, a bivalent anti-von Willebrand factor NB, is currently in Phase III clinical trials against acquired thrombotic thrombocytopenic purpura.^[15]

A recent study has highlighted the high tumor uptake, rapid blood clearance and low liver uptake of a ^{99m}Tc-labeled NB as an imaging probe for epidermal growth factor receptor (EGFR) positive tumors.^[16] This receptor, which is involved in many cellular processes such as proliferation, differentiation and cell survival, represents a crucial target in oncology as it is overexpressed and/or deregulated in a variety of solid tumors, including head and neck, breast, non-small-cell lung and pancreatic cancer. Therefore, EGFR is a major target for cancer therapy.^[16-17] Worthy of note, the successful conjugation of the PS IRDye700DX–maleimide to nanobodies for hepatocyte growth factor receptor targeted PDT was recently demonstrated.^[18]

With this in mind, we report herein the design, synthesis, characterization and in-depth biological evaluation of a NB-containing Ru(II) polypyridyl conjugate (Scheme 1). The conjugate consists of three building blocks: 1) a [Ru(phen)₂(dppz)]²⁺ complex (green), which is known to have an excellent phototoxicity^[1a, 2c, 4], 2) a 7C12 NB (red), which is known for specific binding to EGFR expressing cells^[16, 19] and 3) a peptide chain (blue) with a poly-glycine unit, which is necessary for an efficient and site-specific conjugation by a sortase A (SrtA)-mediated trans-peptidation reaction leading to an 1:1 NB:PS ratio.^[20] To the best of our knowledge, we report herein the first NB-containing Ru(II) polypyridyl conjugate as a PDT PS for EGFR-targeted PDT. As can be seen below, thanks to this design, a highly selective NB-containing [Ru(phen)₂(dppz)]²⁺ conjugate **Ru-NB** could be unveiled.



Scheme 1. Overview of the Sortase A-mediated site-specific modification of the NB derivative 7C12-Strep-Sortag-His₆ with the Ru(phen)₂(dppz-7-maleimidemethyl-S-Cys-(Ser)₂(Gly)₅-NH₂) complex resulting in **Ru-NB** conjugate. PDB entry of Sortase A from *Staphylococcus aureus*: 1t2p.^[21]



Scheme S1. Total synthesis of $[\text{Ru}(\text{phen})_2(\text{dppz}-7\text{-maleimidemethyl-S-Cys-(Ser)}_2(\text{Gly})_5\text{-NH}_3)](\text{TFA})_3$. a) EtOH, reflux 3 h, DMSO, 150°C 2 h; b) 1,10-phenanthroline, LiCl, DMF, reflux overnight under N_2 atmosphere; c) 1,10-phenanthroline, KBr, H_2SO_4 , HNO_3 , 90°C 3 h under N_2 atmosphere; d) EtOH, 80°C 3 h under N_2 atmosphere; e) LiAlH_4 , THF, 60°C 1 h under N_2 atmosphere; f) acetic acid, CH_3CN , reflux 1 h under N_2 atmosphere; g) $(\text{COCl})_2$, DMF, CH_3CN , RT, overnight under N_2 atmosphere; h) Phthalimide, K_2CO_3 , DMF, RT, overnight; i)

NH₂NH₂, MeOH, reflux overnight under N₂ atmosphere; j) maleic anhydride, AcOH, reflux 10 h under N₂ atmosphere; k) (NH₂CO-Cys-(Ser)₂(Gly)₅-NH₃)(TFA), CH₃CN:H₂O 1:1, RT, 30 h.

Results and discussion

Synthesis of the [Ru(phen)₂(dppz-7-maleimidemethyl-S-Cys-(Ser)₂(Gly)₅-NH₃)] complex

The synthetic strategy for the synthesis of the [Ru(phen)₂(dppz-7-maleimidemethyl-S-Cys-(Ser)₂(Gly)₅-NH₃)]³⁺ complex is described in Scheme 1. The [Ru(phen)₂(dppz-7-aminomethyl)](PF₆)₂ complex was synthesized as previously reported in nine synthetic steps.^[4a] The synthesis of the [Ru(phen)₂(dppz-7-maleimidemethyl)](PF₆)₂ complex is already published but, in this study, a slightly different experimental procedure was employed.^[4a] The maleimide-containing Ru(II) complexes was prepared by reacting the [Ru(phen)₂(dppz-7-aminomethyl)](PF₆)₂ complex with maleic anhydride. [Ru(phen)₂(dppz-7-maleimidemethyl)](PF₆)₂ was coupled to the poly-glycine chain *via* a thio-Michael addition reaction. As recently highlighted, this bioconjugation presents important advantages such as synthetic accessibility, excellent reactivity and, importantly, biocompatibility.^[22] Following this synthetic strategy, the thiosuccinimide product [Ru(phen)₂(dppz-7-maleimidemethyl-S-Cys-(Ser)₂(Gly)₅-NH₃)]³⁺ was prepared by reacting thiol of the (NH₃-(Gly)₅(Ser)₂-Cys-CONH₂)(TFA) peptide chain with the [Ru(phen)₂(dppz-7-maleimidemethyl)](PF₆)₂ complex. The product was obtained after an overnight reaction at room temperature and isolated *via* preparative HPLC. The identity of the obtained complexes was confirmed by HR-MS and the purity verified by HPLC (Figures S1-S2).

Sortase A-mediated conjugation

The efficiency of chemoenzymatic bioconjugation was evaluated using the EGFR-specific NB 7C12 and $[\text{Ru}(\text{phen})_2(\text{dppz-7-maleimidemethyl-S-Cys-(Ser)}_2(\text{Gly})_5\text{-NH}_3)]^{3+}$ as a substrate. To this end, the NB was produced with its C-terminus tagged with a $(\text{GGGGS})_3$ spacer followed by a Strep-tag, the LPETGG sortase motif, another $(\text{GGGGS})_3$ spacer and a hexahistidine purification tag (His_6). As successful sortase A-mediated conjugation leads to the elimination of the His_6 -tag, this design allows the removal of the unreacted NB as well as of the His_6 -tagged enzyme by Immobilized Metal Ion Affinity Chromatography (IMAC). To optimize the reaction, the molar ratios of SrtA, NB and $[\text{Ru}(\text{phen})_2(\text{dppz-7-maleimidemethyl-S-Cys-(Ser)}_2(\text{Gly})_5\text{-NH}_3)]^{3+}$ as well as the reaction time were varied (see Figures S3-S4). A 4 h reaction at 30°C with a molar ratio of 1:1:10 was identified as being ideal (Figure 2).

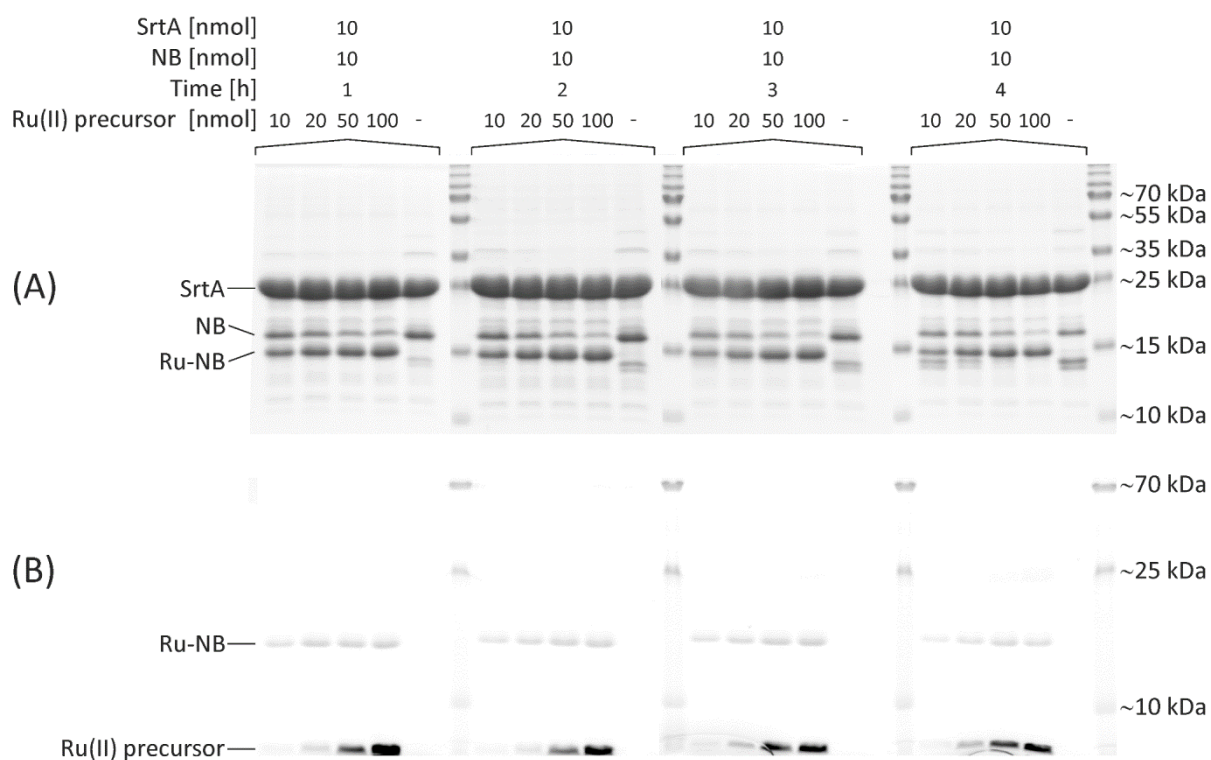


Figure 2. Course of reaction for the chemoenzymatic conjugation of $[\text{Ru}(\text{phen})_2(\text{dppz-7-maleimidemethyl-S-Cys}-(\text{Ser})_2(\text{Gly})_5\text{-NH}_3)]^{3+}$ to the EGFR-specific NB 7C12. While the molar ratio between SrtA and NB was kept constant (1:1), the amount of the Ru(II) precursor was increased (10-100 nmol) to finally achieve molar ratios of 1:1:1, 1:1:2, 1:1:5 and 1:1:10, respectively. The reaction was monitored for up to 4 h and aliquots were separated on 15% SDS polyacrylamide gels. After electrophoresis, gels were imaged with a D-DiGit Gel Scanner (B) to detect the signal of the Ru(II) complex and subsequently stained with colloidal Coomassie G-250 (A).

Consequently, these conditions were kept in an upscaled reaction using 2 μmol SrtA, 2 μmol sdAb and 20 μmol $[\text{Ru}(\text{phen})_2(\text{dppz-7-maleimidemethyl-S-Cys}-(\text{Ser})_2(\text{Gly})_5\text{-NH}_3)]^{3+}$. After purification of the reaction mixture by affinity chromatography, the obtained conjugate 7C12-Strep- $[\text{Ru}(\text{phen})_2(\text{dppz-7-maleimidemethyl-S-Cys}-(\text{Ser})_2(\text{Gly})_5\text{-NH}_3)]^{3+}$ (Ru-NB) was analyzed by MALDI-TOF MS (Figure S5). The mass spectra of the final purified product **Ru-**

NB showed a homogeneous population of a single-conjugated NB with a molecular mass of ~17.7 kDa.

Photophysical properties

With the conjugate in hand, we performed photophysical measurements to evaluate its potential as a PDT agent. At first, the absorptions of $[\text{Ru}(\text{phen})_2(\text{dppz-7-maleimidemethyl})](\text{PF}_6)_2$, $[\text{Ru}(\text{phen})_2(\text{dppz-7-maleimidemethyl-S-Cys-(Ser)}_2(\text{Gly})_5\text{-NH}_3)](\text{TFA})_3$ and **Ru-NB** were measured to investigate if the peptide chain or the NB conjugation had an influence on the photophysical properties of the Ru(II) polypyridyl complexes. Since the conjugate is insoluble in CH_3CN , the measurement of **Ru-NB** was performed in DMSO. The comparison between the absorption spectra (Figure S6) shows small differences in intensity as well as a small shift of the absorption band which can be explained by solvent effects. Since all major bands are still comparable, we assume that the conjugation did not change the photophysical properties of the Ru(II) polypyridyl complex. As a second experiment, the emission and luminescence of the conjugate was investigated upon excitation at 450 nm in DMSO. The maximum of the emission of the complex (Figure S7) was determined to be 633 nm. Consequently, there is a large Stokes shift which results in minimal interference between excitation and luminescence. The luminescence quantum yield (Φ_{em}) was measured upon excitation at 450 nm by comparison with the model complex $[\text{Ru}(\text{bipy})_3]\text{Cl}_2$ in CH_3CN ($\Phi_{\text{em}} = 5.9\%$).^[23] The luminescence quantum yield (Φ_{em}) of the conjugate **Ru-NB** with a value of 3.3% was found to be in the same range than complexes of the type $[\text{Ru}(\text{bipy})_2(\text{dppz})]^{2+}$ and $[\text{Ru}(\text{phen})_2(\text{dppz})]^{2+}$.^[2c, 4] For a deeper investigation of the excited state, the luminescence lifetimes were determined in degassed and air saturated DMSO upon excitation at 450 nm to investigate the influence of the presence of oxygen. As expected, the luminescence lifetime in a degassed solution was much longer (589 ns, Figure S8) than in an aerated solution (134 ns, Figure S9). This shows that oxygen has a

significant influence on the lifetime of the excited state and indicates that $^3\text{O}_2$ can interact with the triplet state of the complex.

Singlet oxygen generation

Knowing that the triplet excited state of the conjugates are able to interact with oxygen, we were interested in determining the singlet oxygen quantum yield $\Phi(^1\text{O}_2)$ of **Ru-NB** using two methods previously described by our group,^[24] namely: 1) by direct method by measurement of the phosphorescence of $^1\text{O}_2$ at 1270 nm. Worthy of note, this method is dependent on the used setup. With the used equipment in our laboratory, we can only detect $\Phi(^1\text{O}_2) > 0.20$; 2) by indirect method by measurement of the change in absorbance of a reporter molecule which is monitored by UV/VIS spectroscopy. Since the measurements were performed in DMSO and aqueous solution, only rather small values (Table 1) could be measured. This is not surprising and has already been investigated for several other $[\text{Ru}(\text{bipy})_2(\text{dppz})]^{2+}$ and $[\text{Ru}(\text{phen})_2(\text{dppz})]^{2+}$ complex derivatives.^[2c, 4a, 4b] In-depth investigations showed that the excited state of the complex is quenched in an aqueous solution due to hydrogen bonding interactions between the nitrogen atoms of the dppz ligand and the solvent.^[25] Comparison of the singlet oxygen quantum yield of **Ru-NB** with the ones obtained for structurally related $[\text{Ru}(\text{bipy})_2(\text{dppz})]^{2+}$ complexes^[2c], revealed that these values are in the same range and therefore indicating that the bioconjugation did not significantly influence this property.

Table 1. Singlet oxygen quantum yields ($\Phi(^1\text{O}_2)$) of **Ru-NB** in DMSO and aqueous solution determined by direct and indirect method by excitation at 450 nm. Average of three independent measurements, $\pm 10\%$ (n.d.=not detectable).

Compound	DMSO direct	D₂O direct	DMSO Indirect	PBS indirect
Ru-NB	n.d.	n.d.	9%	4%

***In vitro* evaluation of EGFR targeting after conjugation**

In order to investigate the targeting ability of the functionalized NB, uptake in the human epithelial cell line A431 originating from an epidermoid carcinoma of the skin was examined by confocal fluorescence microscopy. These squamous carcinoma cells express approximately 2×10^6 EGFR molecules per cell^[26], which represents a high expression level. Confocal imaging of A431 cells showed co-localization of **Ru-NB** with EGFR (Figure 3), thus indicating the preserved targeting ability of 7C12 after site-specific modification. Noteworthy, **Ru-NB** showed a predominant membrane staining even after 48 h of incubation, and only very little intracellular fluorescence was observed. However, it has been shown recently that the free amine ruthenium complex is characterized by a poor cellular uptake even at high micromolar concentrations.^[4a]

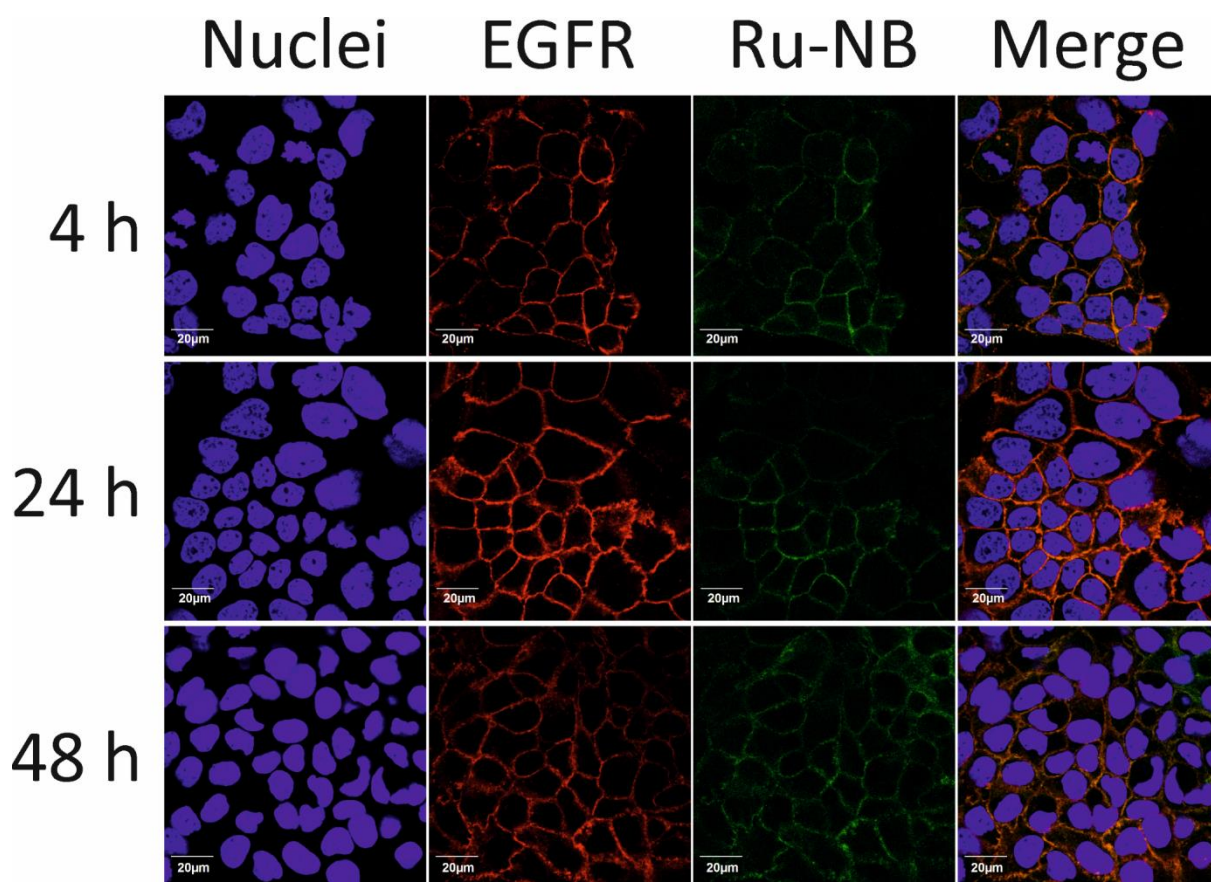


Figure 3. Confocal immunofluorescence microscopy images of A431 cells exposed to **Ru-NB** for 4, 24 and 48 h showing specific binding and co-localization of the single-conjugated NB with EGFR.

Cellular uptake of the bioconjugates

The presence of a metal ubiquitous in a cellular environment as an essential component of the PS allows investigating the cellular accumulation of the bioconjugate by inductively coupled plasma- mass spectrometry (ICP-MS).^[27] In order to demonstrate the receptor-specific uptake, EGFR-positive (A431) and EGFR-negative (MDA-MB-435S) cells were incubated for different periods of time (4, 24, and 48 h) with different concentrations of the bioconjugate in

the dark. The amount of cell-associated ruthenium was determined by ICP-MS and related to the cellular protein content (Figure 4). Although ruthenium was detectable in the cell lysate of both cell lines after 24 and 48 h, respectively, the amount of the metal strongly correlated with the level of EGFR expression. There was more of ruthenium in the EGFR-overexpressing cell line than in the EGFR-negative one. This finding confirmed that cell association was primarily mediated by the NB and not by the PS.

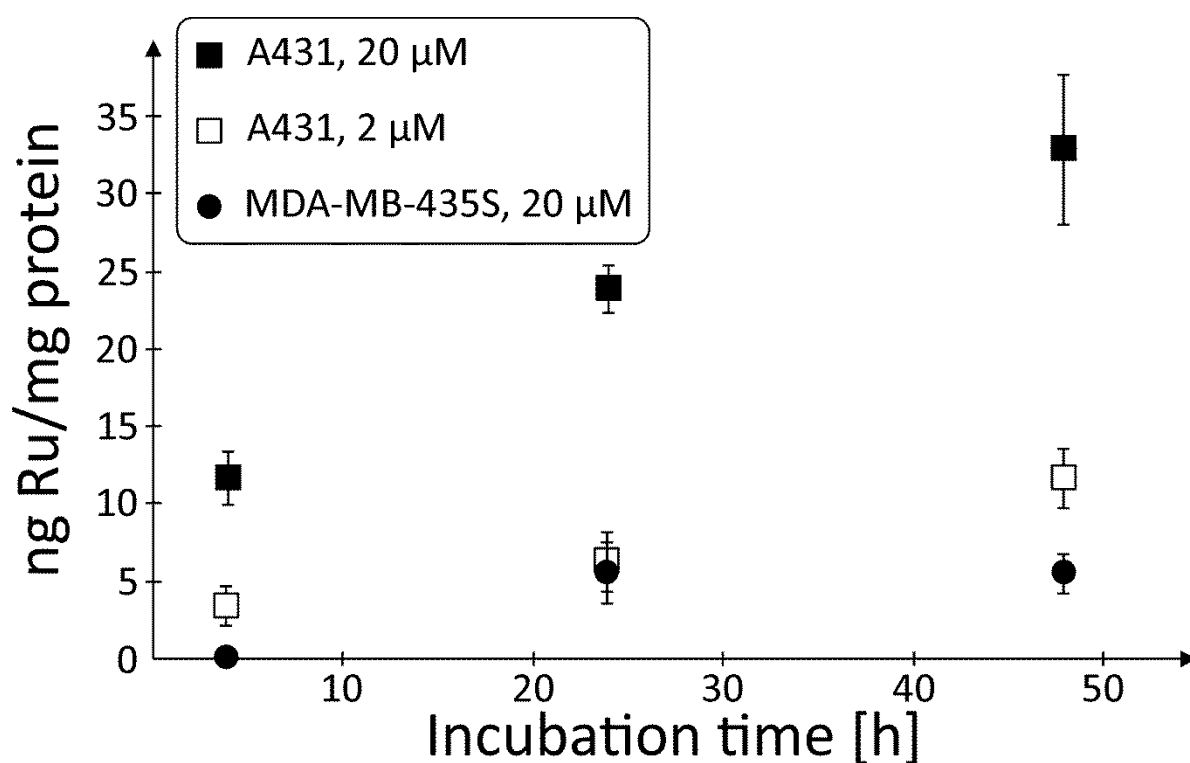


Figure 4. Amount of cell-associated ruthenium after incubation of EGFR-positive A431 and EGFR-negative MDA-MB-435S cells with 2 or 20 μ M of **Ru-NB** for up to 48 h. The level of ruthenium in cell lysates of MDA-MB-435S exposed to 2 μ M of **Ru-NB** were below the analytical limit and are thus not shown.

An identical cell uptake study was performed with the complex [Ru(bipy)₂(dppz-OMe)](PF₆)₂, resulting in comparable ruthenium levels for the A431 cell line (Figure S10 and Table S1). The amount of ruthenium detected in MDA-MB-435S cells upon incubation with this non-targeted Ru-complex was higher at each time point compared to the EGFR-targeting **Ru-NB** conjugate. This result is unsurprising as the latter cells lack these receptor proteins at their surface.

To confirm the receptor specificity of the ruthenium accumulation, A431 cells were incubated in the presence or absence of cetuximab in addition to **Ru-NB**. The epitope for 7C12 partially overlaps the cetuximab epitope on domain III of the EGFR extracellular region and an excess of the mAb can block its interaction with the receptor.^[16, 28] After 24 and 48 h of incubation with 200 nM of **Ru-NB**, 0.77 ng and 2.74 ng ruthenium per mg protein (Table 2), respectively, were detected in the cell lysates. Upon co-incubation of EGFR-overexpressing A431 cells with **Ru-NB** and cetuximab, no cell-associated ruthenium was detectable even after 48 h.

Table 2. Amount of cell-associated ruthenium after incubation of EGFR-positive A431 with 200 nM of **Ru-NB** for 24 or 48 h. The level of ruthenium in cell lysates of A431 co-incubated with 1 μM of the EGFR-blocking antibody cetuximab were below the limit of detection (LOD).

Ru-NB	200 nM	200 nM
Cetuximab	-	1 μM
	ng Ru per mg protein	
24 h	0.77 ± 0.10	< LOD
48 h	2.74 ± 0.12	< LOD

These latter findings corroborate the hypothesis that cellular ruthenium association occurs in a receptor-mediated manner. Overall, **Ru-NB** targets EGFR specifically. Importantly, the free water-soluble PS exhibits only poor cell binding capacity and lacks cell line selectivity, until their conjugation to targeting moieties. These facts together strongly provide the basis for tumor-specific PDT.

Dark cytotoxicity and phototoxicity of Ru-NB

To evaluate the potency of the bioconjugate **Ru-NB** as a PDT agent, its cytotoxicity in the dark and upon light irradiation was determined. For these experiments, the A431 cell line had to be chosen due to the strong light sensitivity of the MDA-MB-435S (EGFR negative) cell line that precluded it from phototoxicity studies. To avoid light sensitivity in A431 cell line, irradiation at 480 nm was performed in sequences. 6 x 3.5 min of irradiation with 15 min gap in between (6.741 J cm^{-2}) were used. Dark treatment and surprisingly light irradiation of the A431 cells (48 h incubation with **Ru-NB**) at 480 nm did not cause any cytotoxic effect ($\text{IC}_{50 \text{ dark}} > 25 \text{ }\mu\text{M}$, $\text{IC}_{50 \text{ light}} > 25 \text{ }\mu\text{M}$, see Figure S11) for **Ru-NB**. We note that we could not go for higher concentration due to conjugate precipitation at $50 \text{ }\mu\text{M}$. Adding polyethylene glycol spacers, changing ionic strength or pH could possibly affect conjugate solubility, and consequently help solving this problem. Lack of cytotoxicity encouraged us to try to enhance the internalization of the conjugate into the cells. For that purpose, an additional step was used, namely temperature change.^[29] Cells treated with **Ru-NB** were incubated for 1 h at $4 \text{ }^\circ\text{C}$. Since EGFR internalization is an energy dependent process, incubating cells at $4 \text{ }^\circ\text{C}$ will inhibit endocytosis processes but not binding of the Ru-NB conjugate to the receptor. A temperature shift to $37 \text{ }^\circ\text{C}$ (for 1 h) allowed then for efficient endocytosis of the receptor with the bound conjugate. This step enables for high accumulation of the Ru-NB in the cells. Due to conjugate precipitation, the highest concentration tested was $35 \text{ }\mu\text{M}$. **Ru-NB** was again found to be non-toxic in the

dark ($IC_{50} > 35 \mu\text{M}$.) Unfortunately, light irradiation at 480 nm (6 x 3.5 min with 15 min gap between irradiations) again did not cause any phototoxic effect ($IC_{50} > 35 \mu\text{M}$, see Figure S12).

Cellular ROS production by Ru-NB

The lack of phototoxicity of **Ru-NB** led us to investigate whether this conjugate could produce ROS in irradiated cells. For that purpose, we have stained A431 cells with the known ROS probe DCFH-DA (2',7'-dichlorodihydrofluorescein diacetate). Cells were then treated with **Ru-NB** (35 μM) using the receptor internalisation protocol, irradiated (480 nm light for 3.5 min; 1,124 J cm^{-2}) and suspended in PBS buffer. The DCFH-DA signal was detected using flow cytometry instrument. As can be seen in Figure S13, there was no ROS production in the A431 cells that were treated with **Ru-NB** and then irradiated, as distinct from the H_2O_2 treated control. This unexpected result might be caused by the impairment of the internalization of **Ru-NB** into the cells. Another explanation would be that the ROS produced are directly reacting with the NB itself. However, this hypothesis is unlikely since $^1\text{O}_2$ was detected during the $^1\text{O}_2$ production measurements.

Conclusion

In summary, in this article, we present the synthesis, characterization and photophysical and biological evaluation of a novel nanobody containing Ru(II) polypyridine conjugate. As a benefit of the linkage to a 7C12 nanobody, the conjugate selectively accumulated at the epidermal growth factor receptor (EGFR). The investigation of the uptake *via* ICP-MS indicated that the conjugate has been successfully internalized inside cancerous A431 cells. Photophysical studies in cuvette suggested that the photophysical properties of the conjugate remain unchanged in comparison to the compound alone. However, DCFH-DA staining

experiments indicated that no significant ROS was produced inside the cells. Consequently, photocytotoxicity investigations did not show any significant effect. Focus of future work will be the successful development of a nanobody-containing Ru(II) polypyridine conjugate with ROS and photocytotoxicity inside cancerous cells.

Experimental Section

Materials

All chemicals were obtained from commercial sources and were used without further purification. Solvents were dried over molecular sieves if necessary. The ligand 5-(aminomethyl)-2,2'-bipyridine^[30] and the Ru(II) complexes [Ru(bphen)₂Cl₂] using the respective ligands^[31], [Ru(phen)₂(dppz-7-aminomethyl)](PF₆)₂ were synthesized as previously reported.^[4a]

Instrumentation and methods

¹H and ¹³C NMR spectra were recorded on a Bruker 400 MHz NMR spectrometer. ESI-MS experiments were carried out using a LTQ-Orbitrap XL from Thermo Scientific (Thermo Fisher Scientific, Courtaboeuf, France) and operated in positive ionization mode, with a spray voltage at 3.6 kV. No Sheath and auxiliary gas was used. Applied voltages were 40 and 100 V for the ion transfer capillary and the tube lens, respectively. The ion transfer capillary was held at 275°C. Detection was achieved in the Orbitrap with a resolution set to 100,000 (at *m/z* 400) and a *m/z* range between 150-2000 in profile mode. Spectrum was analyzed using the acquisition software XCalibur 2.1 (Thermo Fisher Scientific). The automatic gain control (AGC) allowed accumulation of up to 2*10⁵ ions for FTMS scans, Maximum injection time was set to 300 ms

and 1 μ scan was acquired. 10 μ L was injected using a Thermo Finnigan Surveyor HPLC system (Thermo Fisher Scientific) with a continuous infusion of methanol at 100 μ L \cdot min⁻¹. For analytic and preparative HPLC the following system has been used: 2 x Agilent G1361 1260 Prep Pump system with Agilent G7115A 1260 DAD WR Detector equipped with an Agilent Pursuit XRs 5C18 (Analytic: 100Å, C18 5 μ m 250 x 4.6 mm, Preparative: 100Å, C18 5 μ m 250 x 300 mm) Column and an Agilent G1364B 1260-FC fraction collector. The solvents (HPLC grade) were millipore water (0.1% TFA, solvent A) and acetonitrile (0.1% TFA, solvent B). The sample was dissolved in 1:1 (v/v) CH₃CN/ H₂O 0.1% TFA solution and filtered through a 0.2 μ m membrane filter. Gradient: 0-3 minutes: isocratic 95% A (5% B); 3- 17 minutes: linear gradient from 95% A (5% B) to 0% A (100% B); 17-25 minutes: isocratic 0% A (100% B). The flow rate was 1 mL/min (for preparative purposes: 20 mL/min) and the chromatogram was detected at 250 nm, 350 nm, 450 nm.

Synthesis

[Ru(phen)₂(dppz-7-maleimidemethyl)](PF₆)₂

The synthesis of [Ru(phen)₂-dppz-7-maleimidemethyl]²⁺ is already published^[4a] but, in this study, a slightly different synthetic route was employed. [Ru(phen)₂(dppz-7-aminomethyl)](PF₆)₂ (25 mg, 1.0 equiv.) and maleic anhydride (46 mg, 20.0 equiv.) were suspended in acetic acid (10 mL) under a nitrogen atmosphere. The mixture was refluxed for 10 h. The solution was then cooled down and a sat. aqueous solution of NH₄PF₆ was added. The crude product, which precipitated as a PF₆ salt, was collected by filtration and washed three times with H₂O and Et₂O. The product was purified by column chromatography on silica gel with a CH₃CN /aq. KNO₃ (0.4 M) solution (10:1). The fractions containing the product were united and the solvent was removed. The residue was dissolved in CH₃CN and undissolved

KNO₃ was removed by filtration. The solvent was removed and the product was dissolved in H₂O. Upon addition of NH₄PF₆ the product precipitated as a PF₆ salt. The solid was obtained by centrifugation and was washed with H₂O and Et₂O. Yield: 86%. Experimental data fits with the literature. Purity of the sample was assessed by NMR and HPLC analysis. RP-HPLC: R_t = 16.2 min.

[Ru(phen)₂(dppz-7-maleimidemethyl-S-Cys-(Ser)₂(Gly)₅-NH₃)](TFA)₃

[Ru(phen)₂(dppz-7-maleimidemethyl)](PF₆)₂ (16 mg, 1.0 equiv.) and (NH₂CO-Cys-(Ser)₂(Gly)₅-NH₃)(TFA) (11.6 mg, 1.2 equiv.) were dissolved in a 1:1 CH₃CN/H₂O mixture (20 mL) and stirred in the dark at room temperature. The progress of the reaction was followed via HPLC. After 24 h, additional (NH₂CO-Cys-(Ser)₂(Gly)₅-NH₃)(TFA) (4.8 mg, 0.5 equiv.) were added. The reaction mixture was stirred for another 6 h until the complete consumption of the Ru(II) complex was monitored. The solvent was removed under reduced pressure and the product was purified by preparative HPLC. The product was isolated as a red TFA salt. Purity of the sample was assessed by HPLC analysis. Yield: 95%. HRMS (ESI) m/z: Calcd. for [C₆₆H₆₂N₁₈O₁₂RuS-3TFA]³⁺: 445.7874, Found: 445.7875; RP-HPLC: R_t = 14.9 min.

***E. coli* strains and plasmids**

Escherichia coli NEB 5-alpha (*fhuA2* Δ(*argF-lacZ*)U169 *phoA glnV44* Φ80Δ (*lacZ*)M15 *gyrA96 recA1 relA1 endA1 thi-1 hsdR17*) was used in molecular cloning experiments, whereas *E. coli* SHuffle® T7 Express (*fhuA2 lacZ::T7 gene1* [lon] *ompT ahpC gal* λatt::pNEB3-r1-*cDsbC* (Spec^R, *lacI^q*) Δ*trxB sulA11 R(mcr-73::miniTn10--Tet^S)2* [dcm] *R(zgb-210::Tn10 --Tet^S) endA1* Δ*gor* Δ(*mcrC-mrr*)114::IS10) and *E. coli* BL21(DE3) (*fhuA2* [lon] *ompT gal* (λ DE3) [dcm] Δ*hsdS*) were used for expression of the recombinant proteins. All strains were

purchase from New England Biolabs. The generation of pET-28b:7C12 encoding the EGFR-specific single-domain antibody 7C12 has been previously described.^[32] The plasmid pGBMCS-SortA was a gift from Fuyuhiko Inagaki (Addgene plasmid # 21931).^[33]

Molecular cloning

A DNA fragment coding for a (GGGGS)₃ spacer followed by a Strep-tag, the LPETGG sortase motif and another (GGGGS)₃ spacer was commercially synthesized including a 5' restriction site for *Hind*III and a 3' restriction site for *Xho*I, respectively. The ~150-nt fragment was digested with appropriate restriction endonucleases and ligated in-frame into *Hind*III/*Xho*I-linearized pET-28b:7C12 plasmid.^[32] The ligation reactions were transformed into chemically competent *E. coli* NEB 5-alpha cells. The DNA sequences of the resulting recombinant construct pET-28b:7C12-Strep-Sortag-His₆ were checked by Sanger sequencing.

Cultivation and expression of recombinant proteins

Freshly transformed *E. coli* SHuffle® T7 Express or *E. coli* BL21(DE3) harboring the plasmids pET-28b:7C12-Strep-Sortag-His₆ or pGBMCS-SortA were inoculated in 10 mL of LB broth containing 50 µg/mL of kanamycin or 100 µg/mL of ampicillin, respectively, and cultivated at 30°C overnight in an orbital shaker with 50 mm offset and shaking speed of 200 rpm. After that, 5 mL of this pre-culture were transferred into 125 mL MagicMedia™ *E. coli* Expression Medium (Life Technologies) in 1000 mL baffled-bottom glass flasks and grown at 30°C for 24 h. For final harvest, cultures were chilled on ice for 5 min and centrifuged for at least 15 min at 6,000 × g and 4°C. After removal of the supernatant, cell pellets were either stored at -20°C or subjected to purification procedure immediately.

Purification of recombinant proteins

A high-capacity Ni-iminodiacetic acid (IDA) resin in combination with an ÄKTA pure chromatography system (GE Healthcare) was used for purification of hexahistidine tagged proteins by immobilized metal affinity chromatography (IMAC) under native conditions. Efficient cell lysis was achieved by addition of 1 mL RIPA cell lysis buffer (G-Biosciences) supplemented with EDTA-free protease inhibitor cocktail (Roche Diagnostics), 500 µg lysozyme (Sigma-Aldrich) and 25 U endonuclease (Thermo Scientific Pierce) per 200 mg bacterial cell pellet. Prior to incubation on ice for at least 15 min, the pelleted cells were resuspended completely by vortexing or pipetting up and down until no cell clumps remained. After centrifugation at 10,000 x g and 4°C for 20 min to remove cellular debris, the clarified supernatant was loaded using an automated sample pump with a flow rate of 0.5 ml/min. IMAC was performed on a prefilled 5-ml His60 Ni Superflow cartridge (Clontech Laboratories) at a flow rate of 5 mL/min in equilibration buffer (50 mM Tris-HCl, 150 mM NaCl, pH 7.5). Before elution of the hexahistidine tagged proteins by addition of 8 CV elution buffer (50 mM Tris-HCl, 150 mM NaCl, 500 mM imidazole, pH 7.5), the column was washed with 8 CV equilibration buffer and 7 CV wash buffer (50 mM Tris-HCl, 150 mM NaCl, 35 mM imidazole, pH 7.5). Removal of imidazole and buffer exchange after IMAC was achieved by dialysis against sortase buffer (50 mM Tris-HCl, 150 mM NaCl and 10 mM CaCl₂, pH 7.5) using a cellulose ester membrane with a molecular weight cut-off of 3.5-5 kDa (Spectrum® Laboratories).

Gel electrophoresis

Denaturing sodium dodecyl sulfate-polyacrylamide gel electrophoresis (SDS-PAGE) was carried out according to a standard protocol.^[34] For each gel, PageRuler Plus Prestained Protein

Ladder (Thermo Fisher Scientific) was used as molecular weight ladder standard. After electrophoresis, gels were imaged with a D-DiGit Gel Scanner (LI-COR Biosciences) and subsequently stained with PageBlue protein staining solution (Thermo Fisher Scientific) according to the manufacturer's instructions.

Protein determination

Protein concentration was determined with the DC Protein Assay (Bio-Rad Laboratories) according to the manufacturer's microplate assay protocol using bovine serum albumin in sortase buffer (50 mM Tris-HCl, 150 mM NaCl and 10 mM CaCl₂, pH 7.5) as protein standard.

Sortase A-mediated conjugation

Small-scale reactions were set up in 100 μ L with variable molar ratios of SrtA, 7C12-Strep-Sortag-His₆ and [Ru(phen)₂(dppz-7-maleimidemethyl-S-Cys-(Ser)₂(Gly)₅-NH₃)]³⁺ and different incubation times. The optimal conditions were upscaled and the reaction mixture was composed of 2 μ mol SrtA, 2 μ mol NB and 20 μ mol [Ru(phen)₂(dppz-7-maleimidemethyl-S-Cys-(Ser)₂(Gly)₅-NH₃)]³⁺ in sortase buffer (50 mM Tris-HCl, 150 mM NaCl and 10 mM CaCl₂, pH 7.5). Bioconjugation reactions were incubated at 30°C for up to 6 h in the dark with gentle shaking.

Purification of conjugation reactions

In the first purification step, all remaining hexahistidine tagged proteins were eliminated from the reaction mixture by IMAC using prepacked His60 Ni Gravity Columns (Clontech Laboratories). After collection of the flow-through, the gravity-flow column was washed twice with equilibration buffer (50 mM Tris-HCl, 150 mM NaCl, pH 7.5). These wash fractions as

well as the flow-through were analyzed for the presence of the Ru-NB conjugate by SDS-PAGE. Remaining unconjugated $[\text{Ru}(\text{phen})_2(\text{dppz-7-maleimidemethyl-S-Cys}-(\text{Ser})_2(\text{Gly})_5\text{-NH}_3)]^{3+}$ was removed in a second purification step by size-exclusion chromatography using Zeba Spin Desalting Columns (7K MWCO, Thermo Scientific) with elution in PBS. The purified conjugate was sterile filtered using Whatman Puradisc FP 30 cellulose acetate syringe filter units with a pore size of 0.2 μm (GE Healthcare Life Sciences) and stored at 4°C.

Matrix-assisted laser desorption ionization time-of-flight (MALDI-TOF) mass spectrometry of purified sdAb-conjugates

2,5-Dihydroxyacetophenone (2,5-DHAP, Bruker Daltonik) was used as matrix for MALDI-TOF MS. For solubilization of the matrix, 7.6 mg of 2,5-DHAP were dissolved in 375 μL of absolute ethanol. After this, 125 μL of an 18 mg/mL aqueous solution of diammonium hydrogen citrate (Sigma-Aldrich) were added. Protein samples were desalted using mixed cellulose esters membrane filters with a pore size of 0.025 μm and a diameter of 25 mm (MF-Millipore™ Membrane Filter VSWP, Merck Chemicals). Briefly, the filter was placed on the water surface of a beaker filled with distilled water. A 2 μL aliquot of the protein sample was carefully pipetted on top of the membrane. After incubation at room temperature for at least 10 min, 2 μL of the dialyzed sample was mixed with 2 μL of 2% TFA solution. After addition of 2 μL of the matrix solution, the mixture was pipetted up and down until the crystallization starts and the solution became cloudy. Finally, 0.5 μL of the crystal suspension was spotted onto the ground steel target plate and the droplet was air-dried completely at room temperature. Spectra were acquired with an autoflex II TOF/TOF (Bruker Daltonik) in positive linear mode in combination with the flexControl software (Version 3.3, Bruker Daltonik) and analyzed with

the flexAnalysis software (Version 3.3, Bruker Daltonik). Theoretical molecular weights were calculated using the Compute pI/Mw tool on the ExPASy Server.^[35]

Spectroscopic measurements

The absorption of the samples was measured in a cuvette with a Lambda 800 UV/VIS Spectrometer (PerkinElmer Instruments) or in 96 well plates with a SpectraMax M2 Spectrometer (Molecular Devices). The emission was measured by irradiation of the sample in fluorescence quartz cuvettes (width 1 cm) using a NT342B Nd-YAG pumped optical parametric oscillator (Ekspla) at 450 nm. The luminescence was focused and collected at a right angle to the excitation pathway and directed to a Princeton Instruments Acton SP-2300i monochromator. As a detector a XPI-Max 4 CCD camera (Princeton Instruments) was used.

Luminescence quantum yield measurements

For the determination of the luminescence quantum yield, the samples were prepared in a CH₃CN solution with an absorbance of 0.1 at 450 nm. This solution was irradiated in fluorescence quartz cuvettes (width 1 cm) using a NT342B OPO pulse laser Nd-YAG pumped optical parametric oscillator (Ekspla) at 450 nm. The emission signal was focused and collected at a right angle to the excitation pathway and directed to a Princeton Instruments Acton SP-2300i monochromator. As a detector a XPI-Max 4 CCD camera (Princeton Instruments) was used. The luminescence quantum yields were determined by comparison with the reference [Ru(bipy)₃]Cl₂ in CH₃CN ($\Phi_{em}=0.059$)^[23] applying the following formula:

$$\Phi_{em,sample} = \Phi_{em,reference} * \frac{F_{reference}}{F_{sample}} * \frac{I_{sample}}{I_{reference}} * \left(\frac{n_{sample}}{n_{reference}} \right)^2$$

$$F = 1 - 10^{-A}$$

Φ_{em} = luminescence quantum yield, F = fraction of light absorbed, I = integrated emission intensities, n = refractive index, A = absorbance of the sample at irradiation wavelength

Lifetime measurements

For the determination of the lifetimes, the samples were prepared in an air saturated and in a degassed CH₃CN solution with an absorbance of 0.1 at 450 nm. This solution was irradiated in fluorescence quartz cuvettes (width 1 cm) using a NT342B Nd-YAG pumped optical parametric oscillator (Ekspla) at 450 nm. The emission signal was focused and collected at a right angle to the excitation pathway and directed to a Princeton Instruments Acton SP-2300i monochromator. As a detector a R928 photomultiplier tube (Hamamatsu) was used.

Singlet oxygen measurements

- Direct evaluation

The samples were prepared in an air saturated DMSO or D₂O solution with an absorbance of 0.2 at 450 nm. This solution was irradiated in fluorescence quartz cuvettes (width 1 cm) using a mounted M450LP1 LED (Thorlabs) whose irradiation, centred at 450 nm, was focused with aspheric condenser lenses. The intensity of the irradiation was varied using a T-Cube LED Driver (Thorlabs) and measured with an optical power and energy meter. The emission signal was focused and collected at a right angle to the excitation pathway and directed to a Princeton Instruments Acton SP-2300i monochromator. A longpass glass filter was placed in front of the monochromator entrance slit to cut off light at wavelengths shorter than 850 nm. The slits for detection were fully open. As a detector an EO-817L IR-sensitive liquid nitrogen cooled germanium diode detector (North Coast Scientific Corp.) was used. The singlet oxygen

luminescence at 1270 nm was measured by recording spectra from 1100 to 1400 nm. For the data analysis, the singlet oxygen luminescence peaks at different irradiation intensities were integrated. The resulting areas were plotted against the percentage of the irradiation intensity and the slope of the linear regression calculated. The absorbance of the sample was corrected with an absorbance correction factor. As reference for the measurement in an CH₃CN solution phenalenone ($\Phi_{\text{phenalene}}=0.95$)^[36] and for the measurement in a D₂O solution [Ru(bipy)₃]Cl₂ ($\Phi_{\text{Ru(bipy)}_3\text{Cl}_2}=0.22$)^[37] was used and the singlet oxygen quantum yields were calculated using the following formula:

$$\Phi_{\text{sample}} = \Phi_{\text{reference}} * \frac{S_{\text{sample}}}{S_{\text{reference}}} * \frac{I_{\text{reference}}}{I_{\text{sample}}}$$

$$I = I_0 * (1 - 10^{-A})$$

Φ = singlet oxygen quantum yield, S = slope of the linear regression of the plot of the areas of the singlet oxygen luminescence peaks against the irradiation intensity, I = absorbance correction factor, I₀ = light intensity of the irradiation source, A = absorbance of the sample at irradiation wavelength.

- **Indirect evaluation**

For the measurement in DMSO: The samples were prepared in an air-saturated DMSO solution containing the complex with an absorbance of 0.2 at the irradiation wavelength and 1,3-diphenylisobenzofuran (DPBF, 30 μ M). For the measurement in PBS buffer: The samples were prepared in an air-saturated PBS solution containing the complex with an absorbance of 0.2 at the irradiation wavelength, *N,N*-dimethyl-4-nitrosoaniline aniline (RNO, 20 μ M) and histidine (10 mM). The samples were irradiated on 96 well plates with an Atlas Photonics LUMOS BIO irradiator for different times. The absorbance of the samples was measured during these time

intervals with a SpectraMax M2 Microplate Reader (Molecular Devices). The difference in absorbance ($A_0 - A$) at 415 nm for the DMSO solution and at 440 nm for the PBS solution was measured and plotted against the irradiation times. From the plot the slope of the linear regression was calculated as well as the absorbance correction factor determined. The singlet oxygen quantum yields were calculated using the same formulas as used for the direct evaluation.

Cell culture

Cell culture flasks, dishes and plates (CELLSTARS) were supplied by Greiner Bio-One GmbH. The adherent human tumor cell lines A431 (ATCC® number: CRL-1555) and MDA-MB 435S (ATCC® number: HTB-129) were maintained as previously reported.^[32, 38] All cell lines were confirmed to be mycoplasma-negative using the Venor®GeM Advance Mycoplasma Detection Kit (Minerva Biolabs) and were tested monthly.

Cell uptake studies

A total of 300,000 MDA-MB 435S cells and 450,000 A431 cells were seeded in T25 cell culture flasks in 5 mL DMEM supplemented with 10% fetal calf serum (FCS), respectively, and incubated in a humidified atmosphere of 95% air/5% CO₂ at 37°C. After 48 h of incubation, cells were washed twice with warm PBS. The buffer was then replaced by fresh DMEM supplemented with 10% FCS and different concentrations of the Ru-NB conjugate or Ru(bipy)₂(DPPZ-OMe) (PF₆)₂. Following incubation at 37°C for certain time periods, medium was removed and the cells washed three times with warm PBS and trypsinized. After resuspension in warm DMEM with 10% FCS, the pellets were collected by centrifugation at 200 x g for 5 min and washed once with warm PBS. The cell pellets were resuspended in 500 µL

of PBS, lysed by 10 freeze–thaw cycles, and sonicated in an ice-cold ultrasonic bath for 20 min (SONOREX SUPER 10P digital, Bandelin). After determination of the protein content, the lysates were lyophilized on an Alpha 2-4 LSC plus (CHRIST).

ICP-MS studies

After digestion of samples in distilled ultrapure 65% HNO₃ (Roth) and dilution in 1% HNO₃, ICP-MS measurements were performed on an iCap RQ ICP-MS spectrometer (Thermo Fisher Scientific) equipped with a SC-2DX autosampler (ESI). Calibration was done with Ru single element standard (Merck 170347). Rh and Sc were used as internal standards. Limit of detection (LOD) was 50 ng/L Ru.

Dark cytotoxicity and phototoxicity

The dark and light cytotoxicity of the Ru(II)-containing conjugates was assessed by fluorometric cell viability assay using resazurin (ACROS Organics). For dark and light cytotoxicity with the EGFR internalisation step^[39], A431 cells were seeded in triplicates in 96 well plates at a density of 4000 cells per well in 100 µl, 24 h prior to treatment. Cells were then treated with serum free DMEM media containing 0.3% of BSA for 1 h at 37 °C. The medium was then replaced with increasing concentrations of **Ru-NB**, then cells were incubated on ice for 1 h. After that time, cells were transferred for 1 h at 37 °C. The medium was then replaced by fresh complete medium. For the dark and light cytotoxicity without the EGFR internalisation step, A431 cells were seed in triplicates in 96 well plares at a density of 4000 cells per well in 100 µl, 24 h prior to treatment. The medium was then replaced with increasing concentrations of **Ru-NB** for 44 h. Cells used for the light cytotoxicity experiments with **Ru-NB** were exposed to 480 nm light for 6 x 3.5 min with 15 min gap in between irradiations or in a 96-well plate using a LUMOS-BIO photoreactor (Atlas Photonics). Each well was individually illuminated with a 5 lm LED at

constant current (6.741 J cm^{-2}). After 44 h in the incubator, the medium was replaced by fresh complete medium containing resazurin (0.2 mg mL^{-1} final concentration). After 4 h incubation at 37°C , the fluorescence signal of the resorufin product was read by SpectraMax M5 microplate reader (ex: 540 nm em: 590 nm). IC_{50} values were calculated using GraphPad Prism software.

Cellular ROS production

10 cm cell culture plates were seeded with A431 cell line and allowed to adhere overnight. Next, the cells were incubated with a DCFH-DA solution ($100 \text{ }\mu\text{M}$) in DMEM media for 30 min at 37°C . Cells were then washed and treated with serum free DMEM media containing 0.3% of BSA for 1 h at 37°C . The medium was then replaced in the plates with either **Ru-NB** dilution, $0.1 \text{ mM H}_2\text{O}_2$ or media. Cells were then incubated on ice for 1 h. After that time, the cells were transferred for 1 h at 37°C . The medium was then replaced by fresh complete medium. The cells used for the light experiments were exposed to 480 nm light for 3.5 min using a LUMOS-BIO photoreactor (Atlas Photonics; 1.124 J cm^{-2}). All cells were then washed, collected and gated using Fortessa instrument in Cytometry Platform at the Curie Institute.

Data was analysed using FlowJo 10.5.2 software.

Acknowledgments

We gratefully acknowledge financial support from the ERC (Consolidator Grant PhotoMedMet (GA 681679) to G.G.). This work has received support under the program «Investissements d’Avenir » launched by the French Government and implemented by the ANR with the reference ANR-10-IDEX-0001-02 PSL (G.G.). We thank Prof. Philippe Goldner for access to state-of-the-art laser apparatus and S. Beutner and S. Weiss for performing ICP-MS measurements. This work was supported by the Helmholtz Initiative and Networking Fund (Functional Nanomaterials for Multimodality Cancer Imaging (NanoTracking), project ID: VH-VI-421) and we thank Utta Herzog for excellent technical support during the cell culture work.

References

- [1] a) C. Mari, V. Pierroz, S. Ferrari, G. Gasser, *Chem. Sci.* **2015**, *6*, 2660-2686; b) F. Heinemann, J. Karges, G. Gasser, *Acc. Chem. Res.* **2017**, *50*, 2727-2736; c) L. K. McKenzie, H. E. Bryant, J. A. Weinstein, *Coord. Chem. Rev.* **2019**, *379*, 2-29; d) J. Liu, C. Zhang, T. W. Rees, L. Ke, L. Ji, H. Chao, *Coord. Chem. Rev.* **2018**, *363*, 17-28; e) K. Plaetzer, B. Krammer, J. Berlanda, F. Berr, T. Kiesslich, *Lasers Med. Sci.* **2009**, *24*, 259-268; f) L. B. Josefsen, R. W. Boyle, *Met Based Drugs* **2008**, *2008*, 276109.
- [2] a) J. D. Knoll, C. Turro, *Coord. Chem. Rev.* **2015**, *282*, 110-126; b) L. Lilge, *Ruthenium Complexes: Photochemical and Biomedical Applications* **2018**, 117-137; c) C. Mari, V. Pierroz, R. Rubbiani, M. Patra, J. Hess, B. Spingler, L. Oehninger, J. Schur, I. Ott, L. Salassa, *Chem. Eur. J.* **2014**, *20*, 14421-14436; d) J. Karges, O. Blacque, M. Jakubaszek, B. Goud, P. Goldner, G. Gasser, *J. Inorg. Biochem.* **2019**, *198*, 110752; e) M. Jakubaszek, B. Goud, S. Ferrari, G. Gasser, *Chem. Commun.* **2018**, *54*, 13040-13059; f) S. Monro, K. L. Colón, H. Yin, J. Roque III, P. Konda, S. Gujar, R. P. Thummel, L.

- Lilge, C. G. Cameron, S. A. McFarland, *Chem. Rev.* **2019**, *119*, 797-828; g) J. Karges, F. Heinemann, F. Maschietto, M. Patra, O. Blacque, I. Ciofini, B. Spingler, G. Gasser, *Bioorg. Med. Chem.* **2019**, *27*, 2666-2675; h) M. Jakubaszek, J. Rossier, J. Karges, J. Delasoie, B. Goud, G. Gasser, F. Zobi, *Helv. Chim. Acta* **2019**, *accepted*, doi:10.1002/hlca.201900104.
- [3] J. Fong, K. Kasimova, Y. Arenas, P. Kaspler, S. Lazic, A. Mandel, L. Lilge, *Photochem. Photobiol. Sci.* **2015**, *14*, 2014-2023.
- [4] a) C. Mari, V. Pierroz, A. Leonidova, S. Ferrari, G. Gasser, *Eur. J. Inorg. Chem.* **2015**, *2015*, 3879-3891; b) C. Mari, R. Rubbiani, G. Gasser, *Inorg. Chim. Acta* **2017**, *454*, 21-26; c) J. Hess, H. Huang, A. Kaiser, V. Pierroz, O. Blacque, H. Chao, G. Gasser, *Chem. Eur. J.* **2017**, 9888-9896.
- [5] L. H. Hurley, *Nat. Rev. Cancer* **2002**, *2*, 188-200.
- [6] a) P. Kay, in *Semin. Oncol. Nurs.*, Vol. 22, Elsevier, **2006**, pp. 1-4; b) A. Eastman, *Cisplatin. Chemistry and biochemistry of a leading anticancer drug* **1999**, 111-134.
- [7] a) T. Wang, N. Zabarska, Y. Wu, M. Lamla, S. Fischer, K. Monczak, D. Y. Ng, S. Rau, T. Weil, *Chem. Commun.* **2015**, *51*, 12552-12555; b) Y. Ellahioui, M. Patra, C. Mari, R. Kaabi, J. Karges, G. Gasser, S. Gómez-Ruiz, *Dalton Trans.* **2019**, *48*, 5940-5951; c) S. Chakraborty, B. K. Agrawalla, A. Stumper, N. M. Vegi, S. Fischer, C. Reichardt, M. Kögler, B. Dietzek, M. Feuring-Buske, C. Buske, *J. Am. Chem. Soc.* **2017**, *139*, 2512-2519; d) E. Villemin, Y. C. Ong, C. M. Thomas, G. Gasser, *Nat. Rev. Chem.* **2019**, *3*, 261-282.
- [8] P. Kaspler, S. Lazic, S. Forward, Y. Arenas, A. Mandel, L. Lilge, *Photochem. Photobiol. Sci.* **2016**, *15*, 481-495.
- [9] a) A. Zamora, A. Gandioso, A. Massaguer, S. Buenestado, C. Calvis, J. L. Hernández, F. Mitjans, V. Rodríguez, J. Ruiz, V. Marchán, *ChemMedChem* **2018**, *13*, 1755-1762;

- b) V. Novohradsky, A. Zamora, A. Gandioso, V. Brabec, J. Ruiz, V. Marchán, *Chem. Commun.* **2017**, 53, 5523-5526; c) F. Barragán, D. Carrion-Salip, I. Gómez-Pinto, A. González-Cantó, P. J. Sadler, R. de Llorens, V. Moreno, C. González, A. Massaguer, V. Marchán, *Bioconjugate Chem.* **2012**, 23, 1838-1855; d) F. Barragán, P. López-Senín, L. Salassa, S. Betanzos-Lara, A. Habtemariam, V. Moreno, P. J. Sadler, V. Marchán, *J. Am. Chem. Soc.* **2011**, 133, 14098-14108; e) A. Leonidova, V. Pierroz, R. Rubbiani, J. Heier, S. Ferrari, G. Gasser, *Dalton Trans.* **2014**, 43, 4287-4294.
- [10] a) T. M. Allen, P. R. Cullis, *Science* **2004**, 303, 1818-1822; b) C. Alonso, R. W. Boyle, in *Handbook of Porphyrin Science (Volume 4) With Applications to Chemistry, Physics, Materials Science, Engineering, Biology and Medicine*, World Scientific, **2010**, pp. 121-190; c) Y. N. Konan, R. Gurny, E. Allémann, *J. Photochem. Photobiol. B: Biol.* **2002**, 66, 89-106; d) W. M. Sharman, J. E. van Lier, C. M. Allen, *Adv. Drug Del. Rev.* **2004**, 56, 53-76; e) R. Hudson, R. W. Boyle, *J. Porphyr. Phthalocyanines* **2004**, 8, 954-975; f) A. J. Bullous, C. M. Alonso, R. W. Boyle, *Photochem. Photobiol. Sci.* **2011**, 10, 721-750. g) V. del Solar, M. Contel, *J. Inorg. Biochem.* **2019**, accepted. doi: 10.1016/j.jinorgbio.2019.110780
- [11] a) J. Golay, M. Introna, *Arch. Biochem. Biophys.* **2012**, 526, 146-153; b) F. Yuan, M. Dellian, D. Fukumura, M. Leunig, D. A. Berk, V. P. Torchilin, R. K. Jain, *Cancer Res.* **1995**, 55, 3752-3756.
- [12] a) M. Ferrari, *Trends Biotechnol.* **2010**, 28, 181-188; b) D. Vivier, S. K. Sharma, B. M. Zeglis, *J. Labelled Compd. Radiopharm.* **2018**, 61, 672-692.
- [13] a) M. Bhatti, G. Yahioğlu, L. R. Milgrom, M. Garcia-Maya, K. A. Chester, M. P. Deonarain, *Int. J. Cancer* **2008**, 122, 1155-1163; b) L. R. Milgrom, *Sci. Prog.* **2008**, 91, 241-263; c) S. K. Batra, M. Jain, U. A. Wittel, S. C. Chauhan, D. Colcher, *Curr. Opin. Biotechnol.* **2002**, 13, 603-608.

- [14] a) M. Arbabi-Ghahroudi, *Front. Immunol.* **2017**, *8*, 1589; b) Y. Hu, C. Liu, S. Muyldermans, *Front. Immunol.* **2017**, *8*, 1442; c) M. E. Iezzi, L. Policastro, S. Werbajh, O. Podhajcer, G. A. Canziani, *Front. Immunol.* **2018**, *9*, 273.
- [15] <https://clinicaltrials.gov/ct2/show/NCT02553317>, (Accessed 27.06.2019).
- [16] L. O. T. Gainkam, L. Huang, V. Caveliers, M. Keyaerts, S. Hernot, I. Vaneycken, C. Vanhove, H. Revets, P. De Baetselier, T. Lahoutte, *J. Nucl. Med.* **2008**, *49*, 788.
- [17] a) A. Gschwind, O. M. Fischer, A. Ullrich, *Nat. Rev. Cancer* **2004**, *4*, 361-370; b) T. Holbro, N. E. Hynes, *Annu. Rev. Pharmacol. Toxicol.* **2004**, *44*, 195-217.
- [18] R. Heukers, V. Mashayekhi, M. Ramirez-Escudero, H. de Haard, T. C. Verrips, P. van Bergen en Henegouwen, S. Oliveira, *Antibodies* **2019**, *8*, 26.
- [19] S. Albert, C. Arndt, A. Feldmann, R. Bergmann, D. Bachmann, S. Koristka, F. Ludwig, P. Ziller-Walter, A. Kegler, S. Gärtner, M. Schmitz, A. Ehninger, M. Cartellieri, G. Ehninger, H.-J. Pietzsch, J. Pietzsch, J. Steinbach, M. Bachmann, *OncoImmunology* **2017**, *6*, e1287246.
- [20] a) C. P. Guimaraes, M. D. Witte, C. S. Theile, G. Bozkurt, L. Kundrat, A. E. Blom, H. L. Ploegh, *Nat. Protoc.* **2013**, *8*, 1787; b) S. Massa, N. Vikani, C. Betti, S. Ballet, S. Vanderhaegen, J. Steyaert, B. Descamps, C. Vanhove, A. Bunschoten, F. W. van Leeuwen, *Contrast Media Mol. Imaging* **2016**, *11*, 328-339; c) B. M. Paterson, K. Alt, C. M. Jeffery, R. I. Price, S. Jagdale, S. Rigby, C. C. Williams, K. Peter, C. E. Hagemeyer, P. S. Donnelly, *Angew. Chem. Int. Ed.* **2014**, *53*, 6115-6119.
- [21] Y. Zong, T. W. Bice, H. Ton-That, O. Schneewind, S. V. Narayana, *J. Biol. Chem.* **2004**.
- [22] J. M. J. M. Ravasco, H. Faustino, A. Trindade, P. M. p. Gois, *Chem. Eur. J.* **2019**, *25*, 43-59.
- [23] K. Nakamaru, *Bull. Chem. Soc. Jpn.* **1982**, *55*, 1639-1640.

- [24] a) H. Huang, B. Yu, P. Zhang, J. Huang, Y. Chen, G. Gasser, L. Ji, H. Chao, *Angew. Chem. Int. Ed.* **2015**, *54*, 14049-14052; b) J. Karges, P. Goldner, G. Gasser, *Inorganics* **2019**, *7*, 4.
- [25] a) J.-P. Sauvage, N. J. Turro, *J. Am. Chem. Soc.* **1990**, *11*, 4960-4962; b) J. Olofsson, B. Önfelt, P. Lincoln, *J. Phys. Chem. A* **2004**, *108*, 4391-4398; c) E. Olson, D. Hu, A. Hörmann, A. Jonkman, M. Arkin, E. Stemp, J. Barton, P. Barbara, *J. Am. Chem. Soc.* **1997**, *119*, 11458-11467.
- [26] a) Z. Novy, P. Barta, J. Mandikova, M. Laznicek, F. Trejtnar, *Nucl. Med. Biol.* **2012**, *39*, 893-896; b) H. Björkelund, L. Gedda, K. Andersson, *PLoS One* **2011**, *6*, e16536.
- [27] I. Ott, C. Biot, C. Hartinger, *Inorganic Chemical Biology: Principles, Techniques and Applications* **2014**, 63-97.
- [28] K. R. Schmitz, A. Bagchi, R. C. Roovers, P. M. v. B. en Henegouwen, K. M. Ferguson, *Structure* **2013**, *21*, 1214-1224.
- [29] a) M. G. Lampugnani, F. Orsenigo, M. C. Gagliani, C. Tacchetti, E. Dejana, *J. Cell Biol.* **2006**, *174*, 593-604; b) R. Carbone, S. Fre, G. Iannolo, F. Belleudi, P. Mancini, P. G. Pelicci, M. R. Torrisi, P. P. Di Fiore, *Cancer Res.* **1997**, *57*, 5498-5504.
- [30] C. A. Panetta, H. J. Kumpaty, N. E. Heimer, M. C. Leavy, C. Hussey, *J. Org. Chem.* **1999**, *64*, 1015-1021.
- [31] B. P. Sullivan, D. J. Salmon, T. J. Meyer, *Inorg. Chem.* **1978**, *17*, 3334-3341.
- [32] K. Zarschler, S. Witecy, F. Kapplusch, C. Foerster, H. Stephan, *Microb. Cell Fact.* **2013**, *12*, 97.
- [33] Y. Kobashigawa, H. Kumeta, K. Ogura, F. Inagaki, *J. Biomol. NMR* **2009**, *43*, 145.
- [34] U. K. Laemmli, *Nature* **1970**, *227*, 680.
- [35] E. Gasteiger, C. Hoogland, A. Gattiker, M. R. Wilkins, R. D. Appel, A. Bairoch, in *The proteomics protocols handbook*, Springer, **2005**, pp. 571-607.

- [36] I. E. Kochevar, R. W. Redmond, in *Methods Enzymol.*, Vol. 319, Academic Press **2000**, pp. 20-28.
- [37] D. Garcia-Fresnadillo, Y. Georgiadou, G. Orellana, A. M. Braun, E. Oliveros, *Helv. Chim. Acta* **1996**, 79, 1222-1238.
- [38] K. Zarschler, K. Prapainop, E. Mahon, L. Rocks, M. Bramini, P. Kelly, H. Stephan, K. Dawson, *Nanoscale* **2014**, 6, 6046-6056.
- [39] S. Rizzolio, L. Tamagnone, *Cancer Res.* **2012**, 72, 5801-5811.

Supplementary Information

Design of Nanobody-containing Ru(II) Polypyridyl Conjugates as Photosensitizers for Epidermal Growth Factor Receptor Targeted Photodynamic Therapy

Johannes Karges,^{a,#} Marta Jakubaszek,^{a,b,#} Cristina Mari,^{c,#} Kristof Zarschler,^{d,#,} Bruno
Goud,^b Holger Stephan,^d and Gilles Gasser^{a,*}*

^a Chimie ParisTech, PSL University, CNRS, Institute of Chemistry for Life and Health Sciences, Laboratory for Inorganic Chemical Biology, F-75005 Paris, France.

^b Institut Curie, PSL University, CNRS UMR 144, Paris, France.

^c Department of Chemistry, University of Zurich, Winterthurerstrasse 190, CH-8057 Zurich, Switzerland.

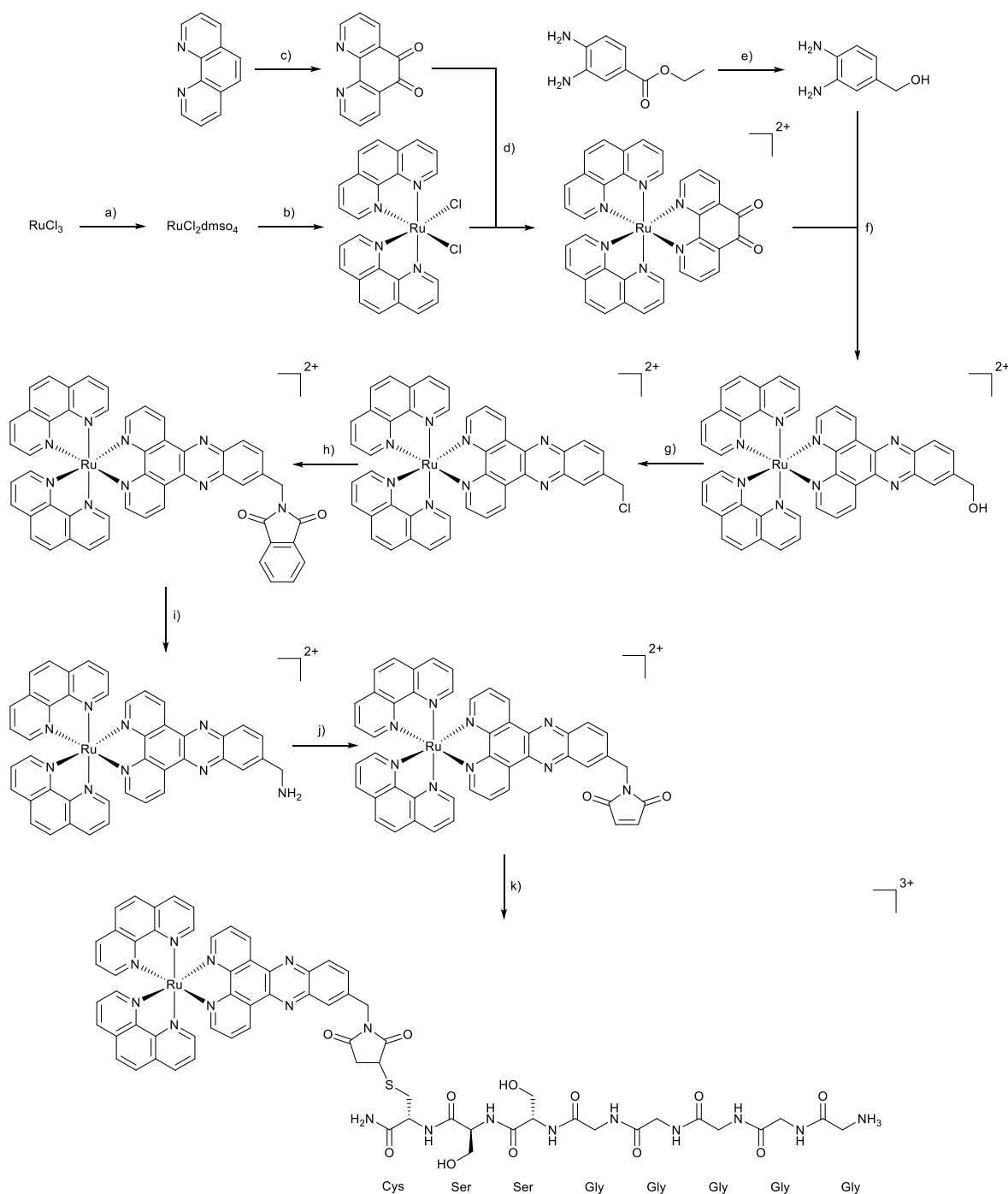
^d Helmholtz-Zentrum Dresden - Rossendorf, Institute of Radiopharmaceutical Cancer Research, Bautzner Landstraße 400, D-01328 Dresden, Germany.

These authors have contributed equally to the work.

*Corresponding authors: Email: k.zarschler@hzdr.de, WWW: www.hzdr.de/NanoscalicSystems, Tel. +49 351 260 3678; Email: gilles.gasser@chimieparistech.psl.eu, WWW: www.gassergroup.com, Tel. +33 1 44 27 56 02.

Table of contents

SCHEME S1. TOTAL SYNTHESIS OF [RU(PHEN) ₂ (DPPZ-7-MALEIMIDEMETHYL-S-CYS-(SER) ₂ (GLY) ₅ -NH ₃)](TFA) ₃	143
FIGURE S1. HPLC CHROMATOGRAM OF [RU(PHEN) ₂ (DPPZ-7-MALEIMIDEMETHYL)] ²⁺	144
FIGURE S2. HPLC CHROMATOGRAM OF [RU(PHEN) ₂ (DPPZ-7-MALEIMIDEMETHYL-S-CYS-(SER) ₂ (GLY) ₅ -NH ₃)] ³⁺	144
FIGURE S3. SDS-PAGE ANALYSIS OF THE REACTION EFFICIENCY FOR CHEMOENZYMATIC CONJUGATION OF THE [RU(PHEN) ₂ (DPPZ-7-MALEIMIDEMETHYL-S-CYS-(SER) ₂ (GLY) ₅ -NH ₃)] ³⁺ TO THE EGFR-SPECIFIC NB 7C12 .	145
FIGURE S4. SDS-PAGE ANALYSIS OF THE REACTION EFFICIENCY FOR CHEMOENZYMATIC CONJUGATION OF THE [RU(PHEN) ₂ (DPPZ-7-MALEIMIDEMETHYL-S-CYS-(SER) ₂ (GLY) ₅ -NH ₃)] ³⁺ TO THE EGFR-SPECIFIC NB 7C12.)	146
FIGURE S5. MALDI-TOF MASS SPECTRA OF THE PURIFIED NB DERIVATIVE 7C12-STREP-SORTAG-HIS ₆ , SINGLE-CONJUGATED NB-CONJUGATE 7C12-STREP-[RU(PHEN) ₂ (DPPZ-7-MALEIMIDEMETHYL-S-CYS-(SER) ₂ (GLY) ₅ -NH ₃)] ³⁺ (RU-NB) AND (C) SORTASE ENZYME SRTA.....	147
FIGURE S6. NORMALISED UV/VIS SPECTRA OF [RU(PHEN) ₂ (DPPZ-7-MALEIMIDEMETHYL)](PF ₆) ₂ , [RU(PHEN) ₂ (DPPZ-7-MALEIMIDEMETHYL-S-CYS-(SER) ₂ (GLY) ₅ -NH ₃)](TFA) ₃ AND RU-NB	148
FIGURE S7. EMISSION SPECTRA OF RU-NB IN DMSO.	149
FIGURE S8. LIFETIME SPECTRA OF RU-NB IN DEGASSED DMSO.	150
FIGURE S9. LIFETIME SPECTRA OF RU-NB IN AERATED DMSO.....	151
FIGURE S10. AMOUNT OF CELL-ASSOCIATED RUTHENIUM IN A431 AND MDA-MB-435S CELL LINES	152
TABLE S1. COMPARISON OF UPTAKE OF RU-NB AND [RU(BIPY) ₂ (DPPZ-OME)](PF ₆) ₂ INTO A431 AND MDA-MB 435S CELLS.	153
FIGURE S11. CYTOTOXICITY OF RU-NB IN A431 CELL LINE.....	154
FIGURE S12. CYTOTOXICITY OF RU-NB IN A431 CELL LINE.....	155
FIGURE S13. CELLULAR ROS PRODUCTION IN A431 CELLS TREATED WITH RU-NB	156



Scheme S1. Total synthesis of $[\text{Ru}(\text{phen})_2(\text{dppz-7-maleimidemethyl-S-Cys-(Ser)}_2(\text{Gly})_5\text{-NH}_3)](\text{TFA})_3$. a) EtOH, reflux 3h, DMSO, 150°C 2 h; b) 1,10-phenanthroline, LiCl, DMF, reflux overnight under N_2 atmosphere; c) 1,10-phenanthroline, KBr, H_2SO_4 , HNO_3 , 90°C 3 h under N_2 atmosphere; d) EtOH, 80°C 3 h under N_2 atmosphere; e) LiAlH_4 , THF, 60°C 1 h under N_2 atmosphere; f) acetic acid, CH_3CN , reflux 1 h under N_2 atmosphere; g) $(\text{COCl})_2$, DMF, CH_3CN , RT, overnight under N_2 atmosphere; h) Phthalimide, K_2CO_3 , DMF, RT, overnight; i) NH_2NH_2 , MeOH, reflux overnight under N_2 atmosphere; j) maleic anhydride, AcOH, reflux 10 h under N_2 atmosphere; k) $(\text{NH}_2\text{CO-Cys-(Ser)}_2(\text{Gly})_5\text{-NH}_3)$ (TFA), $\text{CH}_3\text{CN:H}_2\text{O}$ 1:1, RT, 30 h

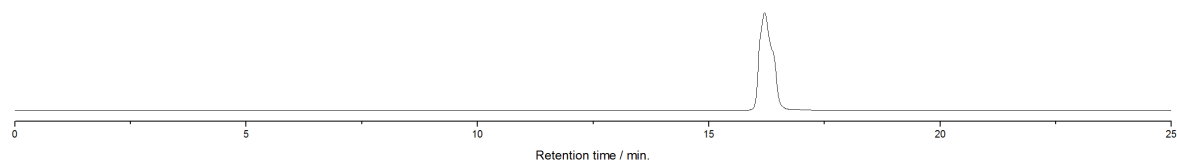


Figure S1. HPLC chromatogram of $[\text{Ru}(\text{phen})_2(\text{dppz-7-maleimidemethyl})]^{2+}$

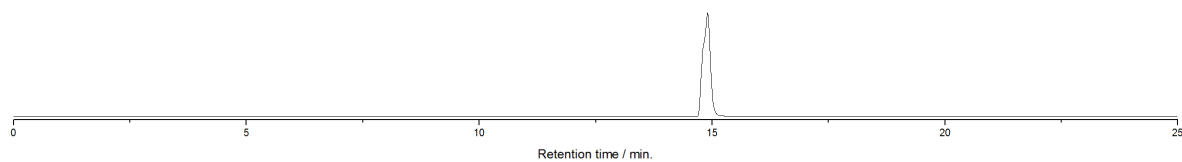


Figure S2. HPLC chromatogram of $[\text{Ru}(\text{phen})_2(\text{dppz-7-maleimidemethyl-S-Cys-(Ser)}_2(\text{Gly})_5\text{-NH}_3)]^{3+}$

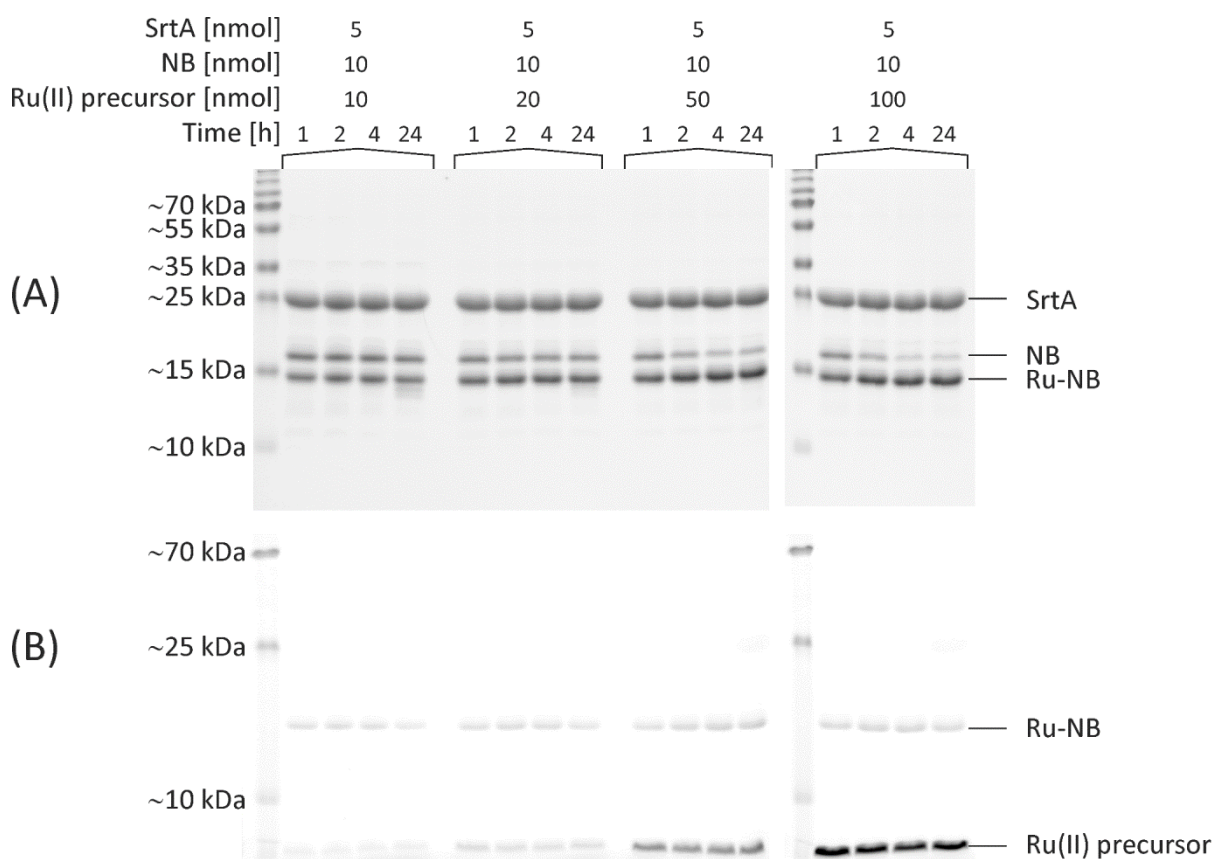


Figure S3. SDS-PAGE analysis of the reaction efficiency for chemoenzymatic conjugation of the $[\text{Ru}(\text{phen})_2(\text{dppz}-7\text{-maleimidemethyl-S-Cys}-(\text{Ser})_2(\text{Gly})_5\text{-NH}_3)]^{3+}$ to the EGFR-specific NB 7C12. The amounts used were 5 nmol SrtA, 10 nmol NB and 10-100 nmol of Ru(II) precursor. The reaction was monitored for up to 24 h and aliquots were separated on 15% SDS polyacrylamide gels. After electrophoresis, gels were imaged with a D-DiGit Gel Scanner (B) to detect the signal of the Ru(II) complex and subsequently stained with colloidal Coomassie G-250 (A).

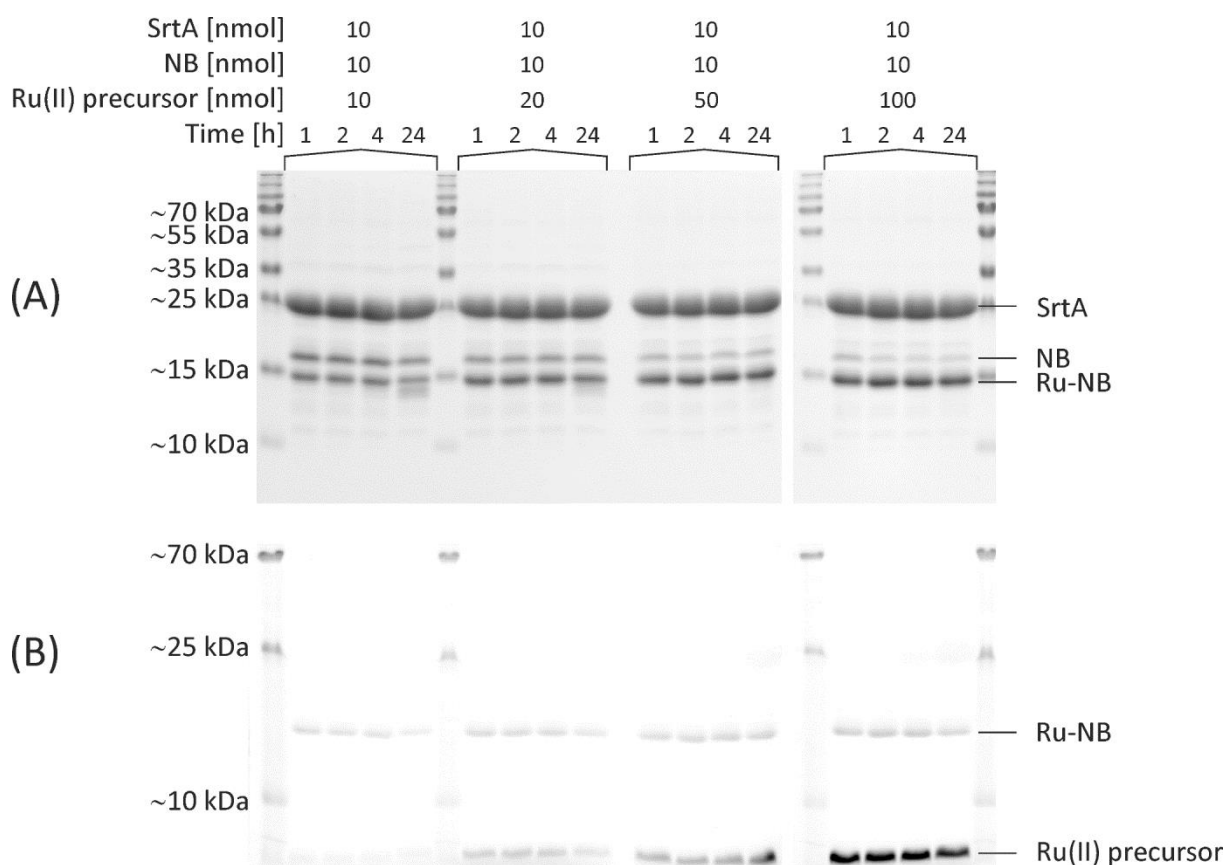


Figure S4. SDS-PAGE analysis of the reaction efficiency for chemoenzymatic conjugation of the $[\text{Ru}(\text{phen})_2(\text{dppz}-7\text{-maleimidemethyl-S-Cys}-(\text{Ser})_2(\text{Gly})_5\text{-NH}_3)]^{3+}$ to the EGFR-specific NB 7C12. The amounts used were 10 nmol SrtA, 10 nmol NB and 10-100 nmol of Ru(II) precursor. The reaction was monitored for up to 24 h and aliquots were separated on 15% SDS polyacrylamide gels. After electrophoresis, gels were imaged with a D-DiGit Gel Scanner (B) to detect the signal of the Ru(II) complex and subsequently stained with colloidal Coomassie G-250 (A)

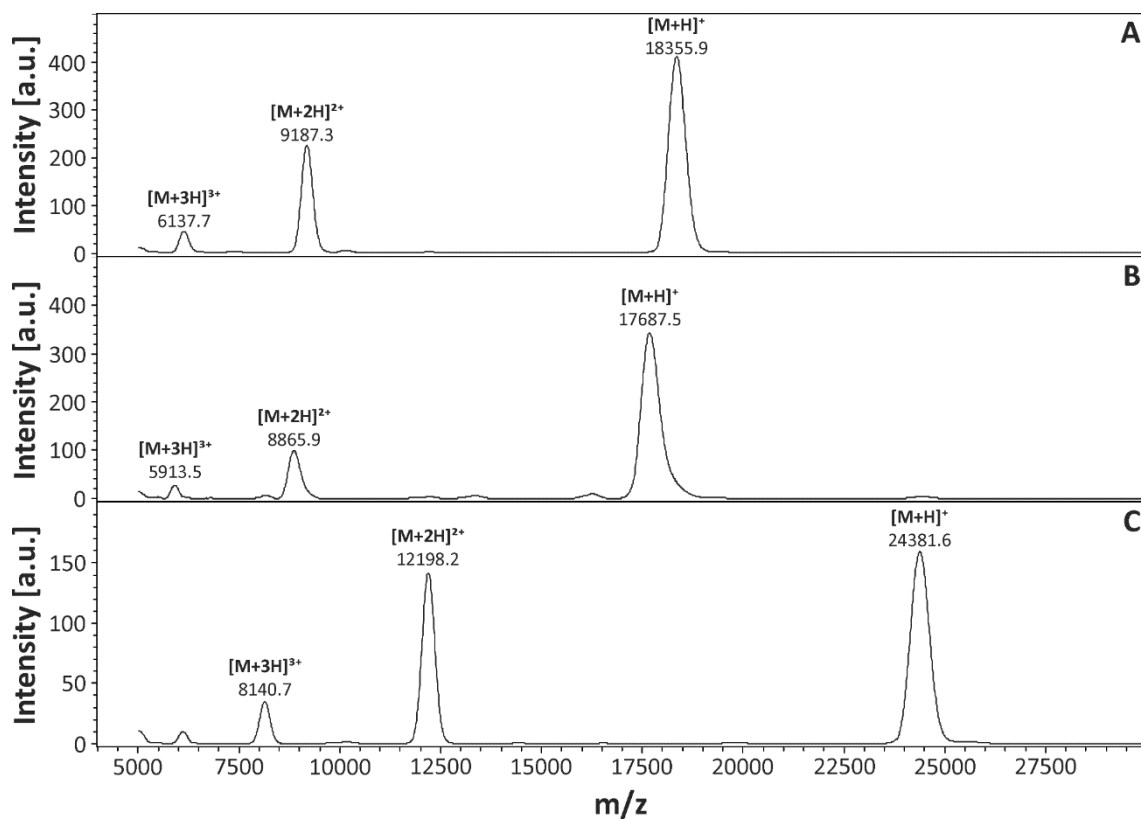


Figure S5. MALDI-TOF mass spectra of the purified (A) NB derivative 7C12-Strep-Sortag-His₆, (B) single-conjugated NB-conjugate 7C12-Strep-[Ru(phen)₂(dppz-7-maleimidemethyl-S-Cys-(Ser)₂(Gly)₅-NH₃)]³⁺ (**Ru-NB**) and (C) sortase enzyme SrtA

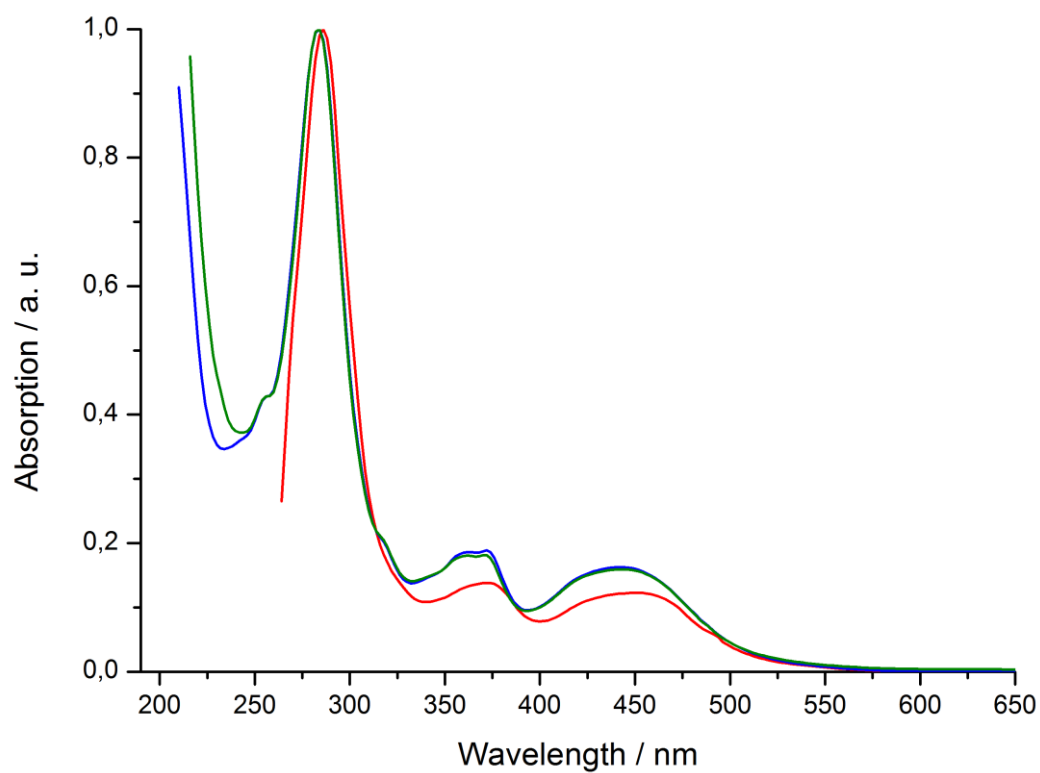


Figure S6. Normalised UV/Vis spectra of $[\text{Ru}(\text{phen})_2(\text{dppz-7-maleimidemethyl})](\text{PF}_6)_2$ in CH_3CN (blue), $[\text{Ru}(\text{phen})_2(\text{dppz-7-maleimidemethyl-S-Cys-(Ser)}_2(\text{Gly})_5\text{-NH}_3)](\text{TFA})_3$ in CH_3CN (green) and **Ru-NB** in DMSO (red).

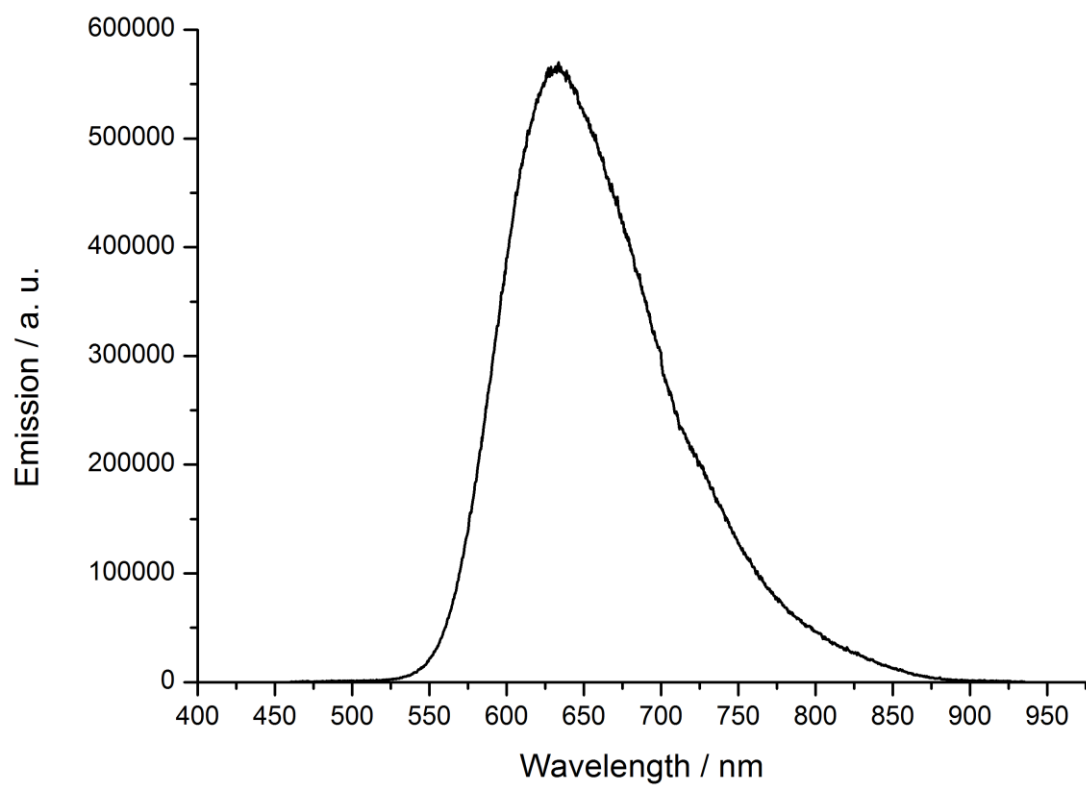


Figure S7. Emission spectra of **Ru-NB** in DMSO.

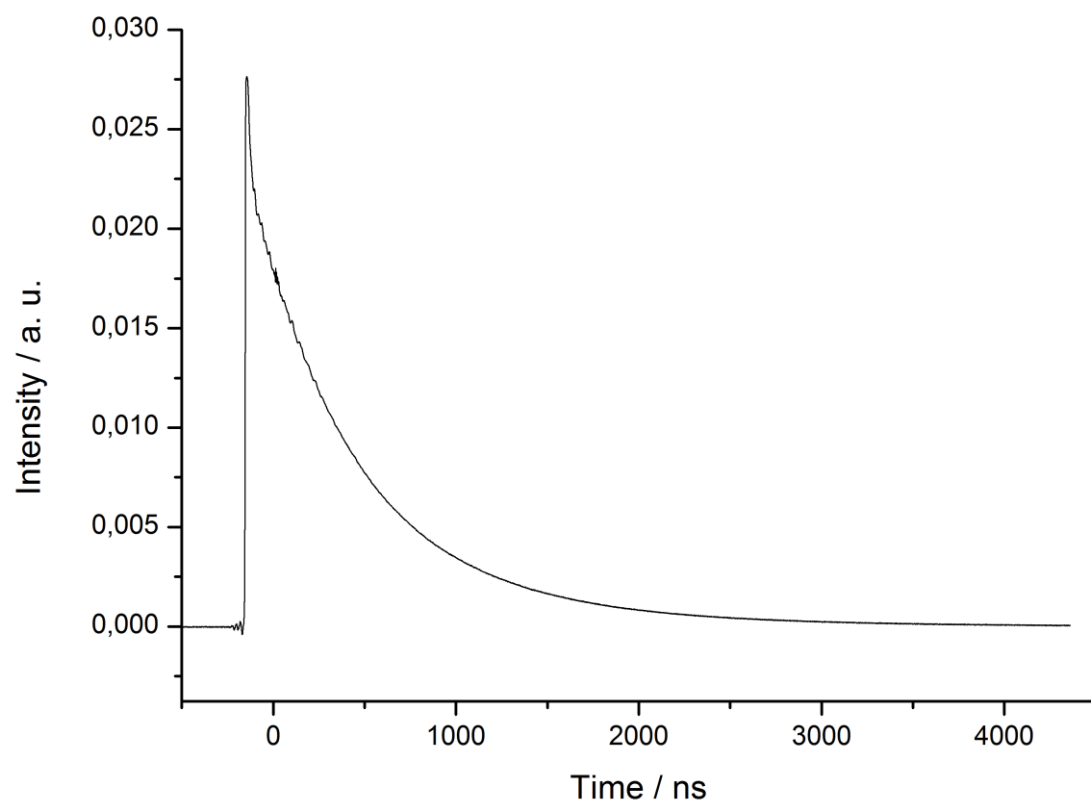


Figure S8. Lifetime spectra of **Ru-NB** in degassed DMSO.

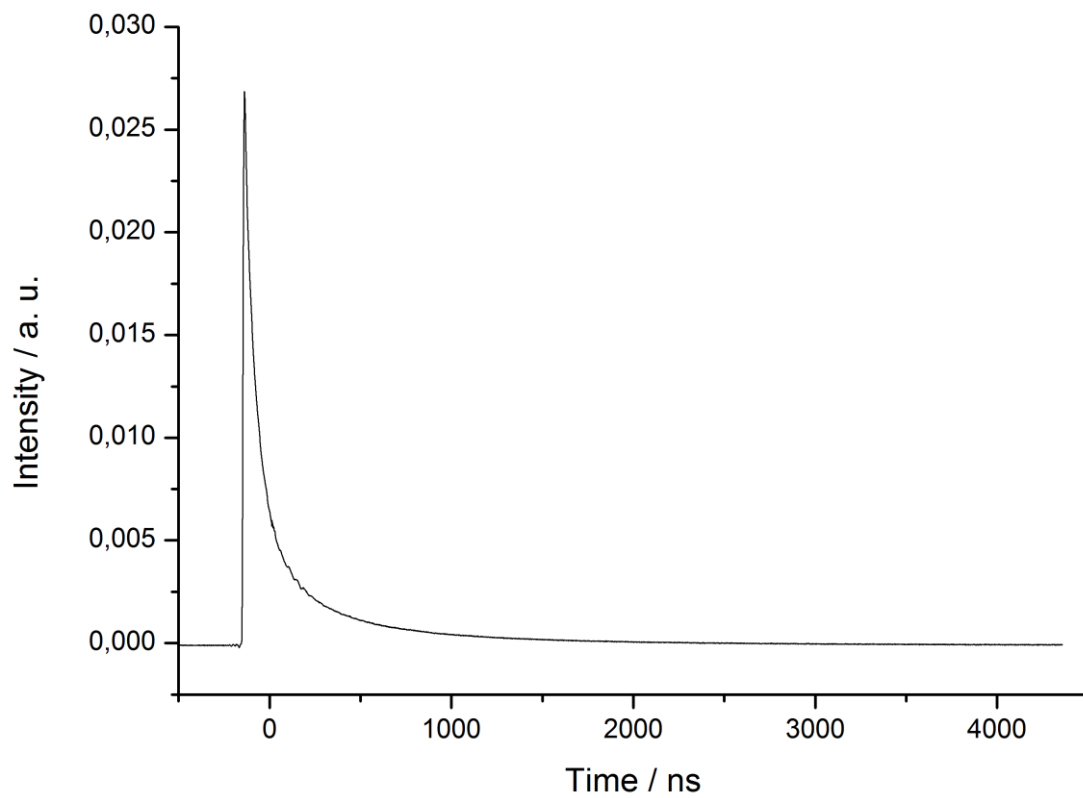


Figure S9. Lifetime spectra of **Ru-NB** in aerated DMSO

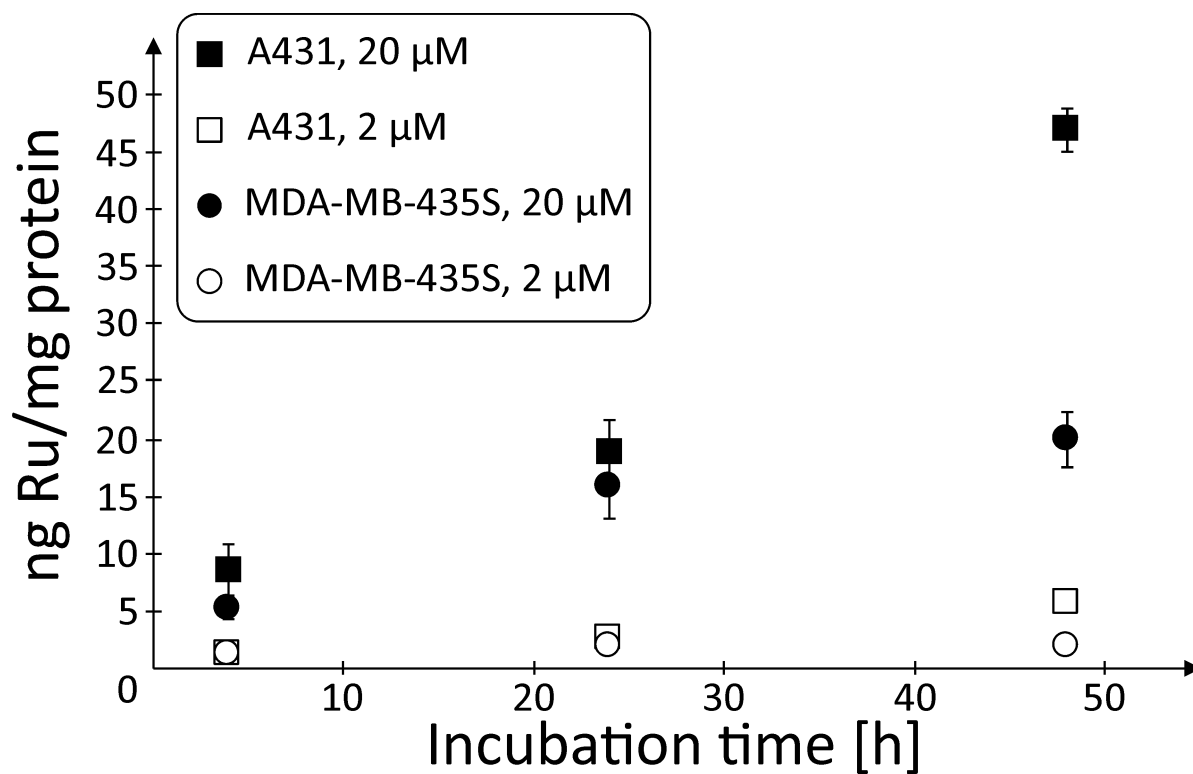
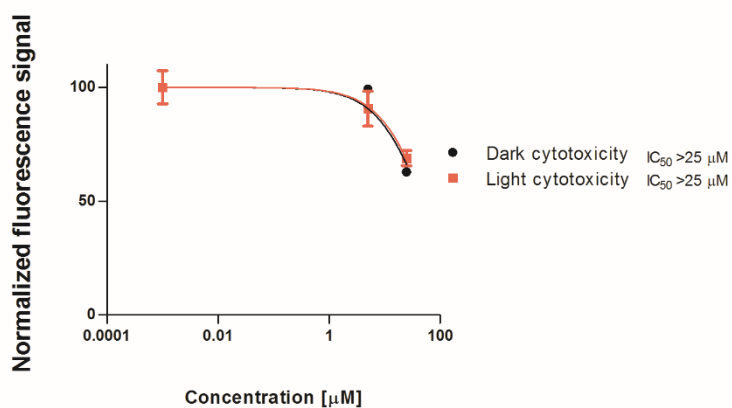


Figure S10. Amount of cell-associated ruthenium after incubation of A431 and MDA-MB-435S cells with 2 or 20 μ M of Ru(bipy)₂(DPPZ-OMe) (PF₆)₂ for up to 48 h.

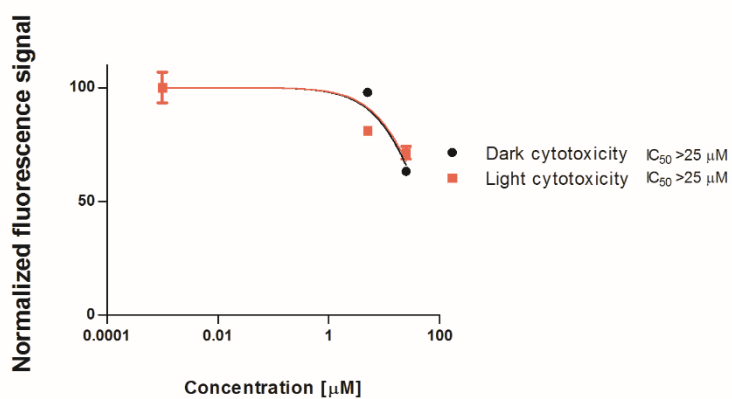
	Ru-NB				Ru(bipy)₂(DPPZ-OMe) (PF₆)₂			
	A431		MDA-MB 453S		A431		MDA-MB 453S	
Time [h]	Concentration of substance [μM]							
	2	20	2	20	2	20	2	20
4	3.26 ±	11.67 ±	< LOD	< LOD	1.20 ±	8.54 ±	1.18 ±	5.20 ±
	1.30	1.70			0.28	2.23	0.14	0.90
24	6.20 ±	23.84 ±	< LOD	5.52 ±	2.51 ±	18.83 ±	1.84 ±	15.84 ±
	1.86	1.54		2.00	0.19	2.84	0.05	2.69
48	11.54 ±	32.87 ±	< LOD	5.45 ±	5.75 ±	46.94 ±	1.92 ±	19.93 ±
	1.89	4.87		1.32	0.74	1.89	0.08	2.39

Table S1. Head-to-head comparison of uptake of **Ru-NB** and [Ru(bipy)₂(DPPZ-OMe)](PF₆)₂ into A431 and MDA-MB 435S cells. The amount of cell-associated ruthenium [ng/mg protein] was measured by ICP-MS

Cytotoxicity of Ru-NB in A431 cell line 1 (48h incubation)



Cytotoxicity of Ru-NB in A431 cell line 2 (48h incubation)



Cytotoxicity of Ru-NB in A431 cell line 3 (48h incubation)

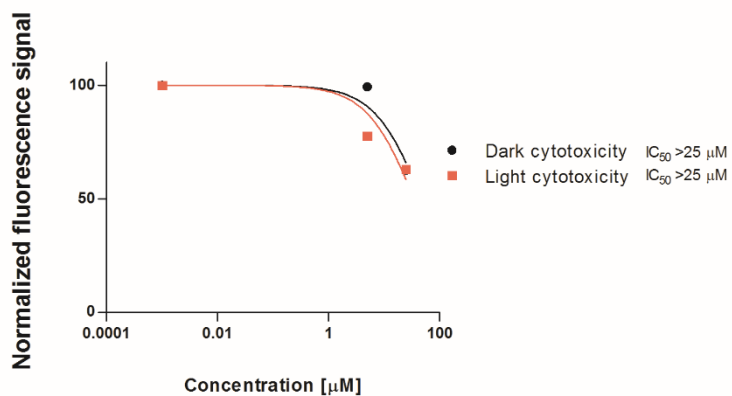
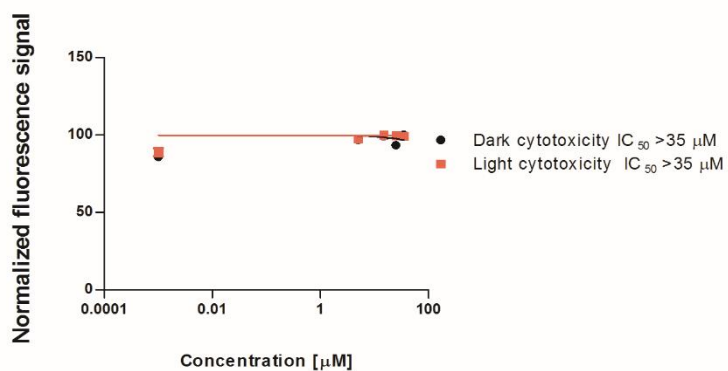
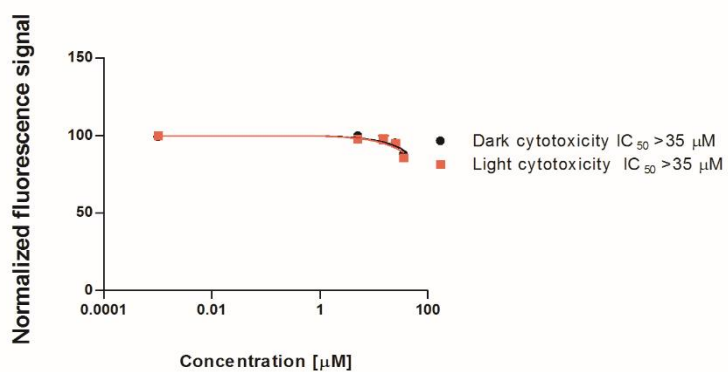


Figure S11. Cytotoxicity of **Ru-NB** in A431 cell line. Cells were treated for 48h, light irradiation: 6x 3.5 min at 480 nm.

Cytotoxicity of Ru-NB in A431 cell line 1 (receptor loading)



Cytotoxicity of Ru-NB in A431 cell line 2 (receptor loading)



Cytotoxicity of Ru-NB in A431 cell line 3 (receptor loading)

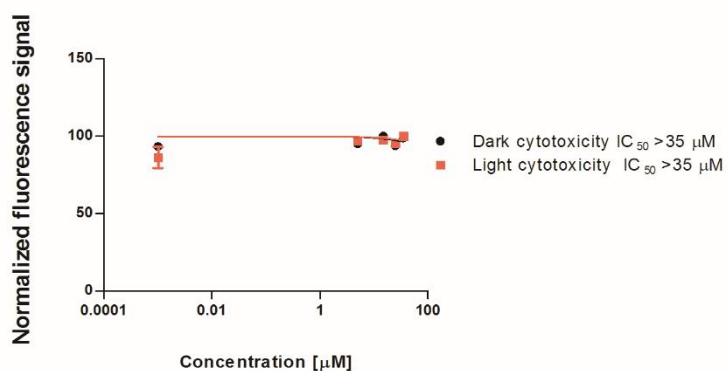
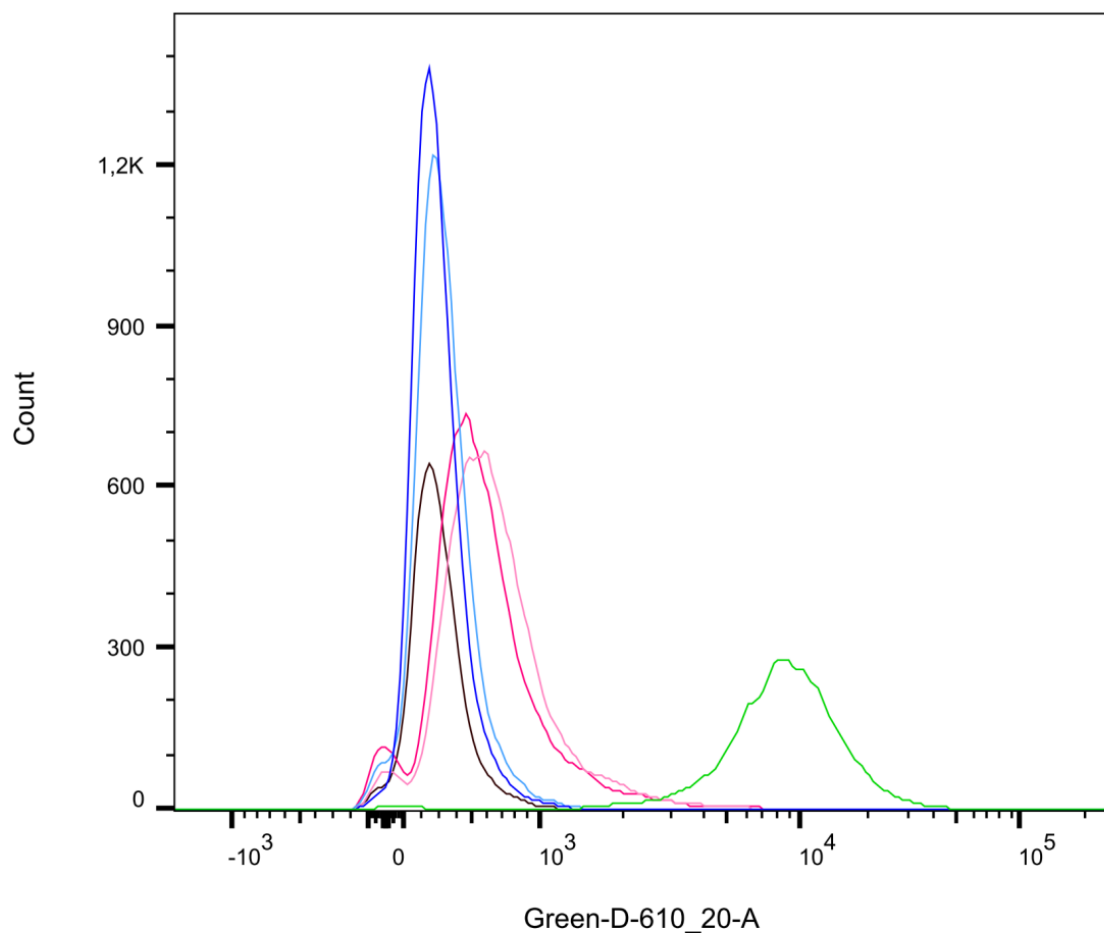


Figure S12. Cytotoxicity of **Ru-NB** in A431 cell line. Cells were treated using receptor internalisation protocol, light irradiation: 6x 3.5 min at 480 nm.



	Sample Name	Count	Mean : Green-D-610_20-A
■	DCFH-DA stained- H2O2 treated.fcs	10000	10186
■	DCFH-DA stained- irradiated.fcs	20000	319
■	DCFH-DA stained-not irradiated.fcs	20000	353
■	DCFH-DA stained- Ru(II) conjugate treated- not irradiated.fcs	20000	843
■	DCFH-DA stained- Ru(II) conjugate- irradiated.fcs	20000	753
■	Cells only.fcs	10000	317

Figure S13. Cellular ROS production in A431 cells treated with **Ru-NB** and stained with DCFH-DA. Cells were gated for DCFH-DA signal (Green-D-610_20-A) using flow cytometry. Cell count for each experimental group with mean of the DCFH-DA signal is provided in the table.

Chapter 4- Systematic Investigation of the Antiproliferative Activity of a Series of Ruthenium Terpyridine Complexes

Johannes Karges,^a Marta Jakubaszek,^{a,b} Bruno Goud,^b Olivier Blacque,^c Philippe Goldner^d and Gilles Gasser^{a,}*

^a Chimie ParisTech, PSL University, CNRS, Institute of Chemistry for Life and Health Sciences, Laboratory for Inorganic Chemical Biology, 75005 Paris, France.

^b Institut Curie, PSL University, CNRS UMR 144, Paris, France.

^c Department of Chemistry, University of Zurich, Winterthurerstrasse 190, 8057 Zurich, Switzerland.

^d Chimie ParisTech, PSL University, CNRS, Institut de Recherche de Chimie Paris, 75005 Paris, France.

* Corresponding author: Email: gilles.gasser@chimieparistech.psl.eu; www.gassergroup.com; Tel. +33 1 44 27 56 02.

This chapter has been published in *Journal of Inorganic Biochemistry*, 2019,**198**, 110752 (DOI: 10.1016/j.jinorgbio.2019.110752.)

Reproduced by permission of Elsevier

(<https://www.sciencedirect.com/science/article/pii/S0162013419300698?via%3Dihub>)

Contribution to the publication:

Marta Jakubaszek performed cytotoxicity studies and the stability experiments. She has contributed to the biological section of this publication.

Marta Jakubaszek

Handwritten signature of Marta Jakubaszek in blue ink.

19.05.2020

Gilles Gasser

Handwritten signature of Gilles Gasser in blue ink.

Keywords

Anticancer, Medicinal Inorganic Chemistry, Metals in Medicine, Photodynamic Therapy, Ruthenium.

Abstract

Due to acquired resistance or limitations of the currently approved drugs against cancer, there is an urgent need for the development of new classes of compounds. Among others, there is an increasing attention towards the use of Ru(II) polypyridyl complexes. Most studies in the literature were made on complexes based on the coordination of N-donating bidentate ligands to the ruthenium core whereas studies on 2,2':6', 2''-terpyridine (terpy) coordinating ligands are relatively scarce. However, several studies have shown that [Ru(terpy)₂]²⁺ derivatives are able to bind to DNA through various binding modes making these compounds potentially suitable as chemotherapeutic agents. Additionally, light irradiation of these compounds was shown to enable DNA cleavage, highlighting their potential use as photosensitizers (PSs) for photodynamic therapy (PDT). In this work, we present the systematic investigation of the potential of 7 complexes of the type [Ru(terpy)(terpy-X)]²⁺ (X = H (**1**), Cl (**2**), Br (**3**), OMe (**4**), COOH (**5**), COOMe (**6**), NMe₂ (**7**)) as potential chemotherapeutic agents and PDT PSs. The compounds were characterized in-depth including X-ray crystallography. Importantly, six of the seven complexes were found to be stable in human plasma as well as photostable in acetonitrile upon continuous LED irradiation. The determination of the logP values for the 7 complexes revealed their good water solubility. Complex **7** was found to be cytotoxic in the micromolar range in the dark as well as to have some phototoxicity upon light exposure at 480 nm in non-cancerous retinal pigment epithelium (RPE-1) and cancerous human cervical carcinoma (HeLa) cells.

1. Introduction

Based on the increasing impact of cancer on the life quality as well as mortality in the world, research efforts are made towards the development of new methods for the treatment of this disease as well as the improvement of existing anticancer drugs. Most commonly, cancer is fought through the combination of different techniques (i.e. chemotherapy, surgery, radiotherapy and immunotherapy).[1-3] To date, the gold standard in the chemotherapeutic treatment of cancer is the platinum drug cisplatin and its derivatives carboplatin and oxaliplatin.[4, 5] However, although the ability of cisplatin for the treatment of patients with cancer is impressive and undeniable, treatments with this drug are also associated with severe side effects that include nerve and kidney damage, nausea, vomiting and bone marrow suppression. Acquired resistances limit also the use of cisplatin and this derivatives. These drawbacks have led, in the last decades, to the search for alternative compounds and, among others, of non-platinum based compounds. Among the new classes investigated, coordinatively saturated, inert Ru(II) polypyridyl complexes are receiving increasing attention due to their promising anticancer and antimicrobial activity as chemotherapeutic agents as well as photodynamic therapy (PDT) photosensitizers (PSs).[6-17] Very importantly, one of Mc Farland and co-workers' ruthenium-based PDT PSs, namely TLD-1433, just completed phase I clinical trial as a PDT PS against bladder cancer.[10]

In the field of ruthenium-based PDT PSs, most studies in the literature are based on a $[\text{Ru}(\text{bipy}/\text{phen}/\text{bphen}/\text{dppz})_3]^{2+}$ (bipy = 2,2'-bipyridine, phen = 1,10-phenanthroline, bphen = 4,7-diphenyl-1,10-phenanthroline, dppz = dipyrido[3,2-a:2',3'-c]phenazine) scaffold due to their interesting redox properties, long excited-state lifetimes as well as intense luminescence.[11, 13, 18-24] In comparison, complexes based on a $[\text{Ru}(\text{terpy})_2]^{2+}$ (terpy = 2,2':6',2''-terpyridine) scaffold have not been very extensively studied. These complexes are

well-known to have a short-lived excited state and to be weakly luminescent at room temperature but long-lived and strongly luminescent at low temperature (77 K). This phenomenon is explained by an unfavourable bite angle of the ligands for the octahedral coordination of the Ru(II). As a result, a relatively low ligand field state 3LF is created which is able to quench the normally emitting 3MLCT state.[20, 25] Despite these unfavourable photophysical properties, several studies have shown that these complexes were still able to bind to DNA and to cleave it upon light irradiation, making them potential PSs for PDT purposes.[26-30] Interestingly, it was demonstrated that these complexes were able to interact in different manners with DNA, including electrostatic interactions, intercalation, and groove binding, depending on the substituents on the terpy ligand.[31-35]

In this work, we present the systematic investigation of the potential of 7 Ru(II) complexes of the type $[Ru(terpy)(terpy-X)]^{2+}$ (X = H (**1**), Cl (**2**), Br (**3**), OMe (**4**), COOH (**5**), COOMe (**6**), NMe₂ (**7**)) as potential chemotherapeutic agents and as PDT PSs. All investigated complexes were fully characterised by 1H and ^{13}C -NMR, ESI-HRMS, elemental analysis as well as single crystal X-ray crystallography. As described below, one of the complexes (compound **7**) was found to be cytotoxic in the micromolar range in the dark as well as to have some phototoxicity upon light exposure at 480 nm, highlighting some potential for this type of complexes.

2. Experimental section

2.1. Materials

All chemicals were obtained from commercial sources and used without further purification. Solvents were dried over molecular sieves if necessary. The Ru(II) precursor $Ru(terpy)Cl_3$ was synthesised as previously published.[36] The substituted 2,2':6',2''-terpyridine ligands (terpy-X): 4'-chloro-2,2':6',2''-terpyridine (terpy-Cl),[37] 4'-bromo-2,2':6',2''-terpyridine (terpy-

Br),[38] 4'-methoxy-2,2':6',2''-terpyridine (terpy-OMe),[39] 4'-carboxy-2,2':6',2''-terpyridine (terpy-COOH),[40] 4'-methylcarboxy-2,2':6',2''-terpyridine (terpy-COOMe),[40] 4'-dimethylamino-2,2':6',2''-terpyridine (terpy-NMe₂)[41] were synthesised as previously reported.

2.2. Instrumentation and methods

¹H and ¹³C NMR spectra were recorded on a Bruker 400 MHz NMR spectrometer. Chemical shifts (δ) are reported in parts per million (ppm) referenced to tetramethylsilane (δ 0.00) ppm using the residual proton solvent peaks as internal standards. Coupling constants (J) are reported in Hertz (Hz) and the multiplicity is abbreviated as follows: s (singlet), d (doublet), dd (doublet of doublet), m (multiplet). ESI-MS experiments were carried out using a LTQ-Orbitrap XL from Thermo Scientific (Thermo Fisher Scientific, Courtaboeuf, France) and operated in positive ionization mode, with a spray voltage at 3.6 kV. No Sheath and auxiliary gas was used. Applied voltages were 40 and 100 V for the ion transfer capillary and the tube lens, respectively. The ion transfer capillary was held at 275°C. Detection was achieved in the Orbitrap with a resolution set to 100,000 (at *m/z* 400) and a *m/z* range between 150-2000 in profile mode. Spectrum was analyzed using the acquisition software XCalibur 2.1 (Thermo Fisher Scientific, Courtaboeuf, France). The automatic gain control (AGC) allowed accumulation of up to 2×10^5 ions for FTMS scans, maximum injection time was set to 300 ms and 1 μ scan was acquired. 10 μ L was injected using a Thermo Finnigan Surveyor HPLC system (Thermo Fisher Scientific, Courtaboeuf, France) with a continuous infusion of methanol at 100 μ L.min⁻¹. Elemental microanalyses were performed on a Thermo Flash 2000 elemental analyser.

2.3. Synthesis

[Ru(terpy)₂](PF₆)₂ (1)

[Ru(terpy)₂PF₆]₂ was synthesized as previously published.[42] Experimental data fits with the literature. Purity of the sample was assessed by HPLC and elemental analysis. *Anal.* Calc. for C₃₀H₂₂F₁₂N₆P₂Ru: C 42.02, H 2.59, N 9.80. Found: C 41.91, H 2.60, N 9.71.

[Ru(terpy)(terpy-Cl)](PF₆)₂ (2)

The synthesis of [Ru(terpy)(terpy-Cl)](PF₆)₂ was previously reported.[43] In this work, another synthetic route was employed. Ru(terpy)Cl₃ (200 mg, 0.45 mmol, 1.0 equiv.), 4'-Chloro-2,2':6',2''-terpyridine (terpy-Cl) (134 mg, 0.50 mmol, 1.1 equiv) and some drops of *N*-ethylmorpholine were dissolved in 8:2 EtOH/H₂O (50 mL). The mixture was heated under reflux for 4 h under nitrogen atmosphere. The crude product was cooled to room temperature and undissolved solid was filtered off over Celite. The solid was washed with EtOH, the solution concentrated and a sat. aqueous solution of NH₄PF₆ was added. The crude product, which precipitated as a PF₆ salt was collected by centrifugation and washed with EtOH, H₂O and Et₂O. The product was isolated by column chromatography on silica gel with an CH₃CN/aq. KNO₃ (0.4 M) solution (10:1). The fractions containing the product were united and the solvent was removed under reduced pressure. The residue was dissolved in CH₃CN and undissolved KNO₃ was removed by filtration. The solvent was removed again and the product was dissolved in H₂O (50 mL). Upon addition of NH₄PF₆ the product precipitated as a PF₆ salt. The solid was obtained by filtration and was washed three-times with H₂O and Et₂O. Experimental data fits with the literature. Purity of the sample was assessed by HPLC and elemental analysis. *Anal.* Calc. for C₃₀H₂₁ClF₁₂N₆P₂Ru + 1.3*H₂O: C 39.36, H 2.60, N 9.18. Found: C 38.99, H 2.50, N 9.68.

[Ru(terpy)(terpy-Br)](PF₆)₂ (**3**)

The synthesis of [Ru(terpy)(terpy-Br)](PF₆)₂ was previously reported.[44] In this work, another synthetic route was employed. Ru(terpy)Cl₃ (200 mg, 0.45 mmol, 1.0 equiv.), 4'-Bromo-2,2':6',2''-terpyridine (terpy-Br) (156 mg, 0.50 mmol, 1.1 equiv) and some drops of *N*-ethylmorpholine were dissolved in 8:2 EtOH/H₂O (50 mL). The mixture was heated under reflux for 4 h under nitrogen atmosphere. The crude product was cooled to room temperature and undissolved solid was filtered off over Celite. The solid was washed with EtOH, the solution concentrated and a sat. aqueous solution of NH₄PF₆ was added. The crude product, which precipitated as a PF₆ salt was collected by centrifugation and washed with EtOH, H₂O and Et₂O. The product was isolated by column chromatography on silica gel with an CH₃CN/aq. KNO₃ (0.4 M) solution (10:1). The fractions containing the product were united and the solvent was removed under reduced pressure. The residue was dissolved in CH₃CN and undissolved KNO₃ was removed by filtration. The solvent was removed again and the product was dissolved in H₂O (50 mL). Upon addition of NH₄PF₆ the product precipitated as a PF₆ salt. The solid was obtained by filtration and was washed three-times with H₂O and Et₂O. Experimental data fits with the literature. Purity of the sample was assessed by HPLC and elemental analysis. *Anal.* Calc. for C₃₀H₂₁BrF₁₂N₆P₂Ru +1 H₂O: C 37.75, H 2.43, N 8.81. Found: C 37.55, H 2.03, N 9.26.

[Ru(terpy)(terpy-OMe)](PF₆)₂ (**4**)

Ru(terpy)Cl₃ (203 mg, 0.46 mmol, 1.0 equiv.), 4'-Methoxy-2,2':6',2''-terpyridine (terpy-Br) (133 mg, 0.51 mmol, 1.1 equiv) and some drops of *N*-ethylmorpholine were dissolved in 8:2 EtOH/H₂O (50 mL). The mixture was heated under reflux for 5 h under nitrogen atmosphere. The crude product was cooled to room temperature and undissolved solid was filtered off over Celite. The solid was washed thoroughly with EtOH and afterwards the solvent was removed

under reduced pressure. The residue was dissolved in H₂O and a sat. aqueous solution of NH₄PF₆ was added. The crude product, which precipitated as a PF₆ salt was collected by centrifugation and washed with EtOH, H₂O and Et₂O. The product was isolated by column chromatography on silica gel with an CH₃CN/aq. KNO₃ (0.4 M) solution (10:1). The fractions containing the product were united and the solvent was removed under reduced pressure. The residue was dissolved in CH₃CN and undissolved KNO₃ was removed by filtration. The solvent was removed again and the product was dissolved in H₂O (50 mL). Upon addition of NH₄PF₆ the product precipitated as a PF₆ salt. The solid was obtained by filtration and was washed three-times with H₂O and Et₂O. 257 mg of [Ru(terpy)(terpy-OMe)](PF₆)₂ (**4**) (0.29 mmol, 63 %) were yielded as a red solid. ¹H-NMR (CD₃CN, 400 MHz): δ = 8.72 (d, *J* = 8.2 Hz, 2H), 8.50-8.46 (m, 4H), 8.36 (t, *J* = 8.2 Hz, 1H), 8.33 (s, 2H), 7.93-7.86 (m, 4H), 7.42 (ddd, *J* = 5.5, 1.4, 0.7 Hz, 2H), 7.29 (ddd, *J* = 5.5, 1.4, 0.7 Hz, 2H), 7.18 (ddd, *J* = 7.5, 5.6 1.3 Hz, 2H), 7.12 (ddd, *J* = 7.5, 5.6 1.3 Hz, 2H), 4.31 (s, 3H). ¹³C-NMR (CD₃CN, 100 MHz): δ = 167.6, 158.8, 158.6, 156.5, 156.4, 153.3, 152.8, 138.5, 138.4, 135.7, 128.0, 127.9, 125.0, 124.8, 124.1, 111.3, 57.8. ESI-HRMS *m/z*: 299.0527 [M]²⁺, calcd for C₃₁H₂₄N₆O₁Ru 299.0522. *Anal. Calc.* for C₃₁H₂₄F₁₂N₆O₂P₂Ru: C 41.95, H 2.73, N 9.47. Found: C 41.79, H 2.64, N 9.45.

[Ru(terpy)(terpy-COOH)](PF₆)₂ (**5**)

The synthesis of [Ru(terpy)(terpy-COOH)](PF₆)₂ was previously reported.[45] In this work, another synthetic route was employed. Ru(terpy)Cl₃ (200 mg, 0.45 mmol, 1.0 equiv.), 4'-Carboxy-2,2':6',2''-terpyridine (terpy-COOH) (139 mg, 0.50 mmol, 1.1 equiv) and some drops of *N*-ethylmorpholine were dissolved in 8:2 EtOH/H₂O (50 mL). The mixture was heated under nitrogen atmosphere at reflux for 4 h. After cooling down to room temperature, the crude product was filtered over Celite and washed thoroughly with EtOH. The solvent was removed and the solid residue dissolved in H₂O. A sat. aqueous solution of NH₄PF₆ was added and the

crude product precipitated as a PF₆ salt. The solid was collected by centrifugation and washed with Ethanol, Water and Et₂O. The product was isolated via fractionated precipitation from Acetonitrile by adding dropwise Et₂O. The yielded solid was isolated by filtration and washed with pentane. Experimental data fits with the literature. Purity of the sample was assessed by HPLC and elemental analysis. *Anal.* Calc. for C₃₁H₂₂F₁₂N₆O₂P₂Ru + 0.1 * C₅H₁₂: C 41.63, H 2.57, N 9.25. Found: C 41.84, H 2.68, N 9.56.

[Ru(terpy)(terpy-COOMe)](PF₆)₂ (**6**)

Ru(terpy)Cl₃ (137 mg, 0.31 mmol, 1.0 equiv.) and AgBF₄ (212 mg, 1.09 mmol, 3.5 equiv.) were suspended in Acetone (50 mL) under nitrogen atmosphere. The mixture was refluxed for 2 h, cooled to room temperature and undissolved solid was filtered off over Celite. The solid was washed with methanol and then the solvent removed under reduced pressure. The residue was dissolved in dry EtOH (50 mL) and 4'-Methylcarboxy-2,2':6',2''-terpyridine (terpy-COOMe) (100 mg, 0.34 mmol, 1.1 equiv.) was added. The mixture was heated under reflux for 18 h under nitrogen atmosphere. The crude product was cooled to room temperature and undissolved solid was filtered off over Celite. The solid was washed with EtOH, the solution concentrated and a sat. aqueous solution of NH₄PF₆ was added. The crude product, which precipitated as a PF₆ salt was collected by centrifugation and washed with EtOH, H₂O and Et₂O. The product was isolated by column chromatography on silica gel with an CH₃CN/aq. KNO₃ (0.4 M) solution (10:1). The fractions containing the product were united and the solvent was removed under reduced pressure. The residue was dissolved in CH₃CN and undissolved KNO₃ was removed by filtration. The solvent was removed again and the product was dissolved in H₂O (50 mL). Upon addition of NH₄PF₆ the product precipitated as a PF₆ salt. The solid was obtained by filtration and was washed three-times with H₂O and Et₂O. 154 mg of [Ru(terpy)(terpy-COOMe)](PF₆)₂ (**6**) (0.17 mmol, 55 %) were yielded as a red solid. ¹H-

NMR (CD₃CN, 400 MHz): δ = 9.20 (s, 2H), 8.76 (d, J = 8.2 Hz, 2H), 8.66-8.62 (m, 2H), 8.50-8.47 (m, 2H), 8.45 (t, J = 8.2 Hz, 1H), 7.98-7.89 (m, 4H), 7.39-7.36 (m, 2H), 7.30-7.27 (m, 2H), 7.23-7.19 (m, 2H), 7.16-7.10 (m, 2H), 4.18 (s, 3H). ¹³C-NMR (CD₃CN, 100 MHz): δ = 165.4, 158.7, 158.4, 157.1, 155.8, 153.5, 153.4, 139.3, 139.1, 137.5, 137.2, 128.8, 128.4, 125.8, 125.5, 124.8, 123.7, 54.2. ESI-HRMS m/z : 313.0502 [M]²⁺, calcd. for C₃₂H₂₄N₆O₂Ru 313.0497. *Anal.* Calc. for C₃₂H₂₄F₁₂N₆O₂P₂Ru: C 41.98, H 2.64, N 9.18. Found: C 41.92, H 2.63, N 9.50.

[Ru(terpy)(terpy-NMe₂)](PF₆)₂ (**7**)

Ru(terpy)Cl₃ (205 mg, 0.47 mmol, 1.0 equiv.), 4'-Dimethylamino-2,2':6',2''-terpyridine (terpy-NMe₂) (141 mg, 0.52 mmol, 1.1 equiv) and some drops of *N*-ethylmorpholine were dissolved in 8:2 EtOH/H₂O (50 mL). The mixture was heated under reflux for 6 h under nitrogen atmosphere. The crude product was cooled to room temperature and undissolved solid was filtered off over Celite. The solid was washed thoroughly with EtOH and afterwards the solvent was removed under reduced pressure. The residue was dissolved in H₂O and a sat. aqueous solution of NH₄PF₆ was added. The crude product, which precipitated as a PF₆ salt was collected by centrifugation and washed with EtOH, H₂O and Et₂O. The product was isolated by column chromatography on silica gel with an CH₃CN/aq. KNO₃ (0.4 M) solution (10:1). The fractions containing the product were united and the solvent was removed under reduced pressure. The residue was dissolved in CH₃CN and undissolved KNO₃ was removed by filtration. The solvent was removed again and the product was dissolved in H₂O (50 mL). Upon addition of NH₄PF₆ the product precipitated as a PF₆ salt. The solid was obtained by filtration and was washed three-times with H₂O and Et₂O. The product was isolated via fractionated precipitation from CH₃CN by adding dropwise Et₂O. 225 mg of [Ru(terpy)(terpy-NMe₂)](PF₆)₂ (**7**) (0.25 mmol, 53 %) were yielded as a dark red solid. ¹H-NMR (CD₃CN, 400

MHz): δ = 8.70 (d, J = 8.2 Hz, 2H), 8.52-8.45 (m, 4H), 8.31 (t, J = 8.2 Hz, 1H), 7.93 (s, 2H), 7.93-7.82 (m, 4H), 7.50-7.48 (m, 2H), 7.24-7.19 (m, 4H), 7.08-7.03 (m, 2H), 3.46 (s, 6H). ^{13}C -NMR (CD_3CN , 100 MHz): δ = 159.9, 159.4, 157.3, 156.3, 154.8, 153.5, 152.9, 138.6, 138.5, 135.2, 128.3, 127.7, 125.0, 124.7, 124.3, 107.4, 40.8. ESI-HRMS m/z : 305.5687 $[\text{M}]^{2+}$, calcd. for $\text{C}_{32}\text{H}_{27}\text{N}_7\text{Ru}$ 305.5680. *Anal.* Calc. for $\text{C}_{32}\text{H}_{27}\text{F}_{12}\text{N}_7\text{P}_2\text{Ru}$: C 42.68, H 3.02, N 10.89. Found: C 42.55, H 2.95, N 10.82.

2.4. X-ray crystallography

X-ray single-crystal data were collected at 160(1) K with Oxford liquid-nitrogen Cryostream coolers on Rigaku OD diffractometers: SuperNova (CCD Atlas detector) for **1_BPh4** and XtaLAB Synergy Dualflex (Pilatus 200K detector) for all the other X-ray analyses. Single wavelength X-ray sources from micro-focus sealed X-ray tubes were used with the Mo K_α radiation (λ = 0.71073 Å)[46] for **1_BPh4** and **2_BPh4** and with the Cu K_α radiation (λ = 1.54184 Å)[46] for all other analyses. The selected single crystals were mounted using polybutene oil on a flexible loop fixed on a goniometer head and transferred to the diffractometer. Pre-experiments, data collections, data reductions and analytical absorption corrections[47] were performed with the program suite *CrysAlisPro*[48]. Using *Olex2*,[49] all structures were solved with the SHELXT[50] small molecule structure solution program and refined with the *SHELXL2018/3* program package[51] by full-matrix least-squares minimization on F^2 . Molecular graphics were generated using *Mercury 4.0*. [52] The crystal data collections and structure refinement parameters for are summarized in Tables S1 – S9. CCDC 1889454 (for **2_PF6**), 1889455 (for **2_BF4**), 1889456 (for **3_BF4**), 1889457 (for **3_PF6**), 1889458 (for **4_BF4**), 1889459 (for **2_BPh4**), 1889460 (for **4_PF6**), 1889461 (for **6_BPh4**), 1889462 (for **6_PF6**), 1889463 (for **6_BF4**), 1889464 (for **5_BPh4**), 1889465 (for **7_PF6**), 1889466 (for **terpy-Br**), 1889467 (for **7_BF4**), 1889468 (for **5_BF4**), 1889469 (for **terpy-Cl**)

and 1889470 (for **1_BPh4**) contain the supplementary crystallographic data for these compounds, and can be obtained free of charge from the Cambridge Crystallographic Data Centre via www.ccdc.cam.ac.uk/data_request/cif.

2.5. Spectroscopic measurements

The absorption of the samples has been measured with a SpectraMax M2 Spectrometer (Molecular Devices). The emission was measured by irradiation of the sample in fluorescence quartz cuvettes (width 1 cm) using a NT342B Nd-YAG pumped optical parametric oscillator (Ekspla) at 450 nm. Luminescence was focused and collected at right angle to the excitation pathway and directed to a Princeton Instruments Acton SP-2300i monochromator. As a detector a PI-Max 4 CCD camera (Princeton Instruments) has been used.

2.6. Luminescence quantum yield measurements

For the determination of the luminescence quantum yield, the samples were prepared in a not degassed CH₃CN solution with an absorbance of 0.1 at 450 nm. This solution was irradiated in fluorescence quartz cuvettes (width 1 cm) using a NT342B Nd-YAG pumped optical parametric oscillator (Ekspla) at 450 nm. The emission signal was focused and collected at right angle to the excitation pathway and directed to a Princeton Instruments Acton SP-2300i monochromator. As a detector a PI-Max 4 CCD camera (Princeton Instruments) has been used. The luminescence quantum yields were determined by comparison with the reference [Ru(bipy)₃]Cl₂ in CH₃CN ($\Phi_{em}=0.059$)[53] applying the following formula :

$$\Phi_{em, sample} = \Phi_{em, reference} * (F_{reference} / F_{sample}) * (I_{sample} / I_{reference}) * (n_{sample} / n_{reference})^2$$

$$F = 1 - 10^{-A}$$

Φ_{em} = luminescence quantum yield, F = fraction of light absorbed, I = integrated emission intensities, n = refractive index, A = absorbance of the sample at irradiation wavelength.

2.7. Lifetime measurements

For the determination of the lifetimes, the samples were prepared in an air saturated and in a degassed CH₃CN solution with an absorbance of 0.1 at 450 nm. This solution was irradiated in fluorescence quartz cuvettes (width 1 cm) using a NT342B Nd-YAG pumped optical parametric oscillator (Ekspla) at 450 nm. The emission signal was focused and collected at right angle to the excitation pathway and directed to a Princeton Instruments Acton SP-2300i monochromator. As a detector a R928 photomultiplier tube (Hamamatsu) has been used.

2.8. Distribution coefficient

The lipophilicity of a compound was determined by measuring its distribution coefficient between the PBS and octanol phase by using the “shake-flask” method. For this technique, the used phases were previously saturated in each other. The compound was dissolved in the phase (A) with its major presence with an absorbance of about 0.5 at 450 nm. This solution was then mixed with an equal volume of the other phase (B) at 80 rpm for 8 h with an Invitrogen sample mixer and equilibrated overnight. The phase A was then carefully separated from phase B. The amount of the compound before and after the sample mixing was determined by UV/VIS spectroscopy at 450 nm with an SpectraMax M2 Microplate Reader (Molecular Devices). The evaluation of the complexes was repeated three times and the ratio between the organic and aqueous phase calculated.

2.9. Stability in human plasma

The stability of the complexes was evaluated with caffeine as an internal standard, which has already shown to be suitable for these experiments.[54] The pooled human plasma was obtained from Biowest and caffeine from TCI Chemicals. Stock solutions of the compounds and caffeine were prepared in DMSO. One aliquot of the solutions was added to 975 μL of human plasma to a total volume of 1000 μL . Final concentrations of the compounds of 50 μM and caffeine of 25 μM were achieved. The resulting solution was incubated for 48 h at 37 $^{\circ}\text{C}$ with continuous gentle shaking (ca. 300 rpm). The reaction was stopped after the incubation time by addition of 4 mL of methanol. The mixture was centrifuged for 45 min at 650 g at 4 $^{\circ}\text{C}$. The methanolic solution was filtered through a 0.2 μm membrane filter. The solvent was evaporated under reduced pressure and the residue was dissolved in 1:1 (v/v) $\text{CH}_3\text{CN}/\text{H}_2\text{O}$ 0.1% TFA solution. The solution was filtered through a 0.2 μm membrane filter and analysed using a 1260 Infinity HPLC System (Agilent Technology). A Pursuit XRs 5 C18 (250x4.6 mm) reverse phase column has been used and the absorption at 250 nm measured. The samples have been measured with a flow rate of 1 mL/min and a linear gradient of 0.1% TFA containing H_2O and CH_3CN (t=0–3 min 95% H_2O 0.1% TFA, 5% CH_3CN ; t=17 min 100% CH_3CN ; t=23 min 100% CH_3CN) has been used.

2.10. Photostability

The samples were prepared in an air saturated CH_3CN solution. To measure the photostability, the samples were irradiated at 450 nm (light dose after 10 min: 13.22 J/cm^2) in 96 well plates with an Atlas Photonics LUMOS BIO irradiator during time intervals from 0-10 min. The absorbance spectrum from 350-700 nm was recorded with an SpectraMax M2 Microplate Reader (Molecular Devices) after each time interval and compared. As a positive control $[\text{Ru}(\text{bipy})_3]\text{Cl}_2$ and as a negative control Protoporphyrin IX has been used.

2.11. Cell culture

HeLa cells were cultured using DMEM media supplemented with 10% fetal calf serum. RPE-1 cells were cultured using DMEM/F-12 media supplemented with 10% fetal calf serum. Cell lines were complemented with 100 U/ml penicillin-streptomycin mixture, and maintained in humidified atmosphere at 37°C and 5% of CO₂. Before an experiment cells were passaged three times.

2.12. (Photo-)Cytotoxicity

The cytotoxicity of the compounds was accessed by measuring the cell viability using a fluorometric resazurin assay. Cells were seeded in triplicates in 96 well plates (4000 cells per well in 100 µL of media). After 24 h media was removed and the cells were treated with increasing concentrations of the compounds diluted in cell media achieving a total volume of 200 µL. The cells were incubated with the compounds for 4 h. After this time, the media was removed and replaced with 200 µL of fresh media. For the phototoxicity studies, the cells were exposed to light with an Atlas Photonics LUMOS BIO irradiator. Each well was constantly illuminated with 480 nm irradiation. During this time, the temperature was maintained at 37 °C. The cells were grown in the incubator for additional 44 h. For the determination of the dark cytotoxicity, the cells were not irradiated and after the media exchange directly incubated for 44 h. After this time, media was replaced with fresh media containing resazurin with a final concentration of 0.2 mg/mL. After 4 h incubation, the amount of the fluorescent product resorufin was determined upon excitation at 540 nm and measurement its emission at 590 nm using a SpectraMax M2 Microplate Reader (Molecular Devices). The obtained data was analysed with the GraphPad Prism software.

3. Results and Discussion

3.1. Syntheses and Characterisation

Ru(II) complexes **1-7** investigated in this work can be visualised in Figure 1. The synthesis and characterisation of compounds **1**,[42] **2**,[43] **3**[44] and **5**[45] have been previously reported in the literature. However, in this work, except for **1**, a different synthetic procedure was employed to prepare them. To the best of our knowledge, complexes **4**, **6** and **7** have never been reported. Specifically, the substituted 2,2':6',2''-terpyridine ligands (terpy-X, Scheme S1), namely 4'-chloro-2,2':6',2''-terpyridine (terpy-Cl),[37] 4'-bromo-2,2':6',2''-terpyridine (terpy-Br),[38] 4'-methoxy-2,2':6',2''-terpyridine (terpy-OMe),[39] 4'-carboxy-2,2':6',2''-terpyridine (terpy-COOH),[40] 4'-methylcarboxy-2,2':6',2''-terpyridine (terpy-COOMe)[40] and 4'-dimethylamino-2,2':6',2''-terpyridine (terpy-NMe₂)[41] were synthesised as previously reported. Analytical data of all synthesised ligands matched with those of the literature. Interestingly, the structures of the ligands terpy-Cl and terpy-Br were confirmed by single crystal X-ray crystallography in this work (see section below). Complexes were synthesised by refluxing the precursor Ru(terpy)Cl₃[36] and the respective terpy ligand in ethanol to give complexes **1-7** (Scheme S2) in moderate yields.[36] Worthy of note, the reaction between Ru(terpy)Cl₃ with terpy-COOMe yielded a mixture of different undesired products, as observed by HPLC (data not shown). To overcome this problem, the synthetic procedure was changed to a two-step reaction. In the first step, the Cl substituents on the Ru(II) core were exchanged with solvent molecules by reaction of Ru(terpy)Cl₃ with AgBF₄ and filtration of the formed AgCl. In the second step, the terpy-COOMe ligand was coordinated to the metal core upon replacement of the solvent molecules. All complexes were analysed by ¹H, ¹³C-NMR, ESI-HRMS as well elemental analysis (Figure S1-S9). Worthy of note, the structures of all Ru(II) complexes prepared in this work were determined by single crystal X-ray crystallography (see below).

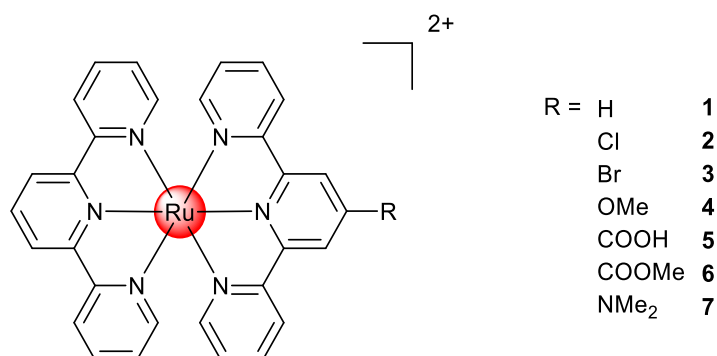


Figure 1. Chemical structures of the $[\text{Ru}(\text{terpy})(\text{terpy-X})]^{2+}$ complexes investigated in this work. The complexes were isolated as PF_6 salts.

3.2. X-ray crystallography

The crystal structures of terpy-Cl, terpy-Br, and all investigated $[\text{Ru}(\text{terpy})(\text{terpy-X})]^{2+}$ complexes **1** – **7** have been determined by single crystal X-ray diffraction studies. Crystal data, structure refinement parameters and molecular structures are presented in Tables S1 – S9 and Figures S10 – S18. In the literature, the $[\text{Ru}(\text{terpy})_2]^{2+}$ cation is well known and can be found in many crystal structures co-crystallizing with various counterions (Cl^- , I^- , BF_4^- , ClO_4^- , PF_6^- and other Pt anionic clusters...) and solvent molecules (H_2O , CH_2Cl_2 , MeCN, NMe_2CHO ...).[42, 55-63] There is also a very large number of other ruthenium terpyridine complexes in the Cambridge Structural Database (version 5.40, last update November 2018).[64] For instance, 142 structures were obtained from a search with terpyridine ligands substituted in *para* position. In the crystal structures of our new metal complexes, the Ru(II) centres are typically in a distorted octahedral environment coordinated by two terpyridine ligands acting as tridentate pincer ligands through the nitrogen atoms. The two ligand planes are always exactly or almost perpendicular to each other. The largest deviation to orthogonality is observed in **6** PF_6 with an angle of $86.9(3)^\circ$ between the calculated mean planes. As a structural feature, the $\text{M-N}_{\text{central}}$ distances are significantly shorter than the $\text{M-N}_{\text{terminal}}$ distances which is typical for

coordination of conjugated terimine systems. The M–N_{central} distances fall in the range 1.973(3) – 1.998(3) Å and the M–N_{terminal} distances in the range 2.063(2) – 2.089(9) Å. In most of the crystal structures of **2** – **7**, the Ru(II) molecules exhibit a positional disorder of the terpyridine ligands. The result of such a disorder is that the group or atom in *para* position on the central pyridine of the substituted terpyridine ligand (and consequently the corresponding H atom of the unsubstituted ligand as well) appears on both terpyridine ligands with a site-occupancy factor of 0.5. It is observed in nine crystal structures over fourteen, only **4**_PF₆, **5**_BF₄, **6**_PF₆, **7**_PF₆ and **7**_BF₄ are free of that kind of disorder. It seems to not be influenced or controlled by the presence of one specific counter ion, neither by the *para* substituent but it is worth noting that when the latter is a “mono-atomic” group like in complexes **2** and **3** (X = Cl, Br) the disorder is always observed (five crystal structures). The crystal packing of [M(terpy)₂] cations have been fully analysed by Scudder *et al.* in 1999.[65] A standard crystal supramolecular motif has been identified as a two-dimensional net of terpy embraces involving molecules attracted by face-to-face $\pi \dots \pi$ interactions and edge-to-face C–H... π interactions between the external rings of the ligands. Despite the *para* substitution of one of the terpyridine ligands, this standard “terpy embrace” motif can be observed in six of our crystal structures: **2**_BF₄, **2**_PF₆, **3**_BF₄, **3**_PF₆, **4**_BF₄ and **7**_BF₄ (Figure S19). The presence of the bulky BPh₄[–] counterion in **1**_BPh₄, **2**_BPh₄, **5**_BPh₄ and **6**_BPh₄ rules out that standard layer structure since no direct interactions are observed between cations anymore, the crystal packing is mainly governed by $\pi \dots \pi$ interactions between the pyridine rings of the cations and the phenyl rings of the anions (Figure S20). The so-called terpy embrace motif still exists in the other crystal structures but the typical face-to-face and edge-to-face interactions only lead to chains in **5**_BF₄ and **7**_PF₆ (Figure S21) or form small units of two molecules in **6**_PF₆ or four molecules in **6**_BF₄ (Figure S22). These chains or units are further connected to via C–H...O hydrogen bondings or C–H... π interactions, and to the counterions via C-

H...F interactions to form a three-dimensional network. Finally, the crystal structure of **4**_PF₆ is the only one to not exhibit π ... π interactions, only C-H... π and C-H...F interactions are observed.

3.3. Photophysical Characterisation

For a complete characterisation, the absorption and emission properties of the synthesised compounds were investigated. The UV/Vis absorption spectra were recorded in CH₃CN (Figure 2) and PBS buffer (Figure S23). The comparison between the different complexes shows that the *para* substituents on the central pyridine of the terpy ligand influences the amount of light absorbed and therefore the excitation coefficient (Table S10). However, no strong shift either to blue or red could be observed. The analysis of the absorption shows that the very intensive band in the UV region is caused by a ligand centred (LC) π - π^* transition. The other broad band in the visible spectrum (~400-550 nm) was attributed to the spin-allowed d- π metal-to-ligand charge transfer (MLCT) transition.[20, 25, 66] Next to the absorption, the emission of the complexes was investigated. The synthesised complexes have a very weak emission from ~550-800 nm (Table S1, Figure S24) upon excitation in CH₃CN at 450 nm at room temperature which was measurable only at the detection limit of our used setup. The luminescence quantum yields were found to be <0.01 % in CH₃CN which is fitting with previous studies of similar complexes.[30, 67-69] The characterisation of the excited state lifetimes was not possible with our apparatus due to a necessary minimal delay between excitation and detection, indicating that the compounds **1-7** have lifetimes < 29 ns. Therefore, as expected, the excited state lifetimes are in the same range than other [Ru(terpy)₂]²⁺ derivatives previously published.[30, 67-69]

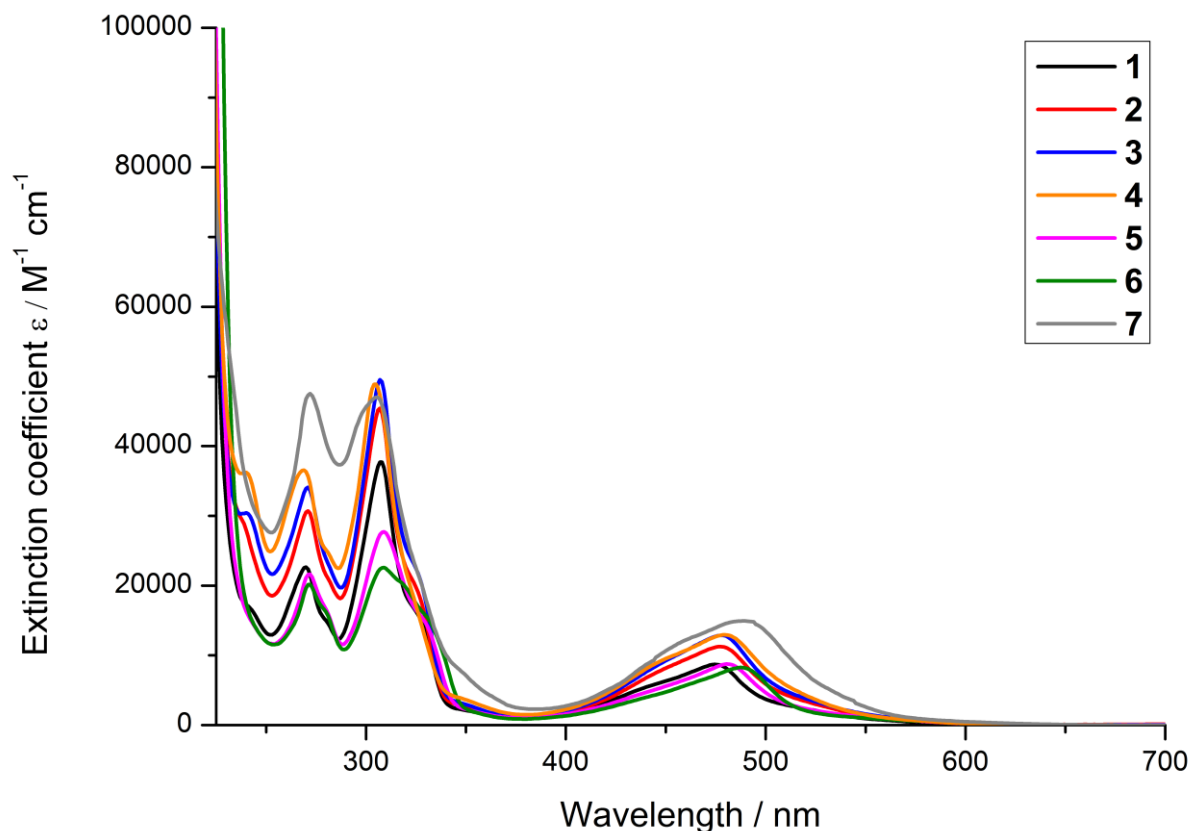


Figure 2. UV/Vis spectra of the complexes **1-7** in CH₃CN.

3.4. Determination of the Log*P* values

After having assessed the photophysical properties of our compounds, we investigated their solubility in an aqueous solution which is crucial for any kind of biological application. For this purpose, we determined the distribution coefficient ($\log P$ values) of the complexes between an aqueous PBS phase and a lipophilic octanol phase by the “shake-flask” method, as previously performed by our group with other metal complexes.[70, 71] All compounds were mostly found in the aqueous phase, which we assume, is due to the positive charge of the metal complexes. As anticipated, the results (Figure 3) show that the $\log P$ values change based on the functional group present on the terpy ligand. Compound **5** bearing a carboxylic acid was found to be the most hydrophilic and complex **3** bearing a bromine substituent the most lipophilic one. The

following order could be made (from the most hydrophilic to the most lipophilic): **5 > 1 > 6 > 2 > 4 > 7 > 3**.

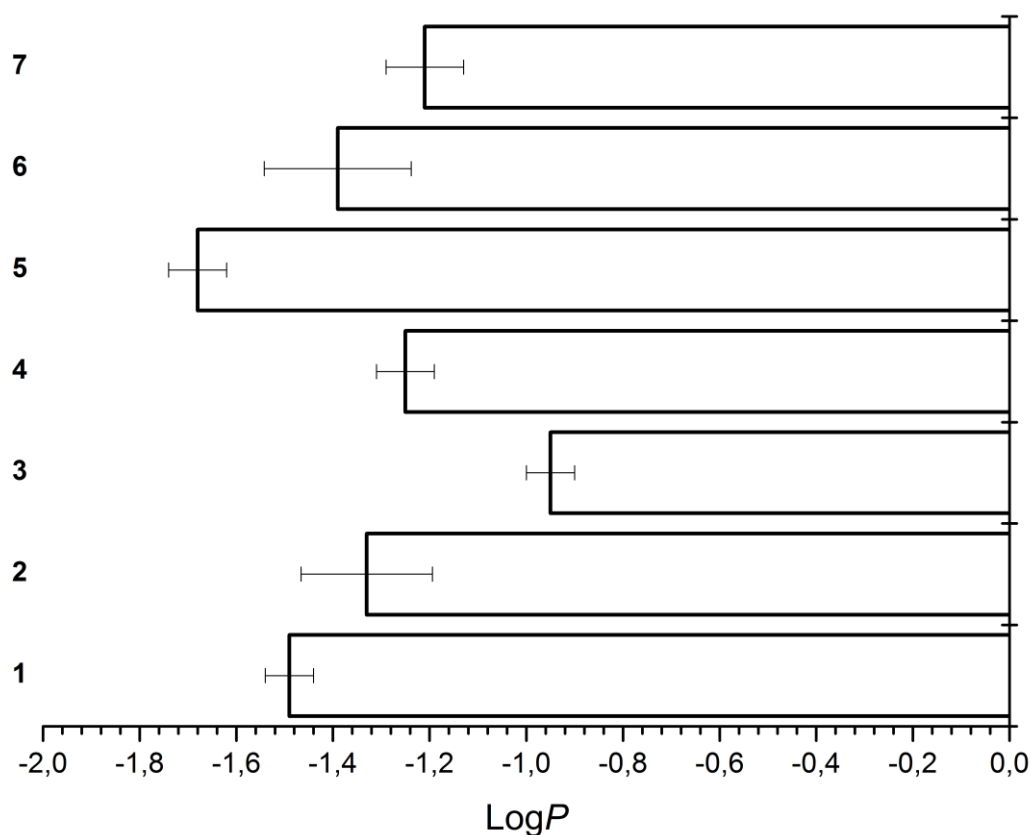


Figure 3. Distribution coefficients ($\text{Log}P$ values) of complexes **1-7**.

3.5. Stability in Human Plasma

In order to have a preliminary insight of the metabolic stability of our compounds, their compatibility under biological conditions was investigated. For this purpose, the complexes were incubated upon the addition of the internal standard caffeine in human plasma at 37 °C for 48 h and their stability investigated, as previously performed by our group with other metal complexes.[21, 23] After extraction from the plasma, the complexes were analysed *via* HPLC and the chromatogram before and after incubation compared. Complexes **1-5** and **7** (Figure S25-S29, S31) were found to be stable for a therapeutically relevant time. However, some degradation of compound **6** (Figure S30) was observed, as indicated by the appearance of small

peaks as well as a decreased of the compound/caffeine ratio. A potential explanation is the activity of esterases in human plasma, which could potential cleave the ester bond in **6**.^[72, 73]

3.6. Photostability

Since Ru(II) complexes are well known to act as PDT PSs, the compounds were investigated to assess if a photobleaching effect, which is a degradation of the compound upon light irradiation, was observed.^[74, 75] To investigate this, the complexes were constantly irradiated at 450 nm in CH₃CN and the potential change in absorbance between 350-700 nm from 0-10 min monitored. As a positive control, [Ru(bipy)₃]Cl₂^[76] (Figure S32) and as a negative control Protoporphyrin IX (PpIX)^[77] (Figure S33) were chosen. Analyses (Figure S34-S40) shows a different photostability of the complexes based on the functional group they bear. In general, a rather small photobleaching effect was observed. From comparison between the different complexes, the following order for photostability can be made from the most photostable to the least photostable: **2 ~ 3 > 4 > 1 > 7 > 5 > 6**.

3.7. Dark Cytotoxicity and (Photo-)toxicity

We then investigated the biological influence of the complexes **1-7**, their corresponding ligands and precursor on non-cancerous retinal pigment epithelium (RPE-1) and human cervical carcinoma (HeLa) cells. For this purpose, cells were treated with the compounds in the dark as well as upon light irradiation at 480 nm and their cell viability measured using a fluorometric resazurin assay. The IC₅₀ values of the compounds are shown in Table 1 and Table 2. Unfortunately, complexes **1-6** did not show a measurable cytotoxic effect in HeLa cells in the dark as well as upon light irradiation. The poor phototoxic effect was expected due to the poor photophysical properties including the short excited state lifetimes of our complexes. However, compound **7** was found to be cytotoxic in the micromolar range in RPE-1 and HeLa cells.

Unfortunately, no selectivity for cancerous cells versus non-cancerous cells was observed. The IC₅₀ values for **7** are 1.4 times higher in RPE-1 and 3.3 times higher in HeLa cells than for the clinically used drug cisplatin. In terms of PDT treatment, an important value for the evaluation of a PS is the comparison between a dark and light treatment. For this purpose, the phototoxic index (PI) is defined as the ratio between the IC₅₀ value in the dark and upon irradiation. Compound **7** was found to be phototoxic with a PI value of 1.4 in RPE-1 and HeLa cells. These values are rather low in comparison to porphyrin based-PSs like Protoporphyrin IX (PpIX). On the contrary all ligands (besides precursor in HeLa and RPE-1 cell line, Terpy-COOH and Terpy-COOMe in RPE-1 cell line) used for the synthesis of the series of the compounds were found to be cytotoxic. Their toxicity did not change much upon light irradiation, obtained PI values were very low (from 0.8 to 2.0).

Table 1. IC₅₀ values in the dark and upon irradiation at 480 nm for the complexes **1-7** incubated in non-cancerous retinal pigment epithelium (RPE-1) and human cervical carcinoma (HeLa) cells. Average of three independent measurements.

Compound	RPE-1			HeLa		
	IC ₅₀ / μM dark	IC ₅₀ / μM 480 nm (10 min, 3.1 J/cm ²)	PI	IC ₅₀ / μM dark	IC ₅₀ / μM 480 nm (10 min, 3.1 J/cm ²)	PI
1	>100	>100	n.d.	>100	>100	n.d.
2	>100	>100	n.d.	>100	>100	n.d.
3	>100	>100	n.d.	>100	>100	n.d.
4	>100	>100	n.d.	>100	>100	n.d.
5	>100	>100	n.d.	>100	>100	n.d.
6	>100	>100	n.d.	>100	>100	n.d.

7	39.7 ± 3.6	27.5 ± 1.1	1.4	35.1 ± 0.6	24.5 ± 2.6	1.4
PpIX	>100	3.8 ± 0.1	>26	>100	2.5 ± 0.1	>40
Cisplatin	29.3 ± 1.4	-	-	10.5 ± 0.8	-	-

n.d. = not determinable

Table 2. IC₅₀ values in the dark and upon irradiation at 480 nm for the ligands as well as Ru(terpy)Cl₃ incubated in non-cancerous retinal pigment epithelium (RPE-1) and human cervical carcinoma (HeLa) cells. Average of three independent measurements.

Compound	RPE-1			HeLa		
	IC₅₀ / μM dark	IC₅₀ / μM 480 nm (10 min, 3.1 J/cm²)	PI	IC₅₀ / μM dark	IC₅₀ / μM 480 nm (10 min, 3.1 J/cm²)	PI
terpy-H	21.8 ± 0.7	21.9 ± 2.4	0.8	26.5 ± 3.0	18.1 ± 0.7	1.5
terpy-Cl	8.7 ± 0.8	8.4 ± 1.2	1.0	12.3 ± 0.6	8.3 ± 1.3	1.5
terpy-Br	10.5 ± 0.4	8.8 ± 0.3	1.1	13.7 ± 3.2	6.9 ± 0.1	2.0
terpy-OMe	18.9 ± 0.8	16.7 ± 0.7	1.1	40.9 ± 2.1	40.2 ± 0.3	1.3
terpy-COOH	>100	>100	n.d.	50.5 ± 9.1	37.5 ± 5.4	1.3
terpy-COOMe	>100	>100	n.d.	23.3 ± 4.0	20.0 ± 2.4	1.2
terpy-NMe₂	14.8 ± 1.4	13.3 ± 2.2	1.1	19.6 ± 1.3	17.7 ± 2.7	1.1
Ru(Terpy)Cl₃	>100	>100	n.d.	96.0 ± 3.5	87.5 ± 8.0	1.1

n.d. = not determinable

4. Conclusion

In this study, we report on the systematic investigation of differently substituted $[\text{Ru}(\text{terpy})(\text{terpy-X})]^{2+}$ ($\text{X} = \text{H}$ (**1**), Cl (**2**), Br (**3**), OMe (**4**), COOH (**5**), COOMe (**6**), NMe_2 (**7**)) complexes as potential chemotherapeutic agents and PDT PSs. The compounds were characterized in-depth including single crystal X-ray crystallography. Photophysical measurements showed that the complexes strongly absorb in the green region of the visible electromagnetic spectrum. Further analysis revealed that they are weakly luminescent and have a short lived excited state. The distribution coefficient ($\log P$ value) of the complexes between an aqueous PBS phase and a lipophilic octanol phase was determined. As expected, all compounds were majorly found in the aqueous phase. Importantly, compounds **1-5** and **7** were found to be stable in human plasma and to have only a small photobleaching effect upon continuous LED irradiation. Complex **6** was found to be not stable in human plasma, probably due to the presence of an ester bond. Biological evaluation on one cancerous and one non-cancerous cell line demonstrated that compounds **1-6** had no cytotoxic effect in the dark as well as upon light irradiation. In comparison, **7** was found to have a dark and (photo-)cytotoxicity in the micromolar range. However, irradiation at 480 nm seems to have only a negligible effect. We assume this is caused by the very short excited state lifetimes of this complex. Overall, this study demonstrates that small structural changes are able to influence significantly the effect the compound has on a cell. Despite unfavourable photophysical properties as a weak emission and short lifetimes, it could have been demonstrated in the literature that ruthenium terpyridine complexes were able to bind to DNA and to cleave it upon light irradiation. Inspired from these works from Thorp and Brewer et al., we considered them as potential candidates as PSs for PDT. Due to a lack of a detailed investigation of Ruthenium Terpyridine complexes in this field, we decided to systematic investigate their

potential. Unfortunately, we could demonstrate that these kind of compounds are not particular interesting as PDT PSs.

Acknowledgements

This work was financially supported by an ERC Consolidator Grant PhotoMedMet to G.G. (GA 681679) and has received support under the program “Investissements d’ Avenir” launched by the French Government and implemented by the ANR with the reference ANR-10-IDEX-0001-02 PSL (G.G.).

References

- [1] D. Cella, E. Cherin, *Compr. Ther.*, vol. 14, 1988, pp. 69-75.
- [2] A. Jemal, F. Bray, M.M. Center, J. Ferlay, E. Ward, D. Forman, *CA Cancer J. Clin.*, vol. 61, 2011, pp. 69-90.
- [3] A. Urruticochea, R. Alemany, J. Balart, A. Villanueva, F. Vinals, G. Capella, *Curr. Pharm. Des.*, vol. 16, 2010, pp. 3-10.
- [4] E.R. Jamieson, S.J. Lippard, *Chem. Rev.*, vol. 99, American Chemical Society, 1999, pp. 2467-2498.
- [5] R. Oun, Y.E. Moussa, N.J. Wheate, *Dalton Transactions*, vol. 47, The Royal Society of Chemistry, 2018, pp. 6645-6653.
- [6] L. Zeng, P. Gupta, Y. Chen, E. Wang, L. Ji, H. Chao, Z.-S. Chen, *Chem. Soc. Rev.*, vol. 46, 2017, pp. 5771-5804.
- [7] A. Notaro, G. Gasser, *Chem. Soc. Rev.*, vol. 46, 2017, pp. 7317-7337.
- [8] F. Li, J.G. Collins, F.R. Keene, *Chem. Soc. Rev.*, vol. 44, 2015, pp. 2529-2542.
- [9] F.R. Keene, J.A. Smith, J.G. Collins, *Coord. Chem. Rev.*, vol. 253, 2009, pp. 2021-2035.

- [10] S. Monro, K.L. Colón, H. Yin, J. Roque III, P. Konda, S. Gujar, R.P. Thummel, L. Lilge, C.G. Cameron, S.A. McFarland, *Chem. Rev.*, vol. 119, 2019, pp. 797-828.
- [11] C. Mari, V. Pierroz, S. Ferrari, G. Gasser, *Chem. Sci.*, vol. 6, 2015, pp. 2660-2686.
- [12] M. Jakubaszek, B. Goud, S. Ferrari, G. Gasser, *Chem. Commun.*, vol. 54, 2018, pp. 13040-13059.
- [13] F. Heinemann, J. Karges, G. Gasser, *Acc. Chem. Res.*, vol. 50, 2017, pp. 2727-2736.
- [14] K. Qiu, Y. Chen, T.W. Rees, L. Ji, H. Chao, *Coord. Chem. Rev.*, 2017.
- [15] A. Yadav, T. Janaratne, A. Krishnan, S.S. Singhal, S. Yadav, A.S. Dayoub, D.L. Hawkins, S. Awasthi, F.M. MacDonnell, *Mol. Cancer Ther.*, 2013.
- [16] F.E. Poynton, S.A. Bright, S. Blasco, D.C. Williams, J.M. Kelly, T. Gunnlaugsson, *Chem. Soc. Rev.*, vol. 46, The Royal Society of Chemistry, 2017, pp. 7706-7756.
- [17] J. Shum, P.K.-K. Leung, K.K.-W. Lo, *Inorg. Chem.*, vol. 58, American Chemical Society, 2019, pp. 2231-2247.
- [18] A. Juris, V. Balzani, F. Barigelletti, S. Campagna, P.I. Belser, A. Von Zelewsky, *Coord. Chem. Rev.*, vol. 84, 1988, pp. 85-277.
- [19] K. Kalyanasundaram, *Coord. Chem. Rev.*, vol. 46, 1982, pp. 159-244.
- [20] S. Campagna, F. Puntoriero, F. Nastasi, G. Bergamini, V. Balzani, in: V. Balzani, S. Campagna (Eds.), *Photochemistry and Photophysics of Coordination Compounds I*, Springer Berlin Heidelberg, Berlin, Heidelberg, 2007, pp. 117-214.
- [21] C. Mari, V. Pierroz, R. Rubbiani, M. Patra, J. Hess, B. Spingler, L. Oehninger, J. Schur, I. Ott, L. Salassa, *Chem. Eur. J.*, vol. 20, 2014, pp. 14421-14436.
- [22] Y. Ellahioui, M. Patra, C. Mari, R. Kaabi, J. Karges, G. Gasser, S. Gómez-Ruiz, *Dalton Trans.*, 2018.
- [23] H. Huang, B. Yu, P. Zhang, J. Huang, Y. Chen, G. Gasser, L. Ji, H. Chao, *Angew. Chem. Int. Ed.*, vol. 54, 2015, pp. 14049-14052.

- [24] C. Mari, V. Pierroz, S. Ferrari, G. Gasser, *Chem. Sci.*, vol. 6, 2015, pp. 2660-2686.
- [25] J.P. Sauvage, J.P. Collin, J.C. Chambron, S. Guillerez, C. Coudret, V. Balzani, F. Barigelletti, L. De Cola, L. Flamigni, *Chem. Rev.*, vol. 94, 1994, pp. 993-1019.
- [26] N. Grover, N. Gupta, P. Singh, H.H. Thorp, *Inorg. Chem.*, vol. 31, 1992, pp. 2014-2020.
- [27] B.T. Farrer, H.H. Thorp, *Inorg. Chem.*, vol. 39, 2000, pp. 44-49.
- [28] N. Grover, H.H. Thorp, *J. Am. Chem. Soc.*, vol. 113, 1991, pp. 7030-7031.
- [29] G.A. Neyhart, N. Grover, S.R. Smith, W.A. Kalsbeck, T.A. Fairley, M. Cory, H.H. Thorp, *J. Am. Chem. Soc.*, vol. 115, 1993, pp. 4423-4428.
- [30] A. Jain, C. Slebodnick, B.S. Winkel, K.J. Brewer, *J. Inorg. Biochem.*, vol. 102, 2008, pp. 1854-1861.
- [31] K.K. Patel, E.A. Plummer, M. Darwish, A. Rodger, M.J. Hannon, *J. Inorg. Biochem.*, vol. 91, 2002, pp. 220-229.
- [32] C.-W. Jiang, H. Chao, H. Li, L.-N. Ji, *J. Inorg. Biochem.*, vol. 93, 2003, pp. 247-255.
- [33] Y. Liu, R. Hammitt, D.A. Lutterman, R.P. Thummel, C. Turro, *Inorg. Chem.*, vol. 46, 2007, pp. 6011-6021.
- [34] H.-Y. Ding, X.-S. Wang, L.-Q. Song, J.-R. Chen, J.-H. Yu, B.-W. Zhang, *J. Photochem. Photobiol. A: Chem.*, vol. 177, 2006, pp. 286-294.
- [35] A. Rilak, I. Bratsos, E. Zangrando, J. Kljun, I. Turel, Z.i.D. Bugarčić, E. Alessio, *Inorg. Chem.*, vol. 53, 2014, pp. 6113-6126.
- [36] B.P. Sullivan, J.M. Calvert, T.J. Meyer, *Inorg. Chem.*, vol. 19, 1980, pp. 1404-1407.
- [37] E.C. Constable, M.D. Ward, *J. Chem. Soc., Dalton Trans.*, 1990, pp. 1405-1409.
- [38] S. Katagiri, R. Sakamoto, H. Maeda, Y. Nishimori, T. Kurita, H. Nishihara, *Chemistry-A European Journal*, vol. 19, 2013, pp. 5088-5096.
- [39] E.C. Constable, K. Harris, C.E. Housecroft, M. Neuburger, J.A. Zampese, *CrystEngComm*, vol. 12, 2010, pp. 2949-2961.

- [40] M.W. Cooke, P. Tremblay, G.S. Hanan, *Inorg. Chim. Acta*, vol. 361, 2008, pp. 2259-2269.
- [41] E. Constable, A.C. Thompson, D. Tocher, M. Daniels, *New J. Chem.*, vol. 16, 1992, pp. 855-867.
- [42] S. Mallakpour, M. Dinari, H. Hadadzadeh, M. Daryanavard, F. Roudi, *Journal of fluorescence*, vol. 24, 2014, pp. 1841-1848.
- [43] E.C. Constable, P. Harverson, C.E. Housecroft, E. Nordlander, J. Olsson, *Polyhedron*, vol. 25, 2006, pp. 437-458.
- [44] E.C. Constable, R.W. Handel, C.E. Housecroft, A. Farràn Morales, B. Ventura, L. Flamigni, F. Barigelletti, *Chemistry-A European Journal*, vol. 11, 2005, pp. 4024-4034.
- [45] E.M. Hahn, N. Estrada-Ortiz, J. Han, V.F. Ferreira, T.G. Kapp, J.D. Correia, A. Casini, F.E. Kühn, *Eur. J. Inorg. Chem.*, vol. 2017, 2017, pp. 1667-1672.
- [46] Rigaku Oxford Diffraction, 2015.
- [47] R. Clark, J. Reid, *Acta Crystallogr. Sect. A: Found. Crystallogr.*, vol. 51, 1995, pp. 887-897.
- [48] CrysAlisPro (version 1.171.38.41), Rigaku Oxford Diffraction, 2016.
- [49] O.V. Dolomanov, L.J. Bourhis, R.J. Gildea, J.A.K. Howard, H. Puschmann, *J. Appl. Crystallogr.*, vol. 42, 2009, pp. 339-341.
- [50] G.M. Sheldrick, *Acta Crystallographica Section A: Foundations and Advances*, vol. 71, 2015, pp. 3-8.
- [51] G.M. Sheldrick, *Acta Crystallographica Section C: Structural Chemistry*, vol. 71, 2015, pp. 3-8.
- [52] C.F. Macrae, P.R. Edgington, P. McCabe, E. Pidcock, G.P. Shields, R. Taylor, M. Towler, J.v.d. Streek, *J. Appl. Crystallogr.*, vol. 39, 2006, pp. 453-457.
- [53] K. Nakamaru, *Bull. Chem. Soc. Jpn.*, vol. 55, 1982, pp. 1639-1640.

- [54] S.J. Bruce, I. Tavazzi, V.r. Parisod, S. Rezzi, S. Kochhar, P.A. Guy, *Anal. Chem.*, vol. 81, 2009, pp. 3285-3296.
- [55] M. Kozłowska, P. Rodziewicz, D.M. Brus, J. Breczko, K. Brzezinski, *Acta Crystallogr. Sect. Sect. E: Struct. Rep. Online*, vol. 68, 2012, pp. m1414-m1415.
- [56] D.C. Craig, M.L. Scudder, W.-A. McHale, H.A. Goodwin, *Aust. J. Chem.*, vol. 51, 1998, pp. 1131-1140.
- [57] M.L. Scudder, D.C. Craig, H.A. Goodwin, *CrystEngComm*, vol. 7, 2005, pp. 642-649.
- [58] A.G. Walstrom, M. Pink, X. Yang, K.G. Caulton, *Dalton Transactions*, 2009, pp. 6001-6006.
- [59] S. Pyo, E. Pérez-Cordero, S.G. Bott, L. Echegoyen, *Inorg. Chem.*, vol. 38, 1999, pp. 3337-3343.
- [60] C.A. Tovee, C.A. Kilner, J.A. Thomas, M.A. Halcrow, *CrystEngComm*, vol. 11, 2009, pp. 2069-2077.
- [61] C. Femoni, M.C. Iapalucci, G. Longoni, T. Lovato, S. Stagni, S. Zacchini, *Inorg. Chem.*, vol. 49, 2010, pp. 5992-6004.
- [62] K. Lashgari, M. Kritikos, R. Norrestam, T. Norrby, *Acta Crystallographica Section C*, vol. 55, 1999, pp. 64-67.
- [63] C.-C. Lin, P. Wang, L. Jin, H.-H. Li, S.-K. Lin, Z.-R. Chen, *J. Cluster Sci.*, vol. 26, 2015, pp. 1011-1022.
- [64] C.R. Groom, I.J. Bruno, M.P. Lightfoot, S.C. Ward, *Acta Crystallographica Section B: Structural Science, Crystal Engineering and Materials*, vol. 72, 2016, pp. 171-179.
- [65] M.L. Scudder, H.A. Goodwin, I.G. Dance, *New J. Chem.*, vol. 23, 1999, pp. 695-705.
- [66] M. Stone, G. Crosby, *Chem. Phys. Lett.*, vol. 79, 1981, pp. 169-173.
- [67] M. Beley, J.-P. Collin, J.-P. Sauvage, H. Sugihara, F. Heisel, A. Miehé, *J. Chem. Soc., Dalton Trans.*, 1991, pp. 3157-3159.

- [68] M. Maestri, N. Armaroli, V. Balzani, E.C. Constable, A.M.C. Thompson, *Inorg. Chem.*, vol. 34, 1995, pp. 2759-2767.
- [69] J.P. Collin, S. Guillerez, J.P. Sauvage, F. Barigelletti, L. De Cola, L. Flamigni, V. Balzani, *Inorg. Chem.*, vol. 30, 1991, pp. 4230-4238.
- [70] V. Pierroz, T. Joshi, A. Leonidova, C. Mari, J. Schur, I. Ott, L. Spiccia, S. Ferrari, G. Gasser, *J. Am. Chem. Soc.*, vol. 134, 2012, pp. 20376-20387.
- [71] J. Karges, P. Goldner, G. Gasser, *Inorganics*, vol. 7, 2019, pp. 4.
- [72] F.M. Williams, *Clin. Pharmacokinet.*, vol. 10, 1985, pp. 392-403.
- [73] B. Vahlquist, *Acta Physiologica*, vol. 72, 1935, pp. 133-160.
- [74] R. Bonnett, G. Martinez, *Tetrahedron*, vol. 57, 2001, pp. 9513-9547.
- [75] T.S. Mang, T.J. Dougherty, W.R. Potter, D.G. Boyle, S. Somer, J. Moan, *Photochem. Photobiol.*, vol. 45, 1987, pp. 501-506.
- [76] X. Zhang, M.A. Rodgers, *The Journal of Physical Chemistry*, vol. 99, 1995, pp. 12797-12803.
- [77] M. Ericson, S. Grapengiesser, F. Gudmundson, A. Wennberg, O. Larkö, J. Moan, A. Rosen, *Lasers Med. Sci.*, vol. 18, 2003, pp. 56-62.

Supplementary Information

Systematic Investigation of the Antiproliferative Activity of a Series of Ruthenium Terpyridine Complexes

*Johannes Karges,^a Marta Jakubaszek,^{a,b} Bruno Goud,^b Olivier Blacque,^c Philippe Goldner,^d and
Gilles Gasser^{a,*}*

^a Chimie ParisTech, PSL University, CNRS, Institute of Chemistry for Life and Health Sciences, Laboratory for Inorganic Chemical Biology, 75005 Paris, France.

^b Institut Curie, PSL University, CNRS UMR 144, Paris, France.

^c Department of Chemistry, University of Zurich, Winterthurerstrasse 190, 8057 Zurich, Switzerland.

^d Chimie ParisTech, PSL University, CNRS, Institut de Recherche de Chimie Paris, 75005 Paris, France.

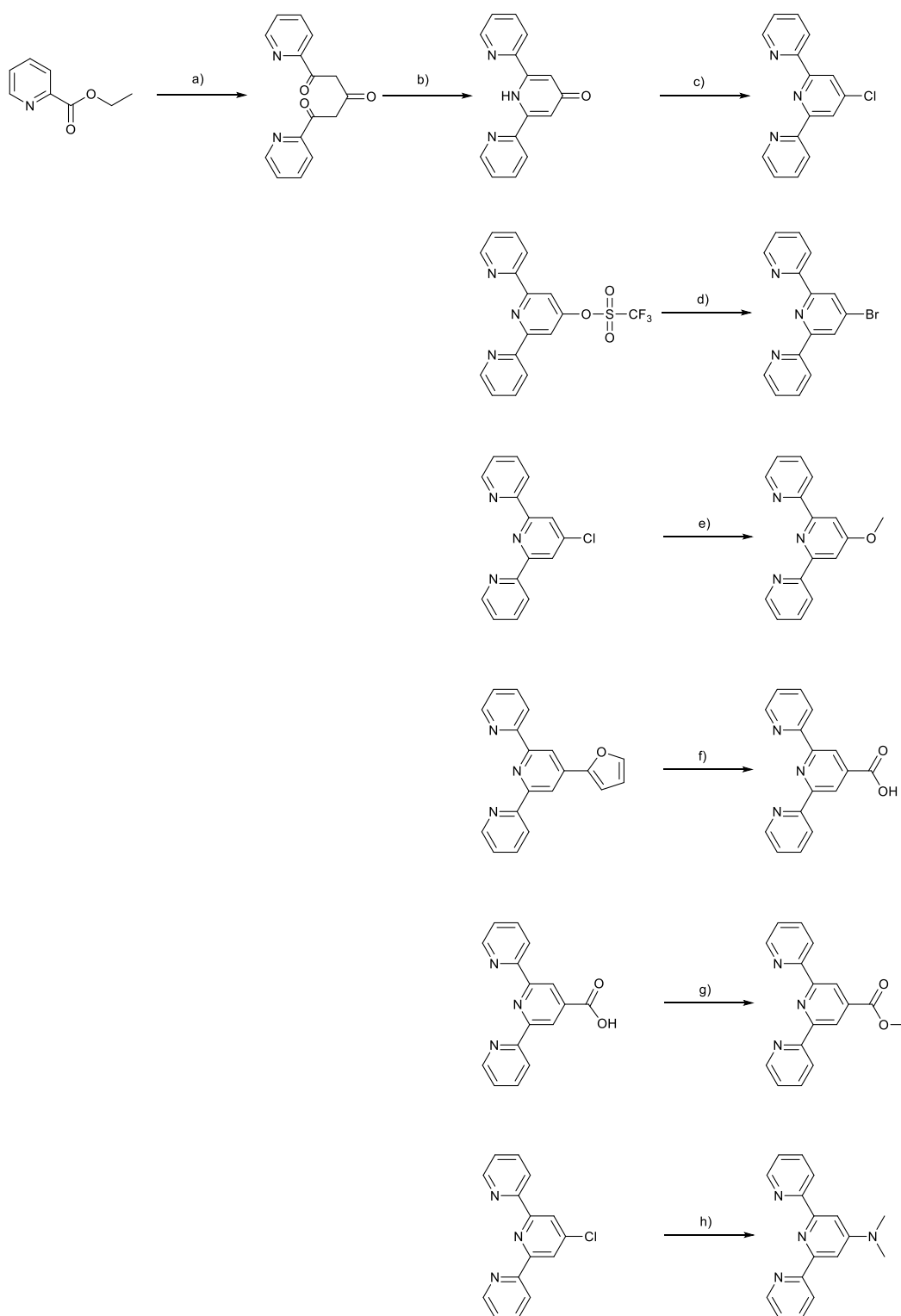
* Corresponding author: Email: gilles.gasser@chimieparistech.psl.eu; www.gassergroup.com; Tel. +33 1 44 27 56 02.

Table of Contents:

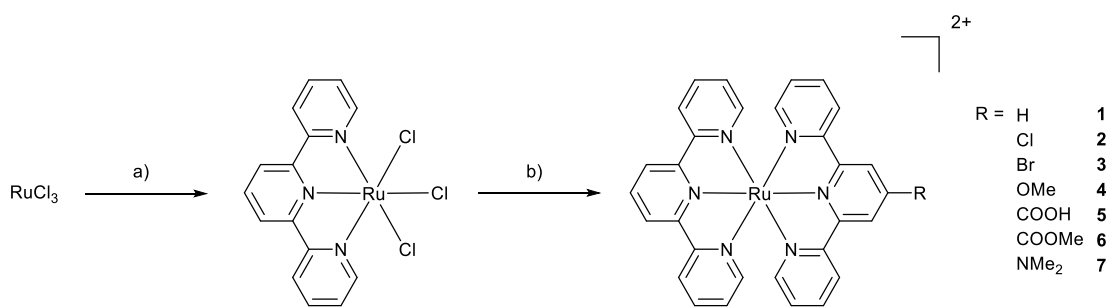
SCHEME S1. SYNTHESIS OF THE TERPY-X LIGANDS.	193
SCHEME S2. SYNTHESIS OF THE COMPLEXES 1-7.	194
FIGURE S1. ¹ H NMR SPECTRUM OF 4 IN CD ₃ CN, 400 MHZ.	194
FIGURE S2. ¹³ C NMR SPECTRUM OF 4 IN CD ₃ CN, 100 MHZ.	195
FIGURE S3. ESI-HRMS SPECTRUM OF 4 (POSITIVE DETECTION MODE).....	195
FIGURE S4. ¹ H NMR SPECTRUM OF 6 IN CD ₃ CN, 400 MHZ.	196
FIGURE S5. ¹³ C NMR SPECTRUM OF 6 IN CD ₃ CN, 100 MHZ.	197
FIGURE S6. ESI-HRMS SPECTRUM OF 6 (POSITIVE DETECTION MODE).....	197
FIGURE S7. ¹ H NMR SPECTRUM OF 7 IN CD ₃ CN, 400 MHZ.	198
FIGURE S8. ¹³ C NMR SPECTRUM OF 7 IN CD ₃ CN, 100 MHZ.	199
FIGURE S9. ESI-HRMS SPECTRUM OF 7 (POSITIVE DETECTION MODE).....	199
TABLE S1. CRYSTAL DATA AND STRUCTURE REFINEMENT PARAMETERS FOR TERPY-CL AND TERPY-BR.	200
TABLE S2. CRYSTAL DATA AND STRUCTURE REFINEMENT PARAMETERS FOR 1_BPH ₄ AND 2_BF ₄	201
TABLE S3. CRYSTAL DATA AND STRUCTURE REFINEMENT PARAMETERS FOR 2_BPH ₄ AND 2_PF ₆	202
TABLE S4. CRYSTAL DATA AND STRUCTURE REFINEMENT PARAMETERS FOR 3_BF ₄ AND 3_PF ₆	203
TABLE S5. CRYSTAL DATA AND STRUCTURE REFINEMENT PARAMETERS FOR 4_BF ₄ AND 4_PF ₆	204
TABLE S6. CRYSTAL DATA AND STRUCTURE REFINEMENT PARAMETERS FOR 5_BF ₄ AND 5_BPH ₄	205
TABLE S7. CRYSTAL DATA AND STRUCTURE REFINEMENT PARAMETERS FOR 6_BF ₄ AND 6_BPH ₄	206
TABLE S8. CRYSTAL DATA AND STRUCTURE REFINEMENT PARAMETERS FOR 6_PF ₆ AND 7_BF ₄	207
TABLE S9. CRYSTAL DATA AND STRUCTURE REFINEMENT PARAMETER FOR 7_PF ₆	208
FIGURE S10. MOLECULAR STRUCTURES OF TERPY-CL AND TERPY-BR 209	209
FIGURE S11. MOLECULAR STRUCTURES OF 1_BPH ₄ AND 2_BF ₄ 210	210
FIGURE S12. MOLECULAR STRUCTURES OF 2_PF ₆ AND 2_BPH ₄ 211	211
FIGURES13.MOLECULAR STRUCTURES OF 3_BF ₄ AND 3_PF ₆ 212	212
FIGURES14.MOLECULAR STRUCTURES OF 4_BF ₄ AND 4_PF ₆ 213	213
FIGURES15.MOLECULAR STRUCTURES OF 5_BF ₄ AND 5_BPH ₄ 214	214
FIGURES16.MOLECULAR STRUCTURES OF 6_BF ₄ AND 6_PF ₆ 215	215
FIGURES17.MOLECULAR STRUCTURES OF 6_BPH ₄ AND 7_BF ₄ 216	216

FIGURES 18. MOLECULAR STRUCTURES OF 7_Pf₆	217
FIGURE S19. BALL-AND-STICK REPRESENTATIONS OF THE TWO-DIMENSIONAL NET OF [RU(TERPY)(TERPY-X)] ²⁺ CATIONS IN 2_Pf₆ AND IN 7_Bf₄	218
FIGURE S20. BALL-AND-STICK REPRESENTATIONS OF THE ARRANGEMENT OF THE [RU(TERPY)(TERPY-X)] ²⁺ CATIONS IN 1_BPh₄ AND IN 2_BPh₄	219
FIGURE S21. BALL-AND-STICK REPRESENTATIONS OF THE ARRANGEMENT OF THE [RU(TERPY)(TERPY-X)] ²⁺ CATIONS IN 5_Bf₄ AND IN 7_Pf₆	220
FIGURE S22. BALL-AND-STICK REPRESENTATIONS OF THE ARRANGEMENT OF THE [RU(TERPY)(TERPY-COOMe)] ²⁺ CATIONS IN 6_Bf₄ AND IN 6_Pf₆	221
TABLE S10. SPECTROSCOPIC PROPERTIES OF THE COMPLEXES 1-7 IN CH ₃ CN AND PBS.....	222
FIGURE S23. UV/VIS SPECTRA OF THE COMPLEXES 1-7 IN PBS.....	223
FIGURE S24. NORMALISED EMISSION SPECTRA OF THE COMPLEXES 1-7 IN CH ₃ CN.....	224
FIGURE S25. HPLC CHROMATOGRAM OF CAFFEINE AND 1 AFTER 0 H AND 48 H INCUBATION IN HUMAN POOLED PLASMA.	224
FIGURE S26. HPLC CHROMATOGRAM OF CAFFEINE AND 2 AFTER 0 H AND 48 H INCUBATION IN HUMAN POOLED PLASMA.	225
FIGURE S27. HPLC CHROMATOGRAM OF CAFFEINE AND 3 AFTER 0 H AND 48 H INCUBATION IN HUMAN POOLED PLASMA.	225
FIGURE S28. HPLC CHROMATOGRAM OF CAFFEINE AND 4 AFTER 0 H AND 48 H INCUBATION IN HUMAN POOLED PLASMA.	226
FIGURE S29. HPLC CHROMATOGRAM OF CAFFEINE AND 5 AFTER 0 H AND 48 H INCUBATION IN HUMAN POOLED PLASMA.	226
FIGURE S30. HPLC CHROMATOGRAM OF CAFFEINE AND 6 AFTER 0 H AND 48 H INCUBATION IN HUMAN POOLED PLASMA.	227
FIGURE S31. HPLC CHROMATOGRAM OF CAFFEINE AND 7 AFTER 0 H AND 48 H INCUBATION IN HUMAN POOLED PLASMA.	227
FIGURE S32. TEMPORAL CHANGE OF THE UV/VIS SPECTRA OF [RU(BIPY) ₃]Cl ₂ BY IRRADIATION AT 450 NM IN CH ₃ CN.	228
FIGURE S33. TEMPORAL CHANGE OF THE UV/VIS SPECTRA OF PROTOPORPHYRIN IX BY IRRADIATION AT 450 NM IN CH ₃ CN.....	228

FIGURE S34. TEMPORAL CHANGE OF THE UV/VIS SPECTRA OF 1 BY IRRADIATION AT 450 NM IN CH ₃ CN.....	229
FIGURE S35. TEMPORAL CHANGE OF THE UV/VIS SPECTRA OF 2 BY IRRADIATION AT 450 NM IN CH ₃ CN.....	229
FIGURE S36. TEMPORAL CHANGE OF THE UV/VIS SPECTRA OF 3 BY IRRADIATION AT 450 NM IN CH ₃ CN.....	230
FIGURE S37. TEMPORAL CHANGE OF THE UV/VIS SPECTRA OF 4 BY IRRADIATION AT 450 NM IN CH ₃ CN.....	230
FIGURE S39. TEMPORAL CHANGE OF THE UV/VIS SPECTRA OF 6 BY IRRADIATION AT 450 NM IN CH ₃ CN.....	231
FIGURE S40. TEMPORAL CHANGE OF THE UV/VIS SPECTRA OF 7 BY IRRADIATION AT 450 NM IN CH ₃ CN.....	232



Scheme S1. Synthesis of the terpy-X ligands. a) NaH, 1,2-dimethoxyethane, 75%; b) NH_4OAc , EtOH, 71%; c) PCl_5 , POCl_3 , 51%; d) HBr, AcOH, 99%; e) NaOMe, MeOH, 90%; f) KMnO_4 , KOH, H_2O , 80%; g) SOCl_2 , MeOH, 72%; h) NMe_2 , FeCl_2 , MeOH, H_2O_2 , 79%.



Scheme S2. Synthesis of the complexes **1-7**. a) terpy, DMF, 87%; b) terpy-X, *N*-ethylmorpholine, EtOH, H₂O, 43-76%.

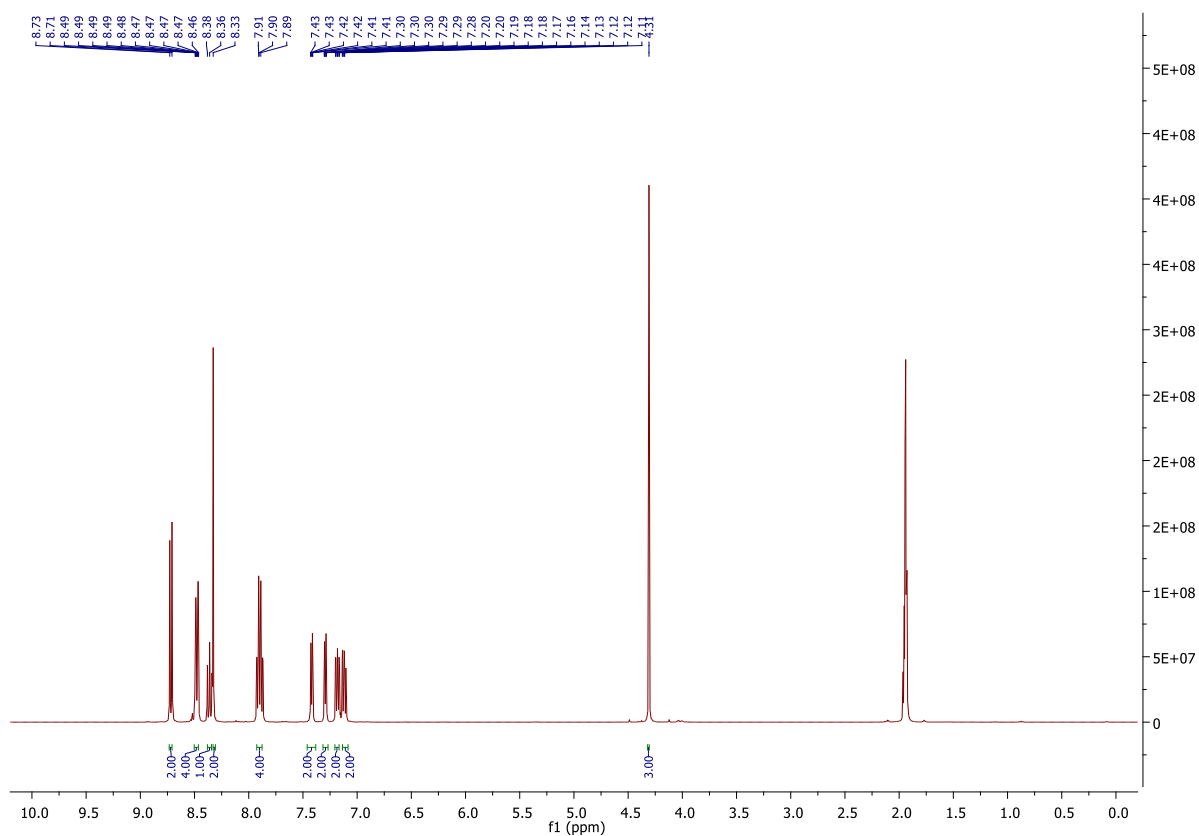


Figure S1. ¹H NMR spectrum of **4** in CD₃CN, 400 MHz.

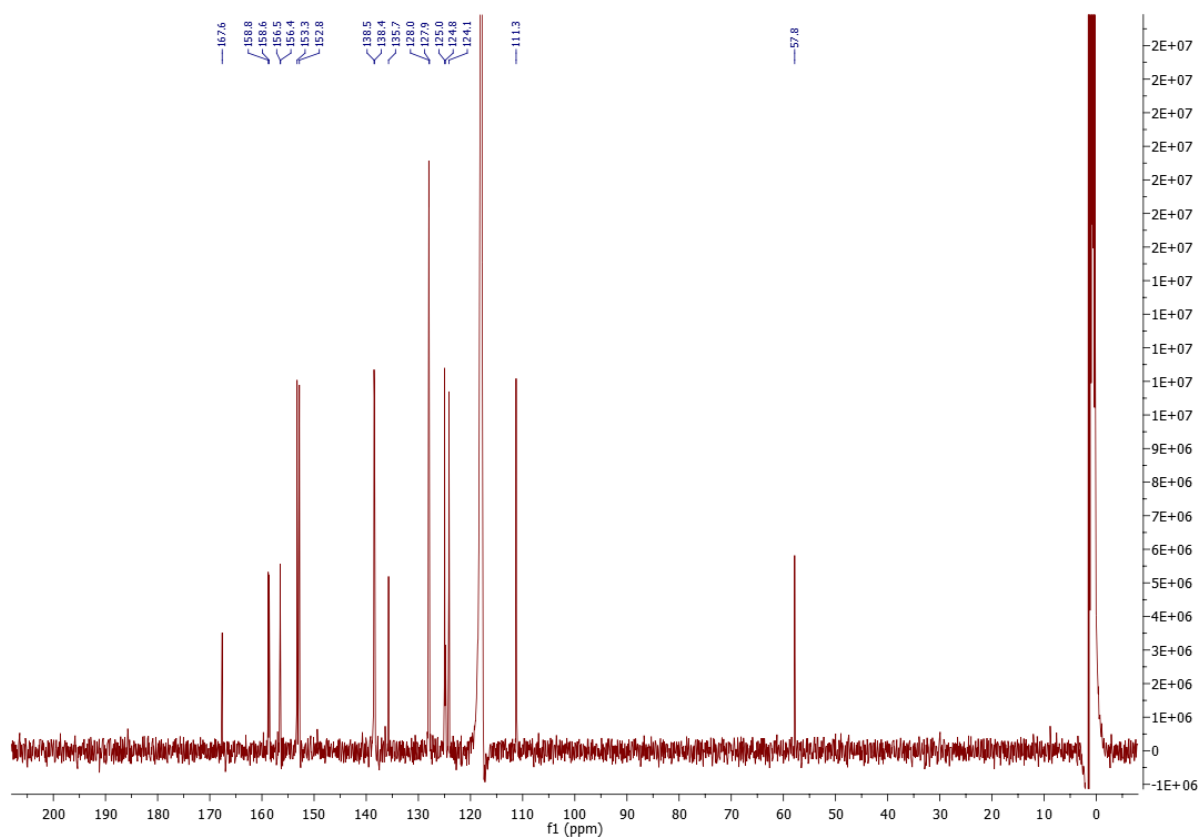


Figure S2. ^{13}C NMR spectrum of **4** in CD_3CN , 100 MHz.

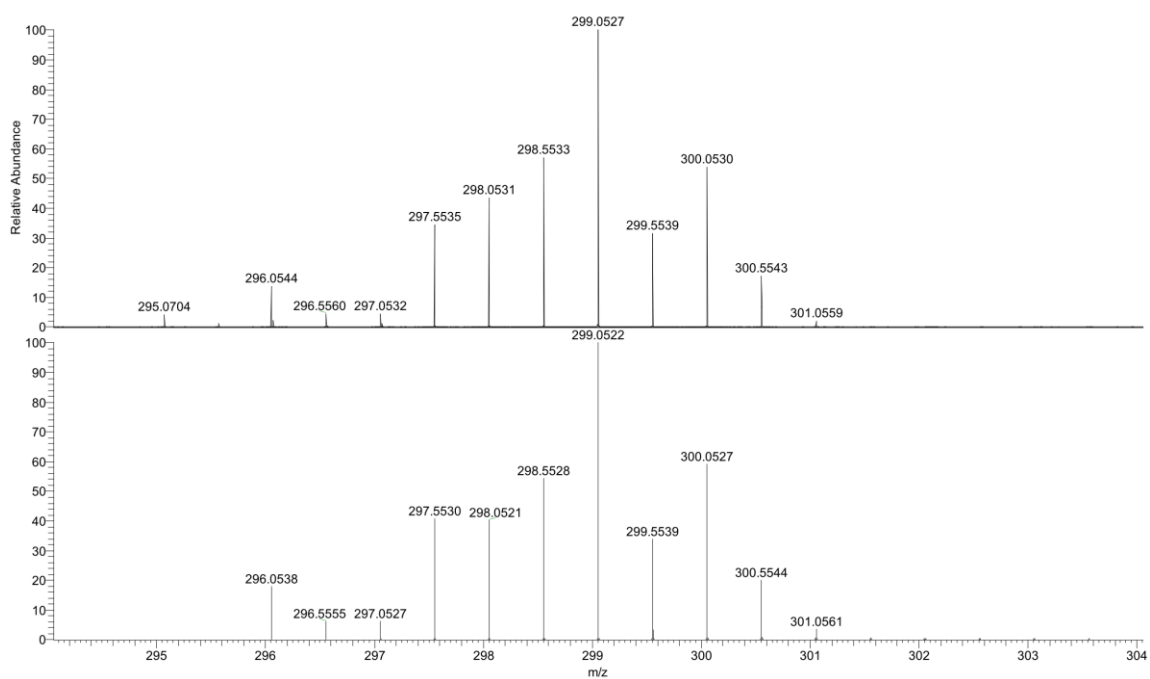


Figure S3. ESI-HRMS spectrum of **4** (positive detection mode).

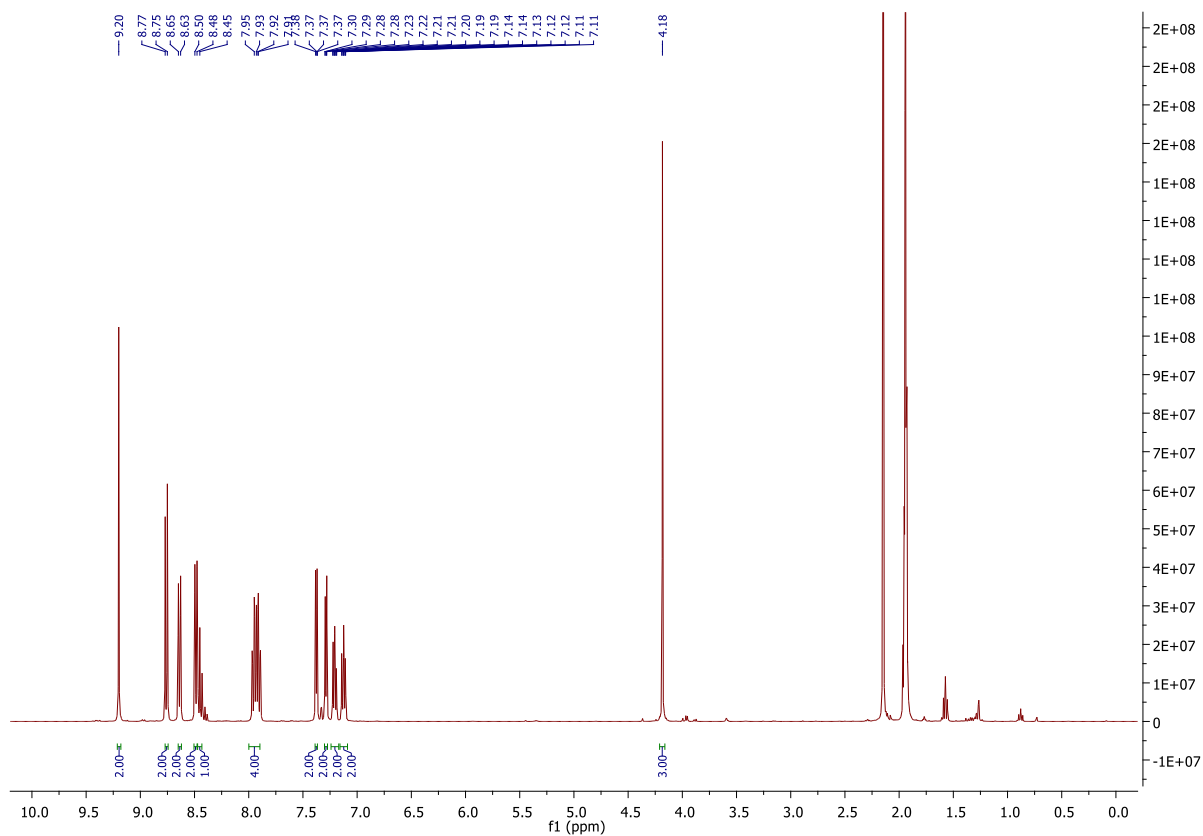


Figure S4. ^1H NMR spectrum of **6** in CD_3CN , 400 MHz.

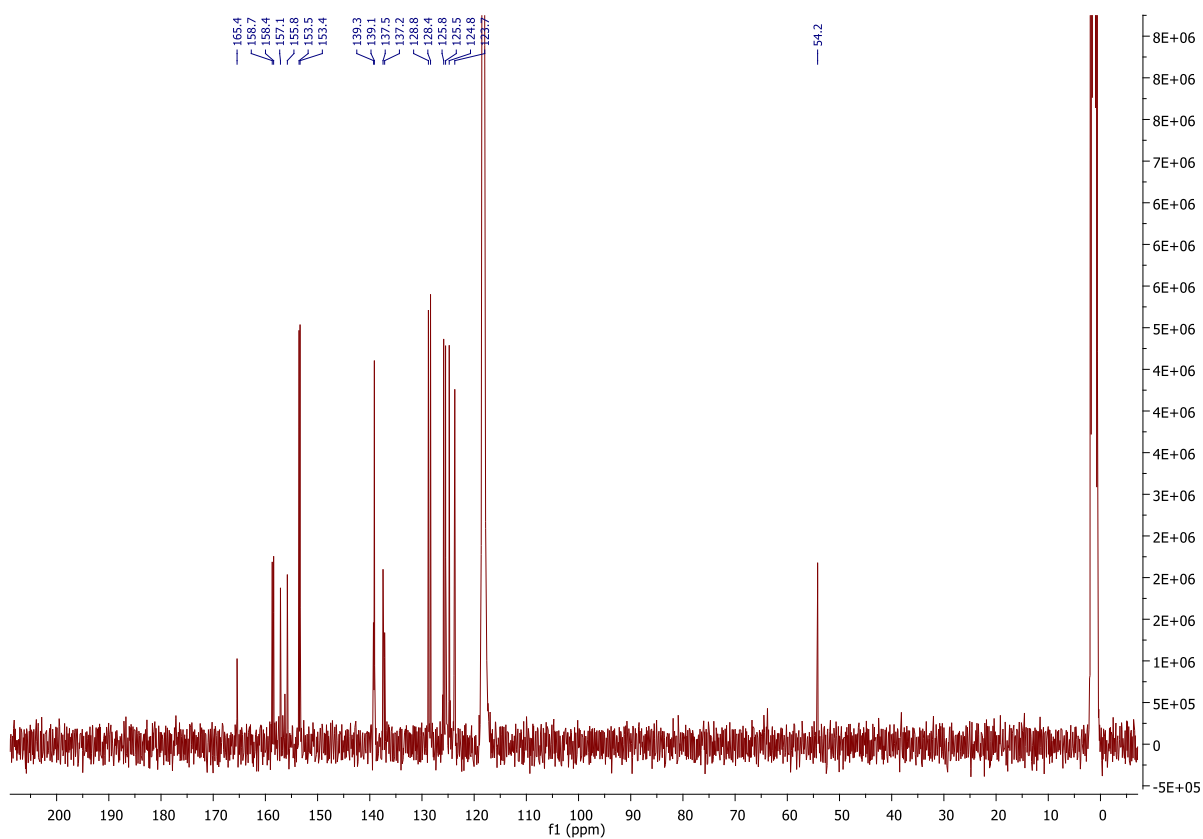


Figure S5. ^{13}C NMR spectrum of **6** in CD_3CN , 100 MHz.

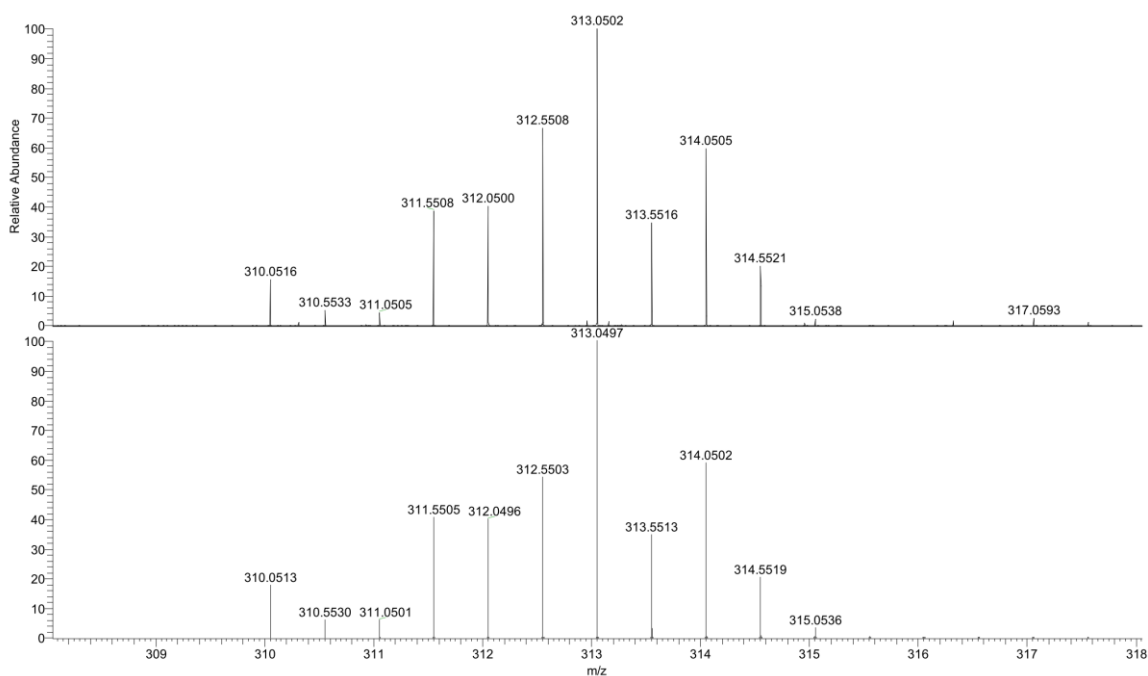


Figure S6. ESI-HRMS spectrum of **6** (positive detection mode).

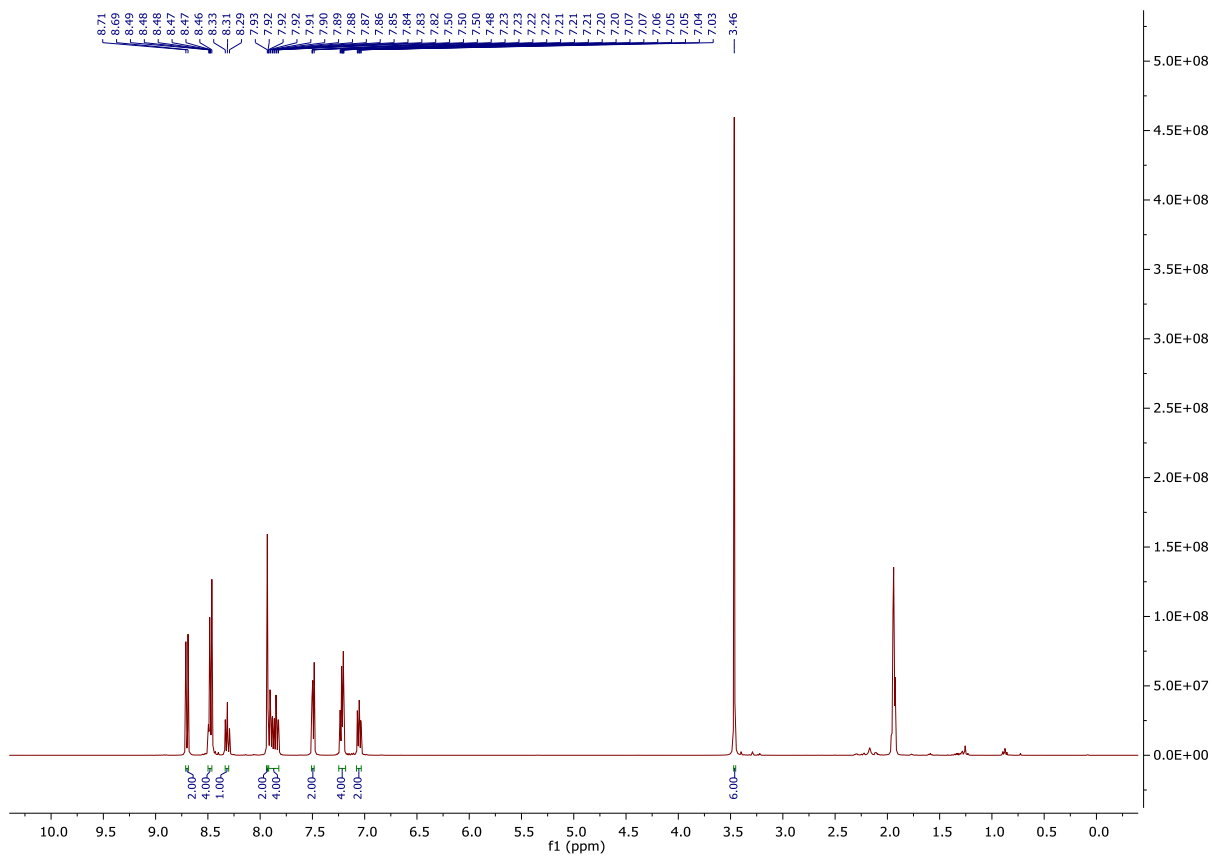


Figure S7. ^1H NMR spectrum of **7** in CD_3CN , 400 MHz.

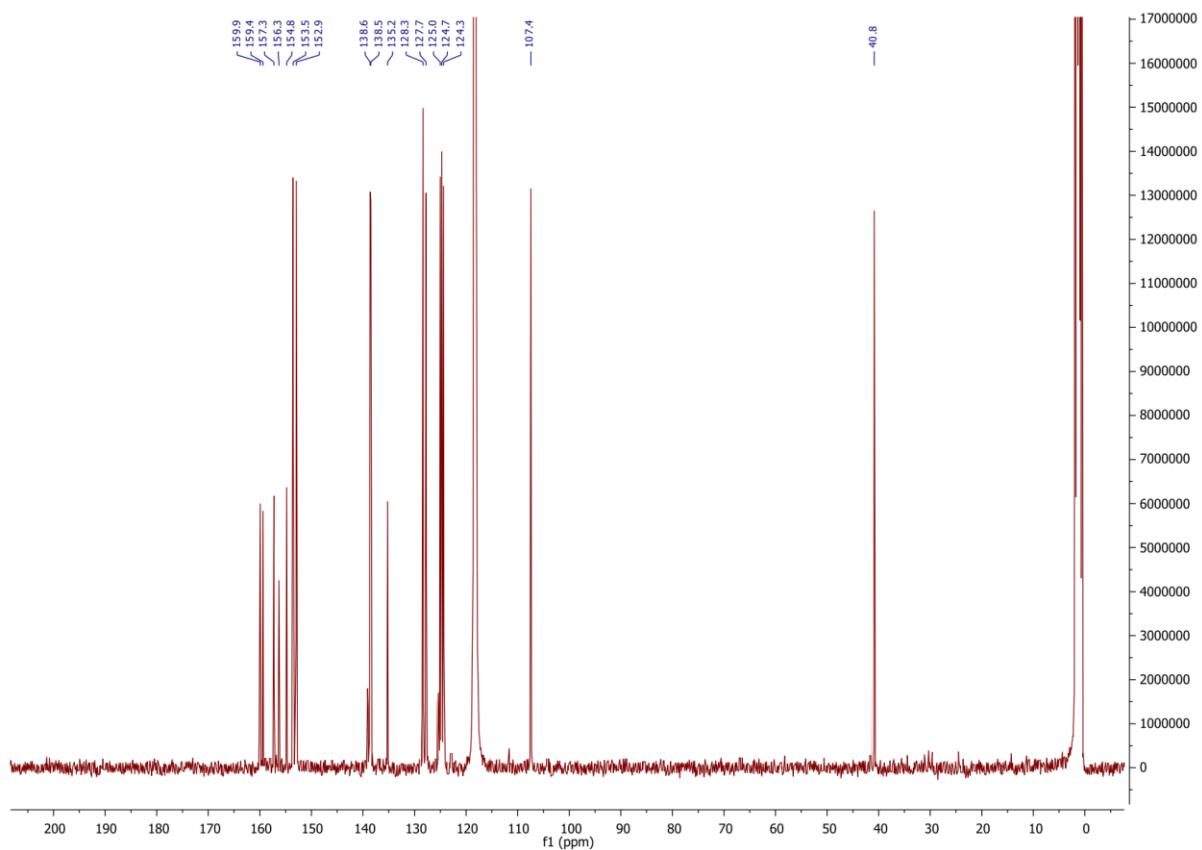


Figure S8. ^{13}C NMR spectrum of **7** in CD_3CN , 100 MHz.

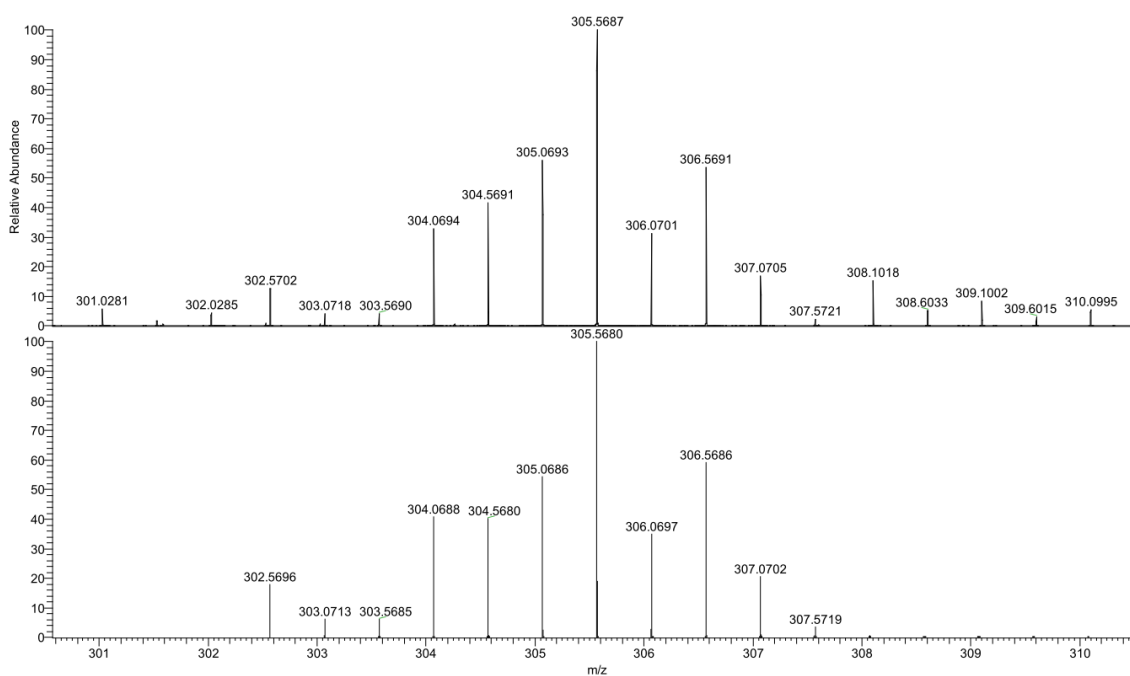


Figure S9. ESI-HRMS spectrum of **7** (positive detection mode).

Identification code	terpy-Cl	terpy-Br
CCDC number	1889469	1889466
Empirical formula	C ₁₅ H ₁₀ ClN ₃	C ₁₅ H ₁₀ BrN ₃
Formula weight	267.71	312.17
Temperature/K	160(1)	160(1)
Crystal system	orthorhombic	orthorhombic
Space group	Pna2 ₁	Pna2 ₁
a/Å	29.8281(6)	29.7043(3)
b/Å	3.82970(10)	3.87802(4)
c/Å	10.6447(2)	10.83185(12)
α/°	90	90
β/°	90	90
γ/°	90	90
Volume/Å ³	1215.97(5)	1247.76(2)
Z	4	4
ρ _{calc} /g/cm ³	1.462	1.662
μ/mm ⁻¹	0.301	4.384
F(000)	552.0	624.0
Crystal size/mm ³	0.24 × 0.2 × 0.11	0.1 × 0.09 × 0.02
Radiation	MoKα (λ = 0.71073)	CuKα (λ = 1.54184)
2θ range for data collection/°	5.462 to 61.008	5.95 to 148.998
Index ranges	-42 ≤ h ≤ 42, -5 ≤ k ≤ 5, -14 ≤ l ≤ 15	-37 ≤ h ≤ 36, -4 ≤ k ≤ 4, -13 ≤ l ≤ 12
Reflections collected	17130	9659
Independent reflections	3719 [R _{int} = 0.0220, R _{sigma} = 0.0188]	2449 [R _{int} = 0.0123, R _{sigma} = 0.0101]
Data/restraints/parameters	3719/1/172	2449/1/172
Goodness-of-fit on F ²	1.065	1.109
Final R indexes [I > 2σ (I)]	R ₁ = 0.0300, wR ₂ = 0.0755	R ₁ = 0.0157, wR ₂ = 0.0424
Final R indexes [all data]	R ₁ = 0.0319, wR ₂ = 0.0770	R ₁ = 0.0157, wR ₂ = 0.0424
Largest diff. peak/hole / e Å ⁻³	0.30/-0.16	0.17/-0.20
Flack parameter	-0.002(15)	-0.015(9)

Table S1. Crystal data and structure refinement parameters for **terpy_Cl** and **terpy_Br**.

Identification code	1_BPh₄	2_BF₄
CCDC number	1889470	1889455
Empirical formula	C ₇₈ H ₆₂ B ₂ N ₆ Ru	C ₃₀ H ₂₁ B ₂ ClF ₈ N ₆ Ru
Formula weight	1206.02	775.67
Temperature/K	160(1)	160(1)
Crystal system	orthorhombic	monoclinic
Space group	Pbca	Cc
a/Å	52.5897(6)	12.61649(13)
b/Å	39.8302(2)	12.24589(13)
c/Å	52.6464(5)	19.3380(2)
α/°	90	90
β/°	90	98.1529(11)
γ/°	90	90
Volume/Å ³	110276.2(17)	2957.52(6)
Z	72	4
ρ _{calc} /g/cm ³	1.308	1.742
μ/mm ⁻¹	2.460	5.891
F(000)	45072.0	1544.0
Crystal size/mm ³	0.09 × 0.06 × 0.04	0.06 × 0.04 × 0.02
Radiation	CuKα (λ = 1.54184)	CuKα (λ = 1.54184)
2θ range for data collection/°	5.242 to 149.002	9.24 to 136.5
Index ranges	-63 ≤ h ≤ 65, -40 ≤ k ≤ 49, -65 ≤ l ≤ 15	-15 ≤ h ≤ 15, -14 ≤ k ≤ 14, -23 ≤ l ≤ 59
Reflections collected	494692	39989
Independent reflections	111841 [R _{int} = 0.0865, R _{sigma} = 0.0698]	5372 [R _{int} = 0.0524, R _{sigma} = 0.0278]
Data/restraints/parameters	111841/270/6980	5372/187/489
Goodness-of-fit on F ²	1.012	1.034
Final R indexes [I ≥ 2σ (I)]	R ₁ = 0.0561, wR ₂ = 0.1284	R ₁ = 0.0360, wR ₂ = 0.0919
Final R indexes [all data]	R ₁ = 0.1000, wR ₂ = 0.1481	R ₁ = 0.0372, wR ₂ = 0.0925
Largest diff. peak/hole / e Å ⁻³	1.45/-1.16	0.80/-0.79
Flack parameter	-	-0.021(8)

Table S2. Crystal data and structure refinement parameters for **1_BPh₄** and **2_BF₄**.

Identification code	2_BPh₄	2_PF₆
CCDC number	1889459	1889454
Empirical formula	C ₉₈ H ₁₀₁ B ₂ ClN ₆ O ₅ Ru	C ₃₀ H ₂₁ ClF ₁₂ N ₆ P ₂ Ru
Formula weight	1600.98	891.99
Temperature/K	160(1)	160(1)
Crystal system	monoclinic	tetragonal
Space group	C2/c	P-42 ₁ c
a/Å	21.3575(5)	8.91426(16)
b/Å	22.5215(4)	8.91426(16)
c/Å	18.3027(3)	20.2372(6)
α/°	90	90
β/°	93.9633(18)	90
γ/°	90	90
Volume/Å ³	8782.6(3)	1608.13(7)
Z	4	2
ρ _{calc} /g/cm ³	1.211	1.842
μ/mm ⁻¹	0.264	6.619
F(000)	3368.0	884.0
Crystal size/mm ³	0.2 × 0.14 × 0.12	0.27 × 0.21 × 0.14
Radiation	MoKα (λ = 0.71073)	CuKα (λ = 1.54184)
2θ range for data collection/°	5.066 to 52.742	8.74 to 148.912
Index ranges	-26 ≤ h ≤ 26, -28 ≤ k ≤ 28, -22 ≤ l ≤ 22	-9 ≤ h ≤ 8, -11 ≤ k ≤ 10, -25 ≤ l ≤ 24
Reflections collected	53511	5988
Independent reflections	8996 [R _{int} = 0.0403, R _{sigma} = 0.0256]	1634 [R _{int} = 0.0388, R _{sigma} = 0.0218]
Data/restraints/parameters	8996/54/428	1634/0/122
Goodness-of-fit on F ²	1.085	1.231
Final R indexes [I >= 2σ (I)]	R ₁ = 0.0583, wR ₂ = 0.1540	R ₁ = 0.0448, wR ₂ = 0.0990
Final R indexes [all data]	R ₁ = 0.0664, wR ₂ = 0.1599	R ₁ = 0.0450, wR ₂ = 0.0991
Largest diff. peak/hole / e Å ⁻³	1.78/-0.90	0.51/-0.93
Flack parameter	-	0.01(2)

Table S3. Crystal data and structure refinement parameters for **2_BPh₄** and **2_PF₆**.

Identification code	3_BF₄	3_PF₆
CCDC number	1889456	1889457
Empirical formula	C ₃₀ H ₂₁ B ₂ BrF ₈ N ₆ Ru	C ₃₀ H ₂₁ BrF ₁₂ N ₆ P ₂ Ru
Formula weight	820.13	936.45
Temperature/K	160(1)	160(1)
Crystal system	monoclinic	tetragonal
Space group	Cc	P-42 ₁ c
a/Å	12.6998(1)	8.93203(8)
b/Å	12.2010(1)	8.93203(8)
c/Å	19.5672(1)	20.3547(3)
α/°	90	90
β/°	98.9220(10)	90
γ/°	90	90
Volume/Å ³	2995.26(4)	1623.92(4)
Z	4	2
ρ _{calc} /g/cm ³	1.819	1.915
μ/mm ⁻¹	6.559	7.240
F(000)	1616.0	920.0
Crystal size/mm ³	0.12 × 0.07 × 0.03	0.23 × 0.18 × 0.12
Radiation	CuKα (λ = 1.54184)	CuKα (λ = 1.54184)
2θ range for data collection/°	9.15 to 149.008	8.688 to 148.908
Index ranges	-15 ≤ h ≤ 15, -15 ≤ k ≤ 15, -24 ≤ l ≤ 23	-11 ≤ h ≤ 10, -9 ≤ k ≤ 10, -25 ≤ l ≤ 25
Reflections collected	44079	13324
Independent reflections	6018 [R _{int} = 0.0235, R _{sigma} = 0.0117]	1647 [R _{int} = 0.0288, R _{sigma} = 0.0120]
Data/restraints/parameters	6018/97/483	1647/0/123
Goodness-of-fit on F ²	1.061	1.229
Final R indexes [I ≥ 2σ (I)]	R ₁ = 0.0280, wR ₂ = 0.0718	R ₁ = 0.0426, wR ₂ = 0.0947
Final R indexes [all data]	R ₁ = 0.0280, wR ₂ = 0.0718	R ₁ = 0.0426, wR ₂ = 0.0947
Largest diff. peak/hole / e Å ⁻³	0.95/-0.60	0.34/-0.77
Flack parameter	-0.007(3)	0.01(3)

Table S4. Crystal data and structure refinement parameters for **3_BF₄** and **3_PF₆**.

Identification code	4_BF₄	4_PF₆
CCDC number	1889458	1889460
Empirical formula	C ₃₁ H ₂₄ B ₂ F ₈ N ₆ ORu	C ₄₁ H ₄₄ F ₁₂ N ₆ O ₃ P ₂ Ru
Formula weight	771.25	1059.83
Temperature/K	160(1)	160(1)
Crystal system	monoclinic	orthorhombic
Space group	P2 ₁	Pccn
a/Å	8.7526(2)	18.5147(2)
b/Å	8.9936(2)	21.4071(2)
c/Å	19.6673(4)	22.1597(2)
α/°	90	90
β/°	99.282(2)	90
γ/°	90	90
Volume/Å ³	1527.89(6)	8782.91(15)
Z	2	8
ρ _{calc} /g/cm ³	1.676	1.603
μ/mm ⁻¹	4.936	4.454
F(000)	772.0	4304.0
Crystal size/mm ³	0.11 × 0.08 × 0.07	0.26 × 0.07 × 0.03
Radiation	CuKα (λ = 1.54184)	CuKα (λ = 1.54184)
2θ range for data collection/°	9.112 to 148.984	7.468 to 148.998
Index ranges	-10 ≤ h ≤ 10, -11 ≤ k ≤ 11, -20 ≤ l ≤ 23	-23 ≤ h ≤ 23, -26 ≤ k ≤ 26, -27 ≤ l ≤ 24
Reflections collected	30909	112638
Independent reflections	6245 [R _{int} = 0.0278, R _{sigma} = 0.0214]	8979 [R _{int} = 0.0300, R _{sigma} = 0.0169]
Data/restraints/parameters	6245/179/546	8979/308/679
Goodness-of-fit on F ²	1.027	1.051
Final R indexes [I ≥ 2σ (I)]	R ₁ = 0.0382, wR ₂ = 0.0996	R ₁ = 0.0572, wR ₂ = 0.1561
Final R indexes [all data]	R ₁ = 0.0384, wR ₂ = 0.0998	R ₁ = 0.0579, wR ₂ = 0.1566
Largest diff. peak/hole / e Å ⁻³	0.93/-0.96	1.20/-0.88
Flack parameter	0.002(6)	-

Table S5. Crystal data and structure refinement parameters for **4_BF₄** and **4_PF₆**.

Identification code	5_BF₄	5_BPh₄
CCDC number	1889468	1889464
Empirical formula	C ₃₈ H ₃₅ B ₂ F ₈ N ₇ O ₃ Ru	C ₁₀₃ H ₁₀₈ B ₂ N ₈ O ₆ Ru
Formula weight	912.42	1676.66
Temperature/K	160(1)	160(1)
Crystal system	monoclinic	monoclinic
Space group	P2 ₁ /n	C2/c
a/Å	10.4076(2)	21.21225(18)
b/Å	24.6965(5)	22.62075(18)
c/Å	14.4928(3)	18.72045(14)
α/°	90	90
β/°	98.1874(19)	92.2918(8)
γ/°	90	90
Volume/Å ³	3687.12(13)	8975.58(13)
Z	4	4
ρ _{calc} /g/cm ³	1.644	1.241
μ/mm ⁻¹	4.245	1.877
F(000)	1848.0	3536.0
Crystal size/mm ³	0.16 × 0.11 × 0.015	0.24 × 0.17 × 0.14
Radiation	CuKα (λ = 1.54184)	CuKα (λ = 1.54184)
2θ range for data collection/°	7.126 to 148.97	5.714 to 148.944
Index ranges	-12 ≤ h ≤ 12, -24 ≤ k ≤ 30, -18 ≤ l ≤ 18	-25 ≤ h ≤ 26, -28 ≤ k ≤ 27, -18 ≤ l ≤ 23
Reflections collected	39087	39430
Independent reflections	7529 [R _{int} = 0.0468, R _{sigma} = 0.0260]	9151 [R _{int} = 0.0229, R _{sigma} = 0.0178]
Data/restraints/parameters	7529/271/589	9151/72/504
Goodness-of-fit on F ²	1.153	1.076
Final R indexes [I >= 2σ (I)]	R ₁ = 0.0899, wR ₂ = 0.2343	R ₁ = 0.0460, wR ₂ = 0.1373
Final R indexes [all data]	R ₁ = 0.0943, wR ₂ = 0.2363	R ₁ = 0.0471, wR ₂ = 0.1385
Largest diff. peak/hole / e Å ⁻³	1.48/-1.89	1.78/-0.72

Table S6. Crystal data and structure refinement parameters for **5_BF₄** and **5_BPh₄**.

Identification code	6_BF4	6_BPh4
CCDC number	1889463	1889461
Empirical formula	C ₃₆ H ₃₂ B ₂ F ₈ N ₆ O ₃ Ru	C ₉₆ H ₉₆ B ₂ N ₆ O ₆ Ru
Formula weight	871.36	1552.47
Temperature/K	160(1)	160(1)
Crystal system	monoclinic	monoclinic
Space group	P2 ₁ /n	C2/c
a/Å	10.42043(19)	21.4964(2)
b/Å	24.4208(5)	22.4535(2)
c/Å	14.4210(2)	18.3461(2)
α /°	90	90
β /°	98.1976(16)	92.8920(10)
γ /°	90	90
Volume/Å ³	3632.29(11)	8843.82(15)
Z	4	4
ρ_{calc} /g/cm ³	1.593	1.166
μ /mm ⁻¹	4.270	1.861
F(000)	1760.0	3264.0
Crystal size/mm ³	0.12 × 0.05 × 0.04	0.13 × 0.07 × 0.03
Radiation	CuK α (λ = 1.54184)	CuK α (λ = 1.54184)
2 θ range for data collection/°	7.174 to 148.998	5.696 to 149.006
Index ranges	-12 ≤ h ≤ 13, -30 ≤ k ≤ 27, -18 ≤ l ≤ 26	-26 ≤ h ≤ 22, -27 ≤ k ≤ 27, -18 ≤ l ≤ 17
Reflections collected	38743	47330
Independent reflections	7421 [R _{int} = 0.0365, R _{sigma} = 0.0229]	9017 [R _{int} = 0.0341, R _{sigma} = 0.0249]
Data/restraints/parameters	7421/802/708	9017/98/496
Goodness-of-fit on F ²	1.056	1.062
Final R indexes [I >= 2 σ (I)]	R ₁ = 0.0609, wR ₂ = 0.1713	R ₁ = 0.0613, wR ₂ = 0.1953
Final R indexes [all data]	R ₁ = 0.0667, wR ₂ = 0.1762	R ₁ = 0.0665, wR ₂ = 0.2014
Largest diff. peak/hole / e Å ⁻³	1.78/-1.16	0.88/-0.45

Table S7. Crystal data and structure refinement parameters for **6_BF4** and **6_BPh4**.

Identification code	6_PF₆	7_BF₄
CCDC number	1889462	1889467
Empirical formula	C ₄₁ H ₄₀ F ₁₂ N ₈ O ₃ P ₂ Ru	C ₃₂ H ₂₇ B ₂ F ₈ N ₇ Ru
Formula weight	1083.82	784.29
Temperature/K	160(1)	160(1)
Crystal system	monoclinic	monoclinic
Space group	P2 ₁ /c	P2 ₁ /n
a/Å	8.57780(10)	8.74499(14)
b/Å	28.6387(2)	9.01167(15)
c/Å	18.51310(10)	39.4349(10)
α/°	90	90
β/°	94.0080(10)	91.7352(16)
γ/°	90	90
Volume/Å ³	4536.75(7)	3106.32(11)
Z	4	4
ρ _{calc} /g/cm ³	1.587	1.677
μ/mm ⁻¹	4.342	4.851
F(000)	2192.0	1576.0
Crystal size/mm ³	0.15 × 0.06 × 0.02	0.1 × 0.03 × 0.01
Radiation	CuKα (λ = 1.54184)	CuKα (λ = 1.54184)
2θ range for data collection/°	5.694 to 154.756	8.974 to 136.576
Index ranges	-10 ≤ h ≤ 10, -34 ≤ k ≤ 36, -23 ≤ l ≤ 10	-10 ≤ h ≤ 10, -10 ≤ k ≤ 10, -47 ≤ l ≤ 22
Reflections collected	62640	7806
Independent reflections	9605 [R _{int} = 0.0343, R _{sigma} = 0.0244]	7806 [R _{sigma} = 0.0286]
Data/restraints/parameters	9605/90/662	7806/36/454
Goodness-of-fit on F ²	1.043	1.099
Final R indexes [I >= 2σ (I)]	R ₁ = 0.0428, wR ₂ = 0.1011	R ₁ = 0.0857, wR ₂ = 0.2364
Final R indexes [all data]	R ₁ = 0.0459, wR ₂ = 0.1029	R ₁ = 0.0976, wR ₂ = 0.2453
Largest diff. peak/hole / e Å ⁻³	0.73/-0.80	2.55/-1.14

Table S8. Crystal data and structure refinement parameters for **6_PF₆** and **7_BF₄**.

Identification code	7_PF₆
CCDC number	1889465
Empirical formula	C ₃₄ H ₃₂ F ₁₂ N ₈ OP ₂ Ru
Formula weight	959.68
Temperature/K	160(1)
Crystal system	triclinic
Space group	P-1
a/Å	8.83260(10)
b/Å	11.05140(10)
c/Å	19.88040(10)
α/°	90.8210(10)
β/°	93.8360(10)
γ/°	104.1870(10)
Volume/Å ³	1876.23(3)
Z	2
ρ _{calc} /cm ³	1.699
μ/mm ⁻¹	5.117
F(000)	964.0
Crystal size/mm ³	0.12 × 0.04 × 0.03
Radiation	CuKα (λ = 1.54184)
2θ range for data collection/°	8.256 to 148.994
Index ranges	-11 ≤ h ≤ 10, -13 ≤ k ≤ 13, -21 ≤ l ≤ 24
Reflections collected	31694
Independent reflections	7646 [R _{int} = 0.0259, R _{sigma} = 0.0225]
Data/restraints/parameters	7646/194/585
Goodness-of-fit on F ²	1.034
Final R indexes [I >= 2σ (I)]	R ₁ = 0.0463, wR ₂ = 0.1332
Final R indexes [all data]	R ₁ = 0.0474, wR ₂ = 0.1342
Largest diff. peak/hole / e Å ⁻³	1.23/-1.45

Table S9. Crystal data and structure refinement parameter for 7_PF₆.

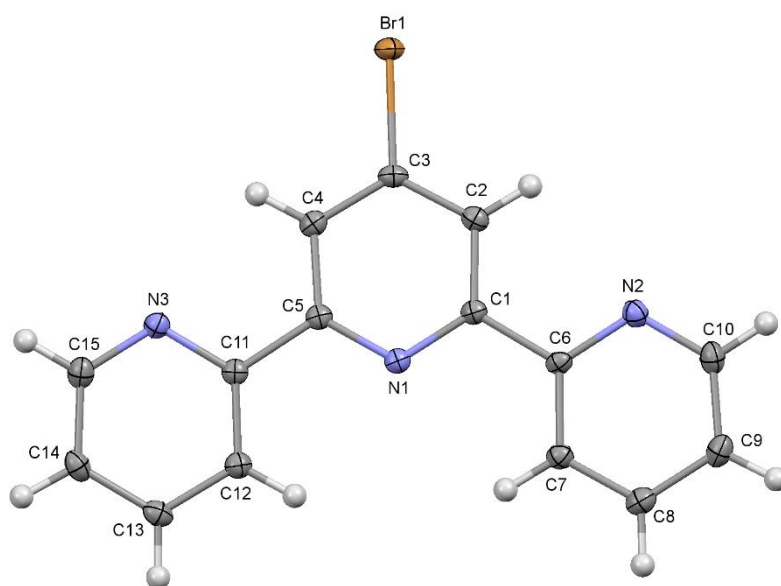
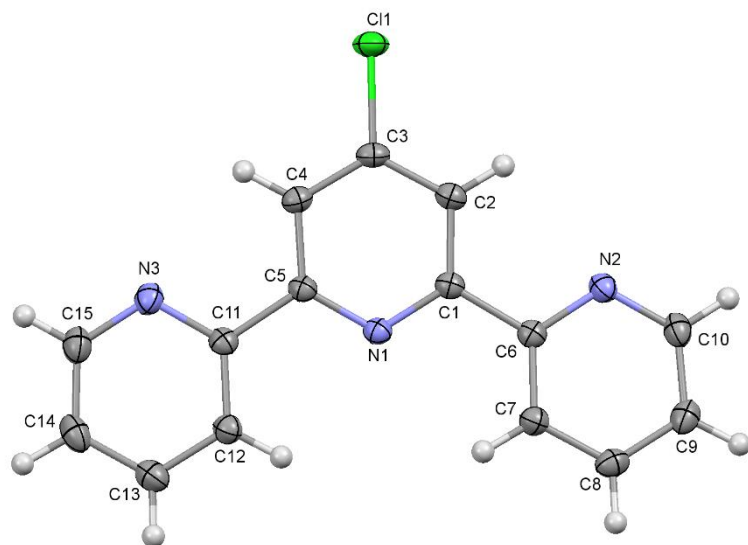


Figure S10. Molecular structures of **terpy-Cl** (top) and **terpy-Br** (bottom). Thermal ellipsoids were drawn at the 30 % probability level.

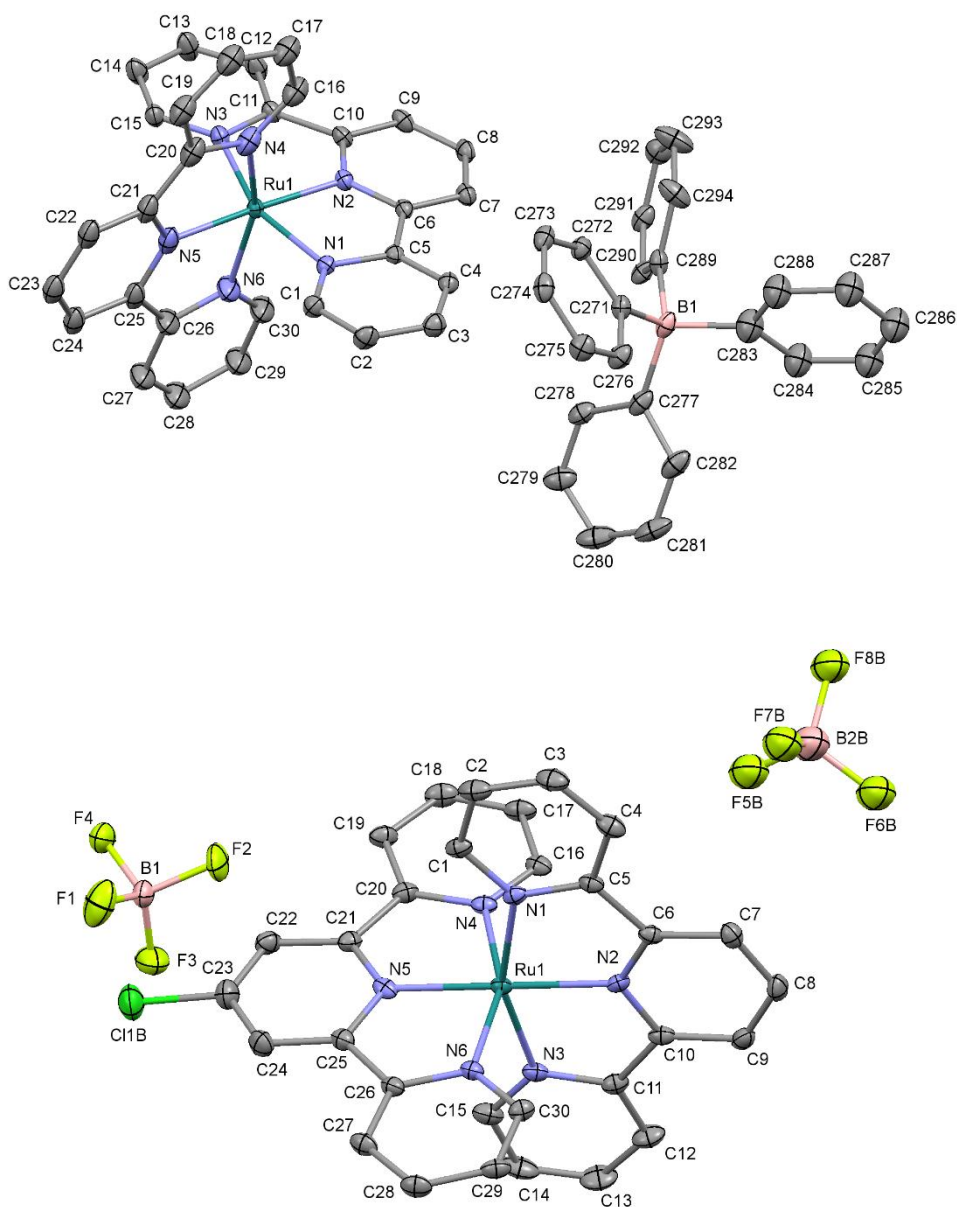


Figure S11. Molecular structures of **1_BPh₄** (top) and **2_BF₄** (bottom). The asymmetric unit of **1_BPh₄** contains 27 independent molecules (9 dications and 18 anions), only one cation and one anion are presented in the figure. Thermal ellipsoids were drawn at the 30 % probability level.

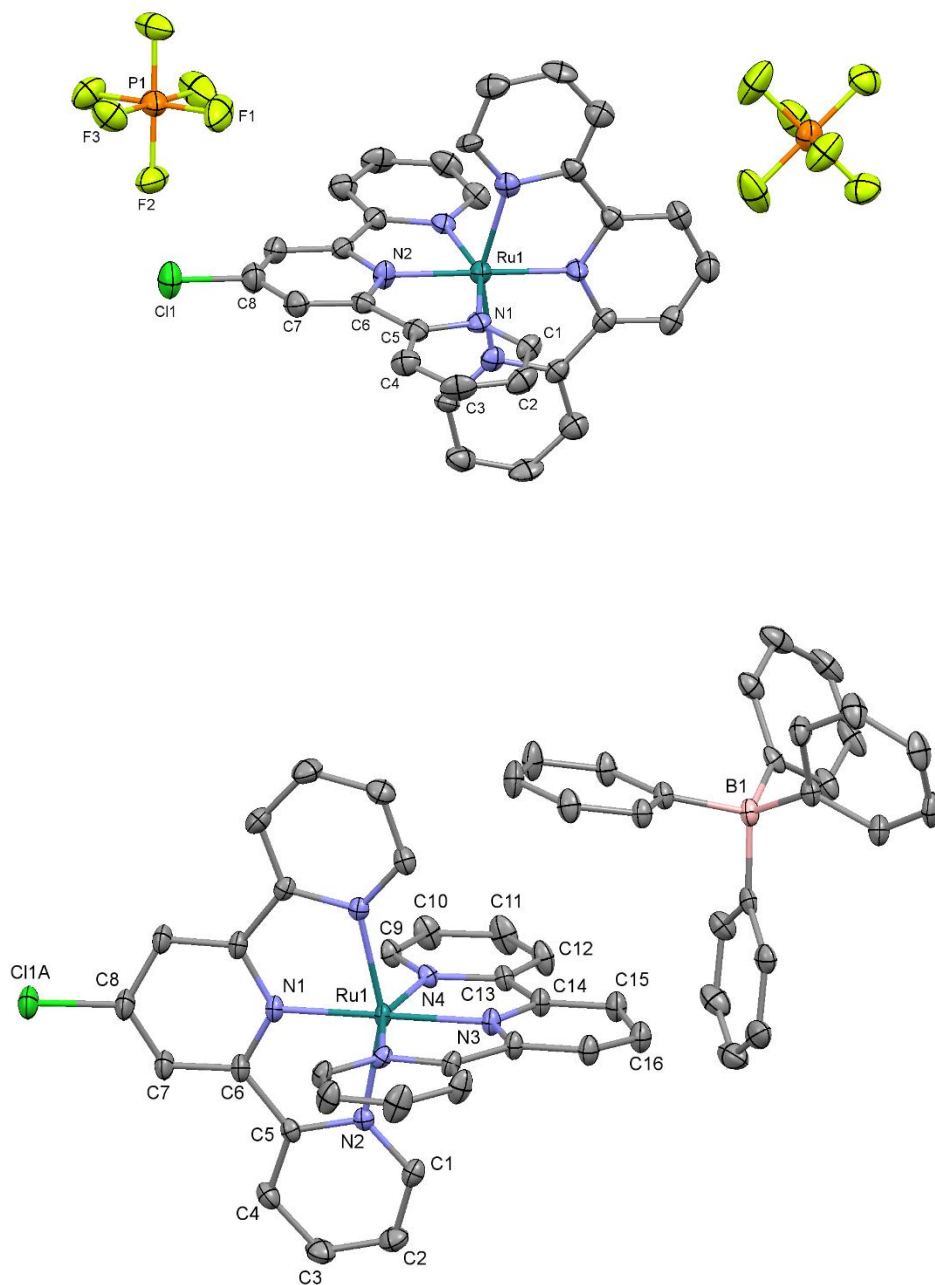


Figure S12. Molecular structures of **2-PF₆** (top) and **2-BPh₄** (bottom; only one BPh₄⁻ counterion is presented in the figure). Thermal ellipsoids were drawn at the 30 % probability level.

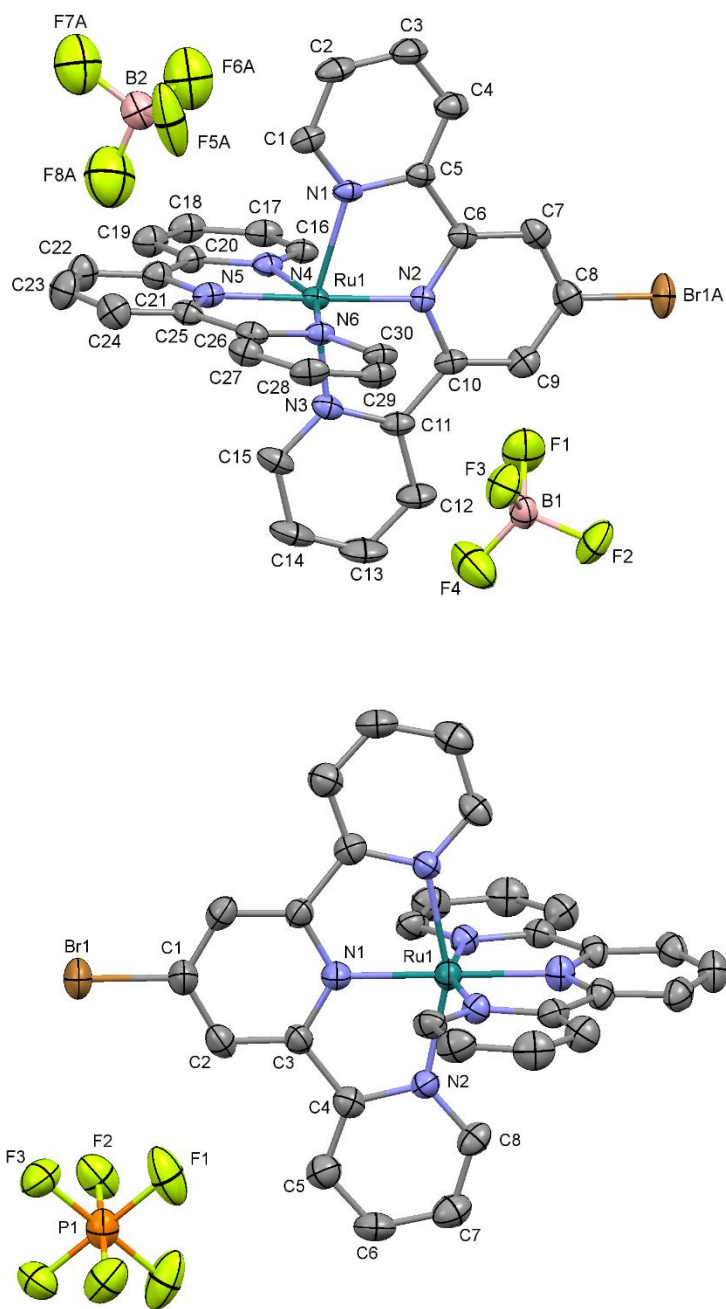


Figure S13. Molecular structures of **3_BF₄** (top) and **3_PF₆** (bottom; only one PF₆⁻ counterion is presented in the figure). Thermal ellipsoids were drawn at the 30 % probability level.

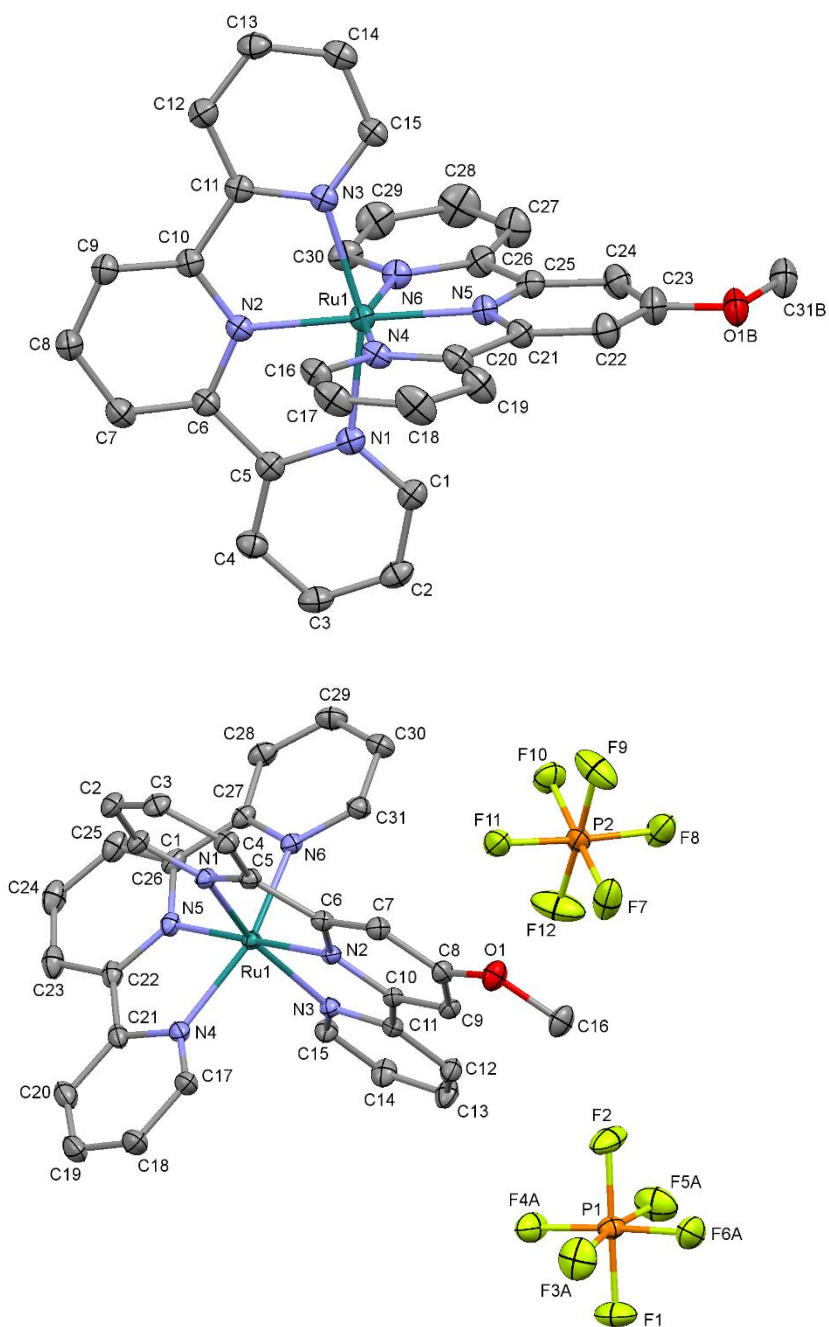


Figure S14. Molecular structures of **4_BF₄** (top; the BF₄⁻ counterions are disordered and are not presented in the figure) and **4_PF₆** (bottom). Thermal ellipsoids were drawn at the 30 % probability level.

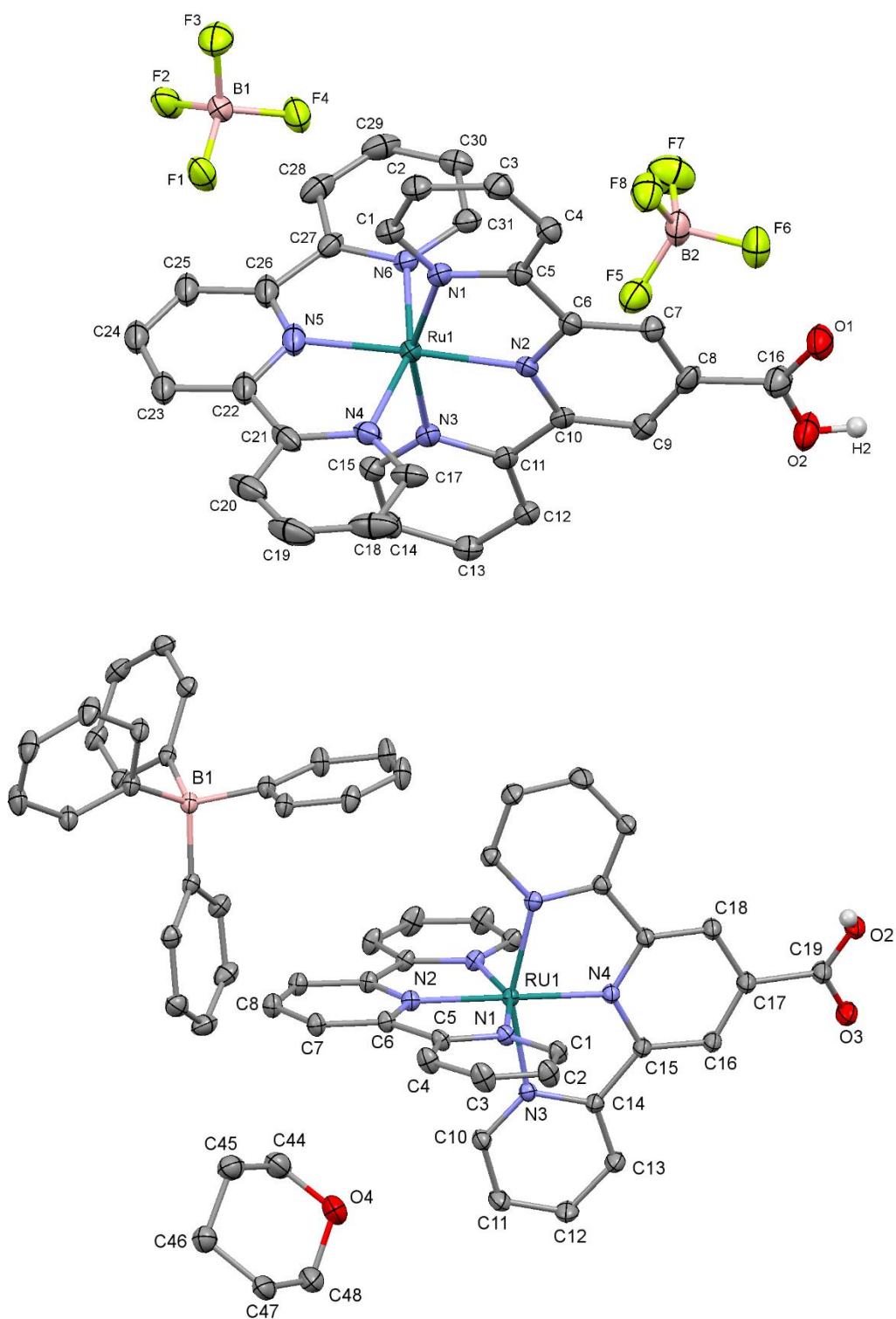


Figure S15. Molecular structures of **5_BF₄** (top) and **5_BPh₄** (bottom; only one BPh₄⁻ counterion is presented in the figure). Thermal ellipsoids were drawn at the 30 % probability level.

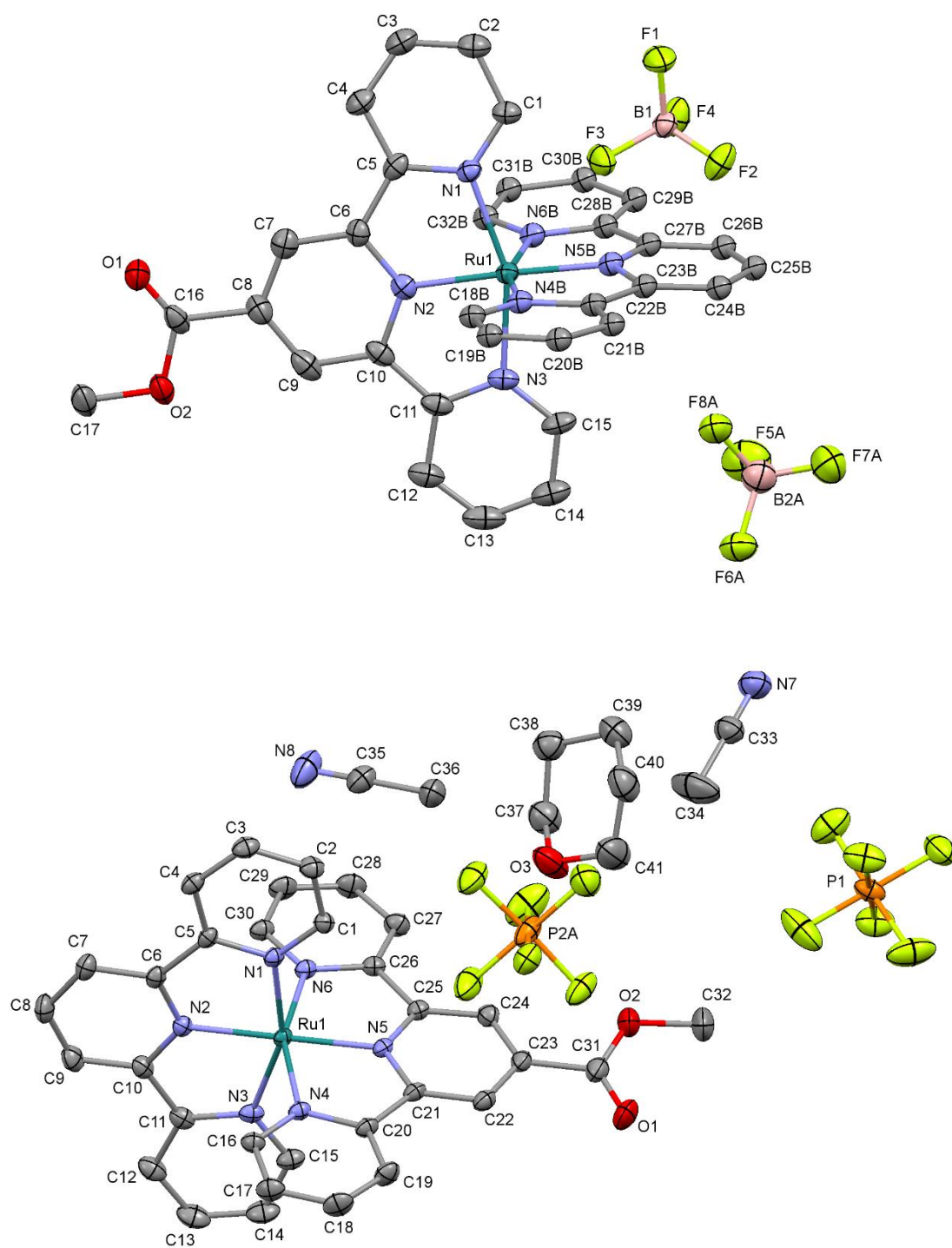


Figure S16. Molecular structures of **6_BF₄** (top) and **6_PF₆** (bottom). Thermal ellipsoids were drawn at the 30 % probability level.

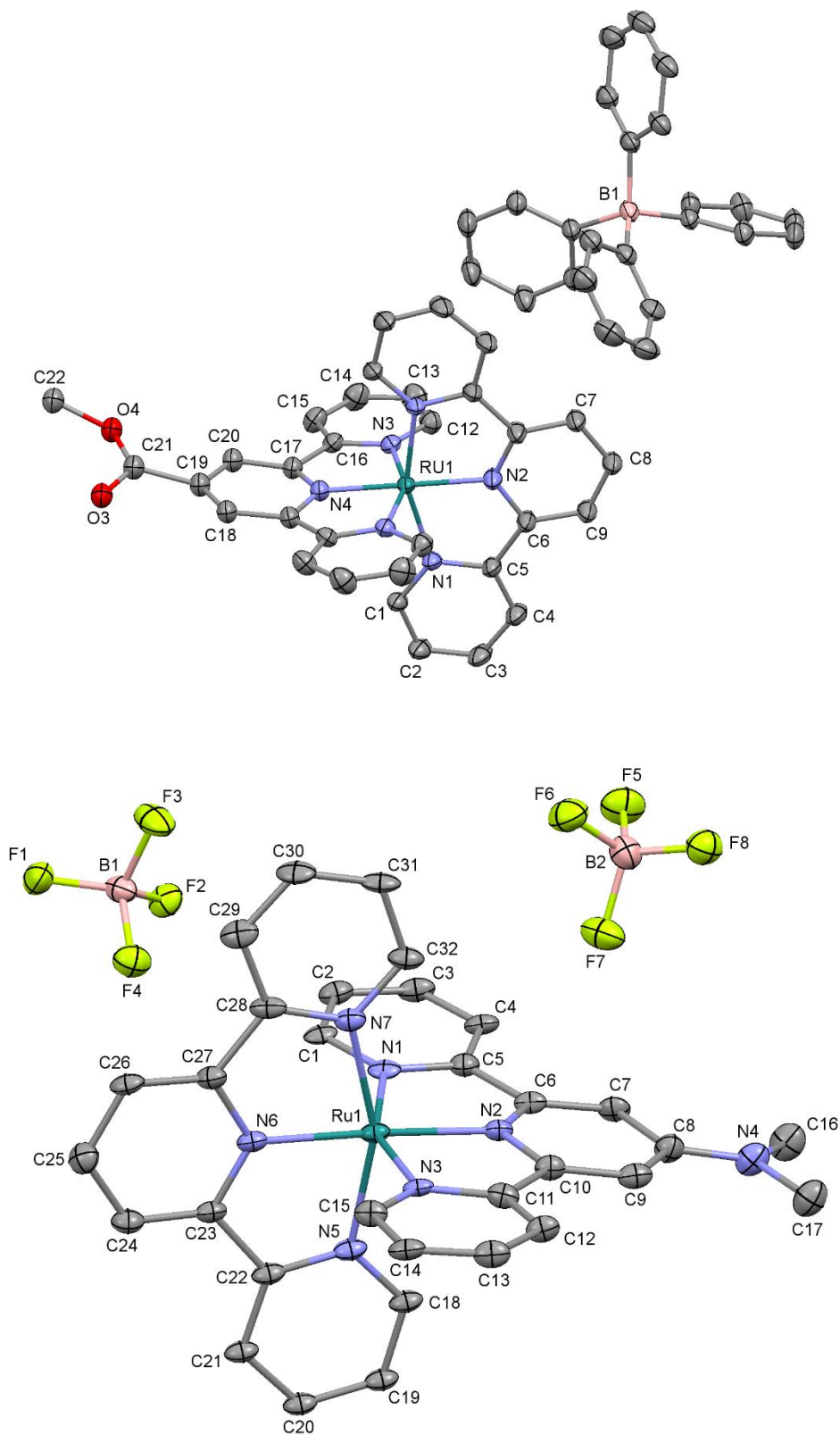


Figure S17. Molecular structures of **6_BPh₄** (top; only one BPh₄⁻ counterion is presented in the figure) and **7_BF₄** (bottom). Thermal ellipsoids were drawn at the 30 % probability level.

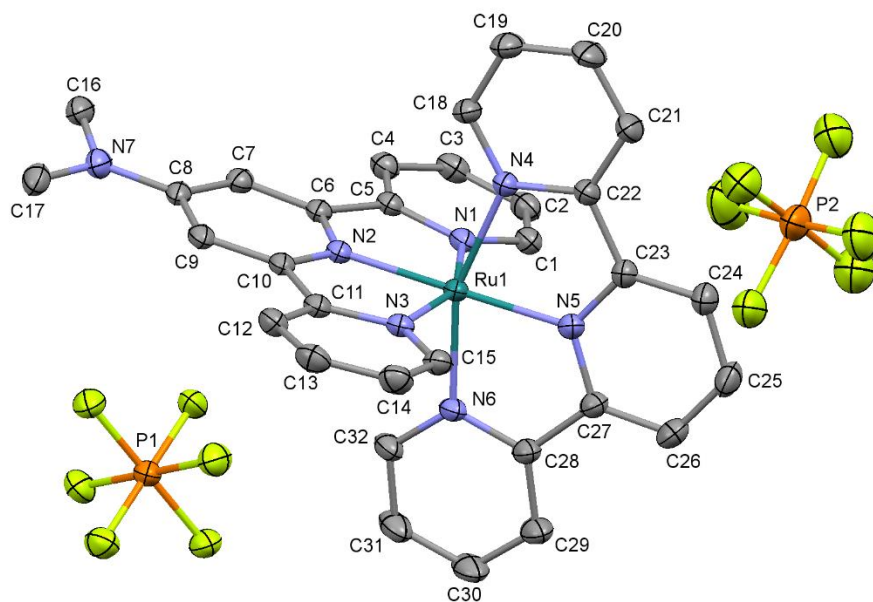


Figure S18. Molecular structures of **7**_PF₆. Thermal ellipsoids were drawn at the 30 % probability level.

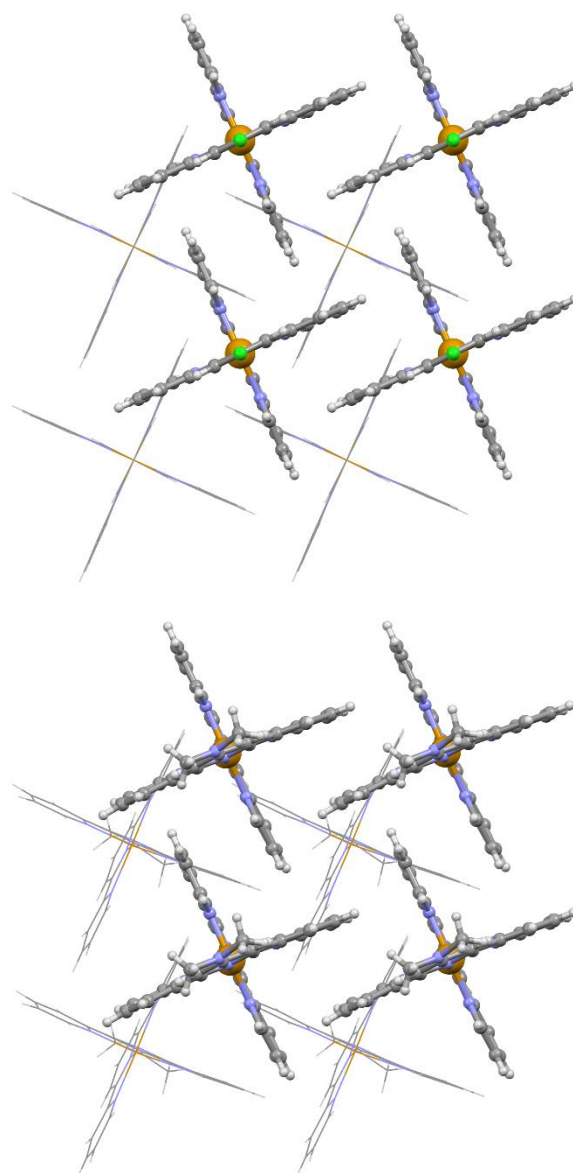


Figure S19. Ball-and-stick representations of the two-dimensional net of $[\text{Ru}(\text{terpy})(\text{terpy-X})]^{2+}$ cations in **2** -PF_6 ($\text{X} = \text{Cl}$, left) and in **7** -BF_4 ($\text{X} = \text{NMe}_2$, right) viewed along the c axis perpendicular to the net. The molecules in the wireframe style belong to adjacent layers while the anions are omitted. In these crystal structures the cations interact with each other through offset face-to-face $\pi \dots \pi$ interactions and edge-to-face $\text{C-H} \dots \pi$ interactions to form the standard “terpy embrace” motif frequently observed in $[\text{M}(\text{terpy})_2]^z$ complexes.

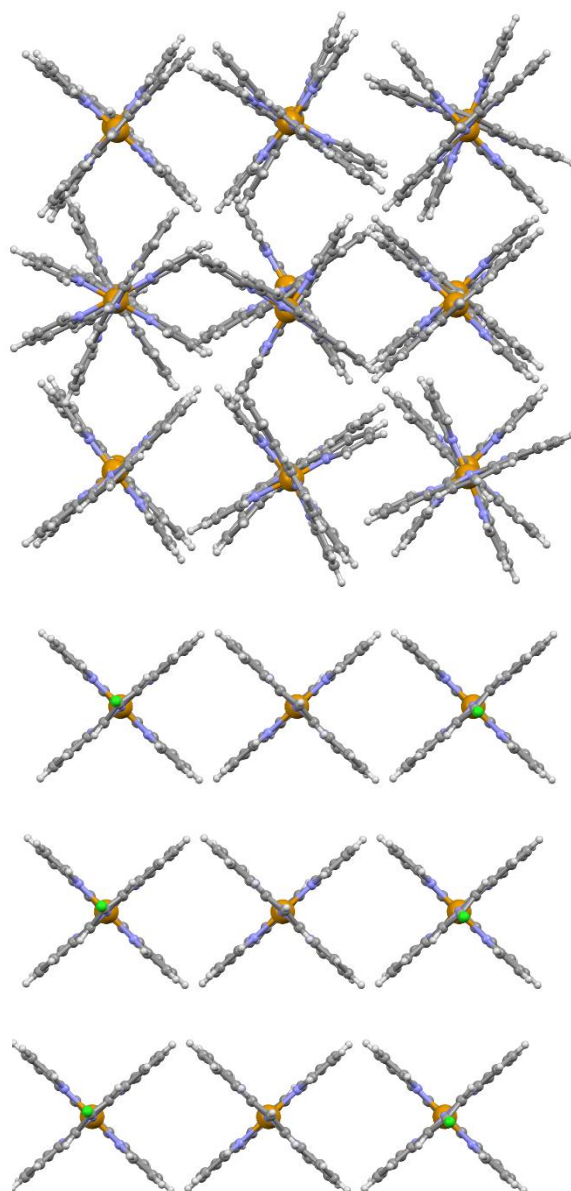


Figure S20. Ball-and-stick representations of the arrangement of the $[\text{Ru}(\text{terpy})(\text{terpy-X})]^{2+}$ cations in **1_BPh₄** (X = H, left) and in **2_BPh₄** (X = Cl, right) viewed along the *b* direction. In the crystal structures the packing of the cations does not respect the standard “terpy embrace” motif, the cations do not interact directly with each other but only with the bulky BPh_4^- ions mainly through $\pi \dots \pi$ interactions between the pyridine and the phenyl rings.

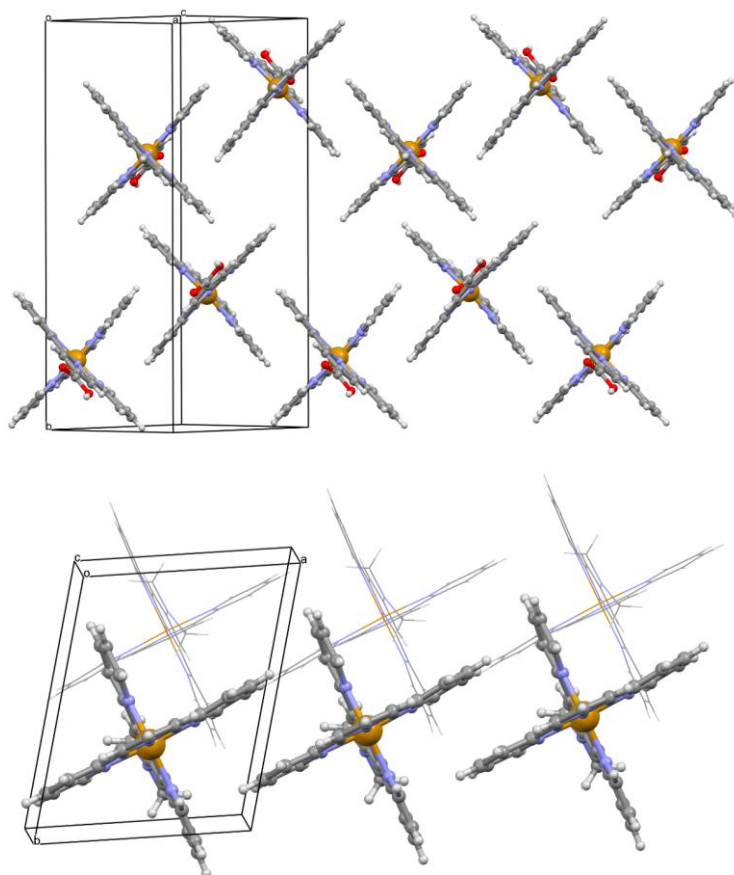


Figure S21. Ball-and-stick representations of the arrangement of the $[\text{Ru}(\text{terpy})(\text{terpy-X})]^{2+}$ cations in **5**_{BF₄} ($X = \text{COOH}$, top, viewed along the $[10\bar{1}]$ direction) and in **7**_{PF₆} ($X = \text{NMe}_2$, bottom, viewed along the c direction). In the crystal structures the packing of the cations does not respect the standard “terpy embrace” motif, the cations still interact with each other through offset face-to-face $\pi\cdots\pi$ interactions and edge-to-face C-H $\cdots\pi$ interactions but to form linear chains instead of layers. The BF₄⁻ and PF₆⁻ anions link the chains together through C-H \cdots F interactions to form a three-dimensional network.

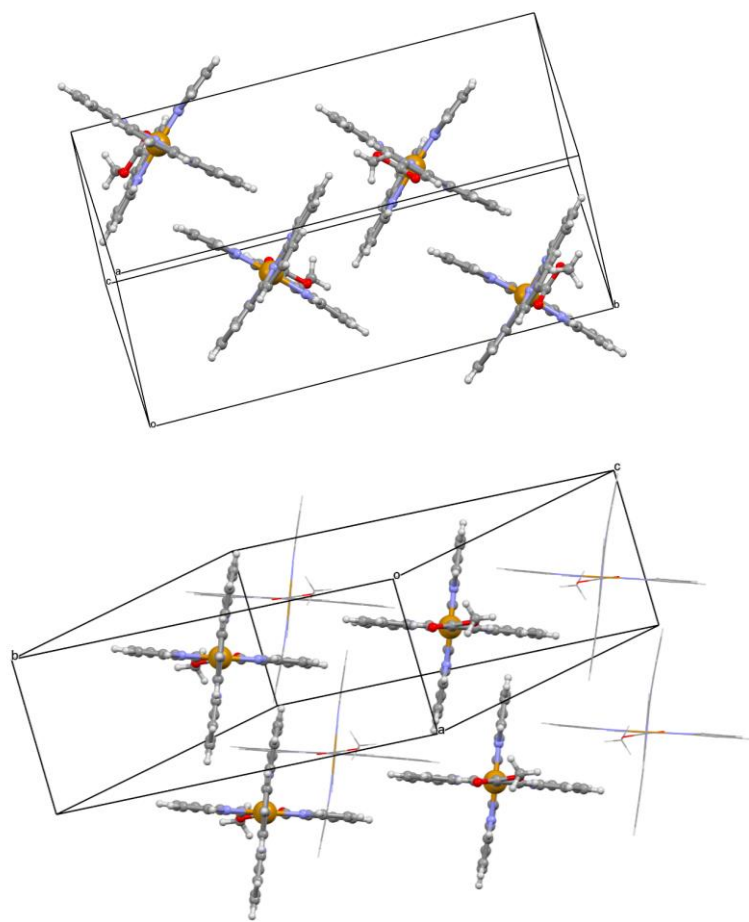


Figure S22. Ball-and-stick representations of the arrangement of the $[\text{Ru}(\text{terpy})(\text{terpy-COOMe})]^{2+}$ cations in **6_BF₄** (top) and in **6_PF₆** (bottom). In the crystal structures the packing of the cations does not respect the standard “terpy embrace” motif, the cations only interact through offset face-to-face $\pi \dots \pi$ interactions by pairs like in **6_PF₆** or by blocks of 4 molecules like in **6_BF₄**. between the pyridine and the phenyl rings. These small units are connected by C-H...O hydrogen bonds while cations and ions interact via weak C-H...F hydrogen bondings.

Compound	UV/Vis λ / nm (ϵ / M ⁻¹ cm ⁻¹ * 10 ⁻³)	Emission λ_{em} / nm
1	CH ₃ CN: 270 (28.7), 308 (47.6), 475 (11.1) PBS: 270 (22.9), 307 (38.0), 475 (8.8)	638
2	CH ₃ CN: 272 (33.3), 308 (49.2), 478 (12.2) PBS: 271 (30.8), 308 (45.5), 478 (11.5)	624
3	CH ₃ CN: 271 (44.3), 308 (65.2), 478 (16.5) PBS: 271 (34.0), 307 (49.8), 478 (13.0)	647
4	CH ₃ CN: 269 (39.7), 305 (52.6), 479 (14.0) PBS: 269 (36.5), 305 (49.1), 479 (13.0)	616
5	CH ₃ CN: 272 (24.5), 309 (30.5), 484 (10.0) PBS: 272 (21.7), 309 (27.6), 480 (8.8)	666
6	CH ₃ CN: 272 (23.7), 310 (26.9), 486 (9.4) PBS: 272 (20.1), 309 (22.3), 488 (8.2)	676
7	CH ₃ CN: 272 (50.8), 306 (50.5), 490 (16.1) PBS: 272 (47.8), 305 (47.1), 490 (15.1)	617

Table S10. Spectroscopic properties of the complexes **1-7** in CH₃CN and PBS.

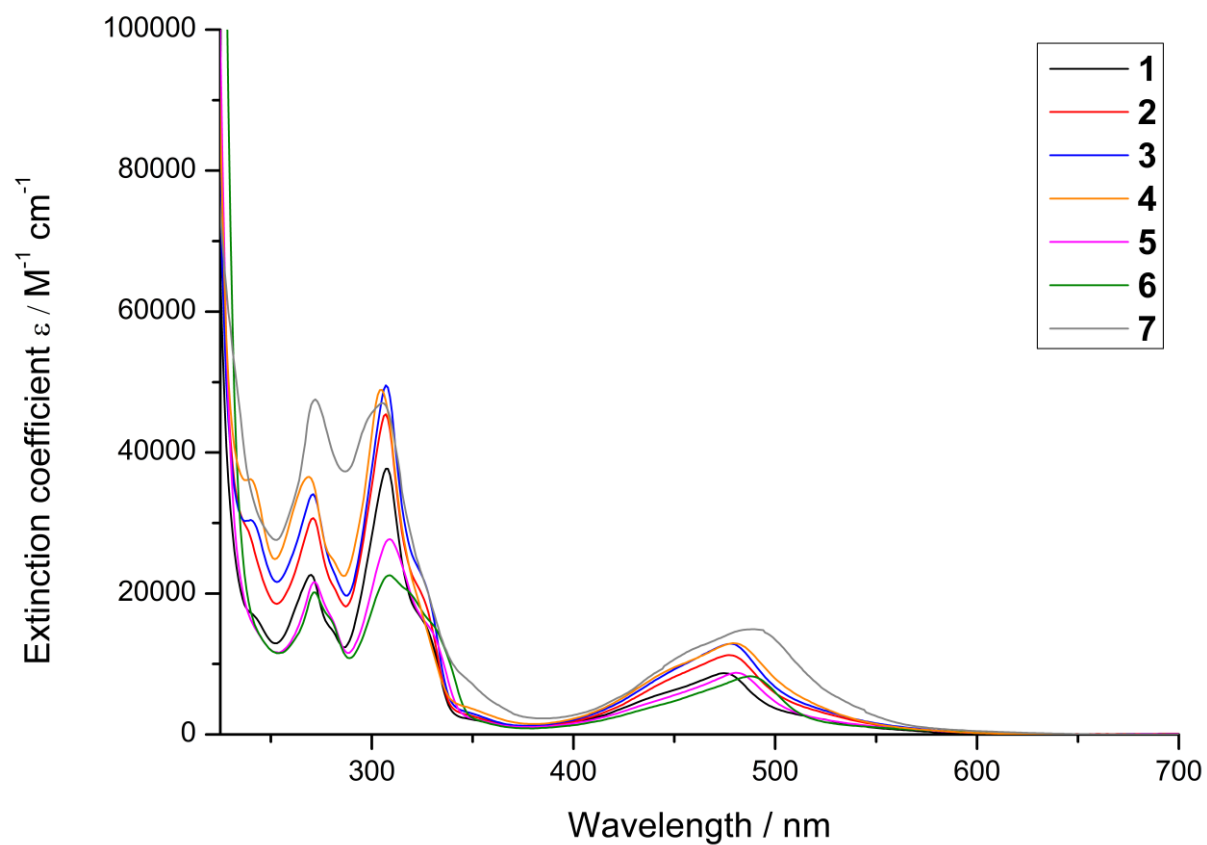


Figure S23. UV/Vis spectra of the complexes **1-7** in PBS.

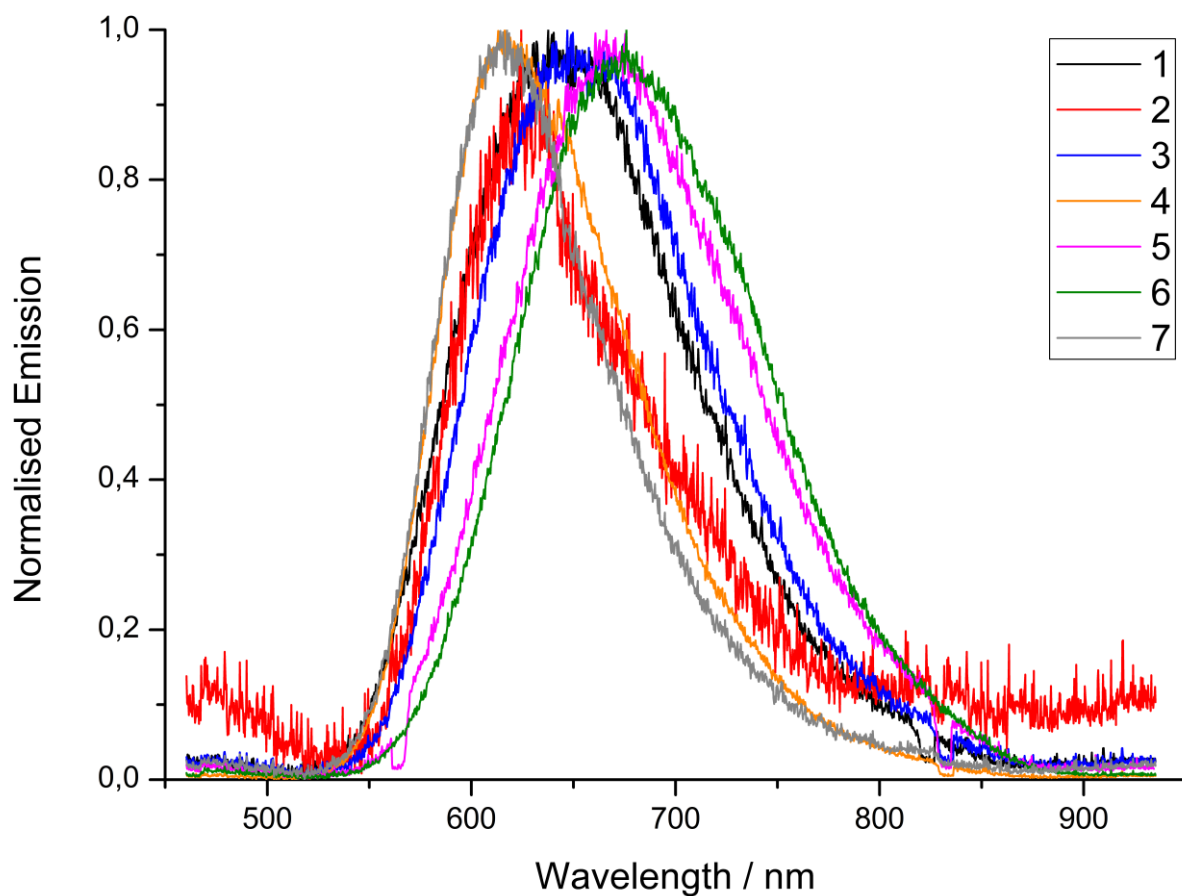


Figure S24. Normalised emission spectra of the complexes **1-7** in CH₃CN.

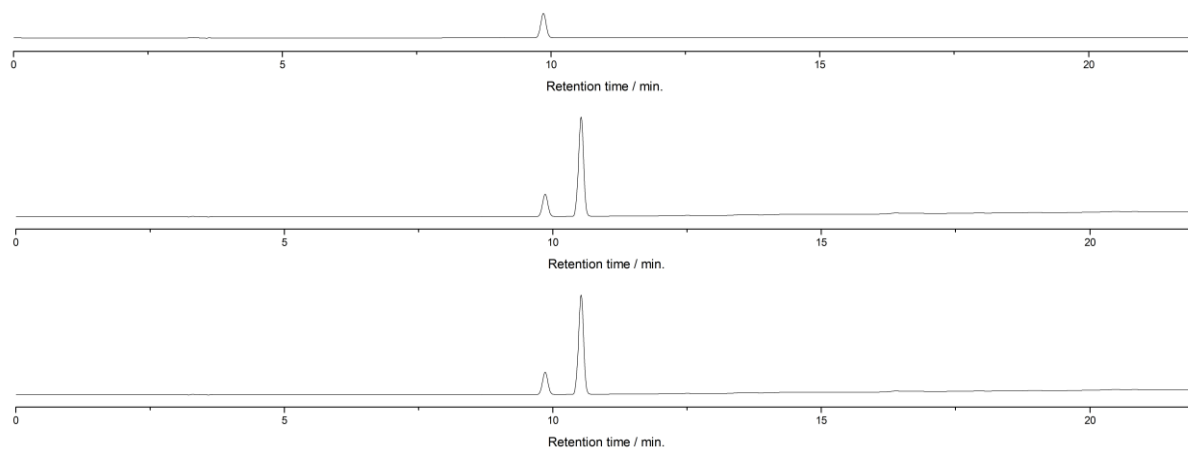


Figure S25. HPLC chromatogram of Caffeine (internal standard, above) and **1** after 0 h (middle) and 48 h (below) incubation in human pooled plasma.

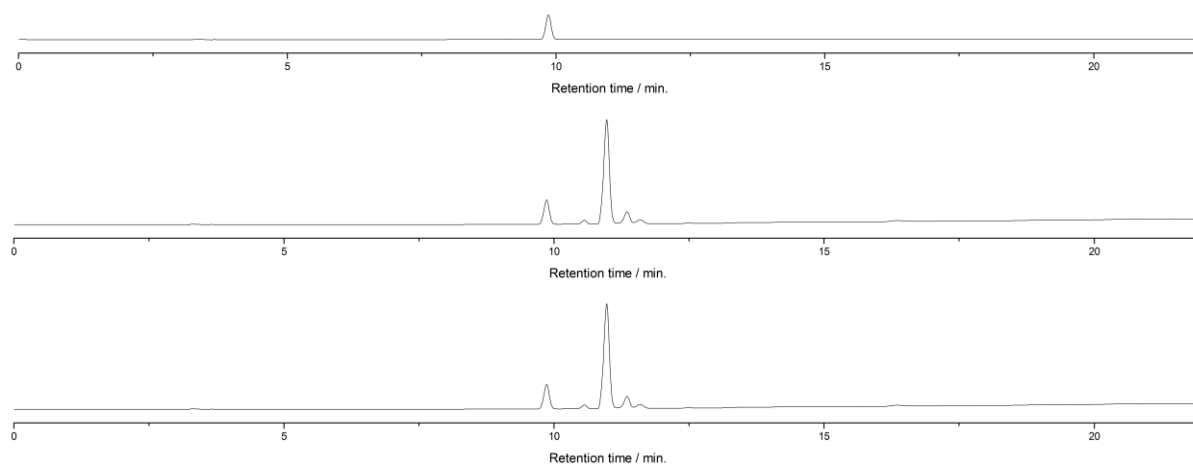


Figure S26. HPLC chromatogram of Caffeine (internal standard, above) and **2** after 0 h (middle) and 48 h (below) incubation in human pooled plasma.

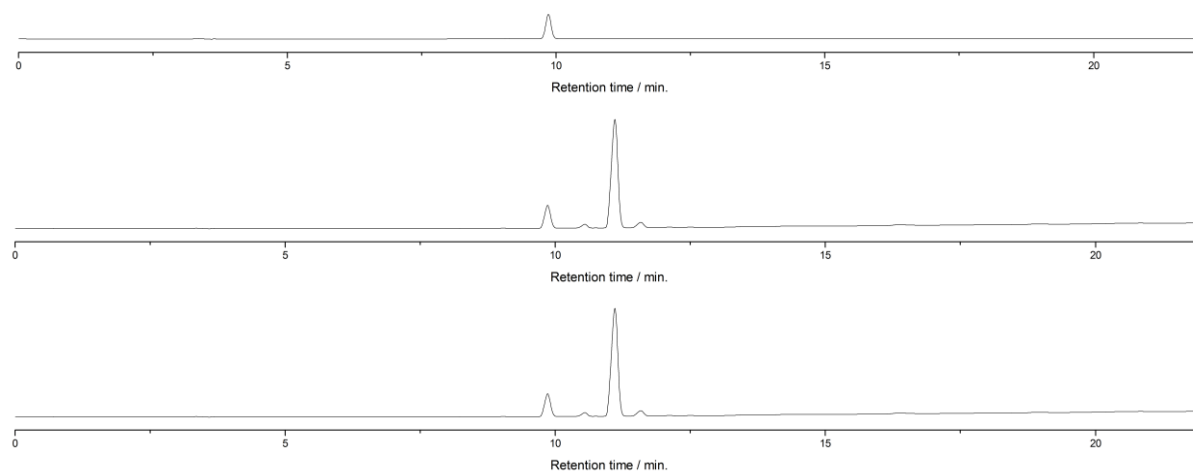


Figure S27. HPLC chromatogram of Caffeine (internal standard, above) and **3** after 0 h (middle) and 48 h (below) incubation in human pooled plasma.

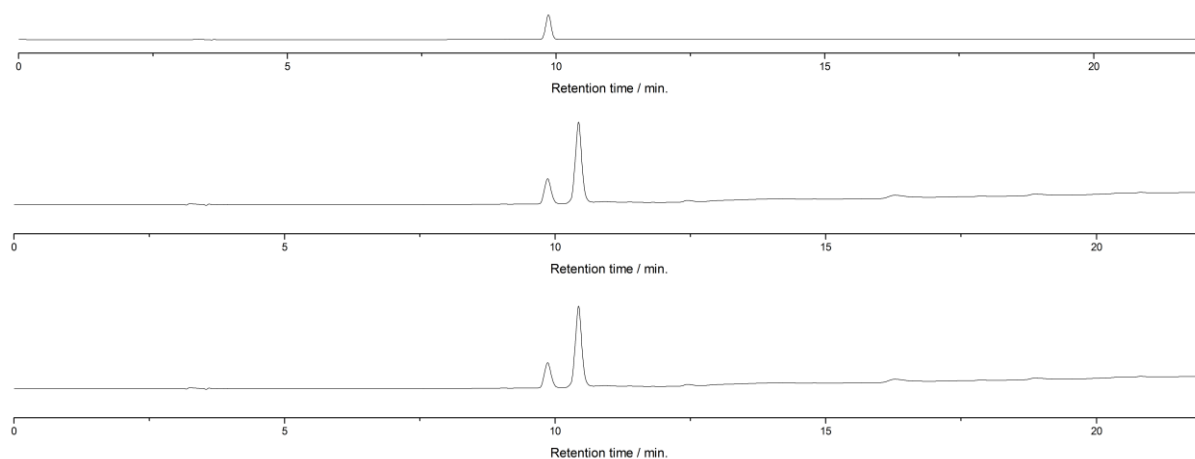


Figure S28. HPLC chromatogram of Caffeine (internal standard, above) and **4** after 0 h (middle) and 48 h (below) incubation in human pooled plasma.

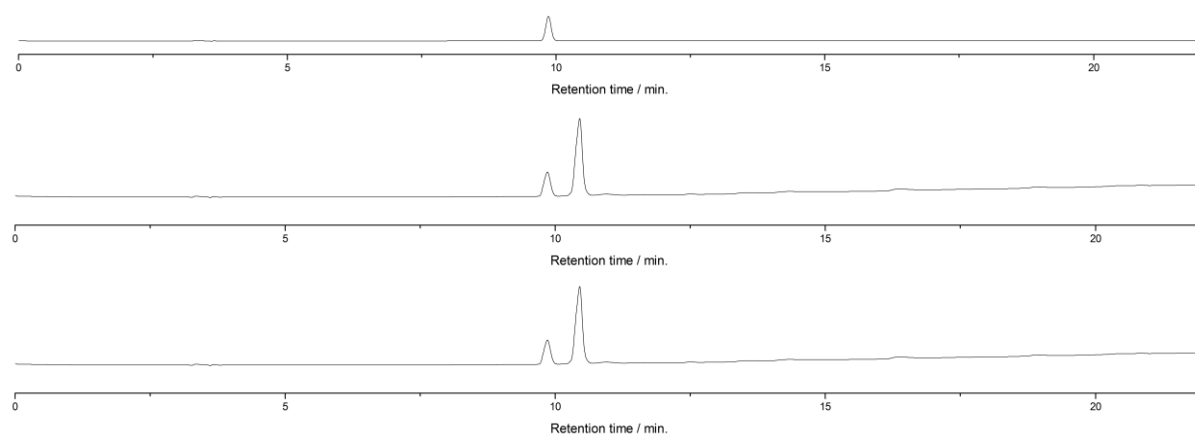


Figure S29. HPLC chromatogram of Caffeine (internal standard, above) and **5** after 0 h (middle) and 48 h (below) incubation in human pooled plasma.

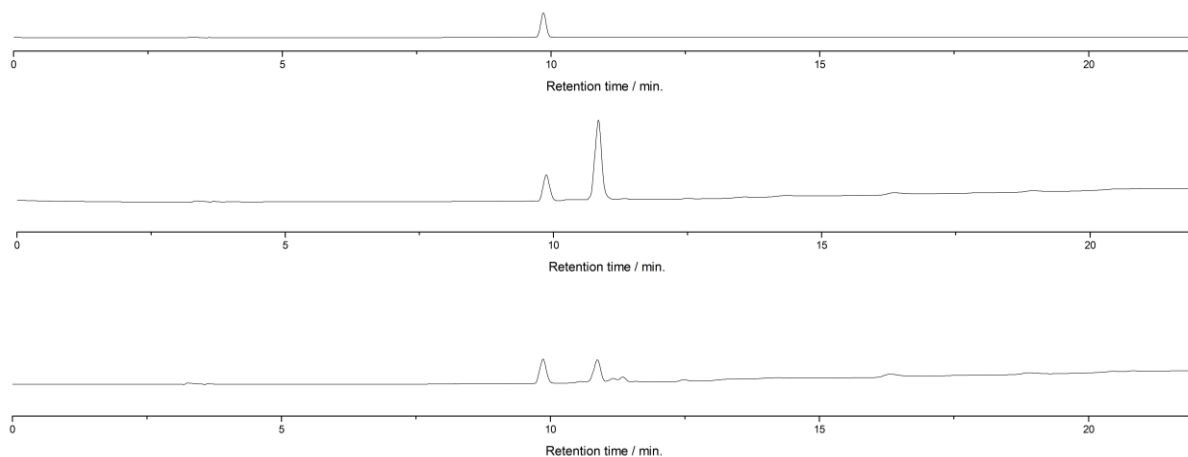


Figure S30. HPLC chromatogram of Caffeine (internal standard, above) and **6** after 0 h (middle) and 48 h (below) incubation in human pooled plasma.

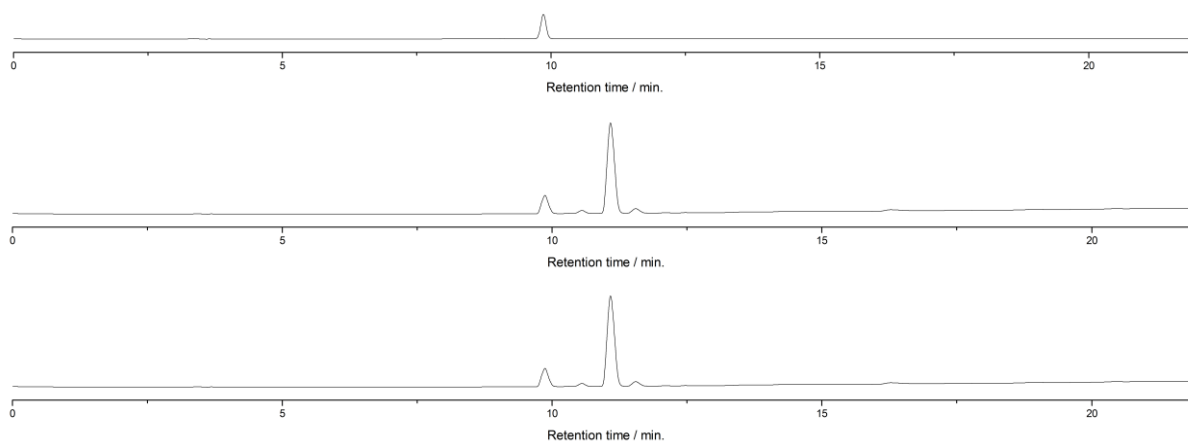


Figure S31. HPLC chromatogram of Caffeine (internal standard, above) and **7** after 0 h (middle) and 48 h (below) incubation in human pooled plasma.

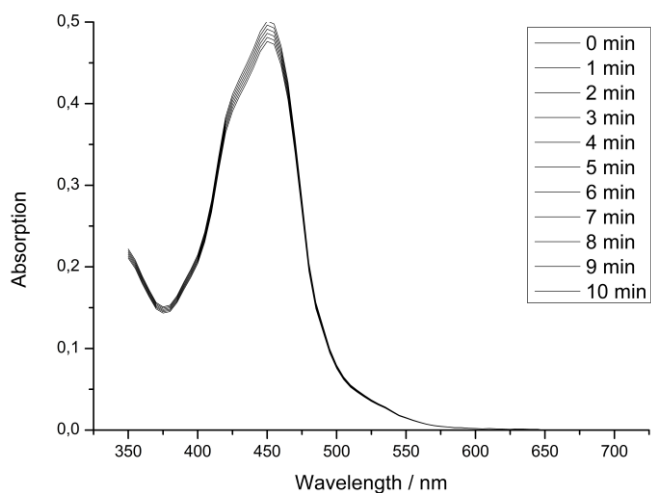


Figure S32. Temporal change of the UV/Vis spectra of $[\text{Ru}(\text{bipy})_3]\text{Cl}_2$ by irradiation at 450 nm in CH_3CN .

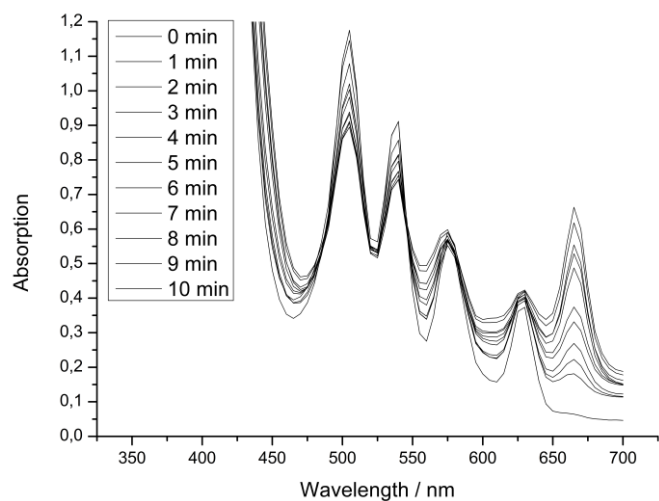


Figure S33. Temporal change of the UV/Vis spectra of Protoporphyrin IX by irradiation at 450 nm in CH_3CN .

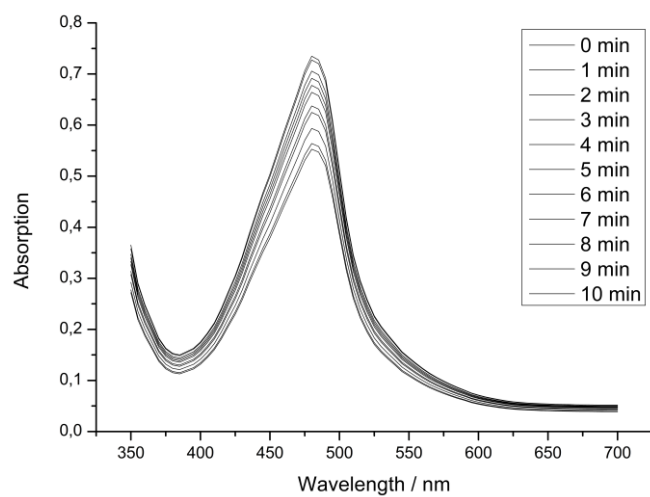


Figure S34. Temporal change of the UV/Vis spectra of **1** by irradiation at 450 nm in CH₃CN.

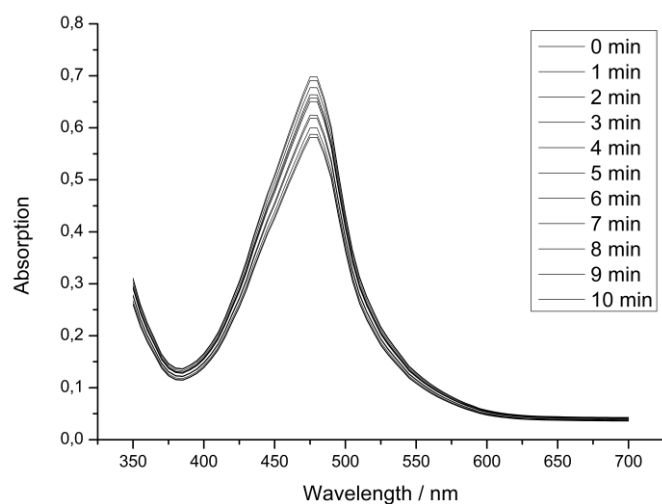


Figure S35. Temporal change of the UV/Vis spectra of **2** by irradiation at 450 nm in CH₃CN.

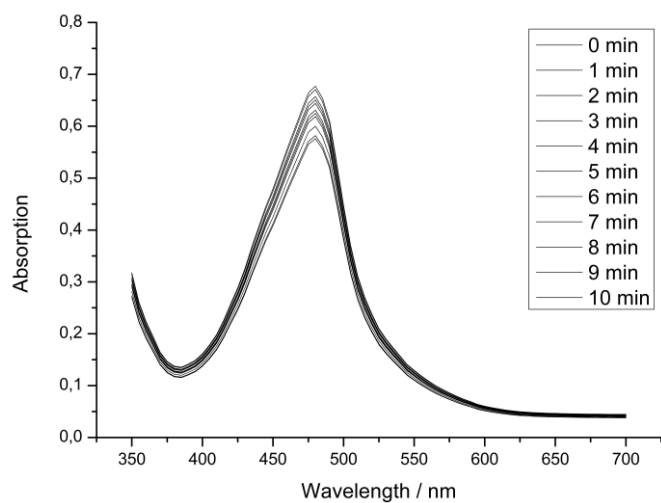


Figure S36. Temporal change of the UV/Vis spectra of **3** by irradiation at 450 nm in CH_3CN .

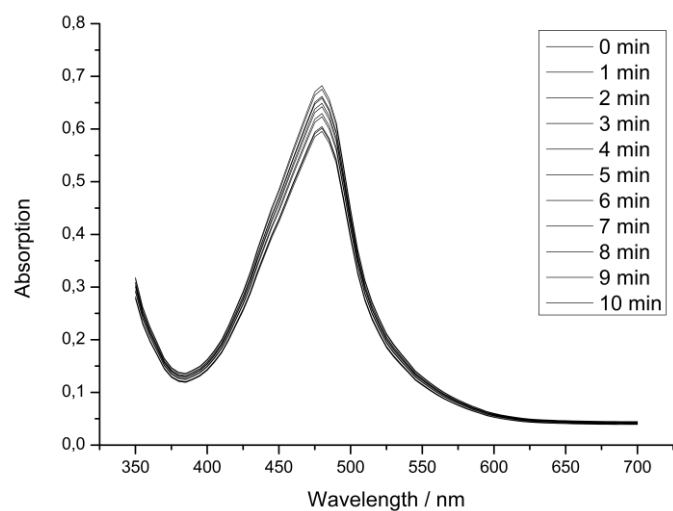


Figure S37. Temporal change of the UV/Vis spectra of **4** by irradiation at 450 nm in CH_3CN .

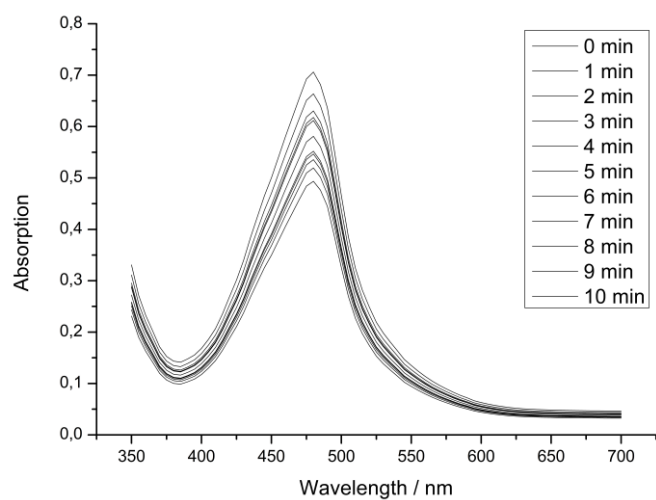


Figure S38. Temporal change of the UV/Vis spectra of **5** by irradiation at 450 nm in CH₃CN.

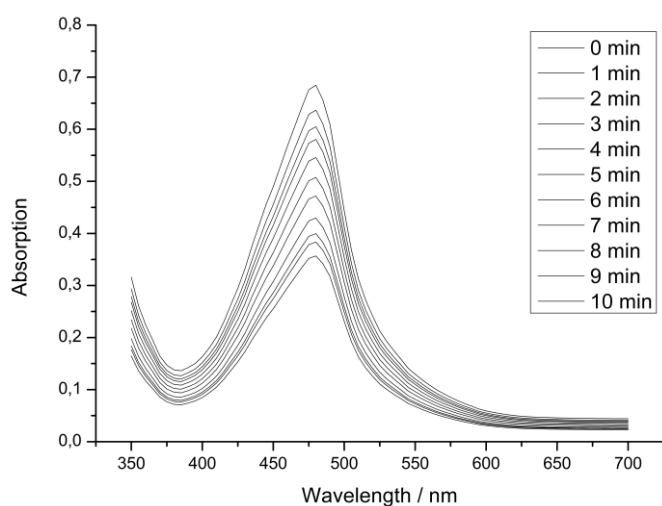


Figure S39. Temporal change of the UV/Vis spectra of **6** by irradiation at 450 nm in CH₃CN.

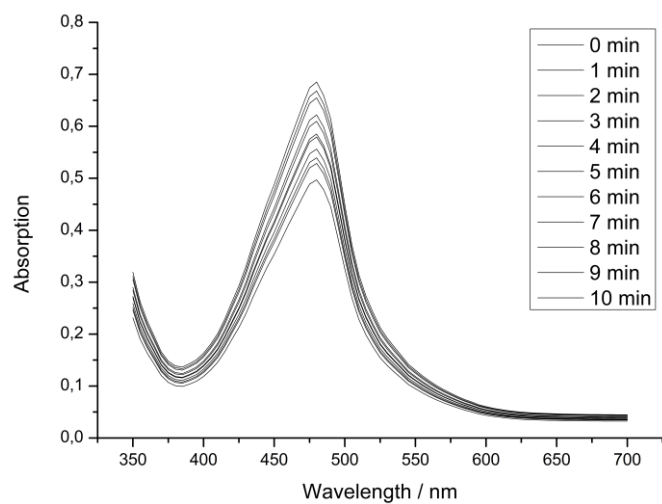


Figure S40. Temporal change of the UV/Vis spectra of **7** by irradiation at 450 nm in CH_3CN .

Chapter 5- Rationally Designed Long-Wavelength Absorbing Ru(II) Polypyridyl Complexes as Photosensitizers for Photodynamic Therapy

Johannes Karges,[†] Franz Heinemann,^{†,‡} Marta Jakubaszek,^{†,¶} Federica Maschietto,[§] Chloé Subecz,[†] Mazzarine Dotou,[†] Olivier Blacque,[‡] Mickaël Tharaud,[§] Bruno Goud,[¶] Emilio Viñuelas Zahinos,[⊥] Bernhard Spingler,^{‡,} Ilaria Ciofini,^{§,*} and Gilles Gasser^{†,*}*

[†] Chimie ParisTech, PSL University, CNRS, Institute of Chemistry for Life and Health Sciences, Laboratory for Inorganic Chemical Biology, 75005 Paris, France.

[‡] Department of Chemistry, University of Zurich, Winterthurerstrasse 190, 8057, Zurich, Switzerland.

[¶] Institut Curie, PSL University, CNRS UMR 144, 75005 Paris, France.

[§] Chimie ParisTech, PSL University, CNRS, Institute of Chemistry for Life and Health Sciences, Theoretical Chemistry and Modelling, 75005 Paris, France.

[§] Université de Paris, Institut de physique du globe de Paris, CNRS, F-75005 Paris, France.

[⊥] Departamento de Química Orgánica e Inorgánica, Facultad de Ciencias, Universidad de Extremadura, 06071 Badajoz, Spain.

* Corresponding authors: spingler@chem.uzh.ch ; Ilaria.ciofini@chimieparistech.psl.eu; gilles.gasser@chimieparistech.psl.eu; www.gassergroup.com; Tel. +33 1 44 27 56 02.

This chapter has been published on 14th of March 2020 in *Journal of the American Chemical Society* 2020, **142**, 14, 6578–6587. (DOI: 10.1021/jacs.9b13620).

Reproduced by permission of American Chemical Society
(<https://pubs.acs.org/doi/10.1021/jacs.9b13620>)

Contribution to the publication:

Marta Jakubaszek supervised Chloé Subecz and Mazzarine Dotou and co-performed the cytotoxicity studies in 2D and 3D cell cultures. She provided fluorescence microscopy results and performed Seahorse Mitostress and Glycostress tests. She wrote the biological section of this publication.

Marta Jakubaszek



19.05.2020

Gilles Gasser



Keywords: Anticancer, Bioinorganic Chemistry, Medicinal Inorganic Chemistry, Metals in Medicine, Photodynamic Therapy

Abstract

The utilization of Photodynamic Therapy (PDT) for the treatment of various types of cancer has gained increasing attention over the last decades. Despite the clinical success of approved photosensitizers (PSs), their application is limited due to poor water solubility, aggregation, photodegradation, and slow clearance from the body. To overcome these drawbacks, research efforts are devoted towards the development of metal complexes and especially Ru(II) polypyridine complexes based on their attractive photophysical and biological properties. Despite the recent research developments, the vast majority of complexes utilize blue or UV-A light to obtain a PDT effect, limiting the penetration depth inside the tissue and therefore, the possibility to treat deep-seated or large tumors. To circumvent these drawbacks, we present the first example of the DFT guided search for efficient PDT PSs with a substantial spectral red shift towards the biological spectral window. Thanks to this design, we have unveiled a Ru(II) polypyridine complex, which causes phototoxicity in the very-low micromolar-to-nanomolar range at clinically relevant 595 nm, in monolayer cells as well as in 3D multicellular tumor spheroids

Introduction

Photodynamic Therapy (PDT) is a non-invasive medical technique for the treatment of various types of cancer (e.g., lung, bladder, esophageal, and brain cancer) as well as bacterial, fungal or viral infections. The effect of PDT relies on the combination of an ideally non-toxic molecule, a so-called photosensitizer (PS), oxygen, and light. The PS is injected either systemically or locally. Upon light irradiation, the PS is uplifted to an excited singlet state from which the PS can undergo an intersystem crossing process to reach an excited triplet state. This state can influence the biological environment either by a Type I or Type II pathway. A Type I mechanism is characterized by an electron or proton transfer from or to the PS, which leads to the formation of reactive oxygen species (ROS) or other highly reactive radicals. In a Type II mechanism, the energy is transferred to triplet oxygen ($^3\text{O}_2$) to generate singlet oxygen ($^1\text{O}_2$). Due to their high reactivity, ROS and $^1\text{O}_2$ can cause oxidative stress and damage in different cellular compartments (i.e., membrane, nucleus, endoplasmic reticulum, lysosome, mitochondria). Both of these mechanisms can happen simultaneously upon light irradiation even so Type II pathway is the predominant one for most approved PSs.¹⁻⁶

Photofrin is the most commonly used PS in PDT. It has been approved for the treatment of bladder cancer, early-stage lung cancer, esophageal cancer, and early non-small cell lung cancer. However, based on its low solubility and low absorption in the therapeutic window (i.e., 600-900 nm), high concentrations, as well as high light doses are required for an adequate tumor treatment making Photofrin not an ideal PS. Additionally, it was shown that this PS has an exceptionally long half-life excretion time leading to severe photosensitivity for the patients. Since the majority of investigated and approved PS are based on a tetrapyrrolic scaffold (i.e., porphyrins, chlorins, phthalocyanines), these PSs are likely to have similar drawbacks which include 1) poor water solubility; 2) tedious synthesis and purification; 3) low cancer selectivity; 4) photobleaching effect and 5) slow clearance from the body causing photosensitivity.

Therefore, a need for modification of existing PSs or the development of new classes of PSs is needed.⁷⁻¹¹

Among the new classes of PSs investigated the development of Ru(II) polypyridyl complexes as PDT PSs has received much attention due to their ideal photophysical and photochemical properties (i.e., high water solubility, high chemical stability and photostability, intense luminescence, large Stokes shifts, high ¹O₂ production).¹²⁻²⁷ Worthy of note, the complex TLD-1433 [Ru(dmb)₂(IP-TT)]²⁺ (dmb=4,4'-dimethyl-2,2'-bipyridine, IP-TT=2-(2',2'':5'',2' ''-terthiophene)-imidazol[4,5-f][1,10]phenanthroline) has just entered phase II clinical trial as a PDT PS for the treatment of non-muscle invasive bladder cancer in Canada.²⁸⁻³¹ Despite these remarkable properties, the majority of Ru(II)-based PS are typically excited using blue or UV-A light and therefore suffer from a lack of absorption in the biological spectral window (600-900 nm) and.³²⁻³⁵ Based on absorption and light scattering effects in the biological environment, the light penetration depth into the tissue is low at this wavelength, which limits their application to treat deep tumors or large tumors.^{36, 37} To overcome this limitation, there is a need for optimization of the absorption properties of Ru(II)-based PSs. It has been well-established that the photophysical properties, including absorption, emission as well as excited-state lifetimes of Ru(II) polypyridyl complexes depend on the ligands bound to the Ru center. This variable can, therefore, be tuned. In this context, we applied a combined experimental and theoretical approach to design new suitable Ru-based PDT PSs. Based on the already well-established biological activity of the complex [Ru(phen)₃]²⁺ (phen = 1,10-phenanthroline) as a minor groove binder³⁸ and [Ru(bphen)₃]²⁺ (bphen = 4,7-diphenyl-1,10-phenanthroline) as a mitochondria and lysosome targeting agent³⁹ and their ability to be effective PDT PSs⁴⁰⁻⁴², we decided to use [Ru(phen)₂(bipy)]²⁺ and [Ru(bphen)₂(bipy)]²⁺ (bipy = 2,2'-bipyridine) derivatives as basic scaffolds. In this investigation, the electronic properties, the origin, and the magnitude of red shift towards the biologic spectral window are disclosed. The resulting

complexes (**1-7**, Figure 1) were synthesized, characterized, and biologically evaluated in-depth. Thanks to this combined study, a highly active Ru(II)-based PDT PS that can be excited up to 595 nm could be unveiled.

Results and discussion

Rational Design

As the basis of the design of Ru(II) polypyridine complexes as PDT PSs with red-shifted absorption near or in the biological spectral window, the $[\text{Ru}(\text{phen})_2(\text{bipy})]^{2+}$ scaffold was used due to its synthetic accessibility and generally high physical stability. To pursue this aim, systematic modification on the bipyridine moiety was investigated, and these effects studied by a theoretical and experimental approach.

It is well known that, in a simplified picture, the highest occupied orbitals in a pseudo-octahedral Ru(II) polypyridyl complex are mainly consisting of the Ruthenium t_{2g} - d -orbitals while the lowest occupied orbitals typically correspond to π^* -orbitals localized on the ligands.^{43,44} Therefore, the lowest intense absorption band is expected to be of metal to ligand charge transfer (MLCT) character stemming from electronic transitions from the t_{2g} manifold to the empty ligands lowest-lying orbitals and leading to the population of a singlet state of MLCT nature under light irradiation. A simple way to red shift the MLCT absorption energy is, therefore, to decrease the HOMO-LUMO gap by an ad-hoc functionalization of the ligands. In particular, functionalization of the ligands with electron-donating and electron-withdrawing (EDG/EWG) groups is expected to increase the occupied MOs and lower the LUMO energy, respectively.

In the case of the unsubstituted compound **1**, the ligands are not strictly equivalent (two phen and one bipy ligand) so that the t_{2g} orbitals are not expected to be strictly degenerate.

Nonetheless, from the computed MOs energies of **1**, it can be seen that the difference in energy between the t_{2g} orbitals is very tiny (roughly 0.04 eV) and the same holds for the LUMOs of π^* character (roughly 0.08 eV) with contributions arising both from the phen and the bipy ligands. As a consequence, the functionalization of any of the two ligands shall induce a shift of the gap but is indeed expected to be easier in the case of the bipy, due to the reduced steric congestion around this ligand. For this reason, EDGs and EWGs were exclusively introduced only on the bipy ligand (**1-5**, Figure 1, optimized cartesian coordinates Table S1-S5).

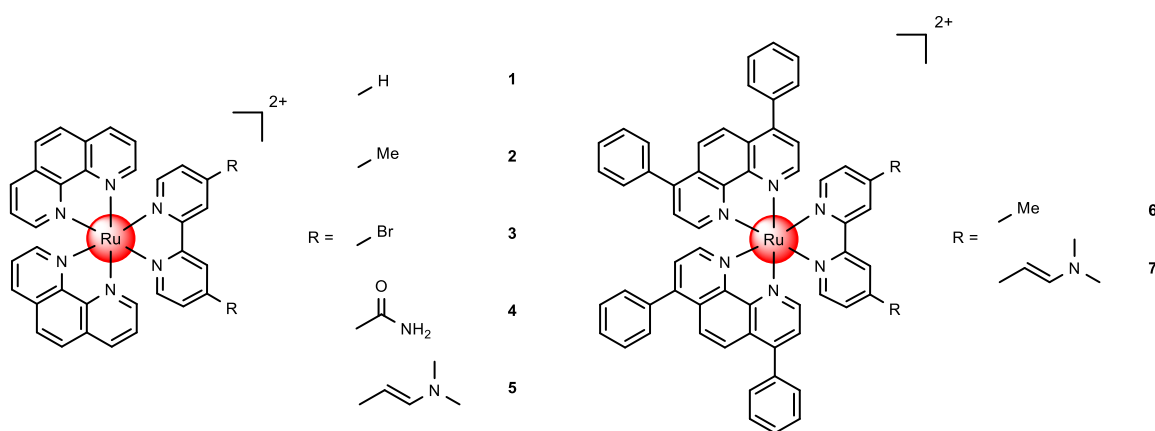


Figure 1. Chemical structures of the Ru(II) polypyridyl complexes investigated in this work. The complexes **1-7** were isolated as PF_6^- salts.

For this purpose, the energies of the frontier molecular orbitals were computed (Figure 2). Indeed, functionalization with -Me (**2**) (a weakly EDG) only negligibly affects the gap (reducing from 3.99 eV for **1** to 3.97 eV for **2**). A slightly more significant effect is obtained by weak EWGs such as -Br (**3**) and -CONH₂ (**4**, 3.83 eV, and 3.77 eV, respectively), which induce a small stabilization of the LUMO. These observations are in line with the results previously obtained by some of us⁴⁵ when functionalizing with a -CHO group, a better EWG for which the computed gap is indeed 3.47 eV. On the other hand, functionalization with the vinyl dimethylamine-EDG (**5**) results in a substantial reduction of the HOMO-LUMO gap (to

3.24 eV, roughly 0.7 eV lower than the native compound (**1**) due to a sizable increase of the HOMO energy. Nonetheless, it should be underlined that the gap is reduced here due to the presence of occupied orbitals centered on the vinyl dimethylamine group in the gap. Therefore, although de facto the gap is substantially reduced, there is no destabilization of the t_{2g} manifold so that the bright MLCT transition (occurring from the t_{2g} orbitals to the π^* ligand orbitals) is expected not to be affected (that is red-shifted).

To capitalize on this theoretical insight, we additionally examined the functionalization with a methyl and vinyl dimethylamine group on the $[\text{Ru}(\text{bphen})_2(\text{bipy})]^{2+}$ scaffold **6-7** (optimized cartesian coordinates Table S6-S7) was also investigated. Interestingly, changing the ligand scaffold from phen to bphen does not significantly affect the gap – as expected due to the small electronic effect induced by the presence of the four phenyl groups on the phen ligands. Indeed comparing compounds **2** and **6** or **5** and **7** (that are the analogous in the two series), a difference of only 0.1 and 0.07 eV in the gap, respectively, can be observed.

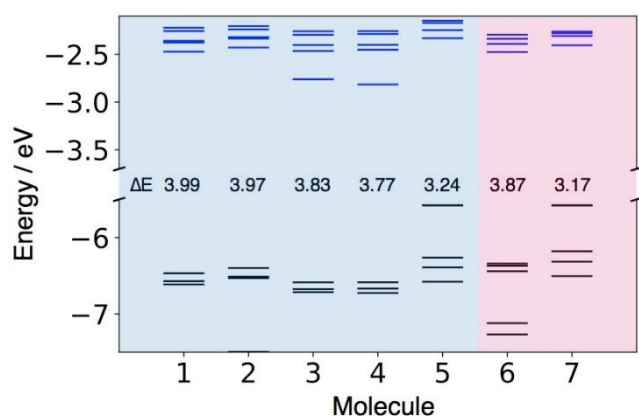


Figure 2. Computed frontier orbitals' energies and HOMO-LUMO gaps (in eV). Occupied/virtual orbitals energies are represented as black/blue line. Blue background: $\text{Ru}(\text{phen})_2(\text{bipy})^{2+}$ skeleton. Purple background: $\text{Ru}(\text{bphen})_2(\text{bipy})^{2+}$ skeleton.

Synthesis and Characterization

Based on the theoretical design, the Ru(II) polypyridine complexes **1-7** (Figure 1) were synthesized. To date, the synthesis of complexes **3-5** and **7** has not been yet reported, while complexes **1**⁴⁶, **2**⁴⁷, and **6**⁴⁸ are known. However, in this study, slightly different experimental procedures than the previously described were employed to obtain these compounds (for experimental protocols see supporting information). The identity of all complexes was confirmed by ¹H, ¹³C-NMR (Scheme S1, Figures S1-S14), HRMS, and the purity by elemental analysis. In addition, the molecular structures of complexes **1-3** (Figure S15-17, Table S8-S9) were confirmed by single-crystal X-ray diffraction studies. The crystal structure of compound **1** has already been characterized by Huang and Ogawa⁴⁹, with the exception that the crystal structure presented here contains one solvent molecule of acetonitrile per ruthenium complex. In all molecular structures, the Ru(II) central atom adopts a distorted octahedral geometry chelated by two 1,10-phenanthroline ligands and one 2,2'-bipyridine ligand with Ru – N bond lengths ranging from 2.046(3) to 2.078(3) Å, N_{phen} – Ru – N_{phen} angles from 79.48(12) to 80.1(2)°, and N_{bipy} – Ru – N_{bipy} angles from 78.55(10) to 78.98(13)°. It is worth to note that the substitution of the bipyridine ligand by methyl groups in **2** and bromo ligands in **3** has no significant influence on the Ru – N bond distances.

Photophysical properties

The absorption spectra of the compounds **1-7** were measured in CH₃CN (Figure S19, extinction coefficients Table S10) and compared with the computed spectra (Figure 3). Although in the simulated spectra the energy of the MLCT band (around 450 nm) is systematically overestimated while the higher energy ligand centered (LE) band (around 300 nm) is better

reproduced, small shifts towards the spectral windows of interest and a rise in intensity for the lowest energy band is indeed observed for the compounds **5**, **6** and **7**.

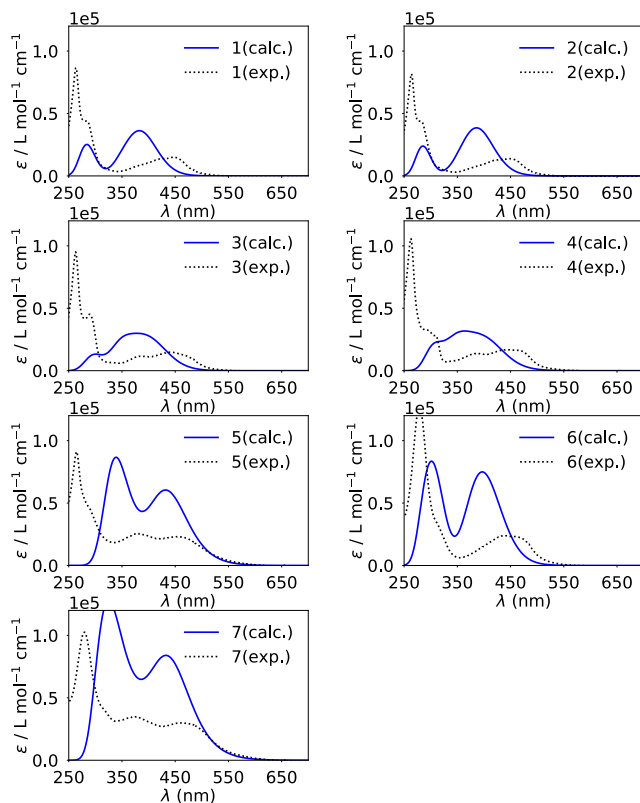


Figure 3. Simulated (blue) and experimental (black) spectra of compounds **1-7** in CH_3CN ($c = 7.5 \mu\text{M}$). Computed vertical electronic transitions are depicted as vertical blue bars. Corresponding oscillator strength (f) is given in a.u.

Of note, in the case of **5** and **7**, several electronic transitions are computed to contribute to the first -lowest energy- absorption band. The most intense has still an MLCT character while the one occurring at lower energy (less intense than those of MLCT character) and responsible for the tail and red-shift of the band are predicted to be essentially ligand centered. These transitions are indeed of HOMO-LUMO type and, as discussed above, corresponding essentially to a transition from the vinyl dimethylamine group to the π^* orbitals of the ligand. This can be visualized and understood from the maps of the difference in density between ground (GS) and

excited state (ES) for two representative transitions of compound **6** (Figure S18a) and **7** (Figure S18b). For both complexes, the lowest energy transition (first electronic transition ES1) and the most intense one contributing to the first band (ES 4 and ES 9 for **6** and **7**, respectively) were analyzed. In Figure S18, density depletion/increase regions upon excitation for each are represented by blue/yellow zones, and the barycenters of these regions - depicted as blue/yellow dots - can be interpreted as the position of the electron and hole upon excitation. It can be clearly seen that while for complex **6**, both transitions have a clear MLCT character though not necessarily involving the same ligand, in the case of **7**, in agreement with the MO diagram, the lowest energy transition is of interligand type and mostly involving the vinyl dimethylamine-part. Therefore, even if a redshift of the first absorption band is predicted and indeed experimentally observed, it is not necessarily expected to correlate with an improvement of the phototherapeutic properties that are indeed linked to the population of a MLCT state.

Following this, the luminescence of the Ru(II) polypyridine complexes upon excitation at 355 nm was investigated. The maxima of the emission signals (Figure S20) were measured and found to be between 600-710 nm. Interestingly, complexes **5** and **7**, which showed the highest red shift in absorption, also demonstrated the strongest red shift in their emission maximum. All complexes demonstrated a large Stokes shift implying minimal inference between excitation and emission. The luminescence quantum yields were found with values between 5.0% - 1.4% (Table S10) for **1-4**, **6** and are therefore in the same range then other Ru(II) polypyridine complexes.^{50, 51} On the contrary, the luminescence of **5** and **7** were barely measurable - with luminescence quantum yields >0.1%. This is consistent with the computed vertical absorption (see before) highlighting that for these two complexes the lowest lying excited states are of LC character. This result is also in agreement with the exceptionally low luminescence quantum yield of (*E,E'*)-4,4'-bis(*N,N'*-dimethylaminovinyl)-2,2'-bipyridine in dichloromethane (1.5%) in comparison to other substituted 2,2'-bipyridines⁵² and of the

[Ru(*(E,E'*)-4,4'-bis(*N,N'*-dimethylaminovinyl)-2,2'-bipyridine)₃]²⁺ complex in CH₃CN (>0.1%),⁵³ which were recently reported.

The excited-state lifetimes were determined in degassed and air-saturated CH₃CN solution to investigate the influence of the presence of oxygen. The obtained values (Figure S21-S27, Table S10) were found to be in the nanosecond scale in a degassed (312 – 1387 ns) and air saturated (55 – 326 ns) solution. All measured lifetimes were found to be in the same range as for other Ru(II) polypyridine complexes.^{50, 51} Importantly, the data shows that the presence of oxygen has a significant influence on the lifetime of the excited state for all complexes indicating that molecular oxygen can interact with the triplet state of the complex.

The generation of singlet oxygen (¹O₂) was quantitatively measured upon excitation at 450 nm by two complementary methods: (i) direct by measurement of the phosphorescence of ¹O₂, (ii) indirect by temporal monitoring the change of absorption of a ¹O₂ scavenger.^{54, 55} Complexes **1-4, 6** were found to have ¹O₂ quantum yields (Table S11) between 53-69% in CH₃CN and 5-36% in an aqueous solution, suggesting an application as a PDT agent. These values are comparable with those previously reported for related compounds.^{56, 57} In comparison, the ¹O₂ quantum yields of the (*E,E'*)-4,4'-bis(*N,N'*-dimethylaminovinyl)-2,2'-bipyridine coordinated complexes **5** and **7** were found to be drastically lower with values of 22-35% in CH₃CN and 7-21% in an aqueous solution. This was expected as these compounds show an untypical excited state behavior (emission, luminescence, lifetime) which is also explained by DFT calculations.

Stability

The stability of a compounds is an essential parameter for their use as a PDT agent. As a first experiment, the stability of the complexes was investigated in a DMSO solution since this solvent was shown to be problematic for certain drug (candidates).⁵⁸⁻⁶⁰ For this purpose, solutions of the complexes in DMSO-d₆ were prepared and stored in a NMR tube in the dark at

room temperature. A $^1\text{H-NMR}$ spectrum was measured directly after preparing the solution after one, two and seven days. For complexes **1-4** and **6** (Figures S28-S31, S33), no significant change in the spectra were observed, indicating that no decomposition occurred. In contrast to this, small changes in the spectra for compounds **5** and **7** could be observed. For both compounds, changes in the signals could be detected after 7 days (Figures S32, S34). This indicates that these compounds are not stable in DMSO. To assess the compatibility of the compounds under biological conditions, the stability of the complexes was tested in pooled human plasma. The complexes were incubated for 48 h in the dark with caffeine as an internal standard, which was previously shown to be stable under these conditions⁶¹ and then analysed by HPLC (Figures S35-41). The stability of complexes **1-4** and **6** and the previously mentioned decomposition of compounds **5** and **7** were confirmed. Based on these findings, the stability of compounds **5** and **7** has been investigated more in detail by incubation of these complexes with shorter time intervals (0 h, 4 h, 12 h, 24 h, 48 h) in the dark. **5** shows first sign of degradation after 12 h and compound **7** after 24 h. The degradation of both complexes advanced in the investigated time interval, but still show unreacted complex even after 48 h incubation.

Following this, the potential decomposition of the complexes upon light irradiation was also tested as previous studies have shown that the stability of metal complexes could be influenced upon light exposure.^{62, 63} This is crucially important as some of the currently approved PDT agents are associated with a strong photobleaching effect. The complexes were exposed to a continuous LED irradiation at 450 nm and the absorption spectra monitored. As a positive control $[\text{Ru}(\text{bipy})_3]\text{Cl}_2$ and as a negative control Protoporphyrin IX was used. The comparison of the spectra shows that complexes **1-4** and **6** (Figure S42-46, 48) have a photobleaching effect in a similar range than $[\text{Ru}(\text{bipy})_3]\text{Cl}_2$ (Figure S41). However, compounds **5** and **7** were found to be strongly affected by light irradiation with a loss of about half of their absorbance after one

minute (Figure S47, 49). This effect is even stronger than that observed for Protoporphyrin IX (Figure S50).

Table 1. IC50 values (μM) for the complexes 1-7 and Protoporphyrin IX (PpIX) in mouse colon carcinoma (CT-26), human glioblastoma (U87), human glioblastoma astrocytoma (U373), human cervical carcinoma (HeLa) and non-cancerous retina pigmented epithelial (RPE-1) cell lines in the dark and upon light irradiation (480 nm, 10 min, 3.21 J cm⁻²).

	CT-26			U87			U373			HeLa			RPE-1		
	Dark	Light	PI	Dark	Light	PI	Dark	Light	PI	Dark	Light	PI	Dark	Light	PI
1	>100	>100	-	>100	93.68 ± 2.50	>1	>100	>100	-	>100	>100	-	>100	>100	-
2	>100	91.24 ± 7.54	>1	>100	71.40 ± 5.67	>1	>100	>100	-	>100	>100	-	>100	>100	-
3	>100	85.71 ± 9.47	>1	>100	>100	-	>100	>100	-	>100	>100	-	>100	>100	-
4	>100	72.59 ± 7.44	>1	>100	>100	-	>100	>100	-	>100	>100	-	>100	>100	-
5	>100	52.54 ± 6.04	>2	>100	>100	-	>100	>100	-	>100	>100	-	>100	>100	-
6	3.09 ± 0.30	0.19 ± 0.04	16.3	28.45 ± 1.97	0.67 ± 0.13	42.5	23.37 ± 0.53	1.89 ± 0.07	12.4	13.57 ± 1.30	0.61 ± 0.06	22.2	28.77 ± 0.94	0.83 ± 0.03	34.9
7	94.47 ± 7.38	6.62 ± 0.07	14.3	>100	7.90 ± 0.54	>12.7	>100	14.85 ± 0.81	>6.7	>100	15.21 ± 1.29	>6.5	>100	8.95 ± 0.50	>11.2

Biological Evaluation

The lipophilicity/hydrophilicity of the compounds was determined by measuring the distribution coefficient (logP) between an organic octanol and aqueous phosphate buffer saline phase (Table S12). The complexes based on a [Ru(phen)₂(bipy)]²⁺ scaffold (1-5) were found with logP values between +0.2 - +0.7 and the complexes based on a [Ru(bphen)₂(bipy)]²⁺ scaffold (6-7) between +1.4 - +1.7. As all complexes were found majorly in the organic phase, their lipophilicity is indicated.

Following this, the cellular uptake of the compounds was investigated. Amount of Ru metal accumulated inside the human cervical carcinoma (HeLa) cells upon incubation for 4 h was

determined by inductively coupled plasma mass spectrometry (ICP-MS). As expected, the compounds 6-7 which are based on a $[\text{Ru}(\text{bphen})_2(\text{bipy})]^{2+}$ scaffold showed a 2.1-5.8 times higher cellular accumulation (Figure S51) in comparison to compounds 1-5, in agreement with their logP values.

To determine the potential of the complexes to act as PDT agents, mouse colon carcinoma (CT-26), human glioblastoma (U87) human glioblastoma astrocytoma (U373), human cervical carcinoma (HeLa) as well as non-cancerous retina pigmented epithelial (RPE-1) cell lines were treated with the complexes. Their cytotoxicity in the dark and upon light exposure was investigated using fluorometric cell viability assay (Table 1). Ideally, a PDT PS should be non-toxic in the dark and highly toxic upon light exposure. Promisingly, complexes 1-5 and 7 were found to be non-cytotoxic in the dark in all chosen cell lines ($\text{IC}_{50} > 100 \mu\text{M}$), while compound **6** showed a cytotoxic profile in the range from 3.09 to 28.77 μM in all investigated cell lines. Upon irradiation at 480 nm (10 min, 3.21 J cm^{-2}), no or only poor toxicity (IC_{50} range from >100 to 52.54 μM) was observed for complexes based on a $[\text{Ru}(\text{phen})_2(\text{bipy})]^{2+}$ scaffold (1-5). In contrast, compounds based on the $[\text{Ru}(\text{bphen})_2(\text{bipy})]^{2+}$ scaffold (6-7) showed a notable phototoxicity upon light irradiation (Phototoxic index (PI)- IC_{50} in the dark/ IC_{50} in upon irradiation, ranges from 6.5 to 42.5). This effect can be attributed to the significantly higher uptake of 6 and 7. Overall, considering the instability of complex 7 in DMSO and human plasma and the absence/low phototoxicity of complexes 1-5, complex 6 was further studied.

Following this preliminary examination, the ability to cause a phototoxic effect at longer wavelengths towards the biological spectral window was further evaluated. CT-26 cell line which was previously shown to be the strongest affected by this compound was chosen for subsequent studies. Importantly, light irradiation of the treated cells at 510 nm or 540 nm caused a phototoxic effect (Table 2). Strikingly, even irradiation at 595 nm generated a phototoxic effect in cells. It has to be noted that the lack of CO_2 atmosphere during irradiation also

contributed to the obtained results. Nevertheless, the calculated PI values are reliable, as cells used as dark control were also incubated for the same amount of time at 37 °C in non-CO₂ atmosphere. Overall, these results make compound **6** an impressive candidate as a PDT agent.

Table 2. IC₅₀ values (μM) for **6** in mouse colon carcinoma (CT-26) cells in the dark and upon light irradiation at 510 nm (40 min, 10.00 J cm⁻²), 540 nm (60 min, 14.25 J cm⁻²) and 595 nm (2 h, 22.47 J cm⁻²).

Wavelength [nm]	Dark	Light	PI
510 nm	4.10 ± 0.56	0.20 ± 0.005	20.6
540 nm	3.27 ± 0.64	0.34 ± 0.005	9.6
595 nm	1.41 ± 0.003	0.06 ± 0.004	23.5

To have a deeper insight in the mechanism of action of compound **6**, its cellular localisation in HeLa cell line was determined by confocal microscopy experiments. After 2 h incubation (14 μM), the complex was detected in the cytoplasm (see Figure S52). Immunofluorescence studies with GM130 (cis-Golgy protein), TGN46 (trans-Golgy protein), KDEL (endoplasmic reticulum protein retention receptor) and LAMP (lysosome- associated membrane glycoprotein) antibodies demonstrated that compound **6** did not colocalize with any of them (Figure 4a). Correlation analysis including Pearson's R value as well as Manders' M1 and Manders's M2 values confirmed the lack of colocalisation of the tested probes with complex **6** (Figure 4b). It is possible that the cytosolic localisation of our complex could be explained by its binding to the cytoskeleton as recently reported for structurally similar complex by the group of MacDonnell.⁶⁴

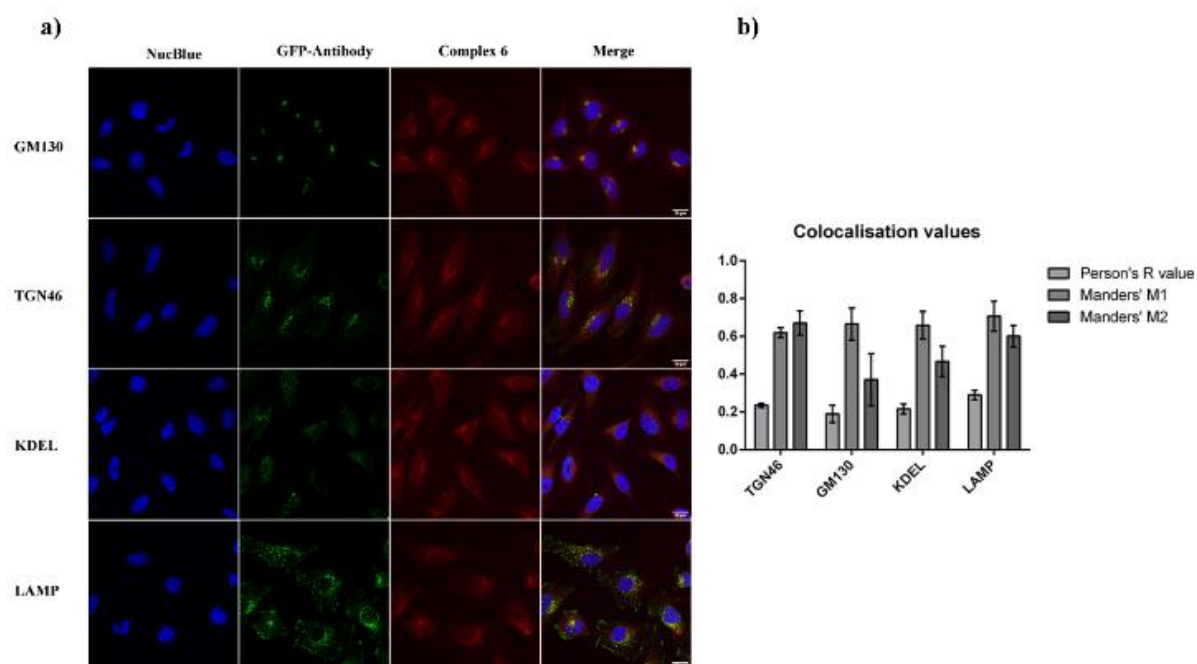


Figure 4. a) Immunofluorescent images of HeLa cells treated with complex **6** (14 μ M, 30 min). DNA visualised by NucBlue staining, immunofluorescence for GM130, TGN46, KDEL and LAMP proteins shown in green, complex **6** shown in red. Scale bar, 20 μ m. b) Person's R, Manders' M1 and Manders' M2 colocalisation values obtained for complex **6** and fluorescent probes

To further study the mechanism of action of complex **6**, its influence on cellular metabolism was studied. Seahorse XF instrument was used which allows for real time measurements of oxygen consumption rate (OCR) and extracellular acidification rate (ECAR) in cells. To observe the effect of the compound **6** on oxidative phosphorylation (ATP production in mitochondria through electron transport chain), the Mito Stress test was performed. In this test, sequential injections of specific inhibitors of the electron transport chain proteins allows for determination of the effect that the compound has on the mitochondrial metabolism of the tested cells. Briefly, the cells were treated (4 h, 1 μ M) with complex **6** as well as with cisplatin and 5-ALA (5-aminolevulinic acid) - precursor of protoporphyrin IX (PpIX), a known photosensitizer, as controls.⁶⁵ After the incubation time, the cells were irradiated at 595 nm (2 h,

22.47 J cm⁻², see Figure S53) and the Mito Stress Test was performed. Strikingly, the data shows that only the cells, which were treated with complex **6** and irradiated, had their metabolism impaired right after the irradiation process. Injection of oligomycin (a specific inhibitor of ATP synthase) or FCCP (an uncoupling agent) did not affect their oxygen consumption rates. The mitochondrial membrane of these cells lost the capacity to restore the proton balance. ATP production was inhibited and spare respiratory capacity (difference between OCR values of maximal respiration and basal respiration) was strongly reduced, contrary to the cells treated with complex **6** that were not irradiated (Figure 5a and Figure S54). Additional tests investigating whether the glycolysis is also affected were performed. Indeed, the glycolysis process is also severely impaired in the cells that are treated with complex **6** and irradiated (Figure 5b and Figure S55). It is known that the glycolysis process is significantly reduced during apoptosis.⁶⁶ Additionally, mitochondria are important compartment, which are responsible for triggering an intrinsic cell death.⁶⁷ It is then likely that the start of apoptosis is responsible for the initial effect in the cellular metabolism observed. A similar metabolic response could not be noticed for the cisplatin. This phenomenon could be explained by the short incubation time (only 4 h) and the very low concentration tested (1 μ M) that is not sufficient to trigger apoptosis by this drug in CT-26 cell line. Overall, compound **6** has an immediate effect on irradiated cells but not in the ones kept in the dark, resulting in disturbed mitochondrial respiration and glycolysis process.

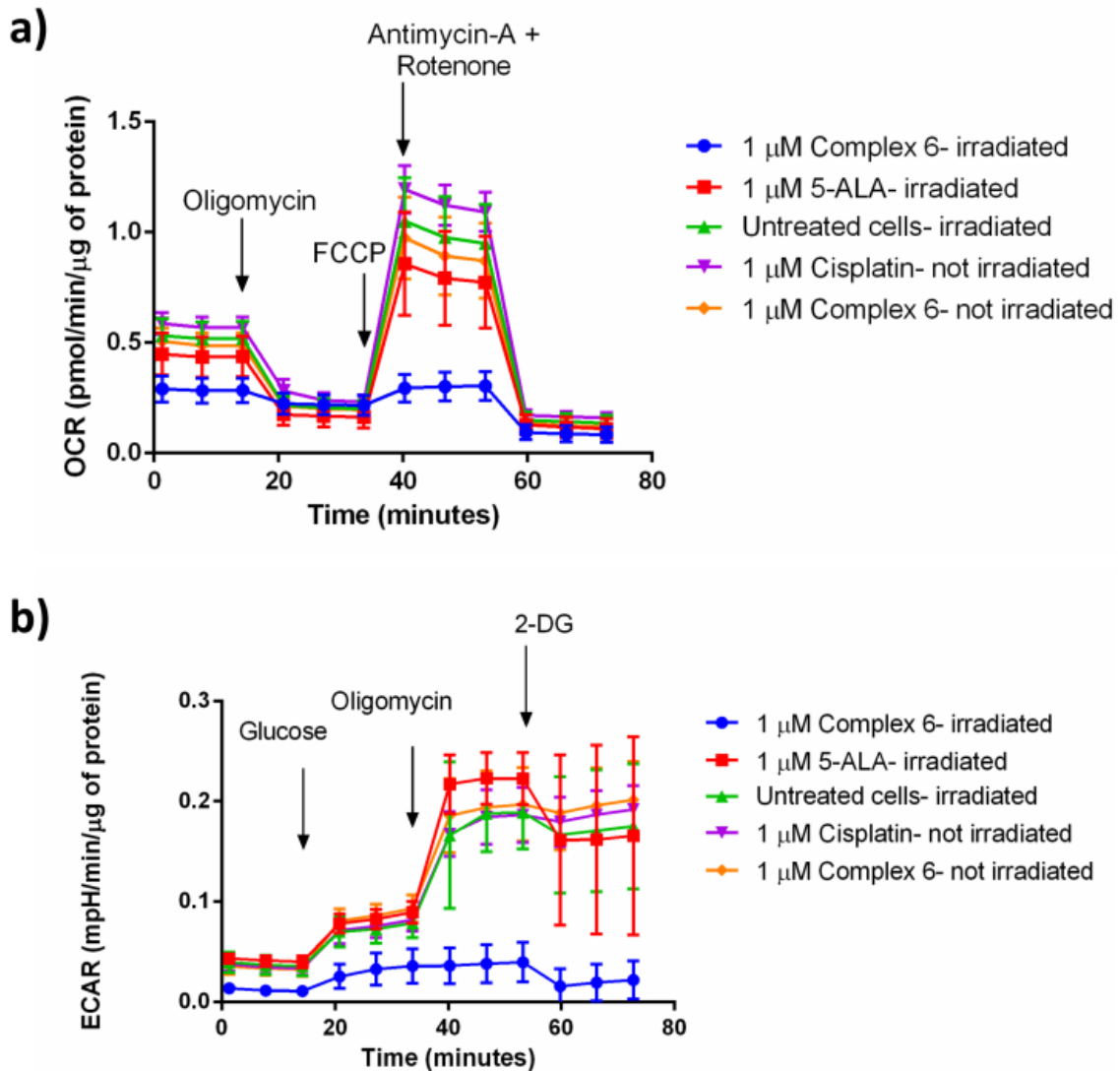


Figure 5. a) Mito Stress Test profile in CT-26 cells after 4 h treatment and 2 h irradiation at 595 nm; oxygen consumption rate changes after treatment with specific electron transport chain inhibitors, namely oligomycin (inhibitor of ATP synthase (complex V)), FCCP (uncoupling agent), antimycin-A (complex III inhibitor) and rotenone (complex I inhibitor). b) Glycolysis Stress Test profile in CT-26 cells after 4 h treatment and 2 h irradiation at 595 nm; extracellular acidification rate that corresponds to the glycolysis process changes after treatment with glucose (basal level of glycolysis in cells), oligomycin (inhibitor of ATP synthase (complex V)- mitochondria inhibition), 2-deoxyglucose (analog of glucose that inhibits glycolytic pathway).

After evaluation of the (photo-)cytotoxicity on 2D monolayer cells, the effect of complex **6** on multicellular tumor spheroids (MCTS) was investigated. This is of special interest as many anticancer drug candidates have failed the translation from monolayer cells to an *in vivo* model due to compromised drug delivery. MCTS are small spherical cell aggregates that mimic cell tumors. They can simulate the gradient of nutrients availability from upper cell layers, that are highly exposed, to lower layers and are able to model the potential penetration of a drug inside a 3D structure.^{66, 67} Therefore, compound **6** was incubated for 24 h in HeLa MCTS and its cytotoxic effect determined by measurement of the ATP concentration. Importantly, upon irradiation at 595 nm (2 h, 22.47 J cm⁻²), compound **6** showed a phototoxic effect (IC_{50, dark} = 29.42 ± 4.60 μM, IC_{50, 595nm} = 20.07 ± 4.15 μM, PI_{595nm} = 1.5), indicating that the compound is able to exert its action inside the 3D MCTS and act as a PDT agent.

Conclusion

In summary, we have combined the theoretical understanding provided by DFT calculations with the photophysical and biological experimental evaluation of Ru(II) polypyridine complexes as PSs for PDT. Thanks to this rational design, ruthenium complexes with a strong red shift in their absorption profile could be successfully prepared. While the (*E,E'*)-4,4'-bis(*N,N'*-dimethylaminovinyl)-2,2'-bipyridine coordinated complexes showed the desired red shift, they were however found to have poor photophysical properties (luminescence, ¹O₂ production) and poor stability. In contrast, the [Ru(bphen)₂(bmb)]²⁺ complex was found to have an absorption tail towards the biological spectral window. While being stable in human plasma as well as upon light irradiation, it was found to localize in the cytoplasm of HeLa cells. Upon irradiation at clinically relevant 595 nm it led to the disturbance of mitochondrial respiration and glycolysis process in 2D monolayer cells as well as 3D MCTS. We strongly believe that the rational design approach to unveil novel (metal-based) PDT PSs have a great potential in

the development of PSs for long-wavelength PDT. We are planning to investigate the *in vivo* efficiency of compound **6** in the future.

Acknowledgment

We thank Dr. Philippe Goldner for access to state-of-the-art laser apparatus. This work was financially supported by an ERC Consolidator Grant PhotoMedMet to G.G. (GA 681679) and has received support under the program “Investissements d’Avenir” launched by the French Government and implemented by the ANR with the reference ANR-10-IDEX-0001-02 PSL (G.G.). I.C and F.M. gratefully acknowledge the European Research Council (ERC) for funding (ERC Consolidator Grant STRIGES to I.C., GA No 648558).

Abbreviations

PDT, Photodynamic Therapy; PS, Photosensitiser; ROS, reactive oxygen species; $^1\text{O}_2$, singlet oxygen; dmb, 4,4'-dimethyl-2,2'-bipyridine; IP-TT, 2-(2',2'':5'',2' ''-terthiophene)-imidazol[4,5-f][1,10]phenanthroline; phen, 1,10-phenanthroline; bphen, 4,7-diphenyl-1,10-phenanthroline; bipy, 2,2'-bipyridine; MLCT, metal to ligand charge transfer; EDG, electron donating group; EWG, electron withdrawing group; LE, ligand centered; GS, ground state; ES, excited state; $^1\text{O}_2$, singlet oxygen; $\log P$, distribution coefficient; PI, phototoxic index; ICP-MS, inductively coupled plasma mass spectrometry; HeLa, human cervical carcinoma cell line; CT-26, mouse colon carcinoma cell line; U87 human glioblastoma cell line, U373, human glioblastoma astrocytoma cell line, RPE-1 retina pigmented epithelial cell line; MCTS, multicellular tumor spheroid.

References

1. D. E. Dolmans, D. Fukumura and R. K. Jain, *Nat. Rev. Cancer*, 2003, **3**, 380-387.
2. K. Plaetzer, B. Krammer, J. Berlanda, F. Berr and T. Kiesslich, *Lasers Med. Sci.*, 2009, **24**, 259-268.
3. S. Bonnet, *Dalton Transactions*, 2018.
4. R. Bonnett, *Chem. Soc. Rev.*, 1995, **24**, 19-33.
5. T. J. Dougherty, C. J. Gomer, B. W. Henderson, G. Jori, D. Kessel, M. Korbelik, J. Moan and Q. Peng, *JNCI: Journal of the national cancer institute*, 1998, **90**, 889-905.
6. B. W. Henderson and T. J. Dougherty, *Photochem. Photobiol.*, 1992, **55**, 145-157.
7. A. E. O'Connor, W. M. Gallagher and A. T. Byrne, *Photochem. Photobiol.*, 2009, **85**, 1053-1074.
8. F. Heinemann, J. Karges and G. Gasser, *Acc. Chem. Res.*, 2017, **50**, 2727-2736.
9. J. Karges, U. Basu, O. Blacque, H. Chao and G. Gasser, *Angew. Chem. Int. Ed.*, **0**.
10. P. Agostinis, K. Berg, K. A. Cengel, T. H. Foster, A. W. Girotti, S. O. Gollnick, S. M. Hahn, M. R. Hamblin, A. Juzeniene and D. Kessel, *CA Cancer J. Clin.*, 2011, **61**, 250-281.
11. S. Callaghan and M. O. Senge, *Photochemical & Photobiological Sciences*, 2018, **17**, 1490-1514.
12. C. Mari, V. Pierroz, S. Ferrari and G. Gasser, *Chem. Sci.*, 2015, **6**, 2660-2686.
13. S. Monro, K. L. Colón, H. Yin, J. Roque III, P. Konda, S. Gujar, R. P. Thummel, L. Lilge, C. G. Cameron and S. A. McFarland, *Chem. Rev.*, 2019, **119**, 797-828.
14. L. Zeng, P. Gupta, Y. Chen, E. Wang, L. Ji, H. Chao and Z.-S. Chen, *Chem. Soc. Rev.*, 2017, **46**, 5771-5804.
15. L. K. McKenzie, H. E. Bryant and J. A. Weinstein, *Coord. Chem. Rev.*, 2019, **379**, 2-29.

16. A. Li, C. Turro and J. J. Kodanko, *Acc. Chem. Res.*, 2018.
17. J. Liu, C. Zhang, T. W. Rees, L. Ke, L. Ji and H. Chao, *Coord. Chem. Rev.*, 2018, **363**, 17-28.
18. F. E. Poynton, S. A. Bright, S. Blasco, D. C. Williams, J. M. Kelly and T. Gunnlaugsson, *Chem. Soc. Rev.*, 2017, **46**, 7706-7756.
19. M. Jakubaszek, J. Rossier, J. Karges, J. Delasoie, B. Goud, G. Gasser and F. Zobi, *Helv. Chim. Acta*, 2019, **0**.
20. J. Shum, P. K.-K. Leung and K. K.-W. Lo, *Inorg. Chem.*, 2019, **58**, 2231-2247.
21. K. Qiu, Y. Chen, T. W. Rees, L. Ji and H. Chao, *Coord. Chem. Rev.*, 2017.
22. J. Karges, M. Jakubaszek, C. Mari, K. Zarschler, B. Goud, H. Stephan and G. Gasser, *ChemBioChem*, **0**.
23. R. Lincoln, L. Kohler, S. Monroe, H. Yin, M. Stephenson, R. Zong, A. Chouai, C. Dorsey, R. Hennigar, R. P. Thummel and S. A. McFarland, *J. Am. Chem. Soc.*, 2013, **135**, 17161-17175.
24. Y. Ellahioui, M. Patra, C. Mari, R. Kaabi, J. Karges, G. Gasser and S. Gómez-Ruiz, *Dalton Transactions*, 2019, **48**, 5940-5951.
25. B. S. Howerton, D. K. Heidary and E. C. Glazer, *J. Am. Chem. Soc.*, 2012, **134**, 8324-8327.
26. J. D. Knoll and C. Turro, *Coord. Chem. Rev.*, 2015, **282-283**, 110-126.
27. A. M. Palmer, B. Peña, R. B. Sears, O. Chen, M. E. Ojaimi, R. P. Thummel, K. R. Dunbar and C. Turro, *Philosophical Transactions of the Royal Society A: Mathematical, Physical and Engineering Sciences*, 2013, **371**, 20120135.
28. *Journal*, 2019.
29. J. Fong, K. Kasimova, Y. Arenas, P. Kaspler, S. Lazic, A. Mandel and L. Lilge, *Photochemical & Photobiological Sciences*, 2015, **14**, 2014-2023.

30. P. Kaspler, S. Lazic, S. Forward, Y. Arenas, A. Mandel and L. Lilge, *Photochem Photobiol Sci*, 2016, **15**, 481-495.
31. S. A. McFarland, A. Mandel, R. Dumoulin-White and G. Gasser, *Curr. Opin. Chem. Biol.*, 2020, **56**, 23-27.
32. S. M. Cloonan, R. B. P. Elmes, M. Erby, S. A. Bright, F. E. Poynton, D. E. Nolan, S. J. Quinn, T. Gunnlaugsson and D. C. Williams, *J. Med. Chem.*, 2015, **58**, 4494-4505.
33. J. Karges, O. Blacque, M. Jakubaszek, B. Goud, P. Goldner and G. Gasser, *J. Inorg. Biochem.*, 2019, **198**, 110752.
34. H. Yin, M. Stephenson, J. Gibson, E. Sampson, G. Shi, T. Sainuddin, S. Monro and S. A. McFarland, *Inorg. Chem.*, 2014, **53**, 4548-4559.
35. E. Wachter, D. K. Heidary, B. S. Howerton, S. Parkin and E. C. Glazer, *Chem. Commun.*, 2012, **48**, 9649-9651.
36. K. Ogawa and Y. Kobuke, *Anti-Cancer Agents in Medicinal Chemistry (Formerly Current Medicinal Chemistry-Anti-Cancer Agents)*, 2008, **8**, 269-279.
37. B. C. Wilson, W. P. Jeeves and D. M. Lowe, *Photochem. Photobiol.*, 1985, **42**, 153-162.
38. M. Eriksson, M. Leijon, C. Hiort, B. Norden and A. Graeslund, *J. Am. Chem. Soc.*, 1992, **114**, 4933-4934.
39. M. Dickerson, Y. Sun, B. Howerton and E. C. Glazer, *Inorg. Chem.*, 2014, **53**, 10370-10377.
40. H. Audi, D. Azar, F. Mahjoub, S. Farhat, Z. El-Masri, M. El-Sibai, R. J. Abi-Habib and R. S. Khnayzer, *J. Photochem. Photobiol. A: Chem.*, 2018, **351**, 59-68.
41. S. Mehanna, N. Mansour, H. Audi, K. Bodman-Smith, M. A. Mroueh, R. I. Taleb, C. F. Daher and R. S. Khnayzer, *RSC Advances*, 2019, **9**, 17254-17265.

42. N. Mansour, S. Mehanna, M. A. Mroueh, H. Audi, K. Bodman-Smith, C. F. Daher, R. I. Taleb, M. El-Sibai and R. S. Khnayzer, *Eur. J. Inorg. Chem.*, 2018, **2018**, 2524-2532.
43. S. Finck, J.-T. Issenhuth, S. Despax, C. Sirlin, M. Pfeffer, C. Poidevin, C. Gourlaouen, A. Boeglin and C. Daniel, *Journal of Organometallic Chemistry*, 2014, **760**, 248-259.
44. S. Campagna, F. Puntoriero, F. Nastasi, G. Bergamini and V. Balzani, in *Photochemistry and Photophysics of Coordination Compounds I*, eds. V. Balzani and S. Campagna, Springer Berlin Heidelberg, Berlin, Heidelberg, 2007, DOI: 10.1007/128_2007_133, pp. 117-214.
45. J. Karges, F. Heinemann, F. Maschietto, M. Patra, O. Blacque, I. Ciofini, B. Spingler and G. Gasser, *Biorg. Med. Chem.*, 2019, **27**, 2666-2675.
46. G. Crosby and W. Elfring Jr, *The Journal of Physical Chemistry*, 1976, **80**, 2206-2211.
47. W. E. Jones Jr, R. A. Smith, M. T. Abramo, M. D. Williams and J. Van Houten, *Inorg. Chem.*, 1989, **28**, 2281-2285.
48. O. Mazuryk, K. Magiera, B. Rys, F. Suzenet, C. Kieda and M. Brindell, *JBIC Journal of Biological Inorganic Chemistry*, 2014, **19**, 1305-1316.
49. W. Huang and T. Ogawa, *Polyhedron*, 2006, **25**, 1379-1385.
50. M. J. Cook, A. P. Lewis, G. S. McAuliffe, V. Skarda, A. J. Thomson, J. L. Glasper and D. J. Robbins, *Journal of the Chemical Society, Perkin Transactions 2*, 1984, 1293-1301.
51. V. Balzani and A. Juris, *Coord. Chem. Rev.*, 2001, **211**, 97-115.
52. O. Maury, J.-P. Guégan, T. Renouard, A. Hilton, P. Dupau, N. Sandon, L. Toupet and H. Le Bozec, *New J. Chem.*, 2001, **25**, 1553-1566.
53. J. Karges, O. Blacque, P. Goldner, H. Chao and G. Gasser, *Eur. J. Inorg. Chem.*, **0**.
54. J. Karges and G. Gasser, *Inorg. Chim. Acta*, 2019, DOI: <https://doi.org/10.1016/j.ica.2019.119196>, 119196.

55. J. Karges, P. Goldner and G. Gasser, *Inorganics*, 2019, **7**, 4.
56. A. A. Abdel-Shafi, P. D. Beer, R. J. Mortimer and F. Wilkinson, *Helv. Chim. Acta*, 2001, **84**, 2784-2795.
57. D. Garcia-Fresnadillo, Y. Georgiadou, G. Orellana, A. M. Braun and E. Oliveros, *Helv. Chim. Acta*, 1996, **79**, 1222-1238.
58. M. Patra, T. Joshi, V. Pierroz, K. Ingram, M. Kaiser, S. Ferrari, B. Spingler, J. Keiser and G. Gasser, *Chem. Eur. J.*, 2013, **19**, 14768-14772.
59. M. D. Hall, K. A. Telma, K.-E. Chang, T. D. Lee, J. P. Madigan, J. R. Lloyd, I. S. Goldlust, J. D. Hoeschele and M. M. Gottesman, *Cancer Res.*, 2014, **74**, 3913-3922.
60. S. Keller, Y. C. Ong, Y. Lin, K. Cariou and G. Gasser, *J. Organomet. Chem.*, 2019, DOI: <https://doi.org/10.1016/j.jorganchem.2019.121059>, 121059.
61. S. J. Bruce, I. Tavazzi, V. r. Parisod, S. Rezzi, S. Kochhar and P. A. Guy, *Anal. Chem.*, 2009, **81**, 3285-3296.
62. U. Basu, J. Karges, F. Chotard, C. Balan, P. Le Gendre, G. Gasser, E. Bodio and R. Malacea Kabbara, *Polyhedron*, 2019, DOI: <https://doi.org/10.1016/j.poly.2019.02.041>, doi.org/10.1016/j.poly.2019.1002.1041.
63. A. K. Renfrew, J. Karges, R. Scopelliti, F. D. Bobbink, P. Nowak-Sliwinska, G. Gasser and P. Dyson, *ChemBioChem*, 2019, **0**.
64. N. Alatrash, F. H. Issa, N. S. Bawazir, S. J. West, K. E. Van Manen-Brush, C. P. Shelor, A. S. Dayoub, K. A. Myers, C. Janetopoulos, E. A. Lewis and F. M. MacDonnell, *Chemical Science*, 2019, DOI: 10.1039/C9SC05671H.
65. K. Mahmoudi, K. L. Garvey, A. Bouras, G. Cramer, H. Stepp, J. G. Jesu Raj, D. Bozec, T. M. Busch and C. G. Hadjipanayis, *J. Neurooncol.*, 2019, **141**, 595-607.
66. J. Friedrich, C. Seidel, R. Ebner and L. A. Kunz-Schughart, *Nat. Protoc.*, 2009, **4**, 309.
67. T. T. Goodman, C. P. Ng and S. H. Pun, *Bioconjugate Chem.*, 2008, **19**, 1951-1959.

Supplementary Information

Rationally Designed Long-Wavelength Absorbing Ru(II) Polypyridyl Complexes as Photosensitizers for Photodynamic Therapy

Johannes Karges,[†] Franz Heinemann,^{†,‡} Marta Jakubaszek,^{†,¶} Federica Maschietto,[§] Chloé Subecz,[†] Mazzarine Dotou,[†] Olivier Blacque,[‡] Mickaël Tharaud,[§] Bruno Goud,[¶] Emilio Viñuelas Zahinos,[⊥] Bernhard Spingler,^{‡,} Ilaria Ciofini,^{§,*} and Gilles Gasser^{†,*}*

[†] Chimie ParisTech, PSL University, CNRS, Institute of Chemistry for Life and Health Sciences, Laboratory for Inorganic Chemical Biology, 75005 Paris, France.

[‡] Department of Chemistry, University of Zurich, Winterthurerstrasse 190, 8057, Zurich, Switzerland.

[¶] Institut Curie, PSL University, CNRS UMR 144, 75005 Paris, France.

[§] Chimie ParisTech, PSL University, CNRS, Institute of Chemistry for Life and Health Sciences, Theoretical Chemistry and Modelling, 75005 Paris, France.

[§] Université de Paris, Institut de physique du globe de Paris, CNRS, F-75005 Paris, France.

[⊥] Departamento de Química Orgánica e Inorgánica, Facultad de Ciencias, Universidad de Extremadura, 06071 Badajoz, Spain.

* Corresponding authors: spingler@chem.uzh.ch ; Ilaria.ciofini@chimieparistech.psl.eu; gilles.gasser@chimieparistech.psl.eu; www.gassergroup.com; Tel. +33 1 44 27 56 02.

Table of Contents

EXPERIMENTAL SECTION	265
COMPUTATIONAL DETAILS	265
MATERIALS	266
INSTRUMENTATION AND METHODS	267
SYNTHESIS	267
(1) <i>[Ru(bpy)(phen)₂](PF₆)₂</i>	267
(2) <i>[Ru(dmb)(phen)₂](PF₆)₂</i>	268
(3) <i>[Ru(Br-bpy)(phen)₂](PF₆)₂</i>	269
(4) <i>[Ru(CONH₂-bpy)(phen)₂](PF₆)₂</i>	270
(5) <i>[Ru(Me₂Nvin-bpy)(phen)₂](PF₆)₂</i>	271
(6) <i>[Ru(dmb)(bphen)₂](PF₆)₂</i> <.....	272
(7) <i>[Ru(Me₂Nvin-bipy)(bphen)₂](PF₆)₂</i>	273
X-RAY CRYSTALLOGRAPHY	274
SPECTROSCOPIC MEASUREMENTS	275
LIFETIME MEASUREMENTS	275
LUMINESCENCE QUANTUM YIELD MEASUREMENTS	276
SINGLET OXYGEN MEASUREMENTS	277
- <i>direct evaluation</i>	277
- <i>indirect evaluation</i>	278
STABILITY IN DMSO	279
STABILITY IN HUMAN PLASMA	279
PHOTOSTABILITY	280
DISTRIBUTION COEFFICIENT	280
CELL CULTURE	281
CELLULAR UPTAKE	281
(PHOTO-)CYTOTOXICITY	281
CELLULAR LOCALISATION	282

<i>Time dependent localisation of complex 6</i>	282
<i>Indirect Immunofluorescence</i>	283
SEAHORSE MITO STRESS TEST	283
SEAHORSE GLYCOLYSIS STRESS TEST	284
GENERATION OF 3D HeLA MCTS	284
(PHOTO-)CYTOTOXICITY IN 3D HeLA MCTS	285
SUPPORTING FIGURES AND TABLES	286
TABLE S1. CARTESIAN COORDINATES OF THE OPTIMIZED STRUCTURE OF COMPLEX 1	286
TABLE S2. CARTESIAN COORDINATES OF THE OPTIMIZED STRUCTURE OF COMPLEX 2	289
TABLE S3. CARTESIAN COORDINATES OF THE OPTIMIZED STRUCTURE OF COMPLEX 3	292
TABLE S4. CARTESIAN COORDINATES OF THE OPTIMIZED STRUCTURE OF COMPLEX 4	295
TABLE S5. CARTESIAN COORDINATES OF THE OPTIMIZED STRUCTURE OF COMPLEX 5	298
TABLE S6. CARTESIAN COORDINATES OF THE OPTIMIZED STRUCTURE OF COMPLEX 6	302
TABLE S7. CARTESIAN COORDINATES OF THE OPTIMIZED STRUCTURE OF COMPLEX 7	307
SCHEME S1. SYNTHESIS OF THE DESIRED COMPLEXES 1-7	313
FIGURE S1. ¹H NMR SPECTRUM OF 1 IN CD₃CN, 500 MHz	314
FIGURE S2. ¹³C NMR SPECTRUM OF 1 IN CD₃CN, 125 MHz	315
FIGURE S3. ¹H NMR SPECTRUM OF 2 IN CD₃CN, 400 MHz	316
FIGURE S4. ¹³C NMR SPECTRUM OF 2 IN CD₃CN, 100 MHz	317
FIGURE S5. ¹H NMR SPECTRUM OF 3 IN CD₃CN, 500 MHz	318
FIGURE S6. ¹³C NMR SPECTRUM OF 3 IN CD₃CN, 125 MHz	319
FIGURE S7. ¹H NMR SPECTRUM OF 4 IN CD₃CN, 400 MHz	320
FIGURE S8. ¹³C NMR SPECTRUM OF 4 IN CD₃CN, 100 MHz	321
FIGURE S9. ¹H NMR SPECTRUM OF 5 IN CD₃CN, 400 MHz	322
FIGURE S10. ¹³C NMR SPECTRUM OF 5 IN CD₃CN, 125 MHz	323
FIGURE S11. ¹H NMR SPECTRUM OF 6 IN CD₃CN, 400 MHz	324
FIGURE S12. ¹³C NMR SPECTRUM OF 6 IN CD₃CN, 125 MHz	325
FIGURE S13. ¹H NMR SPECTRUM OF 7 IN CD₃CN, 500 MHz	326

FIGURE S14. ¹ H NMR SPECTRUM OF 7 IN CD ₃ CN, 125 MHz.....	327
FIGURE S15. THE MOLECULAR STRUCTURE OF 1 WITH DISPLACEMENT ELLIPSOIDS	328
FIGURE S16. THE MOLECULAR STRUCTURE OF 2 WITH DISPLACEMENT ELLIPSOIDS	329
FIGURE S17. THE MOLECULAR STRUCTURE OF 3 WITH DISPLACEMENT ELLIPSOIDS	330
TABLE S8. CRYSTAL DATA AND STRUCTURE REFINEMENT PARAMETERS FOR 1 AND 2	331
TABLE S9. CRYSTAL DATA AND STRUCTURE REFINEMENT PARAMETERS FOR 3	333
FIGURE S18. DIFFERENCE DENSITY PLOTS CALCULATED BETWEEN ES AND GS COMPUTED FOR THE FIRST VERTICAL TRANSITION AND THE FIRST BRIGHT STATE MLCT TRANSITION OF 6 AND 7	335
TABLE S10. SPECTROSCOPIC PROPERTIES OF COMPLEXES 1-7 IN CH ₃ CN AT ROOM TEMPERATURE.....	336
FIGURE S19. MEASURED UV/VIS SPECTRA OF THE COMPLEXES 1-7 IN CH ₃ CN.	337
FIGURE S20. NORMALISED EMISSION SPECTRA OF THE COMPLEXES 1-7 IN CH ₃ CN.	337
FIGURE S21. LIFETIME SPECTRA OF THE COMPLEXES 1 IN AERATED AND DEGASSED) CH ₃ CN.	338
FIGURE S22. LIFETIME SPECTRA OF THE COMPLEXES 2 IN AERATED AND DEGASSED CH ₃ CN.	339
FIGURE S23. LIFETIME SPECTRA OF THE COMPLEXES 3 IN AERATED AND DEGASSED CH ₃ CN.	340
FIGURE S24. LIFETIME SPECTRA OF THE COMPLEXES 4 IN AERATED AND DEGASSED CH ₃ CN.	341
FIGURE S25. LIFETIME SPECTRA OF THE COMPLEXES 5 IN AERATED AND DEGASSED CH ₃ CN.	342
FIGURE S26. LIFETIME SPECTRA OF THE COMPLEXES 6 IN AERATED AND DEGASSED CH ₃ CN.	343
FIGURE S27. LIFETIME SPECTRA OF THE COMPLEXES 7 IN AERATED AND DEGASSED CH ₃ CN.	344
TABLE S11. SINGLET OXYGEN QUANTUM YIELDS ($\Phi(^1\text{O}_2)$) IN CH ₃ CN AND AQUEOUS SOLUTION DETERMINED BY DIRECT AND INDIRECT METHODS BY EXCITATION AT 450 NM.....	345
FIGURE S28. ¹ H NMR SPECTRUM OF 1 IN DMSO-D ₆ AFTER PREPARATION AND 7 DAYS.	346
FIGURE S29. ¹ H NMR SPECTRUM OF 2 IN DMSO-D ₆ AFTER PREPARATION AND 7 DAYS.	347
FIGURE S30. ¹ H NMR SPECTRUM OF 3 IN DMSO-D ₆ AFTER PREPARATION AND 7 DAYS.	348
FIGURE S31. ¹ H NMR SPECTRUM OF 4 IN DMSO-D ₆ AFTER PREPARATION AND 7 DAYS.	349
FIGURE S32. ¹ H NMR SPECTRUM OF 5 IN DMSO-D ₆ AFTER PREPARATION, 1 DAY, 2 DAYS AND 7 DAYS.....	350
FIGURE S33. ¹ H NMR SPECTRUM OF 6 IN DMSO-D ₆ AFTER PREPARATION AND 7 DAYS.	351
FIGURE S34. ¹ H NMR SPECTRUM OF 7 IN DMSO-D ₆ AFTER PREPARATION, 1 DAY, 2 DAYS AND 7 DAYS	352
FIGURE S35. HPLC CHROMATOGRAM OF CAFFEINE AND 1 AFTER 48 H INCUBATION IN HUMAN POOLED PLASMA.....	353

FIGURE S36. HPLC CHROMATOGRAM OF CAFFEINE AND 2 AFTER 48 H INCUBATION IN HUMAN POOLED PLASMA.	353
FIGURE S37. HPLC CHROMATOGRAM OF CAFFEINE AND 3 AFTER 48 H INCUBATION IN HUMAN POOLED PLASMA.	354
FIGURE S38. HPLC CHROMATOGRAM OF CAFFEINE AND 4 AFTER 48 H INCUBATION IN HUMAN POOLED PLASMA.	354
FIGURE S39. HPLC CHROMATOGRAM OF CAFFEINE AND 5 AFTER 0 H, 4 H, 12 H, 24 H AND 48 H INCUBATION IN HUMAN POOLED PLASMA.	355
FIGURE S40. HPLC CHROMATOGRAM OF CAFFEINE AND 6 AFTER 48 H INCUBATION IN HUMAN POOLED PLASMA.	356
FIGURE S41. HPLC CHROMATOGRAM OF CAFFEINE AND 7 AFTER 0 H, 4 H, 12 H, 24 H AND 48 H INCUBATION IN HUMAN POOLED PLASMA.	357
FIGURE S42. TEMPORAL CHANGE OF THE UV/VIS SPECTRA OF [RU(BIPY)₃]CL₂ BY IRRADIATION AT 450 NM IN CH₃CN.	358
FIGURE S43. TEMPORAL CHANGE OF THE UV/VIS SPECTRA OF COMPLEX 1 BY IRRADIATION AT 450 NM IN CH₃CN.	359
FIGURE S44. TEMPORAL CHANGE OF THE UV/VIS SPECTRA OF COMPLEX 2 BY IRRADIATION AT 450 NM IN CH₃CN.	359
FIGURE S45. TEMPORAL CHANGE OF THE UV/VIS SPECTRA OF COMPLEX 3 BY IRRADIATION AT 450 NM IN CH₃CN.	360
FIGURE S46. TEMPORAL CHANGE OF THE UV/VIS SPECTRA OF COMPLEX 4 BY IRRADIATION AT 450 NM IN CH₃CN.	360
FIGURE S47. TEMPORAL CHANGE OF THE UV/VIS SPECTRA OF COMPLEX 5 BY IRRADIATION AT 450 NM IN CH₃CN.	361
FIGURE S48. TEMPORAL CHANGE OF THE UV/VIS SPECTRA OF COMPLEX 6 BY IRRADIATION AT 450 NM IN CH₃CN.	361
FIGURE S49. TEMPORAL CHANGE OF THE UV/VIS SPECTRA OF COMPLEX 7 BY IRRADIATION AT 450 NM IN CH₃CN.	362
FIGURE S50. TEMPORAL CHANGE OF THE UV/VIS SPECTRA OF PROTOPORPHYRIN IX BY IRRADIATION AT 450 NM IN CH₃CN.	362

TABLE S12. DISTRIBUTION COEFFICIENTS OF 1-7 BETWEEN AN ORGANIC OCTANOL AND AQUEOUS PHOSPHATE BUFFER SALINE PHASE.	363
FIGURE S51. COMPARISON OF THE CELLULAR UPTAKE OF COMPLEXES 1-7 AFTER 4 H INCUBATION IN HELa CELLS.	364
FIGURE S52. TIME-DEPENDENT ACCUMULATION OF COMPLEX 6 (14 μ M) IN HELa CELL LINE.	365
FIGURE S53. PLATE ARRANGEMENT FOR SEAHORSE MITO STRESS AND GLYCOLYSIS STRESS EXPERIMENTS.	366
FIGURE S54. OXYGEN CONSUMPTION RATES AND DIFFERENT RESPIRATION PARAMETERS IN CT-26 CELLS ALONE OR AFTER TREATMENT WITH VARIOUS TEST COMPOUNDS.	367
FIGURE S55. EXTRACELLULAR ACIDIFICATION RATES AND DIFFERENT GLYCOLYSIS PARAMETERS IN CT-26 CELLS ALONE OR AFTER TREATMENT WITH VARIOUS TEST COMPOUNDS.	368
REFERENCES.	369

EXPERIMENTAL SECTION

Computational Details

All calculations were performed using the Gaussian 09¹ software package. All calculations were performed using the Los Alamos LANL2² effective core potential and the corresponding triple-zeta basis set for the Ruthenium atom, with all other atoms treated with the Pople double-zeta basis set with a single set of polarisation and diffuse functions on non-hydrogen atoms (6-31+G(d)^{3, 4}. Solvent effects (here acetonitrile) were included using an implicit model (i.e. the Polarizable Continuum Model – PCM⁵. All geometry optimisations were performed using density functional theory (DFT) with the global hybrid B3LYP⁶ exchange-correlation functional and all minima on the potential energy surface were verified via a calculation of vibrational frequencies, ensuring no imaginary frequencies were present. Excited states of all compounds (as shown in Scheme 1) were probed using time dependent density functional theory (TD-DFT⁷) combined with the same exchange correlation functional and basis set. All transitions (singlet-singlet) were calculated vertically with respect to the singlet ground state. Absorption spectra were simulated by convolution with Gaussian functions with a full width at half maximum (FWHM) of 0.3 eV. In order to characterize the nature of the lowest energy states of interest (see discussion), relaxed excited state density was also computed together with the corresponding associated charge transfer distance (D_{CT})⁸. In brief the D_{CT} index provides a measure of the spatial extent of a given transition and yields a coherent representation of the charge rearrangements occurring upon generation of the exciton based on the ground and excited states density distributions. Details on how to calculate the D_{CT} index are reported in refs.^{8, 9}

Materials

All chemicals were obtained from commercial sources and were used without further purification. Solvents were dried over molecular sieves if necessary. The Ru(II) complexes dichlorobis(1,10-phenanthroline)ruthenium(II) [RuCl₂(phen)₂] and dichlorobis(4,7-Diphenyl-1,10-phenanthroline)ruthenium(II) [RuCl₂(bphen)₂] were synthesised as previously published using the respective ligands.¹⁰ The substituted bipyridine ligands 2,2'-bipyridine-4,4'-dicarbonitrile¹¹ and (*E,E'*)-4,4'-bis(*N,N*-dimethylaminovinyl)-2,2'-bipyridine¹² were synthesised as previously reported.

Instrumentation and methods

^1H and ^{13}C NMR spectra were recorded on a Bruker 400 MHz or Bruker 500 MHz NMR spectrometer. Chemical shifts (δ) are reported in parts per million (ppm) referenced to tetramethylsilane (δ 0.00) ppm using the residual proton solvent peaks as internal standards. Coupling constants (J) are reported in Hertz (Hz) and the multiplicity is abbreviated as follows: s (singlet), d (doublet), dd (doublet of doublet), t (triplet), m (multiplet). ESI mass spectra were recorded on a Bruker ESQUIRE-LC quadrupole ion trap spectrometer. Elemental microanalyses were performed on a LecoCHNS-932 elemental analyser or a Thermo Flash 2000 elemental analyser. Inductively coupled plasma mass spectrometry (ICP-MS) experiments were carried out on HR-ICP-MS Element II (Thermo Scientific) apparatus.

Synthesis

Proton and carbon NMR spectra can be found in the supplemental information (Figures S1-14).

(1) **[Ru(bpy)(phen)₂](PF₆)₂**

(2,2'-Bipyridine)bis(1,10-phenanthroline)ruthenium(II)hexafluorophosphate

The synthesis of [Ru(bpy)(phen)₂](PF₆)₂ is already published¹³ but in this study another synthetic route was employed. RuCl₂(phen)₂ (150 mg, 0.28 mmol, 1.0 equiv.) and 2,2'-bipyridine (48 mg, 0.31 mmol, 1.1 equiv.) were dissolved in 8 mL MeOH and refluxed for 18 h under N₂ atmosphere. After this time, the volume of the brown mixture was reduced to 1/4. A saturated, aq. NH₄PF₆ solution was added and the resulting precipitate was collected by vacuum filtration and washed with H₂O (50 mL) and Et₂O (50 mL). The product was dried in high vacuum. Yield: 51%. ^1H NMR (500 MHz, CD₃CN) δ = 8.65 (dd, 2H, J = 8.3, 1.3 Hz), 8.55 (dd, 2H, J = 8.2, 1.3 Hz), 8.52 (d, 2H, J = 8.3 Hz), 8.26 (d, 2H, J = 8.9 Hz), 8.23 (d, 2H, J = 8.9 Hz), 8.20 (d, 2H, J = 5.2 Hz), 8.03 (td, 2H, J = 8.1, 1.4 Hz), 7.88 (dd, 2H, J = 5.3, 1.2 Hz), 7.79 (dd,

2H, $J = 8.3, 5.2$ Hz), 7.67 (d, 2H, $J = 5.6$ Hz), 7.56 (dd, 2H, $J = 8.2, 5.3$ Hz), 7.27 (ddd, 2H, $J = 7.3, 5.6, 1.3$ Hz); ^{13}C NMR (125 MHz, CD_3CN) $\delta = 158.3, 153.8, 153.6, 153.2, 148.8, 148.6, 138.7, 137.8, 137.7, 132.0, 132.0, 129.0, 129.0, 128.3, 127.0, 126.8, 125.1$; HRMS (ESI⁺ m/z): Calcd. for $[\text{C}_{34}\text{H}_{24}\text{F}_{12}\text{N}_6\text{P}_2\text{Ru}-2\text{PF}_6]^{2+}$: 309.05478, Found: 309.05475, Calcd. for $[\text{C}_{34}\text{H}_{24}\text{F}_{12}\text{N}_6\text{P}_2\text{Ru}-\text{PF}_6]^+$: 763.07423, Found: 763.07434; Anal. Calcd. for $\text{C}_{34}\text{H}_{24}\text{F}_{12}\text{N}_6\text{P}_2\text{Ru}$: C, 44.99; H, 2.67; N, 9.26, Found: C, 44.69; H, 2.61; N 9.25.

(2) [Ru(dmb)(phen)₂](PF₆)₂

(4,4'-Dimethyl-2,2'-bipyridine)bis(1,10-phenanthroline)ruthenium(II)

hexafluorophosphate

The synthesis of $[\text{Ru}(\text{dmb})(\text{phen})_2](\text{PF}_6)_2$ is already published¹⁴ but in this study another synthetic route was employed. $\text{RuCl}_2(\text{phen})_2$ (150 mg, 0.28 mmol, 1.0 equiv.) and 4,4'-dimethyl-2,2'-bipyridine (57 mg, 0.31 mmol, 1.1 equiv.) were dissolved in a 1:1 mixture of $\text{H}_2\text{O}/\text{EtOH}$ (7 mL) and were refluxed for 18 h under N_2 atmosphere. The solvent was evaporated to one third of the volume and a saturated, aq. NH_4PF_6 solution was added. The resulting precipitate was collected by vacuum filtration and washed with H_2O (50 mL) and Et_2O (50 mL). The product was dried in high vacuum. Yield: 97%. ^1H NMR (400 MHz, CD_3CN) $\delta = 8.64$ (dd, 2H, $J = 8.3, 1.3$ Hz), 8.53 (dd, 2H, $J = 8.3, 1.3$ Hz), 8.37 (s, 2H), 8.25 (d, 2H, $J = 8.9$ Hz), 8.22 (d, 2H, $J = 8.9$ Hz) 8.20 (dd, $J = 5.3, 1.3$ Hz), 7.88 (dd, 2H, $J = 5.3, 1.3$ Hz), 7.79 (dd, 2H, $J = 8.3, 5.3$ Hz), 7.54 (dd, 2H, $J = 8.2, 5.3$ Hz), 7.47 (d, 2H, $J = 5.8$ Hz), 7.10 (dd, 2H, $J = 5.8, 1.2$ Hz), 2.51 (s, 6H); ^{13}C NMR (100 MHz, CD_3CN) $\delta = 157.8, 153.6, 153.6, 152.2, 151.3, 148.9, 148.7, 137.6, 137.5, 131.9, 131.9, 129.0, 129.0, 129.0, 126.9, 126.8, 125.8, 21.2$; HRMS (ESI⁺ m/z): Calcd. for $[\text{C}_{36}\text{H}_{28}\text{F}_{12}\text{N}_6\text{P}_2\text{Ru}-2\text{PF}_6]^{2+}$: 323.07040, Found: 323.07040; Anal. Calcd. for $\text{C}_{36}\text{H}_{28}\text{F}_{12}\text{N}_6\text{P}_2\text{Ru}+2\text{H}_2\text{O}$: C, 44.50; H, 3.32; N, 8.65, Found: C, 44.43; H, 3.08; N, 8.52.

(3) [Ru(Br-bpy)(phen)₂](PF₆)₂

(4,4'-Dibromo-2,2'-bipyridine)bis(1,10-phenanthroline)ruthenium(II)

hexafluorophosphate

RuCl₂(phen)₂ (150 mg, 0.28 mmol, 1.0 equiv.) and 4,4'-Dibromo-2,2'-bipyridine (105 mg, 0.34 mmol, 1.2 equiv.) were dissolved in a 1:1 mixture of H₂O/EtOH (40 mL) and were refluxed for 18 h under N₂ atmosphere. The solvent was evaporated and the residue redissolved in 5 mL of H₂O. A saturated, aq. NH₄PF₆ solution was added and the resulting precipitate was collected by vacuum filtration. The solid was washed with H₂O (50 mL) and Et₂O (50 mL). The product was isolated by column chromatography on silica gel with an CH₃CN/aq. KNO₃ (0.4 M) solution (10:1). The fractions containing the product were united and the solvent was removed. The residue was dissolved in CH₃CN and undissolved KNO₃ was removed by filtration. The solvent was removed and the product was dissolved in H₂O (50 mL). Upon addition of NH₄PF₆ the product precipitated as a PF₆ salt. The solid was obtained by filtration and was washed with H₂O (50 mL) and Et₂O (50 mL). The product was dried in high vacuum. Yield: 78%. ¹H NMR (500 MHz, CD₃CN) δ = 8.76 (2H, d, *J* = 2.0 Hz), 8.68 (2H, dd, *J* = 8.3, 1.3 Hz), 8.55 (2H, dd, *J* = 8.3, 1.3 Hz), 8.27 (2H, d, *J* = 8.9 Hz), 8.25 (2H, dd, *J* = 5.3, 1.3 Hz), 8.22 (2H, d, *J* = 8.9 Hz), 7.84 (2H, dd, *J* = 5.3, 1.3 Hz), 7.81 (2H, dd, *J* = 8.3, 5.2 Hz), 7.55 (2H, dd, *J* = 8.3, 5.3 Hz), 7.50 (2H, d, *J* = 6.1 Hz), 7.47 (2H, dd, *J* = 6.1, 2.0 Hz). ¹³C NMR (125 MHz, CD₃CN) δ = 158.3, 154.0, 153.9, 153.6, 148.7, 148.4, 138.0, 137.9, 134.7, 132.0, 132.0, 131.7, 129.1, 129.0, 129.0, 127.0, 126.9. HR-MS (ESI⁺ *m/z*): Calcd. [M-2PF₆]²⁺: 386. 96526; found: 386. 96576. Anal. (%): Calcd. for (C₃₄H₂₂Br₂F₁₂N₆P₂Ru): C 38.33, H 2.08, N 7.89; found. C 38.62, H 2.01, N 7.78.

(4) [Ru(CONH2-bpy)(phen)₂](PF₆)₂

(2,2'-bipyridine-4,4'-carboxamide)bis(1,10-phenanthroline)ruthenium(II)

hexafluorophosphate

RuCl₂(phen)₂ (150 mg, 0.28 mmol, 1.0 equiv.) and 2,2'-Bipyridine-4,4'-dicarbonitrile (64 mg, 0.31 mmol, 1.1 equiv.) were dissolved in a 1:1 mixture of H₂O/EtOH (30 mL) and were refluxed for 18 h under N₂ atmosphere. The solvent was evaporated and the residue redissolved in 5 mL of H₂O. A saturated, aq. NH₄PF₆ solution was added and the resulting precipitate was collected by vacuum filtration. The solid was washed with H₂O (50 mL) and Et₂O (50 mL). The product was purified by column chromatography on silica gel with an CH₃CN /aq. KNO₃ (0.4 M) solution (10:1). The fractions containing the product were united and the solvent was removed. The residue was dissolved in CH₃CN and undissolved KNO₃ was removed by filtration. The solvent was removed again and the product was dissolved in H₂O (50 mL). Upon addition of NH₄PF₆ the product precipitated as a PF₆ salt. The solid was obtained by filtration and was washed with H₂O (50 mL) and Et₂O (50 mL). The product was dried in high vacuum. Yield: 16%. ¹H NMR (400 MHz, CD₃CN) δ = 8.97 (2H, s), 8.67 (2H, d, *J* = 8.3 Hz), 8.58 (2H, d, *J* = 8.3 Hz), 8.30-8.22 (4H, m), 8.18 (2H, d, *J* = 5.2 Hz), 7.87-7.84 (4H, m), 7.79 (2H, dd, *J* = 8.3, 5.2 Hz), 7.61-7.57 (4H, m), 7.25 (2H, s), 6.48 (2H, s). ¹³C NMR (100 MHz, CD₃CN) δ = 165.7, 158.8, 154.0, 153.9, 153.5, 148.6, 148.3, 143.0, 138.2, 138.0, 132.1, 132.0, 129.1, 129.0, 127.0, 127.0, 126.0, 123.1. HR-MS (ESI⁺ *m/z*): Calcd. [M-2PF₆]²⁺ : 352.06056; found: 352.06063. Anal. (%): Calcd. for (C₃₆H₂₆F₁₂N₈O₂P₂Ru): C 43.52, H 2.64, N 11.28; found. C 43.33, H 2.47, N 11.15.

(5) [Ru(Me₂Nvin-bpy)(phen)₂](PF₆)₂

((*E,E'*)-4,4'-Bis(*N,N'*-dimethylaminovinyl)-2,2'-bipyridine)bis(1,10-phenanthroline)

ruthenium(II) hexafluorophosphate

[Ru(dmb)(phen)₂](PF₆)₂ (**2**) (100 mg, 0.11 mmol, 1.0 equiv.) was dissolved in dry DMF (1.5 mL) and *tert*-butoxy bis(dimethylamino)methane (0.2 mL, 0.97 mmol, 8.8 equiv.) was added. The mixture was heated at 140 °C for 16 h under N₂ atmosphere. The solution was cooled down and an aq. solution of NH₄PF₆ was added. The resulting precipitate was collected by vacuum filtration and the solid was washed with H₂O (50 mL) and Et₂O (50 mL). The product was isolated via fractionated precipitation from CH₃CN by adding dropwise Et₂O and afterwards dried in high vacuum. Yield: 41%. ¹H NMR (400 MHz, CD₃CN) δ = 8.61 (2H, dd, *J* = 8.3, 1.3 Hz), 8.48 (2H, dd, *J* = 8.3, 1.3 Hz), 8.38 (2H, dd, *J* = 5.3, 1.3 Hz), 8.24 (2H, d, *J* = 8.9 Hz), 8.19 (2H, *J* = 9.0 Hz), 8.08 (2H, d, *J* = 2.2 Hz), 7.87 (2H, dd, *J* = 5.3, 1.3 Hz), 7.82 (2H, dd, *J* = 8.2 Hz, 5.3 Hz), 7.52 (2H, dd, *J* = 8.2 Hz, 5.3 Hz), 7.51 (2H, d, *J* = 13.3 Hz), 6.99 (2H, d, *J* = 6.2 Hz), 6.77 (2H, dd, *J* = 6.2, 2.1 Hz), 5.08 (2H, d, *J* = 13.4 Hz), 2.94 (12H, s). ¹³C NMR (100 MHz, CD₃CN) δ = 157.6, 153.5, 153.5, 151.6, 150.6, 149.2, 149.1, 147.8, 137.0, 137.0, 131.9, 131.9, 129.0, 129.0, 126.9, 126.7, 120.3, 117.1, 92.9, 40.1. HR-MS (ESI⁺ *m/z*): Calcd. [M-2PF₆]²⁺: 378.11260; found: 378.11289. Anal. (%): Calcd. for (C₄₂H₃₈F₁₂N₈P₂Ru): C 48.24, H 3.66, N 10.71; found: C 47.97, H 3.59, N 10.76.

(6) [Ru(dmb)(bphen)₂](PF₆)₂·

(4,4'-Dimethyl-2,2'-bipyridine)bis(4,7-diphenyl-1,10-phenanthroline)ruthenium(II)

hexafluorophosphate

The synthesis of [Ru(dmb)(bphen)₂](PF₆)₂ is already published¹⁵ but in this study another synthetic route was employed. RuCl₂(bphen)₂ (200 mg, 0.24 mmol, 1.0 equiv.) and 4,4'-Dimethyl-2,2'-bipyridine (53 mg, 0.29 mmol, 1.2 equiv.) were dissolved in a 1:1 mixture of H₂O/EtOH (10 mL) and were refluxed for 18 h under N₂ atmosphere. The solvent was evaporated and the residue redissolved in 10 mL of H₂O. A saturated, aq. NH₄PF₆ solution was added and the suspension was sonicated. 60 mL of H₂O were added and the resulting precipitate was collected by vacuum filtration. The solid was washed with H₂O (50 mL) and Et₂O (50 mL). The product was dried in high vacuum. Yield: 93%. ¹H NMR (400 MHz, CD₃CN) δ = 8.44 (2H, s), 8.29 (2H, d, *J* = 5.5 Hz), 8.22-8.16 (m, 4H), 8.10 (2H, d, *J* = 5.5 Hz), 7.75 (2H, d, *J* = 5.5 Hz), 7.72 – 7.53 (24H, m), 7.21 (2H, d, *J* = 5.8, *J* = 1.7 Hz), 2.56 (6H, s). ¹³C NMR (125 MHz, CD₃CN) δ = 157.7, 153.1, 152.9, 152.2, 151.4, 149.9, 149.8, 149.5, 149.4, 136.7, 136.7, 130.8, 130.7, 130.7, 130.6, 130.6, 130.1, 130.1, 130.1, 129.9, 129.9, 129.1, 127.1, 127.0, 127.0, 126.9, 125.8, 21.3. HR-MS (ESI⁺ *m/z*): Calcd. [M-2PF₆]²⁺: 475.13300; found: 475.13388. Anal. (%): Calcd. (C₆₀H₄₄F₁₂N₆P₂Ru)·(H₂O)₂: C 56.47, H 3.79, N 6.59; found: C 56.46, H 3.85, N 6.11.

(7) [Ru(Me₂Nvin-bipy)(bphen)₂](PF₆)₂

((*E,E'*)-4,4'-Bis(*N,N'*-dimethylaminovinyl)-2,2'-bipyridine)bis(4,7-diphenyl-1,10-phenanthroline)ruthenium(II) hexafluorophosphate

[Ru(dmb)(bphen)₂](PF₆)₂ (**7**) (150 mg, 0.12 mmol, 1.0 equiv.) was dissolved in dry DMF (1.5 mL) and *tert*-butoxy bis(dimethylamino)methane (0.3 mL, 1.45 mmol, 12.1 equiv.) was added. The mixture was heated at 140 °C for 18 h under N₂ atmosphere. After this time, more *tert*-butoxy bis(dimethylamino)methane (0.4 mL, 1.94 mmol, 16.2 equiv.) was added the mixture was heated at 145 °C for 72 h under N₂ atmosphere. The solution was cooled down and an aq. solution of NH₄PF₆ was added. The resulting precipitate was collected by vacuum filtration and the solid was washed with H₂O (50 mL) and Et₂O (50 mL). The product was isolated via fractionated precipitation from CH₃CN by adding dropwise Et₂O and afterwards dried in high vacuum. Yield: 67%. ¹H NMR (500 MHz, CD₃CN) δ = 8.48 (2H, d, *J* = 5.5 Hz), 8.20 (2H, d, *J* = 9.4 Hz), 8.16 8.20 (2H, d, *J* = 9.5 Hz), 8.13 (2H, d, *J* = 2.11 Hz), 8.09 (2H, d, *J* = 5.5 Hz), 7.80 (2H, d, *J* = 5.5 Hz), 7.69 – 7.52 (22H, m), 7.21 (2H, d, *J* = 6.2 Hz), 6.87 (2H, dd, *J* = 6.3, 2.0 Hz), 5.14 (2H, d, *J* = 13.4 Hz), 2.96 (12H, s). ¹³C NMR (125 MHz, CD₃CN) δ = 157.4, 152.9, 152.7, 151.5, 150.6, 149.7, 149.6, 149.2, 149.2, 149.2, 149.2, 147.7, 136.9, 136.8, 130.8, 130.7, 130.7, 130.5, 130.5, 130.1, 130.0, 130.0, 129.7, 129.7, 127.1, 126.9, 126.8, 126.8, 120.2, 117.0, 92.7, 40.7. HR-MS (ESI⁺ *m/z*): Calcd. [M-2PF₆]²⁺: 530.17520; found: 530.17584. Anal. (%): Calcd. for (C₆₆H₅₄F₁₂N₈P₂Ru)·(H₂O)_{0.5}: C 58.32, H 4.08, N 8.24; found: C 58.17, H 3.83, N 8.66.

X-ray crystallography

Single crystal X-ray diffraction data were collected at 183(1) K on a Rigaku OD SuperNova (Atlas CCD detector) diffractometer for **1** and **2** and on a Rigaku OD Xcalibur (Ruby CCD detector) diffractometer for **3** equipped with Oxford liquid-nitrogen Cryostream coolers. A single wavelength X-ray source from a micro-focus sealed X-ray tube were used with the Cu K α radiation ($\lambda = 1.54184 \text{ \AA}$) for **1** and **2** and with the Mo K α radiation ($\lambda = 0.71073 \text{ \AA}$) for **3**. The selected single crystals were mounted using polybutene oil on a flexible loop fixed on a goniometer head and transferred to the diffractometer. Pre-experiments, data collections, data reductions and analytical absorption corrections¹⁶ were performed with the program suite *CrysAlisPro*.¹⁷ Using *Olex2*,¹⁸ the structures were solved with the SHELXT¹⁹ small molecule structure solution program and refined with the *SHELXL2018/1* program package²⁰ by full-matrix least-squares minimization on F². The crystal data collections and structure refinement parameters are gathered in Tables S1 and S2. CCDC 1969709 (for **1**), 1969708 (for **2**), and 1969710 (for **3**) contain the supplementary crystallographic data for these compounds, and can be obtained free of charge from the Cambridge Crystallographic Data Centre via www.ccdc.cam.ac.uk/data_request/cif.

In the crystal structure of **1**, solvent molecules of acetonitrile cocrystallized with the main species, one molecule could easily be introduced in the model and freely refined but a second one was observed badly disordered in the asymmetric unit. Consequently, the *PLATON SQUEEZE* tool²¹ was used to take the solvent contribution into account to the calculated structure factors: a total number of 92 electrons were found in the P1 unit cell that were considered as 4 solvent molecules of acetonitrile (one per asymmetric unit). In the crystal structure of **2**, the PF₆ counterions occupy three different positions in the asymmetric unit: one general position and two special positions (centers of inversions). The F atoms of one PF₆ are disordered over two sets of positions. Solvent molecules of tetrahydropyran cocrystallized with

the main species. They occupy two general positions and are disordered over two sets of positions. Solvent molecules of water are also present in the crystal. The non H atoms of the solvent molecules were isotropically refined. In the crystal structure of **3**, the PF₆ counterions occupy two different positions in the asymmetric unit and in both independent molecules the F atoms are disordered over two sets of positions. There are also two solvent molecules of acetonitrile in the asymmetric unit, one is fully disordered over two sets of positions.

Spectroscopic measurements

The absorption of the samples in cuvettes has been measured with a Lambda 800 UV/VIS Spectrometer (PerkinElmer Instruments) and in 96 well plates with a SpectraMax M2 Spectrometer (Molecular Devices) or with a Varian Cary 8454" UV/Visible spectrophotometer and quartz cuvettes (width 1 cm) at $c = 7.5 \mu\text{M}$. The emission was measured by irradiation of the sample in fluorescence quartz cuvettes (width 1 cm) using a NT342B Nd-YAG pumped optical parametric oscillator (Ekspla) at 355 nm. Luminescence was focused and collected at right angle to the excitation pathway and directed to a Princeton Instruments Acton SP-2300i monochromator. As a detector a XPI-Max 4 CCD camera (Princeton Instruments) has been used.

Lifetime measurements

For the determination of the lifetimes, the samples were prepared in an air saturated and in a degassed CH₃CN solution with an absorbance of 0.1 at 355 nm. This solution was irradiated in fluorescence quartz cuvettes (width 1 cm) using a NT342B Nd-YAG pumped optical parametric oscillator (Ekspla) at 355 nm. The emission signal was focused and collected at right angle to the excitation pathway and directed to a Princeton Instruments Acton SP-2300i monochromator. As a detector a R928 photomultiplier tube (Hamamatsu) was used.

Luminescence quantum yield measurements

For the determination of the luminescence quantum yield, the samples were prepared in an CH₃CN solution with an absorbance of 0.1 at 355 nm. This solution was irradiated in fluorescence quartz cuvettes (width 1 cm) using a NT342B OPO pulse laser Nd-YAG pumped optical parametric oscillator (Ekspla) at 355 nm. The emission signal was focused and collected at right angle to the excitation pathway and directed to a Princeton Instruments Acton SP-2300i monochromator. As detector a XPI-Max 4 CCD camera (Princeton Instruments) was used. The luminescence quantum yields were determined by comparison with the reference [Ru(bipy)₃]Cl₂ in CH₃CN ($\Phi_{em} = 0.059$)²² applying the following formula :

$$\Phi_{em,sample} = \Phi_{em,reference} * \frac{F_{reference}}{F_{sample}} * \frac{I_{sample}}{I_{reference}} * \left(\frac{n_{sample}}{n_{reference}} \right)^2$$

$$F = 1 - 10^{-A}$$

Φ_{em} = luminescence quantum yield, F = fraction of light absorbed, I = integrated emission intensities, n = refractive index, A = absorbance of the sample at irradiation wavelength

Singlet oxygen measurements

- direct evaluation

The samples were prepared in an air saturated CH₃CN or D₂O solution with an absorbance of 0.2 at 450 nm. This solution was irradiated in fluorescence quartz cuvettes (width 1 cm) using a mounted M450LP1 LED (Thorlabs) whose irradiation, centred at 450 nm, has been focused with aspheric condenser lenses. The intensity of the irradiation has been varied using a T-Cube LED Driver (Thorlabs) and measured with an optical power and energy meter. The emission signal was focused and collected at right angle to the excitation pathway and directed to a Princeton Instruments Acton SP-2300i monochromator. A longpass glass filter was placed in front of the monochromator entrance slit to cut off light at wavelengths shorter than 850 nm. The slits for detection were fully open. As a detector an EO-817L IR-sensitive liquid nitrogen cooled germanium diode detector (North Coast Scientific Corp.) has been used. The singlet oxygen phosphorescence at 1270 nm was measured by recording spectra from 1100 to 1400 nm. For the data analysis, the singlet oxygen luminescence peaks at different irradiation intensities were integrated. The resulting areas were plotted against the percentage of the irradiation intensity and the slope of the linear regression calculated. The absorbance of the sample was corrected with an absorbance correction factor. As reference for the measurement in an CH₃CN solution phenaleneone ($\Phi_{\text{phenaleneone}} = 0.95$)²³ and for the measurement in a D₂O solution [Ru(bipy)₃]Cl₂ ($\Phi_{\text{Ru(bipy)}_3\text{Cl}_2} = 0.22$)²⁴ was used and the singlet oxygen quantum yields were calculated using the following formula:

$$\Phi_{\text{sample}} = \Phi_{\text{reference}} \times \frac{S_{\text{sample}}}{S_{\text{reference}}} \times \frac{I_{\text{reference}}}{I_{\text{sample}}}$$

$$I = I_0 \times (1 - 10^{-A})$$

Φ = singlet oxygen quantum yield, S = slope of the linear regression of the plot of the areas of the singlet oxygen luminescence peaks against the irradiation intensity, I = absorbance

correction factor, I_0 = light intensity of the irradiation source, A = absorbance of the sample at irradiation wavelength.

- indirect evaluation

For the measurement in CH_3CN : The samples were prepared in an air-saturated CH_3CN solution containing the complex with an absorbance of 0.1 at the irradiation wavelength, *N,N*-dimethyl-4-nitrosoaniline aniline (RNO, 24 μM) and imidazole (12 mM). For the measurement in PBS buffer: The samples were prepared in an air-saturated PBS solution containing the complex with an absorbance of 0.1 at the irradiation wavelength, *N,N*-dimethyl-4-nitrosoaniline aniline (RNO, 20 μM) and histidine (10 mM). The samples were irradiated on 96 well plates with an Atlas Photonics LUMOS BIO irradiator for different times. The absorbance of the samples was measured during these time intervals with a SpectraMax M2 Microplate Reader (Molecular Devices). The difference in absorbance ($A_0 - A$) at 420 nm for the CH_3CN solution or at 440 nm a PBS buffer solution was calculated and plotted against the irradiation times. From the plot the slope of the linear regression was calculated as well as the absorbance correction factor determined. The singlet oxygen quantum yields were calculated using the same formulas as used for the direct evaluation.

Stability in DMSO

The stability of the complexes in DMSO was determined by $^1\text{H-NMR}$ spectroscopy. The complexes were dissolved in 0.7 mL DMSO- d_6 [2 mg/mL] and the filled tube stored at room temperature in the dark. A spectrum was measured directly after preparing the solutions and after 1, 2 and 7 days.

Stability in human plasma

The stability of the complexes was evaluated with Caffeine as an internal standard, which has already shown to be suitable for these experiments.²⁵ The pooled human plasma was obtained from Biowest and caffeine from TCI Chemicals. Stock Solutions of the compounds (40 μM) and caffeine (40 or 20 μM) were prepared in DMSO. One aliquot of the solutions was added to 975 μL of human plasma to a total volume of 1000 μL . Final concentrations of the compounds of 0.5 μM and caffeine of 0.5 or 0.25 μM were achieved. The resulting solution was incubated for 4 h, 12 h, 24 h and 48 h at 37 $^\circ\text{C}$ with continuous gentle shaking (ca. 300 rpm). The reaction was stopped after the incubation time by addition of 2 mL of methanol. The mixture was centrifuged for 45 min at 650 g at 4 $^\circ\text{C}$. The methanolic solution was filtered through a 0.2 μm membrane filter. The solvent was evaporated under reduced pressure and the residue was dissolved in 1:1 (v/v) $\text{CH}_3\text{CN}/\text{H}_2\text{O}$ 0.1 % TFA solution. The solution was filtered through a 0.2 μm membrane filter and analysed using a HPLC System. For analytic HPLC the following system has been used: 2 x Agilent G1361 1260 Prep Pump system with Agilent G7115A 1260 DAD WR Detector equipped with an Agilent Pursuit XRs 5C18 (100 \AA , C18 5 μm 250 \times 4.6 mm) Column and an Agilent G1364B 1260-FC fraction collector. The flow rate was 1 mL/min and the chromatogram was detected at 250 nm. In this study, the chromatograms were recorded using two different methods. Method M1: The solvents (HPLC grade) were millipore water (0.1 % TFA, solvent A) and acetonitrile (solvent B). 0-3 minutes: isocratic 95 %

A (5 % B); 3-17 minutes: linear gradient from 95 % A (5 % B) to 0 % A (100 % B); 17-23 minutes: isocratic 0 % A (100% B). Method M2: The solvents (HPLC grade) were millipore water (0.1 % TFA, solvent A) and acetonitrile (0.1 % TFA, solvent B). 0-3 minutes: isocratic 95 % A (5 % B); 3-17 minutes: linear gradient from 95 % A (5 % B) to 0 % A (100 % B); 17-23 minutes: isocratic 0 % A (100 % B).

Photostability

The samples were prepared in an air saturated CH₃CN solution with an absorbance of about 0.5 at 450 nm. To measure the photostability, the samples were irradiated at 450 nm in 96 well plates with an Atlas Photonics LUMOS BIO irradiator during time intervals from 0-10 min. The absorbance spectrum from 350-700 nm was recorded with a SpectraMax M2 Microplate Reader (Molecular Devices) after each time interval and compared. As a positive control [Ru(bipy)₃]Cl₂ and as a negative control Protoporphyrin IX has been used.

Distribution coefficient

The lipophilicity of a complex was determined by measuring its distribution coefficient between the PBS and Octanol phase by using the “shake-flask” method. For this technique, the used phases were previously saturated in each other. The complex was dissolved in the phase (A) with its major presence with an absorbance of about 0.5 at 450 nm. This solution was then mixed with an equal volume of the other phase (B) at 80 rpm for 8 h with an Invitrogen sample mixer and then equilibrated overnight. The phase A was then carefully separated from phase B. The amount of the complex before and after the sample mixing was determined by UV/Vis spectroscopy at 450 nm using a SpectraMax M2 Microplate Reader (Molecular Devices). The evaluation of the complexes was repeated three times and the ratio between the organic and aqueous phase calculated.

Cell culture

HeLa and CT-26 cell lines were cultured in DMEM media (Gibco, Life Technologies, USA) supplemented with 10 % of fetal calf serum (Gibco). U87 and U373 cell lines were cultured in MEM media with addition of 1 % of MEM NEAA (non-essential amino acids) (Gibco) and 10 % of fetal calf serum. RPE-1 cells were cultured in DMEM/F-12 (Gibco) supplemented with 10 % of fetal calf serum. All cell lines were complemented with 100 U/mL penicillin-streptomycin mixture (Gibco) and maintained in humidified atmosphere at 37 °C and 5 % of CO₂.

Cellular uptake

The cellular uptake of the complex was investigated by the determination of the Ru content inside the cells. The complex with a final concentration of 25 μM (2% DMSO, v%) was incubated for 4 h at 37 °C on a cell culture dish with a density of ca. $5 \cdot 10^6$ cells in 10 mL of media. After this time, the media was removed and the cells were washed with cell media. The cells were trypsinised, harvested, centrifuged and resuspended. The number of cells on each dish was accurately counted. Each sample was digested using a 60% HNO₃ solution for three days. The acid was removed and the residue dissolved in 2% HCl in water. The Ru content was determined using an ICP-MS apparatus and comparing the results with the Ru references. The Ru content was then associated with the number of cells.

(Photo-)cytotoxicity

Dark and light cytotoxicity of the the Ru(II) complexes was assessed by fluorometric cell viability assay using resazurin (ACROS Organics). For dark and light cytotoxicity, cells were seeded in triplicates in 96 well plates at a density of 4000 cells per well in 100 μL, 24 h prior to treatment. The medium was then replaced with increasing concentration of the tested complexes

and cells were incubated for 4 h. Medium was then replaced for fresh complete medium. Cells used for light cytotoxicity experiment were exposed to: 480 nm light for 10 min, 510 nm for 40 min, 540 for 60 min or 595 nm for 120 min in a 96-well plate using a LUMOS-BIO photoreactor (Atlas Photonics). Each well was individually illuminated with a LED at constant current. After irradiation cells were kept for another 44 h in the incubator and the medium was replaced by fresh complete medium containing resazurin (0.2 mg mL^{-1} final concentration). After 4 h incubation at $37 \text{ }^{\circ}\text{C}$, the fluorescence signal of the resorufin product was read by SpectraMax M5 microplate reader (ex: 540 nm em: 590 nm). IC_{50} values were calculated using GraphPad Prism software.

Cellular localisation

HeLa cells were grown on the 12 mm Menzel–Gläser coverslips in 2 ml of complete medium at a density of 1.3×10^5 cells per ml. Cells were then treated with the compounds (IC_{50} concentration in the dark) for 2 h, with NucBlue (2 drops per 1 ml of media) for the last 25 min and with 100 nm Mitotracker Green FM for the last 15 min. HeLa cells were then fixed with paraformaldehyde solution in PBS (4%) and mounted on glass slides using Prolong Glass Antifade Mountant. Leica SP8 confocal microscope was used to analyse the samples. Ru compounds were excited at 488 nm and emission above 650nm was recorded.

Time dependent localisation of complex 6

HeLa cells were grown on the 12 mm Menzel–Gläser coverslips in 2 ml of complete medium at a density of 1.3×10^5 cells per ml. Cells were then treated with the complex 6 ($14 \text{ } \mu\text{M}$) for 5 min, 10 min, 30 min and 2h. Cells were then co-stained with NucBlue (2 drops per 1 ml of media) for the last 25 min and with 100 nm Mitotracker Green FM for the last 15 min. HeLa cells were then fixed and images were taken on Leica SP8 confocal microscope.

Indirect Immunofluorescence

HeLa cells were grown on the 12 mm Menzel–Gläser coverslips in 2 ml of complete medium at a density of 1.3×10^5 cells per ml. Cells were then treated with the complex 6 (14 μM) for 2h. Cells were co-stained with NucBlue (2 drops per 1 ml of media) for the last 25 min and with 100 nm Mitotracker Green FM for the last 15 min. HeLa cells were then fixed with paraformaldehyde solution in PBS (4%). Fixed cells were then incubated in blocking solution (0.2% BSA, 0,05 % Saponin in PBS) for 15 min at RT, and incubated with indicated primary antibodies for 1 h, anti-GM130 (BD Biosciences, catalog number 610823, batch 4324839) anti-TGN46 (AbD Serotec, AHP500), anti-KDEL (Santa Cruz Biotechnology, catalog number sc-58774) and anti-LAMP antibodies (BD Biosciences) were used at 1:1000, 1:1000. 1:50 and 1:3000 dilution, respectively and detected using Alexa 488 conjugated secondary antibodies (Jackson ImmunoResearch Laboratory) at 1:400 dilution. Coverslips were mounted on glass slides using Prolong Glass Antifade Mountant. Leica SP8 confocal microscope was used to analyse the samples. Ru compounds were excited at 488 nm and emission above 650nm was recorded. Images were recorded in Cellular and Molecular Imaging Technical Platform, INSERM UMS 025 - CNRS UMS 3612, Faculty of Pharmacy of Paris, Paris Descartes University, Paris, France. Colocalisation values were calculated using Fiji software.²⁶

Seahorse mito stress test

CT-26 cells were seeded in Seahorse XFe96 well plate at density of 30 000 cells per well in 80 μl . After 24 h cells were treated with 1 μM concentration of: complex 6, cisplatin or 5-ALA according to the plate arrangement (Figure S53). After 4 h incubation media was exchanged for fresh complete media and chosen wells were irradiated for 2 h at 595 nm using a LUMOS-BIO photoreactor (Atlas Photonics). Each well was individually illuminated with a LED at constant current. Wells that were not irradiated were covered with aluminium foil. After irradiation

regular media was removed and the cells were washed thrice using bicarbonate and serum free DMEM, supplemented with glucose, 1.8 mg/ mL; 1% glutamine and 1% sodium pyruvate and incubated in a non-CO₂ incubator at 37 °C for 1 h. Mito Stress assay was run using Oligomycin, 1 μM, FCCP 1 μM and mixture of Antimycin-A/ Rotenone 1 μM each in ports A, B and C respectively using Seahorse XFe96 Extracellular Flux Analyzer.

Seahorse glycolysis stress test

CT-26 cells were seeded in Seahorse XFe96 well plate at density of 30 000 cells per well in 80 μl. After 24 h cells were treated with 1 μM concentration of: complex **6**, cisplatin or 5-ALA according to the plate arrangement (Figure S53). After 4 h incubation media was exchanged for fresh complete media and chosen wells were irradiated for 2 h at 595 nm using a LUMOS-BIO photoreactor (Atlas Photonics). Each well was individually illuminated with a LED at constant current. Wells that were not irradiated were covered with aluminium foil. After irradiation regular media was removed and the cells were washed thrice using bicarbonate and serum free DMEM and incubated in a non-CO₂ incubator at 37 °C for 1 h. Glycolytic stress test was run using glucose, 10 mM, Oligomycin, 1 μM and 2-Deoxyglucose, 50 mM in ports A, B and C respectively using Seahorse XFe96 Extracellular Flux Analyzer.

Generation of 3D HeLa MCTS

HeLa cells were seeded at a density of 5000 cells per well in 200 μL in low attachment round bottom plates (Corning 4515). The single cells would generate MCTS approximately 400 μm in diameter at day 4 at. Plates were kept in the incubator at 37 °C with 5 % CO₂.

(Photo-)cytotoxicity in 3D HeLa MCTSs

HeLa MCTSs after 4 days of growing at 37 °C and 5 % CO₂ were treated by replacing half of the medium in the well by the treatment solutions. For untreated reference MCTS, half of the medium was replaced by fresh medium only. For dark treatment, the cells were treated with increasing concentration of compounds for 24 h. Then medium was removed and replaced by fresh culture medium followed by 44 h incubation in the dark. For phototoxicity treatment, cells were also treated for 24 h with increasing concentration of compounds in the dark. Then medium was removed and replaced by fresh culture medium prior to 2 h of irradiation at 595 nm in using a LUMOS-BIO photoreactor (Atlas Photonics). Each well was individually illuminated with a LED at constant current. Plates were incubated for 44 h. The cytotoxicity was measured using CellTiter-Glo Cell viability kit (Promega, USA).

SUPPORTING FIGURES AND TABLES

Table S1. Cartesian coordinates of the optimized structure of complex **1**.

	X	Y	Z
C	-0.55825800	-1.96095500	2.11992700
C	-1.32520200	-2.95947100	2.73615900
C	-2.57829600	-3.25637400	2.24465400
C	-3.06351800	-2.54957200	1.12647700
C	-4.34971300	-2.77696100	0.53919300
C	-4.76366600	-2.06185400	-0.54228300
C	-3.92623100	-1.06012200	-1.13032600
C	-4.29645200	-0.29247000	-2.25201600
C	-3.41537600	0.64568400	-2.74488300
C	-2.17012700	0.81945000	-2.12553800
C	-2.65677500	-0.81781200	-0.56873200
C	-2.22376500	-1.56600500	0.56718600
C	2.17016700	0.81998000	2.12493100
C	3.41540600	0.64639700	2.74433400
C	4.29647000	-0.29192300	2.25176300
C	3.92622600	-1.05989200	1.13031100
C	4.76365600	-2.06180800	0.54257700
C	4.34968700	-2.77729400	-0.53863300
C	3.06349400	-2.55009700	-1.12600800
C	2.57828400	-3.25721700	-2.24396500
C	1.32523200	-2.96035700	-2.73563200

C	0.55834500	-1.96157600	-2.11979800
C	2.22376000	-1.56630200	-0.56706400
C	2.65675600	-0.81777000	0.56865400
Ru	0.00000600	0.22859500	-0.00022700
N	-0.99051300	-1.27662700	1.06515800
N	0.99057200	-1.27692700	-1.06521200
N	1.79285000	0.10923100	1.06602700
N	-1.79284000	0.10902500	-1.06640500
C	-0.44617000	3.06821300	0.58482200
C	-0.92736500	4.22724500	1.19106300
C	-1.76280900	4.12552500	2.29500100
C	-2.10011900	2.86312400	2.76981300
C	-1.58958200	1.74883800	2.12081700
N	-0.78172800	1.84151000	1.05500000
C	0.44577800	3.06833800	-0.58496600
C	0.92665100	4.22749500	-1.19122600
C	1.76249300	4.12600500	-2.29488000
C	2.10055300	2.86368500	-2.76939100
C	1.59016100	1.74927200	-2.12050900
N	0.78185400	1.84172300	-1.05501100
H	0.42737700	-1.70452600	2.49214500
H	-0.91820400	-3.48203200	3.59416400
H	-3.19246400	-4.02400000	2.70531200
H	-4.99091900	-3.53494500	0.97817000
H	-5.74040200	-2.23999000	-0.98131900

H	-5.26612700	-0.44670400	-2.71513600
H	-3.66460500	1.25466200	-3.60622700
H	-1.46034500	1.54863800	-2.49979900
H	1.46044700	1.54933800	2.49896400
H	3.66460000	1.25561600	3.60551800
H	5.26612700	-0.44607100	2.71494300
H	5.74039300	-2.23979800	0.98167400
H	4.99088400	-3.53545400	-0.97732300
H	3.19236900	-4.02509300	-2.70431500
H	0.91824800	-3.48322900	-3.59345700
H	-0.42724300	-1.70521600	-2.49216800
H	-0.65585400	5.20236000	0.80614600
H	-2.14396300	5.02035900	2.77520200
H	-2.74834400	2.73302700	3.62865400
H	-1.82296300	0.74556400	2.45707300
H	0.65454100	5.20253300	-0.80652900
H	2.14336700	5.02094900	-2.77510000
H	2.74927400	2.73376100	-3.62788300
H	1.82399000	0.74603000	-2.45659800
C	-0.55825800	-1.96095500	2.11992700

Table S2. Cartesian coordinates of the optimized structure of complex **2**.

	X	Y	Z
C	-0.07795000	-2.37011400	2.04174200
C	0.32568500	-3.60818400	2.56061300
C	1.31528700	-4.32403000	1.92216300
C	1.90355100	-3.79521800	0.75601800
C	2.94035400	-4.45376100	0.01953800
C	3.47380500	-3.89001300	-1.09806300
C	3.01386200	-2.62127900	-1.57764400
C	3.52375400	-1.98850100	-2.72878300
C	3.00941000	-0.76736500	-3.10807600
C	1.98774400	-0.17986700	-2.34937000
C	1.99103700	-1.95698000	-0.87205500
C	1.43499600	-2.54604600	0.30320100
C	-1.56193800	-1.78469500	-2.04093000
C	-2.70290000	-2.40839000	-2.56423700
C	-3.91682100	-2.24903100	-1.93155800
C	-3.98555500	-1.46251700	-0.76485100
C	-5.19478500	-1.23175700	-0.03303300
C	-5.20065800	-0.46041000	1.08795300
C	-3.99750700	0.14509900	1.57450900
C	-3.93918300	0.94994600	2.72956400
C	-2.72876200	1.48439400	3.11592000
C	-1.57975800	1.21744900	2.35880200
C	-2.79515500	-0.06740100	0.87056500

C	-2.78949300	-0.87426400	-0.30749800
Ru	-0.01503200	-0.03870600	0.00290600
N	0.45927900	-1.84594200	0.94408400
N	-1.60435600	0.46121700	1.26472800
N	-1.59689100	-1.03364400	-0.94402000
N	1.48548700	-0.75448500	-1.26026800
C	1.50067100	2.41741700	0.53655200
C	2.42028500	3.29933200	1.09947700
C	3.27228800	2.88204500	2.12019800
C	3.15761600	1.55297200	2.53982700
C	2.22400400	0.72332600	1.94523900
N	1.40569800	1.13594600	0.96483800
C	0.56645400	2.78686400	-0.53971200
C	0.50322100	4.05765000	-1.10667100
C	-0.40890400	4.33856700	-2.12228500
C	-1.24015300	3.29281500	-2.53468400
C	-1.12999900	2.05013200	-1.93640200
N	-0.24843700	1.78987300	-0.95969200
C	4.26992100	3.81019400	2.73863800
C	-0.50591700	5.69915200	-2.73788000
H	-0.85122800	-1.78695900	2.52882300
H	-0.14985300	-3.98327900	3.45956300
H	1.64436800	-5.28488300	2.30535500
H	3.29602800	-5.41564000	0.37498400
H	4.26145600	-4.39513300	-1.64839000

H	4.31339100	-2.46417600	-3.30208700
H	3.37626100	-0.25032700	-3.98723400
H	1.56385700	0.77688800	-2.63169300
H	-0.59683400	-1.89347200	-2.52363100
H	-2.61095300	-3.00690200	-3.46313700
H	-4.81443300	-2.72172300	-2.31872100
H	-6.11179700	-1.68614300	-0.39435100
H	-6.12213400	-0.29021100	1.63584300
H	-4.84220000	1.13957100	3.30183200
H	-2.64503500	2.10859500	3.99817600
H	-0.61608700	1.62388300	2.64610800
H	2.47817800	4.32222900	0.74617300
H	3.79053000	1.15908600	3.32862200
H	2.11379600	-0.30878100	2.25742000
H	1.16634900	4.84067500	-0.75845900
H	-1.97288800	3.43801600	-3.32151000
H	-1.75819100	1.22235800	-2.24443200
H	0.30326600	6.35063800	-2.40323800
H	-1.45787400	6.16877300	-2.46884600
H	-0.47506000	5.63420600	-3.82934700
H	5.28477600	3.42546400	2.60120800
H	4.10038400	3.89662000	3.81620100
H	4.21682500	4.80776400	2.29847600

Table S3. Cartesian coordinates of the optimized structure of complex **3**.

	X	Y	Z
C	-2.95990900	1.45739100	1.64568700
C	-3.96399900	2.41394600	1.84886500
C	-4.27762300	3.29701200	0.83843100
C	-3.58135300	3.21976500	-0.38393100
C	-3.82628000	4.08976800	-1.49461600
C	-3.11898000	3.96750300	-2.65083900
C	-2.10802500	2.96383600	-2.79611500
C	-1.34710700	2.78479700	-3.96830200
C	-0.39896700	1.78549600	-4.00844800
C	-0.20846700	0.96578700	-2.88747000
C	-1.84926300	2.09620200	-1.71632800
C	-2.58966500	2.22597200	-0.50312100
C	-0.20847700	-0.96578800	2.88747000
C	-0.39898600	-1.78549300	4.00845000
C	-1.34713200	-2.78478800	3.96830400
C	-2.10804500	-2.96382700	2.79611400
C	-3.11900500	-3.96749000	2.65083700
C	-3.82630000	-4.08975500	1.49461100
C	-3.58136500	-3.21975600	0.38392500
C	-4.27763100	-3.29700200	-0.83844000
C	-3.96400000	-2.41393900	-1.84887400
C	-2.95990700	-1.45738700	-1.64569400
C	-2.58967300	-2.22596700	0.50311600

C	-1.84927500	-2.09619800	1.71632600
Ru	-0.78219500	-0.00000100	-0.00000100
N	-2.28539300	1.36210300	0.50369400
N	-2.28539500	-1.36210000	-0.50369900
N	-0.91194200	-1.11014100	1.76844800
N	-0.91193500	1.11014100	-1.76845000
C	2.05739200	-0.66425700	-0.31634600
C	3.22242900	-1.36150000	-0.62729100
C	3.10534200	-2.60656500	-1.22357200
C	1.85510600	-3.13916700	-1.50235400
C	0.74457800	-2.38206700	-1.16110100
N	0.83186300	-1.17644100	-0.58315100
C	2.05739200	0.66425200	0.31634900
C	3.22243100	1.36149300	0.62729600
C	3.10534500	2.60655700	1.22357700
C	1.85511000	3.13916200	1.50235700
C	0.74458000	2.38206400	1.16110300
N	0.83186400	1.17643700	0.58315200
Br	4.69898900	-3.60306300	-1.66699600
Br	4.69899300	3.60305300	1.66700200
H	-2.69178700	0.75514800	2.42677600
H	-4.47823500	2.44364400	2.80248500
H	-5.05054800	4.04741600	0.97246100
H	-4.59117500	4.85348300	-1.39384900
H	-3.31075100	4.63153800	-3.48778000

H	-1.51426600	3.43141700	-4.82430800
H	0.20512100	1.61696300	-4.89245600
H	0.52832200	0.17060800	-2.89958300
H	0.52831700	-0.17061500	2.89958300
H	0.20509900	-1.61696000	4.89246000
H	-1.51429800	-3.43140400	4.82431100
H	-3.31078200	-4.63152200	3.48777800
H	-4.59119800	-4.85346700	1.39384200
H	-5.05055800	-4.04740400	-0.97247100
H	-4.47823300	-2.44363600	-2.80249600
H	-2.69178100	-0.75514500	-2.42678200
H	4.19826000	-0.94813400	-0.40953300
H	1.73098500	-4.10889300	-1.96798100
H	-0.25478900	-2.74960300	-1.36091800
H	4.19826100	0.94812500	0.40953900
H	1.73098900	4.10888700	1.96798400
H	-0.25478700	2.74960100	1.36091800

Table S4. Cartesian coordinates of the optimized structure of complex **4**.

	X	Y	Z
C	2.67238300	-1.29449200	1.77240700
C	3.66829400	-2.23527000	2.06874500
C	3.96207400	-3.22620600	1.15710600
C	3.25461300	-3.27192300	-0.06043200
C	3.47848000	-4.26014700	-1.07213300
C	2.75978600	-4.25701700	-2.22773600
C	1.75826000	-3.26312600	-2.47172600
C	0.98542300	-3.20576200	-3.64817800
C	0.04694400	-2.20654200	-3.78866500
C	-0.12090700	-1.26552900	-2.76361800
C	1.52177500	-2.27912000	-1.49133000
C	2.27267400	-2.28462300	-0.27728700
C	-0.09831600	1.26289600	2.76188100
C	0.08174400	2.20148300	3.78705500
C	1.02701200	3.19380800	3.64286000
C	1.79439000	3.24660400	2.46261400
C	2.80188200	4.23339100	2.21432100
C	3.51452400	4.23236700	1.05495600
C	3.27839600	3.24664400	0.04355400
C	3.97906700	3.19687600	-1.17779500
C	3.67322000	2.20887800	-2.08868200
C	2.67232300	1.27484900	-1.78777800
C	2.29053400	2.26623700	0.26470700

C	1.54571200	2.26534300	1.48250200
Ru	0.48295100	-0.00262700	-0.00261300
N	1.98660200	-1.31399600	0.63323400
N	1.99286200	1.29828900	-0.64487400
N	0.61210700	1.28694800	1.63801900
N	0.59490300	-1.29372200	-1.64326600
C	-2.35513600	-0.61135500	0.39803600
C	-3.51390200	-1.25720200	0.81200300
C	-3.42732100	-2.41716800	1.57421600
C	-2.16212100	-2.91588000	1.87827800
C	-1.04478800	-2.22903400	1.42714000
N	-1.12879700	-1.09928700	0.71261600
C	-2.35185800	0.62571100	-0.39537100
C	-3.50706500	1.27388000	-0.81531900
C	-3.41529400	2.44581300	-1.55858300
C	-2.14721200	2.92593700	-1.88071000
C	-1.03344800	2.22707100	-1.43906100
N	-1.12299800	1.10595000	-0.71177000
C	-4.72361200	-3.06995700	1.97700100
C	-4.71105300	3.07928700	-1.99441100
O	-5.74488200	2.42029100	-1.98950000
N	-4.65058500	4.36503200	-2.38758800
N	-4.66264300	-3.94037000	3.00203700
O	-5.75595000	-2.80636500	1.37073300
H	2.42023900	-0.51063600	2.47757800

H	4.19113800	-2.16785700	3.01581700
H	4.72714300	-3.96796400	1.36497800
H	4.23685900	-5.01649400	-0.89601800
H	2.93534300	-5.01107300	-2.98861600
H	1.13555600	-3.94508700	-4.42887700
H	-0.56657100	-2.13073900	-4.67895200
H	-0.84990000	-0.46857000	-2.85466800
H	-0.83323100	0.47155900	2.85513000
H	-0.52780700	2.12941400	4.68037600
H	1.18659300	3.93115600	4.42354500
H	2.98688100	4.98543200	2.97496100
H	4.27741000	4.98338600	0.87558200
H	4.74838900	3.93324100	-1.38918600
H	4.19040700	2.13859600	-3.03864900
H	2.41075900	0.49340200	-2.49222400
H	-4.49803000	-0.88490500	0.55412000
H	-2.01707100	-3.83532300	2.43427100
H	-0.04554600	-2.58749300	1.64258900
H	-4.49326200	0.88884000	-0.58576200
H	-1.99471400	3.81085700	-2.48811600
H	-0.03262400	2.56485900	-1.67916900
H	-3.84583700	4.94804300	-2.22977800
H	-5.51422500	4.82025900	-2.64026600
H	-3.86038700	-4.01650800	3.60482100
H	-5.52569400	-4.35443100	3.31935200

Table S5. Cartesian coordinates of the optimized structure of complex **5**.

	X	Y	Z
C	-3.24699200	1.80178400	1.24947200
C	-4.24267300	2.78782100	1.21960900
C	-4.53541800	3.42499900	0.03277500
C	-3.82645500	3.06811200	-1.13105500
C	-4.04862600	3.66798200	-2.41248700
C	-3.32946400	3.28315900	-3.50201300
C	-2.32874800	2.26321600	-3.40466000
C	-1.55470400	1.82115500	-4.49549700
C	-0.61578700	0.83178800	-4.29552800
C	-0.44949200	0.28160400	-3.01704400
C	-2.09372800	1.65730500	-2.15420100
C	-2.84497400	2.06375900	-1.01031100
C	-0.44301300	-0.28189200	3.01493200
C	-0.60500700	-0.83257000	4.29376000
C	-1.54001300	-1.82527300	4.49550100
C	-2.31449400	-2.27015600	3.40611800
C	-3.31149400	-3.29354900	3.50541200
C	-4.03142600	-3.68085600	2.41727400
C	-3.81380200	-3.08021300	1.13542100
C	-4.52393900	-3.43937100	-0.02698900
C	-4.23590100	-2.80097900	-1.21432200
C	-3.24367300	-1.81152300	-1.24611800
C	-2.83595500	-2.07255500	1.01276100

C	-2.08389500	-1.66353300	2.15518800
Ru	-1.05561300	-0.00134200	-0.00048200
N	-2.55980300	1.44484200	0.16817800
N	-2.55535500	-1.45250200	-0.16622800
N	-1.16230900	-0.67871100	1.96894200
N	-1.16833700	0.67573600	-1.96972000
C	1.79365900	0.72187200	0.16529700
C	2.94540100	1.47369000	0.32610100
C	2.89541500	2.84836400	0.64295000
C	1.59440700	3.38505000	0.78178600
C	0.48992200	2.58134100	0.60853400
N	0.56001800	1.27196800	0.30856300
C	1.79565500	-0.71571200	-0.16923800
C	2.94949600	-1.46395200	-0.33200000
C	2.90317800	-2.83767600	-0.65298800
C	1.60388200	-3.37738700	-0.79490400
C	0.49707200	-2.57781400	-0.61698400
N	0.56361000	-1.26928200	-0.31266500
C	4.11786700	3.58173300	0.79619500
C	4.12782100	-3.56767200	-0.80681400
C	4.19511500	-4.90710700	-1.08585200
C	4.18139400	4.91952200	1.08517600
N	5.29938000	5.64415400	1.23380300
N	5.31438900	-5.62400500	-1.26468600
C	6.59996200	5.02459500	1.09381100

C	5.25299800	7.05779100	1.54452200
C	6.61427800	-4.99759900	-1.15425400
C	5.27215200	-7.06025100	-1.44583000
H	-2.99514900	1.29154900	2.17263000
H	-4.76720900	3.03522600	2.13546000
H	-5.30070900	4.19362200	-0.01523000
H	-4.80585600	4.44146200	-2.49644500
H	-3.50348200	3.74479900	-4.46904300
H	-1.70389800	2.26127600	-5.47673300
H	-0.00055000	0.46713000	-5.11015100
H	0.27996300	-0.49941800	-2.83367100
H	0.28329900	0.50171200	2.83012400
H	0.01039800	-0.46563900	5.10723600
H	-1.68585300	-2.26586200	5.47703200
H	-3.48210700	-3.75570900	4.47280200
H	-4.78586600	-4.45689500	2.50269700
H	-5.28648200	-4.21062500	0.02249400
H	-4.76155000	-3.05000800	-2.12909300
H	-2.99558500	-1.30018900	-2.16968800
H	3.91506000	1.00471400	0.20329400
H	1.42998900	4.42855700	1.02499000
H	-0.50920700	2.98958900	0.71461600
H	3.91785500	-0.99253600	-0.20831800
H	1.44274800	-4.41959100	-1.04573600
H	-0.50095100	-2.98840500	-0.72442000

H	5.03627700	3.01776600	0.66626700
H	5.04450300	-3.00020900	-0.68016000
H	3.28291600	-5.48966600	-1.18517500
H	3.26757100	5.49342300	1.21440600
H	6.72066100	4.58994900	0.09468100
H	6.73790800	4.22980800	1.83632700
H	7.37426900	5.77733600	1.24155000
H	4.21507800	7.38632900	1.61457400
H	5.75146100	7.64283800	0.76384900
H	5.74831600	7.26201000	2.50024400
H	6.68385100	-4.13472000	-1.82524100
H	7.38405000	-5.71700300	-1.43414100
H	6.80782000	-4.65737900	-0.12933300
H	4.23674400	-7.38956200	-1.54452700
H	5.72206400	-7.57804400	-0.59060500
H	5.81749800	-7.34797200	-2.35069400

Table S6. Cartesian coordinates of the optimized structure of complex **6**.

	X	Y	Z
C	-0.20433800	-1.17647900	-2.17035000
C	-0.83768700	-2.19745200	-2.88108300
C	-2.14772700	-2.55525600	-2.59848900
C	-2.82562400	-1.81031300	-1.59155300
C	-4.19804200	-2.00280500	-1.23596800
C	-4.79827800	-1.25281400	-0.27122500
C	-4.08926500	-0.22937900	0.43408000
C	-4.65964700	0.58031500	1.45798800
C	-3.81925800	1.47587300	2.10313400
C	-2.48188000	1.60417000	1.72416000
C	-2.73076100	-0.02705700	0.11118900
C	-2.10614700	-0.79978900	-0.91914000
C	0.20420800	-1.17670100	2.17037000
C	0.83744300	-2.19788000	2.88091700
C	2.14742600	-2.55578700	2.59822600
C	2.82542100	-1.81071000	1.59146500
C	4.19786000	-2.00320000	1.23596500
C	4.79817800	-1.25310300	0.27135900
C	4.08924000	-0.22958300	-0.43389700
C	4.65971100	0.58018700	-1.45770400
C	3.81938900	1.47588300	-2.10275500
C	2.48200600	1.60420900	-1.72382100

C	2.73073400	-0.02721900	-0.11103600
C	2.10604300	-0.80002500	0.91919100
Ru	0.00002000	1.00417700	0.00010800
N	-0.80906000	-0.49579700	-1.20172100
N	1.94328200	0.88646700	-0.74342000
N	0.80898600	-0.49594900	1.20182400
N	-1.94323900	0.88651600	0.74365000
C	-0.33309400	3.84788000	-0.65614600
C	-0.68410800	5.00726100	-1.34357000
C	-1.31312700	4.93440100	-2.58495800
C	-1.57105400	3.65697700	-3.09169300
C	-1.19826500	2.54107100	-2.36375700
N	-0.58835100	2.62180000	-1.17170100
C	0.33344400	3.84783200	0.65638400
C	0.68459900	5.00717700	1.34381800
C	1.31361300	4.93424500	2.58518800
C	1.57126200	3.65678000	3.09199900
C	1.19835500	2.54092900	2.36405900
N	0.58852700	2.62173200	1.17194900
C	-1.68879800	6.16523500	-3.34905400
C	1.69010700	6.16500400	3.34900100
H	0.82491600	-0.90956800	-2.38243200
H	-0.27621300	-2.73201400	-3.63936400
H	-4.77001500	-2.76145400	-1.75723800
H	-5.83680100	-1.43482700	-0.02066000

H	-4.20273600	2.11552600	2.89031800
H	-1.83054900	2.31694400	2.21726100
H	-0.82500400	-0.90968800	2.38252700
H	0.27592800	-2.73250800	3.63912200
H	4.76979900	-2.76187300	1.75724200
H	5.83673600	-1.43503800	0.02088900
H	4.20292400	2.11562800	-2.88983600
H	1.83073700	2.31707900	-2.21686700
H	-0.46971000	5.97917200	-0.91455900
H	-2.06111100	3.52524800	-4.05076300
H	-1.38408100	1.54090100	-2.73760400
H	0.47025800	5.97911100	0.91483800
H	2.06115900	3.52499700	4.05114500
H	1.38394300	1.54073100	2.73794600
H	1.52118100	7.06976000	2.76214100
H	2.74308900	6.13076400	3.64399700
H	1.09967500	6.23704100	4.26849500
H	-2.73948600	6.12794100	-3.65161400
H	-1.09201100	6.24102500	-4.26417200
H	-1.52692200	7.06950000	-2.75945000
C	6.08425900	0.50396200	-1.84614200
C	6.43095000	0.38449700	-3.19851800
C	7.10336800	0.60773200	-0.88913300
C	7.76736900	0.35301000	-3.58310200
H	5.64807500	0.29762100	-3.94683800

C	8.43872000	0.58488500	-1.27870900
H	6.84922300	0.73662600	0.15901700
C	8.77400100	0.45296200	-2.62473100
H	8.02230200	0.24873600	-4.63344600
H	9.21836100	0.67673600	-0.52853600
H	9.81699300	0.43141300	-2.92625900
C	2.77721700	-3.67179100	3.33586400
C	3.38981300	-4.73553600	2.65898400
C	2.71668100	-3.70072900	4.73534200
C	3.93544100	-5.79983500	3.36982000
H	3.41301300	-4.74291600	1.57305200
C	3.27176800	-4.76207200	5.44273700
H	2.24914500	-2.87774100	5.26868200
C	3.88231400	-5.81358300	4.76216000
H	4.39779300	-6.62279700	2.83314500
H	3.22827600	-4.76644100	6.52771700
H	4.31273600	-6.64317000	5.31506300
C	-6.08420300	0.50413400	1.84642500
C	-6.43087800	0.38386300	3.19872800
C	-7.10330200	0.60874200	0.88949800
C	-7.76729800	0.35236500	3.58332200
H	-5.64799300	0.29638000	3.94696900
C	-8.43864900	0.58587700	1.27909400
H	-6.84916700	0.73837800	-0.15856700
C	-8.77392800	0.45311400	2.62503600

H	-8.02222000	0.24746100	4.63360600
H	-9.21829100	0.67838100	0.52900200
H	-9.81691900	0.43155200	2.92656400
C	-2.77763800	-3.67097600	-3.33643600
C	-3.39106200	-4.73445800	-2.65989200
C	-2.71642300	-3.69993100	-4.73589000
C	-3.93677300	-5.79852600	-3.37100300
H	-3.41492300	-4.74173200	-1.57397900
C	-3.27159100	-4.76103600	-5.44357200
H	-2.24831100	-2.87712300	-5.26900200
C	-3.88291800	-5.81230200	-4.76331500
H	-4.39977400	-6.62127900	-2.83456600
H	-3.22755900	-4.76540700	-6.52853000
H	-4.31340400	-6.64170500	-5.31644300

Table S7. Cartesian coordinates of the optimized structure of complex **7**.

	X	Y	Z
C	-0.79242200	-1.98975200	2.04237000
C	-1.63210200	-2.95676000	2.59828300
C	-2.85947500	-3.25014500	2.02177900
C	-3.19790600	-2.56234100	0.82163200
C	-4.38992100	-2.80175100	0.06712700
C	-4.66066800	-2.11624900	-1.07750800
C	-3.76177600	-1.12927000	-1.59259700
C	-3.99399800	-0.37741000	-2.77968800
C	-3.06059800	0.59470400	-3.10917100
C	-1.91778100	0.78499800	-2.32985300
C	-2.58111200	-0.86950600	-0.86502200
C	-2.28962900	-1.60032900	0.33120000
C	1.91754400	0.78562200	2.33002000
C	3.06047200	0.59580100	3.10929700
C	3.99438100	-0.37575500	2.77961800
C	3.76258900	-1.12747700	1.59235600
C	4.66205200	-2.11381600	1.07703400
C	4.39165200	-2.79926200	-0.06771800
C	3.19944600	-2.56042800	-0.82210500
C	2.86133100	-3.24826200	-2.02232000
C	1.63374700	-2.95552300	-2.59869300
C	0.79357000	-1.98903500	-2.04261900

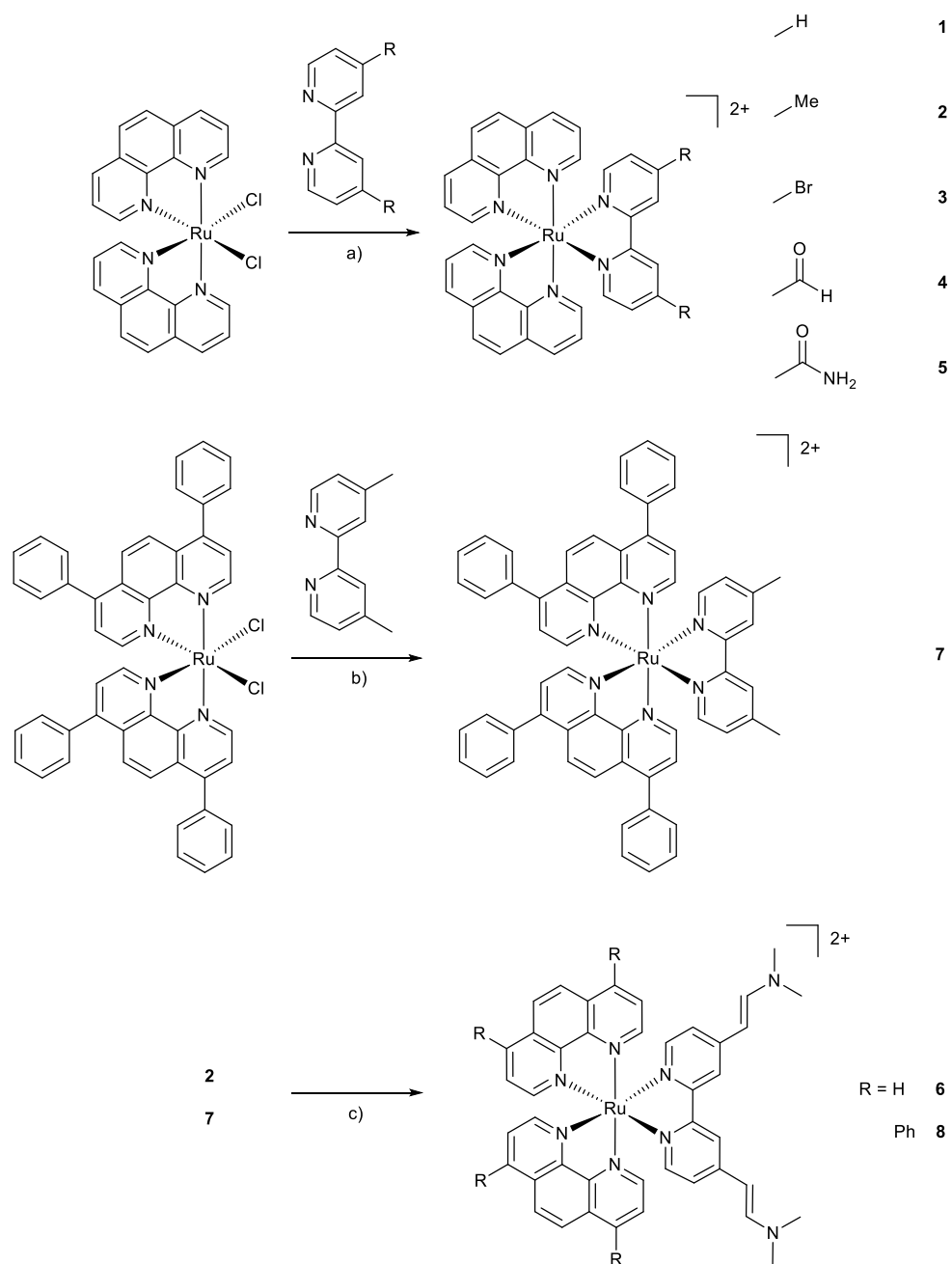
C	2.29065000	-1.59900400	-0.33148500
C	2.58176600	-0.86823300	0.86486000
Ru	0.00001000	0.18367700	0.00004700
N	-1.11021300	-1.30780100	0.94633800
N	1.11104600	-1.30703300	-0.94652500
N	1.66347500	0.06386700	1.24287400
N	-1.66333100	0.06318800	-1.24282900
C	-0.50282300	3.03536600	0.54115400
C	-1.03199700	4.18908700	1.09504000
C	-1.99022800	4.14247900	2.12992600
C	-2.35380400	2.84322900	2.55332700
C	-1.79108200	1.73656300	1.95762000
N	-0.88080700	1.80312200	0.96933800
C	0.50120300	3.03578200	-0.54044500
C	1.02969600	4.18992800	-1.09409800
C	1.98791700	4.14408700	-2.12903100
C	2.35226500	2.84513700	-2.55269200
C	1.79021700	1.73802000	-1.95719100
N	0.87991100	1.80385200	-0.96888900
C	-2.51350000	5.36676100	2.66300600
C	2.51041300	5.36878800	-2.66190700
C	3.47075600	5.43497300	-3.63604400
C	-3.47430400	5.43215400	3.63673700
N	-3.96865800	6.54940200	4.19123700
N	3.96433600	6.55265300	-4.19035100

C	-3.50880600	7.85166500	3.75949900
C	-5.09301700	6.50314400	5.10299600
C	3.50407500	7.85454600	-3.75792700
C	5.08799800	6.50725400	-5.10300800
H	0.15541500	-1.74390700	2.50822100
H	-1.32501900	-3.45291400	3.51248100
H	-5.08824600	-3.55234300	0.41843300
H	-5.58083600	-2.31436200	-1.61465400
H	-3.19057100	1.19671900	-4.00185700
H	-1.17432900	1.52577900	-2.60235600
H	1.17368100	1.52594000	2.60266400
H	3.19012700	1.19770200	4.00210700
H	5.58238800	-2.31144700	1.61407100
H	5.09040700	-3.54937900	-0.41918700
H	1.32686900	-3.45175700	-3.51291800
H	-0.15441600	-1.74365700	-2.50841600
H	-0.71067800	5.15748300	0.72881600
H	-3.07279300	2.68270800	3.34863100
H	-2.06667800	0.73848200	2.28028900
H	0.70780700	5.15807200	-0.72770200
H	3.07133800	2.68521600	-3.34803700
H	2.06640500	0.74015600	-2.28002100
H	-2.11439000	6.28401000	2.24140600
H	2.11097900	6.28570400	-2.23988700
H	3.90462000	4.52198900	-4.03586600

H	-3.90792400	4.51882600	4.03603200
H	-3.83249600	8.07292800	2.73452800
H	-2.41587800	7.90276500	3.79724900
H	-3.91405200	8.61364300	4.42591600
H	-5.29800100	5.46888400	5.38360600
H	-5.99458000	6.92380600	4.64158400
H	-4.87042900	7.07350500	6.01037700
H	2.41111200	7.90521300	-3.79528200
H	3.90878200	8.61696900	-4.42416000
H	3.82802600	8.07551200	-2.73297800
H	5.29340300	5.47317400	-5.38397200
H	5.98965600	6.92839300	-4.64222400
H	4.86435200	7.07763800	-6.01011900
C	-5.16755400	-0.59254900	-3.65354800
C	-5.94945300	0.50099700	-4.04841300
C	-5.48500900	-1.86723700	-4.14295300
C	-7.03403500	0.32100800	-4.90073500
H	-5.71464200	1.49175100	-3.66939900
C	-6.56531800	-2.04196700	-5.00212000
H	-4.86739100	-2.71896900	-3.87270000
C	-7.34487600	-0.95026300	-5.37913100
H	-7.63828000	1.17567000	-5.18993600
H	-6.79401700	-3.03315700	-5.38207200
H	-8.19016300	-1.08947600	-6.04645600
C	-3.74978200	-4.24363100	2.65963600

C	-5.08562900	-3.93836700	2.95538300
C	-3.24165000	-5.49649700	3.02714100
C	-5.89485000	-4.87092900	3.59661000
H	-5.48299400	-2.95817700	2.70800900
C	-4.05618100	-6.42944100	3.66065500
H	-2.20903700	-5.74381800	2.79701400
C	-5.38436800	-6.11937500	3.94629500
H	-6.92511600	-4.61817800	3.82859000
H	-3.65253300	-7.40096600	3.92966400
H	-6.01895300	-6.84729000	4.44292100
C	3.75222000	-4.24110600	-2.66037200
C	3.24500300	-5.49441700	-3.02759900
C	5.08772300	-3.93476500	-2.95655800
C	4.06011400	-6.42675600	-3.66126300
H	2.21266100	-5.74255700	-2.79714100
C	5.89751500	-4.86672300	-3.59794300
H	5.48435300	-2.95422000	-2.70940500
C	5.38795900	-6.11562700	-3.94733900
H	3.65718300	-7.39864000	-3.93005100
H	6.92750200	-4.61314500	-3.83026400
H	6.02299100	-6.84307000	-4.44408300
C	5.16800300	-0.59055100	3.65347500
C	5.48587000	-1.86518800	4.14275100
C	5.94951900	0.50321700	4.04846700
C	6.56621900	-2.03964000	5.00192400

H	4.86852700	-2.71709700	3.87241900
C	7.03414400	0.32350400	4.90079600
H	5.71437200	1.49392800	3.66954900
C	7.34540200	-0.94771200	5.37906400
H	6.79524300	-3.03079100	5.38178200
H	7.63809300	1.17834000	5.19010200
H	8.19072100	-1.08671100	6.04639400



Scheme S1. Synthesis of the desired complexes 1-7. a) EtOH/H₂O (1:1), 18 h reflux under N₂ atmosphere. b) EtOH/H₂O (1:1), 18 h reflux under N₂ atmosphere. c) *tert*-Butoxy bis(dimethylamino)methane, 140 °C, 16 h under N₂ atmosphere.

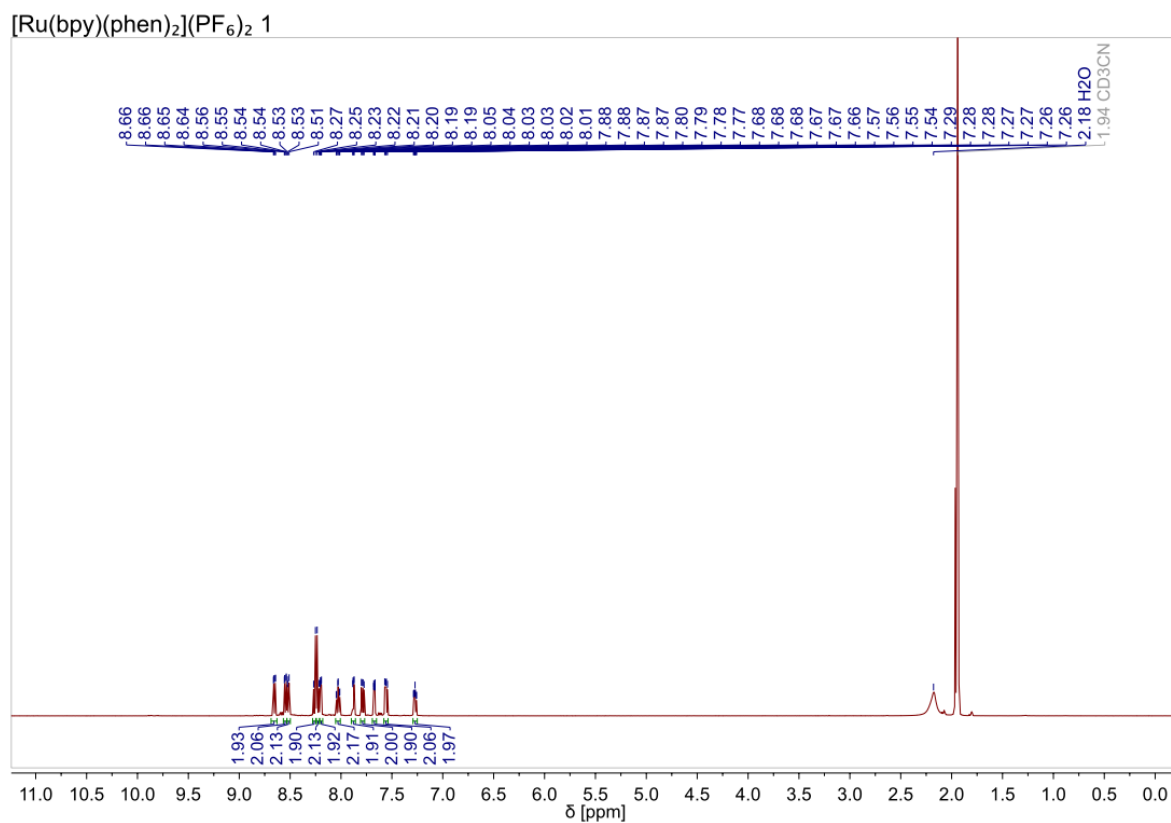


Figure S1. ¹H NMR spectrum of 1 in CD₃CN, 500 MHz.

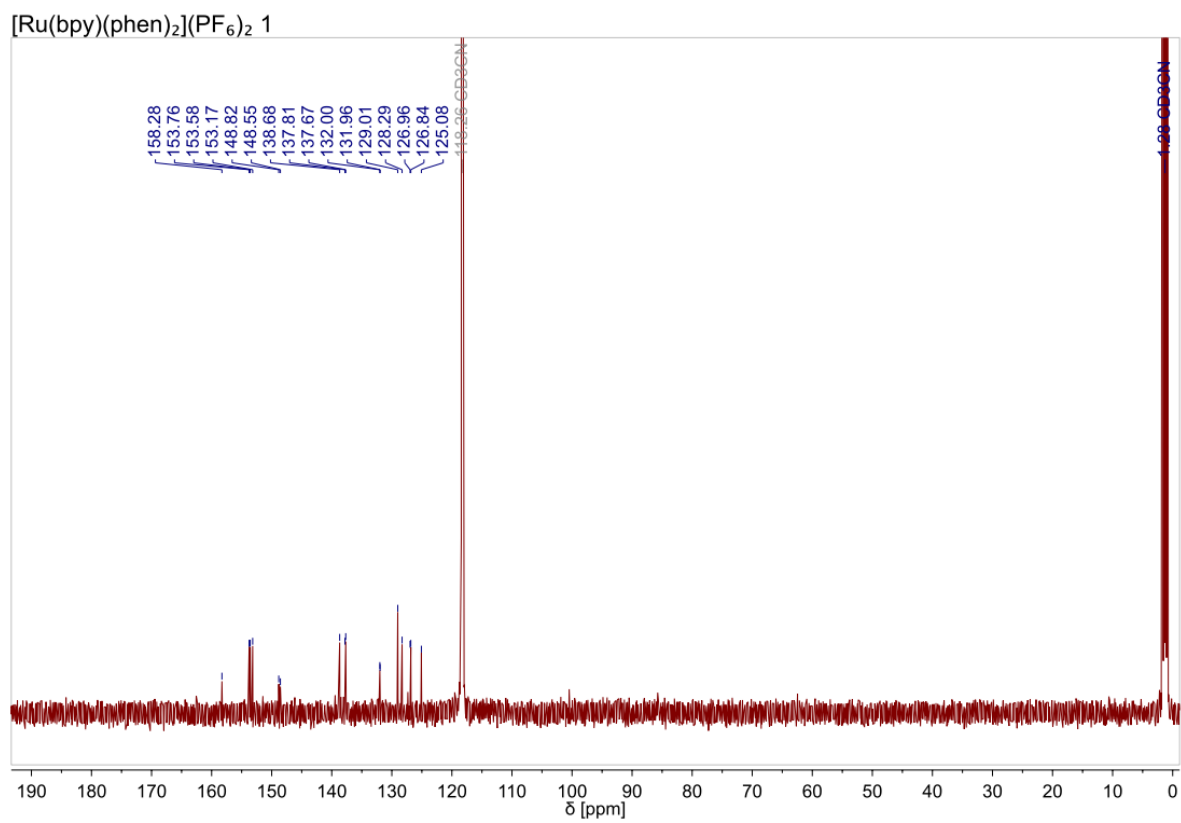


Figure S2. ¹³C NMR spectrum of 1 in CD₃CN, 125 MHz.

[Ru(dmb)(phen)₂](PF₆)₂ 2

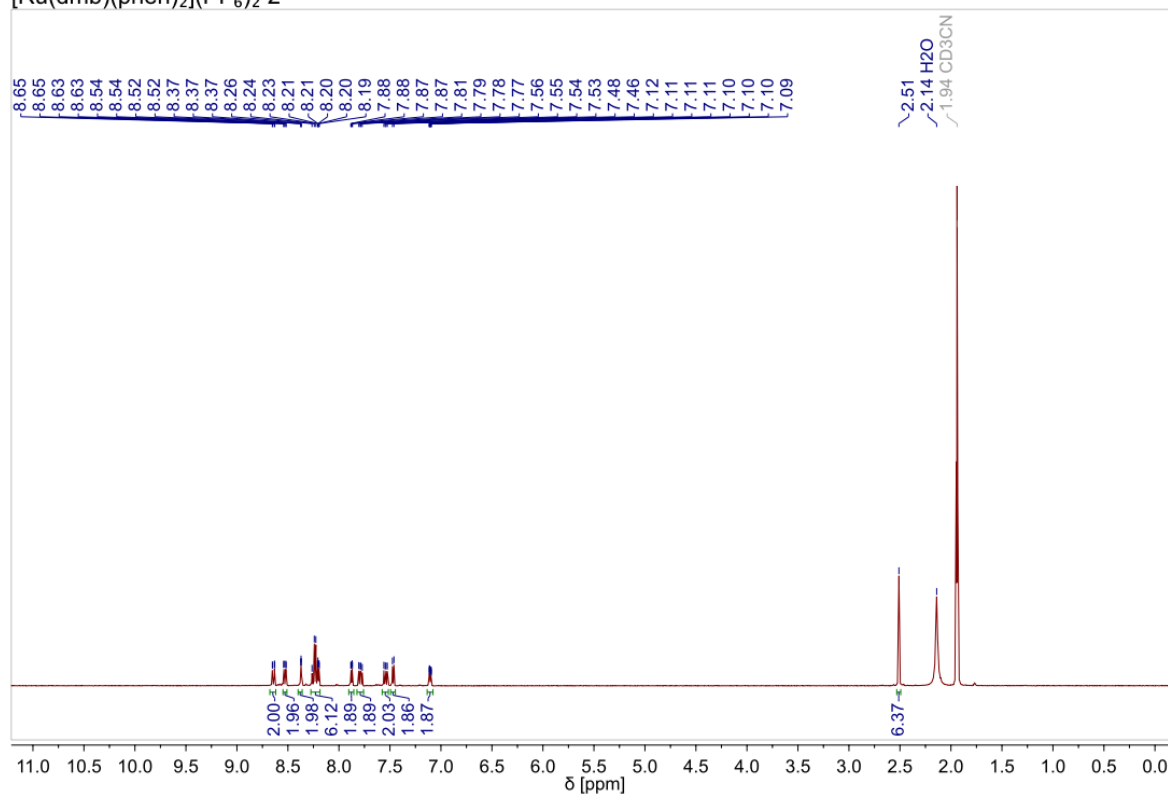


Figure S3. ¹H NMR spectrum of 2 in CD₃CN, 400 MHz.

[Ru(dmb)(phen)₂](PF₆)₂ 2

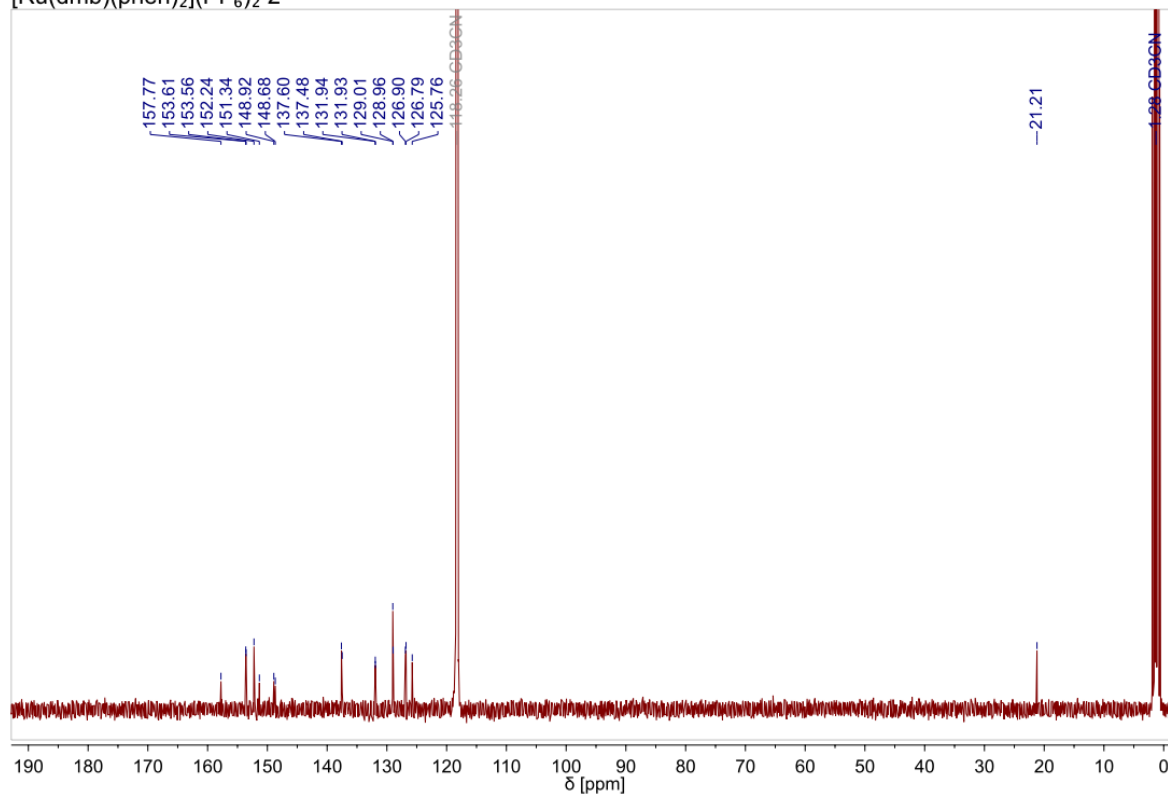


Figure S4. ¹³C NMR spectrum of 2 in CD₃CN, 100 MHz.

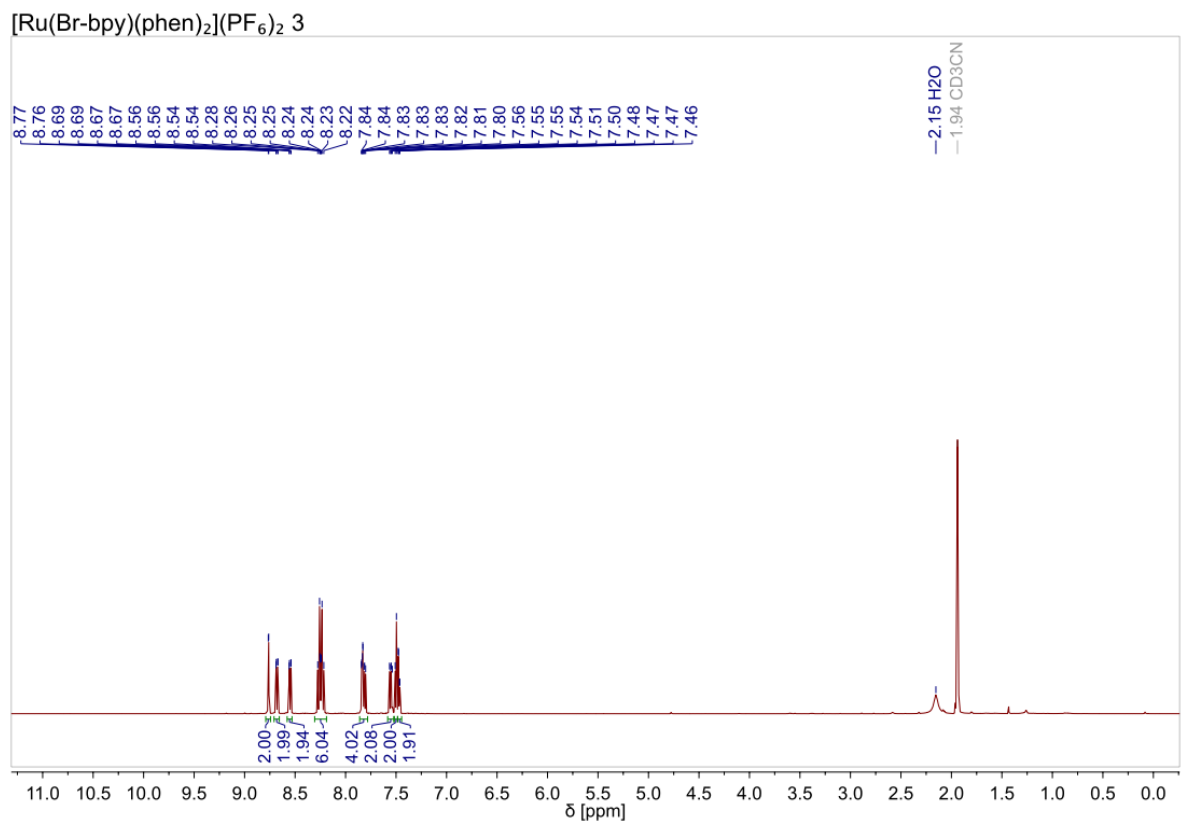


Figure S5. ¹H NMR spectrum of 3 in CD₃CN, 500 MHz.

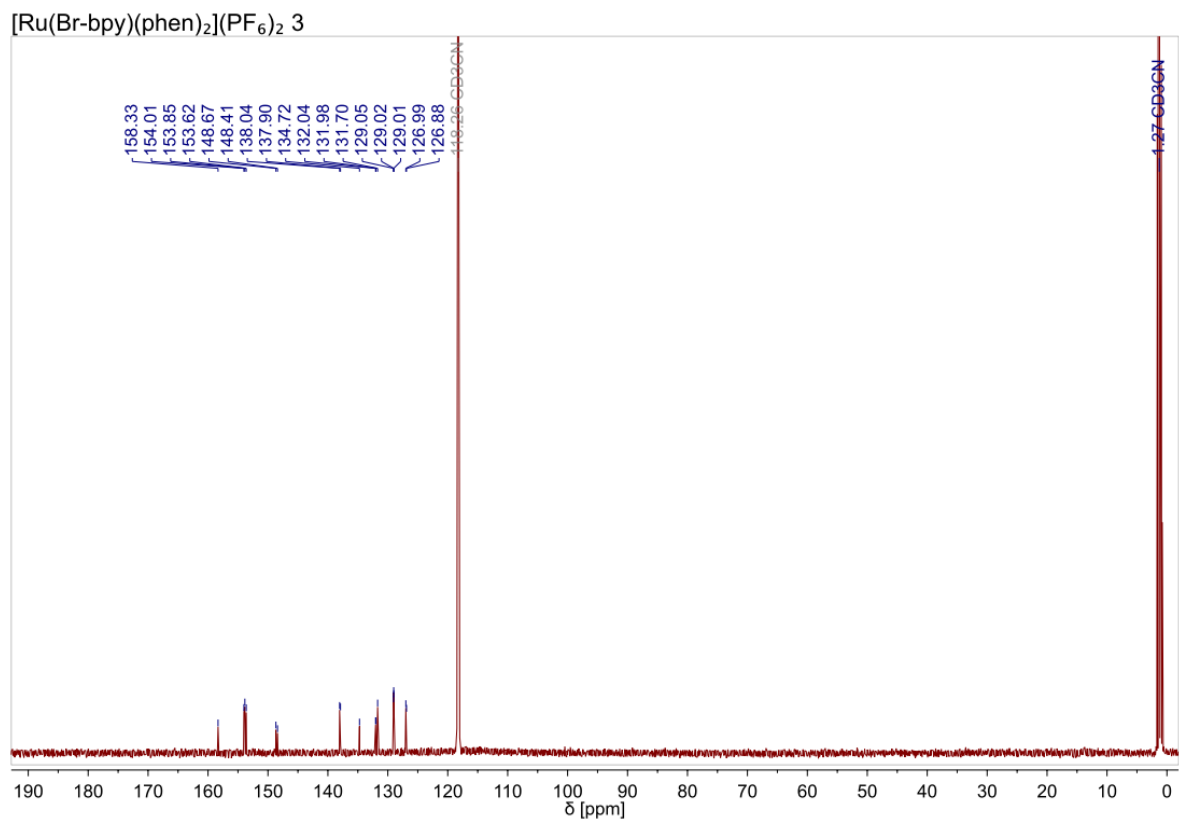


Figure S6. ¹³C NMR spectrum of 3 in CD₃CN, 125 MHz.

[Ru(CONH₂bpy)(phen)₂](PF₆)₂ 4

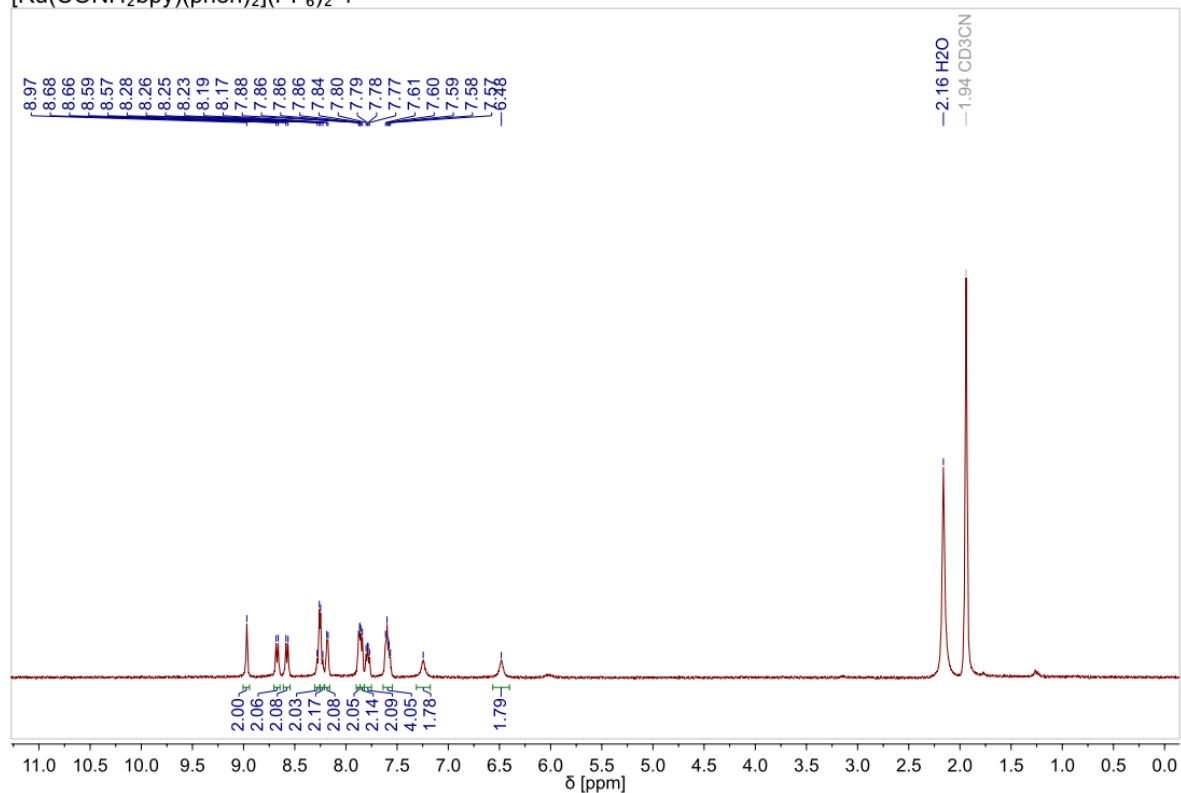


Figure S7. ¹H NMR spectrum of 4 in CD₃CN, 400 MHz.

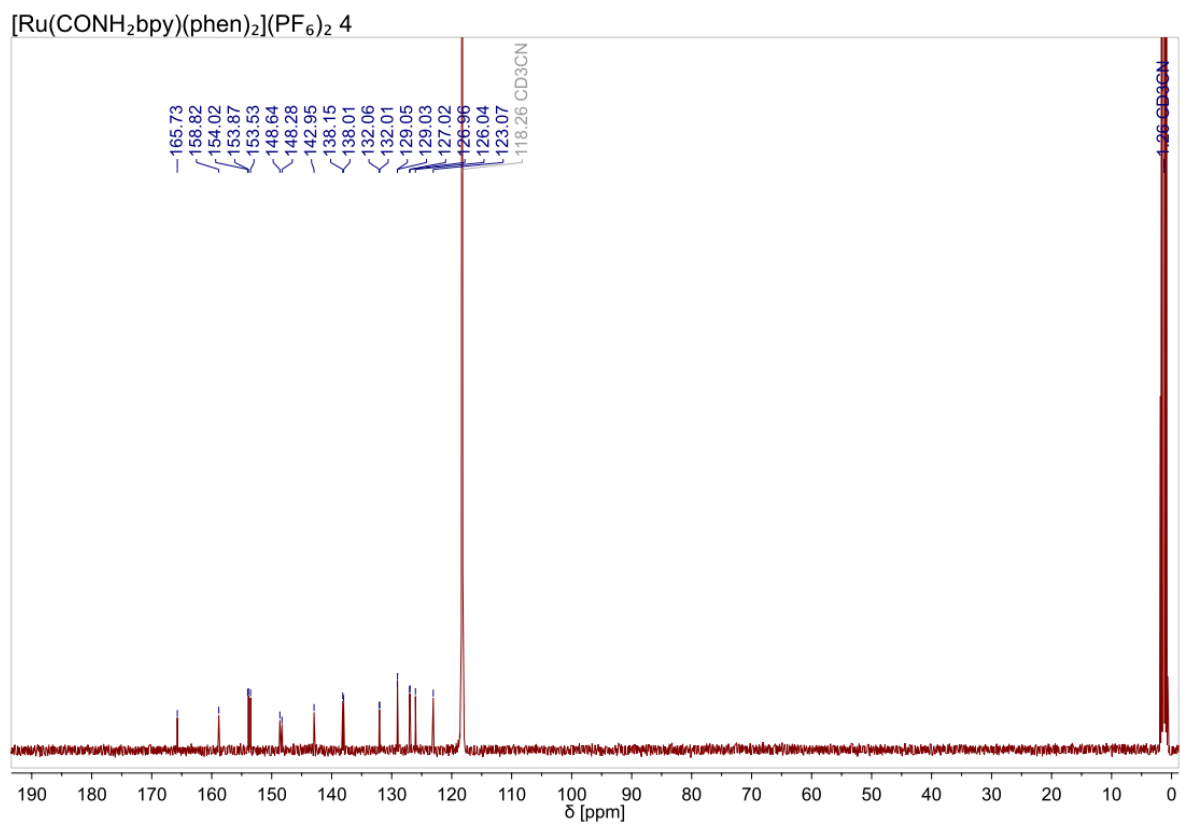


Figure S8. ¹³C NMR spectrum of 4 in CD₃CN, 100 MHz.

[Ru(Me₂Nvin-bpy)(phen)₂](PF₆)₂ 5

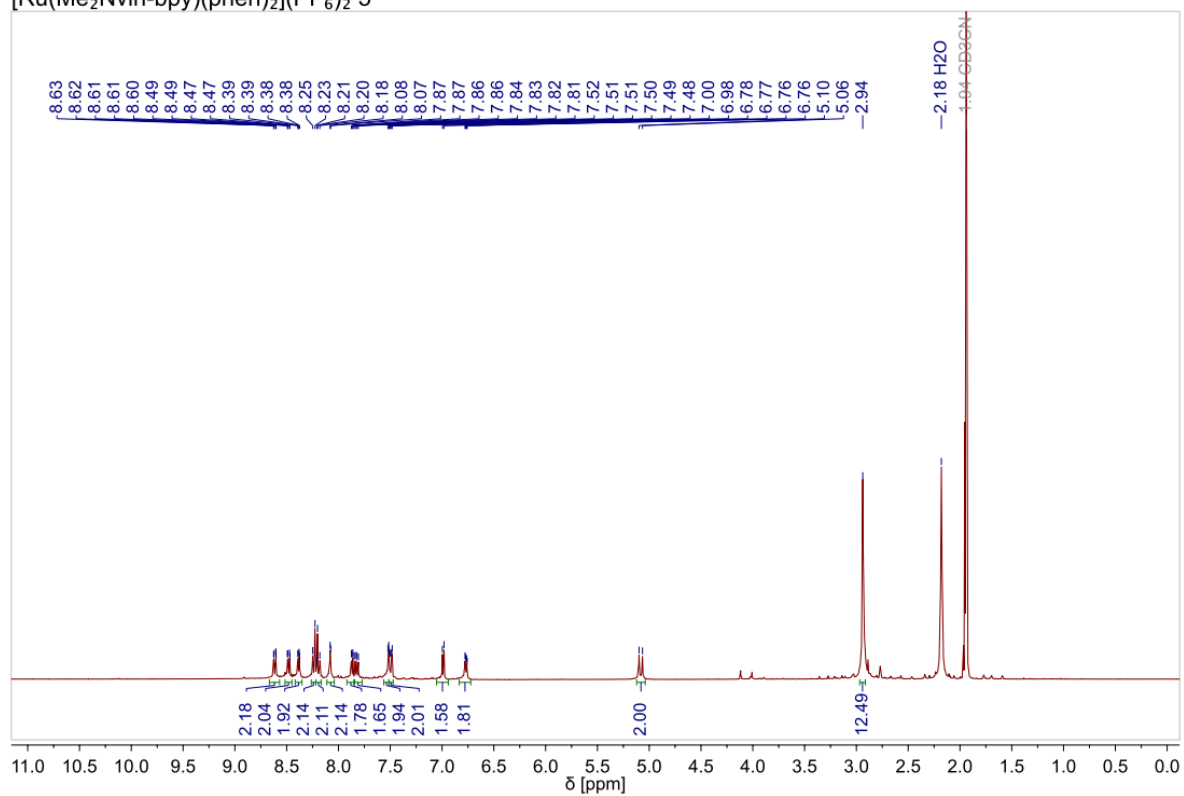


Figure S9. ¹H NMR spectrum of 5 in CD₃CN, 400 MHz.

[Ru(Me₂Nvin-bpy)(phen)₂](PF₆)₂ 5

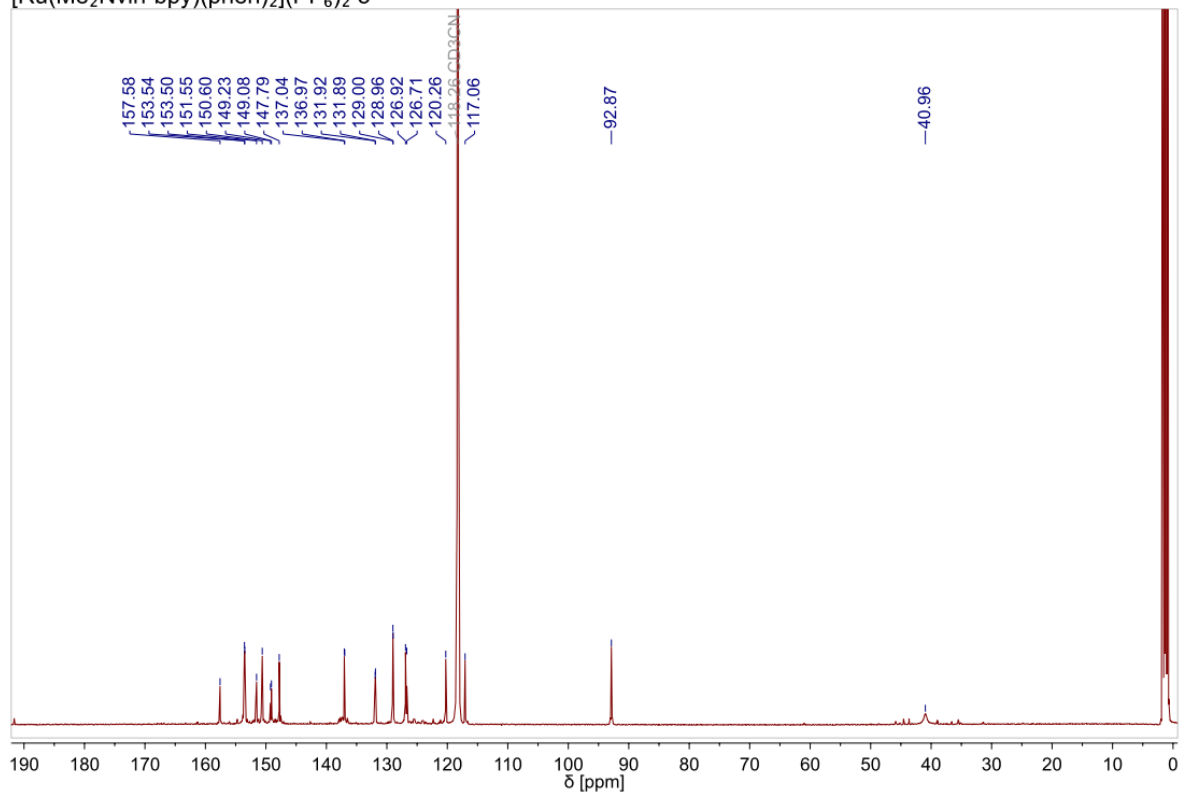


Figure S10. ¹³C NMR spectrum of 5 in CD₃CN, 125 MHz.

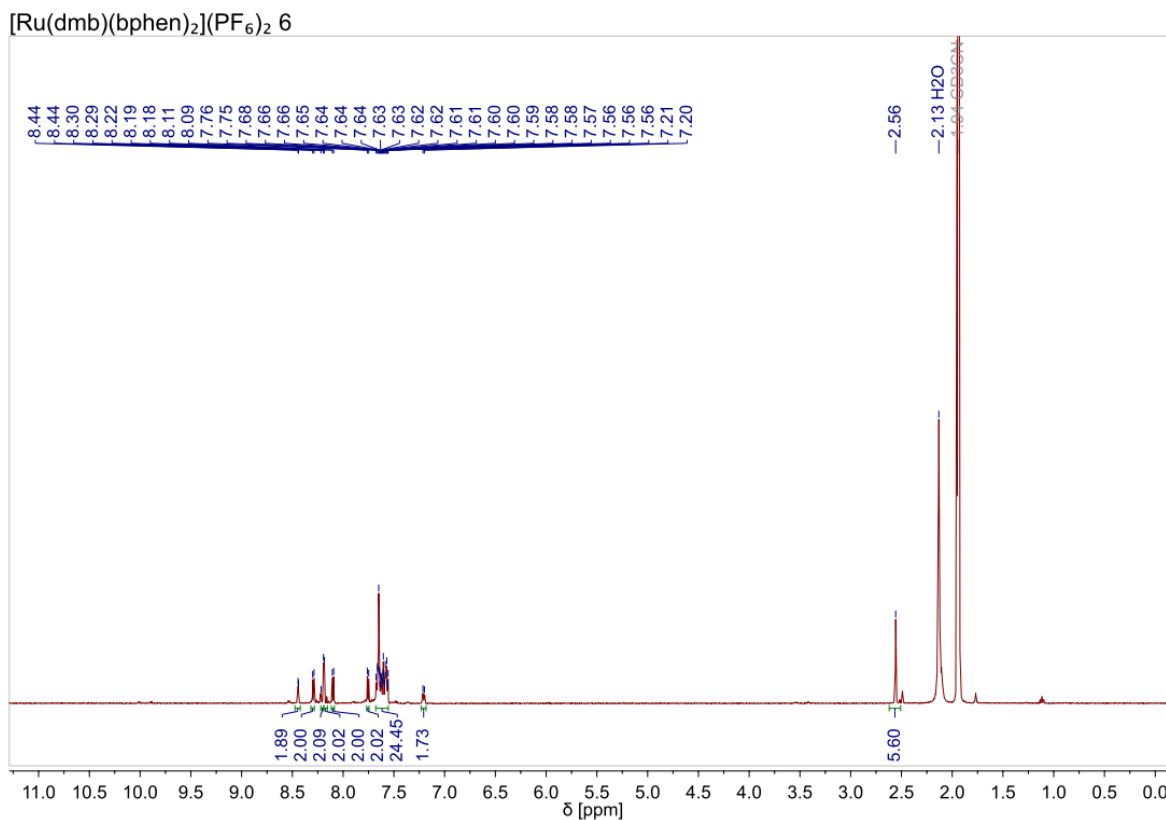


Figure S11. ¹H NMR spectrum of 6 in CD₃CN, 400 MHz.

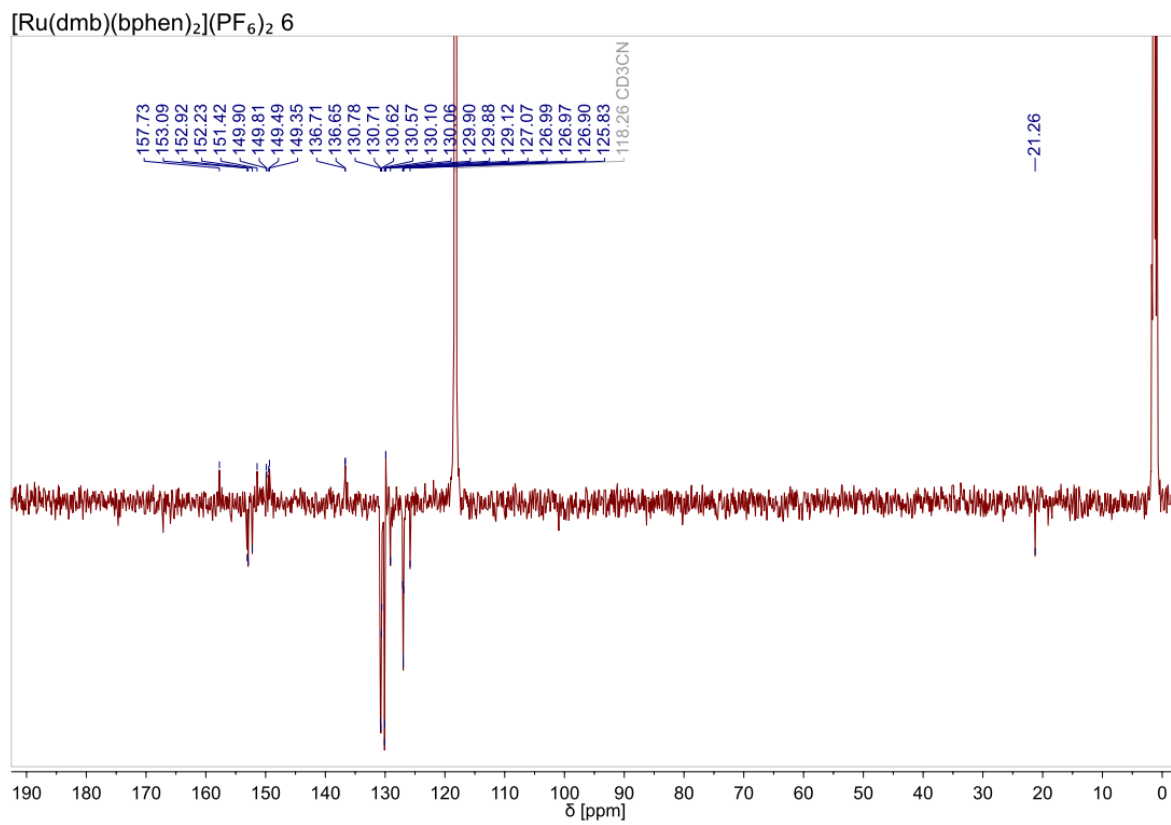


Figure S12. ¹³C NMR spectrum of 6 in CD₃CN, 125 MHz.

[Ru(Me₂Nvin-bpy)(bphen)₂](PF₆)₂ 7

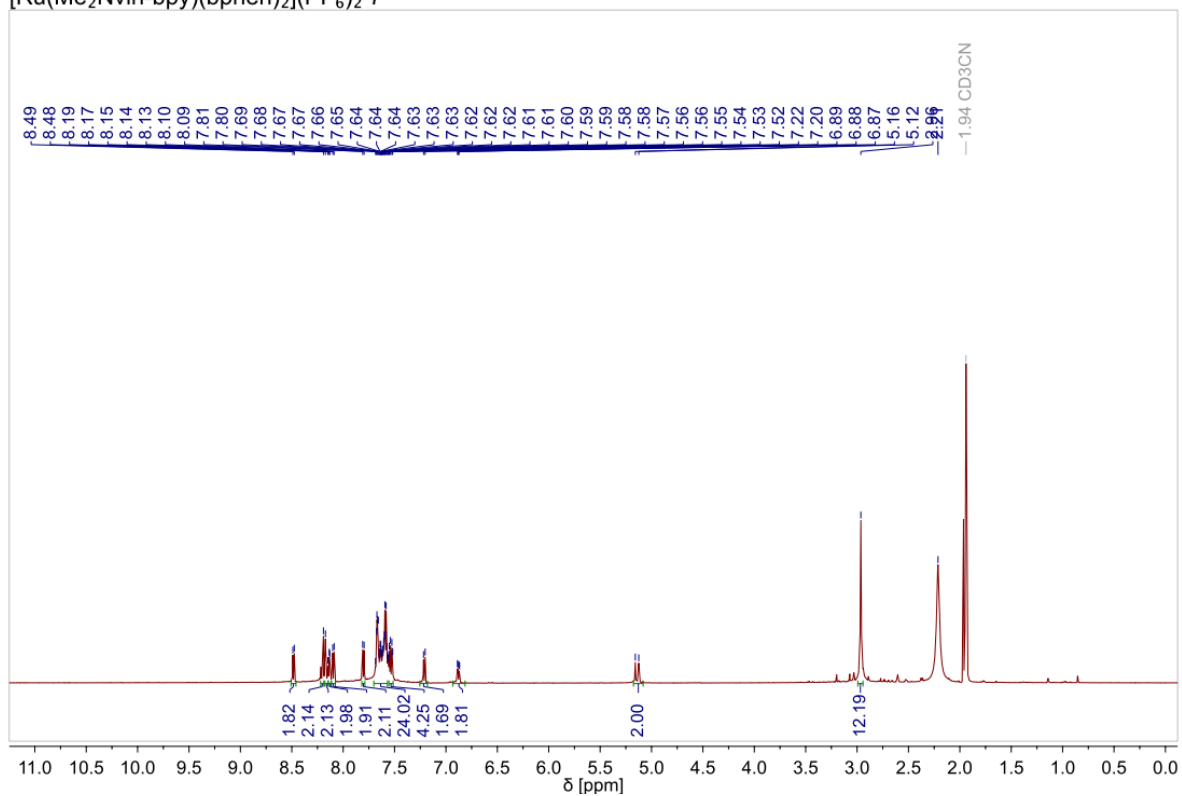


Figure S13. ¹H NMR spectrum of 7 in CD₃CN, 500 MHz.

[Ru(Me₂Nvin-bpy)(bphen)₂](PF₆)₂ **7**

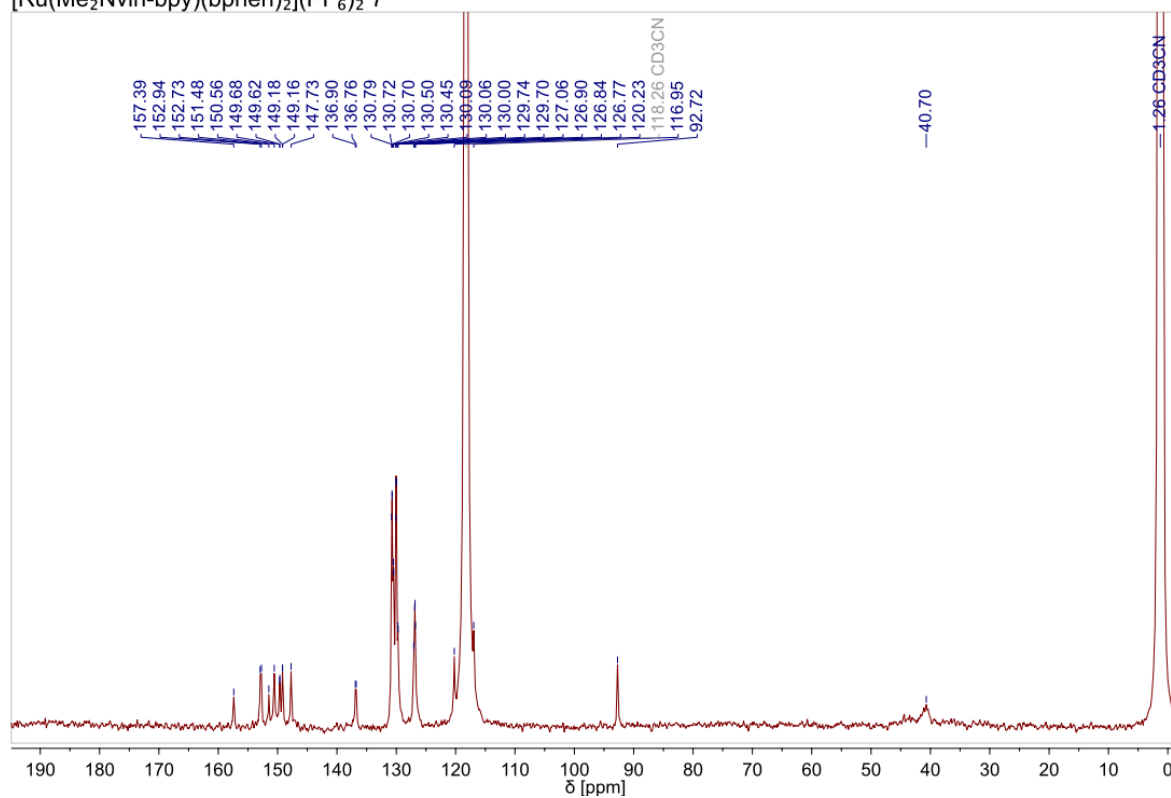


Figure S14. ¹H NMR spectrum of **7** in CD₃CN, 125 MHz.

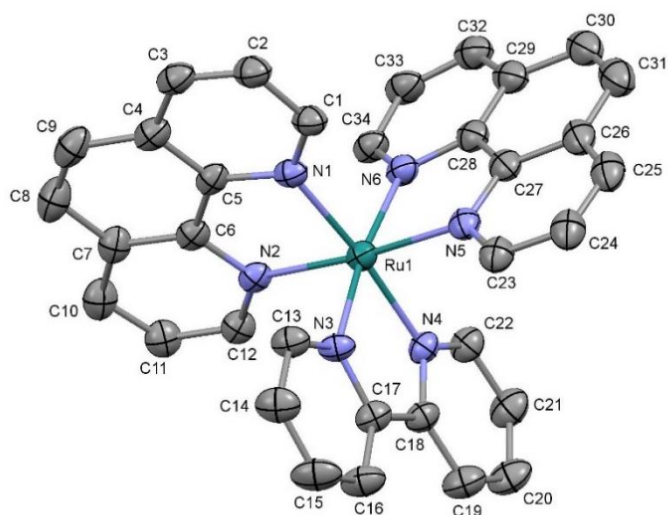


Figure S15. The molecular structure of 1 with displacement ellipsoids drawn at the 20% probability level. Solvent molecules, counterions and hydrogen atoms are excluded for clarity.

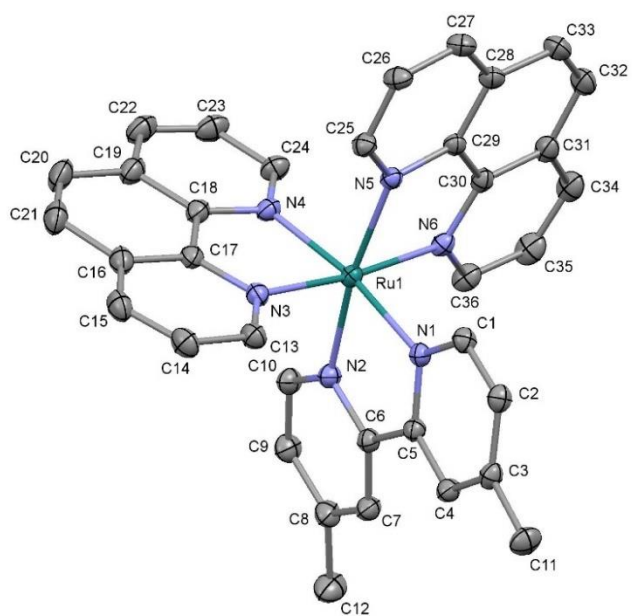


Figure S16. The molecular structure of 2 with displacement ellipsoids drawn at the 20% probability level. Solvent molecules, counterions and hydrogen atoms are excluded for clarity.

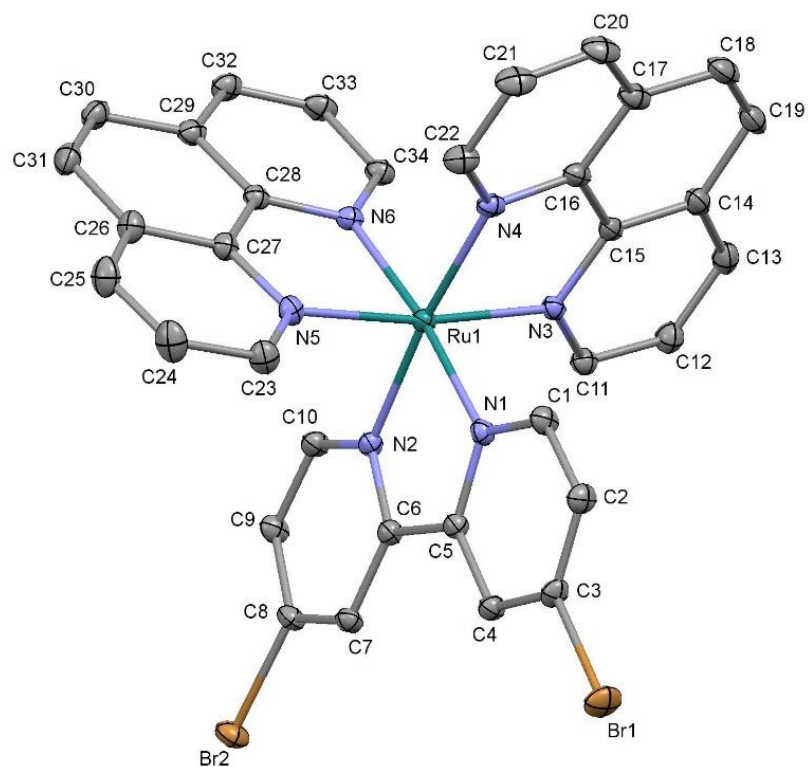


Figure S17. The molecular structure of **3** with displacement ellipsoids drawn at the 20% probability level. Solvent molecules, counterions and hydrogen atoms are excluded for clarity.

Table S8. Crystal data and structure refinement parameters for 1 and 2.

	1	2
CCDC number	1969709	1969708
Empirical formula	C ₃₈ H ₃₀ F ₁₂ N ₈ P ₂ Ru	C ₄₁ H _{38.5} F ₁₂ N ₆ O _{1.25} P ₂ Ru
Formula weight	989.71	1026.29
Temperature/K	183(1)	183(1)
Crystal system	monoclinic	triclinic
Space group	P2 ₁ /c	P-1
a/Å	12.4678(3)	12.8029(3)
b/Å	27.4167(4)	13.1575(2)
c/Å	13.2004(3)	16.2010(4)
α/°	90	79.9877(16)
β/°	118.159(3)	75.692(2)
γ/°	90	62.241(2)
Volume/Å ³	3978.16(16)	2334.63(10)
Z	4	2
ρ _{calc} /cm ³	1.652	1.460
μ/mm ⁻¹	4.832	4.143
F(000)	1984.0	1037.0
Crystal size/mm ³	0.11 × 0.06 × 0.04	0.39 × 0.15 × 0.03
Radiation	CuKα (λ = 1.54184)	CuKα (λ = 1.54184)
2θ range for data collection/°	6.448 to 148.99	7.6 to 149.0

Index ranges	-15 ≤ h ≤ 14, -30 ≤ k ≤ 34, -16 ≤ l ≤ 15, -16 ≤ k ≤ 15, -	
	≤ 16	20 ≤ l ≤ 20
Reflections collected	30861	44520
Independent reflections	8116 [R _{int} = 0.0339, R _{sigma} = 0.0251]	9539 [R _{int} = 0.0221, R _{sigma} = 0.0130]
Data/restraints/parameters	8116/114/524	9539/86/627
Goodness-of-fit on F ²	1.150	1.089
Final R indexes [I ≥ 2σ (I)]	R ₁ = 0.0756, wR ₂ = 0.1785	R ₁ = 0.0491, wR ₂ = 0.1495
Final R indexes [all data]	R ₁ = 0.0782, wR ₂ = 0.1799	R ₁ = 0.0523, wR ₂ = 0.1562
Largest diff. peak/hole / e Å ⁻³	1.13/-0.79	1.36/-0.35

Table S9. Crystal data and structure refinement parameters for **3**.**3**

CCDC number	1969710
Empirical formula	C ₃₈ H ₂₈ Br ₂ F ₁₂ N ₈ P ₂ Ru
Formula weight	1147.51
Temperature/K	183(1)
Crystal system	triclinic
Space group	P-1
a/Å	11.4219(3)
b/Å	12.3760(3)
c/Å	15.0464(4)
α/°	90.834(2)
β/°	98.147(2)
γ/°	101.020(2)
Volume/Å ³	2064.73(10)
Z	2
ρ _{calc} /cm ³	1.846
μ/mm ⁻¹	2.488
F(000)	1128.0
Crystal size/mm ³	0.29 × 0.25 × 0.17
Radiation	MoKα (λ = 0.71073)
2θ range for data collection/°	4.42 to 55.75

Index ranges	-15 ≤ h ≤ 15, -16 ≤ k ≤ 16, -19 ≤ l ≤ 19
Reflections collected	38483
Independent reflections	9850 [R _{int} = 0.0490, R _{sigma} = 0.0378]
Data/restraints/parameters	9850/312/643
Goodness-of-fit on F ²	1.031
Final R indexes [I ≥ 2σ (I)]	R ₁ = 0.0398, wR ₂ = 0.1020
Final R indexes [all data]	R ₁ = 0.0488, wR ₂ = 0.1096
Largest diff. peak/hole / e Å ⁻³	0.79/-0.61

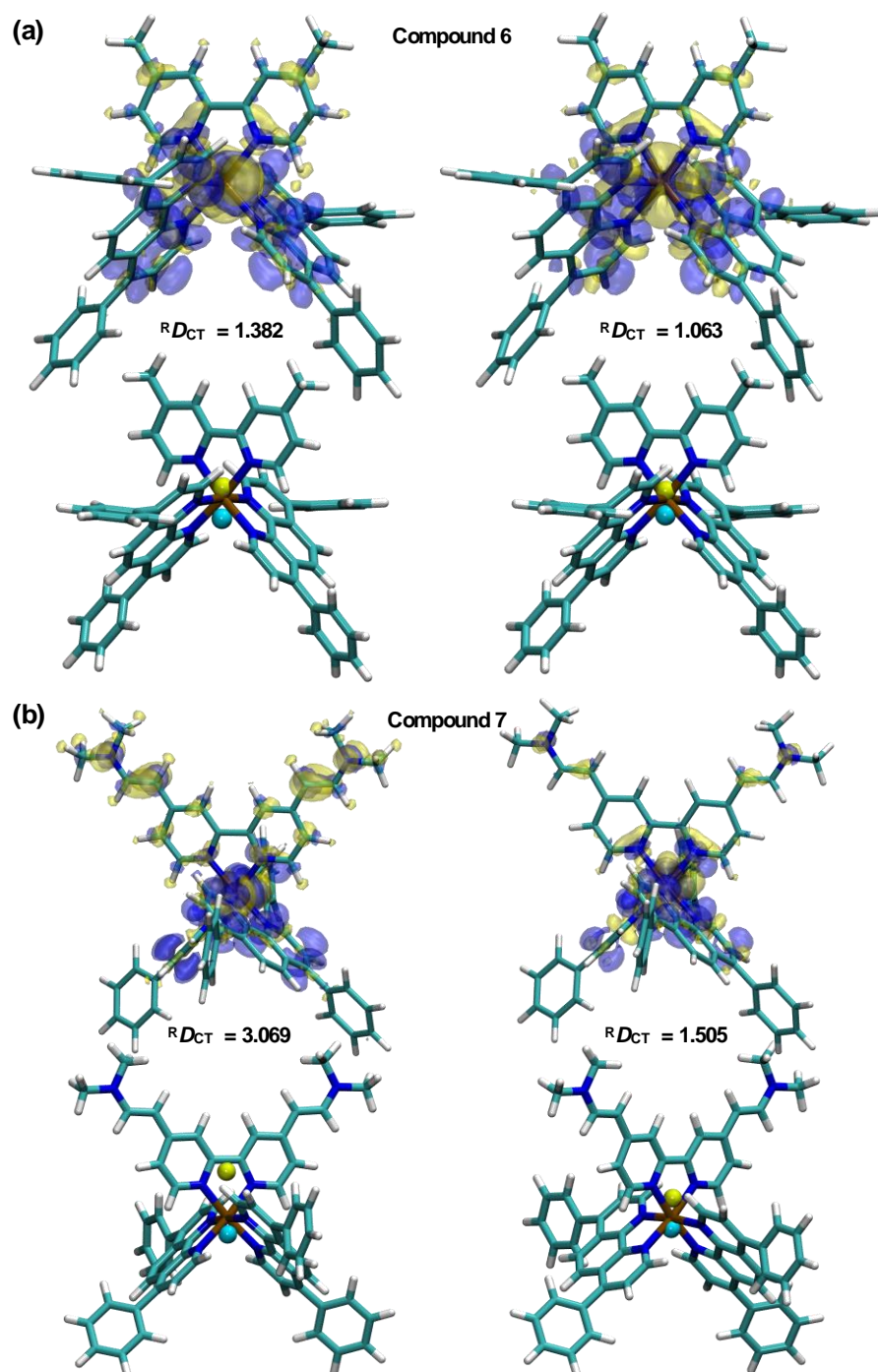


Figure S18. Difference density plots calculated between ES and GS (top row) computed for the first vertical transition and the first bright state MLCT transition of **6** (a) and **7** (b). For **7** both transitions are of MLCT type while the first one of **6** (a) is an inter-ligand charge transfer π - π^* transition. Yellow regions are characterized by an increase in density upon excitation while blue ones show a decrease in electron density. The barycenters are depicted as spheres (bottom rows) and the corresponding distances of charge transfer R_{DCT} (in Å) are stated above. Atoms color scheme: C - green; H - white; N - blue; O - red, Ru - brown.

Table S10. Spectroscopic properties of complexes **1-7** in CH₃CN at room temperature.

	UV/Vis λ [nm] (ϵ [$M^{-1} cm^{-1} \times 10^3$])	Absorption	Emission λ_{em} [nm]	Φ_{em}	Lifetime [ns]	
					Air sat.	degassed
1	200 (73.2), 225 (64.3), 264 (86.5), 284 (44.1), 446 (15.0)		600	0.027	130	766
2	202 (77.9), 222 (61.5), 264 (81.7), 280 (43.9), 421 (12.8), 449 (13.9)		606	0.050	110	918
3	201 (72.9), 223 (91.0), 263 (95.2), 289 (45.1), 388 (11.5), 441 (14.8)		645	0.014	207	617
4	201 (100.1), 223 (91.3), 263 (105.8), 308 (28.2), 386 (13.8), 438 (16.7), 441 (16.8)		654	0.020	326	1387
5	201 (89.3), 224 (81.2), 265 (91.1), 379 (25.6), 458 (23.1)		703	<0.001	75	339
6	192 (183.4), 279 (126.3), 441 (23.2), 457 (23.2)		623	0.021	161	1096
7	192 (168.8), 280 (102.5), 371 (35.0), 465 (30.1)		694	<0.001	55	312

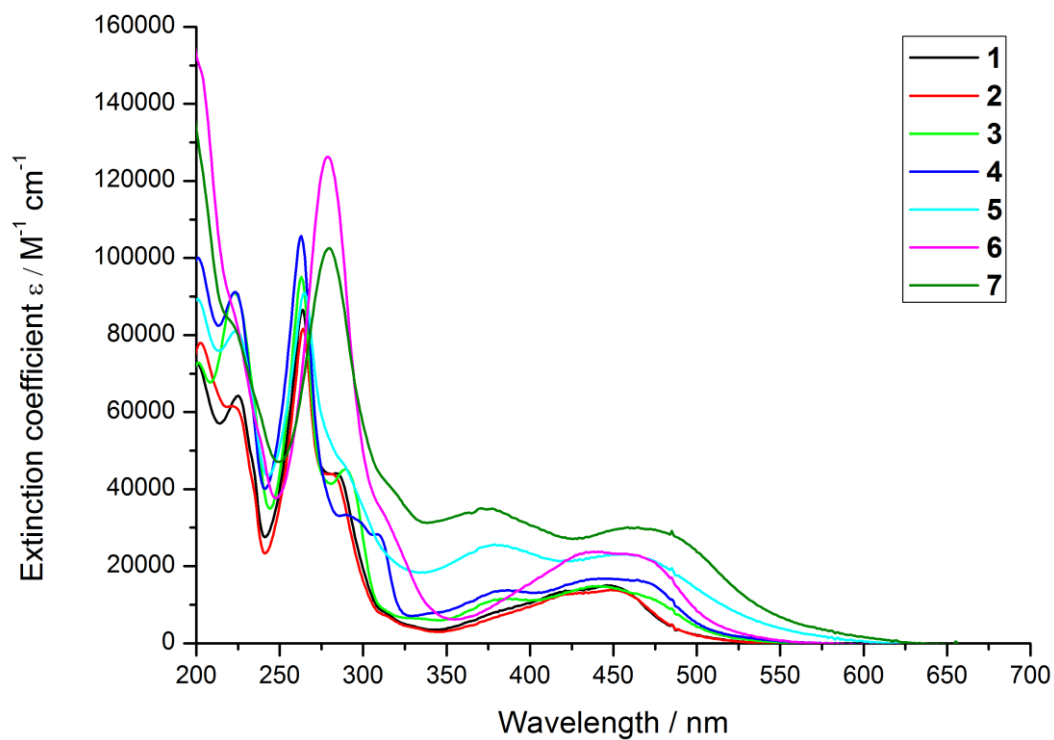


Figure S19. Measured UV/Vis spectra of the complexes **1-7** in CH₃CN.

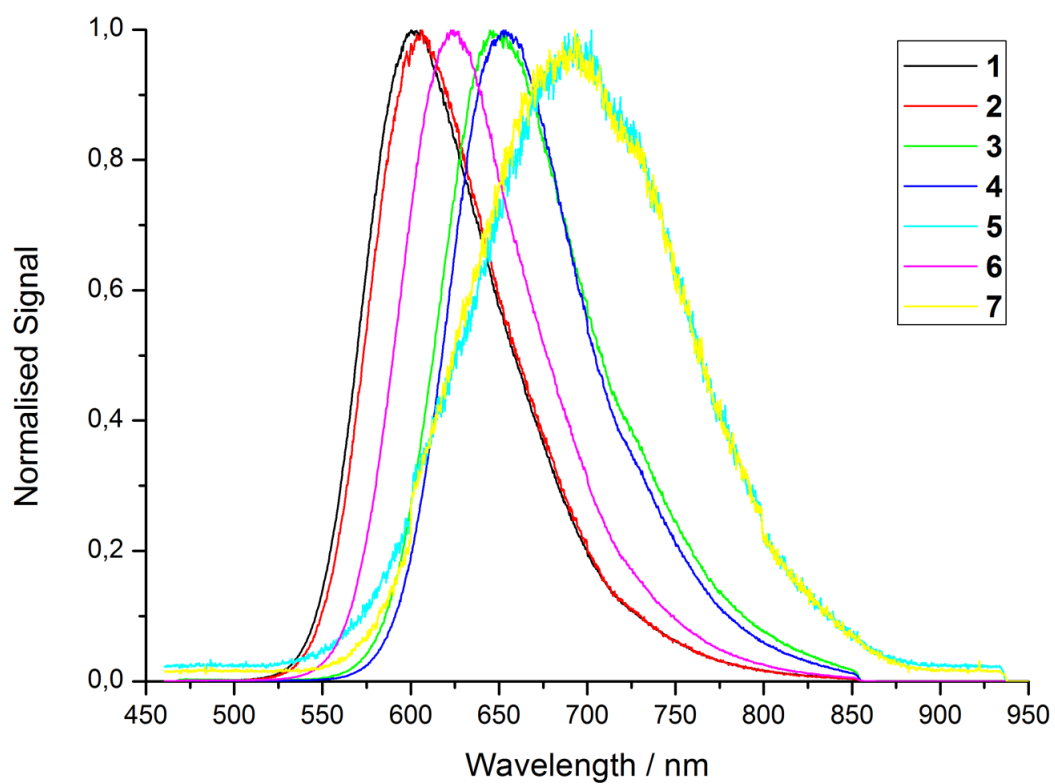


Figure S20. Normalised emission spectra of the complexes **1-7** in CH₃CN.

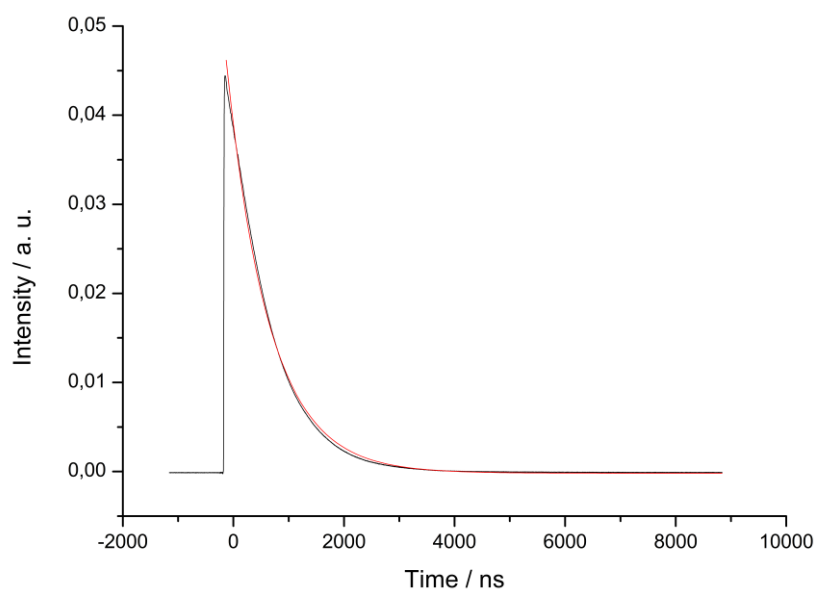
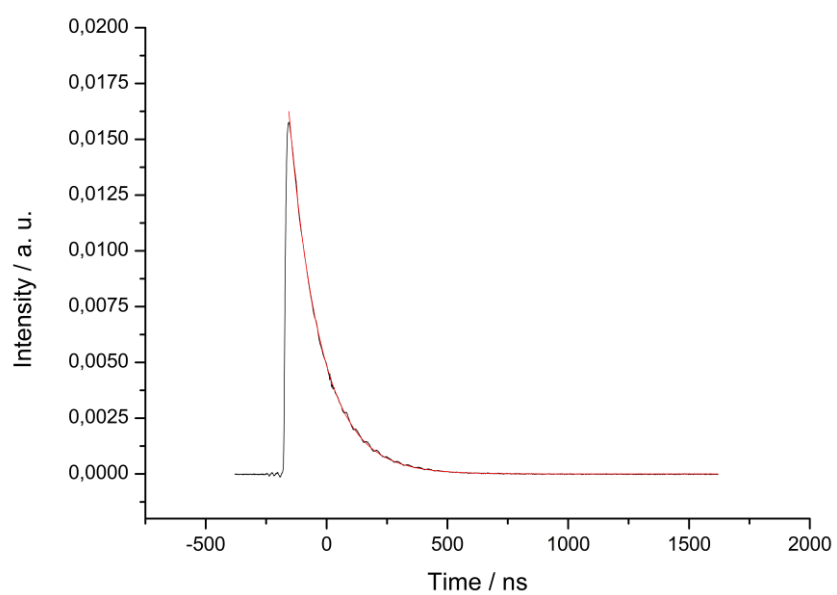


Figure S21. Lifetime spectra of the complexes 1 in aerated (above) and degassed (below) CH_3CN .

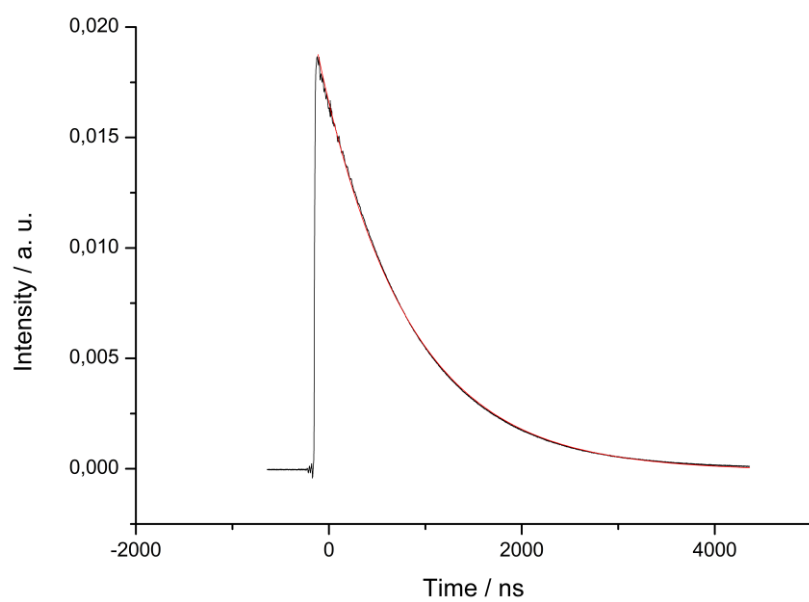
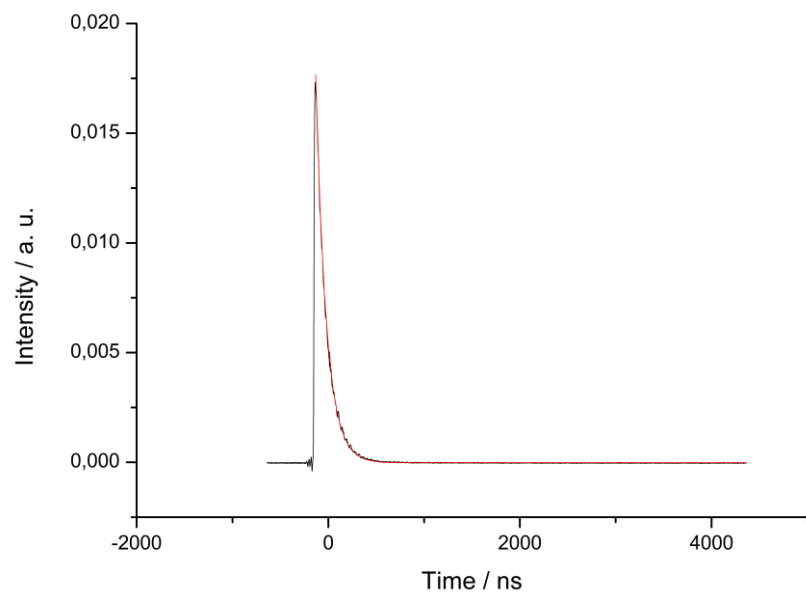


Figure S22. Lifetime spectra of the complexes 2 in aerated (above) and degassed (below) CH₃CN.

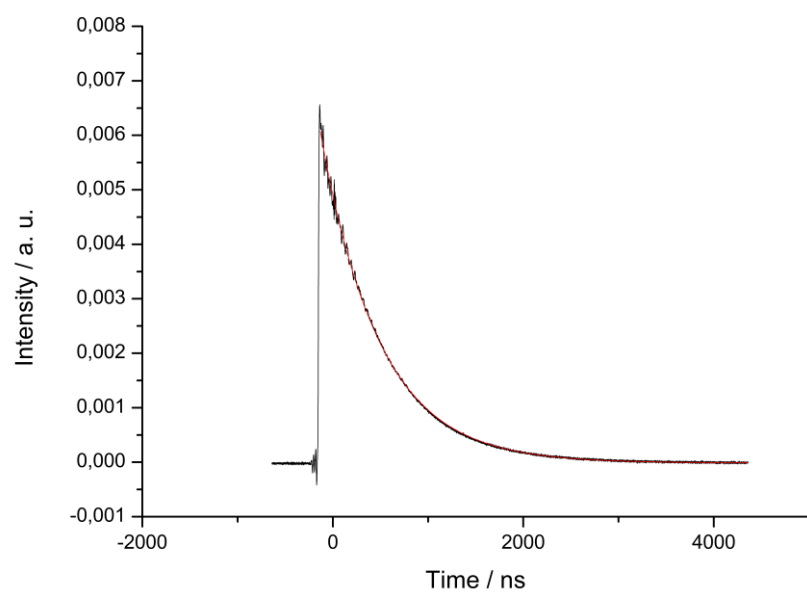
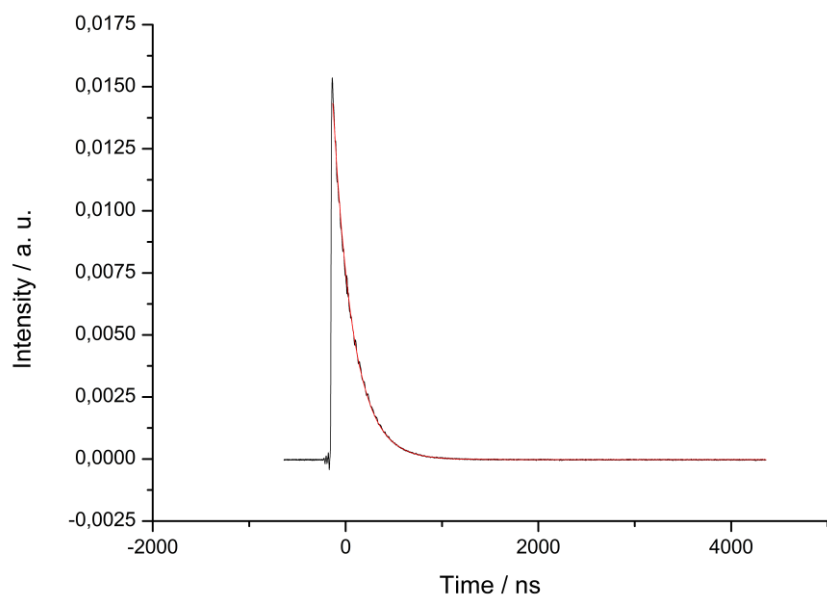


Figure S23. Lifetime spectra of the complexes 3 in aerated (above) and degassed (below) CH_3CN .

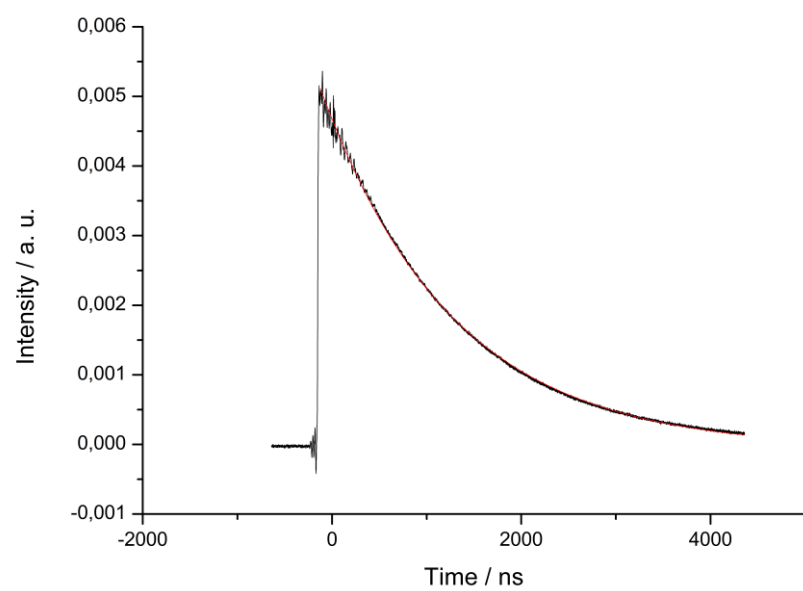
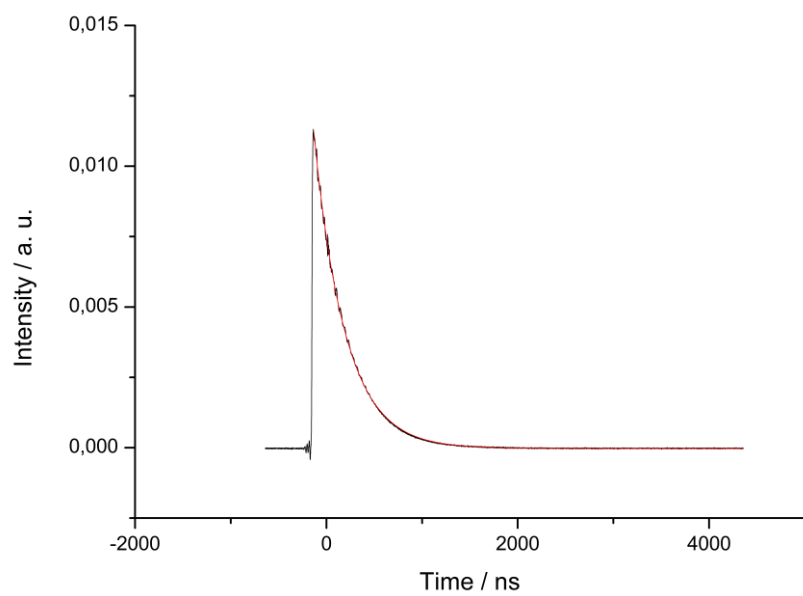


Figure S24. Lifetime spectra of the complexes 4 in aerated (above) and degassed (below) CH_3CN .

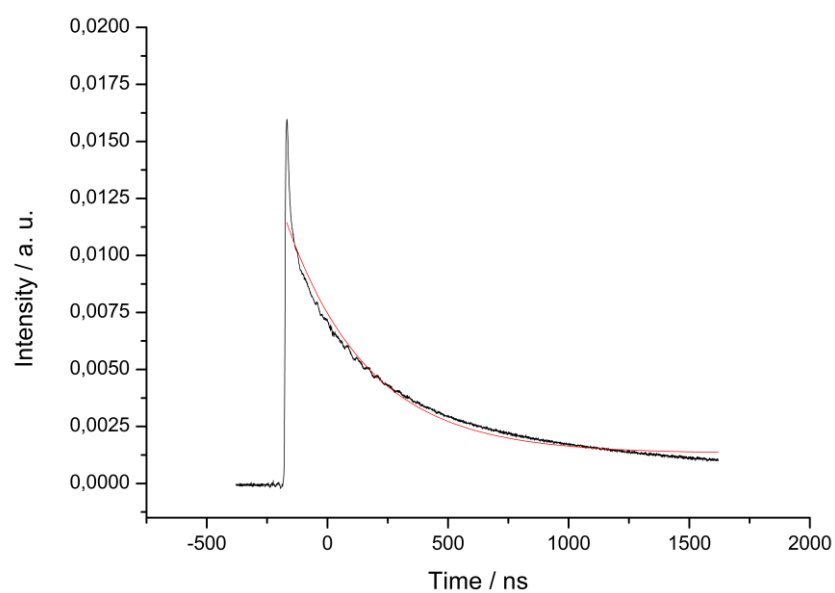
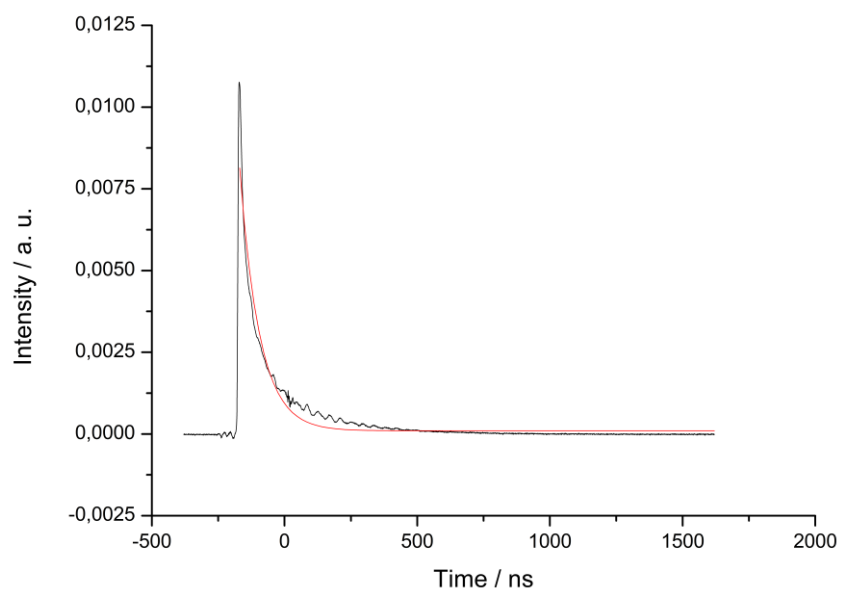


Figure S25. Lifetime spectra of the complexes 5 in aerated (above) and degassed (below) CH_3CN .

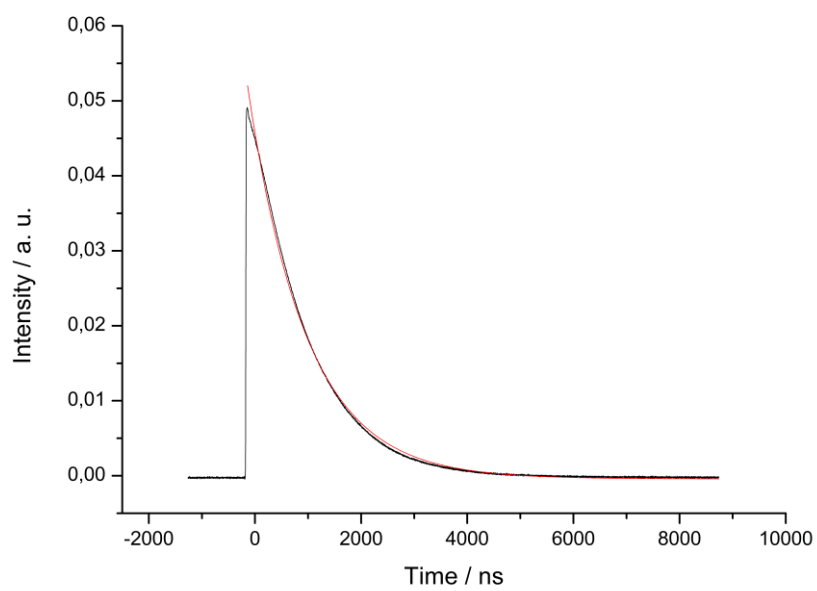
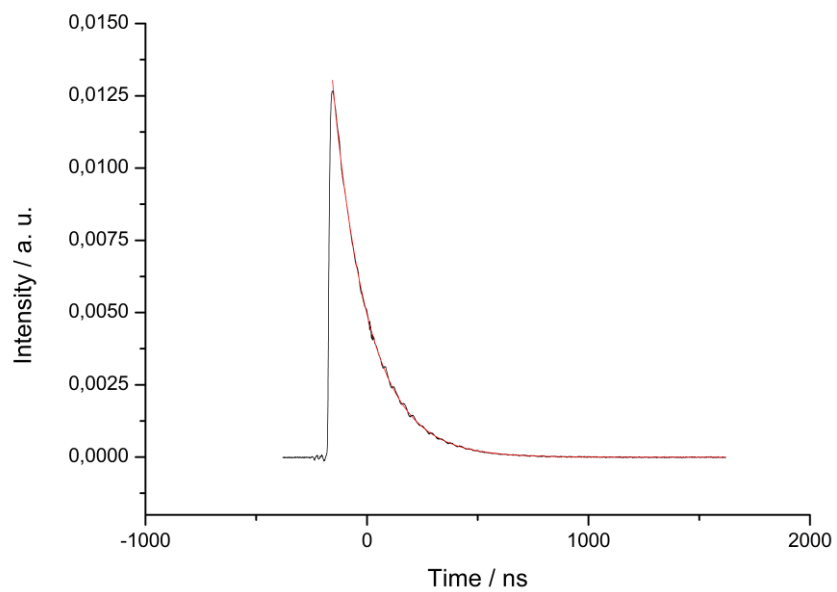


Figure S26. Lifetime spectra of the complexes 6 in aerated (above) and degassed (below) CH₃CN.

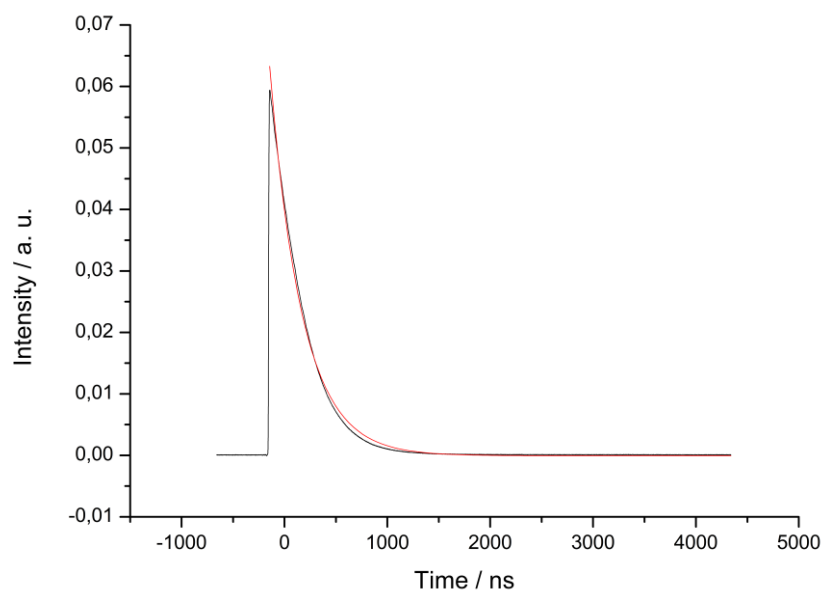
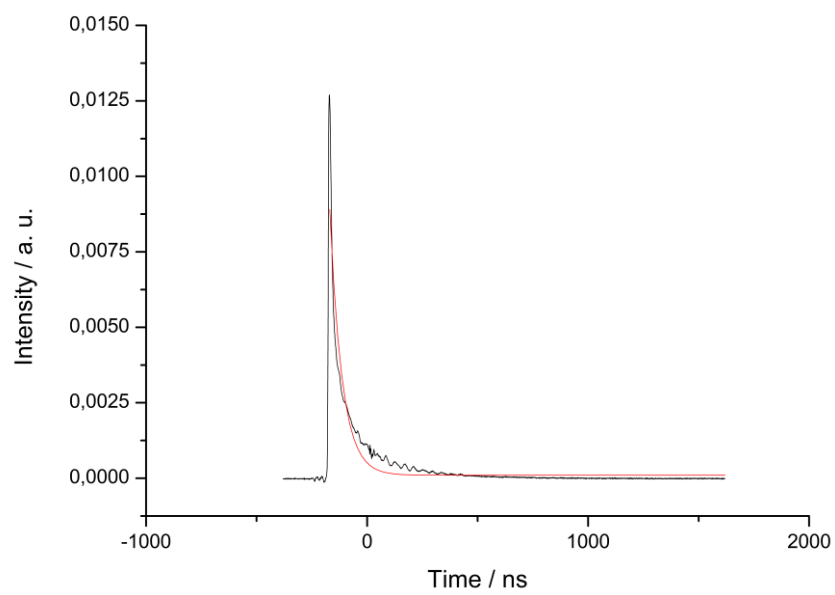


Figure S27. Lifetime spectra of the complexes 7 in aerated (above) and degassed (below) CH_3CN .

Table S11. Singlet oxygen quantum yields ($\Phi(^1\text{O}_2)$) in CH_3CN and aqueous solution determined by direct and indirect methods by excitation at 450 nm. Average of three independent measurements, $\pm 10\%$.

Compound	CH_3CN	CH_3CN	D_2O	PBS
	Direct	Indirect	Direct	indirect
1	0.57	0.54	0.27	0.36
2	0.69	0.53	0.31	0.34
3	0.55	0.56	n.d.	0.21
4	0.62	0.59	0.25	0.26
5	0.24	0.30	n.d.	0.21
6	0.61	0.63	n.d.	0.05
7	0.22	0.35	n.d.	0.07

n.d. = not determinable, $\Phi(^1\text{O}_2) < 0.20$.

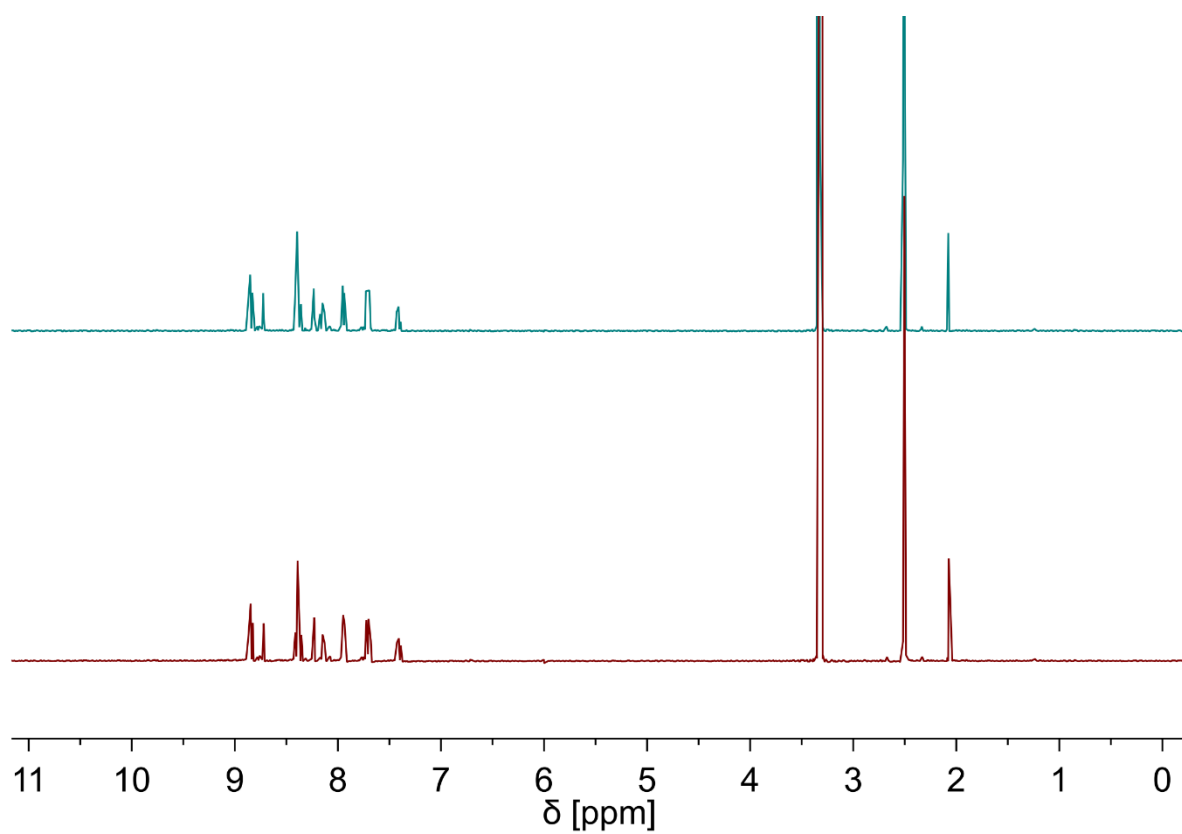


Figure S28. ^1H NMR spectrum of 1 in DMSO-d_6 after preparation (green) and 7 days (red).

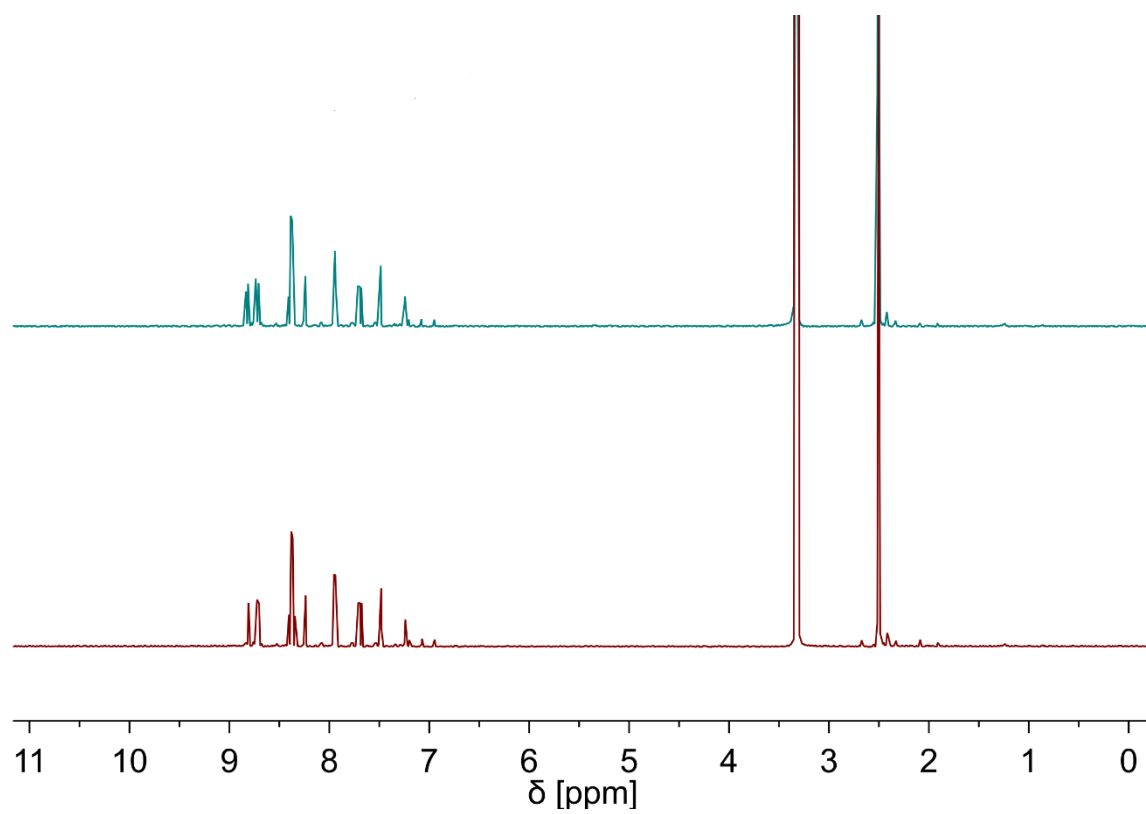


Figure S29. ¹H NMR spectrum of 2 in DMSO-d₆ after preparation (green) and 7 days (red).

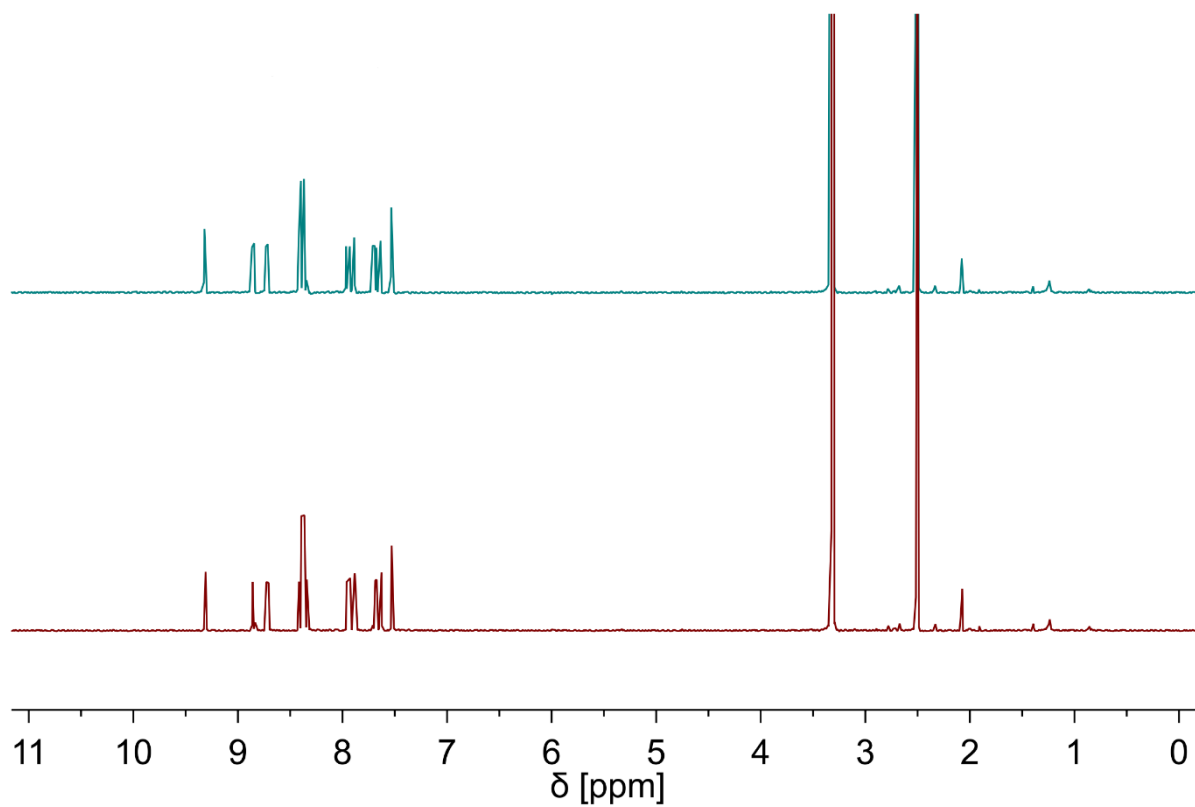


Figure S30. ¹H NMR spectrum of 3 in DMSO-d₆ after preparation (green) and 7 days (red).

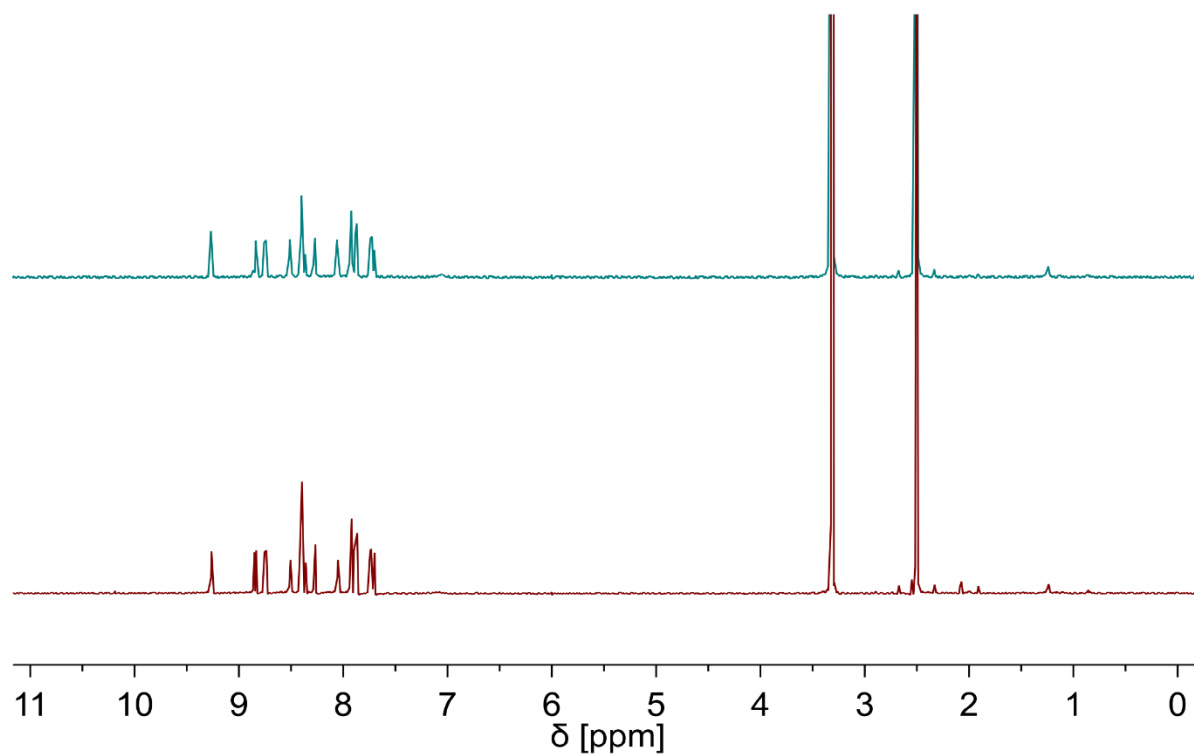


Figure S31. ¹H NMR spectrum of **4** in DMSO-d₆ after preparation (green) and 7 days (red).

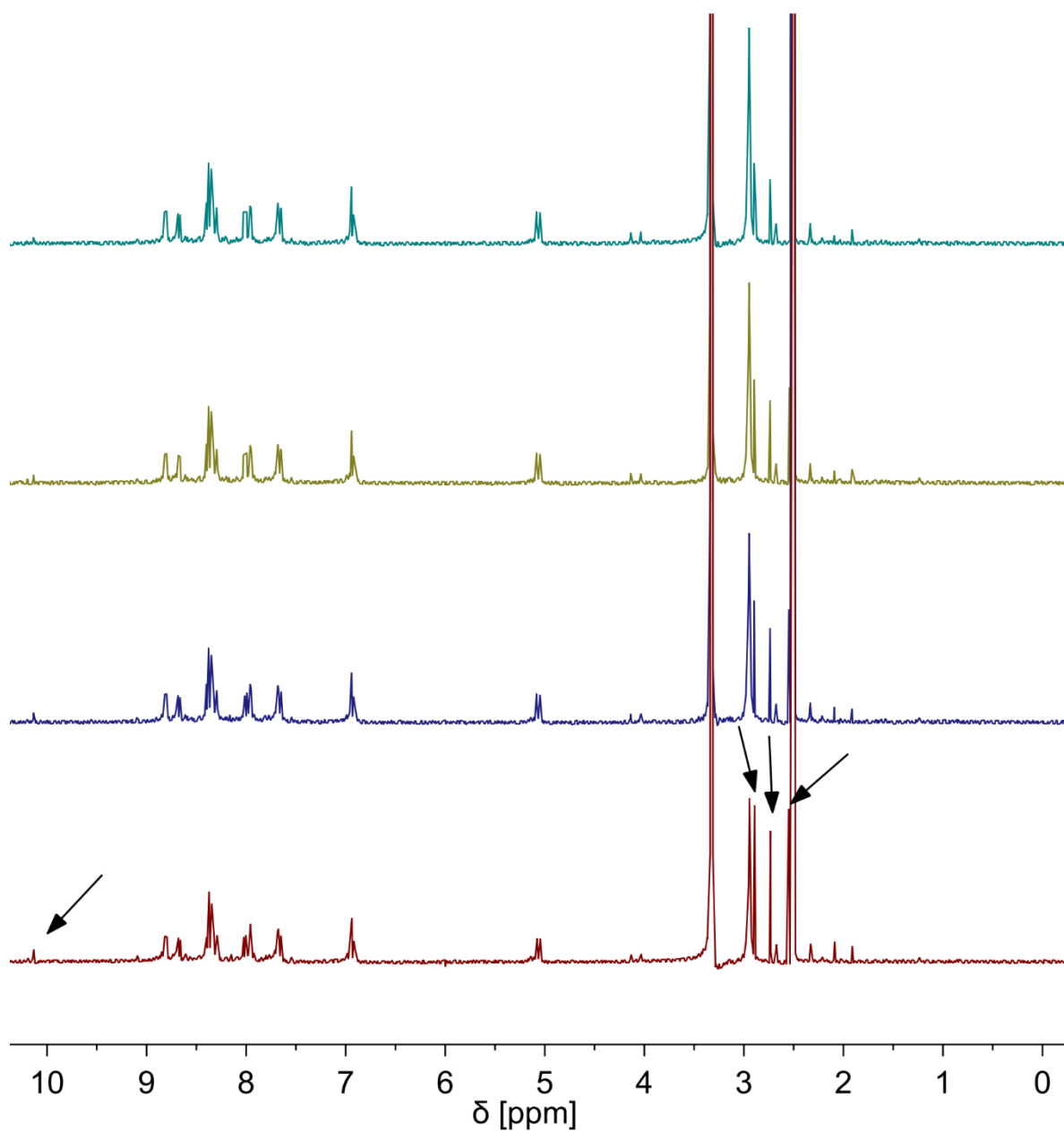


Figure S32. ¹H NMR spectrum of 5 in DMSO-d₆ after preparation (green), 1 day (olive), 2 days (blue) and 7 days (red).

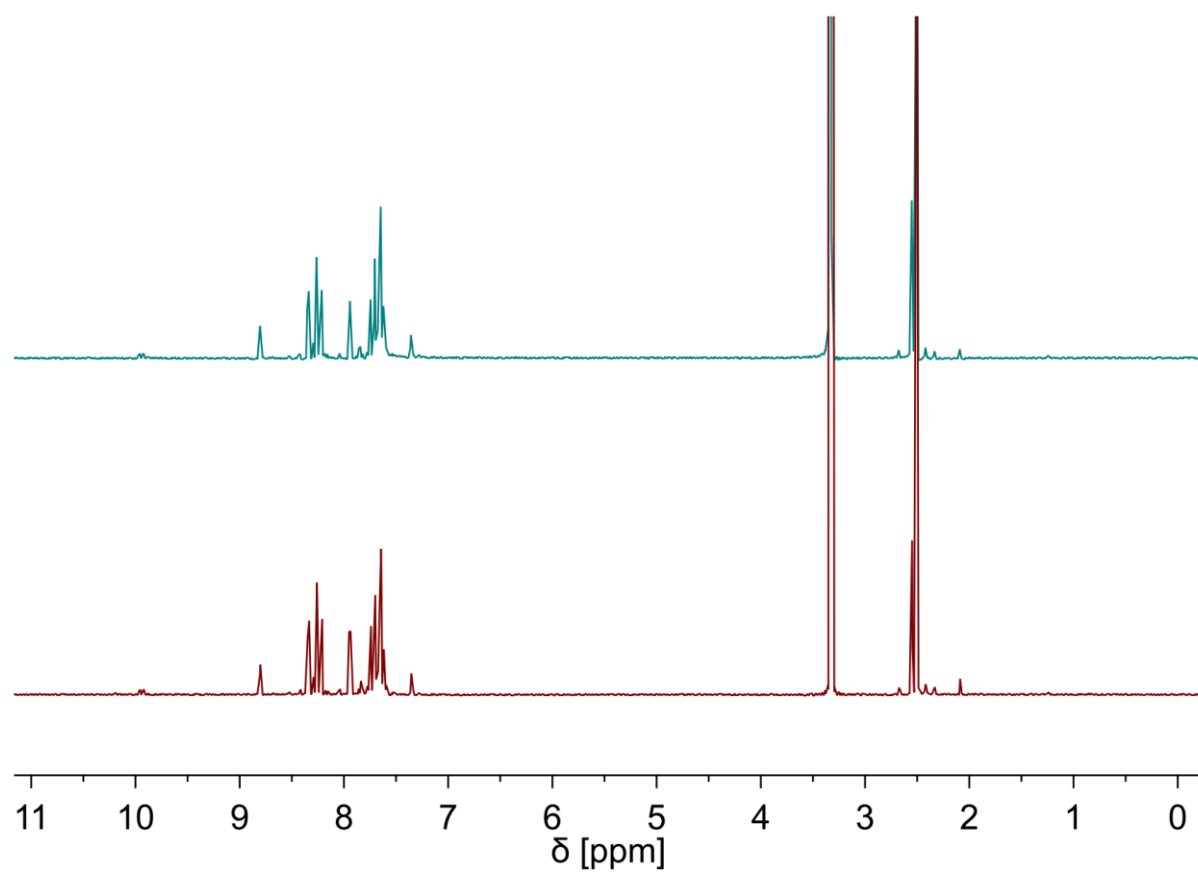


Figure S33. ¹H NMR spectrum of 6 in DMSO-d₆ after preparation (green) and 7 days (red).

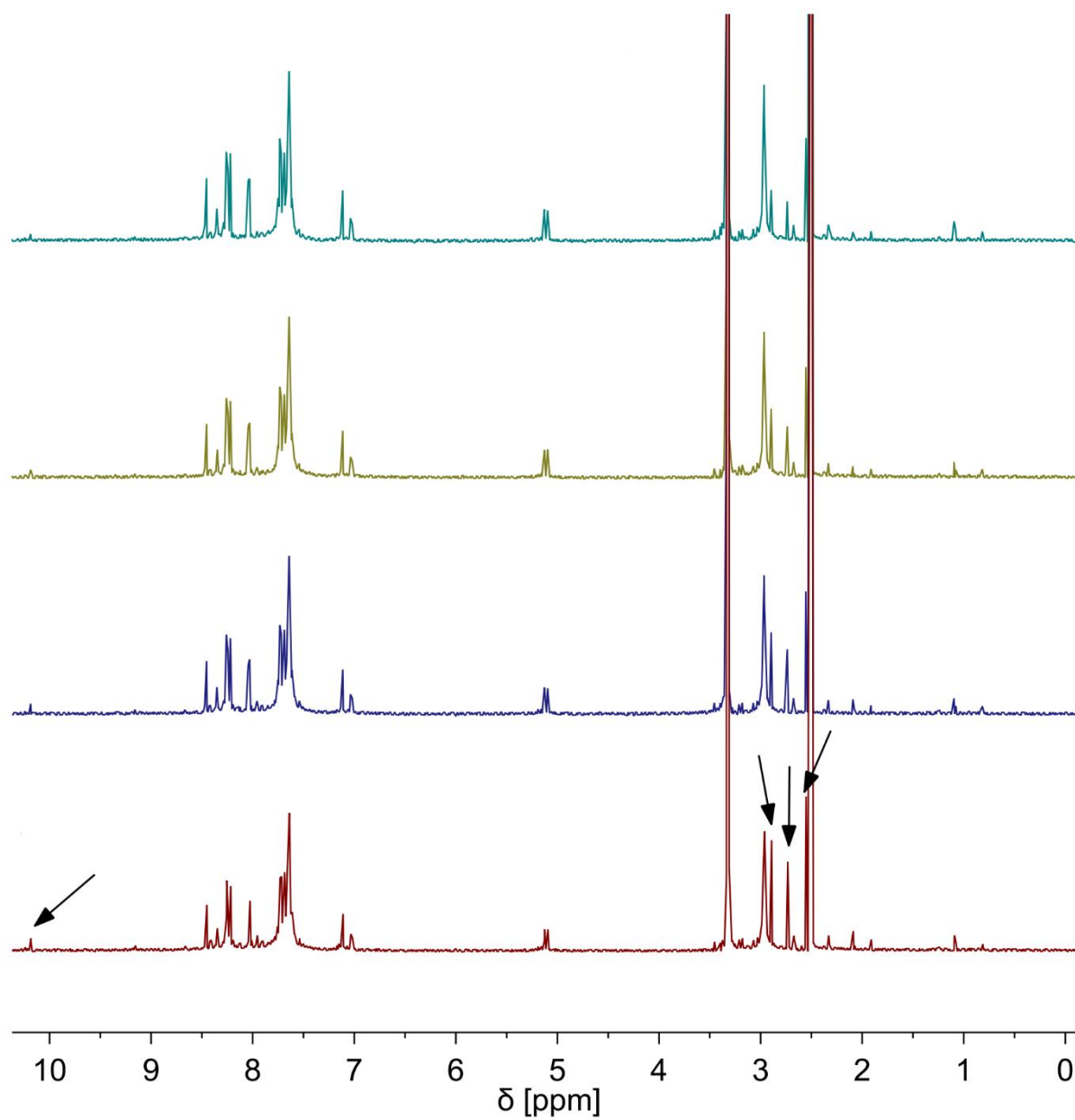


Figure S34. ¹H NMR spectrum of 7 in DMSO-d₆ after preparation (green), 1 day (olive), 2 days (blue) and 7 days (red).

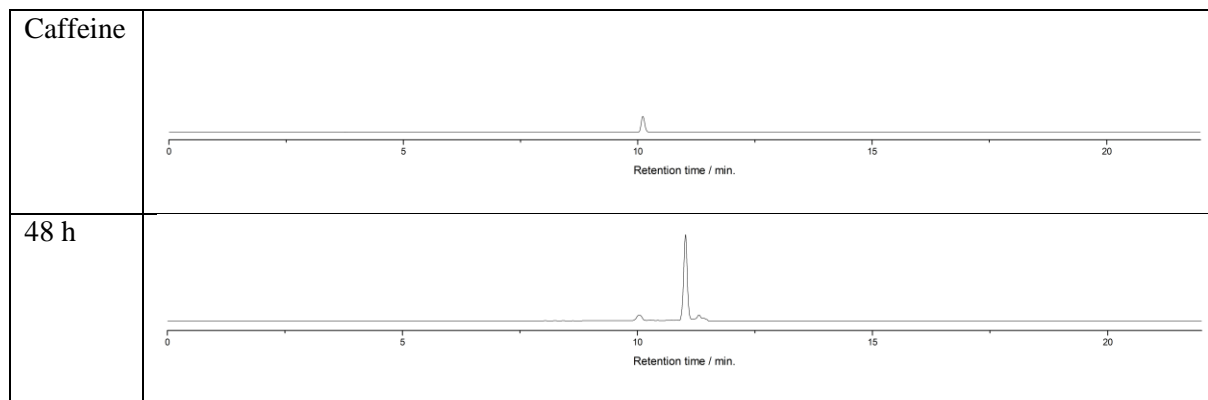


Figure S35. HPLC chromatogram (Method M1) of Caffeine (internal standard) and **1** after 48 h incubation in human pooled plasma.

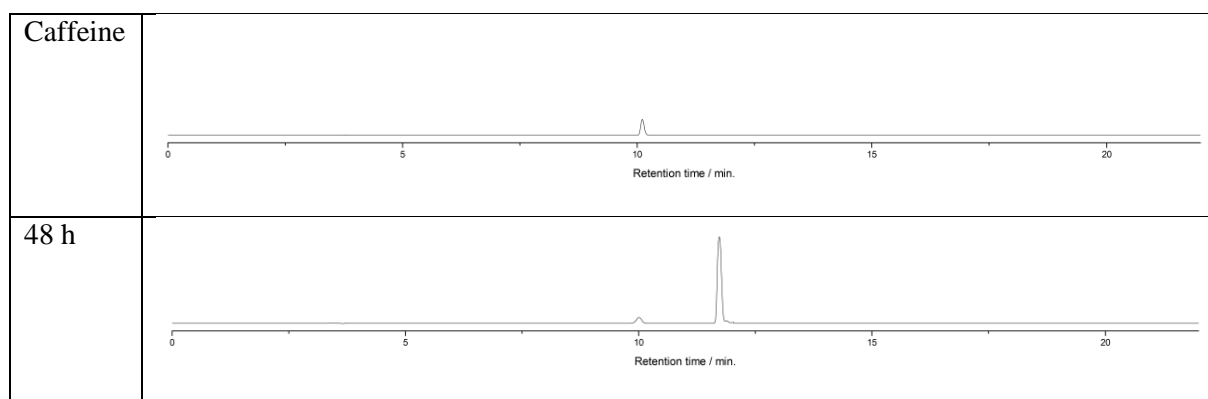


Figure S36. HPLC chromatogram (Method M1) of Caffeine (internal standard) and **2** after 48 h incubation in human pooled plasma.

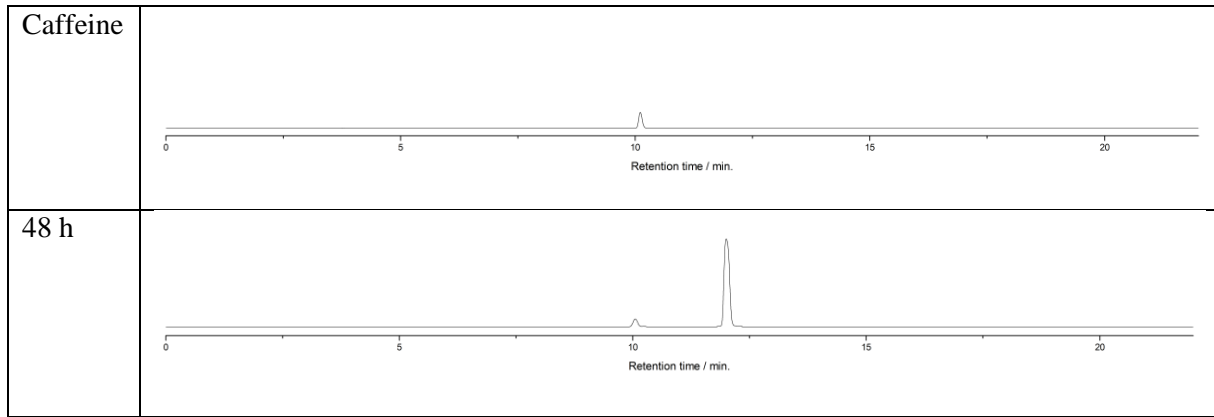


Figure S37. HPLC chromatogram (Method M1) of Caffeine (internal standard) and 3 after 48 h incubation in human pooled plasma.

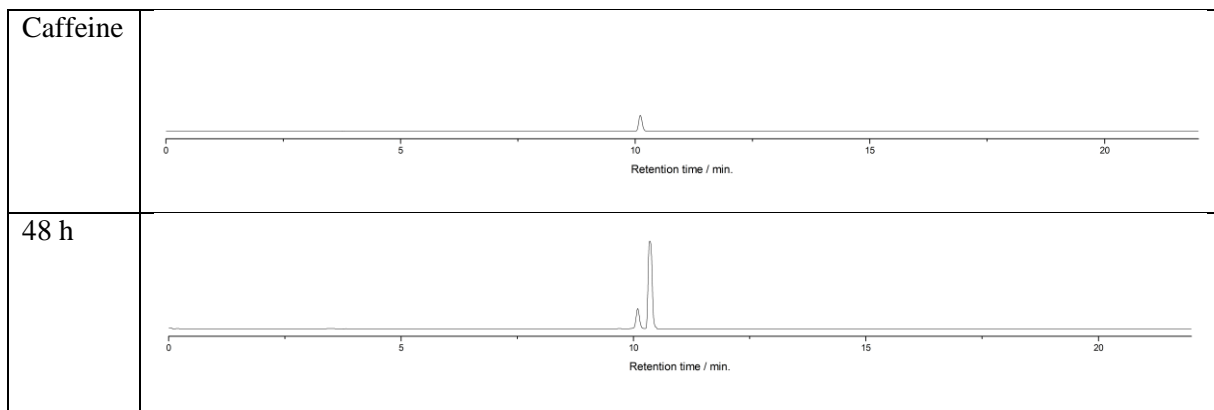


Figure S38. HPLC chromatogram (Method M1) of Caffeine (internal standard) and 4 after 48 h incubation in human pooled plasma.

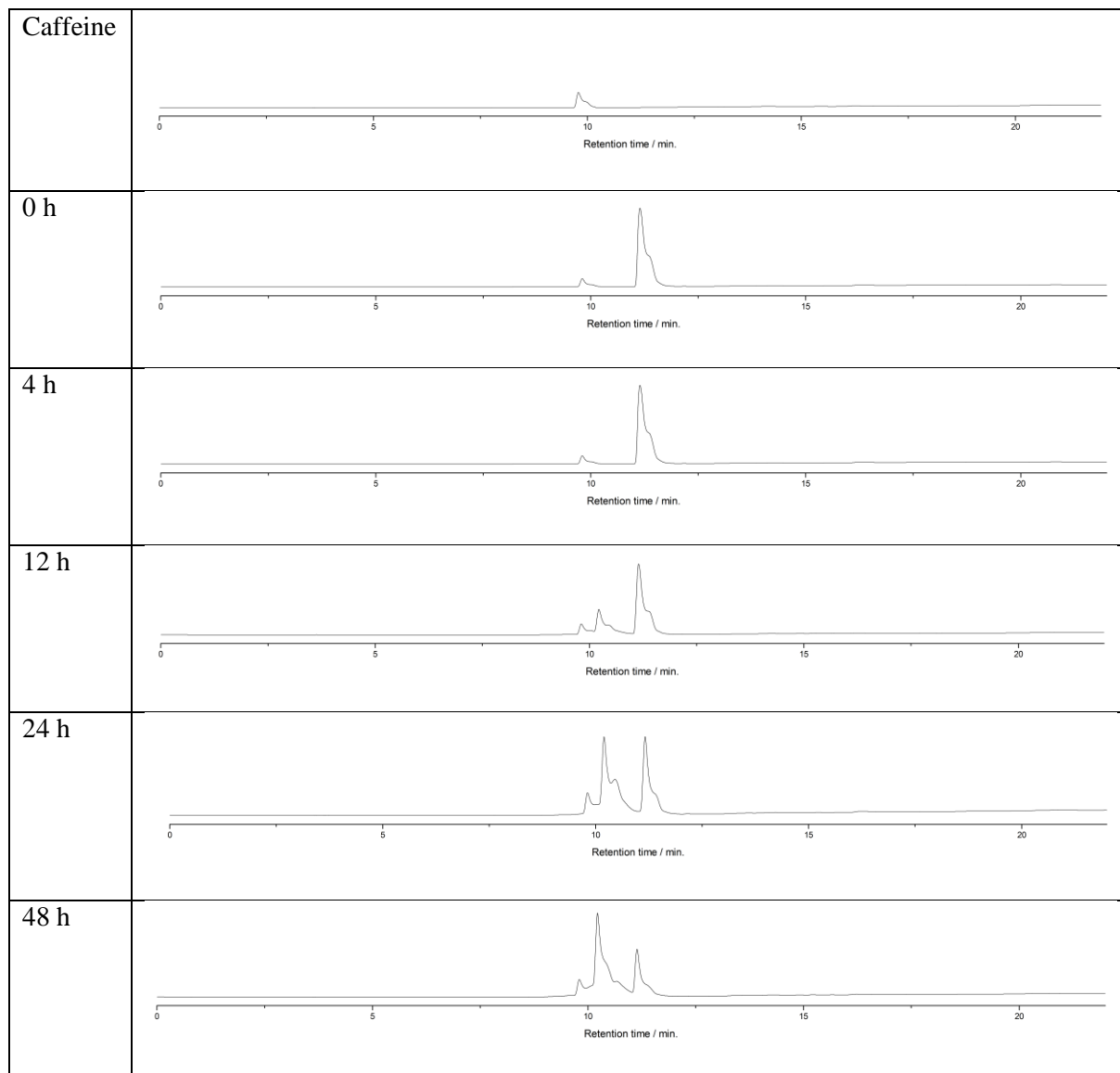


Figure S39. HPLC chromatogram (Method M2) of Caffeine (internal standard) and 5 after 0 h, 4 h, 12 h, 24 h and 48 h incubation in human pooled plasma.

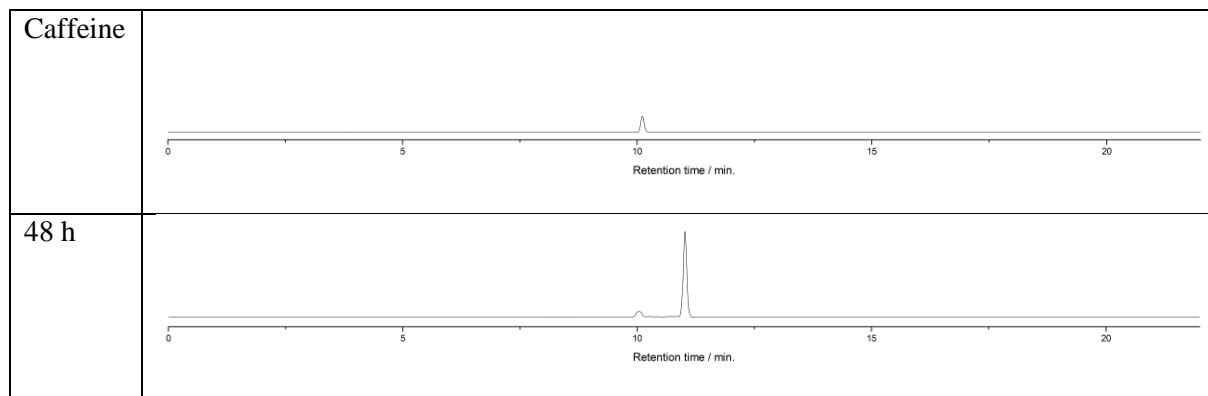


Figure S40. HPLC chromatogram (Method M1) of Caffeine (internal standard) and 6 after 48 h incubation in human pooled plasma.

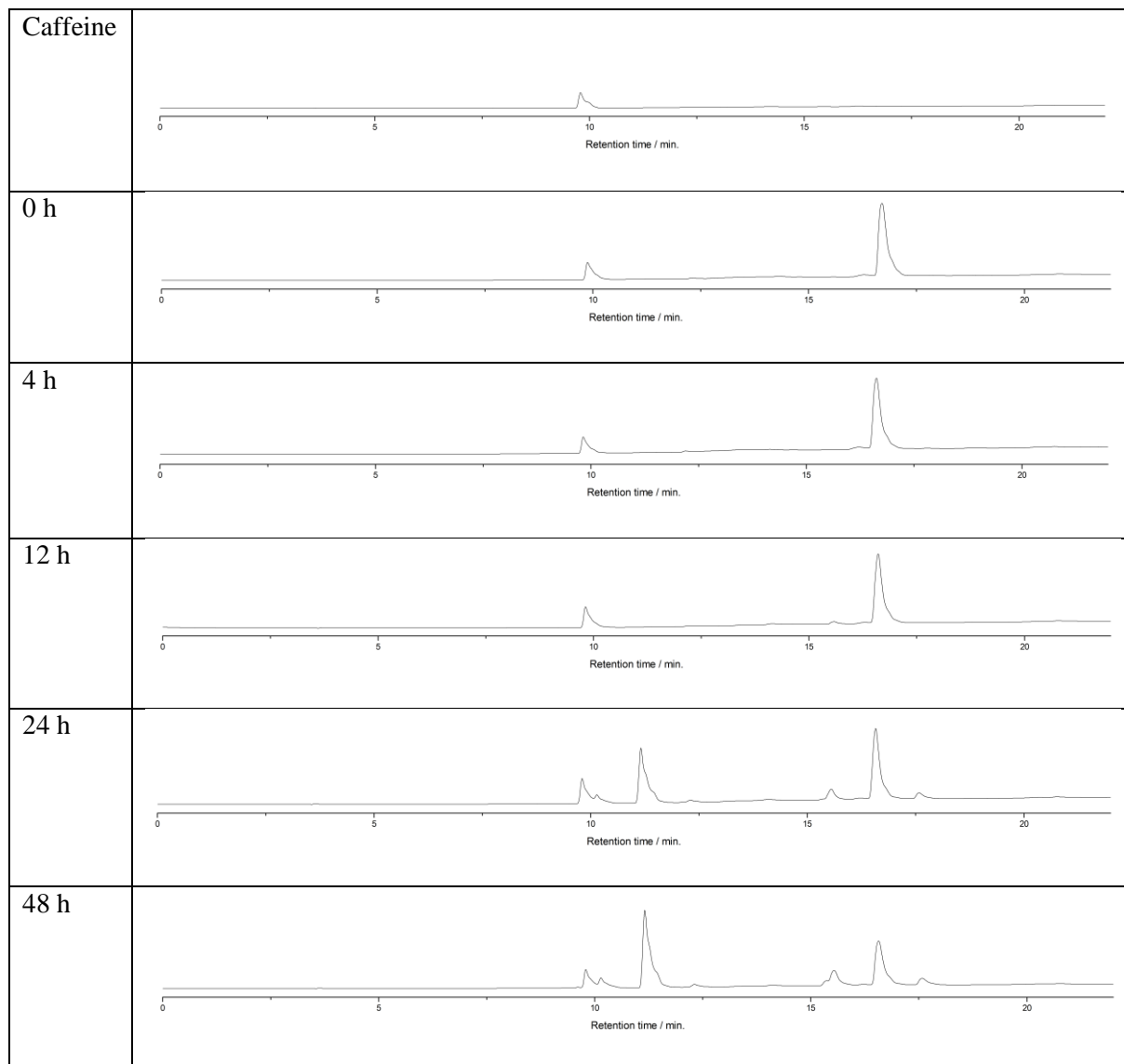


Figure S41. HPLC chromatogram (Method M2) of Caffeine (internal standard) and **7** after 0 h, 4 h, 12 h, 24 h and 48 h incubation in human pooled plasma.

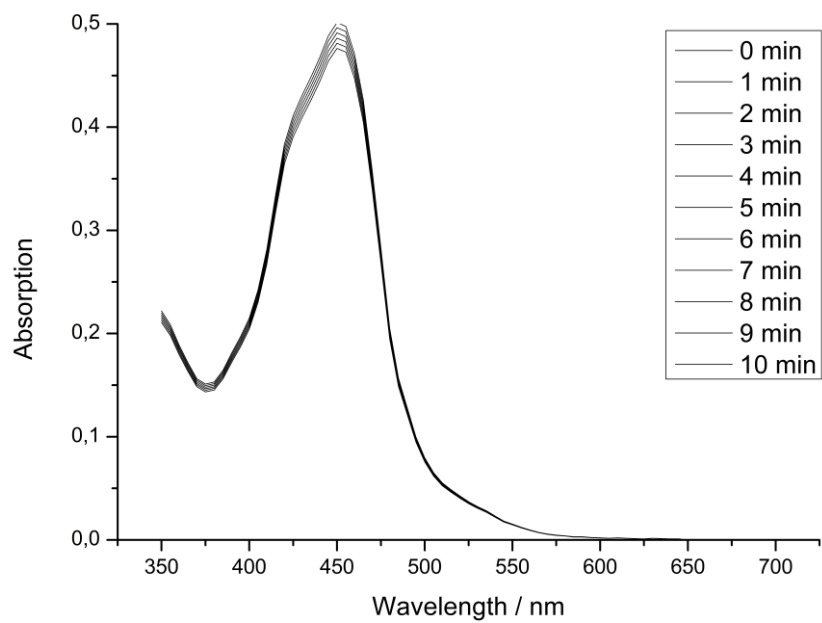


Figure S42. Temporal change of the UV/Vis spectra of [Ru(bipy)₃]Cl₂ by irradiation at 450 nm in CH₃CN.

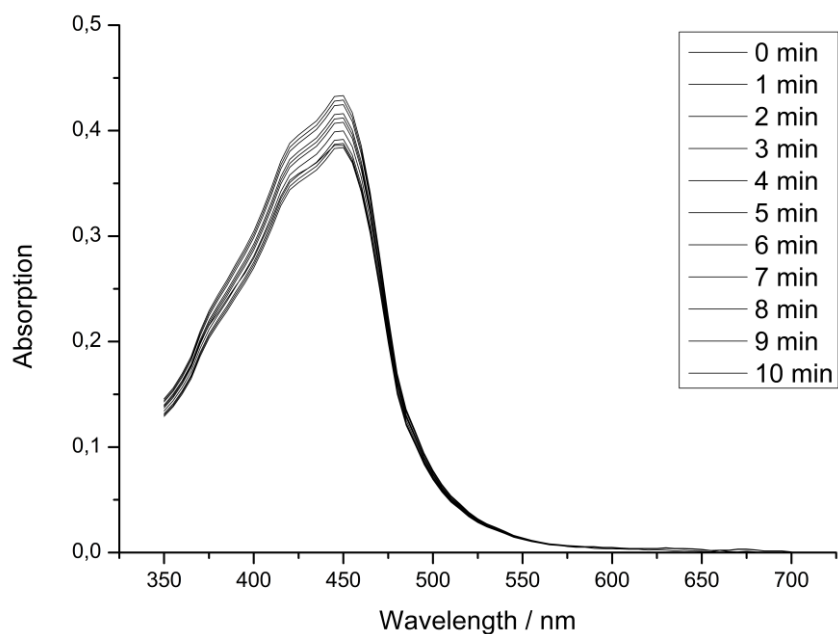


Figure S43. Temporal change of the UV/Vis spectra of complex **1** by irradiation at 450 nm in CH₃CN.

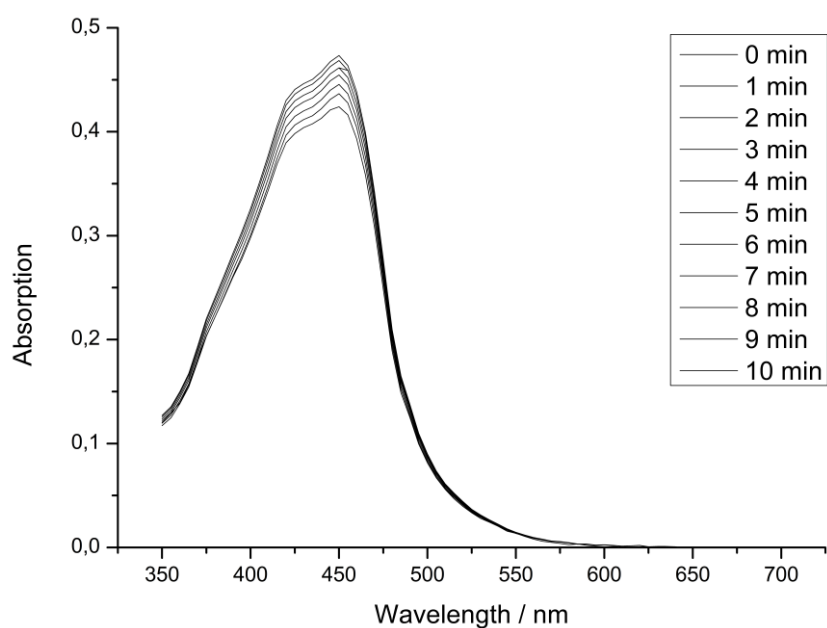


Figure S44. Temporal change of the UV/Vis spectra of complex **2** by irradiation at 450 nm in CH₃CN.

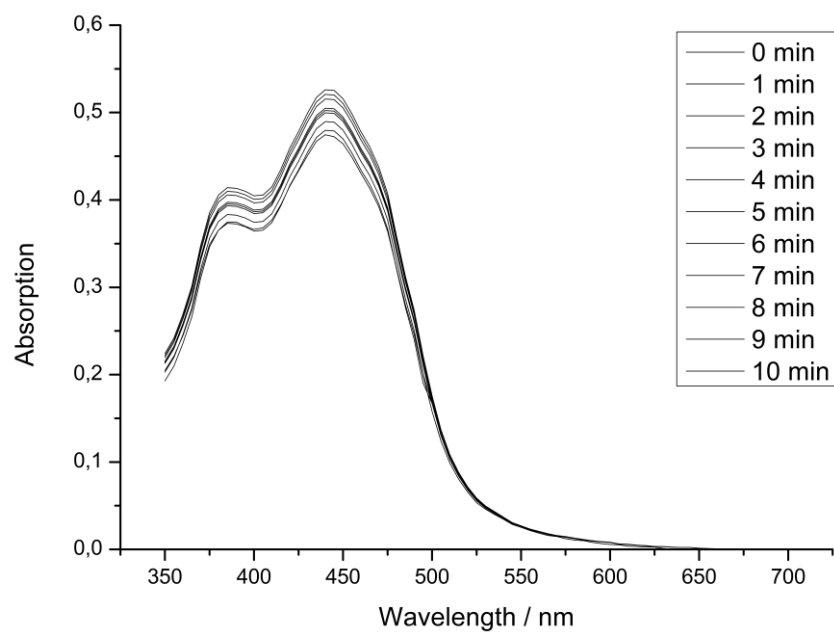


Figure S45. Temporal change of the UV/Vis spectra of complex 3 by irradiation at 450 nm in CH₃CN.

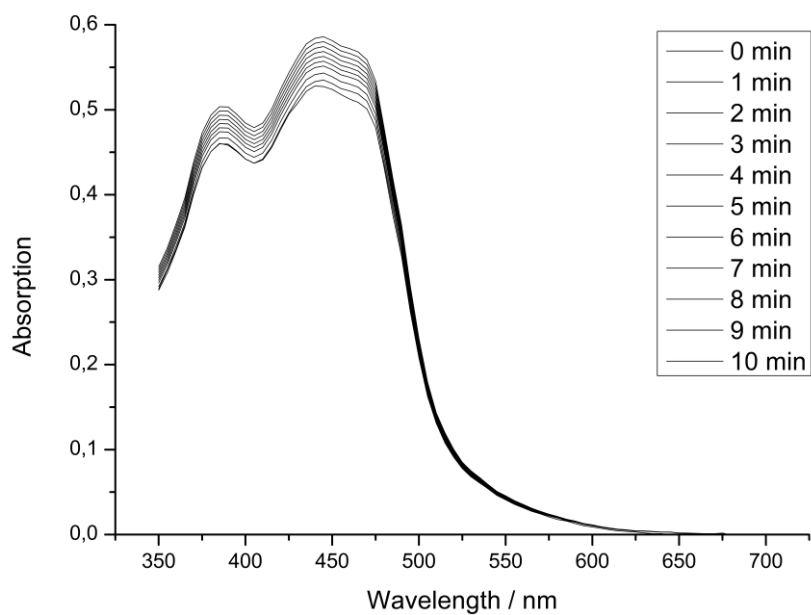


Figure S46. Temporal change of the UV/Vis spectra of complex 4 by irradiation at 450 nm in CH₃CN.

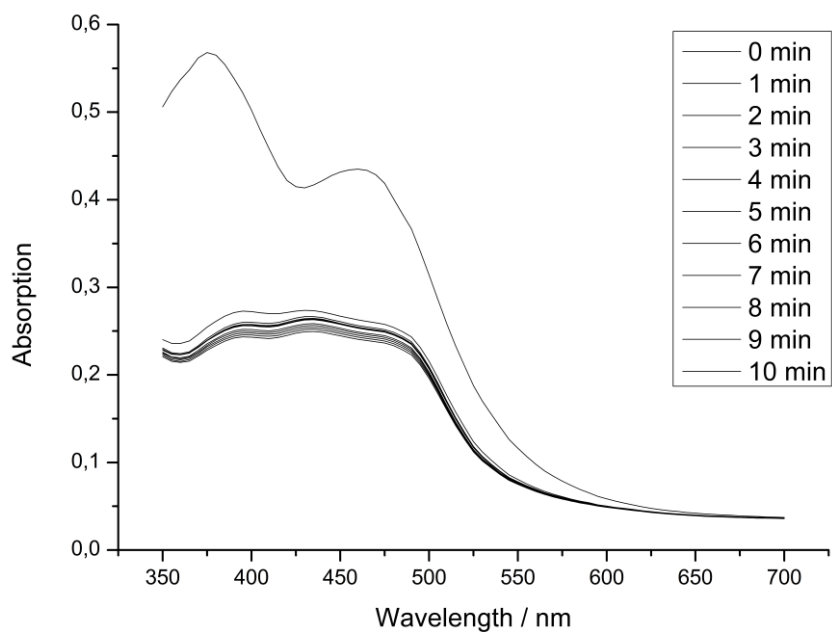


Figure S47. Temporal change of the UV/Vis spectra of complex **5** by irradiation at 450 nm in CH₃CN.

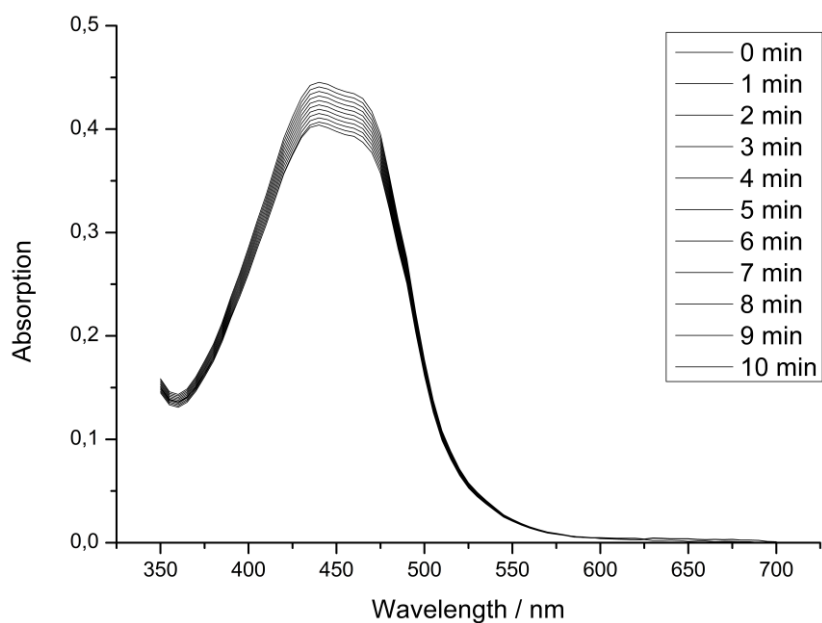


Figure S48. Temporal change of the UV/Vis spectra of complex **6** by irradiation at 450 nm in CH₃CN.

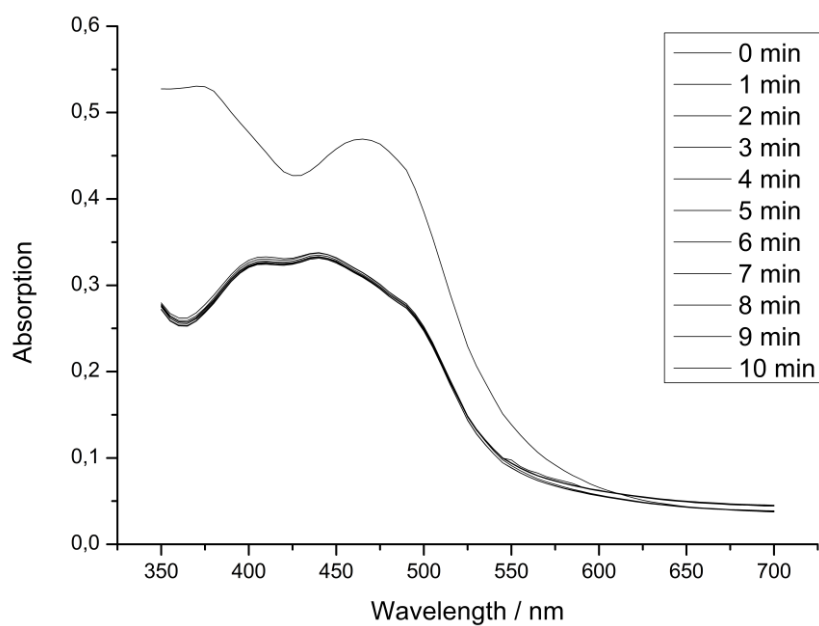


Figure S49. Temporal change of the UV/Vis spectra of complex 7 by irradiation at 450 nm in CH₃CN.

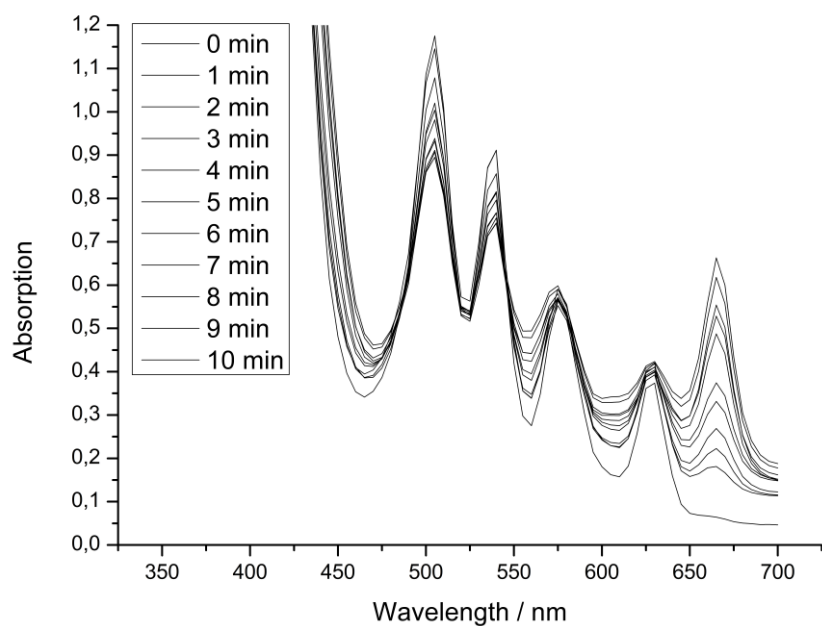


Figure S50. Temporal change of the UV/Vis spectra of Protoporphyrin IX by irradiation at 450 nm in CH₃CN.

Table S12. Distribution coefficients of **1-7** between an organic octanol and aqueous phosphate buffer saline phase.

Compound	log<i>P</i>
1	+0.2 ± 0.2
2	+0.3 ± 0.2
3	+0.4 ± 0.3
4	+0.2 ± 0.2
5	+0.7 ± 0.3
6	+1.4 ± 0.3
7	+1.7 ± 0.2

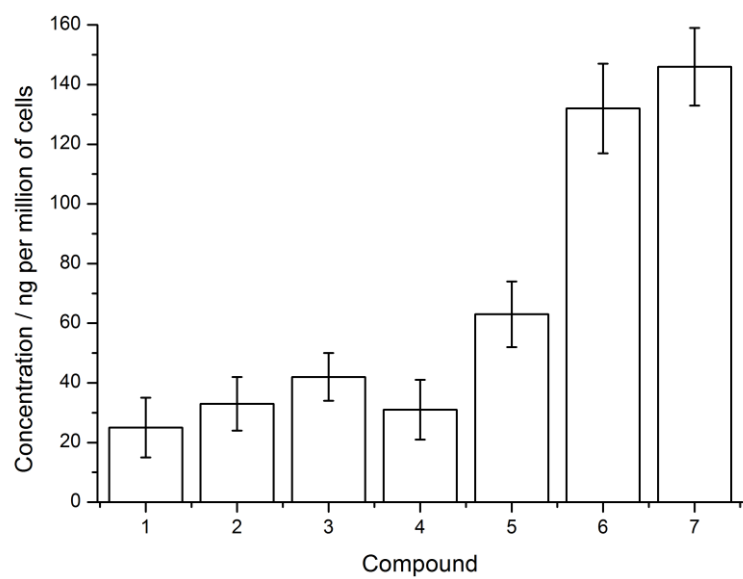


Figure S51. Comparison of the cellular uptake of complexes **1–7** after 4 h incubation in HeLa cells.

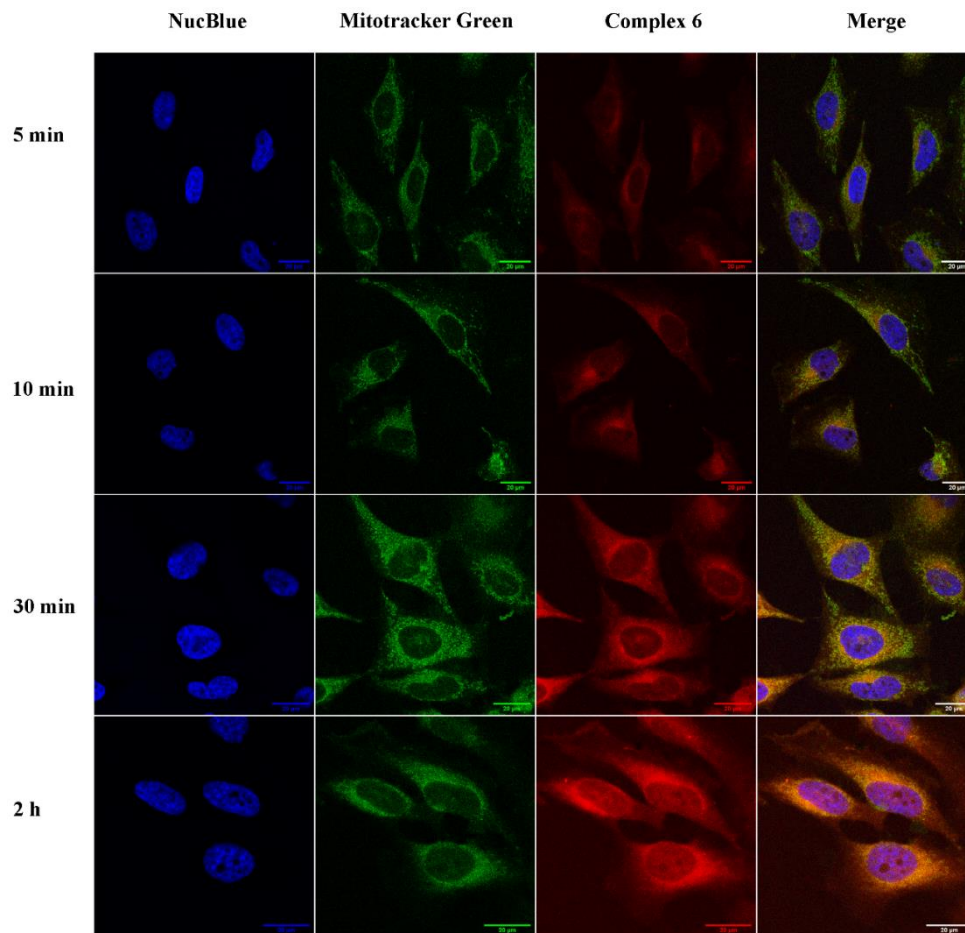


Figure 52. Time-dependent accumulation of complex **6** (14 μ M) in HeLa cell line. DNA visualised by NucBlue staining, mitochondria visualised using Mitotracker Green FM (100 nm), complex **6** shown in red. Scale bar, 20 μ m.

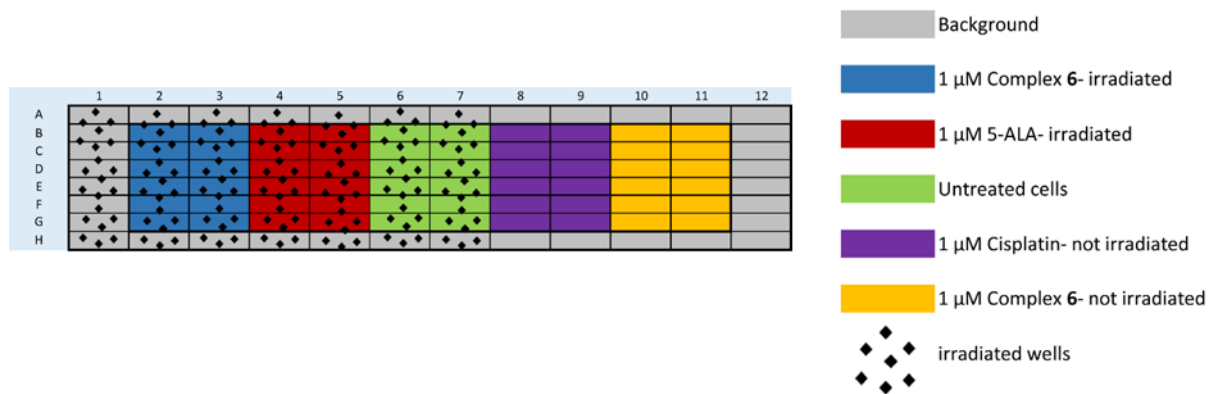


Figure S53. Plate arrangement for Seahorse Mito Stress and Glycolysis Stress experiments.

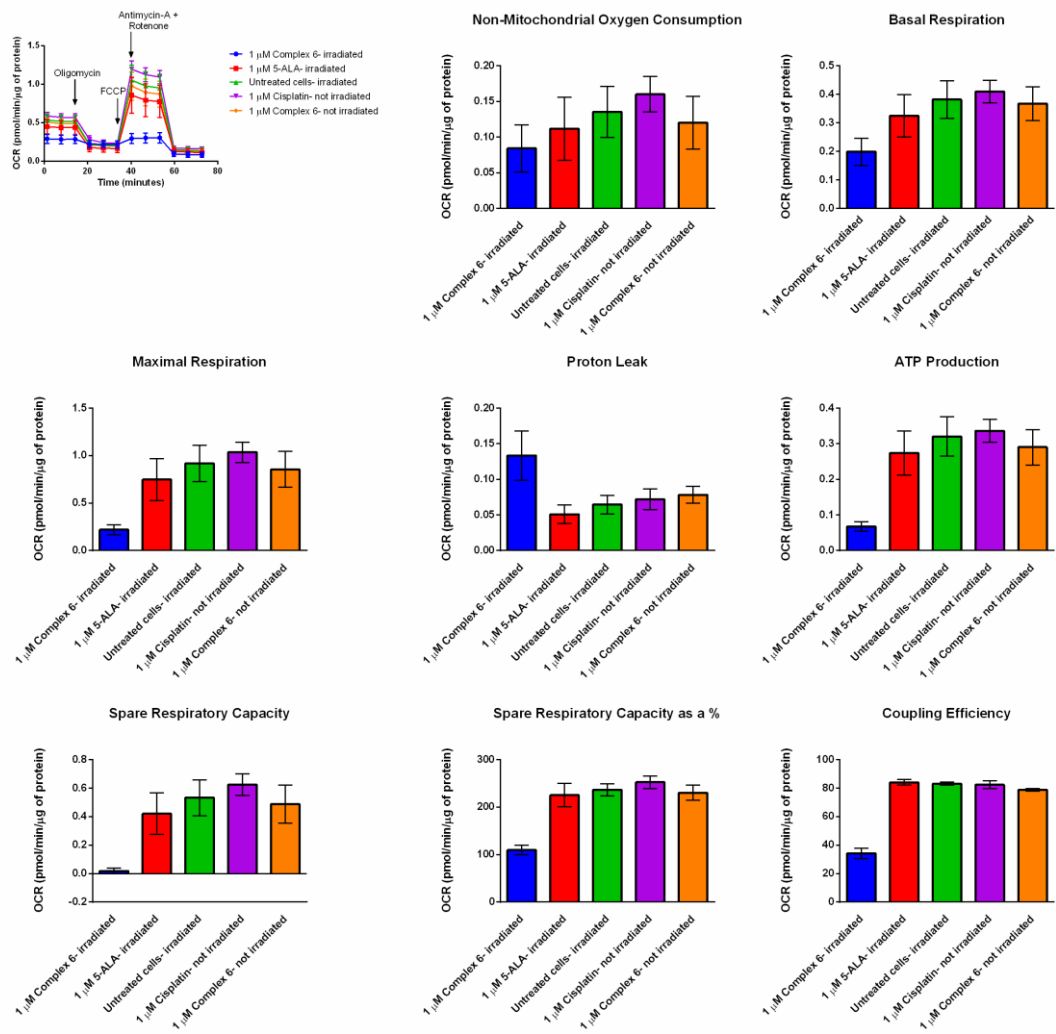


Figure S54. Oxygen consumption rates and different respiration parameters in CT-26 cells alone or after treatment with various test compounds.

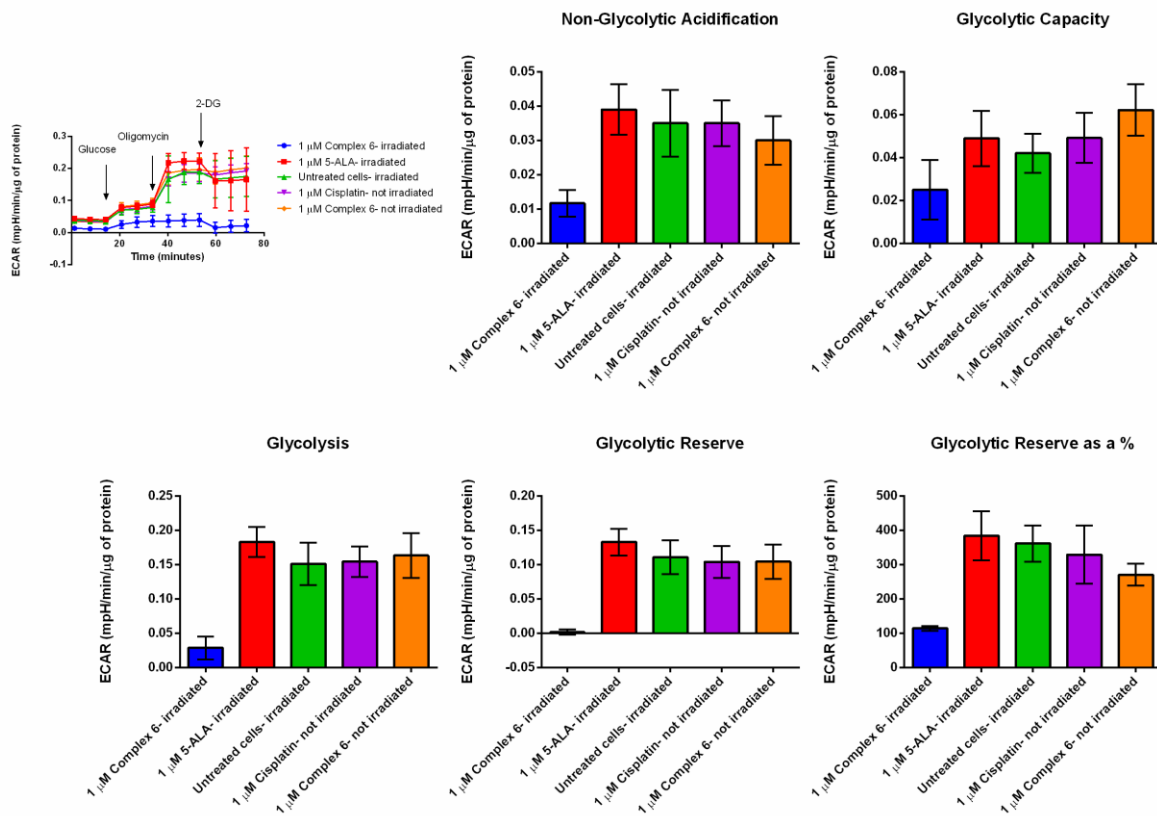


Figure S55. Extracellular acidification rates and different glycolysis parameters in CT-26 cells alone or after treatment with various test compounds.

REFERENCES

1. M. J. Frisch et. al., *Journal*, 2017.
2. T. H. Dunning, Jr. and P. J. Hay, in *Modern Theoretical Chemistry*, ed. H. F. Schaefer III, Plenum, New York, 1977, vol. 3, pp. 1-28.
3. W. J. Hehre, R. Ditchfield and J. A. Pople, *The Journal of Chemical Physics*, 1972, **56**, 2257-2261.
4. P. C. Hariharan and J. A. Pople, *Theoretica Chimica Acta*, 1973, **28**, 213-222.
5. A. Klamt, C. Moya and J. Palomar, *J Chem Theory Comput*, 2015, **11**, 4220-4225.
6. A. D. Becke, *The Journal of Chemical Physics*, 1993, **98**, 5648-5652.
7. C. Ullrich, *Time-Dependent Density-Functional Theory: Concepts and Applications*, Oxford University Press, Oxford, 2012.
8. T. Le Bahers, C. Adamo and I. Ciofini, *J Chem Theory Comput*, 2011, **7**, 2498-2506.
9. F. Maschietto, M. Campetella, M. J. Frisch, G. Scalmani, C. Adamo and I. Ciofini, *Journal of Computational Chemistry*, 2018, **39**, 735-742.
10. B. Sullivan, D. Salmon and T. Meyer, *Inorg. Chem.*, 1978, **17**, 3334-3341.
11. A. Duong, T. Maris, O. Lebel and J. D. Wuest, *The Journal of organic chemistry*, 2011, **76**, 1333-1341.
12. O. Maury, J.-P. Guégan, T. Renouard, A. Hilton, P. Dupau, N. Sandon, L. Toupet and H. Le Bozec, *New J. Chem.*, 2001, **25**, 1553-1566.
13. G. Crosby and W. Elfring Jr, *The Journal of Physical Chemistry*, 1976, **80**, 2206-2211.
14. W. E. Jones Jr, R. A. Smith, M. T. Abramo, M. D. Williams and J. Van Houten, *Inorg. Chem.*, 1989, **28**, 2281-2285.
15. O. Mazuryk, K. Magiera, B. Rys, F. Suzenet, C. Kieda and M. Brindell, *JBIC Journal of Biological Inorganic Chemistry*, 2014, **19**, 1305-1316.
16. R. Clark and J. Reid, *Acta Crystallogr. Sect. A: Found. Crystallogr.*, 1995, **51**, 887-897.
17. *Rigaku Oxford Diffraction*, 2015.

18. A. OLEX, *J. Appl. Crystallogr.*, 2009, **42**, 339-341.
19. G. M. Sheldrick, *Acta Crystallographica Section A: Foundations and Advances*, 2015, **71**, 3-8.
20. G. M. Sheldrick, *Acta Crystallographica Section C: Structural Chemistry*, 2015, **71**, 3-8.
21. A. L. Spek, *Acta Crystallographica Section C: Structural Chemistry*, 2015, **71**, 9-18.
22. K. Nakamaru, *Bull. Chem. Soc. Jpn.*, 1982, **55**, 1639-1640.
23. I. E. Kochevar and R. W. Redmond, in *Methods Enzymol.*, Academic Press 2000, vol. 319, pp. 20-28.
24. D. Garcia-Fresnadillo, Y. Georgiadou, G. Orellana, A. M. Braun and E. Oliveros, *Helv. Chim. Acta*, 1996, **79**, 1222-1238.
25. S. J. Bruce, I. Tavazzi, V. r. Parisod, S. Rezzi, S. Kochhar and P. A. Guy, *Anal. Chem.*, 2009, **81**, 3285-3296.
26. J. Schindelin, I. Arganda-Carreras, E. Frise, V. Kaynig, M. Longair, T. Pietzsch, S. Preibisch, C. Rueden, S. Saalfeld, B. Schmid, J.-Y. Tinevez, D. J. White, V. Hartenstein, K. Eliceiri, P. Tomancak and A. Cardona, *Nat. Methods*, 2012, **9**, 676-682.

Chapter 6- Ruthenium-Initiated Polymerization of Lactide: A Route to Remarkable Cellular Uptake for Photodynamic Therapy of Cancer

Nancy Soliman,^{a,b} Luke K. McKenzie,^{b,c} Johannes Karges,^b Emilie Bertrand,^{a,b} Mickaël Tharaud,^d Marta Jakubaszek,^{b,e} Vincent Guérineau,^f Bruno Goud,^e Marcel Hollenstein,^c Gilles Gasser,^{b,} Christophe M. Thomas^{a,*}*

^a Chimie ParisTech, PSL University, CNRS, Institut de Recherche de Chimie Paris, 75005 Paris, France. E-mail: christophe.thomas@chimie-paristech.fr

^b Chimie ParisTech, PSL University, CNRS, Institute of Chemistry for Life and Health Sciences, Laboratory for Inorganic Chemical Biology, 75005 Paris, France. E-mail: gilles.gasser@chimieparistech.psl.eu

^c Institut Pasteur, Department of Structural Biology and Chemistry, Laboratory for Bioinorganic Chemistry of Nucleic Acids, CNRS UMR 3523, 75015 Paris, France.

^d Université de Paris, Institut de physique du globe de Paris, CNRS, 75005 Paris, France.

^e Institut Curie, PSL University, CNRS UMR 144, 75005 Paris, France.

^f Institut de Chimie des Substances Naturelles, CNRS UPR2301, Université Paris-Sud, Université Paris-Saclay, Avenue de la Terrasse, 91198 Gif-sur-Yvette Cedex, France

* Corresponding authors: Email: gilles.gasser@chimie-paristech.fr;
christophe.thomas@chimie-paristech.fr

This chapter has been published on *Chemical Science* on the 30th of January 2020 (DOI: 10.1039/C9SC05976H)

Reproduced by permission of Royal Society of Chemistry
(<https://pubs.rsc.org/en/content/articlelanding/2020/sc/c9sc05976h#!divAbstract>)

Contribution to the publication:

Marta Jakubaszek advised and consulted biological experiments in this publication (including the cytotoxicity and the microscopy experiments). She contributed to the draft of this publication.

Marta Jakubaszek



19.05.2020

Gilles Gasser



Abstract

Ruthenium complexes have attracted a lot of attention as potential photosensitizers (PSs) for photodynamic therapy (PDT). However, some of these PSs are unsuitable for PDT applications due to their low cellular uptake, which is possibly the consequence of their relatively low degree of lipophilicity, which prevents them from penetrating into tumor cells. Here, we report the simple one-pot synthesis of ruthenium-containing nanoconjugates from a non-cell-penetrating, non-phototoxic ruthenium(II) polypyridyl complex (**RuOH**), by a drug-initiated ring-opening polymerization of lactide through the formation of a zinc initiator. These conjugates were then formulated into nanoparticles by nanoprecipitation and characterized by means of nuclear magnetic resonance spectroscopy (NMR), matrix-assisted laser desorption/ionization - time of flight mass spectrometry (MALDI-TOF MS) and dynamic light scattering (DLS). Finally, their photo-therapeutic activity ($\lambda_{\text{exc}} = 480 \text{ nm}$, $3.21 \text{ J}\cdot\text{cm}^{-2}$) in cancerous human cervical carcinoma (HeLa) and non-cancerous retinal pigment epithelium (RPE-1) cells was tested alongside that of **RuOH** and their cellular uptake in HeLa cells was assessed by confocal microscopy and inductively coupled plasma - mass spectrometry (ICP-MS). All nanoparticles showed improved photophysical properties including luminescence and singlet oxygen generation, enhanced cellular uptake and, capitalizing on this, an improved photo-toxicity. Overall, this study demonstrates how it is possible to transform a non-phototoxic PDT PS into an active PS using an easy, versatile polymerization technique.

Introduction

In recent years, photodynamic therapy (PDT) has gained considerable attention as a complementary/alternative tool in cancer treatment. It consists of a two-stage procedure involving the local or systemic administration of a photosensitizer (PS) followed by local irradiation with light at a specific wavelength. Irradiation leads to the formation of the activated photosensitizer (PS*), which subsequently interacts with surrounding cellular molecular oxygen $^3\text{O}_2$ to generate cytotoxic reactive oxygen species (ROS) including singlet oxygen $^1\text{O}_2$.^{1,2} Most clinically approved PSs are based on cyclic tetrapyrrole structures such as porphyrins, chlorins or phthalocyanines. However, most of these PSs suffer from several drawbacks including (i) poor water solubility, (ii) lack of cancer selectivity and (iii) slow clearance from the body leading to prolonged photosensitivity.³ Numerous efforts have therefore been made to develop new non-tetrapyrrole-based PSs. Among them, transition metal complexes and in particular ruthenium(II) polypyridyl complexes were found to be extremely promising,⁴⁻¹⁰ with one example starting phase II clinical trials in Canada for the treatment of bladder cancer.^{11,12} While a multitude of ruthenium(II) polypyridyl complexes have been reported in the literature, the compound $[\text{Ru}(\text{bipy})_2\text{-dppz-7-hydroxymethyl}][\text{PF}_6]_2$ (**RuOH**) with bipy = 2,2'-bipyridine and dppz = dipyrido[3,2-a:2',3'-c]phenazine was previously found to have no photo-toxicity, due to a lack of cellular uptake owing to its low degree of lipophilicity (Fig. 1).¹³ However, its photophysical properties were ideal for PDT applications.

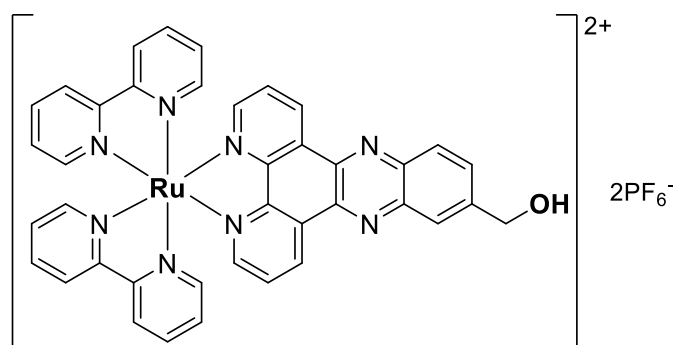


Fig. 1. Structure of the ruthenium complex **RuOH**.

The lipophilicity of drugs has long been established as a crucial physicochemical parameter in determining their potency and toxicity.^{50,51} Numerous studies have shown a strong correlation between the increased lipophilicity of Ru(II) polypyridyl complexes and their biological activity, explained in most cases by an increased cellular uptake (hence, increase intracellular concentrations of the complexes).⁴⁹ Increased lipophilicity of Ru(II) polypyridyl complexes can be achieved either by substitution of the bipy ancillary ligands^{46,47} or by enlargement of the aromatic ring system of the dppz moiety, using the π -expansive ligand dppn (dppn = benzo[*i*]dipyrido[3,2-*a*:2',3'-*h*]quinoxaline) instead.^{48,52,53} However, an increased lipophilicity also raises concern in the way of administration as the drug may have to be dissolved in an organic solvent such as DMSO or DMF, which may lead to serious side effects. To avoid using potentially toxic excipients, encapsulation into nanoparticles with hydrophobic properties may be a better strategy.²¹

Nanoparticles including polymeric nanoparticles offer, as a drug delivery platform, the possibility to improve accumulation at the tumor site by taking advantage of the abnormalities in cancer cells through the enhanced permeability and retention (EPR) effect,¹⁴ therefore improving treatment specificity and reducing side effects. So far, drug delivery systems using the $[\text{Ru}(\text{bipy})_2(\text{dppz})]^{2+}$ scaffold as nanobody-conjugation¹⁵ and mesoporous silica nanoparticle

formulation¹⁶ showed only limited use due to a lack of ROS generation inside the cell and loading limitations.

Biodegradable aliphatic polyester based nanoparticles have been widely used for encapsulation of drugs with an aim to harmlessly deliver them in a controlled and triggered fashion.^{4,17,18} Generally, therapeutic agents are incorporated into the polymer matrix through physical interaction. However, this type of entrapment suffers from strong limitations that hamper intravenous administration such as (i) significant “burst release” effect, (ii) uncontrolled and low encapsulation efficiency and (iii) poor drug loading (generally less than 10 %).¹⁹ To overcome these constraints, Kricheldorf was the first to report the preparation of drug-polyester conjugates by ring-opening polymerization (ROP) of cyclic esters *via* the formation of reactive initiators by mixing triethylaluminium with hydroxyl containing bioactive molecules.²⁰ Inspired by this pioneering work, several research groups developed drug-initiated polymerizations of different monomers.^{21, 25-29} Although the synthetic covalent approaches are interesting, the relationship between the properties of the polymer and the properties of the final polymer-encapsulated complex has rarely been clarified or linked to the physical properties of these conjugates. Therefore, physical encapsulation remains the most common strategy to deliver metal-based complexes because it is often considered simpler and faster than covalent conjugation.

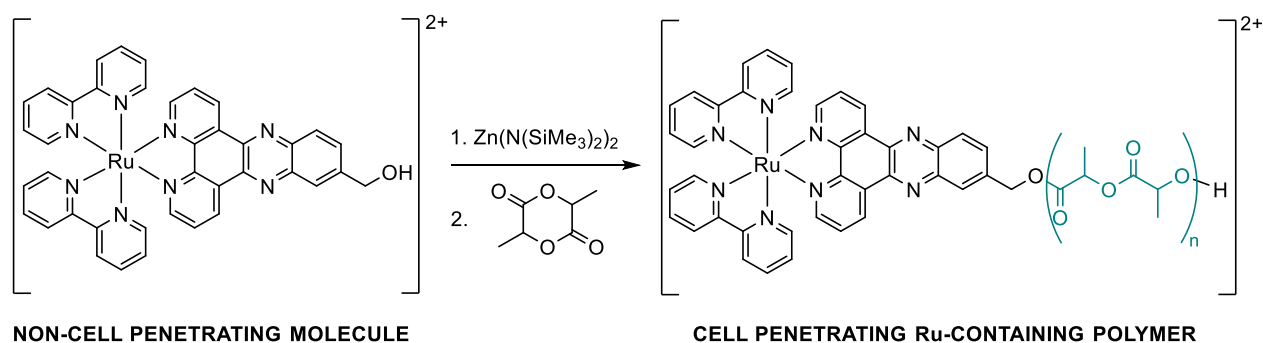
We hypothesized that covalent incorporation of **RuOH** into aforementioned nanoparticles would allow access to the promising photophysical properties of the molecule by improving cellular penetration. Herein, we report the conjugation of **RuOH** to polylactide (PLA), a well-established and FDA-approved biodegradable and biocompatible aliphatic polyester for drug delivery applications,²²⁻²⁴ *via* a simple and straightforward drug-initiated method. We prepared active and easy-to-prepare nanoconjugates from two metal-based precursors for the synthesis of hydrophobic nanoparticles. Polymers of different molecular weight were synthesized from

D,L-lactide, L-lactide and D-lactide yielding respectively, atactic and isotactic polymers that could be formulated into nanoparticles by nanoprecipitation. The influence of molecular weight, tacticity and nanostructure on the photophysical properties, phototherapeutic activity, cellular uptake and photosensitizer release kinetics was evaluated.

Results and discussion

Preparation of Ru-PLA nanoconjugates

ROP of lactide using metal-coordination initiators including metal alkoxides (MORs) is arguably the most efficient method to prepare well-controlled polylactides (PLAs).³⁰ The MORs – synthesized prior to polymerization by mixing a hydroxyl-containing compound with an active metal catalyst – can initiate and control the ROP of LA leading to quantitative insertion of the alcohol into the PLA chain-end.³¹ The commercially available stannous octoate $\text{Sn}(\text{Oct})_2$ has been the most utilized ROP metal catalyst so far. However, it is difficult to be removed entirely from the polymer, raising concerns as the amount of residual tin in polymers for biomedical applications should remain low according to the Food and Drug Administration (FDA).³² Therefore, in view of pharmaceutical applications, special interest has been devoted to non-toxic and biocompatible metal centers such as zinc.^{33,34} As **RuOH** bears a hydroxyl group on the dppz ligand, it can react with $\text{Zn}(\text{N}(\text{SiMe}_3)_2)_2$ to form an active zinc alkoxide to be used for the initiation and control of LA polymerization.



Scheme 1. Synthesis of **Ru-PLA**.

RuOH, as a PF_6^- salt, was only readily soluble in acetonitrile limiting reactions in this solvent system. Anion exchange from PF_6^- to OTf^- , BF_4^- or BPh_4^- did not improve its solubility in non-polar solvents such as toluene or in polar organic solvents such as THF or CH_2Cl_2 . The reaction between equimolar amounts of **RuOH** and $\text{Zn}(\text{N}(\text{SiMe}_3)_2)_2$ resulted in a Schlenk equilibrium that strongly favors the formation of zinc bis(alkoxide) over time, as characterized by ^1H NMR (Figure S1). As zinc bis(alkoxide) is the most thermodynamically stable species, it was used in the ROP of LA by directly adding two equivalents of **RuOH** to a solution of $\text{Zn}(\text{N}(\text{SiMe}_3)_2)_2$ in acetonitrile. Polymerizations of racemic (D,L-lactide) or enantiopure lactide (D-lactide or L-lactide) were performed using the formed zinc alkoxide initiator with a monomer concentration of 3.0 M at 60 °C for 1 h. Conversion was measured by ^1H NMR in CDCl_3 using the signals from the methine protons of the unreacted monomer (q, 5.04 ppm) and the ones of the polymer (5.18 ppm). After 1 h of polymerization, the resulting ruthenium-poly(lactide) (**Ru-PLA**) conjugates were simply isolated by precipitation to remove unreacted monomer (Table 1). Polymers **P1**, **P2** and **P5**, synthesized from D,L-lactide, yielded amorphous polymers as a result of random sequence of D- and L-units along the polymer backbone. As for polymers **P3** and **P4**, derived from the enantiopure monomers, yielded semi-crystalline polymers as the sequence

of the absolute configuration is the same along the polymer backbone. The quantitative conjugation of **RuOH** to PLA through an ester linkage was shown by ^1H and ^{13}C NMR spectroscopy as the peak integrating for the $-\text{CH}_2\text{O}-$ on the dppz ligand of **RuOH** has shifted from 4.98 to 5.54 ppm in the ^1H NMR spectrum and from 64.11 to 66.89 ppm in the ^{13}C NMR spectrum after polymerization (Figures S2-S4). In addition, experimental number-average molecular weights (M_n , calculated by NMR end-group analysis) were close to the theoretical ones, which indicates that the polymerization proceeded in a controlled fashion (i.e., without any significant side reactions), as confirmed by MALDI-TOF mass spectrometry (Figure S5). The MALDI-TOF MS analysis reveals two distribution of peaks, one spaced by $\Delta m/z = 144.03$ corresponding to one lactide unit and the second spaced by $\Delta m/z = 72.02$ attributed to the presence of transesterification reactions which is not surprising with this type of catalyst. Besides, the isotopic pattern of each peak clearly shows the presence of ruthenium. Of note, these polymers could not be analyzed by size exclusion chromatography (SEC) with refractive index detector (RID) and THF or DMF as eluent since the characterization of bipyridine ruthenium complex-containing polymers by SEC is rather difficult. As already reported by Schubert and co-workers,³⁵ this can be explained by the interaction of the metal ions and nitrogen atoms with the SEC column material, which is a highly cross-linked polystyrene divinylbenzene (PS-DVB) gel.

Once these **Ru-PLA** conjugates were synthesized and fully characterized, they were formulated into nanoparticles NPs by a nanoprecipitation method.³⁶ **Ru-PLA** was dissolved in THF, a water-miscible organic solvent and the resulting solution was added dropwise to water, a non-solvent containing 0.3 % w/v of poly(vinyl alcohol) (PVA). The instantaneous diffusion of the organic solvent into the aqueous solution resulted, after solvent removal under reduced pressure, in the formation of narrowly dispersed polymeric NPs as characterized by their intensity-average diameter D_z with a polydispersity index (PDI) lower than 0.3 (Table 1).

Interestingly, the two polymers synthesized from the enantiopure lactide could not be formulated into NPs using these conditions. However, NPs could be obtained by mixing these two at equimolar ratio giving stereocomplex nanoparticles **NPs-3**. The stereocomplex formation was confirmed by differential scanning calorimetry (DSC) showing, for the stereocomplex, a melting temperature (T_m) 60 °C higher than the one of the enantiopure parent polymers. This result is in accordance with what has already been reported. It is, indeed, well documented in the literature that stereocomplexation between poly(D-lactide) and poly(L-lactide) can take place in solution.^{37,38}

Table 1. Macromolecular and colloidal characterization of **Ru-PLA** nanoconjugates^[a]

Entry	LA/Zn	LA	Conv. ^[b] (%)	$M_{n,NMR}$ ^[b] (kDa)	DP ^[b]	$M_{n,theo}$ ^[c] (kDa)	% RuOH ^[d] (wt%)	NPs	$D_z \pm SD$ ^[e] (nm)	$PdI \pm SD$ ^[e]
P1 ^[f]	11	D,L-LA	75	1.9	5	1.7	53	NPs-1	309.7 ± 1.815	0.198 ± 0.022
P2	41	D,L-LA	92	4.0	20	3.7	25	NPs-2	119.6 ± 0.406	0.236 ± 0.003
P3	41	D-LA	91	4.0	20	3.7	25	NPs-3	174.1 ± 1.429	0.192 ± 0.006
P4	41	L-LA	91	3.7	18	3.7	27			
P5	70	D,L-LA	95	7.0	41	5.8	15	NPs-4	248.8 ± 1.601	0.100 ± 0.011

[a] All reactions were performed at 60 °C for 1 h with $[LA]_0 = 3$ M unless otherwise stated. [b] Conversion of monomers, degree of polymerization (DP) and $M_{n,NMR}$ were calculated by ¹H NMR spectroscopy in CD₃CN. [c] Calculated according to $M_{n,theo} = ((LA/Zn) \times conv. \times M(LA))/2 + M(\mathbf{RuOH})$ with $M(LA) = 144.13$ g.mol⁻¹ and $M(\mathbf{RuOH}) = 1015.7$ g.mol⁻¹. [d] Calculated according to $(M(\mathbf{RuOH})/M_{n,NMR}) \times 100$. [e] Determined by dynamic light scattering (DLS) as an average of three measurements, values given with standard deviation (SD). [f] This reaction was performed with $[LA]_0 = 2$ M.

Photophysical properties

After formulation into NPs, their photophysical properties were investigated to determine whether the attachment of a polymer chain or the nanoparticle formulation influenced these properties. As expected, the absorption (Figure S6) and emission spectra (Figure S7) did not show a significant difference. Strikingly, NPs showed a highly improved luminescence in H₂O (Table S1) in comparison to **RuOH** which was only measurable on the detection limit of our apparatus (emission quantum yield $\Phi_{\text{em, NPs-2,3,4}} = 1.3 - 1.4 \%$, $\Phi_{\text{em, RuOH}} < 0.1 \%$). Following this, the excited state lifetimes in a degassed and air saturated aqueous solution were investigated. The obtained values were found in the nanosecond range (Table S1, Figures S8-S11) as for other published ruthenium(II) polypyridyl complexes.^{42,43} Importantly, the lifetime drastically decreases in the presence of air indicating that the excited triplet state of the ruthenium(II) polypyridyl complex can interact with ³O₂ in the air to produce ¹O₂. To validate this and quantify the amount of ¹O₂ generated upon irradiation at 450 nm, singlet oxygen quantum yields $\Phi_{1\text{O}_2}$ were determined by two complementary techniques: 1) direct by measuring the phosphorescence of ¹O₂ at 1270 nm, 2) indirect by measuring the change in absorbance of a ¹O₂ scavenger.⁴⁴ Interestingly, NPs showed a highly improved singlet oxygen production in H₂O (Table S2) in comparison to **RuOH** ($\Phi_{1\text{O}_2, \text{NPs-2,3,4}} = 11 - 12 \%$, $\Phi_{1\text{O}_2, \text{RuOH}} = 3 \%$). These results are a direct consequence of the prevention of quenching effects in water attributed to hydrogen bonding of water to the nitrogen atoms of the phenazine moiety,³⁹⁻⁴¹ which leads to a drastic improvement of the photophysical properties of NPs in comparison to **RuOH**.

Photosensitizer release kinetic studies

As the ruthenium complex is linked to PLA by an ester bond, its release from the resulting nanoconjugates is mainly governed by hydrolysis. The **RuOH** release goes with the degradation of PLA into its shorter oligomers and eventually, lactic acid. The latter is a known, non-toxic

byproduct of several metabolic pathways. There is no systemic toxicity associated with the use of this type of nanoparticles.²¹ Also, the longer the polymer chain is, the slower the release is (Figures S12-S13). It is difficult to establish a rational correlation between the release kinetics of **RuOH** and the nanoparticles' cytotoxicities as the **Ru-PLA** nanoconjugates does not act as a prodrug which becomes active when the linkage between the drug and the polymer gets cleaved. However, as shown by the photophysical studies, the nanoconjugate formulation improves the overall photophysical properties of **RuOH**.

Biological evaluation

The dark and light cytotoxicities of NPs were tested in cancerous human cervical carcinoma (HeLa) and non-cancerous retinal pigment epithelium (RPE-1) cells alongside **RuOH** following a 4, 24 and 48 h incubations (Table 3 and S3). All compounds were non-cytotoxic following a 4 h incubation in the dark ($IC_{50} > 100 \mu M$ for NPs; $> 500 \mu M$ for **RuOH**). Low dose light irradiation ($\lambda_{exc} = 480 \text{ nm}$, 10 min, $3.21 \text{ J}\cdot\text{cm}^{-2}$) yielded photosensitization with NPs in HeLa cells with a phototoxicity index (PI) ranging from > 2.5 to > 6 , while no photosensitization was observed for **NPs-2** and **NPs-3** in RPE-1 cells ($IC_{50} > 100 \mu M$). Notably we chose 480 nm as irradiation wavelength since it is the optimal wavelength for this PDT PS. **RuOH** remained non-cytotoxic following irradiation ($IC_{50} > 500 \mu M$). Following a 24 h incubation, the compounds remained non-cytotoxic in the dark (IC_{50s} 81.3 μM , $> 100 \mu M$ and $> 500 \mu M$ for **NPs-4**, **NPs-1,2,3** and **RuOH**, respectively) while an increase in photosensitization was observed for NPs (PI range > 5.9 to > 11.25) and extremely modest photosensitization close to no photosensitization was observed with **RuOH** in HeLa cells (IC_{50} 274.4 μM). Following a 48 h incubation, all compounds were somewhat cytotoxic in the dark in HeLa cells (IC_{50s} 31.8 – 62.8 μM and 99.1 μM for NPs and **RuOH** respectively) while their light cytotoxicities remained relatively stable. Worthy of note, the blue light irradiation at 480 nm is not toxic to the two cell lines at a fluence of $3.21 \text{ J}\cdot\text{cm}^{-2}$. The cytotoxicity of NPs and **RuOH** in HeLa cells was

correlated to their cellular uptake which was investigated by ICP-MS following 4, 24 and 48 h incubations (Fig. 2). As expected, **RuOH** had limited cellular uptake (0.0019 – 0.0019 pg/cell) while a variation in cellular uptakes was observed for NPs. Relatively low cellular uptake was measured for **NPs-1** (0.038 – 0.064 pg/cell), which is expected due to the short polymer chain length and lower hydrophobicity. **NPs-2,3** were moderately more cell-penetrating (0.174 – 0.230 pg/cell and 0.101 – 0.408 pg/cell for **NPs-2** and **NPs-3**, respectively) with a cellular uptake twice higher after 48 h incubation for **NPs-3** compared to **NPs-2** justifying the interest in forming stereocomplex nanoparticles. As predicted from the higher chain length and hence hydrophobicity (hence implied lipophilicity), **NPs-4** was observed to be the most cell accumulating (0.256 – 2.448 pg/cell) with a 9.5 x increase in cellular ruthenium content from the 4 h timepoint to the 48 h timepoint. The trend in cellular uptake fits with the hydrophobicity of the compounds.

Table 2. Cytotoxic data^[a] for NPs and **RuOH** (μM) in HeLa cells. Light treatment at 480 nm (10 min, $3.21 \text{ J}\cdot\text{cm}^{-2}$).

	4 h			24 h			48 h		
	Light	Dark	PI ^[b]	Light	Dark	PI ^[b]	Light	Dark	PI ^[b]
NPs-1	28.0 ± 3.2	> 100	3.6	18.7 ± 3.6	> 100	5.9	12.7 ± 3.3	43.4 ± 17.8	3.4
NPs-2	34.2 ± 17.4	> 100	2.9	14.5 ± 6.3	> 100	6.9	23.4 ± 3.8	61.4 ± 17.9	2.6
NPs-3	41.3 ± 4.5	> 100	2.5	9.5 ± 1.1	> 100	11.25	8.4 ± 4.3	62.9 ± 13.4	7.5
NPs-4	16.7 ± 4.3	> 100	6	7.8 ± 7.7	81.3 ± 10.9	10.9	4.4 ± 0.8	31.8 ± 7.1	7.5
RuOH	> 500	> 500		274.4 ± 70.1	> 500	1.8	99.1 ± 12.7	248.6 ± 37.7	2.5

[a] IC_{50} values were an average of three measurements. [b] PI refers to the phototoxicity index, which is the ratio between the IC_{50} values in the dark and the ones upon light irradiation.

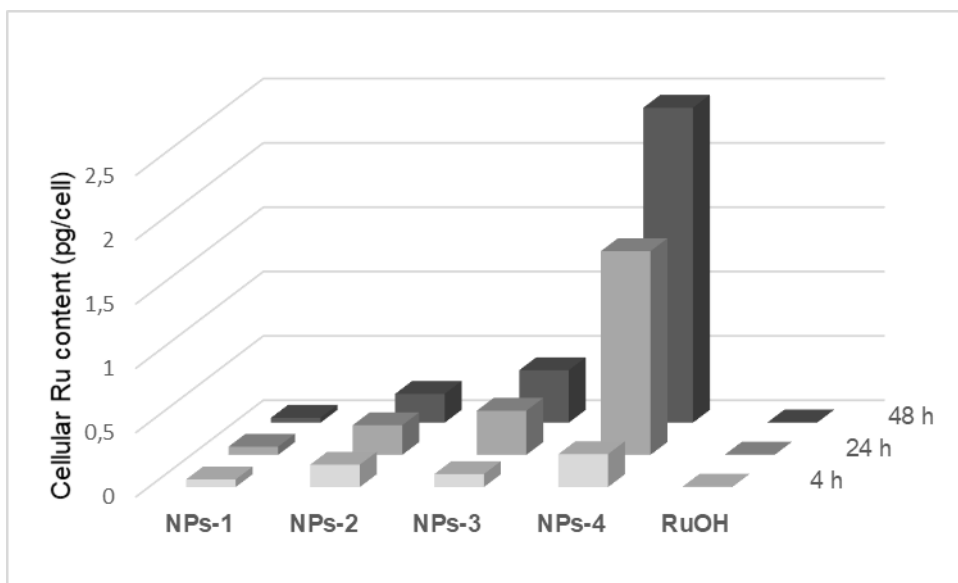


Fig. 2. Cellular uptake in HeLa cells as measured by ICP-MS. Values given in pg/cell.

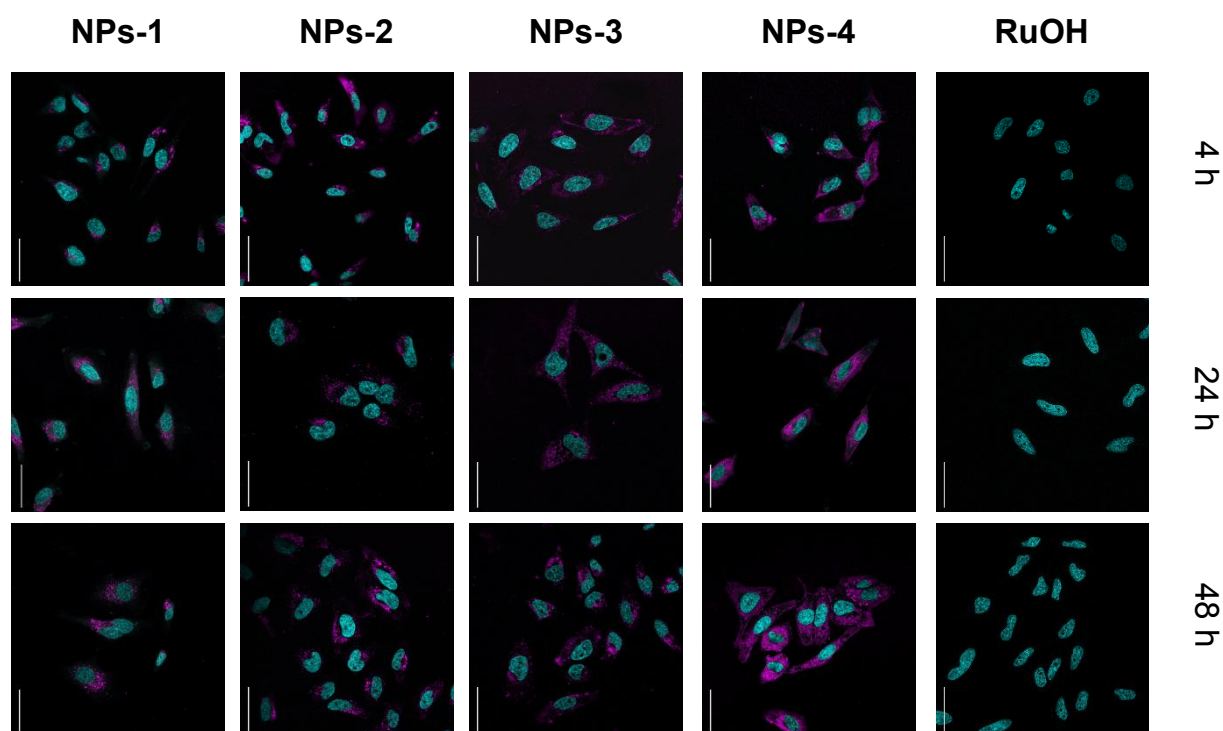


Fig. 3. Confocal microscopy images of HeLa cells incubated with NPs and **RuOH** (50 μ M, 37 $^{\circ}$ C, 4, 24, 48 h, magenta). NPs co-stained with the nuclear stain, NucBlue (cyan), scale bar 50 μ m.

The subcellular localization of the compounds was investigated using confocal microscopy in HeLa cells (Fig. 3 and S14). Cellular localization of NPs can be observed by confocal microscopy ($\lambda_{\text{exc}} = 480 \text{ nm}$, $\lambda_{\text{em}} = 650 - 750 \text{ nm}$) while no luminescence was observed for **RuOH**. Similar staining patterns were observed for NPs with punctuate cytoplasmic signals dominating. Costaining with the anti-LAMP lysosomal antibody indicated no signal overlap (Figure S14). Endocytosis is implicated in the cellular uptake of nanoparticles⁴⁵ and may be, at least, the partial source of the punctate staining. While localization varies slightly between NPs, no significant change in subcellular localization is observed with increased incubation time, suggesting that the increase in photosensitizing effect is not due to a change in localization. These data clearly indicate an increase in cellular uptake, and photosensitization, in cells by the polymer encapsulated ruthenium complex as compared to its 'free' counterpart, **RuOH**. This encapsulation may be suitable for use with small complexes allowing cellular access.

Conclusion

A series of ruthenium-poly(lactide) **Ru-PLA** conjugates with different degrees of polymerization, tacticity and a drug loading up to 53 % has been successfully prepared by the drug-initiated ROP of lactide using a bimetallic initiator formed from **RuOH**. This one-pot synthetic strategy prevents the use of the cost-effective and time-consuming preparative size exclusion chromatography currently applied for purification of ruthenium-polymer conjugates prepared from chelation of a polymeric macroligand to the metal salt, as the only purification step here is precipitation. These conjugates were then formulated into narrowly dispersed nanoparticles with superior photophysical properties including their luminescence and singlet oxygen generation due to lower amount of quenching effects in H₂O. Capitalizing on this, the

particles were biologically tested on HeLa cervical cancer cells, showing an enhanced cellular uptake of **RuOH** overtime and hence, an improved phototherapeutic activity overtime. Owing to its simplicity, this strategy can be expanded and applied to a broad range of ruthenium complexes. This opens new avenues in PDT treatment in which patients could be treated over several days using a single injection.

Conflicts of interest

The authors declare no conflict of interest.

Acknowledgements

This work was financially supported by an ERC Consolidator Grant PhotoMedMet to G.G. (GA 681679) and has received support under the program *Investissements d'Avenir* launched by the French Government and implemented by the ANR with the reference ANR-10-IDEX-0001-02 PSL (G.G.). We thank Dr. Philippe Goldner for access to state-of-the-art laser apparatus. M.H. acknowledges funding from Institut Pasteur. N.S gratefully acknowledges financial support from Cancéropôle Île-de-France for her PhD scholarship. L. K. M. acknowledges a fellowship from the ARC Foundation for cancer research (grant number: S-FB18006). Île-de-France Region is gratefully acknowledged for financial support of 500 MHz NMR spectrometer of Chimie ParisTech in the framework of the SESAME equipment project. We acknowledge the loan of Agilent's equipment to Chimie ParisTech. Part of this work was supported by IPGP multidis-ciplinary program PARI and by Region Île-de-France SESAME Grant no. 12015908. The authors would like to thank Purac for a generous loan of D,L-lactide. C.M.T. is grateful to the Institut Universitaire de France.

References

- 1 D. E. Dolmans, D. Fukumura and R. K. Jain, *Nat. Rev. Cancer*, 2003, **3**, 380-387.
- 2 D. van Straten, V. Mashayekhi, H. S. de Bruijn, S. Oliveira and D. J. Robinson, *Cancers*, 2017, **9**, 19.
- 3 A. E. O'Connor, W. M. Gallagher and A. T. Byrne, *Photochem. Photobiol.*, 2009, **85**, 1053-1074.
- 4 L. Zeng, P. Gupta, Y. Chen, E. Wang, L. Ji, H. Chao and Z.-S. Chen, *Chem. Soc. Rev.*, 2017, **46**, 5771–5804.
- 5 J. Liu, C. Zhang, T. W. Rees, L. Ke, L. Ji and H. Chao, *Coord. Chem. Rev.*, 2018, **363**, 17–28.
- 6 L. K. McKenzie, H. E. Bryant and J. A. Weinstein, *Coord. Chem. Rev.*, 2018, **379**, 2-29.
- 7 M. Jakubaszek, B. Goud, S. Ferrari and G. Gasser, *Chem. Commun.*, 2018, **54**, 13040–13059.
- 8 F. Heinemann, J. Karges and G. Gasser, *Acc. Chem. Res.*, 2017, **50**, 2727-2736.
- 9 S. A. McFarland, A. Mandel, R. Dumoulin-White and G. Gasser, *Curr. Opin. Chem. Biol.*, 2020, **56**, 23-27.
- 10 P. S. Felder, S. Keller and G. Gasser, *Adv. Therap.*, 2019, 1900139.
- 11 Theralase Annouces First Patient Treated in Phase II Non-Muscle Invasive Bladder Cancer Clinical Study, <https://www.streetinsider.com/dr/news.php?id=15879950&gfv=1>, (accessed September 24, 2019).
- 12 S. Monro, K. L. Colón, H. Yin, J. Roque, P. Konda, S. Gujar, R. P. Thummel, L. Lilge, C. G. Cameron and S. A. McFarland, *Chem. Rev.*, 2019, **119**, 797–828.
- 13 C. Mari, V. Pierroz, R. Rubbiani, M. Patra, J. Hess, B. Spingler, L. Oehninger, J. Schur, I. Ott, L. Salassa, S. Ferrari and G. Gasser, *Chem. Eur. J.*, 2014, **20**, 14421–14436.
- 14 H. Maeda, J. Wu, T. Sawa, Y. Matsumura and K. Hori, *J. of Control. Release*, 2000, **65**, 271–284.

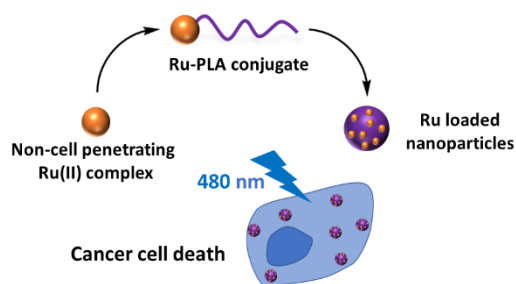
- 15 J. Karges, M. Jakubaszek, C. Mari, K. Zarschler, B. Goud, H. Stephan and G. Gasser, *ChemBioChem*, 2019, accepted. DOI: 10.1002/cbic.201900419.
- 16 Y. Ellahioui, M. Patra, C. Mari, R. Kaabi, J. Karges, G. Gasser and S. Gómez-Ruiz, *Dalton Trans.*, 2019, **48**, 5940-5951.
- 17 E. Villemin, Y. C. Ong, C. M. Thomas and G. Gasser, *Nat. Rev. Chem.*, 2019, **3**, 261–282.
- 18 D. K. Chatterjee, L. S. Fong and Y. Zhang, *Adv. Drug Deliv. Rev.*, 2008, **60**, 1627–1637.
- 19 S. Shen, Y. Wu, Y. Liu and D. Wu, *Int. J. Nanomed.*, 2017, **12**, 4085–4109.
- 20 H. R. Kricheldorf and I. Kreiser-Saunders, *Polymer*, 1994, **35**, 4175–4180.
- 21 J. Nicolas, *Chem. Mater.*, 2016, **28**, 1591–1606.
- 22 B. Tyler, D. Gullotti, A. Mangraviti, T. Utsuki and H. Brem, *Adv. Drug Deliv. Rev.*, 2016, **107**, 163–175.
- 23 S. Farah, D. G. Anderson and R. Langer, *Adv. Drug Deliv. Rev.*, 2016, **107**, 367–392.
- 24 R. James, *Adv. Drug Deliv. Rev.*, 2016, **107**, 277-288.
- 25 R. Tong and J. Cheng, *Angew. Chem. Int. Ed.*, 2008, **47**, 4830–4834.
- 26 R. Tong and J. Cheng, *J. Am. Chem. Soc.*, 2009, **131**, 4744–4754.
- 27 R. Tong and J. Cheng, *Bioconjugate Chem.*, 2010, **21**, 111–121.
- 28 R. Tong and J. Cheng, *Macromolecules*, 2012, **45**, 2225–2232.
- 29 R. M. Johnson and C. L. Fraser, *Biomacromolecules*, 2004, **5**, 580–588.
- 30 C. M. Thomas, *Chem. Soc. Rev.*, 2010, **39**, 165–173.
- 31 The MORs can also synthesized by nucleophilic attack of the metal-based chloride precursor on an epoxide, see for instance: C. Robert, T. E. Schmidt, V. Richard, P. Haquette, S. K. Raman, M.-N. Rager, R. M. Gauvin, Y. Morin, X. Trivelli, V. Guérineau, I. del Rosal, L. Maron and C. M. Thomas, *J. Am. Chem. Soc.*, 2017, **139**, 6217 -6225.
- 32 J. Guo, P. Haquette, J. Martin, K. Salim and C. M. Thomas, *Angew. Chem. Int. Ed.*, 2013, **52**, 13584–13587.

- 33 P. Marin, M. J.-L. Tschan, P. Haquette, T. Roisnel, I. del Rosal, L. Maron and C. M. Thomas, *Eur. Polym. J.*, 2019, **120**, 109208.
- 34 B. M. Chamberlain, M. Cheng, D. R. Moore, T. M. Ovitt, E. B. Lobkovsky and G. W. Coates, *J. Am. Chem. Soc.*, 2001, **123**, 3229–3238.
- 35 M. A. R. Meier, B. G. G. Lohmeijer and U. S. Schubert, *Macromol. Rapid. Commun.* 2003, **24**, 852–857.
- 36 C. J. Martínez Rivas, M. Tarhini, W. Badri, K. Miladi, H. Greige-Gerges, Q. A. Nazari, S. A. Galindo Rodríguez, R. Á. Román, H. Fessi and A. Elaissari, *Int. J. Pharm.*, 2017, **532**, 66–81.
- 37 P. Marin, M. J.-L. Tschan, F. Isnard, C. Robert, P. Haquette, X. Trivelli, L.-M. Chamoreau, V. Guérineau, I. del Rosal, L. Maron, V. Venditto and C. M. Thomas, *Angew. Chem. Int. Ed.*, 2019, **58**, 12585-12589.
- 38 H. Tsuji, *Adv. Drug Deliv. Rev.*, 2016, **107**, 97–135.
- 39 A. E. Friedman, J.-C. Chambron, J.-P. Sauvage, N. J. Turro and J. K. Barton, *J. Am. Chem. Soc.*, 1990, **112**, 4960-4962.
- 40 C. Turro, S. H. Bossmann, Y. Jenkins, J. K. Barton and N. J. Turro, *J. Am. Chem. Soc.*, 1995, **117**, 9026-9032.
- 41 J. Olofsson, B. Önfelt and P. Lincoln, *J. Phys. Chem. A*, 2004, **108**, 4391-4398.
- 42 M. J. Cook, A. P. Lewis, G. S. G. McAuliffe, V. Skarda, A. J. Thomson, J. L. Glasper and D. J. Robbins, *J. Chem. Soc. Perkin Trans. 2*, 1984, 1293-1301.
- 43 A. Juris, V. Balzani, F. Barigelletti, S. Campagna, P. Belser and A. von Zelewsky, *Coord. Chem. Rev.*, 1988, **84**, 85-277.
- 44 J. Karges, O. Blacque, P. Goldner, H. Chao and G. Gasser, *Eur. J. Inorg. Chem.*, 2019, **2019**, 3704-3712.
- 45 S. Zhang, H. Gao and G. Bao, *ACS Nano*, 2015, **9**, 8655–8671.

- 46 C. A. Puckett and J. K. Barton, *J. Am. Chem. Soc.*, 2007, **129**, 46-47.
- 47 C. A. Puckett and J. K. Barton, *Biochemistry*, 2008, **47**, 11711-11716.
- 48 U. Schatzschneider, J. Niesel, I. Ott, R. Gust, H. Alborzinia and S. Wölfl, *ChemMedChem*, 2008, **3**, 1104-1109.
- 49 F.E. Poynton, S. A. Bright, S. Blasco, D. C. Williams, J. M. Kelly and T. Gunnlaugsson, *Chem. Soc. Rev.*, 2017, **46**, 7706-775s6.
- 50 P. D. Leeson and B. Springthorpe, *Nat. Rev. Drug Discov.*, 2007, **6**, 881– 890.
- 51 J. A. Arnott and S. L. Planey, *Expert Opin. Drug Discov.*, 2012, **7**, 863– 875.
- 52 H. Yin, M. Stephenson, J. Gibson, E. Sampson, G. Shi, T. Sainuddin, S. Monro and S. A. McFarland, *Inorg. Chem.*, 2014, **53**, 4548-4559.
- 53 T; Sainuddin, J. McCain, M. Pinto, H. Yin, J. Gibson, M. Hetu and S. A. McFarland, *Inorg. Chem.*, 2016, **55**, 83-95.

Entry for the Table of Contents

This study shows the transformation of a non-phototoxic PDT photosensitizer into an active photosensitizer using an easy, versatile and generalizable one-pot ruthenium-initiated polymerization technique.



Supplementary information

Ruthenium-Initiated Polymerization of Lactide: A Route to Remarkable Cellular Uptake for Photodynamic Therapy of Cancer

Nancy Soliman,^{a,b} Luke K. McKenzie,^{b,c} Johannes Karges,^b Emilie Bertrand,^{a,b} Mickaël Tharaud,^d Marta Jakubaszek,^{b,e} Vincent Guérineau,^f Bruno Goud,^e Marcel Hollenstein,^c Gilles Gasser,^{b,} Christophe M. Thomas^{a,*}*

^a Chimie ParisTech, PSL University, CNRS, Institut de Recherche de Chimie Paris, 75005 Paris, France. E-mail: christophe.thomas@chimie-paristech.fr

^b Chimie ParisTech, PSL University, CNRS, Institute of Chemistry for Life and Health Sciences, Laboratory for Inorganic Chemical Biology, 75005 Paris, France. E-mail: gilles.gasser@chimieparistech.psl.eu

^c Institut Pasteur, Department of Structural Biology and Chemistry, Laboratory for Bioinorganic Chemistry of Nucleic Acids, CNRS UMR 3523, 75015 Paris, France.

^d Université de Paris, Institut de physique du globe de Paris, CNRS, 75005 Paris, France.

^e Institut Curie, PSL University, CNRS UMR 144, 75005 Paris, France.

^f Institut de Chimie des Substances Naturelles, CNRS UPR2301, Université Paris-Sud, Université Paris-Saclay, Avenue de la Terrasse, 91198 Gif-sur-Yvette Cedex, France

* Corresponding authors: Email: gilles.gasser@chimie-paristech.fr; christophe.thomas@chimie-paristech.fr

Table of contents

EXPERIMENTAL	396
SYNTHESIS AND CHARACTERIZATION OF RU-PLA NANOCONJUGATES	396
Materials.....	396
Instrumentation and Methods.....	396
Ring opening polymerization of lactide.	397
NMR determination of the M_n of Ru-PLA conjugates.	398
Nanoparticle preparation.	398
Stereocomplex formation for DSC measurements.	399
Release kinetics of RuOH from nanoparticles.....	399
PHOTOPHYSICAL STUDIES: EMISSION, LUMINESCENCE QUANTUM YIELD, AND LIFETIMES	399
Spectroscopic measurements.....	399
Luminescence quantum yield measurements.	399
Lifetime measurements.	400
Singlet oxygen measurements	400
- Direct evaluation	400
- Indirect evaluation.....	401
BIOLOGICAL EVALUATION.....	402
Cell culture experiments.....	402
Cytotoxicity experiments.	402
ICP-MS cellular uptake.....	403
Confocal microscopy.....	403
SUPPLEMENTARY FIGURES	405
FIGURE S1. AN OVERLAY ^1H NMR SPECTRA OF THE REACTION MIXTURE IN A J. YOUNG NMR TUBE BETWEEN EQUIMOLAR RATIO OF RuOH AND $\text{Zn}(\text{N}(\text{SiMe}_3)_2)_2$ IN DRY CD_3CN	406
FIGURE S2. ^1H NMR SPECTRA OF Ru-PLA PREPARED FROM D,L-LACTIDE , * = H_2O	407
FIGURE S3. AN OVERLAY OF ^1H NMR SPECTRA OF RuOH (GREEN) AND Ru-PLA (RED).	408
FIGURE S4. ^{13}C NMR OF Ru-PLA PREPARED FROM D,L-LACTIDE.....	409
FIGURE S5. MALDI-TOF MS ANALYSIS OF A RU-CONJUGATE	410
FIGURE S6. UV-VIS SPECTRA OF RuOH AND Ru-PLA IN CH_3CN (TOP) AND IN WATER (BOTTOM).....	411

FIGURE S7. EMISSION SPECTRA OF RUOH AND NPs-2,3,4 IN H_2O	412
TABLE S1. PHOTOPHYSICAL PROPERTIES OF RUOH IN COMPARISON TO NPs-2,3,4 IN H_2O ..	412
FIGURE S8. LIFETIME SPECTRA OF RUOH IN AERATED AND DEGASSED H_2O	413
FIGURE S9. LIFETIME SPECTRA OF NPs-2 IN AERATED AND DEGASSED H_2O	414
FIGURE S10. LIFETIME SPECTRA OF THE COMPLEX NPs-3 IN AERATED AND DEGASSED H_2O	415
FIGURE S11. LIFETIME SPECTRA OF THE COMPLEX NPs-4 IN AERATED AND DEGASSED H_2O	416
TABLE S2. SINGLET OXYGEN QUANTUM YIELDS IN H_2O UPON IRRADIATION AT 450 NM..	417
FIGURE S12. STANDARD CURVE OF RUOH	417
FIGURE S13. RUOH RELEASE KINETICS FROM NPs-1,2,4 IN PBS AT 37 °C, OVERTIME	418
TABLE S3. CYTOTOXICITY DATA ^A FOR NPs-1,2,3,4 AND RUOH (MM) IN HeLa AND RPE-1 CELLS.	418
FIGURE S14A. CONFOCAL MICROSCOPY IMAGES OF HeLa CELLS INCUBATED WITH NPs	419
FIGURE S14B. CONFOCAL MICROSCOPY IMAGES OF HeLa CELLS INCUBATED WITH NPs	422
REFERENCES.....	423

Experimental

Synthesis and characterization of Ru-PLA nanoconjugates

Materials

All polymerizations were carried out under a purified argon atmosphere using Schlenk techniques or a glovebox (< 1 ppm O₂, < 2 ppm H₂O). Deuterated acetonitrile (CD₃CN) from Eurisotop and acetonitrile from Carlo Erba was freshly distilled from CaH₂ prior to use. D,L-lactide and L-lactide from Alfa Aesar and D-lactide from Fluorochem were recrystallized from isopropanol then toluene and sublimated before being stored in the glovebox. Zn(N(SiMe₃)₂)₂ was prepared according to the literature^[1] and stored in the glove box freezer. **RuOH** was synthesised as previously reported by our group and dried over CaH₂ overnight.^[2] PVA (*M*_n = 133 000 g/mol, >99% hydrolysed) was purchased from Polysciences, Inc. and used as received. *Trans*-2-[3-(4-*ter*-butylphenyl)-2-propenylidene]malonitrile (DCTB) was purchased from Sigma-Aldrich and used without further purification. Tetrahydrofuran (THF), dichloromethane (DCM), pentane and diethyl ether were purchased from VWR. Phosphate-buffered saline (PBS) was purchased from Gibco.

Instrumentation and Methods.

¹H and ¹³C NMR spectra were recorded on a Bruker Avance 400 spectrometer at room temperature. NMR spectra were calibrated using residual ¹H resonances of deuterated solvents ($\delta = 1.94$ ppm for CD₃CN, $\delta = 7.26$ ppm for CDCl₃) and ¹³C resonances of deuterated solvents ($\delta = 1.32$ ppm, 118.26 for CD₃CN). MALDI-TOF MS analyses of polymers were performed at Institut de Chimie des Substances Naturelles, UPR CNRS 2301, Université Paris-Saclay, using an UltrafleXtreme mass spectrometer (Bruker Daltonics). Acquisitions were performed in reflector ion mode. The laser intensity was set just above the ion generation threshold to obtain peaks with the highest possible signal-to-noise (S/N) ratio without significant peak broadening. The mass spectrometer was externally calibrated using PEG3400. All data were processed using

the program Flex-Analysis (Bruker Daltonics, Bremen). DCTB was used as the matrix for MALDI-TOF MS. Polymer sample for MALDI analysis was prepared at a concentration of 60 mM in THF. The matrix solution was prepared at a concentration of 6 mM in THF. The sample was prepared by mixing the polymer solution with matrix solution at a volume ratio of 1:9. The nanoparticle intensity-average diameters D_z and the polydispersity index (PDI) were determined by dynamic light scattering (DLS) using a Malvern ZetaSizer Nano ZS (scattering angle = 173°) at a temperature of 25°C with an equilibrium time of 120 s. Differential scanning calorimetry (DSC) was carried out with Setaram DSC 131 EVO using high pressure crucibles M30. Polymer samples were analysed under nitrogen flow with a heating/cooling rate of $5^\circ\text{C}/\text{min}$ in the range of 40 to 230°C . Two heating/cooling cycles were performed and the melting temperature (T_m) was determined using the second heating run. DSC data were processed with Calisto software. RP-HPLC equipped with an Agilent Pursuit XRs 5C18 (Analytic: 100 \AA , C18 $5\text{ }\mu\text{m}$ $250 \times 4.6\text{ mm}$, Preparative: 100 \AA , C18 $5\text{ }\mu\text{m}$ $250 \times 300\text{ mm}$) Column was used to assess the hydrolytic release of **RuOH** from **Ru-PLA** nanoconjugates. The C18 reverse phase column was used with a flow rate of $1\text{ mL}\cdot\text{min}^{-1}$ and UV absorption was measured at 300 nm. The runs were performed with a linear gradient of A (CH_3CN containing 0.01 % TFA) and B (distilled water containing 0.01 % TFA): $t=0\text{--}3\text{ min}$, 20 % A; $t=7\text{ min}$, 50 % A; $t=20\text{ min}$, 90 % A.

Ring opening polymerization of lactide.

In a typical polymerization (**P5**), $\text{Zn}(\text{N}(\text{SiMe}_3)_2)_2$ (7.6 mg, 0.020 mmol, 1 equiv.) and **RuOH** (40 mg, 0.039 mmol, 2 equiv.) was dissolved in 0.47 mL of dry acetonitrile. The red solution was stirred at room temperature for a couple of minutes. The solvent was then removed under vacuum to give a red solid which was washed three times with pentane to get rid of the released $\text{HN}(\text{SiMe}_3)_2$. The resulting product was dissolved in 0.47 mL of dry acetonitrile and D,L-lactide (200.5 mg, 1.4 mmol, 70 equiv.) was added. The reaction mixture was heated at 60°C for 1

hour. The polymerization was quenched by contact to air and the reaction mixture was, then, precipitated in cold diethyl ether to remove unreacted monomer, yielding an orange powder.

^1H NMR (400 MHz, CD_3CN): $\delta/\text{ppm} = 9.67 - 9.65$ (d, 2H), 8.56 – 8.51 (dd, 4H), 8.49 – 8.47 (d, 1H), 8.43 (s, 1H), 8.18 – 8.08 (m, 5H), 8.04 – 8.00 (t, 2H), 7.91 – 7.88 (t, 2H), 7.86 – 7.85 (d, 2H), 7.73 – 7.72 (d, 2H), 7.48 – 7.45 (t, 2H), 7.28 – 7.24 (t, 2H), 5.56 (s, 2H), 5.19 – 5.11 (m, PLA, $-\text{CH}_2\text{C}(\text{O})-$), 1.52 – 1.49 (m, PLA, CH_3)

^{13}C NMR (100 MHz, CD_3CN): $\delta/\text{ppm} = 175.25$, 170.49 – 170.31 (PLA), 158.14, 157.94, 154.72, 153.04, 152.91, 151.43, 143.42, 141.62, 141.34, 141.21, 138.96, 138.96, 138.88, 134.46, 132.80, 131.73, 130.90, 128.59, 128.43, 125.29, 125.23, 70.48 - 69.94 (PLA), 67.72, 66.89, 20.72, 17.09 (PLA)

NMR determination of the M_n of Ru-PLA conjugates.

$M_{n,NMR}$ was calculated by integrating the singlet at 5.54 ppm corresponding to two protons from the **RuOH** end-chain and the multiplet (in the case of atactic polymers) or quadruplet (in the case of isotactic polymers) at 5.16 ppm assigned to the protons of the PLA methine group, that allowed determination of LA unit content DP . Given the LA unit content, $M_{n,NMR}$ can be calculated according to: $M_{n,NMR} = DP * MW(\text{LA}) + MW(\text{RuOH})$ with $MW(\text{LA}) = 144.13 \text{ g mol}^{-1}$ and $MW(\text{RuOH}) = 1015.7 \text{ g mol}^{-1}$.

Nanoparticle preparation.

Nanoparticles were prepared by nanoprecipitation. Briefly, 2 mg of polymer was dissolved in 0.5 mL of THF and added dropwise to 1 mL of a 0.3% w/v aqueous solution (Milli-Q water) of PVA under moderate stirring. THF was removed under reduced pressure using a rotary evaporator to give an orange nanoparticle suspension. In the case of **P1**, only 0.5 mg of polymer was dissolved in 0.5 mL of THF. For **NPs-3**, 1 mg of **P3** and 1 mg of **P4** were dissolved in 0.25

mL of THF, respectively. The two solutions were, then, mixed and added dropwise to a 0.3% w/v aqueous solution (Milli-Q water) of PVA under moderate stirring.

Stereocomplex formation for DSC measurements.

10 mg of **P3** and 10 mg of **P4** were dissolved in 1 mL of CH₂Cl₂, respectively and mixed together. The resulting solution was added to an excess of pentane to give an orange powder which was dried under vacuum, prior to analysis.

Release kinetics of RuOH from nanoparticles.

Briefly, 0.5 mL of nanoconjugates were added to 4.5 mL of PBS (1 X, pH = 7.0 - 7.2). The resulting PBS solution was divided into equal portions, added to five separate 1 mL Eppendorf tubes and incubated at 37 °C. At different time points, the corresponding Eppendorf tubes were taken out of the incubator and centrifuged at 10 000 g for 20 min. The supernatant was directly injected into RP-HPLC to quantify the released **RuOH**, based on the calibration curve of **RuOH** (figure S12).

Photophysical studies: emission, luminescence quantum yield, and lifetimes

Spectroscopic measurements.

The absorbance was measured using a Lambda 30 UV/Vis spectrophotometer from Perkin Elmer. The emission was measured by irradiation of the sample in fluorescence quartz cuvettes (width 1 cm) using a NT342B Nd-YAG pumped optical parametric oscillator (Ekspla) at 450 nm. Luminescence was focused and collected at right angle to the excitation pathway and directed to a Princeton Instruments Acton SP-2300i monochromator. As a detector a XPI-Max 4 CCD camera (Princeton Instruments) has been used.

Luminescence quantum yield measurements.

For the determination of the luminescence quantum yield, the samples were prepared in a degassed H₂O solution with an absorbance of 0.2 at 450 nm. This solution was irradiated in

fluorescence quartz cuvettes (width 1 cm) using a NT342B Nd-YAG pumped optical parametric oscillator (Ekspla) at 450 nm. The emission signal was focused and collected at right angle to the excitation pathway and directed to a Princeton Instruments Acton SP-2300i monochromator. As a detector a XPI-Max 4 CCD camera (Princeton Instruments) has been used. The luminescence quantum yields were determined by comparison with the reference [Ru(bipy)₃]Cl₂ in H₂O ($\Phi_{em}=5.5\%$ ^[3]) applying the following formula:

$$\Phi_{em, sample} = \Phi_{em, reference} * (F_{reference} / F_{sample}) * (I_{sample} / I_{reference}) * (n_{sample} / n_{reference})^2$$

$$F = 1 - 10^{-A}$$

Φ_{em} = luminescence quantum yield, F = fraction of light absorbed, I = integrated emission intensities, n = refractive index, A = absorbance of the sample at irradiation wavelength.

Lifetime measurements.

For the determination of the lifetimes, the samples were prepared in an air saturated and in a degassed H₂O solution with an absorbance of 0.2 at 450 nm. This solution was irradiated in fluorescence quartz cuvettes (width 1 cm) using a NT342B Nd-YAG pumped optical parametric oscillator (Ekspla) at 450 nm. The emission signal was focused and collected at right angle to the excitation pathway and directed to a Princeton Instruments Acton SP-2300i monochromator. As a detector a R928 photomultiplier tube (Hamamatsu) has been used.

Singlet oxygen measurements

- Direct evaluation

The samples were prepared in an air saturated D₂O solution with an absorbance of 0.2 at 450 nm. This solution was irradiated in fluorescence quartz cuvettes (width 1 cm) using a mounted M450LP1 LED (Thorlabs) whose irradiation, centred at 450 nm, has been focused with aspheric condenser lenses. The intensity of the irradiation has been varied using a T-Cube LED Driver (Thorlabs) and measured with an optical power and energy meter. The emission signal was

focused and collected at right angle to the excitation pathway and directed to a Princeton Instruments Acton SP-2300i monochromator. A longpass glass filter was placed in front of the monochromator entrance slit to cut off light at wavelengths shorter than 850 nm. As a detector an EO-817L IR-sensitive liquid nitrogen cooled germanium diode detector (North Coast Scientific Corp.) has been used. The singlet oxygen luminescence at 1270 nm was measured by recording spectra from 1100 to 1400 nm. For the data analysis, the singlet oxygen luminescence peaks at different irradiation intensities were integrated. The resulting areas were plotted against the percentage of the irradiation intensity and the slope of the linear regression calculated. The absorbance of the sample was corrected with an absorbance correction factor. As reference for the measurement $[\text{Ru}(\text{bipy})_3]\text{Cl}_2$ ($\Phi_{\text{Ru}(\text{bipy})_3\text{Cl}_2}=0.22^{[4]}$) was used and the singlet oxygen quantum yields were calculated using the following formula:

$$\Phi_{\text{sample}} = \Phi_{\text{reference}} * (S_{\text{sample}} / S_{\text{reference}}) * (I_{\text{reference}} / I_{\text{sample}})$$

$$I = I_0 * (1 - 10^{-A})$$

Φ = singlet oxygen quantum yield, S = slope of the linear regression of the plot of the areas of the singlet oxygen luminescence peaks against the irradiation intensity, I = absorbance correction factor, I_0 = light intensity of the irradiation source, A = absorbance of the sample at irradiation wavelength.

- **Indirect evaluation**

The samples were prepared in an air-saturated PBS solution containing the complex with an absorbance of 0.1 at the irradiation wavelength, *N,N*-dimethyl-4-nitrosoaniline aniline (RNO, 20 μM) and histidine (10 mM). The samples were irradiated on 96 well plates with an Atlas Photonics LUMOS BIO irradiator for different times. The absorbance of the samples was measured during these time intervals with a SpectraMax M2 Microplate Reader (Molecular Devices). The difference in absorbance ($A_0 - A$) at 440 nm a PBS buffer solution was calculated and plotted against the irradiation times. From the plot the slope of the linear regression was

calculated as well as the absorbance correction factor determined. The singlet oxygen quantum yields were calculated using the same formulas as used for the direct evaluation.

Biological evaluation

Cell culture experiments.

Cells lines were treated in appropriate cell culture media of DMEM (Gibco, LifeTechnologies, USA) supplemented with 10% foetal calf serum for the HeLa cell line (Gibco) and DMEM/F-12 (Gibco) supplemented with 10% foetal calf serum (Gibco) for the RPE-1 cell line. All media was also supplemented with 100 U/ml penicillin-streptomycin mixture (Gibco). Cells were incubated at 37 °C in 5 % CO₂. Cells were passaged when 80% confluency was reached and used within 15 passages from initial purchase.

Cytotoxicity experiments.

96-well plates were seeded with HeLa and RPE-1 cell lines (4000, 2000 and 1000 cells per well for 4, 24 and 48 h time points respectively) in media (DMEM, 100 µl) and incubated overnight. Treatment solutions were made by dilution of compound stock solutions (nanoparticles were stored at a concentration **RuOH** of ~500 µM for **NPs-2,3** and at ~300 µM for **NPs-1,4** in 0.3% w/v PVA water, **RuOH** was stored at 50 mM in DMSO) into the cell media. The concentrations of water and DMSO were kept constant throughout all treatment solutions. The incubation media was removed and replaced with treatment media and the cells incubated in the dark. Following 4, 24 or 48 h, the treatment media was replaced with fresh media and the cells were treated with light ($\lambda_{\text{exc}} = 480 \text{ nm}$, 3.21 J cm^{-2} , 10 min) before being incubated in the dark. 48 h post light treatment the cells were treated with resazurin (0.2 mg mL⁻¹ final concentration in appropriate media) and incubated a further 4 h. The plates were read by fluorescence plate reader SpectraMax M5 micro plate reader (λ_{ex} , 540 nm; λ_{em} , 590 nm).

ICP-MS cellular uptake.

6-well plates were seeded with HeLa cells (2×10^4 , 4×10^4 and 10×10^4 cells per well for 48, 24 and 4 h timepoints respectively) in media (2 ml) and incubated overnight. The next morning the cells were treated with nanoparticles or **RuOH** staining solution in media ($5 \mu\text{M}$, 2 wells per condition/timepoint) and the cells were incubated with the staining solution for the stated incubation time. Following incubation, the cells were washed (2 x PBS, 2 ml) and trypsinized ($300 \mu\text{l}$ / well). Once detached the cells were washed by centrifugation (PBS, 1 ml) and the pellet suspended (PBS, 1 ml) and the cells counted by haemocytometer. Once counted the cells were pelleted once again before being suspended in HNO_3 (overnight, 60°C) and subsequently diluted into HCl solution (1/10 dilution, 1 % HCl in distilled H_2O). Daily, prior to the analytical sequence, the instrument (sector-field inductively coupled plasma mass spectrometer, HR-ICP-MS Element II, ThermoScientific) was first tuned to produce maximum sensitivity and stability while also maintaining low Uranium oxide formation ($\text{UO}/\text{U} \leq 5\%$). Ruthenium stock solution (SCP Science, 1g/L) was diluted several times in 1% distilled hydrochloric acid to obtain standards for the calibration range (from 10 ng/L to $10 \mu\text{g/L}$). Then, data were treated as follow: intensities were converted into concentrations using uFREASI (user-FRIendly Elemental dAta proceSsIng)^[5] This software, made for HR-ICP-MS users community, is free and available on <http://www.ipgp.fr/~tharaud/uFREASI>.

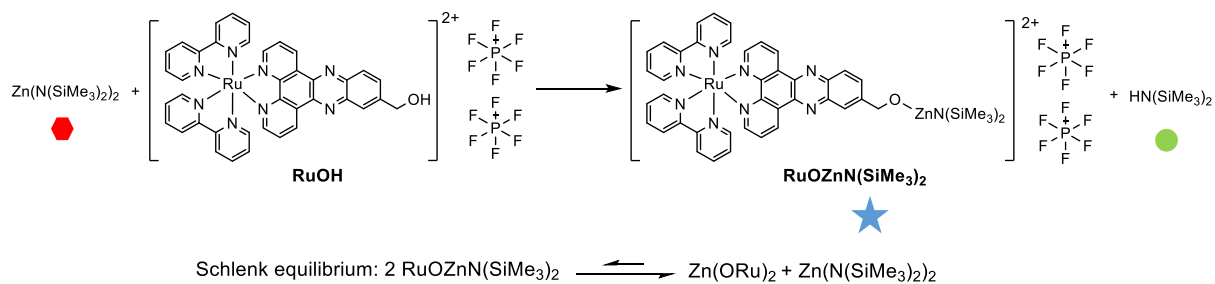
Confocal microscopy.

Into 12-well plates were added pre-sterilized 12 mm *Menzel–Gläser* coverslips before HeLa cells were seeded (2×10^4 , 4×10^4 and 10×10^4 cells per well for 48, 24 and 4 h timepoints respectively) and incubated overnight. The next morning the cells were treated with nanoparticle or RuOH staining solution in media ($50 \mu\text{M}$, 2 wells per condition/timepoint) and the cells were incubated. Nucblue (2 drops/ml) was added for the final 20 minutes of stated incubation time. Cells were then washed (PBS X 2) before being fixed (paraformaldehyde, 4 %

in PBS, 20 mins) and washed (PBS X 2). Samples used later for indirect immunofluorescence were then incubated in blocking solution (0.2% BSA, 0,05 % Saponin in PBS) for 15 min at RT and incubated with primary anti-LAMP (*BD Biosciences*) antibodies for 1 h at 1:3000 dilution and detected using Alexa 488 conjugated secondary antibodies (*Jackson ImmunoResearch Laboratory*) at 1:400 dilution. All samples were then mounted to microscope slides (*Prolong Glass Antifade Mountant*). The slides were imaged using a Leica SP8 confocal microscope. The ruthenium compounds were excited at 488 nm with emission recorded above 650 nm. Images were recorded at the Cellular and Molecular Imaging Technical Platform, INSERMUMS025–CNRSUMS3612, Faculty of Pharmacy of Paris, Paris Descartes University, Paris, France.

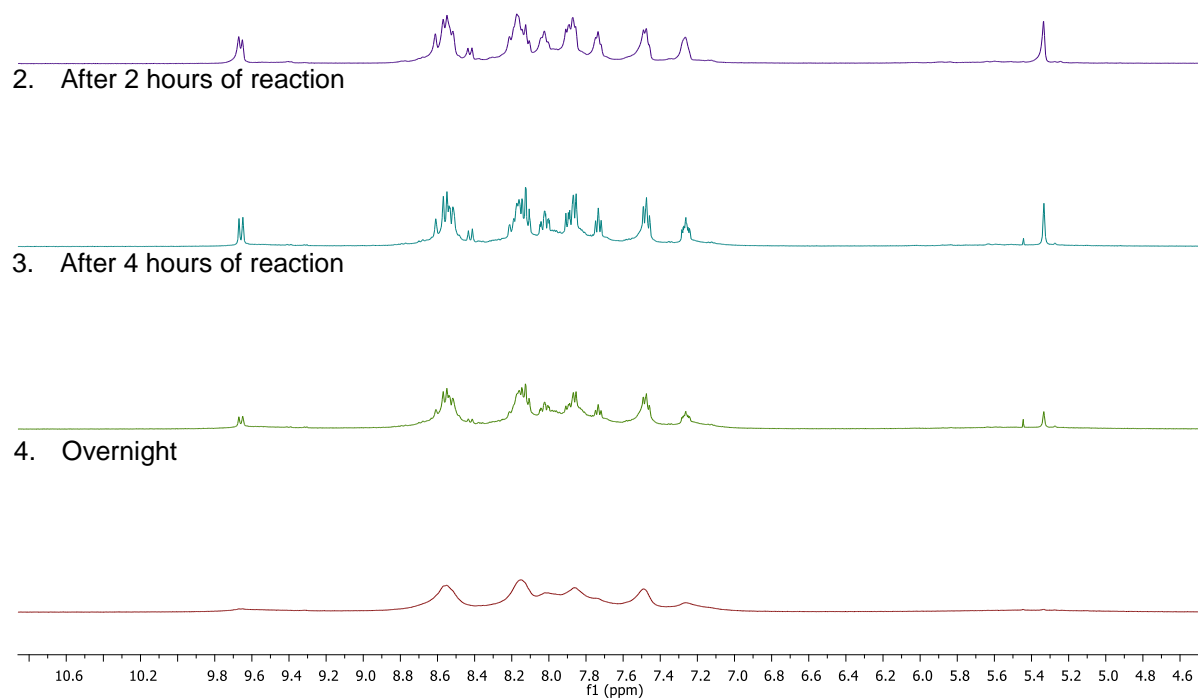
Supplementary figures

a)



b)

1. Equimolar mixture of **RuOH** and $\text{Zn}(\text{N}(\text{SiMe}_3)_2)_2$
Schlenk equilibrium



c)

1. Equimolar mixture of **RuOH** and $\text{Zn}(\text{N}(\text{SiMe}_3)_2)_2$
Schlenk equilibrium

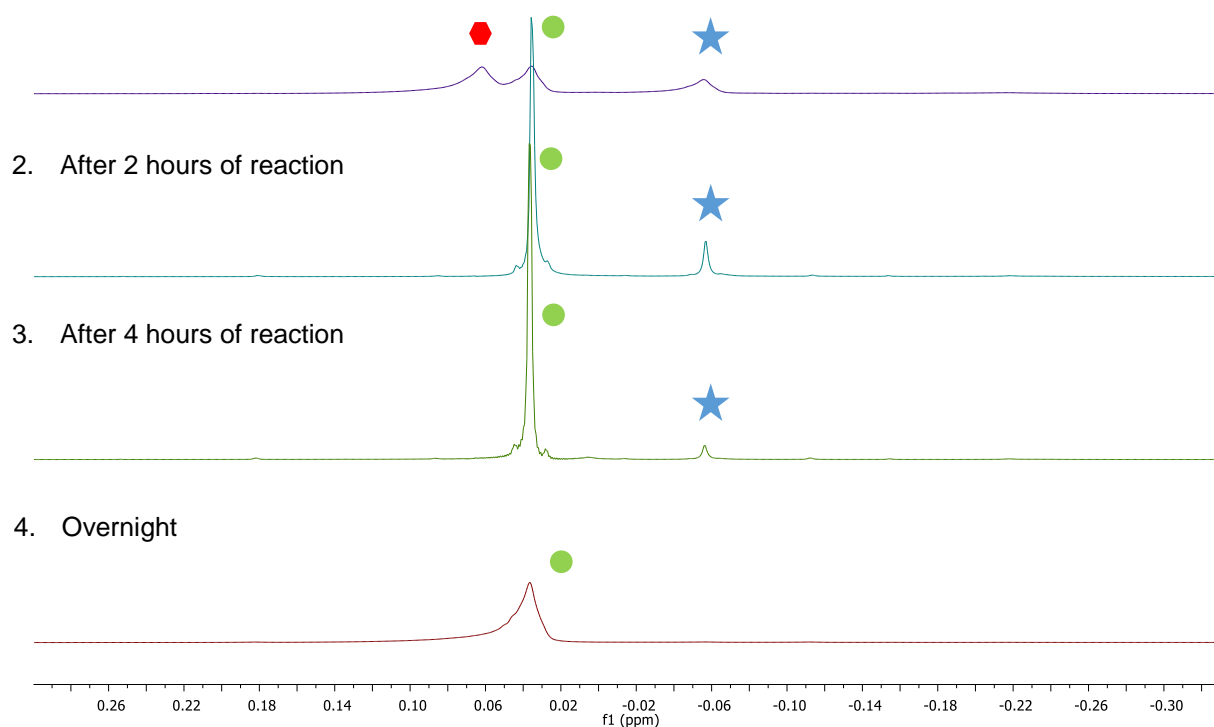


Figure S1. a) Reaction scheme: schlenk equilibrium. b) An overlay ^1H NMR spectra of the reaction mixture in a J. Young NMR tube between equimolar ratio of **RuOH** and $\text{Zn}(\text{N}(\text{SiMe}_3)_2)_2$ in dry CD_3CN and at room temperature overtime, aromatic region, 400 MHz. c) An overlay ^1H NMR spectra of the reaction mixture in a J. Young NMR tube between equimolar ratio of **RuOH** and $\text{Zn}(\text{N}(\text{SiMe}_3)_2)_2$ in dry CD_3CN and at room temperature overtime, amido region, 400 MHz.

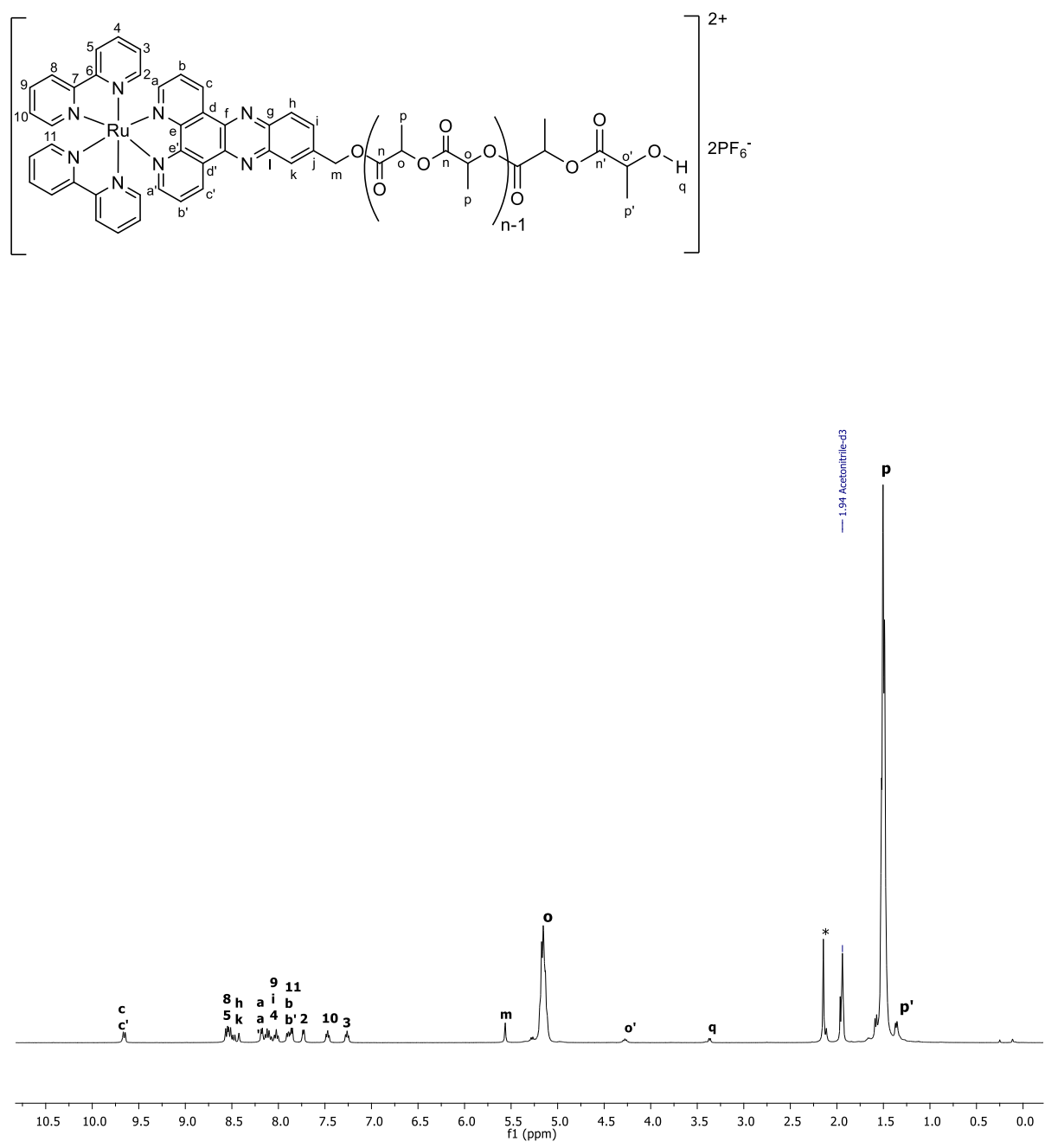


Figure S2. ^1H NMR spectra of **Ru-PLA** prepared from D,L-lactide , * = H_2O .

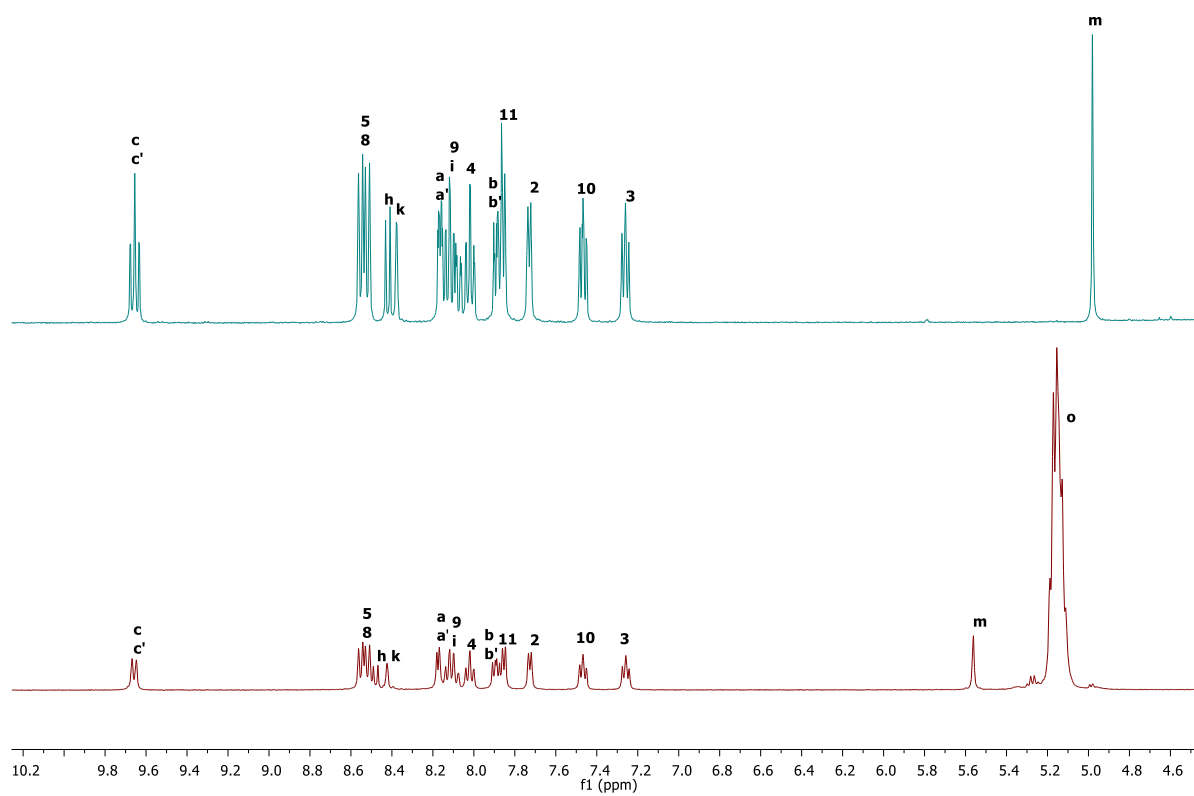


Figure S3. An overlay of ^1H NMR spectra of **RuOH** (green) and **Ru-PLA** (red).

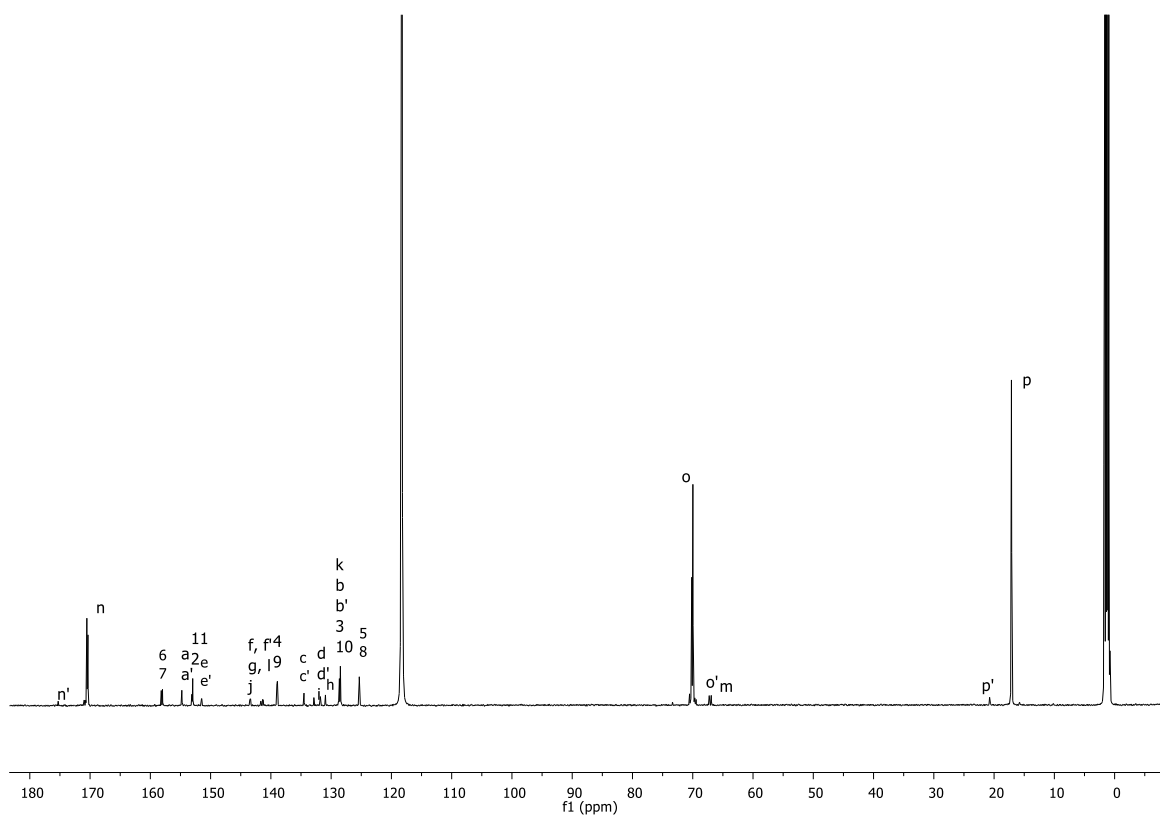
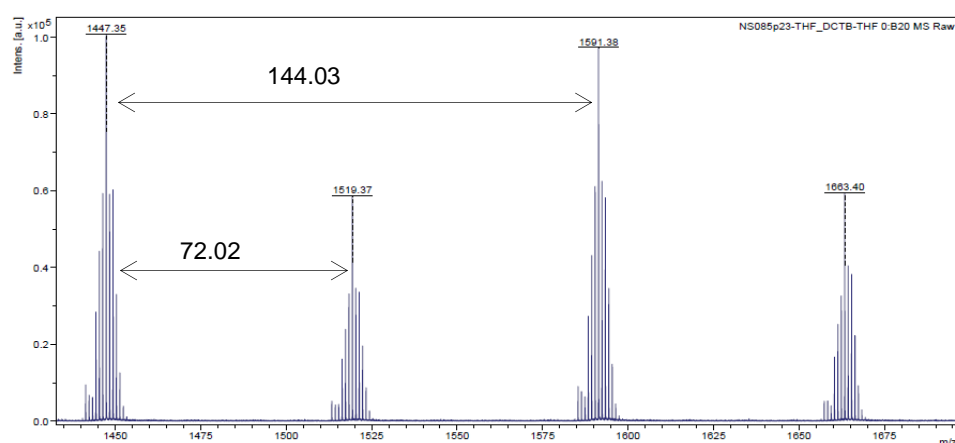
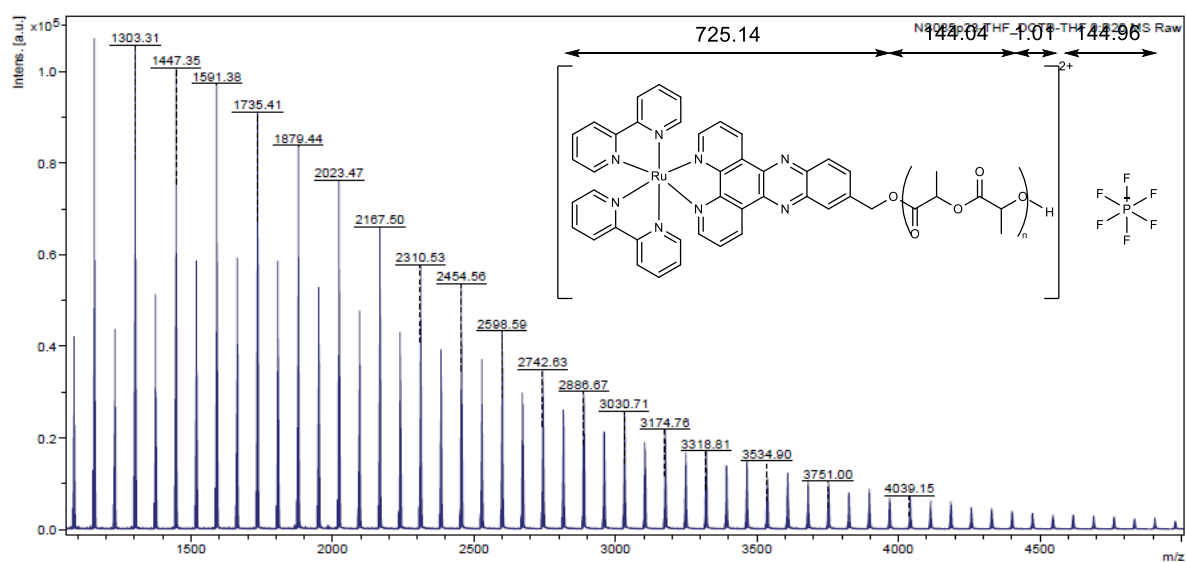
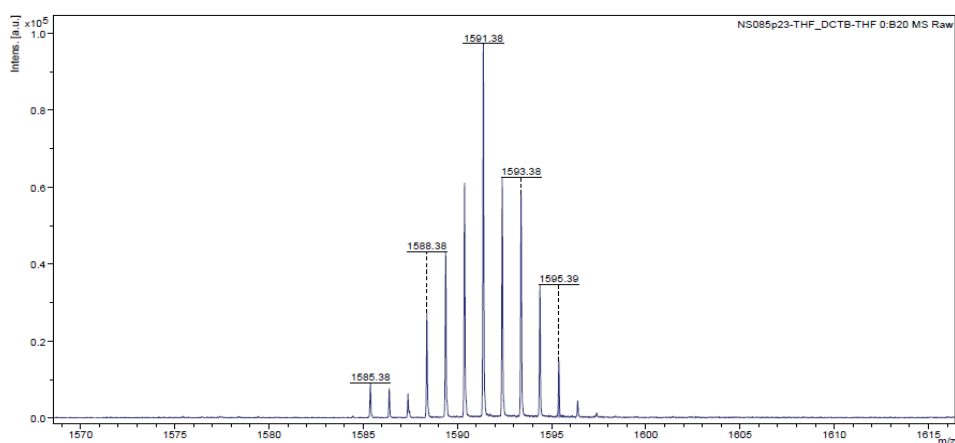


Figure S4. ^{13}C NMR of Ru-PLA prepared from D,L-lactide.



n	m/z (calculated)	m/z MALDI
3	1303,22	1303,31
4	1447,26	1447,35
5	1591,3	1591,38
6	1735,34	1735,41
7	1879,38	1879,44
8	2023,42	2023,47
9	2167,46	2167,5
10	2311,5	2310,53
11	2455,54	2454,56
12	2599,58	2598,59
13	2743,62	2742,63
14	2887,66	2886,67
15	3031,7	3030,71
16	3175,74	3174,76
17	3319,78	3318,81



$M_n = 2\,200$ g/mol

$M_w = 2\,300$ g/mol

$M_w/M_n = 1.07$

Figure S5. MALDI-TOF MS analysis of a Ru-conjugate

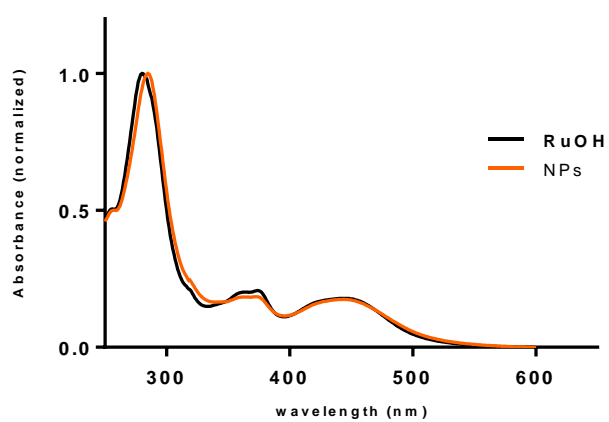
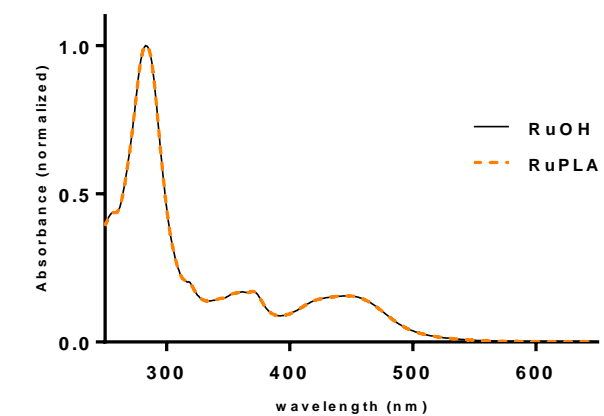


Figure S6. UV-Vis spectra of **RuOH** and **Ru-PLA** in CH₃CN (top) and in water (bottom).

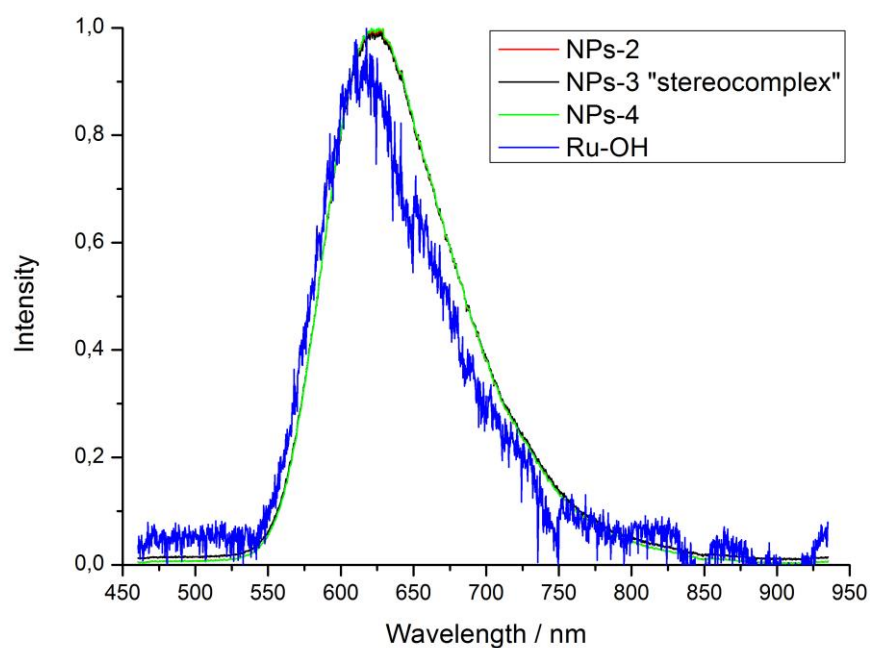


Figure S7. Emission spectra of **RuOH** and **NPs-2,3,4** in H_2O .

Table S1. Photophysical properties of **RuOH** in comparison to **NPs-2,3,4** in H_2O . ^{a)} contains 1% DMSO.

Compound	Emission maximum	Luminescence Quantum Yield	Lifetime / ns	
			degassed	air saturated
RuOH^{a)}	618	>0.1%	950	202
NPs-2	626	1.3%	998	220
NPs-3 “stereocomplex”	626	1.4%	932	231
NPs-4	626	1.4%	1040	207

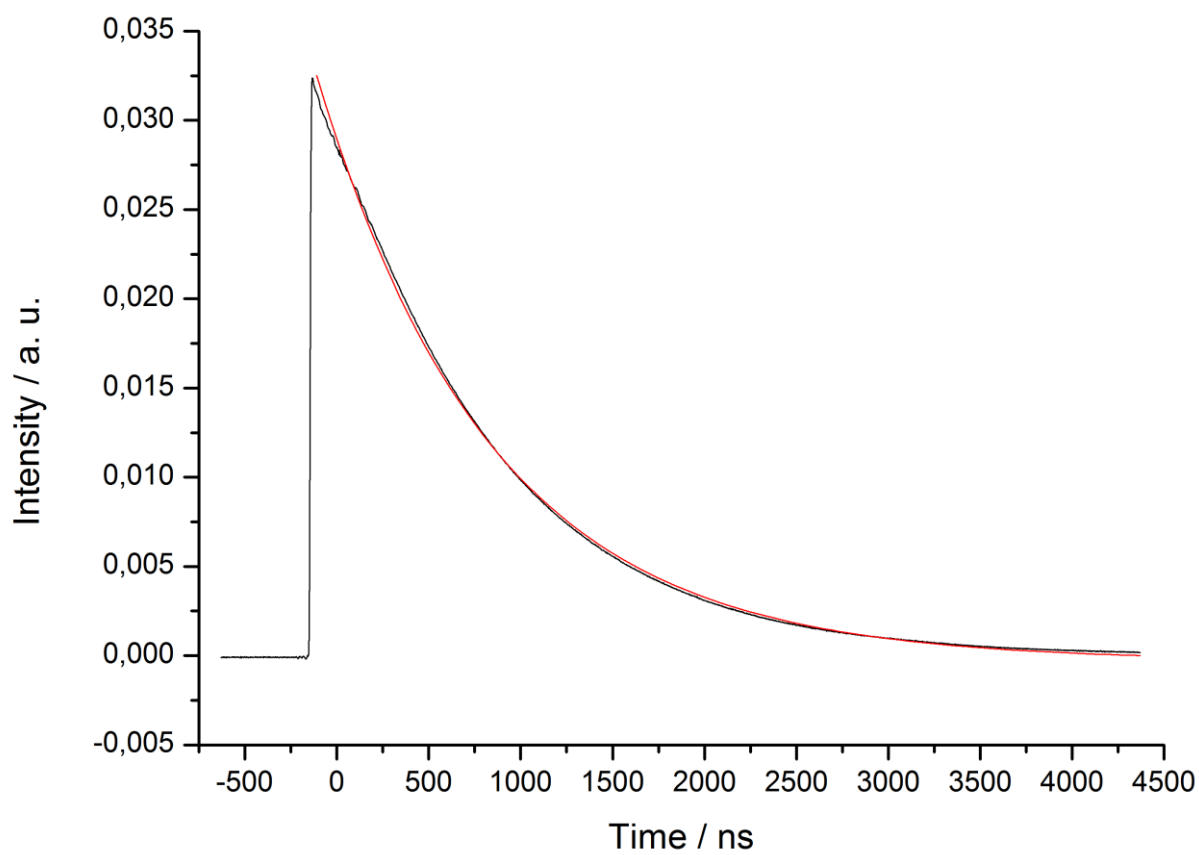
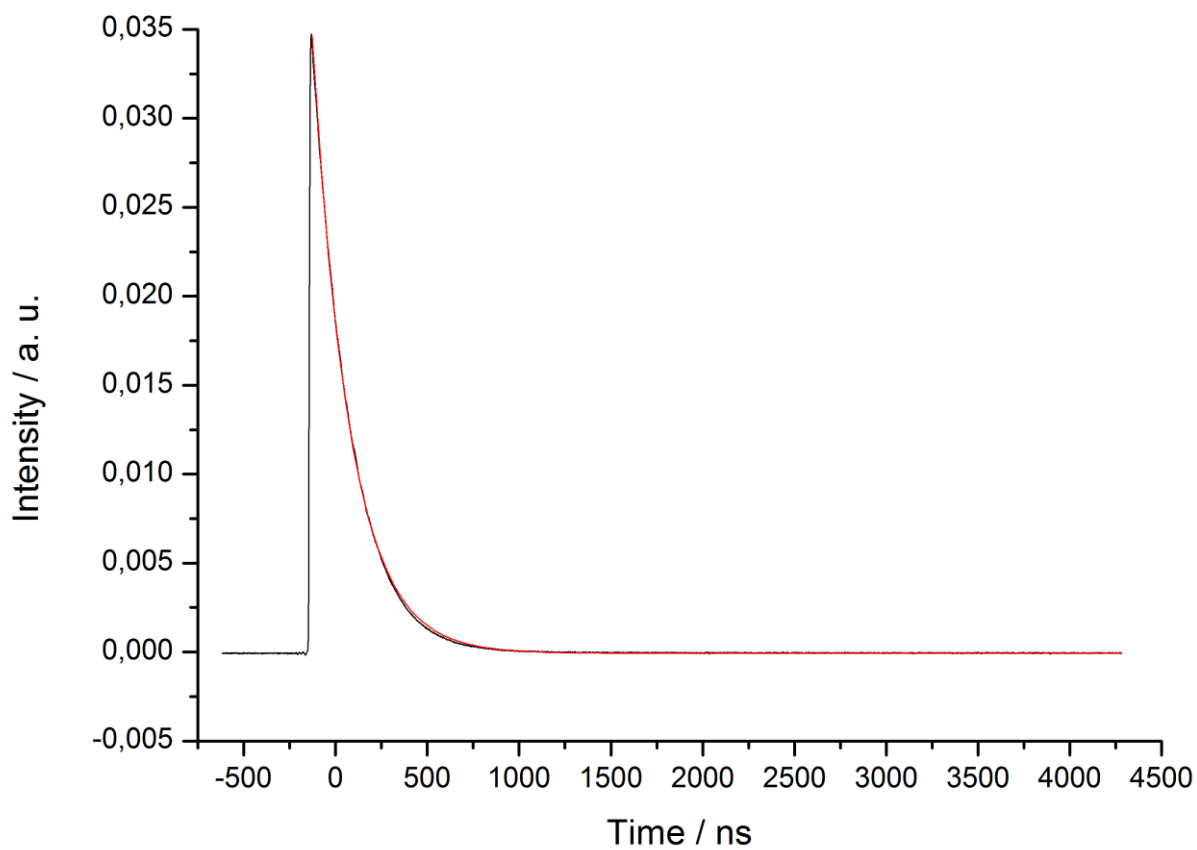


Figure S8. Lifetime spectra of **RuOH** in aerated (above) and degassed (below) H₂O.

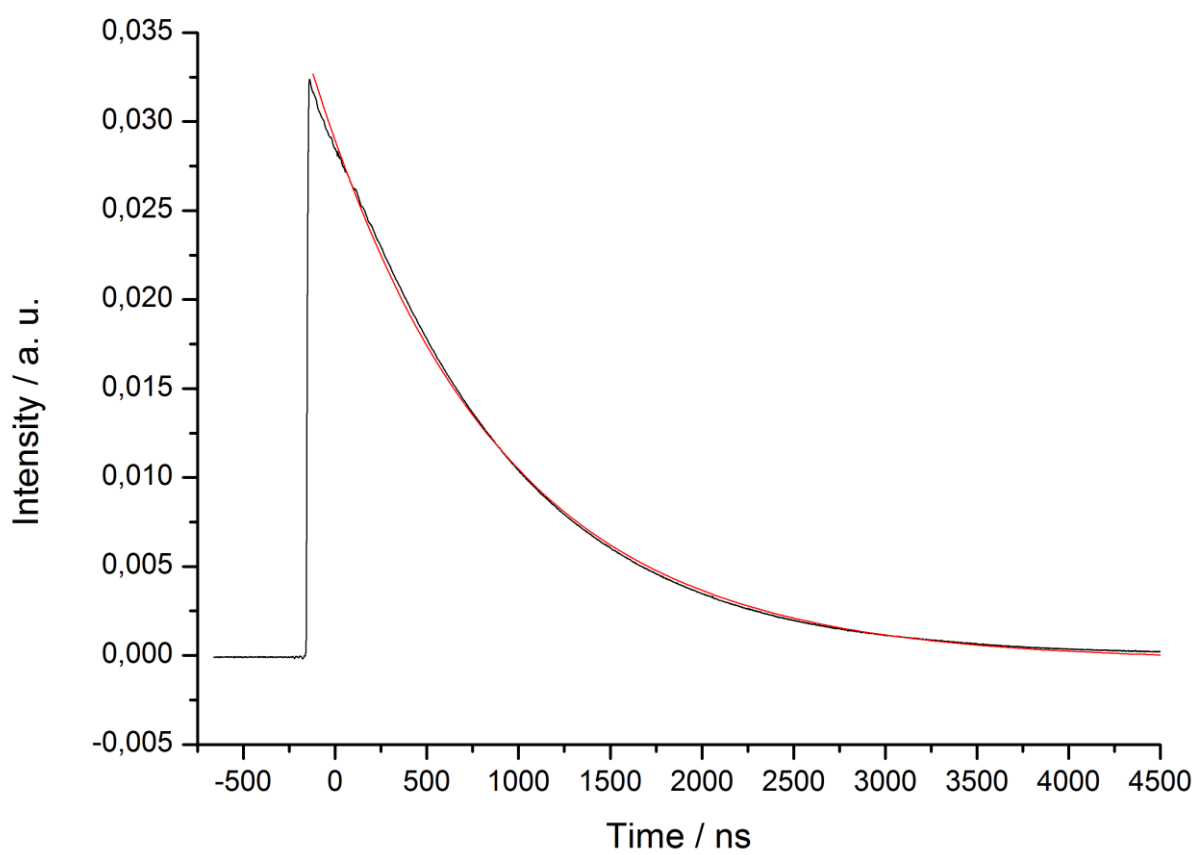
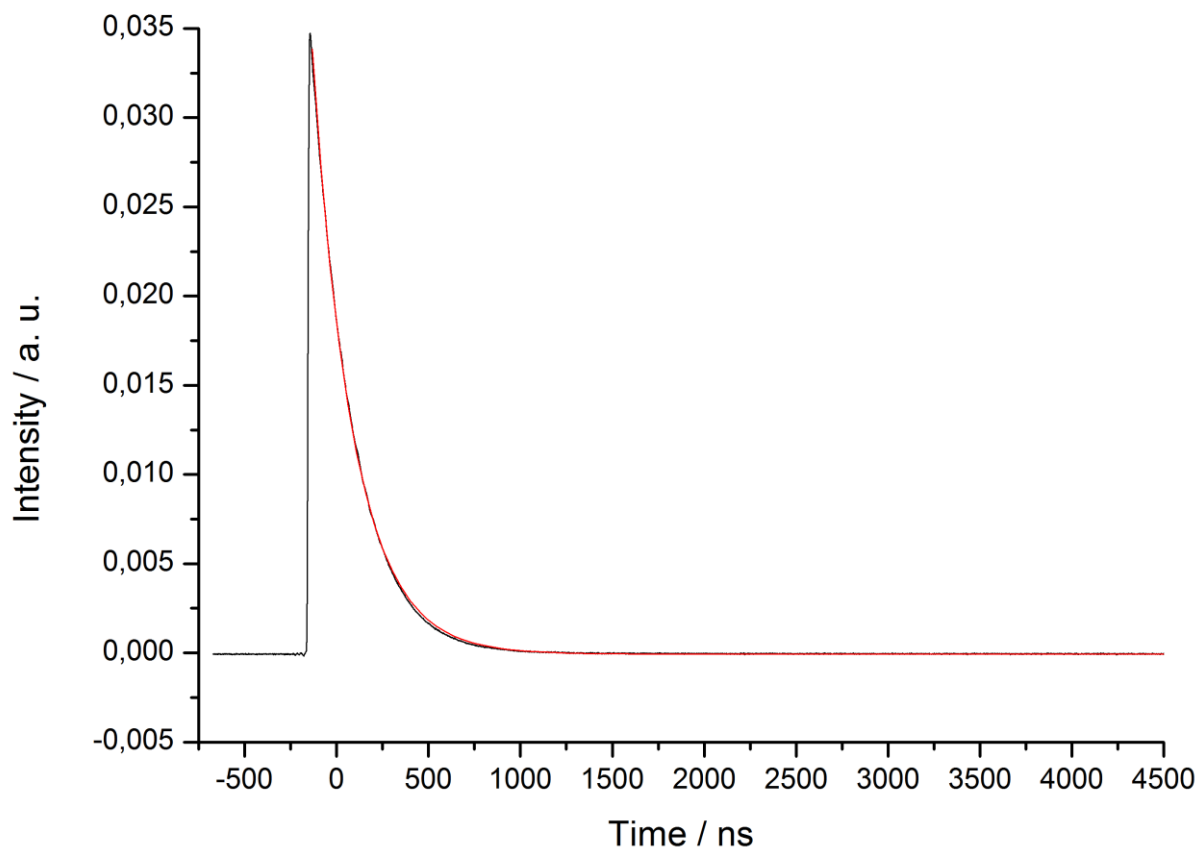


Figure S9. Lifetime spectra of NPs-2 in aerated (above) and degassed (below) H₂O.

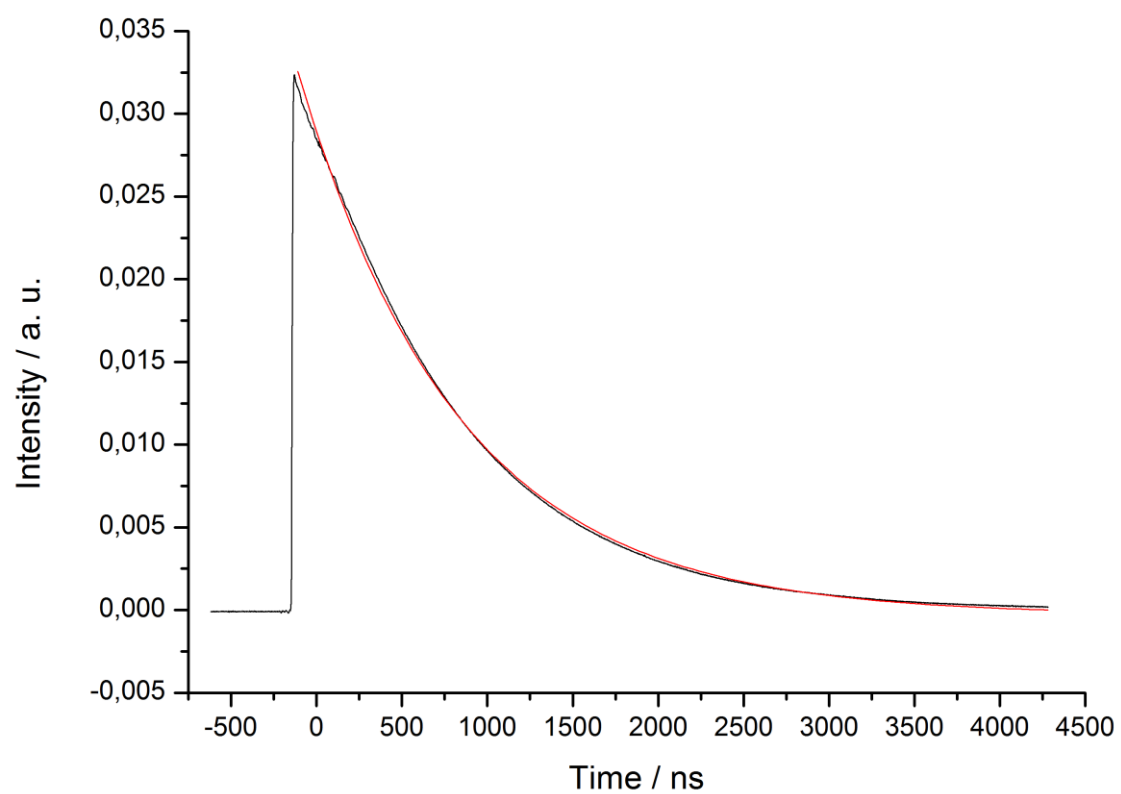
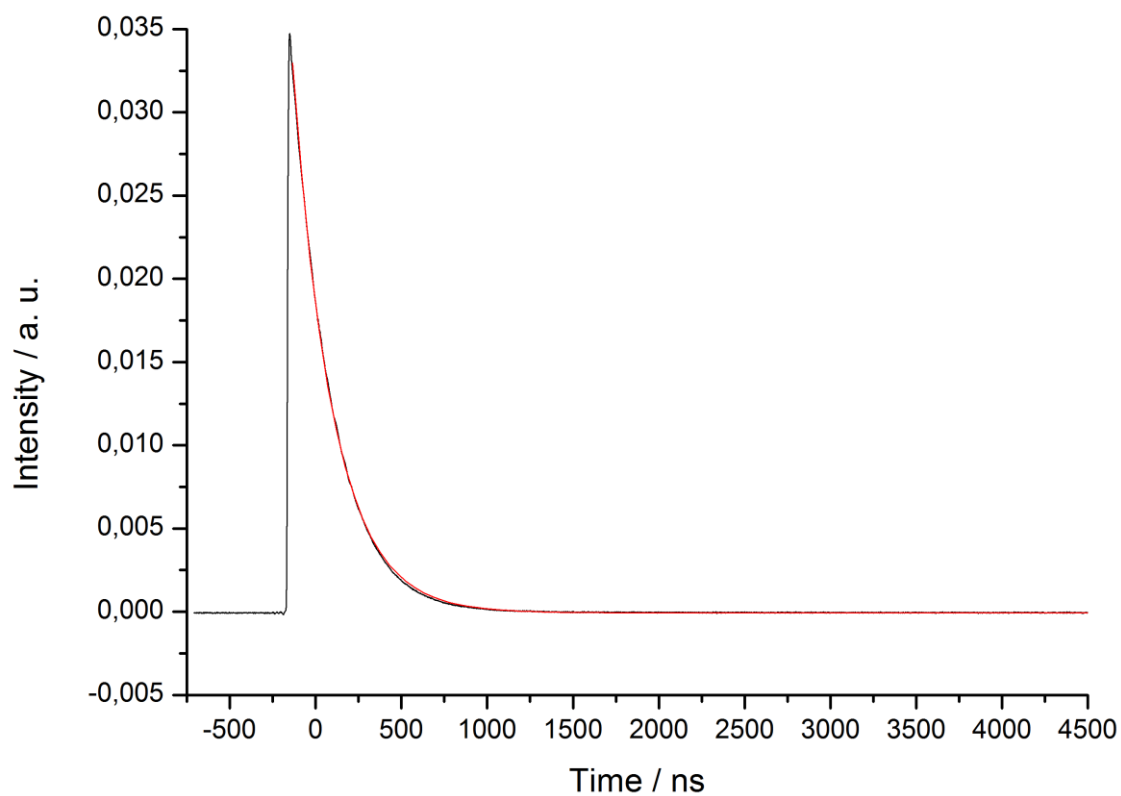


Figure S10. Lifetime spectra of the complex **NPs-3** in aerated (above) and degassed (below) H_2O .

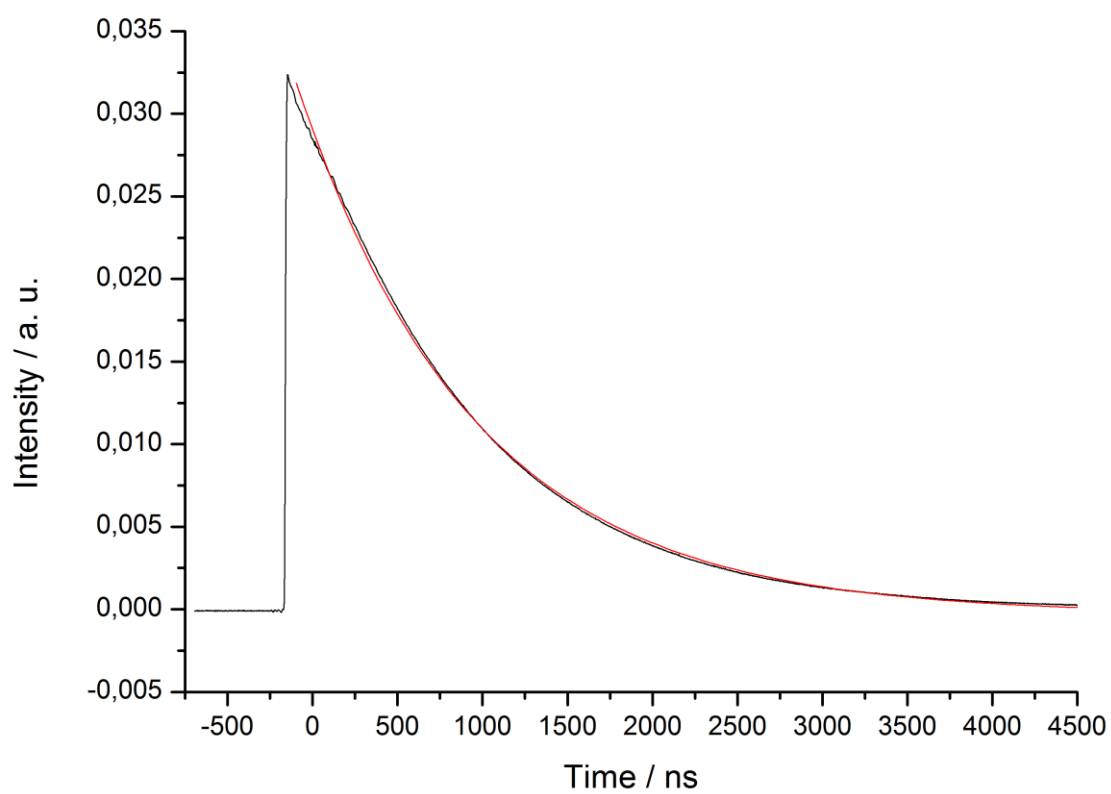
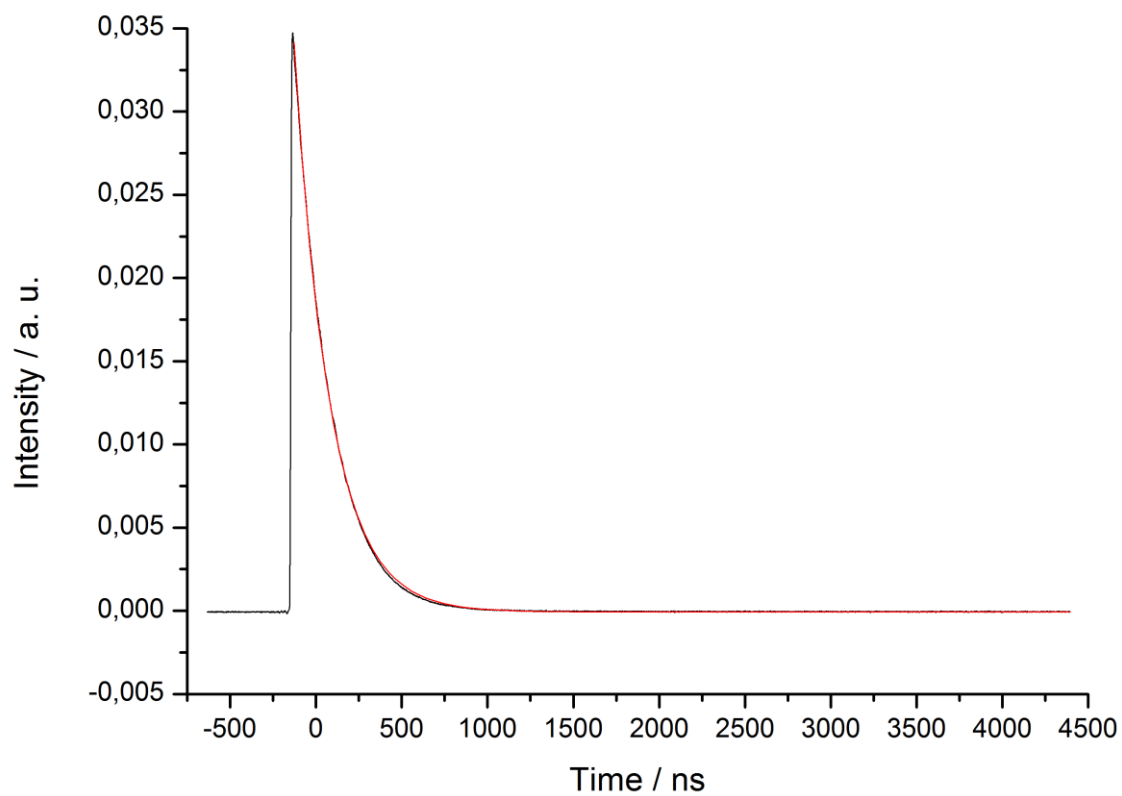


Figure S11. Lifetime spectra of the complex **NPs-4** in aerated (above) and degassed (below) H₂O.

Table S2. Singlet oxygen quantum yields in H₂O upon irradiation at 450 nm. Average of three independent measurements. n.d. = not detectable. ^{a)} contains 1% DMSO.

	Direct D ₂ O	Indirect PBS
RuOH^{a)}	n.d.	3%
NPs-2	n.d.	11%
NPs-3 stereocomplex	n.d.	11%
NPs-4	n.d.	12%

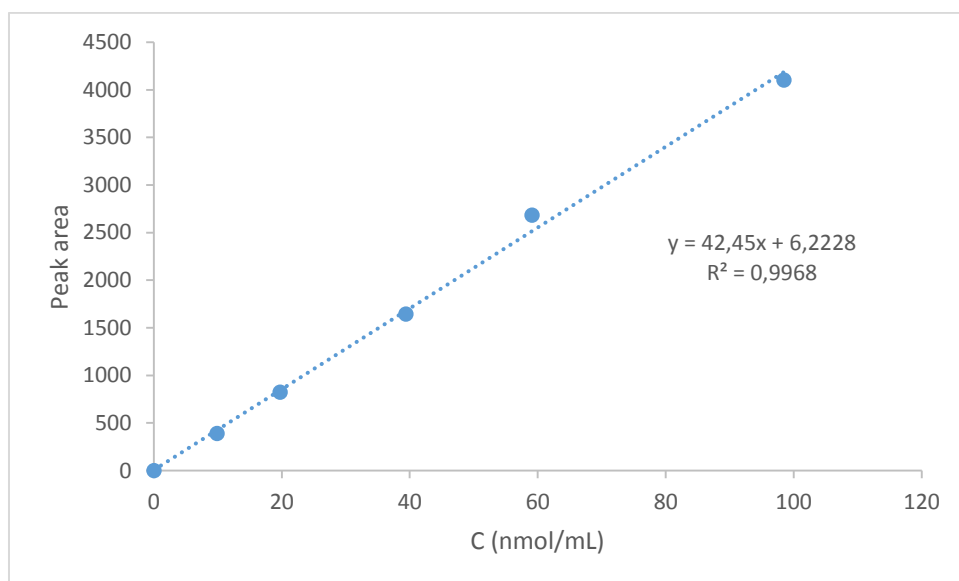


Figure S12. Standard curve of **RuOH**

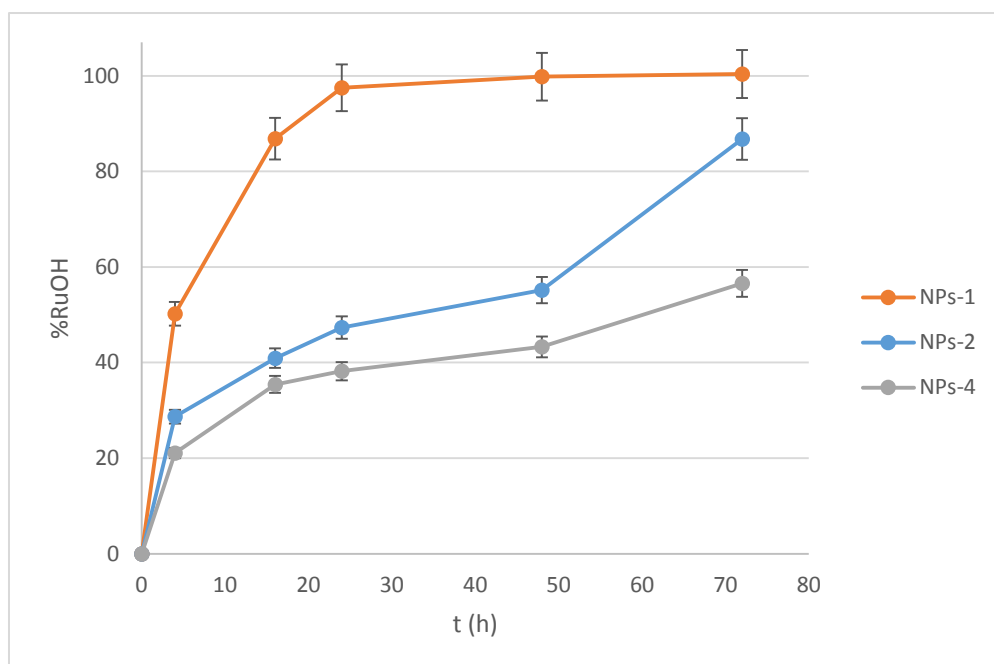


Figure S13. RuOH release kinetics from NPs-1,2,4 in PBS (1 X, pH = 7.0 – 7.2) at 37 °C overtime, with an estimated measurement error of 5 %.

Table S3. Cytotoxicity data^a for NPs-1,2,3,4 and RuOH (μM) in HeLa and RPE-1 cells. Light treatment at 480 nm (10 mins, 3.21 J cm⁻²)

	HeLa 4 hrs			RPE-1 4 hrs			HeLa 24 hrs			RPE-1 24 hrs			HeLa 48 hrs			RPE-1 4 8hrs		
	Light	Dark	PI ^b	Light	Dark	PI ^b	Light	Dark	PI ^b	Light	Dark	PI ^b	Light	Dark	PI ^b	Light	Dark	PI ^b
NPs-1	28.0 ± 3.2	> 100	3.6				18.7 ± 3.6	> 100	5.9				12.7 ± 3.3	43.4 ± 17.8	3.4			
NPs-2	34.2 ± 17.4	> 100	2.9	> 100	> 100		14.5 ± 6.3	> 100	6.9	98.2	> 100		23.4 ± 3.8	61.4 ± 17.9	2.6	53.6 ± 17.6	> 100	1.9
NPs-3	41.3 ± 4.5	> 100	2.5	> 100	> 100		9.5 ± 1.1	> 100	11.25	> 100	> 100		8.4 ± 4.3	62.9 ± 13.4	7.5	76.6 ± 17.5	>100	1.3
NPs-4	16.7 ± 4.3	> 100	6				14.5 ± 6.3	81.3 ± 9.1	10.9				4.4 ± 0.8	31.8 ± 7.1	7.5			
RuOH	> 500	> 500		> 500	> 500		274.4 ± 70.1	> 500	1.8	465.7 ± 85.6	> 500		99.1 ± 12.7	248.6 ± 37.7	2.5	114.5 ± 11.5	234.4 ± 18.7	

^a IC₅₀ values were an average of three measurements. ^bPI refers to the phototoxicity index,

which is the ratio between the IC₅₀ values in the dark and the ones upon light irradiation.

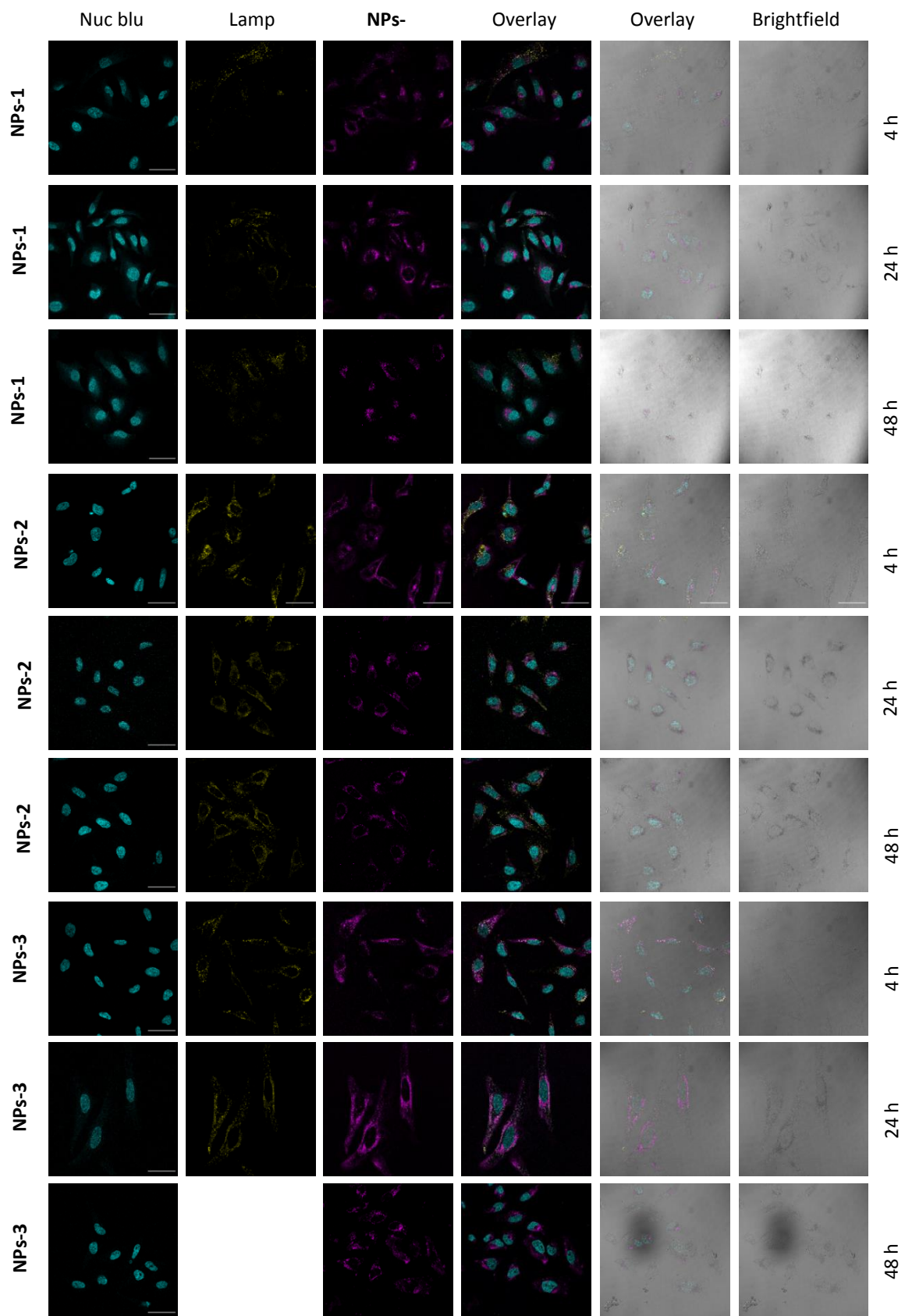


Figure S14a. Confocal microscopy images of HeLa cells incubated with NPs- (50 μ M, 37 $^{\circ}$ C,

4, 24, 48 hr). **NPs** co-stained with the nuclear stain, NucBlue, and the lysosomal specific antibody LAMP. Cells were imaged on a LeicaSP8 confocal microscope. Scale equivalent in all images (scale bar 50 μm).

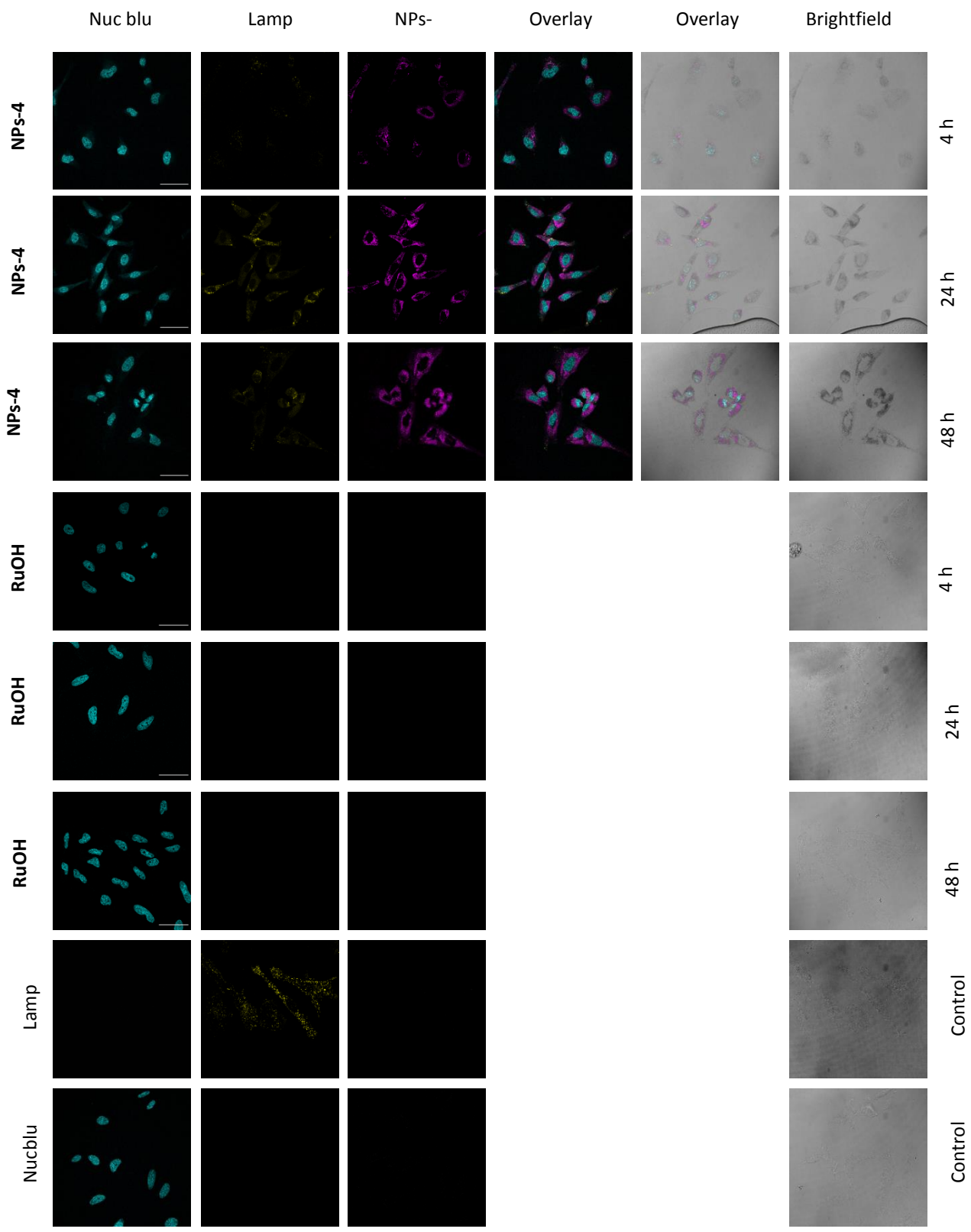


Figure S14b. Confocal microscopy images of HeLa cells incubated with **NPs** (50 μ M, 37 °C, 4, 24, 48 hr). **NPs** co-stained with the nuclear stain, NucBlue, and the lysosomal specific antibody LAMP. Cells were imaged on a LeicaSP8 confocal microscope. Scale equivalent in all images (scale bar 50 μ m).

REFERENCES

- (1) Lee, D.-Y.; Hartwig, J. F. Zinc Trimethylsilylamide as a Mild Ammonia Equivalent and Base for the Amination of Aryl Halides and Triflates. *Org. Lett.* **2005**, *7*, 1169-1172.
- (2) Mari, C.; Pierroz, V.; Rubbiani, R.; Patra, M.; Hess, J.; Spingler, B.; Oehninger, L.; Schur, J.; Ott, I.; Salassa, L.; Ferrari, S.; Gasser, G. DNA intercalating Ru(II) polypyridyl complexes as effective photosensitizers in photodynamic therapy. *Chem. Eur. J.* **2014**, *20*, 14421–14436.
- (3) Nakamaru, K. Solvent Effect on the Nonradiative Deactivation of the Excited State of Tris(2,2'-bipyridyl)ruthenium(II) Ion. *Bull Chem Soc Jpn* **1982**, *55*, 1639-1640.
- (4) Garcia-Fresnadillo, D.; Georgiadou, Y.; Orellana, G.; Braun, A. M.; Oliveros, E. Singlet-Oxygen ($^1\Delta_g$) Production by Ruthenium(II) complexes containing polyazaheterocyclic ligands in methanol and in water. *Helv. Chim. Acta* **1996**, *79*, 1222-1238.
- (5) Tharaud, M.; Gardoll, S.; Khelifi, O.; Benedetti, M. F.; Sivry, Y. uFREASI: user-Friendly Elemental dAta procesSIng. A free and easy-to-use tool for elemental data treatment. *Microchem. J.* **2015**, *121*, 32–40.

Chapter 7- A Ruthenium(II) Complex Containing a Redox-Active Semicuinonate Ligand as Potential Chemotherapeutic Agent: From Synthesis to *in vivo* Studies

Anna Notaro,^{a,#} Angelo Frei,^{b,#} Riccardo Rubbiani,^{b,#} Marta Jakubaszek,^{a, e} Uttara Basu,^a Severin Koch,^b Cristina Mari,^b Mazzarine Dotou,^a Olivier Blacque,^b Jérémie Gouyon,^c Fethi Bedioui,^c Nils Rotthowe,^d Rainer F. Winter,^d Bruno Goud,^e Stefano Ferrari,^{f,g} Mickaël Tharaud,^h Martina Řezáčová,ⁱ Jana Humajová,^j Pavel Tomšik,ⁱ and Gilles Gasser^{a,}*

^a Chimie ParisTech, PSL University, CNRS, Institute of Chemistry for Life and Health Sciences, Laboratory for Inorganic Chemical Biology, F-75005 Paris, France.

^b Department of Chemistry, University of Zurich, Winterthurerstrasse 190, 8057 Zurich, Switzerland.

^c Chimie ParisTech, PSL University, CNRS, Institute of Chemistry for Life and Health Sciences, Team Synthèse, Electrochimie, Imagerie et Systèmes Analytiques pour le Diagnostic, F-75005 Paris, France.

^d Department of Chemistry, University of Konstanz, Universitätsstrasse 10, D-78457 Konstanz, Germany.

^e Institut Curie, PSL University, CNRS UMR 144, Paris, France.

^f Institute of Molecular Cancer Research, University of Zurich, Zurich, Switzerland.

^g Institute of Molecular Genetics of the Czech Academy of Sciences, Videnska 1083, 143 00 Prague, Czech Republic.

^h Université de Paris, Institut de physique du globe de Paris, CNRS, F-75005 Paris, France.

ⁱ Department of Medical Biochemistry, Faculty of Medicine in Hradec Kralove, Charles University, Czech Republic.

^j Department of Medical Biochemistry, Faculty of Medicine in Prague, Czech Republic.

these authors have contributed equally to the work

* Corresponding author: E-mail: gilles.gasser@chimeparistech.psl.eu; WWW: www.gassergroup.com; Phone: +33 1 44 27 56 02

This chapter has been published *Journal of Medicinal Chemistry* on the 22nd of April 2020 (DOI: 10.1021/acs.jmedchem.0c00431)

(<https://pubs.acs.org/doi/abs/10.1021/acs.jmedchem.0c00431>)

Contribution to the publication:

Marta Jakubaszek performed with Anna Notaro the 2D cytotoxicity studies, Annexin V and PI staining, cellular uptake, intracellular distribution and DNA metalation studies. She performed the JC-1 membrane potential test, mitochondrial metabolic studies and Akt-1 protein levels experiments. She supervised Mazzarine Dotou during 3D cell culture experiments. She analysed together with Anna Notaro obtained data and wrote with her contribution the cytotoxicity studies, cellular uptake, intracellular distribution, DNA metalation and JC-1 staining sections. She wrote mechanism of cell death, mitochondrial metabolic studies and Akt-1 protein levels sections.

Marta Jakubaszek



19.05.2020

Gilles Gasser



Keywords: Bioinorganic Chemistry, Cancer, DNA, Medicinal Inorganic Chemistry, Ruthenium.

Abstract

Chemotherapy remains one of the dominant treatments to cure cancer. However, due to the many inherent drawbacks, there is a surge for new chemotherapeutic drugs. More specifically, the discovery of new drug candidates able to overcome severe side effects, the occurrence of resistance and the inefficacy toward metastatic tumours is highly desirable. Many classes of compounds have been investigated over the years in order to discover new targets and synergistic mechanisms of action including multicellular targets. In this work, we designed a new chemotherapeutic drug candidate against cancer, namely $[\text{Ru}(\text{DIP})_2(\text{sq})]\text{PF}_6$ (**Ru-sq**) (DIP = 4,7-diphenyl-1,10-phenanthroline; sq = semiquinonate ligand). The aim was to combine the great potential expressed by Ru(II) polypyridyl complexes and the singular redox and biological properties associated to the catecholate moiety. Experimental evidences (e.g. X-ray crystallography, electron paramagnetic resonance, electrochemistry) demonstrate that the semiquinonate is the preferred oxidation state of the dioxo ligand in this complex. The biological activity of **Ru-sq** was then scrutinised *in vitro* and *in vivo*, and the results highlight the auspicious potential of this complex as a chemotherapeutic agent against cancer. **Ru-sq** was notably found to have a much higher cytotoxic activity than cisplatin (i.e. in the nanomolar range), and, contrary to cisplatin, to have mitochondrial dysfunction as one of its modes of action. The multicellular targets of **Ru-sq** could potentially be the key to overcome one of the main drawbacks of cisplatin i.e. the occurrence of resistance. Moreover, **Ru-sq** exhibited impressive activity on Multi Cellular Tumour Spheroids (MCTS) model, even leading to growth inhibition of the tumour 13 days after treatment (20 μM). Importantly, using two different *in vivo* models, this compound was found to be well-tolerated by mice and has very promising activity.

Introduction

Over the last decades, the search for new chemotherapeutic agents against cancer has challenged scientists worldwide. Chemotherapy, together with surgery, radiotherapy and immunotherapy, is used in a combined modality therapy to treat cancer.¹ The goal of this combination is to overcome the drawbacks of each singular treatment to afford the best chances of survival for the patients.¹

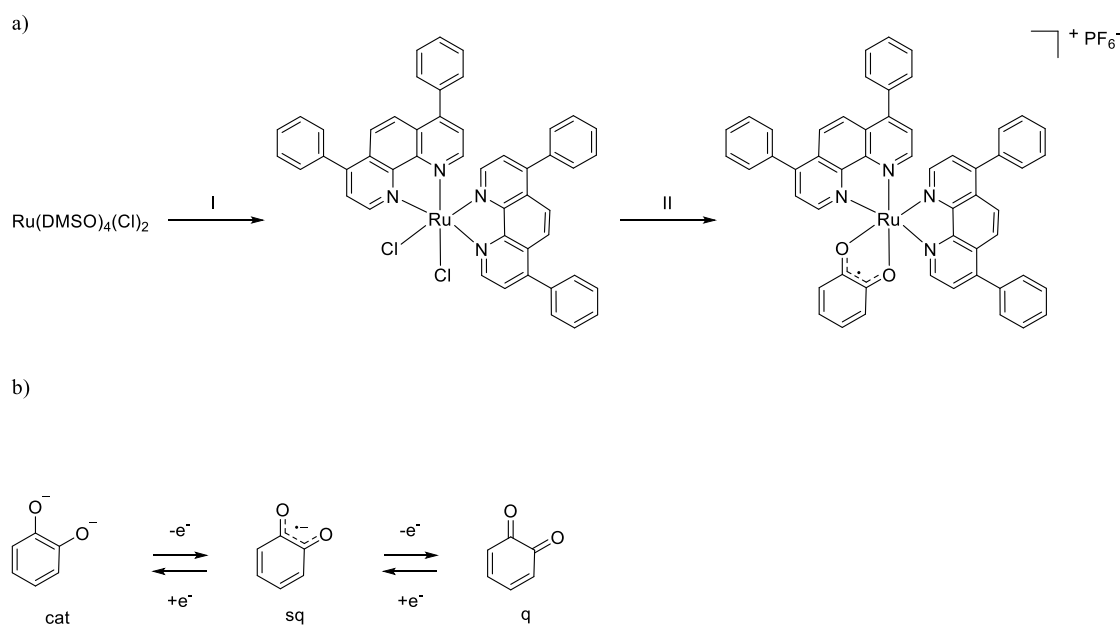
Cisplatin is one of the most common chemotherapeutic agents utilized against cancer. However, its severe side effects are limiting its clinical use.²⁻⁶ Therefore, many other platinum-based drug candidates have been investigated over the last 40 years leading to the worldwide clinical approval of carboplatin and oxaliplatin.^{7,8} On the basis of these ground-breaking discoveries and the observed occurrence of resistance with platinum treatment, a large number of metal complexes based on other metals than platinum have been examined.⁹⁻¹⁷ In this field, ruthenium complexes play a central role due to their inherent advantages (i.e. multiple stable oxidation states, unique properties during pre-clinical trials, etc.).¹⁸⁻²¹ KP-1019, IT-139 (formerly NKP-1339) and NAMI-A are, to date, the only three Ru complexes to have reached clinical trial as anticancer agents. Their mechanism of action involves ligand exchange, resembling therefore the one of cisplatin.²²⁻²⁷ Of note, TLD-1433, a substitutionally inert Ru(II) polypyridyl complex, has recently entered phase II clinical trial as a photosensitizer for photodynamic therapy (PDT).^{28,29} Ruthenium complexes find applications in different fields of medicinal chemistry against cancer, exploiting a large variety of mechanisms of action.³⁰⁻³⁵ A very promising class of ruthenium complexes are the coordinatively saturated and substitutionally inert ruthenium polypyridyl complexes. These compounds have been intensely investigated over the last years and several applications as potential chemotherapeutic agents have been unearthed.³⁰ At first, most of the bio-activity of these compounds was associated with interactions with DNA.³⁶⁻³⁹ However, over the years, many other modes of action were

identified, such as the trigger of mitochondrial dysfunction,^{40–42} Topoisomerases I and II inhibition,^{43,44} modification of cell membranes⁴⁵ and others.³⁰

Towards the discovery of a new class of compounds

Due to the great opportunities offered by this class of Ru compounds, in this work, we designed a new Ru polypyridyl complex, namely [Ru(DIP)₂(sq)](PF₆) (**Ru-sq**, Scheme 1a) where DIP is 4,7-diphenyl-1,10-phenanthroline and sq is a semiquinonate ligand, which was found to be a very interesting anticancer drug candidate. Semiquinonate is a so-called ‘non-innocent’ ligand as its electrochemical properties strongly resemble that of the metal center.⁴⁶ Semiquinonate is the oxidised form of catechol, a well-known dioxo ligand, which can exist in three redox forms, namely catecholate (cat), semiquinonate (sq) and quinone (q) (Scheme 1b).⁴⁷ Catecholate and its oxidation products have already been intensively investigated as ligands.^{48,49} However, the focus of these studies has mostly been on the unique electronic/redox properties of metal complexes containing such ‘non-innocent’ dioxo ligands.^{50–53} Catechols are also known as pan-assay interference compounds (PAINS) due to their redox and chelating properties.⁵⁴ Nevertheless, catecholate and its derivatives have also shown potential in different fields of biological interest,^{55–59} such as cancer chemoprevention,⁵⁷ antifungal activity⁵⁸ and the inhibition of the spontaneous A β fibril formation,⁵⁹ which is a key target for the treatment of Alzheimer’s disease. Worthy of note, vanadium compounds carrying catechol-like ligands have been investigated by Crans and co-workers.^{60,61} During these studies, particularly potent cytotoxic vanadium (V) catecholate complexes toward bone cancer cells were unveiled.⁶⁰ The cytotoxicity on glial cells of [Ru^{III}(NH₃)₄(catecholate)]⁺ was also investigated in 2007 by Almeida and co-workers.⁵⁶ In this case, the catechol was found to be more cytotoxic than the Ru(III) complex itself with an EC₅₀ of 0.342 mM against rat astrocytes and 0.568 mM against human glioblastoma GL-15 cell line, while the [Ru^{III}(NH₃)₄(catecholate)]⁺ complex had EC₅₀

= 1.380 mM and $EC_{50} = 2.6$ mM against rat astrocytes and human glioblastoma, respectively.⁵⁶ Further studies suggested that depletion of glutathione and induction of apoptosis were possible explanations for the cytotoxicity observed for catechol towards mouse neuroblastoma N2a cell line.⁵⁵ These preliminary studies rationalize our choice to integrate catechol and its oxidation products into a Ru(II) polypyridyl complex. To the best of our knowledge, $[Ru(DIP)_2(sq)](PF_6)$ is the first Ru(II) polypyridyl complex containing a catechol moiety to be deeply investigated from both a physico-chemical and biological point of view. The complex was isolated as a racemic mixture of Δ and Λ enantiomers. No effort was made in this work to isolate pure enantiomers. As described below, *in vitro* and *in vivo* studies demonstrate a significant potential of this compound as a chemotherapeutic agent against cancer.



Scheme 1. a) Synthesis of $[Ru(DIP)_2(sq)](PF_6)$. I) DIP, LiCl, DMF, reflux, 24 h, 78%; II) (i) NaOH, catechol 2-propanol, reflux, 24h; (ii) air, 2 h; (iii) NH_4PF_6 , 2-propanol/ H_2O (1:8), 19%. b) Catechol (cat) and its oxidised forms, semiquinonate (sq) and quinone (q).

Results and Discussion

Synthesis and characterization of $[Ru(DIP)_2(sq)](PF_6)$

The synthesis of the target compound **[Ru(DIP)₂(sq)](PF₆)** was achieved in a 2-step synthesis (Scheme 1a). Briefly, the known Ru(DMSO)₂Cl₂⁶², DIP and LiCl were refluxed in DMF to afford Ru(DIP)₂Cl₂ in 72% yield after precipitation with acetone.⁶³ The compound was then refluxed in a nitrogen atmosphere overnight with catechol in the presence of NaOH in 2-propanol. The oxidation step of the catecholate to the semiquinonate was performed by exposing the solution of the Ru complex in 2-propanol to air for 2 h. **[Ru(DIP)₂(sq)](PF₆)** was obtained in 19% yield after precipitation with a large excess of NH₄PF₆ and purification *via* silica gel chromatography. The identity of the product was confirmed by HR-MS and NMR spectroscopy. ¹H-NMR spectra showed a characteristic peak broadening in the aromatic region between 7–9 ppm due to the paramagnetism of the complex. In the ¹³C NMR and 2D ¹H-¹³C HSQC spectra (Figure S1) ten inequivalent CH carbons were observed. The purity of the product was confirmed by microanalysis.

X-ray Crystallography of [Ru(DIP)₂(sq)](Cl)

The crystal structure of **[Ru(DIP)₂(sq)](Cl)** was determined by a single crystal X-ray diffraction study. Suitable single crystals were grown from slow diffusion of diethylether into a solution of the product prior to precipitation with NH₄PF₆ in MeCN. The crystal structure revealed two independent Ru molecules (Ru-1 and Ru-2 in Figure S2), two chloride counter ions (from LiCl) and three water molecules in the asymmetric unit (monoclinic *P*2₁/*c* space group). Both Cl atoms are disordered over two sets of sites with site-occupancy ratios of 0.299/0.701(3) and 0.244/0.756(5). The H atoms of the isolated water molecules could be introduced in the final refinements, but their positions were kept fixed to satisfy reliable hydrogen bonding. The molecular structure of one of the independent Ru molecules is shown in Figure 1 and a selection of the most relevant bond lengths and angles are provided in Tables S1 and S2 (additional crystallographic information can be found in the supporting information). The X-ray crystal

structure determination also provided evidence for the oxidation state of the dioxolene ligand, as it can exist in three different oxidation states; catecholate, semiquinonate and quinone.^{47,51,64} The typical range for the C-O bond length of such a ligand coordinated to a metal is 1.34–1.47 Å for the catecholate form, 1.27–1.31 Å for the semiquinonate form and around 1.23 Å for the quinone.^{47,64} The C-O bond distances of the dioxo ligand in [Ru(DIP)₂(sq)](Cl) are 1.309(4), 1.314(4), 1.315(4) and 1.319(4) Å, which suggest that it is present in its semiquinonate form.⁴⁷

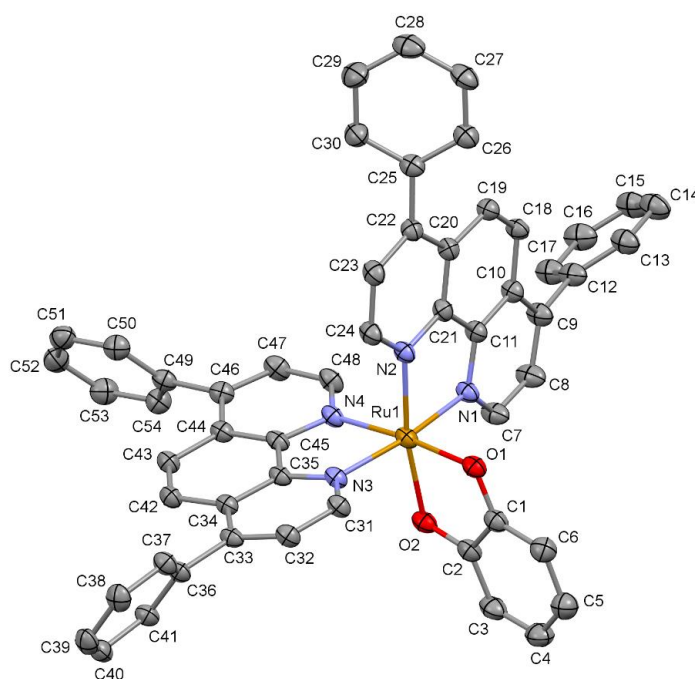


Figure 1. Molecular structure of [Ru(DIP)₂(sq)](Cl). The asymmetric unit contains two crystallographically independent Ru cations, only one of which is presented. The Cl⁻ counter ions, H atoms and solvent molecules are omitted for clarity. The thermal ellipsoids are shown at the 30% probability level.

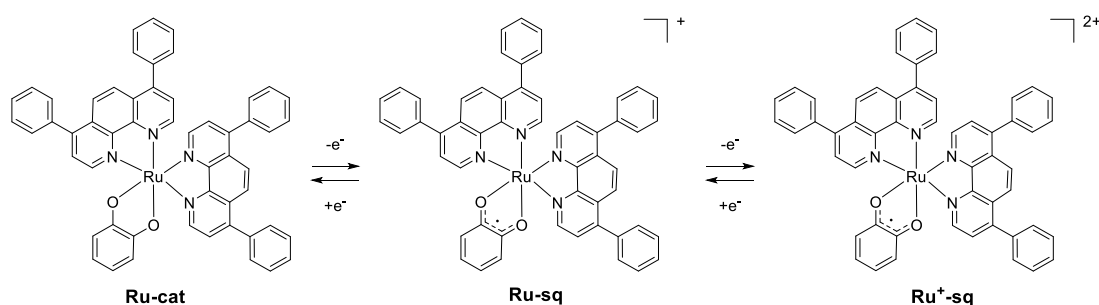
Electrochemistry

The electrochemistry of **[Ru(DIP)₂(sq)](PF₆)** (abbreviated as **Ru-sq**) was investigated using cyclic voltammetry (CV) and rotating disc electrode voltammetry (RDE) in DMF containing tetrabutylammonium hexafluorophosphate 0.1 M. The RDE voltammogram shown in Fig. S3 exhibits four well-defined, reversible waves, in addition to that of decamethylferrocene, which was used as internal reference with a half-wave potential of 0.030 V vs the Saturated Calomel Electrode (SCE). The four features related to the **Ru-sq** have the same intensity, which attests that the related redox processes involve the same number of exchanged electrons. By comparison with the data reported in the literature for closely related complexes under similar conditions,^{50,65,66} the underlying redox processes were assigned as shown in Table S3. The oxidation located at +0.647 V vs SCE can be attributed to the Ru(II)/Ru(III) redox couple while the sq/cat redox couple can be associated to the first reduction process at -0.249 V vs SCE. The following two processes, at more negative potentials, can be assigned to the sequential reductions of the ancillary ligands (DIP^{0/-}). Of note, the latter are separate couples with quite some substantial redox splitting.^{50,65} These data clearly show how the presence of the semiquinonate ligand influences the redox properties of the metal centre, causing a shift to lower potential. The couple of Ru (III)-quinone ligand is not observed in these conditions since they are possibly located outside the anodic limit of a DMF-based electrolyte. Moreover, the CV experiment (Figure S3) indicates the reversibility of the redox processes, at least on the voltammetric timescale.

Electron Paramagnetic Resonance

Ru-sq in its native state is Electron Paramagnetic Resonance (EPR) active in DCM due to the presence of an unpaired spin as already confirmed by X-ray crystallography (Figure S4a). At room temperature, a rather broad isotropic signal was observed. Its *g*-value of 2.0244 is in line with a ligand-centred spin density and deviates only slightly from the free electron value *g_e* of

2.0023. This behaviour is in strong contrast to a metal-centred spin of a Ru(III) complex, which would only become observable at low temperatures due to rapid relaxation and display a broad, axial or rhombic signal with large anisotropy.^{51,67} The reduced form **Ru-cat** (Scheme 2) was generated by the reaction of **Ru-sq** with equimolar amounts of cobaltocene (Cp₂Co, $E_{1/2} = -0.880$ V vs SCE in DMF/0.1 M NBu₄PF₆) (Figure S4b).⁶⁸ Owing to the presence of a low-spin Ru(II) ion and a closed-shell catecholate ligand this species is EPR silent. The same holds also true for oxidized, dicationic **Ru⁺-sq** (Scheme 2), which was prepared by treatment of **Ru-sq** with an excess of 1,1'-diacetylferrocenium hexafluoroantimonate (Ac₂FcSbF₆, $E_{1/2} = 0.940$ V vs SCE in DMF/0.1 M NBu₄PF₆) (Figure S4c).^{68,69} The absence of an EPR signal indicates that the unpaired spins at the Ru(III) ion (**Ru⁺**) and the sq ligand are antiferromagnetically coupled.



Scheme 2. Structures of **Ru-cat**, **Ru-sq**, and **Ru⁺-sq**, carrying a catecholate or a semiquinonate ligand and Ru in oxidation state +II (**Ru**) or +III (**Ru⁺**), respectively.

Stability in DMSO and human plasma

The stability of a compound plays an important role in its biological activity and viability. Therefore, the integrity of **Ru-sq** was first assessed in DMSO-d₆ using ¹H NMR spectroscopy. **Ru-sq** was found to be stable in DMSO over 8 days. No change in the NMR spectra of the complex was observed over 8 days (Figure S5). Next, to obtain a preliminary insight into the behaviour of **Ru-sq** under physiological conditions, the stability of **Ru-sq** in human plasma

was investigated by UPLC following a procedure already established by our group.⁴¹ **Ru-sq** was incubated in human plasma at 37°C for 0 h, 4 h, 6 h, 12 h, 20 h and 24 h using diazepam as an internal standard. The UV traces of the UPLC analysis are shown in Figure S6a. The concentration of **Ru-sq** was normalized with respect to the internal standard and plotted against time. The linear trend shown in Figure S6b clearly demonstrates that between 6 and 20 h, a decomposition of 50% of the compound was observed, to reach a total degradation of the compound after 24 h.

Cytotoxicity Studies

After a full characterisation of **Ru-sq**, its potential activity as a chemotherapeutic agent was investigated starting from the biological evaluation of its behaviour against cancer cells in monolayer cell cultures. The cytotoxicity of **Ru-sq** towards HeLa (human cervical adenocarcinoma) cell line, A2780 (human ovarian carcinoma), A2780 cis (human cisplatin resistant ovarian carcinoma), A2780 ADR (human doxorubicin resistant ovarian carcinoma), CT-26 (mouse colon adenocarcinoma), CT-26 LUC (mouse colon adenocarcinoma stably expressing luciferase), RPE-1 (human normal retina pigmented epithelial) and MRC-5 (human normal lung fibroblast) cell lines was therefore investigated using a fluorometric cell viability assay (single graphs available in Figures S7).⁷⁰ Cytotoxicity of cisplatin and doxorubicin was determined in the same cell lines as positive controls and, as additional controls, **Ru(DIP)₂Cl₂** and catechol were also tested.^{71,72} As shown in Table 1 where IC₅₀ (the half maximal inhibitory concentration) values are reported, **Ru-sq** displayed IC₅₀ values between the high nanomolar and low micromolar range on the cell lines investigated in this study, while the **Ru(DIP)₂Cl₂** precursor and the catechol ligand itself showed much lower cytotoxicity. Very impressively, **Ru-sq** exerted an activity 40 times higher than cisplatin against a cisplatin resistant cell line. On the other hand, the cytotoxicity of doxorubicin and **Ru-sq** against a doxorubicin resistant

cell line appeared to be in the same order of magnitude. Overall, complex **Ru-sq** displays a cytotoxicity, which is comparable to doxorubicin and much higher than the one of cisplatin.

Table 1. IC₅₀ values of **Ru-sq**, the **Ru(DIP)₂Cl₂** precursor and the catechol ligand in tested cell lines; cisplatin and doxorubicin were used as positive controls.

IC ₅₀ (μM)	HeLa	A2780	A2780 ADR	A2780 cis	CT-26	CT-26 LUC	RPE-1	MRC-5
Cisplatin	9.28 ± 0.20	4.00 ± 0.76	8.32 ± 0.71	18.33 ± 2.92	2.60 ± 0.18	2.42 ± 0.23	30.24 ± 5.11	11.20 ± 2.32
Doxorubicin	0.34 ± 0.02	0.19 ± 0.03	5.94 ± 0.58	0.54 ± 0.04	0.082 ± 0.003	0.18 ± 0.006	0.89 ± 0.17	3.37 ± 1.24
Ru-sq	0.50 ± 0.01	0.67 ± 0.04	4.13 ± 0.2	0.45 ± 0.03	1.00 ± 0.03	1.51 ± 0.14	0.90 ± 0.04	0.95 ± 0.09
Ru(DIP)₂Cl₂	15.03 ± 0.4	4.69 ± 0.14	78.27 ± 4.9	6.36 ± 0.57	9.20 ± 1.22	6.65 ± 0.5	3.13 ± 0.07	5.54 ± 0.39
Catechol	>100	22.80 ± 5.96	>100	54.55 ± 11.30	16 ± 4.14	11.56 ± 0.40	>100	>100

Since **Ru-sq** exhibits promising activity in monolayer cell culture, we investigated its behaviour in a Multi Cellular Tumour Spheroids (MCTS) model.⁷³ It was previously shown that such a model mimics the *in vivo* microenvironment and tumour metabolism.^{74,75} Moreover, large MCTS develop a central necrosis core similar to that found in the inner core of tumours.⁷⁶ These unique features give a better representation of a cancer model compared to a 2D model, lowering the disparity between *in vitro* and *in vivo* models.⁷⁶ Table 2 shows the IC₅₀ values obtained *via* a luminescent cell viability assay for compounds that were administered to HeLa MCTS for 48 h (single graphs are available in Figure S8). The **Ru(DIP)₂Cl₂** precursor and the catechol ligand were tested as additional controls and exhibited lower cytotoxicity than **Ru-sq**. Catechol resulted nontoxic with an IC₅₀ > 100 μM while the precursor displayed a cytotoxicity comparable to cisplatin. Cisplatin was used as a positive control and the results are in line with literature data.⁷⁷ The cytotoxicity of **Ru-sq** in HeLa MCTS was impressively high after 48 h

treatment, with $IC_{50} \sim 14 \mu\text{M}$, which is 3 times lower than cisplatin or doxorubicin ($IC_{50} \sim 47 \mu\text{M}$ or $39 \mu\text{M}$, respectively). Noteworthy, the cytotoxicity of **Ru-sq** was comparable to the one of doxorubicin after 72 h treatment ($IC_{50} \sim 11 \mu\text{M}$).⁷⁸ These studies clearly demonstrate the high potential of **Ru-sq** as an anticancer drug candidate. The impressive bioactivity, comparable to doxorubicin in monolayer cell culture, was also confirmed in the 3D tumour model – HeLa MCTS.

Table 2. IC_{50} values for **Ru-sq**, **Ru(DIP)₂Cl₂** precursor and the catechol ligand in multicellular HeLa cancer cell spheroids (approximately 400 μm in diameter); cisplatin and doxorubicin were used as positive controls.

IC_{50} (μM)	Cisplatin	Doxorubicin	Ru-sq	Ru(DIP) ₂ Cl ₂	Catechol
HeLa MCTS	46.49 \pm 4.18	38.59 \pm 0.43	14.11 \pm 0.09	59.84 \pm 3.05	>100

Spheroid integrity and growth upon treatment are very useful tools to determine a potential drug activity.⁷⁶ In this study MCTS were monitored over 13 days after treatment with different concentrations of **Ru-sq** (Figure 2). Every 3 days, the spheroids were washed to remove dead cells and their diameters were measured (Figure 2). It is important to note that at each washing step, half of the media was removed and replaced with fresh one, diluting twice the quantity of the compound in each well. The effect of **Ru-sq** on growth inhibition is dose-dependent and already visible after 3 days. Low concentrations treatments (1 μM and 2.5 μM) led to regrowth of the spheroids after the first 72 h, while for 5 μM and 10 μM treatments, the regrowth is visible after 6 and 9 days, respectively. **Ru-sq** treatment with concentrations higher than IC_{50} (20 μM and 25 μM) completely inhibits the spheroids growth after 13 days of treatment. Overall, we can conclude that **Ru-sq** treatment at 20 μM and 25 μM concentrations, severely affect the size and the integrity of the spheroids after 13 days of treatment.

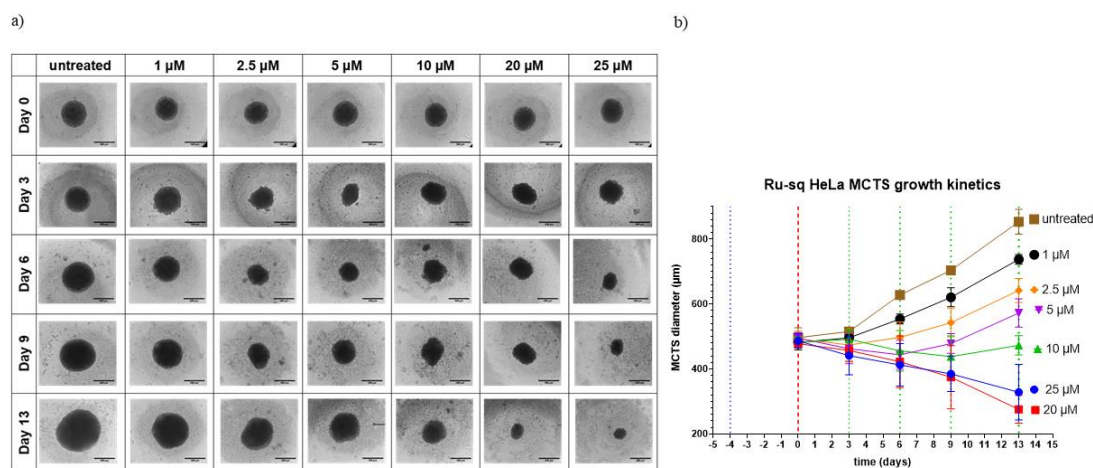


Figure 2. Growth kinetics of HeLa MCTS upon treatment with different concentrations of **Ru-sq** (1, 2.5, 5, 10 and 20 μM). a) Images collected at day 0 (before treatment) and at day 3, 6, 9 and 13. b) MCTS diameter calculated at different time points. Blue dotted line indicates day of seeding, red dashed line indicates day of treatment, green dotted lines indicate days of washing.

Cell Death Mechanism

The excellent activity displayed by **Ru-sq** in HeLa MCTS encouraged us to perform further experiments in order to obtain more insights into its *in vitro* behaviour. The first step was the evaluation of the type of cell death occurring when cancer cells were treated with **Ru-sq**. For this experiment, the Annexin V and PI staining method was used in HeLa cells.⁷⁹ Staurosporine, a known inducer of apoptosis, was employed as a positive control.⁸⁰ As shown in Figure 3 and Figure S9, **Ru-sq** induced significant apoptosis as early as 30 min treatment with progression from early to late apoptosis at 4 h. The level of apoptosis induction by the complex after 4 h was comparable to that caused by 24 h staurosporine treatment. These data clearly demonstrate that **Ru-sq** induces apoptosis as the only type of cell death in HeLa cells.

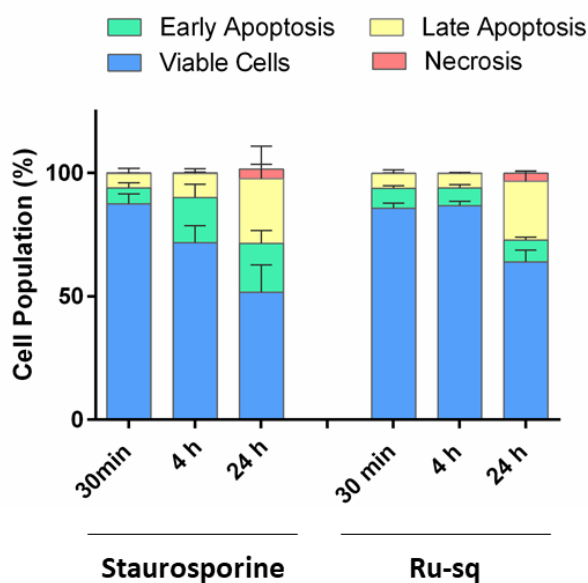


Figure 3. Induction of apoptosis/necrosis in HeLa cells upon treatment with **Ru-sq** (10 μM) and staurosporine (1 μM) at different time frames. The values are expressed as a mean \pm S.D. (standard deviation) of three biological repeats.

Cellular uptake, intracellular distribution and DNA metalation studies

Next, the cellular uptake of **Ru-sq** and cisplatin was investigated in HeLa cells. The amount of ruthenium accumulated was detected by Inductively Coupled Plasma Mass Spectrometry (ICP-MS). Working concentrations and incubation times were chosen to avoid extended cell mass loss due to the high cytotoxicity of the complexes but considering a ruthenium final amount that could afford determination of the metal content. After 2 h treatment (5 μM), **Ru-sq** internalises slightly better than the drug cisplatin (Figure 4a). The low accumulation of cisplatin in these working conditions is in agreement with the literature data.^{81,82} To have more insights about uptake mechanisms of **Ru-sq** into the HeLa cells, additional experiments were performed. Cells were pre-treated with different inhibitors of uptake pathways or kept at different temperatures to assess the energy dependence of the uptake mechanism(s) (Figure S10). More specifically, low temperature (4°C), pre-treatment with metabolic inhibitors (which decreases ATP production), pre-treatment with chloroquine or ammonium chloride (which

mostly impede endocytic pathways), or pre-treatment with tetraethylammonium chloride (mostly inhibiting cation transporters) decreased **Ru-sq** accumulation in cells by half when compared to 37 °C condition (see Figure S10). This outcome indicates that **Ru-sq** might be transported into the HeLa cells by both energy dependent (active) and energy independent (passive) pathways. Further cellular fractionation experiment showed preferential accumulation of **Ru-sq** inside the nucleus (Figure 4b). These findings suggest that the mode of action could be related to the damage caused to DNA and/or to prevention of replication as well as transcription.^{83,84} In order to identify DNA as a potential target for the complex, the genetic material was extracted from HeLa cells after 2 h treatment with **Ru-sq** or cisplatin and the amount of metal analysed by ICP-MS. The DNA of cells treated with **Ru-sq** displayed a metal content much higher when compared to cisplatin. Taken together, these findings strongly suggest direct interaction with DNA as a possible mechanism of action exerted by **Ru-sq**.

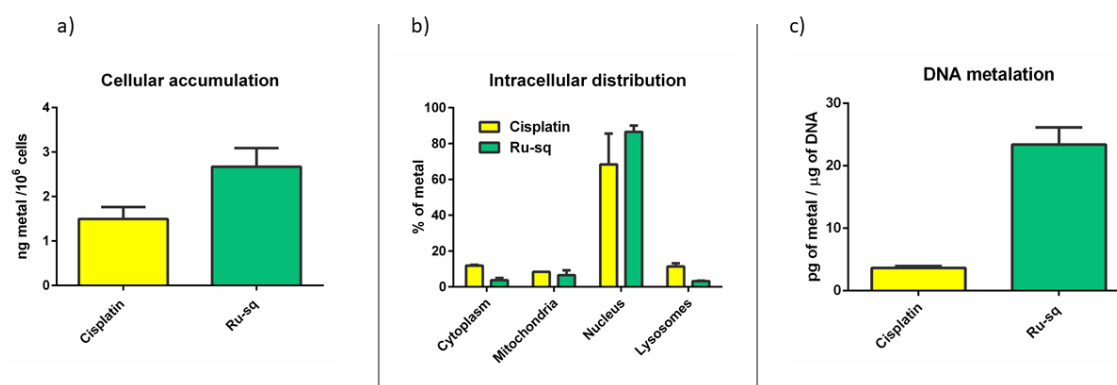


Figure 4. Cellular uptake (a), cellular fractionation (b) and DNA metalation (c) of HeLa cells after treatment with tested compounds (5 μM, 2 h). Data are presented as the mean ± SD of at least 3 technical replicates.

JC-1 Mitochondrial Membrane Potential Test and Metabolic Studies

The search for additional mechanisms of action associated to the treatment of **Ru-sq** led us to the investigation of the mitochondrial metabolism impairment.⁸⁵ Firstly, the mitochondrial membrane potential was studied with the use of a largely used indicator JC-1 (a membrane-permeant dye).^{86,87} At high potentials, the dye forms red emitting aggregates in the mitochondria membrane, whereas at low potentials, it stays as a green emitting monomer.^{86,87} The membrane potential is directly connected to oxidative phosphorylation (the main mitochondrial function).⁸⁸ HeLa cells were treated for 24 h with increasing concentrations of **Ru-sq** (from 0.2 μM to 0.6 μM). Figure 5a shows a slight decrease of the red fluorescence signal with increasing concentrations of **Ru-sq** and a significant drop in the signal around the IC_{50} concentration (0.5 μM , marked in red). However, the dramatic collapse of mitochondrial membrane potential could also be caused by ongoing apoptosis.⁸⁹ Carbonyl cyanide 4-(trifluoromethoxy)phenylhydrazone (FCCP), an uncoupling agent that impairs the membrane potential⁹⁰ was used as positive control.⁹⁰ Comparison of the results obtained with **Ru-sq** (0.5 μM) and FCCP treatment showed that the same loss in potential was detected. These findings strongly suggest a contribution of the membrane potential impairment to the cell death mechanism.

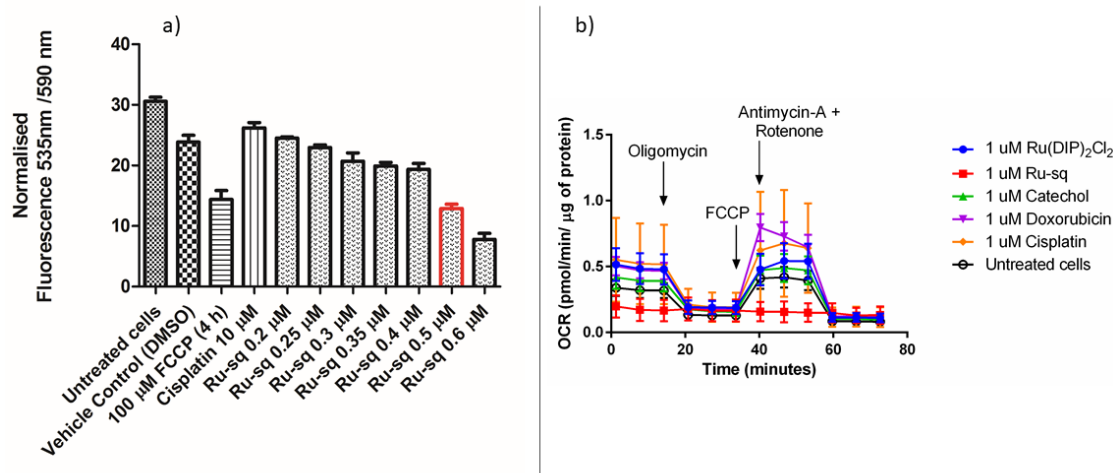


Figure 5. a) Fluorescence signal of JC-1 dye detected in HeLa cells treated for 24 h with different concentrations of **Ru-sq** (from 0.2 μM to 0.6 μM). Bar marked in red indicates the IC_{50} concentration (0.5 μM). FCCP is used as positive control, cisplatin and DMSO (1%) are used as negative controls. b) Mito Stress Test profile in HeLa cells after 24 h treatment; oxygen consumption rate changes after treatment with specific electron transport chain inhibitors. Oligomycin (inhibitor of ATP synthase (complex V)), FCCP (uncoupling agent), Antimycin-A (complex III inhibitor) and Rotenone (complex I inhibitor).

Inspired by these findings, further studies on the metabolic pathways that could be affected by the complex were performed. For this purpose, Seahorse XF Analyzer was used to measure, in real time, the oxygen consumption rate (OCR) and extracellular acidification rate (ECAR) of treated cells. Firstly, the effect of **Ru-sq** on the oxidative phosphorylation in the HeLa cell line was investigated. Mitochondrial respiration was found to be severely impaired in cells treated with **Ru-sq** as opposed to the precursor $\text{Ru}(\text{DIP})_2\text{Cl}_2$. This was evident from the low basal respiration and the inhibition of ATP production compared to untreated cells. The mitochondrial membrane of the cells treated with **Ru-sq**, lost the capacity to restore the proton balance when treated with an uncoupling agent (FCCP). The maximal respiration (the OCR value when the mitochondrial membrane is uncoupled) and spare respiratory capacity

(difference in the OCR values between maximal respiration and basal respiration) of the cells was reduced compared to untreated cells (Figure 5b and Figure S11). The combination of these effects suggests disrupted mitochondrial respiration in cervical cancer cells caused by **Ru-sq**. The effect on glycolysis and the possible metabolic modulation of the three primary fuel pathways (involving glucose, glutamine or fatty acids as substrates) were then examined. In contrast to what was observed for the mitochondrial respiration, the cell glycolysis, which is a cytosolic process, was not affected by **Ru-sq** (Figure S12). Additionally, due to the very low oxygen consumption rate in cells treated with **Ru-sq**, a direct effect on the 3-primary fuel pathways could not be determined (Figure S13). Overall, metabolic studies showed that the accumulation of **Ru-sq** in mitochondria has a significant role in the impairment of oxidative phosphorylation. This effect, together with the results obtained by the JC-1 staining, strongly suggests mitochondrial dysfunction as one of the modes of action of **Ru-sq**. In contrast, the chemotherapeutic drug cisplatin showed no significant effect on the mitochondrial metabolism of HeLa cells. This data suggests fundamental differences between the mode of action of **Ru-sq** and cisplatin. The latter covalently binds to the nuclear DNA and inhibits the replication process. It is widely known that DNA crosslinks can be repaired by different mechanisms such as the nucleotide excision repair (NER) that eventually leads to drug resistance in cancer cells. **Ru-sq**, with its multiple cellular targets, could potentially evade these repair pathways and circumvent such drawbacks associated with cisplatin.

***In vivo* efficacy studies**

It is very difficult to evaluate selectivity of the anticancer drugs *in vitro*, as the proliferation of non-malignant cells is greatly affected by non-physiological conditions of cell culture in 2D and 3D models. The promising results obtained in studies conducted *in vitro* justified the assessment of **Ru-sq** efficacy in the context of whole organism. To this end, we performed *in*

in vivo studies to evaluate the effect on both tumour growth and survival of tumour-bearing mice. The doses were selected according to the dose-finding study, which had revealed a maximum tolerated dose (MTD) of 15 mg/kg of body weight. Two distinct models for testing *in vivo* efficacy of antitumor drugs are possible: a syngeneic (mice) tumour growing in a naturally immunocompetent mouse, or human tumour cells growing in immunodeficient animals. As both approaches have its advantages and pitfalls, we decided to use both models in this study.

Effect of Ru-sq on the growth of Ehrlich mammary carcinoma in immunocompetent NMRI mice and survival of tumour bearing mice

Even though the use of syngeneic tumour allografts in naturally immunocompetent animals had been often considered inferior during the era of athymic mice models, this method made a comeback as the necessity of diversified, near-physiological experimental sets was recognised. In this model, we can observe the effect of the tested compound within the context of the genuine immune system that plays a key role in tumour resistance.⁹¹

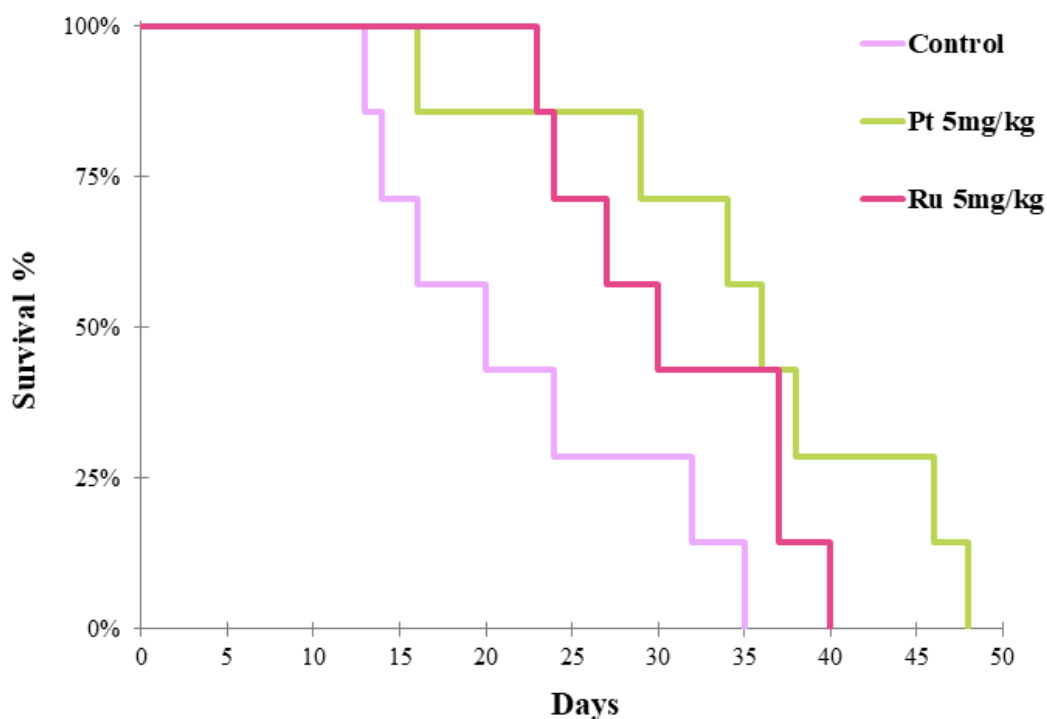


Figure 6. Kaplan-Meier analysis of survival of immunocompetent NMRI mice bearing Ehrlich carcinoma. Only the administration of complex **Ru-sq** 5 mg/kg i.p. and that of cisplatin (5 mg/kg) significantly prolonged the survival of tumour bearing mice when compared with the mixture of co-solvent and water. The compounds were administered i.p. on days 1 and 7 after tumour inoculation, n = 7 in each group.

During the study of the effect on the survival of immunocompetent NMRI mice bearing Ehrlich carcinoma (Figure 6), it was observed that the geometric mean of the overall survival of tumour bearing mice without therapy was 20.6 days. Among the three doses of **Ru-sq** tested, only 5 mg/kg prolonged the survival time significantly when compared with untreated tumour-bearing control mice (geom. mean = 31.9 days, $P = 0.033$). 10 mg and 15 mg/kg of **Ru-sq** seemed to exceed the optimal dose, causing a non-significant prolongation of survival ($P > 0.05$), with the geometric means of 30.2 and 25.5 days, respectively. The explanation may be a subclinical toxic effect that negatively affects immune surveillance as well as other body functions

necessary for the natural cancer defence. Although the optimal intracellular cancer-suppressing concentration may correspond to higher doses, subtle systemic toxicity does not allow to develop the desirable effect in vivo. The positive control cisplatin appeared to have similar efficacy (geom. mean = 33.7 days, P 0.014). An interesting and rare phenomenon was observed in all three groups of **Ru-sq**. Although the tumour was advanced in the later stage of the experiment, all mice treated with **Ru-sq** showed active behaviour, little cachexia and unsuppressed food consumption.

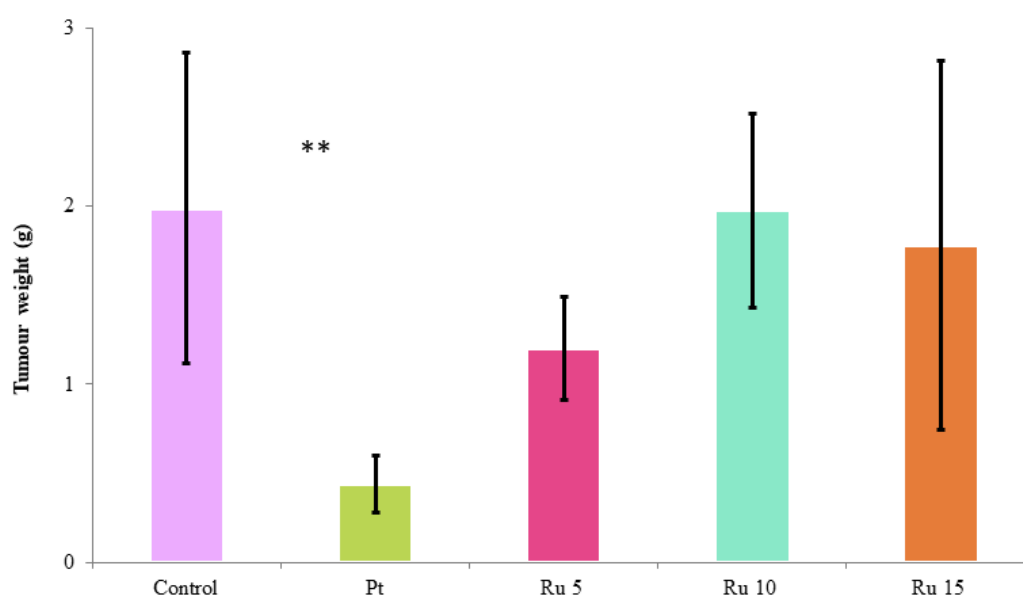


Figure 7. The weight of the solid Ehrlich tumour (in grams) on day 10 of mice injected on days 1 and 7 i.p. with pure vehicle, **Ru-sq** or cisplatin. Values are the means \pm SEM ($n = 7$ in each group). Control – tumour-bearing control treated with mixture of co-solvent and water; Pt – cisplatin 5 mg/kg i.p.; Ru 5 – **Ru-sq** 5 mg/kg i.p.; Ru 10 – **Ru-sq** 10 mg/kg i.p.; Ru 15 – **Ru-sq** 15 mg/kg i.p. Significantly different from the controls (** $P < 0.01$).

Furthermore, the effect of **Ru-sq** on tumour growth was examined. Figure 7 shows the weight of tumours at day 10 in mice treated with mixture of co-solvent and water, **Ru-sq** at 5, 10 or 15 mg/kg, or cisplatin at 5 mg/kg, and documents differences in the effect of the used drugs.

Although only cisplatin exhibited a significant inhibitory effect on tumour growth ($P = 0.0011$), there was a slight but insignificant suppression at 5 mg/kg **Ru-sq** ($P = 0.108$). As in the survival study, also here the optimum dose of **Ru-sq** seems to be in the lower part of the range tested.

Effect of Ru-sq on the growth of A2780 human ovarian cancer in immunodeficient nude mice and survival of tumour bearing mice

To compare the efficacy of the drug, therapeutic and survival experiment was repeated with athymic nude mice and human cancer line. A2780 human ovarian cancer cell line was chosen because of the use of cisplatin as comparative drug. Cisplatin is usually used for the therapy of ovarian cancer. Unfortunately, resistance often arises in treated patients. The use of human tumour xenografts in immunodeficient mice to examine therapeutic effect of potential chemotherapeutics, has several advantages. The major one is the use of actual human tumour tissue, featuring the complexity of genetic and epigenetic abnormalities that exist in the human tumour cell population.^{92,93} We evaluated the growth of A2780 human ovarian cancer cells in immunodeficient nude mice and their survival. Figure 8 shows the survival of animals; the longest average day of death is surprisingly associated to the negative control (42.88 ± 16.97 days). However, there was one surviving mouse in the group treated with **Ru-sq** 10 mg/kg and in the group treated with cisplatin. Two surviving mice were found in the group treated with higher dose of **Ru-sq** (15 mg/kg). Very interestingly, one of them was completely cured with no observable tumour.

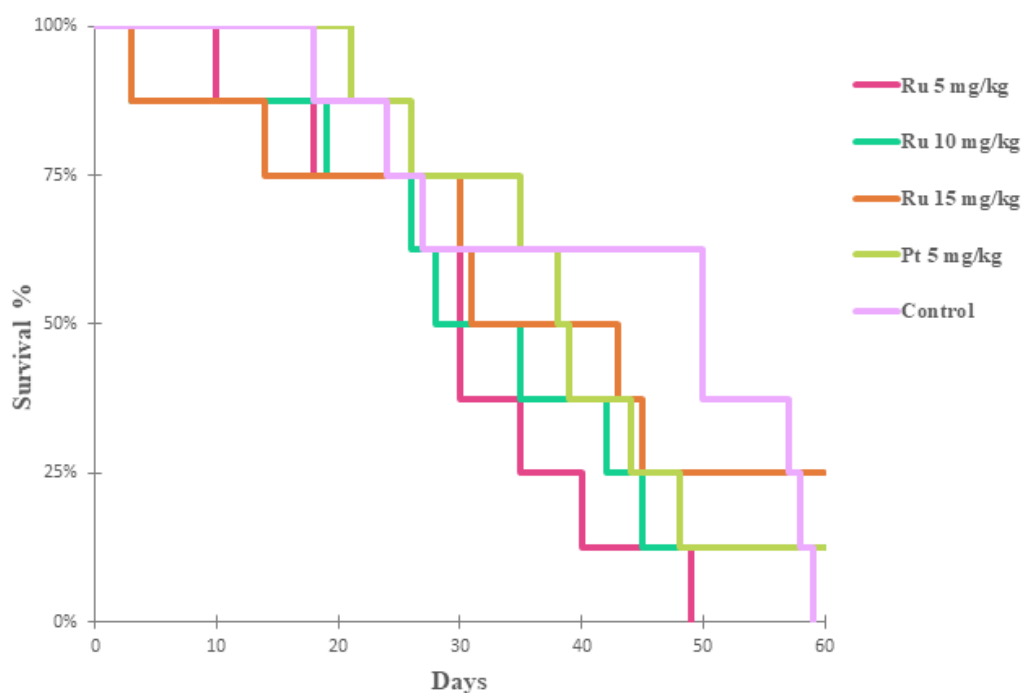


Figure 8. Kaplan-Meier analysis of survival of immunodeficient nude mice bearing A2780 human ovarian cancer. The treatment of Ru 15 mg/Kg led to a completely cancer free mouse. The compounds were administered i.p. on days 1 and 7 after the tumour reached 5 – 8 mm in size, n = 8 in each group.

Looking at the effect of **Ru-sq** on tumour growth (Figure 9), we observed that during the first days of therapy (day 4), there is a significant difference between groups treated with **Ru-sq** 15 mg/kg and cisplatin ($P = 0.00675$). Similar results between these two groups were observed at days 11 and 15 ($P = 0,04246$ for day 11 and $P = 0,0262$ for day 15). Comparison with untreated control group showed significant differences at days 11 and 15 ($P = 0.024$ for day 11; $P = 0.00931$ for day 15). **Ru-sq** administered in the dose of 15 mg/kg also showed decrease in tumour size over 15 days. Very interestingly, one mouse of this group was completely cured, no tumour volume was observed on the day 36 until the end of the experiment (day 60, data not shown). The longer survival of untreated mice observed on the nude model could be rationalised considering the higher sensitivity of immunocompromised animals to any kind of treatment. In

addition, the intraperitoneal administration of the compound itself was found not ideal because of solubility reasons, which could have led to toxic peritonitis and eventually death.

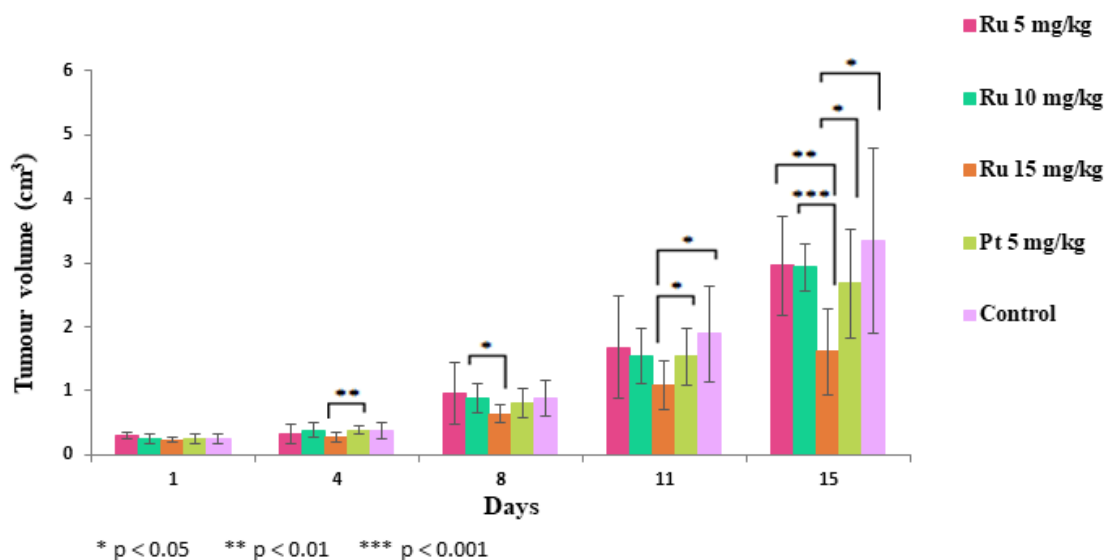


Figure 9. Tumour growth of A2780 cancer line in nude mice in first 15 days of therapy. Tumour size is shown as volume in cm^3 . Control – tumour-bearing control treated with mixture of co-solvent and water; Pt – cisplatin 5 mg/kg i.p.; Ru 5 – **Ru-sq** 5 mg/kg i.p.; Ru 10 – **Ru-sq** 10 mg/kg i.p.; Ru 15 – **Ru-sq** 15 mg/kg i.p. The most significant slowing down of tumour growth is observable in the group with **Ru-sq** 15 mg/kg.

These data demonstrate that the group treated with **Ru-sq** 15 mg/kg experienced a healing effect (in some points better than cisplatin), warranting further research. **Ru-sq** in a dose of 15 mg/kg has shown great potential to be an alternative and better drug candidate than cisplatin.

Taken together, we might conclude that in both models used **Ru-sq** reduces the growth of tumour cells and prolongs tumour-bearing mice survival, although the optimal dose would be different depending on strain of the mice and tumour type.

Akt-1 protein levels in HeLa cells

The interesting results obtained during the *in vivo* studies led us to further investigate the influence of **Ru-sq** on cell proliferation and/or migration. Akt is a serine/threonine kinase that promotes cellular survival.⁹⁴ Three isoforms of this protein exist in mammalian cells: Akt-1, Akt-2 and Akt-3.⁹⁵ Despite their high sequence similarity, they exhibit unique functions.⁹⁶ Akt-1 was found to be involved in the regulation of cell proliferation, transformation and tumour metastasis.⁹⁶ In this study, we assessed the influence of different concentrations of **Ru-sq** on total Akt-1 protein levels in HeLa cells. As shown in Figures 12a and 12b, the treatment with the complex at concentrations lower than the IC_{50} does not change the total Akt-1 protein levels. A similar effect is observed upon treatment with cisplatin and doxorubicin at their IC_{50} concentrations (IC_{50} = 10 and 0.3 μ M, respectively for cisplatin and doxorubicin). On the other hand, Akt-1 protein levels are significantly decreasing when HeLa cells were treated with **Ru-sq** at IC_{50} concentration (0.5 μ M) and higher. It is important to note that GAPDH protein levels (loading control) are also changing at these concentrations, probably indicating ongoing cell death. Although **Ru-sq** complex does not change the total amount of the Akt-1 protein levels, we cannot exclude its impact on the amount of active form of this protein. It is known that Akt-1 needs to be phosphorylated for its activity⁹⁷ and hyper activation of this protein is frequently found in human cancers.⁹⁸ Further studies will be needed to fully understand the influence of our compound on cell proliferation and/or migration.

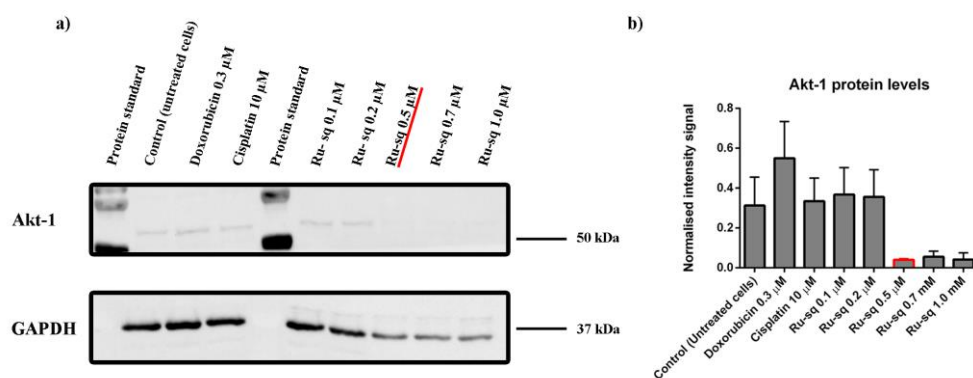


Figure 10. (a) Western blot analysis of Akt-1 protein levels in HeLa cell line after 24 h treatment with different concentrations of **Ru-sq**. Cisplatin, doxorubicin and untreated cells were used as controls. The positions of the nearest molecular weight markers are indicated. (b) Akt-1 protein levels normalised to GAPDH signal. Data is presented as the mean \pm SD of at least 3 independent experiments. The IC₅₀ concentration of the complex is marked in red.

Conclusions

Ru-sq was successfully synthesised and fully characterised. Crystal structure, electrochemical and EPR studies confirmed the oxidation state of the dioxo ligand (semiquinonate), which led to an overall positive charge of the complex. **Ru-sq** was found to be stable at room temperature in DMSO solution over one week and to have a half-life of 12 h upon incubation in human plasma at 37 °C. Cytotoxicity studies were performed in both, cellular monolayer (2D) and Multi Cellular Tumour Spheroids (MCTS) (3D) models. The cytotoxicity in the 2D model was tested against different cell lines showing higher activity than cisplatin with IC₅₀ values mostly in the nanomolar range. The cytotoxicity in HeLa MCTS confirmed the higher activity compared to cisplatin. Great tumour growth inhibition was observed after treatment with **Ru-sq** at 20 μM and 25 μM. Deeper investigation revealed apoptosis as the main cause of cell death. **Ru-sq** was found to be taken up by HeLa cells more efficiently than cisplatin and to accumulate preferentially in nucleus. DNA ruthenation studies suggest that **Ru-sq** might damage the DNA and/or prevent replication as well as transcription processes. Mitochondrial function upon **Ru-**

sq treatment was also studied using an indicator of the mitochondrial membrane potential (JC-1) and mitostress test (Seahorse technology). From these studies, a severe impairment of the mitochondrial potential was observed suggesting mitochondrial dysfunction contributes to the mode of action of **Ru-sq**. *In vivo* studies were performed using two different models: a syngeneic tumour growing in a naturally immunocompetent mouse, or human tumour cells growing in immunodeficient animals. **Ru-sq** reduces the growth of tumour cells and prolongs the survival of tumour-bearing mice. However, the optimal dose would be different depending on strain of the mouse and tumour type. In addition, during this study, especially in the case of the nude animals, the intraperitoneal administration was found to be not ideal because of solubility reasons, which probably lead to some toxicity and eventually death. Worth of note, the patent application for this compound was filed (Eur. Pat. Appl. (2019), EP19305668.6). Further studies are ongoing toward a different formulation of the compound prior administration.

Overall, **Ru-sq** displayed better activity than cisplatin in 2D and 3D cell cultures as well as for some conditions used *in vivo*. In conclusion, in this work, combining the well-known anticancer activity of Ru(II) polypyridyl complexes and the unique properties of the non-innocent ligand semiquinonate, we discovered a remarkable complex, **Ru-sq**, with promising potential as a chemotherapeutic agent against cancer. We strongly believe that further studies might lead our compound to advance towards pre-clinical trials. These findings might represent an inspiration for the scientific community involved in the search for new chemotherapeutic agents.

Experimental Section

Materials.

All chemicals were either of reagent or analytical grade and used as purchased from commercial sources without additional purification. Ruthenium trichloride hydrate was provided by I²CNS, 4,7-Diphenyl-1,10-phenanthroline, Lithium chloride (anhydrous, 99%), and catechol by Alfa Aesar, tetrabutylammonium hexafluorophosphate by Sigma-Aldrich. All solvents were purchased of analytical, or HPLC grade. When necessary, solvents were degassed by purging with dry, oxygen-free nitrogen for at least 30 min before use.

Instrumentation and methods.

Amber glass or clear glassware wrapped in tin foil were used when protection from the light was necessary. Schlenk glassware and a vacuum line were employed when reactions sensitive to moisture/oxygen had to be performed under nitrogen atmosphere. Thin layer chromatography (TLC) was performed using silica gel 60 F-254 (Merck) plates with detection of spots being achieved by exposure to UV light. Column chromatography was done using Silica gel 60-200 μm (VWR). Eluent mixtures are expressed as volume to volume (v/v) ratios. ^1H and ^{13}C NMR spectra were measured on Bruker Avance III HD 400 MHz or Bruker Avance Neo 500 MHz spectrometers using the signal of the deuterated solvent as an internal standard.⁹⁹ The chemical shifts δ are reported in ppm (parts per million) relative to tetramethylsilane (TMS) or signals from the residual protons of deuterated solvents. Coupling constants J are given in Hertz (Hz). The abbreviation for the peaks multiplicity is br (broad). ESI-HRMS experiments were carried out using a LTQ-Orbitrap XL from Thermo Scientific (Thermo Fisher Scientific, Courtaboeuf, France) and operated in positive ionization mode, with a spray voltage at 3.6 kV. Sheath and auxiliary gas were set at a flow rate of 5 and 0 arbitrary units (a.u.), respectively.

Applied voltages were 40 and 100 V for the ion transfer capillary and the tube lens, respectively. The ion transfer capillary was held at 275°C. Detection was achieved in the Orbitrap with a resolution set to 100,000 (at m/z 400) and a m/z range between 200-2000 in profile mode. Spectrum was analysed using the acquisition software XCalibur 2.1 (Thermo Fisher Scientific, Courtaboeuf, France). The automatic gain control (AGC) allowed accumulation of up to 2.105 ions for FTMS scans, Maximum injection time was set to 300 ms and 1 μ scan was acquired. 5 μ L was injected using a Thermo Finnigan Surveyor HPLC system (Thermo Fisher Scientific, Courtaboeuf, France) with a continuous infusion of methanol at 100 μ L.min⁻¹. Elemental analysis was performed at Science Centre, London Metropolitan University using Thermo Fisher (Carlo Erba) Flash 2000 Elemental Analyser, configured for %CHN. IR spectra were recorded with SpectrumTwo FTIR Spectrometer (Perkin–Elmer) equipped with a Specac Golden Gate™ ATR (attenuated total reflection) accessory; applied as neat samples; $1/\lambda$ in cm⁻¹. Analytical HPLC measurement was performed using the following system: 2 x Agilent G1361 1260 Prep Pump system with Agilent G7115A 1260 DAD WR Detector equipped with an Agilent Pursuit XRs 5C18 (100Å, C18 5 μ m 250 x 4.6 mm) Column and an Agilent G1364B 1260-FC fraction collector. The solvents (HPLC grade) were millipore water (0.1% TFA, solvent A) and acetonitrile (0.1% TFA, solvent B). The HPLC gradient used is the following: 0-3 minutes: isocratic 90% A (5% B); 3- 25 minutes: linear gradient from 90% A (5% B) to 0% A (100% B); 25-30 minutes: isocratic 0% A (100% B), 30-35 minutes: linear gradient from 0% A (100% B) to 95% A (5% B). The flow rate was 1 mL/min. Detection was performed at 215nm, 250nm, 350nm, 450nm, 550nm and 650nm with a slit of 4nm. Stability in human plasma was performed on HPLC (Acquity Ultra Performance LC, Waters) that was connected to a mass spectrometer (Bruker Esquire 6000) operated in ESI mode. The ACQUITY UPLC BEH C18 Gravity 1.7 μ m (2.1 \times 50 mm) reverse phase column was used with a flow rate of 0.6 ml/min and UV-absorption was measured at 275 nm. The runs were performed with a linear

gradient of A (acetonitrile (Sigma Aldrich HPLC-grade)) and B (distilled water containing 0.1% formic acid): $t = 0-0.25$ min, 95% A; $t = 1.5$ min, 100% A; $t = 2.5$ min, 100% A. Fractionation ICP-MS measurements were performed on an Agilent QQQ 8800 Triple quad ICP-MS spectrometer (Agilent Technologies) with a ASX200 autosampler (Agilent Technologies), equipped with standard nickel cones and a “micro-mist” quartz nebulizer fed with 0.3 ml/min analytic flow (as a 2% HNO₃ aqueous solution). Cellular Uptake, mechanism of uptake and ruthenation of the DNA was performed using a High-Resolution ICP-MS Element II from ThermoScientific located within the Environmental Biogeochemistry team of the Institut de Physique du Globe de Paris. This ICP-MS enables working in different resolution modes (LR=400, MR=4000 and HR=10000) for a better discrimination between elements of interest and interferences.¹⁰⁰

For the metabolic studies Seahorse XFe96 Analyser by Agilent Technologies was used.

Synthesis and characterization.

Ru(DMSO)₂Cl₂. Ru(DMSO)₂Cl₂ was synthesised following an adapted literature procedure.⁶² Spectroscopic data (¹H NMR) was in agreement with literature.⁶²

Ru(DIP)₂Cl₂. The complex was synthesised following an adapted literature procedure.⁶³ A mixture of Ru(DMSO)₂Cl₂ (3.0 g, 6.19 mmol), 4,7-diphenyl-1,10-phenanthroline (4.11 g, 12.38 mmol) and LiCl (2.0 g, 47.18 mmol) dissolved in DMF (100 mL) was refluxed for 24 h. After cooling to *r.t.*, the solvent was reduced *in vacuo* to 8 mL and 350 mL of acetone were added. The mixture was then stored at -20 °C overnight before filtration with a Buchner funnel and washed with Acetone and Et₂O to afford Ru(DIP)₂Cl₂ as a deep purple solid (3.76 g, 4.49 mmol, 72%). Spectroscopic data (¹H NMR) were in agreement with literature.⁶³

[Ru(DIP)₂(sq)](PF₆) (Ru-sq).

Ru(DIP)₂Cl₂ (0.739 g, 0.88 mmol) and aq. NaOH (0.5 mL, 1 M) were dissolved in 2-propanol (40 mL). The solution was degassed for 15 min and catechol (0.155 g, 1.41 mmol) was added. The mixture was heated to reflux for 24 h under N₂ atmosphere and protected from light. After cooling to *r.t.*, the mixture was stirred opened to air while still protected from light and the solvent was removed under vacuum. The residual solid was dissolved in 2-propanol (7 mL) and H₂O (56 mL) and NH₄PF₆ (0.700 g, 4.3 mmol) were added. The mixture was stored in the fridge (4 °C) overnight. The precipitate was filtered with a Buchner funnel and washed with H₂O (3 x 50 mL) and Et₂O (3 x 50 mL). The solid was collected with DCM and dried under vacuum to deliver a crude product as the PF₆ salt (0.70 g), which was chromatographed on silica (DCM/MeCN 20:1 *R_f* : 0.3). Evaporation of the solvent under vacuum provided [Ru(DIP)₂(sq)](PF₆) as a deep red solid. Further wash with Et₂O and Heptane were necessary in order to obtain clean product. The solid with the washing solvent (10 mL) was sonicated for 10 min and then centrifuged. This procedure was repeated three times for each solvent. Finally the red solid was collected with DCM and dried under vacuum to afford a clean product (0.17 g, 0.167 mmol, 19%). IR (Golden Gate, cm⁻¹): 3345w, 1710m, 1600w, 1520s, 1455s, 1335s, 1270s, 1125s, 820s, 760m. ¹H NMR (400 MHz, CD₂Cl₂): δ/ppm = 8.79–8.20 (br, 5H, *arom.*), 8.09–7.88 (br, 5H, *arom.*), 7.73–7.42 (br, 14H, *arom.*), 7.26–6.92 (br, 10H, *arom.*), 6.92 – 6.63 (br, 2H, *arom.*). ¹³C NMR (125 MHz, CD₂Cl₂): δ/ppm = 149.84, 144.68, 136.10, 133.56, 130.36, 129.89, 129.53, 128.41, 126.21, 125.36, 121.47, 116.35. For the quaternary carbons, only two were observed in the ¹³C NMR spectrum where five were expected. This could be explained by peak overlap or the signal being too weak to be detected within the acquisition time of the experiment which is common for quaternary carbons. HRMS (ESI⁺): *m/z* 874.1887 [M - PF₆]⁺. Elemental Analysis: calcd. for C₅₄H₃₆F₆N₄O₂PRu = C, 63.65; H, 3.56; N, 5.50. Found = C, 63.62; H, 3.52; N, 5.45. HPLC: T_R = 31.304 min.

X-ray Crystallography.

Single-crystal X-ray diffraction data were collected at 183(1) K on a Rigaku OD XtaLAB Synergy, Dualflex, Pilatus 200K diffractometer using a single wavelength X-ray source (Mo K α radiation: $\lambda = 0.71073 \text{ \AA}$)¹⁰¹ from a micro-focus sealed X-ray tube and an Oxford liquid-nitrogen Cryostream cooler. The selected suitable single crystal was mounted using polybutene oil on a flexible loop fixed on a goniometer head and transferred to the diffractometer. Pre-experiment, data collection, data reduction and analytical absorption correction¹⁰² were performed with the program suite *CrysAlisPro*.¹⁰³ Using *Olex2*,¹⁰⁴ the structure was solved with the *SHELXT*¹⁰⁵ small molecule structure solution program and refined with the *SHELXL* program package¹⁰⁶ (version 2018/3) by full-matrix least-squares minimization on F². *PLATON*¹⁰⁷ was used to check the result of the X-ray analysis.

Electrochemical Measurements.

The electrochemical experiments were carried out with a conventional three-electrodes cell (solution volume of 15 mL) and a PC-controlled potentiostat/galvanostat (Princeton Applied Research Inc. model 263A). The working electrode was a vitreous carbon electrode from Orignalys (France) exposing a geometrical area of 0.071 cm² and mounted in Teflon[®]. The electrode was polished before each experiment with 3 and 0.3 μm alumina pastes followed by extensive rinsing with ultra-pure Milli-Q water. Platinum wire was used as counter electrode and saturated calomel electrode, SCE, as reference electrode. Electrolytic solutions, DMF containing tetrabutylammonium hexafluorofosphate 0.1M (TBAPF₆, Aldrich, +99 %) as supporting electrolyte, were routinely deoxygenated by argon bubbling. All the potential values are given versus the calomel saturated electrode SCE and recalculated versus Me₁₀Fc^{0/+} potential value.

EPR.

Electron paramagnetic resonance (EPR) experiments were performed on a MiniScope MS400 table-top X-band spectrometer from Magnettech. Simulation of the experimental EPR spectra was performed with the MATLAB EasySpin program.¹⁰⁸ All samples were dissolved in dry and N₂-saturated DCM at a concentration of ca. 1 mM. Oxidized forms were generated using 1,1'-diacetylferrocenium hexafluoroantimonate (Ac₂FcSbF₆, $E_{1/2} = 0.940$ V vs SCE in DMF/0.1 M NBu₄PF₆).^{68,69} Chemical reduction was achieved by using cobaltocene (Cp₂Co, $E_{1/2} = -0.880$ V vs SCE in DMF/0.1 M NBu₄PF₆).⁶⁸

Stability studies.

The stability in DMSO-d₆ at room temperature was assessed by ¹H NMR over 8 days.

The stability of **Ru-sq** in human plasma at 37 °C was evaluated following a slightly modified procedure already reported by our group.⁴¹ The human plasma was provided by the Blutspendezentrum, Zurich, Switzerland. Diazepam (internal standard) was obtained from SigmaAldrich. Stock solutions of the complexes (20 mM) and diazepam (3.2 mM) were prepared in DMSO. For a typical experiment, an aliquot of the respective stock solutions and DMSO were then added to the plasma solution (975 μL) to a total volume of 1000 μL and final concentrations of 40 μM for the complexes and diazepam. The resulting plasma solution was incubated for either 0, 4, 6, 12, 20, 24 or 48 h at 37°C with continuous and gentle shaking (ca. 600 rpm). The reaction was stopped by addition of 2 mL of methanol, and the mixture was centrifuged for 45 min at 650g at room temperature. The methanolic solution was evaporated and the residue was suspended in 500 μL of 1:1 (v/v) acetonitrile/H₂O solution. The suspension

was filtered and analyzed using UPLC–MS with a total injection volume of 2 μ L.

Cell culture.

HeLa and CT-26 cell lines were cultured in DMEM media (Gibco). CT-26 LUC cell line was cultured in DMEM media (Gibco) supplemented with 1.6 mg/mL of Genticin. RPE-1 cell line was cultured in DMEM/F-12 media (Gibco). MRC-5 cell line was cultured in DMEM/F-10 media (Gibco). A2780, A2780 cis, A2780 ADR cell lines were cultured in RPMI 1640 media (Gibco). The resistance of A2780 cis was maintained by cisplatin treatment (1 μ M) for one week every month. The cells were used in the assays after one week from the end of the treatment in order to avoid interfered results. The resistance of A2780 ADR was maintained by doxorubicin treatment (0.1 μ M) once a week. Cells were used in the assays after three days post doxorubicin treatment in order to avoid interfered results. All cell lines were complemented with 10% of fetal calf serum (Gibco) and 100 U/mL penicillin-streptomycin mixture (Gibco) and maintained in humidified atmosphere at 37°C and 5% of CO₂.

Cytotoxicity Assay using a 2D cellular model.

Cytotoxicity of the tested **Ru-sq** and **Ru(DIP)₂Cl₂** complexes was assessed by a fluorometric cell viability assay using Resazurin (ACROS Organics). Briefly, cells were seeded in triplicates in 96-well plates at a density of 4×10^3 cells/well in 100 μ L. After 24 h, cells were treated with increasing concentrations of the ruthenium complexes. Dilutions for **Ru-sq** were prepared as follows: 2.0 mM stock in DMSO was diluted to 25 μ M with media and then filtrated (0.22 μ m filter VWR). For **Ru(DIP)₂Cl₂** 2.5 mM stock in DMF was prepared, which was further diluted to 100 μ M and filtrated (0.22 μ m filter VWR). After 48 h incubation, medium was removed, and 100 μ L of complete medium containing resazurin (0.2 mg/mL final concentration) was added. After 4 h of incubation at 37 °C, the fluorescence signal of resorufin product was read

(ex: 540 nm em: 590 nm) in a SpectraMax M5 microplate Reader. IC₅₀ values were then calculated using GraphPad Prism software.

Generation of 3D HeLa MCTS.

MCTS were cultured using ultra-low attachment 96 wells plates from Corning® (Fisher Scientific 15329740). HeLa cells were seeded at a density of 5000 cells per well in 200 µL. The single cells would generate MCTS approximately 400 µm in diameter at day 4 with 37 °C and 5 % CO₂.

Treatment of 3D HeLa MCTS.

HeLa MCTS after 4 days of growing at 37 °C and 5 % CO₂ were treated by replacing half of the medium in the well with increasing concentration of compounds for 48 h in the dark. For untreated reference MCTS, half of the medium was replaced by fresh medium only. The cytotoxicity was measured by ATP concentration with CellTiter-Glo® Cell viability kit (Promega, USA).

CellTiter Glo® viability Test.

Cell viability for MCTS was performed *via* ATP assay using luciferase. CellTiter-Glo® kit from Promega was used. The spheroids were incubated for 1 h after replacing half of the media with CellTiter-Glo reagent and the luminescence of the plate was read by SpectraMax M5 microplate reader. IC₅₀ values were calculated using GraphPad Prism software.

HeLa MCTS growth inhibition.

MCTS were grown and treated as previously described (see above). MCTS sizes were observed under a light microscope and pictures were taken with a Samsung Galaxy A5 2017 SM-

A520FZKAXEF thanks to a phone microscope adaptor. Before imaging, the plate was shaken and half of the media was exchanged to remove dead cells. Images were recorded before treatment (day 0) and at day 3, 6, 9 and 13 after treatment. Pictures were first processed using GIMP a cross-platform image editor with a batch automation plug-in. The MCTS sizes were then calculated with SpheroidSizer, a MATLAB-based and open-source software application to measure the size of tumour spheroids automatically and accurately. Data analysis was done using GraphPad Prism software.

Annexin V / PI assay

Apoptosis and necrosis induction in HeLa cells treated with **Ru-sq** was evaluated *via* an AnnexinV/PI staining assay using flow cytometry. Briefly, cells were seeded at density of 2×10^6 cells in 10 cm cell culture dish 24 h prior cell treatments. The medium was removed and replaced with 10 μ M solution of **Ru-sq** or 1 μ M Staurosporin (positive control -Abcam Cat no.120056) and further incubated for 30 min, 4 h or 24 h. Cells were collected, washed twice with ice cold PBS and resuspended in 1x Annexin V binding buffer (10 x buffer composition: 0,1 M HEPES (pH 7.4), 1.4 M NaCl. 25 mM CaCl_2). Samples were processed according to the manufacturer instructions (BD Scientific, cat no 556463 and 556419) and analysed using ZE5 Biorad instrument at Cytometry Platform at Institute Curie. Data were analysed using the FlowJo software.

Sample Preparation for cellular uptake

Cells were seeded at density of 2×10^6 . Next day, cells were treated with 5 μ M concentration of **Ru-sq** or cisplatin. After 2 h, cells were collected, counted and snap frozen in liquid nitrogen and stored at -20 °C. ICP-MS samples were prepared as follows: samples were digested using 70% nitric acid (1 mL, 60 °C, overnight). Samples were then further diluted 1:100 (1% HCl

solution in MQ water) and analysed using ICP-MS.

Sample Preparation for cellular fractionation

HeLa cells were seeded in three 15 cm² cell culture dishes so that on the day of treatment cells were 90% confluent. On the day of treatment cells were incubated with the target complex at a concentration of 5 µM for 2 h. After that time, the medium was removed; cells were washed, collected and counted. After resuspension in cold PBS, the organelles were isolated via different protocols (one cell culture dish per isolation was used).

Mitochondria isolation: To isolate mitochondria, a Mitochondria Isolation Kit (Cat. Nr: MITOISO2, Sigma Aldrich) was used according to the manufacturer procedure for isolation of mitochondria *via* homogenization method.

Lysosome isolation: To isolate lysosomes, a Lysosome Isolation Kit (Cat. Nr: LYSIS01, Sigma Aldrich) was used, according to the manufacturer procedure for isolation of lysosomes *via* Option C.

Nuclear and cytoplasm isolation: To isolate nuclear and cytoplasmic fractions, the ROCKLAND nuclear extract protocol was used.¹⁰⁹ Briefly cells were collected by centrifugation, resuspended in cytoplasmic extraction buffer and incubated on ice. The tubes were centrifuged and supernatant (CE) was removed. Pellets were washed with cytoplasmic extraction buffer without detergent and centrifuged. The pellet (NE) was resuspended in nuclear extraction buffer and incubated on ice. Both CE and NE were centrifuged. Supernatant from CE samples was indicated as cytoplasmic extract, whereas the pellet obtained from NE samples was indicated as nuclear extract.

ICP-MS samples were prepared as follows: isolated cellular fractions were lyophilised and digested using 5 mL of 70% nitric acid (60 °C, overnight). Samples were then further diluted (1:1000 for nuclear pellet samples and 1:100 for all the other samples) MQ water (containing

in 1% HCl solution) and analysed using ICP-MS.

Sample preparation for studies on the mechanism of cellular uptake

Samples were prepared as previously reported.¹¹⁰ Briefly, HeLa cells were seeded at density of 2×10^6 and next day were pre-treated with corresponding inhibitors or kept at specific temperature for 1 h. Next, cells were washed with PBS and were incubated with 5 μ M of **Ru-sq** for 2 h (low temperature sample was still kept at 4 °C). Afterwards cells were washed with PBS, collected, counted and snap frozen in liquid nitrogen. Pellets were stored at -20 °C. ICP-MS samples were prepared as follows: samples were digested using 70% nitric acid (1 mL, 60 °C, overnight), further diluted 1:100 (1% HCl solution in MQ water) and analysed using ICP-MS.

DNA metalation of HeLa cells

Cells were seeded at density of 2×10^6 . The following day, cells were treated with 5 μ M concentration of **Ru-sq** or cisplatin. After 2 h, cells were collected, snap frozen in liquid nitrogen and stored at -20 °C. The following day, DNA was extracted using a PureLink™ Genomic DNA Mini Kit (Invitrogen). DNA purity was checked by absorbance measurements at 260 and 280 nm. Concentrations of genomic DNA were calculated assuming that one absorbance unit equals 50 μ g/mL. ICP-MS samples were prepared as follows: samples were digested using 70% nitric acid (60 °C, overnight) in 1:1.6 DNA to acid volume ratio. Samples were then further diluted 1:10 or 1:100 (1% HCl solution in MQ water) and analysed using ICP-MS.

ICP-MS studies

All ICP-MS measurements were performed on an high resolution ICP-MS (Element II, ThermoScientific) located at the Institut de physique du globe de Paris (France). The monitored isotopes are ^{101}Ru and ^{195}Pt . Daily, prior to the analytical sequence, the instrument was first tuned to produce maximum sensitivity and stability while also maintaining low uranium oxide formation ($\text{UO}/\text{U} \leq 5\%$). The data were treated as follow: intensities were converted into concentrations using uFREASI (user-FRiendly Elemental dAta proceSsIng).¹¹¹ This software, made for HR-ICP-MS users community, is free and available on <http://www.ipgp.fr/~tharaud/uFREASI>.

ICP-MS data analysis

Cellular uptake studies: The amount of metal detected in the cell samples was transformed from ppb into μg of metal. Data were subsequently normalised to the number of cells and expressed as μmol of metal/ amount of cells.

Cellular fractionation: The amount of detected ruthenium in the cell samples was transformed from ppb into μg of ruthenium. Values were then normalised to the number of cells used for specific extraction. Due to low yield of lysosome extraction (only 25%), the values obtained were multiplied by the factor of 4. Because of a low yield of mitochondria extraction (50% of the cells were homogenized), the values obtained for that organelle were multiplied by the factor of 2. Extraction protocols allow for the isolation of pure subcellular fractions. Therefore, the total amount of metal found in the cells was calculated summing the values obtained for the pure organelles.

Mechanism of uptake: The amount of ruthenium detected in cell samples was transformed from ppb into μg of ruthenium and values obtained were normalised to the number of cells used for specific treatment. The value for the ruthenium found in the 37 °C sample was used as a 100%.

Cellular metalation: The amount of ruthenium detected in cell samples was transformed from ppb into μg of ruthenium and value obtained was normalised to the amount of DNA.

JC-1 Mitochondrial Membrane Potential Test.

HeLa cells were seeded at a density of 6000 cells/ well in black 96 well-plate (costar 3916). The next day, the cells were treated with different concentrations of **Ru-sq** and **Ru(DIP)₂Cl₂**. After further 24 h, the cells were treated according to the JC-1 Mitochondrial Membrane Potential Assay Kit (Abcam, ab113850). The data were analysed using GraphPad Prism software.

Mito Stress Test.

HeLa cells were seeded in Seahorse XFe96 well plates at a density of 30,000 cells/ well in 80 μL . After 24 h, the media was replaced with fresh media and cisplatin (10 μM), catechol (10 μM), DIP (1 μM), complex **Ru(DIP)₂Cl₂** (10 μM) or complex **Ru-sq** (1 μM) were added. After 24 h of incubation, the regular media was removed and the cells were washed thrice using bicarbonate and serum free DMEM, supplemented with glucose, 1.8 mg/ mL; 1% glutamine and 1% sodium pyruvate and incubated in a non-CO₂ incubator at 37 °C for 1 h. Mito Stress assay was run using Oligomycin, 1 μM , FCCP 1 μM and mixture of Antimycin-A/ Rotenone 1 μM each in ports A, B and C respectively using Seahorse XFe96 Extracellular Flux Analyzer.

Glycolysis Stress Test.

HeLa cells were seeded in Seahorse XFe96 well plates at a density of 30,000 cells/ well in 80 μL . After 24 h, the media was replaced with fresh media and cisplatin (10 μM), catechol (10 μM), DIP (1 μM), complex **Ru(DIP)₂Cl₂** (10 μM) or complex **Ru-sq** (1 μM) were added. After 24 h of incubation, the regular media was removed and the cells were washed thrice using

bicarbonate, glucose and serum free DMEM, supplemented 1% glutamine and 1% sodium pyruvate and incubated in a non-CO₂ incubator at 37 °C for an hour. Glycolytic stress test was run using glucose, 10 mM, Oligomycin, 1 μM and 2-Deoxyglucose, 50 mM in ports A, B and C respectively using Seahorse XFe96 Extracellular Flux Analyzer.

Mito Fuel Flex Test.

HeLa cells were seeded in Seahorse XFe96 well plates at a density of 30,000 cells/ well in 80 μL. After 24 h, the media was replaced with fresh media and cisplatin (10 μM), catechol (10 μM), DIP (1 μM), complex **Ru(DIP)₂Cl₂** (10 μM) or complex **Ru-sq** (1 μM) were added. After 24 h of incubation, the regular media was removed and the cells were washed thrice using bicarbonate, and serum free DMEM, supplemented with 1.8 mg/mL glucose, 1% glutamine and 1% sodium pyruvate and incubated in a non-CO₂ incubator at 37 °C for an hour. Fuel flex assay for the different fuel pathways viz. glucose, glutamine and fatty acid was studied by measuring the basal oxygen consumption rates and that after addition of the inhibitor of the target pathway in port A and a mixture of the inhibitors of the other two pathways in port B. This gave a measure of the dependency of the cells on a fuel pathway. To study the capacity of a certain fuel pathway, the sequence of addition of the inhibitors was reversed. In port A was added the mixture of inhibitors for the other pathways and in port B was added the inhibitor for the target pathway. UK-5099 (pyruvate dehydrogenase inhibitor, 20 μM) was used as an inhibitor for the glucose pathway. BPTES (selective inhibitor of Glutaminase GLS1, 30 μM) was used as an inhibitor for the glutamine pathway. Etomoxir (O-carnitine palmitoyltransferase-1 (CPT-1) inhibitor, 40 μM) was used as an inhibitor for the fatty acid pathway.

Animals and Tumour Model for Ehrlich mammary carcinoma in immunocompetent NMRI mice.

Due to the poor solubility of Ru-sq in water, dimethyl sulfoxide (DMSO), 1.81 mL / kg of body weight, had to be added to water for injections, for which reason the i.p. route of administration was chosen rather than i.v. Female outbred mice (NMRI) were used for this study, they were obtained from Masaryk University (Brno, Czech Republic). Animal care was conformed to EU recommendations and in accordance with the European convention for the protection of vertebrate animals used for experimental and other scientific purposes; it was approved by the Ethical Commission of the Medical Faculty in Hradec Králové (Nr. MSMT-56249/2012-310). For the MTD assessment, two or three healthy mice per group were observed for weight loss (the limit was 10%) over 14 days after injection of the solution. For the in vivo activity study, 70 NMRI female mice, 7 weeks old and weighting in the average 31.8 g (SD = 1.27) were fed a standard diet and water ad libitum. A solid Ehrlich tumour was purchased from the Research Institute for Pharmacy and Biochemistry (VUFB) in Prague, and then maintained in NMRI mice by periodical transplantations. The homogenised tumour tissue was inoculated subcutaneously into all mice on day 0, using 0.2 mL of 1/1 (v/v) homogenate freshly prepared in isotonic glucose solution. The tumour-bearing mice were then divided into 5 groups of 14 animals as follows: a control group treated with the pure solvent (DMSO and water), 3 groups of animals treated with Ru-sq in doses of 5, 10, and 15 mg/kg i.p. and a positive controls receiving 5 mg/kg cisplatin i.p. (Cisplatin 50 ml/25 mg, EBEWE Pharma, Austria). The solutions were administered on days 1 and 7 in volumes of 0.2 mL per 20 g body weight. On the tenth day, half of the mice were sacrificed, and their tumours were weighed. The remaining animals were left in order to observe their survival.

Statistical Analysis for Ehrlich mammary carcinoma in immunocompetent NMRI mice.

One-Way Analysis of Variance with post-hoc Dunnetts's multiple comparison test was used to detect differences in tumour weight. Kaplan-Meier curves and logrank tests were used to compare survival times in groups. Here, the level of significance was $\alpha=0.05$. MS Excel 2003 and NCSS software was used for the calculations and statistical evaluations.

Animals and Tumour Model for A2780 human ovarian cancer in immunodeficient nude mice.

The animal experiment depicted here after were performed in accordance with the Act on Experimental Work with Animals (Public Notice of the Ministry of Agriculture of the Czech Republic No. 246/1992, No. 311/1997, No. 207/2004; Decree of the Ministry of the Environment of the Czech Republic No. 117/1987; and Act of the Czech National Assembly No. 149/2004), which is fully compatible with the corresponding European Union directives. Athymic nude mice were used for experiment (obtained from AnLab Ltd., Prague, Czech Republic, females, 8 weeks old, $n = 40$). After acclimatization, the A2780 human ovarian cancer cell line was implanted subcutaneously in the shaved right flank of mice (obtained from Sigma-Aldrich, Missouri, USA, used medium RPMI with 10 % fetal bovine serum, 2×10^6 cells per mouse applicated with cells to Matrigel ratio 2:1). The animals were randomly divided into five groups ($n = 8$), when tumour reached the size of 5 – 8 mm in diameter. 5 % DMSO (dimethyl sulfoxide) solution containing Ru-sq 5 mg/kg, 10 mg/kg or 15 mg/kg (in volume 200 μ l per 20 g of mouse weight) were administered intraperitoneally to the first three groups (day 1). Another group received cisplatin (5 mg/kg) in the same manner as positive control. The last group (as negative untreated control) received intraperitoneally 5 % solution of DMSO with physiologic solution. The application of all substances was repeated on day 7 of therapy. The animals were observed 60 days from first application, tumor growth, weight of mice and

survival were monitored in regular intervals. The mice had free access to water and food ad libitum throughout the experiment. At the end of experiment (after 60 days) all surviving mice were sacrificed by using of overdose of intramuscular anesthetic.

Statistical Analysis for A2780 human ovarian cancer in immunodeficient nude mice.

One-Way Analysis of Variance with post-hoc Dunnetts's multiple comparison test was used to detect differences in tumour weight. Kaplan-Meier curves and logrank tests were used to compare survival times in groups. Here, the level of significance was $\alpha=0.05$. MS Excel 2016 and OriginPro 8 software was used for the calculations and statistical evaluations.

Western Blot analysis of Akt-1 protein levels in HeLa cells.

HeLa cells were seeded on a 10 cm dish so that, at the time of the treatment, cells were confluent. The next day, the cells were treated for 24 h with the compounds. After that time, the cells were collected, counted, snap frozen in liquid nitrogen and then stored at -20 °C. Samples were then lysed in 4x SB buffer in reducing conditions, so that 10 μ L of the sample contained 100 000 cells. Samples were passaged ten times through 5 mL syringe with narrow needle then were boiled for 10 min. Samples were then loaded on 10% SDS-PAGE gels (10 μ L). Proteins were then blotted on a nitrocellulose membrane (Amersham Protran 0.2). Detection of Akt-1 and GAPDH proteins was conducted using following primary antibodies: anti-GAPDH (1:10000 sigma-aldrich G9545) and anti-Akt-1 (B-1) (1:50 Santa Cruz Biotechnology sc-5298). Images were taken using ChemiDoc Touch Imaging System by Biorad. Image with non-saturated bands allowed for normalization in Fiji software.

Acknowledgements

This work was financially supported by an ERC Consolidator Grant PhotoMedMet to G.G. (GA 681679) and has received support under the program *Investissements d'Avenir* launched by the French Government and implemented by the ANR with the reference ANR-10-IDEX-0001-02 PSL (G.G.). This work was financed by the Swiss National Science Foundation (Professorships N° PP00P2_133568 and PP00P2_157545 to G.G.), the University of Zurich (G.G), the Novartis Jubilee Foundation (G.G and R.R.), the Forschungskredit of the University of Zurich (R.R.), the UBS Promedica Stiftung (G.G and R.R.) and the Charles University program Progres Q40/01. Ile de France Region is gratefully acknowledged for financial support of 500 MHz NMR spectrometer of Chimie-ParisTech in the framework of the SESAME equipment project. We acknowledge the loan of Agilent's equipment to Chimie ParisTech. Part of this work was supported by IPGP multidisciplinary program PARI and by Region Île-de-France SESAME Grant no. 12015908. Stefano Ferrari is supported by a grant of the Czech Science Foundation (17-02080S). Part of this work was supported by IPGP multidisciplinary program PARI and by Region Île-de-France SESAME Grant no. 12015908.

References

- 1 A. Urruticoechea, R. Alemany, J. Balart, A. Villanueva, F. Viñals and G. Capellá, *Curr. Pharm. Des.*, 2010, **16**, 3–10.
- 2 B. Rosenberg, L. Van Camp and T. Krigas, *Nature*, 1965, **205**, 698–699.
- 3 B. Rosenberg, L. van Camp, E. B. Grimley and A. J. Thomson, *J. Biol. Chem.*, 1967, **242**, 1347–52.
- 4 B. Rosenberg, L. Van Camp, J. E. Trosko and V. H. Mansour, *Nature*, 1969, **222**, 385–386.
- 5 B. B. Rosenberg, *Platin. Met. Rev.*, 1971, **15**, 42–51.
- 6 P. Pieter and S. J. Lippard, *Encycl. Cancer*, 1997, **1**, 525–543.
- 7 E. Wong and C. M. Giandomenico, *Chem. Rev.*, 1999, **99**, 2451–2466.
- 8 D. Lebwohl and R. Canetta, *Eur. J. Cancer*, 1998, **34**, 1522–1534.
- 9 S. P. Fricker, *Dalton Trans.*, 2007, **43**, 4903–4917.
- 10 V. Singh, G. K. Azad, A. Reddy M., S. Baranwal and R. S. Tomar, *Eur. J. Pharmacol.*, 2014, **736**, 77–85.
- 11 E. Jamieson and S. Lippard, *Chem. Rev.*, 1999, **99**, 2467–2498.
- 12 M. J. Clarke, F. Zhu and D. R. Frasca, *Chem. Rev.*, 1999, **99**, 2511–2533.
- 13 M. Jakupec, M. Galanski, V. B. Arion, C. G. Hartinger and B. K. Keppler, *Dalton Trans.*, 2008, 183–194.
- 14 P. J. Dyson and G. Sava, *Dalton Trans.*, 2006, 1929–33.

- 15 G. Gasser, I. Ott and N. Metzler-Nolte, *J. Med. Chem.*, 2011, **54**, 3–25.
- 16 T. Gianferrara, I. Bratsos and E. Alessio, *Dalton Trans.*, 2009, 7588–7598.
- 17 E. Boros, P. J. Dyson and G. Gasser, *Chem.*, DOI:10.1016/j.chempr.2019.10.013.
- 18 B. C. S. Allardyce and P. J. Dyson, *Platin. Met. Rev.*, 2001, **45**, 62–69.
- 19 E. S. Antonarakis and A. Emadi, *Cancer Chemother. Pharmacol.*, 2010, **66**, 1–9.
- 20 M. Pongratz, P. Schluga, M. A. Jakupec, V. B. Arion, C. G. Hartinger, G. Allmaier and B. K. Keppler, *J. Anal. At. Spectrom.*, 2004, **19**, 46–51.
- 21 E. Alessio, *Eur. J. Inorg. Chem.*, 2017, **55**, 1549–1560.
- 22 G. Sava, I. Capozzi, K. Clerici, G. Gagliardi, E. Alessio and G. Mestroni, *Clin. Exp. Metastasis*, 1998, **16**, 371–379.
- 23 F. Lentz, A. Drescher, A. Lindauer, M. Henke, R. a Hilger, C. G. Hartinger, M. E. Scheulen, C. Dittrich, B. K. Keppler and U. Jaehde, *Anticancer. Drugs*, 2009, **20**, 97–103.
- 24 R. Trondl, P. Heffeter, C. R. Kowol, M. a. Jakupec, W. Berger and B. K. Keppler, *Chem. Sci.*, 2014, **5**, 2925–2932.
- 25 C. G. Hartinger, S. Zorbas-Seifried, M. A. Jakupec, B. Kynast, H. Zorbas and B. K. Keppler, *J. Inorg. Biochem.*, 2006, **100**, 891–904.
- 26 H. A. Burris, S. Bakewell, J. C. Bendell, J. Infante, S. F. Jones, D. R. Spigel, G. J. Weiss, R. K. Ramanathan, A. Ogden and D. Von Hoff, *ESMO open*, 2016, 1–8.
- 27 S. A. McFarland, A. Mandel, R. Dumoulin-White and G. Gasser, *Curr. Opin. Chem. Biol.*, 2020, **56**, 23–27.

- 28 H. Yin, J. Roque, P. Konda, S. Monro, K. L. Colo, S. Gujar, R. P. Thummel, L. Lilge, C. G. Cameron and S. A. Mcfarland, *Chem. Rev.*, 2019, **119**, 797–828.
- 29 <https://clinicaltrials.gov/ct2/show/NCT03945162?term=TLD-1433&rank=1>, (accessed the 27/ 09/ 2019).
- 30 A. Notaro and G. Gasser, *Chem. Soc. Rev.*, 2017, **46**, 7317–7337.
- 31 C. G. Hartinger, M. a Jakupec, S. Zorbas-Seifried, M. Groessler, A. Egger, W. Berger, H. Zorbas, P. J. Dyson and B. K. Keppler, *Chem. Biodivers.*, 2008, **5**, 2140–2155.
- 32 J. Shum, P. K. Leung and K. K. Lo, *Inorg. Chem.*, 2019, **58**, 2231–2247.
- 33 M. Patra and G. Gasser, *ChemBioChem*, 2012, **13**, 1232–1252.
- 34 M. Dörr and E. Meggers, *Curr. Opin. Chem. Biol.*, 2014, **19**, 76–81.
- 35 M. Jakubaszek, B. Goud and S. Ferrari, 2018, 13040–13059.
- 36 M. R. Gill, H. Derrat, C. G. W. Smythe, G. Battaglia and J. A. Thomas, *ChemBioChem*, 2011, **12**, 877–880.
- 37 N. Deepika, C. Shobha Devi, Y. Praveen Kumar, K. Laxma Reddy, P. Venkat Reddy, D. Anil Kumar, S. S. Singh and S. Satyanarayana, *J. Photochem. Photobiol. B Biol.*, 2016, **160**, 142–153.
- 38 H. Wang, Y. Liu, M. Li, H. Huang, H. M. Xu, R. J. Hong and H. Shen, *Dalt. Trans.*, 2013, **42**, 4386–4397.
- 39 A. Srishailam, Y. P. Kumar, P. Venkat Reddy, N. Nambigari, U. Vuruputuri, S. S. Singh and S. Satyanarayana, *J. Photochem. Photobiol. B Biol.*, 2014, **132**, 111–123.
- 40 C. Tan, S. Lai, S. Wu, S. Hu, L. Zhou, Y. Chen, M. Wang, Y. Zhu, W. Lian, W. Peng,

- L. Ji and A. Xu, *J. Med. Chem.*, 2010, **53**, 7613–7624.
- 41 V. Pierroz, T. Joshi, A. Leonidova, C. Mari, J. Schur, I. Ott, L. Spiccia, S. Ferrari and G. Gasser, *J. Am. Chem. Soc.*, 2012, **134**, 20376–20387.
- 42 G. Bin Jiang, X. Zheng, J. H. Yao, B. J. Han, W. Li, J. Wang, H. L. Huang and Y. J. Liu, *J. Inorg. Biochem.*, 2014, **141**, 170–179.
- 43 Y. C. Wang, C. Qian, Z. L. Peng, X. J. Hou, L. L. Wang, H. Chao and L. N. Ji, *J. Inorg. Biochem.*, 2014, **130**, 15–27.
- 44 J. F. Kou, C. Qian, J. Q. Wang, X. Chen, L. L. Wang, H. Chao and L. N. Ji, *J. Biol. Inorg. Chem.*, 2012, **17**, 81–96.
- 45 U. Schatzschneider, J. Niesel, I. Ott, R. Gust, H. Alborzinia and S. Wölfl, *ChemMedChem*, 2008, **3**, 1104–1109.
- 46 M. D. Ward, J. A. McCleverty and M. D. Ward, *J. chem. soc. Dalton Trans.*, 2002, 275–288.
- 47 A. Vlček, *Comments Inorg. Chem.*, 1994, **16**, 207–228.
- 48 C. G. Pierpont, *Coord. Chem. Rev.*, 2001, **217**, 99–125.
- 49 C. Creutz, *Prog. Inorg. Chem.*, 1983, **30**, 1–73.
- 50 M. Haga, E. S. Dodsworth and A. B. P. Lever, *Inorg. Chem.*, 1986, **25**, 447–453.
- 51 T. Wada, M. Yamanaka, T. Fujihara, Y. Miyazato and K. Tanaka, *Inorg. Chem.*, 2006, **45**, 8887–8894.
- 52 J. T. Muckerman, D. E. Polyansky, T. Wada, K. Tanaka and E. Fujita, *Inorg. Chem.*, 2008, **47**, 1787–1802.

- 53 S. E. Jones, D. Chin and D. T. Sawyer, *Inorg Chem*, 1981, **20**, 4257–4262.
- 54 J. B. Baell, *J. Nat. Prod.*, 2016, **79**, 616–628.
- 55 R. M. F. Lima, L. D. G. Alvarez, M. F. D. Costa, S. L. Costa and R. S. El-bachá, *Gen. Physiol. Biophys*, 2008, **27**, 306–314.
- 56 W. L. C. Almeida, D. N. Vítor, M. R. G. Pereira, D. S. De Sá, L. D. G. Alvarez, A. M. Pinheiro, S. L. Costa, M. F. D. Costa, Z. N. Da Rocha and R. S. El-Bachá, *J. Chil. Chem. Soc.*, 2007, **52**, 1240–1243.
- 57 D. Lin, F. Dai, L. Di Sun and B. Zhou, *Mol. Nutr. Food Res.*, 2015, **59**, 2395–2406.
- 58 R. Galvao de Lima, A. B. P. Lever, I. Y. Ito and R. Santana da Silva, *Transit. Met. Chem.* 28, 2003, **28**, 272–275.
- 59 V. T. Huong, T. Shimanouchi, N. Shimauchi, H. Yagi, H. Umakoshi, Y. Goto and R. Kuboi, *J. Biosci. Bioeng.*, 2010, **109**, 629–634.
- 60 A. L. and P. A. L. Debbie C. Crans, Jordan T. Koehn, Stephanie M. Petry, Caleb M. Glover, Asanka Wijetunga Ravinder Kaur, *Dalt. Trans.*, 2019, **48**, 6383–6395.
- 61 D. C. C. and M. D. J. Brant G. Lemons, David T. Richens, Ashley Anderson, Myles Sedgwick, *New J. Chem*, 2013, **37**, 75–91.
- 62 I. Brastos, E. Alessio, M. E. Ringenberg and T. B. Rauchfuss, *Inorg. Synth.*, 2010, **35**, 148–163.
- 63 R. Caspar, C. Cordier, J. B. Waern, C. Guyard-Duhayon, M. Gruselle, P. Le Floch and H. Amouri, *Inorg. Chem.*, 2006, **45**, 4071–4078.
- 64 O. Carugo, C. B. Castellani, K. Djinovicb and M. Rizzi, *J. CHEM. SOC. Dalt. TRANS*,

- 1992, **10**, 1–5.
- 65 S. L. H. Higgins, T. A. White, B. S. J. Winkel and K. J. Brewer, *Inorg. Chem.*, 2011, **50**, 463–470.
- 66 M. T. Mongelli and K. J. Brewer, *Inorg. Chem. Commun.*, 2006, **9**, 877–881.
- 67 O. K. Medhi and U. Agarwala, *Inorg Chem*, 1980, **1**, 1381–1384.
- 68 N. G. Connelly and W. E. Geiger, *Chem. Rev.*, 1996, **96**, 877–910.
- 69 D. Bao, B. Millare, W. Xia, B. G. Steyer, A. A. Gerasimenko, A. Ferreira, A. Contreras and V. I. Vullev, *J. Phys. Chem. A*, 2009, **2**, 1259–1267.
- 70 A. Frei, R. Rubbiani, S. Tubafard, O. Blacque, P. Anstaett, A. Felgenträger, T. Maisch, L. Spiccia and G. Gasser, *J. Med. Chem.*, 2014, **57**, 7280–7292.
- 71 V. Cepeda, M. Fuertes, J. Castilla, C. Alonso, C. Quevedo and J. Perez, *Anticancer. Agents Med. Chem.*, 2007, **7**, 3–18.
- 72 H. G. Keizer, H. M. Pinedo, G. J. Schuurhuis and H. Joenje, *Pharmac. Ther*, 1990, **47**, 219–231.
- 73 J. M. Kelm, N. E. Timmins, C. J. Brown, M. Fussenegger and L. K. Nielsen, *Biotechnol. Bioeng.*, 2003, **83**, 173–180.
- 74 H. Ma, Q. Jiang, S. Han, Y. Wu, J. C. Tomshine, D. Wang, Y. Gan and G. Zou, *Mol. Imaging*, 2012, **11**, 487–498.
- 75 M. Kapalczyńska, T. Kolenda, A. Przybyła, Weronika Zajączkowska, Maria Teresiak, V. Filas, M. Ibbs, R. Bliźniak and K. Łuczewski, Łukasz Lamperska, *Arch. Med. Sci.*, 2018, **4**, 910–919.

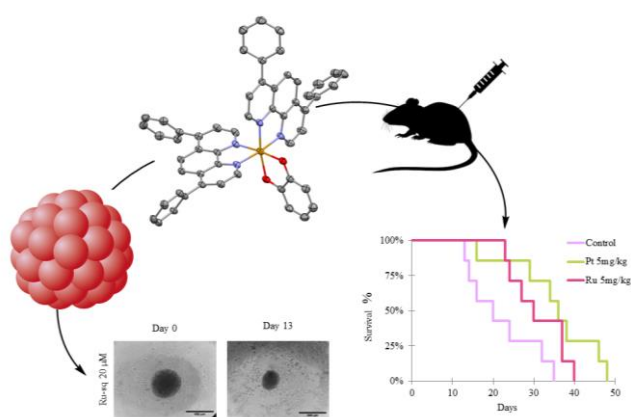
- 76 J. Friedrich, C. Seidel, R. Ebner and L. A. Kunz-schughart, *Nat. Protoc.*, 2009, **4**, 309–324.
- 77 J. Hess, H. Huang, A. Kaiser, V. Pierroz and O. Blacque, 2017, 9888–9896.
- 78 O. W. Seo, M. Kim, J. Hulme and S. S. A. An, 2016, 7207–7218.
- 79 A. M. Rieger, K. L. Nelson, J. D. Konowalchuk and D. R. Barreda, *J. Vis. Exp.*, 2011, 2–5.
- 80 A. C. Belmokhtar, J. Hillion and E. Ségal-Bendirdjian, *Oncogene*, 2001, 3354–3362.
- 81 L. Zeng, Y. Chen, H. Huang, J. Wang, D. Zhao, L. Ji and H. Chao, *Chemistry*, 2015, **21**, 15308–15319.
- 82 J. Zisowsky, S. Koegel, S. Leyers, K. Devarakonda, M. U. Kassack, M. Osmak and U. Jaehde, *Biochem. Pharmacol.*, 2007, **73**, 298–307.
- 83 C. A. Puckett and J. K. Barton, *J. Am. Chem. Soc.*, 2009, **131**, 8738–8739.
- 84 B. M. Goldstein, J. K. Barton and H. M. Berman, *Inorg. Chem.*, 1986, **25**, 842–847.
- 85 Y. Tsujimoto and Osaka, 2000, 134–135.
- 86 V. N. Dedov, G. C. Cox and B. D. Roufogalis, *Micron*, 2001, **32**, 653–660.
- 87 L. Zhuang and X. L. and W. H. Huanjie Wei, Qing Li, Xianlong Su, Shujuan Liu, Kenneth Yin Zhang, Wen Lv, Qiang Zhao, *Chem. Sci.*, 2018, **9**, 502–512.
- 88 L. D. Zorova, V. A. Popkov, E. Y. Plotnikov, D. N. Silachev, B. Pevzner, S. S. Jankauskas, V. A. Babenko, S. D. Zorov, A. V Balakireva, M. Juhaszova, S. J. Sollott and D. B. Zorov, *Anal. Biochem.*, 2018, 50–59.
- 89 J. D. Ly, D. R. Grubb and A. Lawen, *Apoptosis*, 2003, **8**, 115–128.

- 90 S. Sakamuru, M. S. Attene-ramos and M. Xia, in *High-Throughput Screening Assays in Toxicology, Methods in Molecular Biology*, 2016, vol. 1473, pp. 17–22.
- 91 L. Zhen-ge, R. Xiao-hua, W. Sha-sha, L. Xin-hua and T. Ya-ling, *Onco. Targets. Ther.*, 2016, **9**, 545–555.
- 92 J. Jung, *Toxicol. Res.*, 2014, **30**, 1–5.
- 93 C. Xu, X. Li, P. Liu, M. A. N. Li and F. Luo, *Oncol. Lett.*, 2019, **5**, 3–10.
- 94 A. S. Clark, K. West, S. Streicher and P. A. Dennis, *Mol. Cancer Ther.*, 2002, **1**, 707–717.
- 95 J. U. N. Zhang, L. L. I. Zhang, L. E. I. Shen, X. Xu and H. G. Yu, *Oncol. Lett.*, 2013, **5**, 756–760.
- 96 S. A. Santi, A. C. H. Douglas and Lee, *BioMol Concepts*, 2010, **1**, 389–401.
- 97 B. D. Manning and A. Toker, *Cell*, 2017, **169**, 381–405.
- 98 C. Mitchell and J. R. Testa, *Curr. Cancer Drug Targets*, 2013, **13**, 324.
- 99 G. R. Fulmer, A. J. M. Miller, N. H. Sherden, H. E. Gottlieb, A. Nudelman, B. M. Stoltz, J. E. Bercaw and K. I. Goldberg, *Organometallics*, 2010, **29**, 2176–2179.
- 100 M. Krachler, *J. Environ. Monit.*, 2007, **9**, 790–804.
- 101 *Rigaku Oxford Diffraction*, 2015.
- 102 R. C. Clark and J. S. Reid, *Acta Crystallogr. Sect. A*, 1995, **51**, 887–897.
- 103 *CrysAlisPro (version 1.171.39.9f)*, Rigaku Oxford Diffraction, 2015.
- 104 O. V. Dolomanov, L. J. Bourhis, R. J. Gildea, J. A. K. Howard and H. Puschmann, *J.*

- Appl. Cryst.*, 2009, **42**, 339.
- 105 G. M. Sheldrick, *Acta Crystallogr. Sect. A Found. Crystallogr.*, 2015, **71**, 3–8.
- 106 G. M. Sheldrick, *Acta Crystallogr. Sect. C Struct. Chem.*, 2015, **71**, 3–8.
- 107 A. L. Spek, *J. Appl. Crystallogr.*, 2003, **36**, 7–13.
- 108 S. Stoll and A. Schweiger, *J. Magn. Reson.*, 2006, **178**, 42–55.
- 109 <https://rockland-inc.com/Nuclear-Extract-Protocol.aspx>, (accessed the 03.10.2019).
- 110 A. Notaro, A. Frei, R. Rubbiani, M. Jakubaszek, U. Basu, S. Koch, C. Mari, M. Dotou, O. Blacque, J. Gouyon, F. Bedioui, N. Rotthowe, R. F. Winter, B. Goud, S. Ferrari, M. Tharaud, M. Řezáčová, J. Humajová, P. Tomšík and G. Gasser, *ChemRxiv. Prepr.*, , DOI:10.26434/chemrxiv.9582527.v1.
- 111 M. Tharaud, S. Gardoll, O. Khelifi, M. F. Benedetti and Y. Sivry, *Microchem. J.*, 2015, **121**, 32–40.

TOC picture

A ruthenium (II) polypyridyl complex bearing a non-innocent dioxo ligand demonstrates an impressive potential as a chemotherapeutic agent against cancer both *in vitro* and *in vivo*.



Supplementary information

A Ruthenium(II) Complex Containing a Redox-Active
Semiquinonate Ligand as Potential Chemotherapeutic Agent: From
Synthesis to *in vivo* Studies

*Anna Notaro,^{a,#} Angelo Frei,^{b,#} Riccardo Rubbiani,^{b,#} Marta Jakubaszek,^{a, e} Uttara Basu,^a
Severin Koch,^b Cristina Mari,^b Mazzarine Dotou,^a Olivier Blacque,^b Jérémie Gouyon,^c Fethi
Bedioui,^c Nils Rotthowe,^d Rainer F. Winter,^d Bruno Goud,^e Stefano Ferrari,^{f,g} Mickaël
Tharaud,^h Martina Řezáčová,ⁱ Jana Humajová,^j Pavel Tomšik,ⁱ and Gilles Gasser^{a,*}*

- ^a Chimie ParisTech, PSL University, CNRS, Institute of Chemistry for Life and Health Sciences, Laboratory for Inorganic Chemical Biology, F-75005 Paris, France.
- ^b Department of Chemistry, University of Zurich, Winterthurerstrasse 190, 8057 Zurich, Switzerland.
- ^c Chimie ParisTech, PSL University, CNRS, Institute of Chemistry for Life and Health Sciences, Team Synthèse, Electrochimie, Imagerie et Systèmes Analytiques pour le Diagnostic, F-75005 Paris, France.
- ^d Department of Chemistry, University of Konstanz, Universitätsstrasse 10, D-78457 Konstanz, Germany.
- ^e Institut Curie, PSL University, CNRS UMR 144, Paris, France.
- ^f Institute of Molecular Cancer Research, University of Zurich, Zurich, Switzerland.
- ^g Institute of Molecular Genetics of the Czech Academy of Sciences, Videnska 1083, 143 00 Prague, Czech Republic.
- ^h Université de Paris, Institut de physique du globe de Paris, CNRS, F-75005 Paris, France.
- ⁱ Department of Medical Biochemistry, Faculty of Medicine in Hradec Kralove, Charles University, Czech Republic.
- ^j Department of Medical Biochemistry, Faculty of Medicine in Prague, Czech Republic.

these authors have contributed equally to the work

* Corresponding author: E-mail: gilles.gasser@chimeparistech.psl.eu; WWW: www.gassergroup.com; Phone: +33 1 44 27 56 02

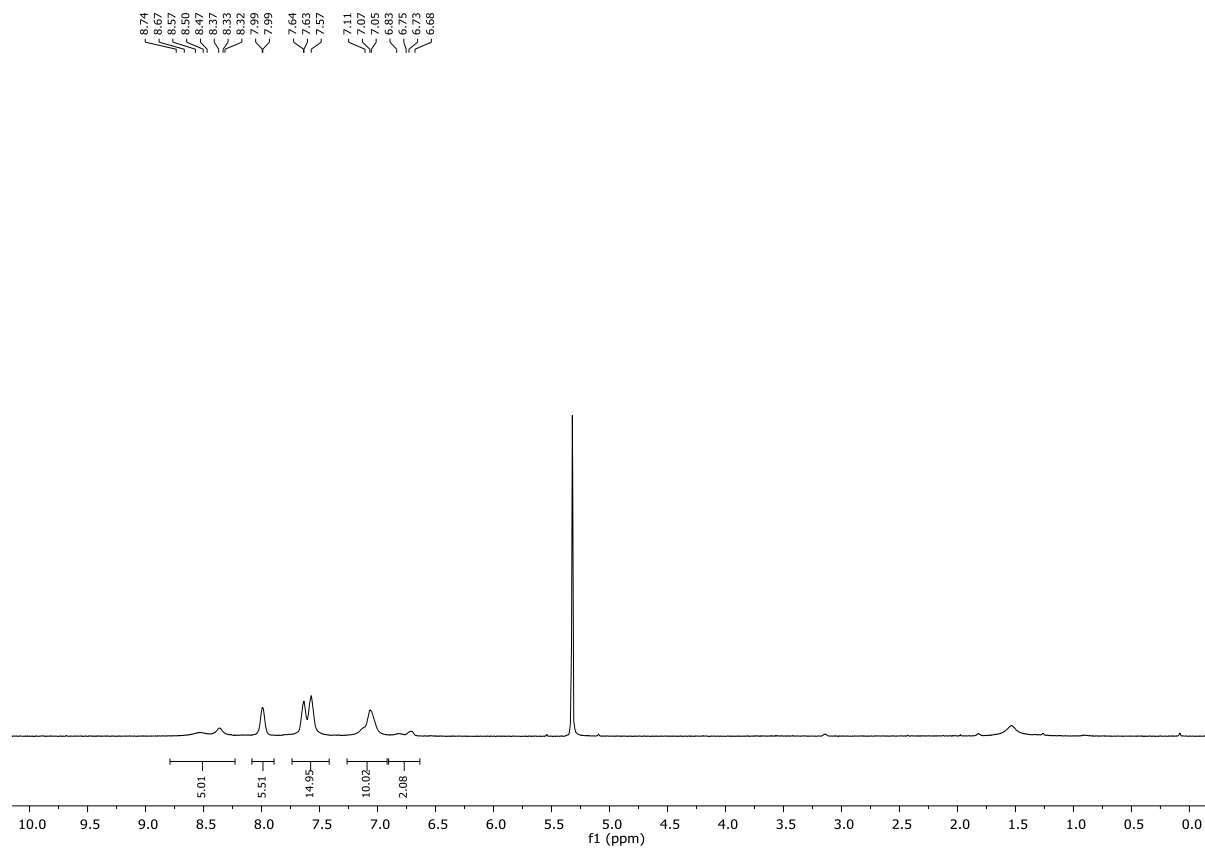
Table of contents:

FIGURE S1. NMR AND HPLC SPECTRA OF RU-SQ.....	485
RU-SQ, ¹ H, CD ₂ CL ₂ , 400 MHZ.....	485
RU-SQ, ¹³ C, CD ₂ CL ₂ , 125 MHZ.....	486
RU-SQ, 2D ¹ H- ¹³ C HSQC, CD ₂ CL ₂ , 125 MHZ	487
RU-SQ, HPLC TRACE RECORDED AT 450NM	487
FIGURE S2. CRYSTALLOGRAPHIC DATA OF [RU(DIP)₂(SQ)](CL).	488
TABLE S1. SELECTED BOND LENGTHS AND ANGLES OF RU-1 MOLECULE.	489
TABLE S2. SELECTED BOND LENGTHS AND ANGLES OF RU-2 MOLECULE.	489
FIGURE S3. CV AND RDE VOLTAMMOGRAMS OF RU-SQ	490
TABLE S3. ELECTROCHEMICAL DATA FOR RU-SQ.....	491
FIGURE S4. EPR SPECTRA OF RU-SQ, ITS REDUCED FORM RU-CAT, AND ITS OXIDIZED FORM RU-Q.....	492
FIGURE S5. OVERLAP OF ¹H SPECTRA OF RU-SQ IN DMSO OVER 8 DAYS.....	493
FIGURE S6. UV TRACES OF UPLC ANALYSIS OF RU-SQ INCUBATED IN HUMAN PLASMA AT 37 °C FOR 0 H, 4 H, 6 H, 12 H, 20 H AND 24 H	494
FIGURE S7. FLUOROMETRIC CELL VIABILITY ASSAY.	495
FIGURE S8. CELLTITER GLO[®] VIABILITY TEST.....	501
FIGURE S9. CELL DEATH MECHANISM.	502
FIGURE S10. CELLULAR UPTAKE MECHANISM OF RU-SQ.	503
FIGURE S11. OXYGEN CONSUMPTION RATES AND DIFFERENT RESPIRATION PARAMETERS IN HELA CELLS ALONE OR AFTER TREATMENT WITH VARIOUS TEST COMPOUNDS.....	504

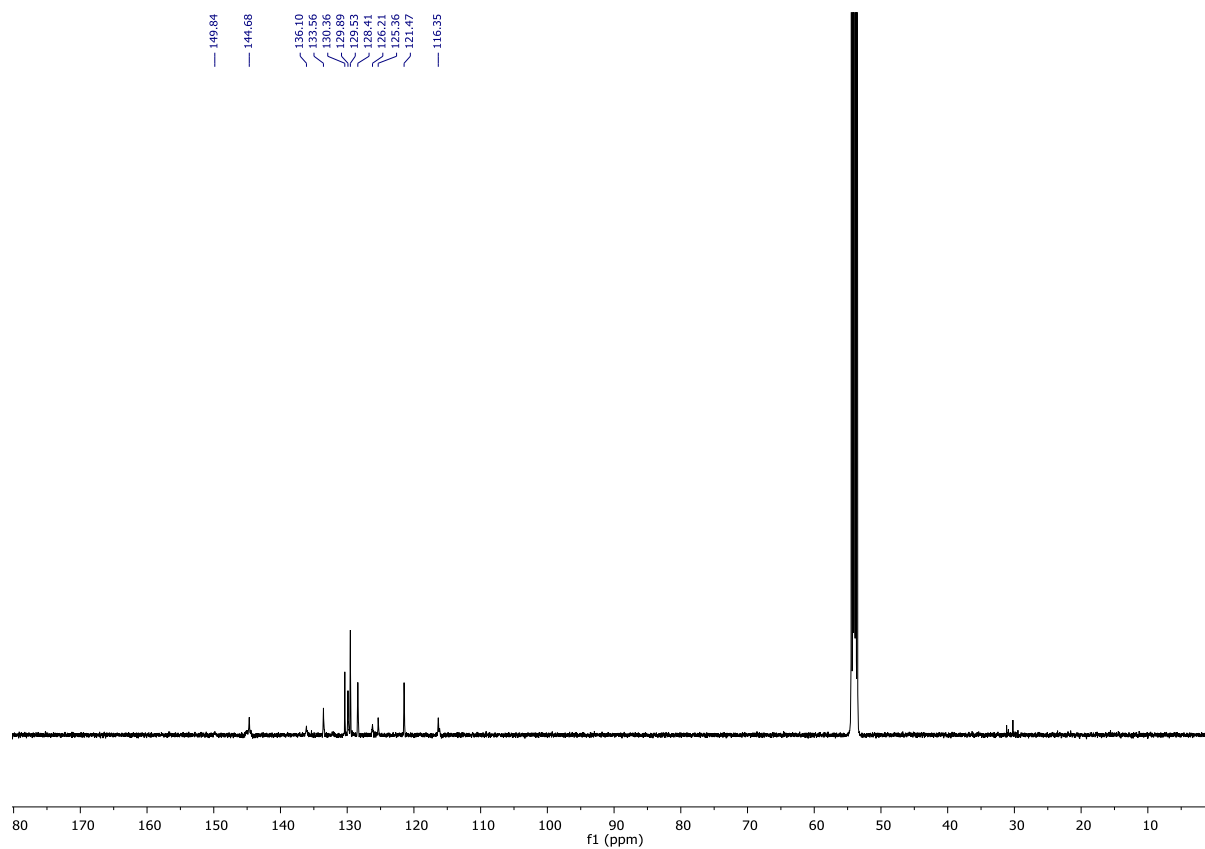
FIGURE S12. EXTRACELLULAR ACIDIFICATION RATE AND DIFFERENT PARAMETERS OF GLYCOLYTIC RESPIRATION IN HELA CELLS ALONE OR AFTER TREATMENT WITH VARIOUS TEST COMPOUNDS.	505
FIGURE S13. FUEL FLEX ASSAY IN HELA CELLS. DEPENDENCY STUDIES.....	506
FIGURE S14. AKT-1 PROTEIN LEVELS IN HELA CELLS TREATED WITH DIFFERENT CONCENTRATIONS OF RU-SQ, DOXORUBICIN AND CISPLATIN.....	507

1) Figure S1. NMR and HPLC spectra of Ru-sq.

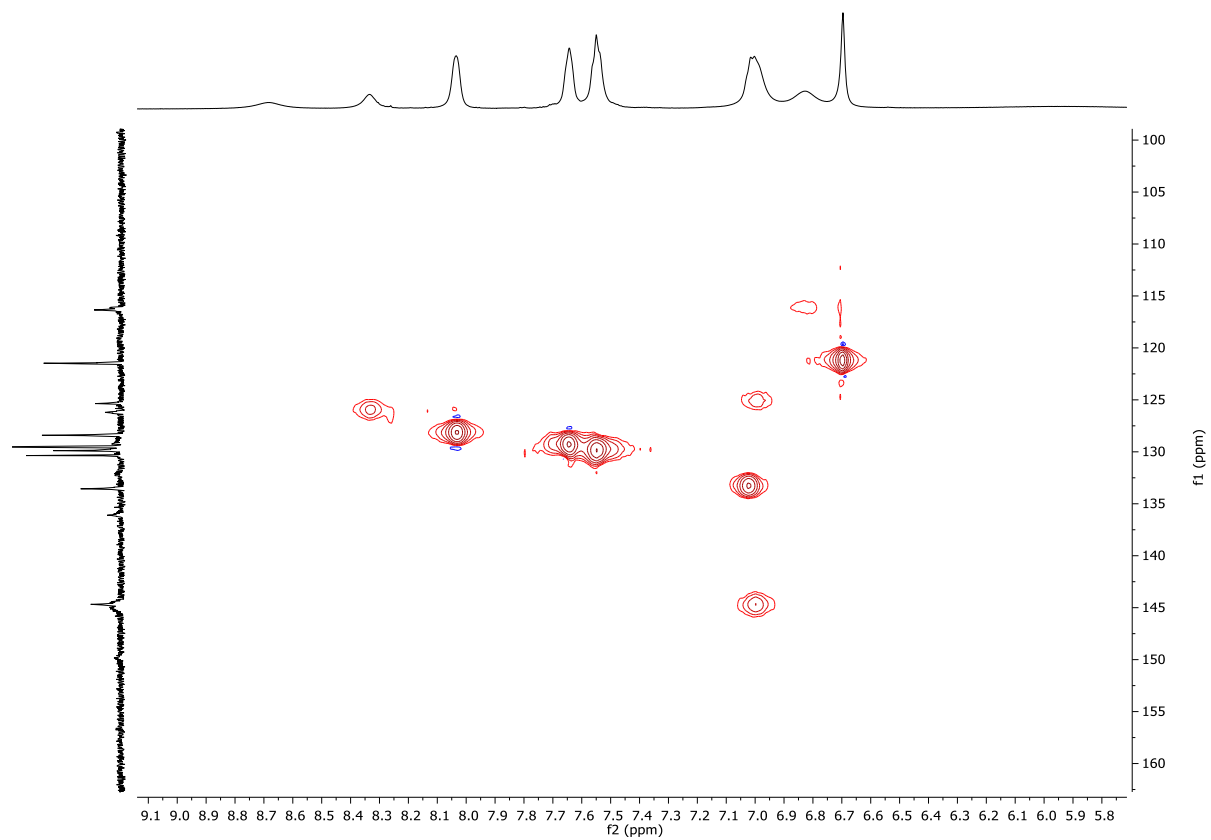
Ru-sq, ^1H , CD_2Cl_2 , 400 MHz



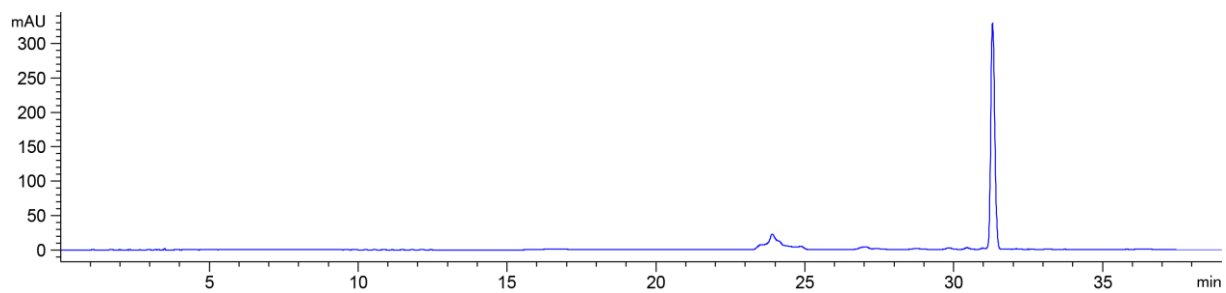
Ru-sq, ^{13}C , CD_2Cl_2 , 125 MHz



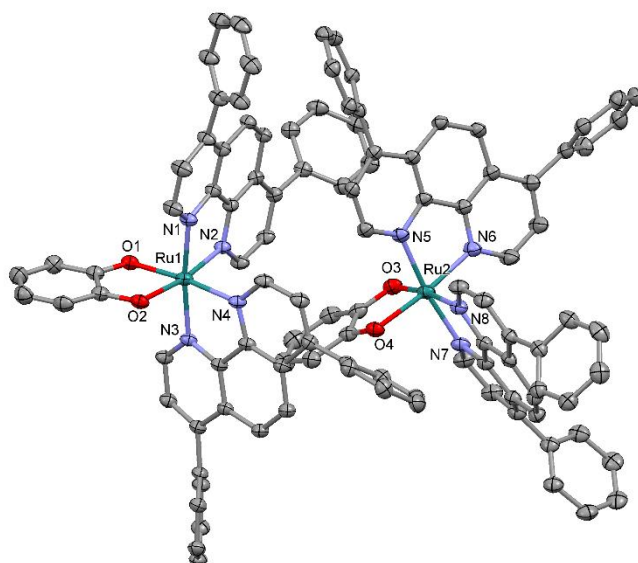
Ru-sq, 2D ^1H - ^{13}C HSQC, CD_2Cl_2 , 125 MHz



Ru-sq, HPLC trace recorded at 450nm



2) **Figure S2.** Crystallographic data of [Ru(DIP)₂(sq)](Cl).



Empirical formula	C ₁₀₈ H ₇₈ Cl ₂ N ₈ O ₇ Ru ₂
Formula weight	1872.82
Temperature/K	183(1)
Crystal system	monoclinic
Space group	P2 ₁ /c
a/Å	14.31140(10)
b/Å	23.42500(10)
c/Å	25.4275(2)
α/°	90
β/°	93.0470(10)
γ/°	90
Volume/Å ³	8512.38(10)
Z	4
ρ _{calc} /cm ³	1.457
μ/mm ⁻¹	3.983
F(000)	4324.0
Crystal size/mm ³	0.22 × 0.03 × 0.02
Radiation	Cu Kα (λ = 1.54184)
2θ range for data collection/°	5.132 to 149.008
Index ranges	-17 ≤ h ≤ 16, -29 ≤ k ≤ 20, -29 ≤ l ≤ 31
Reflections collected	74910
Independent reflections	17374 [R _{int} = 0.0425, R _{sigma} = 0.0339]
Data/restraints/parameters	17374/0/1161
Goodness-of-fit on F ²	1.031
Final R indexes [I ≥ 2σ(I)]	R ₁ = 0.0462, wR ₂ = 0.1187
Final R indexes [all data]	R ₁ = 0.0530, wR ₂ = 0.1237
Largest diff. peak/hole / e Å ⁻³	1.35/-0.79

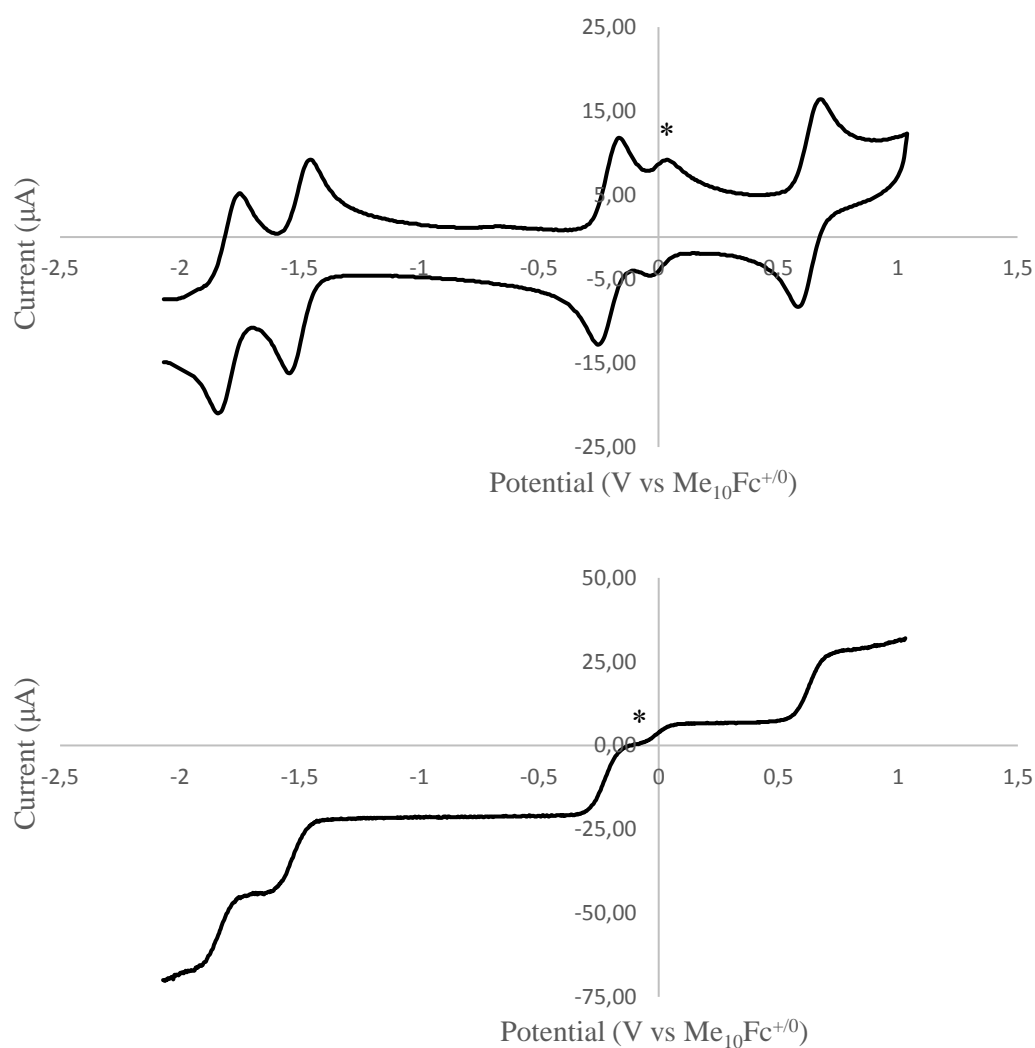
3) **Table S1.** Selected bond lengths and angles of **Ru-1** molecule.

Bond Atoms	Bond Length [Å]	Angle Atoms	Bond Angle [°]
Ru1-N1	2.052(2)	N1-Ru1-N2	79.72(10)
Ru1-N2	2.044(3)	N2-Ru1-N3	98.36(10)
Ru1-N3	2.067(2)	N3-Ru1-N1	172.13(11)
Ru1-N4	2.052(3)	N2-Ru1-N4	90.85(10)
Ru1-O1	2.033(2)	O1-Ru1-N1	92.97(10)
Ru1-O2	2.054(2)	O2-Ru1-N3	89.05(9)
O1-C1	1.309(4)	O1-Ru1-O2	81.03(9)
O2-C2	1.315(4)		

4) **Table S2.** Selected bond lengths and angles of **Ru-2** molecule.

Bond Atoms	Bond Length [Å]	Angle Atoms	Bond Angle [°]
Ru2-N5	2.067(3)	N5-Ru2-N6	79.68(11)
Ru2-N6	2.047(3)	N6-Ru2-N7	93.54(11)
Ru2-N7	2.058(3)	N7-Ru2-N5	171.19(12)
Ru2-N8	2.058(3)	N6-Ru2-N8	92.31(12)
Ru2-O3	2.035(3)	O3-Ru2-N5	92.21(11)
Ru2-O4	2.031(3)	O4-Ru2-N7	91.37(10)
O3-C55	1.319(4)	O3-Ru2-O4	81.19(10)
O4-C56	1.314(4)		

5) Figure S3. CV and RDE voltammograms of **Ru-sq** (from -2.1 to +1 V) at a glassy carbon electrode in DMF (1 mM) containing Bu₄NPF₆ (100 mM) as supporting electrolyte and decamethylferrocene as an internal standard (0.25 mM) versus calomel. Data were recorded versus saturated calomel electrode at scan rate of 100 mV/s and recalculated versus Me₁₀Fc^{0/+} potential value (feature marked with * in Figure S2).



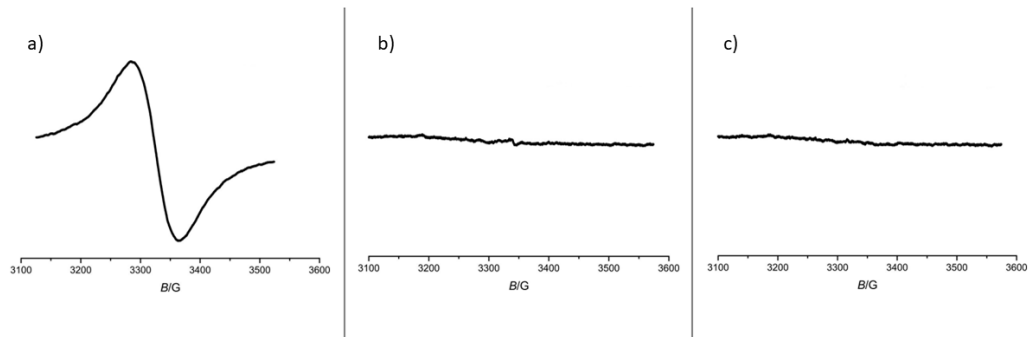
6) Table S3. Electrochemical data for **Ru-sq**.

		DIP^{0/-}	DIP^{0/-}	Sq/cat	Ru^{II/III}
Ru-sq	E_{1/2}^a [V] (RDE)	-1.876 ± 0.039	-1.578 ± 0.035	-0.249 ± 0.010	0.647 ± 0.018
	E_{1/2}^b [V] (CV)	-1.816 ± 0.015	-1.507 ± 0.007	-0.209 ± 0.002	0.623 ± 0.005

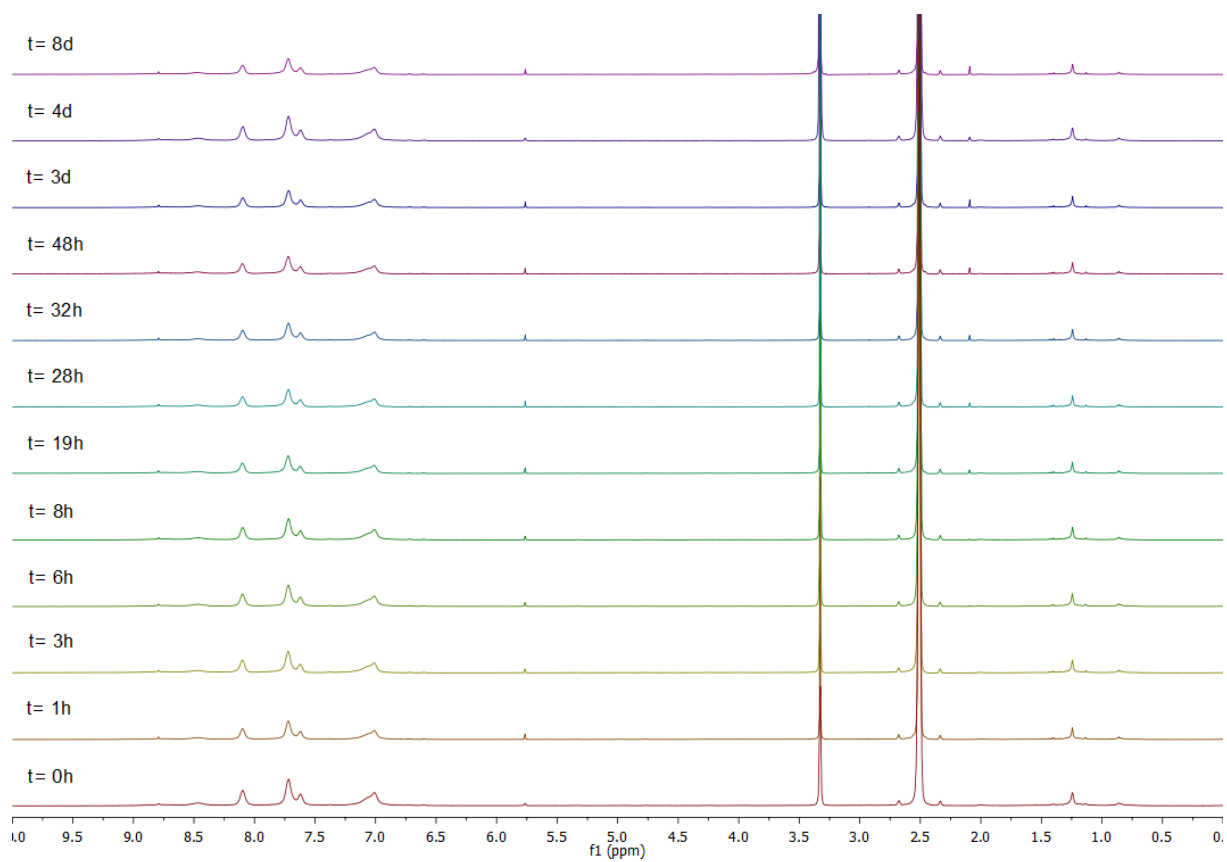
^a E_{1/2} = half-wave.

^b E_{1/2} = (E_{pa} + E_{pc})/2.

7) **Figure S4.** EPR spectra of **Ru-sq** (a), its reduced form **Ru-cat** (b), and its oxidized form **Ru-q** (c).

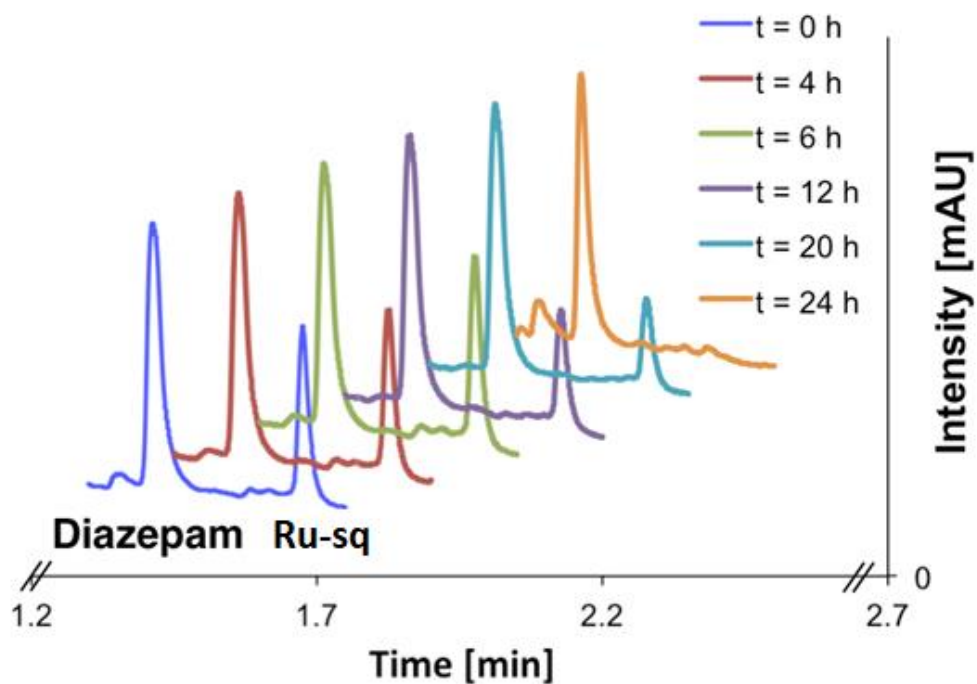


8) **Figure S5.** Overlap of ^1H spectra of **Ru-sq** in DMSO over 8 days.

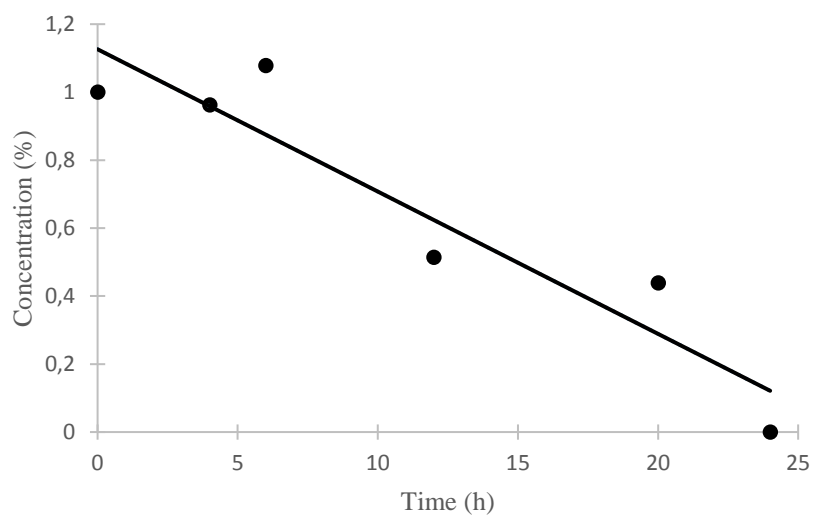


9) **Figure S6.** a) UV traces of UPLC analysis of **Ru-sq** incubated in human plasma at 37 °C for 0 h, 4 h, 6 h, 12 h, 20 h and 24 h using diazepam as an internal standard. b) Percentage concentration of **Ru-sq**, normalized with respect to the internal standard and plotted against time.

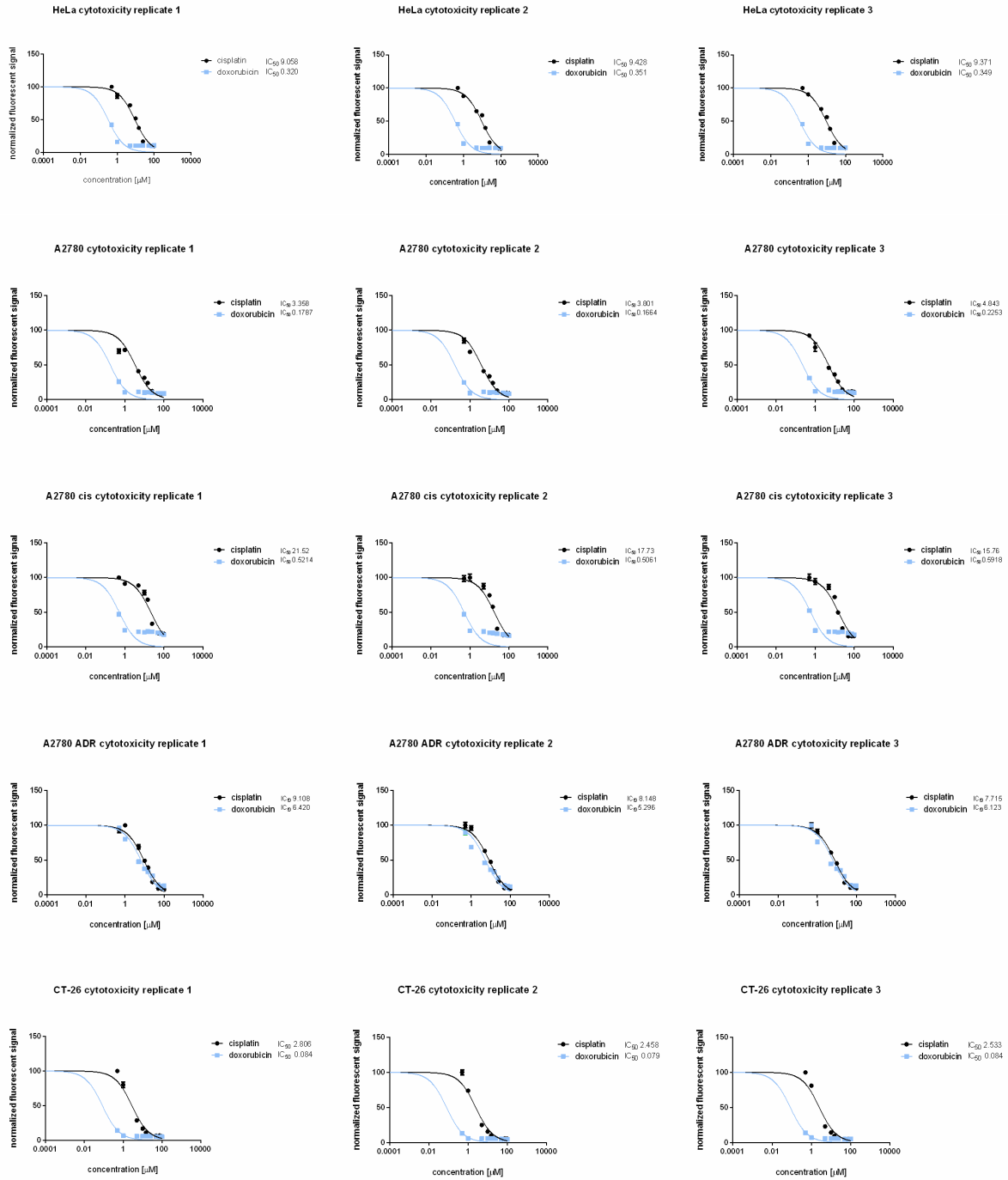
a)



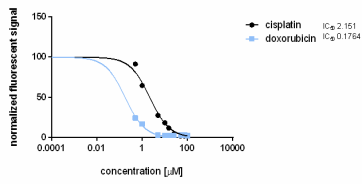
b)



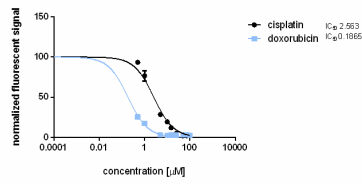
10) Figure S7. Fluorometric cell viability assay.



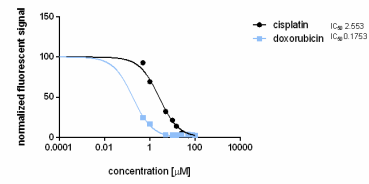
CT-26 LUC cytotoxicity replicate 1



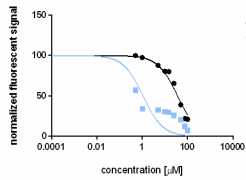
CT-26 LUC cytotoxicity replicate 2



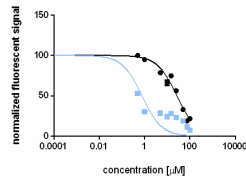
CT-26 LUC cytotoxicity replicate 3



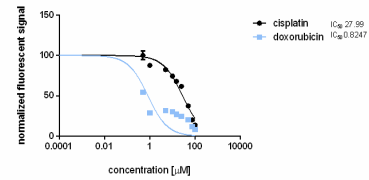
RPE-1 cytotoxicity replicate 1



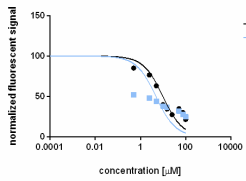
RPE-1 cytotoxicity replicate 2



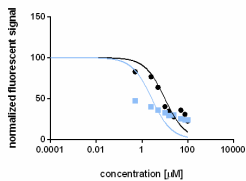
RPE-1 cytotoxicity replicate 3



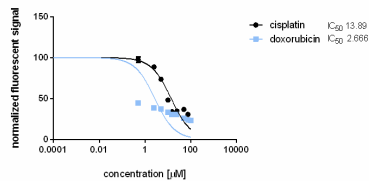
MRC-5 cytotoxicity replicate 1



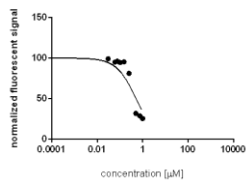
MRC-5 cytotoxicity replicate 2



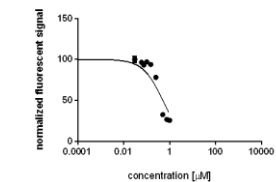
MRC-5 cytotoxicity replicate 3



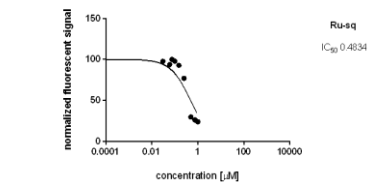
HeLa cytotoxicity replicate 1



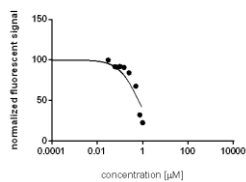
HeLa cytotoxicity replicate 2



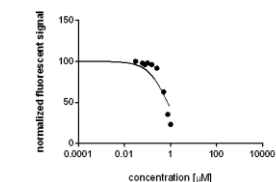
HeLa cytotoxicity replicate 3



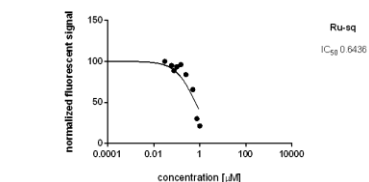
A2780 cytotoxicity replicate 1



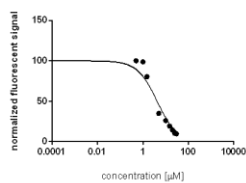
A2780 cytotoxicity replicate 2



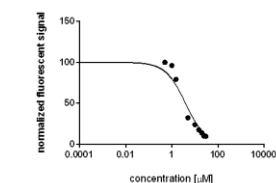
A2780 cytotoxicity replicate 3



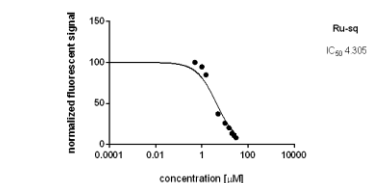
A2780 ADR cytotoxicity replicate 1



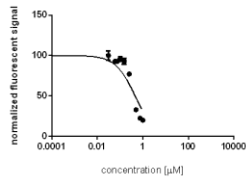
A2780 ADR cytotoxicity replicate 2



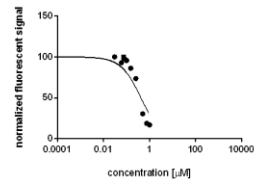
A2780 ADR cytotoxicity replicate 3



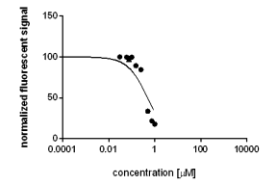
A2780 cis cytotoxicity replicate 1



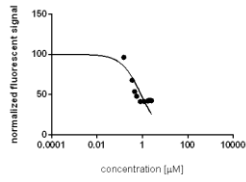
A2780 cis cytotoxicity replicate 2



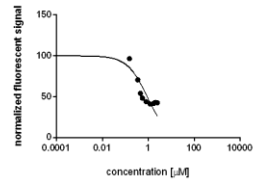
A2780 cis cytotoxicity replicate 3



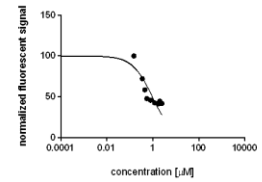
CT-26 cytotoxicity replicate 1



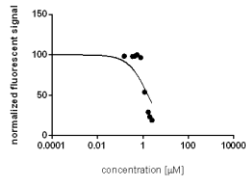
CT-26 cytotoxicity replicate 2



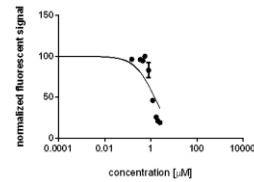
CT-26 cytotoxicity replicate 3



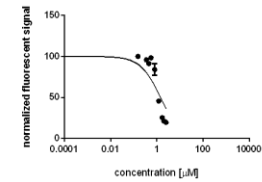
CT-26 LUC cytotoxicity replicate 1



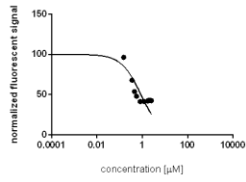
CT-26 LUC cytotoxicity replicate 2



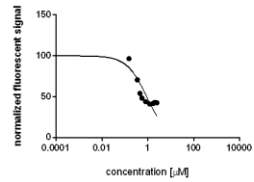
CT-26 LUC cytotoxicity replicate 3



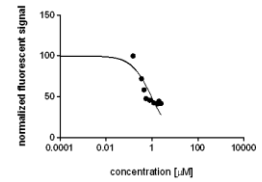
RPE-1 cytotoxicity replicate 1



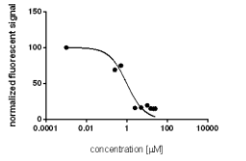
RPE-1 cytotoxicity replicate 2



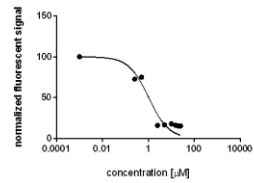
RPE-1 cytotoxicity replicate 3



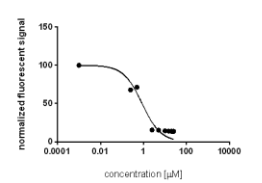
MRC-5 cytotoxicity replicate 1

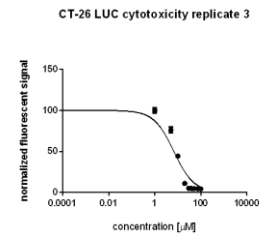
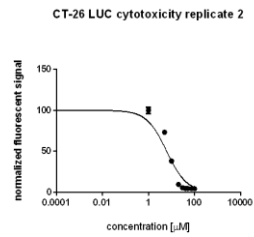
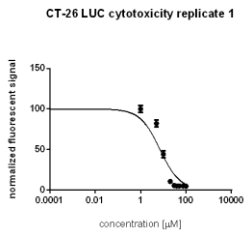
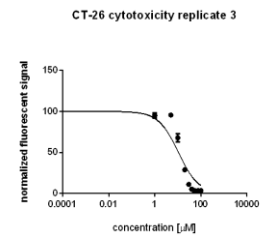
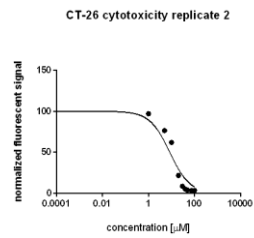
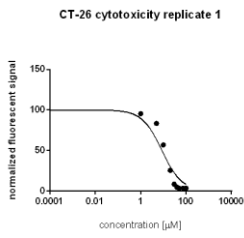
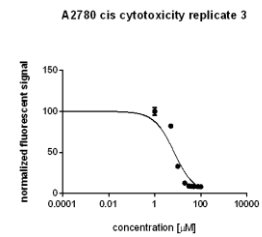
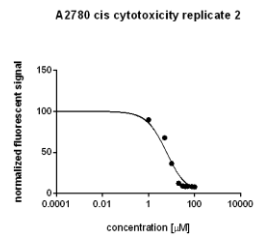
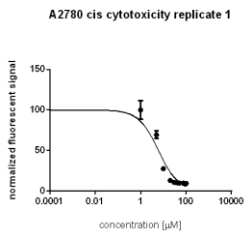
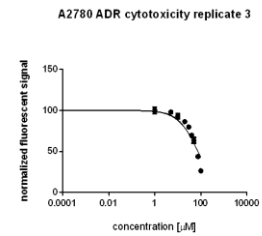
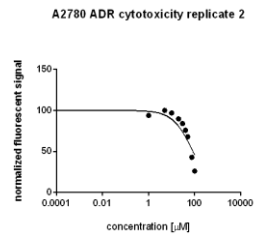
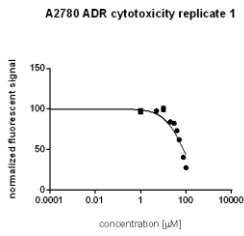
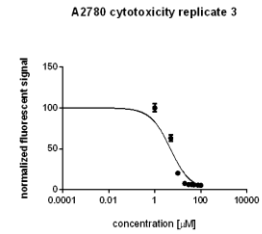
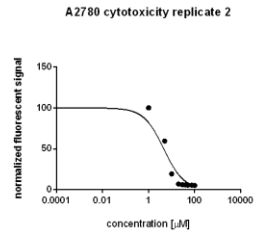
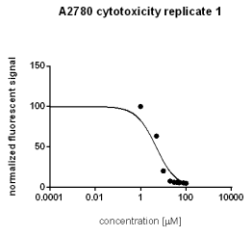
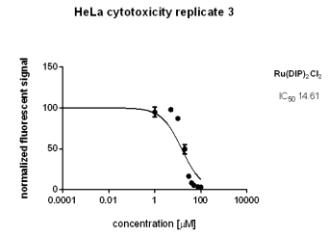
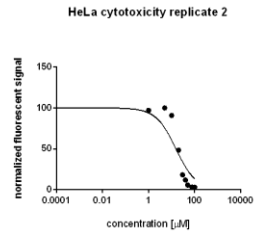
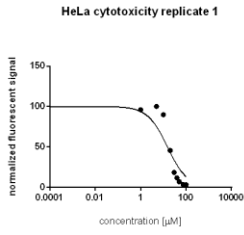


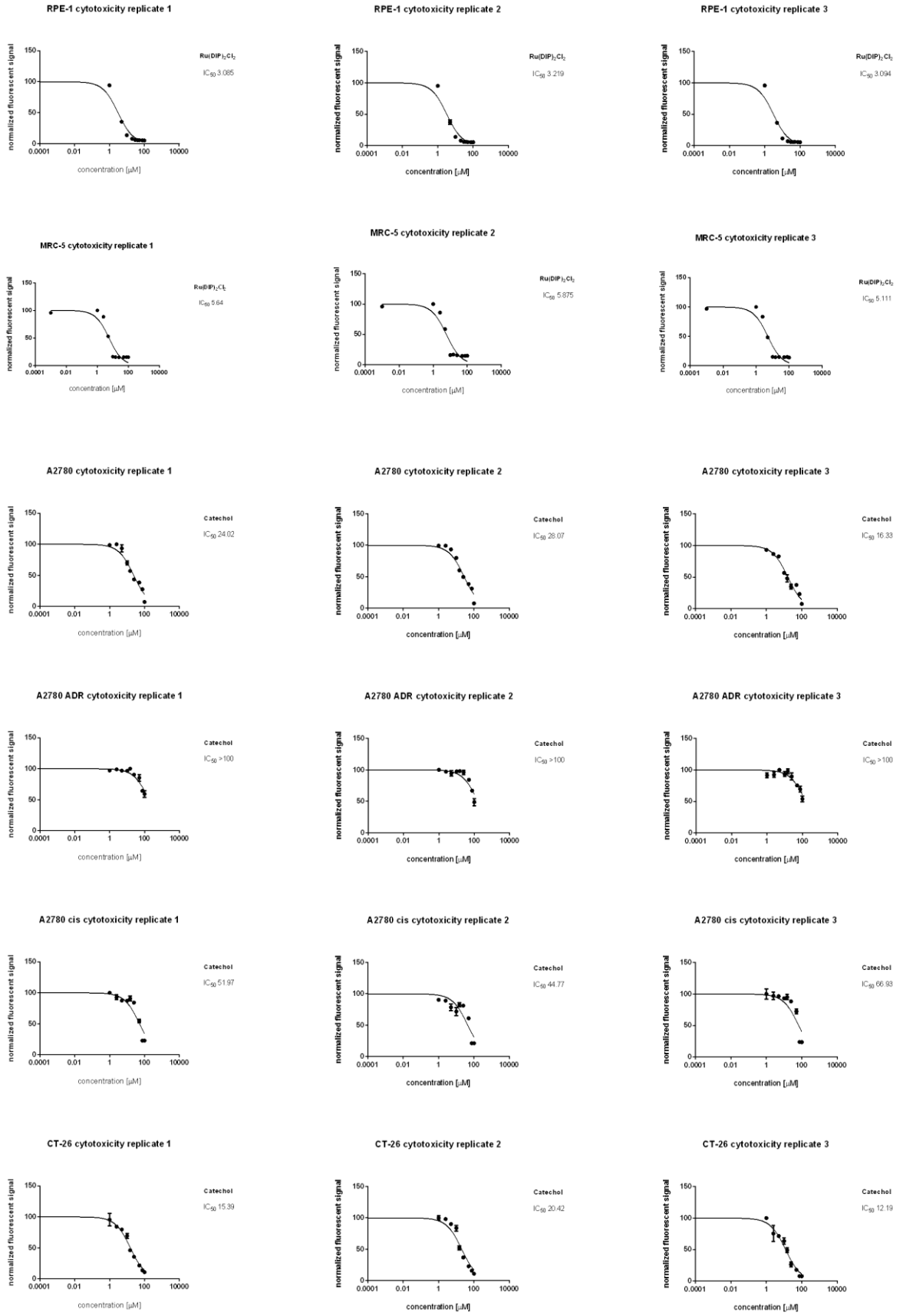
MRC-5 cytotoxicity replicate 2

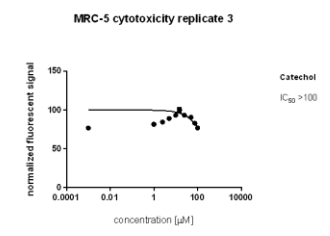
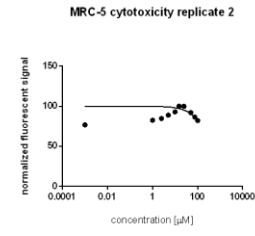
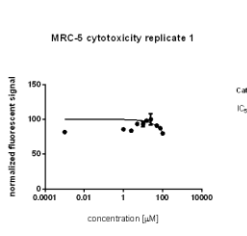
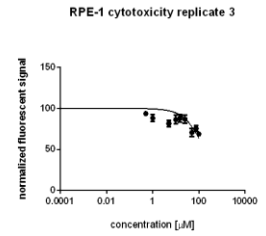
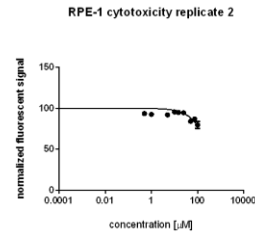
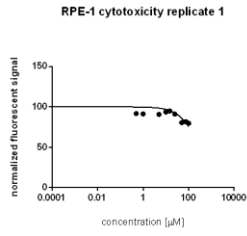
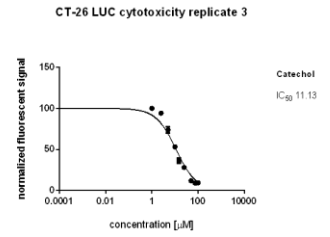
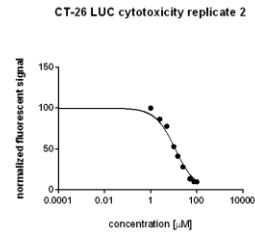
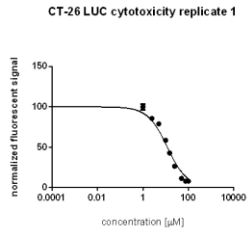


MRC-5 cytotoxicity replicate 3

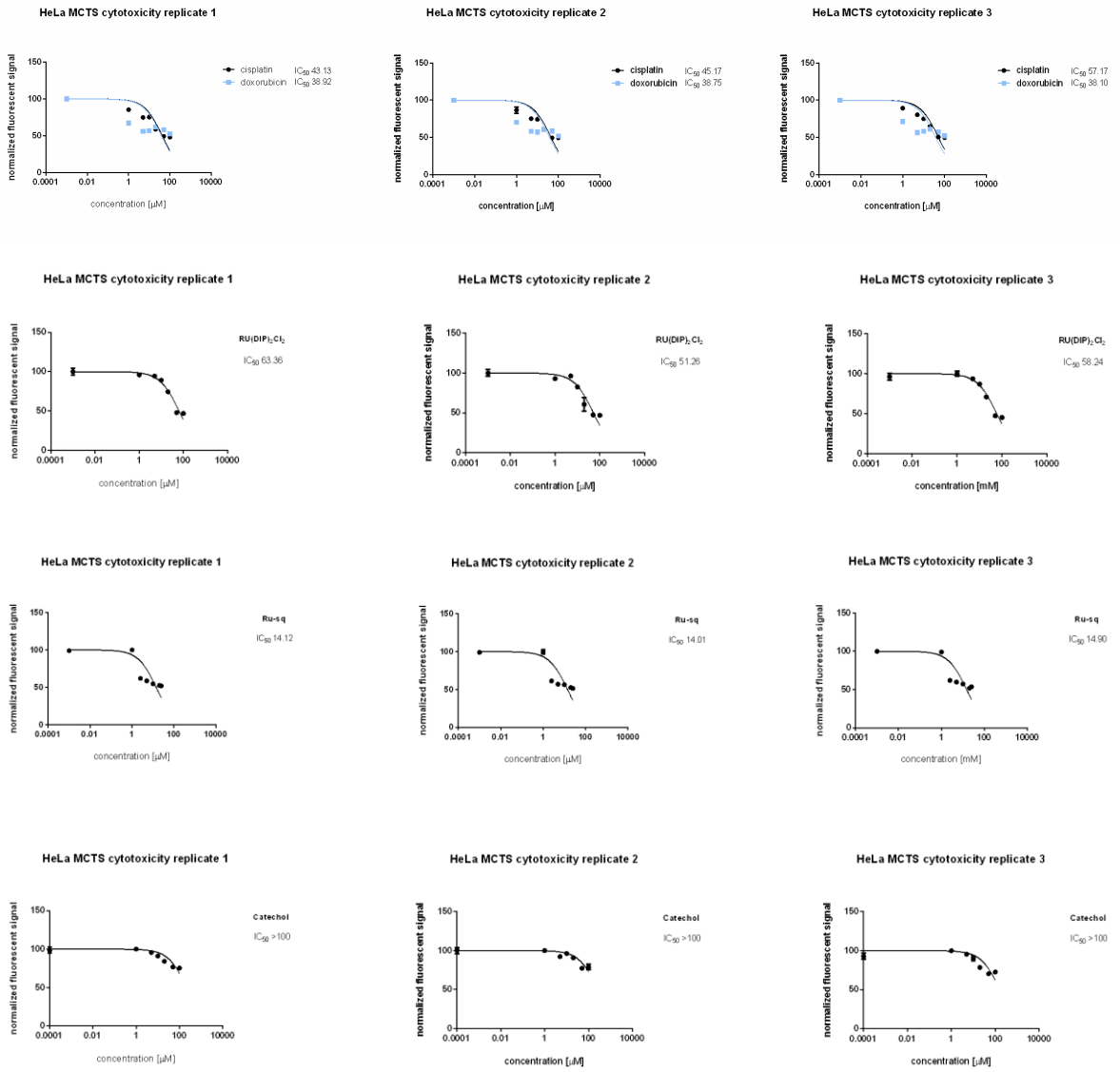




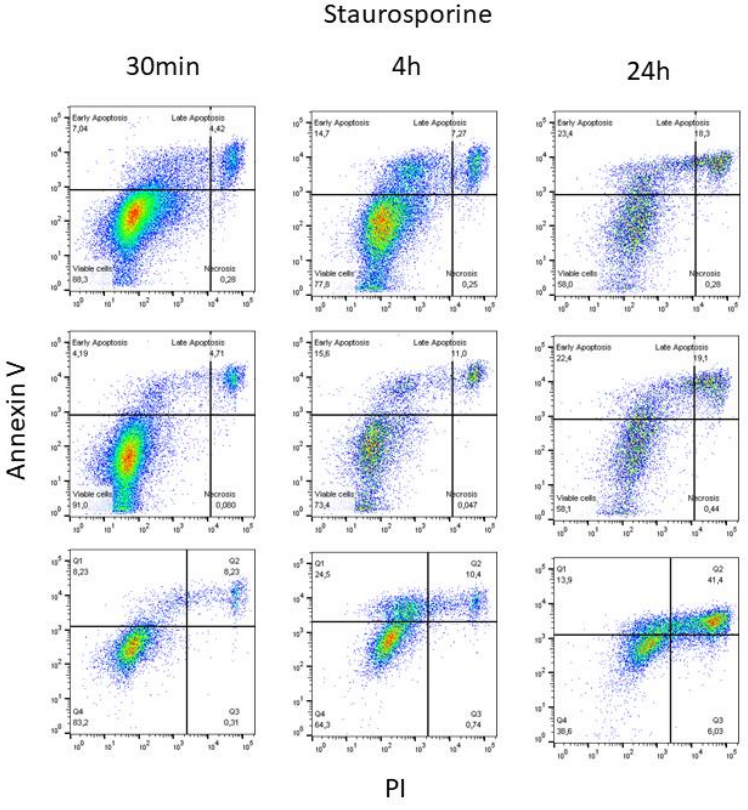
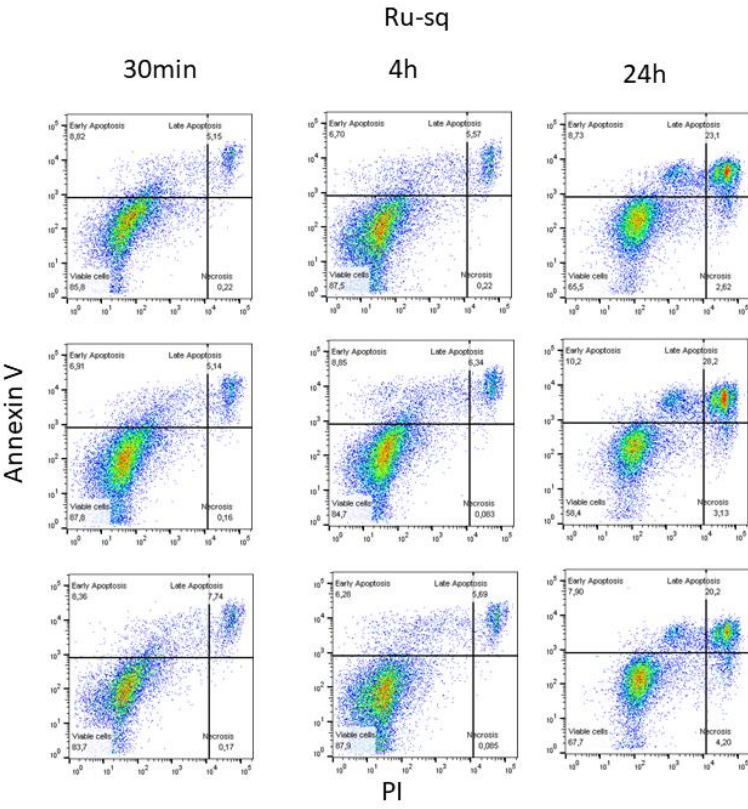




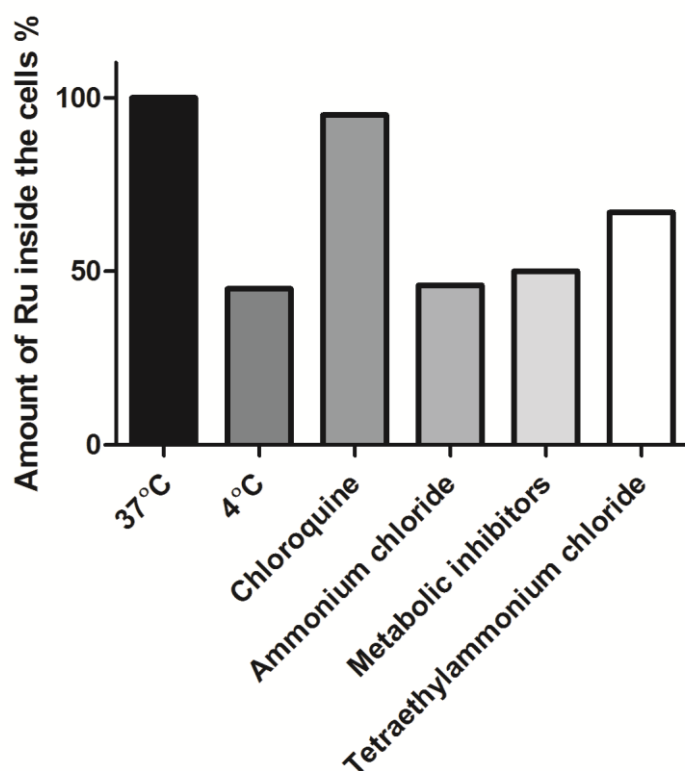
11) Figure S8. CellTiter Glo® viability Test.



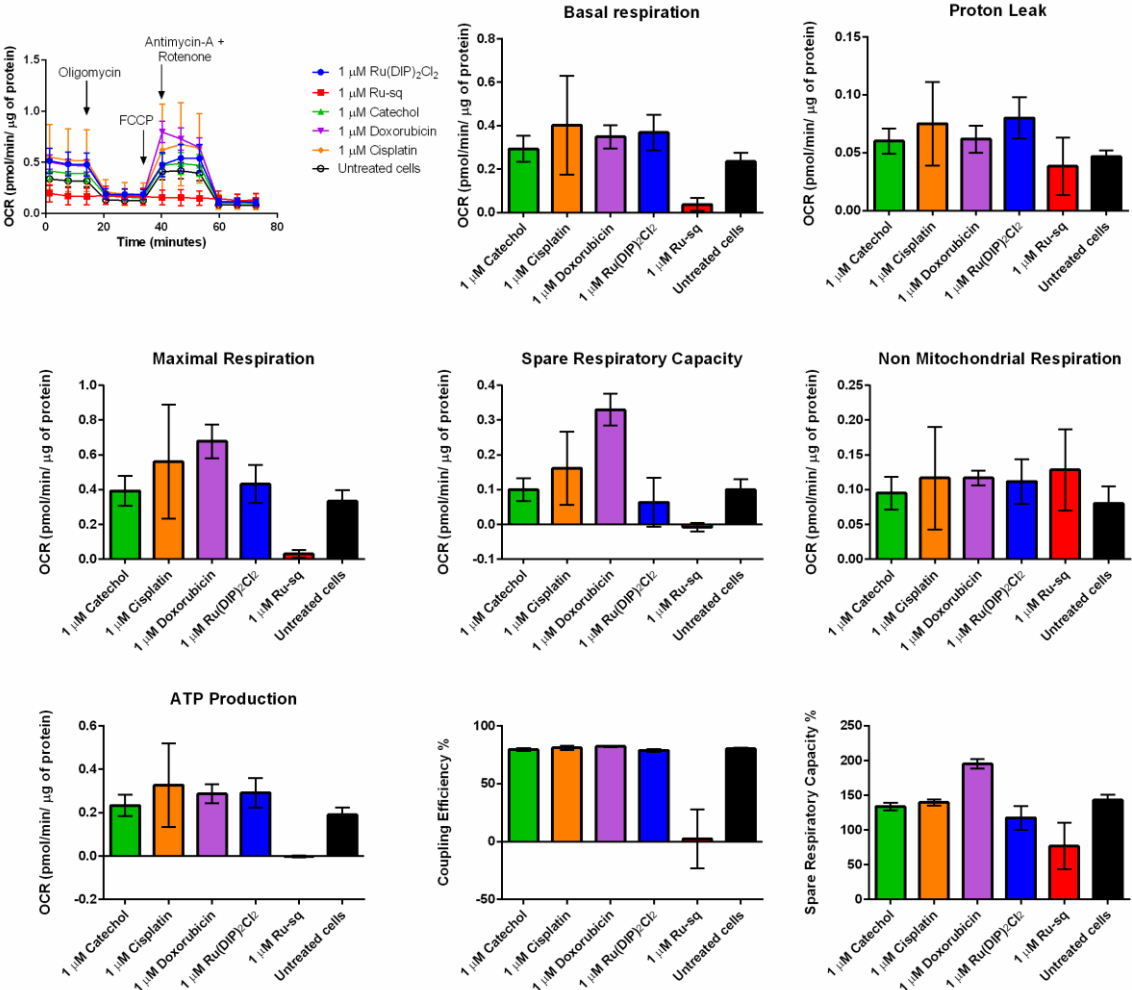
12) Figure S9. Cell Death Mechanism.



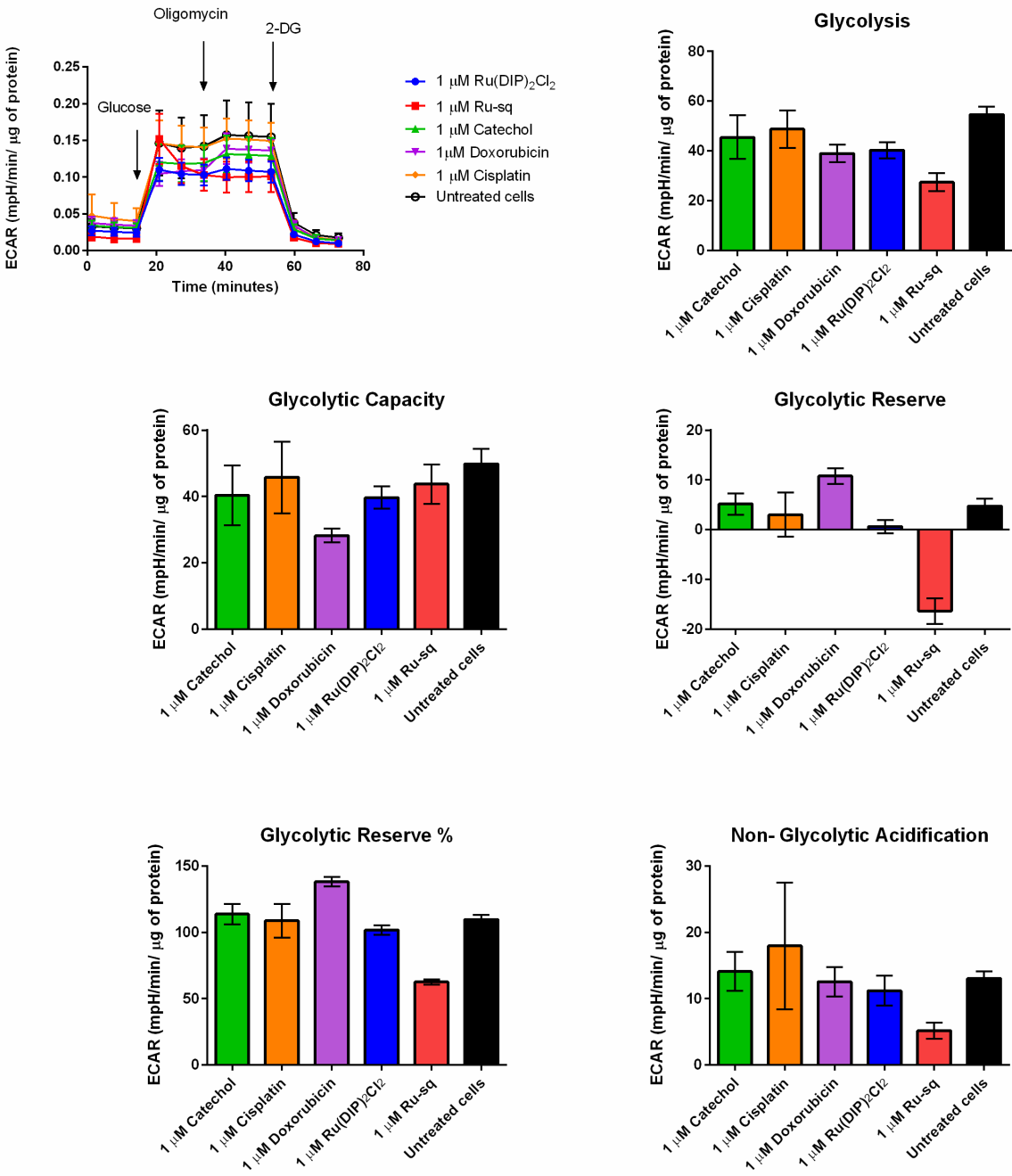
13) Figure S10. Cellular uptake mechanism of **Ru-sq**. Accumulation of ruthenium in HeLa cells in presence of different inhibitors and conditions: low temperature (4°C), blocked cellular metabolism (2-Deoxy-*D*-glucose, oligomycin), blocked endocytic pathways (chloroquine or ammonium chloride), blocked cation transporters (tetraethylammonium chloride). Cells were pre-treated with uptake inhibitors and then incubated with Ru-sq (2 h, 5 μM). Amounts of ruthenium were measured using ICP-MS.



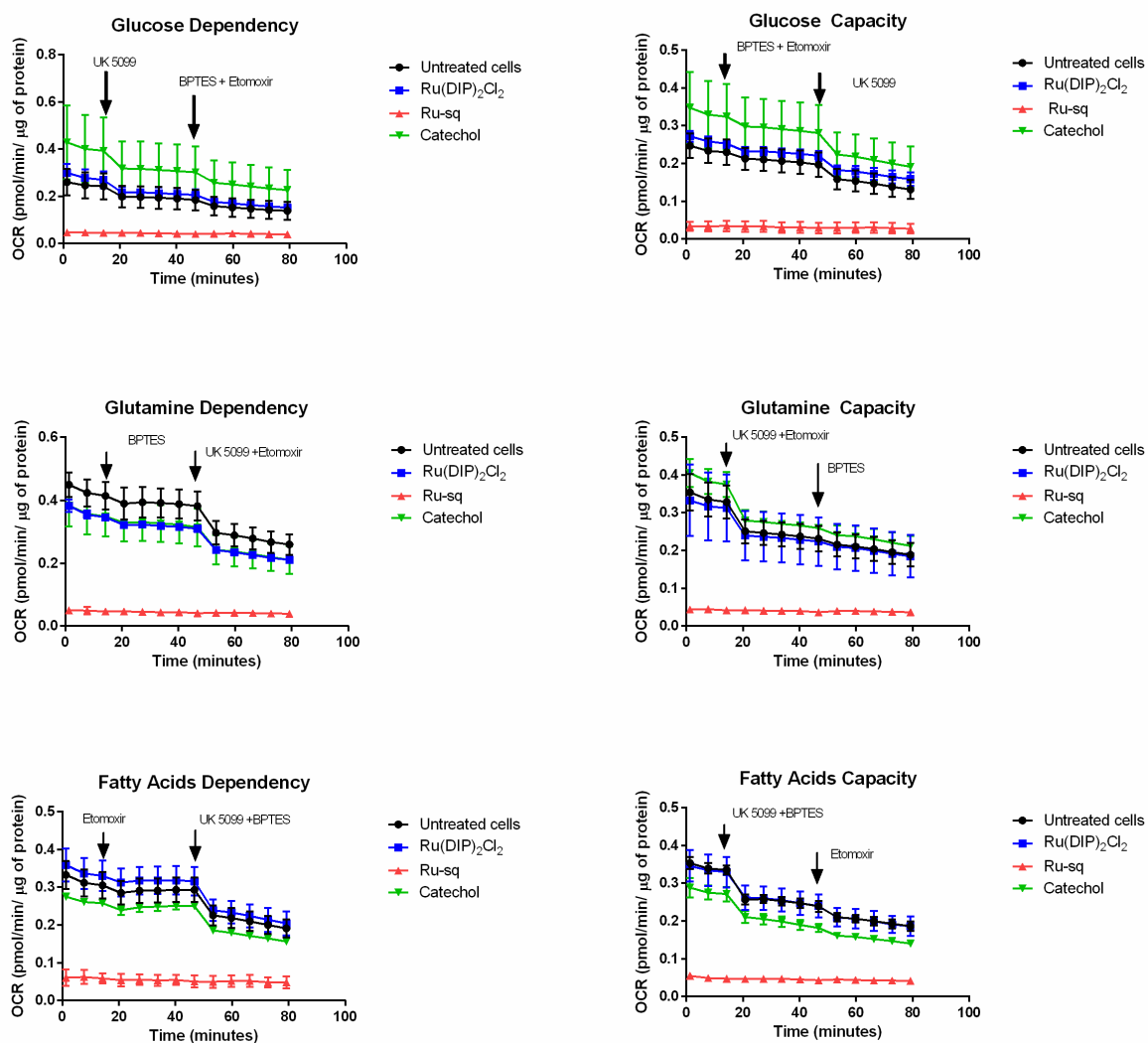
14) Figure S11. Oxygen consumption rates and different respiration parameters in HeLa cells alone or after treatment with various test compounds.



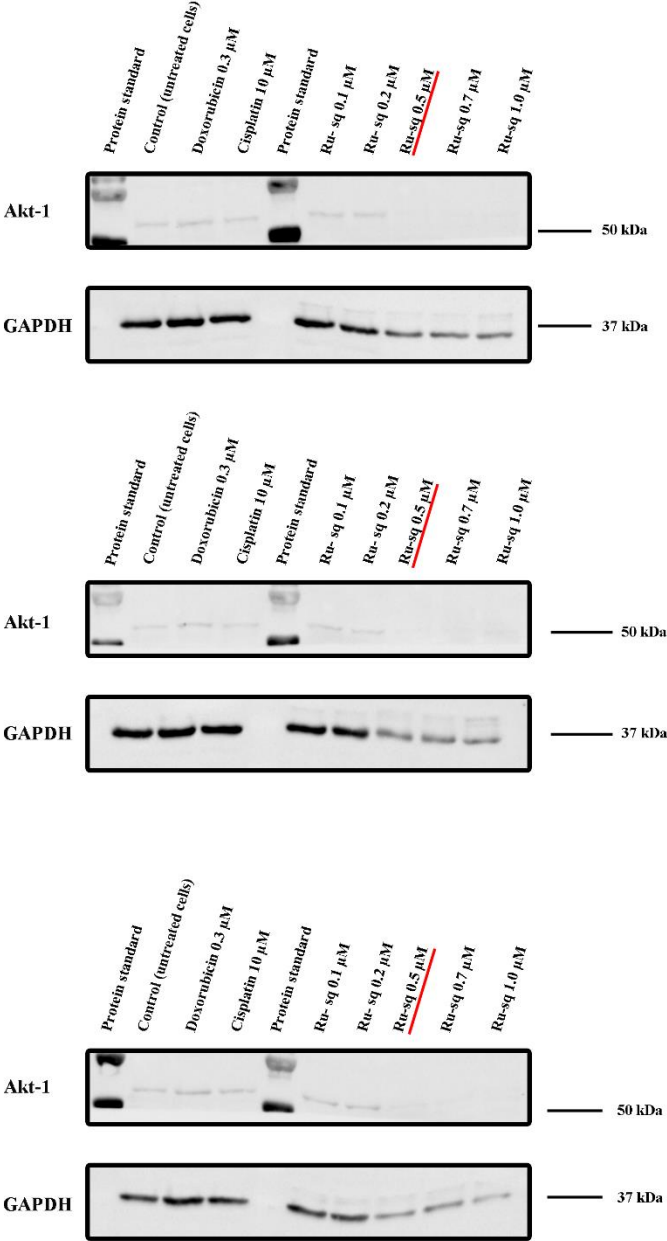
15) **Figure S12.** Extracellular acidification rate and different parameters of glycolytic respiration in HeLa cells alone or after treatment with various test compounds.



16) Figure S13. Fuel flex assay in HeLa cells. Dependency studies were performed by adding the inhibitor for the target pathway in port A and inhibitors for the other two pathways in port B while capacity studies were done using the reverse sequence. UK-5099 (20 μM), BPTES (30 μM) and etomoxir (40 μM) were used as the inhibitors for the glucose, glutamine and fatty acid pathways respectively.



17) **Figure S14.** Akt-1 protein levels in HeLa cells treated with different concentrations of Ru-sq, doxorubicin and cisplatin. Untreated cells were used as a control. Figure represents three independent experiments.



Chapter 8- A maltol-containing Ruthenium Polypyridyl Complex as a Potential Anticancer Agent

*Anna Notaro,^[a] Marta Jakubaszek,^[a, b] Severin Koch,^[c] Riccardo Rubbiani,^[c] Orsolya
Dömötör,^[d] Éva A. Enyedy,^[d, e] Mazzarine Dotou,^[a] Fethi Bedioui,^[f] Mickaël Tharaud,^[g]
Bruno Goud,^[b] Stefano Ferrari,^[h, i] Enzo Alessio,^[j] and Gilles Gasser*^[a]*

- ^[a] Chimie ParisTech, PSL University, CNRS, Institute of Chemistry for Life and Health Sciences, Laboratory for Inorganic Chemical Biology, F-75005 Paris, France.
- ^[b] Institut Curie, PSL University, CNRS UMR 144, Paris, France.
- ^[c] Department of Chemistry, University of Zurich, Winterthurerstrasse 190, 8057 Zurich, Switzerland.
- ^[d] Department of Inorganic and Analytical Chemistry, Interdisciplinary Excellence Centre, University of Szeged, Dóm tér 7. H-6720 Szeged, Hungary.
- ^[e] MTA-SZTE Momentum Functional Metal Complexes Research Group, University of Szeged, Dóm tér 7, H-6720 Szeged, Hungary.
- ^[f] Chimie ParisTech, PSL University, CNRS, Institute of Chemistry for Life and Health Sciences, Team Synthèse, Electrochimie, Imagerie et Systèmes Analytiques pour le Diagnostic, F-75005 Paris, France.
- ^[g] Université de Paris, Institut de physique du globe de Paris, CNRS, F-75005 Paris, France.
- ^[h] Institute of Molecular Cancer Research, University of Zurich, Zurich, Switzerland.
- ^[i] Institute of Molecular Genetics of the Czech Academy of Sciences, Videnska 1083, 143 00 Prague, Czech Republic.
- ^[j] Department of Chemical and Pharmaceutical Sciences, University of Trieste, Via L. Giorgieri 1, 34127 Trieste, Italy.

* Corresponding author: E-mail: gilles.gasser@chimeparistech.psl.eu; WWW: www.gassergroup.com; Phone: +33 1 44 27 56 02

This chapter has been published on 17th of February 2020 on *Chemistry – A European Journal* (10.1002/chem.201904877)

Reproduced by permission of Wiley-VCH Verlag GmbH & Co.

(<https://chemistry-europe.onlinelibrary.wiley.com/doi/abs/10.1002/chem.201904877>)

Contribution to the publication:

Marta Jakubaszek performed with Anna Notaro the 2D cytotoxicity studies, Annexin V and PI staining, cellular uptake, biodistribution and DNA metalation studies. She performed the JC-1 membrane potential test, mitochondrial metabolic studies and 3D cell culture experiments. She analysed together with Anna Notaro obtained data and wrote with her contribution the cytotoxicity studies, cellular uptake, intracellular distribution, DNA metalation and JC-1 staining sections. She wrote mechanism of cell death, mitochondrial metabolic studies and 3D cell culture sections.

Marta Jakubaszek



19.05.2020

Gilles Gasser



Keywords: Bioinorganic Chemistry, Cancer, DNA, Medicinal Inorganic Chemistry, Ruthenium.

Abstract

Cancer is one of the main causes of death worldwide. Chemotherapy, despite its severe side effects, is to date one of the leading strategies against cancer. Metal-based drugs present several potential advantages when compared to organic ones and gained trust from the scientific community after the approval on the market of the drug cisplatin. Recently, we reported a ruthenium complex ($[\text{Ru}(\text{DIP})_2(\text{sq})](\text{PF}_6)$ where DIP is 4,7-diphenyl-1,10-phenantroline and sq is the semiquinonate), with a remarkable potential as chemotherapeutic agent against cancer, both *in vitro* and *in vivo*. In this work, we analyse a structurally similar compound, namely $[\text{Ru}(\text{DIP})_2(\text{mal})](\text{PF}_6)$, carrying the flavour-enhancing agent approved by the FDA, maltol (mal). To possess an FDA approved ligand is crucial for a complex, whose mechanism of action might include ligand exchange. Herein, we describe the synthesis and characterisation of $[\text{Ru}(\text{DIP})_2(\text{mal})](\text{PF}_6)$, its stability in solutions and in conditions which resemble the physiological ones, and its in-depth biological investigation. Cytotoxicity tests on different cell lines in 2D model and on HeLa MultiCellular Tumour Spheroids (MCTS) demonstrated that our compound has higher activity compared to the approved drug cisplatin, inspiring further tests. $[\text{Ru}(\text{DIP})_2(\text{mal})](\text{PF}_6)$ was efficiently internalised by HeLa cells through a passive transport mechanism and severely affected the mitochondrial metabolism.

Introduction

Metal-based drugs are currently playing an essential role in the treatment of cancer.¹ Cisplatin, carboplatin and oxaliplatin are widely used in the clinics.^{2,3} Ruthenium complexes are, to date, the most promising candidates for the next generation of metal-based drugs against cancer.⁴⁻⁶ The Ru(III) complexes KP1019, KP1339 (referred as IT-139 recently) and NAMI-A have entered clinical trials as anticancer drugs,⁷⁻¹¹ while TLD-1433 – a substitutionally inert Ru(II) polypyridyl complex – recently entered phase II clinical trial as a photosensitizer for photodynamic therapy (PDT).^{12,13} Inert Ru polypyridyl complexes hold a tremendous potential as chemotherapeutic agents against cancer.¹⁴⁻¹⁶ Recently, we reported the in-depth biological investigation of a very promising Ru(II) polypyridyl complex carrying a semiquinonate ligand (**[Ru(DIP)₂(sq)](PF₆)**) (Figure 1, DIP = 4,7-diphenyl-1,10-phenantroline, sq = semiquinonate).¹⁷ We could notably show that this complex had a much higher cytotoxicity than cisplatin in several cancer cell lines (i.e. in the nanomolar concentration range), and a very promising *in vivo* activity. Moreover, contrary to cisplatin, **[Ru(DIP)₂(sq)](PF₆)** results in mitochondrial dysfunction as one of its modes of action.¹⁷

Maltol, (3-hydroxy-2-methyl-4-pyrone), belonging to the family of 2-alkyl-3-hydroxy-4-pyrones, is structurally very similar to sq and – upon deprotonation – forms stable 5-membered chelate rings with metal ions. Maltol is a product of carbohydrate degradation, which can be found in coffee, baked cereals, chicory, soybeans and other products.^{18,19} It possesses candy-floss, sweet flavour, and is approved by the FDA as a flavour-enhancing agent.^{18,20,21} Maltol is known for its antioxidative properties²² and its ability to chelate metal ions. It is an effective ligand for increasing absorption and bioavailability of metal ions.²³⁻³³ Maltol has been tested on different human cell lines, confirming lack of toxicity with IC₅₀ (the half maximal inhibitory concentration) values always above 100 μM.^{34,35} In 2006, Thompson and co-workers reported a critical review about the applications of maltol-containing metal complexes in medicinal

chemistry.²⁸ One of them concerns the restoration of iron balance in anaemia. The uptake of iron has indeed been proven to be significantly enhanced in the presence of maltol, in both *in vitro* and *in vivo* models.^{36,37} The bis(maltolato)oxovanadium(IV) complex developed by Orvig and co-workers (better known as **BMOV**, Figure 1) was found to have a high anti-diabetic activity as insulin mimetic agent, and its derivative – the orally administered bis(ethylmaltolato)oxovanadium(IV) (**BEOV** in Figure 1) – was tested in phase IIa.^{24,29,38–41} Gallium maltolate, (tris(3-hydroxy-2-methyl-4H-pyran-4-onato)gallium (**GaM**), Figure 1), recently has completed phase II clinical trials for the treatment of malignant lymphomas, multiple myeloma, bladder neoplasm and prostatic neoplasms.^{42–45} It was found to be better orally absorbed than simple gallium salts (such as the chloride or nitrate).⁴² This higher oral bioavailability offers the possibility of a more convenient and tolerable achievement of therapeutically useful blood gallium levels.^{42,43} The great potential demonstrated by **GaM** led to the investigation of other possible applications of this compound in medicine (e.g., treatment of *Pseudomonas aeruginosa* infection, the neglected tropical disease yaws, and other types of cancer).^{46–49} Mononuclear and dinuclear maltol-containing half-sandwich ruthenium(II) complexes have been extensively investigated in the past decades as chemotherapeutic agents against cancer.^{31,33,50,51} However, only dinuclear species were found to have significant cytotoxicity toward human cancer cell lines ($IC_{50} < 10 \mu M$).^{33,51}

With this mind, in this work we present a novel Ru(II)-maltol polypyridyl complex, namely **[Ru(DIP)₂(mal)](PF₆)** (mal = maltolate) shown in Figure 1. To the best of our knowledge, **[Ru(DIP)₂(mal)](PF₆)** is the first maltol-containing ruthenium polypyridyl complex investigated as a chemotherapeutic agent against cancer. **[Ru(DIP)₂(mal)](PF₆)** is chiral and is isolated as a racemic mixture of Δ and Λ enantiomers. No attempt to work with enantiopure complexes was made in this work. In this study, besides the synthesis and characterisation of **[Ru(DIP)₂(mal)](PF₆)**, we report its binding to human serum albumin (HSA) and its biological

activity against different human cancer cell lines. Due to the high cytotoxicity expressed by **[Ru(DIP)₂(mal)](PF₆)**, additional biological studies were undertaken to obtain more insights about the possible targets and mechanism(s) of action of the compound. As described below, **[Ru(DIP)₂(mal)](PF₆)** was found to be highly cytotoxic against HeLa MCTS (Multicellular tumour spheroids) and to be efficiently internalised by HeLa cells. Its accumulation in cytoplasm, lysosomes, nucleus and mitochondria suggests a mechanism of action involving multicellular targets, which does not exclude ligand exchange at the metal centre.

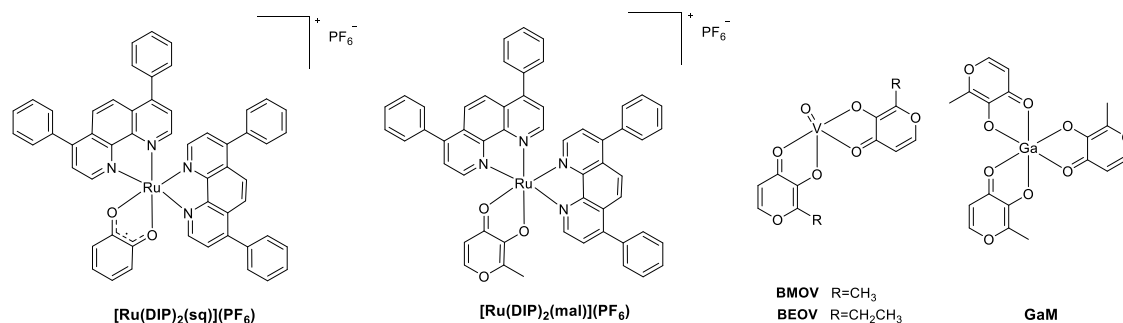


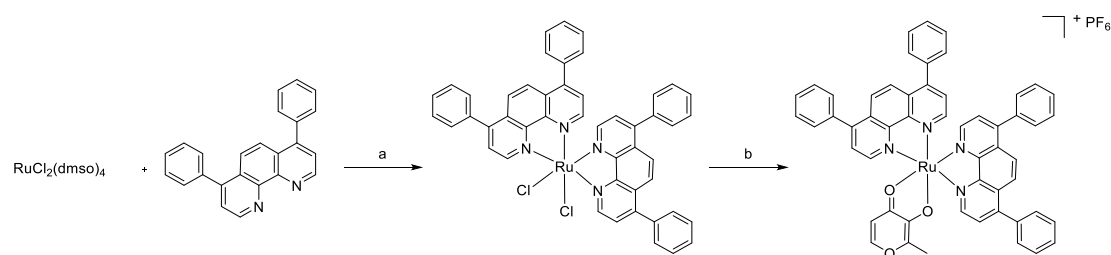
Figure 1. Structures of **[Ru(DIP)₂(sq)](PF₆)**, **[Ru(DIP)₂(mal)](PF₆)**, **BMOV**, **BEOV** and **GaM**.

Results and Discussion

Synthesis and characterization of **[Ru(DIP)₂(mal)](PF₆)**

The synthesis of **[Ru(DIP)₂(mal)](PF₆)** was achieved in two steps (Scheme 1). In the first step the known Ru(II) precursor RuCl₂(dms_o)₄⁵² was treated with DIP and LiCl in refluxing DMF to afford RuCl₂(DIP)₂ in 72% yield after precipitation with acetone.⁵³ The ruthenium intermediate was then refluxed in ethanol with maltol in the presence of NaOH for 3 h. **[Ru(DIP)₂(mal)](PF₆)** was obtained after precipitation with a large excess of NH₄PF₆ in 90% yield. The identity of the product was confirmed by ¹H and ¹³C NMR spectroscopy (Figure S1) as well as HR-MS, and its purity by microanalysis. The number of resonances showed in the

^1H is consistent with the inequivalence of the two DIP ligands, due to the asymmetry of maltolate.



Scheme 1. Synthesis of $[\text{Ru}(\text{DIP})_2(\text{mal})](\text{PF}_6)$. a) LiCl, DMF, reflux, 24 h, 78%; b) (i) NaOH, maltol, ethanol, reflux, 3 h; (ii) NH_4PF_6 , ethanol/ H_2O (1:10), yield: 90%.

Electrochemistry

The electrochemical properties of $[\text{Ru}(\text{DIP})_2(\text{mal})](\text{PF}_6)$ were investigated using cyclic voltammetry (CV) and rotating disc electrode (RDE) voltammetry. The RDE voltammogram (Figure S2) displays three well-defined wave features, in addition to that of decamethylferrocene used as internal reference and located at +0.090 V vs SCE. These electrochemical features are characterized by the same current intensity, which attests that the related redox processes involve the same number of electron transitions (in this case one-electron transition). CV experiment (Figure S2) showed the complete reversibility of the redox processes. The redox potentials were assigned by comparison with the data reported in our recent paper on $[\text{Ru}(\text{DIP})_2(\text{sq})](\text{PF}_6)$ (Table S1).¹⁷ The process taking place at more positive potentials (+0.566 V vs SCE) can be attributed to the Ru(II)→Ru(III) oxidation, while the two processes at negative potentials can be assigned to the reduction of the ancillary ligands ($\text{DIP}^{0/-}$).^{54,55} The potential associated to the metal oxidation of $[\text{Ru}(\text{DIP})_2(\text{mal})](\text{PF}_6)$ is almost 100 mV lower than what was observed for $[\text{Ru}(\text{DIP})_2(\text{sq})](\text{PF}_6)$ in accordance with the higher electron donating property of the maltolate when compared to the semiquinonate ligand. No

redox process involving the maltol appears in the potential range investigated, which is completely in agreement with the literature data.⁵⁶

Solubility and Stability Studies in Different Solvents and Interaction with Human Serum Albumin

The biological ability of a compound is strongly influenced by its solution stability. The stability of $[\text{Ru}(\text{DIP})_2(\text{mal})](\text{PF}_6)$ was first assessed in DMSO- d_6 using ^1H NMR spectroscopy since this solvent was found to be possibly problematic during biological experiments.⁵⁷⁻⁵⁹ The ^1H NMR spectrum of $[\text{Ru}(\text{DIP})_2(\text{mal})](\text{PF}_6)$ remained unchanged over 42 h at room temperature, revealing the stability of the complex in DMSO (Figure S3).

$[\text{Ru}(\text{DIP})_2(\text{mal})](\text{PF}_6)$ shows limited solubility in water and in buffered aqueous media like 20 mM phosphate or HEPES buffer at pH 7.40. Dilution of ethanolic stock solutions of the complex in phosphate or HEPES buffer ($\leq 2\%$ (v/v) ethanol, 20 μM complex) afforded a precipitate after 1 h and 2 h, respectively, while dilution in water (pH ~ 8) afforded solutions that were stable at least for 6 h (Figure S4). It is important to note that in no case decomposition of the complex (i.e. release of maltol) could be detected based on the UV-vis and ultrafiltration studies. Only the different rates of precipitation were observed by varying the type of the media (see more details in the SI, sections S5 and S7). Gradual aggregation followed by precipitation of the complex in buffered samples was seen. *In vitro* biological studies are usually performed in cell culture medium complemented with foetal calf serum (containing albumin as most abundant protein), hence, information about the solubility of the compound in these conditions is required. It was found that RPMI 1640 cell culture medium (non-complemented) could not hinder the precipitation of the complex (Figure S6/A). Therefore, interaction with the most abundant serum protein, albumin, was further investigated. In order to assay the albumin binding, samples were prepared both in phosphate and HEPES buffers (20 mM, $c_{\text{complex}} = 13.8$

μM ; 2% ethanol (v/v); pH = 7.40; T = 25 °C) with a protein-to-metal complex ratio of 6:1. The presence of the protein prevents precipitation of the metal complex in both media (Figure S6/B) confirming the binding interaction between human serum albumin (HSA) and **[Ru(DIP)₂(mal)](PF₆)**. The binding to the protein seems to take place via intermolecular bonding, since no release of maltol or 4,7-diphenyl-1,10-phenanthroline could be detected by UV-vis spectroscopy in ultrafiltration experiments (Figure S7). HSA possesses hydrophobic binding pockets to accommodate small molecules, and binding at sites I and II of HSA was investigated spectrofluorimetrically due to the available site marker probe molecules (see details in Section S7). Interaction at site I was studied via the standard approach, namely following the quenching of the single Trp amino acid of HSA.⁶⁰ Determination of binding data was hindered by the complete overlapping of the weak intrinsic fluorescence of the metal complex with the protein Trp emission band (see Figure S8). The measured intensity upon the addition of the complex to the protein is not the sum of the intensities of the complex and HSA (thus not additive), which indicates the binding interaction at site I and an upper limit of binding constant $\log K' < 4.0$ could be estimated at this site.

Binding at site II was followed via site marker displacement experiment using dansylglycine (DG) as marker. DG was gradually displaced by **[Ru(DIP)₂(mal)](PF₆)** at site II (Figure 2).

Calculated binding constant $\log K'$ (site II) = 4.3 ± 0.1 reveals moderate-to-weak binding affinity of $[\text{Ru}(\text{DIP})_2(\text{mal})](\text{PF}_6)$ at site II.

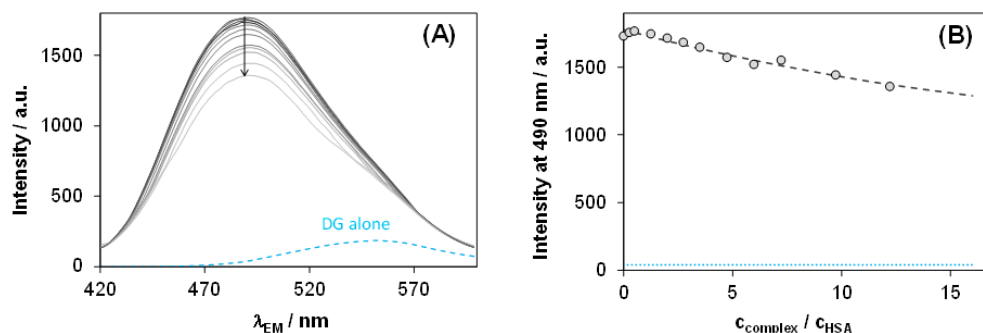


Figure 2. Fluorescence emission spectra obtained by the titration of HSA–DG (1:1) with $[\text{Ru}(\text{DIP})_2(\text{mal})](\text{PF}_6)$ (A); and measured (dots) and calculated (dashed line) intensity values at 490 nm (B). Blue dotted line denotes the emission of free DG. $\{c_{\text{HSA}} = c_{\text{DG}} 2 \mu\text{M}; c_{\text{comp}} = 0\text{--}24 \mu\text{M}; \lambda_{\text{EX}} = 335 \text{ nm}; \text{pH} = 7.40 (20 \text{ mM phosphate buffer}); < 2\% \text{ ethanol}; T = 25 \text{ C}\}$.

All in all, according to our results $[\text{Ru}(\text{DIP})_2(\text{mal})](\text{PF}_6)$ binds to HSA via intermolecular interactions at least at the two hydrophobic sites: I and II. Albumin binding prevents precipitation of the metal complex in aqueous solution.

Stability Studies in Human Plasma

Next, to assess the behaviour of $[\text{Ru}(\text{DIP})_2(\text{mal})](\text{PF}_6)$ under physiological conditions, its stability in human plasma was investigated by Ultra Performance Liquid Chromatography (UPLC) following a procedure already established by our group.⁶¹ $[\text{Ru}(\text{DIP})_2(\text{mal})](\text{PF}_6)$ (0.12 mM) was incubated in human plasma up to 96 h at 37°C using caffeine (1.92 mM) as an internal standard.⁶² The UV traces of the UPLC analysis at different incubation times are shown in Figure S9a. When the concentration of $[\text{Ru}(\text{DIP})_2(\text{mal})](\text{PF}_6)$ was normalized with respect to the internal standard and plotted against time (Figure S9b), no clear decomposition was observed in the first 24 h, whereas a linear decrease in concentration started thereafter. Based

on these changes the half-life of **[Ru(DIP)₂(mal)](PF₆)** could be estimated to be of approximately 48 h under these conditions.

Cytotoxicity Studies and Cell Death Mechanism

After assessment of stability in solution, **[Ru(DIP)₂(mal)](PF₆)** biological activity was investigated. The first step was to evaluate the cytotoxicity in 2D cell culture models, comprising HeLa (human cervical adenocarcinoma), A2780 (human ovarian carcinoma), A2780 cis (human cisplatin resistant ovarian carcinoma), A2780 ADR (human doxorubicin resistant ovarian carcinoma), CT-26 (mouse colon adenocarcinoma), CT-26 LUC (mouse colon adenocarcinoma stably expressing luciferase) and RPE-1 (human normal retina pigmented epithelial) cell lines and using a fluorometric cell viability assay (single graphs available in Figures S10).⁶³ In this study, doxorubicin and cisplatin were tested in the same cell lines and used as positive controls.^{64,65} Cytotoxicity of the **RuCl₂(DIP)₂** precursor and maltol ligand were also determined as additional controls. IC₅₀ values of the tested compounds are reported in Table 1. The cytotoxicity of **[Ru(DIP)₂(mal)](PF₆)** was found very high and comparable to what previously observed for **[Ru(DIP)₂(sq)](PF₆)**¹⁷ in all cell lines tested in this study. The IC₅₀ values obtained are in the high nanomolar concentration range with the exception of the one determined on the doxorubicin-resistant cell line (IC₅₀ = 2.86 μM). The **RuCl₂(DIP)₂** precursor displays much lower cytotoxicity, while maltol, as expected, is non-toxic.^{34,35} **[Ru(DIP)₂(mal)](PF₆)** exerts an overall activity comparable to doxorubicin in all cell lines tested. Interestingly, its cytotoxicity against the cisplatin-resistant cell line is more than 40 times higher than that of cisplatin (IC₅₀ = 0.42 μM vs. 18.33 μM for **[Ru(DIP)₂(mal)](PF₆)** and cisplatin, respectively).

Table 1. IC₅₀ values for **[Ru(DIP)₂(mal)](PF₆)**, cisplatin, doxorubicin, **[Ru(DIP)₂(sq)](PF₆)**, **RuCl₂(DIP)₂** and maltol in different cell lines (48 h).

IC ₅₀ (μM)	HeLa	A2780	A2780 ADR	A2780 cis	CT-26	CT-26 LUC	RPE-1
Cisplatin *	9.28 ± 0.20	4.00 ± 0.76	8.32 ± 0.71	18.33 ± 2.92	2.60 ± 0.18	2.42 ± 0.23	30.24 ± 5.11
Doxorubicin *	0.34 ± 0.02	0.19 ± 0.03	5.94 ± 0.58	0.54 ± 0.04	0.082 ± 0.003	0.18 ± 0.006	0.89 ± 0.17
[Ru(DIP)₂(sq)](PF₆) *	0.50 ± 0.01	0.67 ± 0.04	4.13 ± 0.2	0.45 ± 0.03	1.00 ± 0.03	1.51 ± 0.14	0.90 ± 0.04
[Ru(DIP)₂(mal)](PF₆)	0.45 ± 0.04	0.74 ± 0.05	2.86 ± 0.3	0.42 ± 0.01	0.61 ± 0.02	0.72 ± 0.07	0.86 ± 0.04
RuCl₂(DIP)₂ *	15.03 ± 0.4	4.69 ± 0.14	78.27 ± 4.9	6.36 ± 0.57	9.20 ± 1.22	6.65 ± 0.5	3.13 ± 0.07
Maltol	74.01 ± 14.6	>100	>100	>100	>100	>100	>100

* Values taken from [17] We, however, note that these experiments were performed on the same days.

Due to the promising activity displayed by **[Ru(DIP)₂(mal)](PF₆)** in monolayer cell culture, a MCTS model was also investigated.⁶⁶ 3D cultured cells are recognised as important research tools for their ability to resemble the pathophysiologic environment of the tumor tissue and,^{67–69} along with the 2D model system, they allow for a better estimation of *in vivo* antitumour efficacy of compounds.^{66,68} The cytotoxicity of **[Ru(DIP)₂(mal)](PF₆)**, its **RuCl₂(DIP)₂** precursor, **[Ru(DIP)₂(sq)](PF₆)**, and the maltol ligand were tested *via* a luminescent cell viability assay in HeLa MCTS (single graphs are available in Figure S11). Cisplatin and doxorubicin were also tested in the same conditions as positive controls (Figure S11).^{59,60} The IC₅₀ values of the tested compounds are reported in Table 2. **[Ru(DIP)₂(mal)](PF₆)** preserves the high cytotoxicity observed in the monolayer model with an IC₅₀ value more than 2 times lower than cisplatin or doxorubicin (IC₅₀ ~ 17 μM, 47 μM and 39 μM respectively), and comparable to that of **[Ru(DIP)₂(sq)](PF₆)**. The **RuCl₂(DIP)₂** precursor showed a cytotoxicity comparable to cisplatin while the maltol ligand was proven to be non-toxic also in this model.

Table 2. IC₅₀ values for [Ru(DIP)₂(mal)](PF₆), cisplatin, doxorubicin, RuCl₂(DIP)₂ and maltol in multicellular HeLa cancer cell spheroids.

IC ₅₀ (μM)	Cisplatin*	Doxorubicin*	[Ru(DIP) ₂ (sq)](PF ₆)*	[Ru(DIP) ₂ (mal)](PF ₆)	RuCl ₂ (DIP) ₂ *	Maltol
HeLa	46.49 ±	38.59 ±	14.11 ±	17.00 ±	59.84 ±	>100
MCTS	4.18	0.43	0.09	0.73	3.05	

* Values taken from [17]. Notably, these experiments were performed on the same days.

Next, the size of treated MCTS was studied to evaluate the time dependent effect of the [Ru(DIP)₂(mal)](PF₆). Growth kinetics of treated spheroids was monitored by changes in spheroids diameter. Briefly 400 μm HeLa MCTS were treated with different concentrations of [Ru(DIP)₂(mal)](PF₆), and their diameter was checked every three days (Figure 3). Of note, when the washing step was performed, half of the medium was removed and replaced with fresh one, diluting twice the quantity of the compound in each well. At all concentrations tested, [Ru(DIP)₂(mal)](PF₆) caused a significant decrease in the size of the spheroids. Strikingly, this effect was still dominant even after 13 days of treatment.

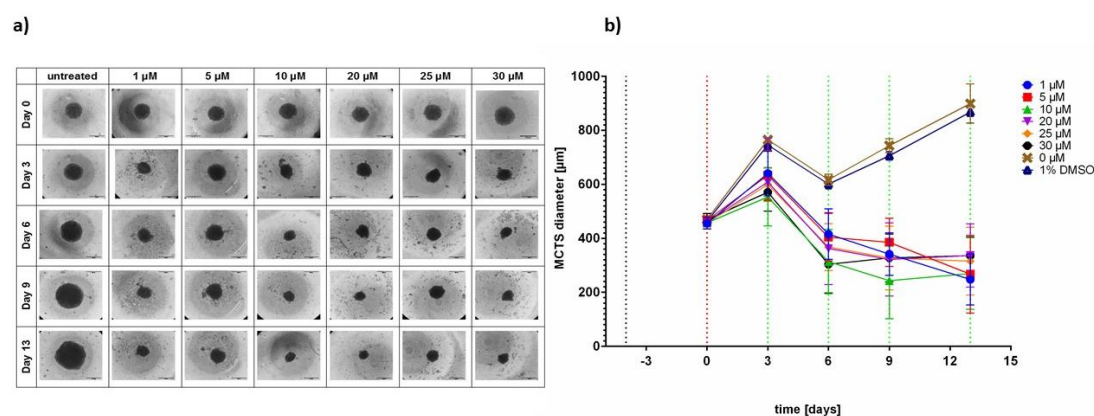


Figure 3. Changes in growth kinetics of MCTS treated with [Ru(DIP)₂(mal)](PF₆) at different concentrations (1, 5, 10, 20, 25 and 30 μM). (a) Images collected at day 0 (before treatment) and at day 3, 6, 9 and 13. b) MCTSs diameter measured at different time points. Blue-dotted line indicates the day of seeding, red-dotted line indicates the day of treatment while green-dotted lines indicate the days of washing.

In summary, **[Ru(DIP)₂(mal)](PF₆)** showed high cytotoxicity in 2D and 3D models, as well as prolonged effect on the spheroids growth. These promising results encouraged further evaluation of the mechanism of cell death caused by the complex. To determine whether cell death occurs by apoptosis or by necrosis process, HeLa cells were analysed by flow cytometry using the Annexin V and PI (propidium iodide) staining method. In this experiment, staurosporin, a known apoptosis inducer, was used as positive control.⁷² 4 h incubation of HeLa cells with **[Ru(DIP)₂(mal)](PF₆)** (10 μM) induced considerable cell death, mostly through apoptosis. Longer incubation of the cells with the complex (24 h) significantly increased the number of cells undergoing apoptotic cell death. In comparison with staurosporin, only a small population of the cells was PI positive after 24 h treatment with **[Ru(DIP)₂(mal)](PF₆)**. Since PI is a vital stain (viable cells with intact membranes will exclude PI), this small population might refer either to dead cells or cells undergoing necrosis. Annexin V and PI staining confirmed that **[Ru(DIP)₂(mal)](PF₆)** induces mostly apoptotic cell death in treated HeLa cells. Specific cell populations are shown in Figures 4 and S12.

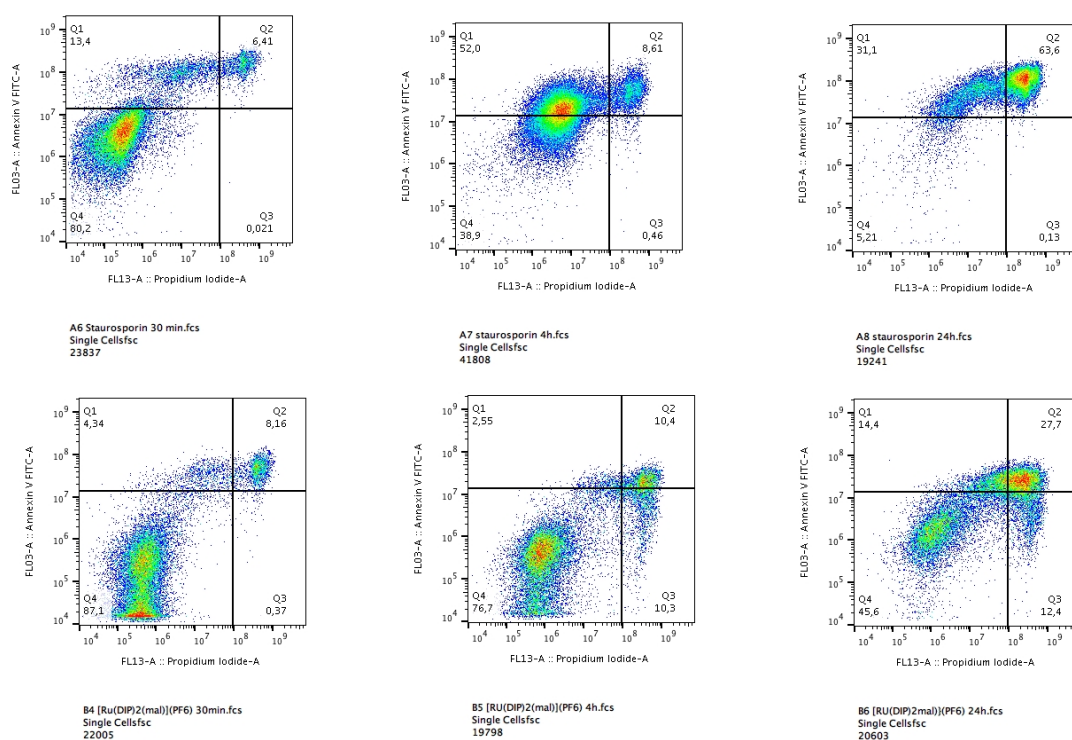


Figure 4. Annexin V and PI staining in HeLa cells treated with $[\text{Ru}(\text{DIP})_2(\text{mal})](\text{PF}_6)$ ($10 \mu\text{M}$) and staurosporine ($1 \mu\text{M}$) at different time points. The fourth quadrant represents living cells (Annexin V, PI negative), first one early apoptotic cells (Annexin V positive, PI negative), second late apoptotic (Annexin and PI positive) and third necrotic or dead cells (Annexin V negative and PI positive).

Cellular Uptake, Biodistribution, and DNA Metalation.

To obtain more insights about the mode of action of $[\text{Ru}(\text{DIP})_2(\text{mal})](\text{PF}_6)$, it is essential to understand its cellular and subcellular accumulation as much as its mechanism of uptake. For this purpose, inductively coupled plasma mass spectrometry (ICP-MS) was utilised. Working concentrations and incubation times were chosen to avoid extended cell mass loss due to the high cytotoxicity of the complex but considering a ruthenium final amount that could allow determination of the metal content. However, the working conditions ($5 \mu\text{M}$ treatment for 2 h), in agreement with literature data, allowed for a minor accumulation of the drug cisplatin used as control.^{73,74} $[\text{Ru}(\text{DIP})_2(\text{mal})](\text{PF}_6)$ accumulation in HeLa cells was found to be higher than

its precursor and cisplatin used as controls and almost three times higher than the **[Ru(DIP)₂(sq)](PF₆)** analogue previously reported by our group (Figure 5a).¹⁷ This could be explained by the different mechanism of cellular uptake associated to the two complexes. To fully understand the uptake mechanism, HeLa cells were pretreated or kept at different temperatures to determine if the uptake mechanism is passive or active. For this purpose low temperature (4°C should slow down passive diffusion as well as ATP required transport) or treatments with active transport inhibitors was utilised. 2-Deoxy-*D*-glucose and oligomycin block cellular metabolism (ATP production), chloroquine or NH₄Cl impeded endocytic pathways and tetraethylammonium chloride stops cation transporters. After pre-treatment, cells were incubated with the compound (2 h, 5 μM) and subsequently analysed *via* ICP-MS (Figure S13). Inhibition of active uptake mechanisms did not perturb accumulation of **[Ru(DIP)₂(mal)](PF₆)** in HeLa cells. These findings clearly suggest that passive transport is the only mechanism responsible for accumulation of **[Ru(DIP)₂(mal)](PF₆)** in HeLa cells, unlike **[Ru(DIP)₂(sq)](PF₆)**, whose mechanism of uptake involves both active and passive transports.¹⁷ Cellular fractionation experiments revealed the relative distribution of **[Ru(DIP)₂(mal)](PF₆)** among the different subcellular compartments (Figure 5b). Most of the complex was found in the cytoplasm, with mitochondria and lysosomes being the next most enriched organelles, while a smaller fraction was detected in the nucleus. **[Ru(DIP)₂(sq)](PF₆)**, on the other hand, accumulated preferentially in the nucleus and only to a small extent in mitochondria, lysosomes and cytoplasm.¹⁷ The accumulation of a compound in the nucleus suggests DNA as one of the potential targets.

Even though only a small amount of ruthenium was found in the nucleus, the reactivity of our compound towards DNA was studied *via* DNA metalation experiment. HeLa cells were treated for 2 h with 5 μM solutions of **[Ru(DIP)₂(mal)](PF₆)** or cisplatin (positive control). The genetic material was then extracted, and the amount of metal was determined by ICP-MS. Data are

shown in Figure 5c in comparison to those obtained for the analogue $[\text{Ru}(\text{DIP})_2(\text{sq})](\text{PF}_6)$.¹⁷ These data point to a significant interaction between DNA and $[\text{Ru}(\text{DIP})_2(\text{mal})](\text{PF}_6)$, regardless of the small accumulation detected in the nucleus. The relative higher amount of metalated DNA found for $[\text{Ru}(\text{DIP})_2(\text{mal})](\text{PF}_6)$ when compared to cisplatin or $[\text{Ru}(\text{DIP})_2(\text{sq})](\text{PF}_6)$, and upon normalization to total DNA, can be explained by the overall higher cellular uptake of the former complex.

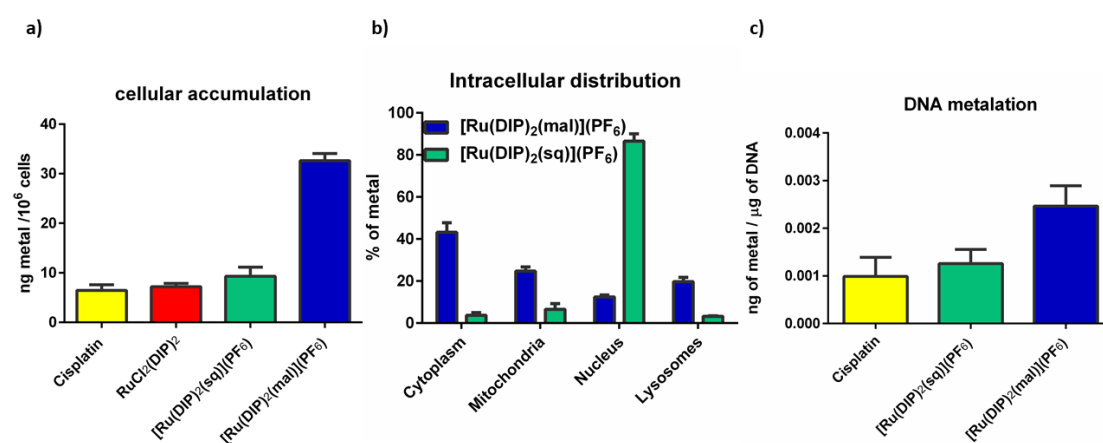


Figure 5. Cellular uptake (a), cellular fractionation (b) and DNA metalation (c) of HeLa cells after treatment with tested compounds (5 μM , 2 h). Data are presented as the mean \pm SD of at least 3 technical replicates. All data related to $[\text{Ru}(\text{DIP})_2(\text{sq})](\text{PF}_6)$ were previously reported by our group.¹⁷ We, however, note that these experiments were performed on the same days.

JC-1 Mitochondrial Membrane Potential Test and Metabolic Studies.

The accumulation of $[\text{Ru}(\text{DIP})_2(\text{mal})](\text{PF}_6)$ in mitochondria suggested studies on possible effects of the compound on mitochondrial function. To this end, we used JC-1, a green fluorescent monomer at low mitochondrial membrane potential (MMP) that aggregates and emits red fluorescence at higher potential.⁷⁵ MMP is a key factor of the mitochondrial function due to its direct correlation to oxidative phosphorylation.⁷⁶ Figure 6a shows the red fluorescence signal observed in HeLa cells upon 24 h treatment with $[\text{Ru}(\text{DIP})_2(\text{mal})](\text{PF}_6)$, FCCP (carbonyl cyanide 4-(trifluoromethoxy)phenylhydrazone, an uncoupling agent used as positive control),⁷⁷ and DMSO (vehicle control). An uncoupling agent is a molecule that inhibits the

coupling between reactions of ATP synthesis and the electron transport chain leading to a disruption of oxidative phosphorylation in mitochondria.⁷⁸ Untreated cells are shown as a negative control. A significant concentration-dependent decrease in the fluorescence signal was observed upon treatment with **[Ru(DIP)₂(mal)](PF₆)** (from 0.1 μM to 0.6 μM). At the IC₅₀ value (0.5 μM, marked in red in Figure 6a), the MMP decrease was comparable to that obtained for the positive control. However, it is important to take into consideration that a dramatic drop in MMP could be triggered by ongoing apoptosis.⁷⁷ These findings strongly suggest a contribution of impaired MMP to the cell death mechanism and inspired further studies on mitochondrial metabolism (i.e. oxidative phosphorylation) in HeLa cells. For this purpose, the Mito stress test was performed using Seahorse XF Analyzer. The low basal respiration observed in cells treated with **[Ru(DIP)₂(mal)](PF₆)** in comparison to untreated cells, clearly demonstrates a severe impairment of mitochondrial respiration. In contrast, the **RuCl₂(DIP)₂** precursor and the maltol ligand did not remarkably affect this process. Additionally, **[Ru(DIP)₂(mal)](PF₆)** caused a loss in the capacity of the mitochondrial membrane to restore the proton balance when treated with an uncoupling agent (FCCP) and inhibited ATP production (Figure 6b and Figure S14). Taken together, these data demonstrate that **[Ru(DIP)₂(mal)](PF₆)** treatment causes complete disruption of mitochondrial respiration in HeLa cells. Furthermore, we investigated effects on other metabolic pathways, such as glycolysis, and the possible metabolic modulation of the three primary fuel pathways (involving glucose, glutamine or fatty acids as substrates) using a Seahorse XF Analyzer. The cytosolic process of glycolysis was not affected by **[Ru(DIP)₂(mal)](PF₆)** or its precursor (Figure S15). Effects on three primary fuel pathways could not be determined due to very low oxygen consumption rate in cells treated with **[Ru(DIP)₂(mal)](PF₆)** (Figure S16). Metabolic studies pointed to a substantial difference in the mode of action of **[Ru(DIP)₂(mal)](PF₆)** and the chemotherapeutic drug cisplatin. The latter is known to interfere with DNA replication and does

not affect mitochondrial metabolism. $[\text{Ru}(\text{DIP})_2(\text{mal})](\text{PF}_6)$, on the other hand, clearly demonstrated that the mitochondrial dysfunction is significantly involved in its mode of action.

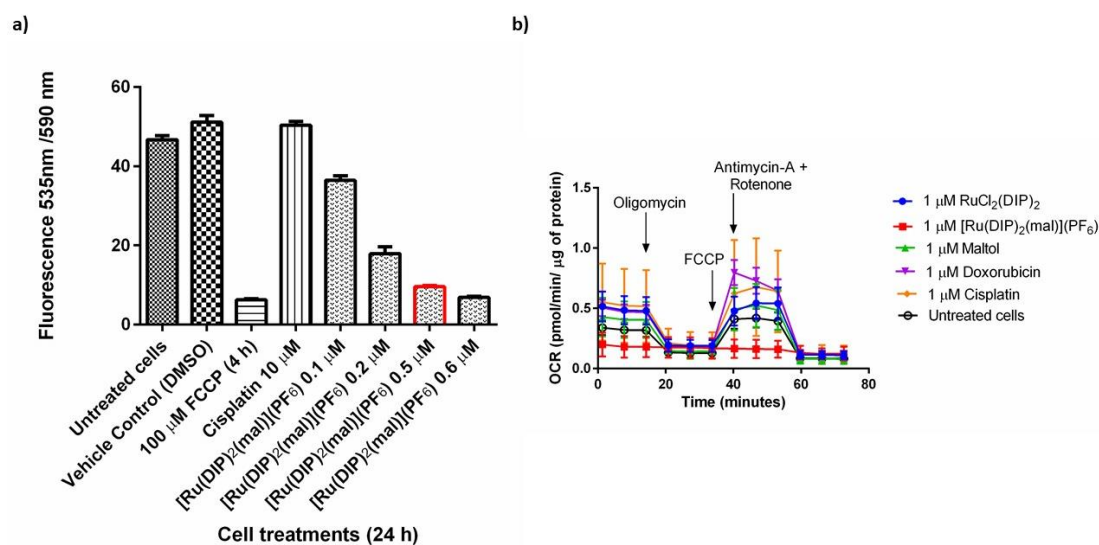


Figure 6. a) Fluorescence signal of JC-1 dye detected in HeLa cells treated for 24 h with different concentrations of $[\text{Ru}(\text{DIP})_2(\text{mal})](\text{PF}_6)$ (from 0.1 μM to 0.6 μM). The bar marked in red indicates the IC_{50} concentration (0.5 μM). FCCCP was used as positive control, cisplatin and DMSO (1%) were used as negative controls. b) Mito Stress Test profile after 24 h treatment; the graph displays oxygen consumption rate changes after treatment with specific electron transport chain inhibitors. Oligomycin (inhibitor of ATP synthase (complex V)), FCCCP (uncoupling agent), Antimycin-A (complex III inhibitor) and Rotenone (complex I inhibitor).

Conclusions

Following the development of the potential anticancer agent $[\text{Ru}(\text{DIP})_2(\text{sq})](\text{PF}_6)$ by our group, here we report synthesis and biological evaluation of an analogue complex, namely $[\text{Ru}(\text{DIP})_2(\text{mal})](\text{PF}_6)$, containing the FDA-approved, flavour-enhancing agent, maltol. It was found that the compound is stable at room temperature in DMSO over 42 h and has a half-life of 48 h in human plasma. Although the complex exhibits poor water solubility, the measurements in human plasma as well as in supplemented media were made possible by the presence of human serum albumin. In the course of this study, we demonstrated that $[\text{Ru}(\text{DIP})_2(\text{mal})](\text{PF}_6)$ binds to HSA via intermolecular interactions at least at the two

hydrophobic sites (I and II), preventing precipitation of the metal complex in aqueous solution. Studies performed on several cancerous cell lines in cellular monolayer culture and on HeLa MCTS indicated remarkable activity by **[Ru(DIP)₂(mal)](PF₆)**, comparable to doxorubicin and much higher than the approved drug cisplatin. It is worth nothing that **[Ru(DIP)₂(mal)](PF₆)** cytotoxicity against the cisplatin-resistant cell line is more than 40 times higher than that of cisplatin (IC₅₀ = 0.42 μM vs. 18.33 μM for **[Ru(DIP)₂(mal)](PF₆)** and cisplatin, respectively) in 2D model cultures. Moreover, HeLa MCTS treated with different concentrations of **[Ru(DIP)₂(mal)](PF₆)** demonstrated a significant decrease in size, even after 13 days of a single treatment. Cellular uptake studies showed efficient cellular accumulation of the compound, when compared to cisplatin or the analogue **[Ru(DIP)₂(sq)](PF₆)**, through a passive transport mechanism. Deeper investigations on **[Ru(DIP)₂(mal)](PF₆)** mode of action by means of cellular fractionation, showed mitochondria as one of the preferred accumulation sites. Mitochondrial dysfunction was assessed through a mito-stress test (Seahorse technology) and changes in MMP (JC-1 staining): both approaches led to establish a conclusive contribution of impaired mitochondria metabolism in the mode of action of **[Ru(DIP)₂(mal)](PF₆)**. Finally, metalation studies confirmed the interaction between **[Ru(DIP)₂(mal)](PF₆)** and DNA, suggesting the latter as another potential target. These findings together with what previously reported on the activity of **[Ru(DIP)₂(sq)](PF₆)**, emphasise the outstanding potential of this class of compounds, which should be taken into account from scientists involved in the search of new chemotherapeutic agents.

Experimental Section

Materials.

All chemicals were either of reagent or analytical grade and used as purchased from commercial sources without additional purification. RuCl₃ hydrate was provided by I²CNS, 4,7-Diphenyl-1,10-phenanthroline, LiCl (anhydrous, 99%), and maltol by Alfa Aesar, tetrabutylammonium hexafluorophosphate by Sigma-Aldrich. All solvents were purchased of analytical, or HPLC grade. When necessary, solvents were degassed by purging with dry, oxygen-free nitrogen for at least 30 min before use.

Instrumentation and methods.

Amber glass or clear glassware wrapped in tin foil was used when protection from light was necessary. Schlenk glassware and a vacuum line were employed when reactions sensitive to moisture/oxygen had to be performed under nitrogen atmosphere. Thin layer chromatography (TLC) was performed using silica gel 60 F-254 (Merck) plates with detection of spots being achieved by exposure to UV light. Column chromatography was done using Silica gel 60-200 μm (VWR). Eluent mixtures are expressed as volume to volume (v/v) ratios. ¹H and ¹³C NMR spectra were measured on Bruker Avance III HD 400 MHz or Bruker Avance Neo 500 MHz spectrometers using the signal of the deuterated solvent as an internal standard.⁷⁹ The chemical shifts (δ) are reported in ppm (parts per million) relative to tetramethylsilane (TMS) or signals from the residual protons of deuterated solvents. Coupling constants J are given in Hertz (Hz). The abbreviation for the peaks multiplicity is s (singlet), d (doublet), dd (doublet of doublet), m (multiplet). ESI-HRMS experiments were carried out using a LTQ-Orbitrap XL from Thermo Scientific (Thermo Fisher Scientific, Courtaboeuf, France) and operated in positive ionization mode, with a spray voltage at 3.6 kV. Sheath and auxiliary gas were set at a flow rate of 5 and 0 arbitrary units (a.u.), respectively. The voltages applied were 40 and 100 V for the ion transfer

capillary and the tube lens, respectively. The ion transfer capillary was held at 275°C. Detection was achieved in the Orbitrap with a resolution set to 100,000 (at m/z 400) and a m/z range between 200-2000 in profile mode. Spectrum was analysed using the acquisition software XCalibur 2.1 (Thermo Fisher Scientific, Courtaboeuf, France). The automatic gain control (AGC) allowed accumulation of up to 2.105 ions for FTMS scans, Maximum injection time was set to 300 ms and 1 μ scan was acquired. 5 μ L was injected using a Thermo Finnigan Surveyor HPLC system (Thermo Fisher Scientific, Courtaboeuf, France) with a continuous infusion of methanol at 100 μ Lmin⁻¹. Elemental analysis was performed at Science Centre, London Metropolitan University using Thermo Fisher (Carlo Erba) Flash 2000 Elemental Analyser, configured for %CHN. IR spectra were recorded with SpectrumTwo FTIR Spectrometer (Perkin–Elmer) equipped with a Specac Golden Gate™ ATR (attenuated total reflection) accessory; applied as neat samples; $1/\lambda$ in cm⁻¹. Stability in human plasma was performed on HPLC (VWR Hitachi Chromaster system) and a Macherey Nager EC 250/3 Nucleosil 100-5 C18 column. UV absorption was measured at 275 nm and the runs (flow rate 0.6 mLmin⁻¹) were performed with a linear gradient of A (distilled water containing 0.1% (v/v) TFA) and B (acetonitrile, Sigma-Aldrich HPLC grade): t = 0 min, 5% B; t = 0.5 min, 5% B; t = 1.5 min, 100% B; t = 2 min, 100% B. Ruthenation of the DNA was performed using a High-Resolution ICP-MS Element II from ThermoScientific located within the Environmental Biogeochemistry team of the Institut de Physique du Globe de Paris. This ICP-MS enables working in different resolution modes (LR=400, MR=4000 and HR=10000) for a better discrimination between elements of interest and interferences.⁸⁰ For the metabolic studies Seahorse XFe96 Analyser by Agilent Technologies was used. **RuCl₂(DMSO)₄** was synthesised following an adapted literature procedure.⁵² Spectroscopic data (¹H NMR) was in agreement with literature.⁵²

Synthesis and characterization.

Ru(DIP)₂Cl₂.

The complex was synthesised following an adapted literature procedure.⁵³ A mixture of RuCl₂(DMSO)₄ (3.0 g, 6.19 mmol), 4,7-diphenyl-1,10-phenanthroline (DIP, 4.11 g, 12.38 mmol) and LiCl (2.0 g, 47.18 mmol) dissolved in DMF (100 mL) was refluxed for 24 h. After cooling to *r.t.* the solvent was reduced *in vacuo* to 8 mL and 350 mL of acetone were added. After overnight storage at -20 °C the deep purple solid was removed by filtration with a Buchner funnel and washed with cold acetone and Et₂O. Ru(DIP)₂Cl₂ was then collected, dried and purified by silica gel chromatography (DCM/MeOH 97:3 *rf* 0.4) to afford the complex in 52% yield (2.71 g, 3.23 mmol,) which purity was confirmed by microanalysis. Spectroscopic data (¹H NMR) were in agreement with literature.⁵³

[Ru(DIP)₂(mal)](PF₆)

Ru(DIP)₂Cl₂ (0.150 g, 0.18 mmol) and aq. NaOH (0.28 mL, 1 M) were dissolved in ethanol (18 mL). The solution was degassed for 30 min and maltol (3-Hydroxy-2-methyl-4H-pyran-4-one) (0.036 g, 0.29 mmol) was added. The mixture was heated to reflux for 3 h under N₂ atmosphere and protected from light. After cooling to *r.t.*, H₂O (200 mL) and NH₄PF₆ (1 g, 6 mmol) were added. The mixture was stored overnight in the refrigerator (4 °C). The precipitate was collected on a Buchner funnel, washed with H₂O (3 × 50 mL) and Et₂O (3 × 50 mL). The solid was sonicated with Et₂O or Heptane (10 mL) for 10 min and then centrifuged. This procedure was repeated three times for each solvent. The solid was eventually dried under vacuum to deliver a clean product as the PF₆ salt (0.17 g, 0.16 mmol, 90%). IR (Golden Gate, cm⁻¹): 1590w, 1545w, 1490w, 1465w, 1445w, 1415w, 1400w, 1275w, 1205w, 1085w, 1025w, 915w, 830s, 765s, 735m, 700s. ¹H NMR (400 MHz, CD₂Cl₂): δ/ppm = 9.49 (d, J = 5.4 Hz, 1H), 9.33 (d, J =

5.5 Hz, 1H), 8.23 (dd, J = 9.4, 4.6 Hz, 2H), 8.13 (dd, J = 9.4, 1.1 Hz, 2H), 8.04 (d, J = 5.6 Hz, 2H), 7.98 (dd, J = 13.5, 5.4 Hz, 2H), 7.78 – 7.60 (m, 11H), 7.59 – 7.47 (m, 10H), 7.33 (dd, J = 5.6, 3.0 Hz, 2H), 6.54 (d, J = 5.1 Hz, 1H), 2.37 (s, 3H). ¹³C NMR (125 MHz, CD₂Cl₃): δ/ppm = 185.00, 159.02, 155.49, 154.10, 154.01, 151.75, 151.47, 151.06, 150.64, 150.17, 149.98, 149.92, 147.66, 147.13, 146.01, 145.71, 136.50, 136.47, 136.23, 136.20, 130.15, 129.86, 129.81, 129.47, 129.44, 129.28, 129.21, 129.10, 128.78, 128.61, 128.55, 128.46, 125.96, 125.82, 125.77, 125.77, 125.69, 125.51, 125.25, 125.05, 112.40, 29.84. HRMS (ESI+): m/z 891.19042 [M - PF₆]⁺. Elemental Analysis: calcd. for C₅₄H₃₉F₆N₄O₄PRu = C, 61.54; H, 3.73; N, 5.32. Found = C, 61.53; H, 3.38; N, 5.17.

Electrochemical Measurements.

Electrochemical experiments were carried out with a conventional three-electrodes cell (solution volume of 15 mL) and a PC-controlled potentiostat/galvanostat (Princeton Applied Research Inc. model 263A). The working electrode was a vitreous carbon electrode from Orignalys (France) exposing a geometrical area of 0.071 cm² and mounted in Teflon[®]. The electrode was polished before each experiment with 3 and 0.3 μm alumina pastes followed by extensive rinsing with ultra-pure Milli-Q water. A platinum wire was used as counter electrode and saturated calomel electrode, SCE, as reference electrode. Electrolytic solutions, DMF containing tetrabutylammonium hexafluoroborate 0.1M (TBAPF₆, Aldrich, +99 %) as supporting electrolyte, were routinely deoxygenated by argon bubbling. All the potential values are given versus the calomel saturated electrode SCE and recalculated versus Me₁₀Fc^{0/+} potential value.

DMSO and Human Plasma stability studies.

The stability in DMSO-d₆ at room temperature was assessed by ¹H NMR over 42 hours. The stability of the complex in human plasma at 37 °C was evaluated following an adapted procedure recently reported by our group.⁸¹ Human plasma was provided by the Blutspendezentrum, Zurich, Switzerland. Caffeine was obtained from Sigma-Aldrich and used as an internal standard.⁶² Stock solutions of the complex (9.6 mM) in DMSO and caffeine (0.15 M) in H₂O were prepared. For a typical experiment, an aliquot of 12.5 μL of each stock solution was added to the plasma solution (975 μL) to a total volume of 1000 μL and final concentration of 1.92 mM for caffeine and 0.12 mM for the complex. The resulting plasma solution was incubated for 0, 1, 2, 4, 6, 24, 48, 72 and 96 h at 37 °C with continuous and gentle shaking (ca. 600 rpm). The reaction was stopped by addition of 2 mL of MeOH, and the mixture was centrifuged for 45 min at 3500 rpm. The methanolic solution was filtered and analysed using HPLC and an injection volume of 6 μL.

Stability of the complex in different solvents and at different conditions.

Preparation of stock solutions: Human serum albumin (HSA as lyophilized powder with fatty acids), Na₂HPO₄, NaH₂PO₄, 4-(2-hydroxyethyl)-1-piperazineethanesulfonic acid (HEPES) and dansylglycine (DG) were obtained from Sigma-Aldrich in *puriss* quality. Powdered RPMI 1640 cell culture medium without indicator for 1 L solution was a Sigma-Aldrich product as well. Milli-Q ultrapure water was used for sample preparations. HSA solution was freshly prepared before the experiments in 20 mM phosphate or in 20 mM HEPES buffer (pH = 7.40). Its concentration was estimated from its UV absorption: $\epsilon_{280\text{ nm}}(\text{HSA}) = 36850\text{ M}^{-1}\text{cm}^{-1}$.⁸² Stock solutions of the complex were freshly prepared every day in ethanol in 1-2 mM concentration.

¹H NMR measurements: ¹H NMR spectroscopic studies were carried out on a Bruker Avance III HD Ascend 500 Plus instrument. The metal complex was dissolved in methanol-*d*⁴ in 3.3 mM concentration. Samples prepared in methanol-*d*⁴, RPMI 1640 medium or in 20 mM phosphate buffer (pH = 7.40) contained 1 mM metal complex and 30% (v/v) methanol-*d*⁴. Spectra for water containing samples were recorded with the WATERGATE water suppression pulse scheme using DSS internal standard.

UV-Vis spectrophotometry and ultrafiltration: An Agilent Carry 8454 diode array spectrophotometer was utilized to record the UV–visible (UV–vis) spectra in the interval 190–1100 nm. The path length (l) was 1 cm. Aqueous stability of the complex was followed in 20 mM phosphate buffer (pH = 7.40), in 20 mM HEPES buffer (pH = 7.40), in RPMI 1640 medium, in the presence of HSA, in ethanol, methanol and in pure water (pH ~ 8). Measurements on the protein binding of the complex were performed at fixed metal complex concentration (20 μM) and various protein-to-complex ratios (from 0.02:1 to 10:1) were applied.

Spectrofluorometric studies: Samples were prepared in 20 mM phosphate or in 20 mM HEPES buffer (pH 7.40); spectra were recorded after 5 min incubation. Samples for quenching experiments contained 1 μM HSA and various HSA-to-metal complex ratios (from 1:0 to 1:15) were used. The excitation wavelength was 295 nm; the emission intensities were read in the range of 305 – 500 nm with 5 nm/5 nm slit widths. In the site marker displacement experiments, the HSA-to-DG ratio was 1:1 (2-2 μM) and the concentration of the metal complex was varied from 0 to 37 μM. The excitation wavelength was 335 nm and the emission intensity was collected in the range of 420 – 600 nm with 5 nm/10 nm slit widths. The conditional binding constant for the site II binding of the complex was calculated with the computer program HypSpec⁸³ as described in our previous works.^{30,84} Corrections for self-absorbance and inner filter effect were done.⁶⁰

Cell culture.

HeLa and CT-26 cell lines were grown in DMEM media (Gibco). CT-26 LUC cell line was cultured in DMEM media (Gibco) supplemented with 1.6 mg/mL of Genticin. RPE-1 cell line was grown and maintained in DMEM/F-12 media (Gibco). A2780, A2780 cis, A2780 ADR cell lines were cultured in RPMI 1640 media (Gibco). The resistance of A2780 cis was maintained by cisplatin treatment (1 μ M) for one week every month. Cells were used in the assays one week after the end of the treatment, in order to avoid interfering results. The resistance of A2780 ADR was maintained by doxorubicin treatment (0.1 μ M) once a week. Cells were used in the assays after three days post doxorubicin treatment in order to avoid interfering results. All cell lines were complemented with 10% of fetal calf serum (Gibco) and 100 U/mL penicillin-streptomycin mixture (Gibco) and maintained in humidified atmosphere at 37°C and 5% of CO₂.

Cytotoxicity Assay using a 2D cellular model.

Cytotoxicity of **[Ru(DIP)₂(mal)](PF₆)** and **RuCl₂(DIP)₂** complexes was assessed by a fluorometric cell viability assay using Resazurin (ACROS Organics). Briefly, cells were seeded in triplicates in 96-well plates at a density of 4 × 10³ cells/well in 100 μ L. After 24 h, cells were treated with increasing concentrations of the ruthenium complexes. Dilutions for **[Ru(DIP)₂(mal)](PF₆)** and **RuCl₂(DIP)₂** were prepared as follows: 2.5 mM stock in DMSO (**[Ru(DIP)₂(mal)](PF₆)**) or DMF (**RuCl₂(DIP)₂**) was prepared, which was further diluted to 100 μ M and filtered (0.22 μ m filter VWR). After 48 h incubation, the medium was removed and 100 μ L of complete medium containing resazurin (0.2 mg/mL final concentration) was added. After 4 h of incubation at 37 °C, the fluorescence signal of resorufin product was read (ex: 540 nm em: 590 nm) in a SpectraMax M5 microplate Reader. IC₅₀ values were then calculated using GraphPad Prism software.

Generation of 3D HeLa MCTS.

MCTS were cultured using ultra-low attachment 96 wells plates from Corning® (Fisher Scientific 15329740). HeLa cells were seeded at a density of 5000 cells per well in 200 µL medium. The single cells would generate MCTS approximately 400 µm in diameter at day 4 with 37 °C and 5 % CO₂.

Treatment of 3D HeLa MCTS.

After 4 days of growing at 37 °C and 5% CO₂, HeLa MCTS were treated for 48 h by replacing half of the medium in the well with medium containing increasing concentration of compounds. For untreated reference MCTS, half of the medium was replaced by fresh medium only. Cytotoxicity was measured by quantification of ATP concentration with CellTiter-Glo® Cell viability kit (Promega, USA).

HeLa MCTSs growth inhibition.

MCTSs were grown and treated as described above. MCTSs sizes were observed under a light microscope and pictures were taken with an iPhone 6s thanks to a phone microscope adaptor. Before imaging, the plate was shaken, and half of the media was exchanged to remove dead cells. Images were recorded before treatment (day 0) and at day 3, 6, 9 and 13 after treatment. Pictures were first processed using GIMP a cross-platform image editor with a batch automation plug-in. The MCTSs sizes were then calculated with SpheroidSizer, a MATLAB-based and open-source software application to measure the size of tumour spheroids automatically and accurately. Data analysis was done using GraphPad Prism software.

Annexin V / PI assay.

Apoptosis and necrosis induction in HeLa cells treated with **[Ru(DIP)₂(mal)](PF₆)** was evaluated *via* an AnnexinV/PI staining assay using flow cytometry. Briefly, cells were seeded at density of 2×10^6 cells in 10 cm cell culture dish 24 h prior cell treatments. The medium was removed and replaced with 10 μ M solution of complex **[Ru(DIP)₂(mal)](PF₆)** or 1 μ M Staurosporin (positive control -Abcam Cat no.120056) and further incubated for 30 min, 4 h or 24 h. Cells were collected, washed twice with ice cold PBS and resuspended in 1x Annexin V binding buffer (10 x buffer composition: 0,1 M HEPES (pH 7.4), 1.4 M NaCl, 25 mM CaCl₂). Samples were processed according to the manufacturer instructions (BD Scientific, cat no 556463 and 556419) and analysed using ZE5 Biorad instrument at Cytometry Platform at Institute Curie. Data were analysed using the FlowJo software.

Sample Preparation for cellular uptake.

Cells were seeded at density of 2×10^6 . Next day, cells were treated with 5 μ M concentration of **[Ru(DIP)₂(mal)](PF₆)** or **RuCl₂(DIP)₂**. After 2 h, cells were collected, counted and snap frozen in liquid nitrogen and stored at -20 °C. ICP-MS samples were prepared as follows: samples were digested using 70% nitric acid (1 mL, 60 °C, overnight). Samples were then further diluted 1:100 (1% HCl solution in MQ water) and analysed using ICP-MS.

Sample Preparation for cellular fractionation.

HeLa cells were seeded in three 15 cm² cell culture dishes so that on the day of treatment cells were 90% confluent. On the day of treatment cells were incubated with the target complex at a concentration of 5 μ M for 2 h. After that time, the medium was removed; cells were washed, collected and counted. After resuspension in cold PBS, the organelles were isolated via different protocols (one cell culture dish per isolation was used).

Mitochondria isolation: To isolate mitochondria, a Mitochondria Isolation Kit (Cat. Nr: MITOISO2, Sigma Aldrich) was used according to the manufacturer procedure for isolation of mitochondria *via* homogenization method.

Lysosome isolation: To isolate lysosomes, a Lysosome Isolation Kit (Cat. Nr: LYSIS01, Sigma Aldrich) was used, according to the manufacturer procedure for isolation of lysosomes *via* Option C.

Nuclear and cytoplasm isolation: To isolate nuclear and cytoplasmic fractions, the ROCKLAND nuclear extract protocol was used.⁸⁵ Briefly cells were collected by centrifugation, resuspended in cytoplasmic extraction buffer and incubated on ice. The tubes were centrifuged and supernatant (CE) was removed. Pellets were washed with cytoplasmic extraction buffer without detergent and centrifuged. The pellet (NE) was resuspended in nuclear extraction buffer and incubated on ice. Both CE and NE were centrifuged. Supernatant from CE samples was indicated as cytoplasmic extract, whereas the pellet obtained from NE samples was indicated as nuclear extract.

ICP-MS samples were prepared as follows: isolated cellular fractions were lyophilised and digested using 5 mL of 70% nitric acid (60 °C, overnight). Samples were then further diluted 1:200 –for nuclear pellet samples and 1:20 for all the other samples (1% HCl solution in MQ water) and analysed using ICP-MS.

Sample preparation for studies on the mechanism of cellular uptake

Samples were prepared as previously reported.¹⁷ Briefly, HeLa cells were seeded at density of 2×10^6 and next day were pre-treated with corresponding inhibitors or kept at specific temperature for 1 h. Next, cells were washed with PBS and were incubated with 5 μ M **[Ru(DIP)₂(mal)](PF₆)** for 2 h (low temperature sample was still kept at 4 °C). Afterwards cells were washed with PBS, collected, counted and snap frozen in liquid nitrogen. Pellets were

stored at -20 °C. ICP-MS samples were prepared as follows: samples were digested using 70% nitric acid (1 mL, 60 °C, overnight), further diluted 1:100 (1% HCl solution in MQ water) and analysed using ICP-MS.

DNA metalation of HeLa cells.

Cells were seeded at density of 2×10^6 . The following day, cells were treated with 5 μ M concentration of **[Ru(DIP)₂(mal)](PF₆)** or cisplatin. After 2 h, cells were collected, snap frozen in liquid nitrogen and stored at -20 °C. The following day, DNA was extracted using a PureLink™ Genomic DNA Mini Kit (Invitrogen). DNA purity was checked by absorbance measurements at 260 and 280 nm. Concentrations of genomic DNA were calculated assuming that one absorbance unit equals 50 μ g/mL. ICP-MS samples were prepared as follows: samples were digested using 70% nitric acid (60 °C, overnight) in 1:1.6 DNA to acid volume ratio. Samples were then further diluted 1:10 or 1:100 (1% HCl solution in MQ water) and analysed using ICP-MS.

ICP-MS studies.

Daily, prior to the analytical sequence, the instrument was first tuned to produce maximum sensitivity and stability while also maintaining low uranium oxide formation ($UO/U \leq 5\%$). The data were treated as follow: intensities were converted into concentrations using uFREASI (user-FRIendly Elemental dAta proceSsIng).⁸⁶ This software, made for HR-ICP-MS users

community, is free and available on <http://www.ipgp.fr/~tharaud/uFREASI>.

ICP-MS data analysis.

Cellular uptake studies: The amount of metal detected in the cell samples was transformed from ppb into μg of metal. Data were subsequently normalised to the number of cells and expressed as μmol of metal/ amount of cells.

Cellular fractionation: The amount of detected ruthenium in the cell samples was transformed from ppb into μg of ruthenium. Values were then normalised to the number of cells used for specific extraction. Due to low yield of lysosome extraction (only 25%), the values obtained were multiplied by the factor of 4. Because of a low yield of mitochondria extraction (50% of the cells were homogenized), the values obtained for that organelle were multiplied by the factor of 2. Extraction protocols allow for the isolation of pure subcellular fractions. Therefore, the total amount of metal found in the cells was calculated summing the values obtained for the pure organelles.

Mechanism of uptake: The amount of ruthenium detected in cell samples was transformed from ppb into μg of ruthenium and values obtained were normalised to the number of cells used for specific treatment. The value for the ruthenium found in the 37 °C sample was used as a 100%.

Cellular metalation: The amount of ruthenium detected in cell samples was transformed from ppb into μg of ruthenium and value obtained was normalised to the amount of DNA.

JC-1 Mitochondrial Membrane Potential Test.

HeLa cells were seeded at a density of 6000 cells / well in black 96 well-plates (Costar 3916). The following day, cells were treated with different concentrations of **[Ru(DIP)₂(mal)](PF₆)** and **RuCl₂(DIP)₂**. After further 24 h, cells were treated according to the instructions of the JC-

1 Mitochondrial Membrane Potential Assay Kit (Abcam, ab113850). The data were analysed using GraphPad Prism software.

Metabolic Studies

HeLa cells were seeded in Seahorse XFe96 well plates at a density of 30,000 cells / well in 80 μ L medium. After 24 h, the medium was replaced with fresh medium and cisplatin (1 μ M), doxorubicin (1 μ M), maltol (1 μ M), complex **RuCl₂(DIP)₂** (1 μ M) or complex **[Ru(DIP)₂(mal)](PF₆)** (1 μ M) were added. After 24 h of incubation, the regular medium was removed, cells were washed thrice using Seahorse Base Media and incubated in a non-CO₂ incubator at 37 °C for 1 h.

Mito Stress Test: Mitostress assay was run using Oligomycin, 1 μ M, FCCP 1 μ M and mixture of Antimycin-A/ Rotenone 1 μ M each in ports A, B and C respectively using Seahorse XFe96 Extracellular Flux Analyzer.

Glycolysis Stress Test: Glycolytic stress test was run using glucose (10 mM), Oligomycin (1 μ M) and 2-Deoxyglucose (50 mM) in ports A, B and C respectively using Seahorse XFe96 Extracellular Flux Analyzer.

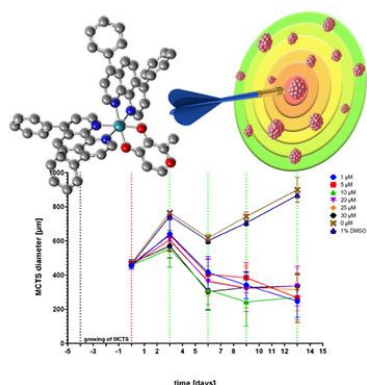
Mito Fuel Flex Test: Fuel flex assay for the different fuel pathways viz. glucose, glutamine and fatty acid was studied by measuring the basal oxygen consumption rates and that after addition of the inhibitor of the target pathway in port A and a mixture of the inhibitors of the other two pathways in port B. This gave a measure of the dependency of the cells on a fuel pathway. To study the capacity of a certain fuel pathway, the sequence of addition of the inhibitors was reversed. In port A was added the mixture of inhibitors for the other pathways and in port B was added the inhibitor for the target pathway. UK-5099 (pyruvate dehydrogenase inhibitor, 20 μ M) was used as an inhibitor for the glucose pathway. BPTES (selective inhibitor of

Glutaminase GLS1, 30 μ M) was used as an inhibitor for the glutamine pathway. Etomoxir (O-carnitine palmitoyltransferase-1 (CPT-1) inhibitor, 40 μ M) was used as an inhibitor for the fatty acid pathway.

Acknowledgements

This work was financially supported by an ERC Consolidator Grant PhotoMedMet to G.G. (GA 681679) and has received support under the program *Investissements d'Avenir* launched by the French Government and implemented by the ANR with the reference ANR-10-IDEX-0001-02 PSL (G.G.). This work was financed by the Swiss National Science Foundation (Professorships N° PP00P2_133568 and PP00P2_157545 to G.G.), the University of Zurich (G.G), the Novartis Jubilee Foundation (G.G. and R.R.), the Forschungskredit of the University of Zurich (R.R.), the University of Trieste (E.A., FRA 2018), and the UBS Promedica Stiftung (G.G. and R.R.). Ile de France Region is gratefully acknowledged for financial support of 500 MHz NMR spectrometer of Chimie-ParisTech in the framework of the SESAME equipment project. We acknowledge the loan of Agilent's equipment to Chimie ParisTech. This work was supported by National Research, Development and Innovation Office-NKFIA through projects GINOP-2.3.2-15-2016-00038, FK 124240. SF is supported by the Czech Science Foundation grant 17-02080S.

TOC picture



References.

- 1 G. Gasser, I. Ott and N. Metzler-Nolte, *J. Med. Chem.*, 2011, **54**, 3–25.
- 2 B. B. Rosenberg, *Platin. Met. Rev.*, 1971, **15**, 42–51.
- 3 E. Wong and C. M. Giandomenico, *Chem. Rev.*, 1999, **99**, 2451–2466.
- 4 E. S. Antonarakis and A. Emadi, *Cancer Chemother. Pharmacol.*, 2010, **66**, 1–9.
- 5 E. Alessio, *Eur. J. Inorg. Chem.*, 2017, **55**, 1549–1560.
- 6 L. Zeng, P. Gupta, Y. Chen, E. Wang, L. Ji, H. Chao, Z.-S. Chen, J. Mai, H. Zhang, Z. Li, M. Guevara, Z.-W. Mao, H. Shen, G. Superti-Furga, B. K. Keppler and C. G. Hartinger, *Chem. Soc. Rev.*, 2017, **46**, 5771–5804.
- 7 E. Alessio and L. Messori, *Molecules*, 2019, **24**, 1995.
- 8 G. Sava, I. Capozzi, K. Clerici, G. Gagliardi, E. Alessio and G. Mestroni, *Clin. Exp. Metastasis*, 1998, **16**, 371–379.
- 9 F. Lentz, A. Drescher, A. Lindauer, M. Henke, R. a Hilger, C. G. Hartinger, M. E. Scheulen, C. Dittrich, B. K. Keppler and U. Jaehde, *Anticancer. Drugs*, 2009, **20**, 97–103.
- 10 R. Trondl, P. Heffeter, C. R. Kowol, M. a. Jakupec, W. Berger and B. K. Keppler, *Chem. Sci.*, 2014, **5**, 2925–2932.
- 11 C. G. Hartinger, S. Zorbas-Seifried, M. A. Jakupec, B. Kynast, H. Zorbas and B. K.

- Keppler, *J. Inorg. Biochem.*, 2006, **100**, 891–904.
- 12 H. Yin, J. Roque, P. Konda, S. Monro, K. L. Colo, S. Gujar, R. P. Thummel, L. Lilge, C. G. Cameron and S. A. Mcfarland, *Chem. Rev.*, 2019, **119**, 797–828.
- 13 <https://clinicaltrials.gov/ct2/show/NCT03945162?term=TLD-1433&rank=1>, (accessed the 27/ 09/ 2019).
- 14 C. A. Griffith, A. Dayoub, T. Janaratne, N. Alatrash, K. Abayan, A. Mohamedi, Z. Breitbach, D. W. Armstrong and F. M. MacDonnell, *Chem. Sci.*, 2017, **8**, 3726–3740.
- 15 F. E. Poynton, S. A. Bright, S. Blasco, D. C. Williams, J. M. Kelly and T. Gunnlaugsson, *Chem Soc Rev*, 2017, **46**, 7706.
- 16 A. Notaro and G. Gasser, *Chem. Soc. Rev.*, 2017, **46**, 7317–7337.
- 17 A. Notaro, A. Frei, R. Rubbiani, M. Jakubaszek, U. Basu, S. Koch, C. Mari, M. Dotou, O. Blacque, J. Gouyon, F. Bedioui, N. Rotthowe, R. F. Winter, B. Goud, S. Ferrari, M. Tharaud, M. Řezáčová, J. Humajová, P. Tomšík and G. Gasser, *ChemRxiv. Prepr.*, , DOI:10.26434/chemrxiv.9582527.v1.
- 18 L. F. B. and H. CHEW, *Mutat. Res.*, 1979, **67**, 367–371.
- 19 H. Ito, *Agric. biol. chem.*, 1977, **41**, 1307–1308.
- 20 C. I--food and H. Services, *CFR Code Fed. Regul.*, 2018, **3**, 1–18.
- 21 A. F. Bingham, G. G. Birch, C. De Graaf, J. M. Behan and K. D. Perring, *Chem. Senses*, 1990, **15**, 447–456.
- 22 V. Kahn, F. Schved and P. Lindner, *J. Food Biochem.*, 1993, **17**, 217–233.
- 23 W. O. Nelson, T. B. Karpishin, S. J. Rettig and C. Orvig, *Inorg. Chem.*, 1988, **27**, 1045–1051.
- 24 P. C. Lucio, G. Nicholas, G. F. Geoffrey, H. Huali, J. H. Mcneill, S. J. Rettig, I. A. Setyawati, E. Shuter, Y. Sun, A. S. Tracey, V. G. Yuen and C. Orvig, *J. Am. Chem. Soc.*, 1995, **117**, 12759–12770.
- 25 K. Murakami, K. Ishida, K. Watakabe, R. Tsubouchi, M. Naruse and M. Yoshino, *Toxicol. Lett.*, 2006, **161**, 102–107.

- 26 B. L. Ellis, A. K. Duhme, R. C. Hider, M. B. Hossain and S. Rizvi, *J. Med. Chem.*, 1996, **2623**, 3659–3670.
- 27 S. J. Lord, N. A. Epstein, R. L. Paddock, C. M. Vogels, T. L. Hennigar, M. J. Zaworotko, N. J. Taylor, W. R. Driedzic, T. L. Broderick and S. A. Westcott, *Can. J. Chem.*, 1999, **1261**, 1249–1261.
- 28 K. H. Thompson, C. A. Barta, C. Orvig and K. Thompson, *Chem. Soc. Rev.*, 2006, **35**, 545–556.
- 29 K. H. Thompson, J. Chiles, V. G. Yuen, J. Tse, J. H. McNeill and C. Orvig, *J. Inorg. Biochem.*, 2004, **98**, 683–690.
- 30 O. Dömötör, S. Aicher, M. Schmidlehner, M. S. Novak, A. Roller, M. A. Jakupec, W. Kandioller, C. G. Hartinger, B. K. Keppler and É. A. Enyedy, *J. Inorg. Biochem.*, 2014, **134**, 57–65.
- 31 W. Kandioller, C. G. Hartinger, A. A. Nazarov, C. Bartel, M. Skocic, M. A. Jakupec, V. B. Arion and B. K. Keppler, *Chem. Eur. J.*, 2009, 12283–12291.
- 32 L. Fang, S. Ming, H. Ling, K. Soo, R. Vikneswaran, S. Guan, M. Ahmad, S. Alan, M. Jamil and C. Hee, *J. Inorg. Biochem.*, 2011, **105**, 339–347.
- 33 V. D. Reddy, D. Dayal, D. J. Szalda, S. C. Cosenza and M. V. R. Reddy, *J. Organomet. Chem.*, 2012, **700**, 180–187.
- 34 M. Hironishi, R. Kordek, R. Yanagihara and R. M. Garruto, *NEURODEGENERATION*, 1996, **5**, 325–329.
- 35 E. Yasumoto, K. Nakano, T. Nakayachi, S. R. Morshed, K. E. N. Hashimoto, H. Kikuchi, H. Nishikawa, M. Kawase and H. Sakagami, *Anticancer Res.*, 2004, **762**, 755–762.
- 36 M. A. Barrand and B. A. Callingham, *Br. J. Pharmacol.*, 1991, **102**, 408–414.
- 37 M. A. Barrand, R. C. Hider and B. A. Callingham, *J. Pharm. Pharmacol.*, 1990, **42**, 105–107.
- 38 K. H. Thompson, J. Lichter, C. Lebel, M. C. Scaife, J. H. McNeill and C. Orvig, *J. Inorg. Biochem.*, 2009, **103**, 554–558.

- 39 K. H. Thompson, Æ. B. D. Liboiron, Æ. Y. Sun, B. O. Patrick, Æ. V. Karunaratne, Æ. G. Rawji, C. Cassidy, Æ. J. H. McNeill and Æ. V. G. Yuen, *J Biol Inorg Chem*, 2003, **8**, 66–74.
- 40 K. H. Thompson and C. Orvig, *J. Chem. Soc., Dalt. Trans.*, 2000, 2885–2892.
- 41 D. C. Crans, S. Schoeberl and D. A. Roess, *J Biol Inorg Chem*, 2011, **16**, 961–972.
- 42 L. R. Bernstein, T. Tanner, C. Godfrey, B. Noll, W. Road and M. Park, *Met. Based. Drugs*, 2000, **7**, 33–47.
- 43 M. A. Jakupec and B. K. Keppler, *Curr. Top. Med. Chem.*, 2004, **4**, 1575–1583.
- 44 C. R. Chitambar, D. P. Purpi, J. Woodliff, M. Yang and J. P. Wereley, *J. Pharmacol. Exp. Ther.*, 2007, **322**, 1228–1236.
- 45 É. A. Enyedy, O. Dömötör, K. Bali and B. K. Keppler, *J Biol Inorg Chem*, 2015, **20**, 77–88.
- 46 K. Deleon, F. Balldin, C. Watters, A. Hamood, J. Griswold, S. Sreedharan and K. P. Rumbaugh, *Antimicrob. Agents Chemother.*, 2009, **53**, 1331–1337.
- 47 L. G. Id, L. R. B. Id, A. M. Haynes, C. Godornes, G. Ciccarese, F. Drago, A. Parodi, S. Valdevit, L. Anselmi, C. F. Tomasini and A. M. Baca, *PLoS Negl. Trop. Dis.*, 2019, 1–14.
- 48 C. R. Chitambar, M. M. Al-gizawiy, H. S. Alhajala, K. R. Pechman, J. P. Wereley, R. Wujek, P. A. Clark, J. S. Kuo, W. E. Antholine and K. M. Schmainda, *Mol Cancer Ther*, 2018, 1–12.
- 49 M. Chua, L. R. Bernstein, R. U. I. Li and S. K. S. So, *Anticancer Res.*, 2006, **1744**, 1739–1743.
- 50 W. Kandioller, C. G. Hartinger, A. A. Nazarov, J. Kasser, R. John, M. A. Jakupec, V. B. Arion, P. J. Dyson and B. K. Keppler, *J. Organomet. Chem.*, 2009, **694**, 922–929.
- 51 C. G. Hartinger, R. E. Eichinger, N. Stolyarova, K. Severin, M. A. Jakupec, A. A. Nazarov and B. K. Keppler, *Organometallics*, 2008, **27**, 2405–2407.
- 52 I. Brastos, E. Alessio, M. E. Ringenberg and T. B. Rauchfuss, *Inorg. Synth.*, 2010, **35**,

- 148–163.
- 53 R. Caspar, C. Cordier, J. B. Waern, C. Guyard-Duhayon, M. Gruselle, P. Le Floch and H. Amouri, *Inorg. Chem.*, 2006, **45**, 4071–4078.
- 54 M. Haga, E. S. Dodsworth and A. B. P. Lever, *Inorg. Chem.*, 1986, **25**, 447–453.
- 55 S. L. H. Higgins, T. A. White, B. S. J. Winkel and K. J. Brewer, *Inorg. Chem.*, 2011, **50**, 463–470.
- 56 P. Sobota, K. Przybylak, J. Utko, L. B. Jerzykiewicz, A. J. L. Pombeiro, M. F. C. Guedes Da Silva and K. Szczegot, *Chem. - A Eur. J.*, 2001, **7**, 951–958.
- 57 M. Patra, T. Joshi, V. Pierroz, K. Ingram and M. Kaiser, *Chem. Eur. J.*, 2013, **19**, 14768–14772.
- 58 M. D. Hall, K. A. Telma, K.-E. Chang, T. D. Lee, J. P. Madigan, J. R. Lloyd, I. S. Goldlust and M. M. Hoeschele, James D. Gottesman, *Cancer Res.*, 2014, **74**, 3913–3922.
- 59 H. Huang, N. Humbert, V. Bizet, M. Patra and H. Chao, *J. Organomet. Chem.*, 2017, **839**, 15–18.
- 60 J. R. Lakowicz, *Principles of Fluorescence Spectroscopy*, 2006. 3rd Edition, Springer-Verlag New York Inc
- 61 V. Pierroz, T. Joshi, A. Leonidova, C. Mari, J. Schur, I. Ott, L. Spiccia, S. Ferrari and G. Gasser, *J. Am. Chem. Soc.*, 2012, **134**, 20376–20387.
- 62 S. J. Bruce, I. Tavazzi, S. Rezzi, S. Kochhar and P. A. Guy, 2009, **81**, 3285–3296.
- 63 A. Frei, R. Rubbiani, S. Tubafard, O. Blacque, P. Anstaett, A. Felgenträger, T. Maisch, L. Spiccia and G. Gasser, *J. Med. Chem.*, 2014, **57**, 7280–7292.
- 64 V. Cepeda, M. Fuertes, J. Castilla, C. Alonso, C. Quevedo and J. Perez, *Anticancer. Agents Med. Chem.*, 2007, **7**, 3–18.
- 65 H. G. Keizer, H. M. Pinedo, G. J. Schuurhuis and H. Joenje, *Pharmac. Ther.*, 1990, **47**, 219–231.
- 66 J. M. Kelm, N. E. Timmins, C. J. Brown, M. Fussenegger and L. K. Nielsen, *Biotechnol. Bioeng.*, 2003, **83**, 173–180.

- 67 H. Ma, Q. Jiang, S. Han, Y. Wu, J. C. Tomshine, D. Wang, Y. Gan and G. Zou, *Mol. Imaging*, 2012, **11**, 487–498.
- 68 M. Kapalczyńska, T. Kolenda, A. Przybyła, Weronika Zajączkowska, Maria Teresiak, V. Filas, M. Ibbs, R. Bliźniak and K. Łuczewski, Łukasz Lamperska, *Arch Med Sci*, 2018, **4**, 910–919.
- 69 J. Friedrich, C. Seidel, R. Ebner and L. A. Kunz-schughart, *Nat. Protoc.*, 2009, **4**, 309–324.
- 70 J. Hess, H. Huang, A. Kaiser, V. Pierroz and O. Blacque, 2017, 9888–9896.
- 71 O. W. Seo, M. Kim, J. Hulme and S. S. A. An, 2016, 7207–7218.
- 72 A. C. Belmokhtar, J. Hillion and E. Ségal-Bendirdjian, *Oncogene*, 2001, 3354–3362.
- 73 L. Zeng, Y. Chen, H. Huang, J. Wang, D. Zhao, L. Ji and H. Chao, *Chemistry*, 2015, **21**, 15308–15319.
- 74 J. Zisowsky, S. Koegel, S. Leyers, K. Devarakonda, M. U. Kassack, M. Osmak and U. Jaehde, *Biochem. Pharmacol.*, 2007, **73**, 298–307.
- 75 V. N. Dedov, G. C. Cox and B. D. Roufogalis, *Micron*, 2001, **32**, 653–660.
- 76 L. D. Zorova, V. A. Popkov, E. Y. Plotnikov, D. N. Silachev, B. Pevzner, S. S. Jankauskas, V. A. Babenko, S. D. Zorov, A. V Balakireva, M. Juhaszova, S. J. Sollott and D. B. Zorov, *Anal. Biochem.*, 2018, 50–59.
- 77 S. Sakamuru, M. S. Attene-ramos and M. Xia, in *High-Throughput Screening Assays in Toxicology, Methods in Molecular Biology*, 2016, vol. 1473, pp. 17–22.
- 78 H. Terada, *Environ. Health Perspect.*, 1990, **87**, 213–218.
- 79 G. R. Fulmer, A. J. M. Miller, N. H. Sherden, H. E. Gottlieb, A. Nudelman, B. M. Stoltz, J. E. Bercaw and K. I. Goldberg, *Organometallics*, 2010, **29**, 2176–2179.
- 80 M. Krachler, *J. Environ. Monit.*, 2007, **9**, 790–804.
- 81 C. Mari, V. Pierroz, R. Rubbiani, M. Patra, J. Hess, B. Spingler, L. Oehninger, J. Schur, I. Ott, L. Salassa, S. Ferrari and G. Gasser, 2014, 1–17.

- 82 G. H. Beaven, S. Chen, A. D. Albis and W. B. Gratzler, *Eur. J. Biochem.*, 1974, **546**, 539–546.
- 83 P. Gans, A. Sabatini and A. Vacca, *Talanta Investig.*, 1996, **43**, 1739–1753.
- 84 O. Domotor, C. G. Hartinger, A. K. Bytzeck, T. Kiss, B. K. Keppler and E. A. Enyedy, *J Biol Inorg Chem*, 2013, 9–17.
- 85 <https://rockland-inc.com/Nuclear-Extract-Protocol.aspx>, (accessed the 03.10.2019).
- 86 M. Tharaud, S. Gardoll, O. Khelifi, M. F. Benedetti and Y. Sivry, *Microchem. J.*, 2015, **121**, 32–40.

Supplementary Information

A maltol-containing Ruthenium Polypyridyl Complex as a Potential Anticancer Agent

*Anna Notaro,^[a] Marta Jakubaszek,^[a, b] Severin Koch,^[c] Riccardo Rubbiani,^[c] Orsolya Dömötör,^[d] Éva A. Enyedy,^[d, e] Mazzarine Dotou,^[a] Fethi Bedioui,^[f] Mickaël Tharaud,^[g]
Bruno Goud,^[b] Stefano Ferrari,^[h, i] Enzo Alessio,^[j] and Gilles Gasser^{*[a]}*

^[a] Chimie ParisTech, PSL University, CNRS, Institute of Chemistry for Life and Health Sciences, Laboratory for Inorganic Chemical Biology, F-75005 Paris, France.

^[b] Institut Curie, PSL University, CNRS UMR 144, Paris, France.

^[c] Department of Chemistry, University of Zurich, Winterthurerstrasse 190, 8057 Zurich, Switzerland.

^[d] Department of Inorganic and Analytical Chemistry, Interdisciplinary Excellence Centre, University of Szeged, Dóm tér 7. H-6720 Szeged, Hungary.

^[e] MTA-SZTE Momentum Functional Metal Complexes Research Group, University of Szeged, Dóm tér 7, H-6720 Szeged, Hungary.

^[f] Chimie ParisTech, PSL University, CNRS, Institute of Chemistry for Life and Health Sciences, Team Synthèse, Electrochimie, Imagerie et Systèmes Analytiques pour le Diagnostic, F-75005 Paris, France.

^[g] Université de Paris, Institut de physique du globe de Paris, CNRS, F-75005 Paris, France.

^[h] Institute of Molecular Cancer Research, University of Zurich, Zurich, Switzerland.

^[i] Institute of Molecular Genetics of the Czech Academy of Sciences, Videnska 1083, 143 00 Prague, Czech Republic.

^[j] Department of Chemical and Pharmaceutical Sciences, University of Trieste, Via L. Giorgieri 1, 34127 Trieste, Italy.

* Corresponding author: E-mail: gilles.gasser@chimeparistech.psl.eu; WWW: www.gassergroup.com; Phone: +33 1 44 27 56 02

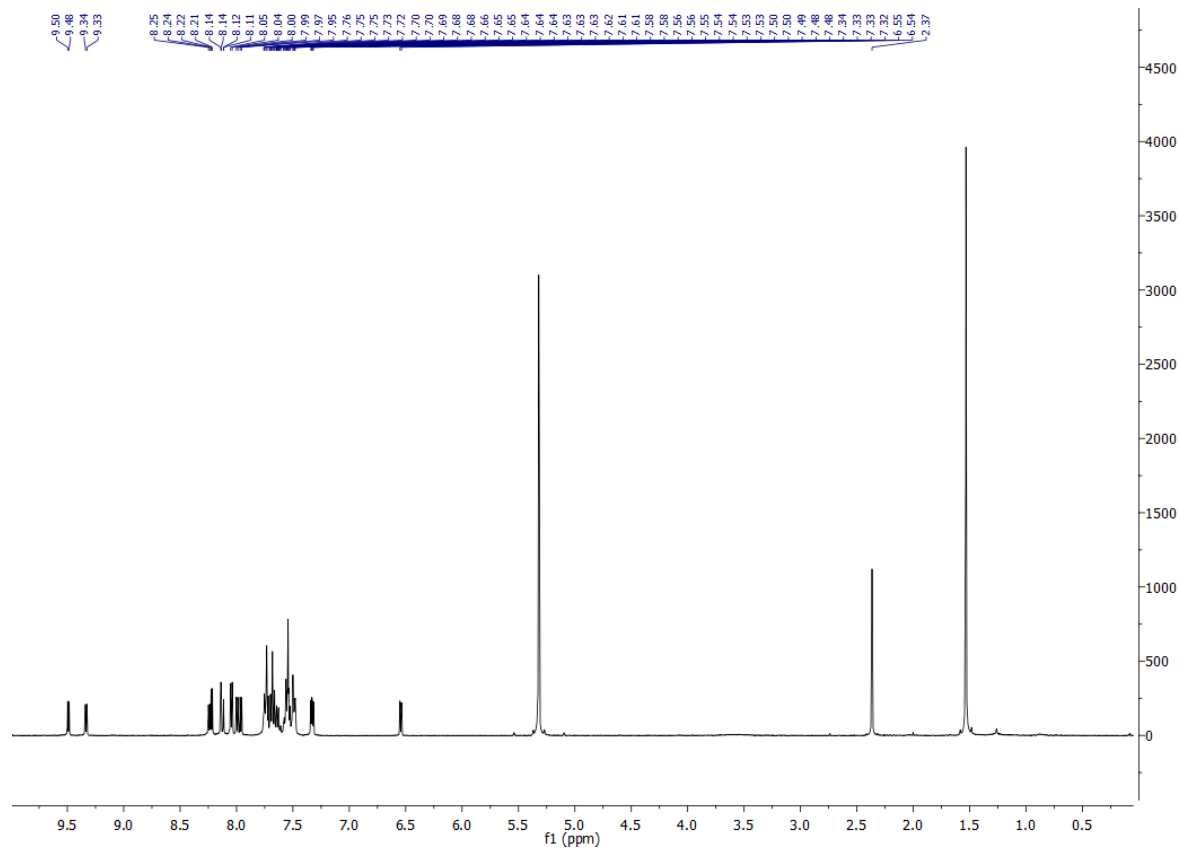
Table of Contents

FIGURE S1. NMR SPECTRA OF [RU(DIP)₂(MAL)](PF₆).....	554
[RU(DIP) ₂ (MAL)](PF ₆), ¹ H, CD ₂ Cl ₂ , 400 MHz	554
[RU(DIP) ₂ (MAL)](PF ₆), ¹³ C{ ¹ H}, CD ₂ Cl ₂ , 125 MHz	555
FIGURE S2. VOLTAMMOGRAMS RECORDED BY CV AND WITH THE USE OF RDE FOR [RU(DIP)₂(MAL)](PF₆)	556
TABLE S1. ELECTROCHEMICAL DATA FOR [RU(DIP)₂(MAL)](PF₆).....	557
FIGURE S3. OVERLAP OF THE ¹H SPECTRA (DOWNFIELD REGION) OF [RU(DIP)₂(MAL)](PF₆) IN DMSO-D₆ AT ROOM TEMPERATURE OVER 42H.	558
DETAILED INVESTIGATION ON THE STABILITY OF THE COMPLEX IN DIFFERENT SOLVENTS AND CONDITIONS.	559
FIGURE S4. TIME-DEPENDENT UV-VIS ABSORBANCE SPECTRA OF [RU(DIP)₂(MAL)](PF₆) IN DIFFERENT CONDITIONS	562
FIGURE S5. NORMALIZED ABSORBANCE VALUES AS A FUNCTION OF TIME AT 286 NM AND 390 NM AT THE INDICATED CONDITIONS.....	562
MORE DETAILS ON INTERACTION WITH HUMAN SERUM ALBUMIN	563
FIGURE S6. UV-VIS ABSORBANCE SPECTRA OF [RU(DIP)₂(MAL)](PF₆) FOLLOWED IN RPMI 1640 CELL CULTURE MEDIUM AND IN 20 MM PHOSPHATE BUFFER CONTAINING 100 MM HSA.	563
FIGURE S7. UV-VIS ABSORBANCE SPECTRA OF [RU(DIP)₂(MAL)](PF₆) ALONE AND IN THE PRESENCE OF 0.03-2.0 EQ OF HSA	564
FIGURE S8. CHANGES OF TRP214 FLUORESCENCE IN HSA IN THE PRESENCE OF [RU(DIP)₂(MAL)](PF₆),	565
EXPERIMENTAL FOR THE ULTRAFILTRATION AND CIRCULAR DICHROISM STUDIES	566
FIGURE S9. RP-UPLC TRACES OF [RU(DIP)₂(MAL)](PF₆) INCUBATED IN HUMAN PLASMA AT 37 °C	567
FIGURE S10. EVALUATION OF THE CYTOTOXICITY IN 2D CELL CULTURE MODELS VIA FLUOROMETRIC CELL VIABILITY ASSAY.	568

FIGURE S12. CELL DEATH MECHANISM.	574
FIGURE S13. CELLULAR UPTAKE MECHANISM OF [RU(DIP)₂(MAL)](PF₆).	575
FIGURE S14. OXYGEN CONSUMPTION RATES AND DIFFERENT RESPIRATION PARAMETERS IN HELA CELLS ALONE OR AFTER TREATMENT WITH VARIOUS TEST COMPOUNDS.	576
FIGURE S15. EXTRACELLULAR ACIDIFICATION RATE AND DIFFERENT PARAMETERS DURING GLYCOLYSIS IN HELA CELLS ALONE OR AFTER TREATMENT WITH VARIOUS TEST COMPOUNDS.	577
FIGURE S16. FUEL FLEX ASSAY IN HELA CELLS.	578

Figure S1. NMR spectra of **[Ru(DIP)₂(mal)](PF₆)**

[Ru(DIP)₂(mal)](PF₆), ¹H, CD₂Cl₂, 400 MHz



[Ru(DIP)₂(mal)](PF₆), ¹³C{¹H}, CD₂Cl₂, 125 MHz

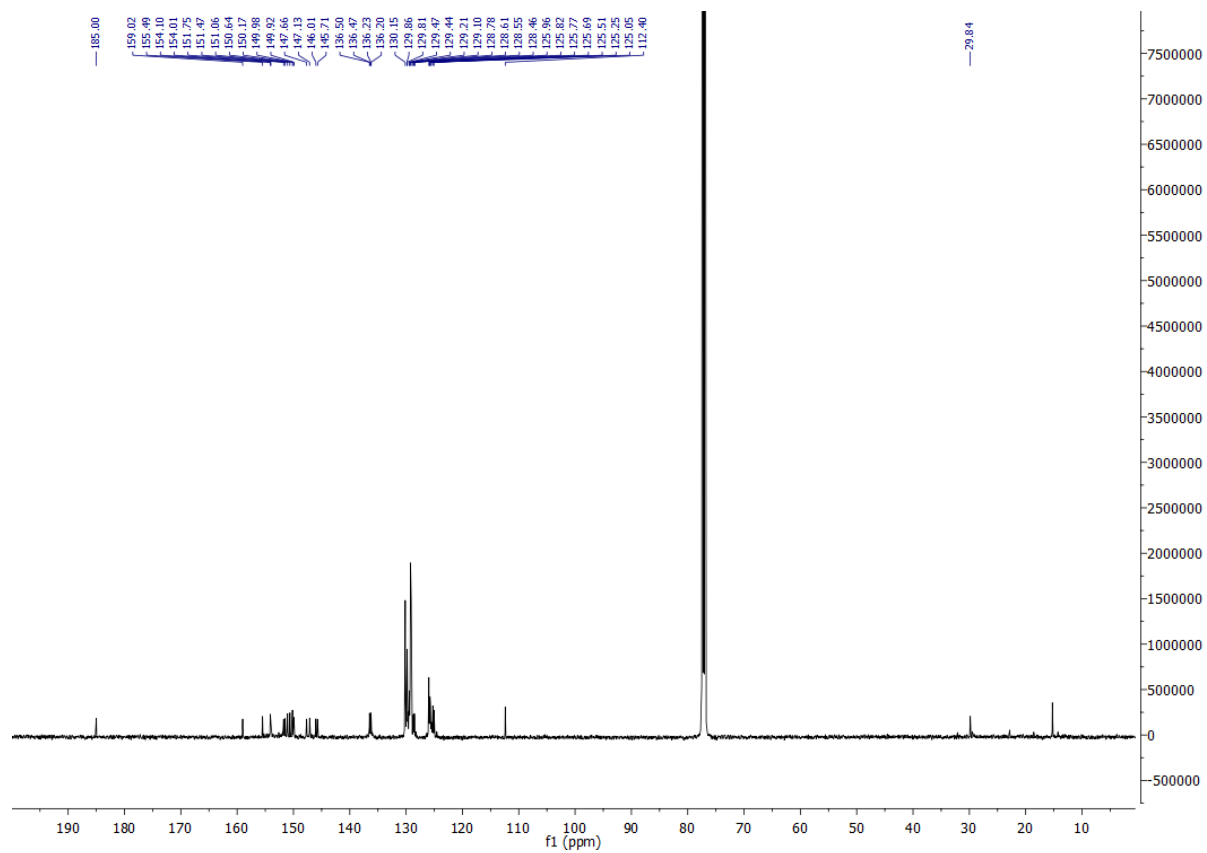


Figure S2. Voltammograms recorded by CV (upper figure) and with the use of RDE (lower figure) for $[\text{Ru}(\text{DIP})_2(\text{mal})](\text{PF}_6)$ (from -2.1 to +1 V) with a glassy carbon electrode in DMF (1 mM) containing Bu_4NPF_6 (100 mM) as supporting electrolyte and decamethylferrocene as an internal standard (0.25 mM). Data were recorded versus saturated calomel electrode at scan rate of 100 mV/s and recalculated versus $\text{Me}_{10}\text{Fc}^{0/+}$ potential value (feature marked with * in Figure S2).

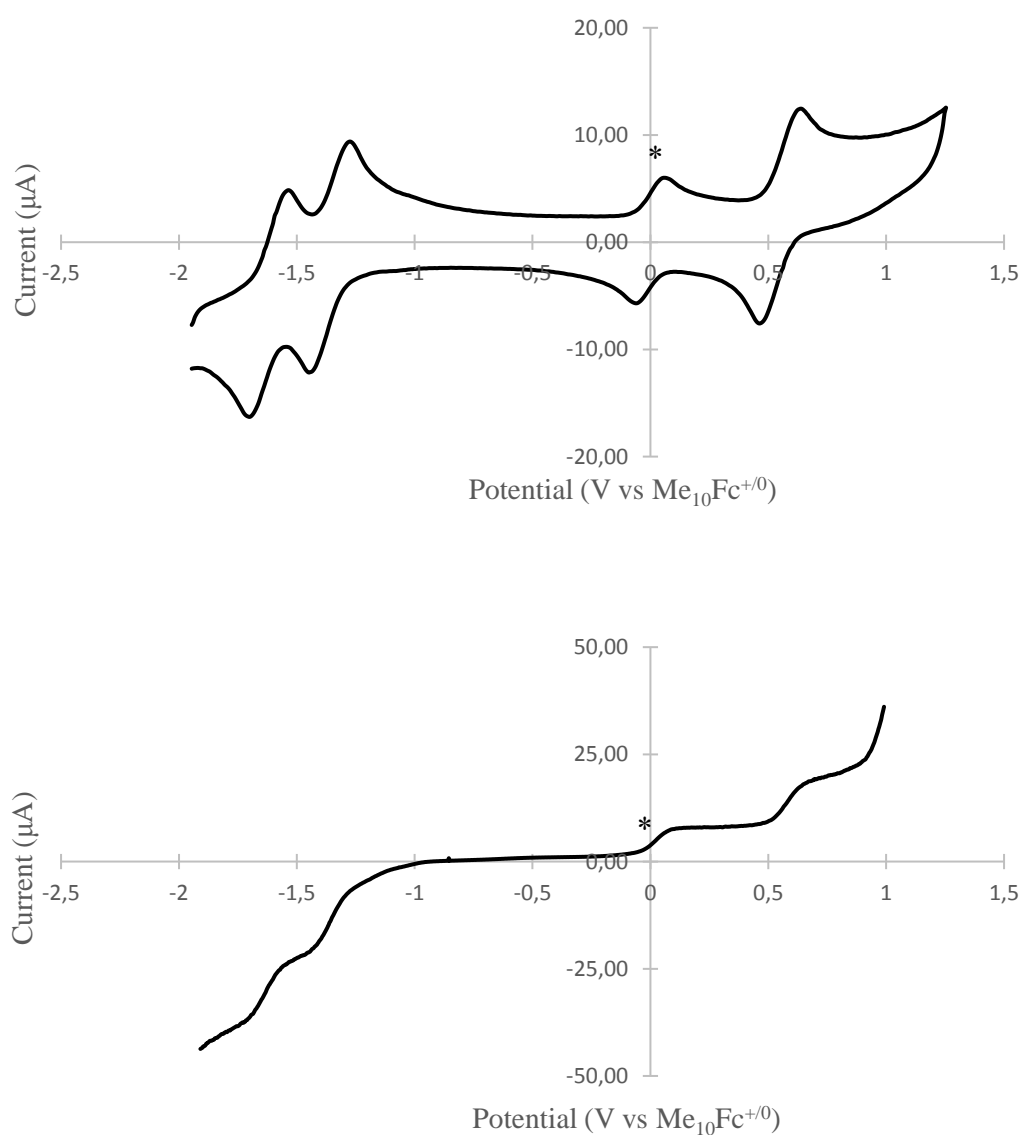
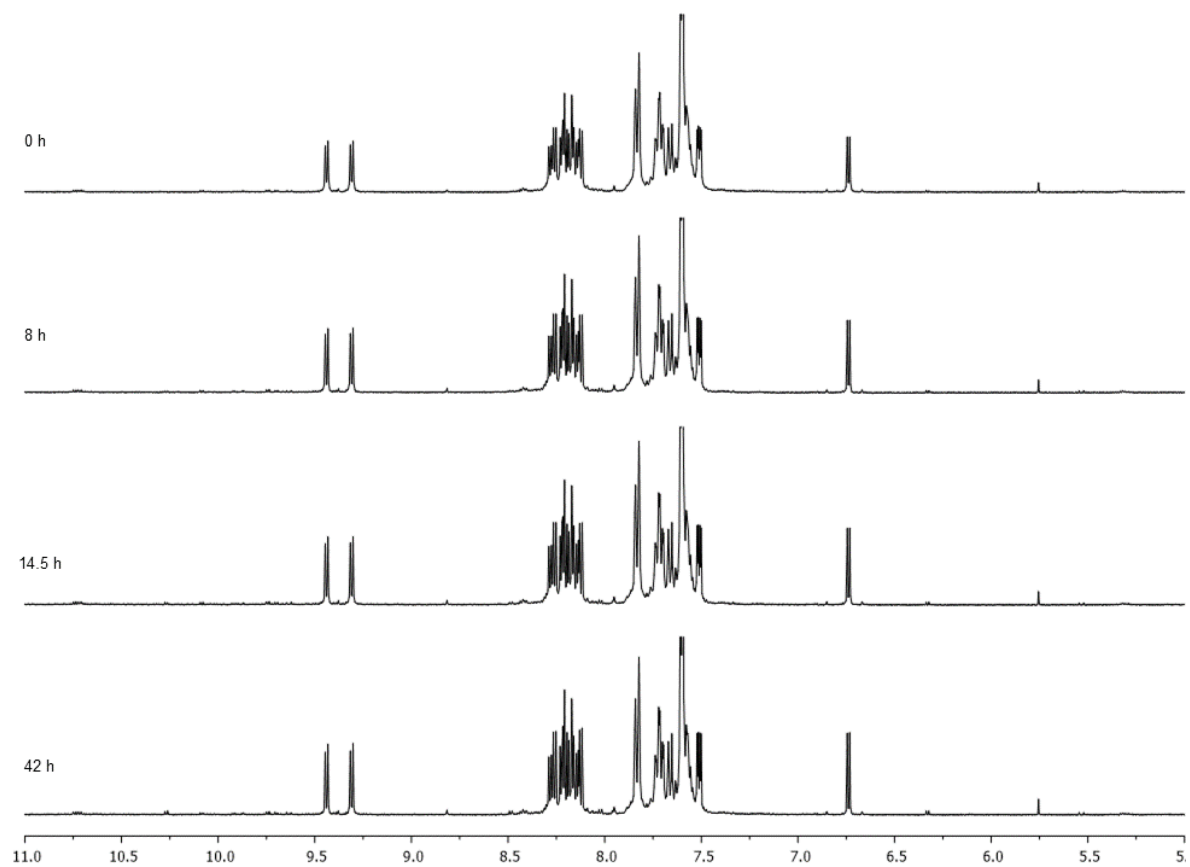


Table S1. Electrochemical data for **[Ru(DIP)₂(mal)](PF₆)**.

		DIP^{0/-}	DIP^{0/-}	Ru^{III/II}
[Ru(DIP)₂(mal)](PF₆)	E_{1/2}^a [V] (RDE)	-1.636 ± 0.020	-1.341 ± 0.017	+0.566 ± 0.037
	E_{1/2}^b [V] (CV)	-1.624 ± 0.030	-1.358 ± 0.004	+0.550 ± 0.005

^a E_{1/2} = half-wave.^b E_{1/2} = (E_{pa} + E_{pc})/2.

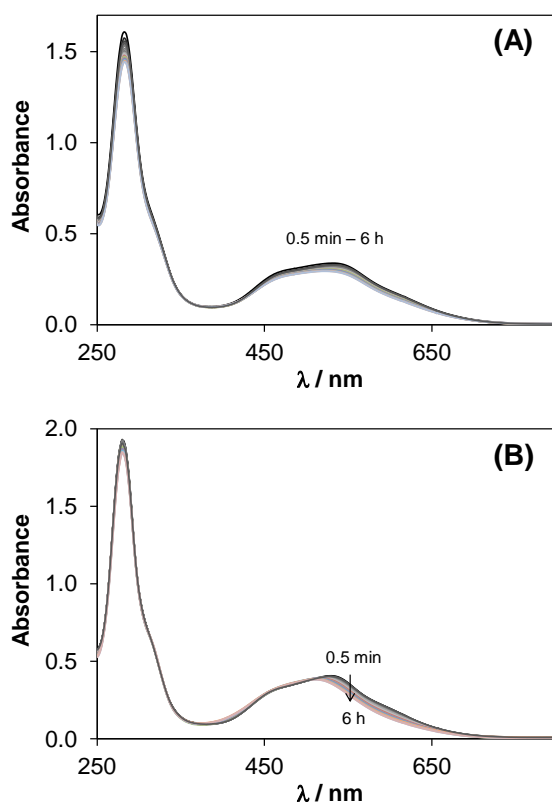
Figure S3. Overlap of the ^1H spectra (downfield region) of $[\text{Ru}(\text{DIP})_2(\text{mal})](\text{PF}_6)$ in DMSO-d_6 at room temperature over 42h.



Detailed investigation on the stability of the complex in different solvents and conditions.

Poor water solubility of $[\text{Ru}(\text{DIP})_2(\text{mal})](\text{PF}_6)$ prevented direct preparation of aqueous samples. Low molecular mass components of the blood serum are often able to solubilize metal complexes as a result of ligand exchange interactions. RPMI 1640 cell culture medium, containing phosphate and hydrogen carbonate buffered saline, inorganic ions Ca^{2+} , Mg^{2+} , K^+ , Na^+ , glucose, essential and some non-essential amino acids in higher concentration, was also not suitable to dissolve $[\text{Ru}(\text{DIP})_2(\text{mal})](\text{PF}_6)$ in aqueous medium. Therefore, stock solutions prepared in ethanol or in methanol were used for further sample preparation; final samples contained $\leq 2\%$ (v/v) alcohol. The alcoholic (ethanol or methanol) stock solutions showed only slight spectral changes within 6 h (Fig. S4/B). The sample in pure ethanol was well filterable by ultrafilter devices and $\sim 100\%$ of the complex could be found in the filtered (bottom) fraction. By ultrafiltration of aqueous samples (containing $\sim 2\%$ (v/v) ethanol), complex stuck to the filter membrane, that allowed us to study the possible appearance of liberated maltol ligand in the filtrate fraction (maltol itself is well filterable). Filtrate fraction of samples filtered immediately after preparation and after 6 h waiting, showed low absorbances (see Fig. S4/C/inset for HEPES buffered sample after 6 h) in the studied wavelength range suggesting that the complex stuck to the filter and did not decompose (i.e. no ligand dissociation occurred). Spectral changes observed in HEPES and phosphate buffers refer to only moderate changes in the complex structure. Aggregation followed by precipitation of the complex is a possible explanation for that. As next step the effect of oxidative, oxygen-free or reductive conditions were investigated; oxygen or argon was bubbled through HEPES buffered samples or 50 eq (1 mM) of GSH was added to the sample containing the $[\text{Ru}(\text{DIP})_2(\text{mal})](\text{PF}_6)$ complex. In Fig. S5/A and B oxygenated sample shows faster and more pronounced spectral changes compared to the only HEPES buffered sample. Data are shown for samples containing no precipitation.

In the oxygenated sample precipitation occurred after 1 h. On the other hand, applying argon atmosphere or the addition of biological reductant GSH seem to prevent partially the spectral changes and delay the concomitant precipitation of the complex (Fig. S5). ^1H NMR spectra recorded for samples containing 1 mM $[\text{Ru}(\text{DIP})_2(\text{mal})](\text{PF}_6)$ complex in methanol- d_4 or in phosphate buffer – methanol- d_4 70:30 (V/V) solvent mixture did not show the appearance of free, non-coordinated maltol or 4,7-diphenyl-1,10-phenantroline, however precipitation occurred in the buffered sample under these conditions providing no reliable result on the solution chemistry of this compound.



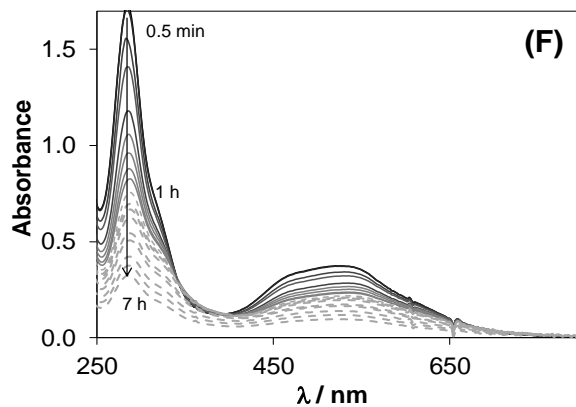
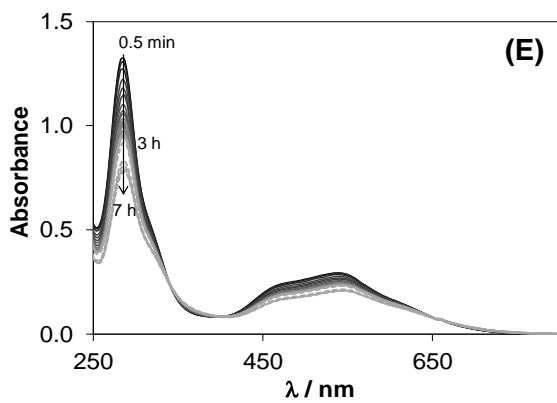
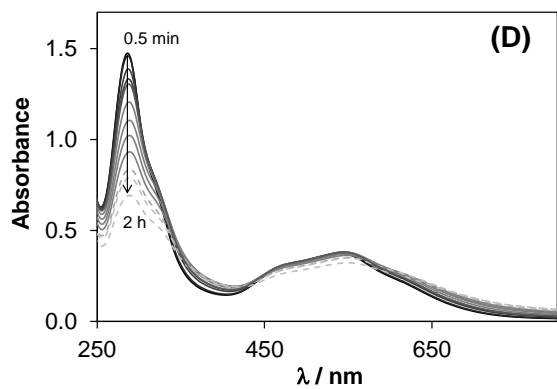
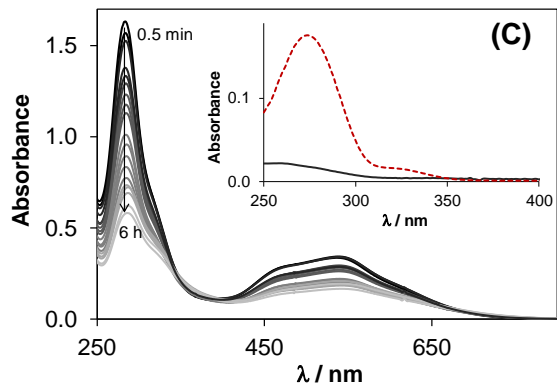


Figure S4. Time-dependent UV-Vis absorbance spectra of $[\text{Ru}(\text{DIP})_2(\text{mal})](\text{PF}_6)$ followed in water/ethanol (pH ~ 8) (A); ethanol (B); 20 mM HEPES/ethanol (pH = 7.4) (C); 20 mM phosphate/ethanol (pH = 7.40) (D); and under argon atmosphere (E) or in oxygen atmosphere (F) in 20 mM HEPES/ethanol (pH = 7.40). Grey dashed spectra refer to the appearance of precipitation. Inset in (C) shows the spectrum of filtrate fraction of sample (C) after 6 h (solid black line) and calculated spectrum (dashed red line) of maltol which should be detected at 100% decomposition of the original complex ($19.8 \mu\text{M}$ maltol) $\{c_{\text{complex}} = 19.8 \mu\text{M}$ (A,C,D) or $21.7 \mu\text{M}$ (B,F) or $17.2 \mu\text{M}$ (E), 2% ethanol (v/v) (in A,C-F), pure ethanol (B); $T = 25 \text{ }^\circ\text{C}\}$.

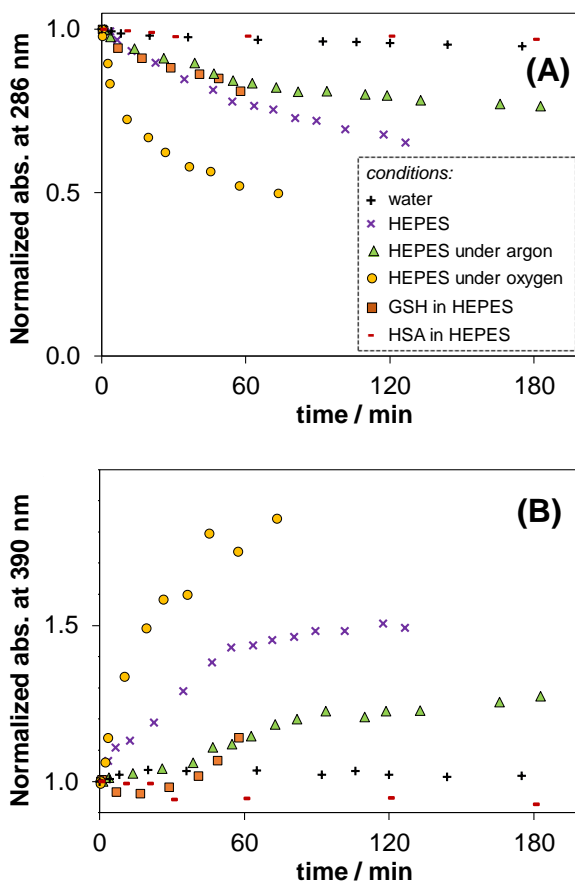


Figure S5. Normalized absorbance values as a function of time at 286 nm (A) and 390 nm (B) at the indicated conditions. Data are shown until no precipitation occurred in the samples. $\{c_{\text{complex}} \approx 20 \mu\text{M}$, $c_{\text{HSA}} = 100 \mu\text{M}$, $c_{\text{GSH}} = 1 \text{ mM}$, 2% ethanol (v/v), $T = 25 \text{ }^\circ\text{C}\}$

More details on interaction with human serum albumin

The presence of human serum albumin (HSA) hindered the precipitation of $[\text{Ru}(\text{DIP})_2(\text{mal})](\text{PF}_6)$ in 20 mM phosphate and HEPES buffered samples, and no liberation of maltol or 4,7-diphenyl-1,10-phenantroline was detected in ultrafiltration experiments.

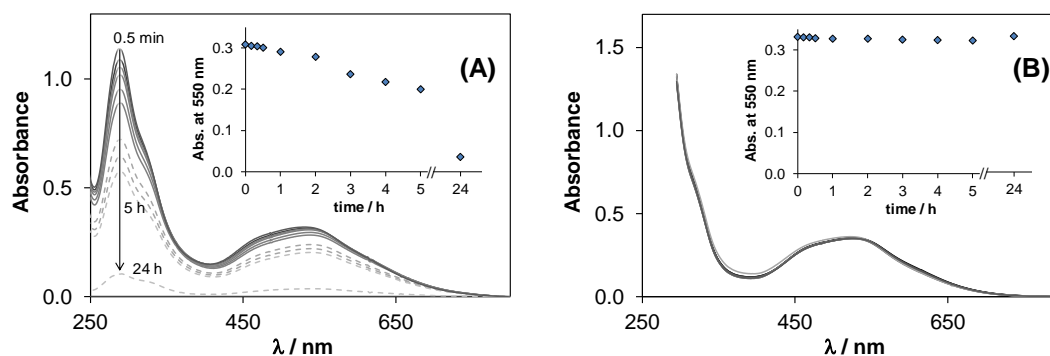


Figure S6. UV-Vis absorbance spectra of $[\text{Ru}(\text{DIP})_2(\text{mal})](\text{PF}_6)$ followed in RPMI 1640 cell culture medium (A) and in 20 mM phosphate buffer containing 100 μM HSA (B). Insets show the time course of the absorbance changes at 550 nm. Dashed spectra refer to precipitation of the complex. $\{c_{\text{complex}} = 13.8 \mu\text{M}; 2\% \text{ ethanol (V/V)}; \text{pH} = 7.40; T = 25 \text{ }^\circ\text{C}\}$.

Binding via intermolecular binding is supported by the UV-Vis spectra of $[\text{Ru}(\text{DIP})_2(\text{mal})](\text{PF}_6)$ recorded in the presence of increasing amount of HSA (see Fig. S8), where practically no spectral changes can be observed, except upon the addition of the first 0.03 eq of HSA. Notably, binding of a small molecule on HSA via secondary binding interactions often does not result in any alteration of UV-Vis absorbance bands.

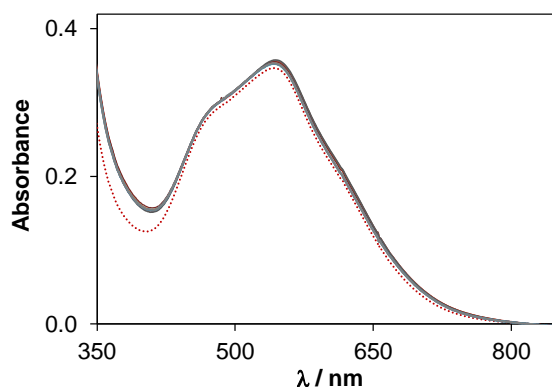


Figure S7. UV-Vis absorbance spectra of **[Ru(DIP)₂(mal)](PF₆)** alone (red dotted spectrum) and in the presence of 0.03-2.0 eq of HSA (grey scale spectra). Spectra are subtracted by the spectrum of HSA. { $c_{\text{complex}} = 20.0 \mu\text{M}$; 2% ethanol (V/V); pH = 7.40 (20 mM phosphate buffer); T = 25 °C}

Binding at sites I and II was investigated by spectrofluorimetry via Trp214 quenching and via dansylglycine (DG) displacement experiments, respectively. Following the selective excitation of Trp214 at 295 nm, its fluorescence emission intensity can be attenuated by the binding of a guest molecule at site I. Intermolecular binding processes usually take place very fast (within seconds), and indeed our time dependent measurement indicated fast kinetics at this site; therefore spectra were recorded after 5 min waiting time. Emission spectra in Fig. S9 show a definite increase of fluorescence, instead of quenching, upon addition of **[Ru(DIP)₂(mal)](PF₆)** to HSA. The increase can be explained by the complete overlapping of the low intrinsic fluorescence of the metal complex with the protein Trp emission band.

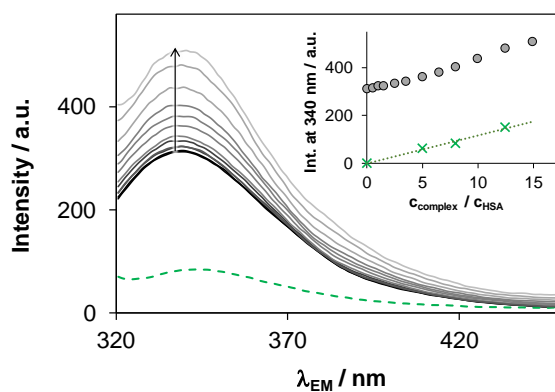


Figure S8. Changes of Trp214 fluorescence in HSA in the presence of $[\text{Ru}(\text{DIP})_2(\text{mal})](\text{PF}_6)$, green dashed spectrum denotes the emission of $8 \mu\text{M}$ metal complex alone. Inset shows the relative emission intensities at 340 nm for HSA– $[\text{Ru}(\text{DIP})_2(\text{mal})](\text{PF}_6)$ system (●) and for $[\text{Ru}(\text{DIP})_2(\text{mal})](\text{PF}_6)$ alone (×). $\{c_{\text{HSA}} = 1 \mu\text{M}; c_{\text{complex}} = 0\text{--}15 \mu\text{M}; \text{pH} = 7.40$ (20 mM phosphate buffer); $< 2\%$ ethanol $\lambda_{\text{EX}} = 295 \text{ nm}; T = 25 \text{ }^\circ\text{C}\}$.

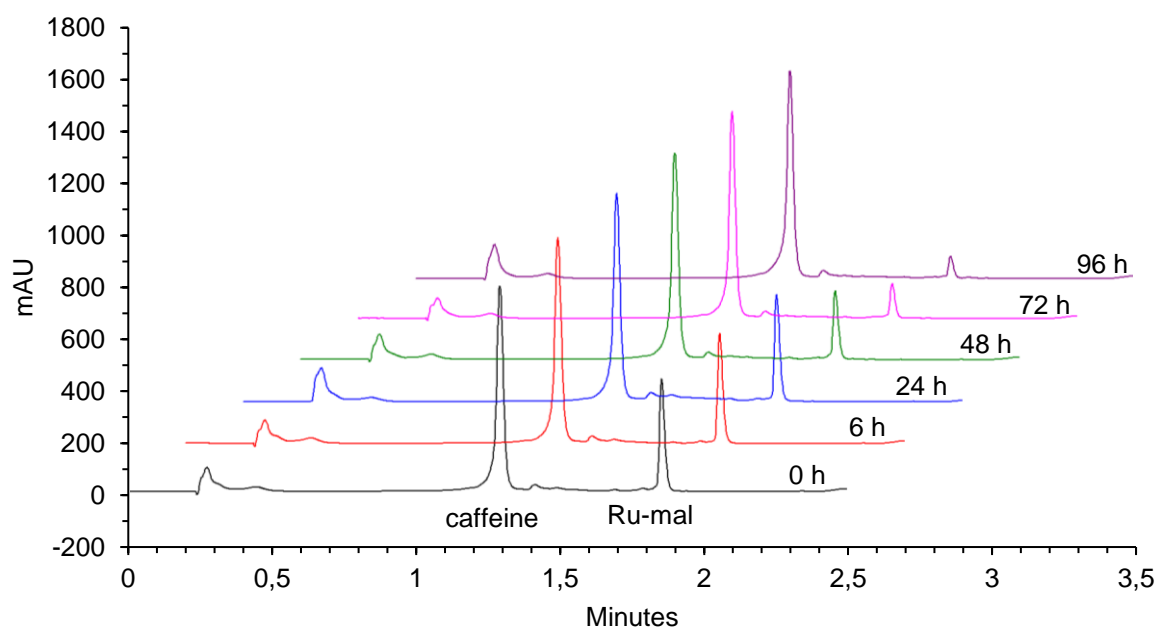
The HSA–DG adduct emits light intensively and displacement of DG by other small molecules results in a considerable decrease in the emission intensity, as it is detailed in the main text DG is gradually displaced by $[\text{Ru}(\text{DIP})_2(\text{mal})](\text{PF}_6)$ at site II.

Experimental for the ultrafiltration and circular dichroism studies

Ultrafiltration studies were carried out in Amicon Ultra-0.5 (Millipore cutoff: 10 kDa) filter devices. 0.5 or 1.0 mL portions were filtered with an Eppendorf MiniSpin plus centrifuge (relative centrifugal force ~ 8000 g; 5–10 min) and the UV–vis spectrum of the filtrate (bottom fraction) was compared to the reference spectra of the original sample or to the ligand spectra. Circular dichroism (CD) spectra for the metal complex – HSA systems were recorded on a Jasco J-815 spectrometer in the wavelength interval from 250 to 1000 nm. Samples contained 24 μM metal complex at pH 7.40 (20 mM HEPES buffer) and increasing amount of HSA (0 – 50 μM) using quartz cell of 1 cm path length.

Figure S9. a) RP-UPLC traces of $[\text{Ru}(\text{DIP})_2(\text{mal})](\text{PF}_6)$ (0.12 mM) incubated in human plasma at 37 °C, using caffeine (1.92 mM) as internal standard, recorded at 275 nm. b) Percentage concentration of $[\text{Ru}(\text{DIP})_2(\text{mal})](\text{PF}_6)$, normalized with respect to the internal standard and plotted against time.

a)



b)

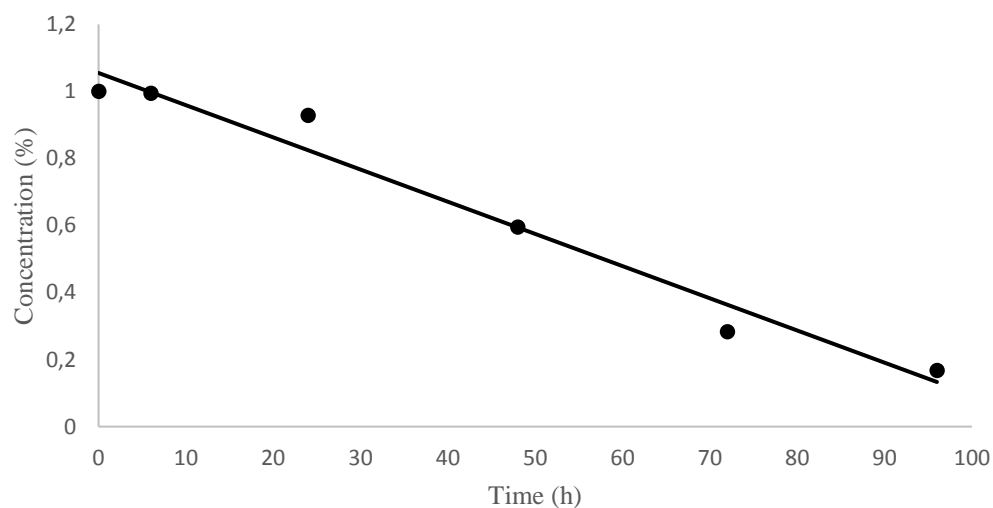
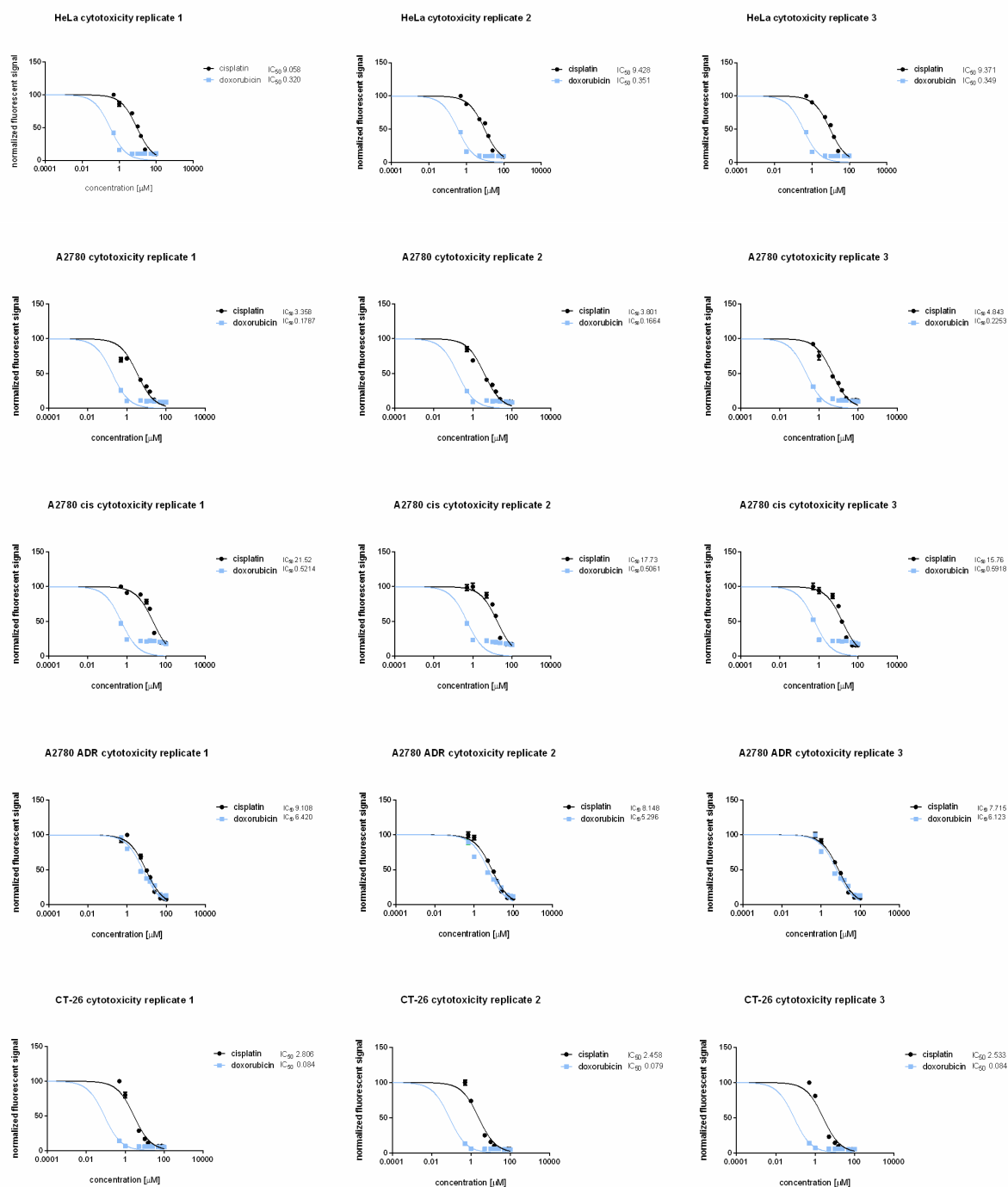
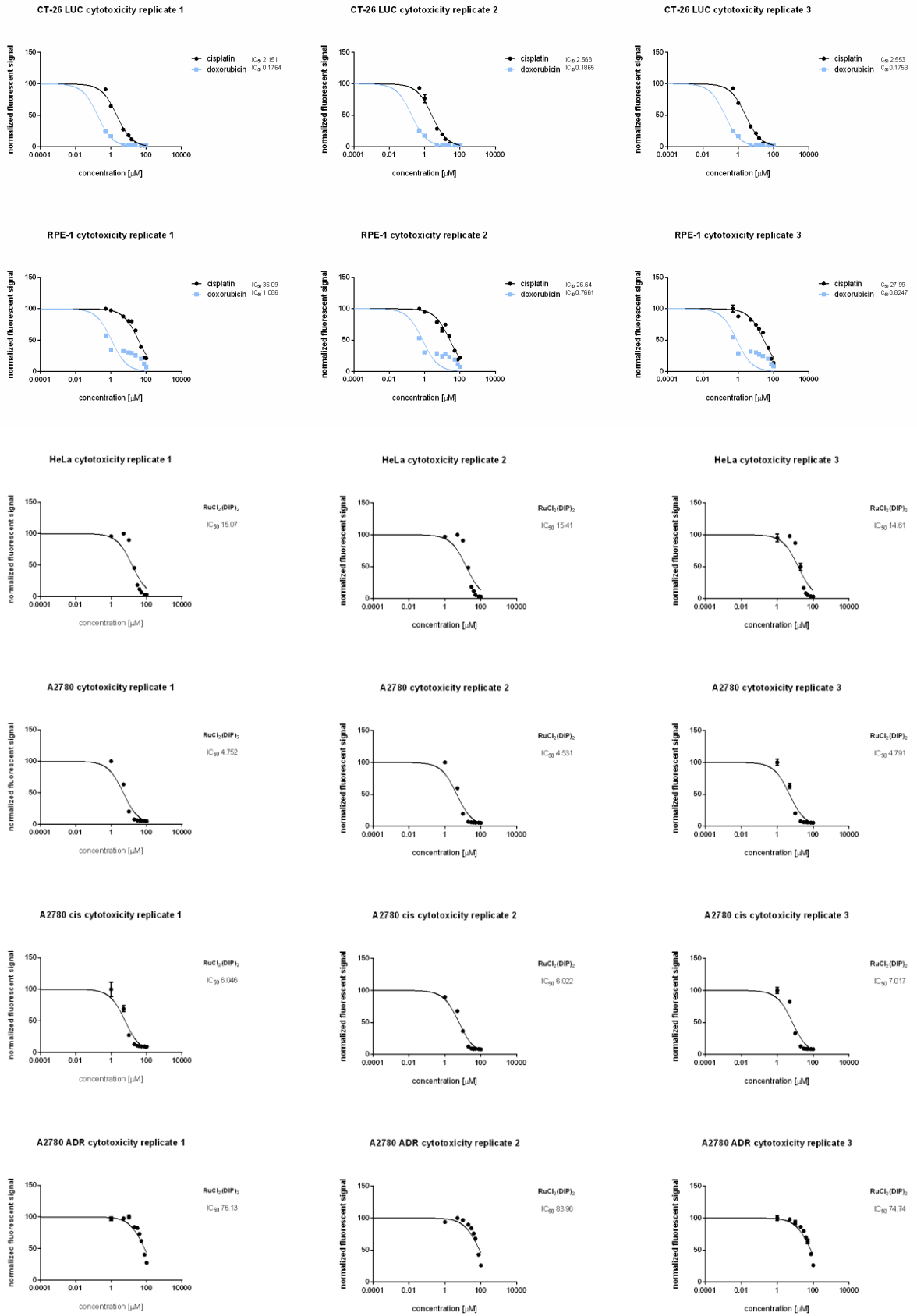
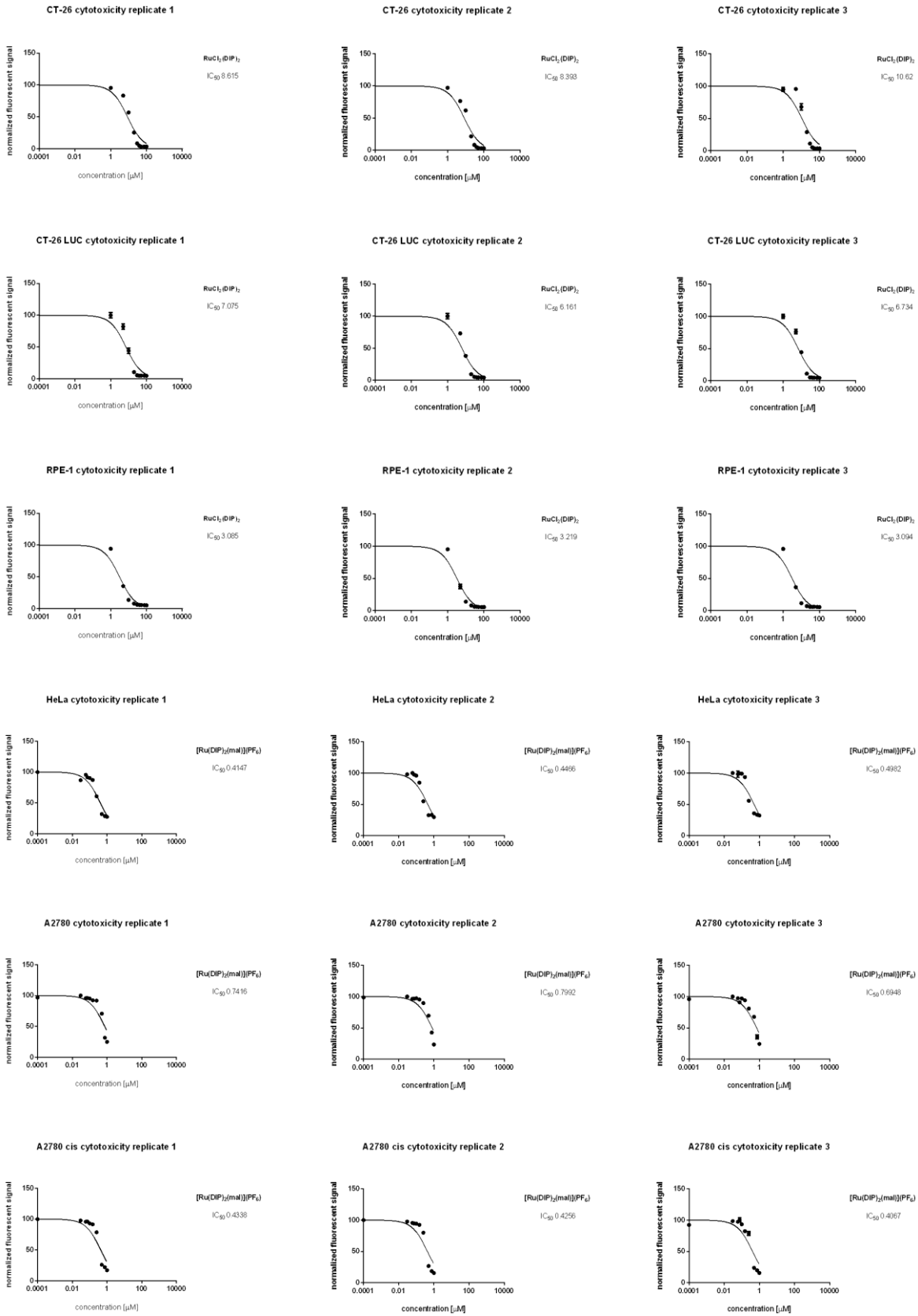
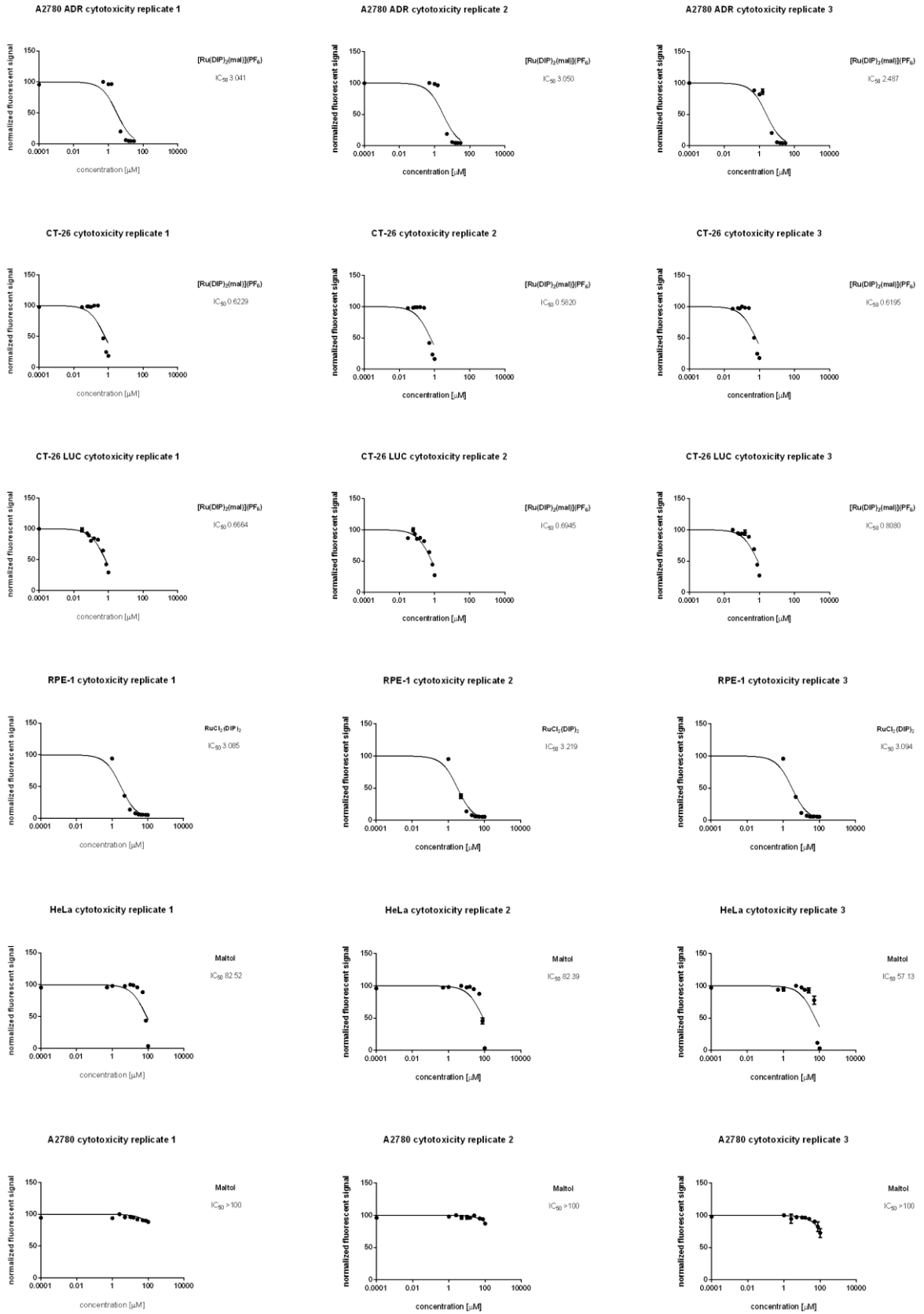


Figure S10. Evaluation of the cytotoxicity in 2D cell culture models *via* fluorometric cell viability assay.

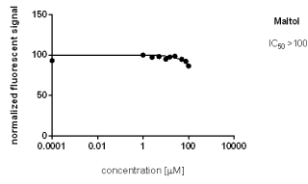




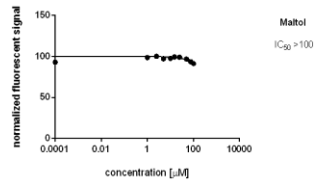




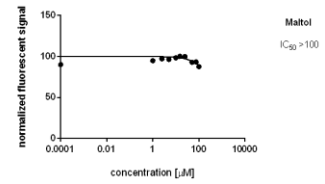
A2780 ADR cytotoxicity replicate 1



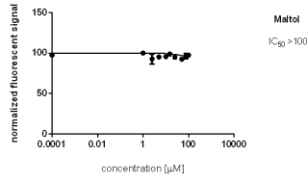
A2780 ADR cytotoxicity replicate 2



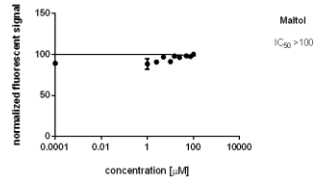
A2780 ADR cytotoxicity replicate 3



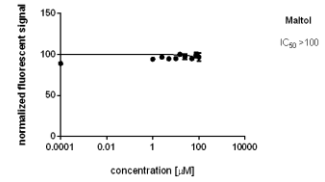
A2780 cis cytotoxicity replicate 1



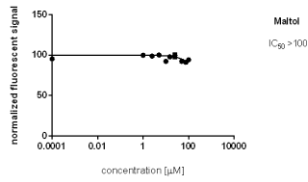
A2780 cis cytotoxicity replicate 2



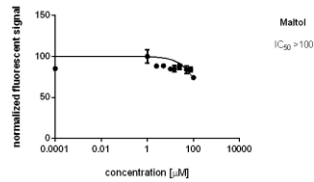
A2780 cis cytotoxicity replicate 3



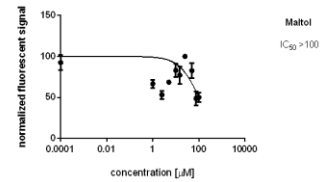
CT-26 cytotoxicity replicate 1



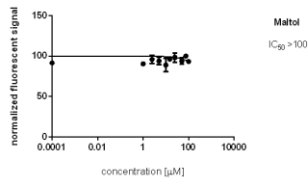
CT-26 cytotoxicity replicate 2



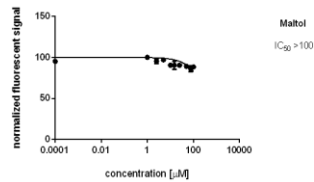
CT-26 cytotoxicity replicate 3



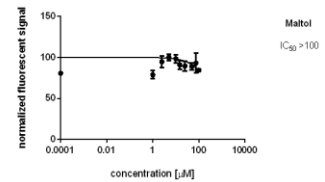
CT-26 LUC cytotoxicity replicate 1



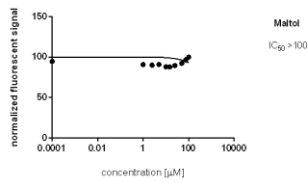
CT-26 LUC cytotoxicity replicate 2



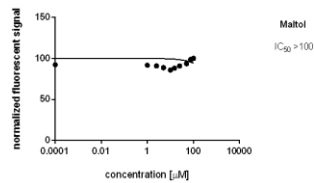
CT-26 LUC cytotoxicity replicate 3



RPE-1 cytotoxicity replicate 1



RPE-1 cytotoxicity replicate 2



RPE-1 cytotoxicity replicate 3

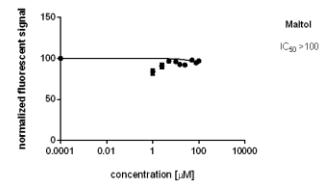


Figure S11. Evaluation of the cytotoxicity in 2D cell culture models *via* CellTiter Glo® viability Test.

4

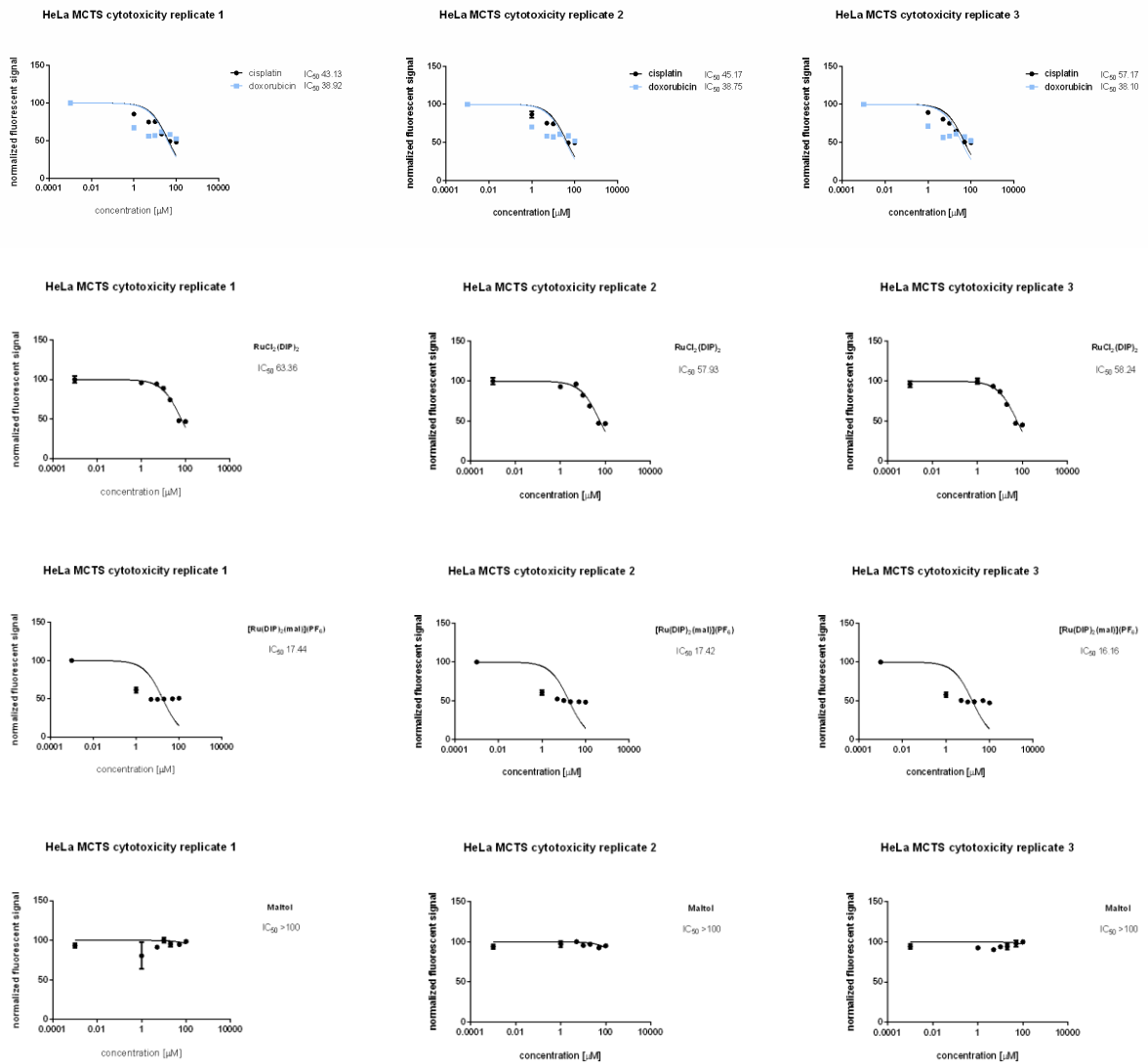


Figure S12. Cell Death Mechanism.

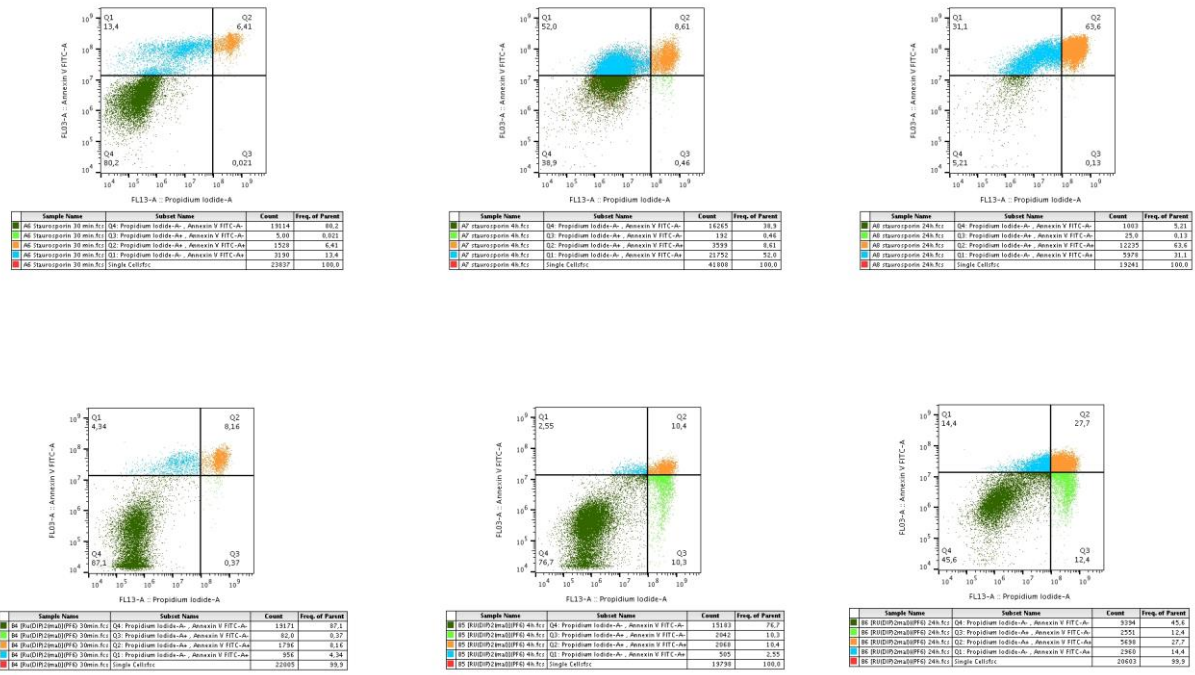


Figure S13. Cellular uptake mechanism of $[\text{Ru}(\text{DIP})_2(\text{mal})](\text{PF}_6)$. Accumulation of ruthenium in HeLa cells in presence of different inhibitors and conditions: low temperature (4°C), blocked cellular metabolism (2-Deoxy-*D*-glucose, oligomycin), blocked endocytic pathways (chloroquine or ammonium chloride), blocked cation transporters (tetraethylammonium chloride). Cells were pre-treated with uptake inhibitors and then incubated with $[\text{Ru}(\text{DIP})_2(\text{mal})](\text{PF}_6)$ (2 h, 5 μM). Amounts of ruthenium were measured using ICP-MS.

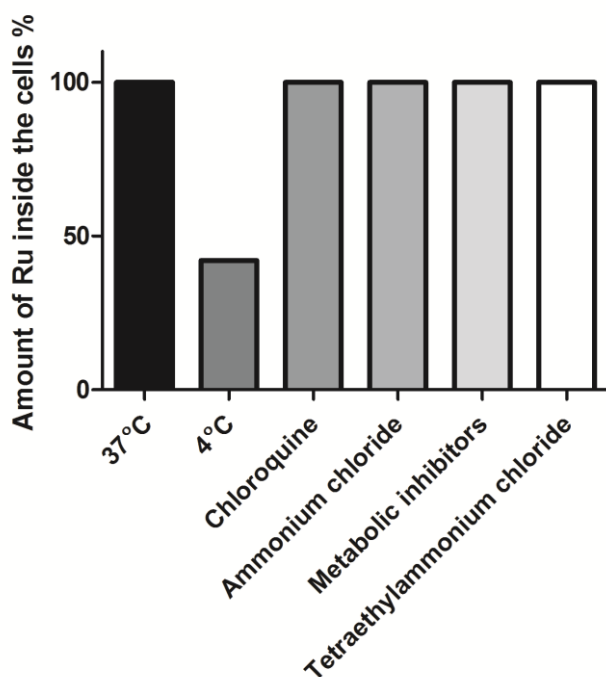


Figure S14. Oxygen consumption rates and different respiration parameters in HeLa cells alone or after treatment with various test compounds.

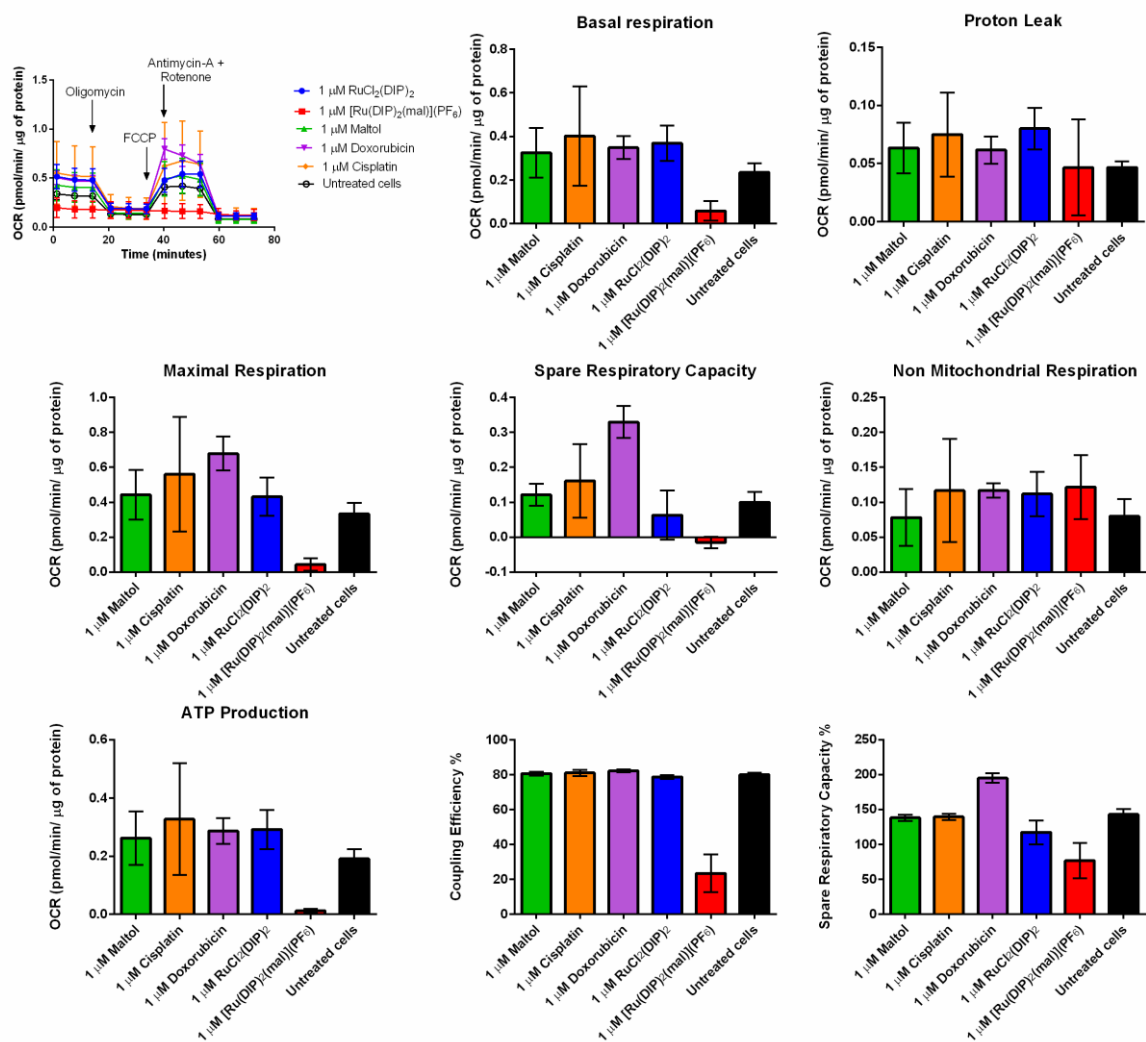


Figure S15. Extracellular acidification rate and different parameters during glycolysis in HeLa cells alone or after treatment with various test compounds.

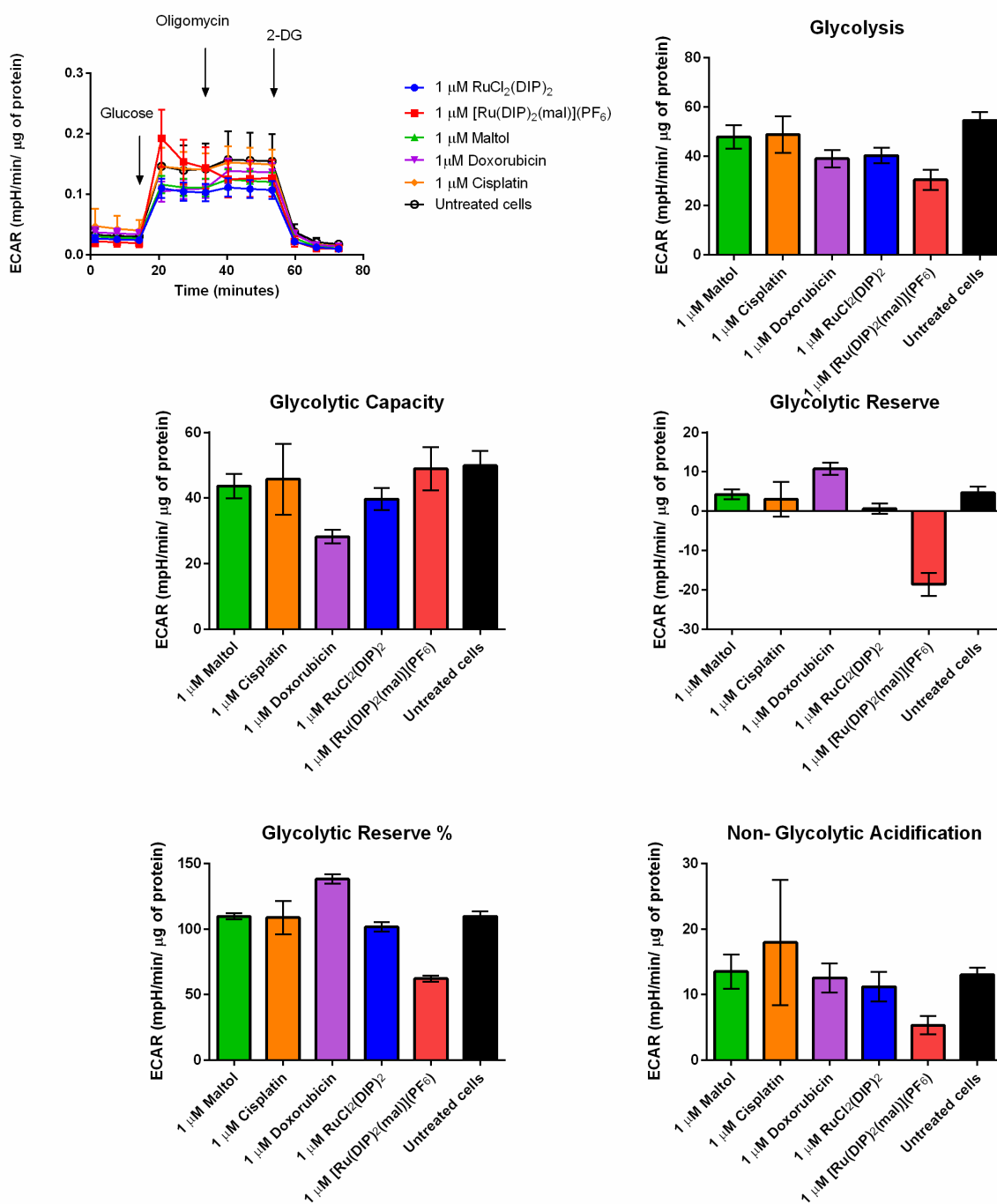
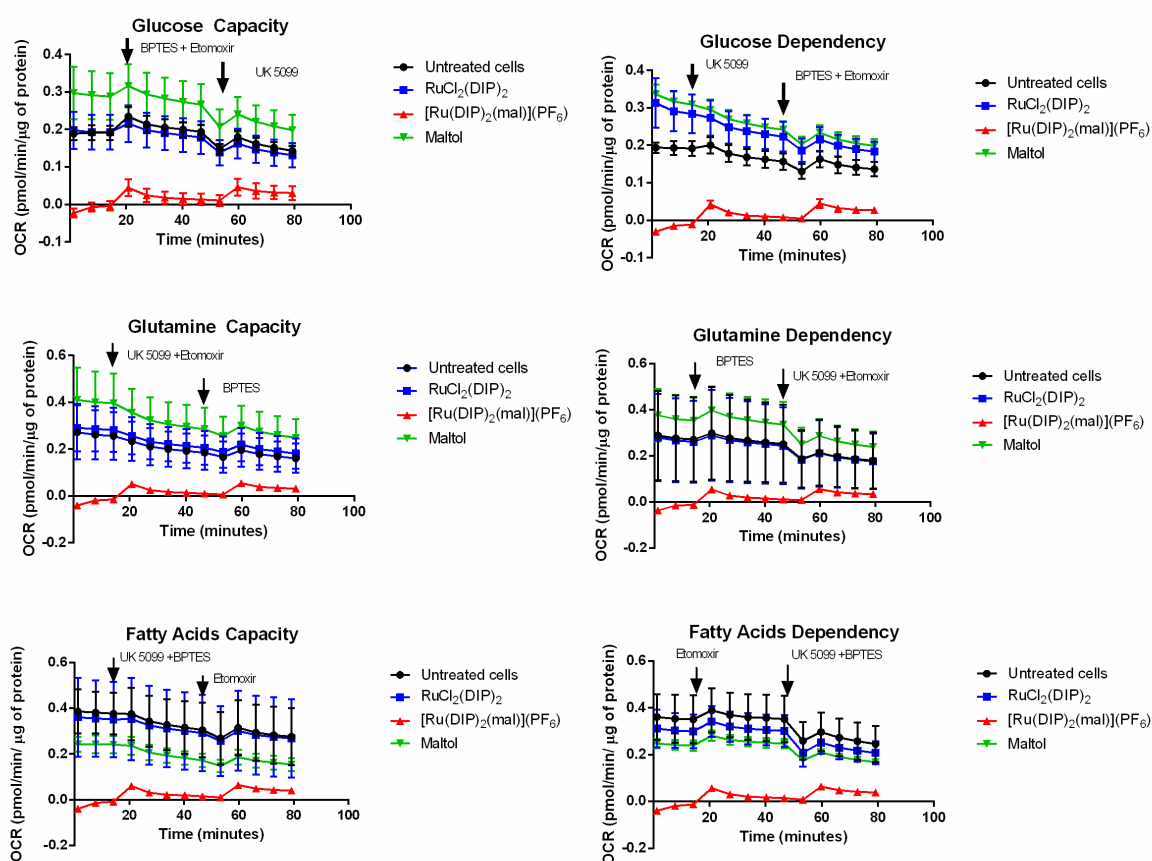


Figure S16. Fuel flex assay in HeLa cells. Dependency studies were performed by adding the inhibitor for the target pathway in port A and inhibitors for the other two pathways in port B while capacity studies were done using the reverse sequence. UK-5099 (20 μ M), BPTES (30 μ M) and etomoxir (40 μ M) were used as the inhibitors for the fuel pathways run by glucose, glutamine and fatty acids.



Chapter 9- Increasing the Cytotoxicity of Ru(II) Polypyridyl Complexes by tuning the Electronic Structure of Dioxo

Ligands

*Anna Notaro,^a Marta Jakubaszek,^{a,b} Nils Rotthowe,^c Federica Maschietto,^d Patrick S. Felder,^a
Bruno Goud,^b Mickaël Tharaud,^e Ilaria Ciofini,^d Fethi Bedioui,^f Rainer F. Winter,^c and Gilles
Gasser^{a,*}*

^a Chimie ParisTech, PSL University, CNRS, Institute of Chemistry for Life and Health Sciences, Laboratory for Inorganic Chemical Biology, F-75005 Paris, France.

^b Institut Curie, PSL University, CNRS UMR 144, Paris, France.

^c Department of Chemistry, University of Konstanz, Universitätsstrasse 10, D-78457 Konstanz, Germany.

^d Chimie ParisTech, PSL University, CNRS, Institute of Chemistry for Life and Health Sciences, Chemical Theory and Modelling Group, F-75005 Paris, France.

^e Université de Paris, Institut de physique du globe de Paris, CNRS, F-75005 Paris, France.

^f Chimie ParisTech, PSL University, CNRS, Institute of Chemistry for Life and Health Sciences, Team Synthèse, Electrochimie, Imagerie et Systèmes Analytiques pour le Diagnostic, F-75005 Paris, France.

* Corresponding author: E-mail: gilles.gasser@chimeparistech.psl.eu; WWW: www.gassergroup.com; Phone: +33 1 44 27 56 02

This chapter has been published on 28th of February 2020, on *Journal of the American Chemical Society* (doi.org/10.1021/jacs.9b12464).

Reproduced by permission of American Chemical Society

(<https://pubs.acs.org/doi/10.1021/jacs.9b12464>)

Contribution to the publication:

Marta Jakubaszek performed with Anna Notaro the 2D cytotoxicity studies, Annexin V and PI staining, cellular uptake, intracellular distribution and the DNA metalation studies. She performed the 3D cell culture studies, JC-1 membrane potential test and mitochondrial metabolic studies. She analysed together with Anna Notaro obtained data and wrote with her contribution the cytotoxicity studies, cellular uptake, intracellular distribution, DNA metalation and JC-1 staining sections. She wrote the mechanism of cell death, the mitochondrial metabolic studies and the 3D cell culture sections.

Marta Jakubaszek



19.05.2020

Gilles Gasser



Abstract

Due to the great potential expressed by an anticancer drug candidate previously reported by our group, namely **Ru-sq** ($[\text{Ru}(\text{DIP})_2(\text{sq})](\text{PF}_6)$ (DIP: 4,7-diphenyl-1,10-phenanthroline, sq: semiquinonate ligand), we describe in this work a structure-activity relationship (SAR) that involves a broader range of derivatives resulting from the coordination of different catecholate-like dioxo ligands to the same $\text{Ru}(\text{DIP})_2$ core. More in detail, we chose catechols carrying either electron-donating or electron-withdrawing groups EDG or EWG and investigated the physico-chemical and biological properties of their complexes. Several pieces of experimental evidences demonstrated that the coordination of catechols bearing EDGs led to deep red positively charged complexes **1–4** in which the preferred oxidation state of the dioxo ligand is the uninegatively charged semiquinonate. Complexes **5** and **6**, on the other hand, are blue/violet neutral complexes which carry an EWG substituted dinegatively charged catecholate ligand. The biological investigation of complexes **1–6** led to the conclusion that the difference in their physico-chemical properties has a strong impact on their biological activity. Thus, complexes **1–4** expressed much higher cytotoxicities than complexes **5** and **6**. Complex **1** constitutes the most promising compound of the series and was selected for a more in-depth biological investigation. Apart from its remarkably high cytotoxicity ($\text{IC}_{50} = 0.07\text{--}0.7 \mu\text{M}$ in different cancerous cell lines) complex **1** was taken up by HeLa cells very efficiently by a passive transportation mechanism. Moreover, its moderate accumulation in several cellular compartments (*i.e.* nucleus, lysosomes, mitochondria and cytoplasm) is extremely advantageous in the search of a potential drug with multiple modes of action. Further DNA metalation and metabolic studies pointed to the direct interaction of complex **1** with DNA and to the severe impairment of the mitochondrial function. Multiple targets, together with its outstanding cytotoxicity, make complex **1** a valuable candidate in the field of chemotherapy research. Noteworthy, a preliminary biodistribution study on healthy mice demonstrated the suitability of complex **1** for further *in vivo* studies.

Introduction

The worldwide approval of the anticancer drug cisplatin and later of carboplatin and oxaliplatin has made platinum-based drugs the leading compounds in the field of medicinal inorganic chemistry.^{1,2} However, the side-effects and resistance associated with these compounds have spurred numerous investigations into other metal-based drugs as potential chemotherapeutic agents against cancer.^{1,3-6} Ruthenium complexes are presently regarded as the successors/alternatives to the aforementioned platinum compounds.⁷⁻¹⁴ Three ruthenium complexes were (i.e., NKP-1019 and NAMI-A, Figure 1) or are (i.e., IT-139, Figure 1) in clinical trials as chemotherapeutic agents. In addition, a Ru(II) polypyridyl complex, namely TLD-1433 (Figure 1) has just entered phase II of clinical trials as a photosensitizer for photodynamic therapy against bladder cancer.¹⁵⁻²⁰ Ru(II) polypyridyl complexes, have been also extensively studied for their cytotoxicity and sowed a great potential ad as potential chemotherapeutic agents.²¹⁻²⁸ Recently, we reported a detailed study on a very promising Ru(II) polypyridyl complex, namely [Ru(DIP)₂(sq)](PF₆) (**Ru-sq**, Scheme 1a), where DIP is 4,7-diphenyl-1,10-phenanthroline and sq is a semiquinonate ligand.²⁹ Semiquinonate (sq) is the product of the first one-electron oxidation of catecholate (cat) and can be further oxidized to quinone (q) (Scheme 1b).^{30,31} Catechol(ate) and its redox congeners semiquinonate and 1,2-benzoquinone are pivotal examples for the class of ‘non-innocent’ ligands.³² This definition is more appropriately referring to a pair of a metal ion and a ligand which are both redox-active and whose frontier orbitals are strongly mixed, defying an unambiguous assignment of redox states to either component.³² Catechols are also considered as pan-assay interference compounds (PAINS) due to their chelating and redox properties.³³

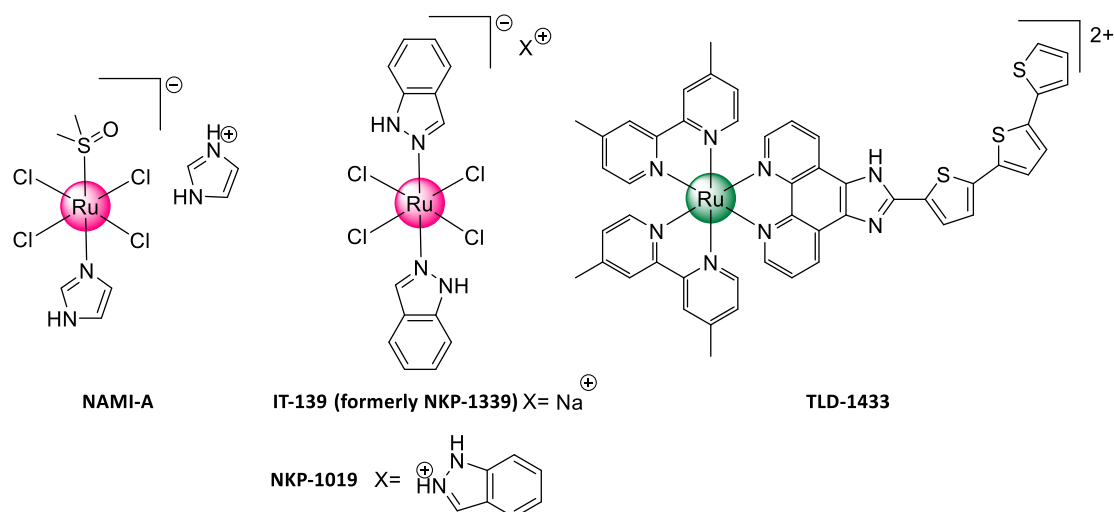
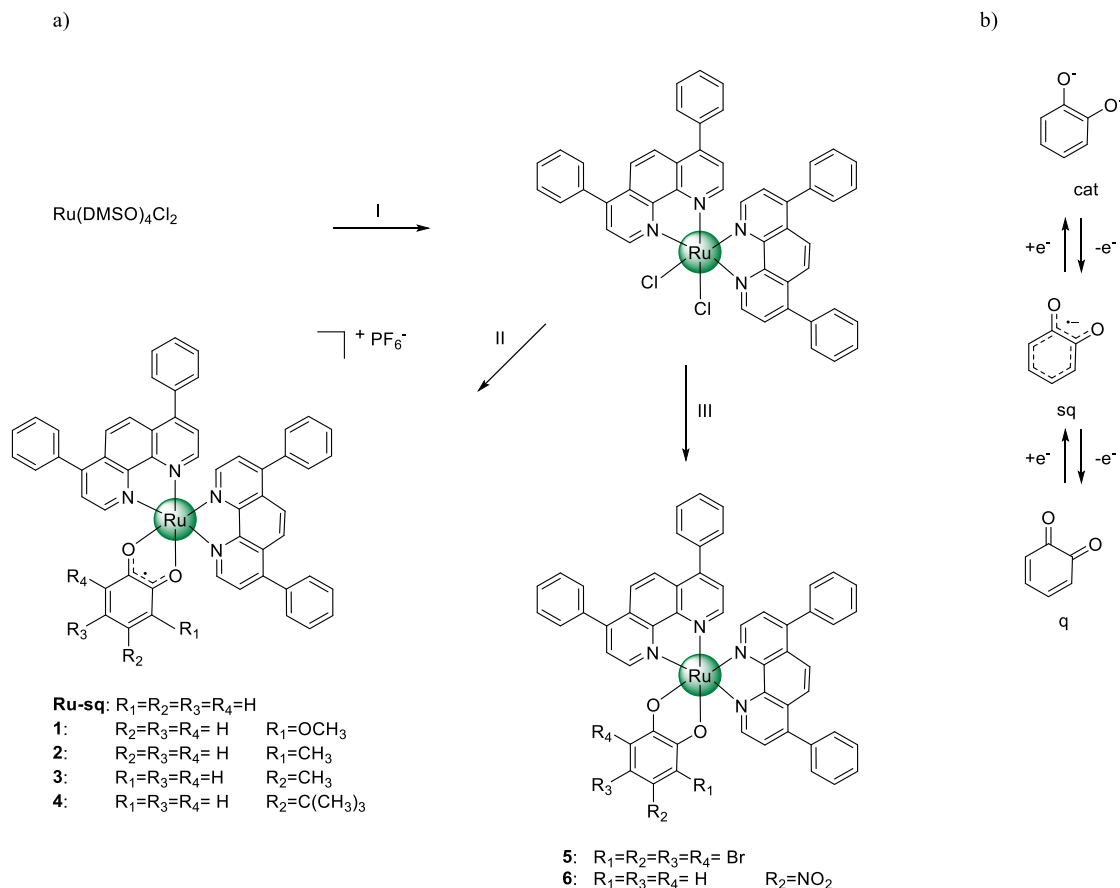


Figure 1. Chemical structures of Ruthenium complexes that were (i.e., NKP-1019 and NAMI-A, Figure 1) or are (i.e., IT-139 and TLD-1433) in clinical trials.

Ru-sq was, to the best of our knowledge, the first Ru(II) polypyridyl complex carrying a semiquinonate moiety which was investigated in-depth as an anticancer drug candidate. We could demonstrate that it is a valuable candidate as a chemotherapeutic agent, both *in vitro* and *in vivo*. Interestingly, its mechanisms of action involve more than one cellular target. This finding could potentially be a key feature to overcome resistance, which is an inherent problem for platinum-based anticancer drug candidates.²⁹ Driven by the promising properties unveiled for **Ru-sq**, we undertook a structure-activity relationship (SAR) study, keeping the same Ru(II) polypyridyl core (i.e. Ru(DIP)₂), but substituting the catechol-type dioxo ligand. Over the years, many studies have been performed focusing on the non-innocent character of different metal complexes both from an experimental and theoretical point of view.^{34–41} In 2006, Wada and co-workers demonstrated how the oxidation state of the dioxo ligand in a given metal-coligand environment depends on the nature of its substituents.⁴² More specifically, the authors investigated a series of [Ru(OAc)(dioxolene)(terpy)] complexes with dioxo ligands carrying electron withdrawing (EWG) or electron donating (EDG) groups.⁴² In particular, they observed that due to the non-innocent nature of the dioxo ligand, all complexes lie on a continuum in

between formal Ru^{II}(sq) and Ru^{III}(cat) descriptions, with an increase of the contribution of the Ru^{II}(sq) form for complexes with an EDG-substituted dioxo ligand and *vice versa*.⁴² Herein, we present, a new series of complexes carrying dioxo ligands substituted with EDGs or EWGs, namely [Ru(DIP)₂(3-methoxysq)](PF₆) (**1**), [Ru(DIP)₂(3-methylsq)](PF₆) (**2**), [Ru(DIP)₂(4-methylsq)](PF₆) (**3**), [Ru(DIP)₂(4-tert-butylsq)](PF₆) (**4**), Ru(DIP)₂(tetrabromocat) (**5**) and Ru(DIP)₂(4-nitrocatechol) (**6**) (Scheme 1a), where DIP is 4,7-diphenyl-1,10-phenanthroline, 3-methoxysq is 3-methoxysemiquinonate, 3-methylsq is 3-methylsemiquinonate, 4-methylsq is 4-methylsemiquinonate, 4-tert-butylsq is 4-tert-butylsemiquinonate, tetrabromocat is tetrabromocatechol and 4-nitrocatechol is 4-nitrocatechol. The physico-chemical and biological properties of these compounds were investigated in-depth. As described in the literature,³⁴⁻⁴¹ the variation of the electron density on the dioxo ligand leads to the modification of its oxidation state when bound as a ligand. The different oxidation states of the dioxo ligands have a strong bearing on the physical properties of the complexes, affecting, among other parameters, their electronic structures and hence the charge state. Of note, we could unveil an interesting correlation between the oxidation state of the dioxo ligand and the biological activity of the complex. Complex **1** was found to be the most promising compound investigated. Its remarkable cytotoxicity in 2D models (IC₅₀ values in the low nanomolar range) was confirmed in a more accurate 3D model, which led to further biological investigation. In the course of this work, we demonstrate how the mechanism of action of complex **1** involves multicellular targets. This is considered a key factor to overcome one of the main drawbacks associated to chemotherapy treatments, which is the occurrence of resistance. Moreover, as most complexes of this kind, complex **1** displays poor water solubility.⁴³ Recently, we reported the formation of colloids of **Ru-sq** and complex **1** in water-DMSO (1% v/v) mixture, which could have been easily mistaken by solutions if no appropriate characterization had been performed.⁴³ Poor aqueous solubility is usually considered a limitation for *in vivo* applications. However, in this

study, we could demonstrate that with an appropriate formulation, complex **1** is able to distribute in healthy BALB/c mice, which renders it a suitable candidate for further *in vivo* studies.



Scheme 1. a) Syntheses of complexes **1–6**. I) DIP, LiCl, DMF, reflux, 24 h, 78%; II) (i) NaOH, 3-methoxycatechol (**1**), or 3-methylcatechol (**2**), or 4-methylcatechol (**3**) or 4-tert-butylcatechol (**4**) 2-propanol, reflux, 24h; (ii) air, 2 h; (iii) NH_4PF_6 , 2-propanol/ H_2O (1:8), 19% (**Ru-sq**), 23% (**1**), 24% (**2**), 29% (**3**), 16% (**4**). III) (i) NaOH, tetrabromocatechol (**5**) or 4-nitrocatechol (**6**), 2-propanol, reflux, 24h; (ii) air, 2 h; (iii) NH_4PF_6 , 2-propanol/ H_2O (1:8), 54% (**5**), 27% (**6**). b) Catecholate (cat) and its oxidised forms, semiquinonate (sq) and quinone (q).

Results and Discussion

Synthesis and characterization of 1–6

The synthesis of compounds **1–6** was achieved by adapting a previously reported procedure.²⁹ Ru(DIP)₂Cl₂ was obtained starting from the known Ru(DMSO)₂Cl₂⁴⁴ as previously reported.⁴⁵ This precursor complex was then refluxed under nitrogen atmosphere with the corresponding catechol derivative in the presence of NaOH in 2-propanol overnight.²⁹ Subsequently, the reaction vessel was opened to air for 2 h to allow for the final oxidation step. Interestingly, oxidation of the catecholate ligand to a semiquinonate occurred only for those complexes bearing catecholate ligands with EDG groups (complexes **1–4** in Scheme 1a). When the synthesis involved catechol derivatives bearing EWG groups, neutral complexes (**5**, **6**) were generated. The drastic change of the electronic properties of the complexes studied in this work is also reflected by their color. EDG-containing derivatives are deep red solids while EWG-containing derivatives are blue/violet. UV/Vis/NIR spectroscopy in DMF solution (Figure 2) confirms the assignment of the EDG-substituted ligands as semiquinonates as compounds **1–4** display a band at ca. 885–900 nm. This absorption is characteristic for ruthenium-bis(diimine) complexes containing a semiquinonate ligand and is due to a Ru(II) → sq transition.⁴⁶ A set of bands, which is responsible for the visual color impression of these compounds, is found in the range of 525 to 470 nm. Based on literature data on similar compounds, this band can be ascribed to MLCT and LL'CT transitions (MLCT = metal-to-ligand charge-transfer; LL'CT = ligand-to-ligand' charge-transfer, electron transfer between a donor and an acceptor ligand). The two neutral compounds **5** and **6** are both characterized by a broad transition at 675 nm alongside two additional bands at ca. 600 and 500 nm; both of which are responsible for their blue/violet color. Their similarity to the absorptions in the precursor complex Ru(DIP)₂Cl₂ is underlined by its similarly convoluted absorption profile with bands at 680, 570 and 485 nm. These data are in agreement with a previous report for the Ru(bpy)₂Cl₂ analogue whose bands

can be assigned as Ru(II) \rightarrow DIP transitions.⁴⁷ An overview over the characteristic absorption bands of all compounds is provided in Table S1.

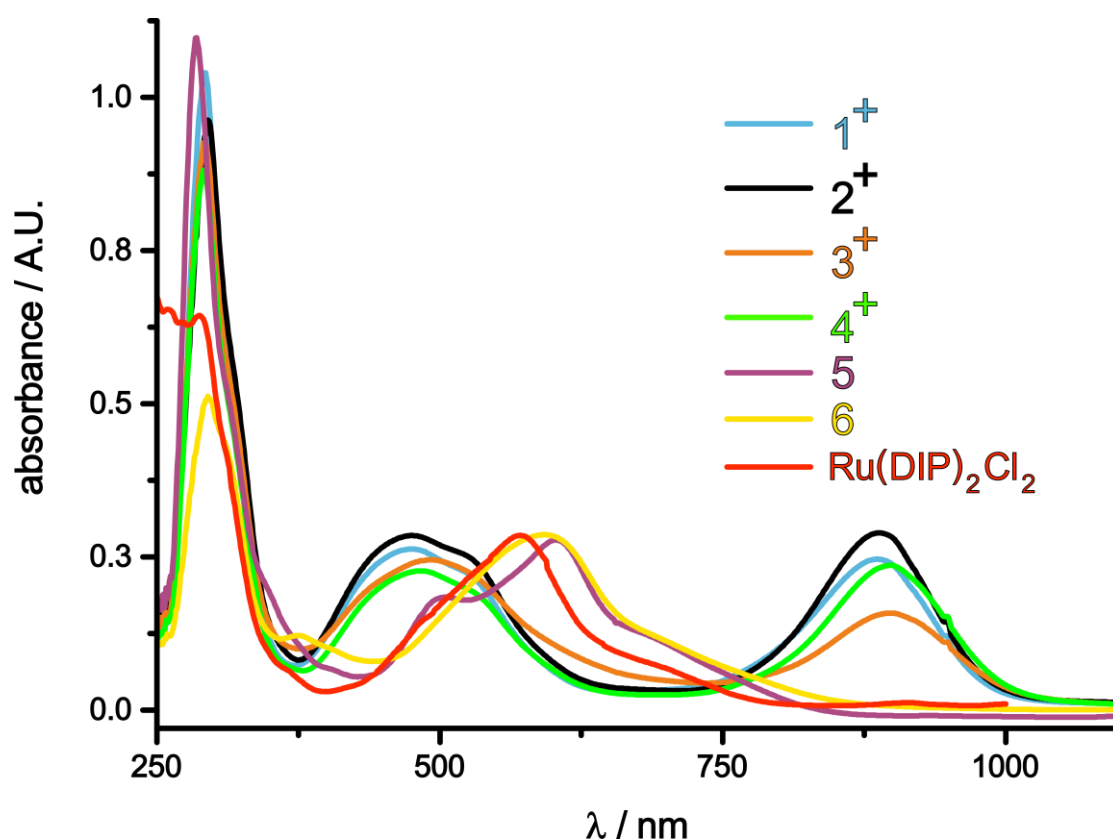


Figure 2. UV/Vis/NIR spectra in DMF solution of the complexes **1-6** and their precursor Ru(DIP)₂Cl₂.

The paramagnetic nature of compounds **1-4** was indirectly confirmed by their characteristically broadened ¹H-NMR spectra (Figure S1). In contrast, compounds **5** and **6**, whose purity was confirmed by the elemental analysis, are neutral and formally diamagnetic. However, the proton NMR spectra also provided severely broadened resonances. The addition of zinc dust to the NMR tube, slightly improves the resolution of NMR signals which suggests the formation of paramagnetic species in solution (Figure S1 (5) and (6)). All complexes were characterized by ESI-MS, and their purity was verified by HPLC (Figure S2) and elemental microanalysis.

EPR, (Spectro-)electrochemistry and Electronic Structures

The oxidation state of the catechololate/semiquinonate ligand of complexes **1–6** was further investigated by electron paramagnetic resonance (EPR) spectroscopy, cyclic voltammetry (CV), rotating disc electrode voltammetry (RDE) as well as UV/Vis/NIR spectroelectrochemistry and supported by density functional theory (DFT) calculations. Compounds **1–4** are, as obtained from the synthesis, EPR active. At room temperature, they display a rather broad, featureless, isotropic signal (Figure 3A), which becomes slightly anisotropic at lower temperatures and in the frozen glass (Figure S3). The substituents on the dioxo ligand and their positions seem to have only little influence on the locus and the distribution of the unpaired spin density. Thus, the g_{iso} values of 1.9893, 1.9891, 1.9872 and 1.9840 for **1–4**, respectively, are all close to the free electron value g_e of 2.0023 and differ only slightly from each other.

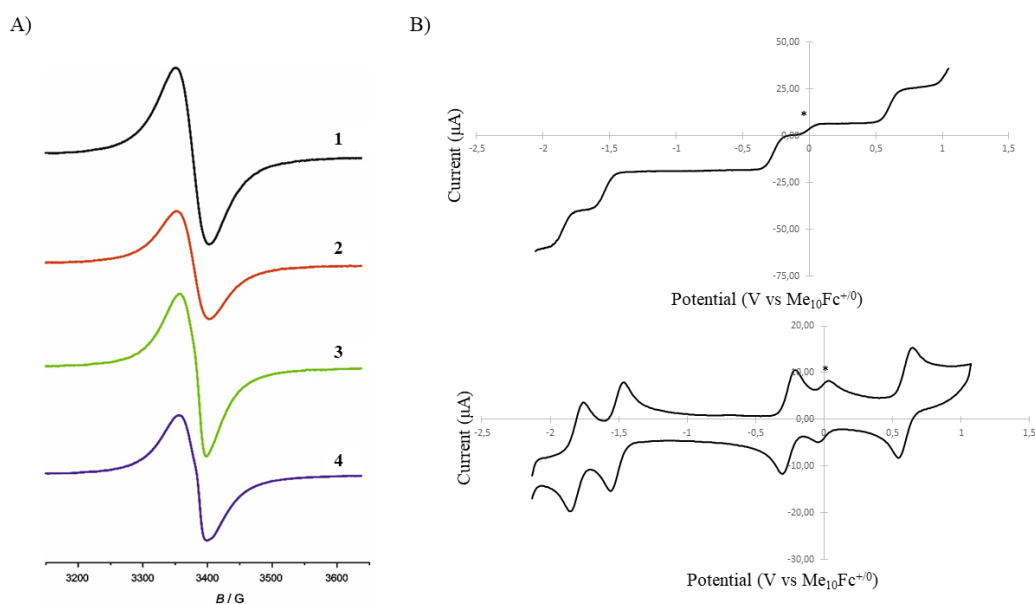


Figure 3. (A) EPR spectra of (from top to bottom) **1–4** at room temperature. (B) RDE and CV voltammograms of **1** (from -2.1 to +1.0 V) at a glassy carbon electrode in DMF (1 mM) containing NBu₄PF₆ (100 mM) as supporting electrolyte and decamethylferrocene as an internal

standard (0.25 mM). Data were recorded versus a saturated calomel electrode (SCE) at a scan rate of 100 mV/s and recalculated versus the $\text{Me}_{10}\text{Fc}^{0/+}$ potential value ($E_{1/2} = 0.040 \text{ V vs SCE}$, feature marked with * in Figure 3B).

These data are also confirmed by the spin density distributions computed for compounds **1** and **3** reported in Table 1 and graphically depicted in Figure 4 (see the Experimental Section for computational details). Indeed, roughly 82% of the spin density is localized on the dioxo ligand with only limited delocalization onto the Ru center (0.19|e-|). Consequently, the computed *g*-tensors (reported as Table S2 in the SI) show very small anisotropies and shifts with respect to the free electron value. These results are consistent with the assumption that the 1,2-dioxo ligand can be formally represented by its semiquinonate form in the case of complexes **1–4**.

Table 1. Computed Mulliken spin densities on the different fragments of the cationic forms of the complexes.

	1	3	5ox	6ox
dioxo ligand	0.8200	0.8268	0.6276	0.6003
ancillary1	-0.0090	-0.0091	-0.0077	-0.0062
ancillary2	-0.0093	-0.0089	-0.0078	-0.0098
Ru	0.1983	0.1913	0.3880	0.4157

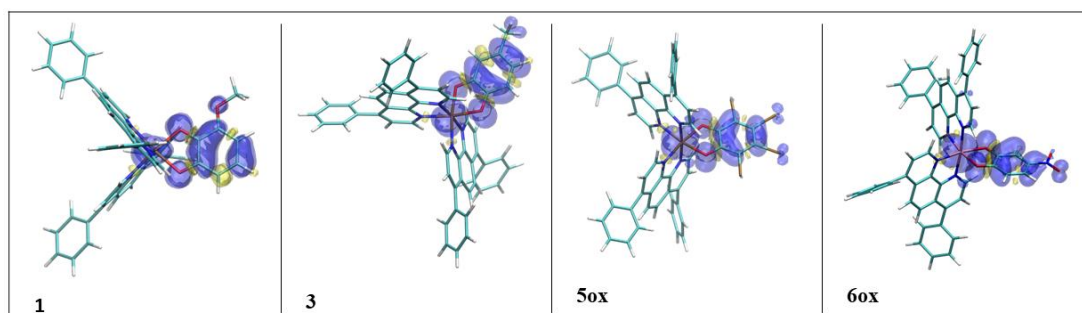


Figure 4. Isodensity plots of computed spin densities. Positive spin density corresponds to blue lobes.

To further investigate the electrochemical properties of compounds **1–4** and to obtain a better insight into the effect of the substituent's position and nature on the redox behavior of the complexes, cyclic voltammetry (CV) and rotating disc electrode (RDE) analyses were performed. Complexes **1–4** display reduction as well as oxidation features in line with what we have reported in our previous work on **Ru-sq**, carrying the non-substituted semiquinonate ligand.²⁹ Figure 3 shows the RDE and cyclic voltammograms of compound **1** while those of **2–4** are available in the SI (Figure S4). Like all other complexes bearing EDG-substituted dioxo ligands, complex **1** exhibits four well-defined reversible redox processes. The RDE experiment shows four features with very similar limiting currents, which indicates that the same number of electrons are exchanged during every process. Based on our previous results,²⁹ the redox process at +0.595 V vs Me₁₀Fc^{0/+} can be attributed to the oxidation of Ru(II) to Ru(III) while the first reduction process at -0.201 V vs Me₁₀Fc^{0/+} can be attributed to the sq/cat redox process. UV/Vis/NIR-spectroelectrochemistry further supports this hypothesis. As evident from Figures 5A and 5B, reducing the complexes **1** or **2** at sufficiently negative potential yields spectra, whose general band structures closely resemble those of compounds **5** and **6**. The observed red-shift with respect to the latter complexes is the result of the higher-lying donor orbitals (cat) and (Ru(II)), which is due to electron rich nature of dioxo ligand in **1**. Oxidation to the

corresponding dications (Figure 5C and Figure 5D) **1ox** and **2ox** leads to a general blue-shift of the Vis/NIR bands. The first visible transition is now found at 675 nm for both complexes. Compared to the Ru(bpy)₂(cat) reference, this corresponds to a red-shift by 810 cm⁻¹.⁴⁶ Adhering to the assignment of a Ru(II) → diimine MLCT transition this effect can be explained through the presence of a more extended π-system in the DIP ligand as compared to bpy. We note, however, that a Ru(III)-sq scenario resulting in a dioxo ligand-to-metal charge-transfer (LMCT) is also possible. The strong electronic coupling between these two redox-active entities prohibits a clear assignment of redox states without additional experimental support or quantum chemical calculations.

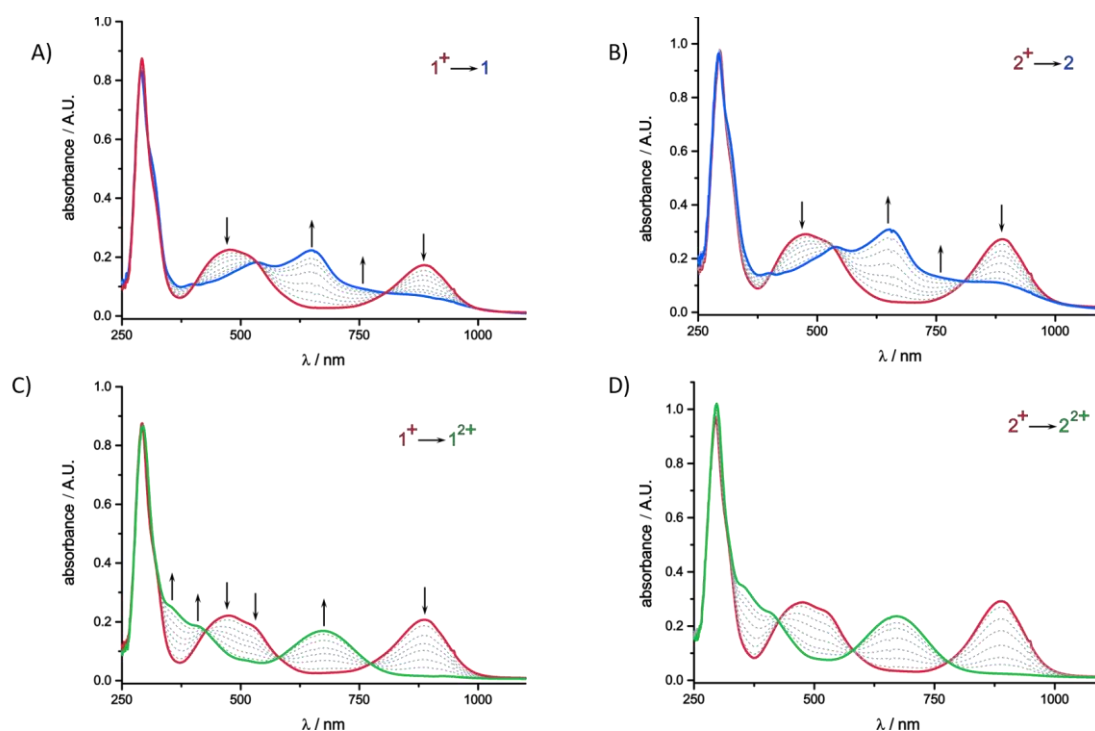


Figure 5. UV/Vis/NIR-spectroelectrochemistry data for compounds **1** and **2**.

The additional two reduction processes at the more negative potentials of -1.463 V and -1.758 V, respectively, are due to the stepwise one-electron reductions of the ancillary ligands (i. e. the DIP^{0/-} couples). These processes were not further studied by spectroelectrochemical investigations due to the high reduction potentials and the irrelevance of these processes to the

bioactivities of these complexes. Table 2 summarizes the redox potentials associated with compounds **1–4** and compares them to those of **Ru-sq** carrying the unsubstituted semiquinonate ligand (see full data in Table S3 of the Supporting Information).²⁹ Comparing the results, it is clear that the presence of an EDG at the dioxo ligand increases the electron density on the metal center, hence shifting its redox process cathodically. These observations are perfectly in agreement with previous work from Wada and co-workers on the charge distribution between the ruthenium ion and the dioxo ligand.⁴² The stronger EDGs OMe and *t*Bu have the predictable effect of shifting the redox potentials of the sq/cat and Ru^{II/III} redox couples cathodically, with however, a different ordering of these couples for complexes **1** and **4**.

Table 2. Electrochemical data for **1–4** and **Ru-sq**.

		DIP ^{0/-}	DIP ^{0/-}	Sq/cat	Ru ^{II/III}
Ru-sq *	E_{1/2}^a [V] (RDE)	-1.876 ± 0.039	-1.578 ± 0.035	-0.249 ± 0.010	0.647 ± 0.018
1	E_{1/2}^a [V] (RDE)	-1.848 ± 0.015	-1.537 ± 0.008	-0.284 ± 0.005	0.595 ± 0.011
2	E_{1/2}^a [V] (RDE)	-1.833 ± 0.007	-1.497 ± 0.012	-0.252 ± 0.011	0.615 ± 0.003
3	E_{1/2}^a [V] (RDE)	-1.836 ± 0.028	-1.472 ± 0.070	-0.265 ± 0.019	0.636 ± 0.011
4	E_{1/2}^a [V] (RDE)	-1.839 ± 0.017	-1.515 ± 0.005	-0.271 ± 0.008	0.574 ± 0.001

* Values taken from^[29] We however note that these experiments were performed on the same days.

^a E_{1/2} = half-wave.

While compounds **1–4** are easily oxidized by air, their reduction to the respective neutral forms within the cell is also feasible. The glutathione system (GSSG/2GSH redox couple) is the most abundant redox couple in a cell and therefore was selected for this experiment.⁴⁸ Nearly full conversion of **1** to its neutral form could be achieved using 5 equivalents of glutathione in a 1:1

mixture of DMF and water containing 20 mM of NaHCO₃ at 40°C, strongly suggesting that compounds **1-4** can at least be partially reduced to their neutral form inside the cell (see Figure S5). Slightly alkaline conditions were thereby necessary in these experiments, most likely to either lower the oxidation potential of the thiol functional group on the cysteine building block through deprotonation or to prevent the formation of HPF₆ (note that in a biological setting basic amino acids or common intracellular buffers can easily serve this function). In addition, these measurements underline the charge-transfer nature of all transitions in the Vis/NIR region as all corresponding absorptions experience a blue-shift with an increase in solvent polarity; i.e., these complexes display negative solvatochromism.

Remarkably, the presence of one or more EWGs on the dioxo ligand causes a distinct change in the electronic structure of the complex. The CV and RDE voltammograms of **5** are shown in Figure 6A, while the voltammograms of compound **6** are available in the SI (Figure S4). The voltammograms of **5** were recorded over two distinct potential ranges, from -1.0 V to -2.0 V and from -1.0 V to 1.0 V to avoid the adsorption of the complex on the electrode (Figure S4).

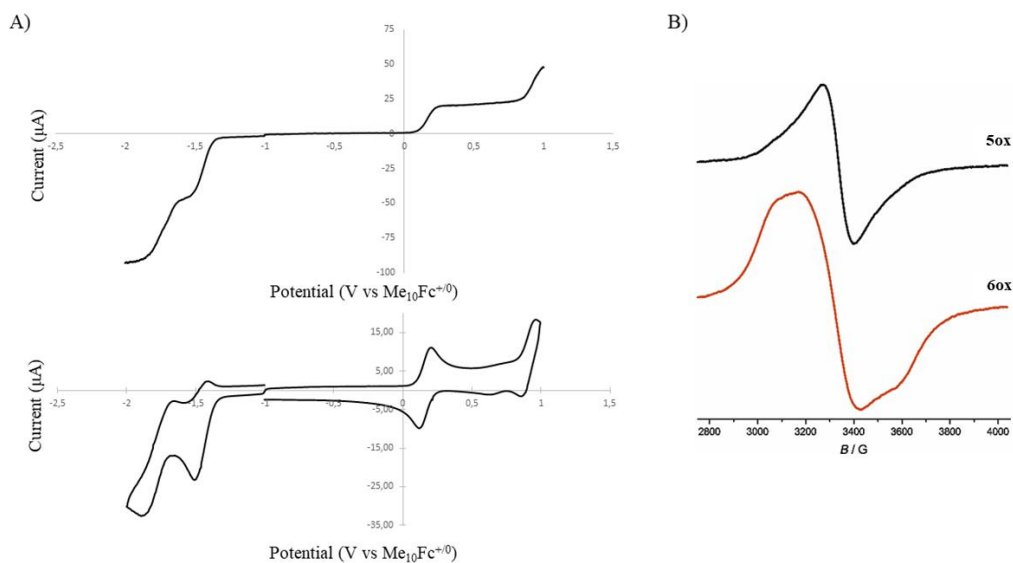
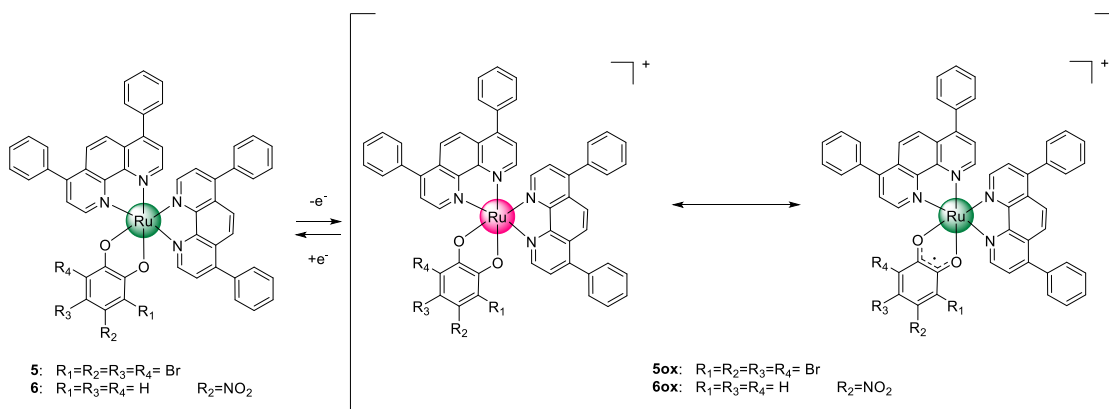


Figure 6. (A) RDE and cyclic voltammograms of complex **5** (from -2.0 to -1.0 V and from -1.0 to +1.0 V) at a glassy carbon electrode in DMF (1 mM) containing NBu_4PF_6 (100 mM) as supporting electrolyte. Data were recorded versus SCE at scan rate of 100 mV/s and recalculated versus $\text{Me}_{10}\text{Fc}^{0/+}$ potential value (-0.001 V and -0.002 V for RDE and CV respectively). (B) EPR spectra of complexes **5ox** and **6ox** at -140 °C.

Complexes **5**, **6** are EPR silent from 20 °C down to -150 °C which confirms that the dioxo ligand is present in its catecholate form as found by UV/Vis/NIR spectroscopy and the elemental analysis. To provide an attribution of the observed voltammetric features in the positive potential range, further EPR experiments were conducted on the monooxidized forms of **5** and **6** (**5ox** and **6ox**, respectively, in Scheme 2). Complexes **5** and **6** were converted to their monocationic forms by treatment with an excess of ferrocenium hexafluorophosphate (FcHPF_6 , $E_{1/2} = 0.450$ V vs SCE in DMF/0.1 M NBu_4PF_6).⁴⁹



Scheme 2. Structures of **5**, **6** and **5ox**, **6ox** represented as two resonance structures. Ru oxidation states +II and +III are marked in green and pink respectively.

5ox and **6ox** are EPR active, giving slightly anisotropic signals at $-140\text{ }^\circ\text{C}$ with a g_{av} of 2.019 for **5ox** and of 2.032 for **6ox** (Figure 4 and 6B). The absence of an EPR signal at room temperature for the oxidized complexes is explained by the electron-poor nature of the per-brominated- and nitro-substituted ligands, which increases the contribution of the Ru center to the spin density in the case of the oxidized complexes at the expense of the dioxo ligand.⁵⁰ Indeed, as reported in Table 1, the spin density on the Ru center increases to 0.4 |e⁻| in the case of **5ox** and **6ox** with a corresponding spin density on the dioxo ligand of roughly 0.6 |e⁻|. Therefore, **5ox** and **6ox** have their spin density nearly equally shared between the Ru ion and the dioxo ligand, corresponding to a strong orbital mixing. This can be represented as the two resonance structures of Scheme 2, where the contribution of the Ru(III)/cat form is nearly as important as the Ru(II)/sq one. A higher metal contribution to the overall spin densities is also indicated by distinct anisotropy of the g -tensor, which is more clearly evident for **6ox** (i.e., showing the larger computed spin density) with individual g -tensor components of $g_x = 1.870$, $g_y = 2.025$, $g_z = 2.190$ as determined by simulation of the experimental spectrum (see Figure S3 of the SI). Table 3 and S4 list the potentials related to the redox processes observed for compounds **5**, **6**.

Table 3. Electrochemical data for complexes **5** and **6**.

		Ph₂Phen^{0/-}	Ph₂Phen^{0/-}	Ox1	Ox2
5	E_{1/2}^a [V] (RDE)	-1.746 ± 0.003	-1.423 ± 0.002	0.182 ± 0.005	0.927 ± 0.008
6	E_{1/2}^a [V] (RDE)	-1.737 ± 0.009	-1.440 ± 0.009	0.164 ± 0.013	0.970 ± 0.009

^a E_{1/2} = half-wave.

To shed additional light on the impact of the substituent on the dioxo ligand, complex **5** was also subjected to UV/Vis/NIR spectroelectrochemical investigations in the positive potential range. As evident from Figure 7A, generation of the monocation furnishes a structured, broad band with a maximum at 940 nm, while the features, characteristic to the neutral forms disappear. The significant red-shift of this band as compared to compounds **1-4** is a clear token of the electron poor nature of the corresponding semiquinonate ligand, which lowers the energy difference between the Ru(II) donor and the dioxo ligand acceptor orbitals. The relatively larger loss of electron density experienced by the ruthenium atom and the rather electron-poor nature of the electrogenerated semiquinonate ligands in oxidized **5ox** are further underlined by the blue shift of the Ru→DIP MLCT and sq→DIP LL'CT bands in the visible range to 465 and 410 nm instead of 510 and 470 nm observed for **1**. Further oxidation to the dication, in agreement with the CV studies, leads to decomposition as rereduction after electrolysis yielded spectra that considerably differed to those of their monocationic or neutral forms (see Figure 7B).

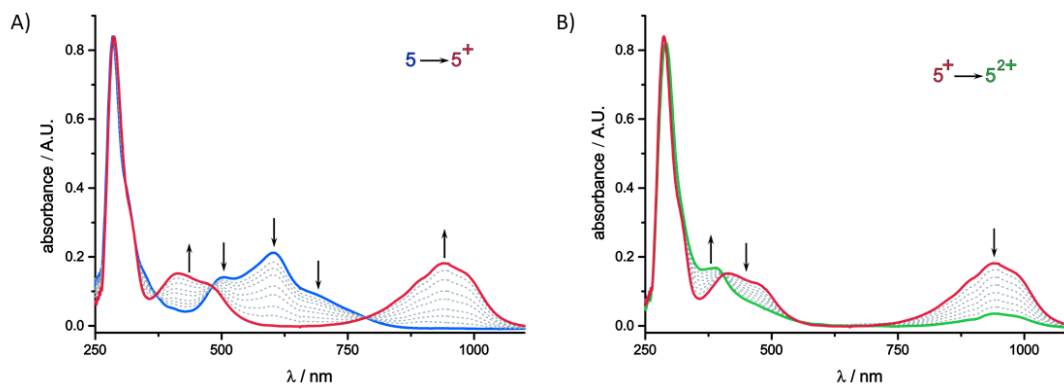


Figure 7. UV/Vis/NIR-spectroelectrochemistry data for complex **5**.

The change from an EDG to an EWG at the sq/cat ligand has therefore two effects. First, the overall redox potential of the molecule is increased in such a manner that, applying the same synthetic procedure and under identical conditions, no longer a paramagnetic, cationic but a neutral, diamagnetic complex is obtained. Secondly, the spin density in the monocationic form presents distinctly larger contributions from the ruthenium center when EWG are present. This occurrence results in a slight increase in EPR signal anisotropy and, more importantly, the absence of a room temperature EPR signal in **5ox** and **6ox**.

Stability in DMSO and human plasma

Next, the stability of compounds **1–6** was investigated in DMSO and in human plasma. DMSO stability is a key factor to consider in medicinal chemistry as this solvent, in some cases, was found to be problematic for biological experiments for its coordinative property.^{51–53} The stability in DMSO was monitored by ¹H NMR spectroscopy over 96 h at room temperature. Overall, all complexes are stable under these conditions as no significant new peaks appear in the spectra (Figure S6). Only complex **3** shows a certain degree of degradation after 96 h, displaying a conversion of about 15% of the initial complex. The spectrum of complex **3** shows

new, more resolved peaks which are a clear indication of the formation of a non-paramagnetic product. Additionally, for estimating the stability under the physiological conditions, the stability of complex **1** (the most promising of the series) was investigated in human plasma. Complex **1** was incubated over 96 h in human plasma at 37 °C in the presence of an internal standard (caffeine). Figure S7 reveals a linear trend of concentration of complex **1** over time and a half-life of 48h.

Cytotoxicity Studies

The first step toward the biological investigation of complexes **1–6** was the evaluation of cell viability in monolayer cultures of HeLa (human cervical adenocarcinoma) cell line, A2780 (human ovarian carcinoma), A2780 cis (human cisplatin resistant ovarian carcinoma), A2780 ADR (human doxorubicin resistant ovarian carcinoma), CT-26 (mouse colon adenocarcinoma), CT-26 LUC (mouse colon adenocarcinoma stably expressing luciferase) and RPE-1 (human normal retina pigmented epithelial) cell lines using a fluorometric cell viability assay (single graphs available in Figures S8).⁵⁴ Doxorubicin and cisplatin, as well as the ligands and the **Ru(DIP)₂Cl₂** precursor were tested in the same cell lines as positive and additional controls (Table 4 and Table S5).^{55,56} Table 4 displays the IC₅₀ (the half maximal inhibitory concentration) values of the tested compounds and the previously reported **Ru-sq**.²⁹ **Ru-sq** is the analogous complex carrying the unsubstituted semiquinonate ligand. The comparison between **Ru-sq** and the derivatives carrying an EDG and EWG substituted dioxo ligand (compounds **1–4** and **5, 6**, respectively) reveals how the electron density on the organic moiety impacts the observed cytotoxicity in the tested cell lines. In general, compounds **1–4** present higher cytotoxicity in most of the cell lines tested. In contrast, complexes **5** and **6** show much lower cytotoxicity with IC₅₀ in the micromolar range for all the cell lines tested. Of particular interest is complex **1** with an IC₅₀ in the low nanomolar range (0.07 μM) against the cisplatin

resistant cell line which makes it 10 times more active than doxorubicin and around 200 times more active than cisplatin (0.54 μM and 18.33 μM for doxorubicin and cisplatin, respectively). Complex **1** presents an IC_{50} of 0.7 μM against the doxorubicin resistant cell line, which is 10 times lower than the values for **Ru-sq** and cisplatin (4.13 μM and 8.32 μM for **Ru-sq** and cisplatin, respectively). Overall, complexes **1–4** display a cytotoxicity which is comparable to that of doxorubicin and much higher than that of cisplatin. The **Ru(DIP)₂Cl₂** precursor (Table 4) and the different catechols (Table S4), display a much lower activity suggesting that the great activity shown by complexes **1–4** is the consequence of the coordination of electron rich sq ligands to the Ru(II) polypyridyl core.

Table 4. IC_{50} values for **1–6**, **Ru-sq**, cisplatin, doxorubicin and **Ru(DIP)₂Cl₂** on different cell lines.

IC_{50} (μM)	HeLa	A2780	A2780 ADR	A2780 cis	CT-26	CT-26 LUC	RPE-1
Cisplatin*	9.28 \pm 0.20	4.00 \pm 0.76	8.32 \pm 0.71	18.33 \pm 2.92	2.60 \pm 0.18	2.42 \pm 0.23	30.24 \pm 5.11
Doxorubicin*	0.34 \pm 0.02	0.19 \pm 0.03	5.94 \pm 0.58	0.54 \pm 0.04	0.082 \pm 0.003	0.18 \pm 0.006	0.89 \pm 0.17
Ru(DIP)₂Cl₂ *	15.03 \pm 0.4	4.69 \pm 0.14	78.27 \pm 4.9	6.36 \pm 0.57	9.20 \pm 1.22	6.65 \pm 0.5	3.13 \pm 0.07
Ru-sq *	0.50 \pm 0.01	0.67 \pm 0.04	4.13 \pm 0.2	0.45 \pm 0.03	1.00 \pm 0.03	1.51 \pm 0.14	0.90 \pm 0.04
1	0.124 \pm 0.004	0.0261 \pm 0.0005	0.70 \pm 0.05	0.076 \pm 0.005	0.067 \pm 0.004	0.269 \pm 0.007	0.764 \pm 0.23
2	0.353 \pm 0.006	0.18 \pm 0.03	1.05 \pm 0.22	0.39 \pm 0.07	0.31 \pm 0.02	0.24 \pm 0.01	0.67 \pm 0.2
3	0.61 \pm 0.07	0.20 \pm 0.01	1.45 \pm 0.14	0.39 \pm 0.03	0.65 \pm 0.04	0.42 \pm 0.01	0.58 \pm 0.01
4	2.11 \pm 0.12	0.53 \pm 0.03	1.91 \pm 0.08	0.80 \pm 0.03	1.167 \pm 0.15	1.147 \pm 0.224	2.965 \pm 0.45
5	10.46 \pm 0.25	10.23 \pm 0.14	15.01 \pm 0.75	17.17 \pm 1.4	13.49 \pm 0.5	11.64 \pm 0.7	23.15 \pm 2.5
6	10.03 \pm 0.44	12.4 \pm 0.8	18.63 \pm 2.02	16.37 \pm 2.04	7.61 \pm 0.11	9.01 \pm 0.19	16.55 \pm 0.98

* Values taken from^[29] We however note that these experiments were performed on the same days.

Since complex **1** was found to be the most promising candidate among the series of complexes investigated in the 2D model due to its remarkably high cytotoxicity and its great activity towards resistant cell lines, its cytotoxicity was explored in a MultiCellular Tumour Spheroids (MCTS) model.⁵⁷ In 3D spheroids, proper cell to cell and cell to environment interactions, as well as cellular morphology and polarity is maintained. Additionally growth pattern, metabolism and gene expression mimic the complexity of initial stages of solid tumours.^{57,58} These features allow for a good estimation of *in vivo* antitumor activity, qualifying MCTS as a more reliable model than monolayer cell cultures in cancer research.⁵⁸⁻⁶⁰ In addition to the complex of interest (**1**), the **Ru(DIP)₂Cl₂** precursor, the 3-methoxycatechol ligand and positive controls (cisplatin and doxorubicin)^{59,60} were tested *via* a luminescent cell viability assay in HeLa MCTS (single graphs are available in Figure S9). Moreover, **Ru-sq** was tested for comparative purposes. Table 5 shows the IC₅₀ values after a 48 h treatment for all the compounds tested. Complex **1** displays high cytotoxicity toward HeLa MCTSs with an IC₅₀ ≈ 21 μM. This value indicates an activity which is almost the double of the current drugs cisplatin and doxorubicin (IC₅₀ ≈ 46 μM and 39 μM, respectively). Nevertheless, the previously reported **Ru-sq** still shows a slightly higher cytotoxicity (IC₅₀ ≈ 14 μM). 3-methoxycatechol proved to be nontoxic and the **Ru(DIP)₂Cl₂** precursor showed a cytotoxicity comparable to cisplatin.

Table 5. IC₅₀ values for complex **1**, cisplatin, doxorubicin, **Ru(DIP)₂Cl₂** and 3-methoxycatechol in multicellular HeLa cancer cell spheroids.

IC ₅₀ (μM)	Cisplatin*	Doxorubicin*	Ru-sq*	1	Ru(DIP)₂Cl₂	3-Methoxycatechol
HeLa MCTSs	46.49 ± 4.18	38.59 ± 0.43	14.11 ± 0.09	21.01 ± 0.66	59.84 ± 3.05*	>100

* Values taken from^[29] We however note that these experiments were performed on the same days.

To evaluate the time dependent effect on the growth of MCTS treated with complex **1**, an additional experiment was performed. 400 μm HeLa MCTS were treated with a range of different concentrations of **1**. Every three days, half of the media in the wells was exchanged

(treatment concentration consequently decreased by half) and pictures of the spheroids were taken (Figure 8a). HeLa MCTS had reduced diameter when treated with concentrations higher than the IC_{50} (20, 25 and 30 μM) of complex **1**. Additionally, Figure 8 indicates that this effect was maintained even after 13 days for the highest concentration, while, a slow regrowth is observed for 20 and 25 μM treatment. These findings are similar to the one previously reported for **Ru-sq** complex.²⁹

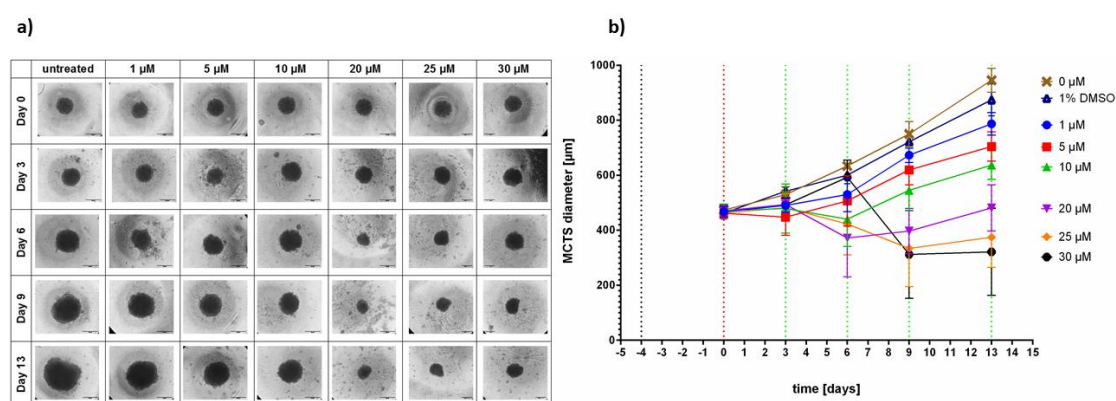


Figure 8. Changes in growth kinetics of MCTSs treated with complex **1** at different concentrations (1, 5, 10, 20, 25 and 30 μM). (a) Images collected at day 0 (before treatment) and at day 3, 6, 9 and 13. b) MCTSs diameter measured at different time points. Blue dotted line indicates day of seeding, red dashed line indicates day of treatment, green dotted lines indicate days of washing.

Overall, the outstanding activities shown by complex **1** in the monolayer cells model is confirmed by a MCTSs model. These findings represent a powerful encouragement to the further investigation of complexes **1** as potential chemotherapeutic agents.

Cell Death Mechanism.

Many of the novel or existing chemotherapeutic agents are developed to trigger cell death through apoptosis.⁶³ This is considered a carefully regulated and energy dependent type of cell

death in contrast to necrosis considered a rapid, unregulated, energy- independent mode of death.⁶⁴ The mode of cell death induced by the treatment with complex **1** was investigated in HeLa cell line *via* flow cytometry using Annexin V and propidium iodide (PI) staining method. Figure 9a shows the obtained dot-plots at t = 24 h (see Figure S10 for the dot plots at each time point). Figure 9b represents the percentage of cell population in different stages of cell death, at different time points in comparison to staurosporin (apoptosis inducer - positive control).⁷² Collected data demonstrated that after 24 h treatment, a large population of HeLa cells was in the late apoptotic/necrotic stage. It is worth noting that apoptosis or necrosis are induced by different pathways and mechanisms, and it is highly unlikely for a cell to undergo necrotic death after several hours of early apoptotic stage. Hence, these data indicate that complex **1** is most probably inducing cell death through apoptosis.

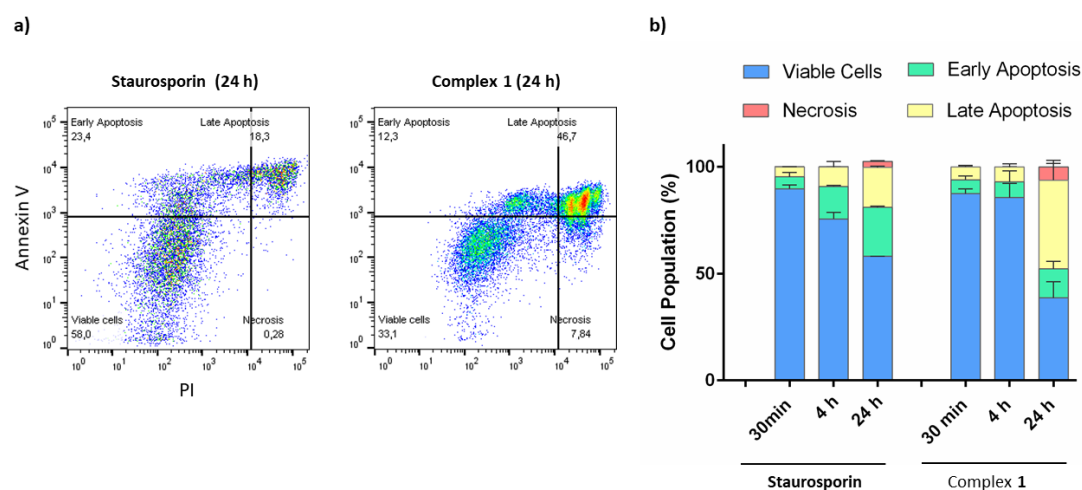


Figure 9. a) Flow cytometry dot-plots of Annexin V and PI staining in HeLa cells treated with complex **1** (10 μ M) and staurosporine (1 μ M) at 24 h. b) Percentage of cell population in different stages of cell death for staurosporin (positive control) and complex

Cellular Uptake, Biodistribution, and DNA Metalation.

The high cytotoxicity of complex **1** in the tested cell lines encouraged its further biological studies. Firstly, cellular uptake, mechanism of uptake and intracellular distribution were tested

using Inductively Coupled Plasma Mass Spectrometry (ICP-MS). Working concentrations and incubation times were chosen accordingly to avoid extended cell mass loss due to the high cytotoxicity of the complexes but considering a final ruthenium amount that allowed for the determination of the metal content. Nevertheless, the working conditions (5 μM treatment for 2 h) allowed for a minor accumulation of the drug cisplatin, which was used as control.^{65,66,67} Complex **1** shows higher cellular accumulation than the positive control cisplatin and the **Ru-sq** analogue previously reported,²⁹(Figure 10a). To clarify whether the mechanism of uptake involves passive or active mechanisms additional experiments were performed. HeLa cells were kept at low temperature (4°C) or were pre-treated with different uptake pathways inhibitors. Thus, 2-deoxy-*D*-glucose and oligomycin were used to block cellular metabolism, chloroquine or ammonium chloride to impede endocytic pathways, and tetraethylammonium chloride to block cation transporters. After pre-treatment, cells were incubated with the tested compounds (2 h, 5 μM). The amounts of ruthenium found in cells were then quantified using ICP-MS. Low temperature slightly inhibited the uptake of complex **1** while all the other conditions (regulating active transportation mechanisms) did not affect the total uptake (Figure S11). These findings strongly suggest that the internalisation of complex **1** is due only to a passive, energy independent mechanism, unlike **[Ru(DIP)₂(sq)](PF₆)**, whose mechanism of uptake involves both active and passive transports.²⁹ Intracellular distribution among cytoplasm, mitochondria, nucleus and lysosomes was determined by isolating pure cellular compartments. Most of the compounds accumulates in nucleus and lysosomes and in a smaller extent to mitochondria and cytoplasm (Figure 10b). To verify whether the accumulation in the nucleus lead to direct interaction with DNA, the genetic material was extracted from treated cells and the metal content analysed *via* ICP-MS. Figure 10c shows that complex **1** successfully binds DNA in a much higher extent when compared to cisplatin, whose results are in perfect agreement with what previously reported.⁶⁷ Even though the accumulation in the nucleus is

lower, the DNA metalation shows comparable results for complex **1** and **Ru-sq**, which can be explained by the overall higher uptake of complex **1**.

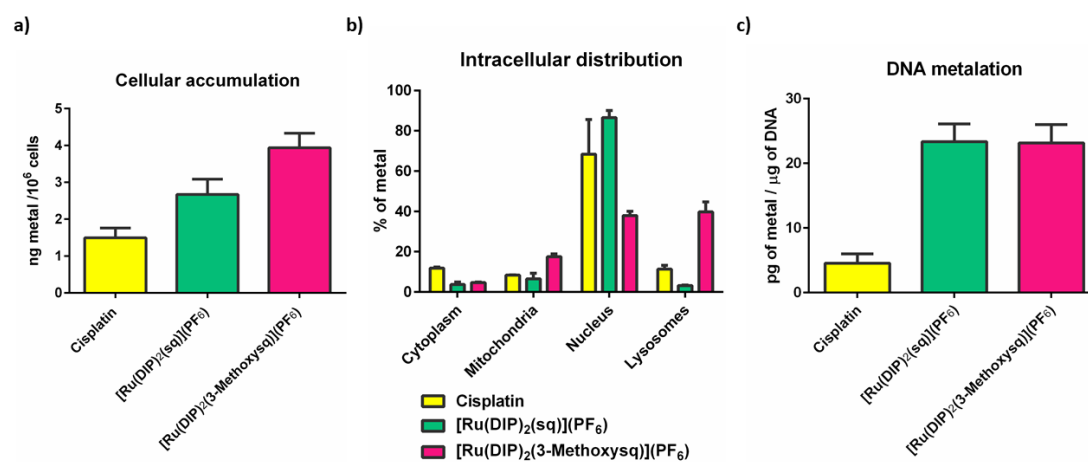


Figure 10. Cellular uptake (a), cellular fractionation (b) and DNA metalation (c) of HeLa cells after treatment with tested compounds (5 μ M, 2 h). Data are presented as the mean \pm SD of at least 3 technical replicates. All data related to **Ru-sq** were previously reported by our group.²⁹ We, however, note that these experiments were performed on the same days.

JC-1 Mitochondrial Membrane Potential Test and Metabolic Studies.

Next, to gain more insights into the possible mechanism of action of complex **1**, its effect on mitochondria membrane potential (MMP) and metabolic pathways was determined. First, the MMP (directly correlated to mitochondrial function⁶⁸) was studied *via* JC-1 staining method. JC-1 is considered the most reliable fluorescent dye to illustrate the MMP in living cells.⁶⁹ It is present as an aggregate (red fluorescent) and as a monomer (green fluorescent), respectively at high and low MMP.⁶⁹ The net distinction allows for an immediate analysis of the MMP.⁶⁹ Figure 11a shows the red fluorescence signal observed in HeLa cells untreated (negative control) and after 24 h treatment with complex **1**, DMSO (vehicle control) and FCCP (carbonyl cyanide 4-(trifluoromethoxy)phenylhydrazone, an uncoupling agent used as positive control).⁷⁰ A slight decrease in the fluorescence is observed in the cells treated with complex **1** (from 0.05 μ M to 0.25 μ M) in a concentration-dependent manner. However, even at the IC₅₀ concentration,

the effect is not as prominent as the one obtained for the positive control. It is worth noting that ongoing apoptosis can also generate a drop in MMP.⁷⁰ Taken together, complex **1** is slightly decreasing mitochondria membrane potential in treated cells. To have more insights into the effect of the complex **1** in the process of oxidative phosphorylation, further experiments were performed. For this purpose, Seahorse XF Analyzer was used. The performed Mito Stress Test pointed to very low basal respiration levels, inhibited ATP production and the loss of the ability to restore proton balance after FCCP treatment (Figure 11b and Figure S12). These data suggest that the mitochondria processes are defective in HeLa cells incubated with complex **1**. On the contrary, the same effects were not observed during treatment with the **Ru(DIP)₂Cl₂** precursor or the 3-methoxycatechol ligand. Furthermore, no influence of compound **1** on the cytosolic process of glycolysis was detected (Figure S13). Unfortunately, no direct impact on three main fuel pathways could be determined due to very low oxygen consumption rates (Figure S14). Metabolic studies confirm that the effects of complex **1** on mitochondria respiration can contribute to cell death, leading to a multiple mode of actions involving at least nucleus and mitochondria as possible targets.

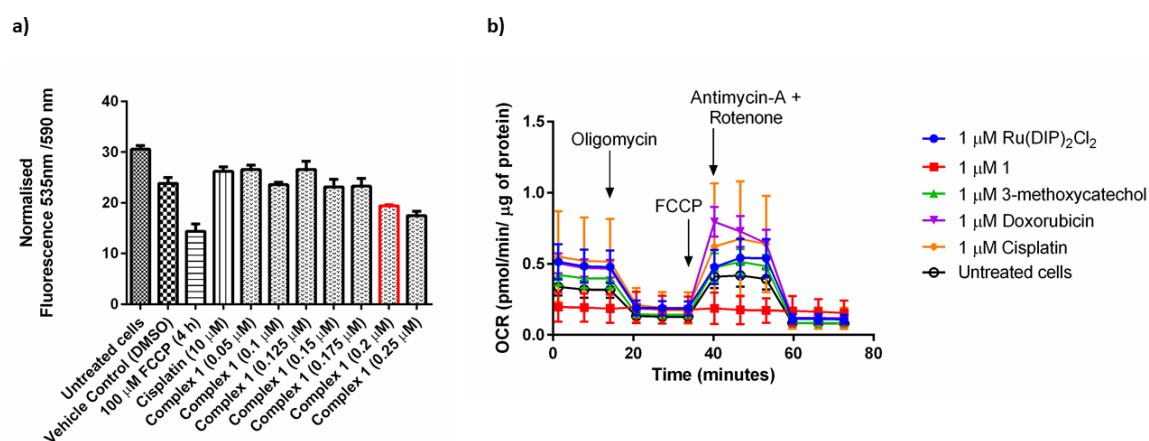


Figure 11. a) Fluorescence signal of JC-1 dye detected in HeLa cells treated for 24 h with different concentrations of complex **1** (from 0.05 μ M to 0.25 μ M). The bar marked in red indicates the IC₅₀ concentration (0.2 μ M). FCCP is used as positive control, cisplatin and

DMSO (1%) are used as negative controls. b) Mito Stress Test profile after 24 h treatment; oxygen consumption rate changes after treatment with specific electron transport chain inhibitors. Oligomycin (inhibitor of ATP synthase (complex V)), FCCP (uncoupling agent), Antimycin-A (complex III inhibitor) and Rotenone (complex I inhibitor).

Preliminary *in vivo* biodistribution studies

In this study, complex **1** demonstrated to be of great interest as potential chemotherapeutic agent. However, one of its main drawbacks is its scarce water solubility, which could limit its potential use *in vivo*. The analogue **Ru-sq**, previously reported by our group, showed potential as anticancer drug in immunocompetent mice bearing Ehrlich tumors.²⁹ Nevertheless, its clinical interest is limited by its poor water solubility, which prevented an intravenous administration. Anticancer drugs such as paclitaxel and docetaxel have faced the same limitation but reached the clinic.^{71,72} Indeed, to overcome this shortcoming, a formulation strategy was used, which allowed for increased apparent aqueous solubility of the drug and therefore their parenteral injection.^{71,72} Following these examples, we successfully developed a formulation of compound **1** using polysorbate 80, a nonionic surfactant generally recognized as safe and already used for docetaxel.⁷³ Using the film rehydration method, usually applied to the preparation of polymeric surfactant micelles and liposomes,^{74,75} up to 0.84 ± 0.06 mg/mL of compound **1** could be dissolved in 50 mg/mL of polysorbate 80, with an encapsulation efficiency of $95 \pm 3\%$. Liver and kidney are the main routes by which drugs and metabolites leave the body, so the effect of complex **1** on them was evaluated.⁷⁶ Complex **1** was tested in

TIB-75 (mouse, epithelial liver) and HEK293 (human, embryonic kidney) cell lines showing cytotoxicity in both cases (Table 6, single graph available in Figure S8).

Table 6. IC₅₀ values for cisplatin, complex **1**, Ru(DIP)₂Cl₂ and 3-methoxycatechol in HEK293 and TIB-75 cell lines.

IC ₅₀ (μM)	Cisplatin*	1	Ru(DIP) ₂ Cl ₂	3-Methoxycatechol
HEK293	6.60 ± 1.49	0.07 ± 0.005	5.42 ± 0.51	18.96 ± 0.88
TIB-75	2.83 ± 0.08	0.02 ± 0.0001	5.06 ± 0.32	19.16 ± 1.15

These results together with the ones shown in Table 4 point out the non-selectivity of complex **1** between cancerous and non-cancerous cell lines. This shortcoming is often faced in medicinal chemistry and it could be improved by the introduction of a targeting moiety. Therefore, we decided to pursue the biodistribution study with the appropriate formulation to verify the ability of the drug to distribute in the organism upon administration, despite its low aqueous solubility. A preliminary biodistribution study was performed on healthy BALB/c mice through the intravenous injection of the formulation at a dose of 5 mg/kg of compound **1**. After 30 minutes, 1 and 2 hours, mice were sacrificed and the ruthenium content was analyzed *via* ICP-MS in relevant tissues (brain, liver, kidneys, spleen, intestine, lungs and blood). Worthy of note, the formulation was well tolerated, and no sign of pain or acute toxicity was observed over the course of the experiment.

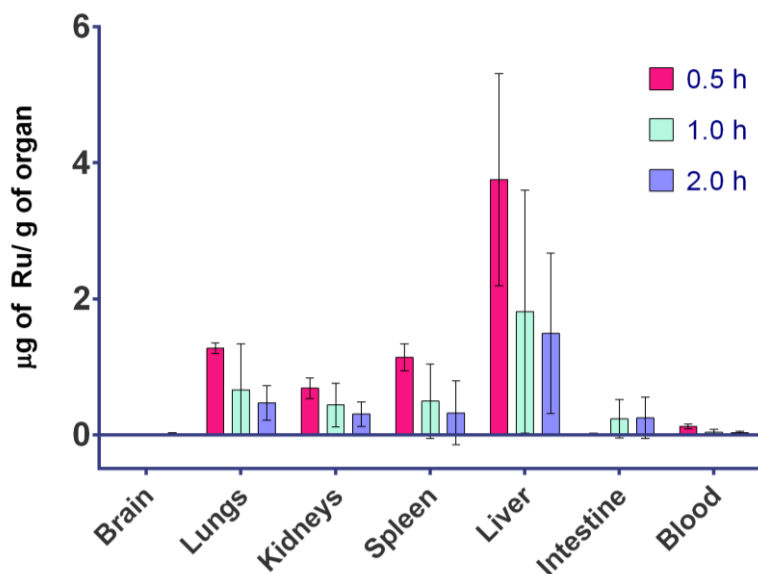


Figure 12. Biodistribution of complex **1** (5mg/kg) over 2 h in BALB/c mice.

According to data shown in Figure 12, compound **1** seems to accumulate preferentially in the liver and the kidneys, and more surprisingly, in the lungs and the spleen. This phenomenon has already been described in the case of doxorubicin formulated in polysorbate 80, and was attributed to this carrier.⁷⁷ The low level of ruthenium detected in the blood at all time point suggest a fast distribution in the tissues, possibly associated to a fast renal and biliary elimination, supported by the increase of the ruthenium content in the intestine over time.

These preliminary results show compound **1**'s ability to distribute in the body despite its hydrophobicity using a formulation strategy. While promising, the formulation with polysorbate 80 has also been associated with side effects.^{78,79} To overcome this drawback, a more biocompatible excipient could be used, as already successfully achieved in the case of docetaxel.⁷²

Conclusions

In this work, we performed a structure activity relationship study (SAR) based on the promising activity expressed by the complex **Ru-sq** recently reported by our group. More specifically, we explored the coordination of differently substituted catechol-type dioxo ligands to the Ru(DIP)₂ core. Electrochemical, EPR and electronic structure studies allowed us to conclude that the two classes of dioxo ligands tested, carrying either electron-donating (EDG) or electron-withdrawing (EWG) groups, gave Ru(II) complexes with either the semiquinonate (sq, for EDG-modified dioxo ligands in complexes **1–4**) or catecholate ligand (cat, for EWG-modified dioxo ligands in complexes **5, 6**). Complexes **1–4** are deep red solids and carry an overall positive charge due to the monoanionic sq ligand. Complexes **5** and **6** are blue/violet in color and overall neutral due to the dianionic charge associated with the catecholate. Both classes of complexes were found to be stable in DMSO and complex **1** displayed a half-life of 48 h in human plasma. Cytotoxicity studies using the monolayer model revealed that complexes **1–4** displayed much higher bioactivities than complexes **5** and **6**. These findings clearly suggest that the high cytotoxicity observed is a direct consequence of the coordination of electron rich semiquinonate ligands to the Ru(II) polypyridyl core. Precisely, complex **1** was found to be the most promising candidate of this series with IC₅₀ values in the low nanomolar range and was chosen for more detailed investigations. Firstly, its cytotoxicity was confirmed using a more reliable 3D model (MCTS), where it displayed an IC₅₀ value of almost half of that of cisplatin and doxorubicin. Complex **1** was found to be taken up by HeLa cells very efficiently through a passive transportation mechanism. Cellular fractionation studies revealed major accumulation in the nucleus, lysosomes and in a smaller extent in the mitochondria and cytoplasm. DNA ruthenation, MMP determination and mitochondria metabolism studies indicated that DNA and mitochondria are both cellular targets of complex **1**. Multiple targets are essential to overcome resistance, which is one of the main drawbacks associated with chemotherapy treatments

nowadays. Moreover, despite its poor water solubility, complex **1** demonstrated to distribute well *in vivo* with the use of an appropriate formulation. These results together with the advantageous modes of action and the outstanding cytotoxicity displayed by complex **1** makes it an interesting compound for clinical application in the search of potential chemotherapeutic agents against cancer.

Experimental Section

Materials

All chemicals were either of reagent or analytical grade and used as purchased from commercial sources without additional purification. Ruthenium trichloride hydrate was provided by I²CNS, 4,7-Diphenyl-1,10-phenanthroline, Lithium chloride (anhydrous, 99%), 3-Methoxycatechol, 4-Methylcatechol, 4-tert-Butylcatechol and 4-Nitrocatechol by Alfa Aesar, 3-Methylcatechol and tetrabutylammonium hexafluorophosphate by Sigma-Aldrich, tetrabromocatechol from BOC Science. All solvents were purchased of analytical, or HPLC grade. When necessary, solvents were degassed by purging with dry, oxygen-free nitrogen for at least 30 min before use.

Instrumentation and methods

Amber glass or clear glassware wrapped in tin foil were used when protection from the light was necessary. Schlenk glassware and a vacuum line were employed when reactions sensitive to moisture/oxygen had to be performed under nitrogen atmosphere. Thin layer chromatography (TLC) was performed using silica gel 60 F-254 (Merck) plates with detection of spots being achieved by exposure to UV light. Column chromatography was done using Silica gel 60–200 μm (VWR). Eluent mixtures are expressed as volume to volume (v/v) ratios. ¹H and ¹³C NMR spectra were measured on Bruker Avance III HD 400 MHz or Bruker Avance Neo 500 MHz spectrometers using the signal of the deuterated solvent as an internal standard.⁸⁰

The chemical shifts δ are reported in ppm (parts per million) relative to tetramethylsilane (TMS) or signals from the residual protons of deuterated solvents. Coupling constants J are given in Hertz (Hz). The abbreviation for the peaks multiplicity is br (broad). ESI experiments were carried out using a 6470 Triple Quad (Agilent Technologies). Elemental analysis was performed at Science Centre, London Metropolitan University using Thermo Fisher (Carlo Erba) Flash 2000 Elemental Analyser, configured for %CHN. IR spectra were recorded with SpectrumTwo FTIR Spectrometer (Perkin-Elmer) equipped with a Specac Golden GateTM ATR (attenuated total reflection) accessory; applied as neat samples; $1/\lambda$ in cm^{-1} . Analytical HPLC measurement was performed using the following system: 2 x Agilent G1361 1260 Prep Pump system with Agilent G7115A 1260 DAD WR Detector equipped with an Agilent Pursuit XRs 5C18 (100Å, C18 5 μm 250 x 4.6 mm) Column and an Agilent G1364B 1260-FC fraction collector. The solvents (HPLC grade) were acetonitrile (0.1% TFA, solvent A) and millipore water (0.1% TFA, solvent B). The flow rate was 1 mL/min. Detection was performed at 215nm, 250nm, 350nm, 450nm, 550nm and 650nm with a slit of 4nm.

Synthesis and characterization

Ru(DMSO)₂Cl₂. Ru(DMSO)₂Cl₂ was synthesised following an adapted literature procedure.⁴⁴ Spectroscopic data (¹H NMR) was in agreement with literature.⁴⁴

Ru(DIP)₂Cl₂. The complex was synthesised following an adapted literature procedure.⁴⁵ A mixture of Ru(DMSO)₂Cl₂ (3.0 g, 6.19 mmol), 4,7-diphenyl-1,10-phenanthroline (4.11 g, 12.38 mmol) and LiCl (2.0 g, 47.18 mmol) dissolved in DMF (100 mL) was refluxed for 24 h. After cooling to *r.t.*, the solvent was reduced *in vacuo* to 8 mL and 350 mL of acetone were added. The mixture was then stored at -20 °C overnight before filtration with a Buchner funnel and washed with acetone and Et₂O to afford Ru(Ph₂Phen)₂Cl₂ as a deep purple solid (3.76 g, 4.49 mmol, 72%). Spectroscopic data (¹H NMR) were in agreement with literature.⁴⁵

General method for the synthesis of 1–6

Ru(DIP)₂Cl₂ (0.250 g, 0.3 mmol) and aq. NaOH (0.45 mL, 1 M) were dissolved in 2-propanol (20 mL). The solution was degassed purging nitrogen through the solution for 15 min and the respective catechol (0.07 g, 0.5 mmol) was added. The mixture was heated to reflux for 24 h under N₂ atmosphere and protected from light. After cooling to *r.t.*, the mixture was stirred open to air for 2 h while still protected from light and the solvent was removed under vacuum. The residual solid was dissolved in 2-propanol (2.5 mL) and H₂O (20 mL) and NH₄PF₆ (0.250 g, 1.5 mmol) was added. The mixture was stored in the fridge (4 °C) overnight. The precipitate was filtered with a Buchner funnel, washed with H₂O (3 × 50 mL) and Et₂O (3 × 50 mL) and collected. The solid was collected with DCM and dried under vacuum to deliver a crude product which was chromatographed on silica (DCM/MeCN 20:1 *R_f*: 0.3 for complexes 1–4, DCM/Et₂O 98:2 *R_f*: 0.8 for complex 5, DCM/MeOH 96:4 *R_f*: 0.4 for complex 6). Evaporation of the solvent under vacuum provided complexes 1–6. Each complex with Et₂O or Heptane (10 mL) was sonicated for 10 min and then centrifuged. This procedure was repeated three times for each solvent. The solid was collected with DCM and dried under vacuum to deliver a clean product. Finally the red solid was collected with DCM and dried under vacuum to afford a clean product.

[Ru(DIP)₂(3-methoxylsq)](PF₆) (1)

Deep red solid (0.073 g, 0.07 mmol, 23%). IR (Golden Gate, cm⁻¹): 3060w, 1620w, 1590w, 1540w, 1460m, 1400m, 1250m, 1160m, 1100m, 1030w, 827s, 764s, 735m, 700s. ¹H NMR (500 MHz, CD₂Cl₂): δ/ppm = 8.91 – 8.50 (br, 1H, *arom.*), 8.43 – 8.08 (br, 3H, *arom.*), 8.07 – 7.79 (br, 7H, *arom.*), 7.75 – 7.46 (br, 15H, *arom.*), 7.46 – 7.28 (br, 2H, *arom.*), 7.28 – 6.93 (br, 10H, *arom.*). ¹³C NMR (125 MHz, CD₂Cl₂): δ/ppm = 149.62, 146.57, 143.72, 140.55, 137.05, 136.03, 133.07, 132.47, 131.27, 130.31, 130.07, 130.00, 129.59, 129.56, 129.33, 128.97,

128.80, 128.57, 125.67, 125.46, 123.55. MS (ESI+): m/z 904.8 $[M - PF_6]^+$. Elemental Analysis: calcd. for $C_{55}H_{40}F_6N_4O_4PRu = C$, 62.76; H, 3.64; N, 5.53. Found = C, 61.67; H, 3.63; N, 5.09. HPLC: 0–3 minutes: isocratic 65% A (35% B); 3–17 minutes: linear gradient from 65% A (35% B) to 100% A (0% B); 17–23 minutes: isocratic 100% A (0% B), $T_R = 11.887$ min.

[Ru(DIP)₂(3-methylsq)](PF₆) (2)

Deep red solid (0.07 g, 0.07 mmol, 24%). IR (Golden Gate, cm^{-1}): 3060w, 1600w, 1540m, 1390m, 1250m, 1150m, 1100w, 1030w, 827s, 764s, 735s, 700s. ¹H NMR (400 MHz, CD₂Cl₂) δ 8.79 – 8.11 (br, 6H, *arom.*), 8.08 – 7.82 (br, 6H, *arom.*), 7.60 (br, 15H, *arom.*), 7.40 – 6.81 (br, 11H, *arom.*). ¹³C NMR (100 MHz): $\delta/ppm = 148.62, 147.00, 142.78, 142.70, 142.59, 136.94, 136.22, 132.88, 130.54, 130.25, 130.13, 129.79, 129.61, 129.56, 128.64, 126.87, 126.52, 124.93, 124.47, 121.72$. MS (ESI+): m/z 888.7 $[M - PF_6]^+$. Elemental Analysis: calcd. for $C_{55}H_{40}F_6N_4O_3PRu = C$, 62.86; H, 3.84; N, 5.33. Found = C, 62.95; H, 3.69; N, 5.20. HPLC: 0–3 minutes: isocratic 65% A (35% B); 3–17 minutes: linear gradient from 65% A (35% B) to 100% A (0% B); 17–23 minutes: isocratic 100% A (0% B), $T_R = 13.568$ min.

[Ru(DIP)₂(4-methylsq)](PF₆) (3)

Deep red solid (0.09 g, 0.09 mmol, 29%). IR (Golden Gate, cm^{-1}): 3060w, 1620w, 1590, 1560, 1510w, 1420m, 1240m, 1120w, 1090w, 1030w, 912w, 827s, 762s, 735m, 698s. ¹H NMR (500 MHz, CD₂Cl₂) δ 8.63 – 8.07 (br, 6H, *arom.*), 8.03 – 7.81 (br, 7H, *arom.*), 7.72 – 7.36 (br, 16H, *arom.*), 7.36 – 7.03 (m, 9H, *arom.*). ¹³C NMR (125 MHz): $\delta/ppm = 149.08, 147.51, 143.55, 142.50, 140.12, 140.01, 136.57, 136.18, 132.83, 132.35, 130.28, 130.19, 129.97, 129.60, 129.49, 128.89, 128.71, 128.37, 126.41, 124.88, 123.69$. MS (ESI+): m/z 888.7 $[M - PF_6]^+$. Elemental Analysis: calcd. for $C_{55}H_{38}F_6N_4O_2PRu = C$, 63.95; H, 3.71; N, 5.42. Found = C, 63.84; H, 3.62; N, 5.29. HPLC: 0–3 minutes: isocratic 85% A (15% B); 3–17 minutes: linear

gradient from 85% A (15% B) to 100% A (0% B); 17–23 minutes: isocratic 100% A (0% B),
 $T_R = 13.532$ min.

[Ru(DIP)₂(4-tert-butylsq)](PF₆) (4)

Deep red solid (0.05 g, 0.05 mmol, 16%). IR (Golden Gate, cm^{-1}): 3060w, 2960w, 1620w, 1580w, 1510m, 1450m, 1420m, 1220m, 1090w, 1030w, 827s, 764s, 735s, 700s. ¹H NMR (400 MHz, CD₂Cl₂): $\delta/\text{ppm} = 8.43 - 8.12$ (br, 6H, *arom.*), 8.09 – 7.81 (br, 9H, *arom.*), 7.70 – 7.46 (br, 16H, *arom.*), 7.46 – 7.24 (br, 4H, *arom.*), 7.24 – 7.04 (br, 8H, *arom.*). ¹³C NMR (125 MHz, CD₂Cl₂): $\delta/\text{ppm} = 147.51, 147.31, 143.70, 136.70, 136.64, 132.77, 132.54, 130.21, 129.63, 129.45, 128.84, 128.75, 127.49, 126.60, 124.85, 124.45$. MS (ESI⁺): m/z 930.8 [M - PF₆]⁺. Elemental Analysis: calcd. for C₅₈H₄₄F₆N₄O₂PRu = C, 64.80; H, 4.13; N, 5.21. Found = C, 64.72; H, 4.13; N, 5.14. HPLC: 0–3 minutes: isocratic 85% A (15% B); 3–7 minutes: linear gradient from 85% A (15% B) to 100% A (0% B); 7–9 minutes: isocratic 100% A (0% B); 9–11 minutes: linear gradient from 100% A to 85% A, $T_R = 9.801$ min.

Ru(DIP)₂(tetrabromocat) (5)

Blue/violet solid (0.192 g, 0.162 mmol, 54%). IR (Golden Gate, cm^{-1}): 3060w, 1600w, 1430s, 1260m, 1080m, 1030w, 914m, 847m, 760m, 731m, 700s. ¹H NMR (400 MHz, CD₂Cl₂): $\delta/\text{ppm} = 8.14 - 8.03$ (br, 5H, *arom.*), 7.74 – 7.63 (br, 10H, *arom.*), 7.60 – 7.43 (br, 15H, *arom.*), 7.40 – 7.31 (br, 2H, *arom.*). ¹³C NMR (125 MHz, CD₂Cl₂): $\delta/\text{ppm} = 146.27, 145.67, 145.62, 145.27, 136.94, 132.87, 132.83, 132.76, 132.64, 132.56, 130.25, 130.19, 129.62, 129.46, 129.35, 128.46, 126.44, 129.35, 128.46, 126.44, 126.38, 125.74, 125.66$. MS (ESI⁺): m/z 1090.4 [M]⁺. Elemental Analysis: calcd. for C₅₄H₃₂Br₄N₄O₂Ru = C, 54.52; H, 2.71; N, 4.71. Found = C, 54.56; H, 2.37; N, 4.89. HPLC: 0–3 minutes: isocratic 85% A (15% B); 3–7 minutes: linear

gradient from 85% A (15% B) to 100% A (0% B); 7–9 minutes: isocratic 100% A (0% B); 9–11 minutes: linear gradient from 100% A to 85% A, $T_R = 8.623$ min.

Ru(DIP)₂(4-nitrocat) (6)

Blue/violet solid (0.07 g, 0.08 mmol, 27%). IR (Golden Gate, cm^{-1}): 3060w, 1550w, 1490m, 1410w, 1240s, 1120m, 1070s, 1030w, 949w, 910w, 845s, 762s, 733s, 698s. ^1H NMR (400 MHz, CD_2Cl_2): $\delta/\text{ppm} = 9.65 - 9.21$ (br, 3H, *arom.*), $8.24 - 7.85$ (br, 8H, *arom.*), $7.81 - 7.40$ (br, 17H, *arom.*), $7.41 - 7.18$ (br, 2H, *arom.*), $6.87 - 6.59$ (br, 1H, *arom.*), $6.60 - 6.27$ (br, 2H, *arom.*), $6.11 - 5.84$ (br, 2H, *arom.*). ^{13}C NMR (125 MHz, CD_2Cl_2): $\delta/\text{ppm} = 153.27, 152.64, 152.53, 150.58, 146.76, 146.65, 144.72, 144.63, 137.40, 137.17, 130.79, 130.69, 130.19, 129.61, 129.50, 129.44, 128.86, 128.38, 126.17, 125.87, 125.49, 125.15, 124.99, 124.87$. MS (ESI+): m/z 919.4 $[\text{M}]^+$. Elemental Analysis: calcd. for $\text{C}_{54}\text{H}_{39}\text{N}_5\text{O}_6\text{Ru} = \text{C}, 67.92; \text{H}, 4.12; \text{N}, 7.33$. Found = C, 68.04; H, 4.11; N, 7.28. HPLC: 0–3 minutes: isocratic 5% A (95% B); 3–17 minutes: linear gradient from 5% A (95% B) to 100% A (0% B); 17–23 minutes: isocratic 100% A (0% B), $T_R = 15.907$ min.

Electrochemical Measurements

The electrochemical experiments were carried out with a conventional three-electrodes cell (solution volume of 15 mL) and a PC-controlled potentiostat/galvanostat (Princeton Applied Research Inc. model 263A). The working electrode was a vitreous carbon electrode from Orignalys (France) exposing a geometrical area of 0.071 cm^2 and mounted in Teflon[®]. The electrode was polished before each experiment with 3 and $0.3 \mu\text{m}$ alumina paste followed by extensive rinsing with ultra-pure Milli-Q water. Platinum wire was used as the counter electrode and saturated calomel electrode, SCE, as the reference electrode. Electrolytic solutions, DMF containing tetrabutylammonium hexafluorophosphate 0.1 M (NBu_4PF_6 , Aldrich, +99%) as

supporting electrolyte, were routinely deoxygenated by argon bubbling. All the potential values are given versus the calomel saturated electrode SCE and recalculated versus the $\text{Me}_{10}\text{Fc}^{0/+}$ redox pair ($E_{1/2} = 0.04 \text{ V vs. SCE}$).

Computational Details

All structural optimizations were performed using the Gaussian16 suite of programs⁸¹, at unrestricted Kohn-Sham⁸² (UKS) level. The non-relativistic double-zeta LANL2DZ⁸³ pseudopotential (effective-core-potential, ECP) were used for Ru and Br atoms, together with the Pople split valence double-zeta basis set for C, N, O, S, and H, coupled with one set of polarization and diffuse functions⁸⁴⁻⁸⁶ on all atoms, except for hydrogens. The B3LYP⁸⁷ exchange-correlation functional was used throughout. Solvent effects (isopropanol) were taken into account using the polarized continuum model in its conductor-like version (CPCM).⁸⁸

Calculations of g-tensors were performed on optimized structures using the Orca 3.0.3 Package.⁸⁹ Scalar relativistic effects were included using the zero-order regular approximation (ZORA).^{90,91} A common gauge origin at the metal nucleus was employed. Such calculations were performed using the segmented all-electron relativistically contracted (SARC) def2-SVP⁹² basis on all atoms except for the Ruthenium atoms, for which the def2-TZVP(-f) basis sets was used. The calculations were sped up by employing the chain-of-sphere (RIJCOSX)⁹³ approximation along with the decontracted auxiliary basis set of def2-SVP/J coulomb-fitting.⁹⁴ Increased integration grids (Grid4) and tight SCF convergence were used throughout the calculations. Solvent effects have been taken into account with conductor-like screening model (COSMO) with a dielectric constant ϵ of 20.7⁹⁵ - closest value to the isopropanol environment simulated in the geometry optimization.

Electron Paramagnetic Resonance Spectroscopy

Electron paramagnetic resonance (EPR) experiments were performed on a MiniScope MS400 table-top X-band spectrometer from Magnettech. Simulation of the experimental EPR spectra was performed with the MATLAB EasySpin program.⁹⁶ All samples were dissolved in dry and N₂-saturated DCM at a concentration of ca. 1 mM. Oxidized forms were generated using ferrocenium hexafluoroantimonate (FcPF₆, $E_{1/2} = 0.450$ V vs SCE in DMF/0.1 M NBu₄PF₆).^{49,97}

UV/Vis/NIR Spectroelectrochemistry (UV/Vis/NIR-SEC)

UV/Vis/NIR spectra were recorded on a TIDAS fibreoptic diode array spectrometer (combined MS UV/NIR and PGS NIR instrumentation) from J&M in HELLMA quartz cuvettes with a 0.1 cm optical path length. The OTTLE (optically transparent thin layer electrolysis) cell used for spectroelectrochemical studies was lab-built according to the design by Hartl et. al.⁹⁸ and comprises a Pt-mesh working electrode, a Pt-sheet counter electrode and a Ag-sheet pseudoreference electrode sandwiched between CaF₂ windows. For regular absorption spectra dry DMF was used as the solvent, while SEC experiments were conducted in a DMF electrolyte containing 0.1M of NBu₄PF₆. A BASi potentiostat was used to apply the necessary voltage to generate the reduced/oxidized species.

Stability studies

The stability in DMSO-d₆ at room temperature was assessed by ¹H NMR over 96h.

The stability of complex **1** in human plasma at 37 °C was evaluated following a slightly modified procedure already reported by our group.²⁹ The human plasma was provided by Biowest. Caffeine (internal standard) was obtained from TCI Chemicals. Stock solutions of the complexes (10 mM in DMSO) and caffeine (10 mM in milliQ water) were prepared. An aliquot of the respective stock solutions was then added to the plasma solution (380 μL) to a total

volume of 500 μL and final concentrations of 400 μM for the complexes and 2mM for caffeine. The resulting plasma solution was incubated for either: 0, 1, 3, 5, 16 or 24 h at 37 °C with continuous and gentle shaking (ca. 600 rpm). The reaction was stopped by addition of 1 mL of methanol, and the mixture was centrifuged for 3 min at 2000 rpm at room temperature. The methanolic solution was directly analysed using HPLC with a total injection volume of 20 μL . HPLC: 0–3 minutes: isocratic 85% A (15% B); 3–7 minutes: linear gradient from 85% A (15% B) to 100% A (0% B); 17–22 minutes: isocratic 100% A (0% B), $T_{R(\text{caff})} = 3.38 \text{ min}$, $T_{R(1)} = 6.51 \text{ min}$.

Cell culture

HeLa and CT-26 cell lines were cultured in DMEM media (Gibco) supplemented with 10% of fetal calf serum (Gibco). CT-26 LUC cell line was cultured in DMEM media (Gibco) supplemented with 10% of fetal calf serum (Gibco) and 1% Gentamicin. RPE-1 cell line was cultured in DMEM/F-12 media (Gibco) supplemented with 10% of fetal calf serum. A2780, A2780 cis, A2780 ADR cell lines were cultured in RPMI 1640 media (Gibco) supplemented with 10% of fetal calf serum (Gibco). The resistance of A2780 cis was maintained by cisplatin treatment (1 μM) for one week every month. The cells were used in the assays after one week from the end of the treatment in order to avoid interfered results. The resistance of A2780 ADR was maintained by doxorubicin treatment (0.1 μM) once a week. Cells were used in the assays after three days post doxorubicin treatment in order to avoid interfered results. Cell lines were complemented with 100 U/ml penicillin-streptomycin mixture (Gibco) and maintained in humidified atmosphere at 37 °C and 5% of CO_2 .

Cytotoxicity assay using a 2D cellular model

Cytotoxicity of the tested Ru complex was assessed by a fluorometric cell viability assay using Resazurin (ACROS Organics). Briefly, cells were seeded in triplicates in 96-well plates at a density of 4×10^3 cells/well in 100 μ L. After 24 h, cells were treated with increasing concentrations of the ruthenium complexes and ligands. Dilutions for complexes **1–4** were prepared as follows: 1.25 mM stock in DMSO was diluted to 100 μ M with media and then filtrated (0.22 μ m filter VWR). Dilutions for complexes **5,6** were prepared as follows: 1.25 mM stock in DMF was diluted to 100 μ M with media and then filtrated (0.22 μ m filter VWR). For **Ru(DIP)₂Cl₂** 2.5 mM stock in DMF was prepared, which was further diluted to 100 μ M and filtrated (0.22 μ m filter VWR). After 48 h incubation, medium was removed, and 100 μ L of complete medium containing resazurin (0.2 mg/mL final concentration) was added. After 4 h of incubation at 37 °C, the fluorescence signal of resorufin product was read (ex: 540 nm em: 590 nm) in a SpectraMax M5 microplate Reader. IC₅₀ values were then calculated using GraphPad Prism software.

Generation of 3D HeLa MCTS

MCTS were cultured using ultra-low attachment 96 wells plates from Corning® (Fisher Scientific 15329740). HeLa cells were seeded at a density of 5000 cells per well in 200 μ L. The single cells would generate MCTSs approximately 400 μ m in diameter at day 4 with 37 °C and 5% CO₂.

Treatment of 3D HeLa MCTS

After 4 days of growing at 37 °C and 5% CO₂, were treated by replacing half of the medium in the well with increasing concentration of compounds for 48 h in the dark. For untreated

reference MCTS, half of the medium was replaced by fresh medium only. The cytotoxicity was measured by ATP concentration with CellTiter-Glo[®] Cell viability kit (Promega, USA).

HeLa MCTSs growth inhibition

MCTSs were grown and treated as described above. MCTSs sizes were observed under a light microscope and pictures were taken with an iPhone 6s thanks to a phone microscope adaptor. Before imaging, the plate was shaken, and half of the media was exchanged to remove dead cells. Images were recorded before treatment (day 0) and at day 3, 6, 9 and 13 after treatment. Pictures were first processed using GIMP a cross-platform image editor with a batch automation plug-in. The MCTSs sizes were then calculated with SpheroidSizer, a MATLAB-based and open-source software application to measure the size of tumour spheroids automatically and accurately. Data analysis was done using GraphPad Prism software.

Annexin V / PI assay

Apoptosis and necrosis induction in HeLa cells treated with complex **1** was evaluated *via* an AnnexinV/PI staining assay using flow cytometry. Briefly, cells were seeded at density of 2×10^6 cells in 10 cm cell culture dish 24 h prior cell treatments. The medium was removed and replaced with 10 μ M solution of complex **1** or 1 μ M Staurosporin (positive control -Abcam Cat no.120056) and further incubated for 30 min, 4 h or 24 h. Cells were collected, washed twice with ice cold PBS and resuspended in 1x Annexin V binding buffer (10 x buffer composition: 0,1 M HEPES (pH 7.4), 1.4 M NaCl. 25 mM CaCl₂). Samples were processed according to the manufacturer instructions (BD Scientific, cat no 556463 and 556419) and analysed using ZE5 Biorad instrument at Cytometry Platform at Institute Curie. Data were analysed using the FlowJo software.

Sample Preparation for cellular uptake

Cells were seeded at density of 2×10^6 . Next day, cells were treated with 5 μM concentration of **1** or **RuCl₂(DIP)₂**. After 2 h, cells were collected, counted and snap frozen in liquid nitrogen and stored at -20 °C. ICP-MS samples were prepared as follows: samples were digested using 70% nitric acid (1 mL, 60 °C, overnight). Samples were then further diluted 1:100 (1% HCl solution in MQ water) and analysed using ICP-MS.

Sample Preparation for cellular fractionation

HeLa cells were seeded in three 15 cm² cell culture dishes so that on the day of treatment cells were 90% confluent. On the day of treatment cells were incubated with the target complex at a concentration of 5 μM for 2 h. After that time, the medium was removed; cells were washed, collected and counted. After resuspension in cold PBS, the organelles were isolated via different protocols (one cell culture dish per isolation was used).

Mitochondria isolation: To isolate mitochondria, a Mitochondria Isolation Kit (Cat. Nr: MITOISO2, Sigma Aldrich) was used according to the manufacturer procedure for isolation of mitochondria *via* homogenization method.

Lysosome isolation: To isolate lysosomes, a Lysosome Isolation Kit (Cat. Nr: LYSIS01, Sigma Aldrich) was used, according to the manufacturer procedure for isolation of lysosomes *via* Option C.

Nuclear and cytoplasm isolation: To isolate nuclear and cytoplasmic fractions, the ROCKLAND nuclear extract protocol was used.⁹⁹ Briefly cells were collected by centrifugation, resuspended in cytoplasmic extraction buffer and incubated on ice. The tubes were centrifuged and supernatant (CE) was removed. Pellets were washed with cytoplasmic extraction buffer without detergent and centrifuged. The pellet (NE) was resuspended in nuclear extraction buffer and incubated on ice. Both CE and NE were centrifuged. Supernatant from

CE samples was indicated as cytoplasmic extract, whereas the pellet obtained from NE samples was indicated as nuclear extract.

ICP-MS samples were prepared as follows: isolated cellular fractions were lyophilised and digested using 5 mL of 70% nitric acid (60 °C, overnight). Samples were then further diluted (1:1000 for nuclear pellet samples and 1:100 for all the other samples) MQ water (containing in 1% HCl solution) and analysed using ICP-MS.

Sample preparation for studies on the mechanism of cellular uptake

Samples were prepared as previously reported.²⁹ Briefly, HeLa cells were seeded at density of 2×10^6 and next day were pre-treated with corresponding inhibitors or kept at specific temperature for 1 h. Next, cells were washed with PBS and were incubated with 5 μ M of complex **1** for 2 h (low temperature sample was still kept at 4 °C). Afterwards cells were washed with PBS, collected, counted and snap frozen in liquid nitrogen. Pellets were stored at -20 °C. ICP-MS samples were prepared as follows: samples were digested using 70% nitric acid (1 mL, 60 °C, overnight), further diluted 1:100 (1% HCl solution in MQ water) and analysed using ICP-MS.

DNA metalation of HeLa cells

Cells were seeded at density of 2×10^6 . The following day, cells were treated with 5 μ M concentration of **1** or cisplatin. After 2 h, cells were collected, snap frozen in liquid nitrogen and stored at -20 °C. The following day, DNA was extracted using a PureLink™ Genomic DNA Mini Kit (Invitrogen). DNA purity was checked by absorbance measurements at 260 and 280 nm. Concentrations of genomic DNA were calculated assuming that one absorbance unit equals 50 μ g/mL. ICP-MS samples were prepared as follows: samples were digested using 70% nitric acid (60 °C, overnight) in 1:1.6 DNA to acid volume ratio. Samples were then further diluted

1:10 or 1:100 (1% HCl solution in MQ water) and analysed using ICP-MS.

ICP-MS studies

All ICP-MS measurements were performed on an high resolution ICP-MS (Element II, ThermoScientific) located at the Institut de physique du globe de Paris (France). The monitored isotopes are ^{101}Ru and ^{195}Pt . Daily, prior to the analytical sequence, the instrument was first tuned to produce maximum sensitivity and stability while also maintaining low uranium oxide formation ($\text{UO/U} \leq 5\%$). The data were treated as follow: intensities were converted into concentrations using uFREASI (user-FRiendly Elemental dAta proceSsIng).¹⁰⁰ This software, made for HR-ICP-MS users community, is free and available on <http://www.ipgp.fr/~tharaud/uFREASI>.

ICP-MS data analysis

Cellular uptake studies: The amount of metal detected in the cell samples was transformed from ppb into μg of metal. Data were subsequently normalised to the number of cells and expressed as μmol of metal/ amount of cells.

Cellular fractionation: The amount of detected ruthenium in the cell samples was transformed from ppb into μg of ruthenium. Values were then normalised to the number of cells used for specific extraction. Due to low yield of lysosome extraction (only 25%), the values obtained were multiplied by the factor of 4. Because of a low yield of mitochondria extraction (50% of the cells were homogenized), the values obtained for that organelle were multiplied by the factor of 2. Extraction protocols allow for the isolation of pure subcellular fractions. Therefore, the total amount of metal found in the cells was calculated summing the values obtained for the pure organelles.

Mechanism of uptake: The amount of ruthenium detected in cell samples was transformed from ppb into μg of ruthenium and values obtained were normalised to the number of cells used for specific treatment. The value for the ruthenium found in the 37 °C sample was used as a 100%.

Cellular metalation: The amount of ruthenium detected in cell samples was transformed from ppb into μg of ruthenium and value obtained was normalised to the amount of DNA.

Biodistribution study: The amount of ruthenium detected in organ digests was transformed from ppb into μg of ruthenium per g of tissue.

JC-1 Mitochondrial Membrane Potential Test

HeLa cells were seeded at a density of 6000 cells / well in black 96 well-plates (Costar 3916). The following day, cells were treated with different concentrations of **1** and **RuCl₂(DIP)₂**. After further 24 h, cells were treated according to the instructions of the JC-1 Mitochondrial Membrane Potential Assay Kit (Abcam, ab113850). The data were analysed using GraphPad Prism software.

Metabolic Studies

HeLa cells were seeded in Seahorse XFe96 well plates at a density of 30,000 cells / well in 80 μL medium. After 24 h, the medium was replaced with fresh medium and cisplatin (1 μM), doxorubicin (1 μM), 3-Methoxycatechol (1 μM), complex **RuCl₂(DIP)₂** (1 μM) or complex **1** (1 μM) were added. After 24 h of incubation, the regular medium was removed, cells were washed thrice using Seahorse Base Media and incubated in a non-CO₂ incubator at 37 °C for 1 h.

Mito Stress Test: Mitostress assay was run using Oligomycin, 1 μM , FCCP 1 μM and mixture of Antimycin-A/ Rotenone 1 μM each in ports A, B and C respectively using Seahorse XFe96 Extracellular Flux Analyzer.

Glycolysis Stress Test: Glycolytic stress test was run using glucose (10 mM), Oligomycin (1 μ M) and 2-Deoxyglucose (50 mM) in ports A, B and C respectively using Seahorse XFe96 Extracellular Flux Analyzer.

Mito Fuel Flex Test: Fuel flex assay for the different fuel pathways viz. glucose, glutamine and fatty acid was studied by measuring the basal oxygen consumption rates and that after addition of the inhibitor of the target pathway in port A and a mixture of the inhibitors of the other two pathways in port B. This gave a measure of the dependency of the cells on a fuel pathway. To study the capacity of a certain fuel pathway, the sequence of addition of the inhibitors was reversed. In port A was added the mixture of inhibitors for the other pathways and in port B was added the inhibitor for the target pathway. UK-5099 (pyruvate dehydrogenase inhibitor, 20 μ M) was used as an inhibitor for the glucose pathway. BPTES (selective inhibitor of Glutaminase GLS1, 30 μ M) was used as an inhibitor for the glutamine pathway. Etomoxir (O-carnitine palmitoyltransferase-1 (CPT-1) inhibitor, 40 μ M) was used as an inhibitor for the fatty acid pathway.

Formulation of compound 1 in polysorbate 80

Formulation protocol: Compound **1** was formulated in polysorbate 80 using the film rehydration method. Briefly, compound **1** (2 mg, 2.2 μ mol) and polysorbate 80 (100 mg) were dissolved in acetone (3 mL). The solvent was removed by rotary evaporation at 40 °C. The red film was then resuspended in PBS (2 mL) at room temperature. The solution was finally sterile filtered on a 0.20 μ m nylon membrane (Corning[®] 431224) to yield a clear red solution.

Compound concentration determination: 50 μ L of the sample was diluted in 100 μ L of acetonitrile and the absorbance was recorded at 480 nm in 96 wells plates from Corning[®] (Fisher Scientific 15329740) using a SpectraMax M5 microplate Reader. The measure was performed in triplicates and compound **1** concentration was determined using a calibration

curve obtained in the same conditions (50 mg/mL polysorbate 80 in PBS/acetonitrile 1:3). Encapsulation efficiency was calculated by comparing the absorbance of the solution before and after filtration using the following equation.

$$\text{Encapsulation efficiency} = 100 * \frac{\text{Absorbance after filtration}}{\text{Absorbance before filtration}}$$

To ensure its repeatability, the procedure was performed in triplicate.

Biodistribution study

This study was carried out in accordance with EU regulations and approved by the Ethical Commission of the faculty of Pharmaceutical and Biological Sciences Paris-Descartes (agreement number: E-75-06-02).

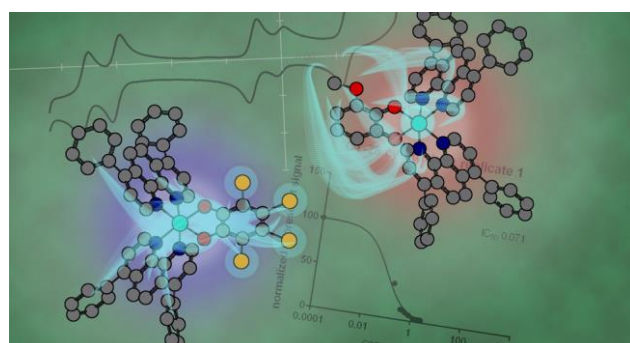
8-week old BALB/c mice (Janvier) were separated into three groups and injected intravenously with 5 mg/kg of compound **1** formulated in polysorbate 80 (280 mg/kg) and PBS. After 30 minutes, 1 or 2 hours, mice were sacrificed and relevant organs including blood, liver, lungs, brain, intestine and kidneys were harvested, weighed, and digested using 70% nitric acid (5 mL, 60 °C, 24 h or 48 h for intestines), further diluted in 1:100 (1% HCl solution in MQ water) and analyzed using ICP-MS.

Acknowledgements

This work was financially supported by an ERC Consolidator Grant PhotoMedMet to G.G. (GA 681679) and has received support under the program *Investissements d'Avenir* launched by the French Government and implemented by the ANR with the reference ANR-10-IDEX-0001-02 PSL (G.G.). Ile de France Region is gratefully acknowledged for financial support of 500 MHz NMR spectrometer of Chimie ParisTech in the framework of the SESAME equipment project. We acknowledge the loan of Agilent's

equipment to Chimie ParisTech. This project has received funding from the European Research Council (ERC) under the European Union’s Horizon 2020 research and innovation programme (grant agreement No 648558, STRIGES CoG grant). Part of this work was supported by IPGP multidisciplinary program PARI and by Region Île-de-France SESAME Grant no. 12015908. The authors would like to thank the LIOPA (the small animal optical imaging platform) and the Animal facility of the faculty of pharmacy from Université de Paris, UTCBS, CNRS, INSERM, F-75006 Paris, France.

TOC



References

- (1) Rosenberg, B. B. Some Biological Effects of Platinum Compounds. *Platin. Met. Rev.* **1971**, *15* (2), 42–51.
- (2) Wong, E.; Giandomenico, C. M. Current Status of Platinum-Based Antitumor Drugs. *Chem. Rev.* **1999**, *99* (August), 2451–2466. <https://doi.org/10.1021/cr980420v>.
- (3) Rosenberg, B.; Van Camp, L.; Krigas, T. Inhibition of Cell Division in Escherichia Coli by Electrolysis Products from a Platinum Electrode. *Nature* **1965**, *205*, 698–699. <https://doi.org/10.1038/205698a0>.
- (4) Rosenberg, B.; van Camp, L.; Grimley, E. B.; Thomson, A. J. The Inhibition of Growth or Cell Division in Escherichia Coli by Different Ionic Species of Platinum (IV)

- Complexes. *J. Biol. Chem.* **1967**, *242* (6), 1347–1352.
- (5) Rosenberg, B.; Van Camp, L.; Trosko, J. E.; Mansour, V. H. Platinum Compounds: A New Class of Potent Antitumour Agents. *Nature* **1969**, *222* (5191), 385–386. <https://doi.org/10.1038/222385a0>.
 - (6) Pieter, P.; Lippard, S. J. Cisplatin and Related Drugs. *Encycl. Cancer* **1997**, *1*, 525–543. <https://doi.org/http://dx.doi.org/10.1016/B0-12-227555-1/00506-2>.
 - (7) Fricker, S. P. Metal Based Drugs: From Serendipity to Design. *Dalton Trans.* **2007**, *43*, 4903–4917. <https://doi.org/10.1039/B705551J>.
 - (8) Singh, V.; Azad, G. K.; Reddy M., A.; Baranwal, S.; Tomar, R. S. Anti-Cancer Drug KP1019 Induces Hog1 Phosphorylation and Protein Ubiquitylation in *Saccharomyces Cerevisiae*. *Eur. J. Pharmacol.* **2014**, *736*, 77–85. <https://doi.org/10.1016/j.ejphar.2014.04.032>.
 - (9) Jamieson, E.; Lippard, S. Structure , Recognition , and Processing of Cisplatin – DNA Adducts. *Chem. Rev.* **1999**, *99* (9), 2467–2498. <https://doi.org/10.1021/cr980421n>.
 - (10) Clarke, M. J.; Zhu, F.; Frasca, D. R. Non-Platinum Chemotherapeutic Metallopharmaceuticals. *Chem. Rev.* **1999**, *99* (9), 2511–2533. <https://doi.org/10.1021/cr9804238>.
 - (11) Jakupec, M.; Galanski, M.; Arion, V. B.; Hartinger, C. G.; Keppler, B. K. Antitumour Metal Compounds: More than Theme and Variations. *Dalton Trans.* **2008**, No. 2, 183–194. <https://doi.org/10.1039/b712656p>.
 - (12) Dyson, P. J.; Sava, G. Metal-Based Antitumour Drugs in the Post Genomic Era. *Dalton Trans.* **2006**, No. 16, 1929–1933. <https://doi.org/10.1039/b601840h>.
 - (13) Gasser, G.; Ott, I.; Metzler-Nolte, N. Organometallic Anticancer Compounds. *J. Med. Chem.* **2011**, *54* (1), 3–25. <https://doi.org/10.1021/jm100020w>.
 - (14) Gianferrara, T.; Bratsos, I.; Alessio, E. A Categorization of Metal Anticancer Compounds Based on Their Mode of Action. *Dalton Trans.* **2009**, No. 37, 7588–7598. <https://doi.org/10.1039/b905798f>.
 - (15) Alessio, E.; Messori, L. NAMI-A and KP1019/1339, Two Iconic Ruthenium Anticancer

- Drug Candidates Face-to-Face: A Case Story in Medicinal Inorganic Chemistry. *Molecules* **2019**, *24*, 1995.
- (16) Sava, G.; Capozzi, I.; Clerici, K.; Gagliardi, G.; Alessio, E.; Mestroni, G. Pharmacological Control of Lung Metastases of Solid Tumours by a Novel Ruthenium Complex. *Clin. Exp. Metastasis* **1998**, *16* (4), 371–379. <https://doi.org/10.1023/A:1006521715400>.
- (17) Lentz, F.; Drescher, A.; Lindauer, A.; Henke, M.; Hilger, R. a; Hartinger, C. G.; Scheulen, M. E.; Dittrich, C.; Keppler, B. K.; Jaehde, U. Pharmacokinetics of a Novel Anticancer Ruthenium Complex (KP1019, FFC14A) in a Phase I Dose-Escalation Study. *Anticancer. Drugs* **2009**, *20* (2), 97–103. <https://doi.org/10.1097/CAD.0b013e328322fbc5>.
- (18) Trondl, R.; Heffeter, P.; Kowol, C. R.; Jakupec, M. a.; Berger, W.; Keppler, B. K. NKP-1339, the First Ruthenium-Based Anticancer Drug on the Edge to Clinical Application. *Chem. Sci.* **2014**, *5* (8), 2925–2932. <https://doi.org/10.1039/c3sc53243g>.
- (19) Hartinger, C. G.; Zorbas-Seifried, S.; Jakupec, M. A.; Kynast, B.; Zorbas, H.; Keppler, B. K. From Bench to Bedside - Preclinical and Early Clinical Development of the Anticancer Agent Indazolium Trans-[Tetrachlorobis(1H-Indazole)Ruthenate(III)] (KP1019 or FFC14A). *J. Inorg. Biochem.* **2006**, *100* (5–6), 891–904. <https://doi.org/10.1016/j.jinorgbio.2006.02.013>.
- (20) Yin, H.; Roque, J.; Konda, P.; Monroe, S.; Colo, K. L.; Gujar, S.; Thummel, R. P.; Lilge, L.; Cameron, C. G.; Mcfarland, S. A. Transition Metal Complexes and Photodynamic Therapy from a Tumor-Centered Approach : Challenges , Opportunities , and Highlights from the Development of TLD1433. *Chem. Rev.* **2019**, *119*, 797–828. <https://doi.org/10.1021/acs.chemrev.8b00211>.
- (21) Notaro, A.; Gasser, G. Monomeric and Dimeric Coordinatively Saturated and Substitutionally Inert Ru(II) Polypyridyl Complexes as Anticancer Drug Candidates. *Chem. Soc. Rev.* **2017**, *46* (23), 7317–7337. <https://doi.org/10.1039/c7cs00356k>.
- (22) Zeng, L.; Gupta, P.; Chen, Y.; Wang, E.; Ji, L.; Chao, H.; Chen, Z.-S.; Mai, J.; Zhang, H.; Li, Z.; et al. The Development of Anticancer Ruthenium(II) Complexes: From Single Molecule Compounds to Nanomaterials. *Chem. Soc. Rev.* **2017**, *46* (19), 5771–

5804. <https://doi.org/10.1039/C7CS00195A>.

- (23) Schatzschneider, U.; Niesel, J.; Ott, I.; Gust, R.; Alborzinia, H.; Wölfl, S. Cellular Uptake, Cytotoxicity, and Metabolic Profiling of Human Cancer Cells Treated with Ruthenium(II) Polypyridyl Complexes [Ru(Bpy) 2(N-N)]Cl₂ with N-N=bpy, Phen, Dpq, Dppz, and Dppn. *ChemMedChem* **2008**, *3* (7), 1104–1109. <https://doi.org/10.1002/cmdc.200800039>.
- (24) Gill, M. R.; Derrat, H.; Smythe, C. G. W.; Battaglia, G.; Thomas, J. A. Ruthenium(II) Metallo-Intercalators: DNA Imaging and Cytotoxicity. *ChemBioChem* **2011**, *12* (6), 877–880. <https://doi.org/10.1002/cbic.201000782>.
- (25) Du, K. J.; Wang, J. Q.; Kou, J. F.; Li, G. Y.; Wang, L. L.; Chao, H.; Ji, L. N. Synthesis, DNA-Binding and Topoisomerase Inhibitory Activity of Ruthenium(II) Polypyridyl Complexes. *Eur. J. Med. Chem.* **2011**, *46* (4), 1056–1065. <https://doi.org/10.1016/j.ejmech.2011.01.019>.
- (26) Pisani, M. J.; Weber, D. K.; Heimann, K.; Collins, J. G.; Keene, F. R. Selective Mitochondrial Accumulation of Cytotoxic Dinuclear Polypyridyl Ruthenium(II) Complexes. *Metallomics* **2010**, *2* (6), 357–432. <https://doi.org/10.1039/c004922k>.
- (27) Pisani, M. J.; Fromm, P. D.; Mulyana, Y.; Clarke, R. J.; Körner, H.; Heimann, K.; Collins, J. G.; Keene, F. R. Mechanism of Cytotoxicity and Cellular Uptake of Lipophilic Inert Dinuclear Polypyridylruthenium(II) Complexes. *ChemMedChem* **2011**, *6* (5), 848–858. <https://doi.org/10.1002/cmdc.201100053>.
- (28) Ye, R. R.; Ke, Z. F.; Tan, C. P.; He, L.; Ji, L. N.; Mao, Z. W. Histone-Deacetylase-Targeted Fluorescent Ruthenium(II) Polypyridyl Complexes as Potent Anticancer Agents. *Chem. - A Eur. J.* **2013**, *19* (31), 10160–10169. <https://doi.org/10.1002/chem.201300814>.
- (29) Notaro, A.; Frei, A.; Rubbiani, R.; Jakubaszek, M.; Basu, U.; Koch, S.; Mari, C.; Dotou, M.; Blacque, O.; Gouyon, J.; et al. A Ruthenium(II) Complex Containing a Redox-Active Semiquinonate Ligand as Potential Chemotherapeutic Agent: From Synthesis to In Vivo Studies. *ChemRxiv. Prepr.* **2019**. <https://doi.org/10.26434/chemrxiv.9582527.v1>.
- (30) Vlček, A. Metal and Ligand Oxidation States in Dioxolene Complexes: Meaning,

- Assignment and Control. *Comments Inorg. Chem.* **1994**, *16* (4), 207–228. <https://doi.org/10.1080/02603599408035860>.
- (31) Wheeler, D. E.; Rodriguez, J. H.; Mccusker, J. K. Density Functional Theory Analysis of Electronic Structure Variations across the Orthoquinone / Semiquinone / Catechol Redox Series. **1999**, 4101–4112. <https://doi.org/10.1021/jp990166q>.
- (32) Ward, M. D.; Mccleverty, J. A.; Ward, M. D. Non-Innocent Behaviour in Mononuclear and Polynuclear Complexes: Consequences for Redox and Electronic Spectroscopic Properties. *J. chem. soc. Dalton Trans.* **2002**, 275–288. <https://doi.org/10.1039/b110131p>.
- (33) Baell, J. B. Feeling Nature 's PAINS: Natural Products, Natural Product Drugs, and Pan Assay Interference Compounds (PAINS). *J. Nat. Prod.* **2016**, *79*, 616–628. <https://doi.org/10.1021/acs.jnatprod.5b00947>.
- (34) Tsai, M.; Rochford, J.; Polyansky, D. E.; Wada, T.; Tanaka, K.; Fujita, E.; Muckerman, J. T. Characterization of Redox States of Ru (OH 2)(Q)(Tpy) 2 + (Q) Related Species through Experimental and Theoretical Studies. *Inorg Chem* **2009**, *48* (10), 4372–4383.
- (35) Sofen, S. R.; Ware, D. C.; Cooper, S. R.; Raymond, K. N. Structural , Electrochemical , and Magnetic Properties of a Four-Membered Redox Series 0-3) in Catechol-Benzoquinone Complexes of Chromium ([Cr (L3) F “ ,. *Inorg. Chem.* **1979**, *18* (2), 234–239. <https://doi.org/10.1021/ic50192a006>.
- (36) Zhao, H. C.; Fu, B.; Schweinfurth, D.; Harney, J. P.; Sarkar, B.; Tsai, M.; Rochford, J. Tuning Oxyquinolate Non-Innocence at the Ruthenium Polypyridyl Core. *Eur. J. Inorg. Chem.* **2013**, *2*, 4410–4420. <https://doi.org/10.1002/ejic.201300373>.
- (37) Ingram, J. D.; Costa, P. J.; Adams, H.; Ward, M. D.; Félix, V.; Thomas, J. A. Ruthenium(II) Thiacrown Complexes Incorporating Noninnocent Redox Active Ligands: Synthesis, Electrochemical Properties, and Theoretical Studies And. *Inorg. Chem.* **2012**, *51*, 10483–10494.
- (38) Haga, M.; Dodsworth, E. S.; Lever, A. B. P. Catechol-Quinone Redox Series Involving Bis (Bipyridine) Ruthenium (II) and Tetrakis (Pyridine) Ruthenium (II). *Inorg. Chem.* **1986**, *25* (4), 447–453. <https://doi.org/10.1021/ic00224a013>.

- (39) Damas, A.; Ventura, B.; Moussa, J.; Degli Esposti, Alessandra Chamoreau, L.-M.; Barbieri, A.; Amouri, H. Turning on Red and Near-Infrared Phosphorescence in Octahedral Complexes with Metalated Quinones. *Inorg. Chem.* **2012**, *51*, 1739–1750. <https://doi.org/10.1021/ic202021w>.
- (40) Kessel, S. L.; Emberson, R. M.; Debrunner, P. G.; Hendrickson, D. N. Iron (III), Manganese (III), and Cobalt (III) Complexes with Single Chelating o -Semiquinone Ligands. *Inorg. Chem.* **1980**, No. Iii, 1170–1178.
- (41) Remenyi, C.; Kaupp, M.; Hubland, A. Where Is the Spin ? Understanding Electronic Structure and g-Tensors for Ruthenium Complexes with Redox-Active Quinonoid Ligands. *J. Am. Chem. Soc.* **2005**, *127* (8), 11399–11413. <https://doi.org/10.1021/ja051811b>.
- (42) Wada, T.; Yamanaka, M.; Fujihara, T.; Miyazato, Y.; Tanaka, K. Experimental and Theoretical Evaluation of the Charge Distribution over the Ruthenium and Dioxolene Framework of [Ru(OAc)(Dioxolene)(Terpy)] (Terpy = 2,2':6',2''-Terpyridine) Depending on the Substituents. *Inorg. Chem.* **2006**, *45* (22), 8887–8894. <https://doi.org/10.1021/ic060696i>.
- (43) Notaro, A.; Gasser, G.; Castonguay, A. Note of Caution for the Aqueous Behaviour of Metal-Based Drug Candidates. *ChemMedChem* *n/a* (n/a). <https://doi.org/10.1002/cmdc.201900677>.
- (44) Brastos, I.; Alessio, E.; Ringenberg, M. E.; Rauchfuss, T. B. Ruthenium Complexes. *Inorg. Synth.* **2010**, *35* (Ii), 148–163. <https://doi.org/10.1002/9780470651568.ch8>.
- (45) Caspar, R.; Cordier, C.; Waern, J. B.; Guyard-Duhayon, C.; Gruselle, M.; Le Floch, P.; Amouri, H. A New Family of Mono- and Dicarboxylic Ruthenium Complexes [Ru(DIP) 2 (L 2)] 2+ (DIP = 4,7-Diphenyl-1,10-Phenanthroline): Synthesis, Solution Behavior, and X-Ray Molecular Structure of Trans -[Ru(DIP) 2 (MeOH) 2][OTf] 2. *Inorg. Chem.* **2006**, *45* (10), 4071–4078. <https://doi.org/10.1021/ic0601236>.
- (46) Masui, H.; Lever, A. B. P.; Auburn, P. R. Control of Orbital Mixing in Ruthenium Complexes Containing Quinone-Related Ligands. *Inorg. Chem.* **1991**, *30*, 2402–2410. <https://doi.org/10.1021/ic00010a033>.
- (47) Allard, M. M.; Odongo, O. S.; Lee, M. M.; Chen, Y.; Endicott, J. F.; Schlegel, H. B.

- Effects of Electronic Mixing in Ruthenium (II) Complexes with Two Equivalent Acceptor Ligands . Spectroscopic , Electrochemical , and Computational Studies. *Inorg. Chem.* **2010**, *49*, 6840–6852. <https://doi.org/10.1021/ic100202h>.
- (48) Schafer, F. Q.; Buettner, G. R. Redox Environment of the Cell as Viewed Through the Redox State of the Glutathione Disulfide/Glutathione Couple. *Free Radic. Biol. Med.* **2001**, *30* (11), 1191–1212.
- (49) Connelly, N. G.; Geiger, W. E. Chemical Redox Agents for Organometallic Chemistry. *Chem. Rev.* **1996**, *96*, 877–910.
- (50) Chakraborty, S.; Laye, R. H.; Paul, R. L.; Gonnade, R. G.; Puranik, V. G.; Ward, D.; Kumar, G. Spectroelectrochemical Properties. *J. Chem. Soc., Dalt. Trans.* **2002**, 1172–1179. <https://doi.org/10.1039/b107307a>.
- (51) Patra, M.; Joshi, T.; Pierroz, V.; Ingram, K.; Kaiser, M. DMSO-Mediated Ligand Dissociation : Renaissance for Biological Activity Of. *Chem. Eur. J.* **2013**, *19*, 14768–14772. <https://doi.org/10.1002/chem.201303341>.
- (52) Hall, M. D.; Telma, K. A.; Chang, K.-E.; Lee, T. D.; Madigan, J. P.; Lloyd, J. R.; Goldlust, I. S.; Hoeschele, James D. Gottesman, M. M. Say No to DMSO: Dimethylsulfoxide Inactivates Cisplatin, Carboplatin and Other Platinum Complexes. *Cancer Res.* **2014**, *74* (14), 3913–3922. <https://doi.org/10.1158/0008-5472.CAN-14-0247>. Say.
- (53) Huang, H.; Humbert, N.; Bizet, V.; Patra, M.; Chao, H. Influence of the Dissolution Solvent on the Cytotoxicity of Octahedral Cationic Ir (III) Hydride Complexes. *J. Organomet. Chem.* **2017**, *839*, 15–18. <https://doi.org/10.1016/j.jorganchem.2016.12.010>.
- (54) Frei, A.; Rubbiani, R.; Tubafard, S.; Blacque, O.; Anstaett, P.; Felgenträger, A.; Maisch, T.; Spiccia, L.; Gasser, G. Synthesis, Characterization, and Biological Evaluation of New Ru(II) Polypyridyl Photosensitizers for Photodynamic Therapy. *J. Med. Chem.* **2014**, *57* (17), 7280–7292. <https://doi.org/10.1021/jm500566f>.
- (55) Cepeda, V.; Fuertes, M.; Castilla, J.; Alonso, C.; Quevedo, C.; Perez, J. Biochemical Mechanisms of Cisplatin Cytotoxicity. *Anticancer. Agents Med. Chem.* **2007**, *7* (1), 3–18. <https://doi.org/10.2174/187152007779314044>.

- (56) Keizer, H. G.; Pinedo, H. M.; Schuurhuis, G. J.; Joenje, H. DOXORUBICIN (ADRIAMYCIN): A CRITICAL REVIEW OF FREE RADICAL-DEPENDENT MECHANISMS OF CYTOTOXICITY. *Pharmac. Ther* **1990**, *47*, 219–231. [https://doi.org/10.1016/0163-7258\(90\)90088-J](https://doi.org/10.1016/0163-7258(90)90088-J).
- (57) Kelm, J. M.; Timmins, N. E.; Brown, C. J.; Fussenegger, M.; Nielsen, L. K. Multicellular Tumor Spheroids Applicable to a Wide Variety of Cell Types. *Biotechnol. Bioeng.* **2003**, *83* (2), 173–180. <https://doi.org/10.1002/bit.10655>.
- (58) Kapalczyńska, M.; Kolenda, T.; Przybyła, Weronika Zajączkowska, Maria Teresiak, A.; Filas, V.; Ibbs, M.; Bliźniak, R.; Łuczewski, Łukasz Lamperska, K. State of the Art Paper 2D and 3D Cell Cultures – a Comparison of Different Types of Cancer Cell Cultures. *Arch. Med. Sci.* **2018**, *4*, 910–919. <https://doi.org/https://doi.org/10.5114/aoms.2016.63743>.
- (59) Ma, H.; Jiang, Q.; Han, S.; Wu, Y.; Tomshine, J. C.; Wang, D.; Gan, Y.; Zou, G. Multicellular Tumor Spheroids as an In Vivo – Like Tumor Model for Three-Dimensional Imaging Of. *Mol. Imaging* **2012**, *11* (6), 487–498. <https://doi.org/10.2310/7290.2012.00012>.
- (60) Friedrich, J.; Seidel, C.; Ebner, R.; Kunz-schughart, L. A. Spheroid-Based Drug Screen : Considerations and Practical Approach. *Nat. Protoc.* **2009**, *4* (3), 309–324. <https://doi.org/10.1038/nprot.2008.226>.
- (61) Hess, J.; Huang, H.; Kaiser, A.; Pierroz, V.; Blacque, O. Evaluation of the Medicinal Potential of Two Ruthenium (II) Polypyridine Complexes as One- and Two-Photon Photodynamic Therapy Photosensitizers. *Chem. A Eur. J.* **2017**, No. Ii, 9888–9896. <https://doi.org/10.1002/chem.201701392>.
- (62) Seo, O. W.; Kim, M.; Hulme, J.; An, S. S. A. Monitoring the Effects of Doxorubicin on 3D-Spheroid Tumor Cells in Real-Time. **2016**, 7207–7218.
- (63) Ricci, M. S.; Zong, W. Chemotherapeutic Approaches for Targeting Cell Death Pathways. *Oncologist* **2006**, *11*, 342–357.
- (64) Elmore, S. Apoptosis : A Review of Programmed Cell Death. *Toxicol. Pathol.* **2007**, *35*, 495–516. <https://doi.org/10.1080/01926230701320337>.

- (65) Zeng, L.; Chen, Y.; Huang, H.; Wang, J.; Zhao, D.; Ji, L.; Chao, H. Cyclometalated Ruthenium(II) Anthraquinone Complexes Exhibit Strong Anticancer Activity in Hypoxic Tumor Cells. *Chemistry* **2015**, *21* (43), 15308–15319. <https://doi.org/10.1002/chem.201502154>.
- (66) Zisowsky, J.; Koegel, S.; Leyers, S.; Devarakonda, K.; Kassack, M. U.; Osmak, M.; Jaehde, U. Relevance of Drug Uptake and Efflux for Cisplatin Sensitivity of Tumor Cells. *Biochem. Pharmacol.* **2007**, *73* (2), 298–307. <https://doi.org/10.1016/j.bcp.2006.10.003>.
- (67) Dong, Y.; Berners-price, S. J.; Thorburn, D. R.; Antalis, T.; Dickinson, J.; Hurst, T.; Qiu, L.; Khoo, S. K.; Parsons, P. G. Serine Protease Inhibition and Mitochondrial Dysfunction Associated with Cisplatin Resistance in Human Tumor Cell Lines : Targets for Therapy. *Biochem. Pharmacol.* **1997**, *53*, 1673–1682.
- (68) Zorova, L. D.; Popkov, V. A.; Plotnikov, E. Y.; Silachev, D. N.; Pevzner, B.; Jankauskas, S. S.; Babenko, V. A.; Zorov, S. D.; Balakireva, A. V.; Juhaszova, M.; et al. Mitochondrial Membrane Potential. *Anal. Biochem.* **2018**, No. 552, 50–59. <https://doi.org/10.1016/j.ab.2017.07.009>.
- (69) Dedov, V. N.; Cox, G. C.; Roufogalis, B. D. Visualisation of Mitochondria in Living Neurons with Single- and Two-Photon ⁻ Uorescence Laser Microscopy. *Micron* **2001**, *32*, 653–660.
- (70) Sakamuru, S.; Attene-ramos, M. S.; Xia, M. Mitochondrial Membrane Potential Assay. In *High-Throughput Screening Assays in Toxicology, Methods in Molecular Biology*; 2016; Vol. 1473, pp 17–22. <https://doi.org/10.1007/978-1-4939-6346-1>.
- (71) Singla, A. K.; Garg, A.; Aggarwal, D. Paclitaxel and Its Formulations. *Int. J. Pharm.* **2002**, *253*, 179–192. [https://doi.org/10.1016/S0378-5173\(01\)00986-3](https://doi.org/10.1016/S0378-5173(01)00986-3).
- (72) Engels, F.; Mathot, R.; Verweij, J. Alternative Drug Formulations of Docetaxel: A Review. *Anticancer. Drugs* **2007**, *18* (2), 95–103. <https://doi.org/10.1097/CAD.0b013e3280113338>.
- (73) Rowe, R. C.; Sheskey, P. J.; Cook, W. G.; Quinn, M. E. Handbook of Pharmaceutical Excipients – 7th Edition. *Pharm. Dev. Technol.* **2013**, *18* (2), 544. <https://doi.org/10.3109/10837450.2012.751408>.

- (74) Zeng, Z. W.; Zhou, G. L.; Wang, J. J.; Li, F. Z.; Wang, A. M. Recent Advances in PEG – PLA Block Copolymer Nanoparticles. *Int. J. Nanomedicine* **2010**, 1057–1065. <https://doi.org/10.2147/IJN.S14912>.
- (75) Zhang, H. Thin-Film Hydration Followed by Extrusion Method for Liposome Preparation. *Methods Mol. Biol.* **2017**, 1522, 17–22. https://doi.org/10.1007/978-1-4939-6591-5_2.
- (76) Montfoort, J. E. van; Hagenbuch, B.; Groothuis, G. M. M.; Koepsell, H.; Meier, P. J.; Meijer, D. K. F. Drug Uptake Systems in Liver and Kidney. *Curr. Drug Metab.* **2003**, 4 (3), 185–211. <https://doi.org/10.2174/1389200033489460>.
- (77) Casazza, A. M.; Pratesi, G.; Giuliani, F.; Formelli, F.; Marco, A. Di. Enhancement of the Antitumor Activity of Adriamycin by Tween 80. *Tumori J.* **1978**, 64 (2), 115–129. <https://doi.org/10.1177/030089167806400202>.
- (78) Lorenz, W.; Schmal, A.; Schult, H.; Lang, S.; Ohmann, C.; Weber, D.; Kapp, B.; Lüben, L.; Doenicke, A. Histamine Release and Hypotensive Reactions in Dogs by Solubilizing Agents and Fatty Acids: Analysis of Various Components in Cremophor El and Development of a Compound with Reduced Toxicity. *Agents Actions* **1982**, 12 (1–2), 64–80. <https://doi.org/10.1007/BF01965109>.
- (79) Bergh, M.; Magnusson, K.; Nilsson, J. L. G.; Karlberg, A.-T. Contact Allergenic Activity of Tween® 80 before and after Air Exposure. *Contact Dermatitis* **1997**, 37 (1), 9–18. <https://doi.org/10.1111/j.1600-0536.1997.tb00368.x>.
- (80) Fulmer, G. R.; Miller, A. J. M.; Sherden, N. H.; Gottlieb, H. E.; Nudelman, A.; Stoltz, B. M.; Bercaw, J. E.; Goldberg, K. I. NMR Chemical Shifts of Trace Impurities: Common Laboratory Solvents, Organics, and Gases in Deuterated Solvents Relevant to the Organometallic Chemist. *Organometallics* **2010**, 29 (9), 2176–2179. <https://doi.org/10.1021/om100106e>.
- (81) Gaussian16 Revision C.01; Frisch, M. J.; Trucks, G. W.; Schlegel, H. B.; Scuseria, G. E.; Robb, M. A.; Cheeseman, J. R.; Scalmani, G.; Barone, V.; Petersson, G. A.; et al. Gaussian16 Revision C.01. 2016.
- (82) Von Bart, U.; Hedin, L. A Local Exchange-Correlation Potential for the Spin Polarized Case : I. *J. Phys. C Solid State Phys.* **1972**, 5, 1629.

- (83) Parr, R. G.; Weitao, Y. *Density-Functional Theory of Atoms and Molecules*; Press, O. U., Ed.; Oxford University Press.
- (84) Ditchfield, R.; Hehre, W. J.; Pople, J. A. Self-Consistent Molecular Orbital Methods. IX. An Extended Gaussian-Type Basis for Molecular Orbital Studies of Organic Molecules. *J. Chem. Phys.* **1971**, *54*, 724. <https://doi.org/10.1063/1.1674902>.
- (85) Hehre, W. J.; Ditchfield, R.; Pople, J. A. Self-Consistent Molecular Orbital Methods. XII. Further Extensions of Gaussian-Type Basis Sets for Use in Molecular Orbital Studies of Organic Molecules. *J. Chem. Phys.* **1972**, *56* (May 2012), 2257. <https://doi.org/10.1063/1.1677527>.
- (86) Hariharan, P. C.; Pople, J. A. The Influence of Polarization Functions on Molecular Orbital Hydrogenation Energies. *Theor. chim. Acta* **1973**, *28*, 213–222.
- (87) Becke, A. D. Density-Functional Thermochemistry. III. The Role of Exact Exchange. *J. Chem. Phys.* **1993**, *98*, 5648. <https://doi.org/10.1063/1.464913>.
- (88) Scalmani, G.; Frisch, M. J. Continuous Surface Charge Polarizable Continuum Models of Solvation. I. General Formalism. *J. Chem. Phys.* **2010**, *132*, 114110. <https://doi.org/10.1063/1.3359469>.
- (89) Neese, F. *ORCA—an Ab Initio, Density Functional and Semiempirical Program Package*; 2007; Vol. 26–35.
- (90) Lenthe, E. Van; Ehlers, A.; Baerends, E. Geometry Optimizations in the Zero Order Regular Approximation for Relativistic Effects. *J. Chem. Phys.* **1999**, *110*, 8943. <https://doi.org/10.1063/1.478813>.
- (91) Wüllen, C. Van. Molecular Density Functional Calculations in the Regular Relativistic Approximation: Method, Application to Coinage Metal Diatomics, Hydrides, Fluorides and Chlorides, and Comparison with First-Order Relativistic Calculations. *J. Chem. Phys.* **1998**, *109*, 392. <https://doi.org/10.1063/1.476576>.
- (92) Pantazis, D. A.; Chen, X.; Landis, C. R.; Neese, F. All-Electron Scalar Relativistic Basis Sets for Third-Row Transition Metal Atoms. *J. Chem. Theory Comput.* **2008**, *4*, 908–

- (93) Neese, F.; Wennmohs, F.; Hansen, A.; Becker, U. Efficient, Approximate and Parallel Hartree–Fock and Hybrid DFT Calculations. A ‘Chain-of-Spheres’ Algorithm for the Hartree–Fock Exchange. *Chem. Phys.* **2009**, *356*, 98–109.
- (94) Weigend, F. Accurate Coulomb-Fitting Basis Sets for H to Rn. *Phys. Chem. Chem. Phys.* **2006**, *8*, 1057–1065. <https://doi.org/10.1039/b515623h>.
- (95) Klamt, A.; Schuurmann, G. COSMO: A New Approach to Dielectric Screening in Solvents with Explicit. *J. Chem. Soc. Perkin Trans.* **1993**, *5*, 799–805.
- (96) Stoll, S.; Schweiger, A. EasySpin , a Comprehensive Software Package for Spectral Simulation and Analysis in EPR. *J. Magn. Reson.* **2006**, *178*, 42–55. <https://doi.org/10.1016/j.jmr.2005.08.013>.
- (97) Bao, D.; Millare, B.; Xia, W.; Steyer, B. G.; Gerasimenko, A. A.; Ferreira, A.; Contreras, A.; Vullev, V. I. Electrochemical Oxidation of Ferrocene : A Strong Dependence on the Concentration of the Supporting Electrolyte for Nonpolar Solvents. *J. Phys. Chem. A* **2009**, *2*, 1259–1267.
- (98) Krejeik, M.; Dangk, M.; Hartl, F. Simple Construction of an Infrared Optically Transparent Thin-Layer Electrochemical Cell Applications to the Redox Reactions of Ferrocene , Mn ,(CO) 1o. *J. Electroanal. Chem.*, **1991**, *317*, 179–187.
- (99) <https://rockland-inc.com/Nuclear-Extract-Protocol.aspx>. (accessed the 03.10.2019).
- (100) Tharaud, M.; Gardoll, S.; Khelifi, O.; Benedetti, M. F.; Sivry, Y. UFREASI: User-Friendly Elemental Data Processing. A Free and Easy-to-Use Tool for Elemental Data Treatment. *Microchem. J.* **2015**, *121*, 32–40. <https://doi.org/10.1016/j.microc.2015.01.011>.

Supplementary Information

Increasing the Cytotoxicity of Ru(II) Polypyridyl Complexes by tuning the Electronic Structure of Dioxo Ligands

*Anna Notaro,^a Marta Jakubaszek,^{a,b} Nils Rotthowe,^c Federica Maschietto,^d Robin Vinck,^a
Patrick S. Felder,^a Bruno Goud,^b Mickaël Tharaud,^e Ilaria Ciofini,^d Fethi Bedioui,^f Rainer F.
Winter,^c and Gilles Gasser^{a,*}*

^a Chimie ParisTech, PSL University, CNRS, Institute of Chemistry for Life and Health Sciences, Laboratory for Inorganic Chemical Biology, F-75005 Paris, France.

^b Institut Curie, PSL University, CNRS UMR 144, Paris, France.

^c Department of Chemistry, University of Konstanz, Universitätsstrasse 10, D-78457 Konstanz, Germany.

^d Chimie ParisTech, PSL University, CNRS, Institute of Chemistry for Life and Health Sciences, Chemical Theory and Modelling Group, F-75005 Paris, France.

^e Université de Paris, Institut de physique du globe de Paris, CNRS, F-75005 Paris, France.

^f Chimie ParisTech, PSL University, CNRS, Institute of Chemistry for Life and Health Sciences, Team Synthèse, Electrochimie, Imagerie et Systèmes Analytiques pour le Diagnostic, F-75005 Paris, France.

* Corresponding author: E-mail: gilles.gasser@chimeparistech.psl.eu; WWW: www.gassergroup.com; Phone: +33 1 44 27 56 02

Table of Contents

TABLE S1. UV/Vis/NIR ABSORPTIONS OF THE COMPLEXES IN THEIR NATIVE AND ELECTROCHEMICALLY GENERATED STATES IN DMF.....	642
FIGURE S1. NMR SPECTRA OF COMPLEXES 1-6.....	643
(1), ¹ H, CD ₂ Cl ₂ , 500 MHz.....	643
(2), ¹ H, CD ₂ Cl ₂ , 400 MHz.....	644
(3), ¹ H, CD ₂ Cl ₂ , 500 MHz.....	645
(4), ¹ H, CD ₂ Cl ₂ , 500 MHz.....	645
(5), ¹ H, CD ₂ Cl ₂ , 400 MHz.....	647
¹ H, CD ₂ Cl ₂ , 400 MHz containing elemental Zinc.....	648
(6), ¹ H, CD ₂ Cl ₂ , 400 MHz.....	649
¹ H, CD ₂ Cl ₂ , 400 MHz containing elemental Zinc.....	650
(1), ¹³ C, CD ₂ Cl ₂ , 125 MHz.....	651
(2), ¹³ C, CD ₂ Cl ₂ , 125 MHz.....	652
(3), ¹³ C, CD ₂ Cl ₂ , 125 MHz.....	653
(4), ¹³ C, CD ₂ Cl ₂ , 125 MHz.....	654
(5), ¹³ C, CD ₂ Cl ₂ , 125 MHz.....	655
(6), ¹³ C, CD ₂ Cl ₂ , 100 MHz.....	656
FIGURE S2. HPLC TRACES AT 450 NM OF COMPLEXES 1-6.....	657
FIGURE S3. EPR SPECTRA OF A) 1, B) 2, C) 3 AND D) 4 AT -40 °C AND -140 °C AND E) 6OX AT -140 °C.	659
TABLE S2. COMPUTED AND EXPERIMENTAL G-TENSORS (ABSOLUTE G-VALUES WITH G-SHIFTS IN PPT IN PARENTHESES). < S ₂ > VALUES CORRESPOND TO THE EXPECTATION VALUES OF THE KOHN-SHAM DETERMINANT.....	660
FIGURE S4. VOLTAMMOGRAMS RECORDED BY CV AND WITH THE USE OF RDE OF COMPLEXES 2-6.	662
TABLE S3. ELECTROCHEMICAL DATA FOR COMPLEXES 1-4.....	667
FIGURE S5. UV/Vis/NIR-SPECTROELECTROCHEMISTRY DATA FOR COMPLEX 1 IN THE PRESENCE OF THE REDUCING AGENT GLUTATHIONE.	668
TABLE S4. ELECTROCHEMICAL DATA FOR COMPLEXES 5 AND 6.....	669
FIGURE S6. OVERLAP OF ¹ H SPECTRA OF COMPLEXES 1-6 IN DMSO OVER 96 H.	670

FIGURE S7. PERCENTAGE CONCENTRATION OF COMPLEX 1 IN HUMAN PLASMA, NORMALIZED WITH RESPECT TO THE INTERNAL STANDARD (CAFFEINE) AND PLOTTED AGAINST TIME.	676
FIGURE S8. FLUOROMETRIC CELL VIABILITY ASSAY.	677
TABLE S5. IC ₅₀ VALUES FOR 3-METHOXYCATECHOL, 3-METHYLCATECHOL, 4-METHYLCATECHOL, 4-TERTBUTYLCATECHOL, TETRABROMOCATECHOL AND 4-NITROCATECHOL.	696
FIGURE S9. CELLTITER GLO® VIABILITY TEST	697
FIGURE S10. CELL DEATH MECHANISM:	698
FIGURE S11. CELLULAR UPTAKE MECHANISM OF COMPLEX 1.....	700
FIGURE S12. OXYGEN CONSUMPTION RATES AND DIFFERENT RESPIRATION PARAMETERS IN HeLA CELLS ALONE OR AFTER TREATMENT WITH VARIOUS TEST COMPOUNDS.....	701
FIGURE S13. EXTRACELLULAR ACIDIFICATION RATE AND DIFFERENT PARAMETERS OF GLYCOLYSIS IN HeLA CELLS ALONE OR AFTER TREATMENT WITH VARIOUS TEST COMPOUNDS.	702
FIGURE S14. FUEL FLEX ASSAY IN HeLA CELLS.....	703

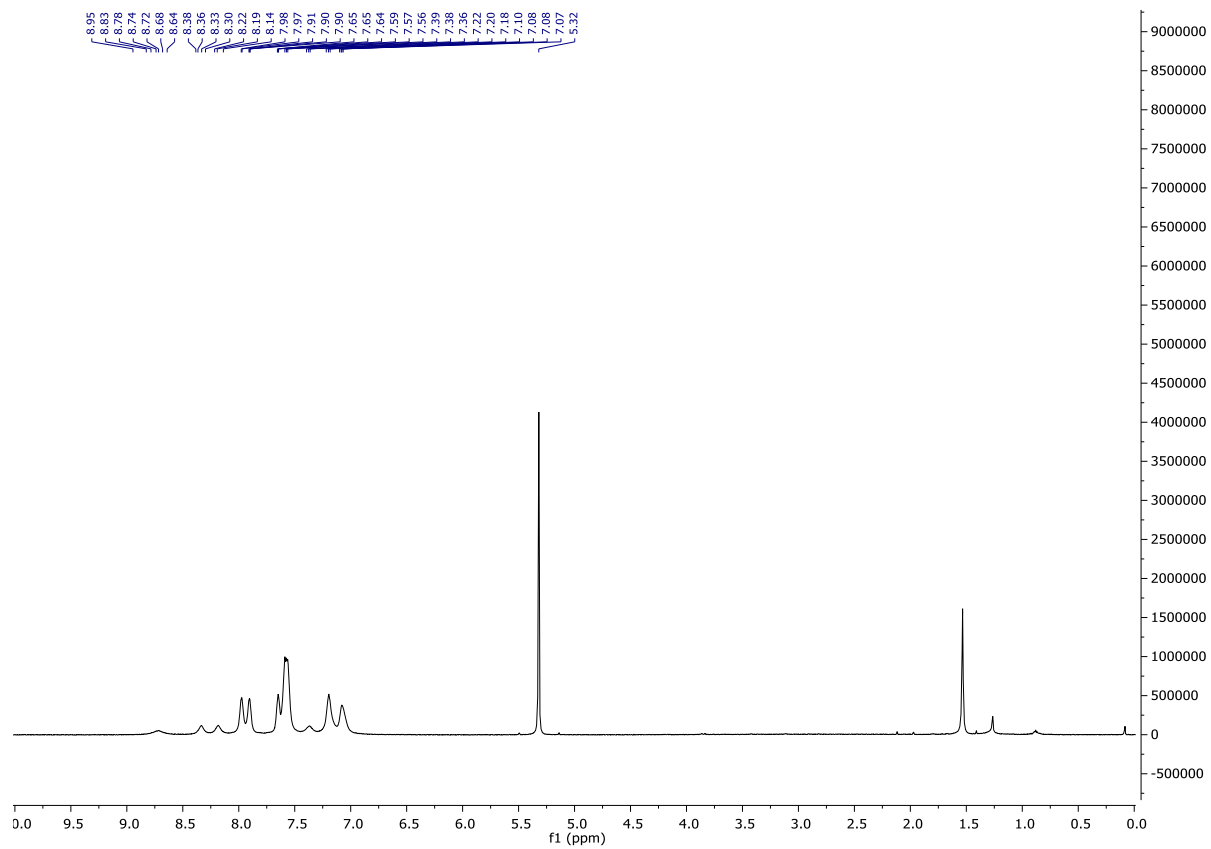
Table S1. UV/Vis/NIR absorptions of the complexes in their native and electrochemically generated states in DMF.

compound	oxidation state	λ_{max}
1	0	810(br) 650 535
	1+	885 510, 470
	2+	675 405(sh) 350(sh)
2	0	810(br) 655 535
	1+	890 520, 470
	2+	675 405(sh) 350(sh)
3	1+	900 525, 490
4	1+	895 525, 480
5	0	675(sh) 600, 505 345(sh)
	1+	985-845 465, 410
	2 ^a	430 (sh), 390
6	0	675(sh) 590, 510(sh) 375

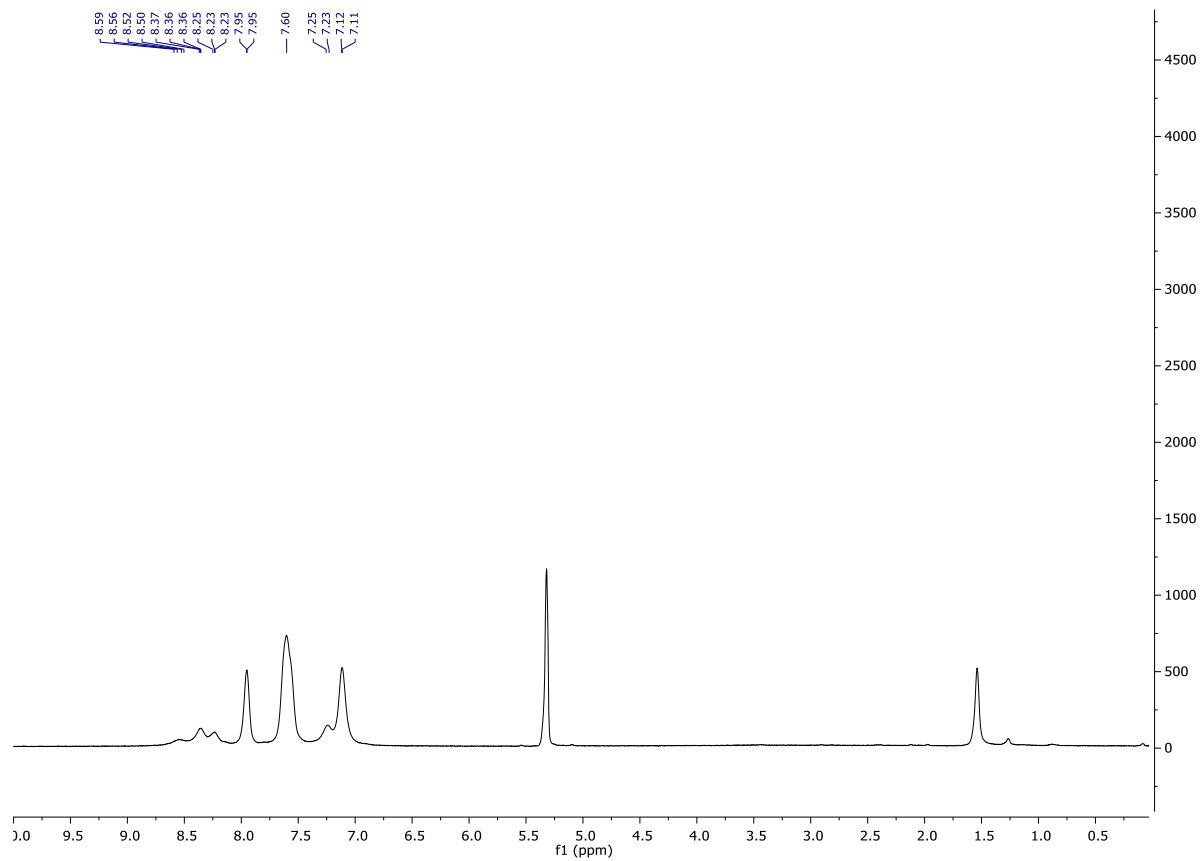
Electrochemically generated species in DMF / 0.1M NBu₄PF₆,

^a irreversible

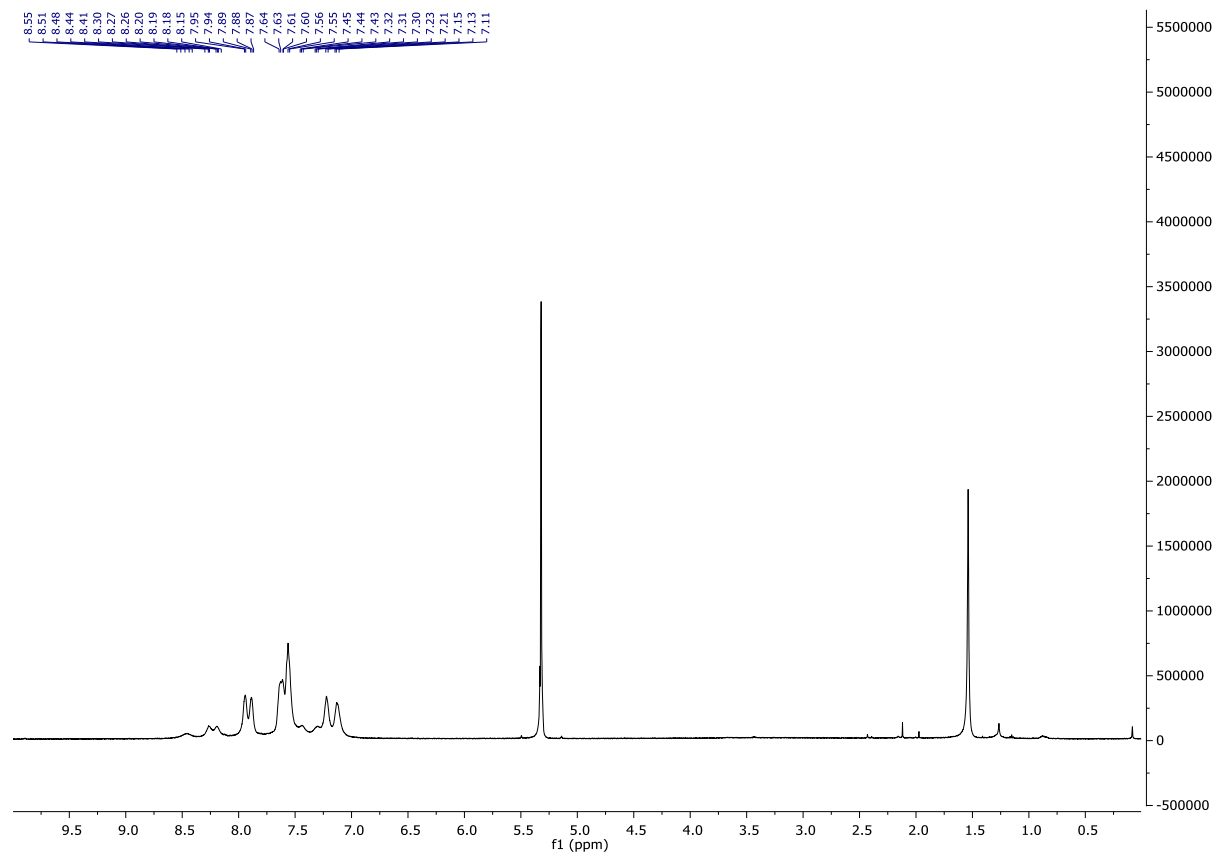
Figure S1. NMR spectra of complexes **1-6**.
(**1**), ^1H , CD_2Cl_2 , 500 MHz



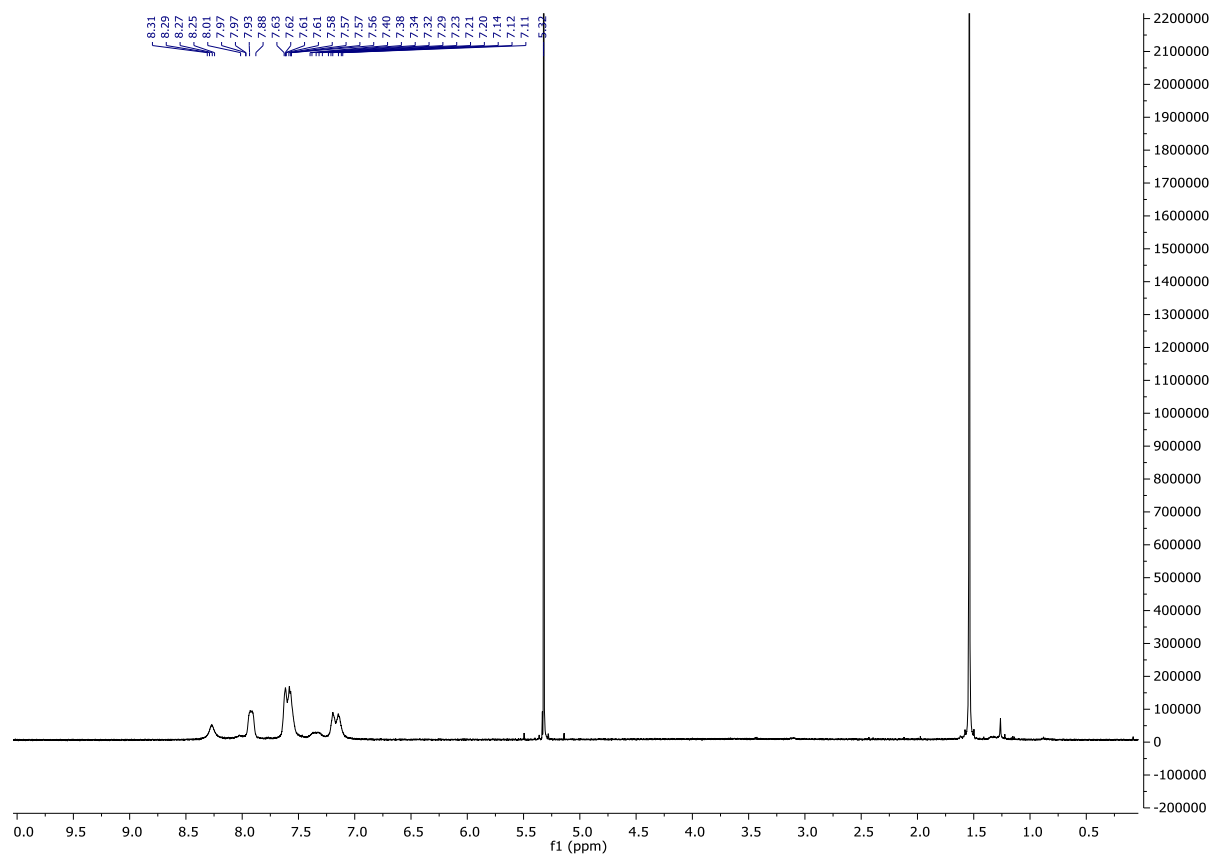
(2), ^1H , CD_2Cl_2 , 400 MHz



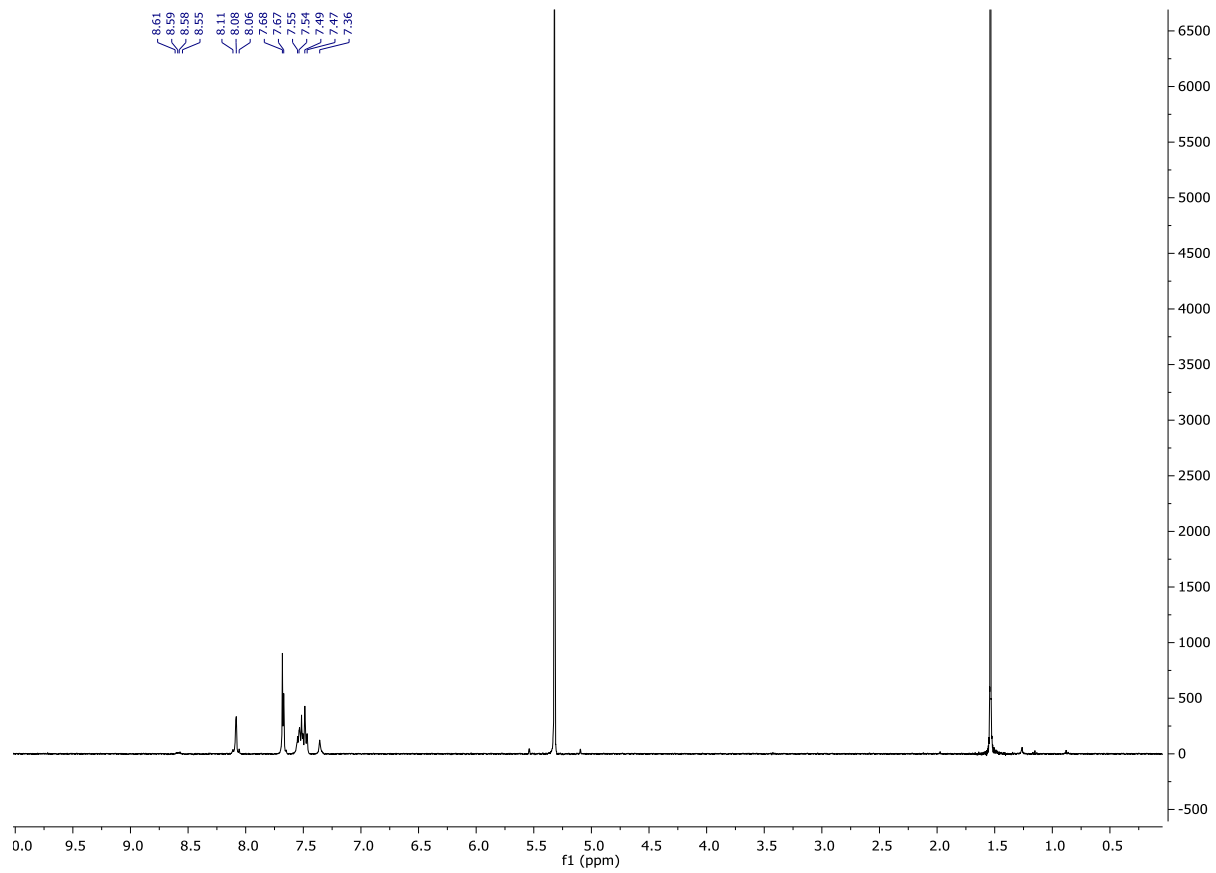
(3), ^1H , CD_2Cl_2 , 500 MHz



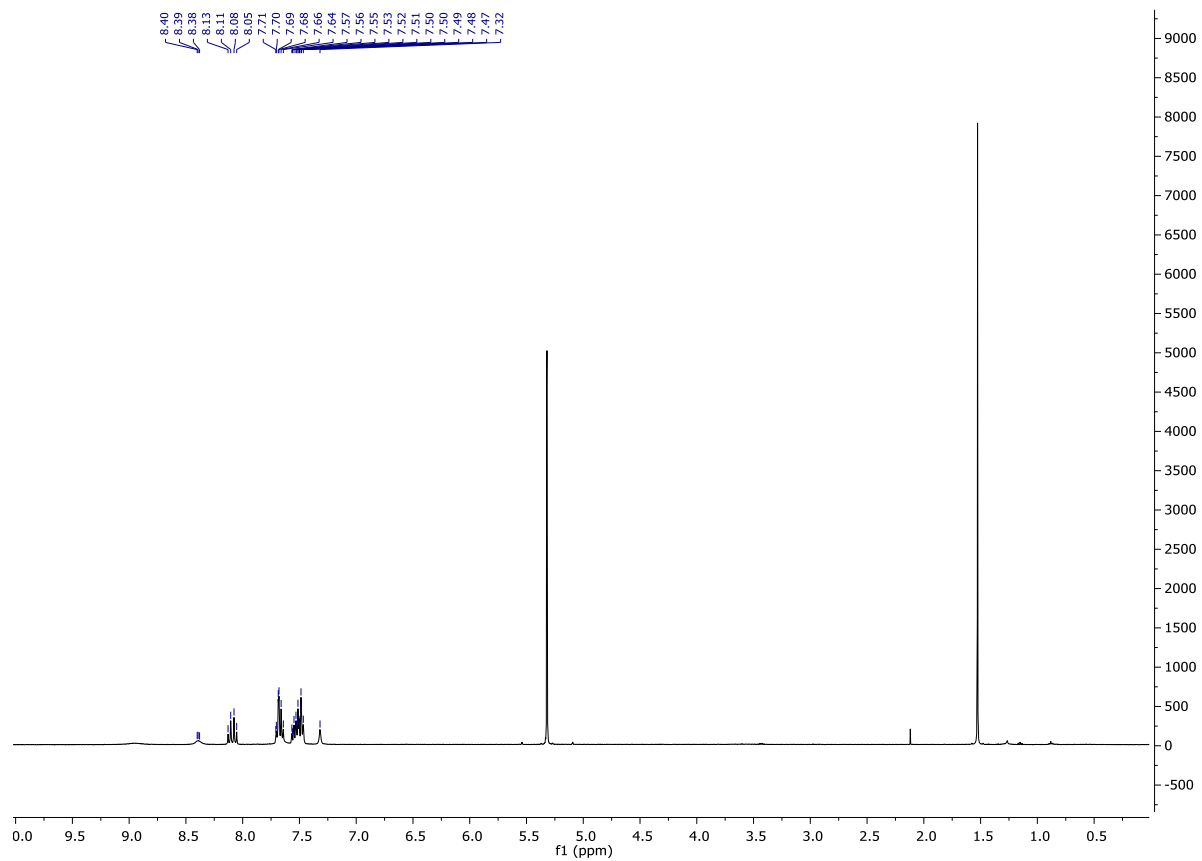
(4), ^1H , CD_2Cl_2 , 500 MHz



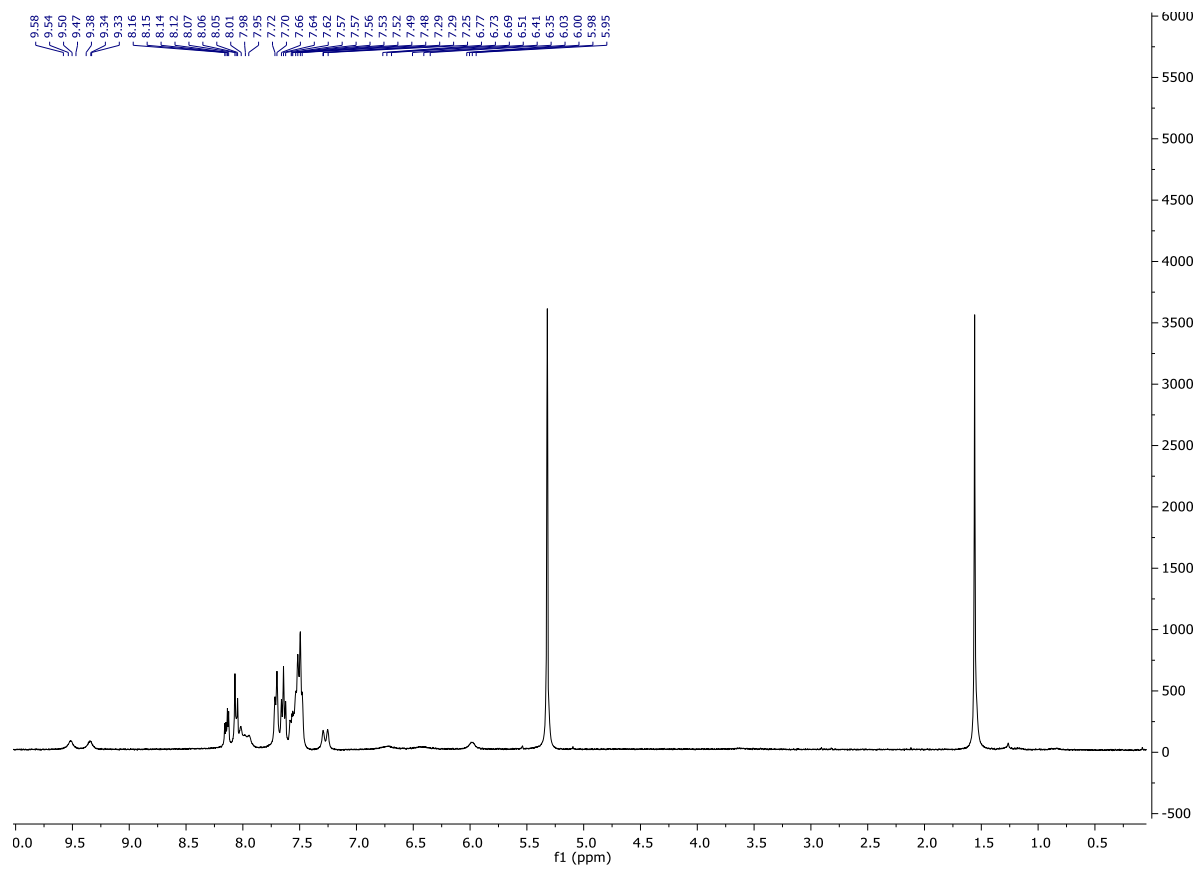
(5), ^1H , CD_2Cl_2 , 400 MHz



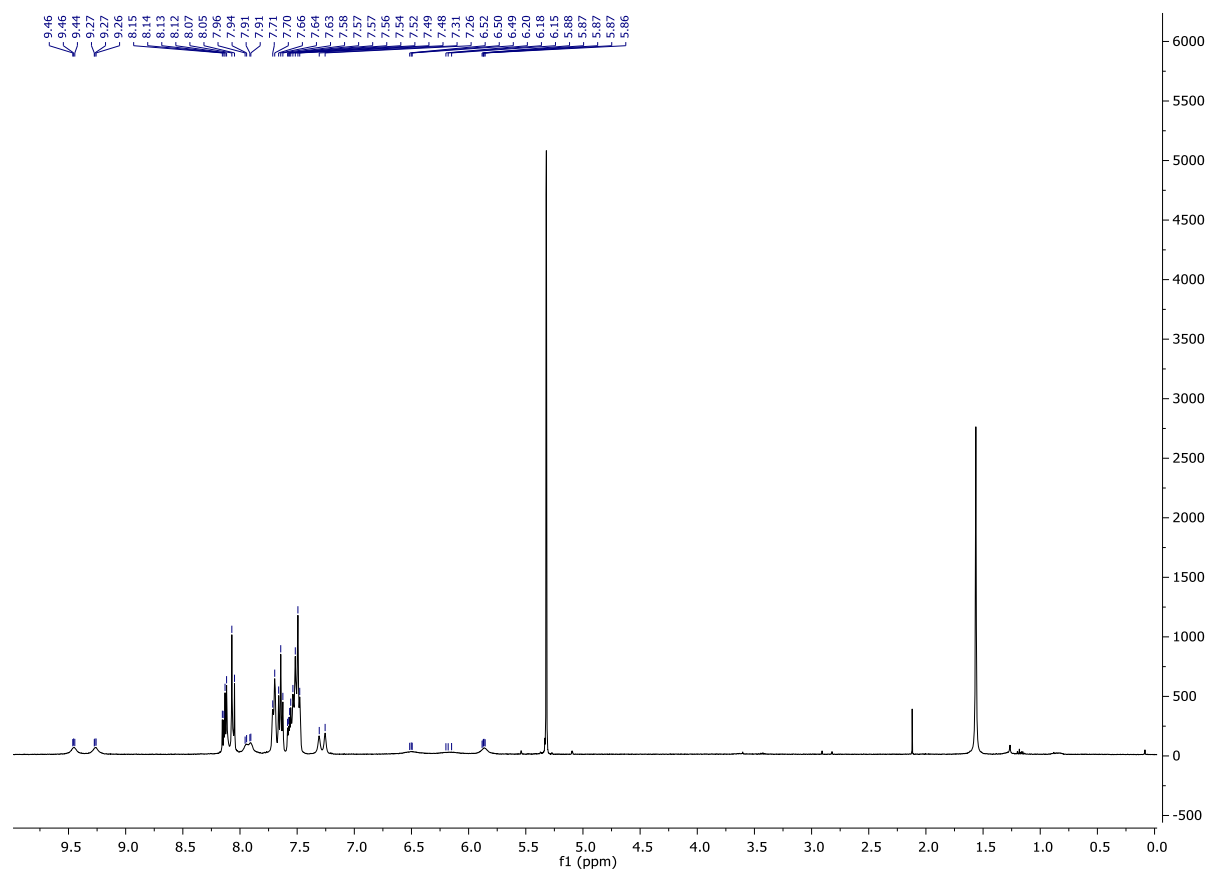
^1H , CD_2Cl_2 , 400 MHz containing elemental Zinc



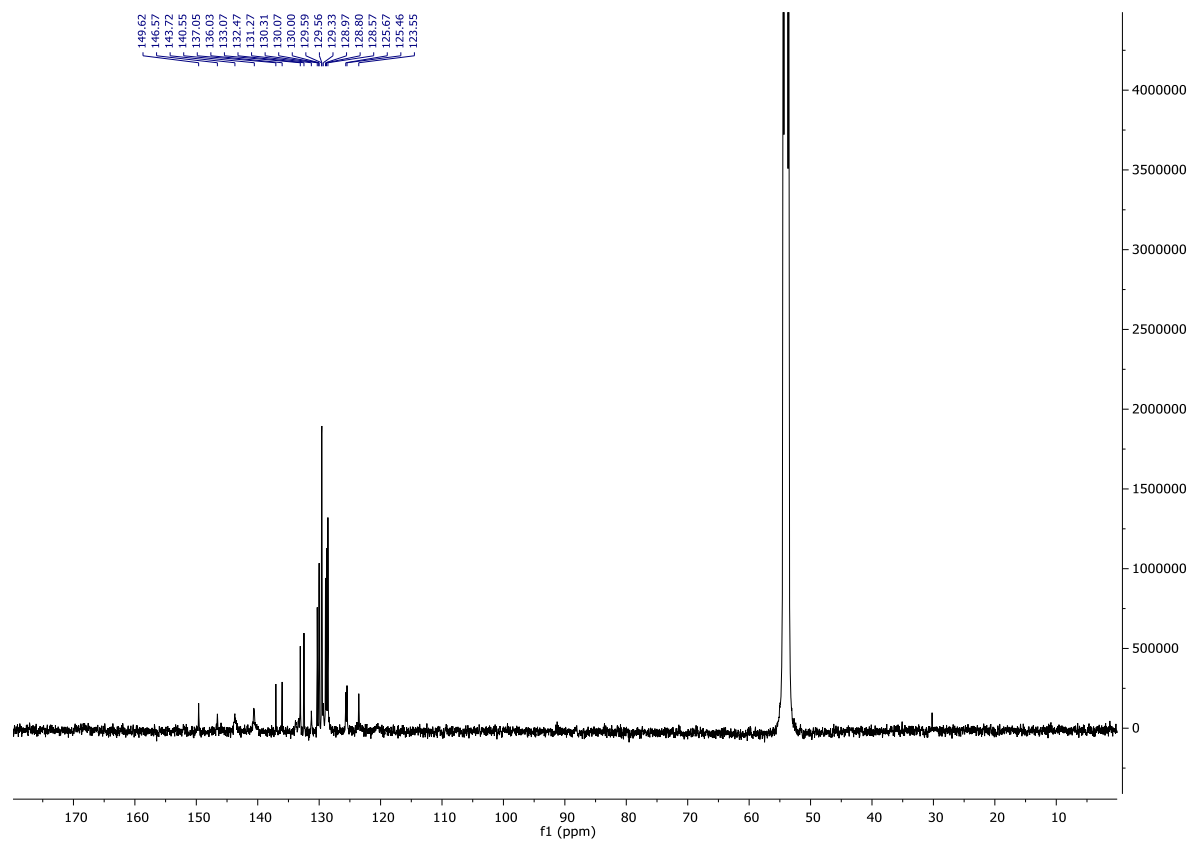
(6), ^1H , CD_2Cl_2 , 400 MHz



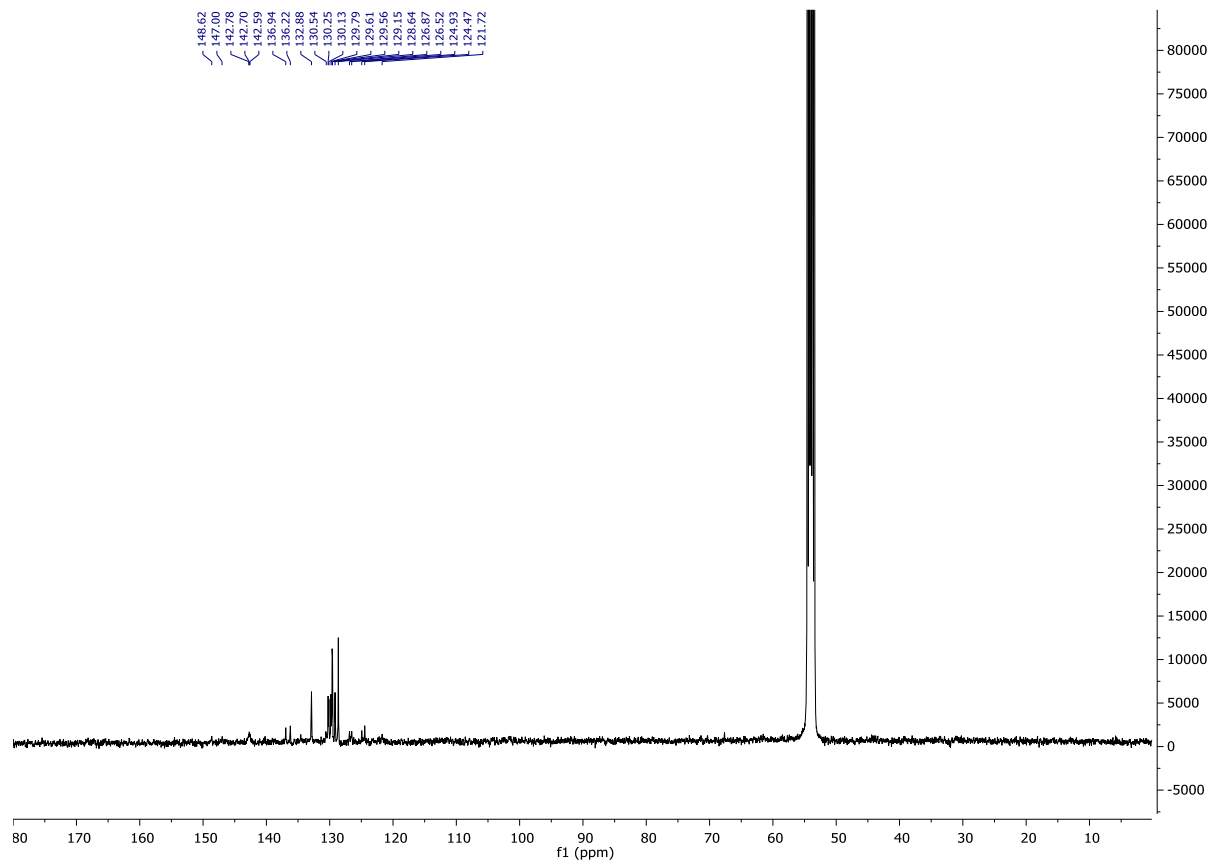
^1H , CD_2Cl_2 , 400 MHz containing elemental Zinc



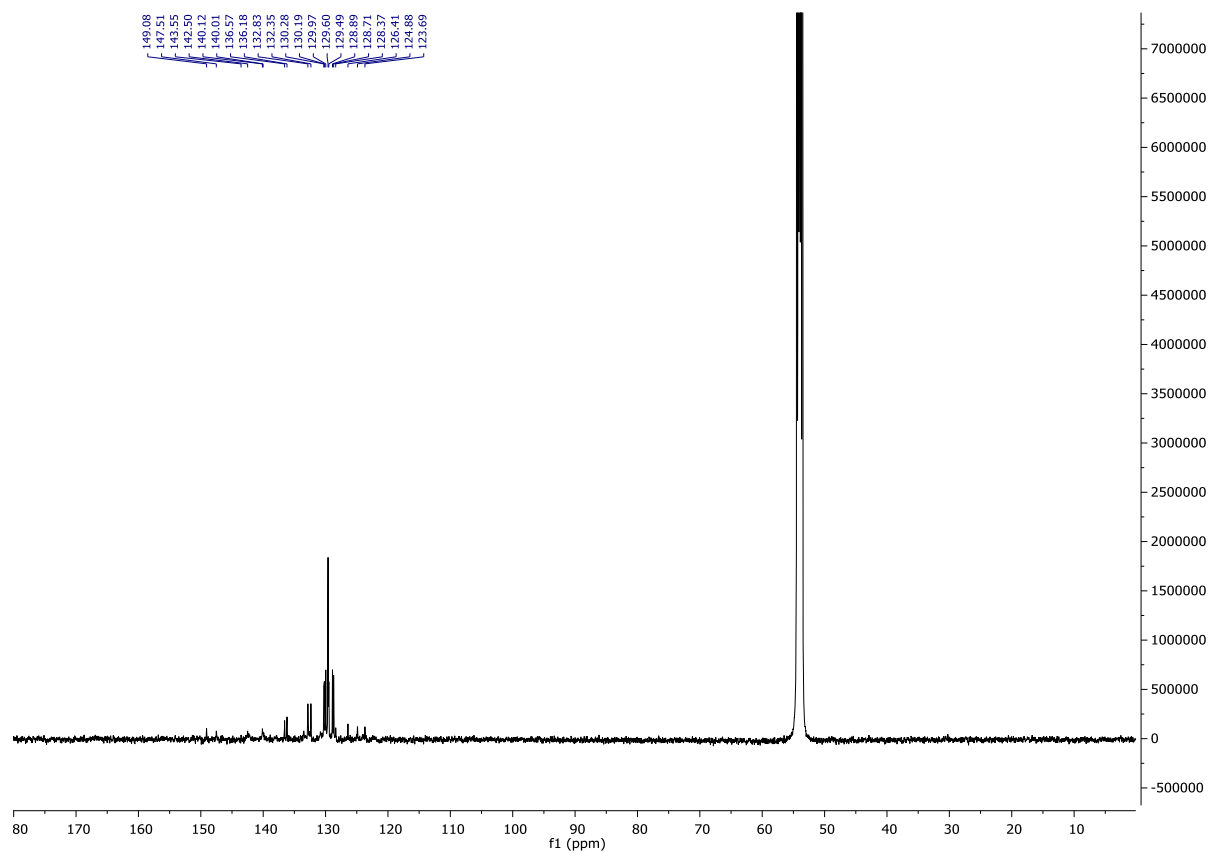
(1), ^{13}C , CD_2Cl_2 , 125 MHz



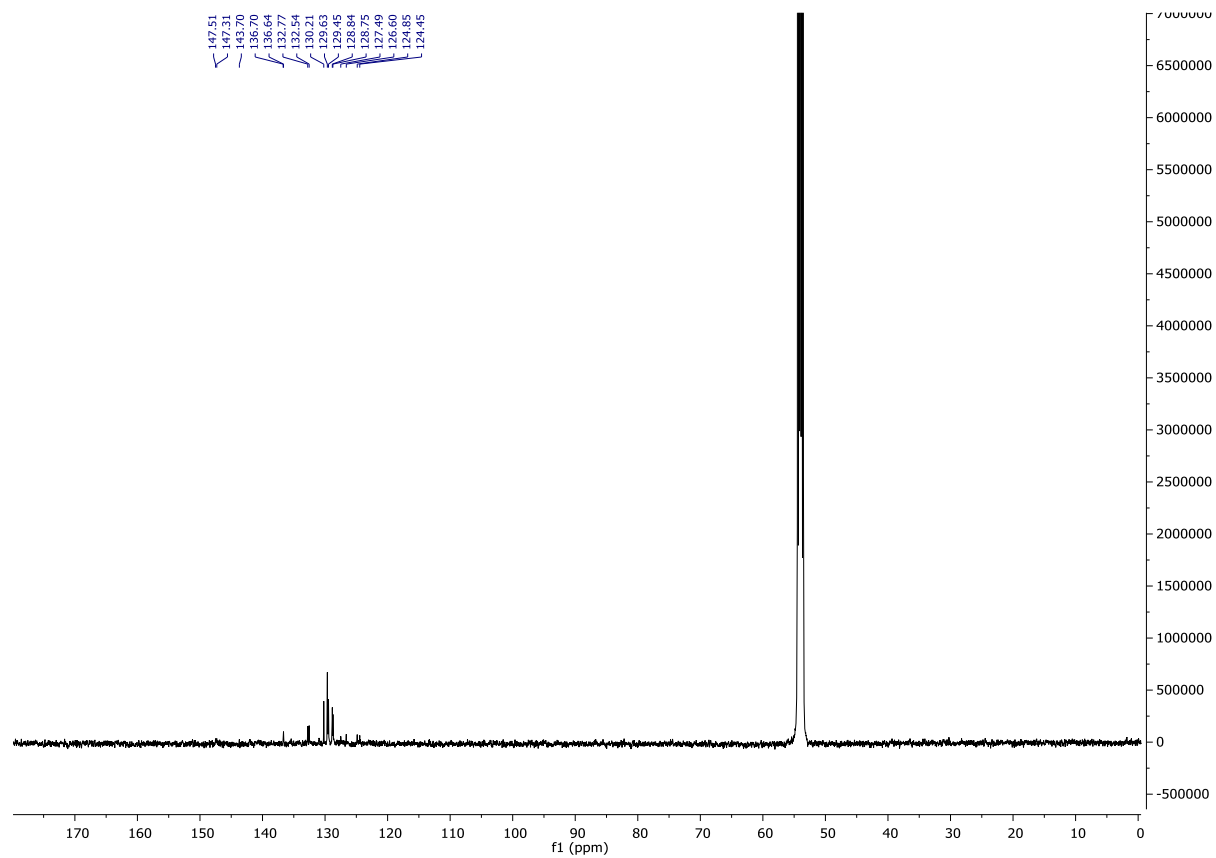
(2), ^{13}C , CD_2Cl_2 , 125 MHz



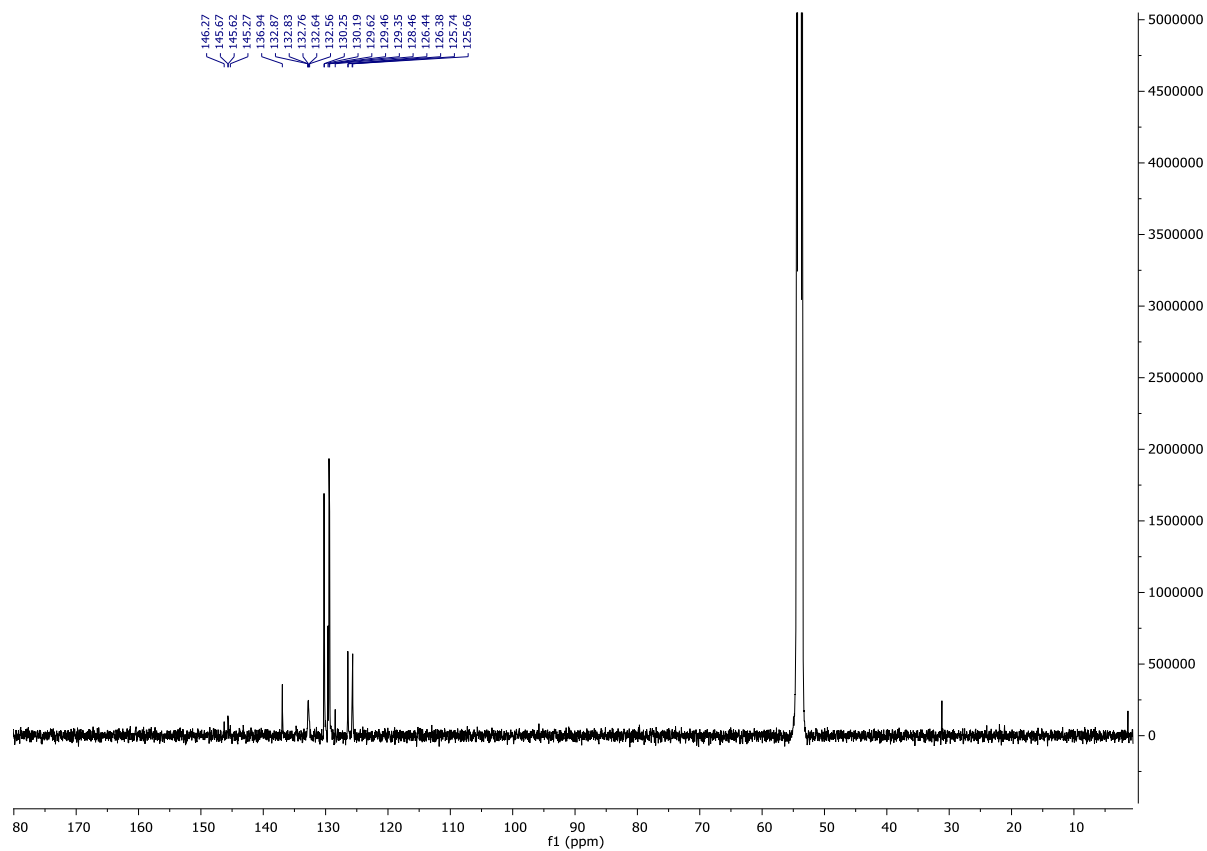
(3), ^{13}C , CD_2Cl_2 , 125 MHz



(4), ^{13}C , CD_2Cl_2 , 125 MHz



(5), ^{13}C , CD_2Cl_2 , 125 MHz



(6), ^{13}C , CD_2Cl_2 , 100 MHz

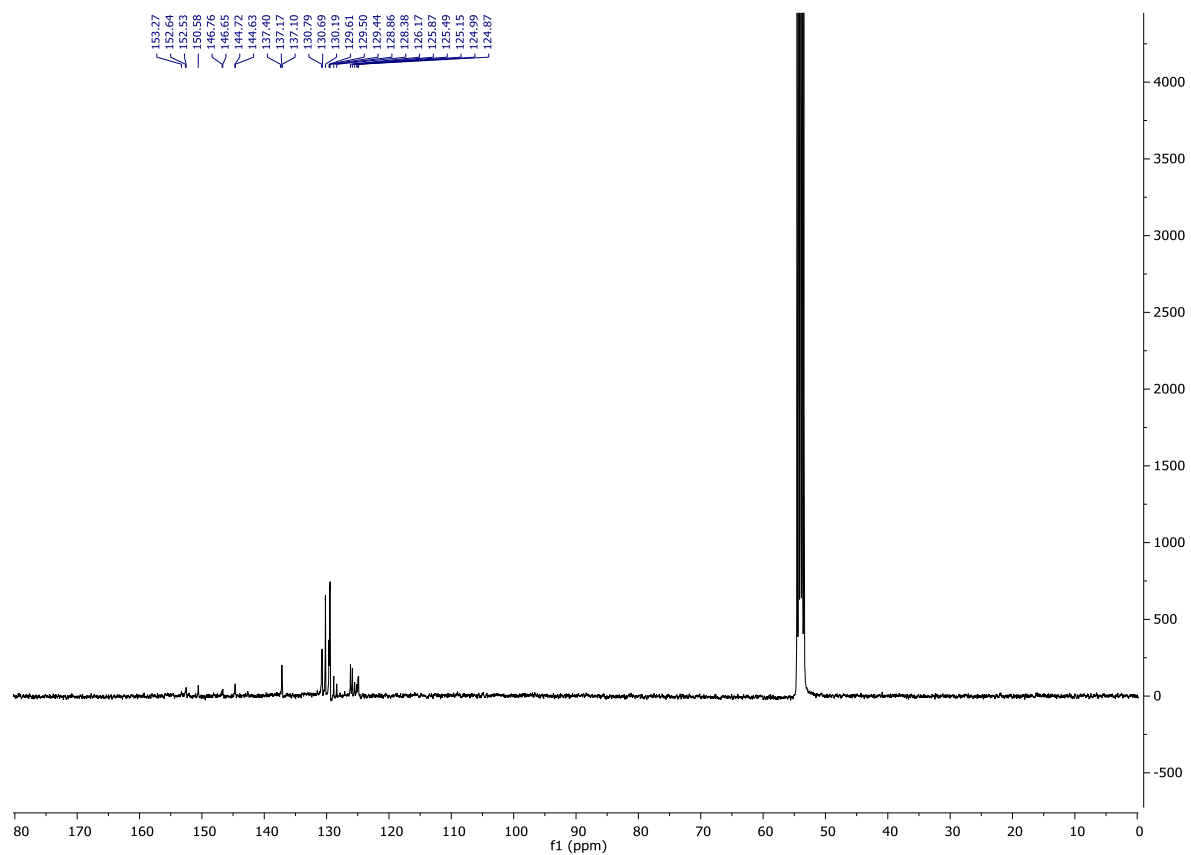
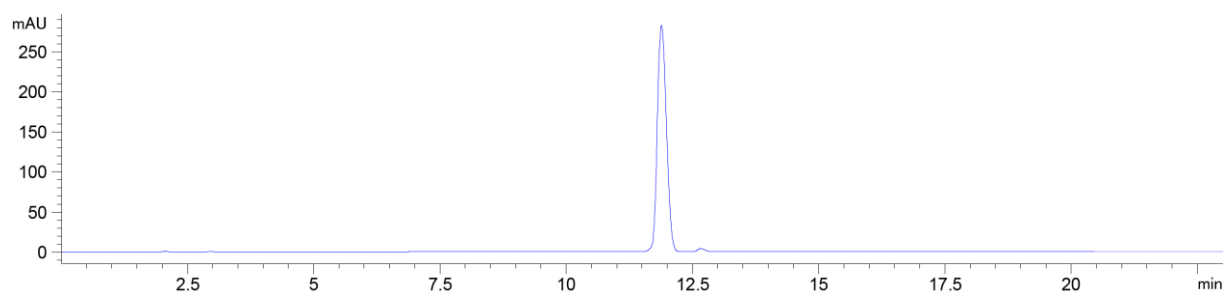
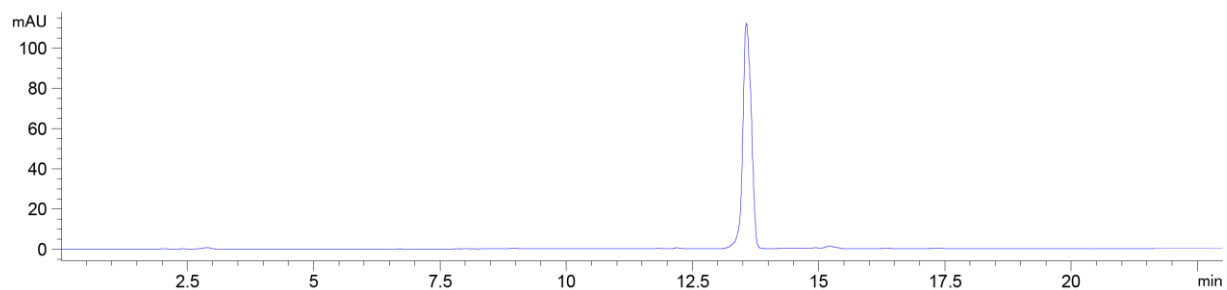


Figure S2. HPLC traces at 450 nm of complexes **1-6**.

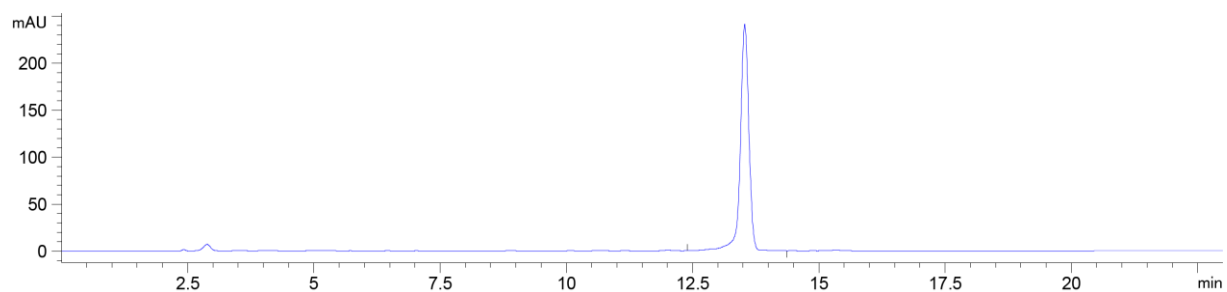
(1), HPLC trace 450 nm.



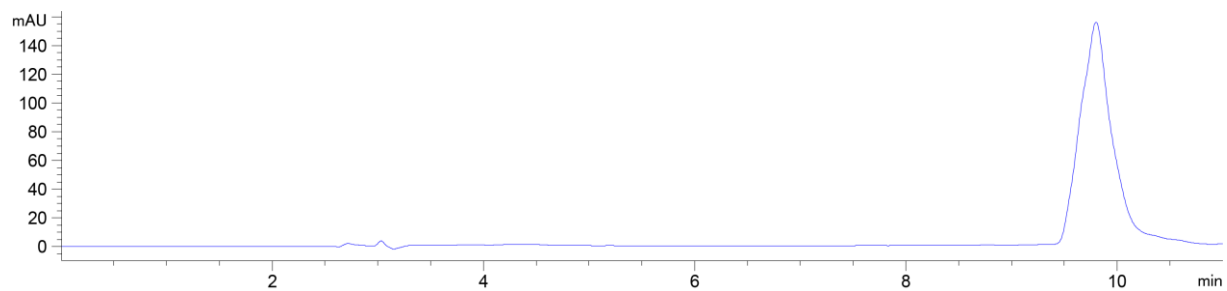
(2), HPLC trace 450 nm.



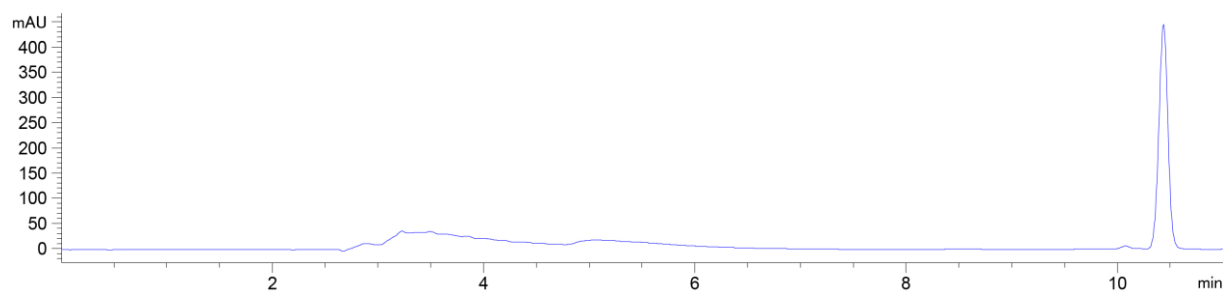
(3), HPLC trace 450 nm.



(4), HPLC trace 450 nm.



(5), HPLC trace 450 nm.



(6), HPLC trace 450 nm.

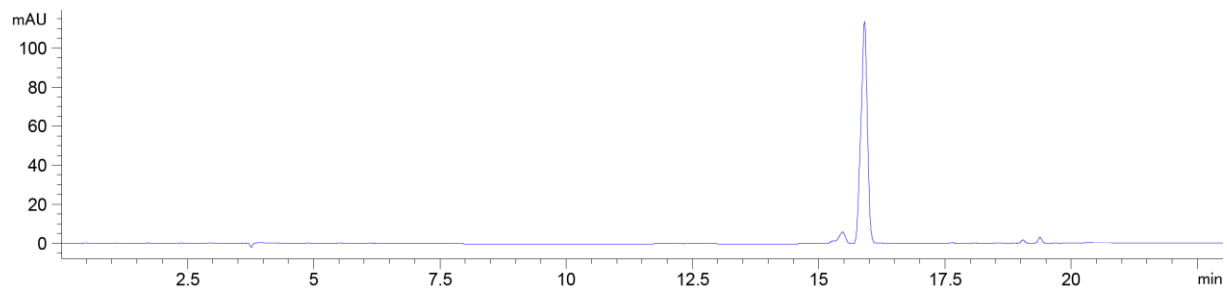


Figure S3. EPR spectra of a) **1**, b) **2**, c) **3** and d) **4** at $-40\text{ }^{\circ}\text{C}$ and $-140\text{ }^{\circ}\text{C}$ and e) **6ox** at $-140\text{ }^{\circ}\text{C}$.

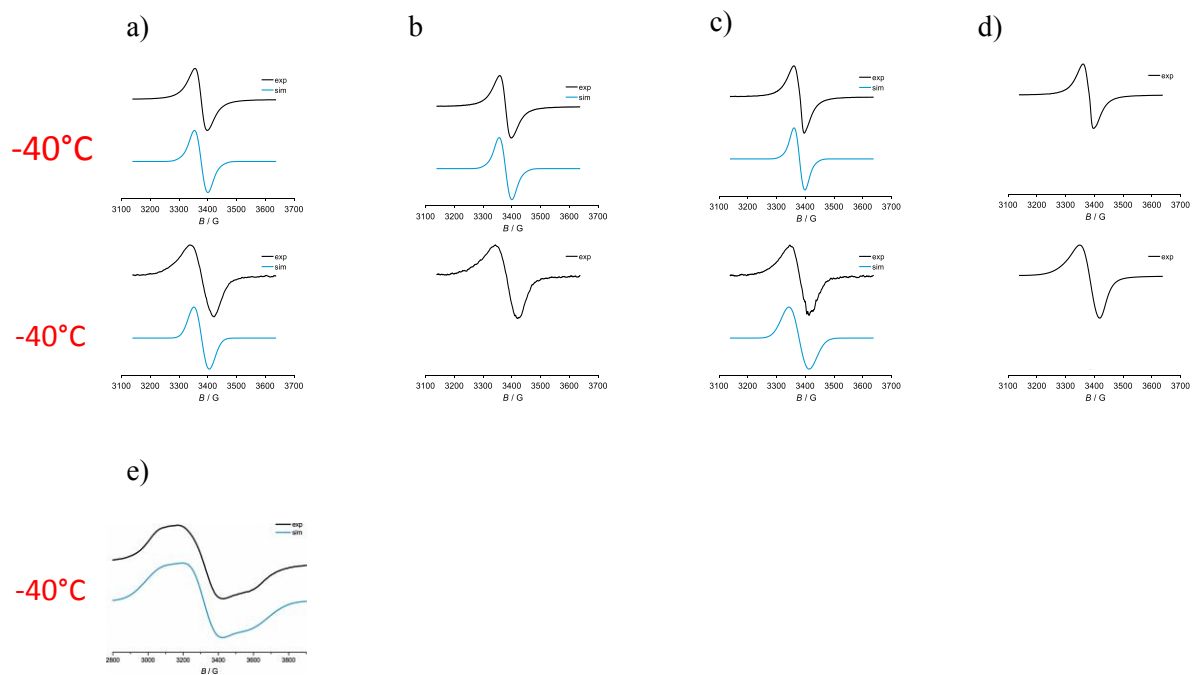


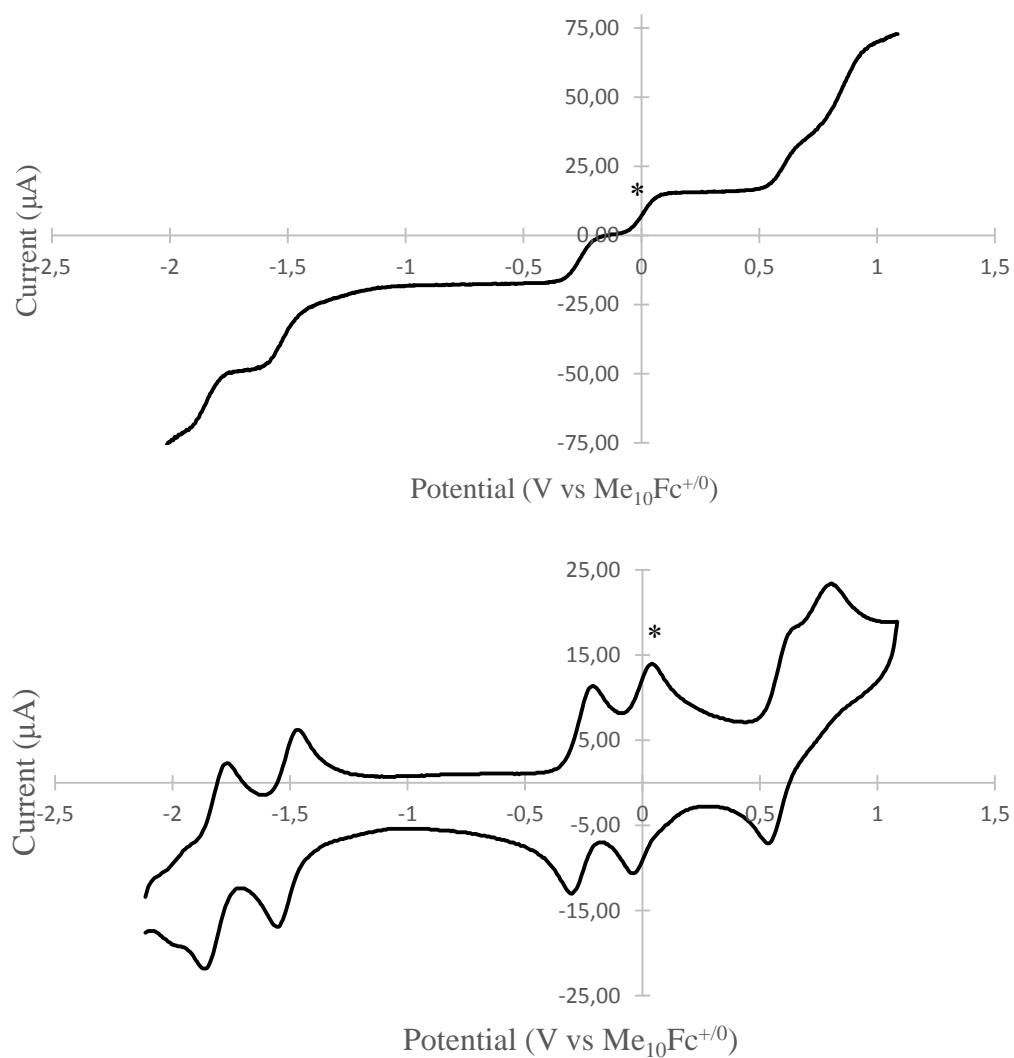
Table S2. Computed and Experimental g-Tensors (absolute g-values with g-shifts in ppt in parentheses). $\langle S^2 \rangle$ values correspond to the expectation values of the Kohn-Sham determinant.

		B3LYP	exp.
(1)	g_{iso}	2.0055 (3.2)	1.9893 (-13.0)
	g_{11}	2.0020 (-0.3)	
	g_{22}	2.0070 (4.7)	
	g_{33}	2.0074 (5.0)	
	$g_{33}-g_{11}$	0.0054	
	$\langle S^2 \rangle$	0.759	
(3)	g_{iso}	2.0054 (3.1)	1.9872 (-15.1)
	g_{11}	2.0020 (-0.3)	
	g_{22}	2.0070 (4.7)	
	g_{33}	2.0071 (4.9)	
	$g_{33}-g_{11}$	0.0051	
	$\langle S^2 \rangle$	0.759	
(50x)	g_{iso}	2.0089 (6.6)	2.019 (16.7)
	g_{11}	2.0019 (-0.4)	
	g_{22}	2.0090 (6.6)	
	g_{33}	2.0159 (13.6)	
	$g_{33}-g_{11}$	0.0140	
	$\langle S^2 \rangle$	0.759	
(60x)	g_{iso}	2.0076 (5.3)	2.032 (29.7)
	g_{11}	2.0038 (1.5)	1.870 (-132.3)
	g_{22}	2.0076 (5.3)	2.025 (22.7)

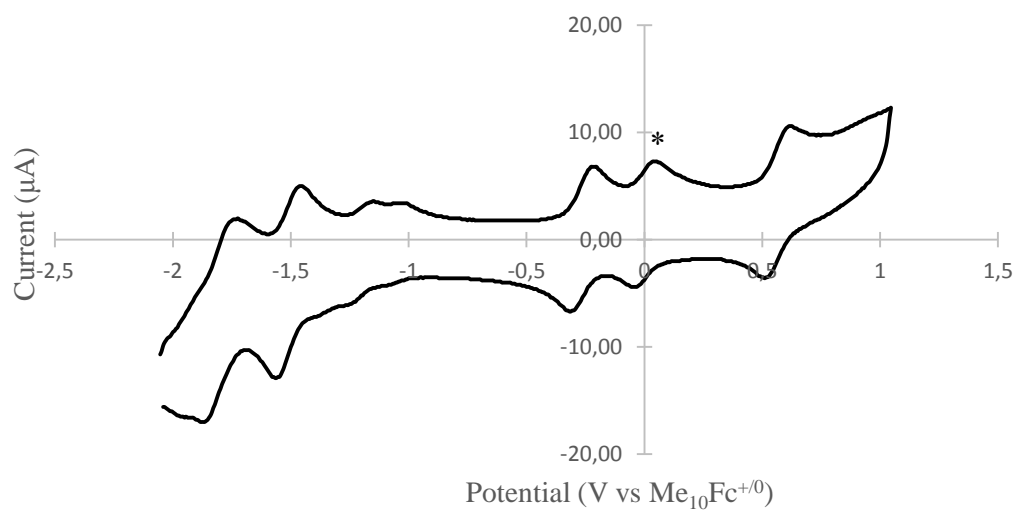
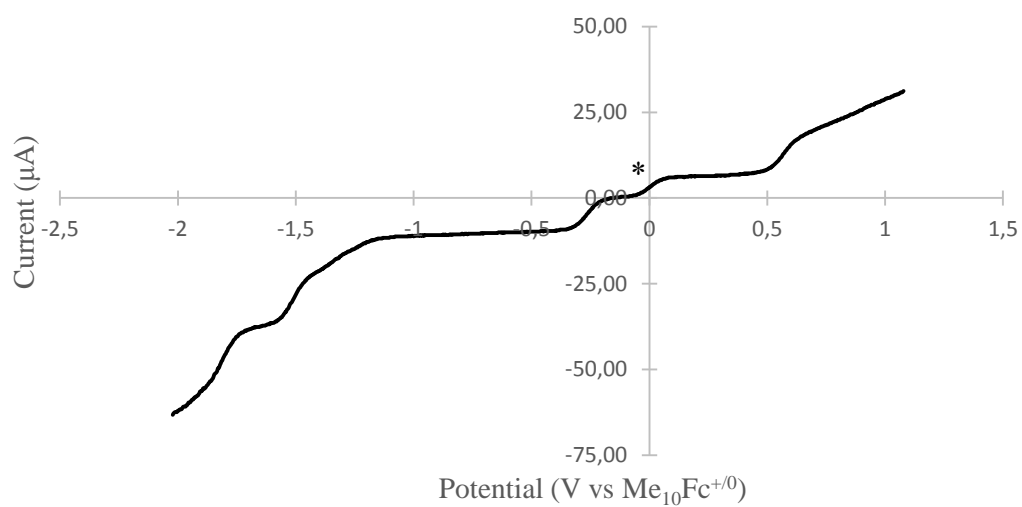
g_{33}	2.0076 (8.9)	2.190 (187.7)
$g_{33}-g_{11}$	0.0074	0.32
$\langle S^2 \rangle$	0.760	

Figure S4. Voltammograms recorded by CV and with the use of RDE of complexes **2-6**.

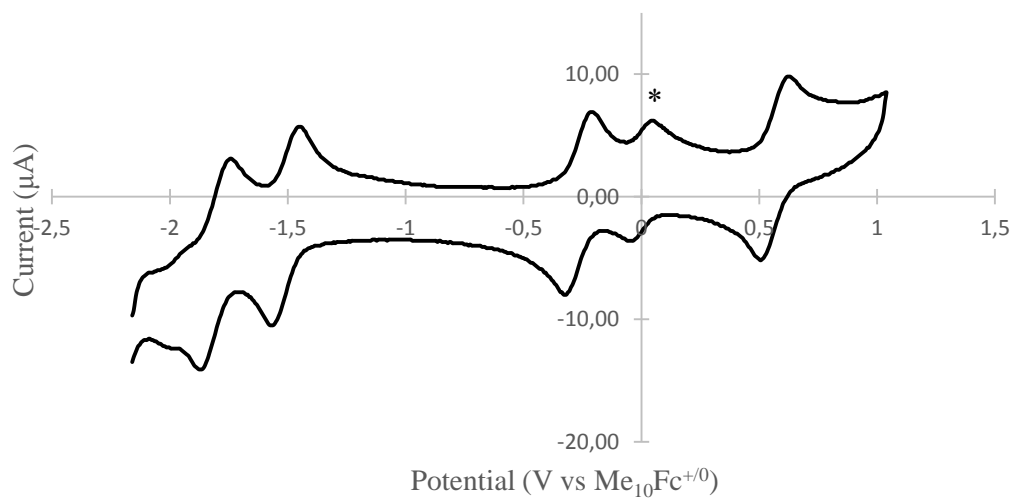
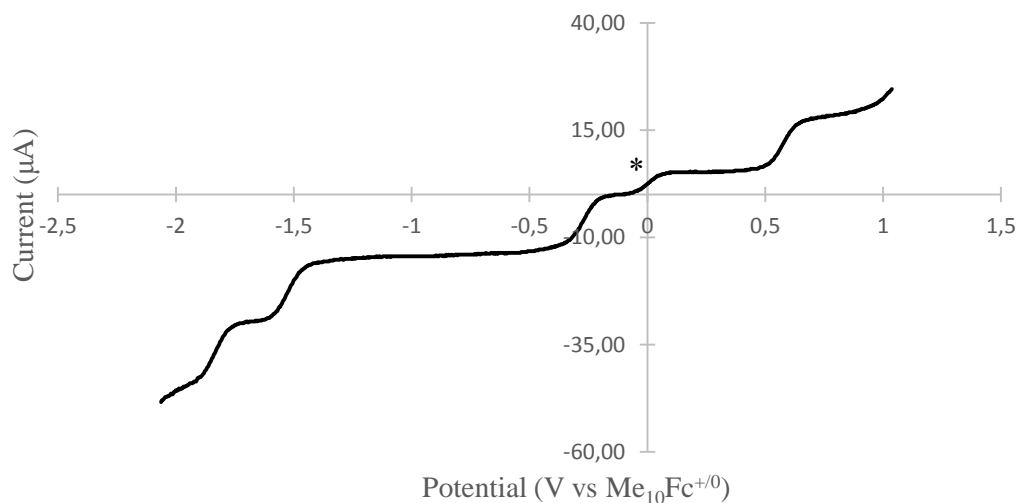
(**2**) (from -2.1 to +1 V) at a glassy carbon electrode in DMF (1 mM) containing Bu_4NPF_6 (100 mM) as supporting electrolyte and decamethylferrocene as an internal standard (0.25 mM). Data were recorded versus saturated calomel electrode at scan rate of 100 mV/s and recalculated versus $\text{Me}_{10}\text{Fc}^{0/+}$ potential value (-0.09 V and -0.09 V for RDE and CV respectively).



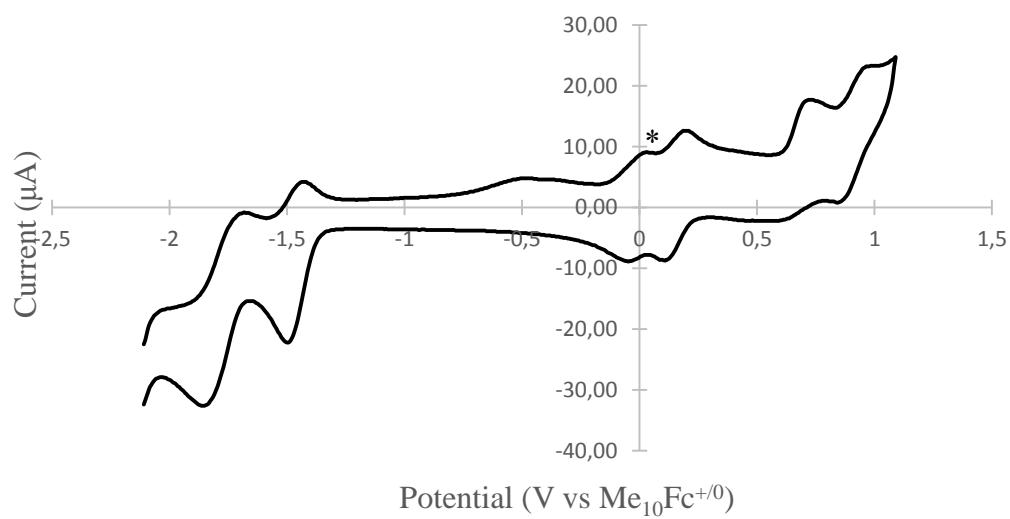
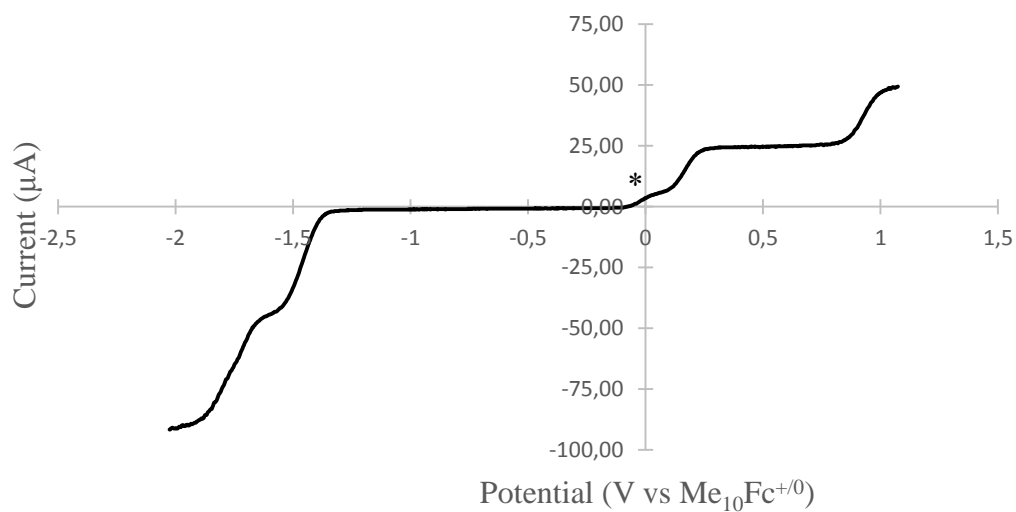
(3) (from -2.1 to +1 V) at a glassy carbon electrode in DMF (1 mM) containing Bu_4NPF_6 (100 mM) as supporting electrolyte and decamethylferrocene as an internal standard (0.25 mM). Data were recorded versus saturated calomel electrode at scan rate of 100 mV/s and recalculated versus $\text{Me}_{10}\text{Fc}^{0/+}$ potential value (-0.07 V and -0.05 V for RDE and CV respectively).



(4) (from -2.1 to +1 V) at a glassy carbon electrode in DMF (1 mM) containing Bu_4NPF_6 (100 mM) as supporting electrolyte and decamethylferrocene as an internal standard (0.25 mM). Data were recorded versus saturated calomel electrode at scan rate of 100 mV/s and recalculated versus $\text{Me}_{10}\text{Fc}^{0/+}$ potential value (-0.04 V and -0.04 V for RDE and CV respectively).



(5) (from -2.1 to +1 V) at a glassy carbon electrode in DMF (1 mM) containing Bu_4NPF_6 (100 mM) as supporting electrolyte and decamethylferrocene as an internal standard (0.25 mM). Data were recorded versus saturated calomel electrode at scan rate of 100 mV/s and recalculated versus $\text{Me}_{10}\text{Fc}^{0/+}$ potential value (-0.07 V and -0.09 V for RDE and CV respectively).



(6) (from -2.1 to +1 V) at a glassy carbon electrode in DMF (1 mM) containing Bu_4NPF_6 (100 mM) as supporting electrolyte and decamethylferrocene as an internal standard (0.25 mM). Data were recorded versus saturated calomel electrode at scan rate of 100 mV/s and recalculated versus $\text{Me}_{10}\text{Fc}^{0/+}$ potential value (-0.07 V and -0.09 V for RDE and CV respectively).

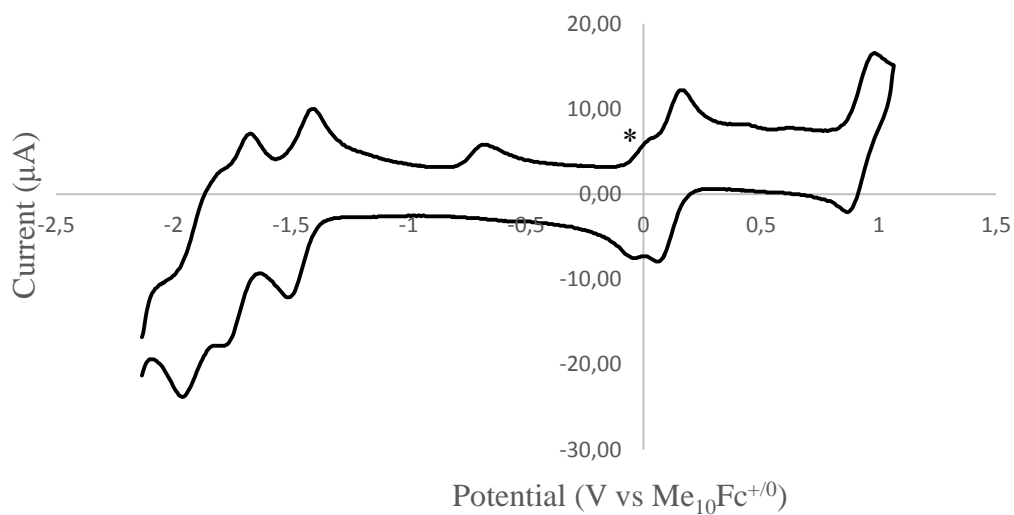
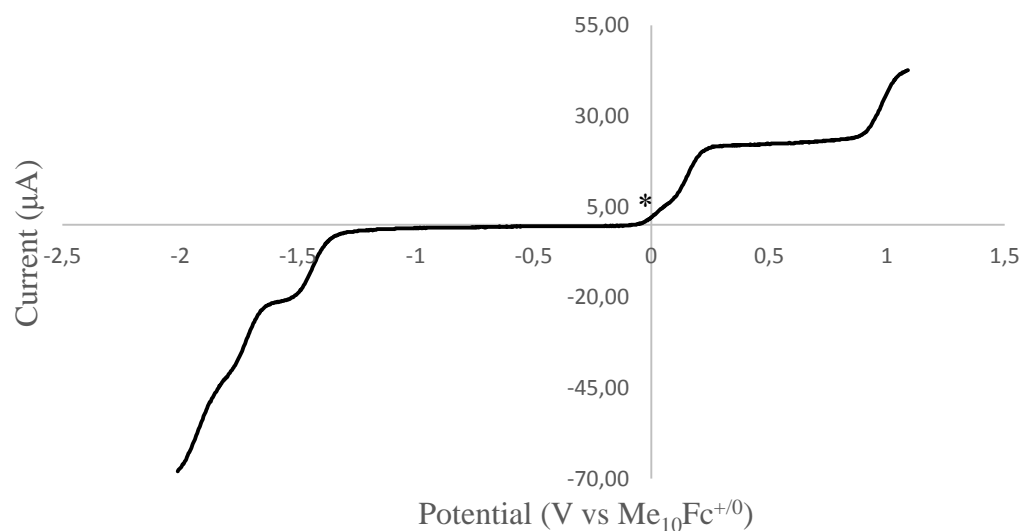


Table S3. Electrochemical data for complexes **1-4**

		Ph₂Phen^{0/-}	Ph₂Phen^{0/-}	sq/cat	Ru^{II/III}
Ru- sq[*]	E_{1/2}^a [V] (RDE)	-1.876 ± 0.039	-1.578 ± 0.035	-0.249 ± 0.010	0.647 ± 0.018
	E_{1/2}^b [V] (CV)	-1.816 ± 0.015	-1.507 ± 0.007	-0.209 ± 0.002	0.623 ± 0.005
1	E_{1/2}^a [V] (RDE)	-1.848 ± 0.015	-1.537 ± 0.008	-0.284 ± 0.005	0.595 ± 0.011
	E_{1/2}^b [V] (CV)	-1.798 ± 0.001	-1.503 ± 0.002	-0.251 ± 0.001	0.602 ± 0.002
2	E_{1/2}^a [V] (RDE)	-1.833 ± 0.007	-1.497 ± 0.012	-0.252 ± 0.011	0.615 ± 0.003
	E_{1/2}^b [V] (CV)	-1.813 ± 0.002	-1.510 ± 0.002	-0.256 ± 0.001	0.592 ± 0.004
3	E_{1/2}^a [V] (RDE)	-1.836 ± 0.028	-1.472 ± 0.070	-0.265 ± 0.019	0.636 ± 0.011
	E_{1/2}^b [V] (CV)	-1.797 ± 0.002	-1.511 ± 0.001	-0.264 ± 0.002	0.569 ± 0.003
4	E_{1/2}^a [V] (RDE)	-1.839 ± 0.017	-1.515 ± 0.005	-0.271 ± 0.008	0.574 ± 0.001
	E_{1/2}^b [V] (CV)	-1.807 ± 0.006	-1.506 ± 0.003	-0.265 ± 0.002	0.567 ± 0.004

* Values taken from^[2] We however note that these experiments were performed on the same days.

^a E_{1/2} = half-wave potential in Volts.

^b E_{1/2} = (E_{pa} + E_{pc})/2 in Volts.

Figure S5. UV/Vis/NIR-spectroelectrochemistry data for complex 1 in the presence of the reducing agent glutathione.

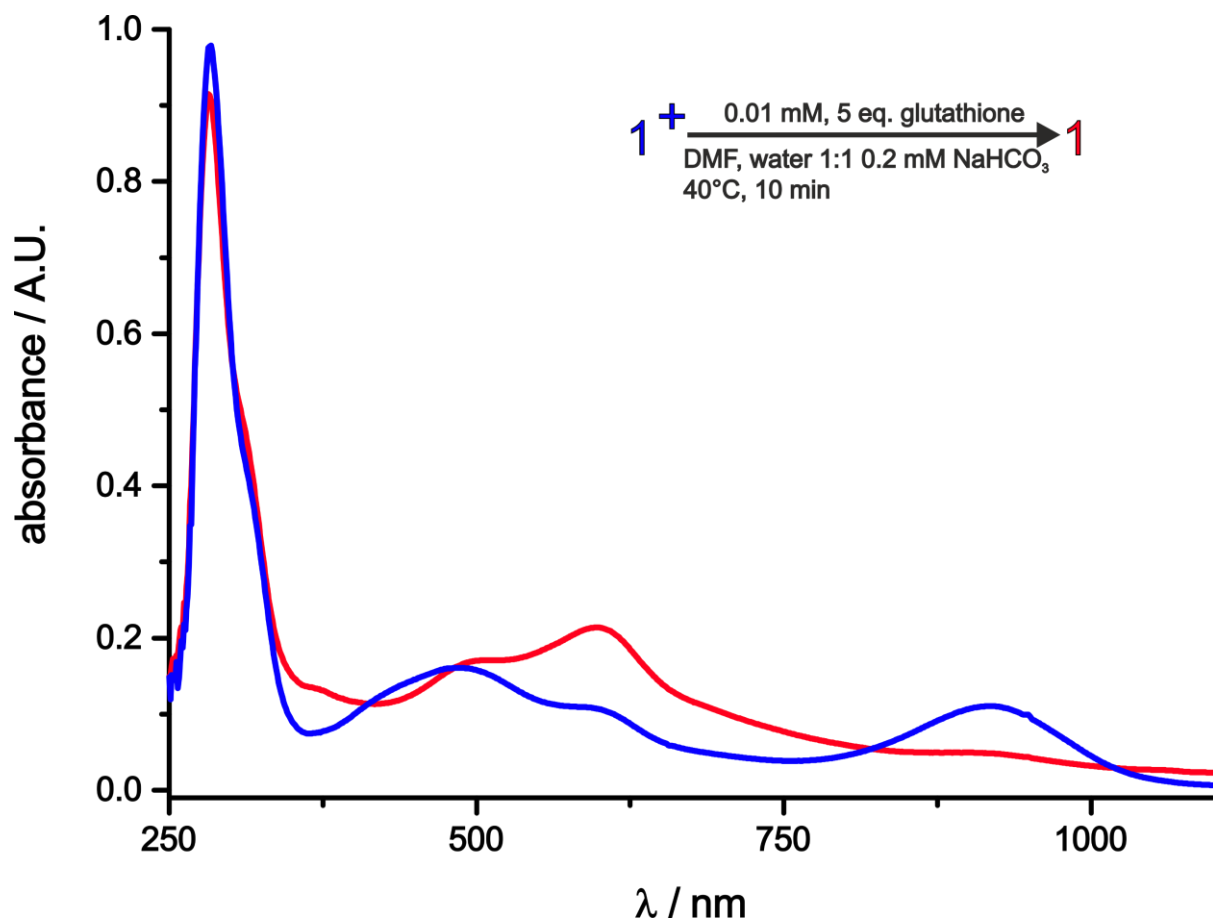


Table S4. Electrochemical data for complexes **5** and **6**.

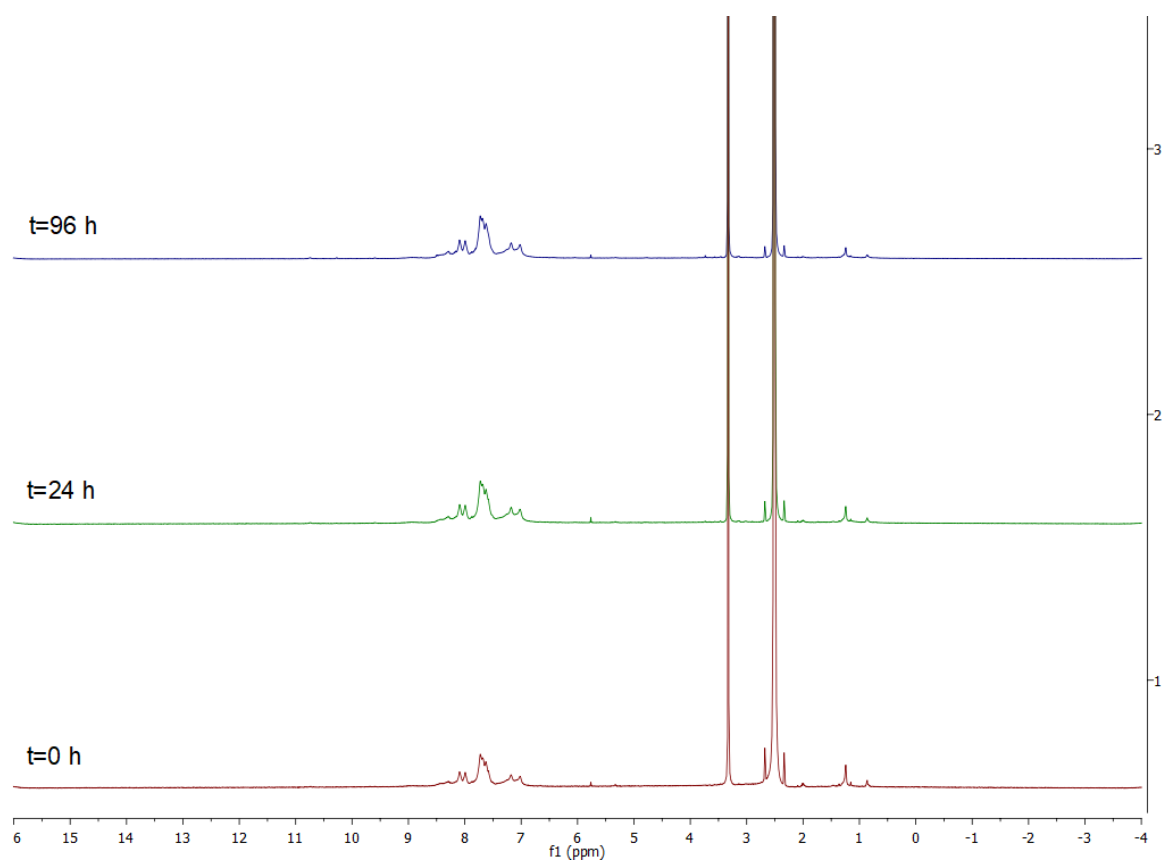
		Ph₂Phen^{0/-}	Ph₂Phen^{0/-}	Ox1	Ox2
5	E_{1/2}^a [V] (RDE)	-1.746 ± 0.003	-1.423 ± 0.002	0.182 ± 0.005	0.927 ± 0.008
	E_{1/2}^b [V] (CV)	-1.764 ± 0.011	-1.456 ± 0.003	0.162 ± 0.001	0.910 ± 0.003
6	E_{1/2}^a [V] (RDE)	-1.737 ± 0.009	-1.440 ± 0.009	0.164 ± 0.013	0.970 ± 0.009
	E_{1/2}^b [V] (CV)	-1.734 ± 0.006	-1.456 ± 0.003	0.114 ± 0.004	0.929 ± 0.007

^a E_{1/2} = half-wave potential in Volts.

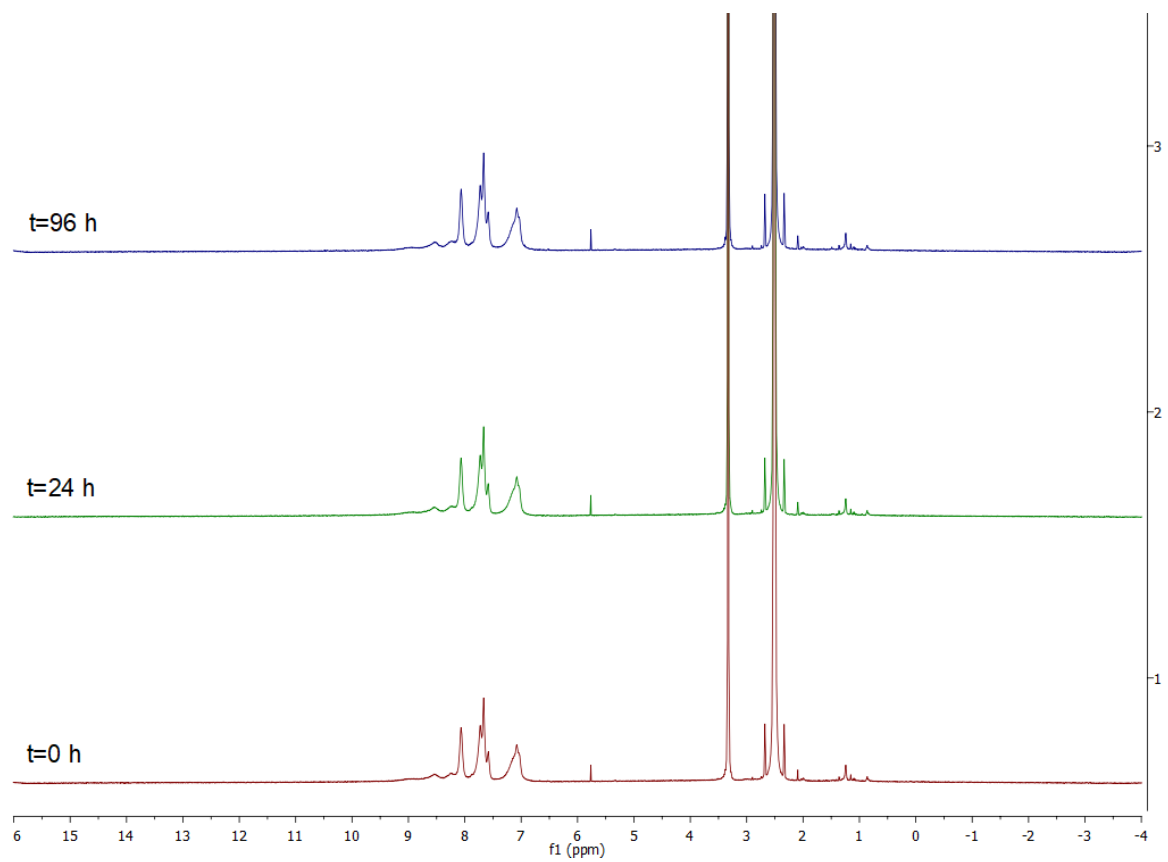
^b E_{1/2} = (E_{pa} + E_{pc})/2 in Volts.

Figure S6. Overlap of ^1H spectra of complexes **1-6** in DMSO over 96 h.

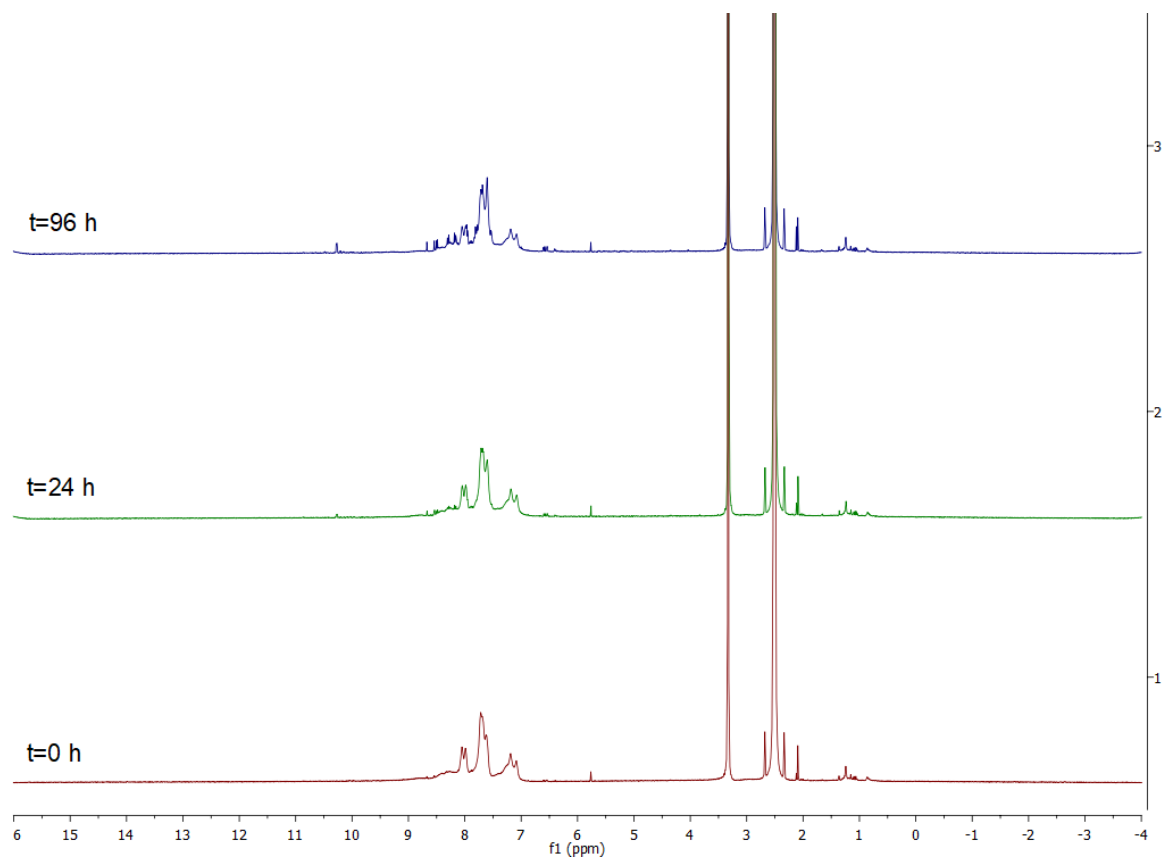
(1)



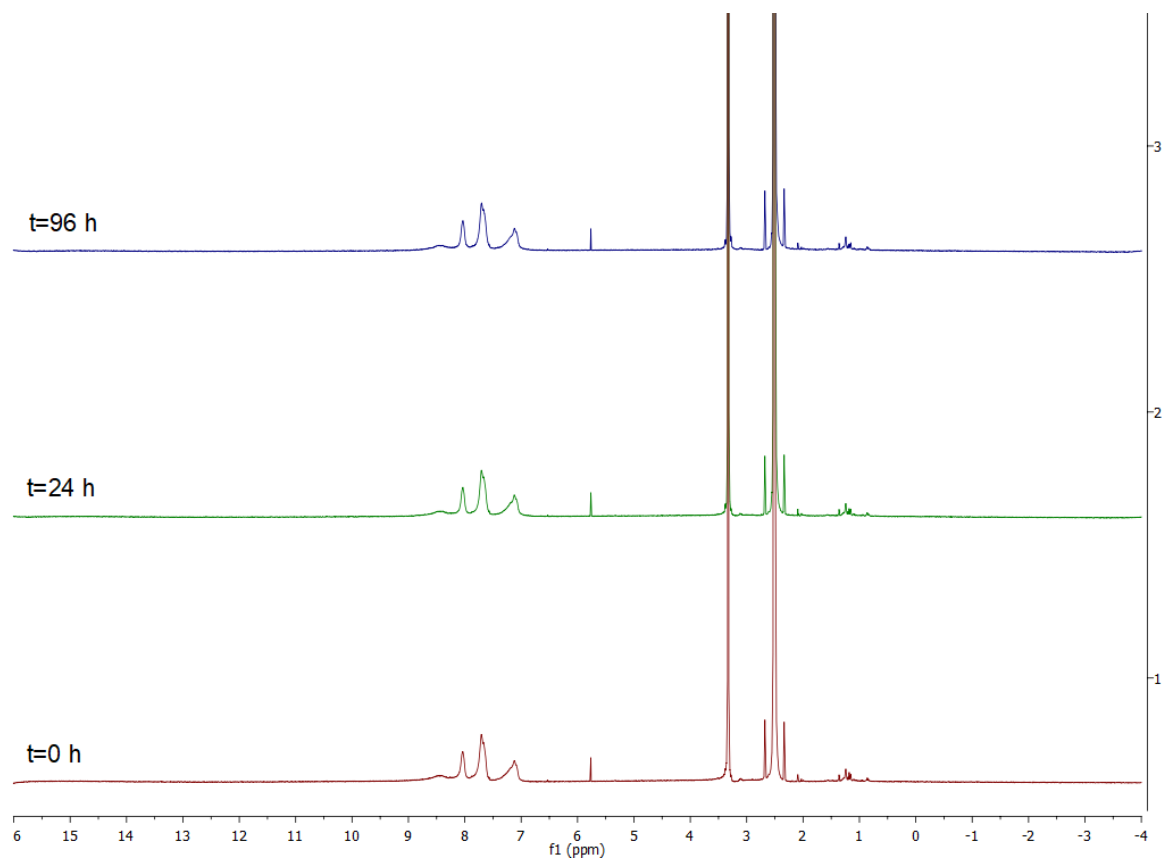
(2)



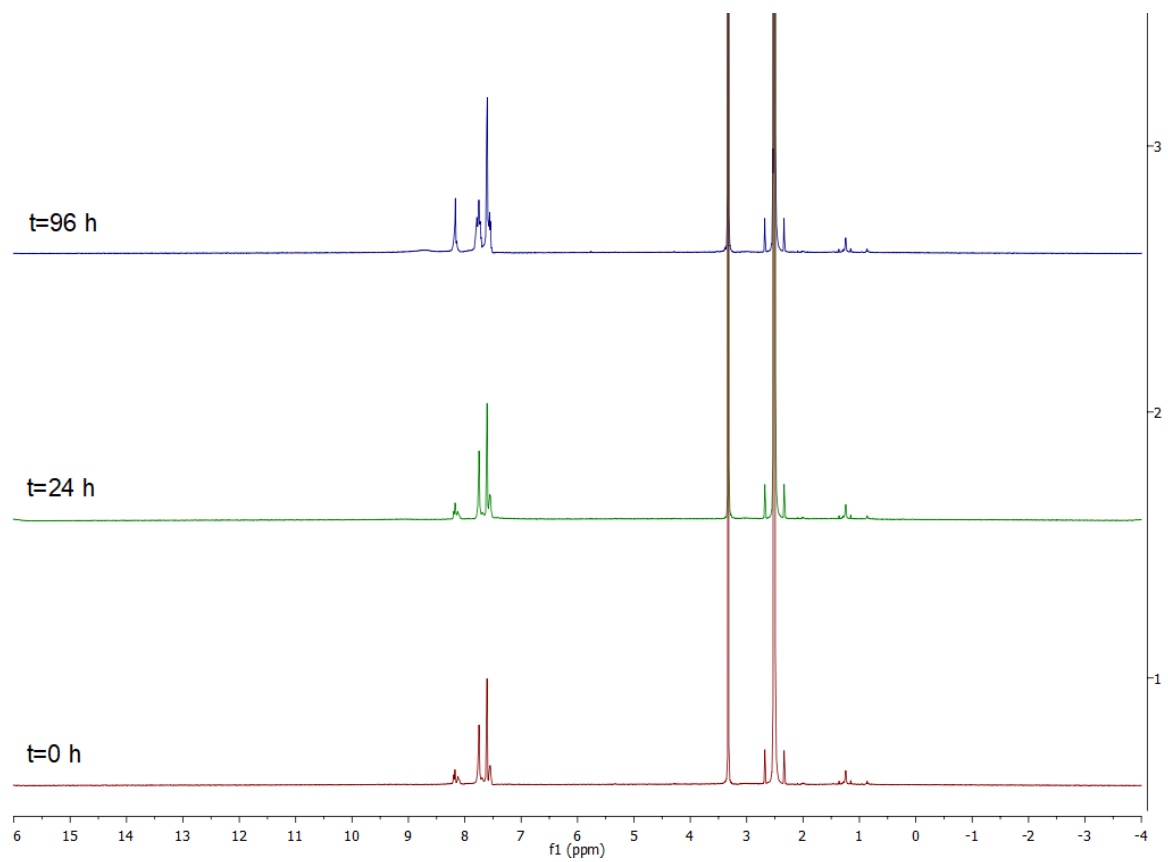
(3)



(4)



(5)



(6)

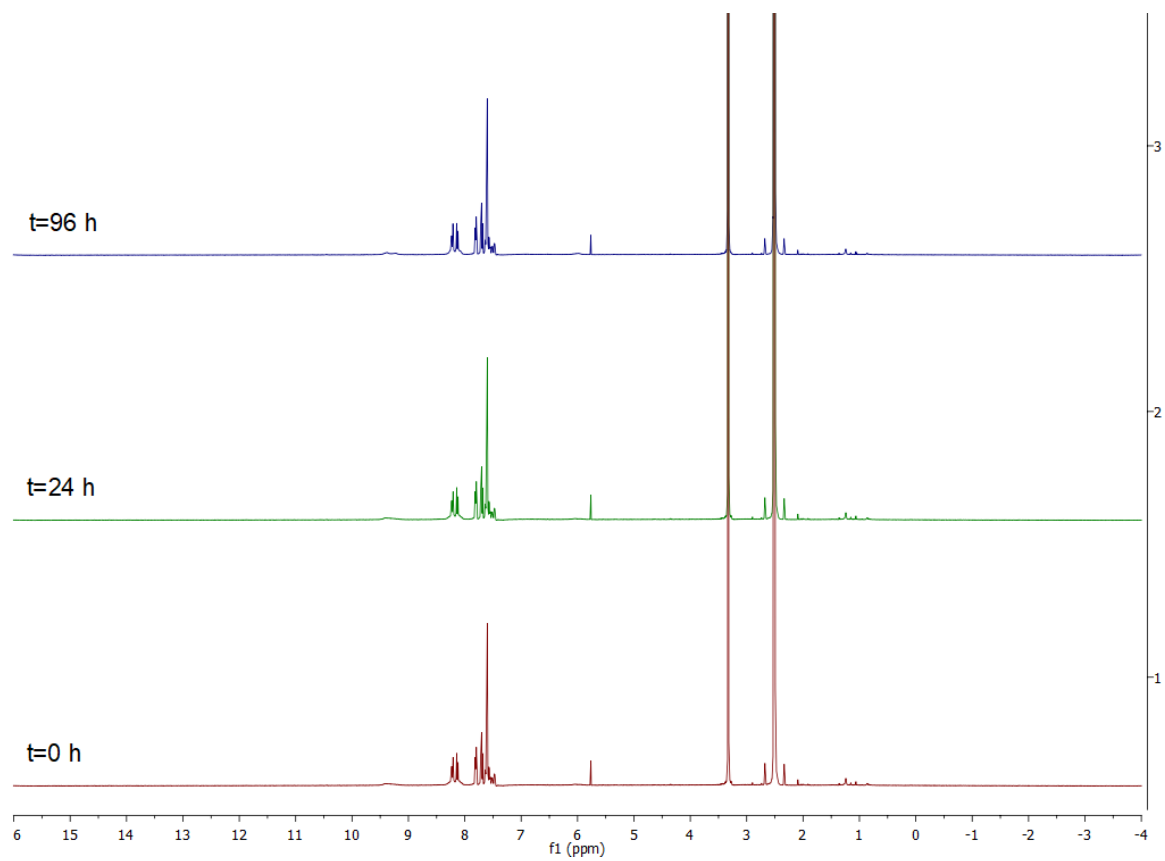


Figure S7. Percentage concentration of complex **1** in human plasma, normalized with respect to the internal standard (caffeine) and plotted against time.

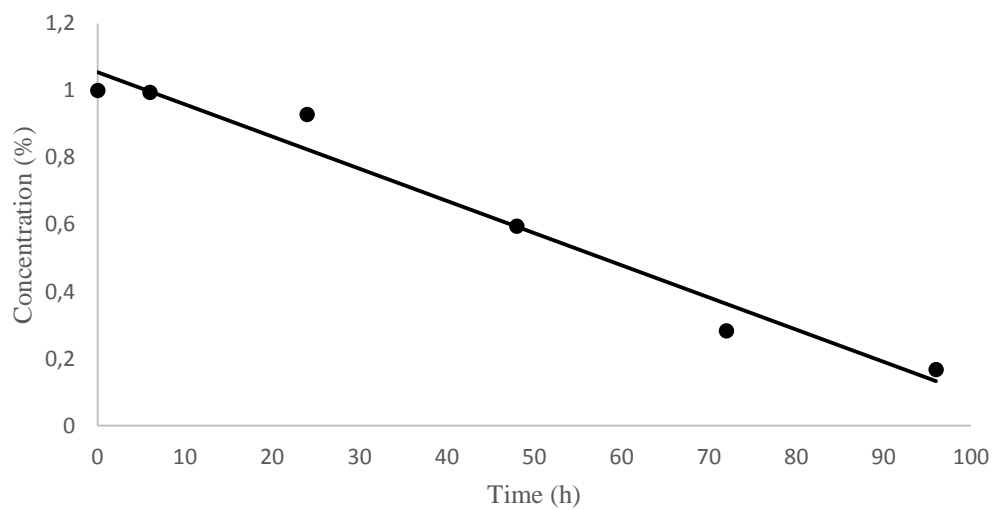
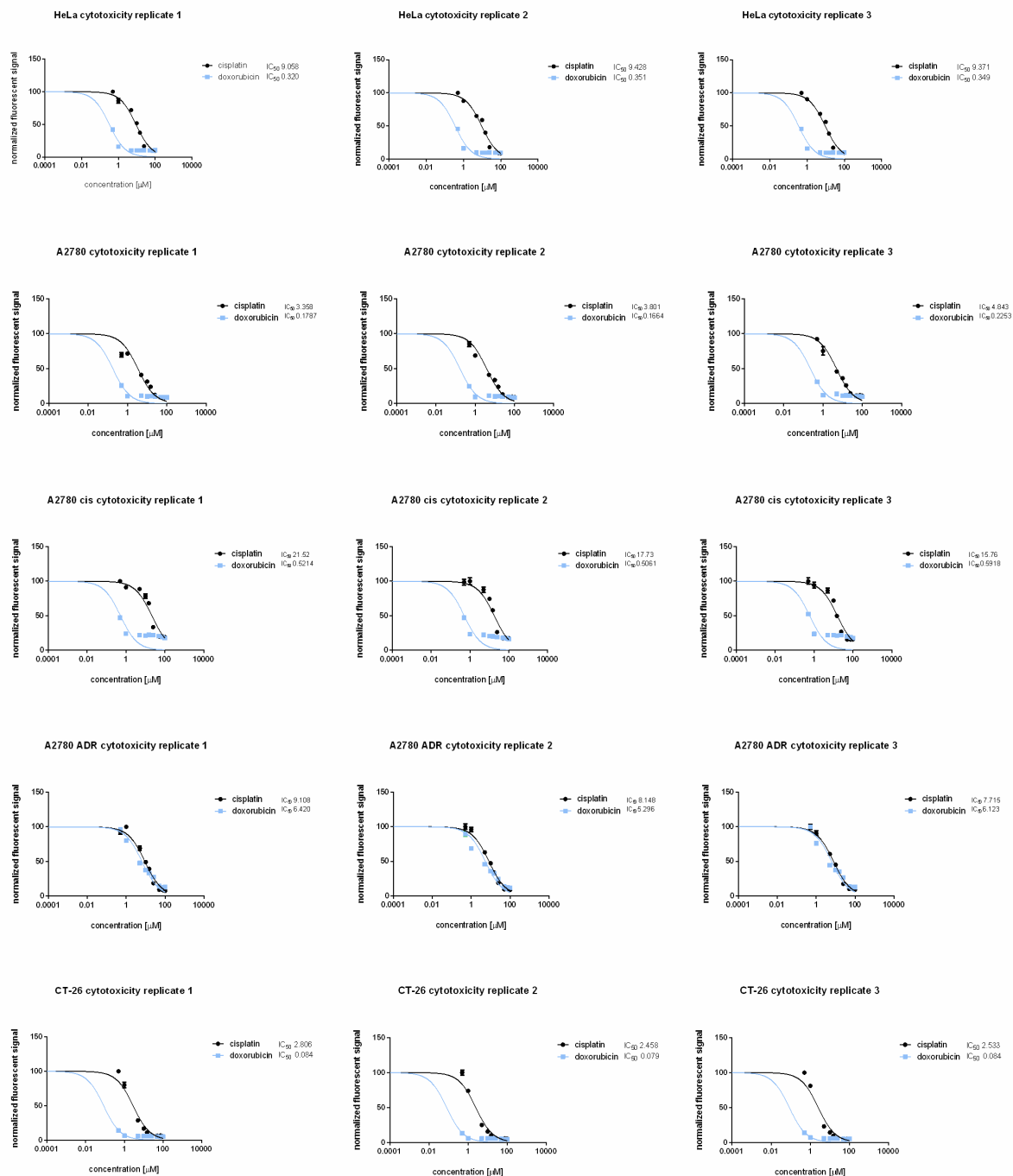
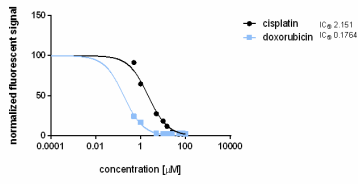


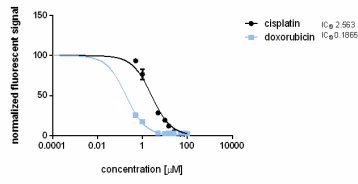
Figure S8. Fluorometric cell viability assay.



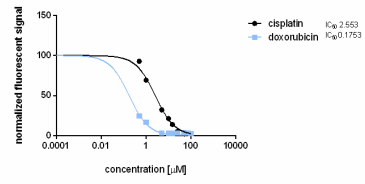
CT-26 LUC cytotoxicity replicate 1



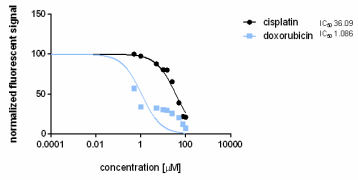
CT-26 LUC cytotoxicity replicate 2



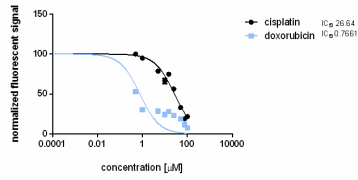
CT-26 LUC cytotoxicity replicate 3



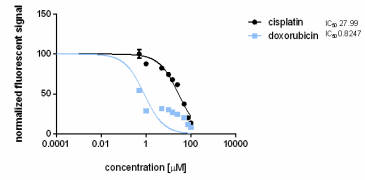
RPE-1 cytotoxicity replicate 1



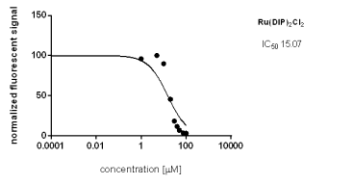
RPE-1 cytotoxicity replicate 2



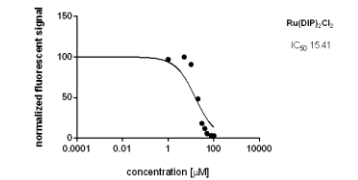
RPE-1 cytotoxicity replicate 3



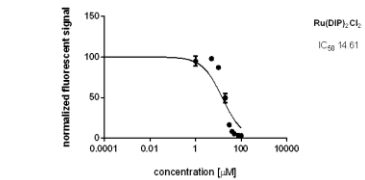
HeLa cytotoxicity replicate 1



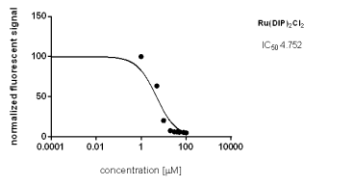
HeLa cytotoxicity replicate 2



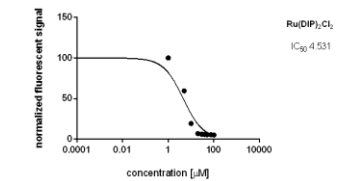
HeLa cytotoxicity replicate 3



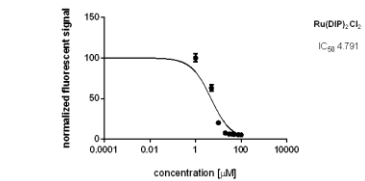
A2780 cytotoxicity replicate 1



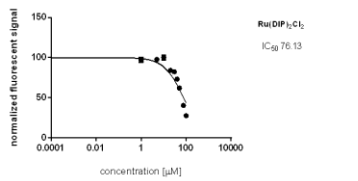
A2780 cytotoxicity replicate 2



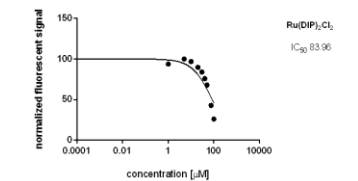
A2780 cytotoxicity replicate 3



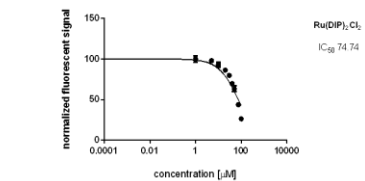
A2780 ADR cytotoxicity replicate 1



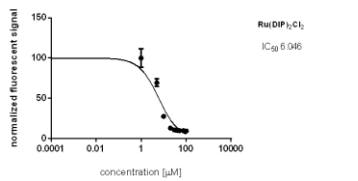
A2780 ADR cytotoxicity replicate 2



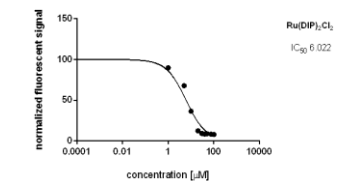
A2780 ADR cytotoxicity replicate 3



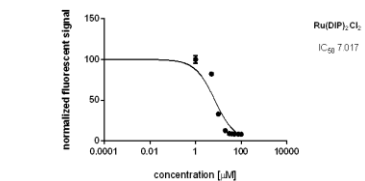
A2780 cis cytotoxicity replicate 1

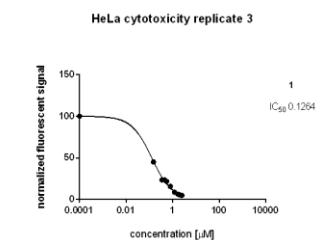
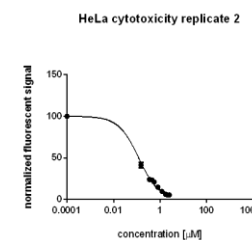
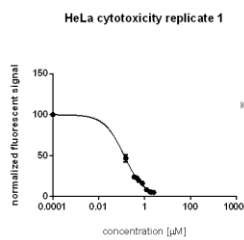
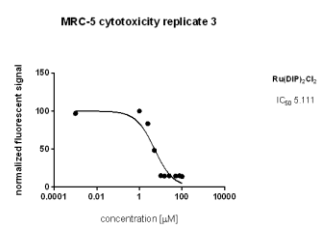
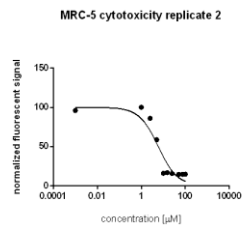
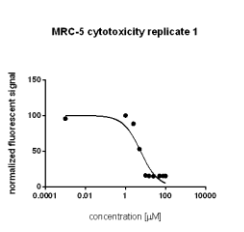
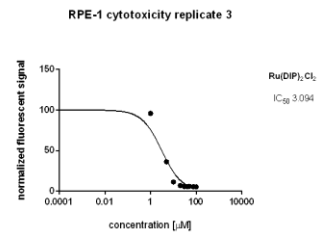
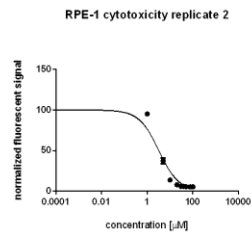
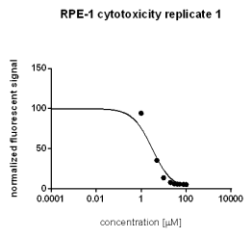
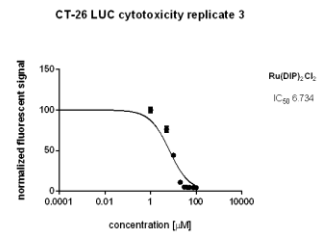
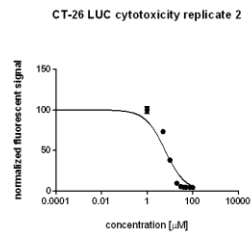
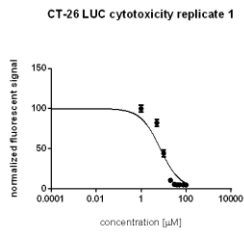
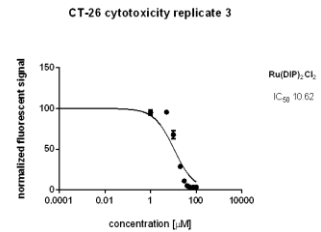
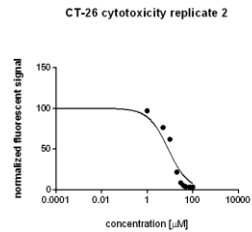
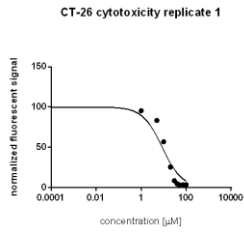


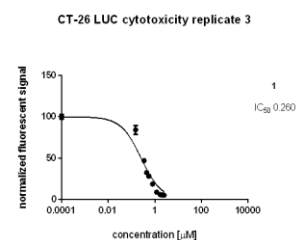
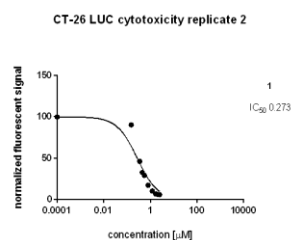
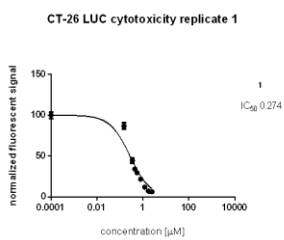
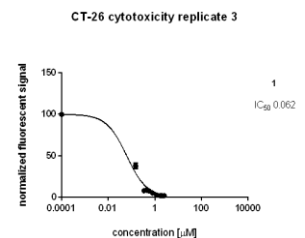
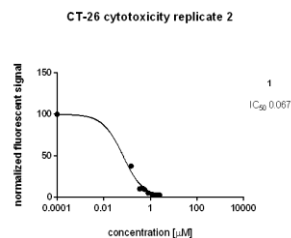
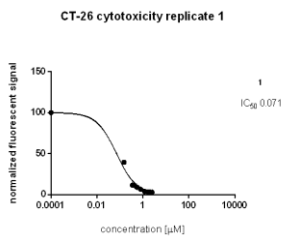
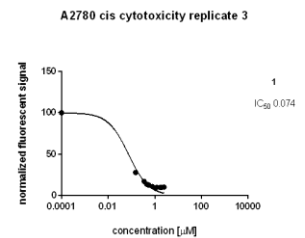
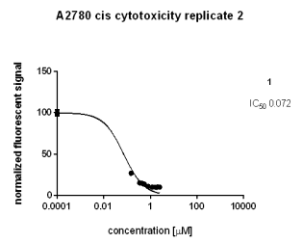
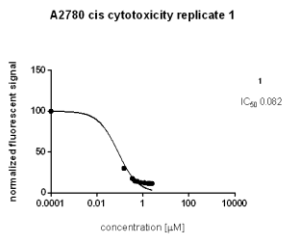
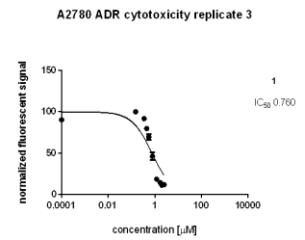
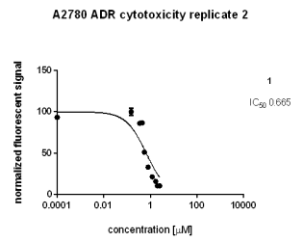
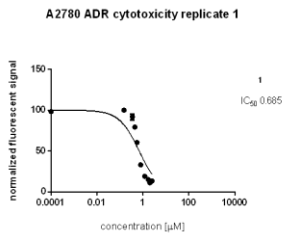
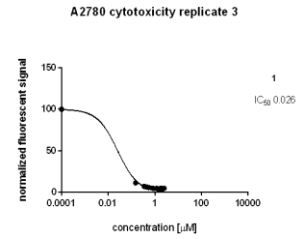
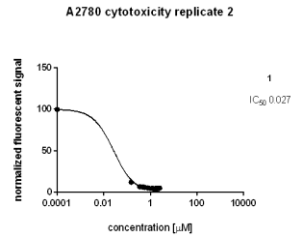
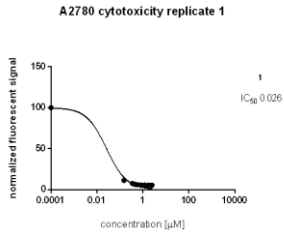
A2780 cis cytotoxicity replicate 2

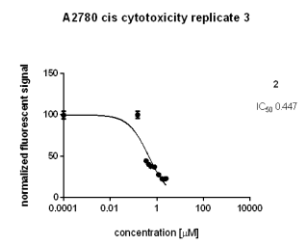
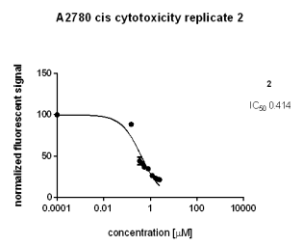
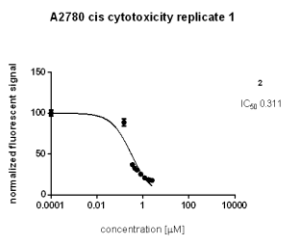
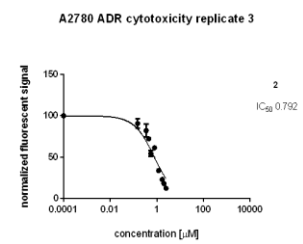
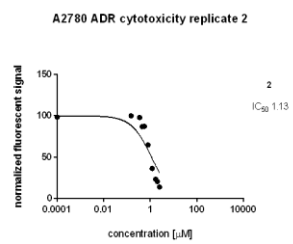
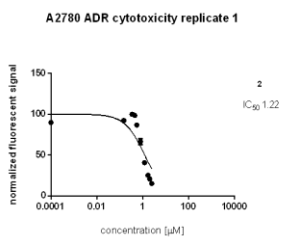
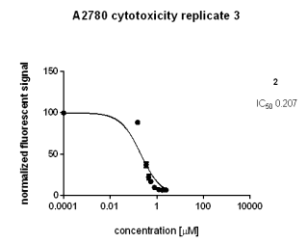
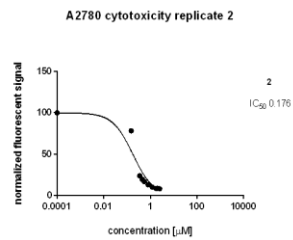
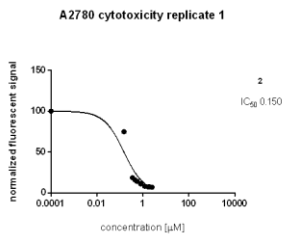
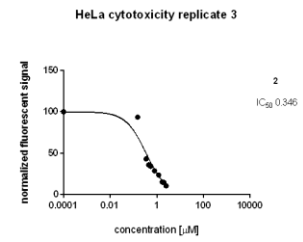
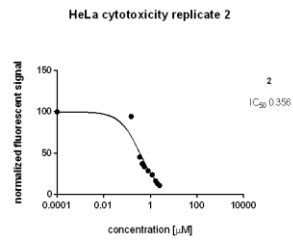
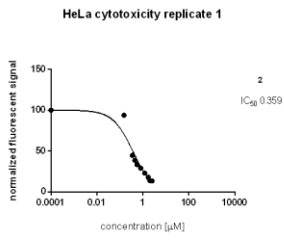
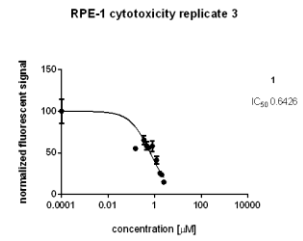
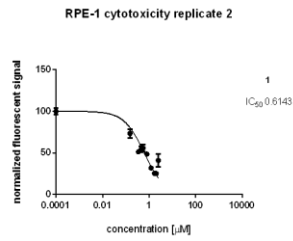
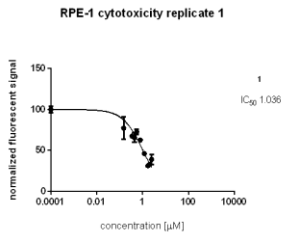


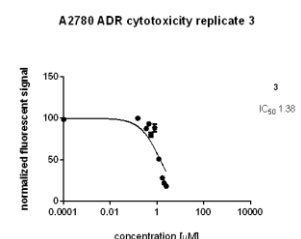
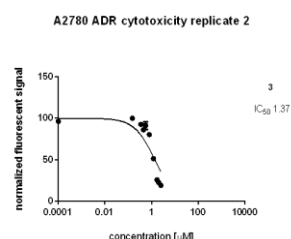
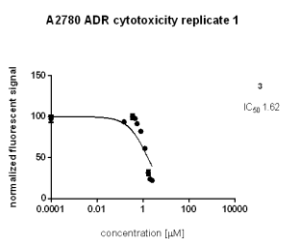
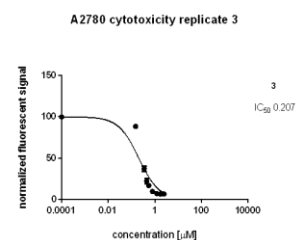
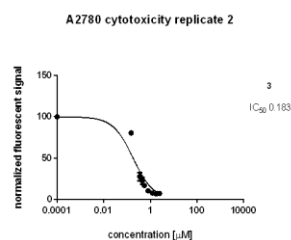
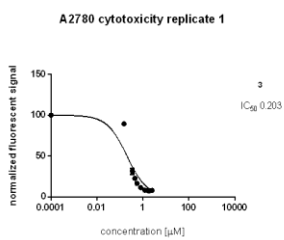
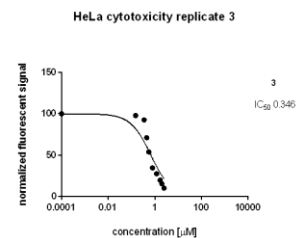
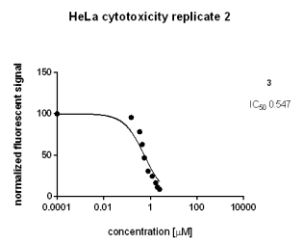
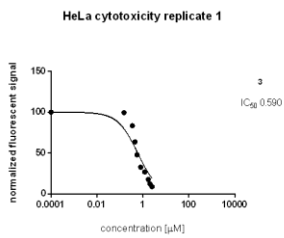
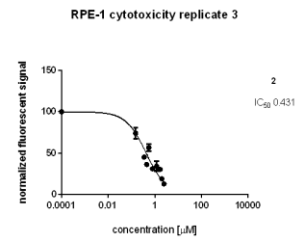
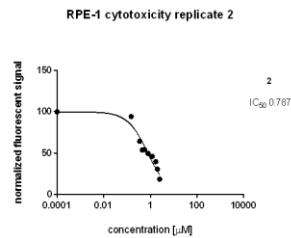
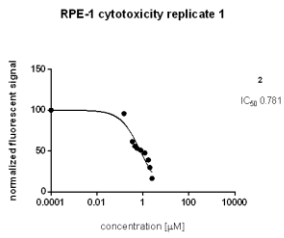
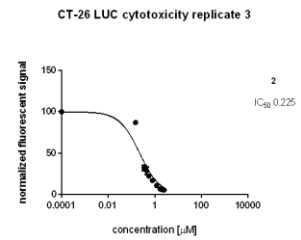
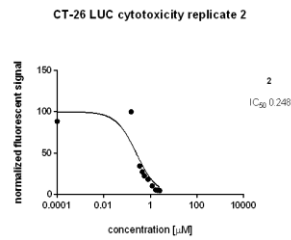
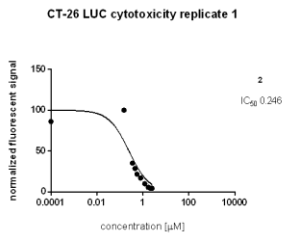
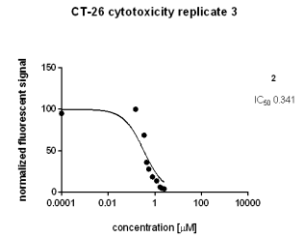
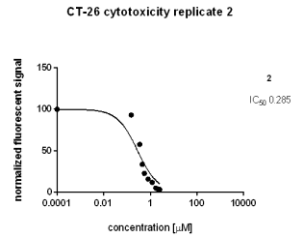
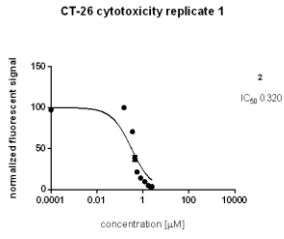
A2780 cis cytotoxicity replicate 3

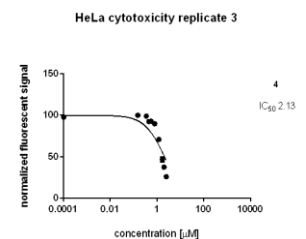
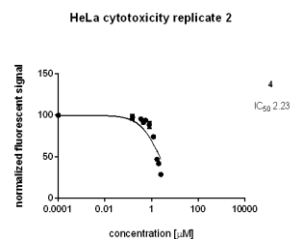
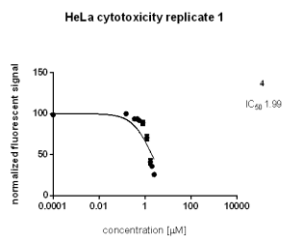
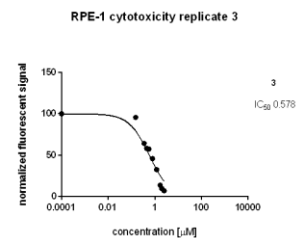
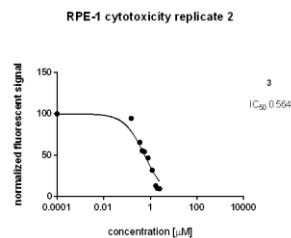
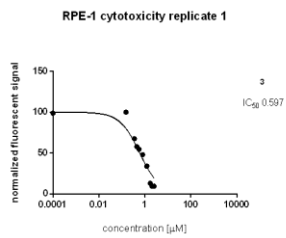
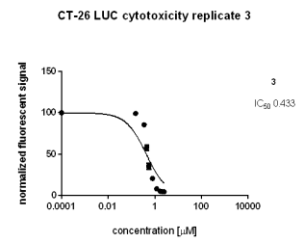
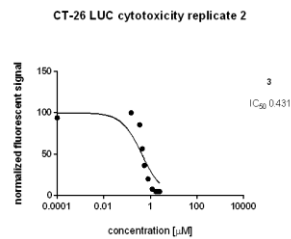
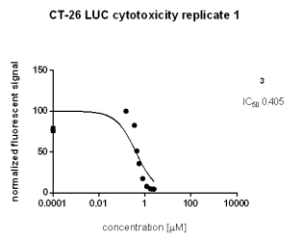
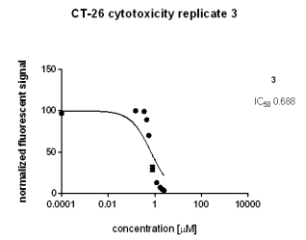
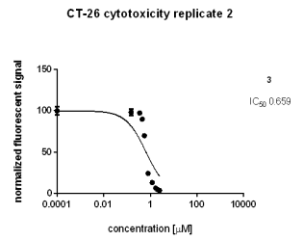
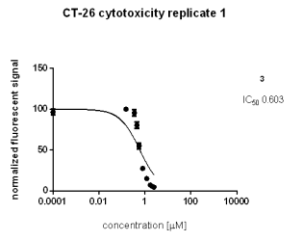
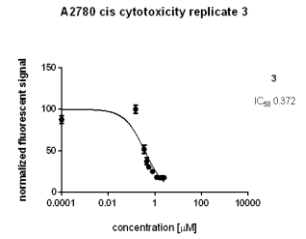
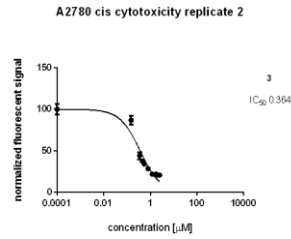
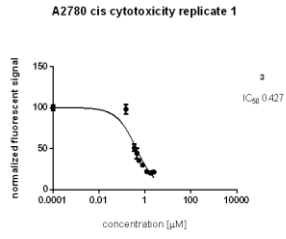


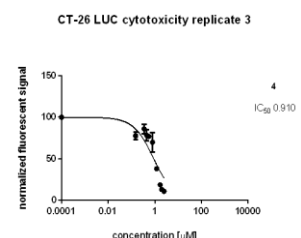
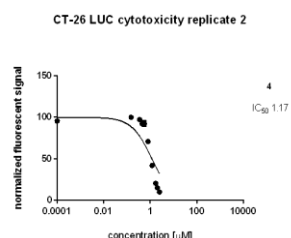
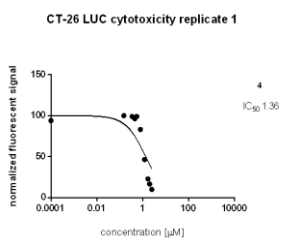
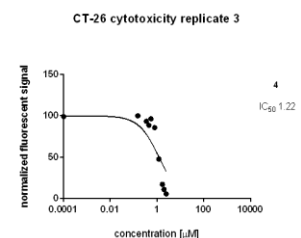
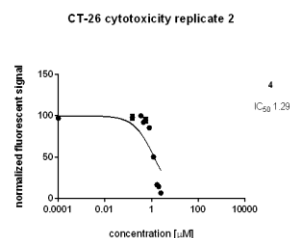
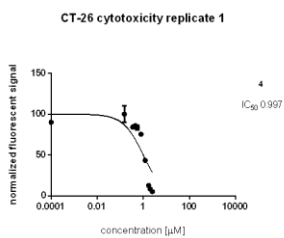
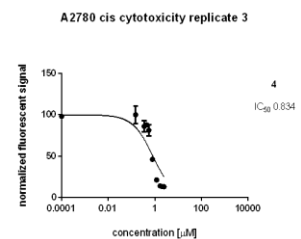
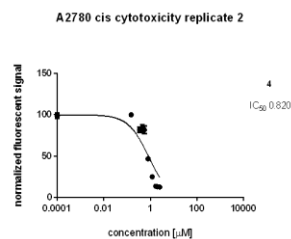
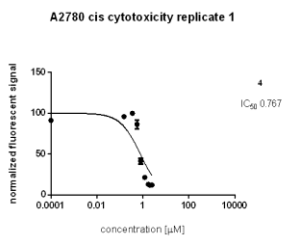
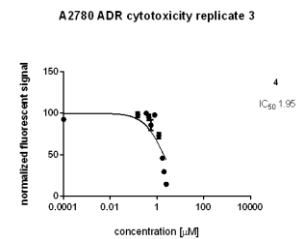
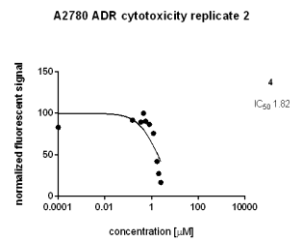
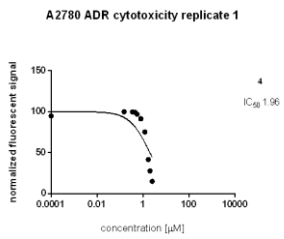
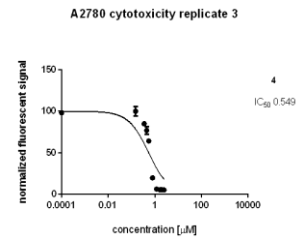
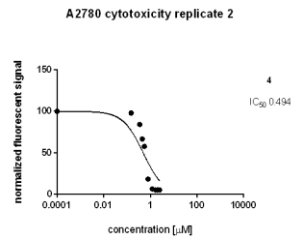
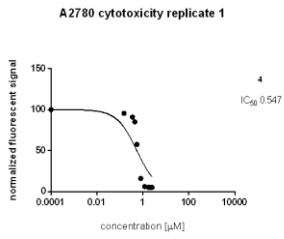


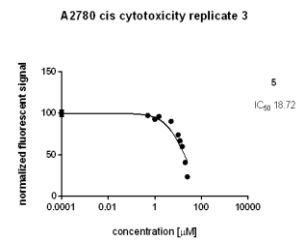
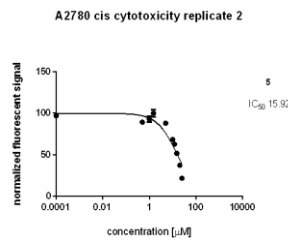
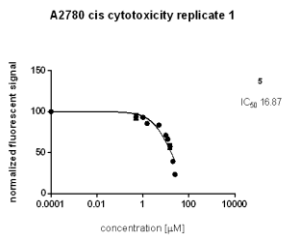
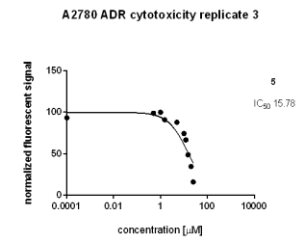
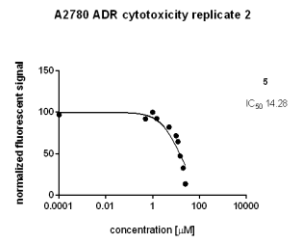
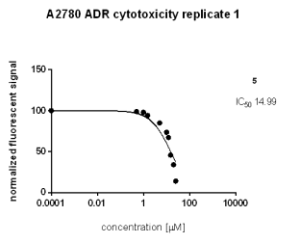
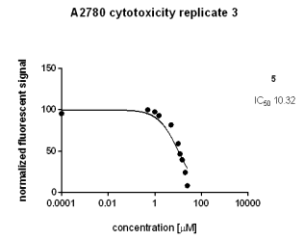
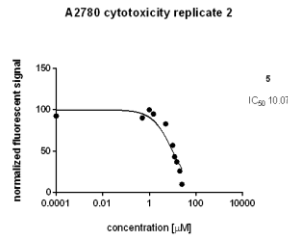
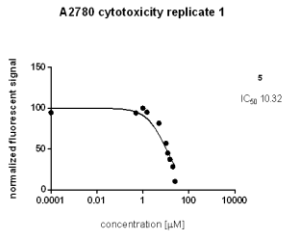
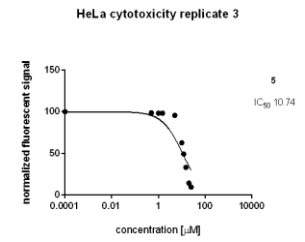
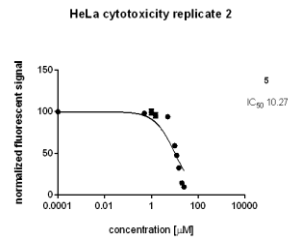
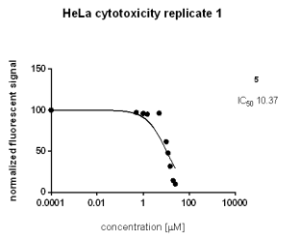
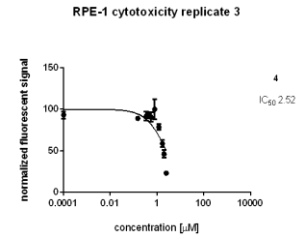
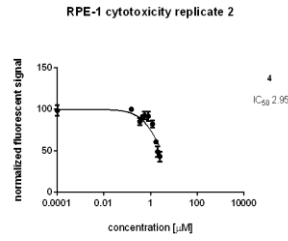
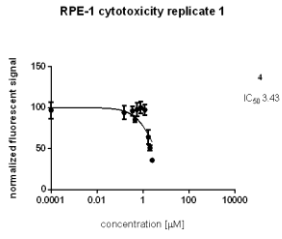


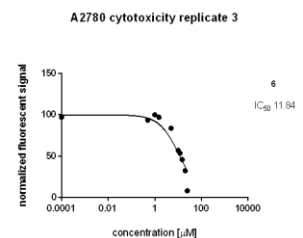
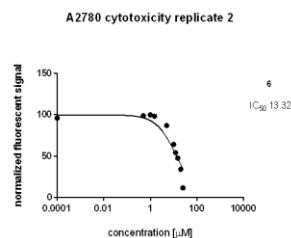
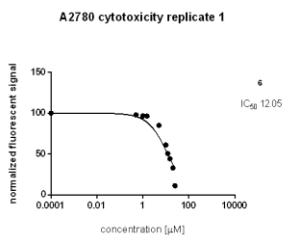
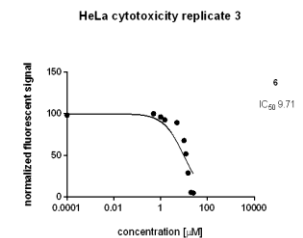
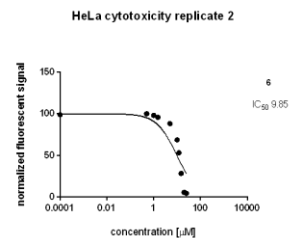
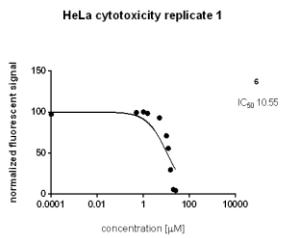
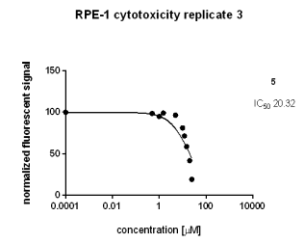
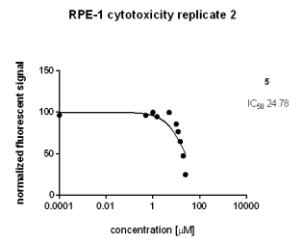
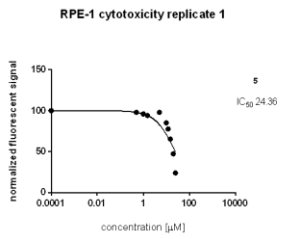
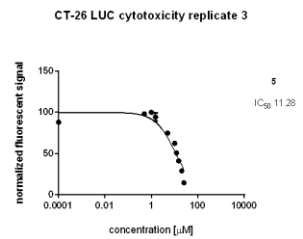
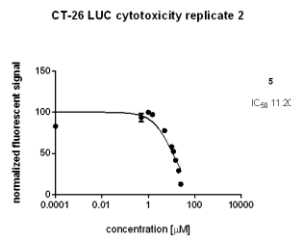
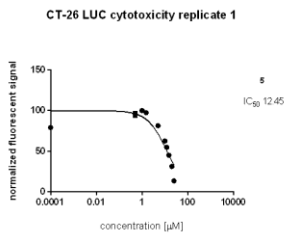
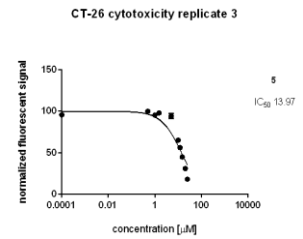
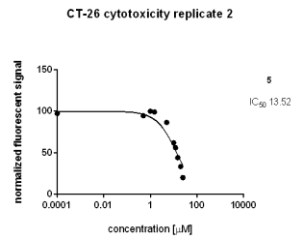
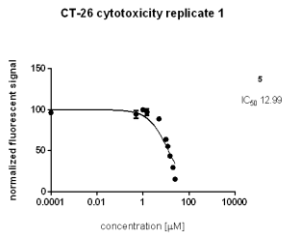


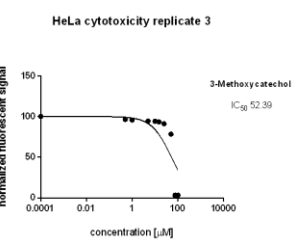
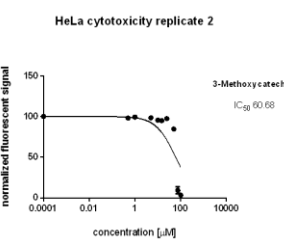
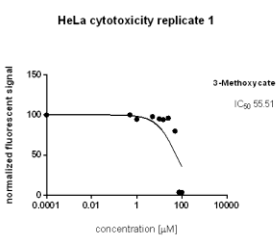
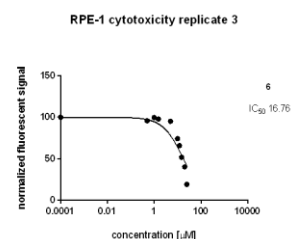
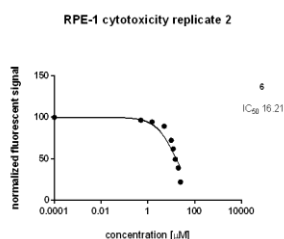
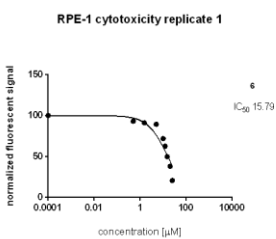
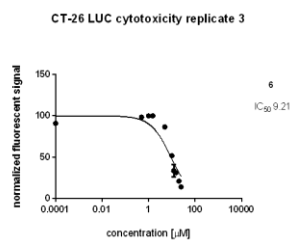
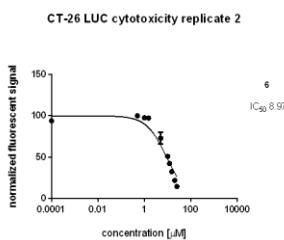
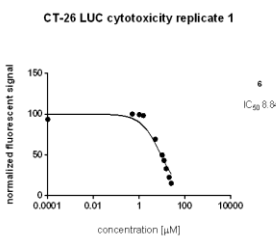
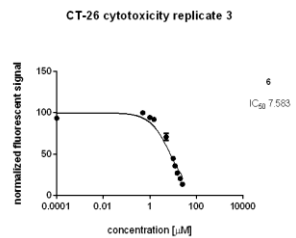
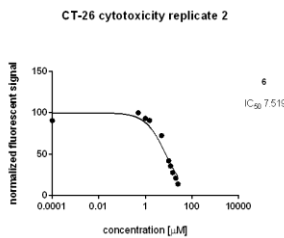
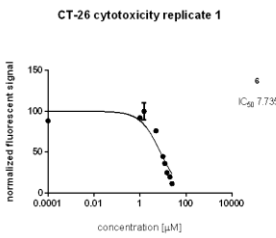
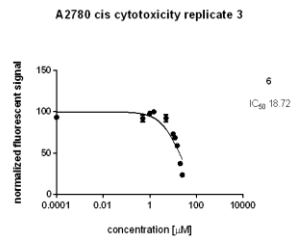
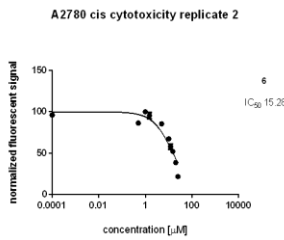
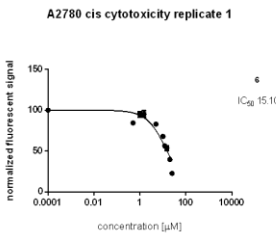
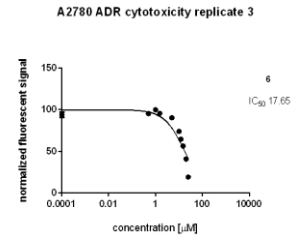
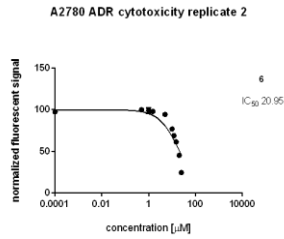
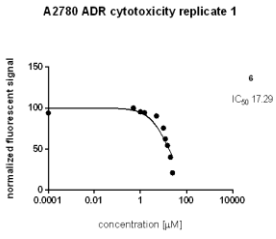


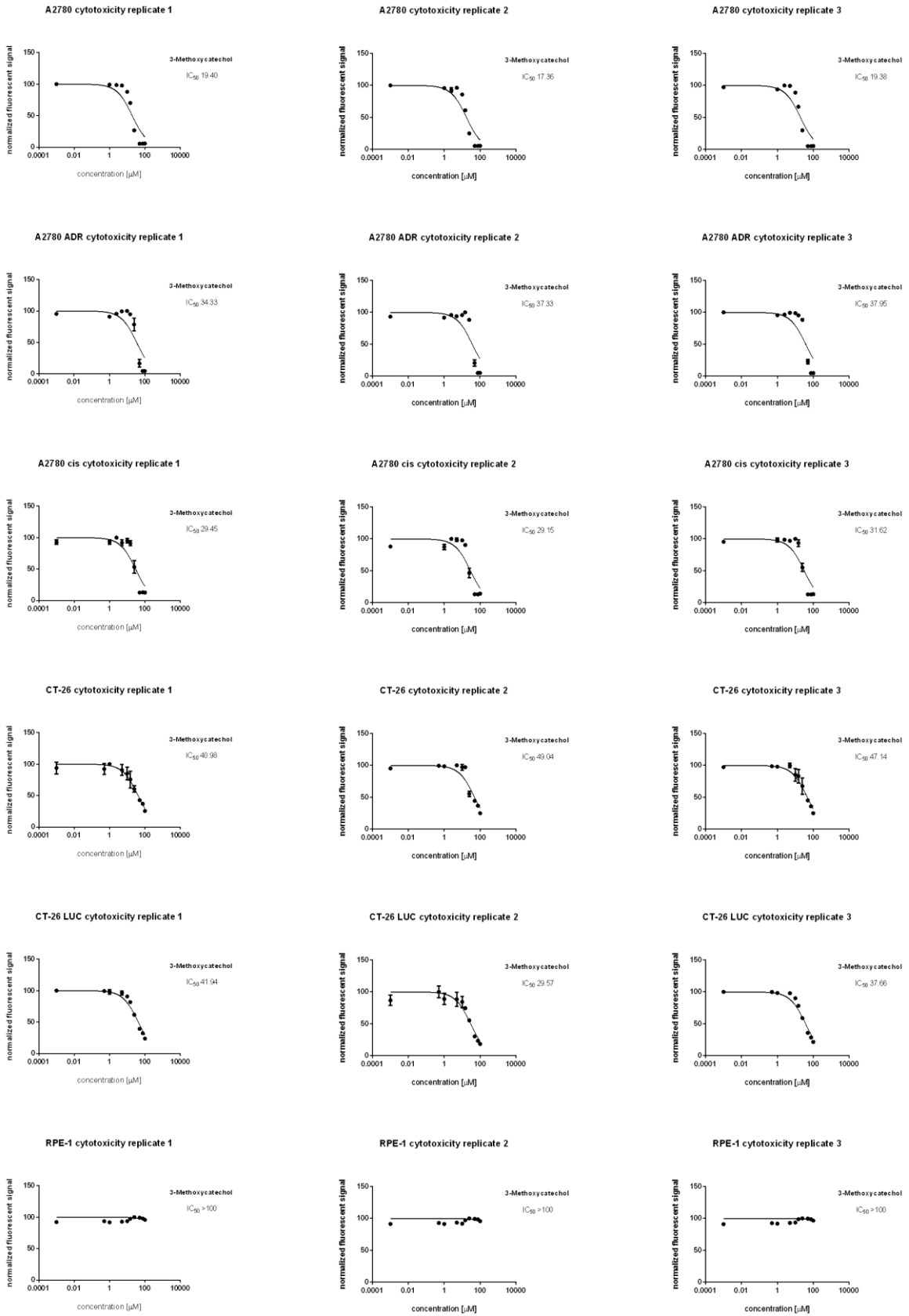


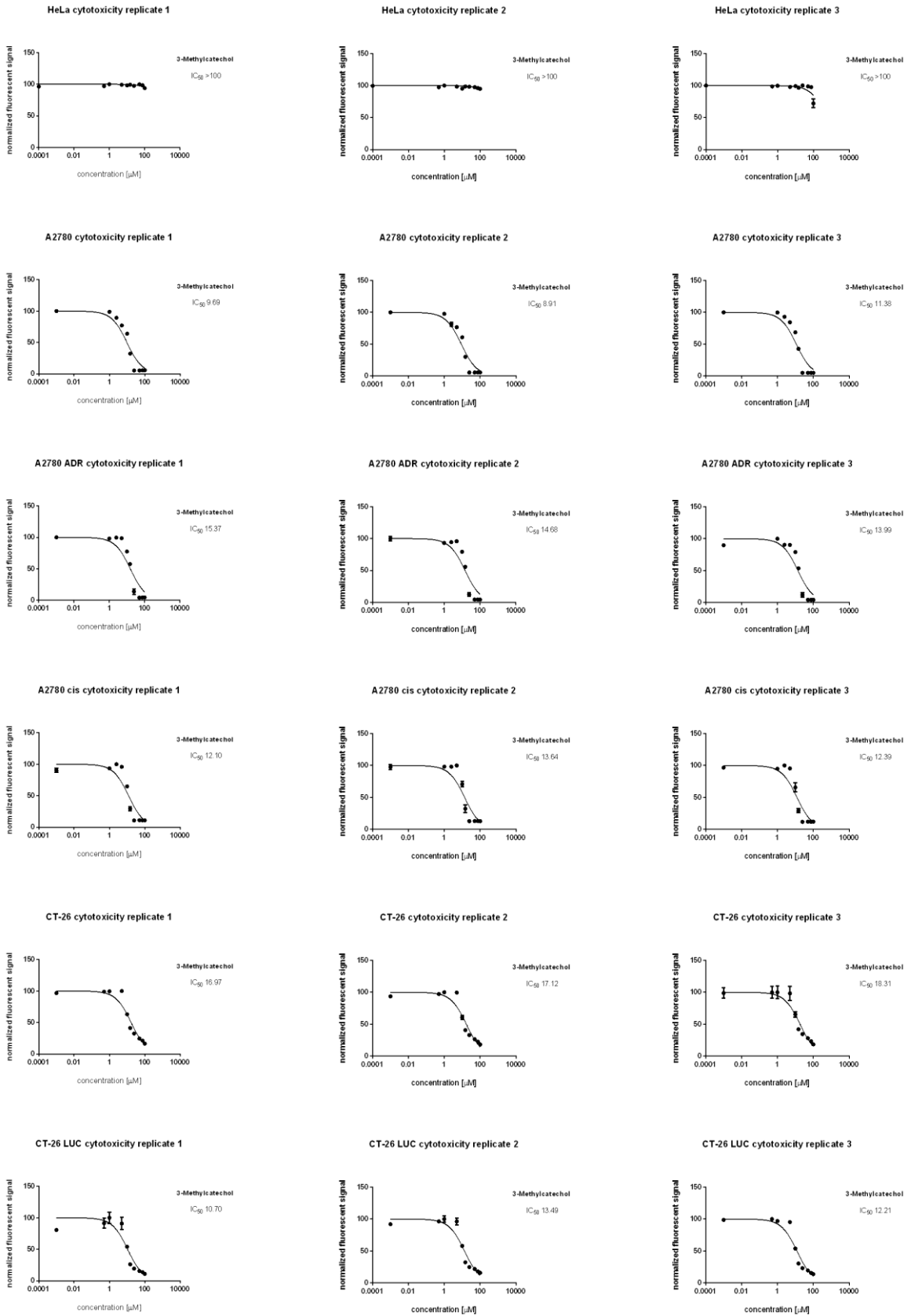


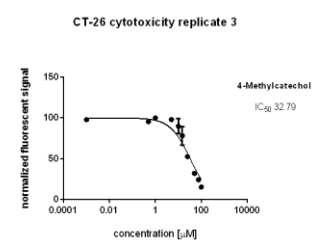
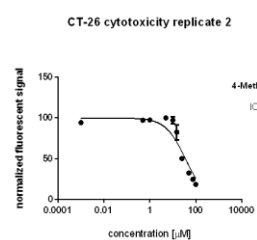
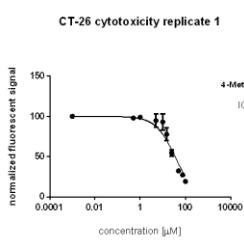
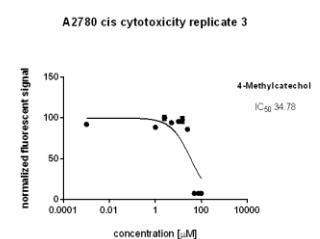
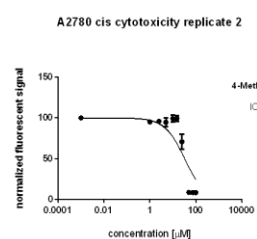
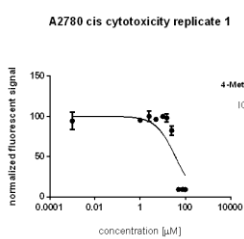
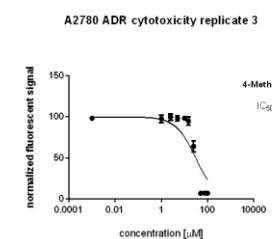
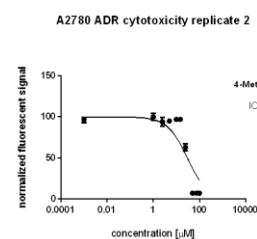
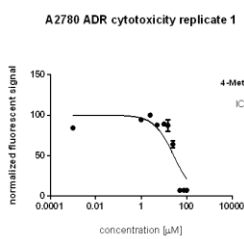
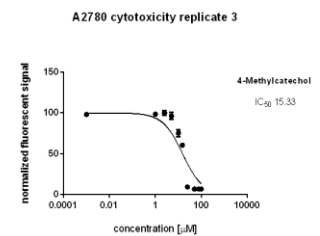
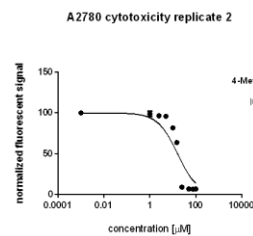
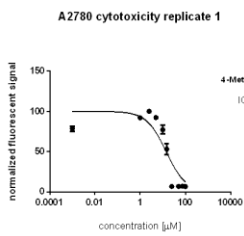
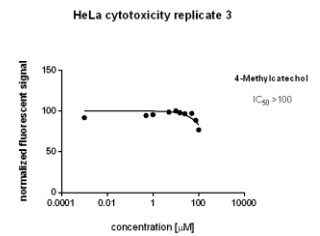
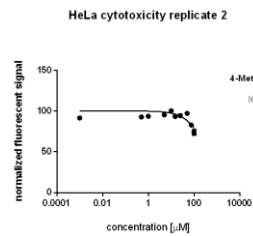
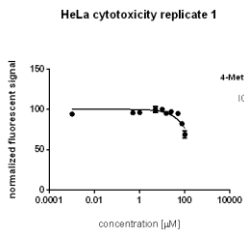
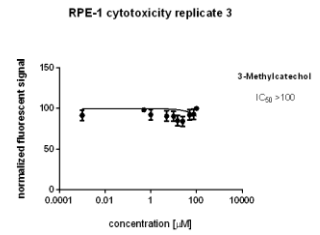
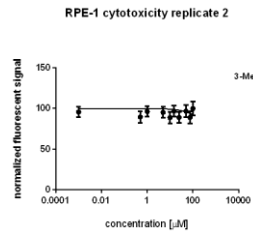
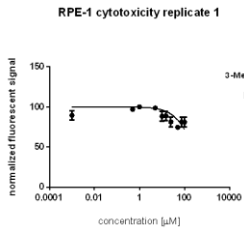


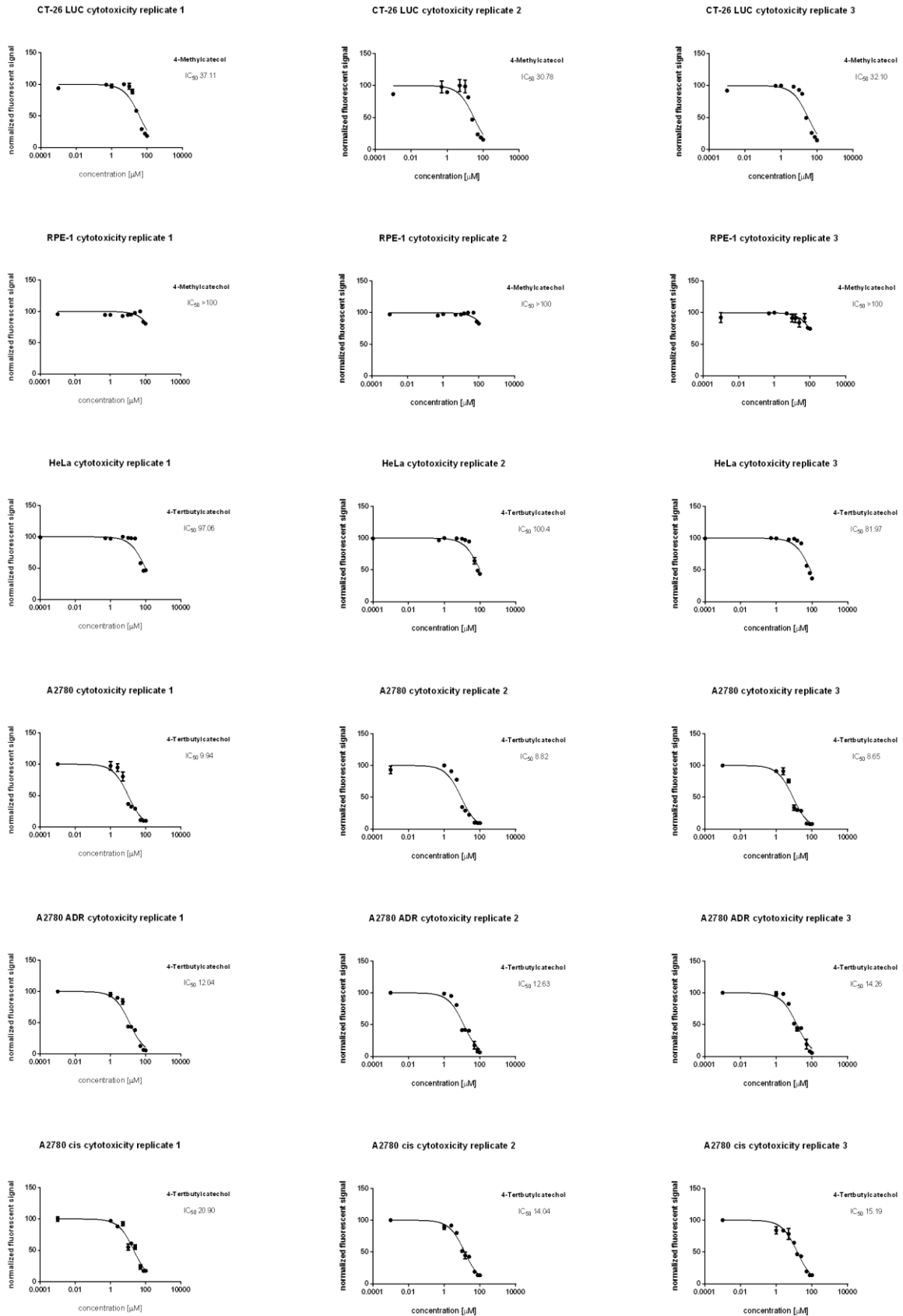


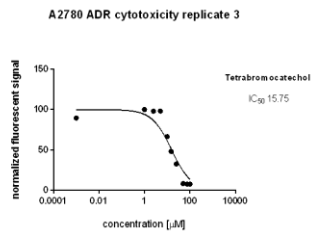
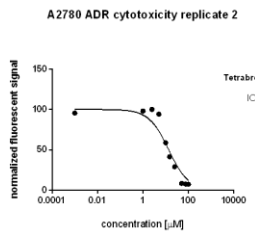
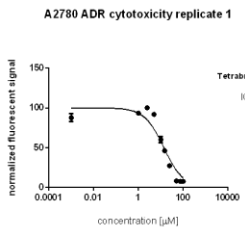
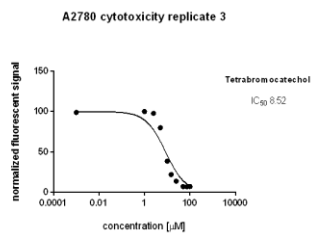
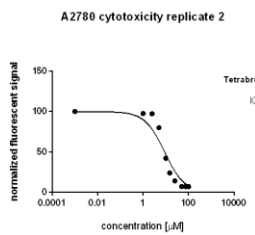
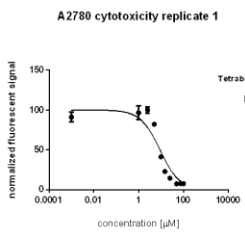
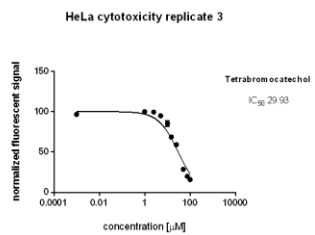
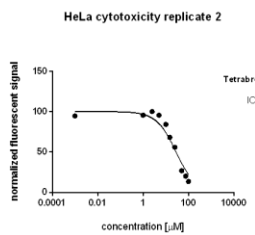
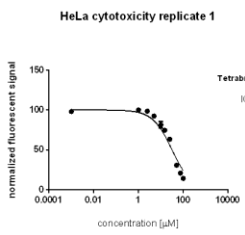
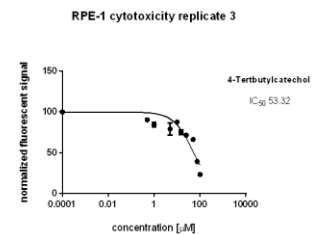
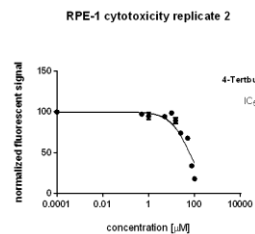
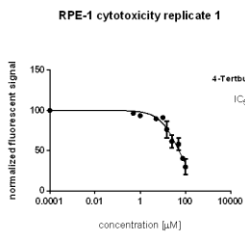
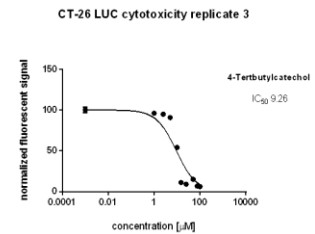
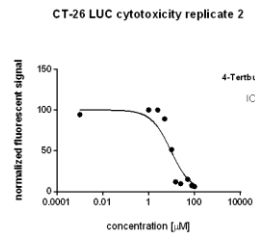
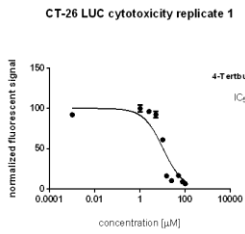
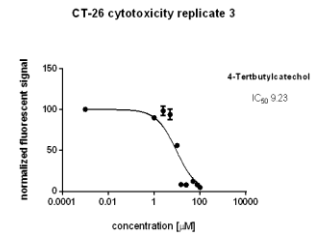
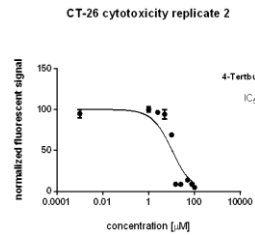
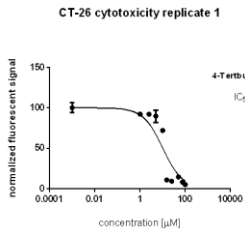


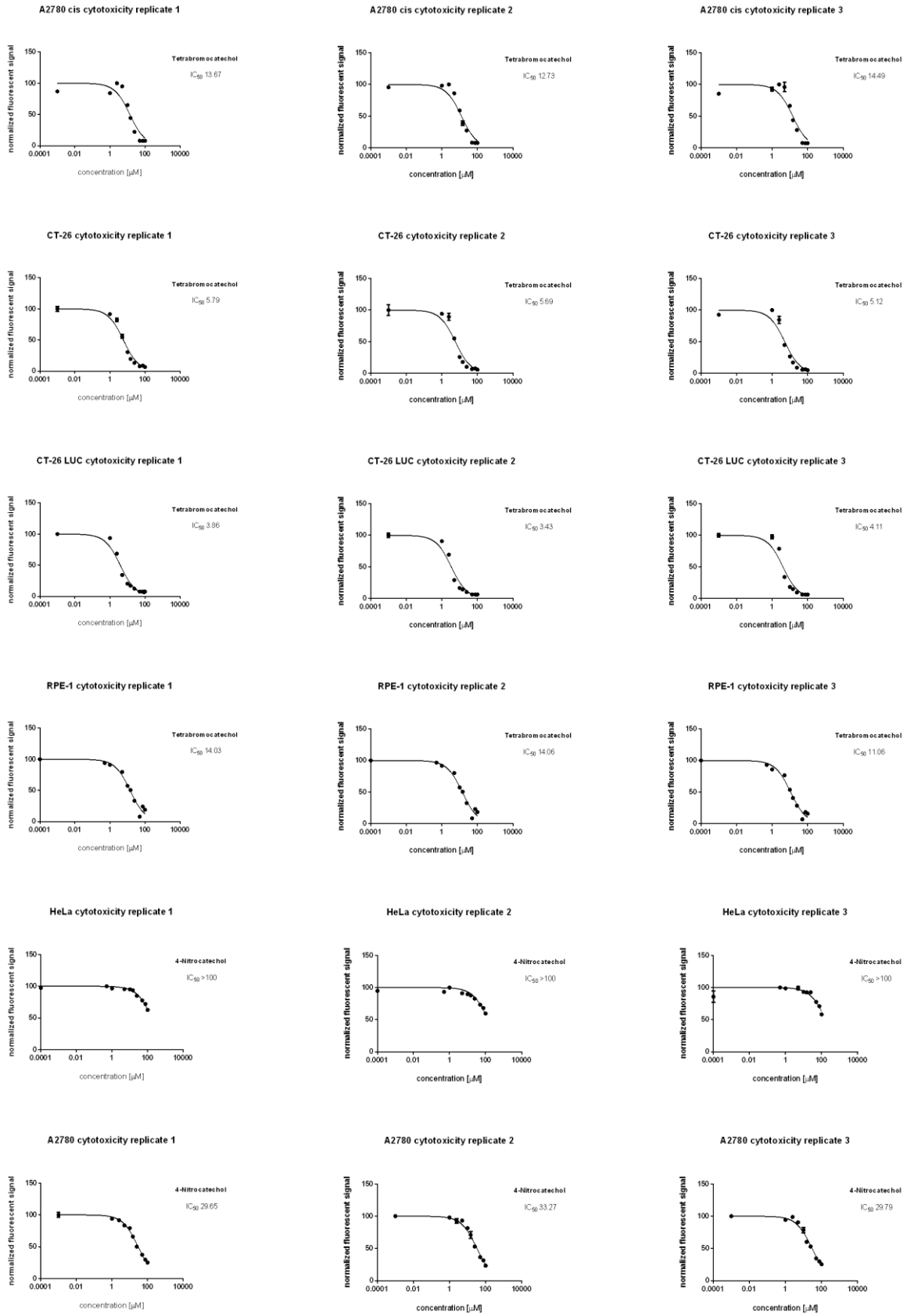


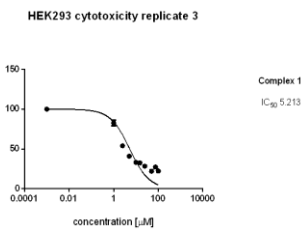
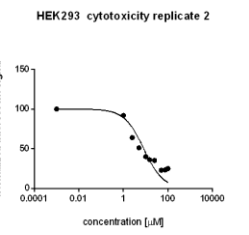
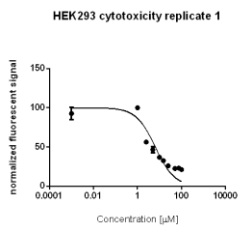
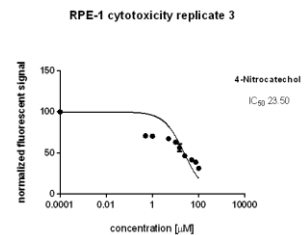
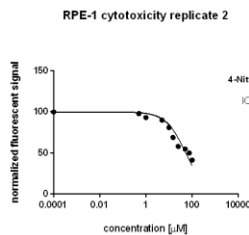
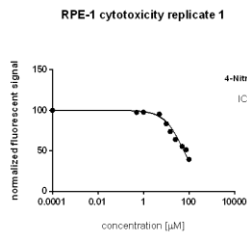
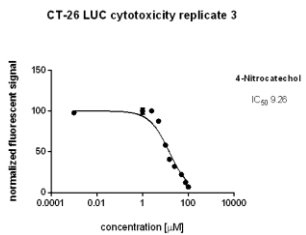
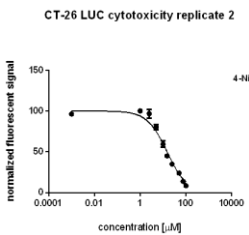
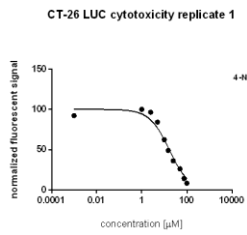
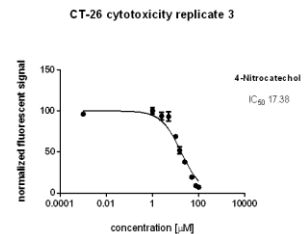
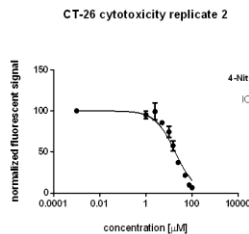
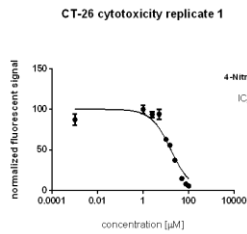
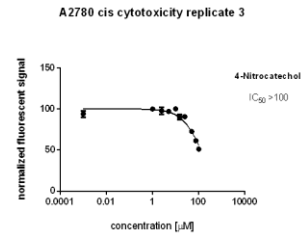
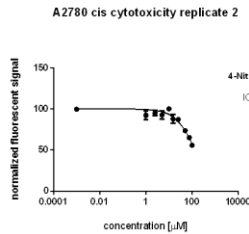
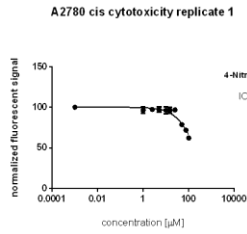
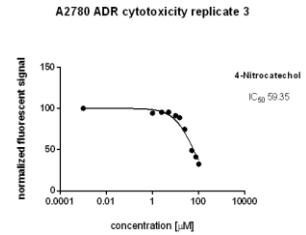
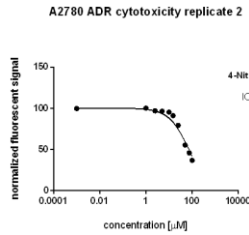
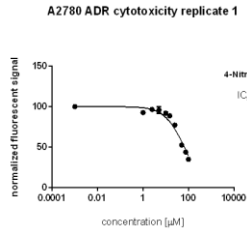


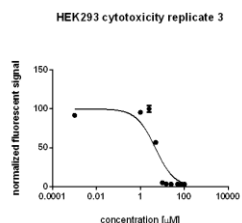
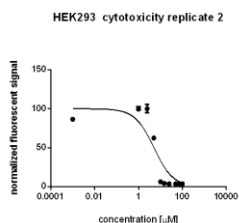
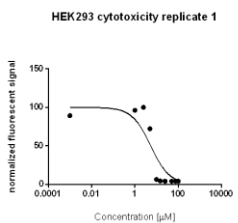
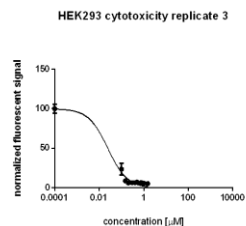
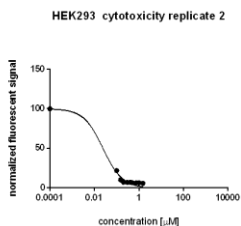
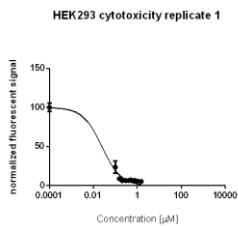
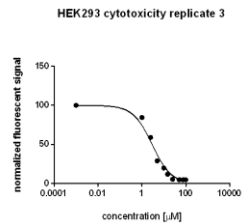
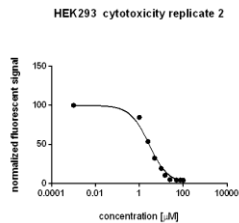
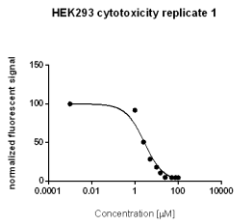
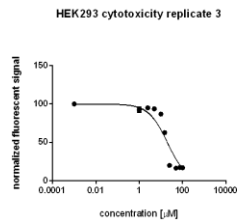
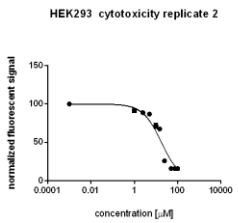
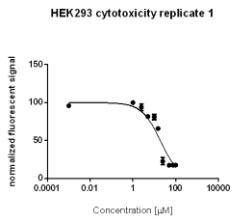
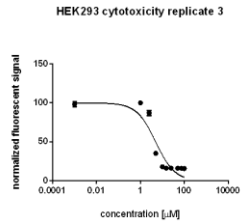
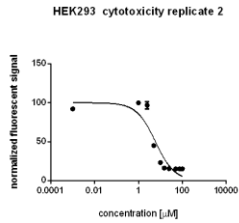
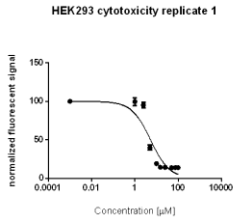
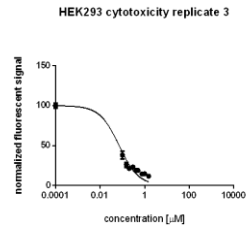
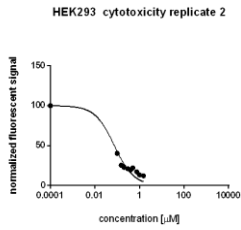
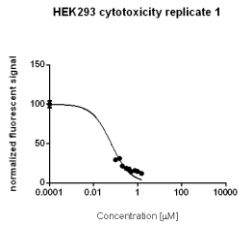












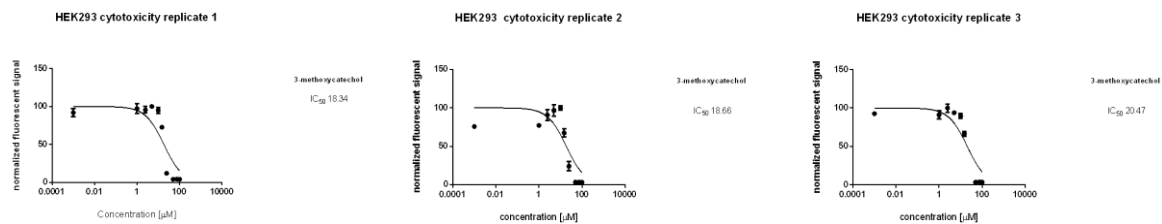


Table S5. IC₅₀ values for 3-methoxycatechol, 3-methylcatechol, 4-methylcatechol, 4-tertbutylcatechol, tetrabromocatechol and 4-nitrocatechol.

IC ₅₀ (μM)	HeLa	A2780	A2780 ADR	A2780 cis	CT-26	CT-26 LUC	RPE-1
3-methoxycatechol	56.19 ± 4.18	18.71 ± 1.17	36.54 ± 1.94	30.07 ± 1.35	45.72 ± 4.21	36.39 ± 6.28	>100
3-methylcatechol	>100	9.99 ± 1.26	14.68 ± 0.69	12.71 ± 0.82	17.47 ± 0.73	12.13 ± 1.40	>100
4-methylcatechol	>100	15.16 ± 1.0	29.27 ± 1.96	34.56 ± 1.49	34.37 ± 1.41	33.33 ± 3.4	>100
4-tertbutylcatechol	93.14 ± 9.8	9.14 ± 0.7	12.89 ± 1.20	16.71 ± 3.67	9.94 ± 0.63	9.72 ± 0.67	55.05 ± 4.64
Tetrabromocatechol	29.95 ± 1.60	8.75 ± 0.20	14.39 ± 1.18	13.63 ± 0.88	5.53 ± 0.37	3.80 ± 0.34	13.5 ± 1.7
4-nitrocatechol	>100	30.90 ± 2.05	65.86 ± 6.62	>100	17.46 ± 1.02	15.31 ± 1.0	45 ± 19

Figure S9. CellTiter Glo® viability Test

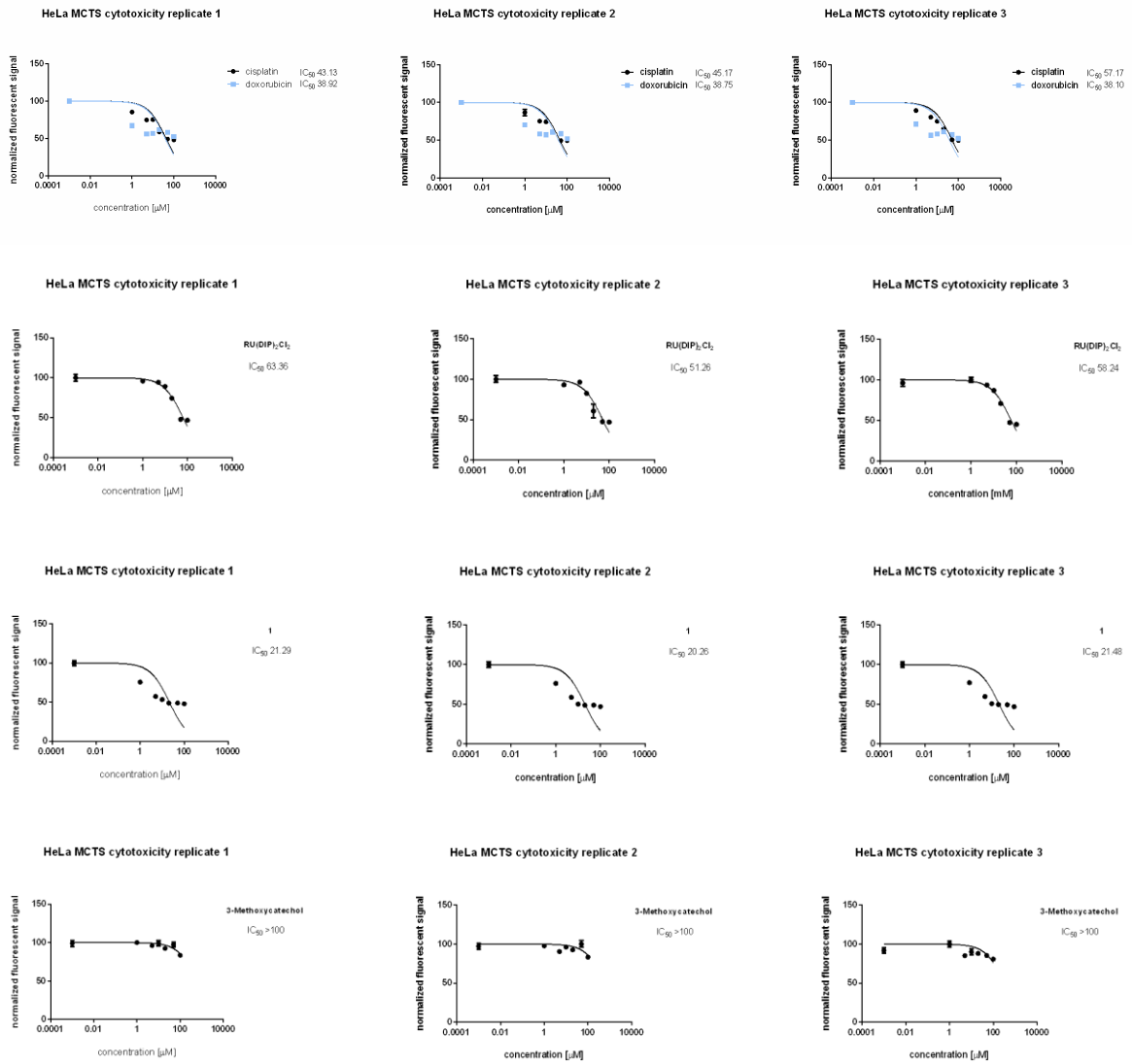
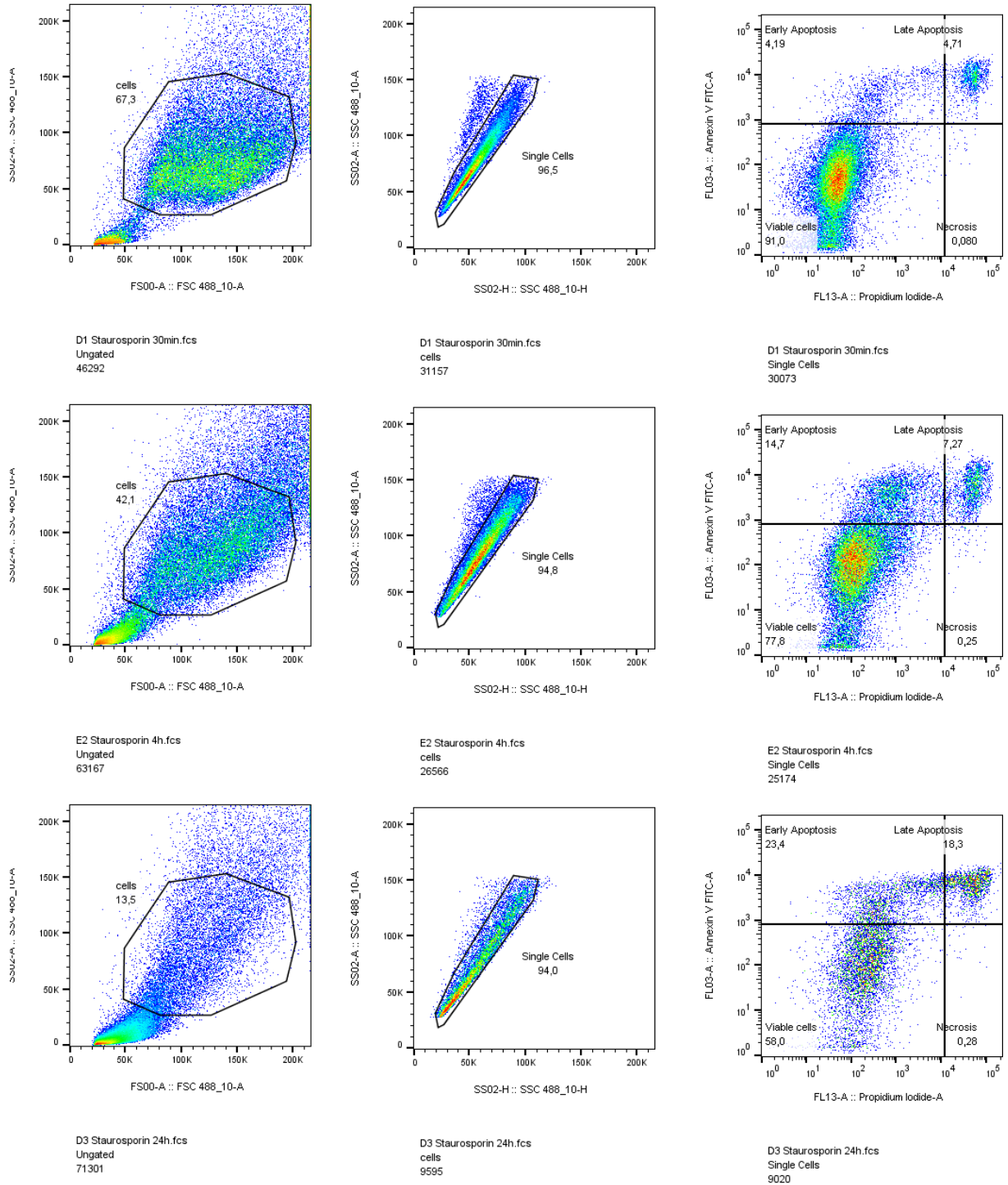


Figure S10. Cell Death Mechanism: Dot plots of staurosporin (a) and complex 1 (b) after 30 min, 4 h and 24 h treatment.

a)



b)

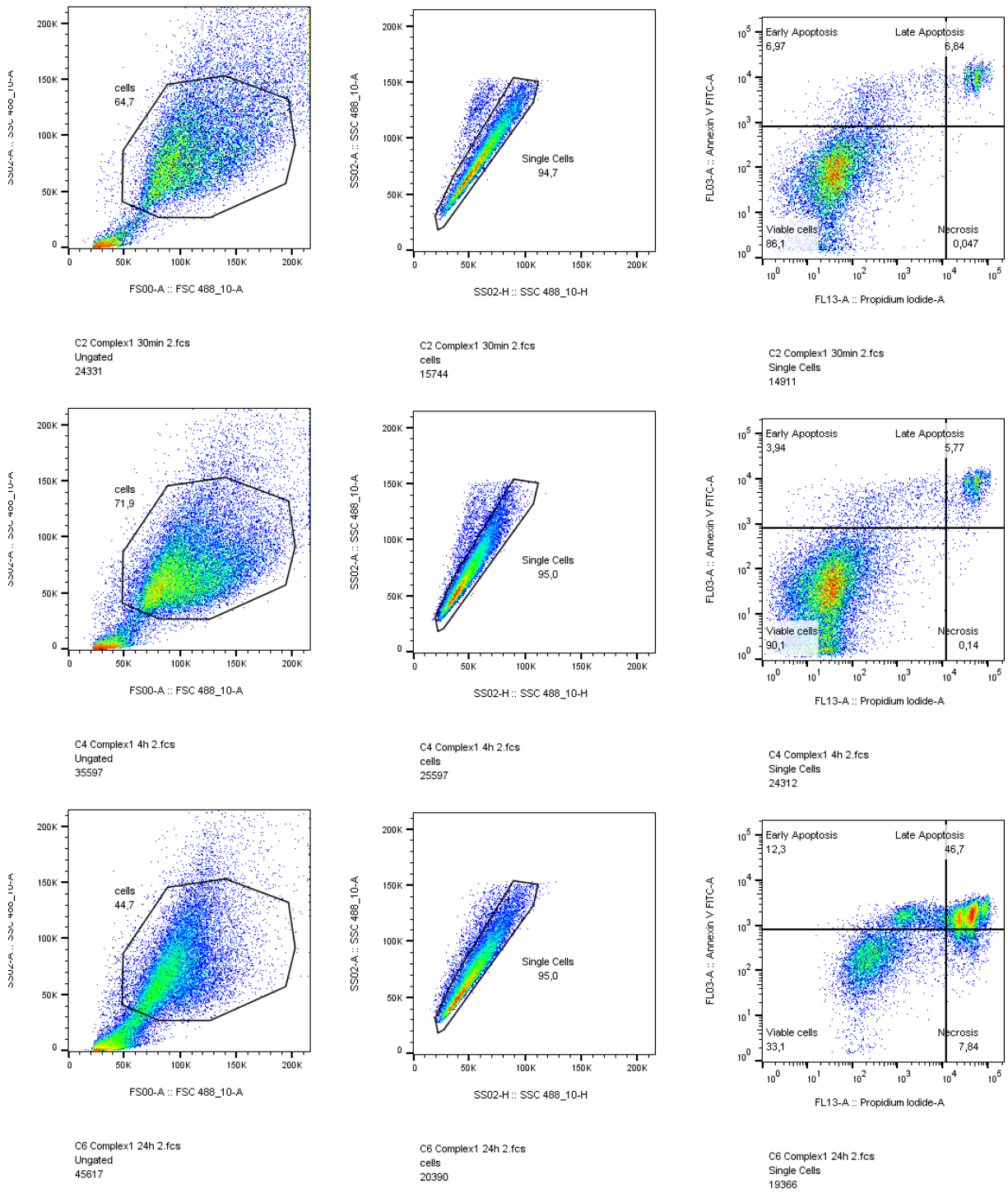


Figure S11. Cellular uptake mechanism of complex **1**. Accumulation of ruthenium in HeLa cells in presence of different inhibitors and conditions: low temperature (4°C), blocked cellular metabolism (2-Deoxy-D-glucose, oligomycin), blocked endocytic pathways (chloroquine or ammonium chloride), blocked cation transporters (tetraethylammonium chloride). Cells were pre-treated with uptake inhibitors and then incubated with **1** (2 h, 5 μ M). Amounts of ruthenium were measured using ICP-MS.

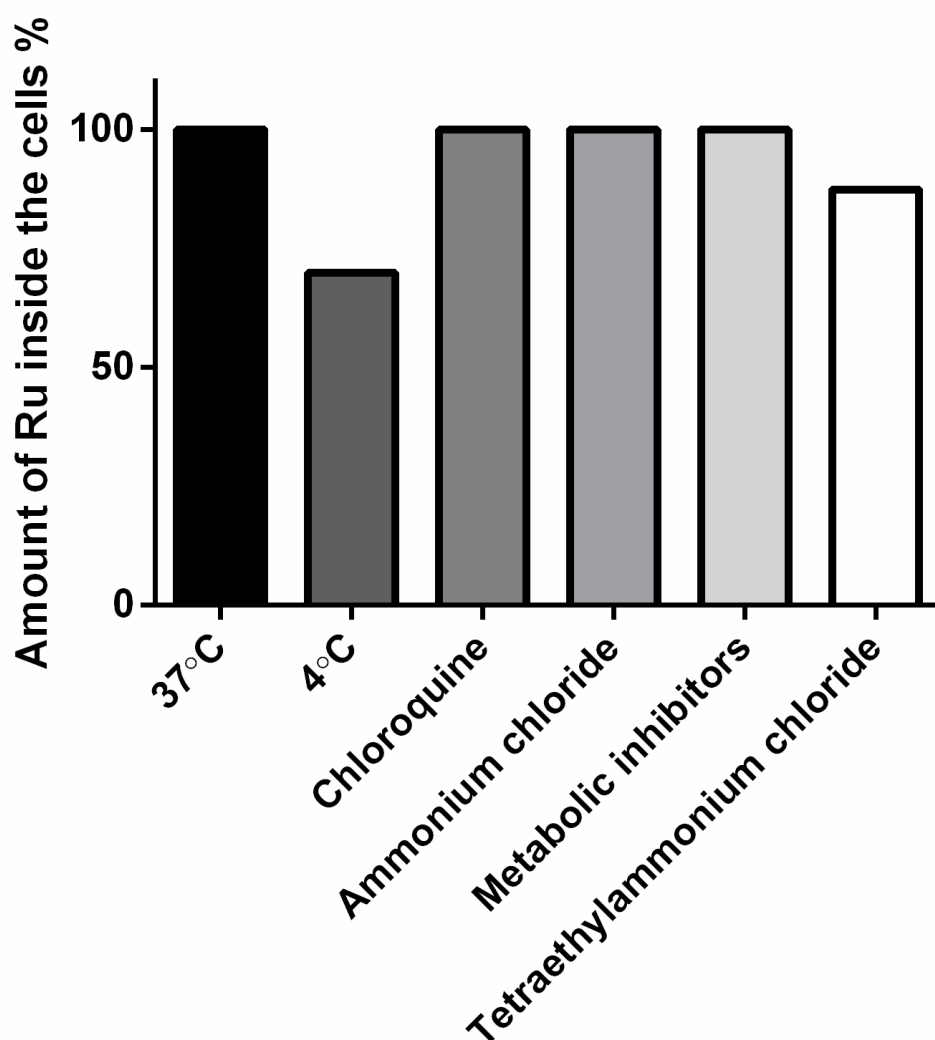


Figure S12. Oxygen consumption rates and different respiration parameters in HeLa cells alone or after treatment with various test compounds.

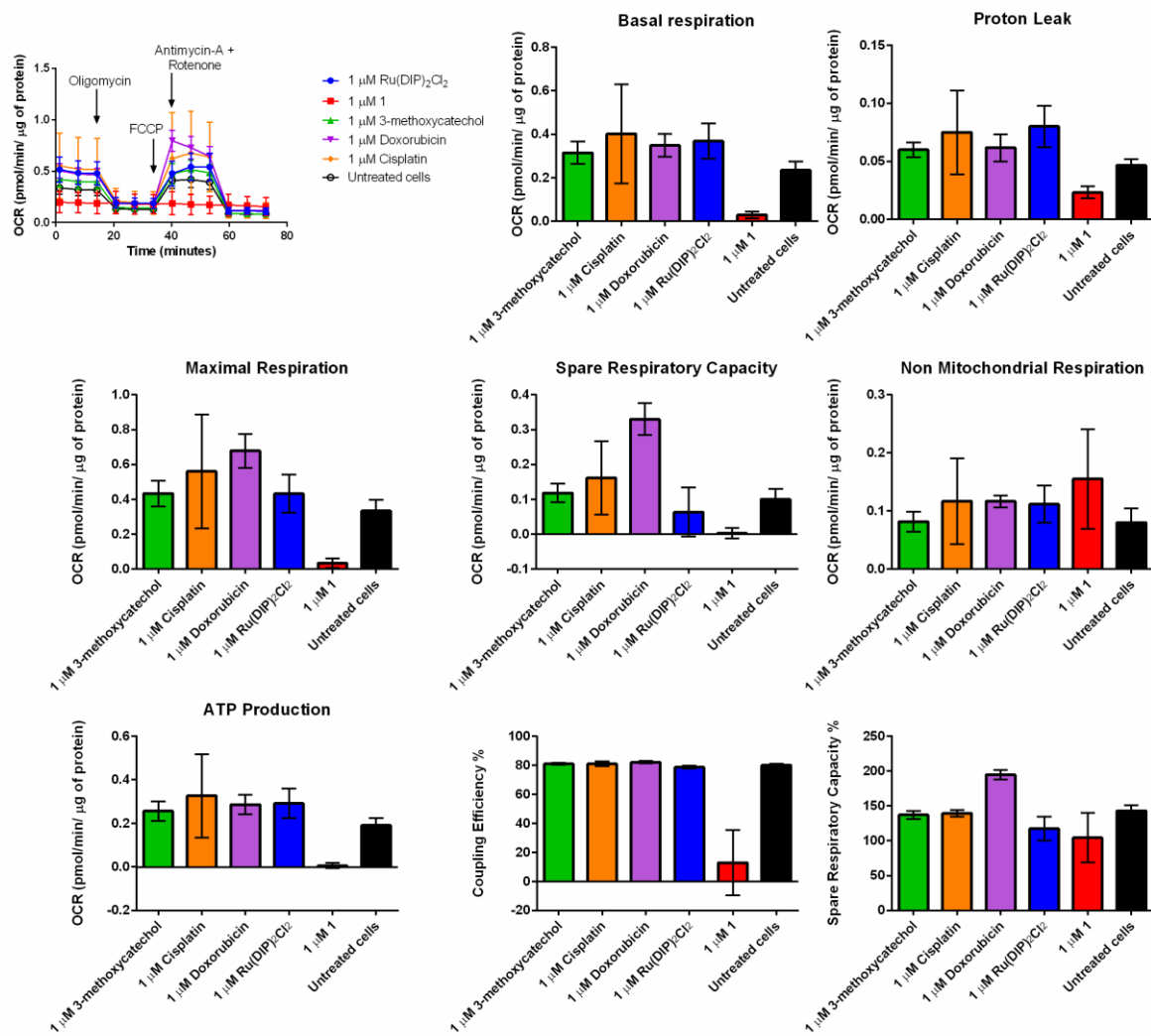


Figure S13. Extracellular acidification rate and different parameters of glycolysis in HeLa cells alone or after treatment with various test compounds.

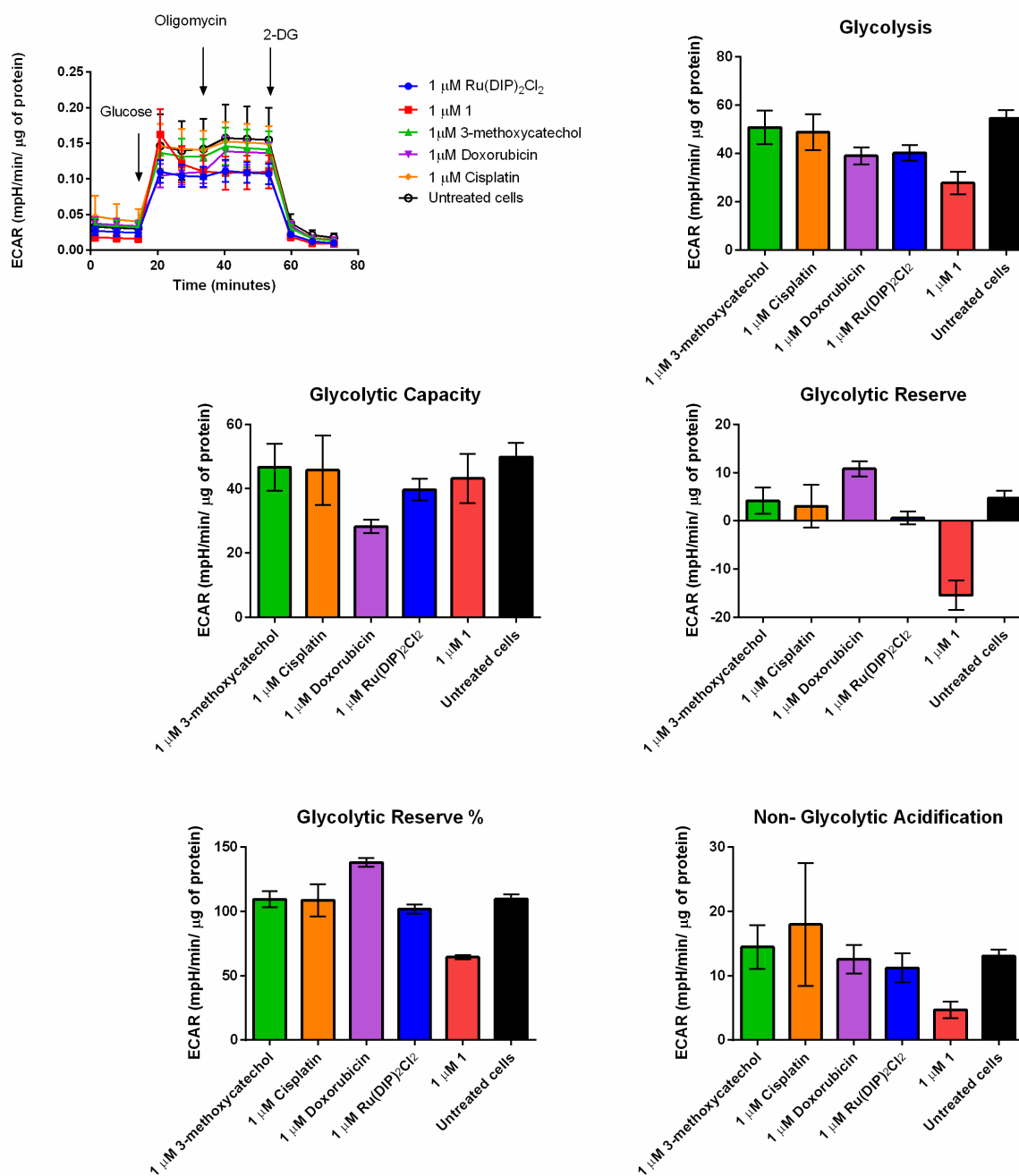
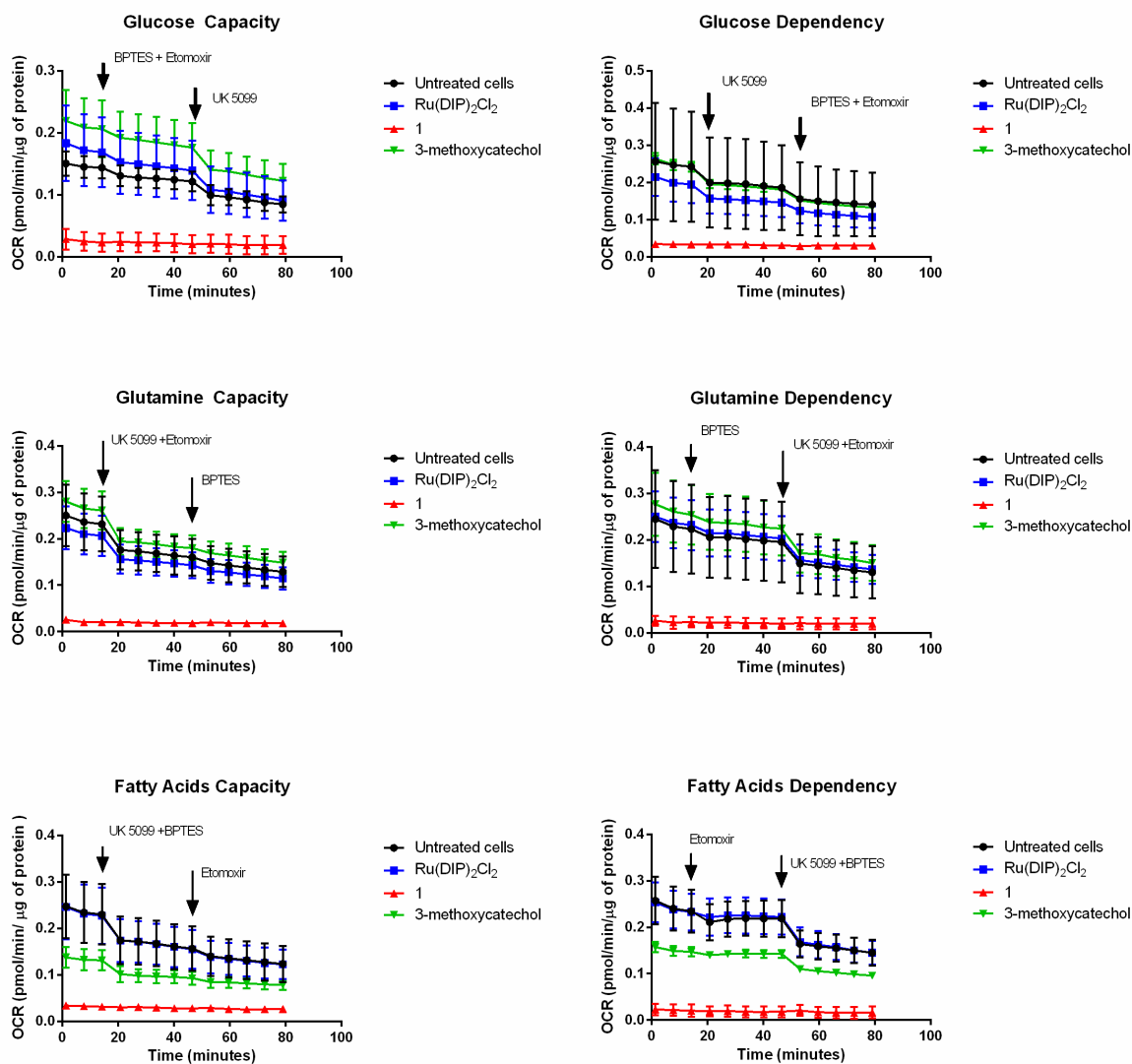


Figure S14. Fuel flex assay in HeLa cells. Dependency studies were performed by adding the inhibitor for the target pathway in port A and inhibitors for the other two pathways in port B while capacity studies were done using the reverse sequence. UK-5099 (20 μM), BPTES (30 μM) and etomoxir (40 μM) were used as the inhibitors for the fuel pathways run by glucose, glutamine and fatty acids.



Chapter 10- Novel Ruthenium (II) Polypyridyl Complexes with Flavonoid Ligands as Anticancer Drug Candidates

Alexandra-Cristina Munteanu,^{a,#} Anna Notaro,^{b,#} Marta Jakubaszek,^{b,c} Joseph Cowell,^b Mickaël Tharaud,^d Bruno Goud,^c Valentina Uivarosi,^a and Gilles Gasser^{b,}*

^a Department of General and Inorganic Chemistry, Faculty of Pharmacy, “Carol Davila” University of Medicine and Pharmacy, 020956 Bucharest, Romania.

^b Chimie ParisTech, PSL University, CNRS, Institute of Chemistry for Life and Health Sciences, Laboratory for Inorganic Chemical Biology, F-75005 Paris, France.

^c Institut Curie, PSL University, CNRS UMR 144, Paris, France.

^d Université de Paris, Institut de Physique du Globe de Paris, CNRS, F-75005 Paris, France.

these authors have contributed equally to the work

* Corresponding author: E-mail: gilles.gasser@chimeparistech.psl.eu; WWW: www.gassergroup.com; Phone: +33 1 44 27 56 02 Bruno Goud: 0000-0003-1227-4159

Valentina Uivarosi: 0000-0002-7165-5069

Gilles Gasser: 0000-0002-4244-5097

Keywords: Bioinorganic Chemistry, Cancer, Flavonoid, Medicinal Inorganic Chemistry, Ruthenium.

This chapter has been published on 19th of March 2020 on *Inorganic Chemistry* (DOI: 10.1021/acs.inorgchem.9b03562)

Reprinted with permission of American Chemical Society

(<https://pubs.acs.org/doi/abs/10.1021/acs.inorgchem.9b03562>)

Contribution to the publication:

Marta Jakubaszek performed with Anna Notaro 2D cytotoxicity studies. She performed the cellular uptake and the mitochondrial metabolic studies. She wrote the cellular uptake and metabolic studies sections of this paper.

Marta Jakubaszek



19.05.2020

Gilles Gasser



Abstract

Four novel monocationic Ru(II) polypyridyl complexes have been synthesized with the general formula $[\text{Ru}(\text{DIP})_2\text{flv}]\text{X}$, where DIP is 4,7-diphenyl-1,10-phenanthroline, flv stands for the flavonoid ligand (5-hydroxyflavone in $[\text{Ru}(\text{DIP})_2(5\text{-OHF})](\text{PF}_6)$, genistein in $[\text{Ru}(\text{DIP})_2(\text{gen})](\text{PF}_6)$, chrysin in $[\text{Ru}(\text{DIP})_2(\text{chr})](\text{OTf})$, and morin in $[\text{Ru}(\text{DIP})_2(\text{mor})](\text{OTf})$) and X is the counterion, PF_6^- , and OTf^- (triflate, CF_3SO_3^-), respectively. Following the chemical characterisation of the complexes by ^1H and ^{13}C -NMR, mass spectrometry and elemental analysis, their cytotoxicity was tested against several cancer cell lines. The most promising complex, $[\text{Ru}(\text{DIP})_2(\text{gen})](\text{PF}_6)$, was further investigated for its biological activity. Metabolic studies revealed that this complex severely impaired mitochondrial respiration and glycolysis processes, contrary to its precursor, $\text{Ru}(\text{DIP})_2\text{Cl}_2$, which showed a prominent effect only on the mitochondrial respiration. In addition, its preferential accumulation in MDA-MB-435S cells (a human melanoma cell line previously described as mammary gland/breast; derived from metastatic site: pleural effusion), that are used for the study of metastasis, explained the better activity in this cell line compared to MCF-7 (human, ductal carcinoma).

Introduction

Cancer, listed as a chronic degenerative non-communicable disease by the World Health Organization (WHO), is a leading cause of death worldwide.¹ Despite the clinical success of several platinum-based drugs (e.g., cisplatin, carboplatin and oxaliplatin)-² their efficacy is impeded by intrinsic and acquired resistance, and dose-limiting toxicity.³ Therefore, the search for more effective therapeutic strategies has led to the development of other metal complexes with anticancer properties.⁴ Ruthenium (Ru)-based compounds have emerged as potential anticancer drug candidates due to their unique physico-chemical and biological properties,⁵⁻⁸ generally lower systemic toxicity (in animal models) and higher cellular uptake compared to platinum complexes.⁵ NAMI-A,^{9,10} KP1019^{11,12} and its water-soluble sodium salt IT-139 (formerly KP1339)¹³ are Ru complexes that have been evaluated in clinical trials as chemotherapeutic agents for the treatment of cancer. NAMI-A is an antimetastatic drug candidate with diverse mechanisms of action.¹⁴⁻¹⁷ Unfortunately, during a phase I/II study, its clinical activity was found to be disappointing, which led to the discontinuation of the trials. These poor results were mainly attributed to dose-limiting adverse events associated with the treatments.¹⁰

Therefore, current trends in the development of novel Ru-based anticancer drug candidates aim to meet the need for more efficient treatments and improved toxicological profiles for the emergent drugs. For instance, Ru(II) polypyridyl complexes have shown great potential,^{18,19} finding applications in tumour diagnosis,²⁰ as antineoplastic agents^{19,21} or photosensitizers for PDT.^{22,23} The most successful compound bearing a Ru(II) polypyridyl scaffold, TLD-1433,²⁴ has recently entered phase II clinical studies as a photosensitizer for intravesical photodynamic therapy (PDT) against bladder cancer.^{25,26}

Moreover, very interesting results have been found for heteroleptic complexes of Ru(II), bearing an *O,O*-chelating ligand. For instance, RAPTA complexes with curcuminoid ligands (IC_{50} values $\leq 1 \mu M$) displayed novel binding modes with biomolecular targets and high, cancer cell selective activity.²⁷ In addition, $Ru^{II}(\eta^6\text{-}p\text{-cymene})$ complexes with flavonol-derived ligands were found to have potent cytotoxic activity against several human cancer cell lines, with IC_{50} values in the low micromolar range.²⁸

These recent discoveries have prompted us towards the study of the therapeutic potential of Ru(II)-polypyridyl complexes with the flavonoids shown in Figure 1, as *O,O*-chelating ligands. Flavonoids are a naturally occurring subclass of polyphenols, with high structural versatility.²⁹ They have been extensively studied in the design of novel anticancer drug candidates. As a result, two derivatives of the flavonoid chrysin (Figure 1), namely flavopiridol and P276-00, have entered clinical trials.^{30,31} Although not yet fully understood, the cytotoxic activity of flavonoids is believed to rely upon the modulation of cellular processes that include proliferation, differentiation, apoptosis, metastasis and oxidative stress.^{29,32,33} Moreover, naturally occurring flavonoid aglycons display exceptionally low, if any, systemic toxicity. It should be noted, however, that the absence of acute toxic effects is related to their low water solubility and bioavailability.^{34,35}

The present work focuses on the synthesis of four novel monocationic Ru(II)-polypyridyl complexes with the general formula $[Ru(DIP)_2flv]X$, where DIP is 4,7-diphenyl-1,10-phenanthroline, flv stands for the flavonoid ligand (5-hydroxyflavone in $[Ru(DIP)_2(5-OHF)](PF_6)$, genistein in $[Ru(DIP)_2(gen)](PF_6)$, chrysin in $[Ru(DIP)_2(chr)](OTf)$, and morin in $[Ru(DIP)_2(mor)](OTf)$) and X is the counterion (PF_6^- or OTf^- (triflate)). Following the successful synthesis and characterisation, the antiproliferative activity of the complexes was tested against

different cell lines. For the most potent compound of the series, metabolic studies were performed and compared with the **Ru(DIP)₂Cl₂** precursor.

Results and Discussion

Synthesis and characterization of the Ru(II) complexes

The synthesis of the Ru(II) complexes was achieved in a 2-step process for [**Ru(DIP)₂(5-OHF)**](PF₆), a 3-step process for [**Ru(DIP)₂(gen)**](PF₆) and [**Ru(DIP)₂(chr)**](OTf) and a 4-step process for [**Ru(DIP)₂(mor)**](OTf), respectively (Scheme 1). Briefly, RuCl₂(dmsO)₄³⁶, DIP and LiCl were refluxed in DMF to afford **Ru(DIP)₂Cl₂** in a 72% yield after precipitation with acetone.³⁷ **Ru(DIP)₂Cl₂** was then refluxed in a nitrogen atmosphere for 1.5-2 hours with the appropriate flavonoid in the presence of sodium ethoxide in dry ethanol. Complexes [**Ru(DIP)₂(5-OHF)**](PF₆) and [**Ru(DIP)₂(gen)**](PF₆) (25% and 13%, respectively) were obtained after precipitation with a large excess of NH₄PF₆ and further purification. Complexes [**Ru(DIP)₂(chr)**](OTf) and [**Ru(DIP)₂(mor)**](OTf) (16% and 35%, respectively) were obtained *via* a ruthenium triflate intermediate. Briefly, **Ru(DIP)₂Cl₂** and silver triflate were stirred to afford [Ru(DIP)₂(OTf)₂], and the appropriate flavonoid was added after filtration of AgCl in the presence of sodium ethoxide.

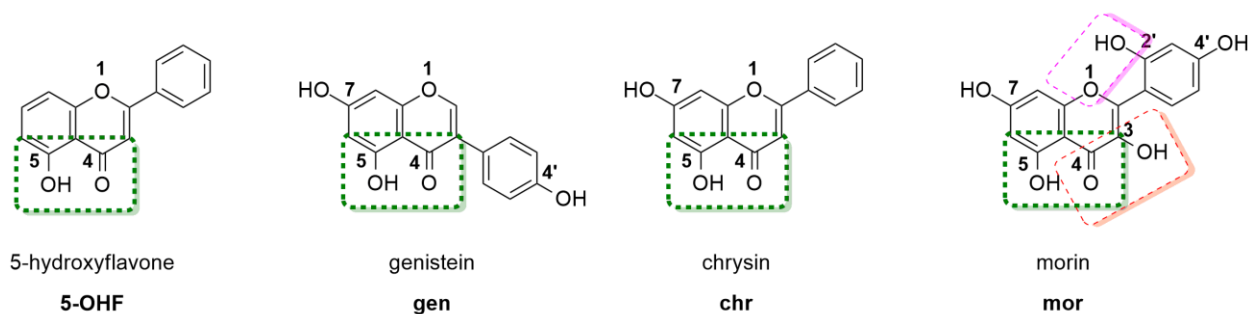
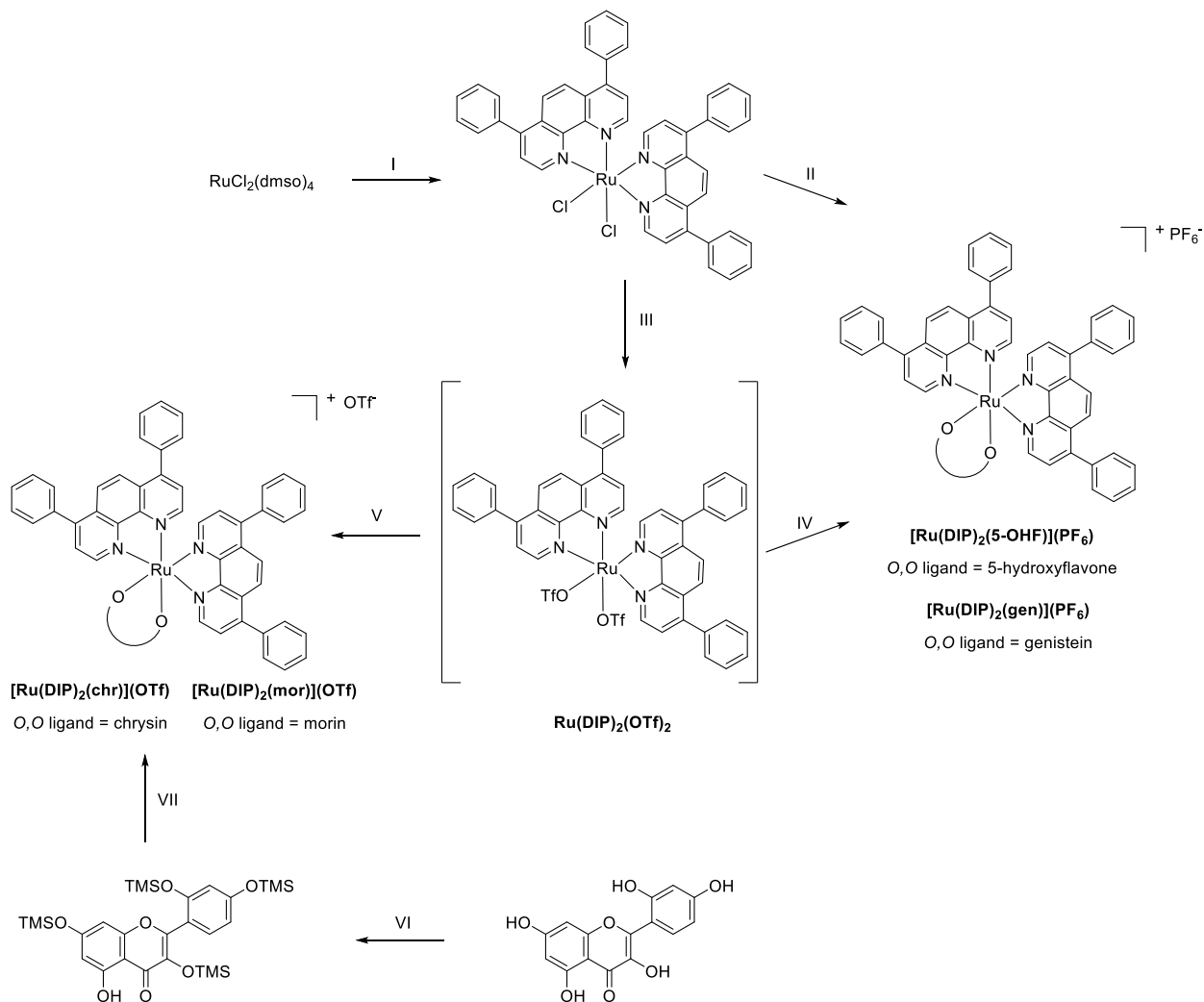


Figure 1. Chemical structures of flavonoids 5-hydroxyflavone, chrysin, genistein and morin.

Worthy of note, morin bears three possible coordination sites (Figure 1) and literature data suggests that the preferred binding site of metal ions to morin is the 3,4-*O,O* site.^{38–41} Therefore, in order to allow for comparison to the Ru(II) complexes of 5-OHF, genistein and chrysin, where the flavonoids coordinate *via* the 4,5-*O,O* site, the selective protection of the oxygen atoms at the 3, 7, 2' and 4' positions was necessary.



Scheme 1. Synthesis of complexes of the type [Ru(DIP)₂(flv)]X, where flv = flavonoid and X = counterion. I) DIP, LiCl, DMF, reflux, 24 h, 78%. II) (i) NaOH, 5-hydroxyflavone, ethanol, reflux, 2 h; (ii) NH₄PF₆, ethanol/H₂O (1:10), 25%. III) (i) silver triflate, ethanol, RT, 1h. IV) sodium ethoxide, genistein, ethanol, reflux, 2 h; (ii) NH₄PF₆, ethanol/H₂O (1:10), 13%. V) sodium

ethoxide, chrysin, ethanol, reflux, 2 h, 16%. VI) NEt_3 , TMSBr , THF, RT, 1h. VII) sodium ethoxide, $\text{Ru(DIP)}_2(\text{OTf})_2$, ethanol, reflux, 2 h, 35%.

Therefore, the synthesis of $[\text{Ru(DIP)}_2(\text{mor})](\text{OTf})$ involved an additional protection step shown in Scheme 1. Following a similar procedure to Qi *et al.*,⁴² the selective protection at the 2', 4', 3 and 7 positions with trimethylsilyl (TMS) protecting group was achieved. The protection step was performed in the presence of triethylamine and TMS-Br in THF and, following an aqueous work-up, the protected morin was used in the complexation step without any further purification. The complexation reaction was performed as described above. Interestingly, during the course of the complexation reaction, the TMS protecting groups were hydrolysed, negating the need for a deprotection step. Following the successful synthesis of $[\text{Ru(DIP)}_2(\text{mor})](\text{OTf})$, coordination at the 4, 5-*O,O* site was confirmed by 1D and 2D NMR studies. It was noticed during the course of the NMR experiments that $[\text{Ru(DIP)}_2(\text{mor})](\text{OTf})$ exists as a mixture of two isomers in solution. The second isomer is presumed to be the result of the morin binding *via* the 3,4-*O,O* site. The rate of isomerisation between the two isomers, however, is slow, with approximately 25% of the 3,4-*O,O* complex being visible by ^1H NMR after 5 days in solution (Figure S5). It should be noted that $[\text{Ru(DIP)}_2(\text{mor})](\text{OTf})$ is stable if stored as a powder at $-20\text{ }^\circ\text{C}$ for over 6 months.

The identity of the compounds was confirmed by ESI-MS and NMR spectroscopy (Figures S1-S9) and their purity confirmed by microanalysis. All complexes are chiral and were isolated as a racemic mixture of Δ and Λ enantiomers. No attempt to obtain enantiopure complexes was made in this work. All four complexes are stable in the solid state and soluble in methanol, DCM, DMSO, DMF and moderately soluble in acetone, acetonitrile. Since the stability and aggregation of metal-based drug candidates is an important parameter, stability studies were undertaken.⁴³⁻⁴⁵

Preliminary studies (Figures S10-S13) showed that $[\text{Ru(DIP)}_2(\text{5-OHF})](\text{PF}_6)$,

[Ru(DIP)₂(gen)](PF₆), and **[Ru(DIP)₂(chr)](OTf)** are stable in DMSO over 5 days. The stability of **[Ru(DIP)₂(mor)](OTf)**, on the other hand, was tested in DMF due to the slower isomerisation rate when compared to DMSO. Taking this into account, NMR analysis in DMF over 5 days shows no degradation of the product (Figure S13).

Cytotoxicity, cellular uptake and metabolic studies

The biological activity of the complexes was tested on MDA-MB-435S (human, melanoma), FaDU (human, pharynx carcinoma), MCF-7 (human, ductal carcinoma), U87 (human, glioblastoma), RPE-1 (human, normal retinal pigmented epithelium) and HEK293 (human embryonic kidney) cell lines using a fluorometric cell viability assay.⁴⁶ Cisplatin and doxorubicin were tested in the same conditions as positive controls.^{47,48} **Ru(DIP)₂Cl₂** as well as the flavonoids 5-hydroxyflavone, genistein, chrysin and morin were used as additional controls. The IC₅₀ (half maximal inhibitory concentration) values obtained in this study are reported in Table 1 (all cytotoxicity graphs are available in Figure S14).

Table 1. IC₅₀ values for flavonoid ligands, cisplatin, doxorubicin, **[Ru(DIP)₂(5-OHF)](PF₆)**, **[Ru(DIP)₂(gen)](PF₆)**, **[Ru(DIP)₂(chr)](OTf)**, **[Ru(DIP)₂(mor)](OTf)**, and **Ru(DIP)₂Cl₂** in different cell lines (48 h treatment).

Compounds	IC ₅₀ (μM)					
	MCF-7	FaDU	MDA-MB-435S	U87	RPE-1	HEK293
5-Hydroxyflavone	>100	>100	>100	>100	>100	>100
Genistein	>100	>100	>100	>100	>100	75.85 ± 0.84

Chrysin	62.59 ± 3.23	95.06 ± 11.55	± 79.37 ± 8.13	91.14 ± 13.76	± >100	26.80 ± 2.79
Morin	>100	>100	>100	>100	>100	>100
Cisplatin	19.69 ± 1.63	5.17 ± 0.21	17.62 ± 0.54	6.94 ± 0.46	39.9 ± 9.14	2.27 ± 0.67
Doxorubicin	9.39 ± 1.37	1.55 ± 0.18	5.55 ± 1.37	0.59 ± 0.03	14.9 ± 1.31	0.21 ± 0.03
Ru(DIP) ₂ Cl ₂	>50	>50	27.73 ± 5.33	25.59 ± 0.29	± 3.13 ± 0.28	12.11 ± 1.30
[Ru(DIP) ₂ (5-OHF)](PF ₆)	>50	38.21 ± 5.22	± 24.48 ± 1.92	30.72 ± 1.48	± 19.72 ± 8.23	26.46 ± 3.20
[Ru(DIP) ₂ (gen)](PF ₆)	16.67 ± 3.93	5.21 ± 0.73	2.64 ± 0.43	5.21 ± 1.74	2.36 ± 0.77	0.72 ± 0.10
[Ru(DIP) ₂ (chr)](OTf)	>50	>50	27.73 ± 5.33	25.59 ± 0.29	± 23.21 ± 8.08	33.02 ± 3.25
[Ru(DIP) ₂ (mor)](OTf)	>50	>50	>50	>50	>50	>50

The literature cites good to excellent cytotoxic activity for other 5-hydroxyflavone, chrysin and morin metal complexes,^{41,49–52} results that prompted us to the design of these compounds. Worthy of note, complexes of morin (bound *via* the 3,4-*O,O* site) and chrysin bearing a Ru(II) polypyridyl scaffold have been previously reported. Their cytotoxic activity was studied on HeLa (cervical carcinoma), SW620 (colorectal adenocarcinoma, metastatic), HepG2 (hepatocellular carcinoma) and MCF-7 cell lines with IC₅₀ values ranging from 7.64 to >100 μM.⁴¹ **[Ru(DIP)₂(mor)](OTf)**, however, was found to be essentially non-toxic, with IC₅₀ values above 50 μM in all the cell lines tested, while **[Ru(DIP)₂(5-OHF)](PF₆)** and **[Ru(DIP)₂(chr)](OTf)** exerted moderate toxicity towards some of the cell lines tested. Interestingly, the most promising complex identified in this study is the complex bearing the flavonoid genistein, (**[Ru(DIP)₂(gen)](PF₆)**), with IC₅₀ values comparable to those of both cisplatin and doxorubicin. Genistein is considered a suitable lead for

anticancer drug development and derivatives have been synthesised in order to enhance its cytotoxic activity.^{53–57} It should be stated that among all chemical derivatives of genistein, only scarce data exists regarding its metal complexes. For instance, a homoleptic copper (II) genistein complex was reported to enhance the cytotoxic activity of the ligand against four cancer cell lines, like the 518A2 melanoma and MCF-7/Topo breast carcinoma cell lines.⁵² Unfortunately, **[Ru(DIP)₂(gen)](PF₆)** exerted no selectivity between cancerous and non-cancerous cell lines with comparable IC₅₀ values. However, this drawback is commonly faced in medicinal chemistry and could be improved by the introduction of a targeting moiety.

[Ru(DIP)₂(gen)](PF₆) showed good activity towards the MDA-MB-435S cell line, with an IC₅₀ of 2.64 μM. Currently, this cell line is identified as a melanoma cell line, which derives from the pleural effusion of a 31-year-old female with metastatic, ductal adenocarcinoma of the breast and considered still valuable for the study of metastasis.^{58,59} The lower activity expressed by the complex towards the MCF-7 cell line (IC₅₀=16.67 μM) led us to study the cellular uptake and mechanism of uptake of this complex in two different cell lines derived from breast tissue. In these experiments, cells were treated with 5 μM of **[Ru(DIP)₂(gen)](PF₆)** for 2 h and the metal content was analysed *via* inductively coupled plasma mass spectrometry (ICP-MS). Cisplatin and **Ru(DIP)₂Cl₂** were tested in the same conditions as controls. The viability of the cells after 2 h treatment was additionally tested, confirming that the acquired results were obtained from living cells (Figure S14). Figure 2a shows that the cellular uptake is much lower for the MCF-7 cell line when compared to MDA-MB-435S for all of the tested compounds. Interestingly, **Ru(DIP)₂Cl₂** accumulates more in MDA-MB-435S compared to **[Ru(DIP)₂(gen)](PF₆)**, in the same cell line, but shows lower cytotoxicity than the flavonoid complex. This observation can be rationalised by the explanation provided by Policar *et al.* in 2014 where they state that IC₅₀ is a resultant value of

cellular uptake, interaction with cellular target and its intrinsic toxicity.⁶⁰ Therefore, one could argue that the higher activity expressed by **[Ru(DIP)₂(gen)](PF₆)** towards MDA-MB-435S when compared to MCF-7 cells, comes as a consequence of its higher cellular uptake. To understand the kinetics of the tested compounds in the chosen cell lines, we have performed time dependent accumulation experiments. Ruthenium and platinum content in treated cells was measured by ICP-MS after 2 h, 12 h, 24 h and 48 h. In this analysis, the concentration of the tested compounds was decreased to 1 μ M to reduce cell loss during the experiment. Figures 2b and 2c show the changes in cellular accumulation in the two cell lines tested. The obtained results confirm previous conclusions that all tested compounds accumulate more in the MDA-MB-435S cell line than in MCF-7 cells. After 24 h incubation time, similar uptake of **Ru(DIP)₂Cl₂** and **[Ru(DIP)₂(gen)](PF₆)** was found in MDA-MB-435S (~ 30 ng of metal in 10⁶ cells) in comparison with cisplatin (~ 4 ng of metal in 10⁶ cells). On the other hand, **[Ru(DIP)₂(gen)](PF₆)** accumulates much more in MCF-7 cells than the two other compounds after 24 h (~ 2 ng of metal in 10⁶ cells as compared to ~ 1 ng) and 48 h (~ 5 ng of metal in 10⁶ cells compare to ~ 1 ng). The discrepancy between the amount of metal detected in total accumulation and time dependent accumulation experiments in both cell lines at 2 h time point (shown in Figures 2a, 2b and 2c), can be explained by different mechanisms of uptake of the Ru complexes (see below), and availability of the complex in cellular media (5 times lower concentration of the compounds in the time dependent experiments).

To understand the nature of the mechanism of uptake (passive or active) of the tested complexes, cells were pre-treated with various inhibitors or kept at different temperatures. A temperature of 4 °C was used to slow down passive diffusion, as well as active transportation. To block cellular metabolism, pre-treatments with ATP production inhibitors 2-deoxy-*D*-glucose and oligomycin

were performed. Chloroquine or ammonium chloride (NH_4Cl) impede endocytic pathways and tetraethylammonium chloride stops the cation transporters. Following pre-treatments, cells were incubated with **[Ru(DIP)₂(gen)](PF₆)** or **Ru(DIP)₂Cl₂** (2 h, 5 μM) and subsequently analysed *via* ICP-MS (Figures 2b and 2c).

Inhibition of active uptake mechanisms did not significantly perturb accumulation of **[Ru(DIP)₂(gen)](PF₆)** in both cell lines tested, demonstrating that the mechanism responsible for its accumulation is energy independent (passive). On the other hand, **Ru(DIP)₂Cl₂** is taken up *via* a passive mechanism by the MCF-7 cell line and an active mechanism by the MDA-MB-435S cell line. As shown for other similar ruthenium complexes, this observation indicates that slight changes in lipophilic properties and structure play a decisive role in the cellular uptake of Ru(II) polypyridyl complexes.⁶¹⁻⁶³

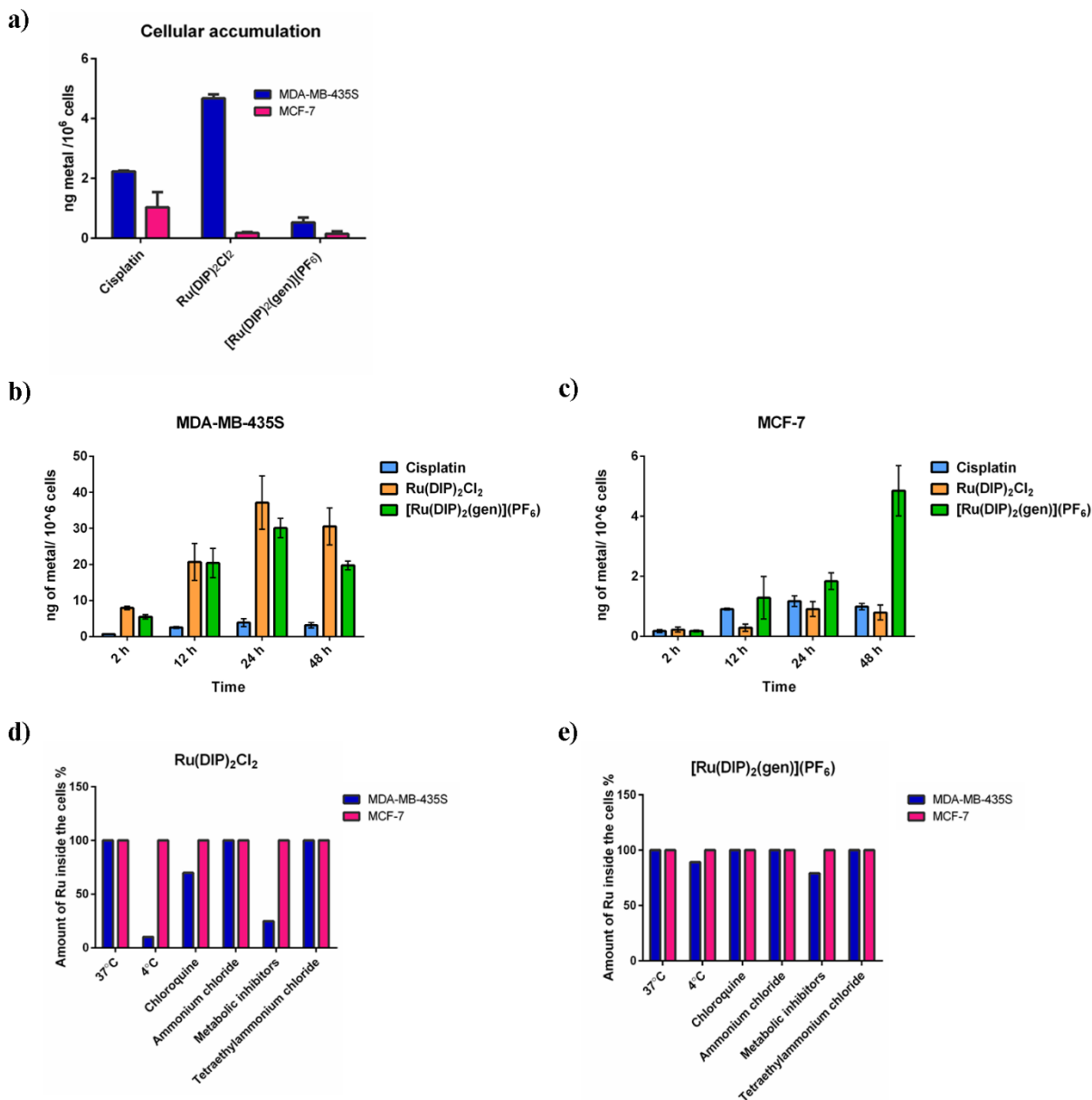


Figure 2. ICP-MS data of cellular uptake of tested compounds in MDA-MB-435S and MCF-7 cell lines. (a) Total cellular accumulation (2 h treatment, 5 μ M) (b) Time dependent cellular accumulation in MDA-MB-435S cell line (c) Time dependent cellular accumulation in MCF-7 cell line (d) Mechanism of cellular uptake of **Ru(DIP)₂Cl₂** in tested cell lines (2 h treatment, 5 μ M) (e) Mechanism of cellular uptake of **[Ru(DIP)₂(gen)](PF₆)** in tested cell lines (2 h treatment,

5 μ M). Data of (a), (d) and (e) is presented as the mean \pm SD of at least 3 technical replicates. Data of (b) and (c) is presented as the mean \pm SD of at least 3 biological replicates

To better understand the effect of the flavonoid complex of interest on the cellular metabolism of MDA-MB-435S cells, a Seahorse XF Analyser was used. This device allows for the real time measurement of the oxygen consumption rate (OCR) and extracellular acidification rate (ECAR) in cells. Firstly, the influence on the oxidative phosphorylation was measured. As shown in Figures 3a and S15, 24 h treatment with the flavonoid complex **[Ru(DIP)₂(gen)](PF₆)** and its precursor **Ru(DIP)₂Cl₂** strongly inhibit mitochondrial respiration. Cells do not respond to the oligomycin injection, which inhibits ATP synthase,⁶⁴ nor to the FCCP which will interfere with the mitochondrial membrane proton gradient.⁶⁵ ATP production, as well as spare respiratory capacity (calculated as the difference between maximal and basal respiration), are extremely low, further confirming non-functioning mitochondria in treated MDA-MB-435S cells.

Next, the effect on the glycolysis process was investigated. Figures 2b and S16 show interesting differences between the modes of action of **[Ru(DIP)₂(gen)](PF₆)** and **Ru(DIP)₂Cl₂**. During the glycolysis stress test the first injection is made with a saturated solution of glucose. This treatment should trigger the glycolysis process in cells and consequently lead to higher ECAR. Surprisingly, MDA-MB-435S cells treated with **[Ru(DIP)₂(gen)](PF₆)** showed no increase in ECAR values following injection of the saturated glucose solution. This observation is a clear indication of the impaired glycolytic process. On the other hand, cells treated with **Ru(DIP)₂Cl₂** showed similar glycolysis levels when compared to those of the untreated cells. This suggests that the cytosolic process of ATP production is impaired in **[Ru(DIP)₂(gen)](PF₆)** treated cells, but not in those treated with **Ru(DIP)₂Cl₂**. Furthermore, the lack of response to the oligomycin injection in cells treated with both complexes, agrees with the results obtained *via* the mito stress test, which

suggests non-functioning mitochondria after both treatments. Interestingly, the complexes $[\text{Ru}(\text{DIP})_2(\text{sq})](\text{PF}_6)$, $[\text{Ru}(\text{DIP})_2(\text{mal})](\text{PF}_6)$ and $[\text{Ru}(\text{DIP})_2(3\text{-methoxysq})](\text{PF}_6)$, recently reported by our group, also showed impaired mitochondrial function but did not show any effect on the glycolysis process.^{66–68} This illustrates how subtle structural changes in the complexes bearing the same $\text{Ru}(\text{DIP})_2$ core but different dioxo ligands, can result in significantly different behaviour of the complexes in living cells.

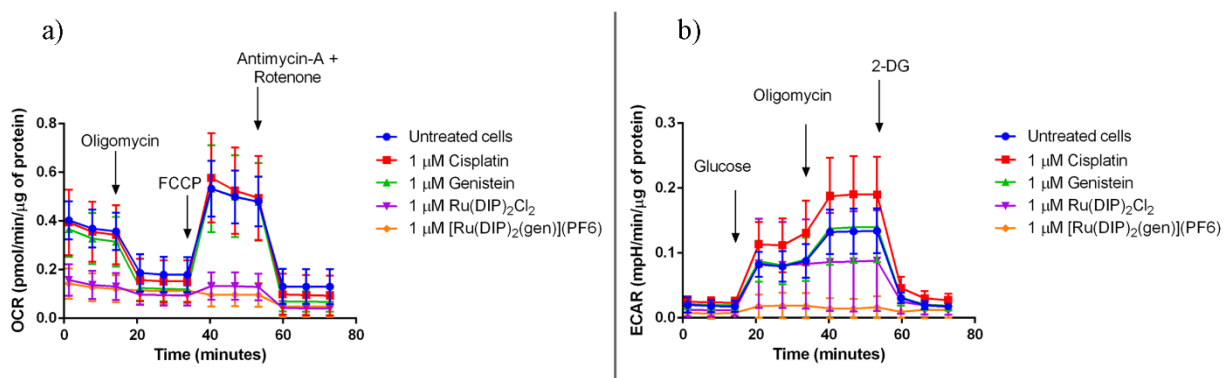


Figure 3. a) Mito Stress Test profile in MDA-MB-435S cells after 24 h treatment. Oxygen consumption rate changes after treatment with specific electron transport chain inhibitors. Oligomycin (inhibitor of ATP synthase (complex V)), FCCP (uncoupling agent), antimycin-A (complex III inhibitor) and rotenone (complex I inhibitor). b) Glycolysis Stress Test profile in MDA-MB-435S cells after 24 h treatment. Extracellular acidification rate that corresponds to the glycolysis process changes after treatment with glucose (basal level of glycolysis in cells), oligomycin (inhibitor of ATP synthase (complex V) - mitochondria inhibition), 2-deoxyglucose (analogue of glucose that inhibits glycolytic pathway).

Conclusions

Briefly, four monocationic Ru(II) polypyridyl complexes with the general formula $[\text{Ru}(\text{DIP})_2\text{flv}]\text{X}$ have been synthesised. The cytotoxicity of these complexes was tested against different cancerous and healthy cell lines and the most promising compound identified is $[\text{Ru}(\text{DIP})_2(\text{gen})](\text{PF}_6)$ with cytotoxicity comparable to that of cisplatin and doxorubicin. The complex displayed good activity towards the MDA-MB-435S cell line ($\text{IC}_{50} = 2.64 \mu\text{M}$), a melanoma cell line derived from the pleural effusion of a female with metastatic breast adenocarcinoma, used for the study of metastasis. Interestingly, genistein was not cytotoxic ($\text{IC}_{50} > 100 \mu\text{M}$) and the precursor, $\text{Ru}(\text{DIP})_2\text{Cl}_2$, was only moderately active ($\text{IC}_{50} = 27.73 \mu\text{M}$). $[\text{Ru}(\text{DIP})_2(\text{gen})](\text{PF}_6)$ was found to be taken up more efficiently by MDA-MB-435S cell lines than MCF-7, a commonly used breast cancer cell line, in both cases *via* a passive transportation mechanism. Further metabolic studies in the MDA-MB-435S cell line revealed that $[\text{Ru}(\text{DIP})_2(\text{gen})](\text{PF}_6)$ not only inhibits mitochondrial respiration, but also interferes with the cytosolic glycolysis process in comparison to $\text{Ru}(\text{DIP})_2\text{Cl}_2$. This result suggests that addition of the flavonoid moiety changes the behaviour of the complex in living cells and allows for a more complex mode of action, leading to cell death. Therefore, we consider $[\text{Ru}(\text{DIP})_2(\text{gen})](\text{PF}_6)$ to be a suitable candidate for further studies, which will aim to identify the cellular targets of the complex and possible interactions with protein transporters. Since the current treatment of advanced melanoma provides modest results, this work may open new opportunities in the search for chemopreventive and/or chemotherapeutic agents for human cancers, especially melanoma.

Experimental Section

Materials

All chemicals were either of reagent or analytical grade and used as purchased from commercial sources without additional purification. Ruthenium trichloride hydrate was provided by I²CNS, 4,7-diphenyl-1,10-phenanthroline, lithium chloride (anhydrous, 99%), the flavonoids and tetrabutylammonium hexafluorophosphate by Sigma-Aldrich. All solvents were purchased of analytical, or HPLC grade. When necessary, solvents were degassed by purging with dry, oxygen-free nitrogen for at least 30 minutes before use. Preparative thin layer chromatography (TLC) glass plates (Analtech, Sigma-Aldrich, Steinheim, Germany, 20 cm × 20 cm; 1500 μm thickness).

Instrumentation and methods

Amber glass or clear glassware wrapped in tin foil were used when protection from the light was necessary. Schlenk glassware and a vacuum line were employed when reactions sensitive to moisture/ oxygen had to be performed under a nitrogen atmosphere. Thin layer chromatography (TLC) was performed using silica gel 60 F-254 (Merck) plates with detection of spots being achieved by exposure to UV light. Eluent mixtures are expressed as volume to volume (v/v) ratios. ¹H and ¹³C NMR spectra were measured on Bruker Avance III HD 400 MHz or Bruker Avance Neo 500 MHz spectrometers using the signal of the deuterated solvent as an internal standard.⁶⁹ The chemical shifts δ are reported in ppm (parts per million) relative to tetramethylsilane (TMS) or signals from the residual protons of deuterated solvents. The following abbreviations were used to designate multiplicities: s = singlet, d = doublet, app t = apparent triplet, m = multiplet, dd = double-doublet, br = broad. Chemical shifts were expressed in ppm. ESI experiments were carried out using a 6470 Triple Quad (Agilent Technologies). Elemental analysis was performed at Science

Centre, London Metropolitan University using Thermo Fisher (Carlo Erba) Flash 2000 Elemental Analyser, configured for %CHN. IR spectra were recorded with a SpectrumTwo FTIR Spectrometer (Perkin–Elmer) equipped with a Specac Golden Gate™ ATR (attenuated total reflection) accessory; applied as neat samples; $1/\lambda$ in cm^{-1} .

Synthesis and characterization

RuCl₂(dmsO)₄

RuCl₂(dmsO)₄ was synthesised following an adapted literature procedure.³⁶ Spectroscopic data were in agreement with the literature.³⁶

Ru(DIP)₂Cl₂

Ru(DIP)₂Cl₂ was synthesised following an adapted literature procedure.³⁶ Spectroscopic data were in agreement with the literature.^{37,66}

[Ru(DIP)₂(5-OHF)](PF₆)

Ru(DIP)₂Cl₂ (0.20 g, 0.24 mmol) and aq. NaOH (0.38 mL, 1 M) were dissolved in ethanol (20 mL). The solution was degassed for 20 min and 5-hydroxyflavone (0.09 g, 0.38 mmol) was added. The resulting mixture was heated to reflux for 1.5 h under a N₂ atmosphere and protected from light. The mixture was cooled to RT, while still protected from light, and the solvent was removed under vacuum. The residual solid was redissolved in ethanol (10 mL), and H₂O (100 mL) and NH₄PF₆ (1.00 g, 6.13 mmol) were added. The precipitate formed was filtered, washed with H₂O (3 × 50 mL) and Et₂O (3 × 50 mL) and collected. The solid with Et₂O (10 mL) and then heptane (10 mL), was sonicated for 10 min and then centrifuged. This procedure was repeated three times for each solvent. The solid was collected with DCM and dried under vacuum to deliver [Ru(DIP)₂(5-OHF)](PF₆) (0.07 g, 0.061 mmol, 25 % yield) as a purple solid. ¹H NMR (400 MHz,

CD₂Cl₂): δ /ppm = 9.54 (d, J = 5.5 Hz, 1H), 9.38 (d, J = 5.5 Hz, 1H), 8.27 (d, J = 8.7 Hz, 2H), 8.21 – 8.16 (m, 3H), 8.11 (d, J = 5.5 Hz, 1H), 7.96 (dd, J = 9.4, 5.5 Hz, 2H), 7.92 – 7.89 (m, 2H), 7.78 – 7.50 (m, 23H), 7.42 (dd, J = 10.5, 5.5 Hz, 2H), 7.35 (app t, J = 8.3 Hz, 1H), 6.74 (s, 1H), 6.65 (dd, J = 11.6, 8.3 Hz, 2H); ¹³C NMR (125 MHz, CD₂Cl₂): δ /ppm = 179.9, 168.1, 160.0, 158.1, 153.5, 153.1, 151.6, 151.1, 151.0, 150.2, 149.8, 149.6, 148.0, 147.7, 146.3, 146.2, 136.2, 136.2, 136.0, 136.0, 134.3, 131.8, 131.0, 129.9, 129.9, 129.7, 129.7, 129.6, 129.5, 129.5, 129.4, 129.2, 129.1, 128.6, 128.6, 128.4, 126.0, 125.9, 125.8, 125.7, 125.6, 125.4, 124.7, 124.5, 118.3, 113.0, 105.9, 100.3. MS (ESI⁺): m/z 1003.22 [M]⁺. Elemental Analysis: calcd. for C₆₃H₄₁F₆N₄O₃PRu = C, 65.91; H, 3.60; N, 4.88. Found = C, 65.70; H, 3.58; N, 4.55.

[Ru(DIP)₂(gen)](PF₆)

Ru(DIP)₂Cl₂ (0.20 g, 0.24 mmol) was dissolved in ethanol (20 mL). The solution was degassed for 20 min and silver triflate (0.13 g, 0.52 mmol) was added. The mixture was stirred at RT for 1 h protected from light, under a N₂ atmosphere. The crude reaction mixture was filtered and the filtrate was degassed for 20 min. To the degassed solution, genistein (0.10 g, 0.38 mmol) and an ethanolic solution of sodium ethoxide (21%, 285 μ L) were added. The mixture was heated to reflux for 2 h under N₂ atmosphere whilst protected from light. The mixture was cooled to RT and the solvent was removed under vacuum. The residual solid was dissolved in ethanol (10 mL), and H₂O (100 mL) and NH₄PF₆ (1.00 g, 6.13 mmol) were added. The precipitate which formed was filtered and washed with H₂O (3 x 50 mL), heptane (3 x 50 mL) and Et₂O (2 x 50 mL). The solid was collected with DCM and dried under vacuum to deliver the crude product. Purification was achieved *via* preparative TLC (DCM/ethylacetate/methanol 79/20/1). The product was collected from the prep TLC with methanol and the solvent was subsequently removed under reduced

pressure. The solid with Et₂O (10 mL) and then heptane (10 mL), was sonicated for 10 min and then centrifuged. This procedure was repeated three times for each solvent. The solid was collected with DCM and dried under vacuum to deliver **[Ru(DIP)₂(gen)](PF₆)** (0.04 g, 0.033 mmol, 14%) as a deep purple solid. ¹H NMR (400 MHz, CD₃OD): δ/ppm = 9.59 (d, *J* = 5.5 Hz, 1H), 9.21 (d, *J* = 5.5 Hz, 1H), 8.42 (d, *J* = 5.5 Hz, 1H), 8.28 (dd, *J* = 9.4, 1.4 Hz, 2H), 8.20 (dd, *J* = 9.4, 3.7 Hz, 2H), 8.10 (dd, *J* = 5.5, 2.3 Hz, 2H), 8.00 (d, *J* = 5.5 Hz, 1H), 7.82 – 7.73 (m, 5H), 7.72 – 7.53 (m, 18H), 7.50 (d, *J* = 5.5 Hz, 1H), 7.38 (d, *J* = 5.5 Hz, 1H), 6.50 (d, *J* = 8.7 Hz, 2H), 6.26 (d, *J* = 8.7 Hz, 2H), 6.10 (s, 1H); ¹³C NMR (125 MHz, CD₃OD): δ/ppm = 178.2, 169.5, 165.5, 160.9, 158.1, 155.2, 155.1, 153.0, 152.7, 152.6, 152.1, 151.2, 150.9, 150.9, 149.6, 149.1, 147.8, 147.5, 137.7, 137.6, 137.6, 137.5, 131.1, 131.1, 131.0, 130.8, 130.5, 130.4, 130.3, 130.2, 130.1, 130.1, 130.1, 129.7, 129.7, 129.6, 129.5, 126.9, 126.8, 126.7, 126.7, 126.6, 125.9, 125.8, 124.2, 123.6, 115.3, 109.3, 92.4, 58.3. MS (ESI+): *m/z* 1035.5 [M]⁺. Elemental Analysis: calcd. for C₆₃H₄₁F₆N₄O₅PRu = C, 64.12; H, 3.50; N, 4.75. Found = C, 64.51; H, 3.45; N, 4.48.

[Ru(DIP)₂(chr)](OTf)·4H₂O

Ru(DIP)₂Cl₂ (0.50 g, 0.60 mmol) was dissolved in ethanol (30 mL). The solution was degassed for 20 min and silver triflate (0.34 g, 1.32 mmol) was added. The mixture was stirred at RT for 1 h protected from light, under a N₂ atmosphere. The crude reaction mixture was filtered and the filtrate was degassed for 20 min before chrysin (0.24 g, 0.96 mmol) and an ethanolic solution of sodium ethoxide (21%, 717 μL) were added. The mixture was heated to reflux for 2 h under N₂ atmosphere and protected from light. The mixture was cooled to RT, while still protected from light, and the solvent was removed under vacuum. The residual solid was collected in DCM (20 mL) and filtered through celite. The solvent was removed under vacuum to deliver the crude

product. Purification was achieved *via* preparative TLC (DCM/ethylacetate/methanol 79/20/1). The product was collected from the prep TLC with methanol and the solvent was subsequently removed under reduced pressure. The solid with Et₂O (10 mL) and then heptane (10 mL), was sonicated for 10 min and then centrifuged. This procedure was repeated three times for each solvent. The solid was collected with DCM and dried under vacuum to afford **[Ru(DIP)₂(chr)](OTf)** (0.12 g, 0.09 mmol, 16% yield) as a deep purple solid. ¹H NMR (400 MHz, CD₂Cl₂-d₂): δ/ppm = 9.56 (d, *J* = 5.5 Hz, 1H), 9.32 (d, *J* = 5.5 Hz, 1H), 8.20 – 8.09 (m, 4H), 8.09 – 7.99 (m, 2H), 7.84 – 7.80 (m, 2H), 7.76 (d, *J* = 7.3 Hz, 2H), 7.69 – 7.36 (m, 24H), 7.34 (d, *J* = 5.5 Hz, 1H), 7.28 (d, *J* = 5.5 Hz, 1H), 6.48 (s, 1H), 6.17 (br d, *J* = 2.2 Hz, 1H), 6.04 (br d, *J* = 2.2 Hz, 1H). ¹³C NMR (125 MHz, CD₂Cl₂): δ/ppm = 178.2, 169.1, 160.0, 159.4, 153.7, 153.4, 152.3, 152.0, 151.6, 150.7, 150.2, 150.2, 147.9, 147.7, 146.3, 146.2, 136.9, 136.8, 136.7, 136.6, 131.8, 131.7, 130.4, 130.4, 130.2, 130.1, 129.9, 129.8, 129.7, 129.6, 129.6, 129.5, 129.0, 129.0, 128.8, 126.3, 126.2, 126.1, 125.8, 125.1, 107.7, 105.5, 104.6, 92.3. MS (ESI+): *m/z* 1019.6 [M]⁺, (ESI-): *m/z* 149.2 [OTf]. Elemental Analysis: calcd. for C₆₄H₄₉F₃N₄O₁₁RuS = C, 61.97; H, 3.99; N, 4.51. Found = C, 62.09; H, 3.93; N, 4.28.

[Ru(DIP)₂(mor)](OTf)

A. Morin (0.56 g, 1.85 mmol) was suspended in dry tetrahydrofuran (50 mL) and triethylamine (1.55 mL, 11.1 mmol) was added. The mixture was stirred at RT under a N₂ atmosphere for 15 minutes before TMS-Br (1.47 mL, 11.1 mmol) was added. The mixture was stirred at RT under a N₂ atmosphere for 2.5 h before being added to a separating funnel. H₂O (50 mL) was added and the product was extracted in DCM and dried on Na₂SO₄. The solvent was removed under vacuum to yield the crude product A.

B. Ru(DIP)₂Cl₂ (0.83 g, 1.00 mmol) was dissolved in ethanol (50 mL). The solution was degassed for 20 min and silver triflate (0.56 g, 2.20 mmol) was added. The mixture was stirred at RT for 1 h protected from light, under a N₂ atmosphere. The crude reaction mixture was filtered and the filtrate was degassed for 20 min before product A and an ethanolic solution of sodium ethoxide (21%, 750 μL) were added. The mixture was heated to reflux for 2 h under N₂ atmosphere and protected from light. The mixture was cooled to RT, while still protected from light, and the solvent was removed under vacuum. The residual solid was collected in DCM (20 mL) and filtered through celite. The solvent was removed under vacuum to deliver the crude product. Purification was achieved *via* preparative TLC (DCM/ethylacetate/methanol 79/20/1). The product was collected from the prep TLC with methanol and the solvent was subsequently removed under reduced pressure. The solid with Et₂O (10 mL) and then heptane (10 mL), was sonicated for 10 min and then centrifuged. This procedure was repeated three times for each solvent. The solid was collected with DCM and dried under vacuum to afford [Ru(DIP)₂(mor)](OTf) (0.42 g, 0.35 mmol, 35% yield) as a deep purple solid. ¹H NMR (400 MHz, DMF-*d*₇): δ/ppm = 11.85 (s, 1H), 9.73 (dd, *J* = 10.1, 5.5 Hz, 2H), 8.53 (d, *J* = 5.5 Hz, 1H), 8.45 (d, *J* = 5.5 Hz, 1H), 8.42 – 8.20 (m, 7H), 7.93 – 7.49 (m, 25H), 6.45 (dd, *J* = 8.7, 2.4 Hz, 1H), 6.06 (d, *J* = 2.4 Hz, 1H), 5.99 (s, 1H), 5.76 (s, 1H). ¹³C NMR (125 MHz, DMF-*d*₇): δ/ppm = 158.9, 158.0, 155.0, 154.7, 151.9, 151.8, 151.8, 151.5, 149.7, 149.6, 147.3, 147.0, 145.7, 145.5, 143.3, 136.4, 136.1, 136.0, 130.3, 130.2, 130.0, 129.4, 129.3, 129.2, 129.1, 128.8, 128.2, 128.0, 126.4, 126.3, 125.9, 125.9, 125.8, 125.7, 125.1, 125.0, 112.5, 108.0, 104.9, 95.7. MS (ESI+): *m/z* 1067.9 [M]⁺, (ESI-): *m/z* 149.3 [OTf]. Elemental Analysis: calcd. for C₆₄H₄₁F₃N₄O₁₀RuS = C, 63.20; H, 3.40; N, 4.60. Found = C, 62.77; H, 3.33; N, 4.45.

Stability studies

The stability in DMSO-*d*₆ or DMF-*d*₇ at room temperature was assessed by ¹H NMR over 96 h.

Cytotoxicity assay using a 2D cellular model

Cytotoxicity of **[Ru(DIP)₂(5-OHF)](PF₆)**, **[Ru(DIP)₂(gen)](PF₆)**, **[Ru(DIP)₂(chr)](OTf)**, **[Ru(DIP)₂(mor)](OTf)**, **Ru(DIP)₂Cl₂**, cisplatin and doxorubicin was assessed by a fluorometric cell viability assay using Resazurin (ACROS Organics). Briefly, cells were seeded in triplicate in 96-well plates at a density of 4×10³ cells/well in 100 μL. After 24 h, cells were treated with increasing concentrations of the ruthenium complexes. Dilutions were prepared as follows: 0.250 mM stock in DMSO (**[Ru(DIP)₂(5-OHF)](PF₆)**, **[Ru(DIP)₂(gen)](PF₆)**, **[Ru(DIP)₂(chr)](OTf)**) or DMF (**[Ru(DIP)₂(mor)](OTf)**, **Ru(DIP)₂Cl₂**), which were further diluted to 100 μM in cell media. After 48 h incubation, the medium was removed and 100 μL of complete medium containing resazurin (0.2 mg/mL final concentration) was added. After 4 h of incubation at 37 °C, the fluorescence signal of resorufin product was read (ex: 540 nm em: 590 nm) in a SpectraMax M5 microplate Reader. IC₅₀ values were then calculated using GraphPad Prism software.

GraphPad Prism calculations of IC₅₀ values

XY analysis with three replicate values in side by side sub-columns were chosen. Inserted raw data obtained from SpectraMax M5 microplate reader was treated as follows: X values were transformed into logarithm; data was normalised to the lowest Y value. Data was then analysed with XY analysis “Nonlinear regression (curve fit)” then “log(inhibitor) vs. normalized response”.

Cytotoxicity assay using a 2D cellular model f (2 h incubation)

Cytotoxicity of $[\text{Ru}(\text{DIP})_2(\text{gen})](\text{PF}_6)$ and cisplatin was assessed by a fluorometric cell viability assay using Resazurin (ACROS Organics). Briefly, cells were seeded in triplicate in 96-well plates at a density of 4×10^3 cells/well in 100 μL . After 24 h, cells were treated with increasing concentrations of the complexes. Dilutions were prepared as described in the section “Cytotoxicity assay using a 2D cellular model”. After 2 h incubation, the medium was removed and 100 μL of complete medium containing resazurin (0.2 mg/mL final concentration) was added. After 4 h of incubation at 37 $^\circ\text{C}$, the fluorescence signal of resorufin product was read (ex: 540 nm em: 590 nm) in a SpectraMax M5 microplate Reader. IC_{50} values were then calculated using GraphPad Prism software as stated before.

Sample Preparation for cellular uptake

MDA-MB-435S and MCF-7 cells were seeded at a density of 2×10^6 in 10 cm plates. Next day, cells were treated with 5 μM concentration of $[\text{Ru}(\text{DIP})_2(\text{gen})](\text{PF}_6)$, $\text{Ru}(\text{DIP})_2\text{Cl}_2$ or cisplatin. Dilutions were prepared as described in the section “Cytotoxicity assay using a 2D cellular model”. After 2 h, cells were washed, collected, counted and snap frozen in liquid nitrogen and stored at -20 $^\circ\text{C}$. ICP-MS samples were prepared as follows: samples were digested using 70% nitric acid (1 mL, 60 $^\circ\text{C}$, overnight). Samples were then further diluted 1:100 (1% HCl solution in MQ water) and analysed using ICP-MS.

Sample preparation for studies on the mechanism of cellular uptake

Samples were prepared as previously reported.⁶⁶ Briefly, MDA-MB-435S and MCF-7 cells were seeded at a density of 2×10^6 in 10 cm dishes and were pre-treated the following day with the

corresponding inhibitors or kept at a specific temperature for 1 h. Next, cells were washed with PBS and were incubated with 5 μM of $[\text{Ru}(\text{DIP})_2(\text{gen})](\text{PF}_6)$ or $\text{Ru}(\text{DIP})_2\text{Cl}_2$ for 2 h (low temperature samples were still kept at 4 °C). Dilutions were prepared as described in the section “Cytotoxicity assay using a 2D cellular model”. Subsequently, cells were washed with PBS, collected, counted and snap frozen in liquid nitrogen. Pellets were stored at -20 °C. ICP-MS samples were prepared as follows: samples were digested using 70% nitric acid (1 mL, 60 °C, overnight), further diluted 1:100 (1% HCl solution in MQ water) and analysed using ICP-MS.

Sample Preparation for time dependent cellular accumulation

MDA-MB-435S and MCF-7 cells were seeded at a density of 3×10^6 in 10 cm plates. Next day, cells were treated with 1 μM concentration of $[\text{Ru}(\text{DIP})_2(\text{gen})](\text{PF}_6)$, $\text{Ru}(\text{DIP})_2\text{Cl}_2$ or cisplatin. Dilutions were prepared as described in the section “Cytotoxicity assay using a 2D cellular model”. After 2 h, 12 h, 24 h and 48 h cells were washed, collected, counted and snap frozen in liquid nitrogen and stored until further use at -20 °C. ICP-MS samples were prepared as follows: samples were digested using 70% nitric acid (0.5 ml for 2 h and 12 h samples; 1 mL for 24 h and 48 h samples, 65 °C, overnight). Samples were then further diluted 1:50 (2 h samples) or 1:100 (12 h, 24 h, 48 h samples) in 1% HCl solution in MQ water and analysed using ICP-MS.

ICP-MS studies

All ICP-MS measurements were performed on a high resolution ICP-MS (Element II, ThermoScientific) located at the Institut de physique du globe de Paris (France). The monitored isotopes are ^{101}Ru and ^{195}Pt . Daily, prior to the analytical sequence, the instrument was first tuned to produce maximum sensitivity and stability while also maintaining low uranium oxide formation

(UO/U \leq 5%). The data were treated as follows: intensities were converted into concentrations using uFREASI (user-FRiendly Elemental dAta proceSsIng).⁷⁰ This software, developed for HR-ICP-MS users community, is free and available on <http://www.ipgp.fr/~tharaud/uFREASI>.

ICP-MS data analysis

Cellular uptake studies: The amount of metal detected in the cell samples was transformed from ppb into μg of metal. Data were subsequently normalised to the number of cells and expressed as ng of metal/ amount of cells.

Mechanism of uptake: The amount of ruthenium detected in cell samples was transformed from ppb into μg of ruthenium and values obtained were normalised to the number of cells used for specific treatment. The value for the ruthenium found in the 37 °C sample was used as a 100%.

Metabolic Studies

HeLa cells were seeded in Seahorse XFe96 well plates at a density of 10×10^3 cells / well in 80 μL . After 24 h, the medium was replaced with fresh medium and cisplatin (1 μM), genistein (1 μM), **Ru(DIP)₂Cl₂** (1 μM) or **[Ru(DIP)₂(gen)](PF₆)** (1 μM) were added. Dilutions were prepared as described in the section “Cytotoxicity assay using a 2D cellular model”. After 24 h of incubation, the regular medium was removed, cells were washed thrice using Seahorse Base Media and incubated in a non-CO₂ incubator at 37 °C for 1 h.

Mito Stress Test: Mitostress assay was run using oligomycin, 1 μM , FCCP 1 μM and mixture of antimycin-A/ rotenone 1 μM each in ports A, B and C respectively using Seahorse XFe96 Extracellular Flux Analyzer.

Glycolysis Stress Test: Glycolytic stress test was run using glucose (10 mM), oligomycin (1 μ M) and 2-Deoxyglucose (50 mM) in ports A, B and C respectively using Seahorse XFe96 Extracellular Flux Analyzer.

Supporting Information

The Supporting Information is at DOI: XXXXX.

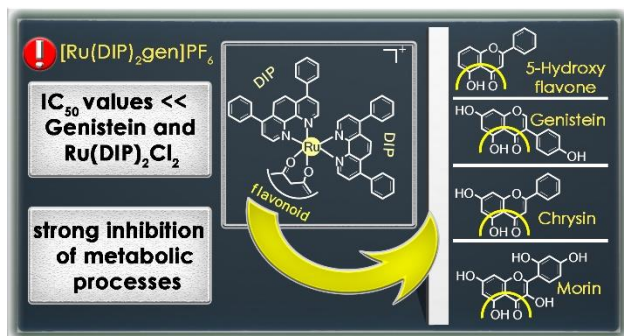
$^1\text{H-NMR}$ spectrum of $[\text{Ru}(\text{DIP})_2(\text{5-OHF})](\text{PF}_6)$ (Figure S1), $^1\text{H-NMR}$ spectrum of $[\text{Ru}(\text{DIP})_2(\text{gen})](\text{PF}_6)$ (Figure S2), $^1\text{H-NMR}$ spectrum of $[\text{Ru}(\text{DIP})_2(\text{chr})](\text{OTf})$ (Figure S3), $^1\text{H-NMR}$ spectrum of $[\text{Ru}(\text{DIP})_2(\text{mor})](\text{OTf})$ (Figure S4), $^1\text{H-NMR}$ spectrum of $[\text{Ru}(\text{DIP})_2(\text{mor})](\text{OTf})$ after 5 days in solution (Figure S5), $^{13}\text{C-NMR}$ spectrum of $[\text{Ru}(\text{DIP})_2(\text{5-OHF})](\text{PF}_6)$ (Figure S6), $^{13}\text{C-NMR}$ spectrum of $[\text{Ru}(\text{DIP})_2(\text{gen})](\text{PF}_6)$ (Figure S7), $^{13}\text{C-NMR}$ spectrum of $[\text{Ru}(\text{DIP})_2(\text{chr})](\text{OTf})$ (Figure S8), $^{13}\text{C-NMR}$ spectrum of $[\text{Ru}(\text{DIP})_2(\text{mor})](\text{OTf})$ (Figure S9), Overlap of $^1\text{H-NMR}$ spectra of $[\text{Ru}(\text{DIP})_2(\text{5-OHF})](\text{PF}_6)$ in DMSO (Figure S10), Overlap of $^1\text{H-NMR}$ spectra of $[\text{Ru}(\text{DIP})_2(\text{gen})](\text{PF}_6)$ in DMSO (Figure S11), Overlap of $^1\text{H-NMR}$ spectra of $[\text{Ru}(\text{DIP})_2(\text{chr})](\text{OTf})$ in DMSO (Figure S12) Overlap of $^1\text{H-NMR}$ spectra of $[\text{Ru}(\text{DIP})_2(\text{mor})](\text{OTf})$ in DMF (Figure S13), Fluorometric cell viability assay (Figure S14), Oxygen consumption rates and different respiration parameters in MDA-MB-435S cells alone or after treatment with various test compounds (Figure S15), Extracellular acidification rate and different parameters during glycolysis in MDA-MB-435S cells alone or after treatment with various test compounds (Figure S16).

Acknowledgements

This work was financially supported by an ERC Consolidator Grant PhotoMedMet to G.G. (GA 681679) and has received support under the program *Investissements d'Avenir*

launched by the French Government and implemented by the ANR with the reference ANR-10-IDEX-0001-02 PSL (G.G.). Ile de France Region is gratefully acknowledged for financial support of 500 MHz NMR spectrometer of Chimie ParisTech in the framework of the SESAME equipment project. We acknowledge the loan of Agilent's equipment to Chimie ParisTech. Part of this work was supported by IPGP multidisciplinary program PARI and by Region Île-de-France SESAME Grant no. 12015908. This project was also financially supported by “Carol Davila” University of Medicine and Pharmacy through Contract no. 23PFE/17.10.2018 funded by the Ministry of Research and Innovation within PNCDI III, Program 1 – Development of the National RD system, Subprogram 1.2 – Institutional Performance – RDI excellence funding projects.

TOC



Synopsis

We report the synthesis, characterisation and biological activity of four heteroleptic Ru(II) polypyridyl complexes containing flavonoid ligands. The most promising compound identified in this study was found to strongly inhibit metabolic processes in MDA-MB-435S melanoma cells. An interesting parallel between this compound and its dichloro precursor highlights the impact of genistein on activity.

References

- (1) Organization, W. H. Noncommunicable diseases <https://www.who.int/news-room/factsheets/detail/noncommunicable-diseases> (accessed Sep 2, 2019).
- (2) Hartinger, C. G.; Zorbas-Seifried, S.; Jakupec, M. A.; Kynast, B.; Zorbas, H.; Keppler, B. K. From Bench to Bedside – Preclinical and Early Clinical Development of the Anticancer Agent Indazolium Trans-[Tetrachlorobis(1H-Indazole)Ruthenate(III)] (KP1019 or FFC14A). *J. Inorg. Biochem.* **2006**, *100* (5), 891–904. <https://doi.org/10.1016/j.jinorgbio.2006.02.013>.
- (3) Oun, R.; Moussa, Y. E.; Wheate, N. J. The Side Effects of Platinum-Based Chemotherapy Drugs: A Review for Chemists. *Dalton Trans.* **2018**, *47* (19), 6645–6653. <https://doi.org/10.1039/c8dt00838h>.
- (4) Boros, E.; Dyson, P. J.; Gasser, G. Classification of Metal-Based Drugs According to Their Mechanisms of Action. *Chem* **2020**, *6* (1), 41–60. <https://doi.org/10.1016/j.chempr.2019.10.013>.
- (5) Mari, C.; Pierroz, V.; Ferrari, S.; Gasser, G. Combination of Ru(II) Complexes and Light: New Frontiers in Cancer Therapy. *Chem. Sci.* **2015**, *6* (5), 2660–2686. <https://doi.org/10.1039/C4SC03759F>.
- (6) Smith, G. S.; Therrien, B. Targeted and Multifunctional Arene Ruthenium Chemotherapeutics. *Dalt. Trans.* **2011**, *40* (41), 10793–10800. <https://doi.org/10.1039/C1DT11007A>.
- (7) Nazarov, A. A.; Hartinger, C. G.; Dyson, P. J. Opening the Lid on Piano-Stool Complexes: An Account of Ruthenium(II)–Arene Complexes with Medicinal Applications. *J. Organomet. Chem.* **2014**, *751*, 251–260.

<https://doi.org/https://doi.org/10.1016/j.jorganchem.2013.09.016>.

- (8) Zeng, L.; Gupta, P.; Chen, Y.; Wang, E.; Ji, L.; Chao, H.; Chen, Z.-S. The Development of Anticancer Ruthenium(II) Complexes: From Single Molecule Compounds to Nanomaterials. *Chem. Soc. Rev.* **2017**, *46* (19), 5771–5804. <https://doi.org/10.1039/C7CS00195A>.
- (9) Rademaker-Lakhai, J. M.; van den Bongard, D.; Pluim, D.; Beijnen, J. H.; Schellens, J. H. M. A Phase I and Pharmacological Study with Imidazolium-Trans-DMSO-Imidazole-Tetrachlororuthenate, a Novel Ruthenium Anticancer Agent. *Clin. Cancer Res.* **2004**, *10* (11), 3717–3727. <https://doi.org/10.1158/1078-0432.CCR-03-0746>.
- (10) Leijen, S.; Burgers, S. A.; Baas, P.; Pluim, D.; Tibben, M.; Van Werkhoven, E.; Alessio, E.; Sava, G.; Beijnen, J. H.; Schellens, J. H. M. Phase I/II Study with Ruthenium Compound NAMI-A and Gemcitabine in Patients with Non-Small Cell Lung Cancer after First Line Therapy. *Invest. New Drugs* **2015**, *33* (1), 201–214. <https://doi.org/10.1007/s10637-014-0179-1>.
- (11) Hartinger, C. G.; Jakupec, M. A.; Zorbas-Seifried, S.; Groessl, M.; Egger, A.; Berger, W.; Zorbas, H.; Dyson, P. J.; Keppler, B. K. KP1019, A New Redox-Active Anticancer Agent – Preclinical Development and Results of a Clinical Phase I Study in Tumor Patients. *Chem. Biodivers.* **2008**, *5* (10), 2140–2155. <https://doi.org/10.1002/cbdv.200890195>.
- (12) Lentz, F.; Drescher, A.; Lindauer, A.; Henke, M.; Hilger, R. A.; Hartinger, C. G.; Scheulen, M. E.; Dittrich, C.; Keppler, B. K.; Jaehde, U. Pharmacokinetics of a Novel Anticancer Ruthenium Complex (KP1019, FFC14A) in a Phase I Dose-Escalation Study. *Anticancer. Drugs* **2009**, *20* (2), 97–103. <https://doi.org/10.1097/CAD.0b013e328322fbc5>.
- (13) Trondl, R.; Heffeter, P.; Kowol, C. R.; Jakupec, M. A.; Berger, W.; Keppler, B. K. NKP-

- 1339, the First Ruthenium-Based Anticancer Drug on the Edge to Clinical Application. *Chem. Sci.* **2014**, *5* (8), 2925–2932. <https://doi.org/10.1039/C3SC53243G>.
- (14) Levina, A.; Mitra, A.; Lay, P. A. Recent Developments in Ruthenium Anticancer Drugs. *Metallomics* **2009**, *1* (6), 458–470. <https://doi.org/10.1039/b904071d>.
- (15) Sava, G.; Bergamo, A.; Dyson, P. J. Metal-Based Antitumour Drugs in the Post-Genomic Era: What Comes Next? *Dalt. Trans.* **2011**, *40* (36), 9069–9075. <https://doi.org/10.1039/C1DT10522A>.
- (16) Bergamo, A.; Gaiddon, C.; Schellens, J. H. M.; Beijnen, J. H.; Sava, G. Approaching Tumour Therapy beyond Platinum Drugs: Status of the Art and Perspectives of Ruthenium Drug Candidates. *J. Inorg. Biochem.* **2012**, *106* (1), 90–99. <https://doi.org/10.1016/j.jinorgbio.2011.09.030>.
- (17) Alessio, E. Thirty Years of the Drug Candidate NAMI-A and the Myths in the Field of Ruthenium Anticancer Compounds: A Personal Perspective. *Eur. J. Inorg. Chem.* **2017**, *2017* (12), 1549–1560. <https://doi.org/10.1002/ejic.201600986>.
- (18) Mital, M.; Ziora, Z. Biological Applications of Ru(II) Polypyridyl Complexes. *Coord. Chem. Rev.* **2018**, *375*, 434–458. <https://doi.org/https://doi.org/10.1016/j.ccr.2018.02.013>.
- (19) Notaro, A.; Gasser, G. Monomeric and Dimeric Coordinatively Saturated and Substitutionally Inert Ru(II) Polypyridyl Complexes as Anticancer Drug Candidates. *Chem. Soc. Rev.* **2017**, *46* (23), 7317–7337. <https://doi.org/10.1039/C7CS00356K>.
- (20) Lin, K.; Zhao, Z.-Z.; Bo, H.-B.; Hao, X.-J.; Wang, J.-Q. Applications of Ruthenium Complex in Tumor Diagnosis and Therapy. *Front. Pharmacol.* **2018**, *9*, 1323. <https://doi.org/10.3389/fphar.2018.01323>.
- (21) Salassa, L. Polypyridyl Metal Complexes with Biological Activity. *Eur. J. Inorg. Chem.*

- 2011**, *2011* (32), 4931–4947. <https://doi.org/10.1002/ejic.201100376>.
- (22) Heinemann, F.; Karges, J.; Gasser, G. Critical Overview of the Use of Ru(II) Polypyridyl Complexes as Photosensitizers in One-Photon and Two-Photon Photodynamic Therapy. *Acc. Chem. Res.* **2017**, *50* (11), 2727–2736. <https://doi.org/10.1021/acs.accounts.7b00180>.
- (23) Jakubaszek, M.; Goud, B.; Ferrari, S.; Gasser, G. Mechanisms of Action of Ru(II) Polypyridyl Complexes in Living Cells upon Light Irradiation. *Chem. Commun.* **2018**, *54* (93), 13040–13059. <https://doi.org/10.1039/C8CC05928D>.
- (24) Monro, S.; Colón, K. L.; Yin, H.; Roque, J.; Konda, P.; Gujar, S.; Thummel, R. P.; Lilge, L.; Cameron, C. G.; McFarland, S. A. Transition Metal Complexes and Photodynamic Therapy from a Tumor-Centered Approach: Challenges, Opportunities, and Highlights from the Development of TLD1433. *Chem. Rev.* **2019**, *119* (2), 797–828. <https://doi.org/10.1021/acs.chemrev.8b00211>.
- (25) Intravesical Photodynamic Therapy (PDT) in BCG Refractory/Intolerant Non-Muscle Invasive Bladder Cancer (NMIBC) Patients <https://clinicaltrials.gov/ct2/show/NCT03945162> (accessed Sep 5, 2019).
- (26) McFarland, S. A.; Mandel, A.; Dumoulin-White, R.; Gasser, G. Metal-Based Photosensitizers for Photodynamic Therapy: The Future of Multimodal Oncology? *Curr. Opin. Chem. Biol.* **2020**, *56*, 23–27. <https://doi.org/10.1016/j.cbpa.2019.10.004>.
- (27) Pettinari, R.; Marchetti, F.; Condello, F.; Pettinari, C.; Lupidi, G.; Scopelliti, R.; Mukhopadhyay, S.; Riedel, T.; Dyson, P. J. Ruthenium(II)–Arene RAPTA Type Complexes Containing Curcumin and Bisdemethoxycurcumin Display Potent and Selective Anticancer Activity. *Organometallics* **2014**, *33* (14), 3709–3715. <https://doi.org/10.1021/om500317b>.

- (28) Kurzwernhart, A.; Kandioller, W.; Bachler, S.; Bartel, C.; Martic, S.; Buczkowska, M.; Muhlgassner, G.; Jakupec, M. A.; Kraatz, H.-B.; Bednarski, P. J.; et al. Structure-Activity Relationships of Targeted RuII(Eta6-p-Cymene) Anticancer Complexes with Flavonol-Derived Ligands. *J. Med. Chem.* **2012**, *55* (23), 10512–10522. <https://doi.org/10.1021/jm301376a>.
- (29) Uivarosi, V.; Munteanu, A.-C.; Nițulescu, G. M. Chapter 2 - An Overview of Synthetic and Semisynthetic Flavonoid Derivatives and Analogues: Perspectives in Drug Discovery; Attar-Rahman, B. T.-S. in N. P. C., Ed.; Elsevier, 2019; Vol. 60, pp 29–84. <https://doi.org/https://doi.org/10.1016/B978-0-444-64181-6.00002-4>.
- (30) Senderowicz, A. M. Flavopiridol: The First Cyclin-Dependent Kinase Inhibitor in Human Clinical Trials. *Invest. New Drugs* **1999**, *17* (3), 313–320.
- (31) Jain, S. K.; Bharate, S. B.; Vishwakarma, R. A. Cyclin-Dependent Kinase Inhibition by Flavoalkaloids. *Mini Rev. Med. Chem.* **2012**, *12* (7), 632–649.
- (32) Chahar, M. K.; Sharma, N.; Dobhal, M. P.; Joshi, Y. C. Flavonoids: A Versatile Source of Anticancer Drugs. *Pharmacognosy Reviews*. India 2011, pp 1–12. <https://doi.org/10.4103/0973-7847.79093>.
- (33) Singh, M.; Kaur, M.; Silakari, O. Flavones: An Important Scaffold for Medicinal Chemistry. *Eur. J. Med. Chem.* **2014**, *84*, 206–239. <https://doi.org/https://doi.org/10.1016/j.ejmech.2014.07.013>.
- (34) Kumar, S.; Pandey, A. K. Chemistry and Biological Activities of Flavonoids: An Overview. *Sci. J.* **2013**, *2013*, 1–20. <https://doi.org/10.1070/RC2004v073n07ABEH000856>.
- (35) Hostetler, G. L.; Ralston, R. A.; Schwartz, S. J. Flavones: Food Sources, Bioavailability, Metabolism, and Bioactivity. *Adv. Nutr.* **2017**, *8* (3), 423–435.

- <https://doi.org/10.3945/an.116.012948>.
- (36) Brastos, I.; Alessio, E.; Ringenberg, M. E.; Rauchfuss, T. B. Ruthenium Complexes. *Inorg. Synth.* **2010**, *35* (li), 148–163. <https://doi.org/10.1002/9780470651568.ch8>.
- (37) Caspar, R.; Cordier, C.; Waern, J. B.; Guyard-Duhayon, C.; Gruselle, M.; Le Floch, P.; Amouri, H. A New Family of Mono- and Dicarboxylic Ruthenium Complexes [Ru(DIP) 2 (L 2)] 2+ (DIP = 4,7-Diphenyl-1,10-Phenanthroline): Synthesis, Solution Behavior, and X-Ray Molecular Structure of Trans -[Ru(DIP) 2 (MeOH) 2][OTf] 2. *Inorg. Chem.* **2006**, *45* (10), 4071–4078. <https://doi.org/10.1021/ic0601236>.
- (38) Porter, L. J.; Markham, K. R. The Aluminium(III) Complexes of Hydroxyflavones in Absolute Methanol. Part II. Ligands Containing More than One Chelating Site. *J. Chem. Soc. C Org.* **1970**, *1970*, 1309–1313. <https://doi.org/10.1039/J39700001309>.
- (39) Panhwar, Q. K.; Memon, S. Synthesis and Properties of Zirconium (IV) and Molybdate (II) Morin Complexes. *J. Coord. Chem.* **2012**, No. 65, 37–41.
- (40) Naso, L. G.; Lezama, L.; Rojo, T.; Etcheverry, S. B.; Valcarcel, M.; Roura, M.; Salado, C.; Ferrer, E. G.; Williams, P. A. M. Biological Evaluation of Morin and Its New Oxovanadium(IV) Complex as Antio-Xidant and Specific Anti-Cancer Agents. *Chem. Biol. Interact.* **2013**, *206* (2), 289–301. <https://doi.org/10.1016/j.cbi.2013.10.006>.
- (41) Zahirović, A.; Kahrović, E.; Cindrić, M.; Kraljević Pavelić, S.; Hukić, M.; Harej, A.; Turkušić, E. Heteroleptic Ruthenium Bioflavonoid Complexes: From Synthesis to in Vitro Biological Activity. *J. Coord. Chem.* **2017**, *70* (24), 4030–4053. <https://doi.org/10.1080/00958972.2017.1409893>.
- (42) Qi, C.; Xiong, Y.; Eschenbrenner-Lux, V.; Cong, H.; Porco, J. A. Asymmetric Syntheses of the Flavonoid Diels–Alder Natural Products Sanggenons C and O. *J. Am. Chem. Soc.*

- 2016**, *138* (3), 798–801. <https://doi.org/10.1021/jacs.5b12778>.
- (43) Huang, H.; Humbert, N.; Bizet, V.; Patra, M.; Chao, H.; Mazet, C.; Gasser, G. Influence of the Dissolution Solvent on the Cytotoxicity of Octahedral Cationic Ir(III) Hydride Complexes. *J. Organomet. Chem.* **2017**, *839*, 15–18. <https://doi.org/10.1016/j.jorganchem.2016.12.010>.
- (44) Patra, M.; Joshi, T.; Pierroz, V.; Ingram, K.; Kaiser, M.; Ferrari, S.; Spingler, B.; Keiser, J.; Gasser, G. DMSO-Mediated Ligand Dissociation: Renaissance for Biological Activity of N-Heterocyclic-[Ru(H6-Arene)Cl₂] Drug Candidates. *Chem. – A Eur. J.* **2013**, *19* (44), 14768–14772. <https://doi.org/10.1002/chem.201303341>.
- (45) Keller, S.; Ong, Y. C.; Lin, Y.; Cariou, K.; Gasser, G. A Tutorial for the Assessment of the Stability of Organometallic Complexes in Biological Media. *J. Organomet. Chem.* **2019**, 121059. <https://doi.org/10.1016/j.jorganchem.2019.121059>.
- (46) Frei, A.; Rubbiani, R.; Tubafard, S.; Blacque, O.; Anstaett, P.; Felgenträger, A.; Maisch, T.; Spiccia, L.; Gasser, G. Synthesis, Characterization, and Biological Evaluation of New Ru(II) Polypyridyl Photosensitizers for Photodynamic Therapy. *J. Med. Chem.* **2014**, *57* (17), 7280–7292. <https://doi.org/10.1021/jm500566f>.
- (47) Cepeda, V.; Fuertes, M.; Castilla, J.; Alonso, C.; Quevedo, C.; Perez, J. Biochemical Mechanisms of Cisplatin Cytotoxicity. *Anticancer. Agents Med. Chem.* **2007**, *7* (1), 3–18. <https://doi.org/10.2174/187152007779314044>.
- (48) Keizer, H. G.; Pinedo, H. M.; Schuurhuis, G. J.; Joenje, H. DOXORUBICIN (ADRIAMYCIN): A CRITICAL REVIEW OF FREE RADICAL-DEPENDENT MECHANISMS OF CYTOTOXICITY. *Pharmac. Ther* **1990**, *47*, 219–231. [https://doi.org/10.1016/0163-7258\(90\)90088-J](https://doi.org/10.1016/0163-7258(90)90088-J).

- (49) Munteanu, A.-C.; Badea, M.; Olar, R.; Silvestro, L.; Mihaila, M.; Brasoveanu, L. I.; Musat, M. G.; Andries, A.; Uivarosi, V. Cytotoxicity Studies, DNA Interaction and Protein Binding of New Al (III), Ga (III) and In (III) Complexes with 5-Hydroxyflavone. *Appl. Organomet. Chem.* **2018**, *32* (12), e4579. <https://doi.org/10.1002/aoc.4579>.
- (50) Deka, B.; Bhattacharyya, A.; Mukherjee, S.; Sarkar, T.; Soni, K.; Banerjee, S.; Saikia, K. K.; Deka, S.; Hussain, A. Ferrocene Conjugated Copper(II) Complexes of Terpyridine and Traditional Chinese Medicine (TCM) Anticancer Ligands Showing Selective Toxicity towards Cancer Cells. *Appl. Organomet. Chem.* **2018**, *32* (4), e4287. <https://doi.org/10.1002/aoc.4287>.
- (51) Roy, S.; Sil, A.; Chakraborty, T. Potentiating Apoptosis and Modulation of P53, Bcl2, and Bax by a Novel Chrysin Ruthenium Complex for Effective Chemotherapeutic Efficacy against Breast Cancer. *J. Cell. Physiol.* **2019**, *234* (4), 4888–4909. <https://doi.org/10.1002/jcp.27287>.
- (52) Spoerlein, C.; Mahal, K.; Schmidt, H.; Schobert, R. Effects of Chrysin, Apigenin, Genistein and Their Homoleptic Copper (II) Complexes on the Growth and Metastatic Potential of Cancer Cells. *J. Inorg. Biochem.* **2013**, *127*, 107–115. <https://doi.org/10.1016/j.jinorgbio.2013.07.038>.
- (53) Fotsis, T.; Pepper, M.; Adlercreutz, H.; Hase, T.; Montesano, R.; Schweigerer, L. Genistein, a Dietary Ingested Isoflavonoid, Inhibits Cell Proliferation and in Vitro Angiogenesis. *J. Nutr.* **1995**, *125* (3 Suppl), 790S–797S. https://doi.org/10.1093/jn/125.suppl_3.790S.
- (54) Peterson, G.; Barnes, S. Genistein Stimulated Inhibits Both Proliferation Estrogen and Growth of Human Breast Cancer. *Cell Growth Differ.* **1996**, *7* (October), 1345–1351.
- (55) Ullah, M. F.; Ahmad, A.; Zubair, H.; Khan, H. Y.; Wang, Z.; Sarkar, F. H.; Hadi, S. M. Soy

- Isoflavone Genistein Induces Cell Death in Breast Cancer Cells through Mobilization of Endogenous Copper Ions and Generation of Reactive Oxygen Species. *Mol. Nutr. Food Res.* **2011**, 55 (4), 553–559. <https://doi.org/10.1002/mnfr.201000329>.
- (56) Marverti, G.; Andrews, P. A. Stimulation of Cis-Diamminedichloroplatinum(II) Accumulation by Modulation of Passive Permeability with Genistein: An Altered Response in Accumulation-Defective Resistant Cells. *Clin. Cancer Res.* **1996**, 2 (6), 991–999.
- (57) Spagnuolo, C.; Russo, G. L.; Orhan, I. E.; Habtemariam, S.; Daglia, M.; Sureda, A.; Nabavi, S. F.; Devi, K. P.; Loizzo, M. R.; Tundis, R.; et al. Genistein and Cancer: Current Status, Challenges, and Future Directions. *Adv. Nutr.* **2015**, 6 (4), 408–419. <https://doi.org/10.3945/an.114.008052>.
- (58) Chambers, A. F. MDA-MB-435 and M14 Cell Lines : Identical but Not M14 Melanoma ? *Perspect. Cancer Res.* **2009**, 63 (13), 5292–5294. <https://doi.org/10.1158/0008-5472.CAN-09-1528>.
- (59) Rae, J. M.; Creighton, C. J.; Meck, J. M.; Haddad, B. R.; Johnson, M. D. MDA-MB-435 Cells Are Derived from M14 Melanoma Cells — a Loss for Breast Cancer , but a Boon for Melanoma Research. *Breast Cancer Res Treat* **2007**, 60, 13–19. <https://doi.org/10.1007/s10549-006-9392-8>.
- (60) Clède, S.; Lambert, F.; Saint-fort, R.; Plamont, M.; Bertrand, H.; Vessières, A.; Policar, C. Influence of the Side-Chain Length on the Cellular Uptake and the Cytotoxicity of Rhenium Triscarbonyl Derivatives : A Bimodal Infrared and Luminescence Quantitative Study. *Chem. - A Eur. J.* **2014**, 3, 8714–8722. <https://doi.org/10.1002/chem.201402471>.
- (61) Puckett, C. A.; Barton, J. K. Methods to Explore Cellular Uptake of Ruthenium Complexes. *J. Am. Chem. Soc.* **2007**, 129 (1), 46–47. <https://doi.org/10.1021/ja0677564>.

- (62) Puckett, C. A.; Barton, J. K. Mechanism of Cellular Uptake of a Ruthenium Polypyridyl Complex. *Biochemistry* **2008**, *47* (45), 11711–11716. <https://doi.org/10.1021/bi800856t>.
- (63) Gill, M. R.; Cecchin, D.; Walker, M. G.; Mulla, R. S.; Battaglia, G.; Smythe, C.; Thomas, J. A. Targeting the Endoplasmic Reticulum with a Membrane-Interactive Luminescent Ruthenium(II) Polypyridyl Complex. *Chem. Sci.* **2013**, *4* (12), 4512–4519. <https://doi.org/10.1039/c3sc51725j>.
- (64) Shchepina, L. A.; Pletjushkina, O. Y.; Avetisyan, A. V.; Bakeeva, L. E.; Fetisova, E. K.; Izyumov, D. S.; Saprunova, V. B.; Vyssokikh, M. Y.; Chernyak, B. V.; Skulachev, V. P. Oligomycin, Inhibitor of the F₀ Part of H⁺-ATP-Synthase, Suppresses the TNF-Induced Apoptosis. *Oncogene* **2002**, *21*, 8149–8157. <https://doi.org/10.1038/sj.onc.1206053>.
- (65) Inho, K. P.; Youngmi, J.; Pak, K.; Hyewhon, S. B.; Suh, R. S.; Jin, S.; Mei, P.; Zhu, H.; So, I.; Kim, K. W. FCCP Depolarizes Plasma Membrane Potential by Activating Proton and Na⁺ Currents in Bovine Aortic Endothelial Cells. **2002**, 344–352. <https://doi.org/10.1007/s004240100703>.
- (66) Notaro, A.; Frei, A.; Rubbiani, R.; Jakubaszek, M.; Basu, U.; Koch, S.; Mari, C.; Dotou, M.; Blacque, O.; Gouyon, J.; et al. A Ruthenium(II) Complex Containing a Redox-Active Semiquinonate Ligand as Potential Chemotherapeutic Agent: From Synthesis to In Vivo Studies. *ChemRxiv* **2019**. <https://doi.org/10.26434/chemrxiv.9582527.v1>.
- (67) Notaro, A.; Jakubaszek, M.; Rotthowe, N.; Maschietto, F.; Felder, P. S.; Goud, B.; Tharaud, M.; Ciofini, I.; Bedioui, F.; Winter, R. F.; et al. Increasing the Cytotoxicity of Ru(II) Polypyridyl Complexes by Tuning the Electronic Structure of Dioxo Ligands. *ChemRxiv Prepr.* **2019**. <https://doi.org/10.26434/chemrxiv.10280507>.
- (68) Notaro, A.; Jakubaszek, M.; Koch, S.; Rubbiani, R.; Domotor, O.; Enyedy, É. A.; Dotou,

- M.; Bedioui, F.; Tharaud, M.; Goud, B.; et al. A Maltol-Containing Ruthenium Polypyridyl Complex as a Potential Anticancer Agent. *ChemRxiv. Prepr.* **2019**. <https://doi.org/10.26434/chemrxiv.10008917.v1>.
- (69) Fulmer, G. R.; Miller, A. J. M.; Sherden, N. H.; Gottlieb, H. E.; Nudelman, A.; Stoltz, B. M.; Bercaw, J. E.; Goldberg, K. I. NMR Chemical Shifts of Trace Impurities: Common Laboratory Solvents, Organics, and Gases in Deuterated Solvents Relevant to the Organometallic Chemist. *Organometallics* **2010**, *29* (9), 2176–2179. <https://doi.org/10.1021/om100106e>.
- (70) Tharaud, M.; Gardoll, S.; Khelifi, O.; Benedetti, M. F.; Sivry, Y. UFREASI: User-FRIENDly Elemental DATA ProcesSIng. A Free and Easy-to-Use Tool for Elemental Data Treatment. *Microchem. J.* **2015**, *121*, 32–40. <https://doi.org/10.1016/j.microc.2015.01.011>.

Supplementary Information

Synthesis, Characterisation, Cytotoxic Activity and Metabolic Studies of Ruthenium(II) Polypyridyl Complexes containing Flavonoid

Ligands

Alexandra-Cristina Munteanu,^{a,#} Anna Notaro,^{b,#} Marta Jakubaszek,^{b,c} Joseph Cowell,^b Mickaël Tharaud,^d Bruno Goud,^c Valentina Uivarosi,^a and Gilles Gasser^{b,}*

^a Department of General and Inorganic Chemistry, Faculty of Pharmacy, “Carol Davila” University of Medicine and Pharmacy, 020956 Bucharest, Romania.

^b Chimie ParisTech, PSL University, CNRS, Institute of Chemistry for Life and Health Sciences, Laboratory for Inorganic Chemical Biology, F-75005 Paris, France.

^c Institut Curie, PSL University, CNRS UMR 144, Paris, France.

^d Université de Paris, Institut de physique du globe de Paris, CNRS, F-75005 Paris, France.

[#] these authors have contributed equally to the work

* Corresponding author: E-mail: gilles.gasser@chimeparistech.psl.eu; WWW: www.gassergroup.com; Phone: +33 1 44 27 56 02

Table of Contents

FIGURE S1. $^1\text{H-NMR}$ SPECTRUM OF $[\text{RU}(\text{DIP})_2(5\text{-OHF})](\text{PF}_6)$	747
FIGURE S2. $^1\text{H-NMR}$ SPECTRUM OF $[\text{RU}(\text{DIP})_2(\text{GEN})](\text{PF}_6)$	748
FIGURE S3. $^1\text{H-NMR}$ SPECTRUM OF $[\text{RU}(\text{DIP})_2(\text{CHR})](\text{OTf})$	749
FIGURE S4. $^1\text{H-NMR}$ SPECTRUM OF $[\text{RU}(\text{DIP})_2(\text{MOR})](\text{OTf})$	750
FIGURE S5. $^1\text{H-NMR}$ SPECTRUM OF $[\text{RU}(\text{DIP})_2(\text{MOR})](\text{OTf})$ AFTER 5 DAYS IN SOLUTION	751
FIGURE S6. $^{13}\text{C-NMR}$ SPECTRUM OF $[\text{RU}(\text{DIP})_2(5\text{-OHF})](\text{PF}_6)$	753
FIGURE S7. $^{13}\text{C-NMR}$ SPECTRUM OF $[\text{RU}(\text{DIP})_2(\text{GEN})](\text{PF}_6)$	754
FIGURE S8. $^{13}\text{C-NMR}$ SPECTRUM OF $[\text{RU}(\text{DIP})_2(\text{CHR})](\text{OTf})$	755
FIGURE S9. $^{13}\text{C-NMR}$ SPECTRUM OF $[\text{RU}(\text{DIP})_2(\text{MOR})](\text{OTf})$	756
FIGURE S10. OVERLAP OF $^1\text{H-NMR}$ SPECTRA OF $[\text{RU}(\text{DIP})_2(5\text{-OHF})](\text{PF}_6)$ IN DMSO	757
FIGURE S11. OVERLAP OF $^1\text{H-NMR}$ SPECTRA OF $[\text{RU}(\text{DIP})_2(\text{GEN})](\text{PF}_6)$ IN DMSO	758
FIGURE S12. OVERLAP OF $^1\text{H-NMR}$ SPECTRA OF $[\text{RU}(\text{DIP})_2(\text{CHR})](\text{OTf})$ IN DMSO	759
FIGURE S13. OVERLAP OF $^1\text{H-NMR}$ SPECTRA OF $[\text{RU}(\text{DIP})_2(\text{MOR})](\text{OTf})$ IN DMF	760
FIGURE S14. FLUOROMETRIC CELL VIABILITY ASSAY	761
FIGURE S15. OXYGEN CONSUMPTION RATES AND DIFFERENT RESPIRATION PARAMETERS IN MDA-MB-435S CELLS ALONE OR AFTER TREATMENT WITH VARIOUS TEST COMPOUNDS.	774
FIGURE S16. EXTRACELLULAR ACIDIFICATION RATE AND DIFFERENT PARAMETERS DURING GLYCOLYSIS IN MDA-MB-435S CELLS ALONE OR AFTER TREATMENT WITH VARIOUS TEST COMPOUNDS.	775

Figure S1. $^1\text{H-NMR}$ spectrum of $[\text{Ru}(\text{DIP})_2(5\text{-OHf})](\text{PF}_6)$

CD_2Cl_2 , 400 MHz

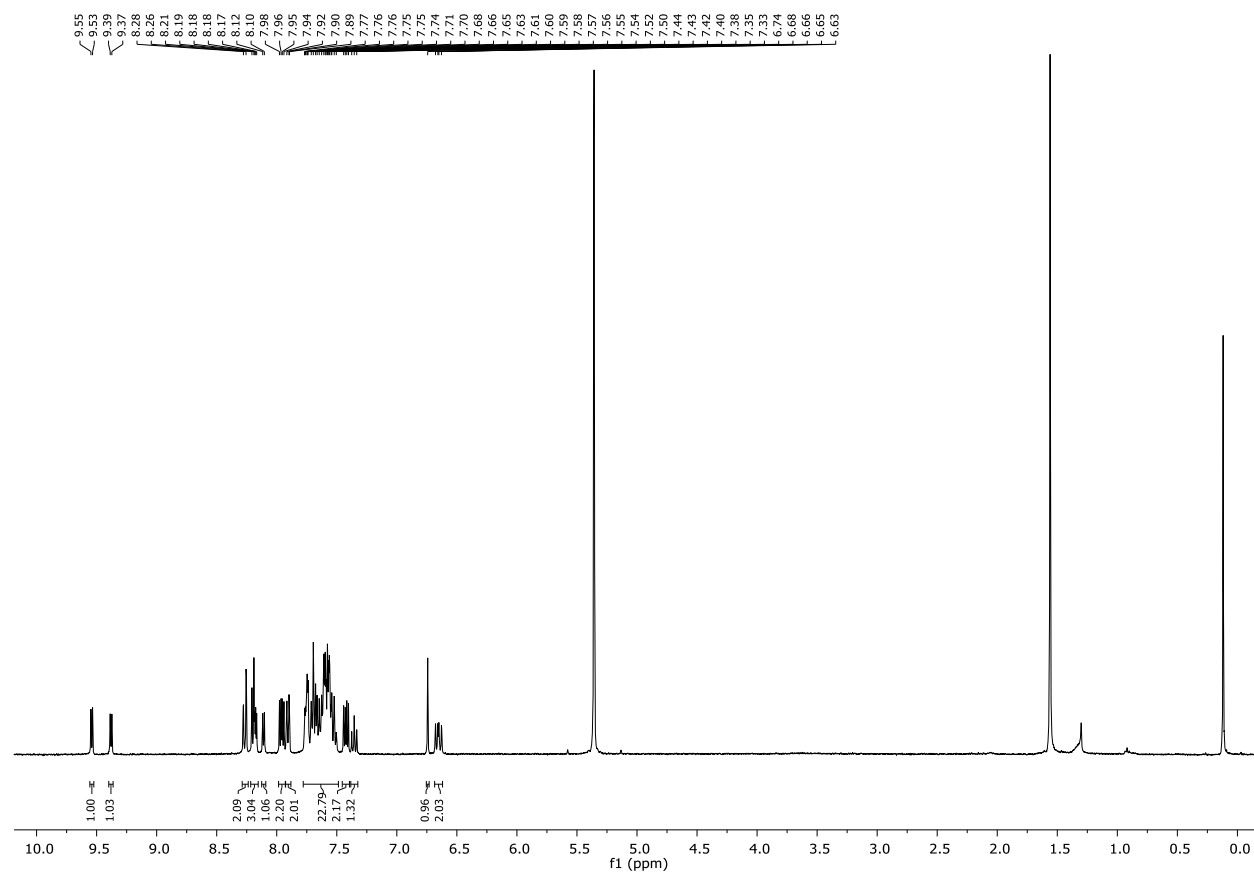


Figure S2. $^1\text{H-NMR}$ spectrum of $[\text{Ru}(\text{DIP})_2(\text{gen})](\text{PF}_6)$

CD_3OD , 400 MHz

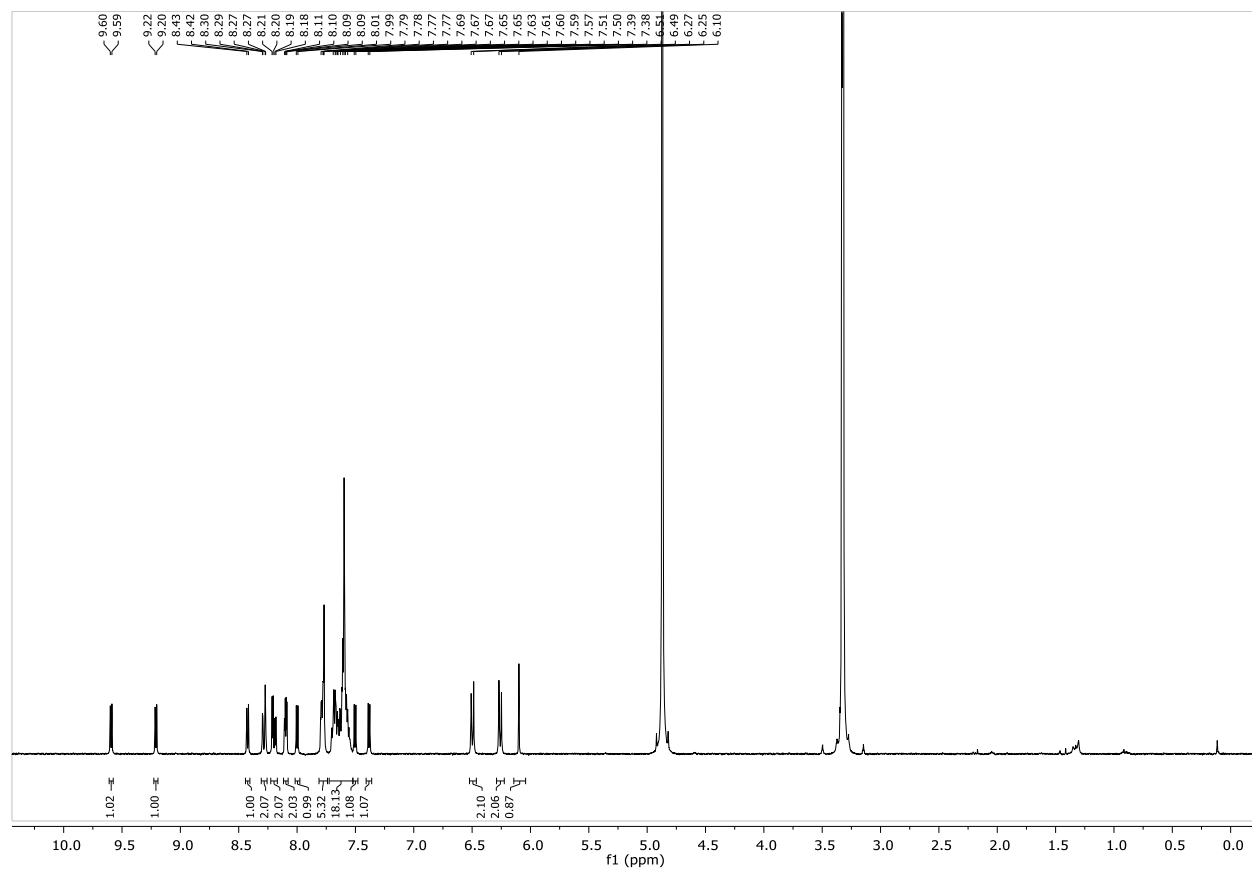


Figure S3. $^1\text{H-NMR}$ spectrum of $[\text{Ru}(\text{DIP})_2(\text{chr})](\text{OTf})$

CD_2Cl_2 , 400 MHz

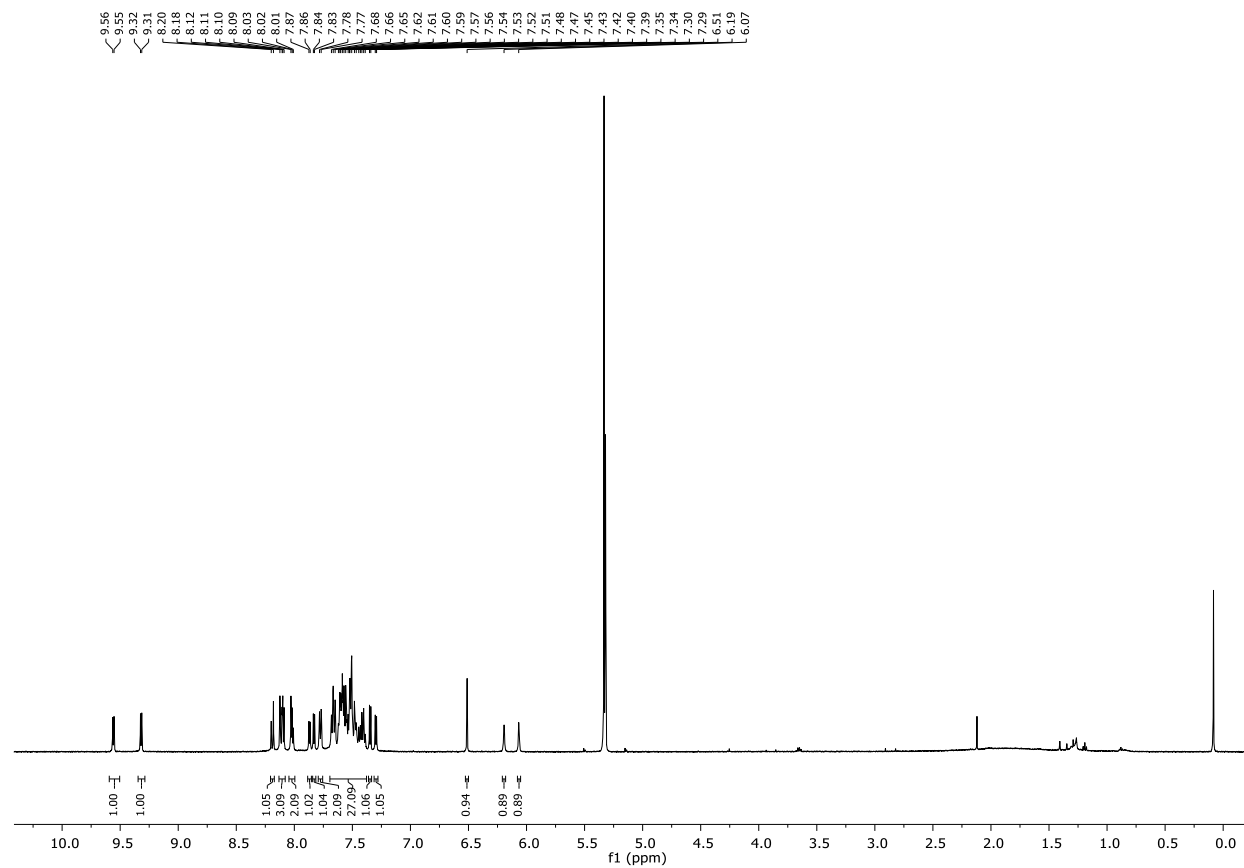


Figure S4. $^1\text{H-NMR}$ spectrum of $[\text{Ru}(\text{DIP})_2(\text{mor})](\text{OTf})$

$\text{DMF-}d_7$, 400 MHz

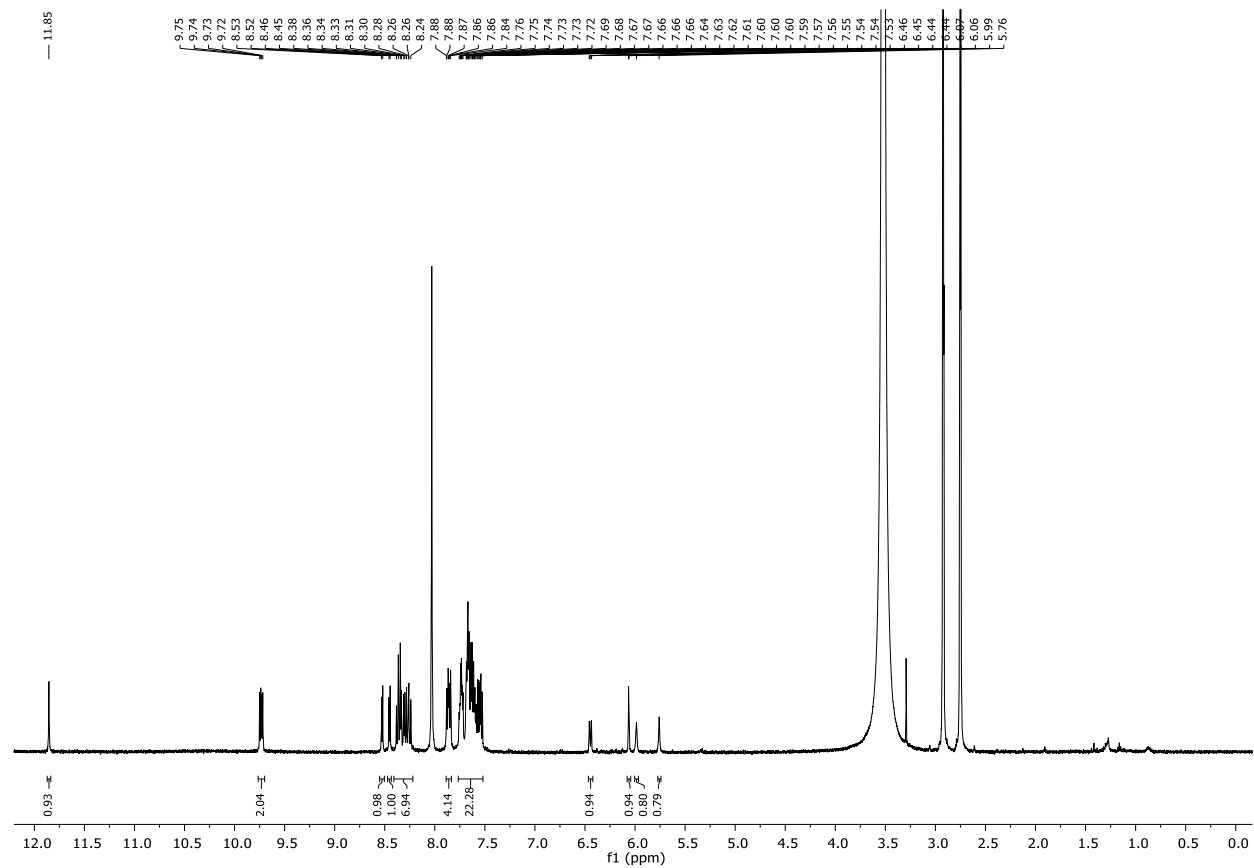
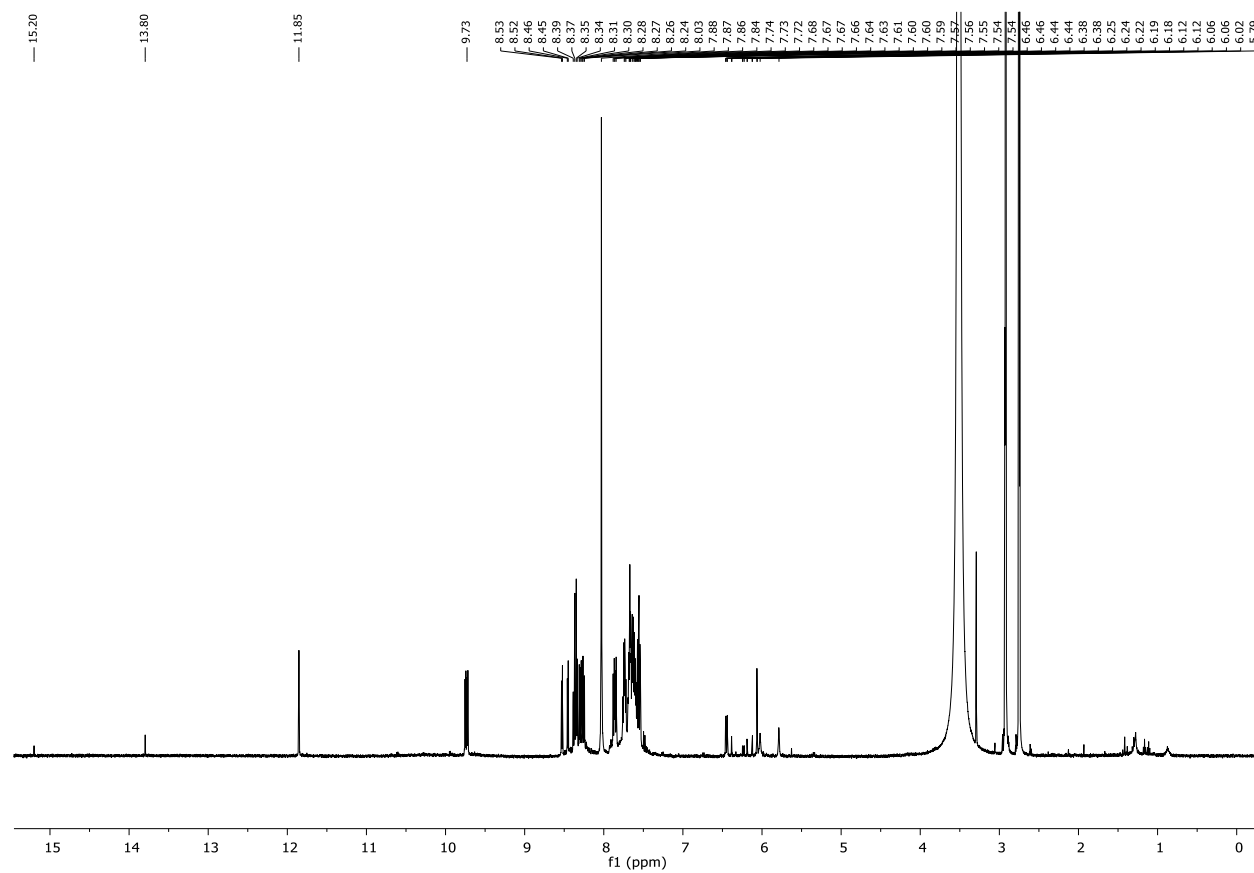


Figure S5. $^1\text{H-NMR}$ spectrum of $[\text{Ru}(\text{DIP})_2(\text{mor})](\text{OTf})$ after 5 days in solution

$\text{DMF-}d_7$, 400 MHz



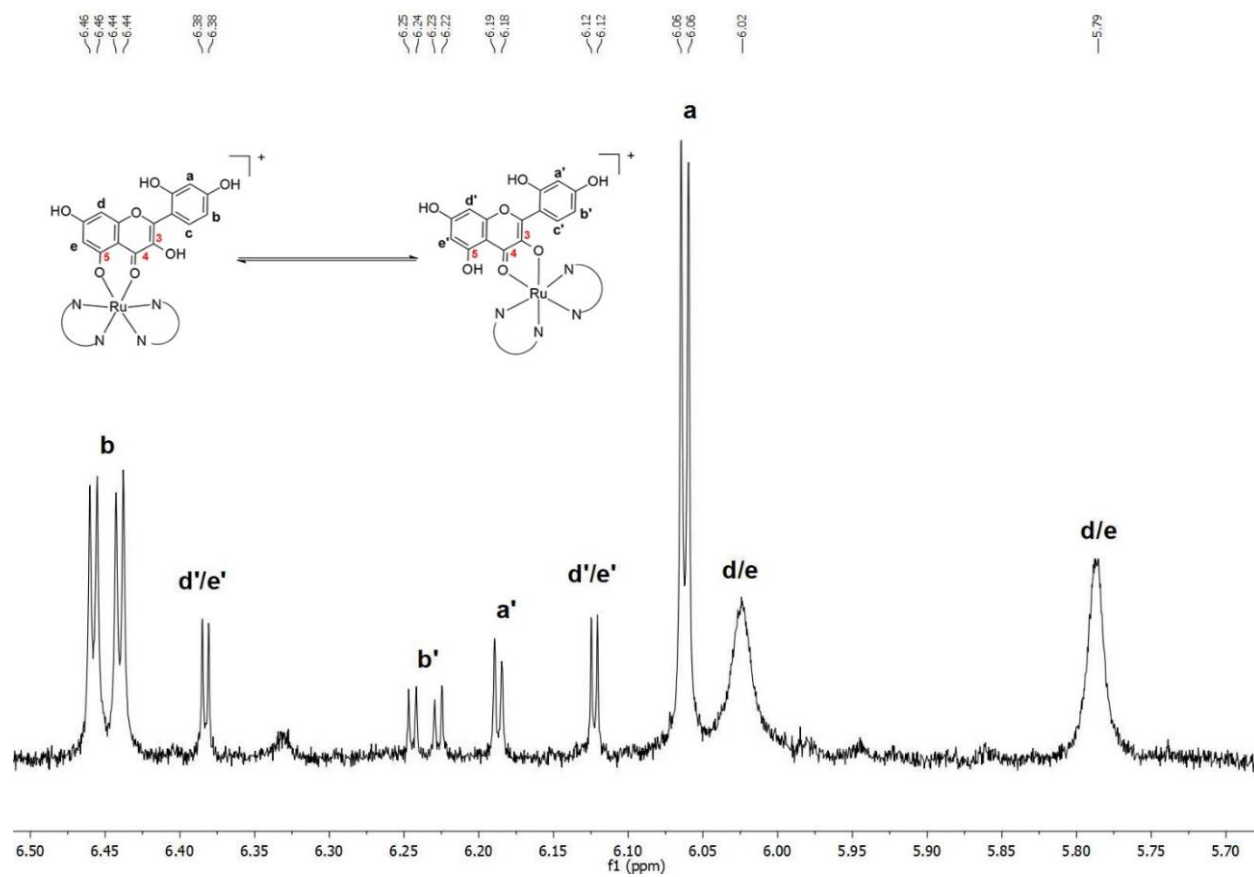


Figure S6. ^{13}C -NMR spectrum of $[\text{Ru}(\text{DIP})_2(5\text{-OHF})](\text{PF}_6)$

CD_2Cl_2 , 125 MHz

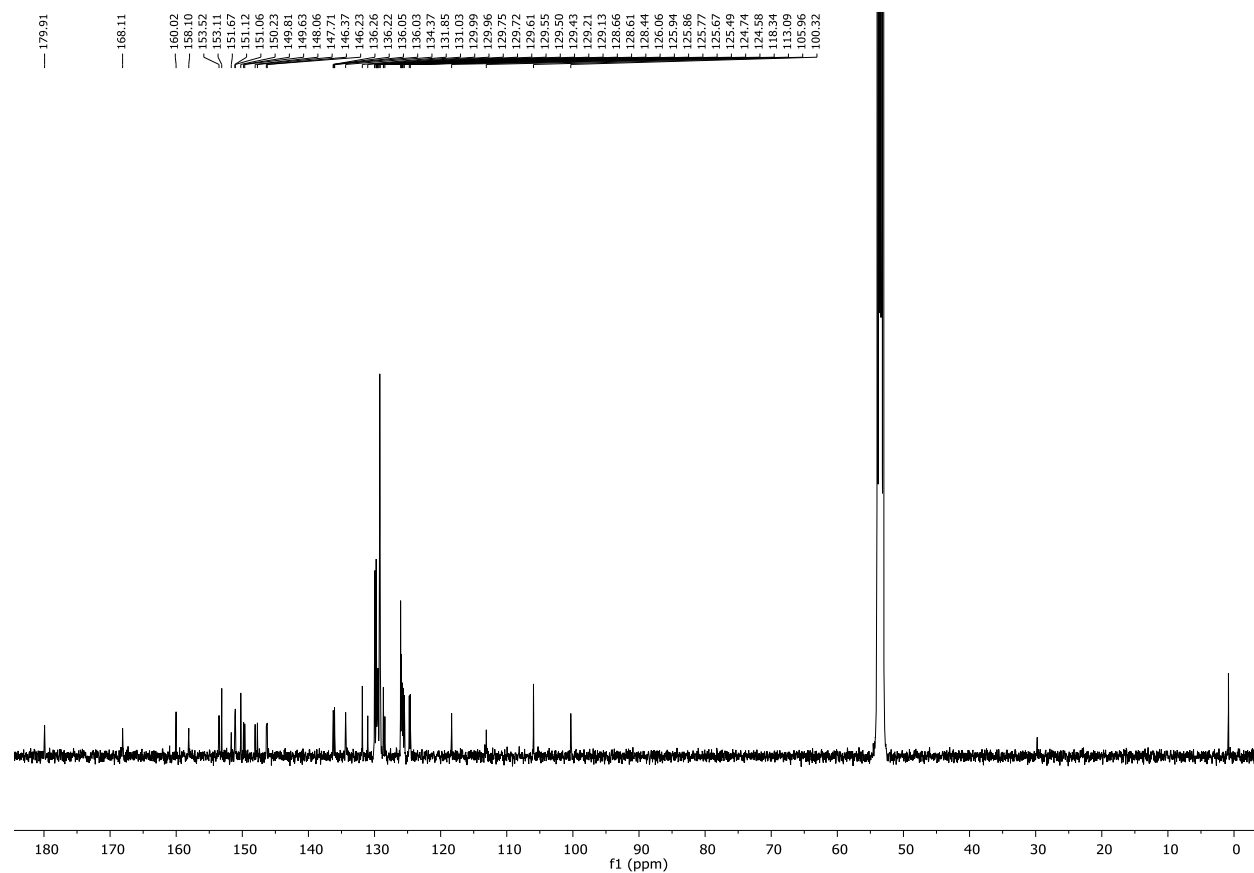


Figure S7. ^{13}C -NMR spectrum of $[\text{Ru}(\text{DIP})_2(\text{gen})](\text{PF}_6)$

CD_3OD , 125 MHz

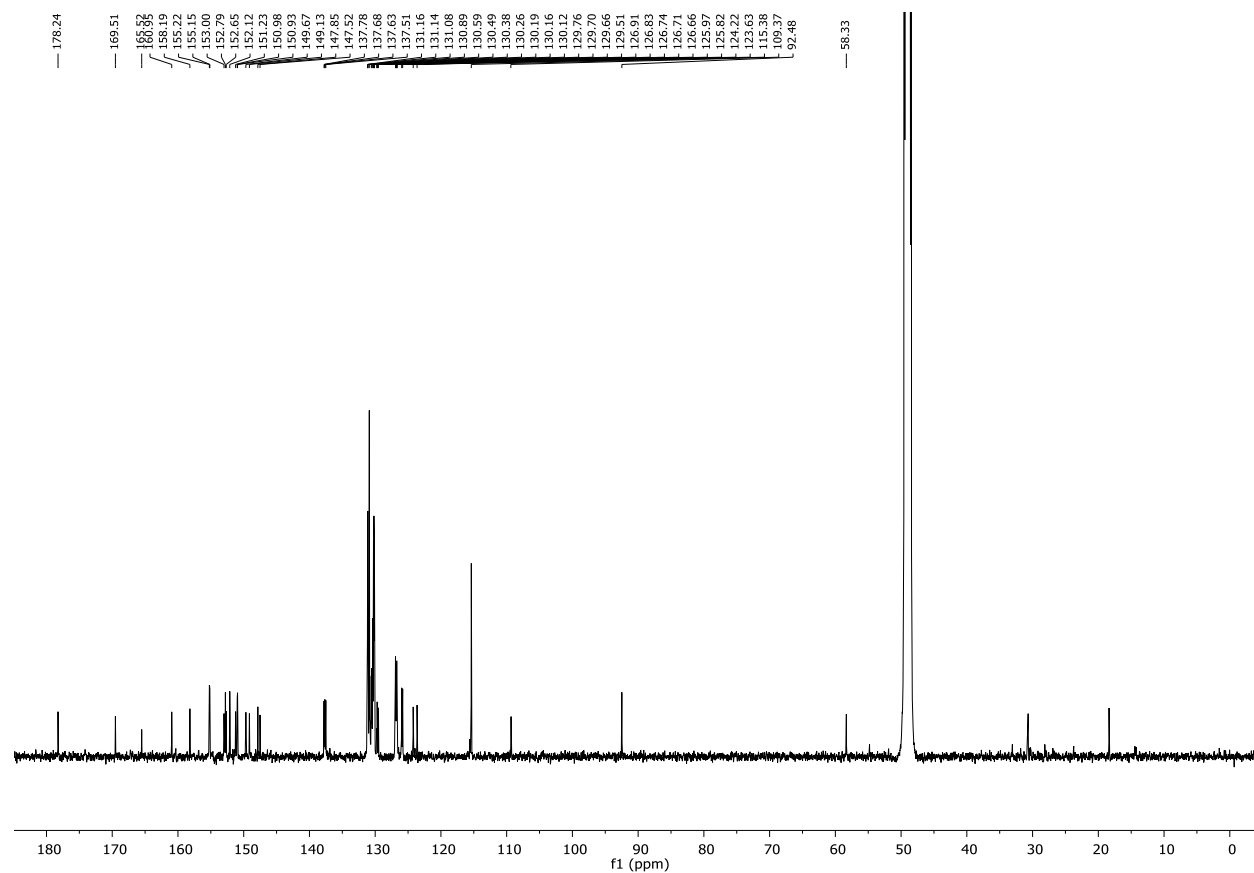


Figure S8. ^{13}C -NMR spectrum of $[\text{Ru}(\text{DIP})_2(\text{chr})](\text{OTf})$

CD_2Cl_2 , 500 MHz

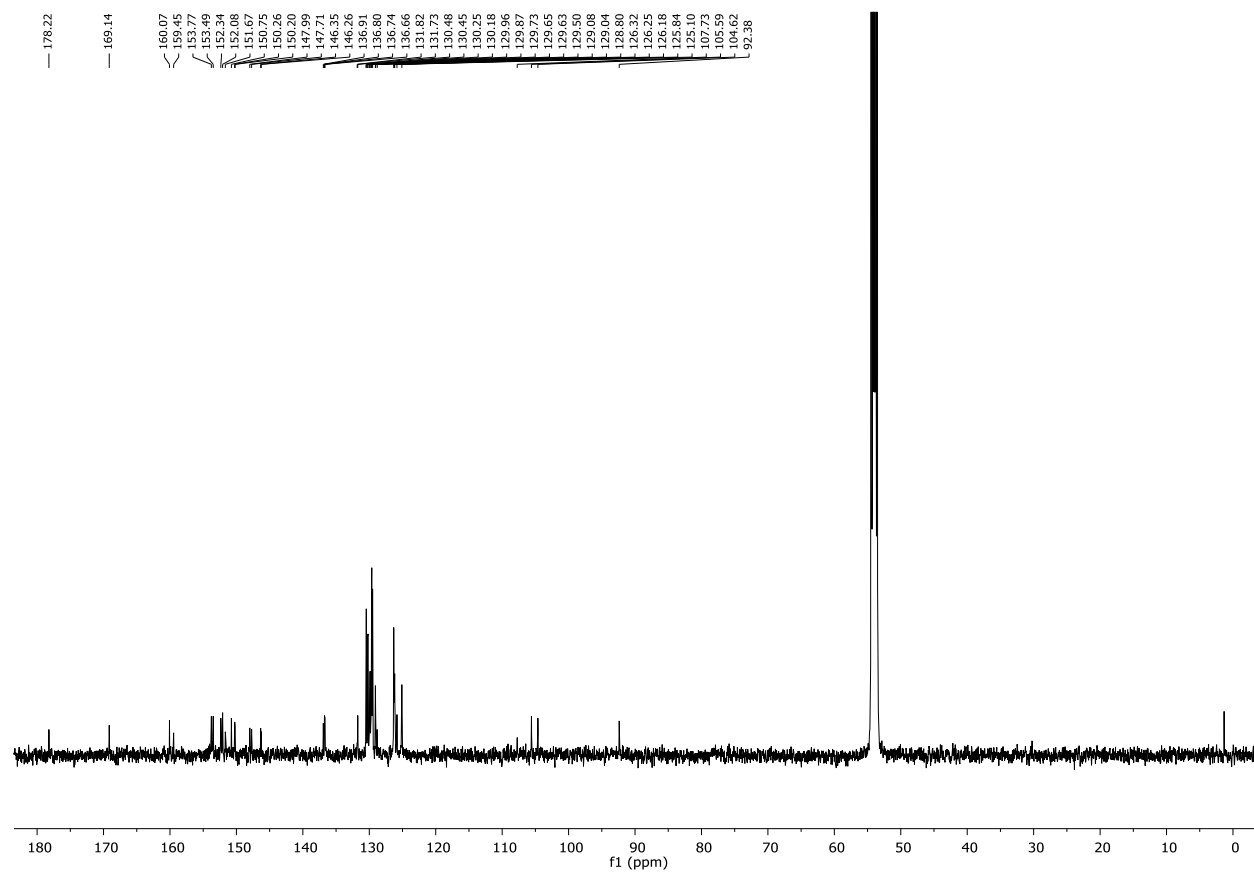


Figure S9. ^{13}C -NMR spectrum of $[\text{Ru}(\text{DIP})_2(\text{mor})](\text{OTf})$

DMF-*d*₇, 125 MHz

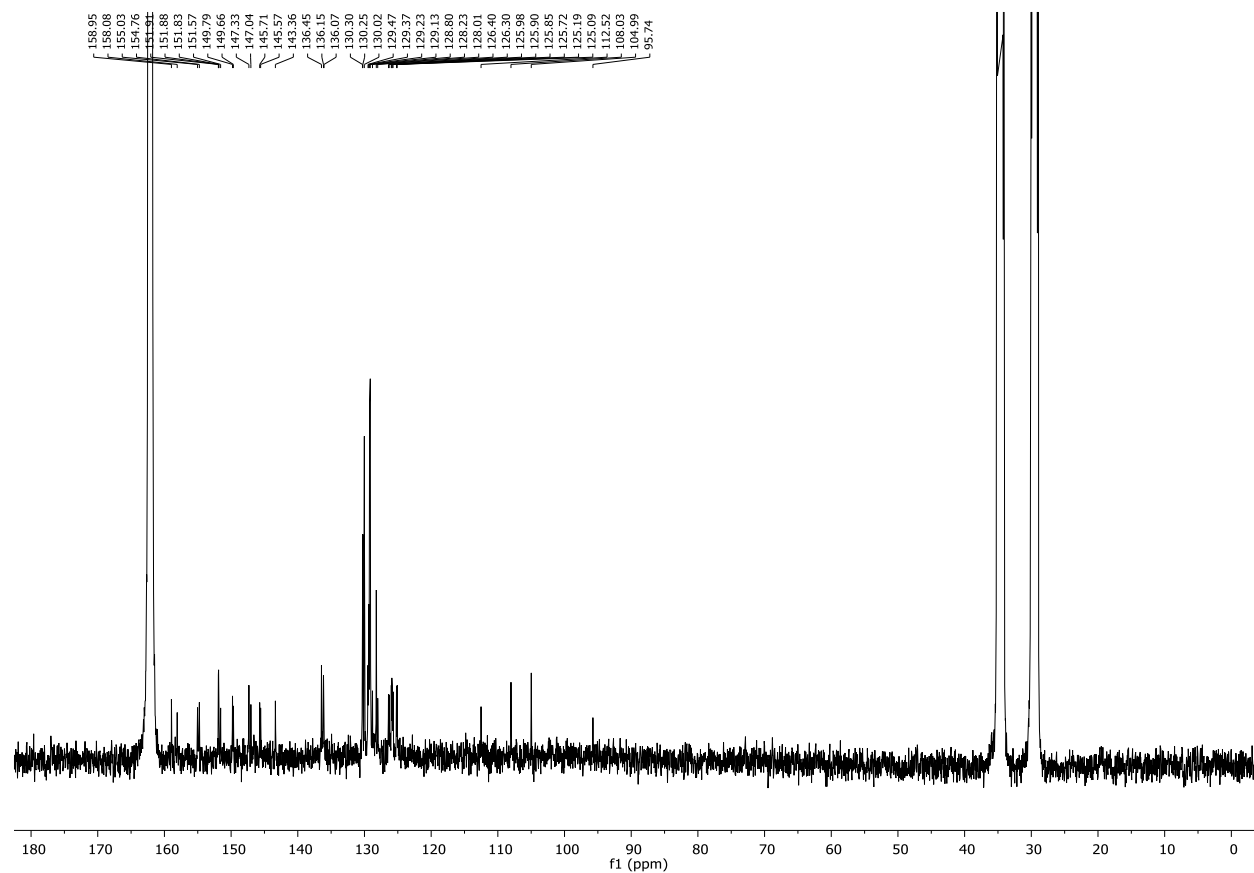


Figure S10. Overlap of ^1H -NMR spectra of $[\text{Ru}(\text{DIP})_2(5\text{-OHF})](\text{PF}_6)$ in DMSO

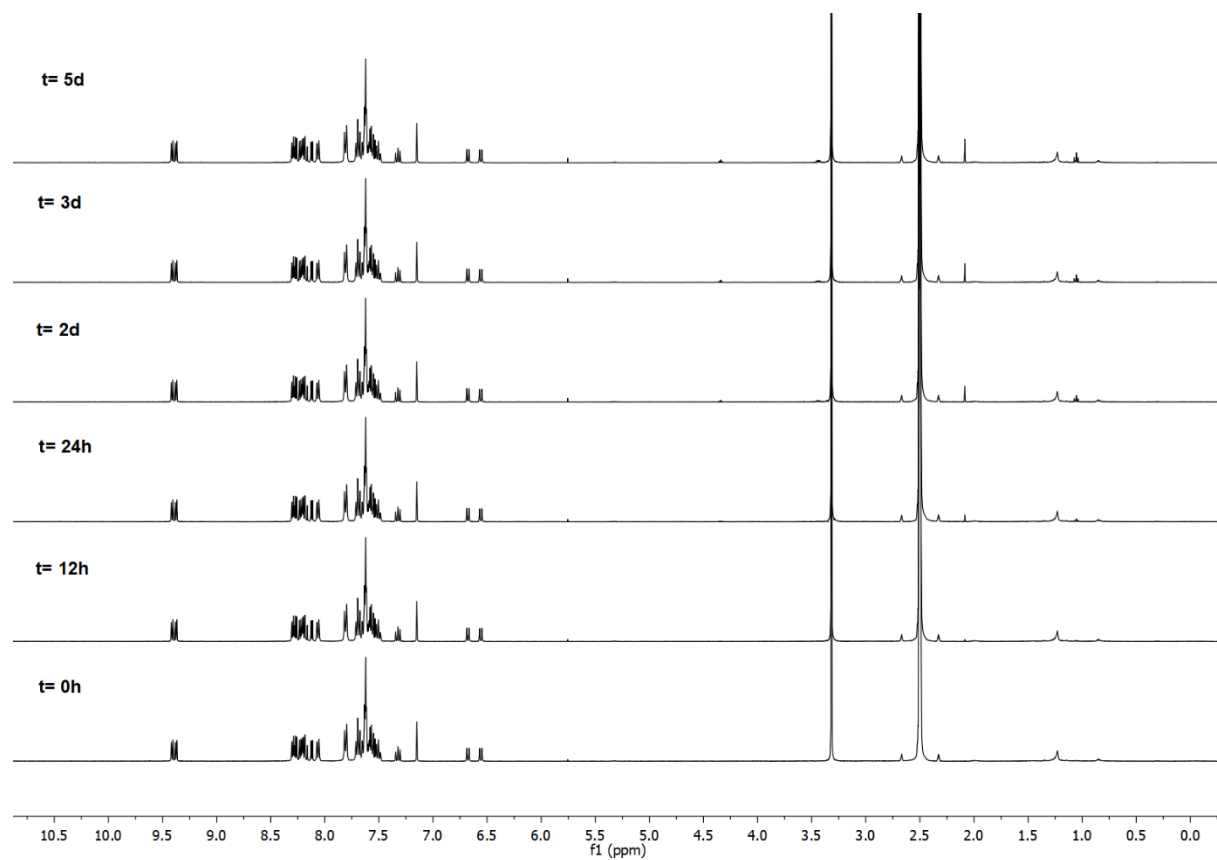


Figure S11. Overlap of ^1H -NMR spectra of $[\text{Ru}(\text{DIP})_2(\text{gen})](\text{PF}_6)$ in DMSO

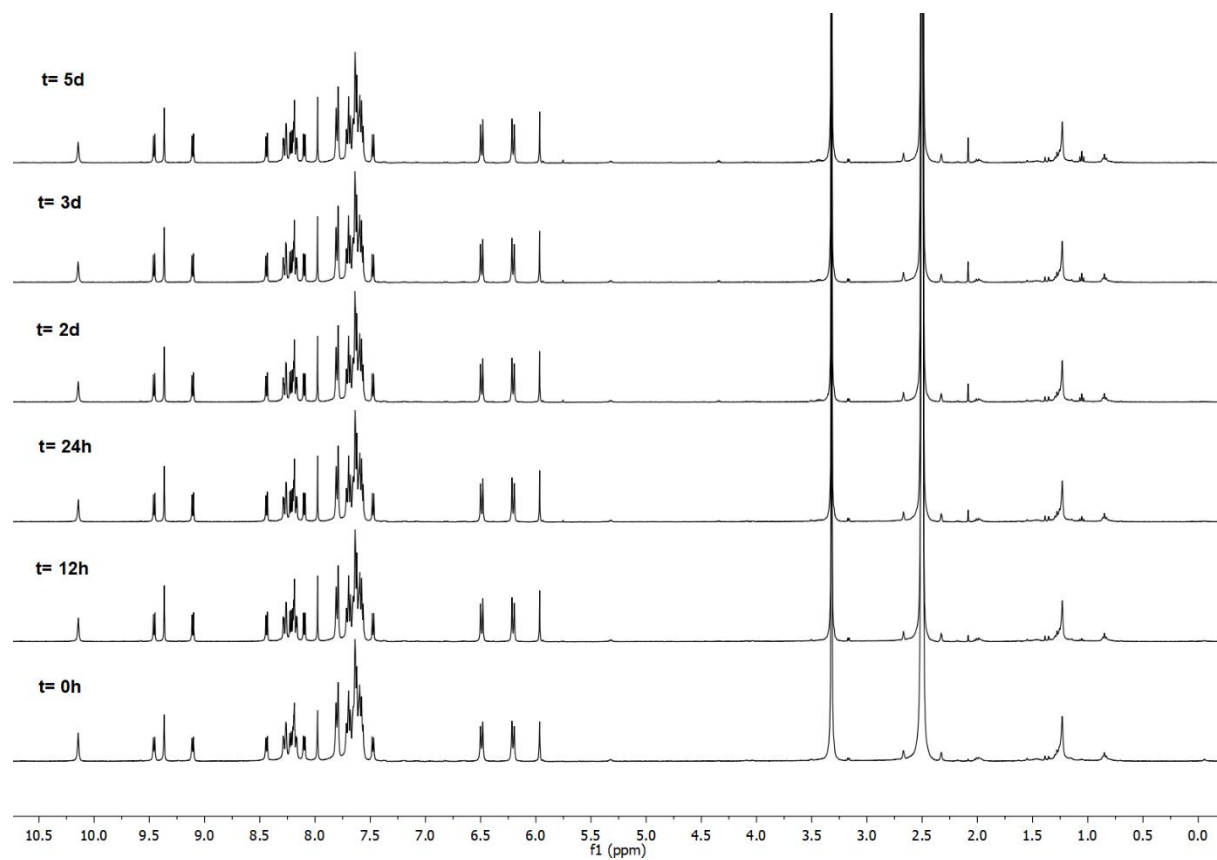


Figure S12. Overlap of ^1H -NMR spectra of $[\text{Ru}(\text{DIP})_2(\text{chr})](\text{OTf})$ in DMSO

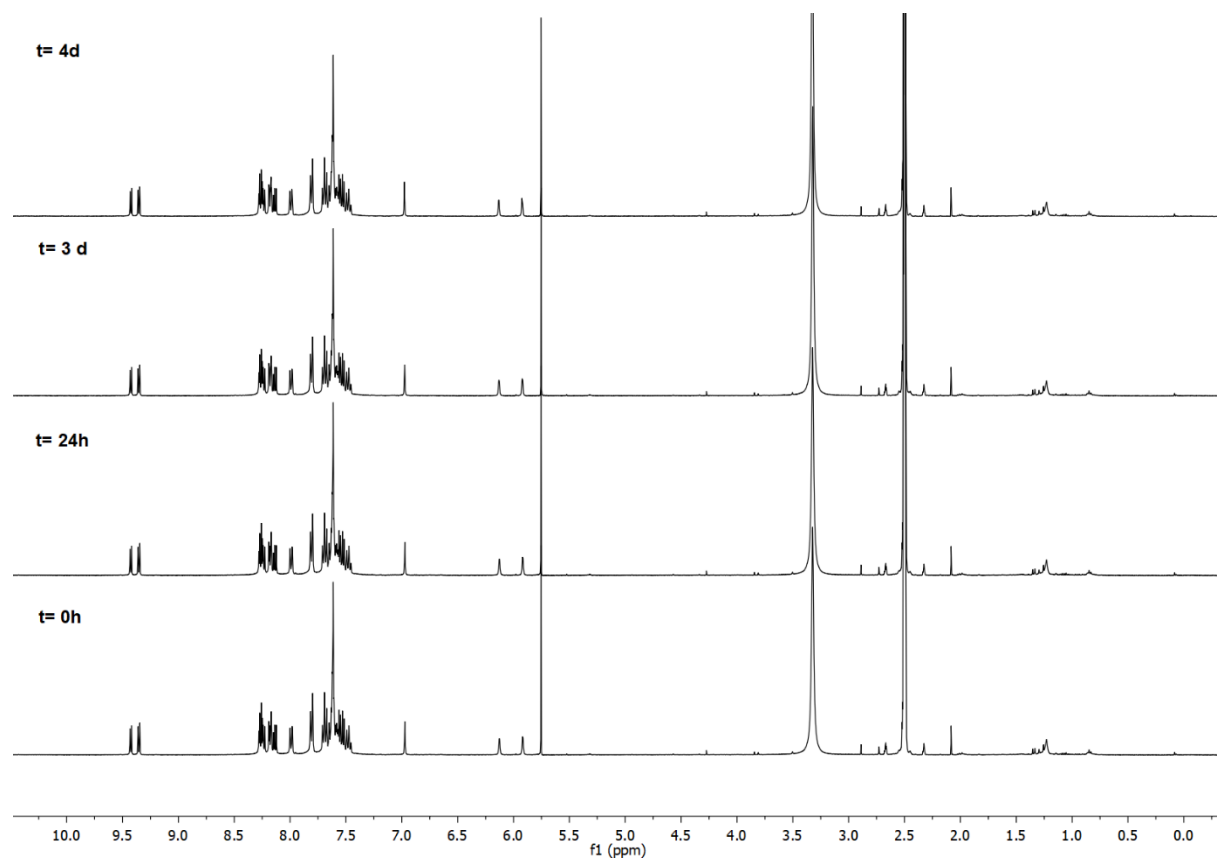


Figure S13. Overlap of ^1H -NMR spectra of $[\text{Ru}(\text{DIP})_2(\text{mor})](\text{OTf})$ in DMF

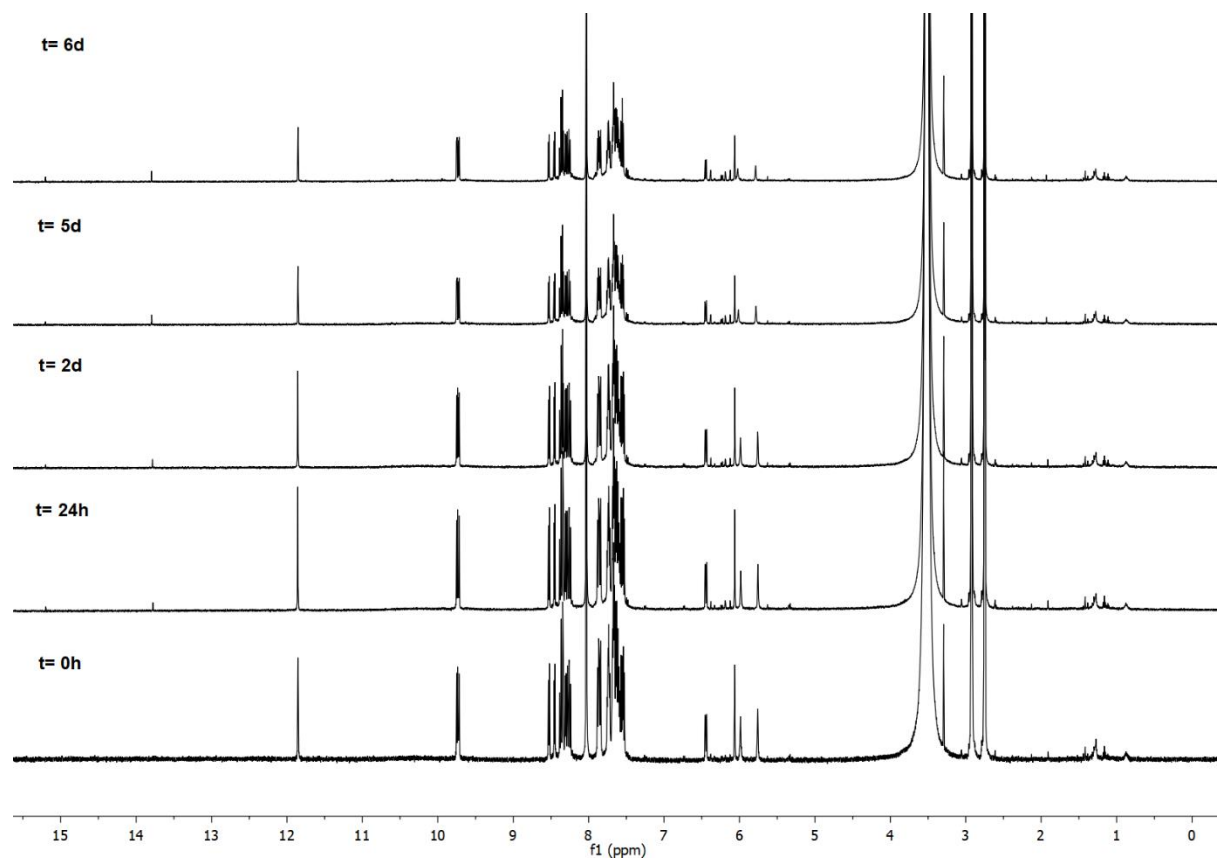
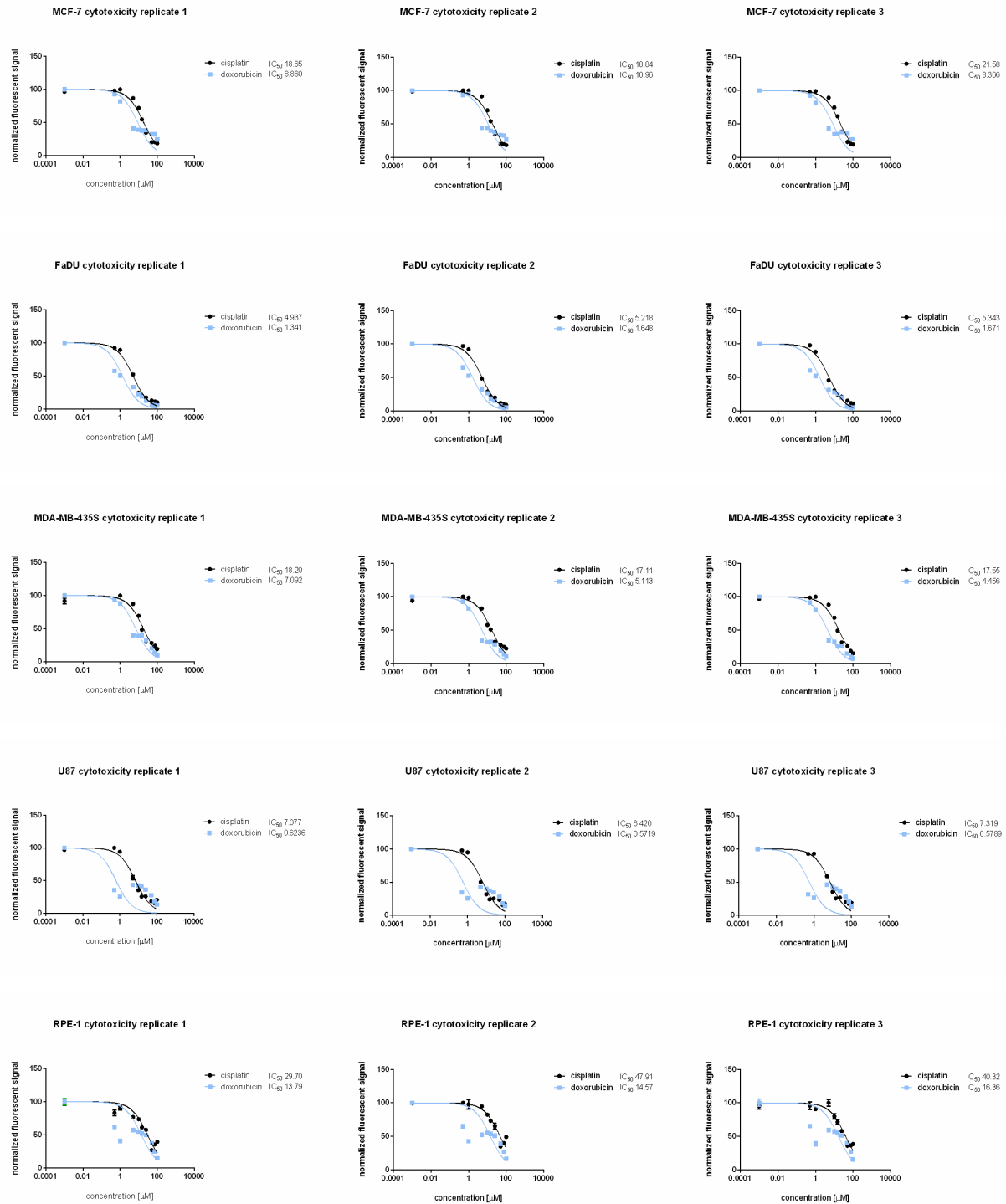
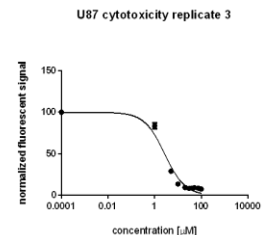
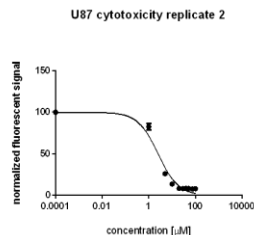
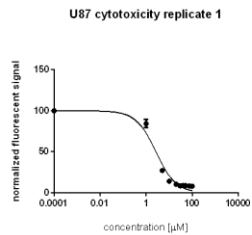
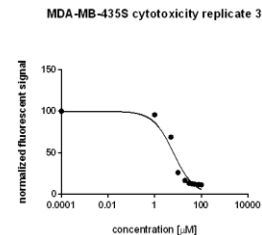
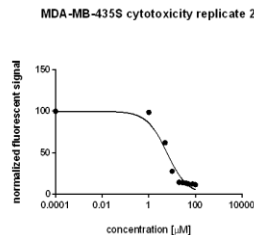
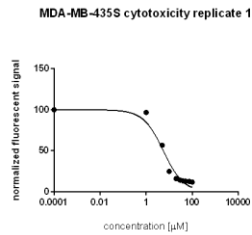
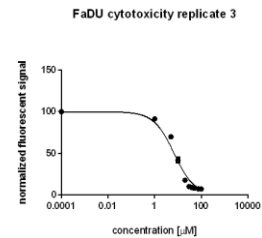
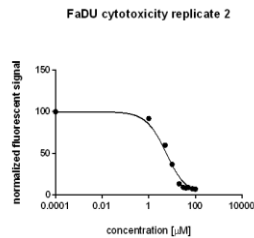
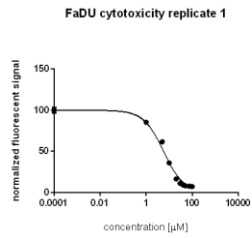
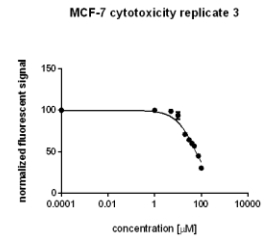
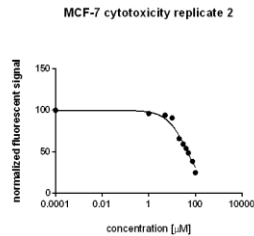
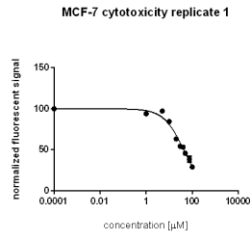
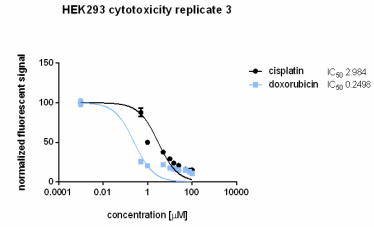
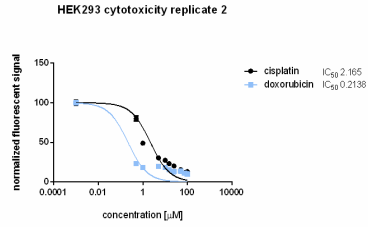
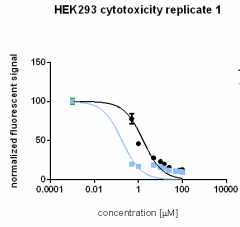
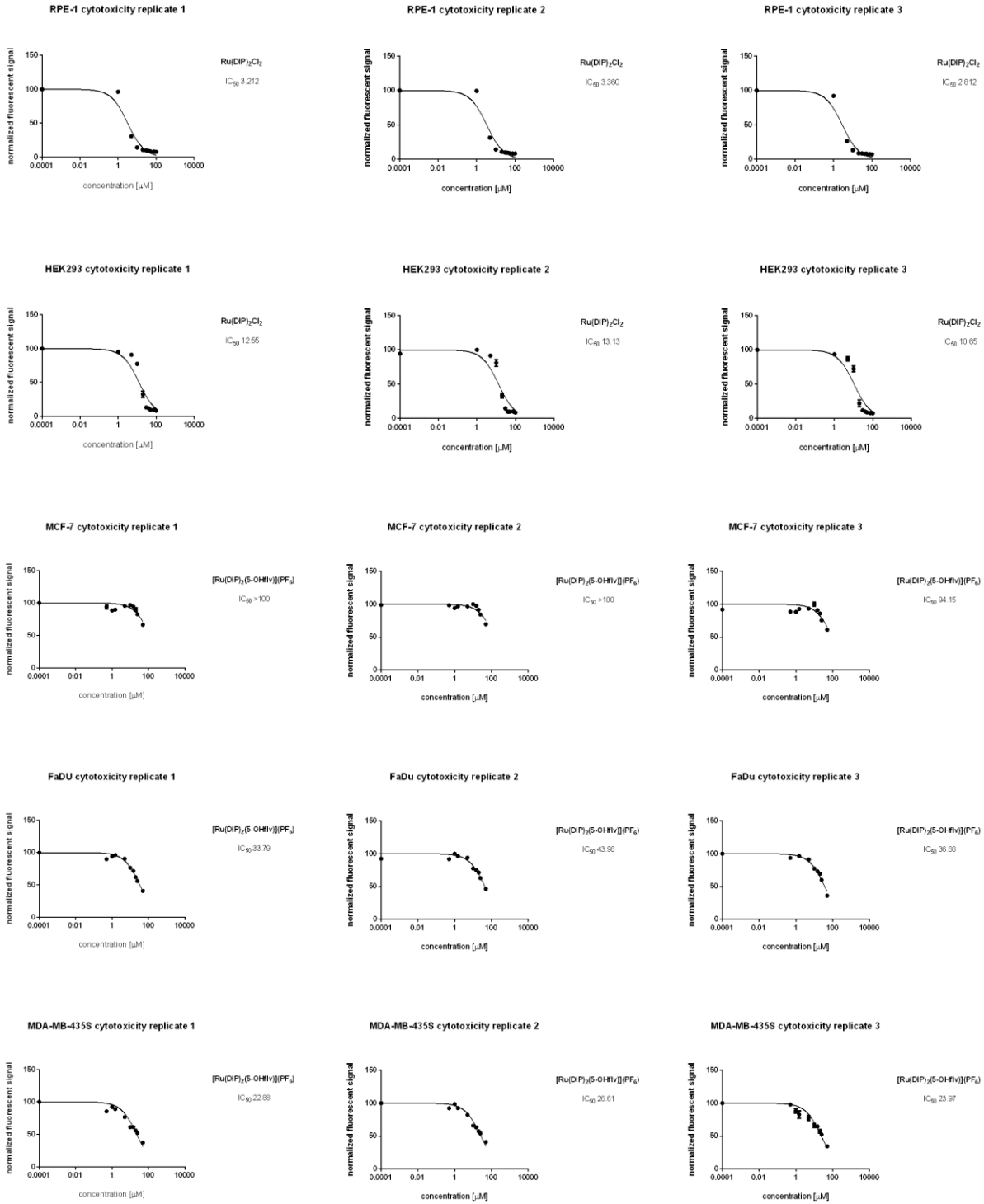
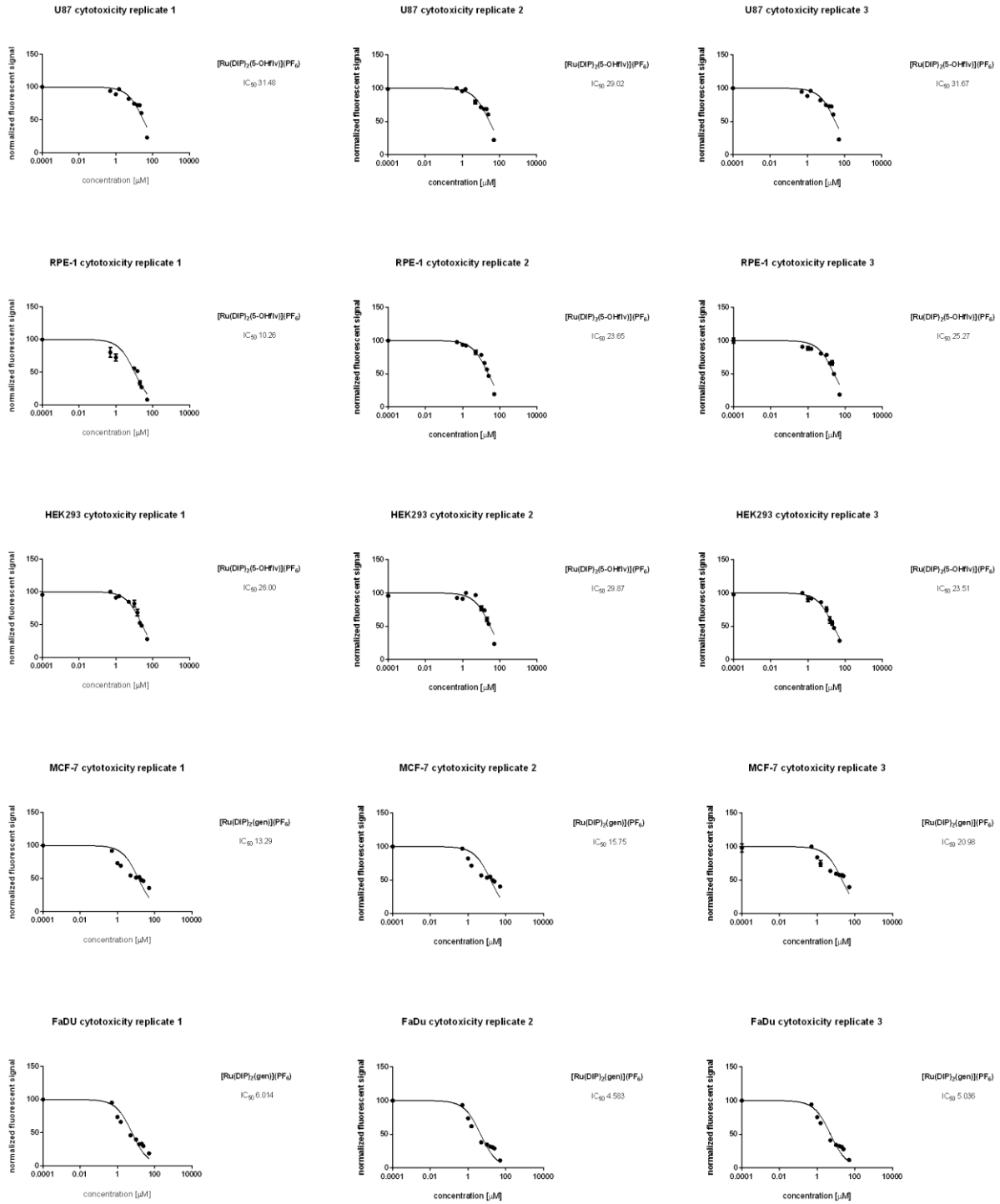


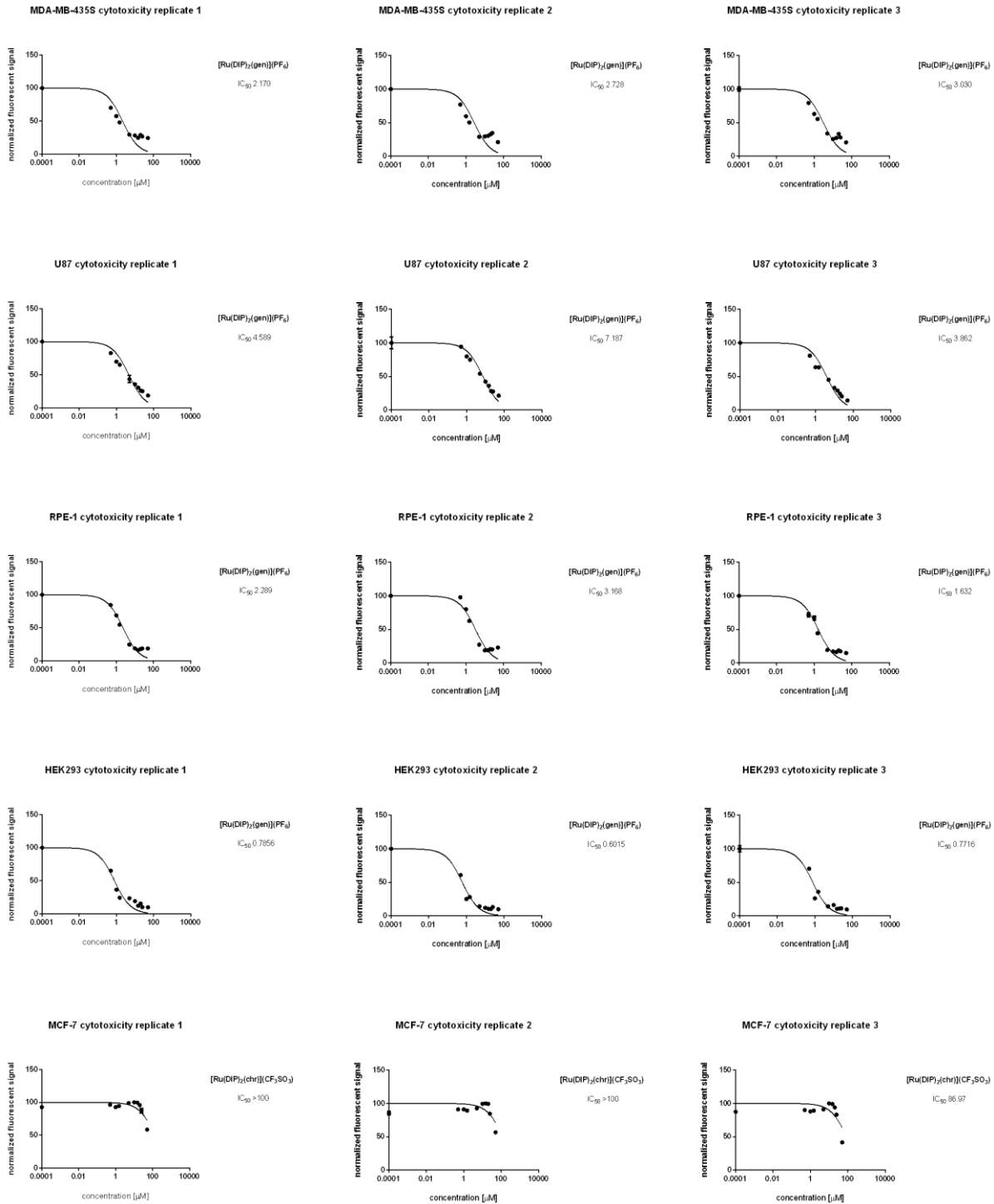
Figure S14. Fluorometric cell viability assay.

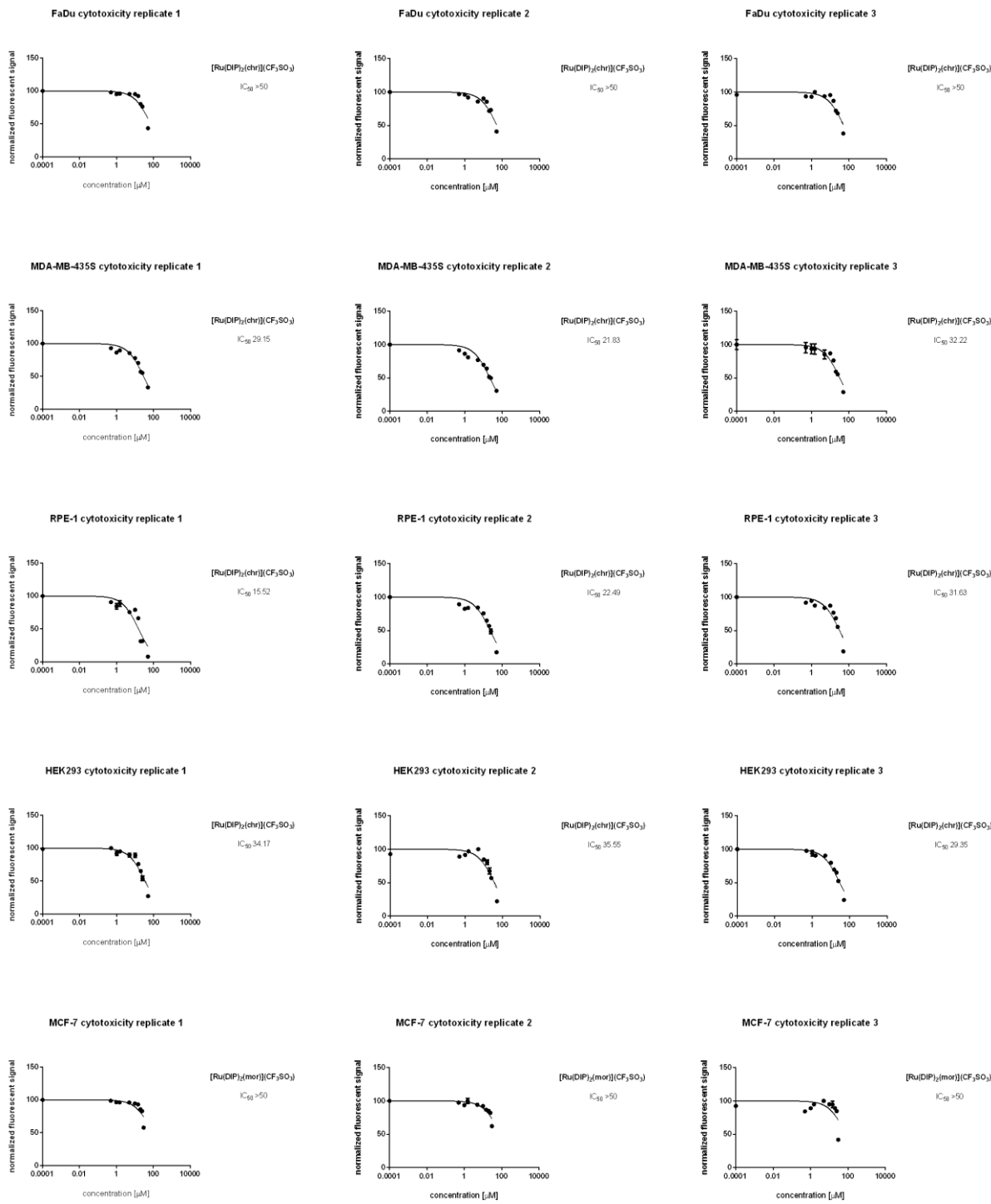


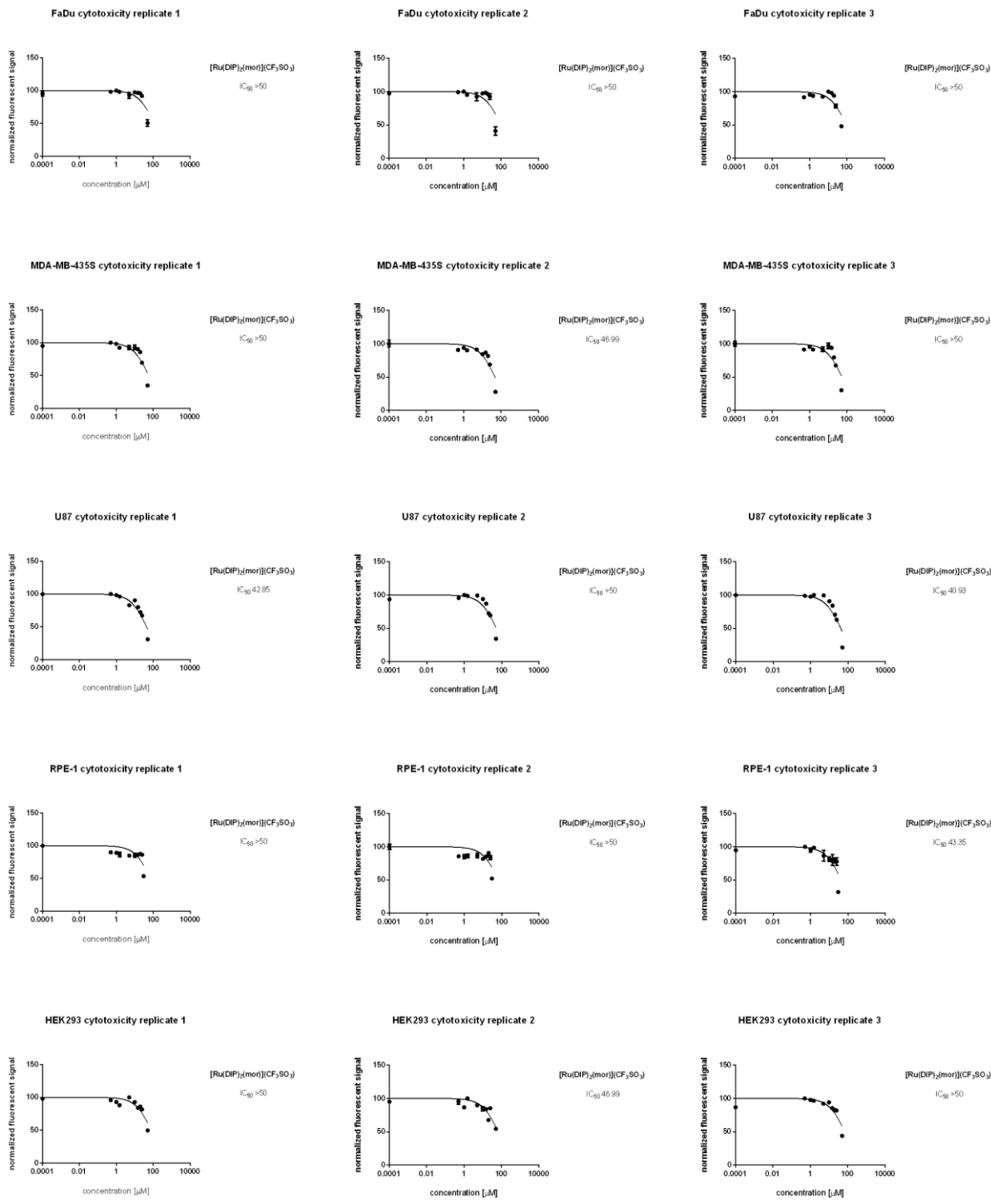


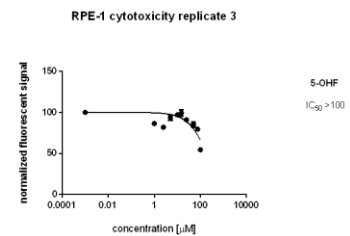
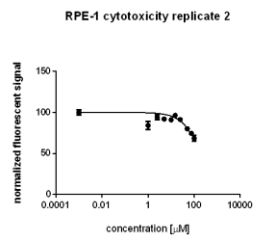
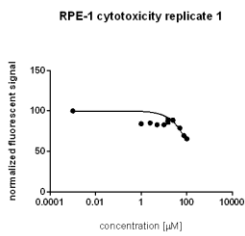
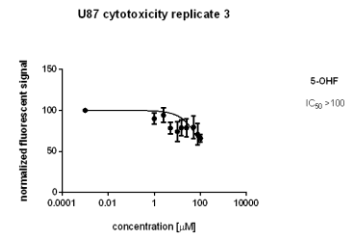
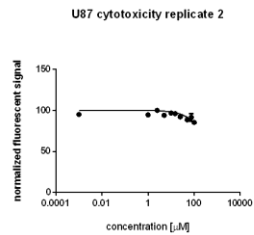
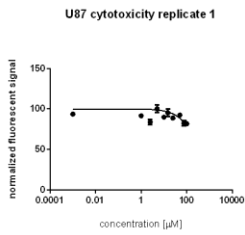
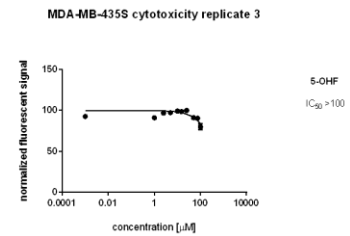
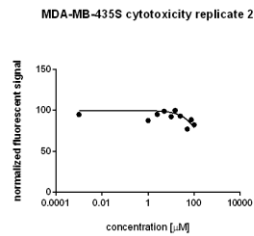
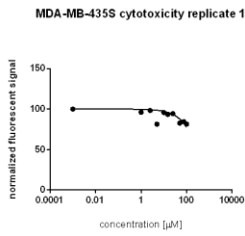
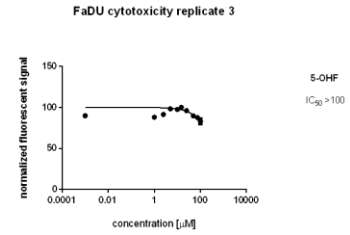
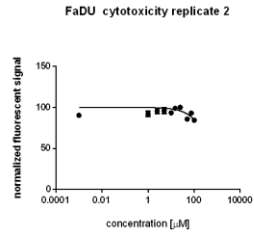
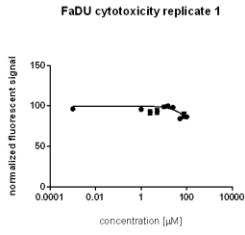
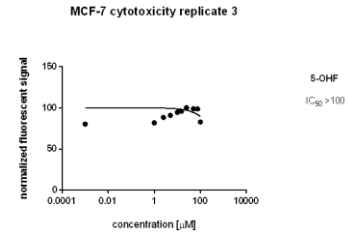
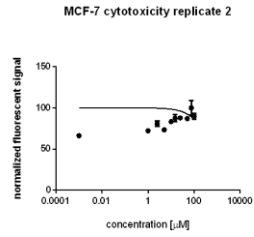
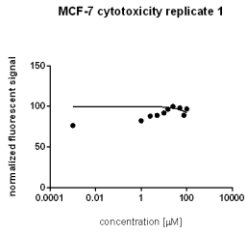


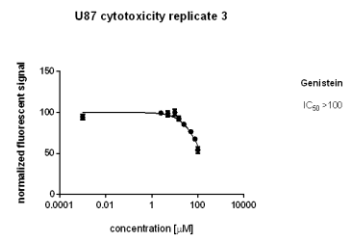
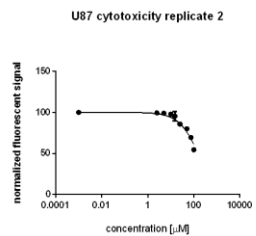
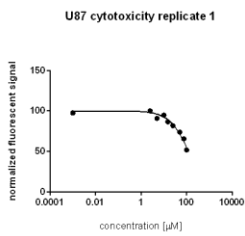
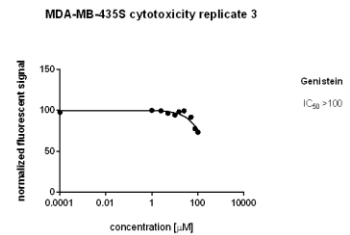
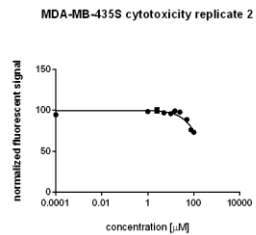
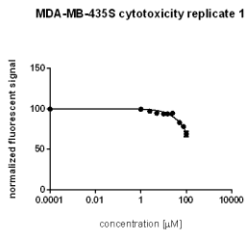
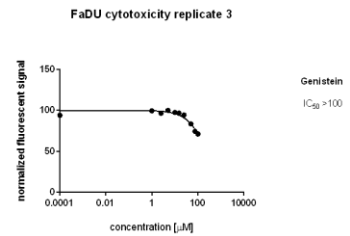
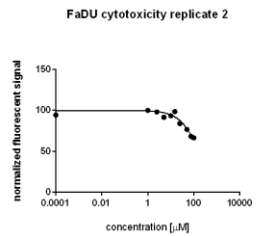
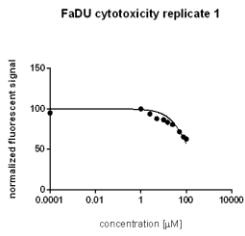
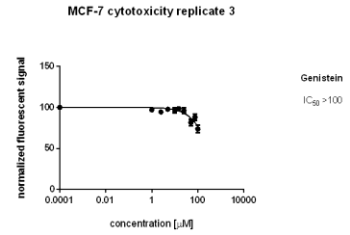
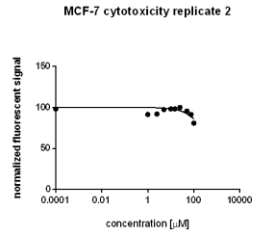
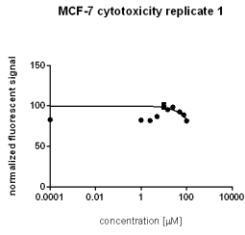
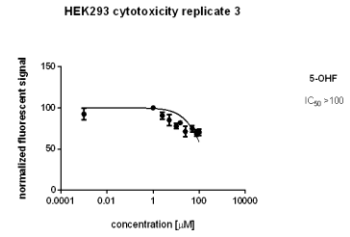
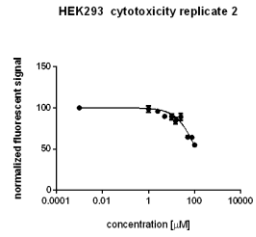
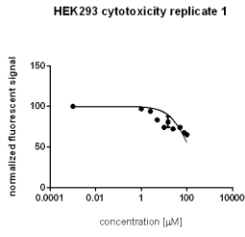


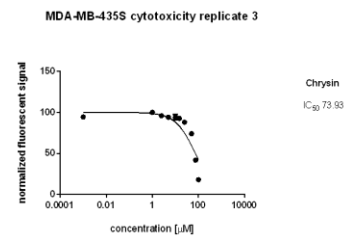
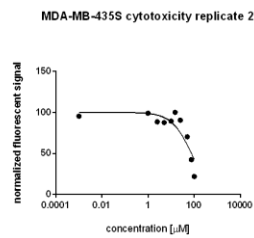
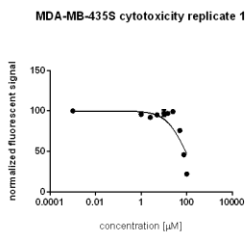
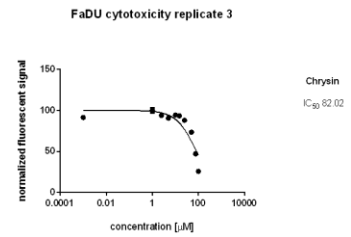
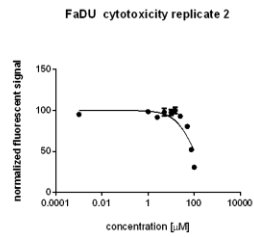
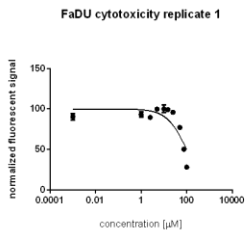
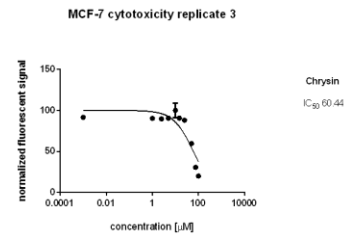
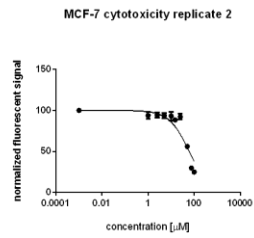
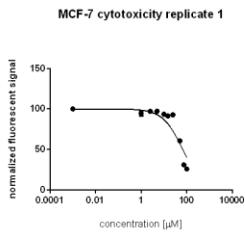
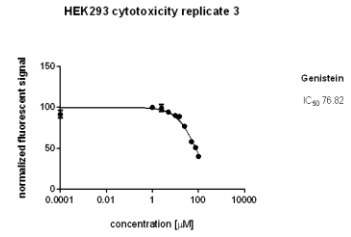
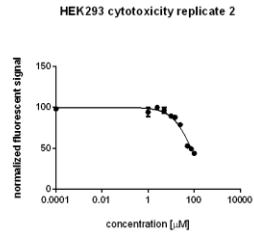
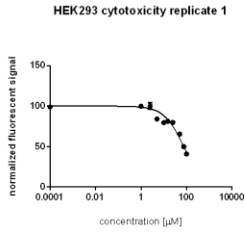
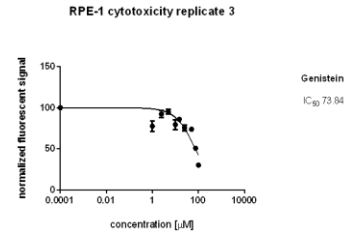
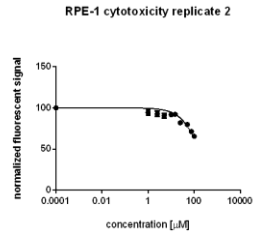
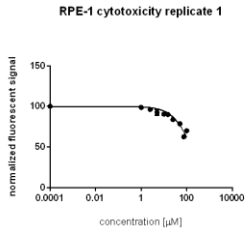


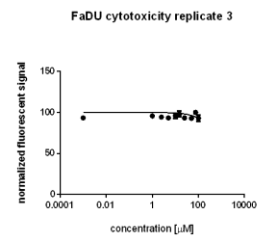
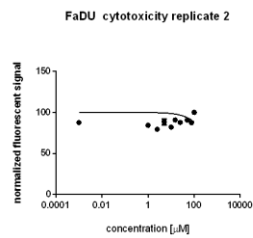
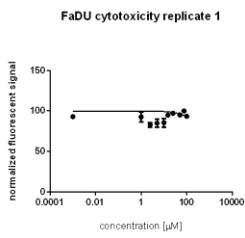
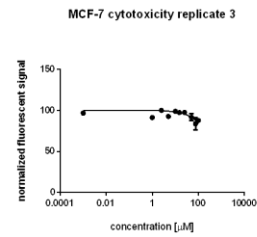
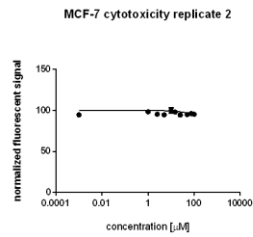
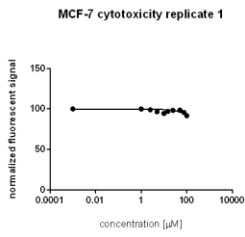
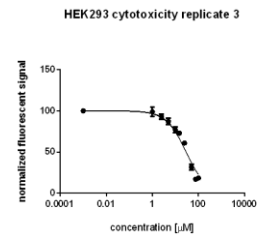
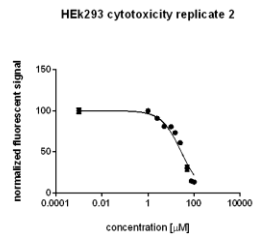
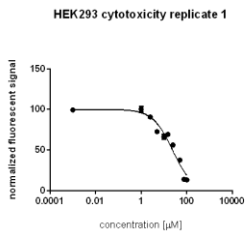
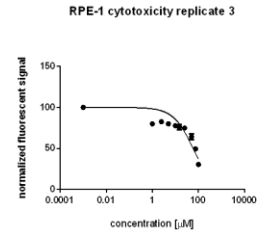
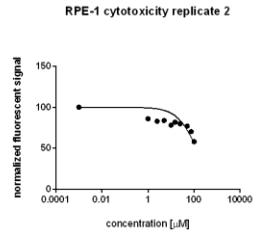
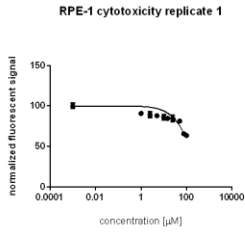
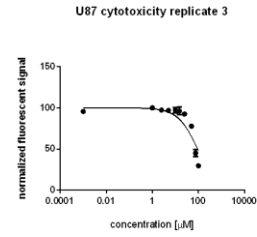
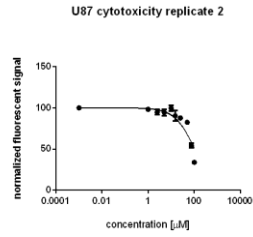
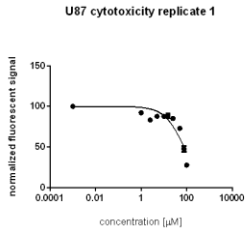


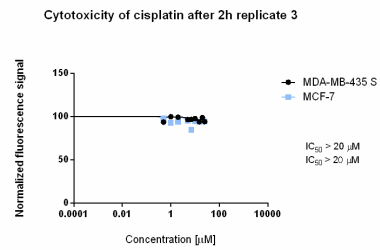
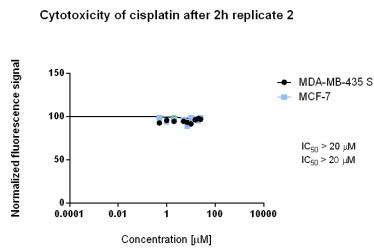
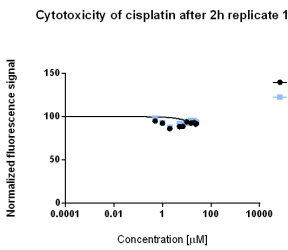
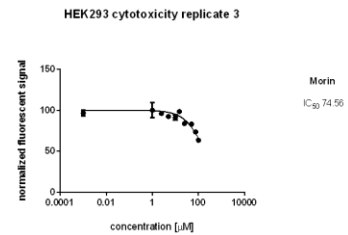
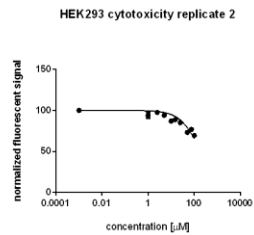
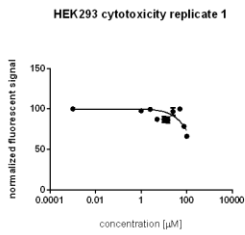
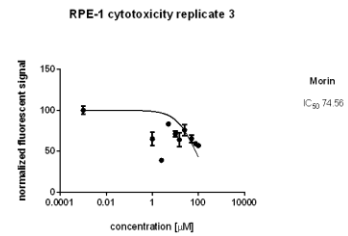
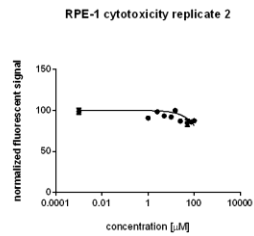
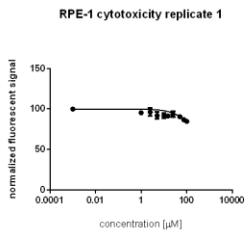
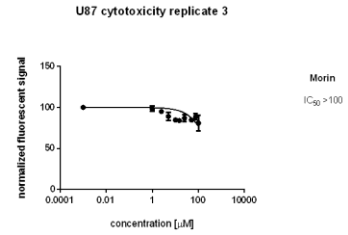
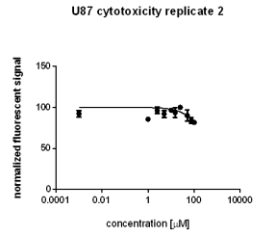
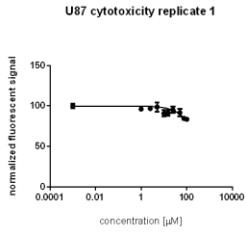
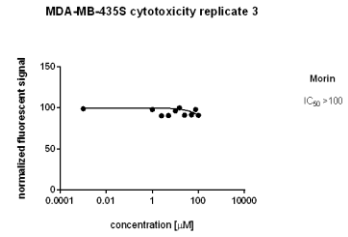
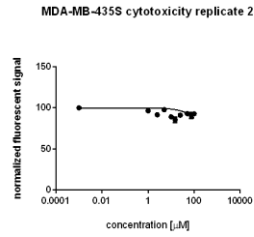
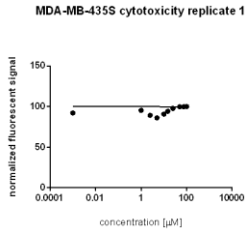




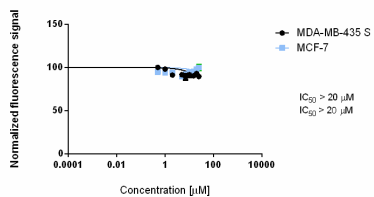




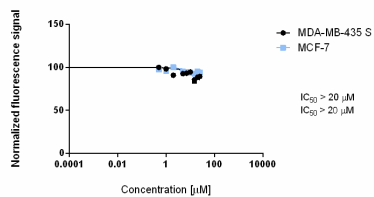




Cytotoxicity of [Ru(DIP)₂(gen)](PF₆) after 2h replicate 1



Cytotoxicity of [Ru(DIP)₂(gen)](PF₆) after 2h replicate 2



Cytotoxicity of [Ru(DIP)₂(gen)](PF₆) after 2h replicate 3

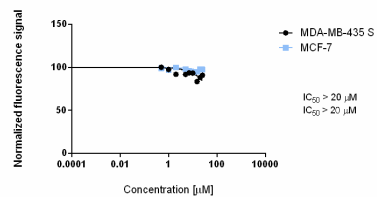


Figure S15. Oxygen consumption rates and different respiration parameters in MDA-MB-435S cells alone or after treatment with various test compounds.

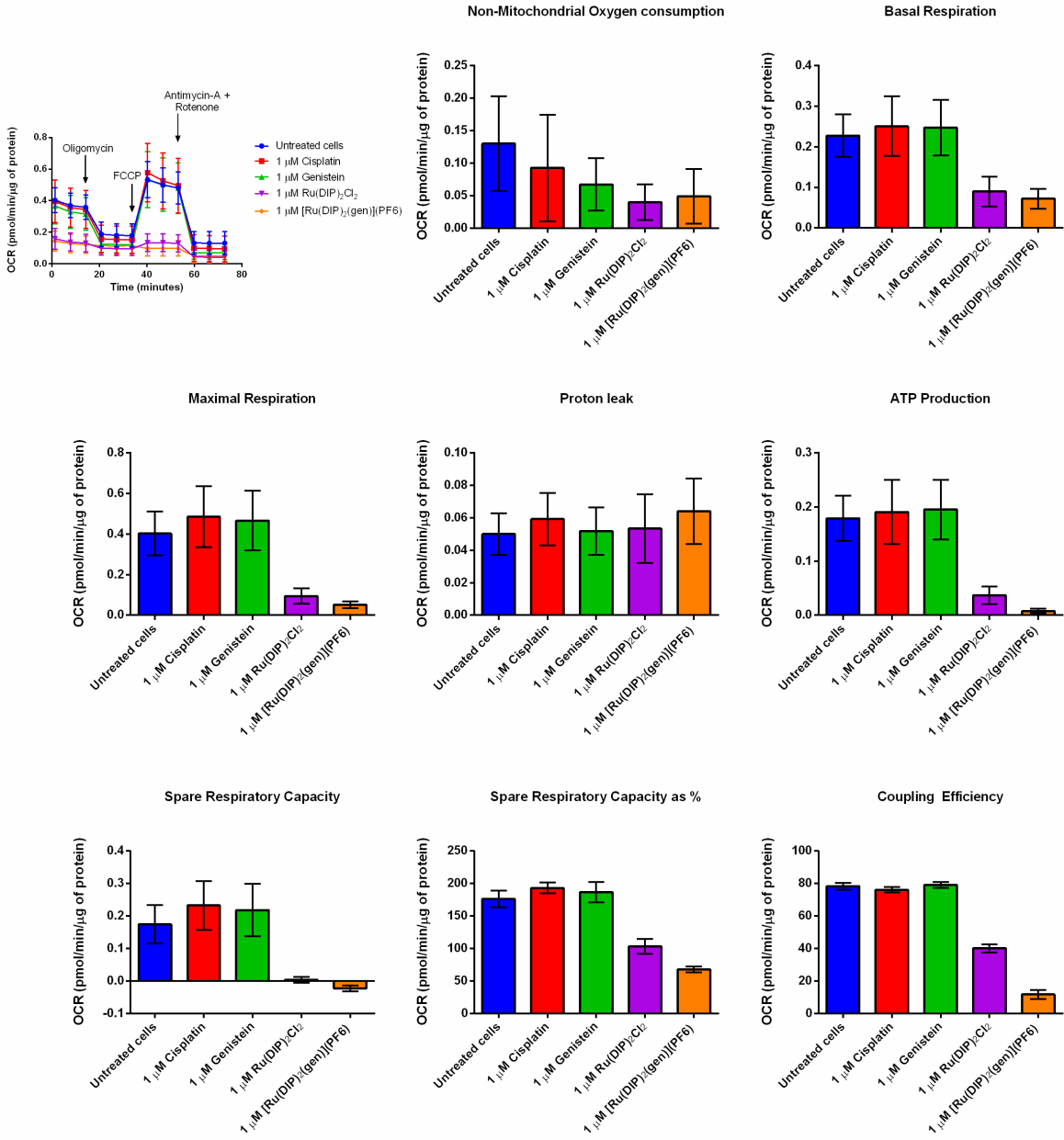
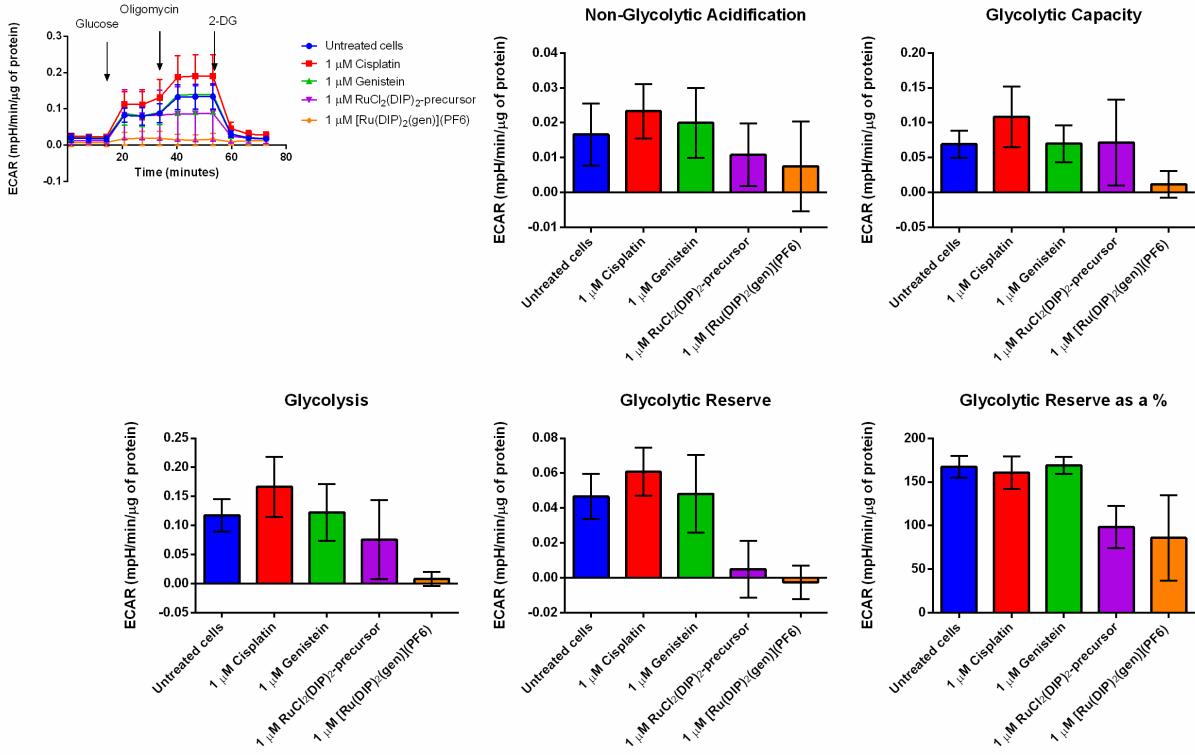


Figure S16. Extracellular acidification rate and different parameters during glycolysis in MDA-MB-435S cells alone or after treatment with various test compounds.



Chapter 11- Conclusions

As discussed in this PhD thesis, Ru(II) polypyridyl complexes are promising PDT PSs and chemotherapeutic agents. Their physico-chemical properties, which include a strong absorption in the visible light, tuneable photophysics and multiple stable oxidation states, make them interesting candidates. Surprisingly however, there are few of studies on Ru(II) polypyridyl complexes which have been looked at from a biological point of view. TLD-1433 (a PS from the McFarland group), KP-1019, IT-139 (formerly NKP-1339) and NAMI-A are Ru complexes that have been deeply characterized and reached clinical trials as anticancer agents.

This thesis has focused on the modes of action of Ru(II) polypyridyl complexes as photodynamic therapy photosensitizers as well as chemotherapeutic agents. Each chapter has described the chemical and biological evaluation of complexes prepared by both our group, and collaborators.

Firstly, Chapters 1-6 are dedicated to the applications of Ru(II) polypyridyl complexes as photosensitizers for photodynamic therapy. The metal complexes were designed to overcome some of the main drawbacks of currently used PSs. The first main objective was to overcome the lack of selectivity of PSs towards cancerous cells. Essential nutrients such as cobalamin (vitamin B₁₂) or nanobodies that are selectively binding to overexpressed receptors on the surface of cancerous cells (Epidermal Growth Factor Receptor- EGFR) were used in this work as targeting moieties. Although the conjugates obtained with vitamin B₁₂ demonstrated higher water solubility than the complex itself, they did not show any phototoxic effect. It could not be precisely determined if this result was due to a low uptake of the compound into the cells or a lack of activity in the cellular environment. In contrast, the novel nanobody-Ru (II) complex conjugate was able to specifically accumulate inside the cell line, which overexpressed the

EGFR on its surface. Unfortunately, ROS production in the cells during light exposure was not high, and no phototoxic effect could be observed. Both studies highlight the difficulty in bringing selective metal-based PDT PSs to cancerous cells that will exert their action efficiently in a cellular environment.

Next, we focused our attention on Ru complexes with 2,2':6', 2''-terpyridine (terpy) coordinating ligands. A systematic investigation into the series of complexes prepared showed that the majority of the compounds had no cytotoxic effect both in the dark, as well as upon light irradiation. However, one of the complexes was found to have a dark (photo-)cytotoxicity in the micromolar range. However, irradiation at 480 nm seems to have a negligible effect. This is probably caused by the very short excited state lifetime of this complex. Overall, this study demonstrates that small structural changes are able to significantly influence the effect that a compound has on a cell. Unfortunately, it also shows that these kinds of complexes are not particularly interesting as PSs for PDT.

Later, a series of Ru(II) polypyridyl complexes, which were specifically designed to have a substantial spectral red shift absorption, was presented. Currently, the PSs used in the clinic usually use UV-A, or blue light to obtain a PDT effect. Unfortunately, this approach, although good for example in the treatment of bladder cancer, does not allow for the treatment of deep-seated or large tumours. With the help of DFT calculations, a promising complex was unveiled. It is characterized by a phototoxicity in the very low micromolar-to-nanomolar range at the clinically relevant 595 nm, in monolayer cells as well as in 3D multicellular tumour spheroids. Additionally, it localises in the cytoplasm of cells and, upon irradiation at 595 nm, this complex led to the disturbance of mitochondrial respiration and the glycolysis process in monolayer cells. This outcome confirms the utility of DFT studies in the design of new metal-based PDT PSs. *In vivo* studies with this complex are scheduled for the near future.

Following studies focused on improving the low cellular uptake of Ru(II)-containing photosensitizers by preparing a series of nanoparticles containing a non-phototoxic Ru(II) polypyridyl complex (**RuOH**) using a drug-initiated ring-opening polymerization of lactide. As anticipated, the nanoparticles were found to have an enhanced cellular uptake (as shown by confocal microscopy and ICP-MS), leading to an improved phototoxic effect. This uncomplicated strategy can be expanded and applied to a broad range of ruthenium complexes. This opens up new avenues in PDT treatments, in which patients could be treated over several days using a single injection.

Chemotherapy is still one of the leading therapies against cancer. Severe side effects and occurring resistance connected with current treatments are the reasons why there is a search for novel anticancer (metal-based) drug candidates. Among them, Ru(II) polypyridyl complexes are an interesting class of compounds. Chapters 7-10 describe a novel class of Ru(II) complexes that were generated as potential anticancer agents for chemotherapy, by coordination of different dioxo ligands to a **Ru(DIP)₂Cl** core.

Firstly, a complex with a semiquinonate ligand was described (**Ru-sq**). A set of experimental evidence including X-ray crystal structure, electrochemical and EPR studies determined the oxidation state of the ligand when bound to the metal core. An in-depth biological investigation revealed that the cytotoxicity of the complex in monolayer cell cultures, as well as in Multi Cellular Tumour Spheroids (MCTS), was higher than for cisplatin. Additionally, impressive spheroid growth inhibition was observed. Further analysis pointed out apoptosis as the main cause of cell death in treated cells. The complex was found to preferentially localise in the nucleus, and bind to DNA, suggesting a possible mode of action related to DNA damage, and/or the prevention of replication as well as transcription processes. Furthermore, disruption of the mitochondrial membrane potential as well as mitochondrial function were observed in treated cells, indicating that **Ru-sq** has more than one mode of action. Preliminary *in vivo* studies were

also performed in two mouse models (syngeneic tumour growing in immunocompetent mice as well as human tumour growing in immunodeficient animals) *via* intraperitoneal administration. **Ru-sq** reduced the growth of the tumour and prolonged survival of the tumour bearing mice in both groups. Unfortunately, solubility issues excluded further *in vivo* studies. A new formulation of the complex is currently prepared that will be used in future studies.

A structurally similar compound to **Ru-sq** was then prepared. Instead of a semiquinonate ligand, this complex bears a maltol moiety. Maltol-taste enhancer is approved by FDA. In addition, the presence of a maltol moiety is an advantage for a complex, whose mode of action does not exclude a ligand exchange mechanism. Similarly to **Ru-sq**, **Ru-mal** was found to be cytotoxic in monolayer cell cultures as well as in MCTS. The values obtained were comparable with doxorubicin and much lower than for cisplatin. MCTS growth inhibition was also observed, even after 13 days post treatment. Contrary to **Ru-sq**, **Ru-mal** was taken up more efficiently by cells and accumulated mostly in the cytoplasm and mitochondria. DNA binding was confirmed by metalation studies. Additionally, the complex had an impact on mitochondrial membrane potential.

A series of six complexes was then prepared during a structure-activity relationship (SAR) study. A range of derivatives were prepared with catecholate-like dioxo ligands (with electro donating or electro withdrawing groups). Analysis of the physico-chemical properties and biological activity of these complexes led to the conclusion that complexes with electro withdrawing groups and neutral charge, are far less cytotoxic than the ones bearing electro donating groups and a positive charge. The most promising complex of the series was further evaluated. Its cytotoxicity in the nanomolar range and activity in MCTS (cytotoxicity and growth inhibition) confirmed its potential as a chemotherapeutic drug candidate. Similarly to the previously described complexes, the compound also targeted DNA and mitochondria.

Despite solubility problems, the use of a formulation with polysorbate 80 allowed some preliminary *in vivo* biodistribution results to be obtained.

Lastly, a series of complexes with the same **Ru(DIP)₂Cl** core and flavonoids as *O,O*-chelating ligands was prepared and characterised. Flavonoids, which are natural products, are broadly studied in anticancer research. All synthesized complexes were tested against different cancerous and non-cancerous cell lines. The complex bearing genistein as its ligand was found to be the most active of the series. Its cellular uptake was found to occur through a passive mechanism and its effect on cellular metabolism was studied. Surprisingly, the genistein complex was found to inhibit not only the mitochondrial respiration like its precursor but also the cytosolic process of glycolysis. This result suggests that the addition of a flavonoid moiety changes the behaviour of the complex in living cells and allows for a more complex mode of action.

Overall, this thesis has focused on the chemical and biological evaluation of Ru(II) polypyridyl complexes as photodynamic therapy photosensitizers and chemotherapy drug candidates. The complexes were designed to overcome the known drawbacks of current treatments (e.g., lack of selectivity against cancerous cells, poor cellular uptake, etc). The Ru(II) complexes with applications as photodynamic therapy photosensitizers showed impressive potential. Nevertheless, there are still some difficulties, like selectively targeting metal-based complexes to cancerous cells and the presence of dark cytotoxicity. The use of DFT studies in the design of new metal-based PDT PSs might help to overcome these issues. Furthermore, this thesis presented also Ru(II) polypyridyl complexes that were design to be used as chemotherapeutic agents. This novel class of complexes with their multiple cellular targets (i.e., DNA and mitochondria), outstanding cytotoxicity and promising preliminary *in vivo* studies makes them interesting compounds for clinical applications as chemotherapeutic agents against cancer.

RÉSUMÉ

Cette thèse de doctorat a pour dessain d'évaluer d'un point de vue chimique, mais surtout biologique les complexes polypyridyle Ru (II). Ces complexes métalliques peuvent être utilisés comme photosensibilisateurs (PS) pour la thérapie photodynamique (PDT), ou encore comme agents chimiothérapeutiques dans le traitement du cancer. La PDT est un traitement alternatif ou complémentaire à la chirurgie, la chimiothérapie ou la radiothérapie. Ses nombreux avantages lui confèrent un intérêt dans le traitement actuel du cancer. Son contrôle spatial et temporel est particulièrement intéressant, ce qui conduit à cibler les tumeurs tout en préservant les tissus sains. De plus, les résistances à répétition et les effets secondaires graves provoqués par la chimiothérapie incitent le monde scientifique à rechercher de nouveaux médicaments candidats anticancéreux. Les complexes de ruthénium sont l'un des groupes les plus prometteurs de médicaments candidats à base de métaux (comme chimiothérapeutiques ou PS) en raison de leurs multiples états d'oxydation stables. Cette thèse décrit un aperçu des modes d'action connus des complexes polypyridyle Ru (II) comme PS pour la PDT et introduit de nouveaux complexes, qui peuvent être utilisés pour des traitements PDT réguliers et ciblés. En outre, cette thèse se concentre également sur la caractérisation d'une nouvelle classe de complexes Ru générés comme agents anticancéreux potentiels pour la chimiothérapie, par coordination de différents dioxoligands au noyau métallique.

MOTS CLÉS

Thérapie photodynamique, chimiothérapie, ruthénium, cancer

ABSTRACT

This PhD thesis aims to evaluate chemically and, more importantly, biologically Ru(II) polypyridyl complexes. These metal complexes can be used as photodynamic therapy (PDT) photosensitizers (PS) or as chemotherapeutic agents in cancer treatment. PDT is an alternative or complimentary treatment to surgery, chemotherapy or radiotherapy. Currently it draws a lot of attention due to its advantages. Especially interesting is its spatial and temporal control, which leads to targeting tumours while preserving healthy tissue. Additionally, repeatedly occurring resistances and severe side effects brought by chemotherapy urges the scientific world to search for new anticancer drug candidates. Ruthenium complexes are one of the most promising groups of metal-based drug candidates (as chemotherapeutics or PSs) owing to their multiple stable oxidation states, etc. This thesis describes an overview of the known modes of action of Ru(II) polypyridyl complexes as PDT PS and introduces new complexes that can be used in regular as well as targeted PDT. Additionally, this thesis also focuses on the characterisation of novel class of Ru complexes that were generated as potential anticancer agents for chemotherapy by coordination of different dioxoligands to the metal core.

KEYWORDS

Photodynamic therapy, chemotherapy, ruthenium, cancer